



IGARSS'97

1997 International Geoscience and
Remote Sensing Symposium

03-08 August 1997

Singapore International Convention & Exhibition Centre • Singapore

Remote Sensing -- A Scientific Vision for
Sustainable Development

DISTRIBUTION STATEMENT A

Approved for public release
Distribution Unlimited

19970801 017

Volume IV

IEEE Catalog Number: 97CH36042
Library of Congress Number: 97-70575

QUANTITY INSPECTED 1

1997 IEEE INTERNATIONAL GEOSCIENCE AND REMOTE SENSING SYMPOSIUM

Editor: Tammy I. Stein
Production: IEEE Publications

Copyright and Reprint Permissions: Abstracting is permitted with credit to the source. Libraries are permitted to photocopy beyond the limits of U.S. copyright law for private use of patrons those articles in this volume that carry a code at the bottom of the first page, provided the per-copy fee indicated in the code is paid through the Copyright Clearance Center, 222 Rosewood Drive, Danvers, MA 01923. For other copying, reprint, or republication permission, write to the IEEE Copyright Manager, IEEE Service Center, 445 Hoes Lane, Piscataway, NJ 08855-1331. All rights reserved. Copyright © 1997 by The Institute of Electrical and Electronics Engineers, Inc.

IEEE Catalog Number: 97CH36042 (softbound)
97CB36042 (casebound)

Library of Congress Number : 97-70575

ISBN Softbound: 0-7803-3836-7
ISBN Casebound: 0-7803-3837-5
ISBN Microfiche: 0-7803-3838-3
CD-ROM: 0-7803-3839-1
ISSN: N/A

Additional copies of this publication are available from the following source:

IEEE Operations Center
P. O. Box 1331
445 Hoes Lane
Piscataway, NJ 08855-1331 USA

1-800-678-IEEE
1-908-981-1393
1-908-981-9667 (FAX)
833-233 (Telex)
email: customer.services@ieee.org



IGARSS'97

1997 International Geoscience and
Remote Sensing Symposium

03-08 August 1997

Sponsors



IEEE

IEEE Geoscience and Remote Sensing Society



Centre for Remote Imaging, Sensing and Processing
The National University of Singapore



National Aeronautics and Space Administration (NASA)



National Oceanic and Atmospheric Administration (NOAA)



Office of Naval Research (ONR)



International Union of Radio Science (URSI) ... Technical Sponsor

ORGANIZING COMMITTEE

Hock Lim
General Chairman

Tat Soon Yeo
 Janet Nichol
 Jian Kang Wu
 Dayalan Kasilingam
Technical Co-Chairmen

Leong Keong Kwoh
Finance Chairman

Karen Wong
Publicity Chairman

Choong Weng Mak
 Ngi Kun Chng
Exhibits Co-Chairmen

Jonnovan Hong
 Chiat Keng Yew
 Fen He
*Local Arrangements
 Co-Chairmen*

Tammy Stein
*GRSS
 Director of Conferences
 and Information Services*

TECHNICAL COMMITTEE

Alpers, Werner
 Aschbacher, Josef
 Bechacq, Yves
 Blanchard, Andrew J.
 Boerner, Wolfgang-Martin
 Cracknell, Arthur
 Chan, Philip
 Chappelle, Emmett W.
 Chen, A.J.
 Choi, Soon Dal
 Chua, Poh Kian
 Chuah, Hean Teik
 Cumming, Ian
 D'Aranjo, Wesley Gerard
 Duchossois, G.
 Durana, Jim
 Forster, Bruce
 Friedman, Ami Ben-Shalom
 Fung, Adrian
 Gasiewski, Albin J.
 Gatlin, James A.
 Goodenough, David
 Guo, Huadong
 Gupta, Avijit
 Hallikainen, Martti T.
 Hardesty, R. Michael
 Ho, Anthony
 Hong, Ye
 Ishimaru, Akira
 Jackson, Thomas J.
 Kam, Suan-Pheng
 Keydel, Wolfgang
 Khazenie, Nahid
 Khorram, Siamak
 Kong, J.A.
 Kuga, Yasuo
 Lau, William K.M.
 Le Toan, Thuy

Lee, Jong-Sen
 Lewis, Anthony J.
 Liew, Soo Chin
 Lin, I-I
 Lu, Yi Hui
 Lui, Pao Chuen
 Luther, Charles
 Mariton, Michel
 Massonet, Didier
 Milne, Anthony K.
 Moon, Wooil M.
 Murai, Shunji
 Nik Nasruddin Mahmood
 Njoku, Eni
 Ong, Jin Teong
 Pampaloni, Paolo
 Prati, C.
 Quegan, Shaun
 Quek, Gim Pew
 Rais, Jacob
 Reagan, John
 Rees, W.G.
 Salomonson, Vincent
 Schumann, Robert
 Shimoda, Haruhisa
 Shu, Peter K.
 Sieber, Alois
 Singh, Kuldip
 Su, Guanng
 Takagi, Mikio
 Tan, Bernard T.G.
 Tilton, James C.
 Tomiyasu, Kiyo
 Tsang, Leung
 Ulaby, Fawwaz
 Wiesbeck, Werner
 Winebrenner, Dale
 Zhang, Cheng Bo



IGARSS'97

1997 International Geoscience and
Remote Sensing Symposium

03-08 August 1997

Table of Contents

IGARSS'97 DIGEST VOLUME I

Interactive Area 1: Aerosols

Aerosol Profile Variations Retrieval Through Kernel Functions in the Oxygen Absorption Band at 762 nm	3
<i>Gabella, M., A. Leone, and G. Perona</i>	
Atmospheric Correction of Landsat-TM Images Using Radiative Transfer Code with Image-Extracted Aerosol Optical Depth	NA
<i>Kwon, T.Y., K.S. Ryu, S.N. Oh, and H.G. Lee</i>	
Seasonality of Ozone Profile at Reunion Island: The Role of Biomass Burning and of Transport	6
<i>Randriambelo, T., S. Baldy and M. Bessafi</i>	
Preliminary Aerosols Observations by Lidar Technique at Reunion Island (20.8° S, 55.5°E)	NA
<i>Riviere, E., and J. Leveau</i>	
Interpretation of Ground-Based Measurements of Atmospheric Aerosols	9
<i>Sano, I., S. Mukai, M. Yasumoto, K. Masuda, M. Sasaki and H. Ishida</i>	
Lidar Investigation of Time and Spatial Distribution of the Atmospheric Aerosol in Mountain Valley	NA
<i>Savov, P., and I. Kolev</i>	

Interactive Area 2: Applications of Radar and SAR Techniques

HF Radar Detection and Tracking of Oil Spills in the Marine Environment	NA
<i>Anderson, S.J.</i>	
High Spatial Resolution Radar Altimetry for Global Earth Topography Mapping	15
<i>Angino, G., F. Impagnatiello and C. Zelli</i>	
Radar-Radiometer Images of the Zone of Underwater Gas Jet Activity	NA
<i>Arakelian, A.K.</i>	
RA-2 Radar Altimeter: Instrument EM Model Performance Results	18
<i>Zelli, C., F. Provvedi, F. Buscaglione and R. Croci</i>	
Ultrawideband Radar Tolerance to Antennas Phase Distortion	NA
<i>Cherniakov, M., and L. Donskoi</i>	
Combined Radar-Radiometer System for the Earth Surface Remote Sensing and Efficiency of Radar-Radiothermal Images in Environmental Monitoring	NA
<i>Hambaryan, A.K., and A.K. Arakelian</i>	
Non-Spherical Hydrometeor Signature in Melting Layer Obtained with Ku-Band Multi-Parameter Radar	NA
<i>Hanado, H., H. Hiroaki, and H. Kumagai</i>	
Relief Restitution by Radargrammetry Using RADARSAT Images: Example in French West Indies	21
<i>Marinelli, L., O. Ferger, L. Laurore and V. Poujade</i>	
SARSCAT-A Ground-Based Scattermeter for Space-Borne SAR Applications	24
<i>Wu, J., and B. Sun</i>	

Interactive Area 3: Applications of Remote Sensing

Artificial Recharge Studies Through Remote Sensing in Central Part of Tamil Nadu, India <i>Anbazhagan, S., S.M. Ramasamy and J.M. Edwin</i>	29
Satellite Remote Sensing of Arctic Marine Mammals Sea-Ice Habitats <i>Belchansky, G.I., I.N. Mordvintsev, V.G. Petrosian, W.G. Garner and D.C. Douglas</i>	NA
Global Survey of Jet Contrails Using AVHRR Data: Spatial Distributions and Optical Property Retrievals <i>Kliche, D.V., J. Chou, J.M. Weiss, S.A. Christopher, R.M. Welch, T. Berendes and K.S. Kuo</i>	32
Reception Condition of Optimization in the Case of Simulated by the Regression Models Earth Surface Parameters Estimation by Passive Remote Sensing <i>Kravchenko, V.F., V.K. Volosyuk and V.R. Tilinskii</i>	NA
Recent Observing System Experiments on the Impact of ERS Scatterometer Wind Data on Numerical Weather Simulations of Cold Surges <i>Lim, T.K., R. Zhang, I.I. Lin, D. Kasilingam and V.H.S. Khoo</i>	35
Coastline Detection with Polynomial Transforms and Markovian Segmentations <i>Moctezuma, M., B. Escalante, R. Mendez, J.R. Lopez, and F. Garcia</i>	38
Applications of ERS SAR-Interferometry in Hydrologic Modelling <i>Riegler, G., K.P. Papathanassiou and W. Mauser</i>	NA
The Concept of Russian Fisheries Industry Service for Satellite Monitoring of Fishing Areas in Global Ocean <i>Romanov, A., A. Rodin and V. Mishkin</i>	41
The Probability Description of Diurnal Solar Radiation Absorption in the Atmosphere Within Different Regions <i>Rublev, A.N., A.N. Trotsenko and N.E. Chubarova</i>	NA
The Estimate of Atmospheric Solar Radiation Absorption Over the Moscow Area Using Data the AVHRR/NOAA <i>Rublev, A.N., A.N. Trotsenko, N.E. Chubarova and P.Y. Romanov</i>	NA
Estimating Potential Mosquito Breeding Sites and Malaria Using Satellite Remote Sensing Techniques <i>Saarnak, C.F., T.T. Nielsen and S. Lindsay</i>	NA
Estimation of Precipitable Water from GSM-5 Split Window Channels <i>Suh, A.S., and S.H. Sohn</i>	NA
Land-Use Classification Using Temporal SAR-Images <i>Torma, M., and J. Koskinen</i>	44
Using RADARSAT-1 for Fisheries Enforcement Operations <i>Wahl, T.</i>	47
The Detection of the Great Wall Using SIR-C Data in North-Western China <i>Xinqiao, L., G. Huadong and S. Yun</i>	50

Interactive Area 4: Atmospheric Sounding

Water Vapor Profile Retrieval Possibilities by Low Angle GPS Data <i>Gaikovitch, K.P., and M.B. Tchernjaeva</i>	NA
Application of Kitt Peak Solar Flux Atlas for Studying Air Pollution in Tokyo Area <i>Jianguo, N., D. Tanaka, X. Yanquen, Y. Sakurada, H. Kuze and N. Takeuchi</i>	55

Atmospheric Temperature Profile Retrieval Using Multivariate Nonlinear Regression	58
<i>Miao, J., K. Zhao and G. Heygster</i>	
Retrieval of Total Water Vapor in Polar Regions Using SSM/T2 Channels	61
<i>Miao, J., N. Schlueter and G. Heygster</i>	
TOVS and ATOVS Retrievals for Local Use	NA
<i>Rochard, G.</i>	
Interferometric Sounding of the Atmosphere for Meteorology	NA
<i>Wilson, S.H.S., N. Atkinson, P.J. Rayer, J. Smith and D.R. Pick</i>	
Simulation on Determination of Cirrus Cloud Optical and Microphysical Properties from Satellite IR Measurements: New Channel Approach	NA
<i>Xu, L., G. Zhang, and J. Ding</i>	
<u>Interactive Area 5: Clouds and Precipitation</u>	
Radiance Thresholds and Texture Parameters for Antarctic Surface Classification	67
<i>Baraldi, A., G. Meloni, and F. Parmiggiani</i>	
Dual-Frequency and Multiparameter Radar Techniques for Rain/Snow Measurements	NA
<i>Horie, H., R. Meneghini, H. Kumagai, and N. Takahashi</i>	
A Rainfall Estimation with the GMS-5 Infrared Split-Window and Water Vapour Measurements	NA
<i>Kurino, T.</i>	
Radar and Microwave Radiometer Sensing of Typhoon Ryan	70
<i>Mitnik, M.L., L.M. Mitnik and M.K. Hsu</i>	
Cloud and Sea Ice Detection Using NOAA/AVHRR Data	73
<i>Muramoto, K., H. Saito, K. Matsuura and T. Yamanouchi</i>	
Lidar Observation of Multiple Scattering in Fogs and Clouds in the Low Atmosphere	NA
<i>Tatarov, B., B. Kaprielov, V. Naboko, A. Blagov and I. Kolev</i>	
<u>Interactive Area 6: Crops, Soils and Forestry</u>	
Technology of the AVHRR Data Processing and Their Application for the Solution of Agronmeteorological Problems	NA
<i>Arushanov, M.L., E.N. Alexeev, and I.N. Kanash</i>	
Improved Fourier Modelling of Soil Temperature Using the Fast Fourier Transform Algorithm	79
<i>Axelsson, S.R.J.</i>	
Modeling Bidirectional Radiance Distribution Functions of Conifer Canopies Using 3-D Graphics	84
<i>Burnett, C.N., G.J. Hay, K.O. Niemann and D.G. Goodenough</i>	
Forest Cartography of Spain Based on the Classification of NOAA-AVHRR Multitemporal Images	87
<i>Gonzalez-Alonso, F., and J.L. Casanova Roque</i>	
Remote Sensing for Estimating Chlorophyll Amount in Rice Canopies	89
<i>Hong, S., S. Rim, J. Lee, and J. Kim</i>	

"NA" indicates not available at time of printing.

Estimation of Leaf Area Index and Total Dry Matter of Rice Canopy by Using Spectral Reflectance Field <i>Lee, J.T., C.W. Lee, S.Y. Hong and M.E. Park</i>	92
Spectral Unmixing and Mapping of Surface Features Related to Soil Erosion <i>Metternicht, G.I., and A. Fermont</i>	95
Simulation of Forest BRDF with the Coupling of High and Medium Resolution Reflectance Models <i>Pinel, V., and J.P. Gastellu-Etcheberry</i>	NA
Forest Decline Dynamics Around the Severonickel Smelter in the Kola Peninsula, Arctic Russia: Remote Sensing and Mathematical Modelling <i>Rigina, O., O. Hagner and H. Olsson</i>	NA
Ku-Band SAR Data for Bare Soil Moisture Retrieval Over Agricultural Fields <i>Sano, E.E., M.S. Moran, A.R. Huete, and T. Miura</i>	98
Airborne Remote Sensing to Support Precision Farming <i>Wehrhan, M.J.G., and T.M. Selige</i>	101
Amazon Rainforest Visualisation/Classification by Orbiting Radar, Enabled by Supercomputers (ARVORES) <i>Siqueira, P., B. Chapman, S. Saatchi, and T. Freeman</i>	104
Utilization of Coherence Information from JERS-1/SAR for Forest Type Discrimination <i>Takeuchi, S., and C. Yonezawa</i>	107
Monitoring Changes in the Tropical Moist Forests of Continental Southeast Asia <i>Wagner, T.W., and K. Nualchawee</i>	NA
<u>Interactive Area 7: Damage Assessment and Management</u>	
A Flexible Environment for Earthquake Rapid Damage Detection and Assessment <i>Casciati, F., P. Gamba, F. Giorgi, A. Marazzi and A. Mecocci</i>	113
Remote Sensing of Global Fire Patterns, Aerosol Optical Thickness and Carbon Monoxide During April 1994 <i>Christopher, S.A., M. Wang, D.V. Kliche, R.M. Welch, S. Nolf, and V.S. Connors</i>	116
Use of SIR-C/X-SAR to Monitor Environmental Damages of the 1991 Gulf War in Kuwait <i>Dobson, M.C., A.Y. Kwarteng and F.T. Ulaby</i>	119
Modelling of Human Dimension on Soil Erosion Processes for Remote Sensing Applications <i>Gaillard, C., F. Zagolski and F. Bonn</i>	122
Moisture and Temperature Condition of Lahar-Affected Area Around Mt. Pinatubo <i>Inanaga, A., M. Watanabe, J.D. Rondal, M. Yoshida, T. Ohkura and A.G. Micoso</i>	125
Evaluation of RADARSAT Image for Landslide Susceptibility Mapping: Application in Bolivia <i>Peloquin, S., Q. Hugh, J. Gwyn, D. Haboudane, R. Mendez and L.A. Rivard</i>	128
The Use of ERS SAR Interferometry for Planning and Monitoring of Siberian Pipeline Tracks <i>Streck, C., and U. Wegmuller</i>	NA

Interactive Area 8: Detection of Buried Objects and Voids

Near Field SAR and Noisy Target Identifications	<i>Afifi, M.S., and A.G. Al-Ghamdi</i>	133
Reconstruction of a 3-Dimensional High-Contrast Penetrable Object in the Pulsed Time Domain by Using the Genetic Algorithm	<i>Choi, H.K., S.K. Park and J.W. Ra</i>	136
The Properties of GPR Antennas Near Lossy Media Calculated by FD-TD Method	<i>Guangyou, F., and Z. Zhongzhi</i>	NA
Imaging Layered Subsurface Using a Multi-Frequency, Coil-Type Sensor	<i>He, X., and C. Liu</i>	NA
Imaging the Shape of a Two-Dimensional Cylindrical Void Near a Plane Surface by Electromagnetic Wave Scattering	<i>Liu, L., and L. Xiao</i>	NA
Generalized Detection Algorithm for Signals with Stochastic Parameters	<i>Tuzlukov, V.P.</i>	139
Applications of Ground Penetrating Radar Forward Calculus with Finite Offset for Point Scattering	<i>Wang, H.</i>	142
Derivative Seismic Processing Method for GPR Data	<i>Yu, H., and X. Ying</i>	145
Detection of the Man-Made Objects (PIPES) with Electromagnetic Induction	<i>Zhu, K., T. Sakurai and F. Tohyama</i>	NA

Interactive Area 9: Detection and Monitoring of Ships and Ocean Pollution

Sea Surface Imaging at Millimeterwave Frequencies	<i>Boehmsdorff, S., and H. Essen</i>	NA
Wind Data in Operational Oil Spill Detection Using ERS SAR	<i>Espedal, H.A., and T. Hamre</i>	NA
Ship and Ship Wake Detection in the ERS SAR Imagery Using Computer-Based Algorithm	<i>Lin, I.I., L.K. Kwok, Y.C. Lin and V. Khoo</i>	151
Oil Spills Detection Using ALMAZ-1 and ERS-1 SAR	<i>Litovchenko, K.T., and A.Y. Ivanov</i>	NA
Adapting Operations of the Radarsat SAR to Enhance Ship Monitoring	<i>Luscombe, A.P., and L. Lightstone</i>	154
Incorporation of Prior Knowledge in Automatic Classification of Oil Spills in ERS SAR Images	<i>Schistad Solberg, A.H., and E. Volden</i>	157
Phytoplankton's Fluorescence-Possible Tool for Remote Detection of the Radioactive Pollution in the Ocean	<i>Tsipenyuk, D. Yu.</i>	NA
Automatic Detection of Ship Tracks in Satellite Imagery	<i>Weiss, J.M., R. Luo, and R.M. Welch</i>	160

"NA" indicates not available at time of printing.

Interactive Area 10: Emission and Scattering

Rainfall Effect on Microwave Thermal Emission Characteristics of Sea Surface <i>Bulatov, M.G., V.G. Pungin and E.I. Skvortsov</i>	NA
Studies of BRDF in Conifer and Deciduous Boreal Forests Using the 4-Scale Model and Airborne POLDER and Ground-Based PARABOLA Measurements <i>Chen, J.M., S.G. Leblanc, J. Cihlar, P. Bicheron, M. Leroy, D. Deering and T. Eck</i>	165
Six Years of Microwave Radiative Transfer Validation Using Airborne Radiometers: The Main Results <i>English, S.J., T.J. Hewison, and P.J. Rayer</i>	NA
Feasability to Measuring Directly Distribution of the Emissivited of Territorial Surface on the Remote Sensing Platforms <i>Zhang, R., X. Sun and Z. Zhu</i>	168
Third Order Microwave Radiative Transfer Equation Solution with SSM/I Data <i>Givri, J.R., and E.A. Decamps</i>	NA
A Comparison of Mixture Modeling Algorithms and Their Applicability to the MODIS Data <i>Kalluri, S.N.V., C. Huang, S. Mathieu-Marni, J.R.G. Townshend, K. Yang, R. Chellappa and A. Fleig</i>	171
Retrieval of Bidirectional Reflectance Distribution Function (BRDF) at Continental Scales from AVHRR Data Using High Performance Computing <i>Kalluri, S.N.V., Z. Zhang, S. Liang, J. Jaja, and J.R.G. Townshend</i>	174
Radiative Transfer Analytical Solutions for Remote Sensing Through the Atmosphere <i>Katkovsky, L. V.</i>	NA
RCS Computation of Dielectric-Coated Bodies Using the Conjugate Gradient Method and the Fast Fourier Transform <i>Neo, C.P., M.S. Leong, L.W. Li and T.S. Yeo</i>	NA
Study of the Polarization Behavior of Complex Natural and Man-Made Clutter at Middle and Grazing Angles <i>Onstott, R.G.</i>	177
Sensitivity Analysis for a SAR Backscatter Model <i>Slatton, K.C., M.M. Crawford, J.C. Gibeaut and R.O. Gutierrez</i>	NA
Determination of the Earth's Emissivity for Use in Studies for Global Climate Change <i>Stephenson-Hawk, D., K. Stephens and A. Shah</i>	180
A New Approach to the Problem of Wave Scattering in Random Media and Its Application to Evaluating the Effective Permittivity of a Random Medium <i>Tateiba, M.</i>	184
Algorithms for Retrieving Land Surface Temperatures and Emissivities from Satellite Radiative Measurements <i>Zhao, G., and H.Q. Wang</i>	NA

Interactive Area 11: Geology and Geomorphology

Influence of Neotectonic Movements on Exogenic Processes on the Territory of the Russian Plane <i>Bronguleyev, V.V.</i>	NA
Spectral and Geomorphometric Discrimination of Environmental Units: Application to the Geomorphological Processes of Land Degradation <i>Haboudane, D., F. Bonn, S. Peloquin, A. Royer, and S. Sommer</i>	189

Geo-Environmental Assessment of Landslide Hazards in the Sikkim Himalaya Utilising Remote Sensing Techniques for Sustainable Development in the Mountain Environment	NA
<i>Krishna, A.P.</i>	
Environmental Geoscientific Assessment for Sustainable Development Priorities in Sikkim Himalaya: An Integrated Remote Sensing Approach	NA
<i>Krishna, A.P., and Y.K. Rai</i>	
Balance and Restoration of Three Cross-Sections in Eastern Tethys-Himalayan Orogeny Belt in Southwest China	NA
<i>Qing, X.</i>	
Analysis of the Areal Vulcanism Zones of Klyuchevskoy Volcano Using SIR-C Data	NA
<i>Shkarin, V.E., V.V. Zaitsev and A.P. Khrenov</i>	
The Design of a Methodology for Volcanic Hazard Mapping Using GIS and Remote Sensing Techniques in the Bulusan Volcano Area, Bicol District, Phillippines	192
<i>Slob, S.</i>	
New Principles of Morphotectonic Mapping of Asia	NA
<i>Timofeev, D.A., and V.V. Bronguleyev</i>	
<u>Interactive Area 12: GIS</u>	
Geographical Information System (GIS) Based on National Base Maps of Iran at 1:100,000 by Satellite Images	NA
<i>Bushehri, S.N., and N. Khorsandian</i>	
Integration of GIS and Remote Sensing Techniques for EIA in Chilika Lake Region (India)	NA
<i>Das, T.K., O. Dikshit, and K.S. Bhatta</i>	
Desertification and Land Degradation Using High Resolution Satellite Data in the Nile Delta, Egypt	197
<i>El-Khattib, H.M., N.M. El-Mowelhi and A.A. El-Salam</i>	
Biodiversity Assessment Using GIS and RS Technology for Protected Area Management and Conservation in Xe Paine, Laos PDR	NA
<i>Kamal, G.M.</i>	
On Integrated Scheme for Vector/Raster-Based GIS's Utilization	200
<i>Kim, K.S., M.S. Kim and K. Lee</i>	
The Application of Rational Formula Based on Remote Sensing and Geographical Information Systems	NA
<i>Leu, C.</i>	
Precision Rectification of Airborne SAR Image	204
<i>Liao, M., and Z. Zhang</i>	
Contribution of Mathematical Morphology and Fuzzy Logic to the Detection of Spatial Change in an Urbanized Area: Towards a Greater Integration of Image and Geographical Information Systems	207
<i>Maupin, P., P. Le Quere, R. Desjardins, M.C. Mouchot, B. St-Onge and B. Solaiman</i>	
Correlation Between Malaria Incidence and Changes in Vegetation Cover Using Satellite Remote Sensing and GIS Techniques	NA
<i>Nualchawee, K., P. Singhasivanon, K. Thimasarn, D. Darasri, K. Linthicum, S. Suvannadabba, P.L. Rajbhandari, and R. Sithiprasasna</i>	
Application of Remote Sensing for Assessing the Habitat Structure of the Whooping Cranes in Nebraska, USA	NA
<i>Richert, A., S. Narumalani, S. Richert and K. Church</i>	

"NA" indicates not available at time of printing.

An Application of GIS Information and Remotely Sensed Data for Extraction of Landslide <i>Shikada, M., Y. Suzuki, T. Kusaka, S. Goto and Y. Kawata</i>	210
Accuracy Assessment of Elevation Data Obtained from Radarsat Stereo Images <i>Singh, K., O.K. Lim, L.K. Kwoh and H. Lim</i>	213
Parallel Ladex Spatial Index Mechanism <i>Xiao, W., and Y. Feng</i>	216
Spatial Information System Applications for Sustainable Development in Korea: Necessity, Possibility and Methodology <i>Xiu-wan, C., C. An, D. Shin, and S. Oh</i>	NA
GIS Modeling in Coastal Flooding Analysis: A Case Study in the Yellow River Delta, China <i>Yang, X.</i>	219
Software Development Project for the National Geographic Information System (NGIS) Initiative <i>Yang, Y.K., J.H. Lee and C.H. Ahn</i>	NA
Combination Between Remote Sensing and Ecosystem Observation Network in China <i>Zhang, Q., and R. Zhang</i>	222
<u>Interactive Area 13: Ground Penetrating Radar</u>	
Full-Wave 3D Modeling of Ground-Penetrating Radars by a Finite Element/Boundary Element-Hybrid Technique <i>Eibert, T.F., V. Hansen and N. Blindow</i>	227
Subsurface Remote Sensing with Electromagnetic Pulsed Beam <i>Kolchigin, N.N., S.N. Pivnenko and V.M. Lomakin</i>	NA
GPR Attenuation Tomography for Sensing Subsurface Contaminants <i>Liu, L.</i>	NA
Mineral Sands Deposits Investigation in Australia Using Subsurface Interface Radar (SIR) <i>Marschall, D.L., and R.A. Marschall</i>	NA
Scattering from Periodically Located Objects Embedded Near the Randomly Rough Surface of a Moist Soil <i>Timchenko, A.I., and V.P. Tishkovets</i>	230
The Applications of GPR to Civil Engineering in China <i>Ying, X., and H. Yu</i>	232
<u>Interactive Area 14: Image Processing</u>	
Separation of Character Strings and High Quality Vectorization for Digitized Korean Cadastral Map Images <i>Bang, K., and D. Hong</i>	237
A Multi-Strategic Approach for Land Use Mapping of Urban Areas by Integrating Satellite and Ancillary Data <i>Caetano, M., J. Santos and A. Navarro</i>	240
Development of a Feature-Based Approach to Automated Image Registration for Multitemporal and Multisensor Remotely Sensed Imagery <i>Dai, X., and S. Khorram</i>	243
Imitation Modeling of Radar Images Using a Complexing Method <i>Gernet, N.D.</i>	NA

A Quality Assurance Algorithm for NASA Scatterometer Wind Ambiguity Removal	Gonzales, A.E., and D.G. Long	246
Mosaicking of ERS SAR Quicklook Imagery of South East Asia	Kwoh, L.K., X. Huang and M. Li	249
Change Detection from Remotely Sensed Multi-Temporal Images Using Morphological Operators	Le Quere, P., P. Maupin, R. Desjardins, M.C. Mouchot, B. St-Onge and B. Solaiman	252
Symbolic Data Analysis of Multitemporal Data: An Application to Seasonal Analysis	Prakash, H.N.S., P. Nagabhushan and K.C. Gowda	NA
Multiscale Markov Random Fields for Large Image Data Sets Representation	Rehrauer, H., K. Seidel and M. Datcu	255
Gibbs Random Field Models for Image Content Characterization	Schroeder, M., K. Seidel and M. Datcu	258
Techniques for Large Zone Segmentation of Seismic Images	Simaan, M.A.	261
SAR Image Interpretation Based on Markov Mesh Random Fields Models	Smits, P.C., F. Giorgini, A. Martuccelli, M. Petrou and S.G. Dellepiane	NA
Automatic Segmentation of Oceanic Linear Structures on AVHRR Thermal Infra-Red Images	Thonet, H., B. Lemmonier and R. Delmas	NA
Segmentation of Multispectral Remote-Sensing Images Based on Markov Random Fields	Tsai, I.W., and D.C. Tseng	264
<u>Interactive Area 15: Land Cover Applications</u>		
Land Cover Change: A Method for Assessing the Reliability of Land Cover Changes Measured from Remotely Sensed Data	Aspinall, R.J., and M.J. Hill	269
Remote Sensing of the Effects of Irrigation Activities on Vegetation Health in Ephemeral Wetlands of Semi-Arid Australia	Benger, S.N.	272
Mapping Pastures in Eastern Australia with NOAA-AVHRR and Landsat TM Data	Hill, M.J., and G.E. Donald	275
Evaluating Quaternary Climatic Change in West Africa Using the NOAA AVHRR 1KM Land Dataset	Nichol, J.	278
Landuse Planning for Sustainable Development of Southeastern Desert of Egypt: An Integrated Remote Sensing and GIS Approach	Rahman, S.I. Abdel	NA
The Method of Early Drought Detection with AVHRR/NOAA Data	Spivak, L., A. Terehov, N. Muratova and O. Arkhipkin	281
Land Cover Classification of East Asia Using Fourier Spectra of Monthly NOAA AVHRR NDVI Data	Sugita, M., and Y. Yasuoka	284
Identifying Urban Features Using RADARSAT Images Taken at Multiple Incidence Angles	Weydahl, D.J.	287

"NA" indicates not available at time of printing.

Interactive Area 16: Optical Measurement of the Ocean

On the Peculiarities of SSM/I Brightness Temperature Variations in Kuroshio Region <i>Cherny, I.V., and V.P. Nakonechny</i>	NA
Simulation of Satellite Measurements of Radiance over Water for Operational Testing of MODIS Ocean Color Algorithms <i>Fleig, A.J., and K. Yang</i>	NA
Resolution Enhancement in SAR Images <i>Guglielmi, V., F. Castanie and P. Piau</i>	293
Diffuse Reflectance of the Optically Deep Sea Under Combined Illumination of Its Surface <i>Haltrin, V.I.</i>	296
Light Scattering Coefficient of Seawater for Arbitrary Concentrations of Hydrosols <i>Haltrin, V.I.</i>	299
Multi-Wavelength Laser Scattering at the Air-Sea Interface <i>Lin, C.S.</i>	302
The MUBEX Experiment - Validation of Satellite Data and Air-Sea Interaction Studies at Mutsu Bay, Japan <i>Llewellyn-Jones, D.T., I.M. Parkes, D.T., R. Yokoyama, S. Tamba, M. Takagi, C.T. Mutlow, T. Nightingale, C. Donlan and V. Bennett</i>	NA
Line Noise Extraction of Thermal Infrared Camera Image in Observing Sea Skin Temperature <i>Tamba, S., and R. Yokoyama</i>	305
Spatial and Temporal Behaviors of Sea Skin Temperature Observed by Thermal Infrared Camera <i>Tamba, S., S. Oikawa, R. Yokoyama, I. Redley, I. Parkes and D. Llewellyn-Jones</i>	308
MUBEX: Japan and U.K. Collaboration for Mutsu Bay Sea Surface Temperature Validation Experiment <i>Yokoyama, R., S. Tamba, T. Souma, D. Llewellyn-Jones and I. Parkes</i>	311
Laser Spark Spectroscopy in Remote Sensing of Sea and Land Surfaces Element Analysis <i>Tsipenyuk, D.Yu, and M.A. Davydov</i>	NA

Interactive Area 17: Remote Sensing Data Processing Techniques

Simulation of Split-Window Algorithm Performance <i>Axelsson, S.R.J., and B. Lunden</i>	317
Analysis of Single and Multi-Channel SAR Data Using Fuzzy Logic <i>Benz, U.</i>	322
Processing and Validation of the ERS-1 Radar Altimeter Data at the Italian PAF <i>Celani, C., A. Bartoloni and F. Nirchio</i>	325
A Visual Tool for Capturing the Knowledge of Expert Image Interpreters: A Picture is Worth More than a Thousand Words <i>Crowther, P., J. Hartnett, and R.N. Williams</i>	328
Data-Driven Decomposition of Mixed Pixels for Crop Area Estimation <i>Gebbinck, M.S.K., and T.E. Schouten</i>	NA

Radarsat Processing Using the Desk-Top Synthetic Aperture Radar Processor <i>Goulding, M., P.R. Lim, L. Wilke and P. Vachon</i>	NA
Congestion Data Acquisition Using High Resolution Satellite Imagery and Frequency Analysis Techniques <i>Kim, K.H., J.H. Lee and B.G. Lee</i>	331
Geoinformation Monitoring System - Gims (The Concept, Structure, Examples of Application) <i>Krapivin, V.F., and A.M. Shutko</i>	NA
The ENVISAT-1 Advanced Synthetic Aperture Radar Generic Processor <i>Lim, P.R., D.R. Stevens, D. Rae, Y.L. Desnos, H. Laur and T. Gach</i>	NA
A Framework for SAR Image Classification: Comparison of Co-Occurrence Method and a Gabor Based Method <i>Manian, V., and R. Vasquez</i>	335
A Network Distributed Processing System for TRMM Ground Validation <i>Merritt, J.H., N.T. Nguyen, D.B. Wolff and D. Han</i>	NA
Fuzzy Supervised Classification of JERS-1 SAR Data for Soil Salinity Studies <i>Metternicht, G.I.</i>	338
Land Cover Change Detection Using Radiometrically-Corrected Multi-Sensor Data <i>Mispan, M.R., and P.M. Mather</i>	NA
Quality Assurance of Global Vegetation Index Compositing Algorithms Using AVHRR Data <i>van Leeuwen, W.J.D., T.W. Laing and A.R. Huete</i>	341
<u>Interactive Area 18: Remote Sensing of the Ocean</u>	
Investigations of Possibilities of Using SAR Data for Monitoring of Volga Estuary and Kalmykija Shore of Caspian Sea <i>Armand, N.A., A.S. Shmalenyuk, Y.F. Knizhnikov, V.I. Kravtsova and E.N. Baldina</i>	347
Laboratory Investigations of Nonlinear Surface Wave Transformation in a Field of Two-Dimensionally Inhomogeneous Currents <i>Bakhanov, V.V., S.D. Bogatyrev, V.I. Kazakov and O.N. Kemarskaya</i>	350
Global Optimization Algorithms for Field-Wise Scatterometer Wind Estimation <i>Brown, C.G., and D.G. Long</i>	353
Retrieval of Air-Water Interaction by Thermal Radio Emission Dynamics at 60 GHZ <i>Gaikovich, K.P.</i>	NA
Ka-Band Ocean Wave-Radar and Wave Envelope-Radar Modulation Transfer Function Measurements and Modeling <i>Grodsky, S.A., V.N. Kudryavtsev and A.N. Bol'shakov</i>	NA
Gulf Stream Signatures and Surface Wave Observation Using ALMAZ-1 SAR <i>Grodsky, S.A., V.N. Kudryavtsev and A.Y. Ivanov</i>	NA
Ocean Wave Spectrum Reconstruction for ERS-1 Satellite Scatterometer Data <i>He, Y., and J. Zhao</i>	356
The Fine Grained Sediment Load of the Mississippi River: A Land Building Commodity <i>Huh, O.K.</i>	NA

"NA" indicates not available at time of printing.

Studies of Ocean Surface Processes Which Influence Climate <i>Jenkins, A.D., H.A. Espedal, H. Drange and O.M. Johannessen</i>	NA
SICH-1 Real Aperture Radar Imagery of Ocean Temperature Fronts <i>Malinovsky, V.V., A.V. Rodin and V.N. Kudryavtsev</i>	NA
Validation of Models and Algorithms for Microwave Radiometric Investigations of Tropical Cyclones <i>Petrenko, B.Z., A.F. Nerushev, L.I. Milekhin and G.K. Zagorin</i>	359
Bistatic Model of Ocean Scattering <i>Picardi, G., R. Seu and S. Sorge</i>	NA
Azimuthal Anisotropy of Sea Surface Polarized Microwave Emission <i>Pospelov, M.</i>	NA
Simultaneous Observation of Oceanic and Atmospheric Internal Waves by Air-Borne Dual Polarization Ku-Band Side Looking Radar <i>Pungin, V.G., and M.I. Mityagina</i>	NA
The Satellite Data "Resource" and NOAA/AVHRR for Black Sea Dynamics Investigation <i>Stanichy, S.V., and D.M. Solov'ev</i>	NA
The Surface Active Sea Films: Properties and Dynamics <i>Talipova, T.</i>	362
Aerocosmic Method of Investigations of Short Time Hydrodynamic Processes and Phenomena at the Surface of Seas and Oceans <i>Tomilov, G.M., and V.P. Bobykina</i>	NA
 <u>Interactive Area 19: Remote Sensing Techniques and Instrumentation</u>	
L-Band 300-Watt Solid State Pulse Power Amplifiers for SAR <i>Deng, Y.</i>	367
Development of a PC Based System for Real-Time, Local Reception of High Resolution Satellite Data for Environmental Monitoring <i>Downey, I.D., J.B. Williams, J.R. Stephenson, R. Stephenson and W. Looyen</i>	370
A Real Aperture Radar for Low Resolution Mapping at Low Costs <i>Impagnatiello, F., G. Angino and G. Leggeri</i>	374
Effects of Faraday Rotation on Microwave Remote Sensing from Space at L-Band <i>Le Vine, D.M., and M. Kao</i>	377
Using JPEG Data Compression for Remote Moving Window Display <i>Leung, P.S., M. Adair and J.H. Lam</i>	380
The Universal Multichannel Technique for Enhancing Images Obtained from Different Sensors <i>Petrenko, B.Z.</i>	383
YSAR: A Compact, Low-Cost Synthetic Aperture Radar <i>Thompson, D.G., D.V. Arnold, D.G. Long, G.F. Miner, T.W. Karlinsey and A.E. Robertson</i>	386

The China Airborne Radar Altimeter Control System	<i>Xu, K., M. Li, N. Zhou, Y.L. Xue and Y.S.Liu</i>	389
Miniature Ocean Radar Altimeter	<i>Xu, K.</i>	NA
Computer Simulation of Spaceborne Multimodes Microwave Sensors	<i>Zhang, Y., and J. Jiang</i>	392
<u>Interactive Area 20: Snow and Glaciers</u>		
Improved Elevation Change Measurements of the Greenland Ice Sheet from Satellite Radar Altimetry	<i>Davis, C.H., and C. Perez</i>	397
Multi-year Ice Concentration from RADARSAT	<i>Fetterer, F., C. Bertioia and J.P. Ye</i>	402
Analysis of a Microwave Airborne Campaign Over Snow and Ice	<i>Hewison, T., and S. English</i>	NA
Vector Radiative Transfer for Scattering Signature from Multi-Layer Snow/Vegetation at SSM/I Channels	<i>Jin, Y.Q.</i>	405
Deriving Glaciers Variation Integrated Remote and GIS in Tibetan Plateau	<i>Li, Z., and Q. Zeng</i>	408
On the Accuracy of Snow Cover Segmentation in Optical Satellite Images	<i>Luca, D., K. Seidel and M. Datcu</i>	411
A Comparison of Antarctic Sea Ice Concentration Derived from SSM/I, SAR, and Ship Observations	<i>Lytle, V.I., and M. Rapley</i>	NA
Sea Ice Concentration and Flow Size Distribution in the Antarctic Using Video Image Processing	<i>Muramoto, K., T. Endoh, M. Kubo and K. Matsuura</i>	414
Spectral RF Reflection from Water and Ice Layers	<i>Noyman, Z. Zlotnick, and A. Ben-Shalom</i>	NA
Comparability of Sea Ice Edges Detected in ERS-SAR Images and SSM/I Data	<i>Schmidt, R., and T. Hunewinkel</i>	417
Snow-Cover Mapping Experiment by EMISAR C Band - Discrimination and Optimum Resolution	<i>Solberg, R., A. Schistad Solberg, E. Volden, H. Koren and A. Teigland</i>	NA
Characterization of Snow Cover from Multispectral Satellite Remote Sensing and Modelling Runoff Over High Mountainous River Basins	<i>Swamy, A.N., and P.A. Brivio</i>	NA

Interactive Area 21: Lidars

Statistical Approach for Lidar Sensing of Turbulence Parameters with a Vi to Atmosphere Pollution	<i>Avramova, R.P.</i>	NA
Accurate Height Information from Airborne Laser-Altimetry	<i>Lemmens, M.J.P.M.</i>	423
Technique Doppler Lidar Measurement of the Atmospheric Wind Field	<i>Li, S.X., B.M. Gentry, and C.L. Korb</i>	NA
A New Airborne Remote Sensing System Integrating Scanning Altimeter with Infrared Scanner	<i>Liu, Z., and S. Li</i>	427
Air Turbulence Measurements Using CCD Camera for Obtaining Laser Spot Fluctuations	<i>Mitev, V.</i>	NA

Interactive Area 22: SAR Interferometry

Local, Global and Unconventional Phase Unwrapping Techniques	<i>Collaro, A., G. Fornaro, G. Franceschetti, R. Lanari, E. Sansosti and M. Tesauro</i>	433
Applicaition of Wavelets to Improve IFSAR DEM Reconstruction	<i>Curlander, J.C., G. Burkhart and C. Johnson</i>	NA
ERS Tandem INSAR Processing for Exploration of the Svalbard Archipelago	<i>Eldhuset, K., Amlien, J., P.H. Andersen, S. Hauge, E. Isaksson, T. Wahl and D.J. Weydahl</i>	NA
Motion Compensation Effects in Wavelength-Resolution VHF SAR Interferomtry	<i>Frolind, P.O., and L.M.H. Ulander</i>	436
The Exact Solution of the Imaging Equations for Crosstrack Interferometers	<i>Goblirsch, W.</i>	439
SAR Interferometric Analysis of ERS Tandem Data over an Alpine Terrain	<i>Kenyi, L.W., and H. Raggam</i>	NA
Baseline Estimation Using Ground Points for Interferomteric SAR	<i>Kimura, H., and M. Todo</i>	442
Development of an Interferometric SAR Data Processing System	<i>Li, J.F., H. Liu and H.D. Guo</i>	NA
Phase Noise Filter for Interferometric SAR	<i>Lim, I., T.S. Yeo, C.S. Ng, Y.H. Lu and C.B. Zhang</i>	445
Calibration and Classification of SIR-C Polarimetric and Interferometric SAR Data in Areas with Slope Variations	<i>Pasquali, P., F. Holecz, D. Small and T. Michel</i>	448
On the Motion Compensation and Geocoding of Airborne Interferometric SAR Data	<i>Sansosti, E., R. Scheiber, G. Fornaro, M. Tesauro, R. Lanari, and A. Moreira</i>	451
A Method for Precise Reconstruction of INSAR Imaging Geometry	<i>ShiPing, S.</i>	NA

Baseline Estimation in Interferometric SAR	<i>Singh, K., N. Stussi, L.K. Kwoh, and H. Lim</i>	454
Removal of Residual Errors from SAR-Derived Digital Elevation Models for Improved Topographic Mapping of Low-Relief Areas	<i>Slatton, K.C., M.M. Crawford, J.C. Gibeaut and R. Gutierrez</i>	457
Digital Elevation Models from SIR-C Interferometric and Shuttle Laser Altimetry (SAL) Data	<i>Sun, G., and K.J. Ranson</i>	460
<u>Interactive Area 23: SAR Techniques</u>		
A High Precision Workstation - Based Chirp Scaling SAR Processor	<i>Breit, H., B. Schattler and U. Steinbrecher</i>	465
Investigations of Coastal Zones in the North West Pacific by Remote Sensing	<i>Bobykina, V.P.</i>	NA
SAR Image Simulation of Moving Targets with LOCOSAR	<i>Cazaban, F., M. Deschaux-Beaume, J.G. Planes and M. Busson</i>	NA
Automated Acquisition of Ground Control Using SAR Layover and Shadows	<i>Gelautz, M., E. Mitteregger, and F. Leberl</i>	468
An Accelerated Chirp Scaling Algorithm for Synthetic Aperture Imaging	<i>Hawkins, D.W., and P.T. Gough</i>	471
Analysis of Code Error Effect in Spaceborne SAR Imaging Processing	<i>Jiang, Z., and J. Song</i>	474
High Quality Spotlight SAR Processing Algorithm	<i>Jin, M.Y.</i>	477
Interpretation of Brightness Temperature Retrieved by Supersynthesis Radiometer	<i>Komiyama, K., Y. Kato and K. Furuya</i>	481
Non-Iterative Spotlight SAR Autofocusing Using a Modified Phase-Gradient Approach	<i>Chan, H.L., and T.S. Yeo</i>	484
Real Time Synthetic Aperture Radar Preprocessor Design Via Three-Dimensional Modular Filtering Architecture	<i>Chan, H.L., and T.S. Yeo</i>	487
High Resolution SAR Processing Using Stepped-Frequencies	<i>Lord, R.T., and M.R. Inggs</i>	490
RADARSAT Attitude Estimates Based on Doppler Centroid of SAR Imagery	<i>Marandi, S.R.</i>	493
A Research of Moving Targets Detection and Imaging by SAR	<i>Pan, R., G. Li and X. Zhu</i>	498
Tree Structured Filter Banks for Speckle Reduction of SAR Images	<i>Sveinsson, J.R., and J.A. Benediktsson</i>	501
Feasibility of Satellite On-Board SAR Processing	<i>Thompson, A., H. Jiang, S. Spenler and A. Macikunas</i>	NA

"NA" indicates not available at time of printing.

Near Real-Time RADARSAT Data System for NOAA CoastWatch Applications <i>Tseng, W.Y., W.G. Pichel, A.K. Liu, P. Clemente-Colon, G.A. Leshkevich, S.V. Nghiem, R. Kwok and R.N. Stone</i>	505
 <u>Interactive Area 24: Surface Temperatures</u>	
Land Surface Temperature Interpretation of Equatorial South America from AVHRR Data <i>Li, G., and P.J. Hardin</i>	511
Tropical Model for Retrieving Surface Temperature from Satellite Data <i>Mansor, S.B.</i>	NA
Sea Surface Temperatures from NOAA Satellites in the Swordfish and Jack Mackerel Fisheries of Chile's Central Zone <i>Yanez, E., M.A. Barbieri, V. Catasti, C. Silva and K. Nieto</i>	NA
 <u>Interactive Area 25: Neural Network and Intelligent Systems</u>	
Pollution Analysis of Hyperdimensional Data Using Neural Networks <i>Benediktsson, J.A., K. Arnason and S. Jonsson</i>	NA
A Classification of Multispectral Landsat TM Data Using Principle Component Analysis of Artificial Neural Network <i>Chae, H.S., S.J. Kim and J.A. Ryu</i>	517
Unsupervised Classification for Remotely Sensed Data Using Fuzzy Set Theory <i>Dinesh, M.S., K.C. Gowda and P. Nagabhushan</i>	521
Development of a Intelligent Image Analysis System for the Detailed Analysis of the Land Surface Information <i>Kim, K.O., Y.L. Ha, I.S. Jung, J.Y. Lee, K.H. Choi and J.H. Lee</i>	524
Study on the Characteristics of the Supervised Classification of Remotely Sensed Data Using Artificial Neural Networks <i>Paek, K.N., Y.S. Song, H.S. Chae and K.E. Kim</i>	528
 <u>Interactive 26: Missions and Programs</u>	
The Advanced Remote Sensing Data from MOMS-2P on PRIRODA <i>Bodechtel, J., and Q. Lei</i>	533
Multi-Frequency and Multi-Polarization SAR System Analysis with Simulation Software Developed at CSA <i>Huang, Y., G. Seguin, and N. Sultan</i>	536
Oceanological Results from the ALMAZ-1 Mission: An Overview <i>Ivanov, A.Y., and K.T. Litovchenko</i>	539
Some Options for RadarSAR-II <i>Parashar, S., E.J. Langham and S. Ahmed</i>	NA
A Summary of the Upper Atmosphere Research Satellite (UARS) <i>Schoeberl, M., A.R. Douglass and C.H. Jackman</i>	542

BEAWARE: Budget Effective All Weather Accurate Radar for Earth Observation	Vincent, N., E. Souleres and N. Suinot	545
Design of MACSIM Cloud Radar for Earth Observation Radiation Mission	Vincent, N., N. Suinot and C.C. Lin	548
<u>Interactive 27: Inverse Techniques</u>		
Ice Concentration Estimation Based on Local Inversion	Arai, K.	553
Retrieving of LAI and FAPAR with Airborne POLDER Data over Various Biomes	Bicheron, P., M. Leroy and O. Hautecoeur	556
The Uncertainty and Confidence in BRDF Model Inversion	Jindi, W., and L. Xiaowen	NA
SAIL Model Experiment of the Inversion of Growth Indices from Rice Canopy Reflectance Using the Information on Variation and Regulation of Leaf Spectral Characteristics	Kushida, K.	NA
Algorithms for Estimating Some Optically Active Substances and Apparent Optical Properties from Subsurface Irradiance Reflectance Measurements in Lakes	Reinart, A.	NA
Geometry-Based Deconvolution of Geophysical Data	Simaan, M.A.	559
A Priori Information in Inverse Problems of Atmospheric Optics	Timofeyev, Y.M.	562
Three-Dimensional DC Resistivity Inversion at a Gasoline Contaminated Site	Xiao, L., and L. Liu	NA
Retrieval of Electrical Properties of a Stratified Medium with Slightly Rough Surface Using an Inversion Method	Zhuck, N.P., D.O. Batrakov and K. Schuenemann	NA
<u>Interactive 28: Calibration</u>		
Characterization of Passive NMMW Backgrounds at 140 and 220 GHz	Ben-Shalom, A., Y. Oreg, and M. Engel	NA
Some Issues on Calibration/Validation Algorithms of SSM/I Data	Jin, Y.Q.	567
Calibration and Validation of ADEOS/NSCAT in Japan	Masuko, H., and Japanese ADEOS/NSCAT CAL/VAL Team	NA
Calibration Experiments of the CRL/NASDA X/L-Band Airborne Synthetic Aperture Radar	Satake, M., T. Kobayashi, H. Masuko and M. Shimada	570

"NA" indicates not available at time of printing.

Interactive 29: Education and Information Systems

Development of Interactive, Graphical, Computer-Based Teaching Tools for Remote Sensing in Tcl/Tk <i>Barnsley, M., and P. Hobson</i>	NA
Ocean Expeditions: El Nino — An Interactive Education Tool Based on Remote Sensing Data <i>Gautier, C.</i>	NA
Meteorological Satellite Image Service via WWW <i>Lee, H.G.</i>	575

Interactive 30: Wavelet Techniques in Remote Sensing

Wavelet Techniques Applied to Lidar Temperature Profiles in the Middle Atmosphere to Study Gravity Waves <i>Chane-Ming, F., F. Molinaro, and J. Leveau</i>	581
Robust Terrain Classification Using Wavelet Packets <i>Keshava, N., and J.M.F. Moura</i>	NA
High Resolution Image Classification with Features from Wavelet Frames <i>Kim, K.O., I.S. Jung and Y.K. Yang</i>	584
A Hierarchical Stereo Matching Algorithm Using Wavelet Representation Based on Edge and Area Information <i>Um, G.M., C.S. Ye and K.H. Lee</i>	588

Interactive 31: Classification

The Impact of the Initial Land-Cover Classification on the Retrieval of Land Use Information from Remotely-Sensed Images Using Structural Pattern Recognition Techniques <i>Barr, S., and M. Barnsley</i>	NA
Snow Covered Area Classification Using Time Series ERS - 1 SAR <i>Li, Z., and J. Shi</i>	NA
From the Satellite to the Airborne Platforms Imagery: Behavioral Classification and Segmentation <i>Orban-Ferauge, F., J.P. Rasson and S. Baudart-Lissoir</i>	NA
Symbolic ISODATA Clustering Procedure Useful for Land Cover Classification: A Case Study Employing IRS-1B LISS II Data for Nagarhole Forest, Karnataka State, India) <i>Prakash, H.N. S., P. Nagabhushan and K.C. Gowda</i>	NA

Interactive 32: Coastal Environment

Retrieval of the Remote Radiance Reflection Coefficient of Coastal Waters from the Inherent Optical Properties <i>Haltrin, V.I.</i>	595
Monitoring Coastal Water Systems: An Integrated Approach <i>Krishnan, P.</i>	598
Near-Bottom Fluxes of Sediment Matter on a Shelf and Their Research by Remote Techniques <i>Likht, F.R., and L.M. Mitnik</i>	601
The Analysis and Comparison of Satellite and “In Situ” Temperature Measurements for Coastal Zone Dynamic Processes Investigation <i>Stanichnaya, R.R., A.S. Kuznetsov, S.A. Shurov, D.M. Solov’ev and S.V. Stanichny</i>	NA

Interactive 33: General Applications

New Method of the Characterization of the Semiconductor Plate Homogeneity by its Thermal Image <i>Bolgov, C., and V. Morozhenko</i>	NA
Ozone Distributions in the Stratosphere-Troposphere System Using the Interdisciplinary Physics Modelling <i>Caldararu, F., S. Patrascu, M. Caldararu, A. Paraschiv and D. Nicolaescu</i>	607
An Improved Description of the MTF of the Moderate Resolution Imaging Spectroradiometer and a Method for Enhancing Its Cross Track Resolution <i>Fleig, A.J., and K. Yang</i>	NA
Spectral Identification of Coral Biological Vigour <i>Holden, H., and E. LeDrew</i>	610
Variance Fractal Dimension Analysis of Crustal Seismic Refraction Signals <i>Jiao, L.X., and W.M. Moon</i>	NA
A Study of the Micro-Scale Disturbances Associated with a Shear Layer in the Lower Atmosphere <i>Natarajan, M.P., and M. Isaac</i>	613
New Architecture for Remote Sensing Image Archives <i>Seidel, K., R. Mastropietro and M. Datcu</i>	616
The Evaluation of Bending Waves and Modified Path Profile <i>Uz, B., O. Yildirim and H.M. El-Khattib</i>	NA
Combined Resistive and Conductive Three-Part Plane: Oblique Incidence Plane Wave <i>Yildirim, O.</i>	NA
Constraint Propagation in the Multi-Granularity World <i>Zequn, G., and L.Deren</i>	NA

A01: Remote Sensing of Snow and Glaciers

A01.01	Improving the MODIS Global Snow-Mapping Algorithm	619
	<i>Klein, A.G., D.K. Hall and G.A. Riggs</i>	
A01.02	The HUT Brightness Temperature Model for Snow-Covered Terrain	622
	<i>Hallikainen, M., J. Pulliainen, L. Kurvonen and J. Grandell</i>	
A01.03	Snow Crystal Shape and Microwave Scattering	625
	<i>Foster, J.L., D.K. Hall, A.T.C. Chang, A. Rango, W. Wergin and E. Erbe</i>	
A01.04	Mapping Snow Cover with Repeat Pass Synthetic Aperture Radar	628
	<i>Shi, J., S. Hensley and J. Dozier</i>	
A01.05	Snow Monitoring Using EMISAR and ERS-1 Data Within the European Multi-Sensor Airborne Campaign EMAC-95	631
	<i>Guneriussen, T., H. Johnsen, R. Solberg and E. Volden</i>	
A01.06	Ground Penetration Radar and ERS SAR Data for Glacier Monitoring	634
	<i>Hamran, S.E., T. Guneriussen, J.O. Hagen and R. Odegard</i>	
A01.07	Comparison of Ranging Scatterometer and ERS-1 SAR Microwave Signatures Over Boreal Forest Zone During Winter Season	637
	<i>Koskinen, J., J. Pulliainen, M. Makynen and M. Hallikainen</i>	
A01.08	Multi-Source Snow Cover Monitoring in the Swiss Alps	640
	<i>Piesbergen, J., and H. Haefner</i>	

A02: Image Processing Techniques

A02.01	The Use of Mathematical Morphology for Accurate Detection and Identification of Microwave Images in the K-Space Domain	643
	<i>Gader, P., and A.J. Blanchard</i>	
A02.02	New Classification Techniques for Analysis of Remote Sensing Integrated Data	646
	<i>Console, E., and M.C. Mouchot</i>	
A02.03	From the Unsupervised Remote Sensing Data Behavioral Classification to the Image Segmentation	NA
	<i>Rasson, J.P., F. Orban-Ferauge and S. Baudart-Lissoir</i>	
A02.04	Hughes Phenomenon in the Spatial Resolution Enhancement of Low Resolution Images and Derivation of Selection Rule for High Resolution Images	649
	<i>Nishii, R., S. Kusanobu and N. Nakaoka</i>	
A02.05	Forming Digital Elevation Models from Single Pass Spot Data: Results on a Generation from Optical Stereo Data	652
	<i>Massonnet, D., A. Giros, and B. Rouge</i>	

A02.06	A Mixed Fractal/Wavelet Based Approach for Characterization of Textured Remote Sensing Images <i>Marazzi, A., P. Gamba, A. Mecocci and E. Costamagna</i>	655
A02.07	Significance-Weighted Classification by Triplet Tree <i>Yoshikawa, M., S. Fujimura, S. Tanaka and R. Nishii</i>	658
A02.08	On-Line System for Monitoring and Forecasting Earth Surface Changes Using Sequences of Remotely-Sensed Imagery <i>Lee, S.</i>	661

A03: Data Fusion I

A03.01	Effect of Scale on the Information Content in Remote Sensing Imagery <i>Niemann, K.O., D.G. Goodenough and G.J. Hay</i>	664
A03.02	Multisensor Classification of Wetland Environments Using Airborne Multispectral and SAR Data <i>Ricard, M.R., A.L. Neuenschwander, M.M. Crawford and J.C. Gibeaut</i>	667
A03.03	Automated Forest Inventory Update with SEIDAM <i>Goodenough, D., D. Charlebois, A.S. Bhogal, S. Matwin and N. Daley</i>	670
A03.04	Modeling Soil Erosion Hazard by Using a Fuzzy Knowledge-Based Approach <i>Metternicht, G.I.</i>	674
A03.05	Comparing Raster and Object Generalization <i>Daley, N., D.G. Goodenough, A.S. Bhogal, Q. Bradley, J. Grant and Z. Yin</i>	677
A03.06	Expert Maps: An Alternative for Integrating Expert Knowledge in Satellite Imagery Classification <i>Campagnolo, M.L., and M. Caetano</i>	680
A03.07	Data Fusion in a Context of Data Mining, Identification and Classification <i>Wu, D., and J. Linders</i>	NA
A03.08	Infusion of Altimeter Data to Same Spatial, Temporal Resolution Infrared Images to Improve the Accuracy of Classification of Images and DEM <i>Liu, Z., and S. Li</i>	683
A03.09	Data Integration in Support of Research on the Gulf of Mexico <i>Mason, M., G.L. Rochon, M. Singletary, N. Blackmon, D. Bardell, C. Jernigan and M. Fernandez</i>	NA

A04: Innovations in Remote Sensing Educational Programs and Information

A04.01	NASA's Mission to Planet Earth Invests in the Future Through a Broad National Education Program <i>Khazenie, N., and S. Stockman</i>	685
A04.02	What is Earth System Science? <i>Johnson, D.R., M. Ruzek, and M. Kalb</i>	688
A04.03	A Web-Based Earth Systems Science Graduate Course for Middle School Teachers <i>Myers, R.J., E.L. Shay, H. Shay, H.B. Davis, and J.A. Botti</i>	692
A04.04	Globe: An International Science and Education Collaboration to Obtain Accurate Data for Monitoring Earth Systems <i>Becker, M.L., R.G. Congalton, R. Budd, and A. Fried</i>	NA

"NA" indicates not available at time of printing.

A04.05	Teacher Enhancement Programs in the Atmospheric Sciences: The American Meteorological Society's Project Atmosphere and DataStreme	NA
	<i>Moore, J.D.</i>	
A04.06	Global Classroom Education Network	NA
	<i>Mesarovic, M., and N. Sreenath</i>	
A04.07	System Thinking and System Modeling in the Earth System Science Classroom	695
	<i>Mahootian, F.</i>	
A04.08	Practical Uses of Math and Science (PUMAS)	698
	<i>Kahn, R.</i>	
A04.09	An Earth System Science Education and Training Program for the Inter American Institute for Global Change Research (IAI)	699
	<i>Johnson, D.R., M. Ruzek, M. Kalb</i>	

A05: Rough Surface Scattering

A05.01	An Exact Technique for Calculating the Scattering from Roughness Surfaces	NA
	<i>Kasilingam, D.</i>	
A05.02	Application of an Extended IEM to Multiple Surface Scattering and Backscatter Enhancement	702
	<i>Hsieh, C.Y., and A.K. Fung</i>	
A05.03	Numerical Study of Shadowing in Electromagnetic Scattering from Rough Dielectric Surfaces	705
	<i>West, J.C., and J.M. Sturm</i>	
A05.04	Precise Estimation of Surface Roughness Parameters for Field-Measured Ground Truth Data	708
	<i>Oh, Y.</i>	
A05.05	Some Features of Low-Grazing-Angle Backscatter from the Sea Surface in X- and Ka-Bands: Modeling and Observations	NA
	<i>Skirta, E.A., L.A. Ostrovsky, M.B. Kanevsky, V.I. Titov, E.M. Zuikova, N.A. Sedunov and V.Y. Karaev</i>	
A05.06	Laboratory Study of Polarized Microwave Scattering from Steep Waves at Grazing Incidence	711
	<i>Rozenberg, A., D. Quigley, M. Ritter and W.K. Melville</i>	
A05.07	Inside the Sea-Spike: Low Grazing Angle Radar Imaging of Laboratory Waves Repeatedly Breaking in Wave Groups	714
	<i>Fuchs, J., S. Welch, T. Waseda, D. Regas and M.P. Tulin</i>	
A05.08	Monte Carlo Simulation of Backscattering from Natural Soil Surfaces	719
	<i>Casarano, D., F. Posa, F. Mattia, G. De Carolis, J.C. Souyris, T. Le Toan and G. Pasquariello</i>	
A05.09	Qualitative Analysis of the Effect of Roughness on Backscattered Signal Derived from SIR-C Data	NA
	<i>Rao, Y.S., and K.S. Rao</i>	

A06: SAR Processing Algorithms

A06.01	A Processing Algorithm for the ENVISAT Alternating Polarization Mode Single Look Complex Product	722
	<i>Stevens, D.R., F. Wong, P. Lim and Y.L. Desnos</i>	
A06.02	Phase Preserving Processing of ScanSAR Data with Modified Range Doppler Algorithm	725
	<i>Wong, F., D.R. Stevens and J. Cumming</i>	

A06.03	Synthetic Aperture Radar Out of Slant Plane Motion Compensation	728
	<i>Stacy, N.J.S.</i>	
A06.04	A Comparison of Phase-Preserving Algorithms for Burst-Mode SAR Data Processing	731
	<i>Cumming, I., Y. Guo and Y. Wong</i>	
A06.05	Precision Two-dimensional Focusing of Spaceborne Synthetic Aperture Radar Data with Range-Varying Doppler Centroid	734
	<i>Heng, A.W.C., H. Lim, S.C. Liew and B.T.G. Tan</i>	
A06.06	SAR Image Interpretation Based on Markov Mesh Random Fields Models	737
	<i>Smits, P.C., F. Giorgini, A. Martuccelli, M. Petrou and S.G. Dellepiane</i>	
A06.07	The Spaceborne SAR Imaging Algorithms Research	740
	<i>Li, G., M. Zhu and X. Zhu</i>	
A06.08	Speckle Filter Based on Correlation Between Wavelet Transform Scales	NA
	<i>Zhang, K., and M. Zhu</i>	
 <u>A07: Geology and Geomorphology</u>		
A07.01	Joint Analysis of Radar and VNIR/SWIR Images for Mapping Alluvial Fans	NA
	<i>Gillespie, A.R.</i>	
A07.02	Multisensoral Approach for Studying the Geology and Tectonics of the Dead Sea Rift/Israel	743
	<i>Bodechtel, J., M. Frei, T. Wever, H. Kaufmann, Y. Xia and M. Beyth</i>	
A07.03	Mapping Evolutive Surface Deformations in Semi-Industrial and Urban Areas by Differential SAR Interferometry and Modelisation	NA
	<i>Carnec, C., C. Delacourt, E. Burov, D. Legendre, H. Fabriol and C. King</i>	
A07.04	Estimation of SiO ₂ Content from TIR Spectra Measured on Weathered Surfaces of Igneous Rocks	NA
	<i>Ninomiya, Y., and T. Matsunaga</i>	
A07.05	Volcanic Mapping with SIR-C/X-SAR Data for Western Kunlun of China	746
	<i>Wang, C., G. Huadong, and J. Liào</i>	
A07.06	Modeling Spatial Data Applied for Geomorphologic Mapping	NA
	<i>Tuan, V.A., N.T. Cong, P.V. Cu, P.T. Hai, C.X. Huy, D.V. Khac, N.T. Thanh and L.A. Tuan</i>	
A07.07	Viewing China with the ERS-1 WSC Data	749
	<i>Wang, X., C. Wang, and G. Huadong</i>	
A07.08	Integrated Imaging of RADARSAT and Other SAR Data for Earthquake Tectonic Investigation of the Nahanni Earthquake Area in Northwest Territories, Canada	NA
	<i>Moon, W.M., J. Ristau, V. Singhroy, Y. Yamaguchi, M. Lamontagn and R. Kuoda</i>	
A07.09	Effects of Terrain Types on the Selection of RADARSAT Beam Modes for Geological Mapping	752
	<i>Singhroy, V.</i>	

"NA" indicates not available at time of printing.

A08: Properties and Processing of SAR Speckle

A08.01	Comparison of the Statistical Properties of SAR Data, and Their Applications to SAR Classification <i>Sant'Anna, S.J., C.F. Yanasse, and S. Quegan</i>	NA
A08.02	Influence of Canopy Shape on SAR Speckle Distributions Over Woodland <i>Williams, M.L.</i>	755
A08.03	Prior Scene Knowledge for the Bayesian Restoration of Mono- and Multi-Channel SAR Images <i>Nezry, E., A. Lopes, and F. Yakam-Simen</i>	758
A08.04	Statistical Properties of Speckle and Full Polarimetric Filters in SAR <i>Sery, F., and A. Lopes</i>	761
A08.05	Effects of Parameter Tuning and De-Speckle Filtering on the Accuracy of SAR Image Classification Based on Gray-Level Co-Occurrence Matrix Features <i>Bruzzone, L., S.B. Serpico, and G. Vernazza</i>	764
A08.06	Bayesian Approach to SAR Image Reconstruction <i>Walessa, M., and M. Datcu</i>	767
A08.07	Validation of Segmentation Techniques for SAR Images <i>Preston, M.I., and S. Quegan</i>	770
A08.08	The Effect of Forest Understory on Synthetic Aperture Radar Backscatter <i>Silva, T., and J.B. Dias</i>	773
A08.09	Block-Based Maximum Likelihood Classification for Hyperspectral Remote Sensing Data <i>Jia, X.</i>	778

A09: Radar Observations of Forest

A09.01	SAR Image Analysis Methods for Forest Applications <i>Quegan, S., and J. Yu</i>	781
A09.02	On the Coupling of Backscatter Models with Tree Growth Models - Part I: A Realistic Description of the Canopy Using the AMAP Tree Growth Model <i>Castel, T., A. Beaudoin, J.F. Barcz, Y. Caraglio, N. Floury, T. Le Toan and L. Castagnas</i>	784
A09.03	On the Coupling of Backscatter Models with Tree Growth Models - Part II: RT Modelling of Forest Backscatter <i>Floury, N., T. Le Toan, J.A. Kong, T. Castel, A. Beaudoi and, J.F. Barcz</i>	787
A09.04	Forest Applications of ERS, JERS, and SIR-C SAR Interferometry <i>Wegmuller, U., T. Strozzi and C. Werner</i>	790
A09.05	Use of SAR Interferometry for Monitoring Clear Cutting of Forests <i>Smith, G., and J. Askne</i>	793
A09.06	Analysis of CARABAS VHF SAR Data from BALTASAR-96 <i>Ulander, L.M.H., P.O. Frolind, A. Gustavsson, H. Hellsten, T. Jonsson, B. Larsson and G. Stenstrom</i>	797
A09.07	Modelling of VHF Radar Backscattering from Forests Based on Radiative Transfer <i>Israelsson, H., J. Askne and L. Ulander</i>	800
A09.08	Radar Backscatter from Boreal Forest in Winter <i>Hallikainen, M., M. Makynen, J. Pulliainen and T. Vanska</i>	803

A10: Coastal Environments

- A10.01 Air/Sea/Land Interaction in the Coastal Zone Seen by Satellite RAR and SAR 806
Mitnik, L., V.B. Lobanov, M.K. Hsu, R.S. Tseng and K.S. Chen
- A10.02 Remote Sensing Analysis of Submerged Coral Reefs: Applications for Integrated Coastal Management in Fiji 809
LeDrew, E., D. Knight and H. Holden
- A10.03 Active and Passive Remote Sensing of Colored Dissolved Organic Matter (CDOM) in Marine Waters NA
Blough, N.V., A. Vodacek, F.E. Hoge and R.N. Swift
- A10.04 Landcover Classification Using ERS SAR/INSAR Data Over Tropical Areas 813
Stussi, N., S. Liew, L.K. Kwok, H. Lim, J. Nichol and K.C. Goh
- A10.05 Potential Applications of Remote Sensing in the Coastal Environmental Management of Bangladesh NA
Khan, M.H., M. Emch and A. Islam
- A10.06 Preliminary Study on Development and Management Information System of China Coastal Resources Environment 816
Jiang, X., and C. Yun
- A10.07 Radarsat SAR Investigations of South Coasts of Korea for Coastal Zone Management: Preliminary Results NA
Won, J.S., J.K. Park and K.H. Chi
- A10.08 Status of the Development of an In Situ Plankton Monitor 819
Campbell, W., J. Nault and R.A. Warner

B01: Marine Biochemistry

- B01.01 Microbial Particles and Oceanic Optics: Where Do We Go Next? 821
Stramski, D.
- B01.02 Light Absorption Measurements of Aquatic Particles: Status and Prospects 825
Tassan, S., B.G. Mitchell, D. Stramski and A. Bricaud
- B01.03 Physico-Biological Oceanographic Remote Sensing of the East China Sea: Satellite and In Situ Observations NA
Ning, X., M. Fang, Z. Liu and J.C. Chen
- B01.04 The Dependence of the Spectrum-Derived Chlorophyll a Concentration on the Profile of Chlorophyll a Concentration NA
Liu, C.T., M.H. Chang, C.L. Lee and Y.L.L. Chen

B02: Clouds and Precipitation I

- B02.01 Retrieval of Liquid Water Distribution in Convective Clouds Using Microwave Computerized Tomography 830
Bobylyev, L.P.
- B02.02 Microwave Brightness Temperature Difference of Vertical and Tilted Tropical Convective Systems NA
Hong, Y., J. Haferman, and C.D. Kummerow
- B02.03 Low Cost Digitalization of an X-Band, Non Coherent Weather Radar 833
Galati, G., G. Russo, G. Dargaud and G. Pavan
- B02.04 Cloud Contamination in Cross Track and Conical Scanning Configurations NA
Divakarla, M.G., and L.M. McMillin

"NA" indicates not available at time of printing.

B03: Remote Sensing and Urban Planning

- B03.01 Environmental Quality and Changes: A View from NDVI in Hong Kong 836
Fung, T.
- B03.02 Urban Planning Using Data Fusion of Satellite and Aerial Photo Images 839
Cheng, P., and T. Toutin
- B03.03 Information System for Monitoring the Urban Environment Based on Satellite Remote Sensing: Shanghai as an Example 842
Zhang, Y.
- B03.04 Test of a Digital Camera Integrated with INS/GPS for Urban Environment Monitoring NA
Gong, P., G. Biging, K.P. Schwarz, M. Mostafa and Y. Sheng

B04: Educational Initiatives/Student Programs

- B04.01 Investigation of the North-East Monsoon Characteristics in the Region of South East Asia Using ERS Wind Scatterometer Data 845
Guo, Y., J. Toh, Z. M. Zhang, I.I. Lin and V.H.S. Khoo
- B04.02 Remote Sensing Educational Resources on the World Wide Web 848
Sivaprakash, S., J. Ng, N.L. Teo, V.H.S. Khoo and S.C. Liew
- B04.03 National GIS Training Program: Korean Experiences 850
Lee, K., H.G. Lee and M.S. Kim
- B04.04 Issues of WWW-Based Data Visualization in the Earth System Science Classroom 854
Mahootian, F.

B05: Remote Sensing of Sea Ice

- B05.01 Temperature Corrected Bootstrap Algorithm 857
Comiso, J.C., and H.J. Zwally
- B05.02 An Evaluation of Error Sources in the Retrieval of Antarctic Sea Ice Concentrations from Satellite Passive Microwave Data NA
Massom, R.A., J.C. Comiso, A.P. Worby, V. Lytle and I. Allison
- B05.03 Bistatic Microwave Investigations of Media with Sea Ice-Like Properties NA
May, G.C., J.W. Bredow, A.K. Fung, S. Nadimi and J. Jin
- B05.04 Wave Dispersion by Frazil-Pancake Ice from SAR Imagery 862
Wadhams, P., G. De Carolis, F. Parmiggiani, and M. Tadross

B06: SAR Interferometry: Phase Unwrapping

- B06.01 Multiresolution Signal Representation for Phase Unwrapping and Interferometric SAR Processing 865
Bamler, R., and G.W. Davidson
- B06.02 Phase Unwrapping by Fusion of Local and Global Methods 869
Reigber, A., and J. Moreira

B06.03	Comparison of Path-Following and Least-Squares Phase Unwrapping Algorithms	Pritt, M.D.	872
B06.04	Congruence in Least-Squares Phase Unwrapping	Pritt, M.D.	875
B06.05	How Global and Local Phase Unwrapping Techniques Are Connected	Fornaro, G., G. Franceschetti, R. Lanari, E. Sansosti and M. Tesauro	878

B07: Remote Sensing of Coral and Coastal Environments

B07.01	Modeling Water Surface Reflectance Signatures and In-Water Irradiance Profiles in Shallow Tropical Waters Influenced by Bottom Reflectance	Bostater, C.	881
B07.02	Analysis of the Diffuse Attenuation Coefficients for Radiance and the Implications for Retrieval of the Spectral Signature of Submerged Tropical Corals	LeDrew, E., and H. Holden	885
B07.03	Coastal Water Studies in Hong Kong -- Satellite Remote Sensing and Realtime Hydrology	Fang, M., D.R. Kester, Y. Li and X.R. Ning	NA
B07.04	Environmental Monitoring of the Venice Lagoon Using MIVIS Data	Barducci, A., and I. Pippi	888

B08: Monitoring Urban Settlements

B08.01	Analysis of Radar Response from Urban Areas	Forster, B., C. Ticehurst and Y. Dong	891
B08.02	Inferring Urban Land Use from Very Fine Resolution Satellite Sensor Images Using Region-Based, Graphic-Theoretic Techniques	Barnsley, M., and S. Barr	NA
B08.03	Road Network Extraction from Airborne Digital Camera Images: A Multi-Resolution Comparison	Gong, P., and J. Wang	895
B08.04	A Complex Spatial Analysis of Urban Areas Using Airborne Thermal Radiometry and GIS Techniques	Ben-Dor, E., H. Saaroni, A. Tshudnovski and A. Bitan	NA
B08.05	Remote and In Situ Monitoring of Peri-Urban Wetlands	Fernandez, M., G.L. Rochon, J.K. Terry, J. Smith, C. Jernigan, D. Bardell and M. Mason	NA

B09: Microwave Emission & Scattering from Rough Surfaces

B09.01	On the Surface Roughness Characterization for SAR Data Analysis	Mattia, F., J.C. Souyris, T. Le Toan, D. Casarano, F. Posa and M. Borgeaud	898
B09.02	Bare Soil Surface Observations and Modelling	Le Toan, T., P. Borderies, M. Borgeaud, I. Chenerie, F. Mattia, T. Mannenen and J.C. Souyris	NA

"NA" indicates not available at time of printing.

B09.03 Electromagnetic Scattering Interaction Between a Dielectric Cylinder and a Slightly Rough Surface 901
Chiu, T., and K. Sarabandi

B09.04 Experimental Validation of Surface Scattering and Emission Models 904
Coppo, P., S. Lolli, G. Macelloni, G. Nesti, P. Pampaloni, R. Ruisi and D. Tarchi

B10: Image Processing and Feature Extraction

B10.01 Discontinuity Adaptive MRF Model for Remote Sensing Image Analysis 907
Smits, P.C., and S.G. Dellepiane

B10.02 Application of Adaptive Filters for Multisensoral Image Fusion 910
Steinnocher, K.

B10.03 Classification of Hyperdimensional Data Using Data Fusion Approaches 913
Benediktsson, J.A., and J.R. Sveinsson

B10.04 Integrated Mineral Exploration Using Multiple Exploration Data and JERS-1 SAR Data 914
(East Java, Indonesia)
Jiang, W.W., S.K. Choi, Y. Yamaguchi, C.S. So, L. Feng and W.M. Moon

B11: NOAA Data Processing

B11.01 ATOVS & AVHRR Processing Package 915
Rochard, G.

B11.02 Comparison of Land Cover Indices of AVHRR Data 916
Sakurai-Amano, T., J. Iisaka, and M. Takagi

B11.03 Global Land Surface Temperature Products from AVHRR 917
Arino, O., Y. Kerr, J.P. Lagouarde, F. Nezry and C. Ottle

B11.04 Satellite-Derived Atmosphere Aerosol Optical Thickness and Size Distribution 918
Lynch, M.

C01: Electrical Geophysics Related to Complex Media

C01.01 Monte Carlo Simulations of Scattering of Electromagnetic Waves from Dense Distributions of Nonspherical Particles 919
Tsang, L., K.H. Ding and S.E. Shih

C01.02 A finite Difference Time Domain Simulation of Electromagnetic Wave Propagation and Scattering in a Partially Conducting Layered Earth 922
Calhoun, J.

C01.03 Complex Permittivity Measurements of Two Conifers 925
Franchois, A., R. Lang and Y. Pineiro

C01.04 3D Electromagnetic Modeling Using Staggered Finite Differences 929
Newman, G.A., and D.L. Alumbaugh

C01.05 3D Electromagnetic Inversion Using Conjugate Gradients 933
Newman, G.A., and D.L. Alumbaugh

C01.06	A Stable Algorithm for Simualtion of Two-and-Half Dimensional Problems in Electromagnetic Well Logging <i>Tian, X., C. Liu and L.C. Shen</i>	NA
C01.07	Inversion of 6FF40 Induction Tool Measurement Using the Distorted Born Iterative Method <i>Chen, S., W.C. Chew and W.D. Kennedy</i>	938
C01.08	A New Numerical Method for Large-Scale Complex Media: The PSTD Algorithm <i>Liu, Q.H.</i>	942
C01.09	3D PML-FDTD Simulation of Ground Penetrating Radar on Dispersive Earth Media <i>Teixeira, F.L., W.C. Chew, M. Straka, M.L. Oristaglio and T. Wang</i>	945

C02: Educational Technologies/Student Programs

C02.01	The NASA Academy: A Four Year Experiment in Education <i>Soffen, G.</i>	NA
C02.02	Applications of Satellite Imagery, Visualizations, and Remote Sensing in Environmental/Science Education: An Earth Systems Science Approach <i>Moore, J.D.</i>	NA
C02.03	The International Space University: Its Mission and Programs <i>Bali, S.</i>	948
C02.04	Project SUN (Students Understanding Nature) <i>Yanow, G., and A. Herzog</i>	951
C02.05	The CSU-Chill Fully Polarimetric S-Band Weather Radar Facility: Providing Research Experience to Undergraduates <i>Bringi, V.N., and V. Chandrasekar</i>	954
C02.06	Using the World Wide Web for Distributed Learning: Two Examples <i>Skiles, J.W., K.D. Kennedy, W.B. Rundberg, and D.L. Peterson</i>	957
C02.07	"Winds of Change:" The NSCAT CD-ROM <i>Yanow, G.</i>	960
C02.08	Landuse Study of the Sentosa Island Using SPOT Images <i>Zhao, L., F.Y. Tan, W. Quek, P. Chen and S.C. Liew</i>	963

C03: Image Analysis and Information Fusion Technologies

C03.01	Evaluation of Elevation Derived form Interferometric SAR Data with DEM <i>Iwamoto, M., T. Fujisaka, C. Satoh, K. Kawabata and Y. Hara</i>	966
C03.02	Applicability of Category Decomposition for the Fusion of Multi-Resolution Data <i>Takeuchi, S., and A. Inanaga</i>	969
C03.03	Estimation of Topographic Effects in NVI Data Obtained form Satellite Images <i>Kusaka, T., and M. Sakane</i>	972

"NA" indicates not available at time of printing.

C03.04	A Method for Object-Oriented Feature Extraction Hyperspectral Data - Generation of New Channels by Fusion of Data	975
	<i>Fujimura, S., and S. Kiyasu</i>	
C03.05	Bayesian Feature Selection for Classifying Multi-Temporal SAR and TM Data	978
	<i>Yamagata, Y., and H. Oguma</i>	
C03.06	Rainfield Detection Comparison in Small Regions with Particular Microclimatic Characteristics Using Meteosat and SSM/I Navigated Images	981
	<i>Piazza, E., P.F. Pellegrini and M. Tommasini</i>	
C03.07	Terrain Classification of SAR Images by Combined Distributional and Contextual Classifier	NA
	<i>Muller, H.J., and P. Vieira</i>	
C03.08	Automatic Interaction Detector (Aid) Applied on Classified Images	NA
	<i>Ho, L.L., and J.A. Quintanilha</i>	
 <u>C04: Emerging Technologies and Techniques</u>		
C04.01	Meeting Future Landsat Requirements with Emerging Technologies	NA
	<i>Irons, J.R., D.L. Williams and S.G. Unger</i>	
C04.02	Geosynchronous Technology Infusion Studies	984
	<i>Hilliard, L., D. Jenstrom, D. Chesters and P. Racette</i>	
C04.03	Technologies for Future Remote Sensing Systems	987
	<i>Dionisio, C., M. Oricchio and F. Mura</i>	
C04.04	An Outlook for European Spaceborne Synthetic Aperture Radar	990
	<i>Heer, C., S. Mahdi, G. Angino, and A. Torre</i>	
C04.05	Future Operational Spaceborne Synthetic Aperture Radar System Considerations	993
	<i>Velten, E., and C. Heer</i>	
C04.06	The Radar Sail: An Innovative Satellite Concept for Reduced Cost and High Performance Radar Mission	NA
	<i>Aguttes, J.P., J. Sombrin and E. Conde</i>	
C04.07	Next-Generation Coherent Radar Depth Sounder for Measurement of Greenland Ice Sheet Thickness	996
	<i>Legarsky, J., T. Chuah and S.P. Gogineni</i>	
C04.08	A New Airborne Remote Sensing Platform for Acquiring Spatial and Radiation Information	999
	<i>Liu, Z., and S. Li</i>	
 <u>C05: Remote Sensing of Ocean Surface Parameters</u>		
C05.01	Combined High-Resolution Active and Passive Imaging of Ocean Surface Winds from Aircraft	1001
	<i>Gasiewski, A.J., J.R. Piepmeier, R.E. McIntosh, C.T. Swift, J.R. Carswell, W.J. Donnelly, E. Knapp, E.R. Westwater, V.I. Irisov, L.S. Fedor and D.C. Vandemark</i>	
C05.02	High-Resolution Multiband Passive Polarimetric Observations of the Ocean Surface	1006
	<i>Piepmeier, J.R., and A.J. Gasiewski</i>	
C05.03	Multi-Frequency Polarimetric Ocean Wind Direction Retrievals	1009
	<i>Chang, P., P.W. Gaiser, K. St.Germain and L. Li</i>	

C05.04	Satellite Remote Sensing of Air-Sea Energy Fluxes	<i>Schluessel, P.</i>	NA
C05.05	Sea Surface Temperature Estimation Using Active/Passive Microwave Remote Sensing	<i>Wang, N.Y., and J.F. Vesecky</i>	NA
C05.06	Development of a Sea Surface Temperature Algorithm for the ADEOS II/AMSR	<i>Galloway, J., M. Goodberlet and C. Swift</i>	1012
C05.07	A Neural Network Approach to the Determination of Ocean Latent Heat Flux from Multisensor Satellite Data	<i>Gautier, C., P. Peterson and C. Jones</i>	NA
C05.08	Estimation of Ocean Wave Height from Grazing Incidence Microwave Backscatter	<i>Buckley, J.R., and J. Aler</i>	1015
<u>C06: High Resolution 3D SAR</u>			
C06.01	Ramses Interferometer: A Step to High Resolution	<i>Pairault, B., D. Sicard and J.M. Boutry</i>	NA
C06.02	A Comparison of Two Airborne Interferometric SAR Systems	<i>Huelskamp, R.M., D.L. Bickel and D.A. Yocky</i>	NA
C06.03	The JPL Dual Frequency/Dual Baseline Interferometer for Geophysical Topographic Mapping Research	<i>Hensley, S., P. Rosen, E. Rodriguez, E. Chapin, A. Freeman and Y. Kim</i>	NA
C06.04	Calibration of a High Resolution Airborne 3-D SAR	<i>Dall, J., J. Grinder-Pederson and S.N. Madsen</i>	1018
C06.05	The Mount Etna Case Study: A Multisensoric View	<i>Horn, R., K.P. Papathanassiou, A. Reigber, R. Scheiber, P. Hausknecht, P. Strobl, R. Boehl, M. Scheele, R. Reulke, W. Baerwald, G. Puglisi and M. Coltelli</i>	1022
C06.06	Results of the German DO-SAR in C- and X-Band Interferometric	<i>Fritsch, B.</i>	NA
C06.07	An Airborne Radar for High Precision Digital Elevation Model Generation	<i>Moreira, J.R.</i>	NA
C06.08	First Results in 3D SAR Imaging Using a Three Antenna Sensor	<i>Schmitt, K., and W. Wiesbeck</i>	NA
<u>C07: Neural Networks</u>			
C07.01	Feature Extraction for Neural Network Classifiers Using Wavelet and Tree Structured Filter Banks	<i>Sveinsson, J.R., J.A. Benediktsson and O. Hilmarsson</i>	1026
C07.02	Two-Layer Perceptrons for Urban Landuse Classification: Evaluation of Conjugate Gradient Based Learning	<i>Staufer, P., and M.M. Fischer</i>	NA
C07.03	Neural Network-Based Cloud Classification Using Textural Features	<i>Tian, B., M.A. Shaikh, M.R. Azimi-Sadjadi, T.H. Vonder Haar and D. Reinke</i>	NA

"NA" indicates not available at time of printing.

C07.04	Evaluation of the Performance of the Self Organized Feature Map Neural Network Using Various Texture Descriptions for Cloud Detection	NA
	<i>Stephanidis, C.N., T. Parrinello, A.P. Cracknell and R.A. Vaughan</i>	
C07.05	Development of New Automated Land Cover Change Detection System for Remotely Sensed Imagery Based on Artificial Neural Networks	1029
	<i>Dai, X., and S. Khorram</i>	
C07.06	Characterisation of Agricultural Land Using Signal Processing and Cognitive Learning Techniques	1032
	<i>Herries, G.M., and T. Selige</i>	
C07.07	The Implementation of a Fuzzy Self Organised Feature Map Neural Network for Digital Image Classification	NA
	<i>Stephanidis, C.N., and A.P. Cracknell</i>	
C07.08	The Prediction of the Upwelling Phenomenon at the Northwest African Atlantic Coast — A Connectionist Approach	1035
	<i>Kriebel, S.K.T.</i>	
 <u>C08: SAR Speckle Filtering and Classification</u>		
C08.01	Polarimetric SAR Speckle Filtering and Its Impact on Classification	1038
	<i>Lee, J.S., M.R. Grunes and G. De Grandi</i>	
C08.02	The Principles of Polarimetric Filtering	1041
	<i>Quegan, S., and J. Schou</i>	
C08.03	Optimal Bayesian Texture Estimators for Speckle Filtering of Detected and Polarimetric Data	1044
	<i>Lopes, A., J. Bruniquel, F. Sery and E. Nezry</i>	
C08.04	Radar Reflectivity Estimation Using Multiple SAR Scenes of the Same Target: Techniques and Applications	1047
	<i>De Grandi, G.F., M. Leysen, J.S. Lee and D. Schuler</i>	
C08.05	Control Systems Principles Applied to Speckle Filtering and Geophysical Information Extraction in Multi-Channel SAR Images	1051
	<i>Nezry, E., F. Zagolski, I. Supit and F. Yakam-Simen</i>	
C08.06	Multiresolution Adaptive Speckle Filtering: A Comparison of Algorithms	1054
	<i>Aiazzi, B., L. Alparone, S. Baronti and G. Borri</i>	
C08.07	The Application of Wavelet Transform for Speckle Suppression in Radar Imagery	1057
	<i>Dong, Y., B. Forster, A. Milne and C. Ticehurst</i>	
 <u>C09: RADARSAT</u>		
C09.01	RADARSAT Applications Development at CCRS	NA
	<i>Brown, R.J., B. Brisco and M.A. D'Iorio</i>	
C09.02	Use of RADARSAT ScanSAR Products for Regional Mapping in Southeast Asia	1060
	<i>Nazarenko, D.M., G. Mitchell and G.C. Staples</i>	
C09.03	Assessment of RADARSAT Data for Tropical Forest Observations	NA
	<i>Le Toan, T., F. Ribbes, J. Bruniquel, N. Stussi, S.C. Liew, H. Lim, U.R. Wasrin</i>	
C09.04	Using the RADARSAT SAR Versatility to Enhance Fine Resolution Imaging Capabilities	1063
	<i>Luscombe, A.P., D.A. Furseth, S. Srivastava and W.C. Jefferies</i>	

C09.05	Interferometric RADARSAT Data for Topographic Mapping of the Three Gorge Area and Yellow River Delta	NA
	<i>Huadong, G., S. Yun, L. Jingjuan, W. Changling, L. Hao and L. Junfei</i>	
C09.06	Delineating and Mapping Rainfed Dry Direct-Seeded Rice in the Mekong River Delta, Vietnam, Using RADARSAT SAR Imagery	NA
	<i>Kam, S.P., T.P. Tuong, L. Balababa, V.Q. Minh and R. Brown</i>	
C09.07	RADARSAT Image Quality and Calibration Results	1066
	<i>Srivastava, S.K., R.K. Hawkins, T.I. Lukowski, B. Banik and M. Adamvic</i>	
C09.08	A Preliminary Study of Phenological Growth Stages of Wetland Rice Using ERS1/2 SAR Data	1069
	<i>Bakar, S.B.A., A.T. Shaari, H.T. Chuah and H.T. Ewe</i>	
<u>C10: Monitoring Crops and Forests</u>		
C10.01	Application of Radar Remote Sensing in Mapping and Monitoring Tropical Forest Types in Amazon Basin	NA
	<i>Saatchi, S., B. Nelson, A. Freeman and B. Chapman</i>	
C10.02	Effects of Within-Season Dielectric Variations on Terrain Classification Using SIR-C/X-SAR	1072
	<i>Bergen, K., M.C. Dobson, L. Pierce and F. Ulaby</i>	
C10.03	Scale Integration of Bi-Directional Reflectance Effects in Remotely Sensed Vegetated Surfaces	1075
	<i>Burgess, D.W., J.R. Dymond, D. Pariman and J. Shepherd</i>	
C10.04	Airborne SAR in an End-To-End System for Sustainable Forest Management	1078
	<i>Greidanus, H., D.H. Hoekman, R.J.A. Grim and W.J. Looyen</i>	
C10.05	Comparing Accuracy of Satellite and Airborne Remote Sensing Data in the Retrieval of Forest Stand Attributes	1081
	<i>Hyypä, J., M. Inkinen, H. Hyypä, M. Engdahl and M. Hallikainen</i>	
C10.06	Tasseled Cap Transformation and Spectral Angle Mapper Classification of Fujo 1 OPS Data for Winter Cover Monitoring	NA
	<i>Kim, C.</i>	
C10.07	Application of Multitemporal ERS Synthetic Aperture Radar in Delineating Rice Cropping Systems in the Mekong River Delta	1084
	<i>Liew, S.C., S.P. Kam, T.P. Tuong, P. Chen, V.Q. Minh, L. Balababa and H. Lim</i>	
C10.08	Combined ERS SAR and Optical Satellite Data for the Estimation of Forest Structural Attributes	1087
	<i>Kattenborn, G., and E. Nezry</i>	

"NA" indicates not available at time of printing.

IGARSS'97 DIGEST VOLUME III

D01: Soil Moisture I

- | | | |
|--------|---|------|
| D01.01 | Soil Moisture Estimation Under Sparse Vegetation Using Microwave Radiometry at C-Band
<i>Chanzy, A., Y. Kerr, J.P. Wigneron, and J.C. Calvet</i> | 1090 |
| D01.02 | Microwave Remote Sensing of Soil Moisture for Estimation of Soil Properties
<i>Mattikalli, N.M., E.T. Engman, and T.J. Jackson</i> | 1093 |
| D01.03 | Retrieval of Soil Moisture Using a Dynamic Learning Neural Network Trained with a 1-Dimensional Hydrology/Radiobrightness Model
<i>Liou, Y.A., Y.C. Tzeng and A.W. England</i> | 1096 |
| D01.04 | Passive Microwave Observation of Soil Water Infiltration
<i>Jackson, T.J., T.J. Schmugge, W.J. Rawls, P.E. O'Neill and M.B. Parlange</i> | 1099 |
| D01.05 | Land Surface Hydrological Processes Using Satellite Data
<i>Lakshmi, V., and J. Susskind</i> | 1102 |
| D01.06 | Soil Moisture Profile Determination Using Remote Sensing Techniques
<i>Timchenko, A.I., and Y.V. Gorishnya</i> | 1105 |
| D01.07 | Dielectric Model of Bound Water in Wet Soils for Microwave Remote Sensing
<i>Tikhonov, V.V.</i> | 1108 |

D02: Remote Sensing of Precipitation

- | | | |
|--------|---|------|
| D02.01 | Rain/No-Rain Discrimination for TRMM Precipitation Radar
<i>Kumagai, H., T. Kozu and T. Igushi</i> | 1111 |
| D02.02 | Assessment of Multiparameter Radar Rain Rate Algorithms Using an Optimal Area Approach
<i>Bolen, S., V.N. Bringi and V. Chandrasekar</i> | 1114 |
| D02.03 | Non-Uniform Beam Filling Correction for Spaceborne Rain Radar Measurement: A Simulation Study by Using Shipborne Radar Data Over Tropical Pacific
<i>Kozu, T., and T. Iguchi</i> | 1117 |
| D02.04 | Space-Borne Remote Sensing of Cloud Liquid Water Content by Combined Radarmeter
<i>Liu, J., L. Zhang and D. Lu</i> | 1120 |
| D02.05 | Applications of Self-Consistency Principle to Multiparameter Radar Measurements in Rainfall
<i>Scarchilli, G., and E. Gorgucci</i> | NA |
| D02.06 | Attenuation Compensation Technique for an X-Band Polarimetric Weather Radar
<i>Galati, G., G. Pavan and G. Scarchilli</i> | 1123 |
| D02.07 | Dual Polarisation and Multifrequency Measurements of Rain Rate and Drop Size Distribution by Ground-Based Radar and Radiometers
<i>Hornbostel, A., A. Schroth, B.G. Kutuza and A. Evtuchenko</i> | 1126 |
| D02.08 | Indian Doppler Weather Radar System - An Overview
<i>Viswanathan, G., Members of Project Team, R.C. Bhatia, V.P. Kamble and S.R. Rao</i> | 1129 |

H08: Aerosols

- H08.01 The Aerosol Optical Thickness Retrieval from GOME Spectra 1908
Bartoloni, A., M. Mochi, C. Serafini, M. Cervino, R. Guzzi and F. Torricella
- H08.02 Aerosol Optical Thickness Over Ocean Areas and Its Relationship With Cloud Droplet Size 1911
Han, Q., J. Chou, and R.M. Welch
- H08.03 Effects of Atmospheric Aerosol Models on the Single Scattering Point Spread Function in Optical Remote Sensing 1914
Liew, S.C.
- H08.04 Aerosol Retrieval Using Synthetic POLDER Multi-Angular Data 1917
Kuo, K.S., R.C. Weger and R.M. Welch
- H08.05 Aerosol Optical Thickness and Scattering Phase Function Retrieval from Solar Radiances Recorded over Water: A Revised Approach 1920
Paronis, D.K., and J.N. Hatzopoulos
- H08.06 The Long Distance Transport of Sand Dust and Aerosols from Northern China to Hong Kong NA
Fang, M., M. Zheng, K.S. Chim and S.C. Kot
- H08.07 Comparing Optical Models of Atmospheric Aerosol with Results of Multi-Wavelength Laser Sounding NA
Chaikovsky, A.P., A.P. Ivanov, F.P. Osipenko, and V.N. Shcherbakov
- H08.08 Satellite Remote Sensing of Fires, Smoke and Regional Radiative Energy Budgets 1923
Christopher, S.A., M. Wang, K. Barbieri, R.M. Welch and S.K. Yang

H09: Advance Sensors and Sensor Calibration II

- H09.01 Polarimetric Effects in Repeat-Pass SAR Interferometry 1926
Papathanassiou, K.P., and S.R. Cloude
- H09.02 Height Model Generation, Automatic Geocoding and Mosaicing Using of Airborne AES-1 InSAR Data 1929
Holecz, F., J. Moreira, P. Pasquali, S. Voigt, E. Meier and D. Nuesch
- H09.03 Calibration of Airborne AES INSAR Data NA
Holecz, F., J. Moreira and P. Pasquali
- H09.04 InSAR Takes over the Former Roll of Photogrammetry NA
Moreira, J., and F. Holecz
- H09.05 Coherence Optimisation in Polarimetric SAR Interferometry 1932
Cloude, S.R., and K.P. Papathanassiou
- H09.06 The X-Band SAR Demonstrator Development 1935
Zahn, R., H. Braumann and M. Schlott
- H09.07 A Novel Model of the Platform Attitude Drift for SAR 1938
Song, H., M. Zhu and Y. Bai
- H09.08 SIR-C Polarimetric Calibration by Using Polarization Selective Dihedrals and a Polarimetric Active Radar Calibrator 1941
Fujita, M., T. Masuda, Y. Fujino and M. Satake

"NA" indicates not available at time of printing.

D05: Remote Sensing of Mesoscale Features

D05.01	Coastal Wind Field Retrievals from ERS SAR Images <i>Korsbakken, E., J. A. Johannessen and O.M. Johannessen</i>	1153
D05.02	Climatology of Wind and Waves from Satellite Altimeters <i>Hwang, P.A., W.J. Teague and G.A. Jacobs</i>	1156
D05.03	Towards Extracting Fine-Scale Winds from Synthetic Aperture Radar Images <i>Mourad, P.D.</i>	1159
D05.04	Study of Atmospheric Boundary Layer Rolls Near Spitsbergen by Using ERS SAR Images of the Sea Surface and a Numerical Model <i>Alpers, W., G. Muller and B. Brummer</i>	1162
D05.05	COASTWATCH'95: Upper Ocean Features from ERS SAR Imagery <i>Johannessen, O.M., E. Korsbakken, H.A. Espedal, V. Jensen, A.D. Jenkins and J.A. Johannessen</i>	1165
D05.06	Remote Sensing of Estuarine Ocean Fronts During the Chesapeake Bay Outflow Plume Experiment (COPE-1) <i>Trizna, D., M. Sletten, N. Allen, G. Marmarino and T. Donato</i>	NA
D05.07	ERS-1/2 SAR Detection of Natural Film on the Ocean Surface <i>Espedal, H.A., O.M. Johannessen, J.A. Johannessen, E. Dano, D. Lyzenga and J. Knulst</i>	1168
D05.08	Tilting Effect on the Derivation of Wind Speed from Satellite Altimeters <i>Hwang, P.A., W.J. Teague, G.A. Jacobs and D.W. Wang</i>	1171

D06: SAR Image Filters & Non-Bayesian Classification Techniques

D06.01	Automated Hierarchical Classification of SAR Images <i>Smits, P.C., R. Vaccaro and S. Dellepiane</i>	1174
D06.02	Identifying Classes in SAR Sea Ice Imagery Using Correlated Texture <i>Soh, L.K., and C. Tsatsoulis</i>	1177
D06.03	Use of SAR Image Texture in Terrain Classification <i>Dobson, M.C., L. Pierce, J. Kellndorfer and F. Ulaby</i>	1180
D06.04	Efficiency of Bi-Polarization and Correlative Radar-Radiometer System for Detection and Identification of Observed Surfaces Anomalous Formations <i>Arakelian, A.K.</i>	NA
D06.05	Fuzzy Clustering of Textured SAR Images Based on a Fractal Dimension Feature <i>Alparone, L., M. Barni, M. Betti and A. Garzelli</i>	1184
D06.06	A Knowledge Based Approach for Mapping of Road Networks Using GIS Database <i>Forghani, A.</i>	NA
D06.07	Multiresolution Analysis and Processing of Synthetic Aperture Radar Images Using Wavelets <i>Fukuda, S., and H. Hirosawa</i>	1187
D06.08	Suitability of Selected Structural Properties and Relations for Inferring Land Use from an Initial Land Cover Classification of Remotely-Sensed Images <i>Barr, S., and M. Barnsley</i>	NA

D07: Neural Network Applications in Remote Sensing

D07.01	Trends on Information Processing for Remote Sensing	Chen, C.H.	1190
D07.02	Artificial Neural Network-Based Inversion Technique for Extracting Ocean Surface Wave Spectra from SAR Images	Kasilingam, D., and J. Shi	1193
D07.03	Neural Computing for Seismic Principal Components Analysis	Huang, K.Y	1196
D07.04	Filtering Effects on Polarimetric SAR Image Classification	Chen, K.S., Y.C. Tzeng, C.T. Chen and J.S. Lee	1199
D07.05	Training of Neural Networks for Classification of Imbalanced Remote-Sensing Data	Serpico, S.B., L. Bruzzone	1202
D07.06	Land Use Analysis of Remote Sensing Data by Kohonen Nets	Nogami, Y., Y. Jyo, M. Yoshioka and S. Omatu	1205
D07.07	Wind Reconstruction from ERS-1 Scatterometer Data Using Neural Network	Tzeng, Y.C., and K.S.Chen	1208
D07.08	The Application of Artificial Neural Networks and Standard Statistical Methods to SAR Image Classification	Ghinelli, B.M.G., and J.C. Bennett	1211

D08: Satellite and Airborne Missions

D08.01	First Airborne Tests with the New VHF SAR CARABAS II	Gustavsson, A., B. Flood, P.O. Frolind, H. Hellsten, T. Jonsson, B. Larsson, G. Stenstrom and L.M.H. Ulander	1214
D08.02	RADARSAT-1 Background Mission for a Global SAR Coverage	Mahmood, A.	1217
D08.03	The MODIS BRDF/Albedo Product: Prototyping Albedo Retrieval Using AVHRR and GOES	Strahler, A., R. d'Entremont, W.W. Lucht, B. Hu, X. Li and C. Schaaf	1220
D08.04	A Cost-Effective, Airborne Digital Video System for Producing Rectified, Geo-Referenced Digital Images	Kemppinen, M., and T. Auer	1224
D08.05	A Test Site Network for EOS-MODIS Global Land Cover Classification Based on Representativeness Criteria	Muchoney, D., J. Hodges, A. Hyman and A. Strahler	1227
D08.06	First In-Flight Results from POLDER/ADEOS over the Terrestrial Biosphere	Leroy, M., and O. Hautecoeur	1230
D08.07	Activities at the Institute of Industrial Science, University of Tokyo as a Distributed Data Center Via Network	Takagi, M.	NA
D08.08	The Remote Sensing Programme of the German Aerospace Research Establishment (DLR)	Ottl, H.	NA

"NA" indicates not available at time of printing.

D09: Surface Temperature: Observations and Applications

D09.01	Instrumentation for Land Surface Temperature Measurements	<i>Kahle, A.B.</i>	NA
D09.02	Temperature and Emissivity Separation from Advanced Spaceborne Thermal Emission and Reflection Radiometer (ASTER) Images	<i>Gillespie, A.</i>	NA
D09.03	Application of the TES Algorithm to TIMS Data Acquired in HAPEX-Sahel	<i>Schmugge, T., S. Hook and C. Coll</i>	1233
D09.04	Hyperspectral TIR Remote Sensing of Fans and Bedrock Near Yuma, Arizona, USA	<i>Gillespie, A.</i>	NA
D09.05	Potential Interest of a Combined Use of MODIS and ASTER Data for the Determination of Surface Temperature and Emissivity	<i>Becker, F., and Z.L. Li</i>	NA
D09.06	Lithologic Mapping in the Iron Hill, Colorado, USA Area Using Airborne Multispectral Thermal-Infrared Data and Simulated Advanced Spaceborne Thermal Emission and Reflection Radiometer (ASTER) Data	<i>Rowan, L.C., and K. Watson</i>	NA
D09.07	An Overview of Volcanological Application of Infrared Remote Sensing	<i>Realmuto, V.J.</i>	NA
D09.08	ASTER Observations for the Monitoring of Land Surface Fluxes	<i>Schmugge, T.</i>	1236
D09.09	Application of High Resolution Side-Looking MSS Data to Heat Island Potential in Urban Area	<i>Hoyano, A., and A. Iino</i>	1239

D10: Data Standards and Distributions

D10.01	Derivative Analysis of Hyperspectral Data for Detecting Spectral Features	<i>Tsai, F., and W. Philpot</i>	1243
D10.02	Reading SAR Data: A New General Reader and a Proposed New Standard	<i>Pierce, L.</i>	1246
D10.03	Operational Performance of Radarsat's Canadian Data Processing Facility	<i>Jefferies, W.C., D.J. Wilson and R. Periard</i>	NA
D10.04	Standard Data Products from the MODIS Science Team	<i>Fishtahler, L.E.</i>	1249
D10.05	Intelligent Guide to Earth Observation - IGEOs	<i>Zingler, M.</i>	NA
D10.06	Towards a Common Language in Satellite Data Management: A New Processing Level Nomenclature	<i>Gutman, G., and A. Ignatov</i>	1252
D10.07	Innovations in Response to Floods of Data	<i>Ziskin, D.C., and P. Chan</i>	1255
D10.08	A Catalog-Browse System with Quick-Look Images for SPOT, ERS and RADARSAT Data Archives	<i>Kwoh, L.K.</i>	1257

E01: Soil Moisture II

- E01.01 Soil Moisture Estimation with RADARSAT
Brisco, B., T.J. Pultz, R.J. Brown and Q.H.J. Gwyn NA
- E01.02 Estimating Hydrological Parameters with Multifrequency SAR Data
Paloscia, S., G. Macelloni, P. Pampaloni and S. Sigismondi 1260
- E01.03 Profile Soil Moisture Estimation Using the Modified IEM
Walker, J.P., P.A. Troch, M. Mancini, G.R. Willgoose and J.D. Kalma 1263
- E01.04 Examination of Soil Moisture Retrieval Using SIR-C Radar Data and a Distributed Hydrological Model
Hsu, A.Y., P.E. O'Neill, E. F. Wood and M. Zion 1266
- E01.05 A Hybrid Algorithm for Soil Surface Backscattering and Its Use for Soil Moisture Retrieval
Su., Z., P.A. Troch and R. Hoeben NA
- E01.06 Estimation of Soil Moisture for Vegetated Surfaces Using Multi-Temporal L-Band SAR Measurements
Shi, J., G. Sun, A. Hsu, J. Wang, P. O'Neill, J. Ranson and E.T. Engman 1269
- E01.07 On the Retrieval of Soil Moisture Retrieval from SAR Data Over Bare Soils
Pasquariello, G., G. Satalino, F. Mattia, D. Casarano, F. Posa, J.C. Souyris, and T. Le Toan 1272
- E01.08 Soil Moisture Estimation Using SIR-C Data: A Case Study Over Bhavnagar Test Site, India
Rao, K.S., and Y.S. Rao NA

E02: Hydrological Cycle

- E02.01 Global Pattern of Potential Evaporation Calculated from the Penman-Monteith Equation Using Satellite and Assimilated Data
Choudhury, B.J. NA
- E02.02 Precipitation Efficiency, Free-Tropospheric Vapor, and Global Warming
Spencer, R.W., and W.D. Braswell NA
- E02.03 Climatological Features of the East Asian Summer Monsoon Based on Satellite Estimates of Heat Budget and Hydrological Variables
Sohn, B. NA
- E02.04 Passive Microwave Signatures of the Melting Layer in Stratiform Clouds
Bauer, P., J.P.V. Poiares Baptista and M. de Iulio 1275
- E02.05 Atmospheric Latent Heating Distributions Retrieved from SSM/I Passive Microwave Measurements
Smith, E.A., and S. Yang NA
- E02.06 Recent Advances in Observing the Distribution and Variability of Thunderstorms from Space
Goodman, S.J., H.J. Christian, K.T. Driscoll, R.J. Blakeslee, D.J. Boccippio, D.A. Mach, and D.E. Buechler NA
- E02.07 The TRMM Mission
Kummerow, C., J. Simpson, and Y. Hong NA
- E02.08 Linking Passive Microwave Observations to a Summertime LSP/Radiobrightness Model for Northern Prairie Grassland
Judge, J., and A.W. England NA

"NA" indicates not available at time of printing.

E03: Detection of Buried Objects and Voids II

E03.01	Range of Effectiveness of Electromagnetic Detection of Buried Cylindrical Conductors <i>Moses, R.W., J.M. Mack and L.G. Stolarczyk</i>	NA
E03.02	Ultrawideband Radar Detection of Buried Objects <i>Daniels, D.J.</i>	1278
E03.03	Preliminary Field Results of an Ultra-Wideband (10-620 MHz) Stepped-Frequency Ground Penetrating Radar <i>Stickley, G.F., D.A. Noon, M. Cherniakov and I.D. Longstaff</i>	1282
E03.04	Extraction of Discriminant Features from Impulse Radar Data for Classification of Buried Objects <i>Brunzell, H.</i>	1285
E03.05	Radar Detection of Near-Surface Buried Metallic Reflectors in Wet Soil <i>O'Neill, K.</i>	1288
E03.06	Radar Detection of a Void in Lossy Clay Ground <i>Murray, W., C. Williams and C. Lewis</i>	NA
E03.07	The Mapping of Buried Pipes and Cables in a Street Environment <i>Chignell, R.J., H. Dadis and H. West</i>	NA
E03.08	Short-Pulse Ground Penetrating Radar (SP-GPR) for Buried Objects Detecting: Signal Processing and 3-D Mapping <i>Fang, G., Zengyi, J. Guo, C. Wang, Zhanyi, Y. Yuan and X. Chen</i>	NA

E04: Sea Ice Remote Sensing and Applications to Global Change Detection

E04.01	A Comparison of Sea Ice Type, Sea Ice Temperature, and Snow Thickness Distributions in Arctic Seasonal Sea Ice Zones With the DMSP SSMI <i>St.Germain, K., D.J. Cavalieri and T. Marcus</i>	1291
E04.02	Global Sea Ice Cover - Retreating in the North and Advancing in the South <i>Cavalieri, D.J., C.L. Parkinson, P. Gloersen, J.C. Comiso, and H.J. Zwally</i>	NA
E04.03	Results of Satellite and In-Situ Remote Sensing Measurement and Modeling Studies of Arctic Sea Ice Which Support the Monitoring of Changes in the Global Climate <i>Onstott, R.G.</i>	1294
E04.04	SeaSAT Scatterometer Observations of Sea Ice <i>Swift, C.T.</i>	1297
E04.05	Surface Temperatures from 1979 Through 1995 in the Antarctic Region Derived from Satellite Infrared Data <i>Comiso, J.C., and L. Stock</i>	1300
E04.06	Modeling and Interpretation of Ultra-Wideband Microwave Scattering Measurements of Simulated Sea Ice <i>Kanagaratnam, P., S.P. Gogineni and K. Jezek</i>	1305
E04.07	Modeling Interpretation of Active and Passive Measurements from Sea Ice <i>Fung, A.K., and S. Tjuatja</i>	1308

E04.08	The Influence of the Atmosphere on the Remote Sensing of Sea Ice Using Passive Microwave Radiometers <i>Oelke, C.</i>	1311
E04.09	Analysis of Sea Ice Thickness and Mass Estimation with a Spaceborne Laser Altimeter <i>Luntama, J.P., S. Koponen and M. Hallikainen</i>	1314
<u>E05: Hydrodynamic Modeling of Oceanic Interactions</u>		
E05.01	Wave-Breaking Effects in Radar Signatures from 2-Dimensional Modelling of the HI-RES-1 Rip Features <i>Chubb, S.R., A.L. Cooper, R.A. Fusina and R.W. Jansen</i>	1317
E05.02	Intercomparison and Validation of Bathymetry Radar Imaging Models <i>Greidanus, H., C. Calkoen, I. Hennings, R. Romeiser, J. Vogelzang and G.J. Wensink</i>	1320
E05.03	The Bathymetry Assessment System <i>Wensink, G.J., C.J. Calkoen and G.H.F.M. Hesselmans</i>	NA
E05.04	Stress Modulation Account in the Problem of the Wave Spectrum Transformation Caused by Nonuniform Currents <i>Trohkimovski, Y.</i>	1323
E05.05	On the Polarization-Dependent Signatures of Atmospheric and Oceanic Features in Radar Images of the Ocean Surface <i>Romeiser, R.</i>	1326
E05.06	Dynamics and Statistics of Intense Internal Waves Over a Continental Slope <i>Talipova, T., E. Pelinovsky and P.E. Holloway</i>	1331
E05.07	Spectral Nonlinearities of the Gravity-Capillary Waves and Their Effect on Sea Surface Radar Signatures <i>Pavakis, P.J.</i>	1332
E05.08	Radar and Optical Measurements of Damping of Small-Scale Wind Waves in Artificial Slicks <i>Ermakov, S.A., E.M. Zuikova, I.A. Sergievskaya, Yu.B. Shchegolkov, S.V. Kijashko, A.G. Luchinin, J.C. da Silva, N. Stapleton and J.C. Scott</i>	1335
<u>E06: SAR Interferometry: DEM Generation and Assessment</u>		
E06.01	Producing Ground Deformation Maps Automatically: The DIAPASON Concept <i>Massonnet, D.</i>	1338
E06.02	RADARSAT Repeat-Pass SAT Interferometry Results <i>Geudtner, D., and P.W. Vachon</i>	NA
E06.03	A Flexible System for the Generation of Interferometric SAR Products <i>Eineder, M., and N. Adam</i>	1341
E06.04	Operational DEM Generation by Means of SAR Interferometry <i>Herland, E.A., and A. Vuorela</i>	1344
E06.05	Calibrating Interferograms with High-Quality DEMs <i>Seymour, M., and I. Cumming</i>	NA
E06.06	ERS SAR Interferometry: An Operational Evaluation of the DTM Production <i>Dupont, S., P. Nonin, L. Renouard, G. Pichon and M. Berthod</i>	1347

"NA" indicates not available at time of printing.

E06.07	Map Generation Utilizing IFSARE Imagery and Digital Elevation Models from the Intermap STAR-3i System	1350
	<i>Bullock, M.E., G. Lawrence, R.V. Dams and K. Tennant</i>	
E06.08	The AIRSAR/TOPSAR Integrated Multi-Frequency Polarimetric and Interferometric SAR Processor	1358
	<i>van Zyl, J.J., A. Chu, S. Hensley, Y. Lou, Y. Kim and S.N. Madsen</i>	
<u>E07: Terrain Scattering Models and Their Applications</u>		
E07.01	Implementation of the Integral Equation Model for Rough Surfaces with Generic Isotropic Autocorrelation Functions	1361
	<i>Nesti, G., R. Estevan de Quesada, J.M. Lopez and A.J. Sieber</i>	
E07.02	A Reappraisal of the Validity of IEM Model	1365
	<i>Wu, T.D., K.S. Chen, A.K. Fung, Z. Su, P.A. Troch, R. Hoeben and M. Mancini</i>	
E07.03	Sensitivity of Radar Backscattering to Soil Surface Parameters: A Comparison Between Theoretical Analysis and Experimental Evidence	1368
	<i>Hoeben, R., P.A. Troch, Z. Su, M. Mancini and K.S. Chen</i>	
E07.04	Topography Sensing by Polarimetric SAR: Theoretical Basis and Application Using Orthogonal-Pass AIRSAR Data	1371
	<i>De Grandi, G.F., D.L. Schuler, T.L. Ainsworth and J.S. Lee</i>	
E07.05	Interpretation of Radar Measurements from Rough Soil Surface with a Permittivity Profile	1376
	<i>Fung, A.K., J. Boisvert and B. Brisco</i>	
E07.06	Polarimetric Radar Response of Forest Canopies: A Sensitivity Study Based on a Monte Carlo Coherent Model	NA
	<i>Lin, Y.C., and K. Sarabandi</i>	
E07.07	A Successive Approximation Series for TE and TM Scattering from One-Dimensional Conducting Rough Surfaces	1379
	<i>Moyssidis, M.A., C.N. Vazouras, P.G. Cottis and J.D. Kanellopoulos</i>	
<u>E08: Advance Sensors and Sensor Calibration I</u>		
E08.01	Influence of the Radiometer System Parameters and the Frequency Used in the Ground-Based Microwave Measurement of the Atmospheric Water Vapor	NA
	<i>Hashimoto, S., N. Yamashita, and T. Mikami</i>	
E08.02	Radarsat Elevation Antenna Pattern Determination	1382
	<i>Lukowski, T.I., R.K. Hawkins, C. Cloutier, J. Wolfe, L.D. Teany, S.K. Srivastava, B. Banik, R. Jha and M. Adamovic</i>	
E08.03	The Effect of Atmospheric Correction on AVIRIS Data to Obtain Consistent Multiyear Foliage Chemistry Results	1385
	<i>Goetz, A.F.H., K.B. Heidebrecht and B. Kindel</i>	
E08.04	The Airborne X/L-Band SAR System of CRL/NASDA: System Description and Preliminary Results	1389
	<i>Kobayashi, T., M. Satake, H. Masuko, M. Shimada, H. Oaku and T. Umehard</i>	
E08.05	A Study on Radiometric Calibration of Next Generation Spaceborne SAR	1392
	<i>Hara, Y., C. Ohno, M. Iwamoto, N. Kondo, Y. Kamiya and Y. Nemoto</i>	

E08.06	Efficient Technique for Holographic Imaging Diagnostic to Antennas in Cylindrical Near-Field Scanning	NA
	<i>Hussein, Z.A.</i>	
E08.07	ARIES - A Simulator for the Next Generation of Spaceborne IR Meteorological Sounders	1395
	<i>Wilson, S.H.S., N.C. Atkinson, P.J. Rayer, J. Smith and D.R. Pick</i>	
E08.08	Calibration of AVHRR Data Generated by the On-Board TIROS-N Using Ocean and Cloud Views	1398
	<i>Cracknell, A.P., and I. Busu</i>	
E08.09	93 GHz Dual-Channel Airborne Imaging Radiometer (AIR-93) and its Data Examples	NA
	<i>Kemppinen, M., T. Auer, I. Mononen and M. Hallikainen</i>	

E09: Polarimetric and Interferometric Remote Sensing

E09.01	Polarimetry in Remote Sensing: Basic and Applied Concepts	1401
	<i>Boerner, W.M., H. Mott and E. Luneburg</i>	
E09.02	The NASA/JPL Airborne Synthetic Aperture Radar's 1996 Pacrim Deployment	1404
	<i>Lou, Y., Y. Kim, J. van Zyl, L. Maldonado, T. Miller, E. O'Leary, G. Romero, W. Skotnicki and V. Taylor</i>	
E09.03	Littoral Remote Sensing Using Polarimetry SAR	1407
	<i>Lee, J.S., D.L. Schuler, T.L. Ainsworth and L.J. Du</i>	
E09.04	Classification Using Polarimetric and Interferometric SAR-Data	1411
	<i>Hellmann, M., S.R. Cloude and K.P. Papathanassiou</i>	
E09.05	Radar Polarimetry: A New Dimension in Geological Mapping and Exploration Within Australia's Arid and Semi-Arid Lands	NA
	<i>Tapley, I.J.</i>	
E09.06	Texture and Speckle Statistics in Polarimetric SAR Synthesized Images	1414
	<i>De Grandi, G.F., J.S. Lee and D.L. Schuler</i>	
E09.07	Model Based Decomposition in Polarimetric Radar Remote Sensing of Coniferous Forests	NA
	<i>Robin, E. and A. Guissard</i>	
E09.08	A Feature Motivated Sinclair Matrix Sphere-Diplane-Helix Decomposition and its Application to Polarimetric Remote Sensing in Agriculture, Forestry and Hydrology	NA
	<i>Krogager, E., S.R. Madsen and W.M. Boerner</i>	

E10: Remote Sensing Research in Asia

E10.01	Remote Sensing Research in Malaysia	1418
	<i>Mahmood, N.N., K.F. Loh and S. Ahmad</i>	
E10.02	GIS for Natural Disaster Monitoring and Estimation in Mongolia	NA
	<i>Ykhanbai, H., and M. Bayasgalan</i>	
E10.03	Multisource Data Integration for Cartography of Humid Zones and Flooding Risk Evaluation in the Red River Delta, Vietnam	NA
	<i>Cu, P.V., L.A. Tuan, C.X. Huy, J. Simoneau-Coulombe, P. Lafrance, B. Brisco and N.C. Tuyet</i>	

"NA" indicates not available at time of printing.

E10.04	An Overview of Microwave Remote Sensing Research at the University of Malaya, Malaysia	<i>Chuah, H.T.</i>	1421
E10.05	The Use of Satellite Imagery for Monitoring Coastal Environment in Taiwan	<i>Chen, C.F., K.S. Chen, L.Y. Chang and A.J. Chen</i>	1424
E10.06	A Study of Dense Medium Effect in a Simple Backscattering Model	<i>Ewe, H.T., and H.T. Chuah</i>	1427
E10.07	Estimation of Rice Growth Stage Using RADARSAT Data	<i>Yun, S., C. Wang, X. Fan and H. Lim</i>	1430
E10.08	Forest Biodiversity Study in Thailand Using Remote Sensing Techniques	<i>Wara-Aswapati, P., and L. Garcia</i>	NA
E10.09	PACRIM, Deployment of AIRSAR in the Australian-ASEAN Region	<i>Milne, A.K.</i>	1433

IGARSS'97 DIGEST VOLUME IV

F01: Global Monitoring and Remote Sensing for Climate Studies

F01.01	The Earth's Radiation Field: Comparison Between Models and Observations	<i>Arking, A.</i>	NA
F01.02	Observation of the Interactions of Clouds and Radiation from EOS	<i>Barkstrom, B.R.</i>	NA
F01.03	Observation of Global Ocean-Atmosphere Exchanges from Spaceborne Sensors	<i>Liu, W.T.</i>	1435
F01.04	Water Vapor and Cloud Feedback Mechanisms: Inferences from Satellite Observations and Numerical Modeling	<i>Lau, W.K.M.</i>	1438
F01.05	Wavelet Analysis of Satellite Images for Coastal Monitoring	<i>Liu, A.K., S.Y. Wu and W.Y. Tseng</i>	1441
F01.06	Cloud Macrostructure and Radiation	<i>Cahalan, R.F., A. Davis, A. Marshak, D. Silberstein and W. Wiscombe</i>	1444
F01.07	Global Monitoring and Retrievals of Atmospheric Aerosols and Clouds	<i>Tsay, S.C.</i>	1448
F01.08	Effects of Large Structure in Wet Snow Cover on SAR Measurements	<i>Shi, J., R. Kattlemann and J. Dozier</i>	1451

F02: Clouds and Precipitation II

F02.01	Microwave Rainfall Monitoring: A Tuscany Study Case	<i>Nativi, S., M. Padoin, P. Mazzetti, L. Baldini, and D. Giuli</i>	1454
F02.02	Simultaneous Radar and In-Situ Aircraft Based Observations of Convective Storms: Intercomparison Study	<i>Abou-El-Magd, A.M., V. Chandrasekar, V.N. Bringi, and J.W. Strapp</i>	1458

F02.03	Airborne W-Band Radar Measurements of the Doppler Spectrum of Light Precipitation <i>Galloway, J., A. Pazmany, R. McIntosh, D. Leon, J. French, S. Haimov, R. Kelly and G. Vali</i>	1460
F02.04	Development of Model for Predicting the Rainfall Rate Around Singapore Using Radar Reflectivity Measurements <i>Ong, J.T., Y.Y. Shan, T.K. Lim, D. Kasilingam, I.I. Lin and V. Khoo</i>	NA
F02.05	Analysis of the Structure of a Tropical Squall Line, a Stratiform System and a Cyclone Using the NASA Millimeter-Wave Imaging Radiometer (MIR, 89-220 GHz), MODIS Airborne Simulator (MAS, 0.66-13.95 μ m) and Advanced Microwave Moisture Sounder (AMMS, 90-183 GHz) in TOGA/COARE <i>Zhan, J., and J. Wang</i>	NA
F02.06	Tracking the Evolution of Rain Patterns by Mean of Modal Matching <i>Dell'Acqua, F., P. Gamba and A. Marazzi</i>	1463
F02.07	The NASADC-8 Airborne Cloud Radar: Design and Preliminary Results <i>Sadowy, G.A., R.E. McIntosh, S.J. Dinardo, S.L. Durden, W.N. Edelstein, F. Li, A.b. Tanner, W.J. Wilson, T.L. Schneider and G.L. Stephens</i>	1466
F02.08	High Performance Digital Pulse Compression and Generation <i>Mavrocordatos, C., M. Martin-Neira, N. Vincent and N. Suinot</i>	1470
<u>F03: Detection of Buried Objects and Voids III</u>		
F03.01	Microwave Imaging Radar System for Detecting Buried Objects <i>Chen, F.C., and W.C. Chew</i>	1474
F03.02	A High-Resolution Imaging of Objects Embedded in a Lossy Dispersive Medium <i>Sato, T., K. Takemura, and P. Huimin</i>	1477
F03.03	The Influence of Ground Stratification Upon a Field of Magnetic Dipole <i>Dmitriev, W.V.</i>	1480
F03.04	Selection of Optimum Correlation Functions for the Processing of GPR Data for Point Scatterers <i>Detlefsen, J., and D. Felbach</i>	NA
F03.05	Magnetic Dipole Localization with a Gradiometer: Obtaining Unique Solutions <i>Wynn, W.M.</i>	1483
F03.06	Numerical Analysis of Radar Cross-Sections of a Conducting Cylinder in a Strong Turbulent Medium <i>Tateiba, M., and T. Hanada</i>	1486
F03.07	Genetic Algorithm Applied to the Detection of a Buried Conducting Cylinder <i>Shi, S.Y, Y.B. Yan and D.B. Ge</i>	NA
F03.08	Imaging of a Penetrable Object Buried in a Lossy Half-Space for a Multipoint Bistatic Measurement Configuration Above the Interface <i>Lyu, J.W., and J.W. Ra</i>	1489

F04: Data Processing

F04.01	Selection of an Optimum Patch for an Area-Based Stereo Matching Algorithm	<i>Kim, T., and S.D. Choi</i>	1492
F04.02	Visualization of Satellite Derived Time-Series Datasets Using Computer Graphics and Computer Animation	<i>Meisner, R.E., M. Bittner and S.W. Dech</i>	1495
F04.03	Passive Microwaves Protection	<i>Rochard, G.</i>	NA
F04.04	Super Computing of 10-Years HRPT Data Set of AVHRR-Derived SSTs for Analysis	<i>Kawamura, H., F. Sakaida and J.I. Kudo</i>	1499
F04.05	Online Access to Weather Satellite Imagery through the World Wide Web	<i>Emery, W.J.</i>	1502
F04.06	ESA Fire Product: The Algorithm, the Products, the Results, the Operations, the Services, the Plans for the Future	<i>Arino, O., and J.M. Melinotte</i>	NA
F04.07	Operational Generation of AVHRR-Based Level-3 Products at the German Remote Sensing Data Centre: Status and Perspectives	<i>Dech, S.W., R.E. Meisner and P. Tungalagsaikhan</i>	1505
F04.08	Incorporating Remotely-Sensed Land Surface Parameters in a Land Surface Parameterization	<i>Oleson, K.W., P.S. Thames and W.J. Emery</i>	1509
F04.09	A Fast Forward Model for the Satellite Data Assimilation with Numerical Weather Forecasting	<i>Aoki, T.</i>	NA

F05: Remote Sensing of the Ocean by Radar Techniques

F05.01	A Study of the Effect of Swell in Scatterometer Wind Measurements Using SAR Wave Mode Data	<i>Kasilingam, D., I.I. Lin, V. Khoo and L. Hock</i>	1512
F05.02	SAR Imaging of the Ocean Surface: Nonlinearities Simulation and Estimation	<i>Garello, R., and J.M. Le Caillec</i>	1515
F05.03	Observation of Internal Waves in the Andaman Sea by ERS SAR	<i>Alpers, W., W.C. Heng and H. Lim</i>	1518
F05.04	Study of Gulf Stream Features with a Multi-Frequency Polarimetric SAR from the Space Shuttle	<i>Askari, F., S.R. Chubb, T. Donato, W. Alpers and S.A. Mango</i>	1521
F05.05	Effect of Azimuth Bandwidth Spreading on SAR Imaging and SAR Interferometry Over the Ocean	<i>Zhou, B., and D. Kasilingam</i>	1524
F05.06	A Quantitative Study of Tropical Rain Cells from ERS SAR Imagery	<i>Lin, I.I., D. Kasilingam, W. Alpers, T.K. Lim, H. Lim and V. Khoo</i>	1527
F05.07	Signature of the Gulf Stream in Wavebreaking Field Observations	<i>Dulov, V., V. Kudryavtsev, S. Grodsky and O. Sherbak</i>	NA
F05.08	Experimental Investigation of Doppler Spectra of Microwave Signals Backscattered from Sea Slicks	<i>Kanevsky, M.B., S.A. Ermakov, E.M. Zuikova, V.Y. Karaev, V.Y. Goldblat, I.A. Sergievskaya, Y.B. Shchegol'kov, J.C. Scott and N. Stapleton</i>	1530

F06: SAR Interferometry: Systems and Applications

- F06.01 Probing the Ultimate Capabilities of Radar Interferometry for Deformation with Low Gradient: A New Mission? 1533
Massonnet, D., and F. Adragna
- F06.02 Reduction of the Phase-Unwrapping Drawbacks by the Three-Antenna Interferometric SAR System 1536
Corsini, G., M. Diani, F. Lombardini and G. Pinelli
- F06.03 A Comparison of Interferometric Radar Ocean Surface Velocity Measurements to Subsurface Current Structure 1539
Moller, D., D.L. Porter, S. Frasier and R. McIntosh
- F06.04 The Use of Man-Made Features for Long Time Scale INSAR 1542
Usai, S.
- F06.05 The Effect of Scattering from Buildings on Interferometric SAR Measurements 1545
Bickel, D.L., W.H. Hensley and D. A. Yocky
- F06.06 Quality Assessment of Coherence Between 35-Day and Tandem Modes in ERS-1/2 Interferometric Studies 1548
Stussi, N., S.C. Liew, K. Singh, L.K. Kwok and H. Lim
- F06.07 Quantitative Analysis of Atmospheric Effects on ERS Interferometric SAR Data NA
Kenyi, L.W., and H. Raggam
- F06.08 Combination of Linear and Circular SAR for 3D Features 1551
Rudolf, H., D. Tarchi and A.J. Sieber
- F06.09 Results of the Mt. Etna Interferometric E-SAR Campaign 1554
Coltelli, M., G. Fornaro, G. Franceschetti, R. Lanari, A. Moreira, G. Puglisi, E. Sansosti, R. Scheiber and M. Tesaro

F07: Tropical Forest Monitoring

- F07.01 Detecting Change in Equatorial Regions of Brazil Using Medium Resolution Satellite Imagery 1557
Emmett, C.F., R.R. Jensen, P.J. Hardin and D.G. Long
- F07.02 Deforestation Monitoring in Tropical Regions Using Multitemporal ERS/JERS SAR and INSAR Data 1560
Ribbes, F., T. Le Toan, J. Bruniquel, N. Floury, N. Stussi, S.C. Liew and U.R. Wasrin
- F07.03 Reconstructed Imagery for Equatorial Monitoring: Combining AVHRR with Reconstructed NSCAT 1563
Hardin, P.J., D.G. Long and R.R. Jensen
- F07.04 BRDF Behavior of a Tropical Forest Surveyed from Space 1566
Gastellu-Etchegorry, J.P., V. Demarez, V. Trichon, D. Ducrot and F. Zagolski
- F07.05 Spectral and Textural Features of Amazon Rain Forests Obtained from Landsat-TM NA
Chen, S.C., and R. Herz
- F07.06 Remote Sensing and GIS Tools to Support Vegetation Fire Management in Developing Countries 1569
Flasse, S.P., P. Ceccato, I.D. Downey, M.A. Raimadoya and P. Navarro
- F07.07 Mapping Forest Fragments in Atlantic Coastal Moist Forest of Bahia, Brazil: A Case Study for Conservation and Biodiversity NA
Saatchi, S., K. Alger, S. Filoso, C. Alves, C.A. Mesquita and R. Rice
- F07.08 Identifying and Monitoring Change in Wetland Environments Using SAR 1573
Milne, A.K.

"NA" indicates not available at time of printing.

F08: Interferometric and Differential Interferometric SAR

- F08.01 A Study of the Rainforests of borneo by the JERS-1 Repeat-Pass InSAR NA
Ouchi, K., S. Takeuchi, Y. Suga, C. Yonezawa, I.B. Ipor and S. Maedoi
- F08.02 SAR Interferometry for the Study of Earth Crust Movement and Topography NA
Rao, K.S., and Y.S. Rao
- F08.03 Terrain Elevations from InSAR Incorporating Ground Control Data 1576
Mirbagheri, M., J.C. Trinder and B.C. Forster
- F08.04 Improved Digital Elevation Models Via Multi-Baseline Interferometric SAR 1579
Homer, J., I.D. Longstaff and Z. She
- F08.05 SAR Data Processing for Interferometry Using a Personal Computer 1582
Omura, M., K. Koike, K. Doi and S. Aoki
- F08.06 Development of JERS-1 SAR Interferometry Software Set NA
Ono, M.
- F08.07 Fault Model of 1995 Neftegorsk, Northern Sakhalin, Earthquake Based on Crustal Deformation Detected by JERS-1/SAR Interferometry 1585
Nakagawa, H., M. Tobita, S. Fujiwara, S. Ozawa, K. Nitta, M. Murakami, M. Murakami, M. Shimada and P.A. Rosen
- F08.08 Multi Baseline SAR Interferometry for Automatic DEM Reconstruction NA
Ferretti, A., A. Monti Guarnieri, C. Prati and F. Rocca

F09: PS-PR Polarimetric Propagation and Scattering, Sounding and Radiometry

- F09.01 Optimum Antenna Elevation for HF Surface Wave Radars NA
Anderson, S.J., G.J. Frazer and G.M. Warne
- F09.02 Synthetic Aperture Radar Image Reconstruction Algorithms Designed for Subsurface Imaging 1588
Gough, P.T., and B.R. Hunt
- F09.03 On the Proper Polarimetric Scattering Matrix Formulation of the Forward Propagation Versus Backscattering Radar Systems Description 1591
Luneburg, E., S.R. Cloude and W.M. Boerner
- F09.04 HF Skywave Radar Measurements of Wind and Sea Condition in the SE Asian Region NA
Anderson, S.J.
- F09.05 Scattering and Cascading Matrices of the Lossless Reciprocal Polarimetric Two-Port Microwave Versus Millimeter-Wave Optical Polarimetry NA
Czyz, Z.H., and W.M. Boerner
- F09.06 Determination of Propagation Parameters from Fully Polarimetric Radar Data 1594
Santalla del Rio, V., and Y.M.M. Antar
- F09.07 A Low Cost Polarimetric Radiometer for Real Time Stokes Parameter Measurements 1597
Lahtinen, J., and M. Hallikainen
- F09.08 Volume Scattering Properties of Glass Particles as a Function of Size and Absorption Coefficient 1600
Betty, C.L., A.K. Fung and S. Tjuatja

F10: Surface Backscatter Modeling

F10.01	Modeling of Extremely Heterogeneous Radar Backscatter	Muller, H.J.	1603
F10.02	Electromagnetic Scattering and Fractal Analysis of Bare Soil Surfaces <i>Rouvier, S., E. Bachelier, P. Borderies, I. Chenerie, J.C. Souyris, T. Le Toan and M. Borgeaud</i>		1606
F10.03	Investigation of Surface Scattering Mechanisms by Means of High Resolution SAR Imaging <i>Tarchi, D., G. Nesti and A.J. Sieber</i>		NA
F10.04	Semi-Rough Surface Scattering and Its Fading Effects for Active Microwave Sensors <i>Wu, J., J. Jiang and L. Wang</i>		1609
F10.05	Empirical and Theoretical Backscattering Behavior as a Function of Roughness for Arid Land Surfaces <i>Remond, A., and J.P. Deroin</i>		1612
F10.06	Simulation of Unpolarized Scattering in Synthetic Aperture Radar Images <i>Tomiyasu, K.</i>		1615
F10.07	3-D Landscapae Modeling Using High Resolution Data <i>Lavoie, P., D. Ionescu and K.B. Fung</i>		NA
F10.08	Modelling and Experimental Study of Scattering from a Heterogeneous Random Medium Embedded with Seeds <i>Nedeltchev, N.M., J.C. Peuch and H. Baudrand</i>		NA

G01: Soil and Vegetation Biophyscial Properties I

G01.01	On the Retrieval of Rice Crop Parameters from ERS, JERS and RADARSAT Data <i>Le Toan, T., F. Ribbes, N. Floury, L. Wang, K.H. Ding and J.A. Kong</i>		NA
G01.02	Relating Vegetation Aerodynamic Roughness Length to Interferometric SAR Measurements <i>Saatchi, S., and P. Siqueira</i>		NA
G01.03	Assesement of ERS-1/2 Interferometric Data for Soil Moisture Estimation <i>Souyris, J.C., T. Le Toan, O. Casamian, F. Mattia, E. Bachelier, F. Borderies, I. Chenerie and M. Borgeaud</i>		NA
G01.04	A Vegetation Classification Scheme Validated by Model Simulations <i>Ferrazzoli, P., L. Guerreiro and G. Schiavon</i>		1618
G01.05	The Role of Frequency and Polarization in Terrain Classification Using SAR Data <i>Dobson, M.C., L.E. Pierce and F.T. Ulaby</i>		1621
G01.06	Mapping Vegetation Structure for Biodiversity Analysis Using Synthetic Aperture Radar <i>Imhoff, M.L., A.K. Milne, T.D. Sisk, W.T. Lawrence and K. Brennan</i>		1624
G01.07	Relationship Between Surface Temperature Diurnal Range and Vegetation Cover as Derived from Meteorological Satellite <i>Gutman, G.</i>		NA

"NA" indicates not available at time of printing.

- G01.08 Comparative Assessment of Multisensor Data for Suitability in Study of the Soil Salinity Using Remote Sensing and GIS in the Fordwah Irrigation Division, Pakistan 1627

Ahmed, I., and H.H. Andrianasolo

- G01.09 Scientific Visualization of Drought-Related Famine Conditions in Sudan: An Approach to Temporal and Spatial Analysis of Remotely-Sensed Multi-Spectral Data NA

Rochon, G.L.

G02: TRMM Precipitation Radar: Its Algorithm and Validation

- G02.01 Development Results of TRMM Precipitation Radar 1630

Oikawa, K., T. Kawanishi, H. Kuroiwa, M. Kojima and T. Kozu

- G02.02 Rain Type Classification Algorithm for TRMM Precipitation Radar 1633

Awaka, J., T. Iguchi, H. Kumagai and K. Okamoto

- G02.03 Rain Profiling Algorithm for the TRMM Precipitation Radar 1636

Iguchi, T., T. Kozu, R. Meneghini and K. Okamoto

- G02.04 Effects of Non-Uniform Beam-Filling on TRMM PR Rainfall Measurements 1639

Durden, S.L., Z.S. Haddad, A. Kitiyakara and F.K. Li

- G02.05 Bayesian Fusion of TRMM Passive and Active Measurements 1642

Haddad, Z.S., S.L. Durden and E. Im

- G02.06 Simultaneous Observation of a Rain Event Using the MU Radar and an Airborne Doppler Radar for Simulating TRMM Ground Validation 1645

Sato, T., R. Peng, H. Hanado and H. Horie

- G02.07 Radar Measurements from Papua New Guinea and Their Implications for TRMM PR Retrieval Algorithm 1648

Ladd, D.N., C.L. Wilson and M. Thurair

- G02.08 The Dual Beam Airborne Technique as a Tool for Validation of the TRMM Rain Radar Retrieval 1651

Testud, J., and S. Oury

G03: Data Fusion II

- G03.01 A Comprehensive Data Management and Fusion System for Multi-Band Imaging Systems and Associated Data 1654

Cooley, T., L. Standley and J. Erickson

- G03.02 An MSOM Framework for Multi-Source Fusion and Spatio-Temporal Classification 1657

Wan, W., and D. Fraser

- G03.03 Urban Land Use Mapping with Multi-Spectral and SAR Satellite Data Using Neural Networks 1660

Heikkonen, J., I. Kanellopoulos, A. Varfis, A. Steel and K. Fullerton

- G03.04 Multisource and Multisensor Data in Land Cover Classification Tasks: The Advantage Offered by Neural Networks 1663

Chiuderi, A.

- G03.05 Fusion of Optical and Microwave Remote Sensing Data for Vegetation Studies NA

Qi, J., M.S. Moran and E.E. Sano

G03.06	Combining Structural and Spectral Information for Discrimination Using Pulse Coupled Neural Networks in Multispectral and Hyperspectral Data	1666
	<i>Cooley, J.H., and T.W. Cooley</i>	
G03.07	Classification of Hyperdimensional Data Using Data Fusion Approaches	1669
	<i>Benediktsson, J.A., and J.R. Sveinsson</i>	
G03.08	A Self-Organizing Map Based on Framework for Data Fusion II	NA
	<i>Wan, W., and D. Fraser</i>	
G03.09	Application of Fuzzy Logic for Integration of SIR-C and Geological Exploration Data for Base Metal Exploration in Hwang-Gang-Ri District, Korea	NA
	<i>Jiang, W.W., C.S. So, S.K. Choi, L. Feng and W.M. Moon</i>	
 <u>G04: Sea Ice, Climate and Weather Applications in Polar Region</u>		
G04.01	The Origin and Evolution of Sea-Ice Anomalies in the Beaufort Sea	NA
	<i>Tremblay, B., and L.A. Mysak</i>	
G04.02	Determination of the Dominant Spatial Modes of Terrestrial Snow Cover Over North America Using Passive Microwave Derived Data	1672
	<i>LeDrew, E., C. Derksen and B. Goodison</i>	
G04.03	Microwave Measurements of Sea Ice in the Kara and Laptev Sea	1675
	<i>Johnsen, K.P., A. Darovskikh, G. Heygster and A. Wiesmann</i>	
G04.04	Identification of Clear-Sky Sea-Ice Albedo Feedbacks with Advanced Very High Resolution Radiometer Data	NA
	<i>De Abreu, R., and E. LeDrew</i>	
G04.05	First Realtime Use of RADARSAT SAR Imagery for Ship Navigation in Antarctica	1678
	<i>Danduran, P., M.C. Mouchot, R. Garello, D. Fleury and I. Thepaut</i>	
G04.06	ICEWATCH - Real-Time Sea Ice Monitoring of the Northern Sea Route Using Satellite Radar Techniques	1681
	<i>Johannessen, O.M., S. Sandven, L.H. Pettersson, K. Kloster, T. Hamre, J. Solhaug, A.M. Volkov, V. Asmus, O.E. Milekhin, V.A. Krovotytsev, V.D. Grischenko, V.G. Smirnov, L.P. Bobylev, V.V. Melentyev and V. Alexandrov</i>	
G04.07	Comparison of Cloud Parameters and Downwelling Radiative Fluxes over Sea Ice Computed from TOVS and AHHRR	NA
	<i>Schweiger, A., J. Francis, J. Key and D. Lubin</i>	
G04.08	Sea Ice Concentration in Response to Weather Systems in the Weddell Sea: Comparison Between SSM/I Data and Model Simulations	1686
	<i>Fischer, H., and C. Oelke</i>	
G04.09	Design and Development of an Operational Sea Ice Mapping System for Meteorological Applications in the Antarctic	1689
	<i>Williams, R.N., P. Crowther and S. Pendlebury</i>	

"NA" indicates not available at time of printing.

G05: Sea Surface Modelling

- G05.01 Beyond the Two-Scale Composite Backscatter Model for Modelling Radar Return from the Ocean Surface NA
Chubb, S.R., A.L. Cooper and G.M. Nedlin
- G05.02 Microwave Scattering from a Slightly Rough Surface of a Medium Possessing a Finite Large Dielectric Constant, and Application to an Air-Water Scattering 1692
Nedlin, G.M., S.R. Chubb and A.L. Cooper
- G05.03 On Combining Satellite Altimetry Data With Models in Improving the Simulation of Ocean Circulation NA
Fu, L.L.
- G05.04 Ocean Wave-Radar Modulation Transfer Function: A Nonlinear System Modelling Approach NA
Bao, M., and A. Schmidt
- G05.05 Validation of Wave Model Using ERS Altimeter and SAR Wave Mode Data 1695
Zhang, R., T.K. Lim, D. Kasilingam, I.I. Lin, and V. Khoo
- G05.06 On the Cross Spectrum Between Individual-Look Synthetic Aperture Radar Images of Ocean Waves NA
Bao, M., and W. Alpers
- G05.07 Studying the Monsoon Circulation in the Indian Ocean Using Altimeter Data 1698
Jensen, V.E., P. Samuel and O.M. Johannessen
- G05.08 Ekman Heat Transport Estimated by Using Microwave Scatterometer Data NA
Kubota, M., A. Tamada and H. Yokota

G06: SAR Interferometry: Simulation and Noise Reduction

- G06.01 Efficient Simulation of SAR Interferometric Raw Signal Pairs 1701
Franceschetti, G., A. Iodice, M. Migliaccio and D. Riccio
- G06.02 Simulator for Repeat-Pass Satellite InSAR Studies 1704
Xu, W., and I. Cumming
- G06.03 High Doppler Centroid CSA Based SAR Raw Data Simulator NA
Carrasco, D., J. Closa and A. Broquetas
- G06.04 Optimization of SAR Interferogram by Using Coherence Information 1707
Yonezawa, C., and S. Takeuchi
- G06.05 Decorrelation by Interpolation Errors in InSAR Processing 1710
Bamler, R., and R. Hanssen
- G06.06 An Interferometric SAR Processor Avoiding Phase Ambiguities 1713
Schmitt, K., and W. Wiesbeck
- G06.07 Processing Low Noise Interferograms from ERS1 - SLC Radar Images NA
Michel, R., J.P. Avouac and J. Taboury
- G06.08 Suppressing the Noise of Single-Look InSAR Interferogram with Wavelet Analysis NA
Tang, J., and Z.S. Wang
- G06.09 A New Technique for Noise Filtering of SAR Interferogram Phase Images 1716
Lee, J.S., K.P. Papathanassiou, T.L. Ainsworth, M.R. Grunes and A. Reigber

G07: Ecosystem Studies with Microwave Remote Sensing

- G07.01 Toward Consistent Global Physiognomic Vegetation Mapping Using ERS/JERS SAR Classification 1719
Kellndorfer, J.M., M.C. Dobson and F.T. Ulaby
- G07.02 Agro-Ecosystem Monitoring in Canada with RADARSAT NA
Brown, R.J., B. Brisco, T. Huffman, T. Hirose and D. Major
- G07.03 Effect of Environmental Temperatures on SAR Forest Biomass Estimates 1722
Ranson, K.J., and G. Sun
- G07.04 Enhanced Flood Mapping Using ERS SAR Interferometric Data: An Example in South France NA
Beaudoin, A., L. Marinelli, R. Michel, and J. Astier
- G07.05 The Global Rain Forest Mapping - An Overview NA
Rosenqvist, A., M. Shimada, B. Chapman and G. De Grandi
- G07.06 The ERS-1 Central Africa Mosaic: A New Role for Radar Remote Sensing in Global Studies of the Tropical Ecosystem 1725
Malingreau, J.P.G., G. De Grandi, M. Leysen, P. Mayaux and M. Simard
- G07.07 Land Cover Type and Forest Biomass Assessment in the Colombian Amazon 1728
Hoekman, D.H., and M.J. Quinones
- G07.08 Radar Monitoring for Sustainable Forest Management in Indonesia 1731
Hoekman, D.H.
- G07.09 Tabular Summary of SIR-C/X-SAR Results: Synthetic Aperture Radar Frequency and Polarization Requirements for Applications in Ecology and Hydrology 1734
Schmullius, C.C., and D.L. Evans

G08: Remote Sensing of Clouds and Aerosols

- G08.01 Airborne Millimeter-Wave Radiometric Observations of Cirrus Clouds 1737
Wang, J.R., and P. Racette
- G08.02 Application of Space Lidar to the Remote Sensing of Clouds and Aerosols 1740
Winker, D.M.
- G08.03 Ground-Based Validation of the EOS Multiangle Imaging SpectroRadiometer (MISR) Aerosol Retrieval Algorithms and Science Data Products 1743
Conel, J.E., W.C. Ledeboer, S.H. Pilorz, J.V. Martonchik, R. Kahn, W. Abdou, C. Bruegge, M.C. Helmlinger and B.J. Gaitley
- G08.04 LITE Aerosol Retrievals 1749
Reagan, J.A., and H. Liu
- G08.05 Lidar Measurements of Stratospheric Aerosol Over Hefei, China During 1990-1996 NA
Hu, H., and J. Zhou, and Y.W. Anhui
- G08.06 A New Method for Detection of Absorbing Aerosols (Dust and Smoke) from TOMS Data NA
Herman, J.R., C. Hsu, O. Torres, P.K. Bhartia and M. Schoeberl
- G08.07 Non-Rayleigh Scattering Applied to Hydrometeor Size Estimation 1753
Sekelsky, S.M., R.E. McIntosh, W.L. Ecklund and K.S. Gage

"NA" indicates not available at time of printing.

G08.08 Modified Gamma Model for Singapore Rain Drop Size Distribution *Ong, J.T., and Y.Y. Shan* 1757

G08.09 Relationship Between Cirrus Particle Size and Cloud Top Temperature *Han, Q., J. Chou, and R.M. Welch* 1760

G09: Accuracy Assessment Issues in Remote Sensing

G09.01 A Review of Sampling Strategies for Determining the Accuracy of Change Maps *Biging, G.S., and R.C. Congalton* NA

G09.02 Techniques for Managing Errors Associated with Geometric and Attribute Data Derived from Remote Sensing Sensors *Karimi, H.A., and M.A. Chapman* NA

G09.03 Application of Adaptive Sampling in the Assessment of Accuracy of Landcover Maps Developed from Remotely-Sensed Data *Colby, D.R.* NA

G09.04 Earth Observation in Understanding Terrestrial Dynamics *Clandillon, S., N. Tholey and K. Fellah* NA

G09.05 Quantification of the Impact of Misregistration on the Accuracy of Remotely Sensed Change Detection *Dai, X., and S. Khorram* 1763

G09.06 Assessing the Accuracy of High Spatial Resolution Image Data and Derived Products *Stow, D., A. Hope, S. Phinn, A. Brewster and B. Bradshaw* 1766

G09.07 NOAA's Coastal Change Analysis Program (C-CAP): Field Verification *Dobson, J.E.* NA

G09.08 Accuracy Assessment Issues for Global Data: Lessons form the Grass Global CD-Rom Project *Madry, S.* NA

G09.09 An Introduction to Using Generalized Linear Models to Enhance Satellite-Based Change Detection *Morisette, J.T., and S. Khorram* 1769

G10: IRS-1C Data Products and Applications

G10.01 A Total Solution Approach Using IRS-1C and IRS-P3 Data *Jayaraman, V., and M.G. Chandrasekhar* NA

G10.02 Role of NIC in RS and GIS Applications A Case Study: Srirama Sagar Command Area *Rao, N.V.K.* NA

G10.03 Image Classification and Performance Evaluation of IRS 1C LISS-III Data *Muralikrishna, I.V.* 1772

G10.04 IRS-1C Applications for Land Use/Landcover Mapping, Change Detection and Planning *Gautam, N.C.* 1775

G10.05 IRS-1C Applications for Forest Resources Assessment *Dutt, C.B.S.* NA

G10.06	IRS IC's LISS-III Data Application Potential in Coastal Studies	NA
	<i>Krishnamoorthy, R., I. Gnappazham and V. Selvam</i>	
G10.07	Contrast Enhancement of IRS - 1C LISS Sensors	1778
	<i>Ramesh Babu, I., and I.V. Murali Krishna</i>	
G10.08	IRS-1C Data Applications	NA
	<i>Rao, P.S., G. Chandrasekhar and V.R. Hegde</i>	
G10.09	Operationalisation of New Tehcnology - A Case Study of IRS-1C Application	NA
	<i>Rao, T.G., and G.S. Kumar</i>	

H01: Soil and Vegetation Biophysical Properties II

H01.01	Angular Signatures of NASA/NOAA Pathfinder AVHRR Land Data and Applications to Land Cover Identification	1781
	<i>Liang, S., and J.R.G. Townshend</i>	
H01.02	Spatial Assessment of Soil Properties for Agricultural Land Using Remotely Sensed Imagery, Relief Analysis and GIS	1784
	<i>Selige, T.M.</i>	
H01.03	A Modelling Study of BRDF Canopy and Radiation Regime for Boreal Forests	1787
	<i>Zagolski, F., P. Guillevic, J.P. Gastellu-Etchegorry, C. Gaillard, D. Deering and M. Leroy</i>	
H01.04	Ground Reflectance and Albedo Extracted from NOAA-AVHRR Time-Series in a Topographically Complex Terrain	NA
	<i>Eibl, B., and W. Mauser</i>	
H01.05	Estimation of Surface Reflection Parameters Over Lands Using Linear Polarization Data by Airborne POLDER	1790
	<i>Takemata, K., and Y. Kawata</i>	
H01.06	Radiometric Estimates of Grain Yields Related to Crop Aboveground Net Production (ANP) in Paddy Rice	1793
	<i>Hong, S., J. Lee, S. Rim and J. Shin</i>	
H01.07	Passive Microwave Technology of Rice Crop Fields Monitoring at the Different Stages of Vegetation	NA
	<i>Yazerian, G.G., A.M. Shutko and E.P. Vorobeichick</i>	
H01.08	A Simple Model for the Estimation of Biomass Density of Regenerating Tropical Forest Using JERS-1 SAR and Its Application to Amazon Region Image Mosaics	1796
	<i>Luckman, A., and J. Baker</i>	

H02: Fluorescent Measurements in Remote Sensing

H02.01	New Instrumentation for Plant/Crop Monitoring Uses Fluorescence Imaging and Image Processing to Detect Pre-Symptomatic Plant Stress	NA
	<i>Lussier, R.R.</i>	
H02.02	Time Resolved Laser Induced Flourescence Spectroscopy of Chemicals and Phytoplankton in Waters	NA
	<i>Vebe, U., J. Kubitz, J. Wienke and A. Anders</i>	

"NA" indicates not available at time of printing.

H02.03	Flourescence and Reflectance Spectral Response of Crop Residue for Assessing Erosion Control and Analysis of Previous Crop Condition <i>McMurtrey, J.E., M.S. Kim, E.W. Chappelle, L.A. Corp and C.S.T. Daughtry</i>	NA
H02.04	Laser Induced Imaging of Blue/Red and Blue/Far-Red Fluorescence Ratios, F440/F690 and F440/F740, as a Means of Early Stress Detection in Plants <i>Lichtenthaler, H.K., N. Subhash, O. Wenzel and J.A. Miehe</i>	1799
H02.05	Non-Destructive Detection of Increased Tropospheric Ozone Carbon Dioxide Effects on Crops with Fluorescence Imaging System <i>Kim, M.S., C.L. Mulchi, C.S.T. Daughtry, E.W. Chappelle, J.E. McMurtrey and L.A. Corp</i>	NA
H02.06	Characterization of Soybean Flavonol Isolines with Fluorescence Imaging <i>Kim, M.S., E. Lee, C.L. Mulchi, J.E. McMurtrey and E.W. Chappelle</i>	NA
H02.07	Applications of Fluorescence Imaging and Spectal Measurements to the Remote Assessment of Plant Nitrate Supply <i>Corp, L.A., E.W. Chappelle, J.E. McMurtrey and M.S. Kim</i>	NA
H02.08	Bark and Leaf Fluorescence as Potential Tool in Remote Sensing: A Reflection of Some Aspects of Problems in Comparative Analysis <i>Kharouk, V.I.</i>	NA
<u>H03: HF Radar Remote Sensing</u>		
H03.01	Over-the-Horizon Radar: Ground-Based Ocean Remote Sensing on Basin-Wide Scales <i>Georges, T.M., and J.A. Harlan</i>	1802
H03.02	A Study of SeaSonde Bearing and Signal Stability Using Transponder Measurements <i>Barrick, D.E., and J.D. Paduan</i>	NA
H03.03	A Comparison of Surface Current Fields Derived by Beam Forming and Direction Finding Techniques as Applied by the HF Radar WERA <i>Gurgel, K.W., G. Antonischki and T. Schlick</i>	1805
H03.04	Initial Observations of Ocean Currents and Current Shears, Wind Direction Using Multifrequency HF Radar <i>Teague, C.C., J.F. Vesecky, P.E. Hansen, N.G. Schnepf, J.M. Daida, R.G. Onstott, K. Fischer and D.M. Fernandez</i>	1808
H03.05	Observations of Near-Surface Currents at Varying Depths Using a New Multifrequency HF Radar <i>Vesecky, J.F., C.C. Teague, R. Onstott, P. Hansen, N. Schnepf, D. Fernandez, J. Daida and K. Fischer</i>	1811
H03.06	Two-Dimensional Diurnal to Monthly Period Surface Currents in Monterey Bay from CODAR-Type HF Radar <i>Paduan, J.D., M.S. Cook and D.M. Fernandez</i>	1814
H03.07	Coastal Near-Inertial Wave Bursts Detected by OSCAR <i>Shay, L.K.</i>	1817
H03.08	Measurement of Surface Current Fields with High Spatial Resolution by the HF Radar WERA <i>Gurgel, K.W., and G. Antonischki</i>	1820

H04: Scatterometer Applications

- H04.01 Snow Accumulation on Greenland Estimated from ERS Scatterometer Data 1823
Wismann, V., D.P. Winebrenner, K. Boehnke and R.J. Arthern
- H04.02 Thawing Processes During Siberian Spring Observed by ERS Scatterometer and SAR 1826
Boehnke, K., and V. Wismann
- H04.03 Assessment of Scatterometer Data for Environmental Studies in Thar Desert 1829
Stephen, H., R.L.G. Schumann, K. Honda and K. Nualchawee
- H04.04 Observations and Simulations of the ERS Wind Scatterometer Response over a Sahelian Region 1832
Frison, P.L., E. Mougin and P. Hiernaux
- H04.05 Characterizing Earth's Surface Using Moderate Resolution 14 Ghz Scatterometer Imagery: Early Results 1835
from NSCAT Reconstruction
Hardin, P.J., D.G. Long, R.R. Jensen
- H04.06 Ice Classification in the Southern Ocean Using ERS-1 Scatterometer Data 1838
Early, D.S., and D.G. Long
- H04.07 Automated Antarctic Ice Edge Detection Using NSCAT Data 1841
Remund, Q.P., and D.G. Long
- H04.08 Enhanced Resolution Imaging from Irregular Samples 1844
Early, D.S., and D.G. Long

H05: Radar Measurements of Ocean Winds

- H05.01 Wind Field Models and Model Order Selection for Wind Estimation 1847
Brown, C.G., P.E. Johnson, S.L. Richards and D.G. Long
- H05.02 A Neural Network-Based Model for Estimating the Wind Vector Using ERS Scatterometer Data 1850
Kasilingam, D., I.I. Lin, V. Khoo and L. Hock
- H05.03 On a New Relationship Between Radar Cross Section and Wind Speed Using ERS-1 Scatterometer Data and 1853
ECMWF Analysis Data Over the Mediterranean Sea
Migliaccio, M., P. Colandrea, A. Bartoloni and C. D'Amelio
- H05.04 Backscatter Observed in C-Band and Ku-Band Scatterometer Data 1856
Johnson, P.E., and D.G. Long
- H05.05 An Aggregate Spectral Model for ERS-1 Wind Retrievals 1859
Lettvin, E., and J. Vesecky
- H05.06 An Inversion Technique for Estimating the Wind-Dependent Short Wave Spectral Density from the CMOD4 1862
and Composite Surface Models
Chen, J., and D. Kasilingam
- H05.07 The Influence of Topography on Wind Over the Sea of Japan 1865
Wu, P., H. Kawamura, and F. Kimura
- H05.08 A Synergistic Approach for Estimation of High Winds Within Tropical Cyclones NA
Sarker, A., B.M. Rao, C.M. Kishtawal and M. Mohan

"NA" indicates not available at time of printing.

H06: Application of SAR/INSAR in Forestry

- H06.01 A Study of SAR Interferometry over Forests: Theory and Experiment 1868
Floury, N., T. Le Toan, J.C. Souyris and J. Bruniquel
- H06.02 An Electromagnetic Scattering Model for Tree Trunks Over a Tilted Rough Ground Plane 1871
Esteban, H., J.M. Lopez, M. Baquero, J. Fortuny, G. Nesti, and A.J. Sieber
- H06.03 Effect of Temporally Varying Parameters on L- and C-Band SAR Observations of Boreal Forests 1874
Pulliainen, J., L. Kurvonen and M. Hallikainen
- H06.04 Numerical Studies of Forest Backscatter in the VHF-Band 1878
Ulander, L.M.H., T. Martin and H. Israelsson
- H06.05 Estimating Soil Moisture in a Boreal Old Jack Pine Forest 1881
Moghaddam, M., S. Saatchi and R. Treuhaft
- H06.06 Forest Vertical Structure from Multibaseline Interferometric Radar for Studying Growth and Productivity 1884
Treuhaft, R.N., M. Moghaddam, and B.J. Yoder
- H06.07 Simulation of Interferometric SAR Response to Deciduous and Coniferous Forest Stands 1887
Sarabandi, K., and Y.C. Lin
- H06.08 Processing and Analysis Techniques for Continental Scale Radar Maps of the Tropical Forest 1890
Simard, M., G. De Grandi, S. Sattchi, M. Leysen and K.P.B. Thomson

H07: Atmospheric Radiation

- H07.01 Adjacent Effects Over Rugged Terrains NA
Li, X., and B. Hu
- H07.02 Atmospheric Correction Over a Composite Land and Water Surface 1893
Takashima, T., and K. Masuda
- H07.03 Algorithms for Atmospheric Correction for Ocean Color Data 1896
Mukai, S., I. Sano and K. Masuda
- H07.04 Multi-Angle Remote Sensing of Aerosols Over Ocean NA
Kahn, R., J. Martonchik, D. Diner and R. West
- H07.05 An Atmospheric Correction Algorithm for Space Remote Sensing Data and Its Validation 1899
Yamazaki, A., M. Imanaka, M. Shikada, T. Ohumura and Y. Kawata
- H07.06 Estimation of Adjacent Effects in Polarization Measurements over the Coastal Zone 1902
Kusaka, T., N. Taniguchi and Y. Kawata
- H07.07 Information Content of Outgoing Reflected and Scattering Solar Radiation in UV and Visible Spectral Ranges 1905
Timofeyev, Y.M., A.V. Vasilyev and V.V. Rozanov
- H07.08 Correction of Atmospheric Effects on Earth's Image - Mathematical Model & Analysis NA
Wang, A.P., and S. Ueno

H08: Advance Sensors and Sensor Calibration II

- H08.01 The Aerosol Optical Thickness Retrieval from GOME Spectra 1908
Bartoloni, A., M. Mochi, C. Serafini, M. Cervino, R. Guzzi and F. Torricella
- H08.02 Aerosol Optical Thickness Over Ocean Areas and Its Relationship With Cloud Droplet Size 1911
Han, Q., J. Chou, and R.M. Welch
- H08.03 Effects of Atmospheric Aerosol Models on the Single Scattering Point Spread Function in Optical Remote Sensing 1914
Liew, S.C.
- H08.04 Aerosol Retrieval Using Synthetic POLDER Multi-Angular Data 1917
Kuo, K.S., R.C. Weger and R.M. Welch
- H08.05 Aerosol Optical Thickness and Scattering Phase Function Retrieval from Solar Radiances Recorded over Water: A Revised Approach 1920
Paronis, D.K., and J.N. Hatzopoulos
- H08.06 The Long Distance Transport of Sand Dust and Aerosols from Northern China to Hong Kong NA
Fang, M., M. Zheng, K.S. Chim and S.C. Kot
- H08.07 Comparing Optical Models of Atmospheric Aerosol with Results of Multi-Wavelength Laser Sounding NA
Chaikovsky, A.P., A.P. Ivanov, F.P. Osipenko, and V.N. Shcherbakov
- H08.08 Satellite Remote Sensing of Fires, Smoke and Regional Radiative Energy Budgets 1923
Christopher, S.A., M. Wang, K. Barbieri, R.M. Welch and S.K. Yang

H09: Aerosols

- H09.01 Polarimetric Effects in Repeat-Pass SAR Interferometry 1926
Papathanassiou, K.P., and S.R. Cloude
- H09.02 Height Model Generation, Automatic Geocoding and Mosaicing Using of Airborne AES-1 InSAR Data 1929
Holecz, F., J. Moreira, P. Pasquali, S. Voigt, E. Meier and D. Nuesch
- H09.03 Calibration of Airborne AES INSAR Data NA
Holecz, F., J. Moreira and P. Pasquali
- H09.04 InSAR Takes over the Former Roll of Photogrammetry NA
Moreira, J., and F. Holecz
- H09.05 Coherence Optimisation in Polarimetric SAR Interferometry 1932
Cloude, S.R., and K.P. Papathanassiou
- H09.06 The X-Band SAR Demonstrator Development 1935
Zahn, R., H. Braumann and M. Schlott
- H09.07 A Novel Model of the Platform Attitude Drift for SAR 1938
Song, H., M. Zhu and Y. Bai
- H09.08 SIR-C Polarimetric Calibration by Using Polarization Selective Dihedrals and a Polarimetric Active Radar Calibrator 1941
Fujita, M., T. Masuda, Y. Fujino and M. Satake

"NA" indicates not available at time of printing.

H10: Weather Information Systems & Data Analysis Methods

H10.01	Knowledge Based Weather Image Processing Classification	<i>Siddiqui, K.J.</i>	1944
H10.02	Remote Sensing of Surface UV Radiation from Multi-Sensor Satellite Observations	<i>Gautier, C., and M. Landsfeld</i>	NA
H10.03	Infectious Disease and Climate Change: Detecting Contributing Factors and Predicting Future Outbreaks	<i>Andrick, B., B. Clark, K. Nygaard, A. Logar, M. Penaloza and R. Welch</i>	1947
H10.04	Infectious Disease and Climate Change: A Fuzzy Database Management System Approach	<i>Penaloza, M.A., and R.M. Welch</i>	1950
H10.05	Environmental Monitoring in Italy Using the Optical Sensors of the Priroda Module	<i>Armand, N.A., V.V. Efremenko, L. Pantani and I. Pippi</i>	1953
H10.06	Climatology of Light Equivalents of Integral and Photosynthetically Active Radiation and of PAR Portion in Integral Solar Radiation Derived from Ground-Based Surface Measurements	<i>Shilovtseva, O.A.</i>	NA
H10.07	Variability of Solar Radiation in Different Solar Spectrum and Natural Illuminance by Clear Sky on the Ground-Based Long-Term Measurements	<i>Abakumova, G.M., E.V. Gorbarenko, E.I. Nezval, and O.A. Shilovtseva</i>	NA
H10.08	A Joint Chain Between Thermal Interia Model and Geometric Optical Model of BRDF	<i>Zhang, R.</i>	1956

I01: Soil and Vegetation Process Model

I01.01	Importance of Soil Depth in the Estimation of Net CO ₂ Exchange Over the FIFE Site	<i>Divakarla, M.G., and J.M. Norman</i>	NA
I01.02	Retrieval of Land Surface Temperature and Water Vapor Content from AVHRR Thermal Imagery Using an Artificial Neural Network	<i>Liang, S.</i>	1959
I01.03	A Combined Temperature and Water Content Model for Bare Soil	<i>Kjellgren, J.</i>	1962
I01.04	The Use of Vegetation Indices in Forested Regions: Issues of Linearity and Saturation	<i>Huete, A.R., H. Liu and W.J.D. van Leeuwen</i>	1966
I01.05	A Sensitivity Analysis of a Coupled Leaf-Canopy-Growth Model	<i>Hobson, P., and M. Barnsley</i>	NA
I01.06	Validation of a Summertime LSP/Radiobrightness Model for Bare Soils in Northern Prairie	<i>Judge, J., J.R. Metcalfe and A.W. England</i>	NA
I01.07	Investigating Surface Heterogeneity in Semi-Arid Lands	<i>Chehbouni, A., and J. Qi</i>	NA
I01.08	Scaling Issues Related to Estimating Land Surface Evapotranspiration Using Remote Sensing Data	<i>Toll, D.L., and F.M. Vukovich</i>	NA

I02: Atmospheric Processing and Dynamics

- I02.01 Examining the Influences of Water Vapor Profile on the SSM/I - Derived Column Water Vapor Over the Global Oceans NA
Sohn, B.J.
- I02.02 Simultaneous Measurements of Water Vapor Profiles from Airborne MIR and LASE 1969
Wang, J.R., P. Racette, M.E. Triesky, E.V. Browell, S. Ismail and L.A. Chang
- I02.03 Volume Imaging Radar Observations of Atmospheric Boundary Layer Turbulence with Large Eddy Simulations 1972
Pollard, B.D., S.J. Frasier and R.E. McIntosh
- I02.04 BIAS: A Straightforward Algorithm for the Retrieval of Tracegas Vertical Columns from Near Infra-Red Earthshine Measurements by the SCIAMACHY Remote Sensing Spectrometer NA
Spurr, R.J.D.
- I02.05 A Tomographic Infrared System for Monitoring Atmospheric Pollution in Urban Areas 1975
Giuli, D., F. Cuccoli, L. Facheris, and S. Tanelli
- I02.06 Data Analysis of Lidar Measurements of Atmospheric Boundary Layer Aerosols from a Black Hawk Helicopter NA
Karl, Jr., R.R., W.K. Grace, JR. Busse, J.G. Sutton, N.A. Kurnit, A. Koskelo, O.G. Peterson and W.S. Huntgate
- I02.07 A Study of Gravity Waves in the Atmospheric Boundary Layer Using Sodar and Microbarograph NA
Reddy, K.K., and D.N. Rao
- I02.08 Aerosol Atmospheric Pollution in Some Industrial Cities of Former Soviet Union NA
Gorbarenko, E.V.

I03: Remote Sensing Research in China

- I03.01 Remote Sensing in China: Techniques and Applications 1978
Huadong, G.
- I03.02 Several Airborne Imaging Spectrometers Developed in China NA
Wang, J., and Y. Xue
- I03.03 Data Fusion of China Advanced Microwave Remote Sensor 1981
Zhang, X., and J. Jiang
- I03.04 Research and Development on Synthetic Aperture Radar System in China 1984
Zhu, M.H.
- I03.05 A New Airborne Remote Sensing Platform for Generating Geocoding Image Without Ground Control Point 1987
Li, S., Y. Xue and Z. Liu
- I03.06 Short-Term and Imminent Earthquake Prediction and Satellite Remote Sensing Thermal Infrared Technology NA
Zuji, Q., D. Changgong and L. Linzhi
- I03.07 The Development of China's Meteorological Satellite and Satellite Meteorology NA
Fang, Z., J. Xu and L. Guo
- I03.08 GIS Development and Application in China NA
Zhou, C.

"NA" indicates not available at time of printing.

I03.09	Mission Analysis of the China - Brazil Earth Resources Satellite (CBERS)	<i>Yiyuan, C.</i>	NA
--------	--	-------------------	----

I04: Data Compression Techniques and Visualization

I04.01	Reversible Compression of Multispectral Imagery Based on an Enhanced Inter-Band JPEG Prediction <i>Aiazzi, B., P.S. Alba, L. Alparone and S. Baronti</i>	1990
--------	---	------

I04.02	A DCT-Based Adaptive Compression Algorithm Customized for Radar Imagery <i>Andreadis, A., G. Benelli, A. Garzelli and S. Susini</i>	1993
--------	--	------

I04.03	SPOT Image Compression Using Block Truncation Coding Techniques <i>Ma, K.K., L. Huang, S. Zhu and A.T.S. Ho</i>	1996
--------	--	------

I04.04	Effects on Image Quality for MPEG Video Over Satellite Channel <i>Liren, Z.</i>	NA
--------	--	----

I04.05	Lossless Compression of Satellite Images Using Neural Network & Arithmetic Coding <i>Yann, S.I., Y.C. Kiat and H.Y. Yi</i>	NA
--------	---	----

I04.06	Construction of Multi-Resolution Terrain Models Using Hierarchical Delaunay Triangulated Irregular Networks <i>Huang, S.J., and D.C. Tseng</i>	1999
--------	---	------

I04.07	Raw Data Compressing Technology Study in Spaceborne SAR <i>Ru-liang, Y., and W.Y. Bai ping</i>	NA
--------	---	----

I05: Sea Surface Temperature and Its Validation

I05.01	Wind Speed Forcing of the Bulk-Skin Sea Surface Temperature Difference as a Function of Wind Speed and Heat Flux <i>Emery, W.J., and C.J. Donlon</i>	2002
--------	---	------

I05.02	Characteristics of the AVHRR-Derived Sea Surface Temperature in the Oceans Around Japan <i>Kawamura, H., and Y. Kawai</i>	2005
--------	--	------

I05.03	Global and Regional Pathfinder SST Fields: Characterization and Validation <i>Casey, K., P. Cornillon, R. Evans and G. Podesta</i>	2008
--------	---	------

I05.04	Spatial and Temporal Variability of Sea Surface Temperature in the Seas Around Korea Using Satellite Data (NOAA/AVHRR) <i>Park, K.A., and J.Y. Chung</i>	NA
--------	---	----

I05.05	The Detection of the Diurnal Variation of SST by GOES <i>Wu, X.Q.</i>	NA
--------	--	----

I05.06	Investigation of Large-Scale Oceanographic Phenomena Using Data from ATSR on ERS-1 and Other Satellite Sensors <i>Llewellyn-Jones, D.T., S.P. Lawrence, Y. Xue and C.T. Mutlow</i>	NA
--------	---	----

I05.07	The Retrieval and Validation of Ocean Color Products <i>Lynch, M.</i>	NA
--------	--	----

I06: SAR Techniques

I06.01	Passive SAR Reusing Digital Television Signals	<i>Caroti, L., I. Pippi and C. Prati</i>	NA
I06.02	Measurement of Interferometer Instrument Line Shape	<i>Atkinson, N.C., and S.H.S. Wilson</i>	2011
I06.03	Progress on the SASAR System - First Results	<i>da Silveira, M., J. Horrell, M. Inggs and E. Abenat</i>	2015
I06.04	SASAR External Polarimetric Calibration Considerations	<i>de Silveira, M.</i>	2018
I06.05	Spotlight SAR Processing Using the Extended Chirp Scaling Algorithm	<i>Mittermayer, J., and A. Moreira</i>	2021
I06.06	Wavelet Based Approaches for Efficient Compression of Complex SAR Image Data	<i>Brandfaß, M., W. Coster, U. Benz and A. Moreira</i>	2024
I06.07	A SAR Auto-Focus Technique Based on Azimuth Scaling	<i>Moreira, A., J. Mittermayer and R. Scheiber</i>	2028
I06.08	Speckle Reduction in SAR Images - Techniques and Prospects	<i>Schwarz, G., M. Walessa and M. Datcu</i>	2031

I07: Crop Monitoring and Classification

I07.01	Early Identification and Surface Estimation of Agricultural Crops Using ERS SAR Images	<i>Nezry, E.</i>	2035
I07.02	Landcover Classification Over the Mekong River Delta Using ERS and RADARSAT SAR Images	<i>Liew, S.C., S.P. Kam, T.P. Tuong, P. Chen, V.Q. Minh and H. Lim</i>	2038
I07.03	Comparison Between Classified Result of Paddy Field and Statistic Data of the Production	<i>Tsuhasa, H., and S.A.P. Ceballos</i>	2041
I07.04	Winter Crops Classification Using Satellite Data	<i>Kryvobok, O.</i>	2044
I07.05	Shortperiodic Variability of Different Landscapes in MM-Wave Range	<i>Vasilyev, Y.F., B.D. Zamaraev, V.L. Kostina and A.N. Roenko</i>	2047
I07.06	Ground Surface Sensing Through Wheat Foliage	<i>Noyman, Y., I. Shmulevich, and A. Ben-Shalom</i>	NA
I07.07	Monitoring Crop Growth on China Plains by Using SSM/I Data	<i>Jin, Y.Q.</i>	2050

"NA" indicates not available at time of printing.

I08: SAR Image Processing

I08.01	An Exploration of Features for SAR Classification	<i>Pierce, L.E.</i>	2053
I08.02	Segmentation of Radar Imagery Using Gaussian Markov Random Field Models and Wavelet Transform Techniques	<i>Dong, Y., B. Forster and A. Milne</i>	2054
I08.03	Efficient Calculation in the Map Domain of SAR Layover and Shadow Masks	<i>Pairman, D., and S. McNeill</i>	2057
I08.04	Different Approaches to Multiedge Detection in SAR Images	<i>Fjortoft, R., A. Lopes, P. Marthon and E. Cubero-Castan</i>	2060
I08.05	Terrain Classification Via Texture Modeling of SAR and SAR Coherency Images	<i>Meagher, J., J. Homer, R. Paget, and D. Longstaff</i>	2063
I08.06	Multifractal Analysis of the Digital Terrain Model for Terrain Classification in a Polarimetric SAR Image	<i>Martinez, P., D. Schertzer and K. Pham</i>	NA
I08.07	Adaptive Texture-Preserving Filtering of Multitemporal ERS-1 SAR Images	<i>Aiazzi, B., L. Alparone, S. Baronti and R. Carla</i>	2066
I08.08	Internal Waves Detection and Characterization from ERS-1 SAR Images Using the 2-D Wavelet Transform	<i>Rodenas, J.A., D. Cabarrocas and R. Garelllo</i>	2069

I09: ADEOS

I09.01	Results of CAL/VAL and Preliminary Scientific Results of ADEOS	<i>Shimoda, H.</i>	2072
I09.02	OCTS (Ocean Color and Temperature Scanner)	<i>Kawamura, H., M. Shimada, H. Nakumura, H. Oaku, Y. Mitomi and A. Mukaida</i>	2075
I09.03	Calibration and Validation of AVNIR Data	<i>Yasuoka, Y., M. Naka, and M. Shimada</i>	NA
I09.04	Atmospheric Trace Species Measurements by ILAS and RIS	<i>Sasano, Y., and N. Sugimoto</i>	2078
I09.05	Initial Result of IMG on Board ADEOS	<i>Ogawa, T., H. Shimoda, H. Kobayashi, S. Kadokura, A. Shimoda, R. Imasu, and M. Hayashi</i>	NA
I09.06	Studies of Atmospheric and Oceanic Phenomena with the NASA Scatterometer	<i>Liu, W.T.</i>	2082
I09.07	TOMS-ADEOS Initial Results	<i>Krueger, A.J.</i>	NA
I09.08	The Analysis of the Polder Data	<i>Kawata, Y., Y. Yamazaki K. Takemata and T. Kusaka</i>	2084

I10: Atmospheric Profile

I10.01	Cloud Classification and Retrieval from Spaceborne Microwave Radiometry Using a Simulated Cloud Database	2087
	<i>d'Auria, G., F.S. Marzano, N. Pierdicca, R. Pinna Nossai, P. Basili and P. Ciotti</i>	
I10.02	On the Measurement of Stratus Cloud Properties with a Cloud Radar and Microwave Radiometer	2090
	<i>Frisch, A.S., T. Uttal, C.W. Fairall and J.B. Snider</i>	
I10.03	Remote Sensing of Boundary-Layer Temperature Profiles by a Scanning 5mm Microwave Radiometer and RASS: A Comparison Experiment	2093
	<i>Westwater, E.R., Y. Han, V.G. Irisov, V. Leuski, E.N. Kadygrov and S.A. Viazankin</i>	
I10.04	A Neural Network Algorithm for the Retrieval of Atmospheric Profiles from Radiometric Data	2097
	<i>Del Frate, F., and G. Schiavon</i>	
I10.05	The Role of a priori Information in Designing Retrieval Algorithms for Microwave Radiometric Profiling of the Atmosphere	2100
	<i>Basili, P., P. Ciotti, G. d'Auria, F.S. Marzano, N. Pierdicca and S. Bonafoni</i>	
I10.06	Cirrus Characteristics and Remote Sensing Retrievals from Airborne Active/Passive Observations	NA
	<i>Spinhirne, J.D</i>	
I10.07	Calibration/Validation of Wind Profile Measurement by V.H.F. Radar	NA
	<i>Givri, J.R.</i>	
I10.08	Developmental Studies for Remote and In-Situ Detection of Halogenated Compounds by Laser-Induced Photofragmentation/Fragment Detection Spectrometry	2103
	<i>Sausa, R.C., and J.B. Simeonsson</i>	

Author's Index

Volume I	<i>Follows page</i>	618
Volume II	<i>Follows page</i>	1089
Volume III	<i>Follows page</i>	1434
Volume IV	<i>Follows page</i>	2106

Observation of Global Ocean-Atmosphere Exchanges from Spaceborne Sensors

W. Timothy Liu

Jet Propulsion Laboratory 300-323

California Institute of Technology

Pasadena, CA 91109, U.S.A.

(Tel: 1-818-354-2394; Fax: 1-818-393-6720; email: liu@pacific.jpl.nasa.gov)

INTRODUCTION

The ocean and the atmosphere are coupled by the fluxes of momentum, heat, and water, but in situ measurements of these fluxes are sparse and uneven. Global fields of these fluxes can be derived from satellite data or obtained from operational numerical weather prediction (NWP) models. The NWP models provide quality control and dynamic interpolation of sparse and uneven data. However, dynamic interpolation is only as good as the model physics and parameterization scheme, and over most of the ocean, there may not be sufficient data for any useful interpolation. Operational NWP models change frequently; the results are inconsistent of climatic studies. Reanalysis to produce long period of consistent data have only been started recently. Adequate observations at temporal and spatial scales significant to global change research can only be achieved from the vantage point of space. Spaceborne sensors provide repeated global observations of some parameters from which these fluxes can be derived. The status and shortfalls of spacebased estimation of the fluxes will be summarized and assessed in this report. Satellite data can be assimilated into numerical model to simulate surface fluxes, but the progress in developing assimilation technique of unconventional satellite data has been slow.

MOMENTUM FLUX

The flux of momentum and kinetic energy are resulted from wind shear. There are three sets of spacebased global wind field available now and in the near future. The Special Sensor Microwave /Imager (SSM/I) on the operational spacecraft of the Defense Meteorological Space Program has provided continuous wind speed measurements over global ocean since July 1987 [1]. It has a wide scan and, therefore, good coverage, but lacks directional information. The wind speed from SSM/I has been combined with other available wind data through a variation method to produce wind vector fields at 6 hourly interval and 2° by 2.5° resolution. These wind fields were found to generate more realistic anomalous ocean cooling in an ocean general circulation model [2]. SSM/I is an operational sensor and data availability will be continued well into the next century. The production of wind vector, however, is a research effort.

There are scatterometers on board European Remote Sensing Satellites (ERS) which were specifically designed to measure surface wind vector [3]. ERS-1 was launched in 1991 with a C-band scatterometer and it was replaced by a duplicate on ERS-2 in 1996. Unfortunately the ERS scatterometers scan a narrow 475 km swath only on one side of the spacecraft and leaves large data gaps between passes; the coverage is less than half of SSM/I. ERS winds from January 1992 have been available but the distribution is restricted. The next European scatterometer will be on the Meteorology Operational Platform (METOP) to be launched in 2002.

The NASA scatterometer (NSCAT) was launched in August 1996 on the Japanese spacecraft ADEOS-1. It will scan two 600 km swaths on both sides and will have more than twice the coverage of ERS scatterometers. It will cover over 87% of the ocean in one days, and 97% in two days, under both clear and cloudy conditions. NSCAT measures at Ku-band which has been studied more vigorously than C-band. NSCAT will be followed by an improved version, called SeaWinds, on ADEOS-2 to be launched in 1999. A third scatterometer is being proposed for ADEOS-3 to be launched in 2002. The third version will incorporate a polarimetric radiometer as a proof-of-concept study of measuring wind vector with a passive sensor. Spacebased observations of wind vector will be continued on the National Polar-orbiting Operational Satellite System (NPOESS) in the next century. Summaries of scatterometry and examples of applications are given in [4].

HEAT FLUX

Air-sea heat flux can be divided into four components; sensible heat resulted from thermal gradient, latent heat (LF) carried by evaporation, shortwave radiation (SR) from the sun and longwave radiation from the atmosphere and the ocean. Shortwave radiation and latent heat flux are the larger variable components over most of the tropical and temperate oceans.

Global SR has been computed from the Earth Radiation Budget Experiment (ERBE) data from 1985 to 1989 [5]. The variability of SR is largely controlled by the variability of

clouds and most of the computations of SR make use of the high resolution and high sampling of data from geostationary satellites. The International Satellite Cloud Climatology Project (ISCCP) has provided calibrated and standardized cloud data from 4 geostationary satellites operated by the U.S., the Japanese, and the European space agencies. A number of methods [6, 7, 8] have been used to compute SR at daily and 2° by 2.5° resolution, including the operational effort by the Surface Radiation Budget Program at Langley Research Center. The availability of ISCCP data is expected well into the future. The launching of sensors for the Earth Observation Program, including CERES (Clouds and Earth Radiant Energy System) will advance the derivation of SR.

The computation of LF requires sea surface temperature (SST), wind speed (u), and humidity at a level within the surface layer (q). Over ocean, u and SST have been directly retrieved from satellite data, but not q . A method of estimating q and LF from the ocean, using satellite data was proposed [9] which is based on an empirical relation between the integrated water vapor (measured by spaceborne microwave radiometer) and q (required to compute evaporation) in the monthly time scale [10]. The physical rationale is that the vertical distribution of water vapor through the whole depth of atmosphere is coherent for period longer than a week [11]. The relation does not work well at synoptic and shorter time scales and also fails in some regions during summer [12]. The relation have also been scrutinized in a number of studies [13, 14, 15]. Methods which include other geophysical parameters or EOF functions as estimators have also been proposed [16, 17, 18, 19]. Future advanced microwave humidity sounders may improve the accuracy and temporal resolution of evaporation estimation.

It is much more difficult to estimate sensible heat flux and longwave radiation from satellite data. The magnitude and variability of sensible heat are relatively small over much of the ocean and near surface air temperature is difficult to retrieve with sufficient accuracy. It can be derived from LF if the relative humidity or the Bowen Ratio is known, but the accuracy is uncertain [20]. Longwave radiation is strongly affected by atmospheric properties below cloud base which are hidden from spaceborne sensors. Methods that combined cloud information with atmospheric soundings and numerical models have been attempted [21, 22]. Improved atmospheric temperature sounders such as Atmospheric Infrared Sounder (AIRS), scheduled to be launched early next decade may advance the estimation of these fluxes.

WATER FLUX

Hydrologic forcing is the difference between precipitation and evaporation. The estimation of evaporation is the same

as the estimation of latent heat flux discussed above. Attempts have also been made to estimate precipitation from spaceborne sensors at visible, infrared, and microwave wavelengths [23, 24]. Passive microwave sensors have the advantage of more directly related to rain but are limited by the insufficient sampling of the diurnal cycle by the polar orbiters. Data production and validation have been undertaken by the Global Precipitation Climatology Project (GPCP) and data at 2.5° and monthly resolutions from 1986 to 1994 are available. Precipitation for a very long period of time has also been derived from the operational Microwave Sounding Unit [25]. Improvement in rain measurement is expected with the launching the Tropical Rain Measuring Mission (TRMM) in 1997.

ASSESSMENT

At present, we have the ability of monitoring momentum flux over global ocean using spacebased data. We could discern the annual variations over a large part of the global ocean and El Niño anomalies over the tropical ocean of the two major components of heat flux. However, we do not have the absolute accuracy of the net heat flux to compute the average meridional ocean heat transport from spacebased heat flux estimates. The retrieving method of q does not work well at high frequencies and over some region. The validation of spacebased estimation of precipitation has been hampered by the lack accurate standard. Surface wind measurement is sustainable if the series of planned scatterometers are approved. While present methods of estimating heat and water fluxes rely on operational sensors which are sustainable, the estimation of the fluxes from the satellite data are largely research efforts that need to be supported, before more stable and operational methods emerge.

The studies of air-sea fluxes involve the interaction of the atmospheric and ocean and are intrinsically interdisciplinary. Spacebased estimation of these fluxes required synergistic combination of multiple sensors from different flight projects. To pursue such studies, traditional disciplinary separations (in the research institutes or in the funding agencies) have to be overcome and individual flight project prepossession also has to be challenged. Coordination in sensor deployment and data processing is needed to have coincident or continuous data. The limited life-span of a single sensor requires continuous sensor deployment to study interannual to decadal changes. Because spaceborne sensors are expensive and require long lead time to develop, continuous vigilance from the scientific community to advocate and coordinate is necessary to shepherd these space programs to fruition.

ACKNOWLEDGMENTS

This study was performed at the Jet Propulsion Laboratory, under contract with the National Aeronautics and Space Administration (NASA). It was supported by the Earth Observing System Interdisciplinary Science Program and the Physical Oceanograph Program of NASA's Mission to Planet Earth.

REFERENCES

- [1] Wentz, F.J., "Measurement of oceanic wind vectors using satellite microwave radiometer", *IEEE Trans. Geosci. Remote Sens.*, 30, 960-972, 1992.
- [2] Liu, W.T., W. Tang, and R. Atlas, "Responses of the tropical Pacific to wind forcing as observed by spaceborne sensors and simulated by an ocean general circulation model", *J. Geophys. Res.*, 101, 16,345-16,359, 1996.
- [3] Attema, E.P.W., "The active microwave Instrument on board the ERS-1 satellite", *Proc. IEEE*, 79, 791-799, 1991.
- [4] Liu, W.T. and W. Tang, "Spaceborne scatterometer in studies of atmospheric and oceanic phenomena from synoptic to interannual time scales". *Space Remote Sensing of Subtropical Ocean*. C.T. Liu (ed.), Elsevier Press, Amsterdam, in press.
- [5] Li, Z., and H.G. Leighton, "Global climatologies of the solar radiation budgets at the surface and in the atmosphere from 5 years of ERBE data.", *J. Geophys. Res.*, 98, 4919-4930, 1993.
- [6] Gautier, C., G. Diak, and S. Masse, "A simple physical model to estimate incident solar radiation at the surface from GOES satellite data" *J. Appl. Meteor.*, 19, 1821-1844, 1980.
- [7] Bishop, J.K.B., and W.B. Rossow, "Spatial and temporal variability of global surface solar irradiance" *J. Geophys. Res.*, 96, 16839-16858, 1991.
- [8] Pinker, R.T., and I. Laszlo, "modeling surface solar irradiance of satellite applications on a global scale", *J. Appl. Meteor.*, 31, 194-211, 1992.
- [9] Liu, W.T., and P.P. Niiler, "Determination of monthly mean humidity in the atmospheric surface layer over oceans from satellite data", *J. Phys. Oceanogr.*, 14, 1451-1457, 1984.
- [10] Liu, W.T., "Statistical relation between monthly precipitable water and surface-level humidity over global oceans. *Mon. Wea. Rev.*, 114, 1591-1602, 1986.
- [11] Liu, W.T., W. Tang, and P.P. Niiler, "Humidity profiles over ocean", *J. Clim.*, 4, 1023-1034, 1991.
- [12] Liu, W.T., W. Tang, and F. J. Wentz, "Precipitable water and surface humidity over global oceans from SSM/I and ECMWF", *J. Geophys. Res.*, 97, 2251-2264, 1992.
- [13] Hsu, S.A., and B.W. Blanchard, "The relationship between total precipitable water and surface-level humidity over the sea surface: a further evaluation", *J. Geophys. Res.*, 94, 14539-14545, 1989.
- [14] Esbensen, S.K., D.B. Chelton, D. Vickers, and J. Sun, "An analysis of errors in Special Sensor Microwave Imager evaporation estimates over the global oceans" *J. Geophys. Res.*, 98, 7081-7101, 1993.
- [15] Jourdan, D. and C. Gautier, "Comparison between global latent heat flux computed from multi-sensor (SSM/I and AVHRR) and from in-situ data", *J. Atmos. and Oceanic Tech.*, 12, 46-72, 1994.
- [16] Wagner, D., E. Ruprecht, and C. Simmer, "A combination of microwave observations from satellite and an EOF analysis to retrieve vertical humidity profiles over the ocean", *J. Appl. Meteor.*, 29, 1142-1157, 1990.
- [17] Cresswell, S., E. Ruprecht, and C. Simmer, "Latent heat flux over the North Atlantic Ocean-A case study. *J. Appl. Meteor.*, 30, 1627-1635, 1991.
- [18] Miller, D.K., and K.B. Katsaros, "Satellite-derived surface latent heat fluxes in a rapidly intensifying marine cyclone" *Mon. Wea. Rev.*, 120, 1093-1107, 1991.
- [19] Chou, S.H., R.M. Atlas, and J. Ardizzone, "Estimates of surface humidity and latent heat fluxes over oceans from SSM/I data", *Mon. Wea. Rev.*, 123, 2405-2435, 1995.
- [20] Liu, W.T., and P.P. Niiler, 1990: The sensitivity of latent heat flux to the air humidity approximations used in ocean circulation models. *J. Geophys. Res.*, 95, 9745-9753, 1990.
- [21] Frouin, R., C. Gautier, and J. Morcrette, 1988: Downward longwave irradiance at the ocean surface from satellite data: methodology and in situ validation. *J. Geophys. Res.*, 93, 597-619.
- [22] Gupta, S.K., W. Darnell, and A.C. Wilber, 1992: A parameterization for longwave surface radiation from satellite data: recent improvements. *J. Appl. Meteor.*, 31, 1361-1367.
- [23] Arkin, P.A., P.E. Ardanuy, "Estimating climatic-scale precipitation from space: a review", *J. Climate*, 2, 1229-1238, 1989.
- [24] Wilheit, T.T., A.T.C. Chang, and L.S. Chiu, "Retrieval of monthly rainfall indices from microwave radiometric measurements using probability distribution functions", *J. Atmos. Oceanic Tech.*, 8, 118-136, 1991.
- [25] Spencer, R.W., "Global oceanic precipitation from the MSU during 1979-92 and comparisons to other climatologies", *J. Clim.*, 6, 1301-1326, 1993.

Water vapor and cloud feedback mechanisms: inferences from satellite observations and numerical modeling

William K. M. Lau

Climate and Radiation Branch, Code 913

NASA/Goddard Space Flight Center, Greenbelt, MD USA

(Tel: 301-286-7208, Fax: 301-286-1759, email: lau@climate.gsfc.nasa.gov)

Abstract -- Satellite observations show large sensitivity of water vapor and cloud forcings to sea surface temperature changes during major climate events such as the El Nino Southern Oscillation (ENSO). This lead to two very important questions: What are the mechanisms of the observed large sensitivity? and can we use ENSO as a surrogate to understand mechanisms for climate change? This paper addresses the above questions. We have studied the sensitivity of water vapor and cloud forcings to ocean temperature changes and their relationship with large scale circulation regimes using AVHRR and ERBE satellite outgoing longwave radiation, sea surface temperature and large scale circulation data. Results show that on interannual time scales, changes in the large scale circulation regimes contribute substantially to anomalies in the water vapor and cloud forcing observed during major climate events such as ENSO. Experiments show that over 75% of the observed apparent sensitivity of water vapor and cloud feedback sensitivity are due to changes in the large scale circulation with direct radiative feedback accounting for less than 20% of the observed changes. On interannual time scales, when adjustments are made for changes in the large scale circulation, the so-called supergreenhouse effect, i.e., run away greenhouse warming, does not exist. The results point to possible pitfalls in interpreting results for cloud and radiation feedback processes and that ENSO or other natural climate variations such as the seasonal cycle cannot simply be used as a surrogates for climate change without taking into account the effect of large scale dynamics.

CLIMATE FEEDBACK FORMALISM

The results of this paper are based on the following climate feedback formalism. In the following, we define the change in the clear sky water vapor greenhouse, shortwave and longwave cloud forcing at the top of the atmosphere (TOA) as:

$$\Delta G_a = \Delta(\sigma T_s^4 - LW_{clear})$$

$$\Delta C_t = \Delta(LW_{clear} - LW_{total})$$

$$\Delta C_s = \Delta(SW_{total} - SW_{clear}) \text{ where } \sigma \text{ is the Stefan-Boltzman's constant, } T_s \text{ the SST; } LW_{clear} \text{ and } LW_{total}$$

the clear sky and total TOA longwave fluxes, defined positive upward. The clear and total shortwave fluxes SW_{clear} and SW_{total} are defined positive downward. The symbol Δ denotes the difference between the anomaly experiments and the control E1. To understand the relationship of the above quantities to climate feedback, we define a climate sensitivity from changes in these radiative flux quantities following Arking (1991). Let N be the total radiative imbalance at the top of the atmosphere due to, say change in atmospheric CO_2 and T_s be the surface temperature then a climate sensitivity factor can be defined as

$$\Delta T_s = K \Delta N$$

However the radiative imbalance will be further modified by individual processes which are functions of the induced T_s . The modified flux can be expressed as

$$\Delta N^* = \Delta N + \sum \alpha_i \Delta T_s$$

where the α_i is the sensitivity coefficient representing changes in net flux due to a specific process per unit change in surface temperature for different physical processes. If we define a new climate sensitivity factor K_o including the feedback terms, i.e., $\Delta T_s = K_o \Delta N^*$, and a feedback factor, $f_i = \alpha_i K_o$, then the expression for change in surface temperature becomes

$$\Delta T_s = \frac{K_o}{(1 - \sum f_i)} \Delta N.$$

From (4), we can see that a strong amplifying surface temperature signal will result if the sum of the feedback factors is closed to one, even if the initial imposed radiative forcing ΔN is small. Most important, the feedback factor is dependent on the sensitivity of the various radiative flux changes with respect to T_s . In the above formalism, the feedback factors are defined in the global and long-term sense. In this paper, we will identify ΔT_s with the ENSO

SST changes and the α_i 's the rate of change with respect to

SST i.e., $\frac{\partial G_a}{\partial T_s}$, $\frac{\partial C_t}{\partial T_s}$, $\frac{\partial C_s}{\partial T_s}$ for water vapor, longwave

and shortwave cloud forcing respectively. The key question is can we estimate these feedback factors based on climate processes over a regional domain over time periods relatively short (seasonal to interannual) compared to those (interdecadal or longer) for climate change.

RESULTS

Comparing the greenhouse effect for the warm vs. the cold events, it was found that there is a large increase in the atmospheric greenhouse effect over the region of warm water during El Nino, with magnitude up to 30 Wm^{-2} near the dateline. However negative greenhouse effects are found over the western Pacific and the subtropical regions. Clouds have strong local effects on the IR and solar radiation, but the net effect at the top of the atmosphere between 35°N - 25°S is quite small. Overall, the earth-atmosphere system receives less radiative energy order of $4\text{--}5 \text{ Wm}^{-2}$ during El Nino, primarily due to the reduced clear sky greenhouse effect. To understand the mechanisms for the changes in the greenhouse effect and cloud radiative forcing, it is important to bear in mind that changes in water vapor and cloudiness can be brought about by (a) the changes in the atmospheric circulation induced by the changes in SST and (b) direct feedback effects on the local SST change. Obviously, the large scale atmospheric circulation is related to the large scale SST gradient, which is dependent on oceanic circulation. Therefore, it is important to distinguish the contribution of dynamics vs. radiative feedback to the sensitivity of radiative forcing to SST. Fig. 1 illustrates schematically the important factors that contribute to the apparent climate feedback parameters. During ENSO, it is likely that the apparent feedback parameter is much larger, because there is a large change in the circulation regime. In the global warming scenario, where changes in atmospheric circulation is small, the radiative climate feedback sensitivity is expected to be much smaller than those computed from ENSO conditions. To unravel the causes of the large feedback factors associated with ENSO, we carried out the following experiments using the Goddard Earth Observing System (GEOS) general circulation model.

Four experiments have been conducted:

E1: a 90-day control integration with climatological January insolation, SST and other surface boundary conditions.

E2: Same as in E1, except that the model is forced by SST anomalies derived from the difference between

two phases of ENSO, i.e., a composite of the warm events of 1986-87, 1992-93, and the cold event of 1988-89.

E3: Same as in E2, except that the radiative feedback is disabled at every time step, with the radiation flux terms replaced by the means of the equilibrium state of E2.

E4: Same as in E2, with disabled radiative feedback, but with the radiation flux terms replaced by the means of the equilibrium state of E1.

All the above experiments have been carried out with identical initial conditions. E1 is the control experiment and E2 through E4 are anomaly experiments. E2 has full physics; E3 and E4 have no radiative feedback and differ only in the mean radiative flux terms. In E3, the total mean radiative fluxes of the atmosphere are the same as in E2, except for the nonlinear effects of the cloud-radiation interaction at each time step. We shall refer to this as a partial removal of radiative feedback. In E4, all anomalous radiative effects are removed. Here, clouds and water vapor are generated and advected by atmospheric circulation but they are completely passive with respect to the radiation budget. In all the above experiments, the atmosphere reaches an equilibrium state within the first 20 days. In the following, an anomaly field (also referred to as the response) is defined as the difference between the equilibrium state of the anomaly experiments (E2, E3 and E4) and that of the control experiment (E1), based on the average of the last 70 days of the integration. In addition, we carried out two extra experiments

G1: same as in E1, but with the SST increased by 2°C everywhere.

G2: same as in G1, but with SST decreased by 2°C everywhere.

For each of the above experiments, the sensitivity parameters $\frac{\partial G_a}{\partial T_s}$, $\frac{\partial C_t}{\partial T_s}$, $\frac{\partial C_s}{\partial T_s}$ have been computed by a

regression analysis (cf. Bony et al, 1995). It can be seen that the model simulates quite well the sensitivity of the observed sensitivities in the full physics experiment (E2),

with $\frac{\partial G_a}{\partial T_s}$, $\frac{\partial C_t}{\partial T_s}$, $\frac{\partial C_s}{\partial T_s}$ equal to 9.4, 24.3 and -29.3

$\text{Wm}^{-2}/^\circ\text{C}$ respectively. As long as the mean radiative forcing is prescribed, the sensitivity appears to be changed very little (E3). When the radiative feedback is removed, there is by design no radiative sensitive to SST, because

the radiative forcing is kept at the climatological value. But an apparent sensitivity can still be computed in E4 that is all due to the effect of the large scale circulation. The difference between E2 and E4 then yields the inferred radiative feedback for greenhouse effect at $1.8 \text{ Wm}^{-2}/^{\circ}\text{C}$ and cloud longwave and shortwave at 6.5 and $-8.7 \text{ Wm}^{-2}/^{\circ}\text{C}$ respectively. These values are considerably smaller than that deduced directly from ERBE for ENSO conditions. This indicates that using ENSO conditions tends to overestimate the climate feedback effects. This is confirmed by the results of the G1 and G2 experiments. In these two experiments, the atmosphere response mostly through thermodynamic effects, i.e., increase water vapor due to increasing temperature and changes in the

atmospheric circulation is relatively small compared to ENSO. In this case, the greenhouse sensitivity is estimated to be $1.7 \text{ Wm}^{-2}/^{\circ}\text{C}$ about the same as that inferred from E2- E4. Interestingly, the cloud feedback is very small. This is because there is no large scale circulation to organize the clouds, therefore the cloud radiative feedback effect is very small. The above results show the importance of the large scale dynamics in organizing clouds and water vapor in interannual variability. In the absence of large scale dynamic forcing, the water vapor feedback is about $1.7 \text{ Wm}^{-2}/^{\circ}\text{C}$, in agreement with that deduced from (E4-E2). However, the cloud feedback is negligible.

Wavelet Analysis of Satellite Images for Coastal Monitoring

Antony K. Liu, Sunny Y. Wu

NASA Goddard Space Flight Center, Code 971, Greenbelt, Maryland USA
Tel: (301)286-8534, Fax: (301)286-0240, E-Mail: liu@neptune.gsfc.nasa.gov

and William Y. Tseng

Interactive Processing Branch, NOAA/NESDIS, Washington, D.C. 20233 USA
Tel: (301)763-8142, Fax: (301)899-9196, E-Mail: wtseng@nesdis.noaa.gov

Abstract -- In this paper, algorithms and techniques for automated detection and tracking of mesoscale features from satellite imagery employing wavelet analysis are presented. The wavelet transform has been applied to satellite images, such as those from Synthetic Aperture Radar (SAR), Advanced Very High-Resolution Radiometer (AVHRR), and Coastal Zone Color Scanner (CZCS) for feature extraction and Special Sensor Microwave/Imager (SSM/I) data for sea ice drift. The evolution of mesoscale features such as oil slicks, fronts, eddies, and ice floes/textures can be tracked by the wavelet analysis using satellite data from repeating paths.

INTRODUCTION

A new method for time-varying signal analysis, called the Wavelet Transform, has been developed for ocean applications at NASA/GSFC during the past three years, and gives spectral decompositions via the scale concept. Basically, wavelet transforms are analogous to Fourier transforms, but are localized both in frequency and time, i.e., they enable the study of processes by localizing their properties in both time and frequency [1]. The Two-dimensional wavelet transform is a highly efficient band-pass filter, which can be used to separate various scale processes and show their relative phase/location information. Two-dimensional Gaussian wavelet (often referred to as Mexican hat) transform of SAR image for small scale features can be used with threshold as an edge detector. In the marginal ice zone study by [2], the ice edge in each SAR image has been delineated by using two-dimensional wavelet transform.

Several examples of the wavelet analysis applied to various satellite images demonstrate the feasibility of this technique for coastal monitoring [3]. The wavelet transforms of satellite images can be used for near real-time "quick look" screening of satellite data (feature detection), data reduction (binary image), and image enhancement (edge linking). Wavelet analysis of SSM/I 85 GHz radiance data can be used to obtain daily sea ice drift information for both the northern and southern polar regions. Reliable imaging of such mesoscale features, combined with a definition of the conditions under which imaging is feasible, would lead to an important data product; satellite-derived maps for tracking mesoscale features in the coastal zone and sea ice drift in the polar regions.

OCEAN FEATURE TRACKING

Satellite data will first be divided into subscenes with coastal land and clouds masked. The histogram of each subscene will also be examined for data screening. The promising subscenes will then be wavelet transformed with various scales to separate various texture or features. The Laplacian of the Gaussian (Mexican hat) wavelet will be used as a band-pass-filter, and its first derivative as a threshold for feature detection. Heuristic edge linking methods will be used to enhance the images. Finally, a binary image can be produced in order to reduce the data volume. By overlaying ocean color, IR, and SAR binary images with some data fusion techniques, the evolution of mesoscale features such as ice edge, fronts, oil slicks, ship wakes, and eddies can be monitored by wavelet analysis using satellite data from subsequent passes.

Satellite remote sensing has become a useful tool to study marine pollution [4]. Recently, RADARSAT ScanSAR Narrow data has been obtained by NESDIS in response to a major oil spill in Uruguay on February 8, 1997 in the La Plata river mouth. The SAR image (with pixel size of 25 km) in Figure 1 collected on February 26, 1997 shows the spreading of oil slicks (in dark areas) near the Uruguay coast. For demonstration purposes, Figure 1 also shows the oil slick areas extracted by the Mexican hat wavelet transform with a median scale $a = 8$ units of pixel spacing to separate the oil slick areas (in white contours) from the open water. A 0.6 standard deviation of the first derivative is chosen as the threshold for feature extraction. In addition, the method of edge linking based on the neighboring point was applied and the short segments were removed. Notice that the oil slicks have been dispersed by coastal current and wind over a large SSM/I coastal area after 18 days.

In order to understand the evolution of the oil spill, several AVHRR images between February 8 to 26 have been examined. Due to heavy cloud cover over the oil spill area, only February 13 and 15 can be used for oil slick tracking. An AVHRR image (with pixel spacing of 0.01°) of sea surface temperatures collected over the Uruguay coast collected on February 15, 1997 after the oil spill is shown in Figure 2. First the cloud/land and ocean features are separated by using different gray scales for different temperature ranges. Then, the land (dark areas) is

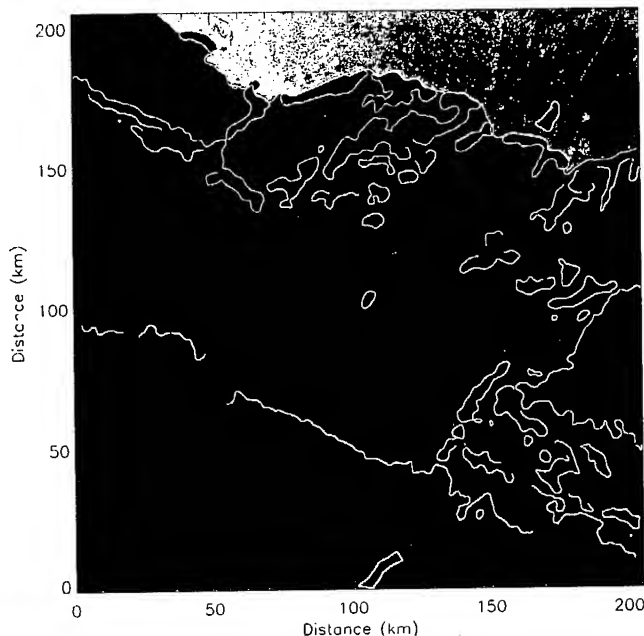


Figure 1. A RADARSAT ScanSAR Image of the Uruguay Oil Spill on February 26, 1997, and the Wavelet Transform to Separate the Oil Spill Areas (in White Contours) from the Open Water.

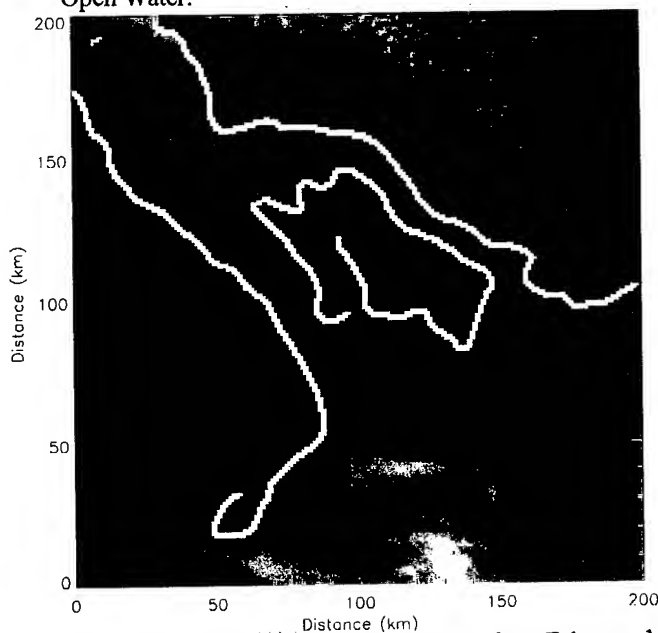


Figure 2. An AVHRR Image of Uruguay from February 15, 1997 with land and Oil Spill Area Delineated by White Curves Processed by the Wavelet Transform.

delineated by the white lines and the oil spill on ocean surface (gray area) is extracted by white contour using wavelet transforms with a small scale ($a = 4$ units of pixel spacing) as an edge detector and a threshold about 0.1 standard deviation. By combined use of gray scale and wavelet transform, we can detect (with gray scale), track (with wavelet transform), and enhance (with edge linking) the satellite images. Notice that after a week, the oil spill is still confined near the La Plata river mouth.

SEA ICE DRIFT

Wavelet analysis of DMSP SSM/I 85 GHz radiance data can be used to obtain daily sea ice drift information for both the northern and southern polar regions. This technique provides improved spatial coverage over the existing array of Arctic Ocean buoys and better temporal resolution over techniques utilizing data from satellite synthetic aperture radars. Figure 3 shows an 85 GHz SSM/I image (12.5 km resolution) of the Arctic Ocean for December 12, 1992 where the ice cover is clearly distinguishable from the open ocean. In this SSM/I image of size 512*512 pixels, the wavelet transform using the Mexican-hat wavelet with a scale, $a=2$ units of pixel spacing or 25 km, is first computed. With such a small wavelet scale, many zero-crossings which correspond to the boundary of ice features, exist in the image. To associate a single closed contour with an isolated ice features, we apply a 5% threshold above the minimum of the wavelet transform as the contour value. Next, each closed contour is framed in a rectangular window with its four sides just tangent to the four extreme locations of the closed contour. Each window at a given starting date is used as a template to be matched. Note that the template window is not fixed in size, but it is determined by the ice feature at a particular location.

With the template defined, we then perform the template matching with the results from the wavelet transform of the SSM/I image two days later. Because of the 12.5 km resolution of the SSM/I image, the displacement of the ice feature may move just a few pixels in a few days. Thus, the domain of the template matching can be restricted to an area with a few pixels (e.g., 10 pixels) larger than the template window. The template match is done by shifting the template over each pixel in the domain. The summation of the absolute value of the differences between the shifted template values and the target values is computed at each location. The sequence of the summation values is then used as a metric of the degree of match of the ice feature. Its minimum indicates a possible match of two displaced ice features. Once the shapes have been matched, the velocity vector can be easily estimated from dividing the relative displacement over a time interval of four days. Several different scales ($a=1, 1.414, 2$) can be used and then the resultant motion vectors can be block averaged with outlier filtered. As an example, a grid of 100*100 km is used for the final sea-ice drift map of the Arctic basin as shown in Figure 3. Figure 4 shows the ice motion in Fram Strait/Baffin Bay and Greenland coast.

DISCUSSION

The coastal zone is a highly productive and dynamic environment. Because of the fast growth of industry, the coastal pollution is one of the major issues for environmental protection. Increasingly, coastal regions need reliable, high quality resource and environmental

information from remote sensing to better manage this vital area. Remote sensing with repeated coverage is the most efficient method to monitor and study the marine productivity and pollution. The mapping of mesoscale ocean features in the coastal zone is a major potential application for satellite SAR data, especially for the ScanSAR on RADARSAT with 500 km swath. The use of SAR-derived observations to track eddies, surface temperature-related features, and river and estuarine plumes can aid in the management of fisheries. The NOAA (National Oceanic and Atmospheric Administration) CoastWatch provides near real-time mapped satellite and in-situ data and information for U.S. coastal waters for hazard warning, ice and ocean monitoring, and environmental management [5].

The wavelet transforms of satellite images can be used for near real-time "quick look" screening of satellite data (feature detection), data reduction (binary image), and image enhancement (edge linking). By combining ocean color SeaWiFS/OCTS, ERS-2/RADARSAT SAR, and infrared AVHRR images (wavelet transformed binary images) by some data fusion technique, mesoscale features of various physical processes such as oil spills, surface slicks, fronts, upwelling, and eddies can be detected and tracked in the coastal area. Wavelet analysis can provide a more cost-effective monitoring program that would keep track of changes in important elements of the coastal watch system and sea-ice motion.

ACKNOWLEDGMENTS

The authors wish to thank Bill Pichel and Pablo Clemente-Colon of NOAA/NESDIS and Don Cavalieri for their valuable discussions and suggestions. The RADARSAT SAR image collected by CSA satellite is also acknowledged. This work was supported by NASA and NOAA.

REFERENCES

- [1] J. M. Combes, A. Grossmann, and Ph. Tchamitchian, "Wavelet: time frequency methods and phase space", Proc. International Conference, Marseille, France, Springer-Verlag, 331pp, 1989.
- [2] A. K. Liu, C. Y. Peng, and T. J. Weingartner, "Ocean-ice interaction in the marginal ice zone using SAR", J. Geophys. Res., 99, 22391-22400, 1994.
- [3] A. K. Liu, C. Y. Peng, and S. Y.-S. Chang, "Wavelet analysis of satellite images for coastal watch", IEEE Journal of Oceanic Engineering, 22, No. 1, 9-17, 1997.
- [4] Park, P. K., J. A. Elrod, and D. R. Kester, "Application of satellite remote sensing to marine pollution studies", Chemistry and Ecology, 5, 57-73, 1991.
- [5] W. Pichel, J. Sapper, C. Duda, E. Maturi, K. Jarva, and

J. Stroup, "CoastWatch operational mapped AVHRR imagery", Proceedings of IGARSS'94, 1994.

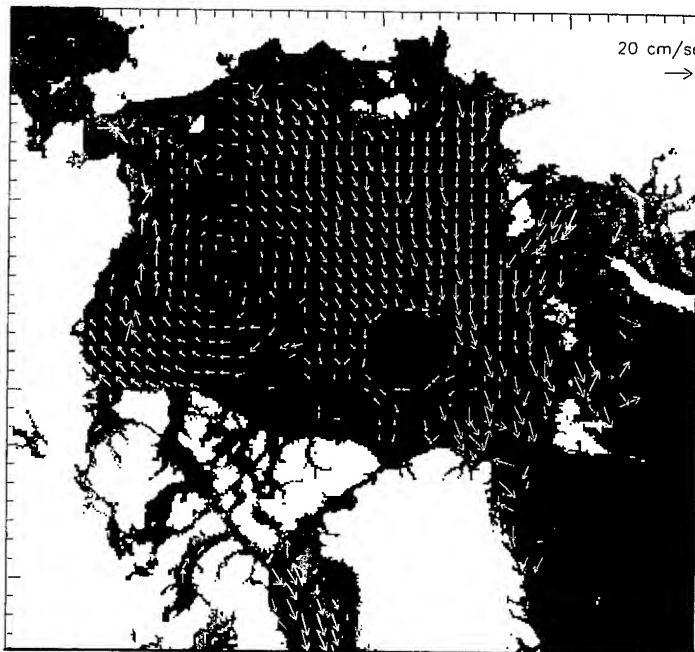


Figure 3. Arctic Ocean Ice Displacement Vectors for December 12, 1992 with Grid Size of 100 km. In This 85 GHz SSM/I Image, White Arrows Indicate Velocities Derived from Feature Tracking Using Wavelet Analysis.

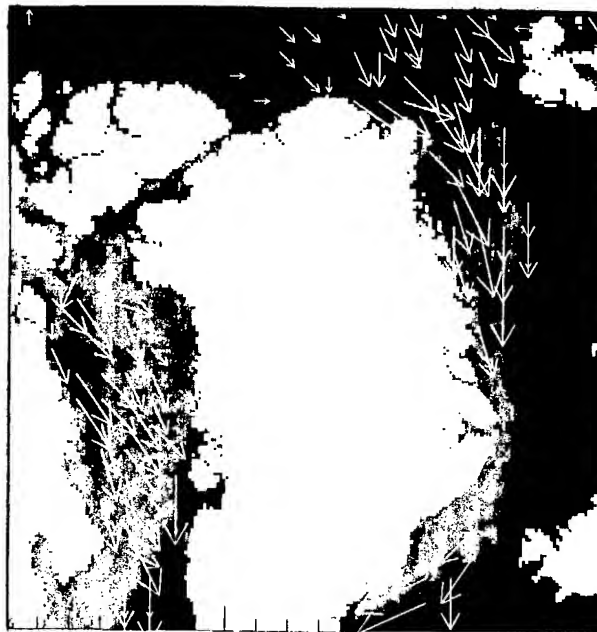


Figure 4. Ice Motion in Fram Strait/Baffin Bay and Greenland Coast from Wavelet Analysis of SSM/I Data.

Cloud Macrostructure and Radiation

Robert F. Cahalan, A. Davis, A. Marshak, D. Silberstein, and W. Wiscombe
Goddard Laboratory for Atmospheres
NASA-Goddard Space Flight Center, Greenbelt, MD 20771 USA

ABSTRACT

Cloud radiative properties are sensitive not only to drop size and other parameters of cloud micro-structure, but also cloud shape, spacing, other parameters of cloud macro-structure. Field programs such as DoE/ARM and DoE/UAV are now underway to improve the measurement and modelling of physical and radiative properties of clouds under a variety of meteorological conditions. A parallel effort is underway to improve cloud remote sensing from current GOES and AVHRR platforms as well as the upcoming NASA suite of EOS instrument which will provide higher spectral and/or spatial resolution, such as MODIS and ETM+/LATI. Corrections to plane-parallel theory to account for cloud inhomogeneity take different forms for the 100 km scale of climate model grids, and for the 1 km scale of typical satellite pixels. A first approximation for grid-scale fluxes is obtained by a linear weighting of clear and cloudy fractions, using an "effective cloud thickness" which depends on the within-cloud variability. A key finding for improving pixel-scale retrievals is that there is a characteristic "radiative smoothing" scale of several hundred meters. This scale has been observed as a change in the spatial spectrum of Landsat cloud radiances, and was also recently found with the help of Spinhirne's lidar at NASA-Goddard, by searching for returns from directions nonparallel to the incident beam. "Offbeam" Lidar returns are now being used to estimate the cloud "Green's function", which will be applied to improving simple IPA estimates of cloud radiative properties. This and other measurements of 3D transfer in clouds, coupled with 3D Monte Carlo transfer methods, are beginning to provide a better understanding of the dependence of radiation on cloud inhomogeneity, and to suggest new retrieval and parameterization algorithms which take account of cloud inhomogeneity.

1. INTRODUCTION

The large-scale terrestrial climate is well-known to be very sensitive to small changes in the average albedo of the earth-atmosphere system. Sensitivity estimates vary, but typically a 10% change in global albedo, with all other quantities held fixed, changes the mean equilibrium surface temperature by 5 °C, more than, say, a doubling of CO₂. [See, for example, Cahalan and Wiscombe, 1993.] Atmospheric absorption also has a profound effect on the climate, through its impact on the intensity of the Hadley circulation and convective processes in general [For example Kiehl et al, 1995]. Current global climate models are beginning to attempt to predict cloud liquid water, and from that the albedo and cloud absorption in each gridbox, rather than simply to adjust the albedo and absorption to what are believed to be observed values, as in the past. The ability of the models to compute the albedo is largely a function of their inability to predict the microphysical and macrophysical statistical properties of cloud liquid water within each gridbox. As Stephens (1985) has emphasized, the mean albedo of each gridbox depends not only on the mean properties of the clouds within each box, but also upon the variability of the clouds, which involves not only the fractional area covered by clouds, but also the cloud structure itself.

The dependence of average albedo and absorption on cloud structure has been found to be particularly striking in the case of marine stratocumulus, a major contributor to net cloud forcing. A study based on the FIRE observations of California

stratocumulus in July 1987 showed that cloud structure has a greater impact on average albedo than does cloud fraction (Cahalan et al, 1994a and 1994b). That study employed a "bounded cascade" model to distribute the cloud liquid, with parameters f and c adjusted to fit the variance of the log(LWP), and the exponent of the power spectrum, respectively. In order to isolate the effects of horizontal liquid water variations on cloud albedo, the usual microphysical parameters were assumed homogeneous, as was the geometrical cloud thickness. In order to simplify comparison with plane-parallel clouds, the area-averaged vertical optical depth was kept fixed at each step of the cascade. The albedo bias was found as an analytic function of the fractal parameter, f , as well as the mean vertical optical thickness, τ_v , and sun angle, θ . For typical values observed in FIRE ($f = 0.5$, $\tau_v = 10$, and $\theta = 60^\circ$) the absolute bias is 0.09, or 15% of the plane-parallel albedo of 0.69.

In the following, we first briefly review plane-parallel biases in cloud albedo and absorption estimated from NASA/FIRE and DoE/ARM field observations; then discuss the "nonlocal independent pixel approximation", or nIPA, which provides a practical alternative to the simple IPA with accuracies often approaching full 3D Monte Carlo in computations of plane-parallel albedo biases, and in the retrieval of cloud properties from satellite radiances; thirdly we show measurements of the "cloud Green's function" used by the nIPA technique, made with a "wide-angle" configuration of the Goddard lidar facility; and finally, we show that under certain commonly-

observed conditions the albedo can be obtained from the plane-parallel albedo by employing a "reduced optical thickness" where the reduction factor increases with cloud variability.

2. PLANE-PARALLEL BIASES

Figure 1 dramatizes the importance of cloud structure in determining cloud albedo. It shows the diurnal cycle of the "plane-parallel albedo bias", namely the bias in plane-parallel estimates of cloud albedo based only on the mean cloud quantities in a given gridbox. The upper curve is the total bias computed with 100% uniform cloud cover, while the lower curve shows "cloud fraction bias", or that portion of the bias found by using the actual diurnally varying cloud fraction, but still treating the clouds as uniform. This cloud fraction bias vanishes at about 11 AM when the cloud fraction is nearly 100%. Yet that is precisely when the total bias is largest (ignoring the sharp rise at sunset, which is an artifact of the computation due to the neglect of surface albedo). The middle curve explains the peak at 11 AM - it is the bias due only to the internal variability of the cloud, namely the "fractal structure bias". That bias is largest when the cloud fraction is largest, because that occurs when the convection is strongest, so that the most extensive clouds are not only thickest, but also most variable. This observation has also been born out by microwave observations of cloud liquid over Porto Santo in the Atlantic Madeira Islands during the June 1992 ASTEX program, and during the year following.

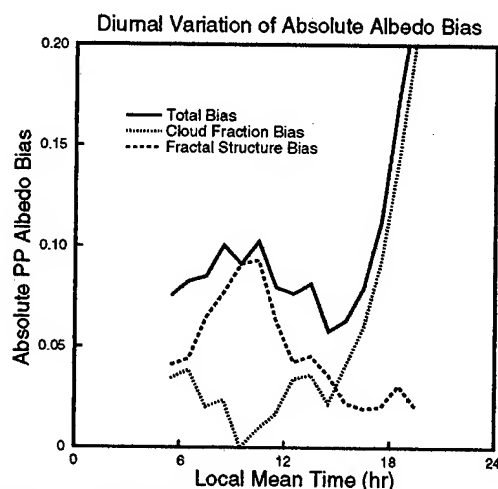


Figure 1. Albedo of a uniformly cloud-covered region minus that of a region 82% uniformly covered (lower curve); albedo of an 82% uniformly covered minus that of a region 82% fractal (middle); and sum (top).

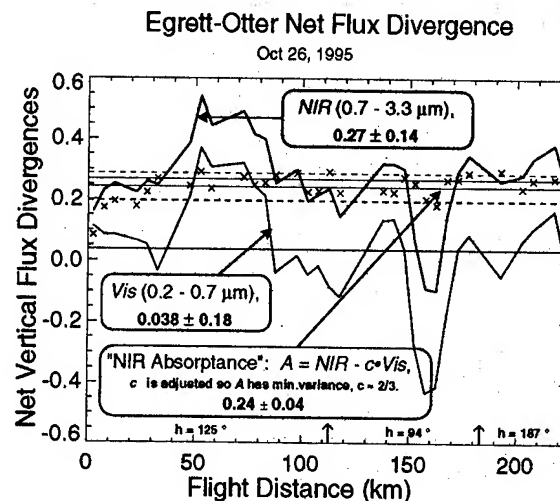


Figure 2. Apparent absorption measured by up and down-looking broadband flux radiometers on high-altitude Egrett and low-altitude Otter aircraft during DoE/ARESE field experiment during September 1995. Vertical axis is net vertical flux divergence (as a percentage of incident flux in each band at the upper aircraft) between 13 km Egrett altitude and 1 km Otter altitude in the near-infrared (red curve, 0.7 to 3.3 microns) and visible (blue curve, 0.2 to 0.7 microns), as measured by up and down-looking hemispheric broadband radiometers onboard the Egrett (at 13 km) and Otter (at 1 km) aircraft near the DoE Southern Great Plains ARM site on October 26, 1995 during the ARESE Intensive Observation Period. The horizontal axis shows both the flight distance and the location of two turns (arrows) with the headings labelled in between (h is measured clockwise from 0° = North). The large correlated excursions in both NIR and Vis are due to horizontal fluxes caused by cloud inhomogeneity. To cancel horizontal fluxes between NIR and Vis, a weighted difference $A = \text{NIR} - c \cdot \text{Vis}$ is computed, where c is chosen to minimize the spatial variance, which occurs when $c = \text{linear correlation coefficient of NIR and Vis}$. In this case $c \sim 2/3$, and the resulting values of A are plotted as X's. The mean of A is only slightly reduced from that of NIR, but the variance of A is reduced by nearly a factor of 4!

Figure 2 shows the large excursions in "apparent" absorption observed during the DoE/ARESE field experiment in September 1995. The large excursions even to negative numbers caused by horizontal radiative fluxes, can be eliminated by cancelling them between different bands, as shown here for broadband visible and near-infrared. To minimize the variance of the difference, the linear correlation coefficient "c" is used as a multiplier.

3. NONLOCAL INDEPENDENT PIXEL APPROXIMATION

To correct for the effect of horizontal fluxes on satellite cloud retrievals, we employ the nonlocal IPA, or nIPA (Marshak et al., 1997). This simulates the smoothing effect of horizontal fluxes via a "smoothing kernel". The inverse of the smoothing kernel has the effect of sharpening the distribution of cloud optical thickness and liquid water. Figure 3 shows a comparison of both IPA and NIPA retrievals with the exact but expensive 3D Monte Carlo. The NIPA points show dramatically improved retrievals.

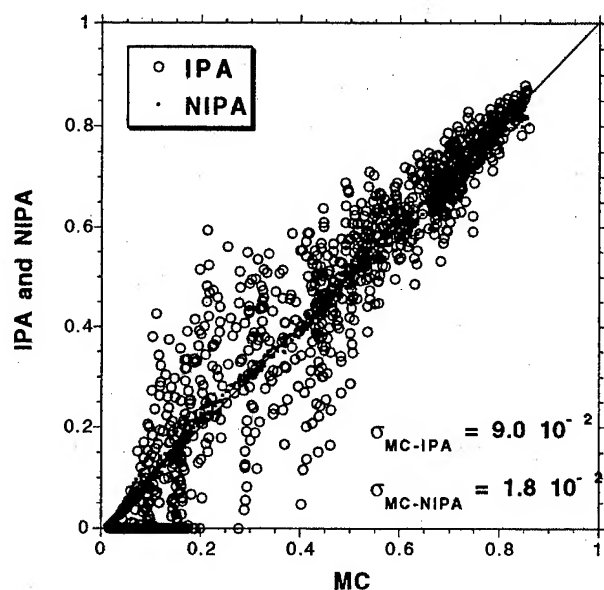
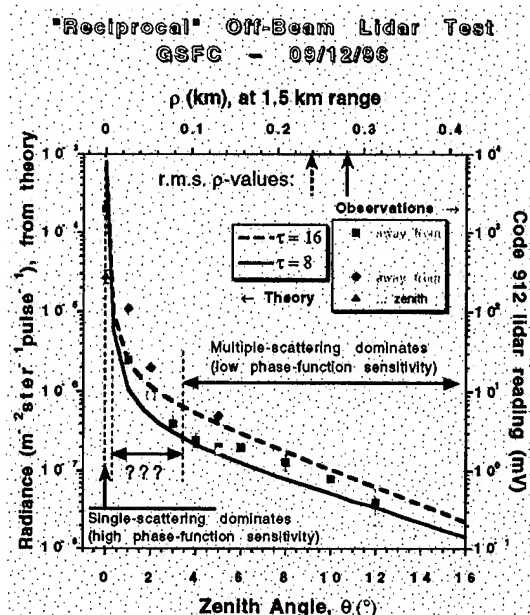


Figure 3. Scatter plot of IPA (red) and NIPA (blue) albedo versus Monte Carlo albedo from a bounded cascade having 77% cloud. NIPA is much faster than Monte Carlo, and much more accurate than IPA.

4. CLOUD GREEN'S FUNCTION

The smoothing in the nIPA approach is accomplished by the cloud radiative Green's function, which is the pattern of reflected (or transmitted) radiation produced by an incident localized beam, such as that of a laser. Most of the reflected light is backscattered in the direction of the incident beam, but the rms distance between the beam and the reflected photons, the "spot size" increases with cloud thickness. An example, (as far as we know the first such) is shown in Figure 4 (Davis et al., 1997a and b). This is the intensity as a function of angle between the incident lidar beam and the detected return photons. Note the characteristic exponential falloff associated with photon diffusion at large angle. Integrating this function

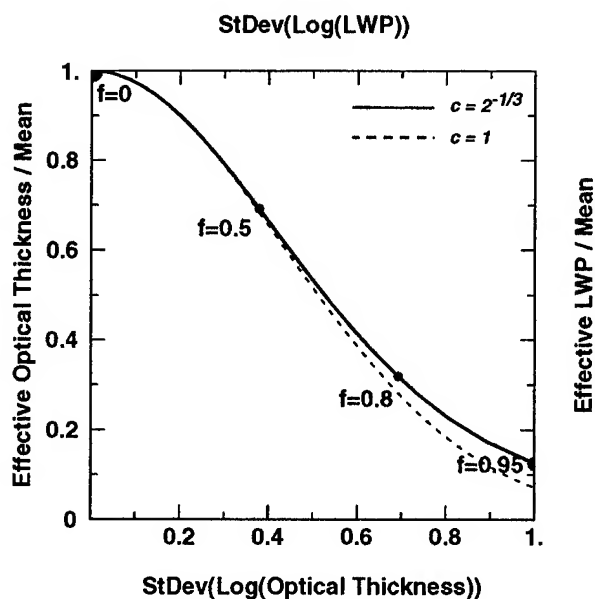
times the squared distance gives the rms distance, shown for



two cloud optical thicknesses.

5. REDUCED THICKNESS

For a range of intermediate mean cloud thicknesses, the



mean albedo can be computed from a "reduced" mean thickness, where the reduction factor is a known function of f , approximately 0.7 when $f = 0.5$. Harshvardhan and Randall suggested that globally cloud liquid must be reduced by approximately 0.3 in order to obtain the correct global albedo. In the fractal bounded cascade model this requires an increase in the fractal parameter to $f = 0.8$; and increases the albedo bias by a factor of 5, presumably due to the contribution of deep convective cloudiness. This approach has been used to improve the ToA fluxes in the ECMWF model (Tiedke, 1996).

6. DISCUSSION

A number of new results on the mesoscale-average albedo and absorptivity of stratocumulus clouds, known to be a major contributor to net cloud forcing, have been obtained by both 3D Monte Carlo and analytic methods, and compared to field observations of cloud albedo and absorption. The "apparent" absorption measured by two aircraft in ARESE, in broadband visible and near-infrared bands, shows large excursions from the mean due to horizontal fluxes. The excursions in different bands are strongly correlated, so that appropriate differences may be defined which are largely unaffected by the horizontal transports. The effect of horizontal transports on cloud retrievals can be approximated with a "smoothing kernel", and its inverse has the effect of sharpening the radiatively smoothed cloud distributions obtained by IPA. The kernel in this nonlocal IPA, or NIPA technique is physically related to the "cloud radiative Green's function", which has recently been measured by off-beam lidar technique, and used to interpret the results in terms of a "radiative smoothing scale" which increases with cloud thickness. Finally, one example of the kind of cloud parameterization provided by fractal cloud studies was shown -- the cloud effective optical thickness, which is a simple function of the variance of the logarithm of the cloud liquid water. Climate models are now beginning to incorporate the effects of such internal variability on cloud optical properties.

7. REFERENCES

- R. F. Cahalan and W. J. Wiscombe, "Impact of Cloud Structure on Climate," in **Current Problems in Atmospheric Radiation**, A. Deepak Publishing, 565+pp, pp. 120-124, 1993.
- R. F. Cahalan, W. Ridgway, W. J. Wiscombe, T. L. Bell and J. B. Snider, "The Albedo of Fractal Stratocumulus Clouds," *J. Atmos. Sci.* **51**, 2434-2455, 1994a.
- R. F. Cahalan, W. Ridgway, W. J. Wiscombe, Harshvardhan and S. Gollmer, "Independent Pixel and Monte Carlo Estimates of Stratocumulus Albedo," *J. Atmos. Sci.* **51**, 3776-3790, 1994b.
- R. F. Cahalan, "Bounded Cascade Clouds: Albedo and Effective Thickness," *Nonlinear Proc. Geophys.* **1**, 156-167, 1994c.
- R. F. Cahalan, D. Silberstein and J. B. Snider, "Liquid Water Path and Plane-parallel Albedo Bias during ASTEX," *J. Atmos. Sci.*, **52**, 3002-3012, 1995.
- Kiehl, H. Grassl, L. Shi, "Warm pool heat budget and shortwave cloud forcing: A missing physics?," *Science* **267**, 499-503, 1995.
- A. Marshak, A. Davis, W. Wiscombe and R. F. Cahalan, "Radiative smoothing in fractal clouds," *J. Geophys. Res.-Atmospheres*, **100**, 26,247-26,261, 1995.
- A. Davis, A. Marshak, R. F. Cahalan and W. Wiscombe, "The Landsat scale break in stratocumulus as a three-dimensional radiative transfer effect, implications for cloud remote sensing," *J. Atmos. Sci.*, **54**, 241-260, 1997a.
- A. Davis, D. Winker, A. Marshak, J. Spinhirne, R. Cahalan, S. Love, S. Melfi and W. Wiscombe, "Retrieval of Physical and Optical Cloud Thicknesses from Space-borne and Wide-angle Lidar," *Proceedings of the 18th Int'l Laser Radar Conference*, Berlin, in press, 1997b.
- A. Marshak, A. Davis, R. Cahalan, and W. Wiscombe, "Nonlocal Independent Pixel Approximation: Direct and Inverse Problems," *Trans. Geosci. Rem. Sensing.*, accepted, January, 1997a.
- A. Marshak, A. Davis, R. Cahalan, and W. Wiscombe, "Physical Simulation of High-res. Satellite Images for Fractal Cloud Models, in **Fractals in Geophysics**, World Scientific, M. Novak and T. G. Dewey, Eds., 301-310, 1997b.
- A. Marshak, A. Davis, W. Wiscombe, W. Ridgway and R. Cahalan, "Biases in Shortwave Column Absorption in the Presence of Fractal Clouds," *Journal of Climate*, accepted, April, 1997c.
- A. Marshak, A. Davis, W. Wiscombe and R. Cahalan, "Inhomogeneity Effects on Reflectance versus Transmittance Estimates of Cloud Shortwave Absorption: Two-aircraft Simulations," *J. Geophys. Res.*, accepted March, 1997d.
- G. L. Stephens, "Reply to Harshvardhan and Randall," *Mon. Wea. Rev.* **113**, 1834-1835, 1985.
- M. Tiedke, "Extension of Cloud-Radiation Parameterization in the ECMWF Model: Representation of Subgrid-Scale Variations in Optical Depth," *Mon. Wea. Rev.* **124**, 745-750, 1996.

Global Monitoring and Retrievals of Atmospheric Aerosols and Clouds

Si-Chee Tsay

Climate and Radiation Branch, Code 913

NASA Goddard Space Flight Center, Greenbelt, MD USA

(Tel: 301-286-9710, Fax: 301-286-1759, email: tsay@climate.gsfc.nasa.gov)

Abstract -- A knowledge of aerosol and cloud radiative properties and their variation in space and time is especially crucial to the understanding of the radiative forcing in all climate related studies. The role of clouds in modifying the Earth's radiation balance - albedo cooling effect in short-wave radiation and greenhouse warming effect in longwave radiation - is well recognized as a key source of uncertainty. Man-made processes, both burning of fossil fuels and biomass, generate greenhouse gases and aerosol particles. Directly, aerosol particles can scatter and absorb the sun light. Indirectly, these particles may serve as cloud condensation nuclei and alter cloud albedo. Ship tracks have provided intriguing examples of cloud albedo modification by anthropogenic aerosols. There has been a general concern that the potential climate forcing from the indirect effects of aerosol on clouds can be of comparable magnitude, but opposite in sign, to greenhouse gas radiative forcing.

Global monitoring of aerosol and cloud radiative effects relies on advanced Earth Observing Systems (e.g., NASA's EOS and NASDA's ADEOS). Key advances include simultaneous observation of radiation budget and aerosol/cloud properties, additional information on particle size, phase, and vertical layer structure. Comprehensive radiation models are used to develop retrieval algorithms. This paper presents an overview of the science and technique in remote sensing and retrievals of atmospheric aerosols and clouds. High quality multi-spectral imagery, together with nadir propagating lidar measurements, acquired from high altitude aircraft in many field experiments are served as examples for discussion.

EARTH OBSERVING SYSTEMS

Observations by remote sensing from space broaden our view and perception of the Earth Sciences, and permit for the first time a systematic view of the Earth. Current and future Earth observing satellites can provide opportunities for global monitoring and retrievals of atmospheric aerosols and clouds. For example, a comprehensive suite of instruments onboard the first Japanese ADEOS (ADvanced Earth Observing Satellite) was successfully launched and operated in orbit since August 1996; the first U.S. EOS (Earth Observing System) AM-1 is scheduled to launch in June 1998. These series of satellites, including those from other countries, form the basis for a comprehensive International EOS and assure the capability of continuous operation for at least 15 years. Sustained observations will allow scientists to monitor Earth's climate variables over time to determine trends and to estimate magnitudes.

It has been a long-standing goal to quantify global cloud and aerosol properties from spaceborne observations, such as cloud cover, cloud particle thermodynamic phase, cloud optical thickness and effective particle radius, cloud top altitude and temperature, aerosol optical thickness, and aerosol columnar mass concentration, etc. The development of retrieving atmospheric aerosol and cloud properties can benefit greatly from using the multi-spectral, multi-angle, and high spatial and temporal resolution EOS data. For example, simultaneous determination of cloud optical thickness and effective particle radius can be achieved by inverting visible and near-infrared radiometric data, with the help of forward radiative transfer calculations. The underlying principle on which these techniques are based is the fact that the reflectance of clouds at a non-absorbing band in the visible wavelength region is primarily a function of the cloud optical thickness, whereas the reflectance at a water (or ice) absorbing band in the near-infrared is primarily a function of cloud particle size. More sophisticated approaches in retrieving cloud properties may utilize more spectral information. For example, the MODIS (MODERate resolution Imaging Spectroradiometer, EOS AM-1) algorithms (King et al. 1996) apply seven bands (0.65, 0.86, 1.24, 1.64, 2.13, 3.75, and 11.03 μm) in cloud retrievals for optimal performance. Different MODIS bands are used for different surface types (i.e., 0.65 μm over land, 0.86 μm over ocean, and 1.24 μm over snow/ice) to enhance retrieval sensitivity; and others for atmospheric corrections.

Similarly, the retrievals of aerosol properties can take advantage of the MODIS wide spectral range and high spatial resolution. Using the shortwave infrared bands (e.g., 2.1 and 3.7 μm) to identify dark objects and to estimate their reflectance at the visible bands (e.g., 0.47, and 0.66 μm), the aerosol optical thickness and mass concentration can be retrieved from measured radiance field (Kaufman and Tanré 1996). An alternative method is utilizing the ultraviolet techniques (e.g., channels available in Total Ozone Mapping Spectrometer, ADEOS), in which the radiative signatures of biomass burning aerosols are spectrally dependent as opposed to clouds and background environments. By taking the reflectivity differences between ozone non-absorbing wavelengths, the effects of multiple scattering between the Rayleigh molecules and aerosols are dominant and can be represented as a measure of the abundance of aerosols in the atmosphere (e.g., Hsu et al. 1996).

DISCUSSIONS

For many Earth remote sensing applications, cloud de-

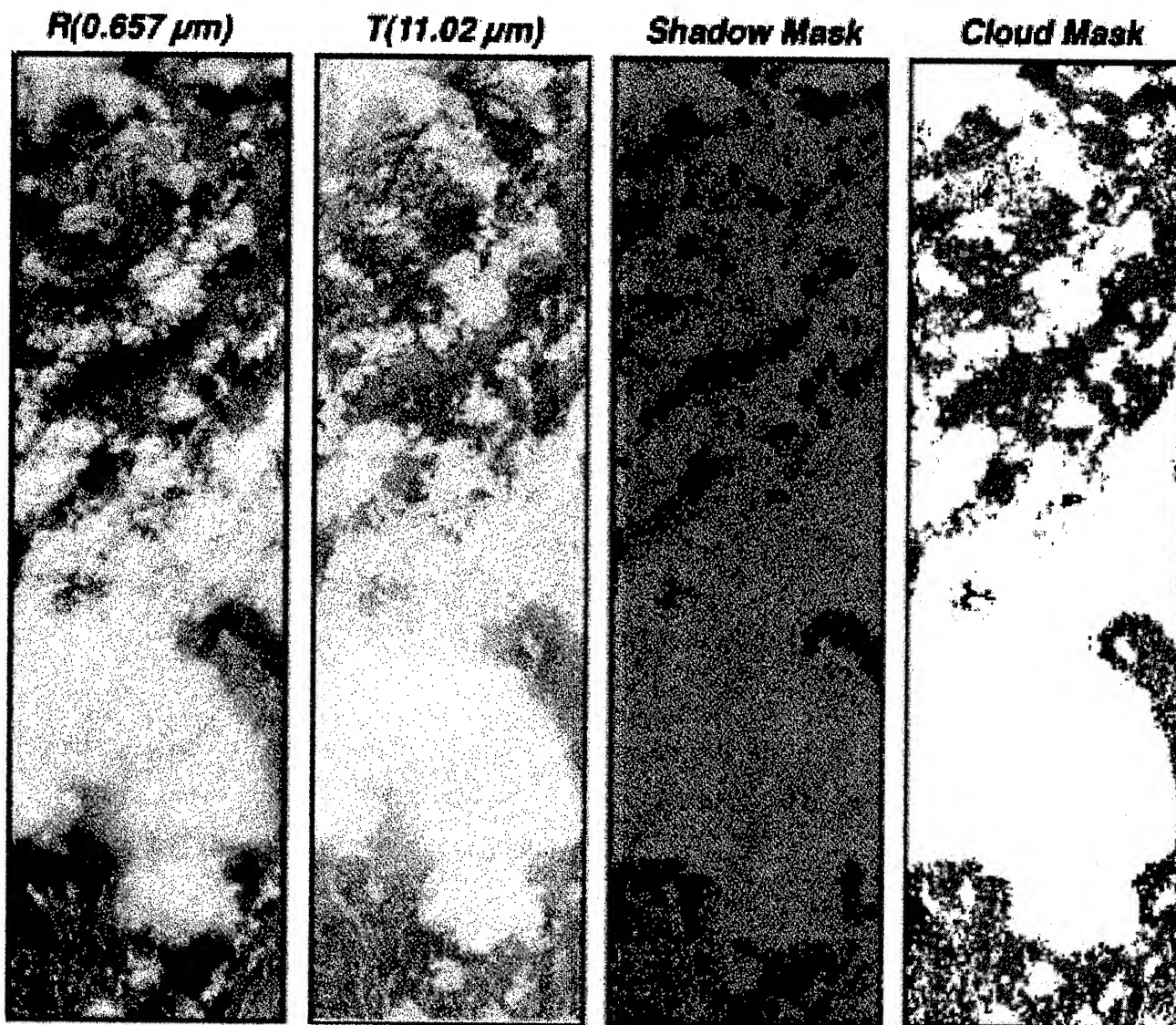


Fig. 1. Results of reflectance, brightness temperature, cloud and cloud shadow masks derived from the MAS measurements obtained on 7 June 1995 during ARMCAS field experiment

tection (or derivation of a cloud mask) is vital because the Earth is frequently covered by various types of clouds. The cloud mask indicates whether a given field of view has an unobstructed view of the Earth surface, or whether the pixel is cloud free but affected by cloud shadows or thick aerosol (Ackerman et al. 1996). Spectral information from up to 14 MODIS channels (visible, near-IR and IR) is used, for the first time. Below, we use the 50-channel MAS (MODIS Airborne Simulator, 0.47 - 14.35 μm) measurements for discussions. With their high spatial resolution (~ 50 m at ER-2 20 km altitude), MAS measurements help to assess ways of convolving small scale variations to the larger scales typical of satellite sensors (like MODIS, with its primary resolution of 1 km) and serve as a prototype for cloud mask development.

Figure 1 shows the results of cloud and cloud shadow

masks, together with 0.657 μm reflectance and 11.02 μm brightness temperature measurements from ARMCAS (Arctic Radiation Measurements in Column Atmosphere-surface System, conducted in Alaska and Beaufort Sea area in June 1995) experiment. Images of a convective cumulonimbus cloud (lower center) surrounded by lower level water clouds on the northern foothills of the Brooks Range, Alaska, were acquired on 7 June 1995. The first panel on the left (0.657 μm) shows high contrast between the optically thick (and therefore bright) cumulonimbus cloud, diffuse cirrus anvil, and remnants of the snow pack lying in ravines and topographic depressions (lower right of image), less reflective altocumulus clouds (upper and center portion of image), and dark tundra. The second panel (11.02 μm) appears quite cold (low radiance) in the coldest portion of the cumulonimbus cloud (-50°C), warmer at the top of the altocumulus cloud (-18°C), where the cloud must be composed

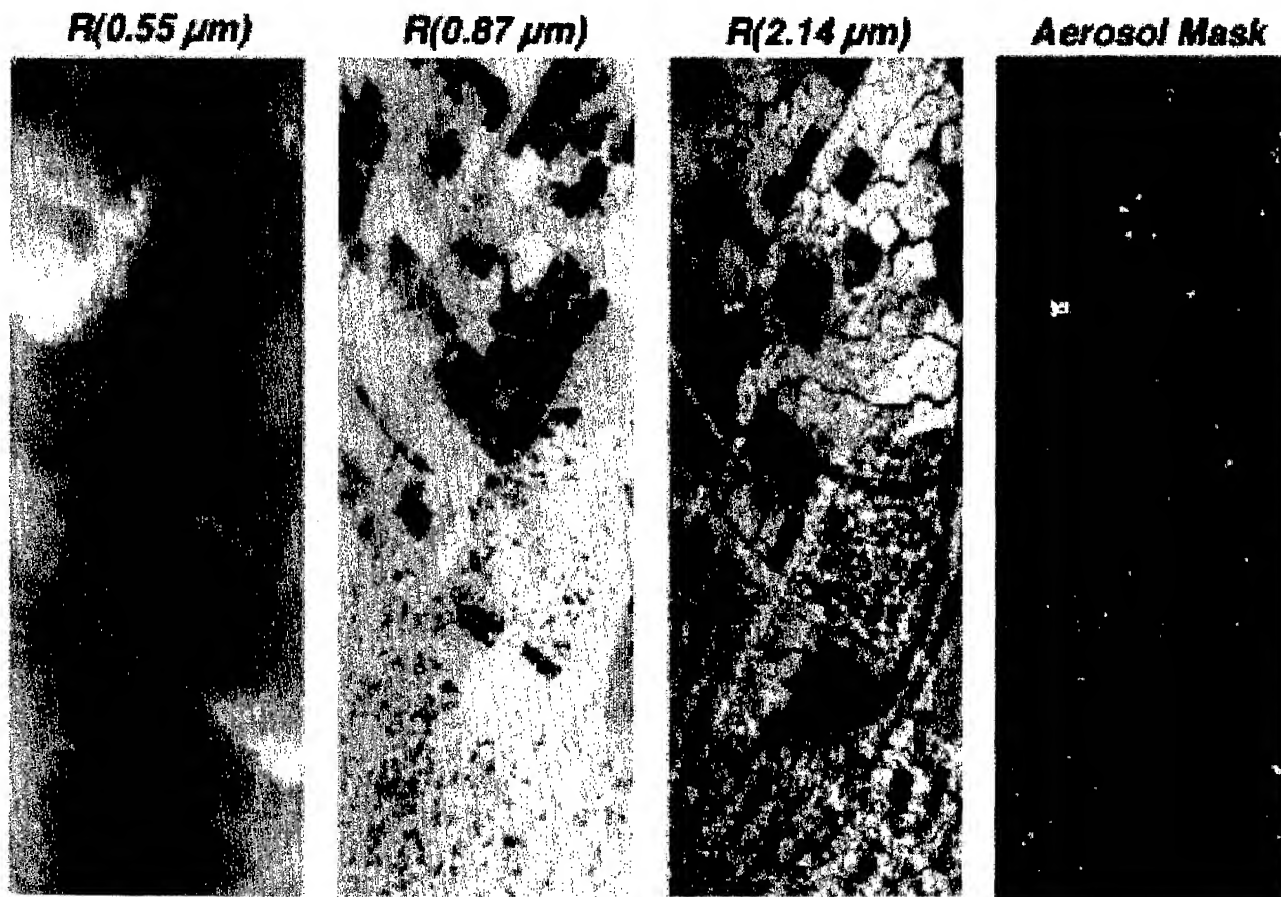


Fig. 2. Results of spectral reflectance and cloud mask, with indication of heavy aerosol loading (or aerosol mask), derived from the MAS measurements obtained on 4 September 1995 during SCAR-B field experiment.

of supercooled water rather than ice (according to the 1.609 and 1.879 μm channels, not shown), and warmest at the surface (+17°C). By comparing to the 0.657 and 11.02 μm images, the detection of cloud shadow mask (blue color in the third panel) and cloud mask (white color in the last panel) was very successful.

In the springtime burning season in Brazil, thick haze is generated by burning of cerrado and primary forest, producing much haze as well as burning and smoldering fires and clouds. Figure 2 shows an example of the application of the cloud mask (clear sky with aerosol loading) to such biomass burning aerosols in SCAR-B (Smoke, Clouds, And Radiation - Brazil, August - September 1995. At 0.55 μm it is difficult to see the ground due to the heavy smoke and aerosol from extensive biomass burning. At 0.87 μm (second panel from left), on the other hand, surface reflectance is high and the haze is transparent, except where the ground has already been burned and is dark from burn scars. At 2.14 μm (third panel), the burn scars are again quite reflective, as if often the case over pavement in cities. The resultant aerosol mask (last panel) was derived from a combination of tests on 12 different MAS channels. Most of the scene is classified as high confident clear with heavy aerosol

(red in aerosol mask), and correctly noting that this scene is not composed of cloud as suggested from 0.55 μm band.

REFERENCES

- Ackerman, S., K. Strabala, P. Menzel, R. Frey, C. Moeller, L. Gumley, B. Baum, C. Schaaf, G. Riggs and R. Welch, 1996: *Discriminating clear-sky from cloud with MODIS Algorithm Theoretical Basis Document (MOD35)*. Algorithm Theoretical Basis Document ATBD-MOD-06, NASA Goddard Space Flight Center, 119 pp.
- Hsu, N. C., J. R. Herman, P. K. Bhartia, C. J. Seftor, O. Torres, A. M. Thompson, J. F. Gleason, T. F. Eck, and B. N. Holben, 1996: Detection of biomass burning smoke from TOMS measurements. *Geophys. Res. Lett.*, **23**, 745-748.
- Kaufman, Y. J., and D. Tanré, 1996: Strategy for direct and indirect methods for correcting the aerosol effect on remote sensing: From AVHRR to EOS-MODIS. *Remote Sens. Environ.*, **55**, 65-79.
- King, M. D., S. C. Tsay, S. E. Platnick, M. Wang, and K. N. Liou, 1996: *Cloud Retrieval Algorithms for MODIS: Optical Thickness, Effective Particle Radius, and Thermodynamic Phase*. Algorithm Theoretical Basis Document ATBD-MOD-05, NASA Goddard Space Flight Center, 70 pp.

Effects of large structure in Wet Snow Cover on SAR Measurements

Jiancheng Shi, Rich Kattlemann, and Jeff Dozier

*Institute For Computational Earth System Science (ICESS)
University of California, Santa Barbara, CA 93106, U.S.A
Tel: 805-893-2309, Fax: 805-893-2578, E-mail: shi@icess.ucsb.edu*

INTRODUCTION AND BACKGROUND

The movement of liquid water through snow occurs in distinct flow paths rather than as uniform flow. Lateral down-slope flow along textural discontinuities may account for a greater fraction of total water movement than has been realized. Flow fingers can deliver water through the snowpack for weeks before the entire pack becomes wet. Although water flow in snow is not uniform, we normally lack knowledge of the spatial and temporal distributions of the flow paths, so many models (both microwave and snow melt) of water movement treat the pack as a homogeneous porous medium. Information about spatial and temporal distributions of flow paths will provide an opportunity to improve modeling of snowmelt. Moreover, lateral down-slope flow along textural discontinuities may generate a thin saturation layer, which will weaken the stability of the snowpack and increase the probability of avalanches. If we can identify flow paths remotely, we can provide information for snowmelt modeling, analysis of ionic pulses from the snow, and avalanche control.

Radar measurements at long wavelengths (mainly L-band with 24 cm wavelength) from SIR-C over some wet snow covered regions have shown unexpected signatures [2], e.g., backscattering coefficient, σ^0 , at L-band greater than that at C-band (5.6 cm wavelength), L-band σ^0 at VV polarization smaller than at HH polarization.

In modeling backscatter and polarization properties of a wet snow cover, we generally consider the volume scattering contribution and the surface scattering contributions from the air-snow interface and snow-ground interface or from the air-snow interface only depending on the frequency and amount of free liquid water content in snow pack. The surface backscattering is characterized as $VV \geq HH$ polarization signal. The

volume scattering from snow pack commonly assumed to be due to randomly orientated (or spherical) ice particles and water inclusions which have no difference in extinction properties in VV and HH polarization. The direct volume backscattering from snow pack is also characterized as $VV > HH$ polarization since the power transmissivity of VV is always greater than that of HH polarization at air-snow interface. In addition, both the volume scattering and the surface backscattering for a typical air-snow roughness range increase as the radar frequency increases. Therefore, the currently available microwave models for snow cover fail to explain these observations over wet snow at long wavelength (24 cm) because free liquid water is treated as uniformly distributed in snowpack. This assumption may be valid at C-band [3] since it only penetrates a few cm where a thin wet snow surface layer (a few cm) is commonly found even during the early snow melt season. At longer wavelengths, however, the microwave sensor can "see" through the thin surface wet layer and observe the signals generated by flow paths.

We have developed a microwave model to evaluate the effects of large structures in wet snow cover, such as draining fingers and channels, on backscattering and polarization properties, especially at L-band. With the numerical simulation, we demonstrate the characteristics of backscattering and polarization signatures at each stage of draining finger and channel developments. Thus, it will show the potential of SAR applications for both snow melting model improvement and snow avalanche prediction and control.

MODEL CONSTRUCTION

In most seasonally snow-covered areas, a distinct transition occurs between a winter accumulation season and a spring melt season. During this transition period, the character of snow cover changes drastically and

sustained snow melt runoff begins. As liquid water enters the snow pack, a series of processes collectively known as *ripening*, *aging*, or *melt metamorphism* ensue [4]. One of the most important processes is the creation of a flow network in snow pack [1].

When liquid water is generated at the snow surface by melting or is added by rainfall, it will be retained by capillary pressure in the pore spaces. Where fine-grain snow overlies coarse-grain snow, water will accumulate in the upper layer, forming a commonly found wet snow layer at the top of the snow surface, until the pressure difference between the layers is relieved and water flows into the lower layer. If there is a sufficient discontinuity in snow texture, water will accumulate in a saturated layer until water pressure at the interface approaches atmospheric pressure at which point water begins to flow into the lower layer. If the saturated layer is inclined, water will tend to flow down slope. These fingers and channels become preferred pathways for additional flow as grain size and permeability increase within them. In general, flow fingers should become better developed in warmer snow packs. Creation of saturated layers and flow fingers contributes to an irregular distribution of liquid water beyond that at the grain scale.

Based on the above characteristics of flow fingers and channels, we consider four states of melting conditions for microwave modeling in order to evaluate the effects of draining finger and channels in a wet snow pack on the backscattering and polarization properties at L-band as shown in Figure 1. We model wet snow pack as multi-layers with

1. the first wet snow layer at the top snow surface with a few cm thickness - an uniformly distributed liquid water inclusion,
2. the second layer - vertically orientated flow fingers as the dielectric cylinders (with higher liquid water content) embedded in a dry or slightly wet snow background medium,
3. the third layer - vertical orientated lateral flow fingers (normal to surface) and channels as the dielectric discs (high wetness) embedded in a dry or slightly wet snow background medium,
4. the fourth layer is same as the second layer to account for the further development of flow fingers and channels during the later transition season.

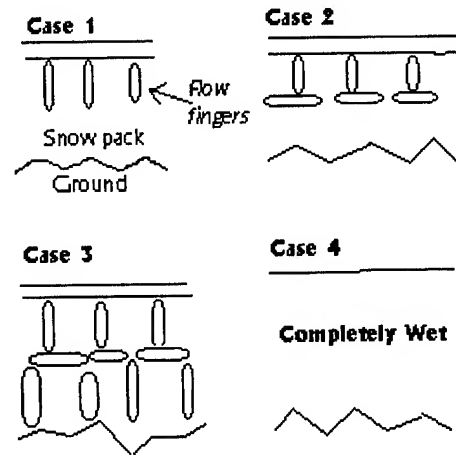


Figure 1. *Geometric considerations for the different characteristics of draining fingers and channels.*

Later in the spring season, the snow pack becomes completely wet and there is no significant dielectric discontinuity within snow pack as shown in Figure 1, case 4. The microwave model will be same as the traditional used models.

NUMERICAL SIMULATION AND DISCUSSION

Figure 2 shows the simulated backscattering components at 30° for HH polarization (top) and VV/HH ratio and VH polarization (bottom) for case 1 (as in Figure 1, where there are only vertical flow fingers - the second layer) at L-band with fixed cylinder size parameters. The effect of flow fingers is quite small on radar backscattering measurements when there are only a few flow fingers at very early transition season. The ground surface backscattering is the dominant scattering source. However, the calculated backscattering coefficients at C-band and X-band are even smaller than that at L-band since the penetration depth are only about a wavelength. Therefore, the radar at L-band can “see” the different scattering source (snow-ground interface) as compared with C-band and X-band. As shown in Figure 2, the volume scattering and surface-volume interaction terms increase significantly as the volume fraction increase (more flow fingers). It can increase about 4 dB when the volume fraction of the flow fingers is 5 %. The VV to HH ratio continuously increase as the volume fraction of flow fingers increases. Since the backscattering models for both the surface and the volume (for random orientated particles) predict $VV \geq HH$, it will be difficult to detect

the existence of flow fingers even with higher volume fraction by only using backscattering and VV/HH ratio at L-band.

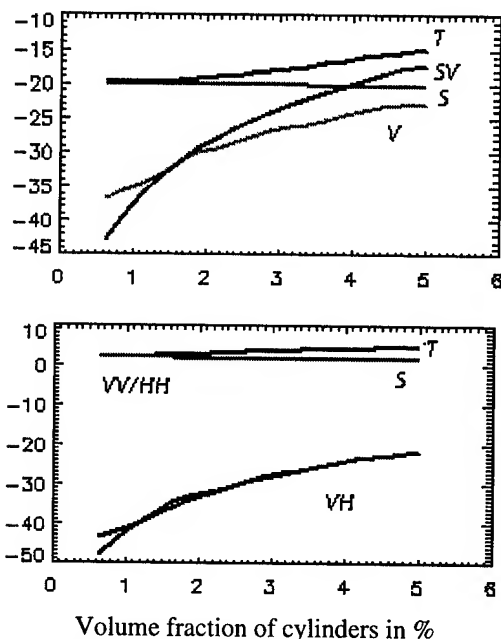


Figure 2. Simulated case 1 backscattering components at 30° for HH polarization (top) and VV/HH ratio and VH polarization (bottom) at L-band with fixed cylinder size parameters. In Figure, T - total backscattering; S - ground surface backscattering component; V - volume backscattering component generated by flow fingers as vertical orientated dielectric cylinders; and SV - the surface and volume interaction component.

However, a significant increase in backscattering will be observed when lateral flow fingers and channels have been developed in snow pack as shown in Figure 3. The volume scattering from lateral flow fingers increase very quickly as the disc radius increase. For the small radius cases, VV > HH is observed since the surface backscattering from snow-ground interface, which is characterized as VV ≥ HH, is the major scattering source. As the disc radius further increases, up to about 6 cm, the volume scattering contribution becomes greater than that from snow-ground interface. The HH becomes greater than VV polarization. This is because the normal vertical discs generate larger volume scattering in HH polarization than that in VV polarization. Therefore, HH > VV in radar measurements will be expected as shown in Figure 3 (bottom). This phenomena indicates that the

relationship between HH and VV might be used to identify or detect flow fingers and paths. Thus, it has high potential to provide information on snow pack stability.

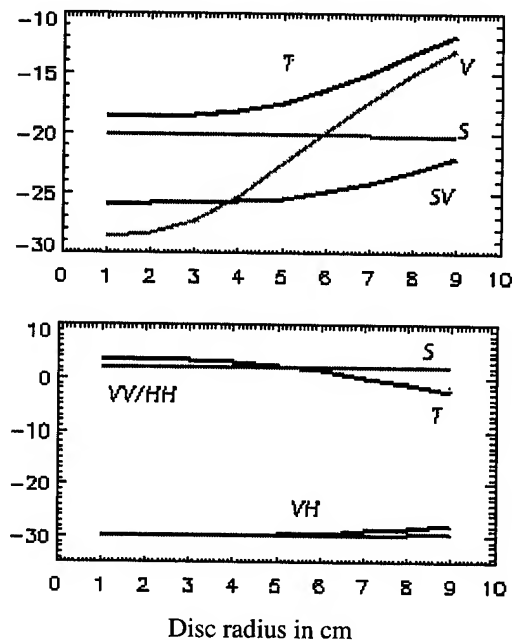


Figure 3. Simulated case 2 backscattering components at 30° for HH polarization (top) and VV/HH ratio and VH polarization (bottom) at L-band with fixed number density and disc thickness.

REFERENCES

- [1] R. Kattelmann, "Water movement and ripening processes in snowpacks of the Sierra Nevada", Ph.D. thesis, Department of Geography, University of California, Santa Barbara, 1995.
- [2] J. Shi and J. Dozier, "Mapping Seasonal Snow with SIR-C/X-SAR in Mountainous Areas", *Remote Sensing Environment*, vol. 59, no. 2, pp. 294-307, 1997.
- [3] J. Shi and J. Dozier, "Inferring snow wetness using SIR-C C-band polarimetric synthetic aperture radar", *IEEE Transactions on Geoscience and Remote Sensing*, vol. 33, no. 4, pp. 905-914, 1995.
- [4] S. C. Colbeck, "The physical aspects of water flow through snow", in *Advances in Hydrosience*, edited by V. T. Chow, vol. 11, pp. 165-206, Academic Press, New York, 1978.

Microwave rainfall monitoring: a Tuscany study case

S. Nativi, M. Padoin, P. Mazzetti, L. Baldini, D. Giuli

Department of Electronical Engineering University of Florence

Via S. Marta, 3 - 50139 Florence - ITALY

Phone: +39-574-602532 ; Fax: +39-574-602515 ; e-mail: nativi@pinet.ing.unifi.it

Abstract -- The present work empirically deals with the challenging problem of the integration of data obtained from passive and active microwave sources, in order to develop procedures to suitably calibrate and validate satellite-based passive microwave rainfall algorithms by means of near-simultaneous multi-parameter radar information acquired over the same area. SSM/I passive microwave radiometer precipitation related parameters have been compared with multi-parameter radar Zh and Zdr constant-altitude and vertical profile maps, obtained from CAPPI and RHI data from the POLAR-55C meteorological radar, located near Florence in Italy. As a result, such investigation proved the importance of considering the different vertical penetrations due to the diverse microwave channels, in order to work out better regression laws between the passive and active data.

INTRODUCTION

The ability of satellite-born passive microwave sensors to detect precipitation events has been demonstrated by several investigators lately. In particular the DMSP series of SSM/I have been used to map regions of precipitation and ongoing validation studies through international projects have confirmed the ability of such passive sensor to generate rain fields reliably [1].

Although there are several techniques available to identify areas of rain from these instruments, the conversion to an instantaneous rainrate results difficult for the inhomogeneity of the rain fields in the relatively large microwave footprints causing the so-called "beam-filling" effect. Additionally, the estimation of rainfall values has strict regional dependence based upon the physical processes of the precipitation regime. This problem is compounded by the scarcity of validation data, especially in midlatitude regions as the European one. Surface-based radar measurements of precipitation are based on the estimation of hydrometeors falling from the bases of clouds, they view the atmosphere from the bottom upwards way. The temporal and spatial resolution is very good; therefore, radar data may be very useful to tackle passive microwave satellite data shortcomings. The utilisation of multi-parameter radar information is very useful in order to estimate the amount of certain hydrometeor types. That is, a classification of the

cloud vertical structure (even if uncompleted) is achieved through Montagnana radar data.

Referring to Mugnai et al. [2] the different wavelengths of the SSM/I sensor can not penetrate all the same atmospheric strata; this work separated the radar data in several layers in order to go into this issue.

MONTAGNANA RADAR DATA

Montagnana radar is a multi-parameter C-band radar, located near Florence (17 km far from it). Data sets, derived from the Montagnana radar are based on volume acquisitions. The obtained 3-D Zh and Zdr blocks were sliced along the altitude axis, producing a set of Constant Altitude PPI (CAPPI) maps. Therefore, each CAPPI characterises a different layer of the cloud structure.

SSM/I DATA

The Special Sensor Microwave Imager (SSM/I) is a passive sensor which detects radiances at four frequencies: 19.35, 22.235, 37.0 and 85.5 GHz. The 19, 37 and 85 channels have dual polarisation (vertical and horizontal), the water vapour line at 22.235 GHz has only vertical polarisation. This instrument is aboard of the operating Defense Meteorological Satellite Program (DMSP) Block 5D-2 Spacecrafts: F10, F11, F13. The seven channels have different spatial resolutions (i.e. EFOV on earth surface in the cross-track direction) from roughly 43 Km at 19.35 GHz to approximately 13 Km at 85.5 GHz). Considering these spatial resolution differences and the definitely better radar spatial resolution, we used a deconvolution scheme developed initially by Poe [3], but subsequently corrected and improved by staff of the Centre for Remote Sensing of Bristol, in order to increase SSM/I data resolution.

DATA PROCESSING

SSM/I images were spatially deconvoluted and projected according to UTM system with a resolution of 5x5 km per cell. They were then processed in order to correct possible navigation errors and are centred on the Montagnana radar site. Snow and cold ground pixels were filtered according to the Ferraro and Grody algorithm [4]. Several SSM/I

parameters related to precipitation over land have been achieved, among them:

$$\text{I and Q Stokes parameters: } \begin{cases} I_{85} = \frac{T_{b85v} + T_{b85h}}{2}; \\ Q_{85} = \frac{T_{b85v} - T_{b85h}}{2}; \end{cases}$$

Polarization Corrected Temperature:

$$\begin{cases} PCT_{85} = \frac{T_{b85v} - \beta \cdot T_{b85h}}{1 - \beta}; \\ \beta = \frac{1 - \epsilon_v}{1 - \epsilon_h}; \end{cases}$$

they take into account the total amount of energy as well as the polarisation characteristic of the measured signal. Moreover, each brightness temperature estimated from the instrument (i.e. the SSM/I radiometer) was considered in order to analyse their vertical atmospheric penetration. Each Zh and Zdr CAPPI radar map was subdivided into bins -made up of several radar map pixels- of the same dimension of SSM/I map pixel. Thus, it was possible to correlate each radar bin with the correspondent SSM/I pixel. Radar bins were characterised by means of the following calculated parameters: average reflectivity values ($\langle Zh \rangle$, $\langle Zdr \rangle$), number (N) of useful -i.e. significant- reflectivity values belonging to the bin, and the fractional standard deviation of reflectivity values (FSD).

Hydrometeor classification

Several algorithms have been written to classify hydrometeor types according to reflectivity in multi polarised radars. All these algorithms, from Zrnice and Straka [5] or Holler and Meischner [6] use the Linear Depolarization Ratio (LDR). Montagnana radar does not provide LDR, so we have to set our own classification using only Zh and Zdr. The schema defined by Doviak and Zrnice [7] was utilised; it is reported in Tab. 1. Starting from this schema, empirical thresholds were estimated for the classification of the cloud structures analysed in the present work. Radar and SSM/I parameters maps were geographically co-registered, and overlaid, correlating the diverse achieved information. In particular, correlation values for each SSM/I estimated parameter against $\langle Zh \rangle$ and $\langle Zdr \rangle$ values were worked out, and the following main analyses considered:

- Analysis of the behaviour of the correlation values as the CAPPI altitude value is changing.
- Analysis of the influence that the N parameter has on the correlation values.
- Analysis of the improved correlation values, obtained filtering the radar data according to the classification of

Tab. 1, and the results obtained from the previous analyses.

Furthermore, the spatial variance related to each SSM/I pixel was estimated through FSD, and its influence on the regression were considered.

Hydrometeor Type	Zh	Zdr	Comments
Rain	High	High	Includes large oblate drops
Drizzle, Cloud or Fog	Low	Low	Small spherical drops of water and/or small ice particles
Dry Snow Flakes	Medium-Low	Medium-Low	Large horizontally oriented low-density aggregates
Sleet / Wet Snow	High	High	Large oblate horizontally oriented particles
Wet Graupel	High	Negative	Large conical vertically oriented particles
Wet Hail	High	Variable	Large particles, seldom spheres
Dry Hail, High density Ice particles	Medium	Low	

Tab. 1 Expected characteristics of Zh and Zdr for various Hydrometeor types

RESULTS AND PERSPECTIVES

As far as our data set is concerned, the statistical analysis suggests that:

- different strata have definitively diverse influence for the SSM/I channels; and therefore the same is true as far as the parameters related to rainfall are considered;
- both N and FSD are critical parameters for the fusion and correct correlation of the active and passive microwave data; in a certain way, they take into account the beam-filling problem;
- from our analysis, it is quite evident the necessity to consider different hydrometeor classification schemes, for the different layers of achieved CAPPI map; it is likely, that this is due to the lack of more significant parameters (e.g. the LDR one);
- filtering radar data according to parameters values, derived from the previous analyses, it is possible to

definitively improve the correlation between SSM/I and radar data; this was particularly true for PCT parameter calculated from 85 GHz values.

The present results must be assessed through further study cases.

ACKNOWLEDGMENTS

The authors would like to thank the Marshall Space Flight Center Distributed Active Archive Center (MSFC-DAAC) for SSM/I brightness temperature data.

REFERENCES

- [1] E.C. Barrett, and M.J. Beaumont, "Satellite Rainfall Monitoring: an Overview," Remote Sensing Review, vol. 11, pp. 23-48, 1994.
- [2] A. Mugnai, E.A. Smith, H.J. Cooper, G.J. Tripoli, and X.W. Xiang, "Foundations for statistical physical precipitation retrieval from passive microwave satellite measurements. Part I brightness temperature properties of a time dependent cloud-radiation model", J. Appl. Meteor., vol. 31, pp 506-531, 1992.
- [3] G. Poe, "Optimum interpolation of imaging microwave radiometer data," IEEE Trans. Geosci. Remote Sensing, vol. 28, No 5, pp. 800-810, September 1990.
- [4] R.R. Ferraro, N.C. Grody, G.F. Marks, "Effect of Surface Conditions on Rain Identification using the DMSP-SSM/I," Remote Sensing Reviews, vol. 11, No 14, pp. 195-209, 1994.
- [5] D.S. Zrnica, J.M. Straka, "An Algorithm to Deduce Hydrometeor Types and Contents From Multi-Parameter Radar Data", 26th International Conference of Radar Meteorology, 513-515, 1993.
- [6] H. Holler, P.F. Meischner, "Identification of Severe Storm Types by Combined Polarization and Doppler Measurements", Cost 75 Weather Radar Systems International Seminar. Report EUR 16013 EN. 736-743, 1995
- [7] R.J. Doviak, D.S. Zrnica, "Doppler radar and weather observations", Academic Press, Inc., Orlando, Florida, 1984.

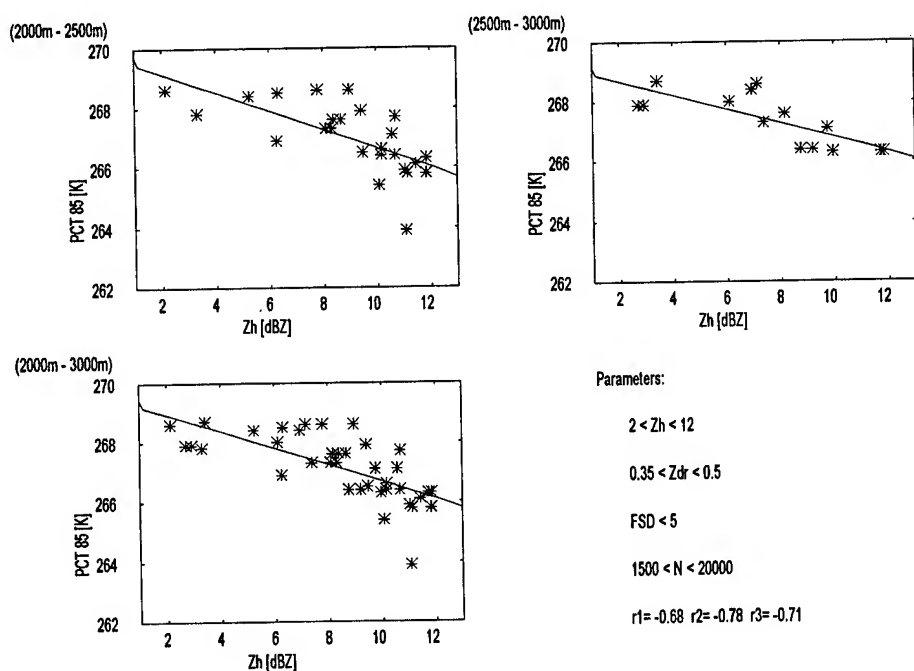


Fig.1 Scatterplot of PCT 85 GHz against Zh values for three different strata: 2000-2500 m, 2500-3000 m and 2000-3000 m respectively ; radar values were filtered according to the reported parameters thresholds. Correlation values are reported (i.e. r1, r2 and r3).

Simultaneous Radar and In-situ Aircraft Based Observations of Convective Storms: Intercomparison Study

A. M. Abou-El-Magd, V. Chandrasekar, V. N. Bringi

Colorado State University, Fort Collins, CO 80523

email : chandra@engr.colostate.edu

J. W. Strapp, Atmospheric Environment Services, Canada.

Abstract – During the summer of 1995 the CSU-CHILL multiparameter radar and an instrumented aircraft (T-28 operated by the South Dakota School of Mines and Technology) were used to collect coordinated measurements over summer-storms in Northern Colorado. This paper presents comparison of the radar and aircraft data collected over a hailstorm which occurred on 22 June 1995. The predominant precipitation observed by T-28 was mixed phase consisting mainly of wet spherical hail and rain particles. The T-28 aircraft was equipped, for the first time, with a High Volume Particle Spectrometer, (HVPS), capable of collecting two dimensional images of hydrometeors encountered in the flight path. Simultaneously, the radar was collecting data in a PPI sector scan mode covering the elevations of the aircraft track. A comparative study of the multiparameter radar data and the in-situ aircraft observation for this storm is presented with the objective of interpreting multiparameter radar signatures.

INTRODUCTION

The CSU-CHILL multiparameter radar provides a set of polarization diversity measurements [1], namely the radar reflectivity at horizontal polarization, Z_H , differential reflectivity between horizontal (H) and vertical (V) polarization, Z_{DR} , specific differential propagation phase, K_{DP} , Copolar correlation coefficient, $\rho_{HV}(0)$, and Linear depolarization ratio, LDR . The size, shape, orientation distributions as well as the density of the hydrometeors in the radar resolution volume determine the values and variabilities of the multiparameter radar measurements. For example Z_{DR} is a measure of the reflectivity weighted shape, K_{DP} is independent of the isotropic constituents of the precipitation, (such as spherical or tumbling hail), $\rho_{HV}(0)$, is mainly affected by the mixed phase precipitation due to inhomogeneities in H and V backscattered signals, and finite LDR occurs only if the particles in the radar resolution volume are not symmetric with respect to the H/V axis. We refer to the review article by Bringi and Hendry [1] for a full description of the multiparameter radar measurements. In this paper, the multiparameter radar signatures of mixed phase precipi-

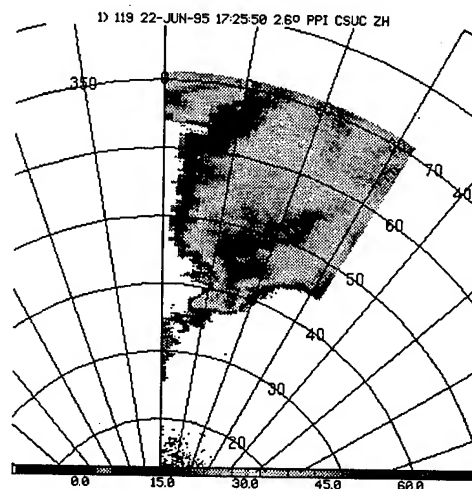


Figure 1: The Cell Location

tation collected in a hailstorm that occurred on June 22, 1995 are studied. The radar signatures along the T-28 tracks were simulated using an electromagnetic scattering model based on the HVPS observations with the objective of interpreting these signatures.

THE JUNE 22, 1995 HAILSTORM

A severe Hailstorm occurred on June 22, 1995 near Fort Collins, Colorado. This storm grew to a height of 12.5 km and upon collapsing produced heavy rain and hail of sizes up to 3-4 cm. The T-28 made four passes through a storm cell located 35 km range away North East of the CSU-CHILL radar, (fig.1). The radar continuously scanned the storm approximately every 1 to 2 minutes through the time interval 17:25:00 to 17:45:00 in PPI mode covering the aircraft tracks. The time history of K_{dp} , and ρ_{hv} for this storm, shown in fig.2, show that K_{dp} reaches to values above 5.8 deg/km, which confirms the heavy rain observed during this event. At the same time the area of $\rho_{hv} \leq 0.96$ extended all over the cell, indicating the mixed phase event. Gradually, with the decrease of K_{dp} values, the area of $\rho_{hv} \leq 0.96$ decreases. Fig.3 shows the reflectivity contours and the aircraft track for one of the

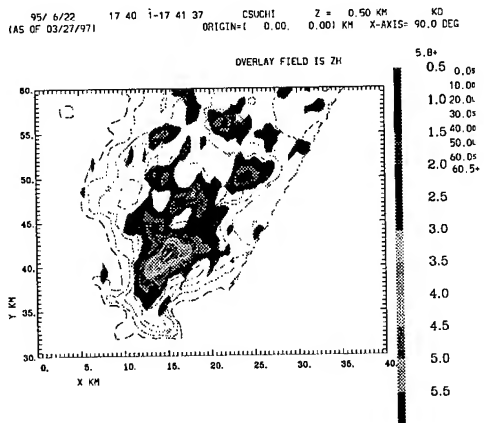


Figure 2: The K_{dp} contours with overlaid contours of reflectivity.

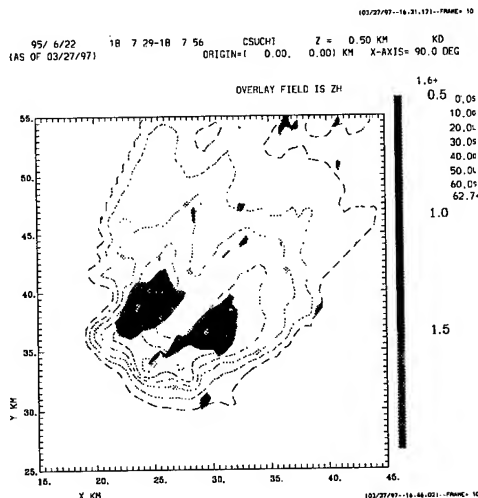


Figure 3: The T28 track overlaid on reflectivity contours.

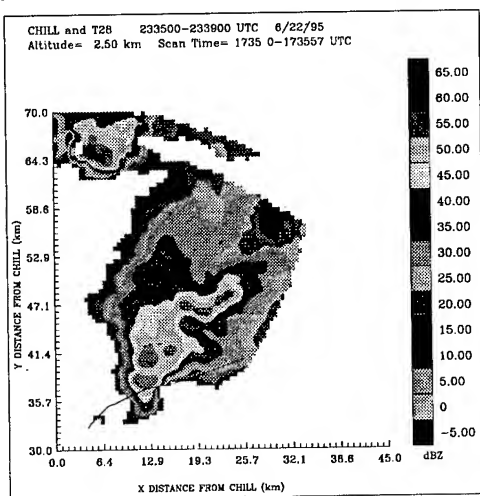


Figure 3: The T28 track overlaid on reflectivity contours.

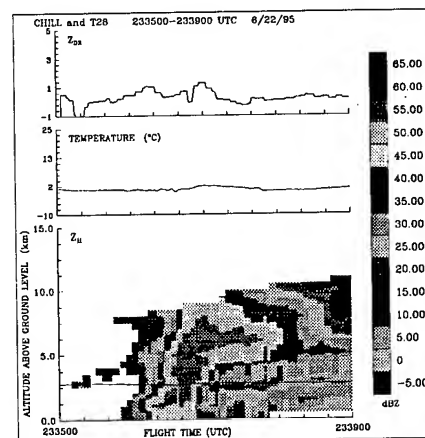


Figure 4: Vertical profile of Z_H along the T28 track

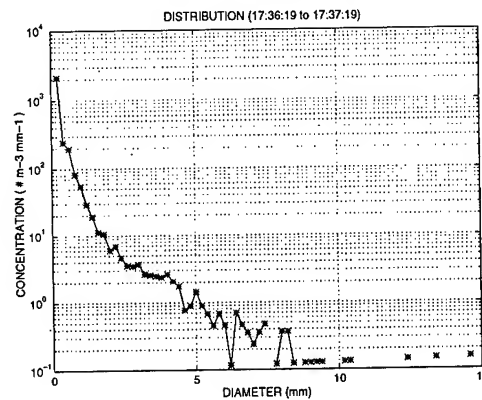


Figure 5: Particle size distribution observed by HVPS; 17:36:19 to 17:37:19

passes during 173500-173900 UTC. The vertical profiles along the T-28 pass, (fig.4), show that Z_H reaches to 60 dBZ along the T-28 pass, the corresponding Z_{DR} value is about zero and the LDR values is around -20 dB, all these indicative of melting ice. The four T-28 passes were studied in detail. Each pass corresponding to several radar volumes. The radar signatures were evaluated for each volume at the corresponding T-28 flight track. The particle size distribution corresponding to each radar volume was evaluated using the HVPS data, (fig.5). The particles were modeled according to their HVPS images into classes of rain/hail or melting ice. Fig.6 shows an example of hail particle. The melting and shedding of hailstones as observed with HVPS are shown in fig.7. We notice that the hailstones accumulate meltwater on its surface and this behaviour causes its axis ratio to decrease as a water torus builds up around its equator. Once an unstable amount of meltwater accumulates on the surface of the hailstone, shedding of water begins (see fig.7). The radar signatures along T-28 tracks were simulated based

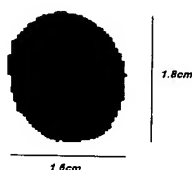


Figure 6: 2D-HVPS Hail image, 17:36:46, June22,95 at 2.5 km altitude.

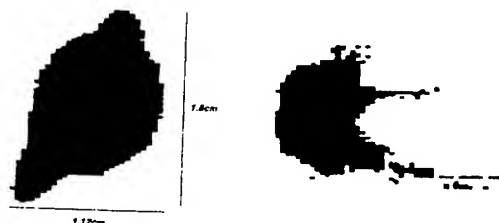


Figure 7: Hailstone melting, 17:36:46, and shedding, 17:42:59, 2D-HVPS image, June22,1995, at 2.5 km altitude.

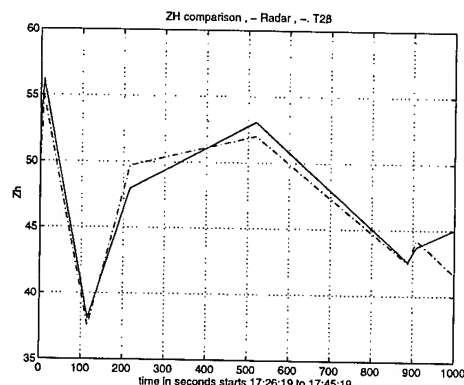


Figure 8: Radar and T28 Z_{HH} comparison; June22,1995

on HVPS data. Fig.8-fig10 show the comparison of radar measurements and the simulation results.

CONCLUSIONS

Multiparameter radar measurements of a hailstorm are described. The storm was simultaneously sampled by airborne HVPS probe to collect coordinated in-situ measurements. The radar signatures along the flight tracks were simulated based on the in-situ observations, thereby providing an indirect verification of the microphysical and electromagnetic models. The radar/aircraft intercomparison results show good agreement between the measured radar data and the estimated radar signatures using the HVPS particle images.

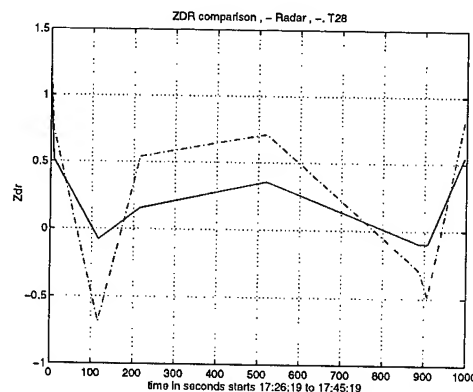


Figure 9: Radar and T28 Z_{DR} comparison; June22,1995

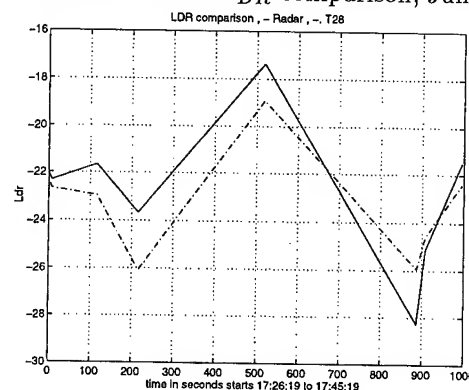


Figure 10: Radar and T28 LDR comparison; June22,1995

ACKNOWLEDGMENTS

The authors acknowledge support from AFOSR via grant FA 9620-95-1-0133 and NSF. The field program was funded by CSU center for Geosciences via DOD grant DAA04-94-G-0402.

REFERENCES

- [1] Bringi, V. N., and A. Hendry, 1990: Technology of polarization diversity radar for meteorology . chapter (19a), from Radar in Meteorology, Atlas, D. American Society, pp 153-190.

Airborne W-band Radar Measurements of the Doppler Spectrum of Light Precipitation

John Galloway, Andrew Pazmany, Robert McIntosh

Microwave Remote Sensing Lab

Knowles Engineering Building, University of Massachusetts at Amherst, Amherst, MA 01003

T: (413) 545-0723, F: (413) 545-4652, galloway@alex.ecs.umass.edu

David Leon, Jeff French, Sam Haimov, Robert Kelly, Gabor Vali

University of Wyoming, Department of Atmospheric Science

Laramie, WY 82071

T: (307) 766-4955, F: (307) 766-2635, rkelly@grizzly.uwyo.edu

Abstract — This paper presents Doppler spectrum measurements of drizzle and marine stratocumulus clouds from the University of Wyoming King Air W-band radar taken during the Coastal Stratus experiment off the coast of Oregon during late 1995. Comparisons with 2D PMS laser size spectrometer measurements of the same region indicate substantial agreement between the two approaches to drop size spectrum measurement.

INTRODUCTION

Both highly resolved W-band measurements of precipitation and aircraft drop size spectrometer measurements are available from this experiment. Comparisons between these two data sets allow determination of the relationships between the properties of the precipitation and the W-band measurements. Examples of such properties include the total drop concentration, the drop size spectrum, and development of the drop size spectrum throughout a precipitating cloud. This provides information about precipitation initiation.

Topics covered in this paper include the radar measurement technique and calibration, the post-processing required to relate the measurements to the drop size spectrum, and comparisons with drop size spectra measured with the wingtip size spectrometers on the King Air. Evaluation of the measurements and their interpretation is carried out for four different observations of marine stratocumulus clouds.

MEASUREMENT AND CALIBRATION

The University of Wyoming 95 GHz, airborne, cloud profiling, polarimetric radar is a pulsed, fully coherent, dual receiver radar system with programmably switched linear (H and V) polarization from pulse to pulse. An antenna mounted to the fuselage of the King Air is shielded by a faring containing a motor-driven reflector plate and two dielectric windows, providing the capability to direct the radar beam up or to the side during flight. The outputs of the two receivers are sampled by digitizers which stream data to DSP's running in parallel for data pre-processing. Further information on this radar may be found in [3], which discusses the details of a similar polarimetric radar system developed for the King Air by the University of Massachusetts.

This work was supported by NSF Grant No. ATM-9320672.

The radar sampled groups of 64 transmit pulses, all H polarization, directed up at either 15 or 5 kHz to form Doppler spectrum estimates. One case of the high PRF data is available from September 14, and 3 cases of data taken at the lower PRF are available from September 16. The real-time signal processing system calculated a periodogram from each group of 64 samples. Eight (16) such estimates were formed and averaged for each of the Doppler spectrum estimates and were stored at a rate of 15.5 Hz (4.24 Hz). This processing was done for each of 100 range gates separated by 15 m (30 m), starting at a range of 60 m (90 m). Corner reflector measurements obtained before and after each flight provided the absolute calibration.

POST-PROCESSING

Averaging of the Doppler spectrum estimates along track was performed to match the intervals at which 2DC and 2DP data were reported (1 second or about 85 m along track, depending on air speed). The resultant number of periodograms averaged for each reported Doppler spectrum was 124 (68). Since the pulse repetition frequency of the radar was 15 kHz (5 kHz), the folding velocity for the spectral estimates was 11.9 ms^{-1} (3.95 ms^{-1}).

The procedure used for inversion of the Doppler spectra to drop size distributions assumes that the measured spectra are related to the drop distribution by the following [1, eq. 8.77]:

$$S_n(w - w_t)dw_t = \frac{\sigma_b(D)N(D)dD}{\eta}, \quad (1)$$

where $S_n(w - w_t)$ is the measured spectrum normalized to the total reflectivity, $\eta (= \int_0^\infty \sigma_b(D)N(D)dD)$, shifted by the amount required to remove vertical air motion (w), w_t is the terminal fall speed of the drops of a given diameter, D , σ_b is the volume backscatter coefficient and $N(D)$ is the drop size distribution in terms of drop diameter.

Inversion of $S_n(w - w_t)$ to $N(D)$ is accomplished by solving (1) for $N(D)$:

$$\frac{S_n(w - w_t)\eta}{\sigma_b(D)} \frac{dw_t}{dD} = N(D), \quad (2)$$

where the values for $\sigma_b(D)$ may be calculated for spherical drops of water using Mie's solution for backscatter from dielectric spheres [2]. For the purposes of this analysis, the form

of the Mie solution developed by Deirmendjian and presented in [5] was used.

The velocity for a particular bin, v_k , including the effect of aircraft motion, is:

$$v_k = k \frac{\lambda}{2MT_s} + v_{acbeam} + v_{updraft}, \quad (3)$$

where λ is 3.16 mm, T_s is the PRT (66.7 μ s or 200 μ s), v_{acbeam} is the offset velocity for aircraft motion resolved into the radar beam pointing direction, $v_{updraft}$ is the air motion into the radar beam, $-\frac{M}{2} \leq k \leq \frac{M-1}{2}$ and M is the number of FFT bins.

The relation between w_t and D used to find the drop diameters corresponding to the measured velocities was one proposed in [4]:

$$w_t(D) = \begin{cases} KD(1 - e^{-kD}) & D \leq D_0, \\ A - Be^{-CD} & D \geq D_0, \end{cases} \quad (4)$$

where $K = 4 \text{ ms}^{-1}\text{mm}^{-1}$, $k = 12 \text{ mm}^{-1}$, $A = 9.65 \text{ ms}^{-1}$, $B = 10.43 \text{ ms}^{-1}$, $C = 0.6 \text{ mm}^{-1}$, and $D_0 = 0.745 \text{ mm}$. This relation was chosen principally due to its tractable nature in carrying out the derivative required in (2). A correction for air density was also applied using the pressure and temperature measurements available from the King Air sensors. The relationship used for correction from air at a reference density of ρ_0 given a temperature, T_0 , of 293 K, and reference pressure, P_0 , of 760 mm Hg was [1]:

$$w_t(D, \rho) = w_t(D) \left(\frac{T_0 P}{T P_0} \right)^{0.5}, \quad (5)$$

where ρ is the air density at a temperature of T and pressure of P .

DROP SIZE SPECTRUM COMPARISONS

Plots of the drop size spectra as measured by the aircraft probes and estimated from the Doppler spectrum measurements may be found in figures 1 to 5. The representative drop spectra in figure 1 display substantial agreement between the radar estimates and probe measurements, particularly for the 2DC probe data. The following figures, one for each of four cases, show the scatter between the 2DC probe concentration density measurements and radar estimates for the drop diameters relevant in these four cases. Ten seconds of data from both systems were averaged to obtain each point on these scatter plots, providing a trade off between convergence of the probe measurements and the amount of available data. Time stamps on each plot indicate the start and stop times of the available data segments. For all four cases, the 75 μ m bin results indicate substantial disagreement between the two systems. Higher diameters, however, show better agreement. Quantization effects in the probe data complicate interpretation of the higher diameter results (225 μ m or more).

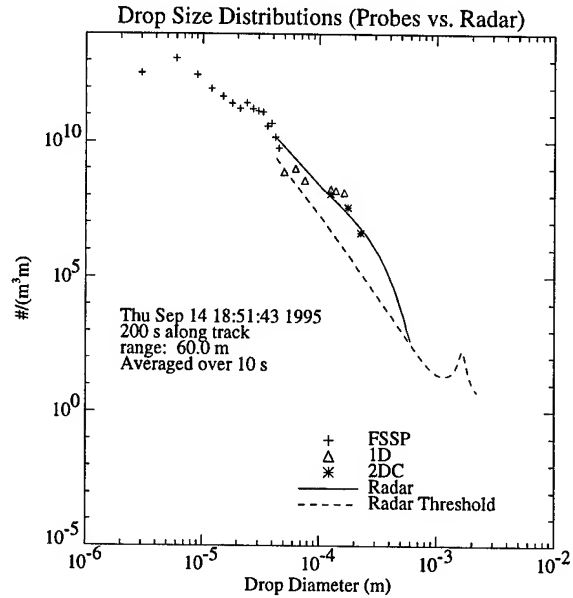


Fig. 1. Representative drop size spectra from aircraft probes and radar data (September 14 case)

CONCLUSIONS

The measurements of the drop size spectrum from both wing tip probes and the University of Wyoming W-band radar agree to a substantial degree. Further effort in this regard will likely address the issues of distortion due to aircraft motion and turbulence and error analysis for both systems. The use of the W-band data samples further away from the aircraft will be hampered by a lack of information regarding the air motion away from the aircraft and the attenuation encountered along the transmission path. However, the results obtained from this current study provide reasonable indication that relationships between the radar measurements of Doppler spectra and the drop size spectrum in a cloud and light precipitation may be examined in fine detail using this airborne radar system.

REFERENCES

- [1] R.J. Doviak and D.S. Zrnić. *Doppler Radar and Weather Observations*. Academic Press, Inc., 1993.
- [2] G. Mie. Betirage zur Optik Truber Medien, Speziell Kollidaler Metalasungen. *Ann. Physik*, 25, 1908.
- [3] A. L. Pázmány, R. E. McIntosh, R. Kelly, and G. Vali. An Airborne 95 GHz Dual-Polarized Radar for Cloud Studies. *IEEE Transactions on Geoscience and Remote Sensing*, 32(4):731–739, July 1994.
- [4] R. R. Rogers, D. Baumgardner, S. A. Ethier, D. A. Carter, and W. L. Ecklund. Comparison of Raindrop Size Distributions Measured by Radar Wind Profiler and by Airplane. *Journal of Applied Meteorology*, pages 694–699, April 1993.
- [5] F. Ulaby, R. Moore, and A. Fung. *Microwave Remote Sensing; Active and Passive vol. 1*. Artech House, 1982.

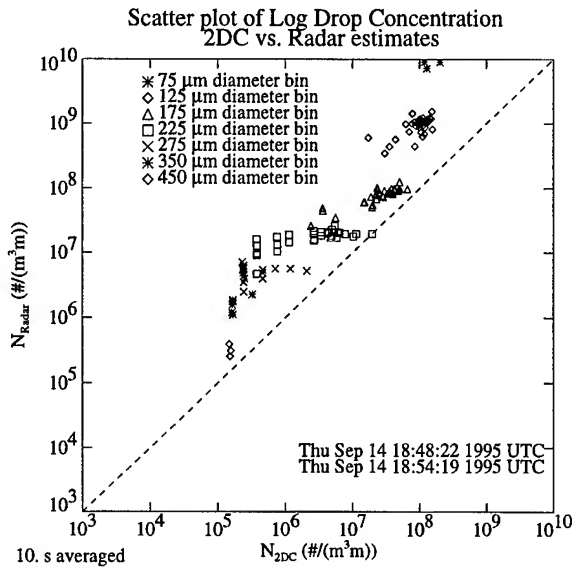


Fig. 2. Scatter plot of drop concentration density for particular bins (2DC probe vs. radar data) from the September 14 measurement.

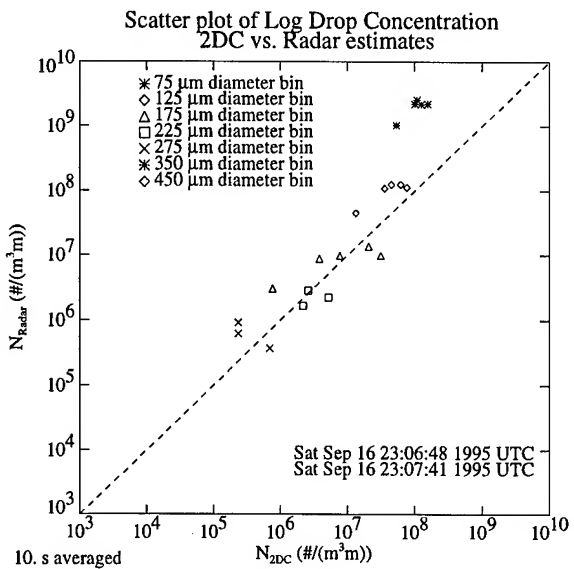


Fig. 4. Scatter plot of drop concentration density for particular bins (2DC probe vs. radar data) from the second September 16 measurement.

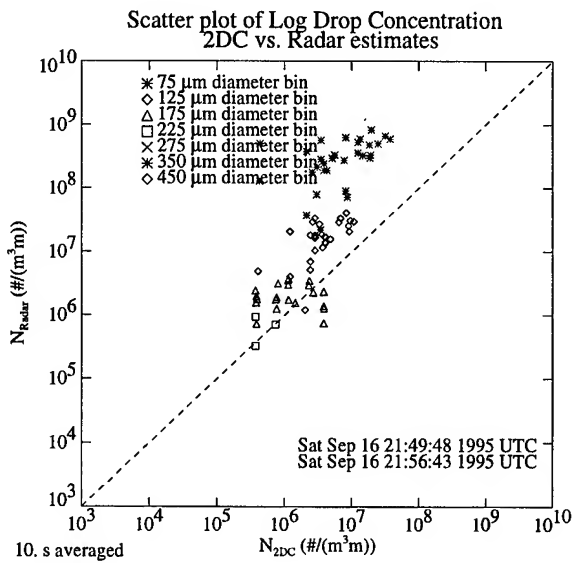


Fig. 3. Scatter plot of drop concentration density for particular bins (2DC probe vs. radar data) from the first September 16 measurement.

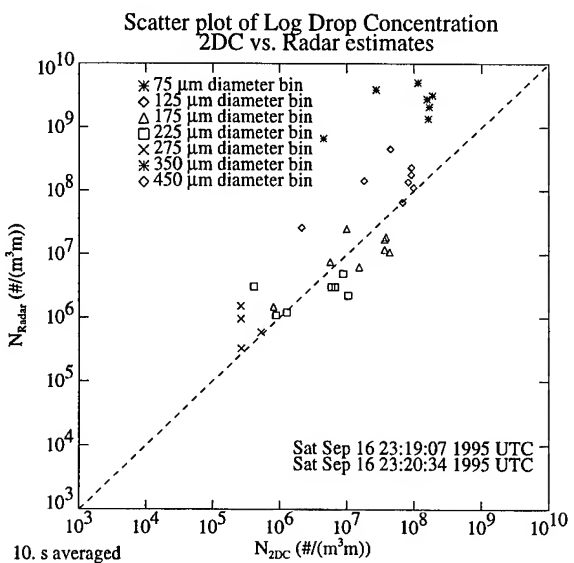


Fig. 5. Scatter plot of drop concentration density for particular bins (2DC probe vs. radar data) from the third September 16 measurement.

Tracking the Evolution of Rain Patterns by means of Modal Matching

Fabio Dell'Acqua, Paolo Gamba, Andrea Marazzi

Dipartimento di Elettronica, Università di Pavia, Via Ferrata, 1, I-27100 Pavia

Tel: +39-382-505923 Fax: +39-382-422583 E-mail:{fabiodll,gamba,maraz}@comel1.unipv.it

Abstract – In this paper the usefulness of the modal matching approach for shape analysis to meteorological data interpretation is shown.

A tracking chain for the detection and the analysis of rain patterns or the rainfall area of a given rain event is developed and tested on actual meteorological radar sequences.

A morphing procedure to guess the evolution of the structures of interest between two radar frames is also introduced.

1. INTRODUCTION

The wide variety of visible and microwave sensors able to obtain an estimation of rainfall areas at the scale of wide geographic regions (satellites), but also at medium and small scales (meteorological radars), allow the study with different resolution of the spatial structure of precipitation, whose knowledge is mandatory to achieve a deeper insight on the hydrological characteristics of the area basin. However, the raw data supplied by the measuring systems must be processed to provide the information on the spatial/temporal characteristics of the rain events [1, 2]. In particular, we need a system able to track the spatial evolution of rain patterns: from the synoptic external scale of frontal systems to the meso-gamma scale of convective cells, each rain pattern displays its own dynamic, which is sometimes coupled with the others, sometimes not, and we must deal with targets continuously changing their shape while moving. Shape evaluation is therefore one of the key problems in meteorological data understanding.

In the last years many techniques have been developed for shape analysis in machine vision, employing eigen-shapes, eigensnakes or eigenpictures. More recently, a robust technique named modal matching has been proposed [3]: in our work we want to present the application of this method to rain pattern tracking (also possible at different scales, by means of the integration of satellite and meteorological radar measurements), enlightening the spatio/temporal relationships among the spatial scales of a rain event.

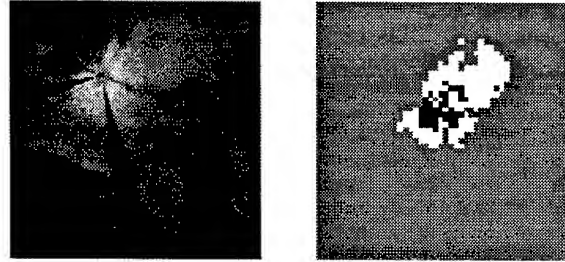


Figure 1: A radar frame of the sequence of October 8th, 1992, and the extracted rain patterns.

2. THE MODAL MATCHING TECHNIQUE

More in detail, the modal matching technique is based on the representation of an object by means of N points, generally (but not only) from its boundary. Each point is considered as a concentrated mass element (or *node*), bounded to its neighbors by elastic relations. The ensemble of all points follows the so called dynamic equilibrium equation:

$$\mathbf{M} \frac{\partial^2 \vec{U}}{\partial t^2} + \mathbf{D} \frac{\partial \vec{U}}{\partial t} + \mathbf{K} \vec{U} = \vec{R} \quad \text{in } \mathbb{R}^2 \quad (1)$$

that rules the elastic behavior of the whole structure, when forced by external strengths. The same equation allows to express the displacement in each node due to these forcing strengths by means of the resonating modes of the same structure, computed as the solution of an eigenvalue matrix system corresponding to the unconstrained counterpart of the dynamic equilibrium equation.

$$\mathbf{K} \Phi = \Gamma^2 \mathbf{M} \Phi \quad (2)$$

Practically, this last equation is obtained by means of the introduction of N two-dimensional Gaussian basis functions, each centered on a node, and a FEM (Finite Element Method) procedure. The solution of (2) gives some eigenvalues (representing the *natural* resonating frequencies of the shape) and the associated eigenvectors, i.e. the deformation to which the boundary is submitted as a consequence of each resonance.

The first eight modes of a mesoscale rain pattern extracted from actual radar data are presented in fig. 2.

The eigenvalues found forms an effective basis $\Omega = \{\omega_1, \omega_2, \dots, \omega_N\}$ for shape analysis and recognition, ex-

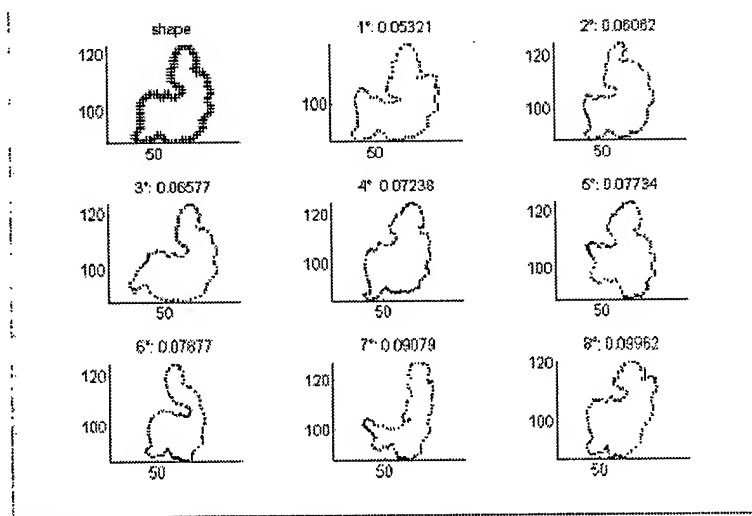


Figure 2: The first eight modes of a rain pattern extracted from radar data.

Table 1: The characteristics of the Teolo radar

Geographical location	Northern Italy
Height	500 m asl
Type	conventional or Doppler
Frequency	5.4 GHz
Resolution	≥ 1 Km
Maximum range	240 Km
Polarization	vertical or horizontal
Peak power	250 Kw

remely useful to track and monitor any change in meteorological data. The modal matching technique allows in fact to find easily the correspondences between similar shapes with a high degree of precision, as the authors have outlined in [6]; therefore, it corresponds to a valuable mean to characterize in great detail the evolution of rain patterns at different mesoscale not only by tracking each pattern during the temporal sequence of radar data, but also by allowing a deeper insight in the evolution of the different parts of these patterns.

3. EXPERIMENTAL RESULTS

The complete procedure to test the suitability and reliability of the method for rain pattern tracking has been applied to several actual radar data sequences. In particular, here we report the results for the rain event happened in Northern Italy on October 4th, 1992, as it was recorded by the weather radar in Teolo (near Venice), whose electromagnetic characteristics are summarized in Table 1.

For this sequence, the rain patterns at two different mesoscale have been extracted by means of a wavelet analysis procedure recently developed by the authors [4, 5],

particularly suited for rain structures' detection. Then, a shape extraction routine determined the points of the images corresponding to the boundaries of the different patterns to be tracked, and, finally, the modal matching analysis has been applied to retrieve, for each silhouette, a modal representation.

Object belonging to the same scale but in different radar frames have been compared by computing their distance in the *modal space*. The analysis led to the recognition of the position of the same structure (even with substantial changes in shape) in subsequent frames independently from its position, and without the need to compute before a *possible* future position, for instance by extrapolating the past behavior of the pattern.

Moreover, by computing the similarity between the sets of points representing two correlated shapes, but now in the deformation space, we were able to extract point correspondences, and to retrieve a more detailed analysis of the movements of each rain pattern.

In fig. 1 a radar frame and the corresponding extracted patterns is presented, while in fig. 3 the point correspondences between two rain patterns at the same scale (but in different time frames) is shown.

4. MODAL MORPHING

Moreover, modal matching allows to introduce a morphing process, useful for instance to guess rain-pattern shape variations in the time-intervals between the recorded frames, or for short-time forecasts.

Once the points from the two shapes have been matched, adding complete modal deformations results in turning one shape into an other; so, *gradually* introducing them, one gets progressive transformation of the first shape into



Figure 4: The results of the morphing procedure applied to the two shapes of fig. 3.

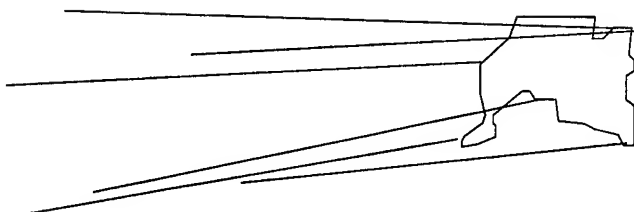


Figure 3: Point correspondences between two rain patterns at the same scale, but in subsequent frames of the radar sequence.

the second. *Gradual* introduction consists essentially in adding subsequently small parts of spatial deformation until the reaching of the complete transformation. A simple way to attain morphing is therefore to build each following frame from the previous by adding to point positions the displacement due to a calculated quantity of modal deformations. Acting this way, the last frame obtained (the one in which modal deformations have been completely introduced) superimpose exactly to the final desired shape.

If $\mathbf{x}_{i,1}(t)$ is the position of the i -th point of the point set representing the starting shape, it changes in time according to the following equation:

$$\mathbf{x}_{i,1}(t + \Delta t) = \mathbf{x}_{i,1}(t) + a(t) \Delta \mathbf{i} \quad (3)$$

where

$$a(t) = \frac{1 + \sin\left(-\frac{\pi}{2} + \frac{\pi t}{T}\right)}{2} \quad (4)$$

T is the time interval of the evolution, $\tilde{\Delta} = \Phi' \tilde{\Delta}'$ are the nodal deformations needed, and $\tilde{\Delta}'$ the modal ones. The raised cosine law in (4) has been chosen according to standard morphing procedures in computer graphics.

Applying this procedure to the shapes of fig. 2, we obtain the sequence of fig. 4.

5. CONCLUSIONS

In this paper we have shown how the modal matching technique could be applied to meteorological data analysis.

With respect to the methods that are usually found in literature for this problem, like Shape Fourier Descriptors [7], modal matching exploits better the physical meaning

of the data, since it gives global information about the whole shape, and not about its local characteristics. It has also a scaling property, since it is possible to use only lower eigenvalues (corresponding to less detailed images) for recognition and tracking, and higher eigenvalues (corresponding to the higher details of the images) for more precise characterization of the movement of each part of the meteorological structure to be investigated.

REFERENCES

- [1] A. Pawlina, "Rain patterns motion over a region deduced from radar measurement," *Alta Frequenza*, Vol. LV (2), pp. 99-103, 1987.
- [2] A. Pawlina, "Radar rain patterns: automatic extraction, collection and description for modeling purposes," *Alta Frequenza*, Vol. LVI (1-2), pp. 153-159, 1987.
- [3] S. Scarloff and A. Pentland, "Modal matching for correspondence and recognition," *IEEE Trans. Pattern Analysis and Machine Intelligence*, vol. PAMI-17, no. 6, pp. 545-561, June 1995.
- [4] A. Marazzi, A. Mecocci, P. Gamba, M. Barni, "Texture segmentation in remote sensing images by means of packet wavelets and fuzzy clustering," *European Symposium on Satellite Remote Sensing II*, Paris, 25-29 Sept. 1995.
- [5] A. Marazzi, P. Gamba, R. Ranzi, "Rain pattern detection by means of packet wavelets," *Proc. of the 1996 IEEE International Geoscience and Remote Sensing Symposium (IGARSS '96)*, Vol. I, pp. 266-268, Lincoln, Nebraska, USA, 27-31 May 1996.
- [6] F. Dell'Acqua, P. Gamba, A. Mecocci, "Modal matching for rainfall patterns shape evaluation at different scales," *Proc. of the European Symposium on Satellite Remote Sensing III*, Taormina, Italy, 23-27 Sept. 1996.
- [7] P. Kumar and E. Foufoula-Georgiou, "Fourier domain shape analysis methods: a brief overview and an illustrative application to rainfall area evolution," *Water Resour. Res.*, Vol. 26 (9), pp. 2219-2227, 1990.

The NASA DC-8 Airborne Cloud Radar: Design and Preliminary Results

Gregory A. Sadowy, Robert E. McIntosh
Microwave Remote Sensing Laboratory
University of Massachusetts at Amherst
Amherst, MA 01003
T: (413) 545-0723, F: (413) 545-4652
sadowy@alex.ecs.umass.edu

Steven J. Dinardo, Stephen L. Durden, Wendy N. Edelstein,
Fuk K. Li, Alan B. Tanner, William J. Wilson
Jet Propulsion Laboratory
4800 Oak Grove Drive
Pasadena, CA 91109-8099

Timothy L. Schneider, Graeme L. Stephens
Department of Atmospheric Science
Colorado State University
Fort Collins, CO 80523

Abstract -- The University of Massachusetts Microwave Remote Sensing Laboratory and NASA Jet Propulsion Laboratory have developed a 95 GHz airborne radar system for remote sensing of clouds. This instrument was recently operated aboard NASA's DC-8 Airborne Laboratory and participated in the Cloud Layer Experiment (CLEX) in the central U.S. and in the Southern Alps Experiment (SALPEX) in New Zealand. The development of this system was motivated by the need for a sensitive, well-calibrated millimeter-wave cloud radar that can probe clouds from above. This geometry avoids the attenuation suffered by ground based systems that look up through precipitation and also simulates the viewing geometry of a spaceborne sensor. This paper describes the design and operating characteristics of the instrument as well as preliminary results from the initial deployments. Engineering test flights were conducted during June 1996, concurrent with CLEX. The instrument also collected data during two flights from California to Hawaii and New Zealand and another flight near New Zealand. Data from the flights are used to demonstrate the instruments capabilities. The data from both experiments are classified into the four classes of cloud systems used by the GEWEX Cloud System Study (GCSS). Reflectivity statistics for each class of cloud system are presented.

INTRODUCTION

In recent years, the utility of millimeter wave radars for sensing clouds has been demonstrated [1] and such instruments have been successfully used for cloud microphysical studies [2][3]. Also, studies of the impact of cloud feedbacks on the earth's radiation budget have underscored the importance of having a means of measuring the ver-

TABLE I
SYSTEM SPECIFICATIONS

Frequencies	94.905, 94.915, 94.215, 94.935 GHz
Peak Power	1.4 kW
Max. Average Power	15 W
Pulse Widths	250, 500, 1000 ns
Noise Figure (includes front end loss)	8.0 dB
Antenna Aperture	30 cm
3 dB Beamwidth	0.8 deg.

tical distribution of clouds [4][5]. Millimeter wave radars can provide this information under most conditions, with high resolution, using a relatively compact system. In 1993, the GEWEX Tropical Workshop recommended that a 94 GHz spaceborne radar be developed for this purpose and that it be supported by airborne observations [6]. The DC-8 airborne cloud radar was developed to determine the feasibility of a future spaceborne radar program and to conduct cloud studies similar to those planned for the spaceborne system, albeit on a smaller geographical scales.

SYSTEM DESIGN

Important goals of the system design were calibration stability and sensitivity. It was also quite important to achieve the receiver dynamic range required to accommodate the range of signals that are typically encountered in cloud sensing applications. Additionally, the system was designed to be rugged, serviceable and compact.

The system consists of an RF/IF subsystem, a digital

signal processor and data handling and control electronics. The RF/IF subsystem uses a combination of frequency mixing and multiplication to generate the transmitted signal at one of four frequencies in a 50 MHz band centered at 94.92 GHz. The power of the transmitted signal is supplied by an extended interaction amplifier (EIA). The transmit RF pulses can be routed to either the V or H port of an orthomode transducer (OMT) using a ferrite switch matrix. The OMT then feeds a 30 cm lens antenna. A small portion of the transmitted power is coupled through an attenuator into the receiver for calibration purposes.

The ferrite switches route the returned signals from the OMT to a low-noise amplifier. The signal then undergoes three down conversion steps to reach the final IF of 2.5 MHz. The IF signal is digitized and sent to a signal processor (that is based on four i860 vector processors) where it is digitally demodulated and filtered to achieve the final system bandwidth. The signal processor then calculates power, pulse-pair and (optionally) polarimetric correlation estimates and accumulates these estimates in real time. These processed data are then combined with auxiliary data and stored.

The calibration stability of the system is maintained by using a calibration path to remove fluctuations in transmitted power and receiver gain. The calibration path consists of two 20 dB cross-guide couplers and two attenuators with a combined loss of 47.5 dB. The calibration signal is injected into the receiver just before the LNA during the transmit interval. This path can be removed as a unit and has been characterized using a vector network analyzer.

The calibration loop presented a design challenge because of the difficulty of achieving isolation between the transmitter and receiver. Coherent leakage from unwanted paths causes fluctuations in the calibration signal. To reduce the fluctuations to a level of ± 0.1 dB, the leakage signal must be suppressed to 38 dB below the level of the calibration signal. If the calibration signal is set to a level near the receiver compression point, transmitter to receiver isolation of greater than 120 dB is required. Additional switch junctions can be added to the switching network but this increases front-end loss, thereby decreasing sensitivity. Instead, a calibration mode where the full transmitter power is dumped to an internal load was used. The switching network was designed so that an extra junction provides the additional isolation that is required during calibration mode only. These calibration mode pulses are interlaced with the data mode pulses on a time scale of 1-2 ms. This calibration data is accumulated and stored separately and used in post-processing to calibrate the reflectivity data.

The receiver design provides excellent sensitivity while maintaining high dynamic range. The 95 GHz LNA de-

termines both the system noise figure and compression point. Highly linear IF components were chosen in order to preserve this compression point. System gain can be controlled by a step attenuator in the 120 MHz IF chain, but gain reduction is only required during the transmit interval. The system has enough instantaneous dynamic range to accommodate the strongest signals encountered (ocean surface returns) at typical flight altitudes.

The final system bandwidth is achieved by using digital down conversion and matched filtering. Filter coefficients for the matched filters are derived from complex time series data collected using a corner reflector as a point target. This technique yields close approximations of matched filters for all available transmitter pulse widths, thereby maximizing sensitivity for a given pulse width.

The system can utilize frequency hopping between four frequencies in order to increase the number of independent samples. At typical flight speeds, successive pulses are only independent with respect to fading induced fluctuations after approximately 1 ms. By hopping through a sequence of four nonoverlapping frequency bands, independent samples can be collected at a rate of four kHz. When scanning limits the dwell time for each pixel, this technique is needed to reduce the variance of reflectivity estimates.

FIELD EXPERIMENTS

Test Flights / CLEX II

During May of 1996, the system was integrated into NASA's DC-8 Airborne Laboratory and engineering test flights began. A fixed nadir-viewing geometry was used for these flights. The radar was operated as a secondary instrument during JPL AIRSAR flights over the Cascades near Seattle, WA and over the Aleutian Peninsula in Alaska. Cloud radar data was collected during two flight days at each location and during the transits in between. A range of cloud types were encountered, including cirrus, stratiform precipitating systems as well as systems that contain multiple layers consisting of different cloud types.

On June 24-26 the instrument was flown in conjunction with CLEX II in southern Oklahoma. Radar data of altocumulus and cirrostratus clouds were collected while the University of Wyoming King Air aircraft collected *in situ* measurements. Also, observations were made of thunderstorms near Galveston, TX and in southern Arkansas during this time period.

On July 1st, marine stratocumulus were observed in an area approximately 350 km west of Los Angeles.

Pacific transit / SALPEX

Near the end of October 1996, the system was operated on transit flights from Moffet Field, CA to Honolulu, HI,

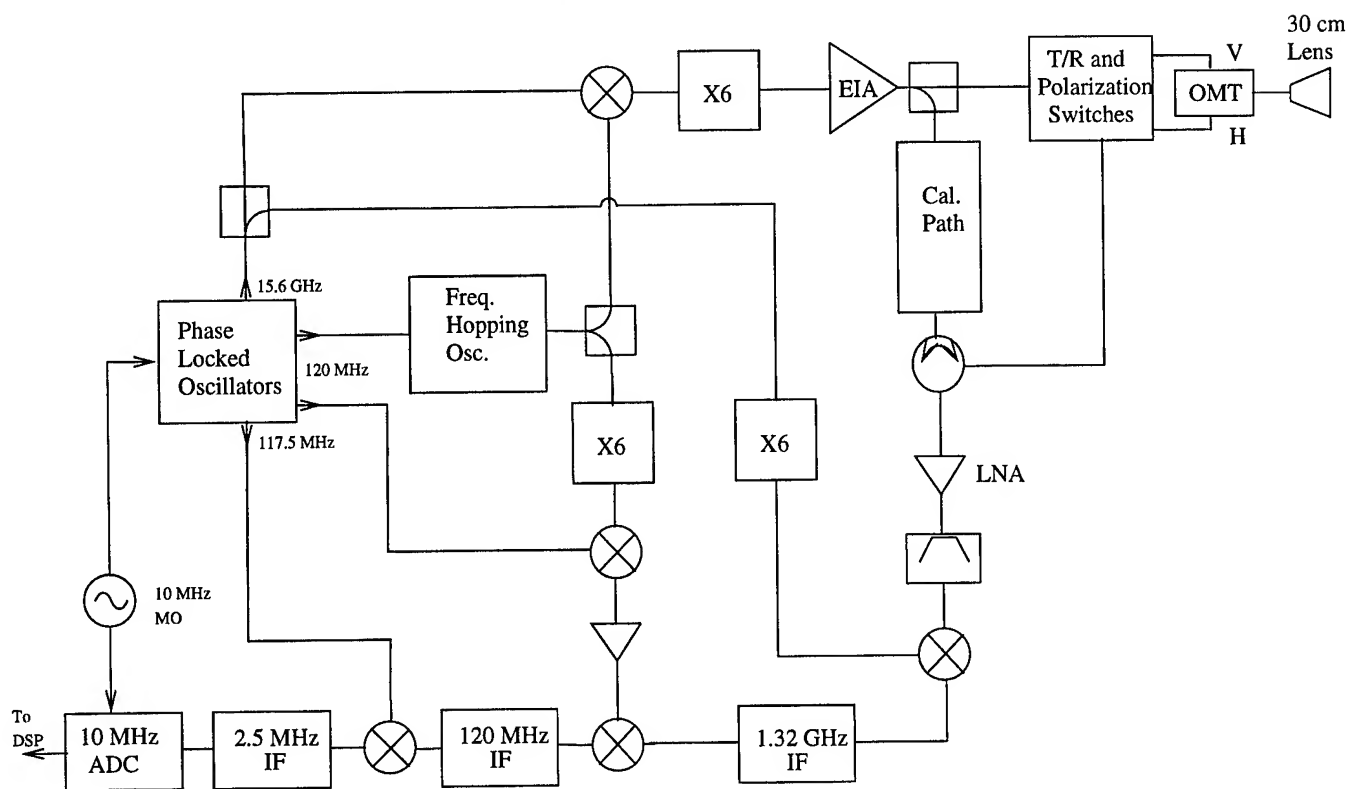


Fig. 1. Simplified block diagram of RF/IF subsystem

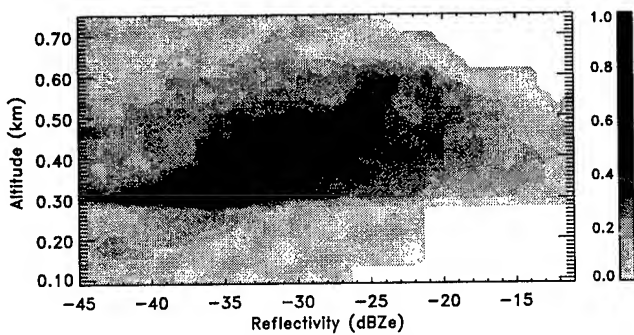


Fig. 2. CFAD for boundary layer clouds

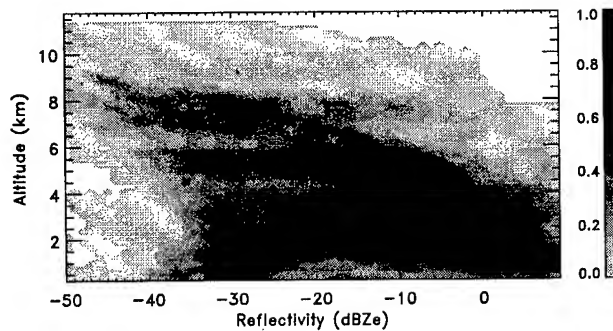


Fig. 4. CFAD for extratropical layer clouds

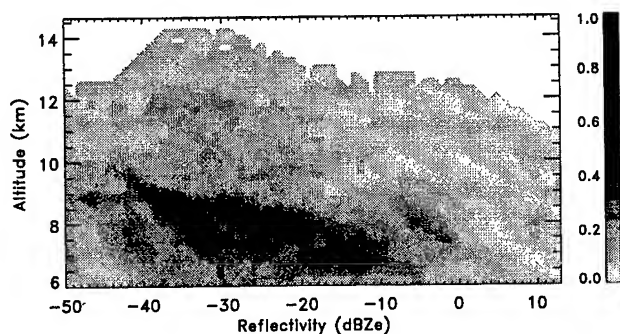


Fig. 3. CFAD for cirrus clouds

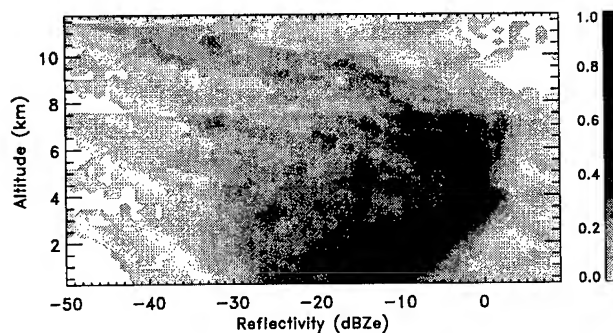


Fig. 5. CFAD for precipitating, convective clouds

and then to Christchurch New Zealand. During these flights the radar was installed in a zenith viewing geometry. During the transit some cirrus were observed but the cirrus cover was not extensive.

In Christchurch, the instrument was operated in conjunction with SALPEX. Marine stratocumulus were observed from below as the DC-8 flew 300 m above the ocean surface. During this flight, a CSIRO's Fokker 27 aircraft collected *in situ* data.

REFLECTIVITY VS. ALTITUDE FREQUENCY ANALYSIS

All the radar data for the two flight campaigns were processed and classified into four groups according to the system used by the GCSS. Histograms of reflectivity occurrence versus altitude, sometimes known as contoured frequency by altitude diagrams (CFADs) were generated for each cloud class. These are shown in Fig. 2-5. Pulse widths and along track velocities were used to normalize all the differing sample volumes of the data files. These diagrams are based on 67 hours of data.

Classifications were based on the visual observations recorded during the flights for clouds that were visible and on reflectivity imagery for clouds that were not visible from the aircraft (eg. a layer that was obscured by another layer.) In most cases classifications were straightforward and unambiguous, but in a few cases the classifications are somewhat subjective.

Boundary Layer Clouds

The histogram in figure Fig. 2 is composed of data from marine stratocumulus clouds over the Pacific ocean near Los Angeles, CA and Christchurch, New Zealand. The reflectivity factors ranged from about -15 to -45 dBZe with a but were mostly concentrated between -28 to -38 dBZe. The horizontal discontinuity near 3 km is caused by the lack of data below 3 km during the New Zealand flight.

Cirrus Clouds

Fig. 3 shows the the distribution of cirrus clouds in data throughout most of the flights. The reflectivity factors ranged from about +5 to -50 dBZe but the distribution is strongly peaked in -30 to 35 dBZe range. The part of the histogram that is above about 10 km altitude is biased lower because of limited opportunities to collect data at the highest altitude. The 12-14 km portion is based on data from only the two Pacific transit flights.

Extra Tropical Layer Clouds

The distribution of extra tropical layer clouds is shown in Fig. 4. This histogram is based on data from throughout the June 1996 flights. The reflectivity factors ranged from +10 to almost -50 dBZe with a strong peak at the high end that is due to precipitation. As a result of the

wide variety of clouds that fall into this class, the reflectivities were much more evenly distributed than reflectivities of data in the other classes. The classifications were most subjective for this group. It was sometimes difficult to classify high altitude stratiform systems as cirrus or extra tropical layers. Also it is difficult to tell what degree of convection is present in large precipitating systems, especially when the layer top is visually obscured by another layer.

Convective Precipitating Clouds

The histogram for convective precipitating clouds, Fig. 5 is based on data from flights on June 24-26 over the gulf coast of Texas and southern Arkansas. The reflectivity ranged from about +5 to -40 dBZe. The main peak of this histogram is caused by precipitation. The reflectivities at the lower altitudes are biased downward as a result of attenuation. The peak in the upper portion is caused by anvils associated with these storms. The horizontal discontinuity just below 8 km is caused by the lower frequency of high altitude data flights.

CONCLUSIONS

The data presented here demonstrate the successful development and deployment of the NASA DC-8 Airborne Cloud Radar. The CFADs demonstrate the sensitivity of the instrument as well as serving as compact summary of the data that was collected during the two experimental campaigns. As more data is collected during future campaigns, the statistics can be merged with the existing data sets in order to form distributions that are representative of a wider range of conditions.

REFERENCES

- [1] J.B. Mead, A.L. Pazmany, S.M. Sekelsky, and R.E. McIntosh, "Millimeter-Wavelength Radars for Remotely Sensing Clouds and Precipitation", *Proceedings of the IEEE*, vol. 82, no. 12, pp. 1891-1906, December 1994.
- [2] G. Vali, R. Kelly, A. L. Pazmany, and R. E. McIntosh, "Airborne radar and in-situ observations of a shallow stratus with drizzle", *L. Appl. Meteor.*, vol. Submitted, 1993.
- [3] J. Galloway, A. Pazmany, J. Mead, R. E. McIntosh, D. Leon, J. French, R. Kelly, and G. Vali, "Detection of Ice Hydrometeor Alignment Using an Airborne W-Band Polarimetric Radar", *Journal of Atmospheric and Oceanic Technology*, vol. 14, no. 1, pp. 3-12, February 1997.
- [4] G.L. Stephens, S. Tsay, P.W. Stackhouse, Jr., and P.J. Flatau, "The relevance of the microphysical and radiative properties of cirrus clouds to climate and climactic feedback", *Journal of the Atmospheric Sciences*, vol. 47, no. 14, pp. 1742-1753, July 1990.
- [5] T.L. Schneider and G.L. Stephens, "Climatically relevant clouds as sensed by a space-borne cloud radar", in *Proceedings of the International Radiation Symposium*, Fairbanks, AK, August 1996.
- [6] Report of the GEWEX Topical Workshop, Pasadena, CA, *Utility and Feasibility of a Cloud Profiling Radar*, January 1994.

High performance digital pulse compression and generation

C. Mavrocordatos, M. Martin-Neira

ESA-ESTEC, Keplerlaan 1, 2200 AG Noordwijk, THE NETHERLANDS
Phone: (31) 71 565 5536, (31) 71 565 4052, Fax: (31) 71 565 4596
E-Mail: cmavroco@estec.esa.nl, mneira@estec.esa.nl

N. Vincent, N. Suinot

ALCATEL ESPACE, 26 av. J.F. Champollion, 31037 Toulouse Cedex, FRANCE
Phone: (33) 561 19 52 25, (33) 561 19 61 04, Fax: (33) 561 19 61 63
E-Mail: frdk8n58@ibmmail.com, frdk8hx8@ibmmail.com

Abstract -- The European Space Agency (ESA) with an industrial team led by Alcatel Espace, has developed an all digital pulse generation and compression system for spaceborne Rain Radar application. The particular and most challenging constraint for this system was the capability to achieve a compressed pulse shape with very low range side-lobe level (<-60 dB). This objective was met and the results were published in a recent paper. More recently and as a continuation of this breadboarding activity, possible implementation in a real system was investigated taking into account different configurations, such as centralized amplification instruments or active array antennas. Performance improvement was also investigated and all factors limiting the actual performance were identified. Hardware integration using space qualified technologies was also assessed. Encouraged by the overall positive results of these activities, ESA is now planning to adapt this technique -or elements of this technique- to next generation spaceborne radars, such as topographic Radar Altimeters or future SARs.

INTRODUCTION

Pulse compression is used in several spaceborne radar instruments since it can either increase the sensitivity of the radar, or improve the resolution, or decrease the RF peak power needed. However, there is also a drawback associated with pulse compression as it generally leads to a long impulse response, which in turn presents the risk of interference between adjacent targets - especially when their dynamic range is high.

This is particularly the case of spaceborne weather radars (rain or cloud radars) where the surface clutter is several times higher than the signal to be measured (rain or cloud echo). To avoid interference, the side-lobe level (SLL) of the Impulse Response Function (IRF) must be as low as possible (lower than typically -60 dB) which requires particular care in the design of the pulse compression sub-system.

CONTROLLING THE IRF

The SLL that can effectively be met depends essentially on the selection of an appropriate set of transmitted waveform $s(t)$ and compression filter response $r(t)$. Nevertheless, due to distortions of the signal by the hardware or the propagation path, the signal $s'(t)$ which enters the compression filter may differ from $s(t)$. Alternatively, the actual IRF of the compression filter $r'(t)$ may differ from the ideal $r(t)$ depending on the technology of this filter. These deviations can affect the IRF of the radar and consequently degrade the SLL performance, unless they are compensated for.

There are 2 ways to control the shape of the IRF and make it match the ideal shape in spite of these deviations:

- a) Pre-distort the transmitted waveform and compensate for hardware distortions and compression filter deviations
- b) Use a compression filter with an adaptive IRF compensating for hardware distortions.

The advantage of the first method is that it involves a relatively simple hardware. However, it generally implies the capability to transmit amplitude modulated and longer pulses than would otherwise be needed [1], which may be undesirable.

The second method was investigated in a breadboarding activity by ESA with Alcatel Espace [2], and requires a digital compression filter since its transfer function needs to be varied. The principle can be briefly described as follows:

Noting $IRF(t)$ the ideal response obtained with a set of undistorted functions $s(t)$ and $r(t)$, we can write in the frequency domain:

$$IRF(f) = S(f) \cdot R(f) \quad (1)$$

Assuming that an image of the transmitted/received pulse $s'(t)$ acquired at the input of the compression filter is available, we can define a new transfer function for that filter as:

$$R'(f) = IRF(f) / S'(f) \quad (2)$$

If now $R'(f)$ is used instead of $R(f)$ to compress the distorted signal $s'(t)$, the ideal IRF will be obtained:

$$IRF'(f) = S'(f) \cdot R'(f) = S'(f) \cdot IRF(f) / S'(f) = IRF(f) \quad (3)$$

It is clear from this discussion that the efficiency of this method is related to the accuracy in acquiring $s'(t)$.

IMPLEMENTATION IN A REAL SYSTEM

The simplest possible implementation on board a real system of the adaptive compression technique addressed in [2], is shown in Fig.1 which depicts a typical transmit/receive chain of a radar. The acquisition of $s'(t)$ -also called calibration pulse-

noise amplifier (LNA) and high attenuation values have to be applied in the calibration path, leading to extremely stringent isolation requirements between the transmit and receive chains. In this case, it is more convenient to replace the calibration coupler in Fig.1 by the circuit drawn with a dashed line. The calibration signal $s'(t)$ can then be reconstructed by combining 3 different measurements acquired in a 3-step calibration procedure.

In the first step (Fig.2a), the waveform is taken just before the

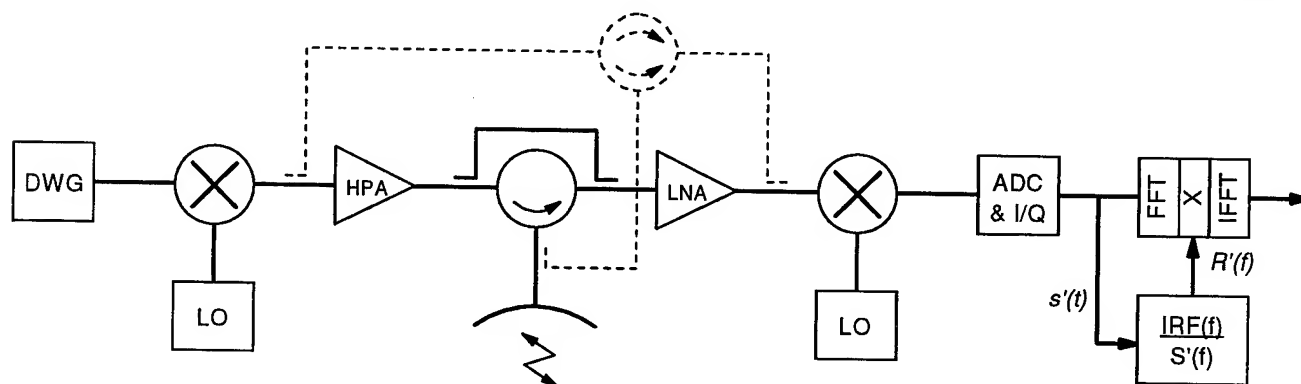


Figure 1: Implementation of adaptive pulse compression in a radar

is achieved by the means of a coupler which by-passes the diplexer. During transmission, a fraction of the high power signal is coupled into the receive chain, demodulated and digitised. At this point, it is routed into a processing unit where the adaptive transfer function $R'(f)$ is derived according to (2). The compression of the echoes received is then carried out in the spectral domain in a classical way (FFT, multiplication, inverse-FFT). An interesting feature is that the acquisition of $s'(t)$ can be done during the transmission time slots without interruption of the normal operation of the radar. Thus, real time adaptive compression is feasible.

Unfortunately, this simple technique is not implementable in any radar. In fact, the transmitted power is often too high with respect to the level nominally present at the input of the low

HPA and fed into the down-conversion chain (after the LNA). In the second step (Fig.2b), the same waveform is applied to the input of the LNA. In the last step (Fig.2c), the high power signal bypasses the LNA and enters directly the down-conversion chain. It is assumed that appropriate attenuation is applied at each step to match the dynamic range of each active stage.

Noting $S_1(f)$, $S_2(f)$, $S_3(f)$ the spectrum of the signals acquired at the input of the compression filter in steps 1, 2 and 3 respectively, the calibration signal $s'(t)$ can be derived from:

$$S'(f) = S_2(f) \cdot S_3(f) / S_1(f) \quad (4)$$

assuming that the receiver chain from the LNA down to the input of the compression filter is linear and that no distortions are generated by the calibration hardware.

This technique is still compatible with instruments using

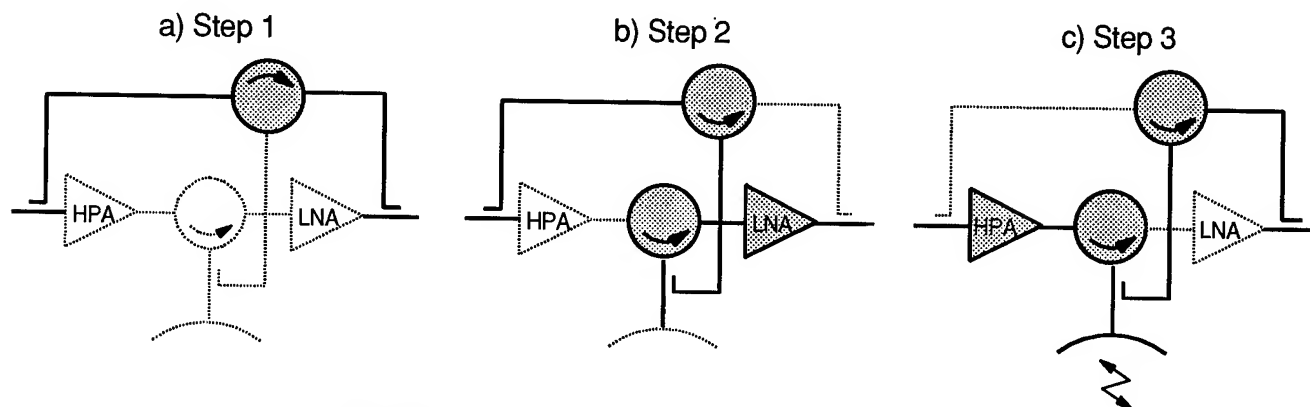


Figure 2: 3-step calibration concept for adaptive compression

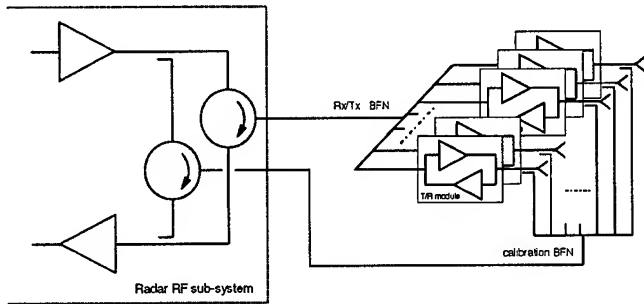


Figure 3: Active antenna with 3-step calibration

antenna arrays (active or passive) such as TRMM Rain Profiler instrument [3] or the reflector antenna Rain Radar assessed in ESA studies [4]. In an active array instrument the 3-step calibration is accomplished by combining the outputs of the individual HPA's in step 2 -and inputs of the LNA's in step 3- through a dedicated beamforming network (BFN) as shown in Fig.3, or simply using a dedicated calibration horn facing the antenna [4]. It should be noticed that real time operation is more difficult to achieve since 3 pulses need to be generated and routed through different paths within a single pulse repetition interval (PRI). However, as the most unstable or noisy element needing frequent calibration is usually the HPA, real time operation is still achievable by acquiring only step 3 pulse at PRF rate and using step 1 and 2 pulses acquired at slower rates.

PERFORMANCE LIMITATIONS & IMPROVEMENTS

-60dB SLL was demonstrated under laboratory environment in [2]. Although this figure is sufficient for a Rain Radar,

further investigations were carried out to identify the factors that currently limit the performance. Further improvement of SLL was also tentatively addressed with the objective to increase the margin available for a Rain Radar or approach the requirement of even more demanding instruments such as a Cloud Radar (-80dB SLL).

Noise level

Fig.4 shows the IRF measured on the breadboard [2] and compares it to the ideal IRF. It can be seen that the measured SLL is limited by a noise level at about -70dB which also masks the shape of the side-lobes. This noise floor results from the combination of quantisation noise in the acquisition of $s'(t)$ and of processing noise in the compression filter. Thermal noise during calibration doesn't affect the shape of the IRF since its level is about 20dB lower than the other two. These results were obtained with a 12-bit ADC -with 9 effective bits under the actual operating conditions- sampling at 20MHz and 16-bit floating point FFT / inverse-FFT processors. The length of the FFT's was 2048 complex points.

Doppler effect

Doppler shift of the received echoes -generated for example by antenna mispointing- cannot be cancelled automatically by the calibration since it takes place out of the instrument chain. Nevertheless, if the frequency shift is known $r'(f)$ can also be shifted accordingly to compensate for this effect.

Another type of Doppler effect is a spread of the spectrum of the received echoes due to the fact that the antenna footprint intersects a range of iso-Doppler lines on ground. This effect is directly related to the antenna beamwidth and cannot be

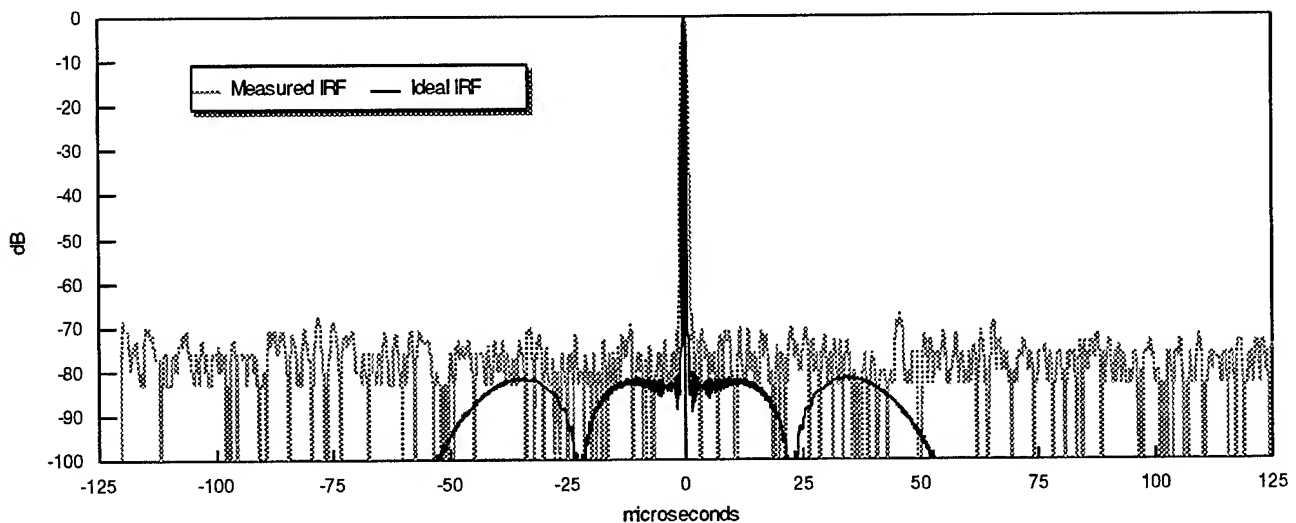


Figure 4: Measured and ideal IRF

cancelled. However, the impact on SLL is lower than that of Doppler shifts.

Simulations have shown that the SLL can rise from ideally -70dB to about -65dB at 13.7GHz and -60dB at 24GHz carrier due to Doppler spread and shift with a 6mrad (0.17deg) antenna beamwidth and a 3mrad residual pointing error. Associated Doppler shifts are 2KHz and 3.4KHz at 13.7 and 24GHz.

Uncalibrated paths

As little hardware as possible should be left out of the calibration loop since uncalibrated errors can dramatically affect the SLL. The sensitivity to different types of amplitude and phase errors was assessed. SLL performance was found quite tolerant to linear/quadratic errors but extremely sensitive to ripple errors. As an example, residual (uncompensated) amplitude ripple of only 0.2dB generates paired side-lobes of -45dB. It is believed however that ripple errors are unlikely to be generated out of the calibration loop, considering pulse parameters close to those selected in [2] ($B=4.5\text{MHz}$, $T=60\mu\text{s}$).

Improvements

An optimisation of the ideal IRF was carried out by varying the transmit waveform parameters. An improvement of the order of 3dB was obtained in SLL performance. Even lower SLL could in theory be met by multiplying the $IRF(t)$ function involved in the computation of $r'(f)$ by a rectangular window increasing the level of the main lobe only and leaving the side-lobes unchanged. A 20dB improvement using this window was already implemented in the breadboard to generate the $IRF(t)$ function in Fig.4, but still higher values could in principle be used to decrease the SLL.

However, simulations demonstrated that all benefits from any optimisation were lost in the presence of uncompensated Doppler shifts of the order of 5KHz.

TECHNOLOGY

If a flight model was to be manufactured, different components and technologies than those in the breadboard would be used, in order to reduce mass/power and enhance the reliability. The preliminary design of such a sub-system led to the definition of a 2 board equipment, composed of:

a) **the digital waveform generator**, with:

- a 12-bit DAC, sampling at 40MHz
- an analogue section
- a RAM, where the waveform is stored
- a microcontroller for interfacing functions

b) **the digital compression unit**, with the following functions:

- 12-bit ADC, sampling at 20MHz
- digital I&Q demodulation and downsampling at 8MHz
- compression (FFT, multiplication, inverse-FFT)
- near real-time (real-time x 20) replica computation $r'(f)$.

The digital signal processing (demodulation and FFT) can be

implemented using only 3 ASIC's in MGRT technology and several RAM chips. FFT and IFFT ASIC's can be made identical, thus reducing development costs.

Although real-time compensations are feasible, the study focused on a near-real time concept using a ADSP21020 processor. The replica computation rate was assumed to be 8ms in a system having a PRI of 400 μs .

The design of the waveform generator is simplified with the use of an FPGA integrating most of the digital control functions.

Estimated power consumption is 5W for the generation unit and 25W for the compression unit.

CONCLUSION

It was demonstrated that very low SLL can be achieved in spaceborne pulse compression radars with the implementation of an adaptive error compensation loop. A SLL of the order of -60 to -70dB can be met in the case of a Rain Radar.

Uncompensated Doppler seems to be dominating the performance. Therefore, adaptation of this concept to more demanding instruments in terms of SLL and/or operating at higher frequencies -as a Cloud Radar [5]- seems unrealistic without significant impact on the instrument design (antenna size, mispointing knowledge etc) to minimise Doppler effects.

The overall results obtained are quite encouraging and ESA is now planning to pursue these activities under the General Support Technology Programme (GSTP-2). The possibility to adaptively control the shape of the IRF on board other spaceborne pulse compression radars will be assessed and performance will be verified at breadboard level. Candidate instruments are wide bandwidth SAR and Topographic Altimeter.

REFERENCES

- [1] K.Sato, H.Hanado, H.Kumagai, "A Low Range-Sidelobe Pulse Compression Technique for Spaceborne Rain Radar", Proc. IGARSS'96, Vol. I, pp. 487-489.
- [2] N.Vincent, J.Richard, N.Suinot, P.Mancini, C.Mavrocordatos, "Very low side-lobe level pulse compression for rain radar", Proc. Europto'95, Vol. 2584, pp. 487-489.
- [3] T.Kozu, M.Kojima, K.Oikawa, K.Okamoto, T.Ihara, T.Manabe, "Development status of Rain Radar for Tropical Rainfall Measuring Mission", Proc. IGARSS'92, Vol. II, pp. 1722-1724
- [4] N.Vincent, J.Chenebault, N.Suinot, P.Mancini, "Spaceborne rain radar mission and instrument analysis", Proc. IGARSS'96, Vol. I, pp. 279-281.
- [5] N.Vincent, N.Suinot, C-C.Lin, "Design of MACSIM Cloud Radar for Earth Observation Radiation Mission", Proc. IGARSS'97, in press.

Microwave Imaging Radar System For Detecting Buried Objects

Fu-Chiarng Chen* and Weng Cho Chew

Electromagnetics Laboratory
Center For Computational Electromagnetics
Department of Electrical and Computer Engineering
University of Illinois
Urbana, IL 61801
Tel: (217) 333-9365 (Chen)
Tel: (217) 333-7309 (Chew)
Fax: (217) 244-7345

Email: fchen@sunchew.ece.uiuc.edu (Chen)

Email: chew@sunchew.ece.uiuc.edu (Chew)

Abstract—A time-domain microwave imaging radar system for nondestructive evaluation purposes has recently been developed at the University of Illinois. This system will be used for rapid nondestructive evaluation and quality control of civil structures. This paper describes both the radar system development and the inverse scattering algorithm used for imaging shallow buried objects in a concrete slab.

TIME-DOMAIN RADAR SYSTEM

Time-domain ultra-wideband microwave radar system is one of the new technologies which has the potential for important applications in nondestructive evaluation (NDE)[1,2,3]. Compared to conventional narrow-band CW radar systems, the time-domain ultra-wideband radar system has several advantages. The time-domain ultra-wideband radar system can provide much more information for target sensing purposes. In addition, it costs less and takes less measurement time compared to the coherent step-frequency radar system. However, the time-domain system has a worse signal-to-noise ratio (SNR) compared to the frequency domain system. To improve the SNR in the time-domain system, typical averaging and time-gating techniques can be applied to suppress the noise level.

The system block diagram of the time-domain radar system is shown in Fig. 1. This radar system consists of a Picosecond Pulse Lab (PSPL) 4050B step generator, a PSPL 4050RPH remote pulse head, two PSPL 5210 impulse forming networks, a Hewlett-Packard (HP) 54120B digitizing oscilloscope mainframe, an HP 54121A 20 GHz four-channel test set, two ultra-wideband amplifiers, a dual motor positioning system, and an ultra-wideband antenna system. The antenna system can be an ultra-wideband Vivaldi antenna [9] array or a pair of ridge horn antennas. The whole system is controlled and automated by a personal computer via the IEEE-488 bus. The dual motor positioning system makes the radar system a synthetic aperture radar (SAR) system. The PSPL 4050B step generator with the PSPL 4050RPH remote pulse

head generates a 10 volt, 45 ps rise-time pulse. A 1.5 volt, 10 GHz monocycle pulse is generated by attaching two PSPL 5210 impulse forming networks. The monocycle pulse was chosen as the transmitting signal in order to match the operational frequency of the antenna system. Fig. 2 shows a typical time-domain measurement data of a plastic pipe using a pair of Vivaldi antennas. Fig. 2(a) shows the measured data of the clutter of the system. The clutter includes background noise and coupling between the transmitting antenna and receiving antenna. Fig. 2(b) shows the measured data of the plastic pipe. Fig. 2(c) shows the subtraction of the clutter from the measured plastic pipe data. We can clearly observe the multiple reflected pulse shapes of the plastic pipe. Fig. 3 shows the one-dimensional SAR time-domain measurement data using a pair of ridge horn antennas. The test target is a embedded metallic cylinder (2.5 cm radius) which is located 15 cm beneath a concrete slab surface. Fig. 4 shows the data from Fig. 3 after background subtraction. The reflected signal of the embedded target can be clearly observed.

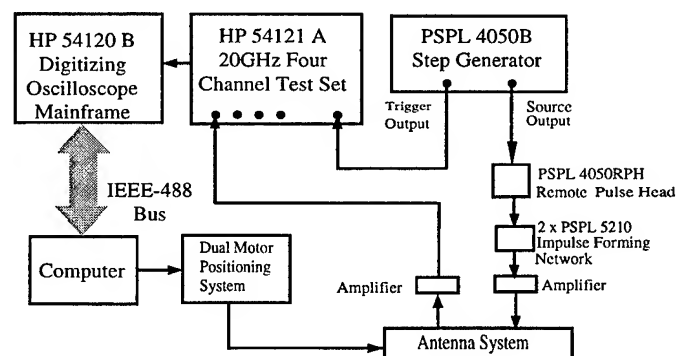


Fig. 1 The system block diagram of the time-domain microwave imaging radar system.

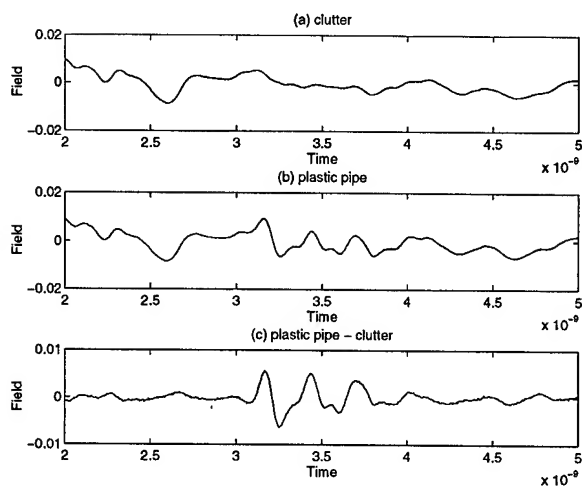


Fig. 2 The time-domain measurement data of a plastic pipe. (a) is the measurement data of the clutter without tested target. (b) is the measurement data of a plastic pipe. (c) is the subtraction of (a) from (b).

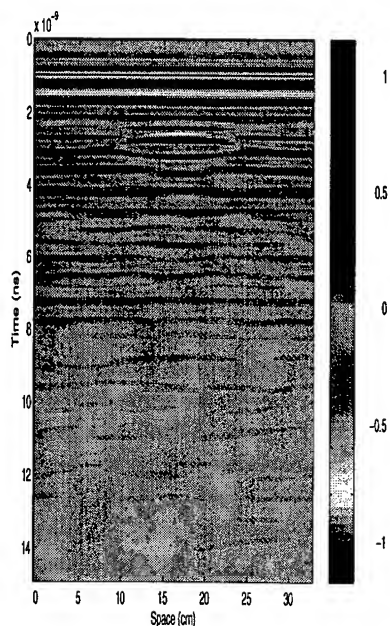


Fig. 3 The raw time-domain measurement data of a metallic cylinder embedded in a concrete slab.

INVERSE SCATTERING IMAGING

Two iterative nonlinear reconstructive algorithms, the distorted Born iterative method (DBIM) [4,5] and the local shape function (LSF) method [6,7,8], have been developed to process the measurement data for image reconstruction. The DBIM and LSF methods account for multiple scattering effects of the test targets and show a high resolution image reconstruction capability. However,

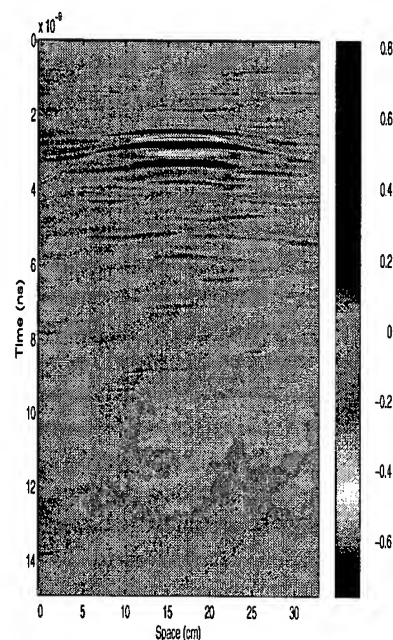


Fig. 4 The time-domain measurement data of Fig.3 after background subtraction.

when the multiple scattering effect is not significant, the first order Born approximation method such as diffraction tomography can be applied in order to save the expensive computational time of DBIM and LSF. In the past, the DBIM and LSF have been demonstrated successfully to reconstruct images for both dielectric objects and metallic objects [2,3]. In this paper, we apply a limited-angle, multi-frequency diffraction tomography algorithm to reconstruct the buried metallic cylinder in the concrete slab. The reconstructed image is shown in Fig. 5.

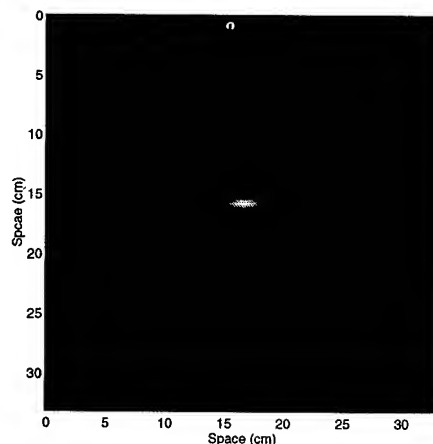


Fig. 5 The reconstructed image of the metallic cylinder embedded in the concrete slab.

CONCLUSIONS

A time-domain microwave imaging radar system has been developed for detecting shallow buried objects. This system successfully combines the time-domain impulse radar systems hardware and inverse scattering imaging software. The imaging radar system shows a high potential capability for nondestructive evaluation and quality control of civil structures.

REFERENCES

- [1] F.-C. Chen and W. C. Chew, "Time-Domain Ultra-Wideband Radar System For Nondestructive Evaluation", *URSI Radio Science Meeting Digest*, Baltimore, Maryland, July 21-27, 1996.
- [2] F.-C. Chen, W. C. Chew, and W. H. Weedon, "Inverse Scattering Imaging Using Time-Domain Ultra-Wideband Radar", *URSI Radio Science Meeting Digest*, Baltimore, Maryland, July 21-27, 1996.
- [3] F.-C. Chen and W. C. Chew, "An Impulse Radar Nondestructive Evaluation System", *Twenty-third Annual Review of Progress in Quantitative Nondestructive Evaluation*, Brunswick, Maine, July 28-Aug. 2, 1996.
- [4] W. C. Chew, *Waves and Fields in Inhomogeneous Media*. New York: Van Nostrand, 1990.
- [5] W. C. Chew and Y. M. Wang, "Reconstruction of Two-Dimensional Permittivity Distribution Using the Distorted Born Iterative Method," *IEEE Trans. Medical Imag.*, vol. 9, no. 2, pp. 218-225, 1990.
- [6] W. C. Chew and G. P. Otto, "Microwave Imaging of Multiple Metallic Cylinders Using Shape Functions," *Micro. Guided Wave Lett.*, vol. 2, no. 7, pp. 284-286, 1992.
- [7] G. P. Otto and W. C. Chew, "Microwave Inverse Scattering - Local Shape Function (LSF) Imaging for Improved Resolution of Strong Scatters," *IEEE Trans. Microwave Theory Tech.*, Vol. MTT-42 No. 1, pp. 137-141, July 1994.
- [8] W. H. Weedon and W. C. Chew, "A Local Shape Function (LSF) Method for Time-Domain Inverse Scattering," *IEEE Antennas and Propagation Society International Symposium Digest*, Ann Arbor, MI, June 28-July 2, 1993.
- [9] K. M. Frantz, "An Investigation of the Vivaldi Flared Radiator." M.S. Thesis, University of Illinois, Urbana, 1992.

A High-Resolution Imaging of Objects Embedded in a Lossy Dispersive Medium

Toru Sato, Kazuhisa Takemura, and Pan Huimin

Department of Electronics and Communication, Kyoto University

Kyoto 606-01, Japan

Corresponding Author: T. Sato

Phone: +81-75-753-5960, Fax: +81-75-751-8201

E-mail: tsato@kuee.kyoto-u.ac.jp

INTRODUCTION

Most of techniques used in subsurface radar applications, such as the aperture synthesis or the pulse compression, are developed originally for conventional radars which use the air as the propagation medium. Among the features that specialize subsurface radar, the loss and dispersion of the medium together with the existence of strong clutters strictly limit the usefulness of these techniques.

For an accurate imaging of subsurface objects, it is thus essential to develop an algorithm which can handle these features. While it is very hard to include the effect of loss and dispersion in inverse scattering problems, various numerical procedures have already been developed for the forward scattering case. Our approach has been to model the target with a limited number of parameters, and to recursively modify them so that the observed signal waveforms fit the estimated ones computed for the model[1, 2].

Our previous algorithm[3] is, however, applicable only to the case of lossless and non-dispersive medium. In this paper, we extend it to handle a more realistic case of target imaging in a two-dimensional homogeneous lossy and dispersive medium.

ALGORITHM

At the first step, outstanding targets are estimated as a group of point targets. Position of each target is estimated from the peaks in the received signal waveform, which gives the distance of the points from each antenna. All possible combinations of these points determined from two received signals at different antenna locations are plotted on a plane.

For each prominent target found in the first step, the shape estimation procedure is applied. The shape of the target is expressed in terms of the points which represents its outer boundary. These points are selected so that the distance between adjacent points are on the order of 1/10 of the radar wavelength, and they are connected smoothly. Non-linear least squares fitting is used to improve the model in an iterative manner in estimating the parameters. The shape estimation starts from the single point found in the first step, and then the algorithm increase the number of points in a stepwise manner. the second point is searched in the two opposite transverse directions, among which the direction which gives a better fit is chosen. The extension is terminated when the direction of the reflected

ray from the extended surface falls away from the receiving antenna position.

For each trial in this recursive model fitting process, the entire forward scattering problem should be solved. Use of FD-FDTD method is too time consuming for this purpose. In order to save the machine time, we compute the estimated scattered wave by using a modified ray tracing method which include the effect of diffraction. Unlike conventional ray tracing where individual ray is traced independently, the rays are treated as groups, each of which represents a wave front. The diffraction rays from an edge are generated and appended to the outer limits of a ray group each time when the ray group that represents a wave front passes the edge. The magnitude of the diffracted rays are computed by using the physical optics method so that they connect smoothly to the reflected wave at the reflection boundary.

The attenuation and dispersion of the transmitted waveform is taken care of by applying proper filter functions which are synthesized in the frequency domain. The model parameters to be determined are the permittivity and conductivity of the medium, their frequency derivatives, and the location of several points that characterize the outer contour of the object.

NUMERICAL SIMULATION

The performance of the developed algorithm is quantitatively examined by numerical simulations. The simulated data are generated using the Frequency- Dependent FDTD method[4]. In this case, the complex permittivity of the medium is expressed by

$$\epsilon_r = a + \frac{c}{1 + j\omega b}, \quad (1)$$

where a , b , and c are the constants representing the medium characteristics. The phase velocity v , attenuation constant β , and conductivity σ are approximately expressed in terms of these constants as

$$v = c_0 / \sqrt{a + \frac{c}{1 + \omega^2 b^2}} \quad (2)$$

$$\beta = 60\pi \frac{\epsilon_0 \omega^2 b c}{1 + \omega^2 b^2} / \sqrt{a + \frac{c}{1 + \omega^2 b^2}} \quad (3)$$

$$\sigma = \frac{\epsilon_0 \omega^2 b c}{1 + \omega^2 b^2}, \quad (4)$$

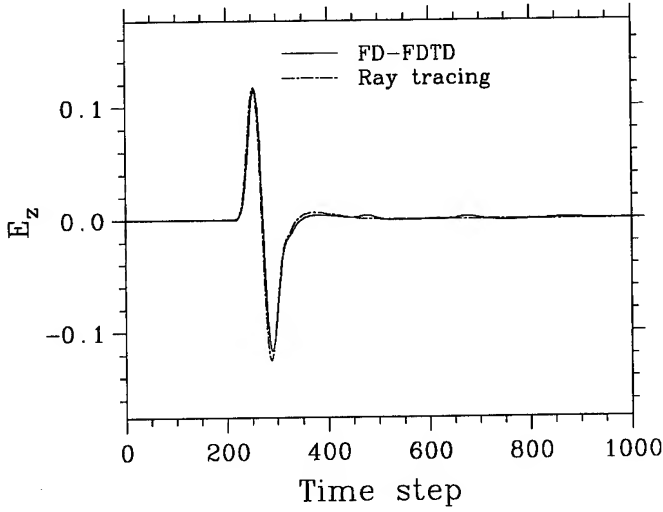


Figure 1: Simulated received waveform by FD-FDTD method (solid line) and by the extended ray tracing method (dot-dashed line).

where c_0 is the speed of light, and ϵ_0 is the permittivity of the free space.

Target shapes assumed are conductive cylinders and plates whose size is a few wavelengths at the center frequency of the pulse. Fig. 1 compares the scattered waveform by the FD-FDTD method and the developed ray tracing method. The signal is computed for the case of a mono-cycle pulse scattered from a conductive cylinder embedded in a lossy dispersive medium. The medium parameters used are for typical dry rock, namely

$$\begin{aligned} v &= 1.36 \times 10^8 \quad (\text{m/s}) \\ \beta &= 23.3 \quad (\text{dB/m}) \\ \sigma &= 3.16 \times 10^{-2} \quad (\text{S/m}) \end{aligned}$$

The phase velocity is roughly constant in the frequency band of 0.5–2GHz, while the attenuation has a gradient of 23 dB/m/GHz. The developed ray tracing algorithm generates the estimated scattered wave roughly 100 times faster than the FD-FDTD method.

The developed model fitting algorithm works almost equally well as for the case of non-dispersive medium, and the shape of the upper surface of the targets are precisely reconstructed. Current simulations assume the TM mode for the transmitted and received waves, so the creeping wave which may contain the information of the lower side of the target is very weak compared with the direct scattering from the upper surface.

EFFECT OF CLUTTERS

In order to examine the tolerance of the algorithm against clutters, 200 point targets with various permittivity are randomly

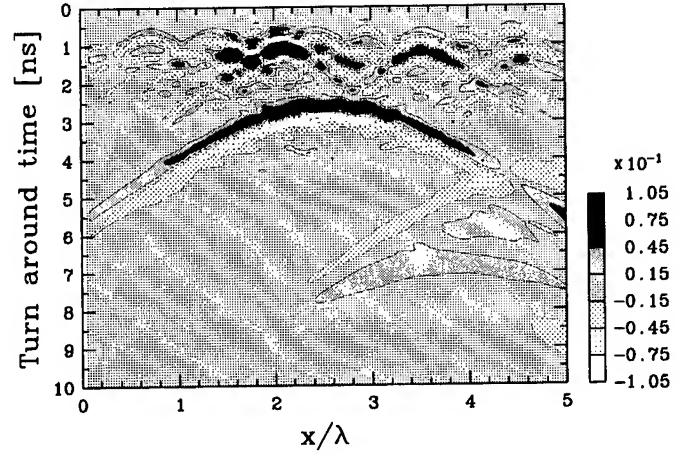


Figure 2: Simulated echo from a cylinder in an clutter environment (S/C = 4dB).

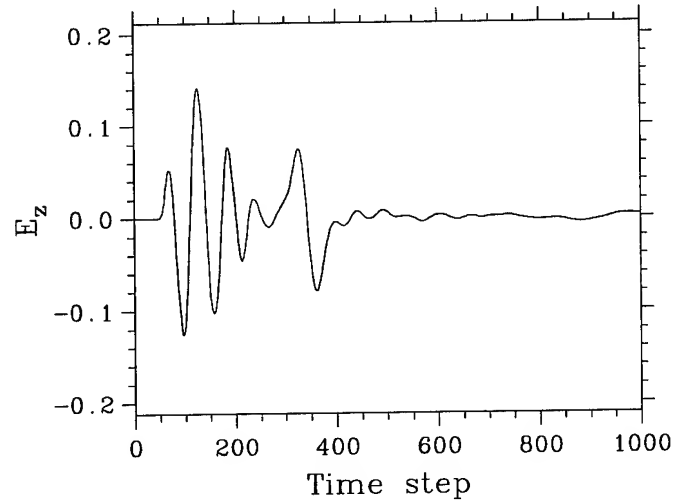


Figure 3: Signal waveform at $x = 1.5\lambda$ in Fig. 2.

embedded in the simulated medium. Fig. 2 shows the simulated echoes from a cylinder of 0.8λ in diameter in a strong clutter environment. The hyperbola peaked at $x = 2.5\lambda$ and the delay of 2.5 ns is the reflection from the cylinder, and other echoes are from the point scatterers representing the clutter. The signal-to-clutter (S/C) ratio is controlled by adjusting the standard deviation of the distribution of the permittivity of random points, and is set to 4dB for this case.

Fig. 3 shows the simulated waveform at a point of $x = 1.5\lambda$. The desired echo from the cylinder shows up from about 250 time steps, but the clutters at shallower locations appears

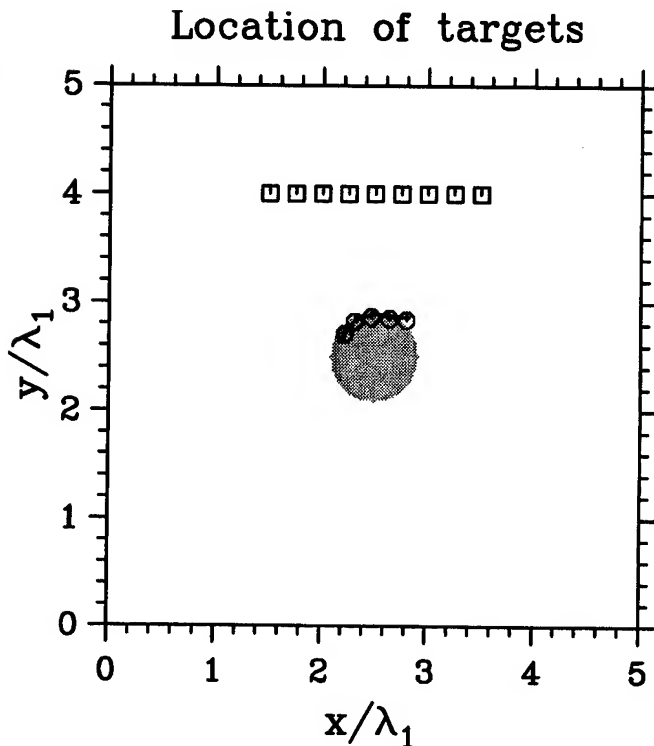


Figure 4: Estimation of a cylinder in a clutter environment ($S/C = 4\text{dB}$).

stronger than the desired echo. The clutter echoes at deeper locations are not only suppressed by the attenuation, but also low-pass filtered due to the dispersion of the medium.

The same model fitting algorithm was applied to the cases with various magnitude of the clutter. No special means was taken to remove clutter echoes in the first and the second step of the algorithm. It was found that the algorithm can accurately reconstruct the target shape for the signal-to-clutter ratio of larger than 10dB . The reason that fairly strong clutters do not affect the estimate is because the non-linear least squares fitting find the local minima which is affected only by clutters that occurs at the same time window as the desired echo.

The shape estimation gradually deteriorates when the clutter level is further increased, and the points which represent the outer contour of the target start to deviate from the true locations. However, the size of the target can be still correctly estimated with S/C of up to about 4dB . Fig. 4 shows the estimated shape of the cylinder for the S/C of 4dB . The shaded circle indicates the given shape of the target, and small circles shows the estimated outer contour. The right-most point of the estimated shape does not agree with the given contour, but the horizontal extent of the points well represents the target size. When the clutter level exceeds this threshold, the algorithm mistakes the strongest clutter point as the target.

For a higher clutter level, it is necessary to take care of strong individual clutters. We have separately developed an algorithm which considers the target to be a group of point targets[1]. Although it is in principle possible to combine this method with the current algorithm, the number of parameters may become prohibitively large to make a stable estimate.

SUMMARY

A two-dimensional shape estimation algorithm was developed for the situation of a solid conductive target embedded in a lossy dispersive medium. Numerical simulations confirmed the capability of the algorithm, which showed equally good performance as is the case of non-dispersive medium. The simulation with clutters also revealed the robustness of the algorithm even under a fairly strong clutter environments.

The major limitation of the algorithm is that we have to model the given situation precisely. The current model assumes a uniform medium, which is still too simple to deal with realistic cases of field excavations. We are currently extending the algorithm to fit the medium consisting of multiple layers.

REFERENCES

- [1] T. Wakayama, T. Sato and I. Kimura, "High-Resolution Radar Image Reconstruction Using an Arbitrary Array", *IEICE Trans. Commun.*, Vol. E76-B, No. 10, pp. 1305-1312, 1993.
- [2] T. Sato, K. Takeda, T. Nagamatsu, T. Wakayama, I. Kimura, and T. Shinbo, "Automatic signal processing of front monitor radar for tunneling machines", *IEEE Trans. Geosci. Remote Sens.*, Vol. 35, No. 2, pp. 354-359, 1997.
- [3] T. Sato, T. Wakayama, K. Takemura, and I. Kimura, "A High-Resolution Imaging of Small Objects for Subsurface Radar Data Processing", *Proc. Int. Geosci. Remote Sens. Symp.*, pp. 775-777, 1996.
- [4] R. Luebbers, K. S.Kunz, R. B. Standler, and M. Schneider, "A Frequency-Dependent Finite-Difference Time-Domain Formulation for Dispersive Materials", *IEEE Trans. Electromagn. Compat.*, Vol. EMC-32, No. 3, pp. 222-227, 1990.

The influence of ground stratification upon near field of magnetic dipole.

W.V.Dmitriev

Omsk State Pedagogical University,
14, Tukhachevsky Embankment, Omsk, 644099, Russia
Tel.: 7 381-2-24-37-95 Fax: 7 381-2-23-12-20
E-Mail: fis@lvt.ospi.omsk.su

Abstract -- In work the influence of ground stratification upon a near field of loop is studied. The results is: a) inclined stratification causes the change of shape of azimuthal dependencies of magnetic loop field; b) coupling coefficient of two loops became a function of azimuthal angle; c) by using azimuthal dependence of coupling coefficient it's possible to retrieve some characteristics of ground layers; d) method enabling to locate the horizontal space inclusion is offered.

INTRODUCTION

At some applications for example: underground sensing, antennas technics ets., it is necessary to know the ground stratification. Stratification include the dates about order, depth, grade angle of soil layers ets and the dates about theirs dielectric properties

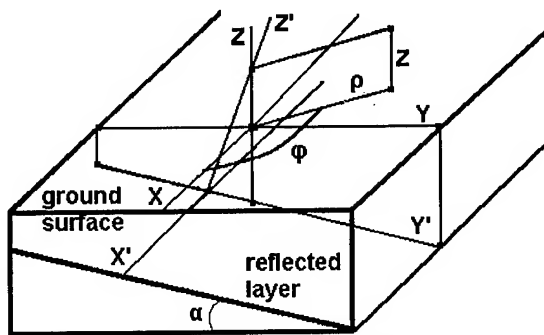


Fig 1 Geometry of task

(relative dielectric constant and conductivity).

In that paper the influence of ground stratification upon a near field of magnetic loop is studied. More correctly we described the case of inclined reflected layer (water-bearing layer). The main purpose is to investigate the resources of solution of inverse problem, i.e. the resources of determination of ground stratification using knowledge about near field of magnetic loop.

In papers of previous authors influence of ground stratification on near field of antennas always was examined[1,2]. However they investigated the case when ground layers were parallel to ground surface. At first in that paper the method of calculation of near

magnetic field of loop and coupling coefficient of two perpendicular loops in case inclined ground layer is proposed. At second some theoretical results is discussed.

1.THEORY

At Fig.1 the geometry of task is shown. In work the cylinder coordinates (r, j, z) is used mainly.

As known, strong determination of field of antennas at or above ground surface is difficult problem and is based on Sommerfeld's results [3]. It's necessary to calculate Sommerfeld's integral:

$$U \approx \int_0^{\infty} f(\alpha) J_0(\alpha \rho) e^{-i\sqrt{k^2 - \alpha^2} z} d\alpha \quad (1)$$

f - function is defined from boundary conditions,

J_0 - Bessel, first kind, zero order function.

Commonly (1) needs the numerical methods. At some cases this task assumes simplification. The near field of magnetic loop is the quasi-static field. It may be determined by using

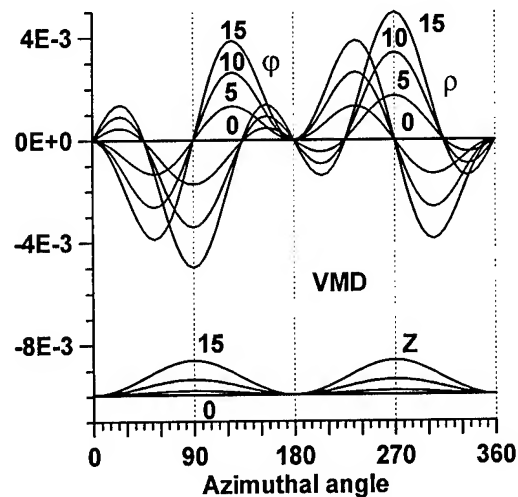


Fig 2 Azimuthal dependencies of VMD field with grade angle as parameter.

image theory [2].

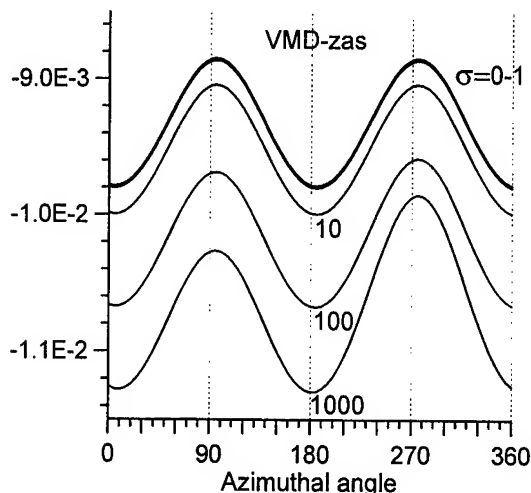


Fig 3 Azimuthal dependencies of Hz component of VMD field with soil conductivity as parameter

The calculation of near field of magnetic loop above stratified ground with grade layers is based on Bannister's expressions [2]. At first our task is reduced to known cause when soil layers is parallel to ground surface. To do it we pass on new X'Y'Z' coordinates (see Fig.1). In that cause the horizontal magnetic dipole (HMD) and vertical magnetic dipole (VMD) in XYZ coordinates is reduced to HMD' and VMD' in X'Y'Z' coordinates:

$$\text{VMD}' = \text{VMD} \cos(\alpha) + \text{HMD} \sin(\varphi) \sin(\alpha);$$

$$\text{HMDx}' = \text{HMD} \cos(\varphi);$$

$$\text{HMDy}' = \text{HMD} \sin(\varphi) \cos(\alpha) - \text{VMD} \sin(\alpha).$$

At second we calculate the magnetic field in new coordinates and pass on old coordinates

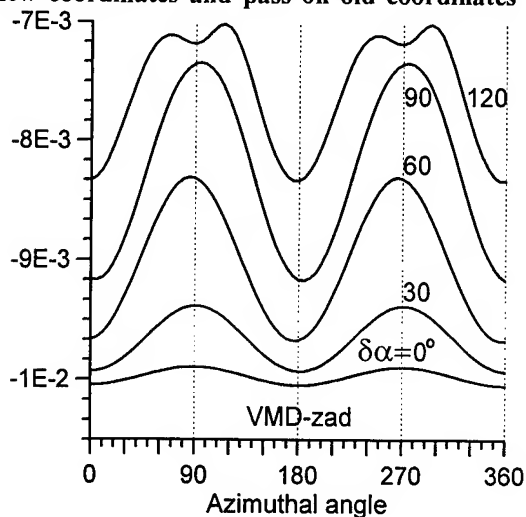


Fig 4 Azimuthal dependencies of Hz component of VMD field with $\delta\alpha$ as parameter

XYZ or (r, j, z).

2. SINGLE LOOP FIELD

By using described in part 1 methods we have calculated values of all components (H_r - radial, H_j - azimuthal and H_z - z axis) near field single magnetic antenna as a function of azimuthal angle - j, grade angle of reflected layer - a, conductivity of ferlected layer - σ , etc. For testing computer program we calculated the magnetic field with non-inclined reflected layer. The followed values of magnetic field intensity was calculated by using next parameters of task usually:

- 1) distance between transmitter and receiver $\rho = 2$ meters (m);
- 2) distance between ground surface and magnetic loop - $h = 1$ m;
- 3) soil conductivity - $\sigma = 0.01 \Omega^{-1} \text{m}^{-1}$;
- 4) HMD (or VMD) = 1 A/m^2 , it was oriented to angle $\varphi = 0^\circ$ - HMDx or to angle $\varphi = 90^\circ$ - HMDy (see Fig.1).

As a result we have investigated the dependencies of H_r , H_j and H_z from j, a, σ , ρ , h and $\delta\alpha$ - range of α variance. Main attention has directed to influence of grade angle, conductivity and $\delta\alpha$ to components of field. For example on Fig.2 shown azimuthal dependencies of H_z , H_φ and H_r with grade angle as parameter. Evolution of field characteristics in case of HMDx and HMDy is analogous. We see that some components (H_ρ and H_φ) which were absent become non-zero. Another (H_z) field components which had no azimuthal dependence become the function from azimuthal angle. Moreover the functions has anisotropical shape. That results may be used to solving of inverse problem (value of α and slope direction). Some results of investigation of field dependencies from σ and

HMDx-Hr

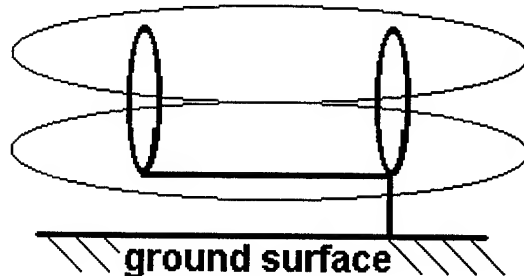


Fig 2 The example of two loops configuration

$\delta\alpha$ is shown on Fig.3 and Fig.4 respectively. Ones were calculated at case VMD, $\alpha = 5^\circ$, another parameters as listed early. We see that soil conductivity has influence upon quasi-static field of magnetic loop at case very large value ($\sigma > 1 \Omega^{-1} \text{m}^{-1}$). As is known the usually values of conductivity is near 0.01-0.1 $\Omega^{-1} \text{m}^{-1}$. At the contrary the influence of range of α -variance (for really values of that

parameter) is more perceptible (see Fig.4). Consequently we believe that the inverse problem for $\delta\alpha$ must be more simple then one for soil conductivity.

3. COUPLING COEFFICIENT OF TWO LOOPS

In previous part of work we show that near field of magnetic loop demonstrate strong dependence from grade angle of reflected soil layer, layer conductivity and range of α -variance. Consequently the value of field components may used for investigation of ground stratigraphy. However measurements of real value of near magnetic field of antenna is difficult experimental task.

Experimental difficulties may be reduced by using two loops simultaneously. In that case

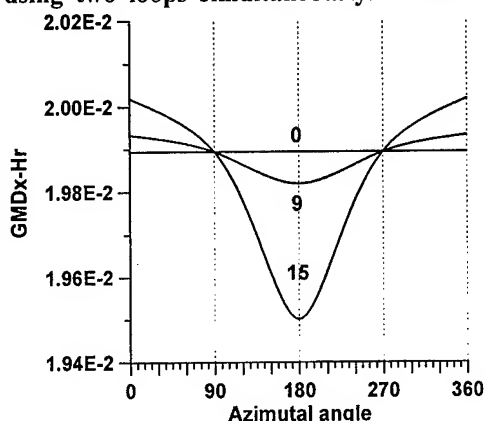


Fig 3 Azimuthal dependencies of coupling coefficient with α as parameter.

we may to measure by using numerous difference methods or by relative measurements.

We know 9 main variants of mutual configurations of two loops. For example we consider one of there - Fig.5. The signal at second antenna is defined of $H\rho$. In case on nought grade angle of reflected layer it is independent from azimuthal angle. Hence the coupling coefficient is independent too. In case on nonzero of grade angle $H\rho$ is changed at $j = 0^\circ$ and 180° . It cause changes of signal at second antenna. Hence the coupling coefficient become dependenced from azimuthal angle - Fig.6. By using that dependencies we may to determine grade angle and slope direction.

At next step we make calculation experiment for solving of particulare inverse problem. On Fig.7 shown the initial distribution of $\delta\alpha$ (below) and the results of recovering of that distribution (above). Recovering was made with next parameters of task: mean value

grade angle - 10° , minimal and maximal $\delta\alpha$ - 10° and 60° respectively.

4. CONCLUSIONS

As a result we see that:

- a) inclined stratification causes the change of quasi-static field and coupling coefficient of two perpendicular magnetic loops;
- b) by using azimuthal dependence of coupling coefficient of two loops it's possible to retrieve grade angle, slope direction of reflected (water-bearing) layer of soil and range of variance of grade angle;
- c) next step must be the multilayered surface model.

ACKNOWLEDGMENTS

I thanks Maslennikov N.M. for purpose of task.

REFERENCES

- [1] P.R.Bannister, "Summary of image theory expressions for the quasi-static fields of antennas at or above the earth's surface," Proc.IEEE, V.67, pp.1001-1008, July,

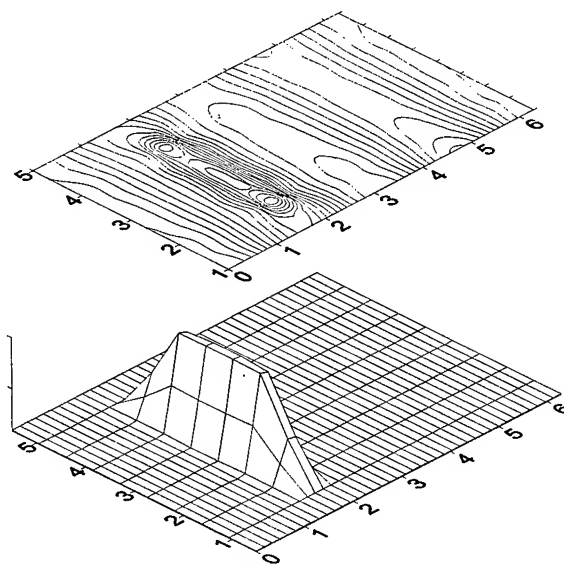


Fig 4 The results of calculation experiment: below - initial $\delta\alpha$ distributions, above - recovered one.

- [2] J.R.Wait, "Electromagnetic waves in stratified media." NY: Pergamon, 1970, ch.2.
- [3] A.Sommerfeld, "On the propagation of waves in wireless telegraphy," Ann.Phys, V.81, pp.1135-1153, 1926 [.

Magnetic Dipole Localization With a Gradiometer: Obtaining Unique Solutions

W. M. Wynn

Naval Surface Warfare Center, Coastal Systems Station
Code R22, 6703 West Hwy 98, Panama City, FL 32407, USA
904.234.4682/904.235.5462/wynn_mike@ccmail.ncsc.navy.mil

Abstract--The five independent equations describing the field gradient tensor at a point for a static magnetic dipole source can be inverted to give the bearing vector to the source and the source moment vector divided by the fourth power of the range. The equations have four solutions, two of which are related in a non-trivial way, and two more that are obtained by reflections through the field point. The symmetry of the four solutions in the principal-axis frame of the gradient tensor can be used to express the solutions directly in terms of one another in an arbitrary frame without executing the inversion. This relationship has been exploited to construct explicit proofs that a unique solution for magnetic moment vector and relative position between source and field point can be obtained if either the magnetic field vector, or the rate of change of the gradient tensor and the relative motion of source and field point is known.

INTRODUCTION

For a magnetic dipole source of moment \mathbf{m} located at the origin, the magnetic field \mathbf{b} at a point located at \mathbf{r} is given by

$$\mathbf{b} = \frac{\mu_0}{4\pi} \left[\frac{3(\mathbf{m} \cdot \mathbf{r})\mathbf{r}}{r^5} - \frac{\mathbf{m}}{r^3} \right] \quad (1)$$

and the gradient tensor has the form

$$G_{ij} = \frac{\mu_0}{4\pi} \left[-\frac{15(\mathbf{m} \cdot \mathbf{r})r_i r_j}{r^7} + \frac{3m_i r_j}{r^5} + \frac{3m_j r_i}{r^5} + \frac{3(\mathbf{m} \cdot \mathbf{r})\delta_{ij}}{r^5} \right] \quad (2)$$

which, with the introduction of the bearing vector $\mathbf{n} = \mathbf{r}/r$ and the scaled moment vector $\mathbf{M} = 3\mu_0 \mathbf{m}/(4\pi r^4)$, can be expressed as

$$G_{ij} = -5(\mathbf{M} \cdot \mathbf{n})n_i n_j + M_i n_j + M_j n_i + (\mathbf{M} \cdot \mathbf{n})\delta_{ij}. \quad (3)$$

Equation (3) has five unknowns, and there are five independent elements of the gradient tensor, since $\nabla \cdot \mathbf{b} = 0$, and $\nabla \times \mathbf{b} = 0$ for static magnetic sources in nonmagnetic media. Equation (3) has been inverted [1], and the details can be found in the references cited therein, or in [2]. There are four solutions for \mathbf{M} and \mathbf{n} and they have a symmetric

arrangement in the plane, defined by \mathbf{m} and \mathbf{r} , which forms a coordinate plane in the gradient tensor's principal-axis system. This arrangement is shown in Fig.1. These solutions can be expressed directly in terms of one another in an arbitrary frame without executing the inversion [3]. If we physically generate the gradient tensor with the scaled moment \mathbf{M} and bearing vector \mathbf{n} , then solutions for scaled moment \mathbf{R} and bearing vector \mathbf{u} not trivially related to the input scaled moment and bearing vector are given by

$$\mathbf{R} = \pm \frac{[10(\mathbf{M} \cdot \mathbf{n})^2 - 2M^2]\mathbf{n} - 5(\mathbf{M} \cdot \mathbf{n})\mathbf{M}}{\sqrt{4M^2 + 5(\mathbf{M} \cdot \mathbf{n})^2}}, \quad (4)$$

$$\mathbf{u} = \pm \frac{5(\mathbf{M} \cdot \mathbf{n})\mathbf{n} - 2\mathbf{M}}{\sqrt{4M^2 + 5(\mathbf{M} \cdot \mathbf{n})^2}}, \quad (5)$$

with identical expressions giving \mathbf{M} and \mathbf{n} in terms of \mathbf{R} and \mathbf{u} .

The bearing vectors \mathbf{u} and \mathbf{n} will lie in the same half-space ($\mathbf{u} \cdot \mathbf{n} \geq 0$) if we choose the positive sign in (4) and (5) when $\mathbf{M} \cdot \mathbf{n} \geq 0$ and the negative sign otherwise. We will refer to the solution for \mathbf{R} and \mathbf{u} selected this way as the "ghost" solution. Equations (4) and (5) are essential to the uniqueness proofs to be developed below

UNIQUENESS PROOF: KNOWN FIELD VECTOR

Expressed in terms of the scaled moment \mathbf{M} and bearing vector \mathbf{n} , (1) becomes

$$\mathbf{b} = r \left[(\mathbf{M} \cdot \mathbf{n})\mathbf{n} - \frac{\mathbf{M}}{3} \right]. \quad (6)$$

By inspection, if \mathbf{M}, \mathbf{n} is a solution of (3) that satisfies (6), then $-\mathbf{M}, -\mathbf{n}$ cannot satisfy (6), and the number of acceptable solutions of (3) has been reduced from four to two. Next, we will assume that \mathbf{M}, \mathbf{n} satisfies (3) and (6), and ask if the "ghost" solution \mathbf{R}, \mathbf{u} defined by (4) and (5) can also satisfy (6), possibly with a different range \hat{r} . That is, can we satisfy

$$r \left[(\mathbf{M} \cdot \mathbf{n})\mathbf{n} - \frac{\mathbf{M}}{3} \right] = \hat{r} \left[(\mathbf{R} \cdot \mathbf{u})\mathbf{u} - \frac{\mathbf{R}}{3} \right] \quad (7)$$

Sponsored by the Office of Naval Research Independent Research Program.

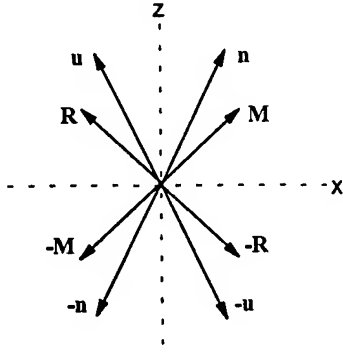


Figure 1. Principal-Axis Frame Solution Arrangement.

with \mathbf{R}, \mathbf{u} given by (4) and (5)? If we square both sides of (7) we get

$$r^2[3(\mathbf{M} \cdot \mathbf{n})^2 - M^2] = \hat{r}^2[3(\mathbf{R} \cdot \mathbf{u})^2 - R^2]. \quad (8)$$

However, we know [3] that $(\mathbf{M} \cdot \mathbf{n})^2 = (\mathbf{R} \cdot \mathbf{u})^2$ and $M^2 = R^2$ so we conclude $\hat{r} = r$. Thus, we attempt to satisfy (7) with the range factor removed. Equations (4) and (5) are valid in any reference frame and this means that upon substitution in (7), the resulting scalar coefficients of the vectors on the two sides of the equation must be identical. In particular, for the coefficient of \mathbf{M} we get the equation

$$\frac{(\mathbf{M} \cdot \mathbf{n})}{\sqrt{5(\mathbf{M} \cdot \mathbf{n})^2 + 4M^2}} = 1 \Rightarrow (\mathbf{M} \cdot \mathbf{n})^2 + M^2 = 0, \quad (9)$$

which is unphysical. Consequently, we conclude that the solution \mathbf{M}, \mathbf{n} common to (3) and (6) is unique, and the two together lead to a solution for r via (6) and thus a unique solution for \mathbf{m} and \mathbf{r} .

GRADIENT RATE TENSOR

When there is relative motion between the field measurement point and the dipole source, a tensor gradiometer can be used to measure the rate of change of the gradient tensor, which we will refer to simply as the rate tensor. Taking the time derivative of (2) gives

$$R_{ij} = \frac{dG_{ij}}{dt} = \mathbf{v} \frac{dG_{ij}}{ds} = \frac{\mu_0}{4\pi} \left[\frac{105(\mathbf{m} \cdot \mathbf{r})(\mathbf{v} \cdot \mathbf{r})r_i r_j}{r^9} - \frac{15(\mathbf{m} \cdot \mathbf{v})r_i r_j}{r^7} - \frac{15(\mathbf{m} \cdot \mathbf{r})v_i r_j}{r^7} - \frac{15(\mathbf{m} \cdot \mathbf{r})v_j r_i}{r^7} - \frac{15(\mathbf{v} \cdot \mathbf{r})m_i r_j}{r^7} - \frac{15(\mathbf{v} \cdot \mathbf{r})m_j r_i}{r^7} - \frac{15(\mathbf{m} \cdot \mathbf{r})(\mathbf{v} \cdot \mathbf{r})\delta_{ij}}{r^7} + \frac{3m_i v_j}{r^5} + \frac{3m_j v_i}{r^5} + \frac{3(\mathbf{m} \cdot \mathbf{v})\delta_{ij}}{r^5} \right], \quad (10)$$

where we have shown two forms, a time derivative, and, via the chain rule, a spatial derivative along the path of motion of the field point. The first form is useful for a stationary source and a field point of known velocity, such as in localization from air borne or water borne platforms. The second form is useful when the field measurements are sampled along a line in space without regard to speed, such as in a survey mode seeking buried objects. In this latter case, the speed can be factored from (10) and only the direction of relative motion matters. Equation (10) has been inverted [4] to give solutions for bearing vector and the moment vector scaled by the fifth power of the range. That process produces multiple solutions, and previous numerical work indicates that the solution common to the new inversion and the gradient tensor inversion is unique. The present work establishes a unique solution rigorously, and does so without inversion of the gradient rate equations.

In terms of the scaled moment vector and the bearing vector, the rate equations can be written in the form

$$R_{ij} = \frac{1}{r} [35(\mathbf{M} \cdot \mathbf{n})(\mathbf{v} \cdot \mathbf{n})n_i n_j - 5(\mathbf{M} \cdot \mathbf{v})n_i n_j - 5(\mathbf{M} \cdot \mathbf{n})v_i n_j - 5(\mathbf{M} \cdot \mathbf{n})v_j n_i - 5(\mathbf{v} \cdot \mathbf{n})M_i n_j - 5(\mathbf{v} \cdot \mathbf{n})M_j n_i - 5(\mathbf{M} \cdot \mathbf{n})(\mathbf{v} \cdot \mathbf{n})\delta_{ij} + M_i v_j + M_j v_i + (\mathbf{M} \cdot \mathbf{v})\delta_{ij}], \quad (11)$$

In the following, we will interpret \mathbf{v} to be the field point velocity when R_{ij} is the time rate tensor, and a unit vector in the direction of field point translation when R_{ij} represents the along-track space rate of change.

UNIQUENESS PROOF: KNOWN RATE TENSOR

We assume that \mathbf{v} is specified, and that \mathbf{M}, \mathbf{n} is a solution of (3) that satisfies (11). By inspection of (11), $-\mathbf{M}, -\mathbf{n}$ cannot be a solution, so the number of possible solutions satisfying (3) and (11) is at most two. Next, we assume that the "ghost" solution given by (4) and (5) satisfies (11), possibly for a different range \hat{r} . We substitute \mathbf{R}, \mathbf{u} from (4) and (5) into (11) and expand, and equate the resulting expression to the explicit form in (11). We will not write this expression out, but will just examine selected terms. Again, rotational invariance is invoked, and in the resulting expression, coefficients of specific elementary tensors on both sides of the equation must be identical. In particular, for the coefficient of $M_i v_j + M_j v_i$ we get the equation

$$\frac{5(\mathbf{M} \cdot \mathbf{n})}{\hat{r} \sqrt{5(\mathbf{M} \cdot \mathbf{n})^2 + 4M^2}} = \frac{1}{\hat{r}}, \quad (12)$$

and for the coefficient of $n_i v_j + n_j v_i$ we get

$$\frac{25(\mathbf{M} \cdot \mathbf{n})^2 + 2M^2}{\hat{r} \sqrt{5(\mathbf{M} \cdot \mathbf{n})^2 + 4M^2}} = \frac{5(\mathbf{M} \cdot \mathbf{n})}{r}, \quad (13)$$

and when we combine (12) and (13) we conclude $M^2 = 0$, which is unphysical. Consequently, we conclude that the solution of (3) that satisfies (11) for specified \mathbf{v} is unique. It remains now to use the rate tensor to perform the scaling to obtain moment and position vectors.

EXPLOITING THE RATE TENSOR

Equation (11) can be written in tensor form (summation convention) as

$$R_{ij} = \frac{1}{r} Q_{ijk} v_k \Rightarrow \frac{v_k}{r} = \tilde{Q}_{ijk} R_{ij} \quad (14)$$

where Q_{ijk} is mathematically similar to the tensor T_{ijk} appearing in the direct inversion of the gradient rate equations [4], with \mathbf{M} replacing \mathbf{v} in the latter expression. Consequently, we can immediately write the inverse tensor \tilde{Q}_{ijk} as

$$\begin{aligned} \tilde{Q}_{ijk} = & \frac{M^2(\mathbf{M} \cdot \mathbf{n})^2}{[M^4 - (\mathbf{M} \cdot \mathbf{n})^4]} n_i n_j n_k \\ & - \frac{3(\mathbf{M} \cdot \mathbf{n})^2 + 5M^2}{8[M^4 - (\mathbf{M} \cdot \mathbf{n})^4]} (M_i n_j + M_j n_i) n_k \\ & + \frac{1}{2[M^2 - (\mathbf{M} \cdot \mathbf{n})^2]} [n_i n_j M_k \\ & - (\mathbf{M} \cdot \mathbf{n})(\delta_{ik} n_j + \delta_{jk} n_i) + \delta_{ik} M_j + \delta_{jk} M_i]. \end{aligned} \quad (15)$$

Given the prescribed platform motion \mathbf{v} , the rate tensor R_{ij} , and either expression in (14), the range r can be determined, and \mathbf{m} and \mathbf{r} are uniquely determined. We have included this last step (15) to provide the basis for further analysis of the gradient-gradient rate inversion procedure when the relative motion of field point and source is not known *a priori*. This will be the topic of a future paper.

CONCLUSION AND COMMENTS

Given the gradient tensor at a point due to a magnetic dipole source, knowledge of either the field vector at the

same point, or the gradient rate tensor at the same point along with the relative motion of source and field point, leads to a unique solution for the relative position of source and measurement point and the magnetic moment vector of the source. In practice, due to the large background magnetic field of the earth, the field vector due to a source can be used only when the measuring device is stationary, so this mode only has utility in, say, tracking a moving magnetic source with a fixed sensor. However, for this case, no *a priori* knowledge of the relative motion of source and sensor is needed. For mobile sensor applications, the gradient and gradient rate tensors appear to be the only practical candidates for point-by-point dipole localization, and this process as we have described it above requires precise knowledge of the motion of the sensor relative to the source. Consequently, the two cases we have described are complementary, and both have useful applications.

As a final practical note, the uniqueness proofs do not constitute prescriptions for obtaining the unique solution. In practice, all four gradient tensor solutions (two if the source halfspace is known) must be tested to see which produces the associated field vector or gradient rate tensor.

REFERENCES

- [1] W. M. Wynn, C. P. Frahm, P. J. Carroll, R. H. Clark, J. Wellhoner, and M. J. Wynn, "Advanced Superconducting Gradiometer/Magnetometer Arrays and a Novel Signal Processing Technique", IEEE Trans. Mag. Vol. MAG-11, No. 2, pp. 701-707, March 1975.
- [2] W. M. Wynn, "Detection, Localization, and Characterization of Static Magnetic Dipole Sources", in Detection and Identification of Visually Obscured Objects, C. E. Baum, Ed., New York: Taylor and Francis, Chapter 12, In Press.
- [3] W. M. Wynn, "Direct Relation between Solutions in the Magnetic Dipole Gradient Equations Inversion", Naval Coastal Systems Center Technical Memorandum NCSC TM 301-81, Panama City, Florida, February, 1981.
- [4] W. M. Wynn, "Magnetic Dipole Localization using the Gradient Rate Tensor Measured by a Five-Axis Gradiometer with Known Velocity", In A.C. Dubey, I. Cindrich, M. Ralston, and K. Rigano, Eds., Detection Technologies for Mines and Minelike Targets, SPIE Proceedings, Vol. 2496, pp. 357-367, April, 1995.

Numerical Analysis of Radar Cross-sections of a Conducting Cylinder in a Strong Turbulent Medium

M. Tateiba and T. Hanada

Department of Computer Science and Communication Engineering
Kyushu University

6-10-1 Hakozaki, Higashi-ku, Fukuoka 812-81, Japan

Tel: +81-92-642-4047, Fax: +81-92-642-4084

E-mail: tateiba@csce.kyushu-u.ac.jp

INTRODUCTION

When a body is surrounded by a random medium, the radar cross-section (RCS) is expected to be sometimes remarkably different from that in free space. In general, the problem of wave scattering from a body in a random medium needs to be treated by taking account of the boundary conditions of incident and scattered waves on the body. Recently, we have presented a method for solving it as a boundary value problem and analyzed numerically RCS of a conducting elliptic cylinder in such a strong turbulent medium that an incident wave becomes incoherent[1,2]. The numerical analysis shows that the spatial coherence length of an incident wave on the body plays a central role in determining RCS as well as the effect of double passage which results in backscattering enhancement. Through the analysis, we have made clear the characteristics of RCS for some elliptic cylinders: that is, some convex cylinders.

When the spatial coherence length becomes comparable to an effective width of the illuminated surface of a body, RCS changes largely and is enhanced or diminished as compared with that in free space. In this case, the curvature of a body surface has also an important effect on RCS. This paper makes more clear the curvature effect on RCS in a random medium, by assuming the E wave incidence and analyzing numerically RCS of a conducting cylinder with a concave-convex surface.

FORMULATION

Consider the problem of wave scattering from a conductive body surrounded by a random medium. An approach to the scattering problem can be described as Fig. 1 where the current generator is a deterministic operator which transforms incident waves into surface currents. We now consider the scattering of E waves radiated from a line source which is far from a conducting cylinder embedded in a turbulent medium and parallel to the y axis (Fig. 2).

The surface of the cylinder is expressed by

$$r = a[1 - \delta \cos 3(\theta - \phi)] \quad (1)$$

where a is a average radius, δ and ϕ are constant.

We assume that the local intensity of turbulent medium is sufficiently small and the local correlation length of turbulent medium is much longer than the wavelength of the wave in free space. Therefore the scalar wave and the forward scattering approximations are valid in the turbulent medium. That is, the re-incident wave in Fig. 1 is neglected and the feedback loop is suppressed. Then, using Green's function in the turbulent medium $G(\mathbf{r}|\mathbf{r}')$ and surface current on the cylinder $J(\mathbf{r}_1)$, the scattered wave $u_s(\mathbf{r})$ is given by

$$u_s(\mathbf{r}) = \int_S G(\mathbf{r}|\mathbf{r}_1) J(\mathbf{r}_1) d\mathbf{r}_1 \quad (2)$$

where S denotes the cylinder surface. Here $J(\mathbf{r}_1)$ is expressed in terms of the current generator Y_E :

$$J(\mathbf{r}_1) = \int_S Y_E(\mathbf{r}_1, \mathbf{r}'_1) u_{in}(\mathbf{r}'_1) d\mathbf{r}'_1 \quad (3)$$

for an incident wave $u_{in}(\mathbf{r})$ which is now given by $G(\mathbf{r}|\mathbf{r}_t)$ on the assumptions of line source and E wave incidence. Note that Y_E depends only on the cylinder surface. From (2) and (3), we can obtain the average intensity of backscattered waves given by

$$\langle |u_s|^2 \rangle = \int_S d\mathbf{r}_1 \int_S d\mathbf{r}_2 \int_S d\mathbf{r}'_1 \int_S d\mathbf{r}'_2 [Y_E(\mathbf{r}_1|\mathbf{r}'_1) Y_E^*(\mathbf{r}_2|\mathbf{r}'_2) \cdot \langle G(\mathbf{r}|\mathbf{r}_1) G^*(\mathbf{r}|\mathbf{r}'_1) G(\mathbf{r}_2|\mathbf{r}_t) G^*(\mathbf{r}'_2|\mathbf{r}'_t) \rangle] \quad (4)$$

where the angular brackets $\langle \rangle$ denote the ensemble average and the asterisk the complex conjugate.

The current generator is constructed in the sense of mean by applying Yasuura's method[1].

$$Y_E(\mathbf{r}|\mathbf{r}') \simeq \Phi^*(\mathbf{r}) A_E^{-1} \langle \Phi^T(\mathbf{r}') \rangle \quad (5)$$

where $\Phi = [\phi_{-N}, \phi_{-N+1}, \dots, \phi_N]$, $\phi_m(\mathbf{r}) = H_m^{(1)}(kr) \exp(jm\theta)$, and A_E is a positive definite Hermitian

matrix given by

$$A_E = \begin{bmatrix} (\phi_{-N}, \phi_{-N}) & (\phi_{-N}, \phi_{-N+1}) & \cdots & (\phi_{-N}, \phi_N) \\ (\phi_{-N+1}, \phi_{-N}) & (\phi_{-N+1}, \phi_{-N+1}) & \cdots & (\phi_{-N+1}, \phi_N) \\ \vdots & \vdots & \ddots & \vdots \\ (\phi_N, \phi_{-N}) & (\phi_N, \phi_{-N+1}) & \cdots & (\phi_N, \phi_N) \end{bmatrix} \quad (6)$$

in which the m, n elements are the inner products of ϕ_m and ϕ_n on S :

$$(\phi_m, \phi_n) \equiv \int_S \phi_m(\mathbf{r}) \phi_n^*(\mathbf{r}) d\mathbf{r} \quad (7)$$

In addition, $\langle\langle \Phi^T$ denotes the following operation of each element of Φ^T and the function u_{in} to the right of Φ^T

$$\langle\langle \phi_m(\mathbf{r}), u_{in}(\mathbf{r}) \rangle\rangle = \phi_m(\mathbf{r}) \frac{\partial u_{in}(\mathbf{r})}{\partial n} - \frac{\partial \phi_m(\mathbf{r})}{\partial n} u_{in}(\mathbf{r}) \quad (8)$$

Here $\partial/\partial n$ denotes the outward normal derivative on S .

The Y_E converges to the true operator in the sense of mean as $M \rightarrow \infty$.

NUMERICAL RESULTS OF RADAR CROSS-SECTIONS

Suppose that the turbulent medium is so strong that the incident wave becomes incoherent about the cylinder and only the backscattering from the cylinder is dealt with. Then the Green's function may be regarded as a complex Gaussian random function. In such a situation, the radar cross-sections are calculated for two cases of the spatial coherence length of an incident wave $l : kl = 2, 6$ where k is the wavenumber in free space and l is defined as the distance ρ at which the degree of spatial coherence

$$\Gamma(\rho, z) = \frac{\langle G(\rho, 0|0, z) G^*(-\rho, 0|0, z) \rangle}{\langle G(0, 0|0, z) \rangle^2} \quad (9)$$

takes $e^{-1} = 0.367 \dots$.

Figs. 3 and 4 show RCS when waves are incident on the convex part of the cylinder surface. The RCS is nearly twice as large as that in free space because of backscattering enhancement, and the effect of l on RCS is not so large. The characteristics of RCS are almost the same as shown in [2]. On the other hand, Figs. 5 and 6 show that the effect of l of RCS becomes remarkable when the concavity of the surface becomes large and l becomes small, because l becomes smaller than the effective width of the illuminated surface which is mainly contributed on backscattering.

CONCLUDING REMARKS

The comparison of the present results with the previous ones shows that the spatial coherence length of an incident

wave about a body plays a more active role in determining the radar cross-section of a partially concave body than a convex body. The case of H wave incidence is expected to show more noticeable effect due to creeping of surface currents, but the analysis is a forthcoming study.

REFERENCES

- [1] M. Tateiba and Z. Q. Meng, PIER14: Electromagnetic Scattering by Rough Surfaces and Random media, ed. by M. Tateiba and L. Tsang, Ch.7, 317-361, PMW Publishing, Cambridge, MA, USA, 1996.
- [2] Z. Q. Meng and M. Tateiba, Waves in Random Media, vol. 6, no. 4, 335-345, 1996.

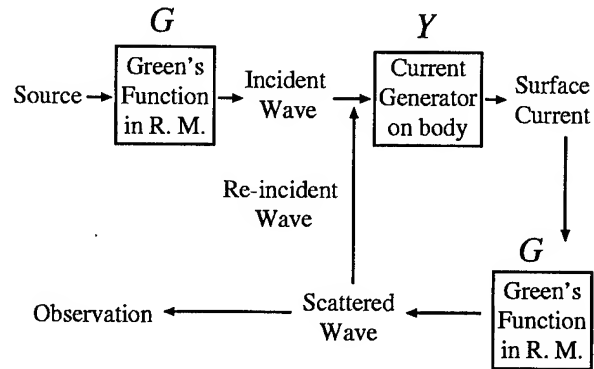


Figure 1. Schematic diagram for solving the scattering problem where a conducting body is surrounded by a random medium.

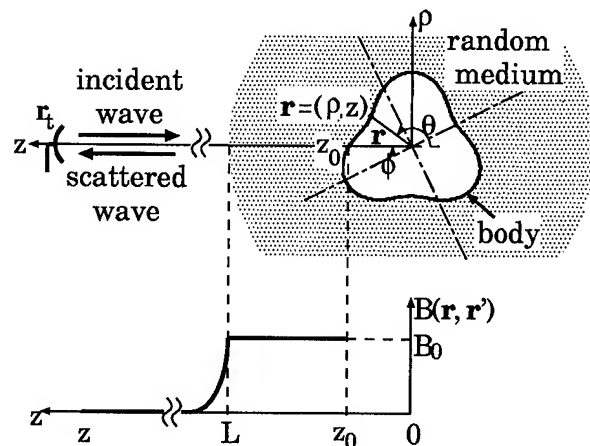


Figure 2. Geometry of the problem of wave scattering from a conducting cylinder in a turbulent medium.

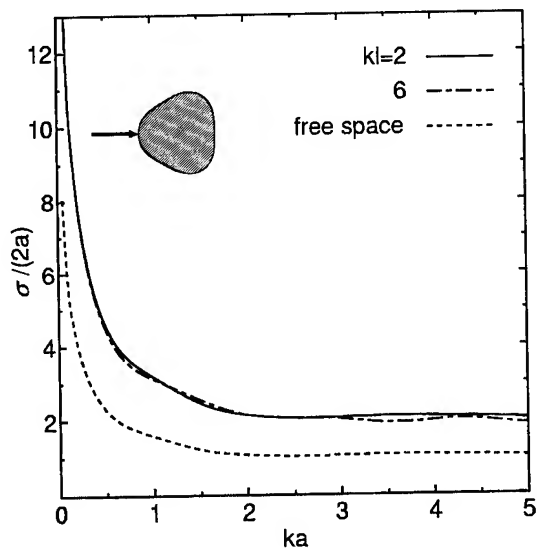


Figure 3. RCS of the concave-convex body of $\delta = 0.1$ and $\phi = 0$ in Fig. 2.

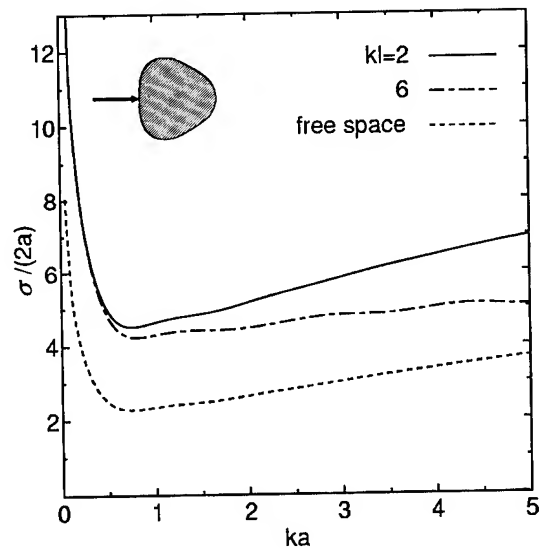


Figure 5. As Fig. 3, but with $\delta = 0.1$ and $\phi = \pi$

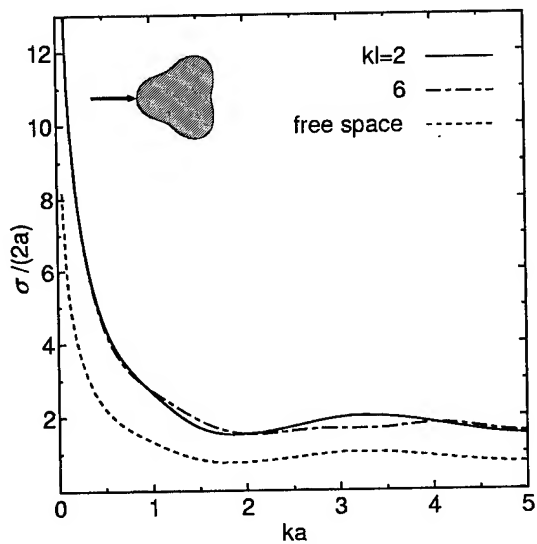


Figure 4. As Fig. 3, but with $\delta = 0.2$ and $\phi = 0$

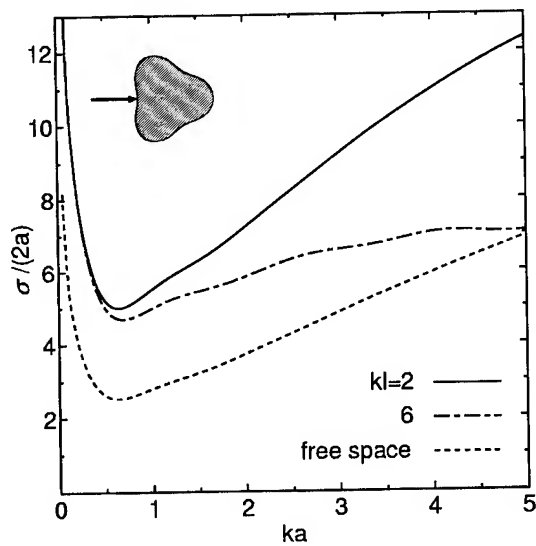


Figure 6. As Fig. 3, but with $\delta = 0.2$ and $\phi = \pi$

Imaging of a Penetrable Object Buried in a Lossy Half-Space for a Multipoint Bistatic Measurement Configuration above the Interface

Jae-Woo Lyu* and Jung-Woong Ra

Department of Electrical Engineering, KAIST
373-1, Kusong-dong, Yusong-gu, Taejeon, 305-701, Korea
Tel : 82-42-869-3414, Fax : 82-42-869-3410
Email : rawoong@ee.kaist.ac.kr

Abstract -- Underground object of one wavelength by one wavelength is reconstructed from the simulated measured fields in the air above the ground interface. By using the transmitting and receiving antenna separated about half a wavelength, one eliminates the direct coupling including the reflections from the interface and reconstructs the object from the fields scattered by the object. Iterative inversion method with the optimization algorithm of the Levenberg-Marquardt and the simulated annealing is used for the reconstruction of high-contrast, large, and slightly lossy object in the presence of Gaussian noise in the measured field.

1. Introduction

In the subsurface exploration of objects such as pipes, cables, voids, etc, electromagnetic pulse[1] and FM-CW radars[2] are used. Detection of shallow targets requires an extremely short pulse or, equivalently, a large-bandwidth FM-CW operation. Continuous-wave(CW) multifrequency radar for subsurface exploration is advantageous over that of impulse in coping with the detection in the shallow depth and the dispersion of the medium. It requires, however, mutual coupling between the transmitting and receiving antennas, which determines the dynamic range of the system, as small as possible. Impulse radar isolates the coupling by the gating of the transmitted pulse.

In order to reduce the mutual coupling between the transmitting and the receiving (T/R) antenna, two transmitting dipoles symmetrically located with respect to one receiving dipole in the center may be fed with the opposite polarity[4]. This antenna reduces not only the direct coupling but also the symmetrically scattered fields from the target. Cross polarized dipoles[5] may be used to reduce the co-polarized coupling and detect the cross-polarized scattered fields. Without reducing the scattered field, the direct coupling may be reduced by a decoupled planar dipoles[6]. Isolation between T/R antenna elements is not large enough, however, and does not give the sufficient dynamic range for the detection of the underground objects.

In addition to the isolation by the physical antennas, it is shown here that the direct coupling as well as the strong reflection from the interface of the half space may be eliminated by filtering out the zero-frequency component in the spatial frequency spectrum of the scattered field. The scattered field including the coupling between T/R antennas and from the interface may be measured by moving this T/R antenna along the interface and may be Fourier transformed into its spatial frequency domain. By filtering out the undesirable couplings, the buried object may be reconstructed successfully by using the iterative inversion algorithm[8].

A two-dimensional object of one wavelength by one wavelength with its permittivity and conductivity of $25 \epsilon_0$ and 0.01 S/m is assumed to be buried in the ground with its permittivity and conductivity of $10 \epsilon_0$ and 0.005 S/m , respectively, in the depth of half a wavelength, where μ_0 and ϵ_0 is the permeability and the permittivity of the free space. An iterative inversion method [8] minimizes the cost function to obtain the distribution of the object permittivity. Numerical simulation for this two-dimensional object is shown to be successfully reconstructed by using the hybrid inversion algorithm combining the steepest descent type Levenberg - Marquardt algorithm and the stochastic type simulated annealing algorithm[8]. The simulated annealing algorithm is needed to reach the global minimum when the iterative process is trapped in one of the local minima of its cost function.

2. FORMULATION

When a time harmonic electric line source is located at (x_s, y_s) in the air region along the z -direction, in the presence of a two dimensional penetrable object in the lossy half space, as shown in Fig.1, the electric field polarized in the z -direction, $\underline{z}_0 u$, is given by

$$u = u_h + u_o, \quad (1)$$

where u_h is the total field in the absence of the object and u_o is the field due to the presence of the object. They are given as[7],

$$u_h(x, y : x_s, y_s) = \frac{-\omega\mu_0}{4\pi} \int_{-\infty}^{+\infty} \frac{1}{\sqrt{k_1^2 - k_y^2}} \left[e^{-\sqrt{k_1^2 - k_y^2}|x-x_s|} + \frac{\sqrt{k_1^2 - k_y^2} - \sqrt{k_2^2 - k_y^2}}{\sqrt{k_1^2 - k_y^2} + \sqrt{k_2^2 - k_y^2}} \right. \\ \left. \cdot e^{-\sqrt{k_1^2 - k_y^2}(x+x_s)} \right] e^{-jk_y(y-y_s)} dk_y, \quad x_s > 0, x > 0, \quad (2a)$$

$$\frac{-\omega\mu_0}{2\pi} \int_{-\infty}^{+\infty} \frac{1}{\sqrt{k_1^2 - k_y^2} + \sqrt{k_2^2 - k_y^2}} e^{-\sqrt{k_1^2 - k_y^2}x_s} e^{\sqrt{k_2^2 - k_y^2}x} \\ \cdot e^{-jk_y(y-y_s)} dk_y, \quad x_s > 0, x < 0, \quad (2b)$$

$$u_o(x, y) = k_0^2 \int_S [\varepsilon_3(x', y') - \varepsilon_2 - \frac{j}{\omega\varepsilon_0}(\sigma_3(x', y') - \sigma_2)] u(x', y') G(x, y : x', y') dx' dy' \quad (3)$$

where k_i , ε_i and σ_i are the wave number, the relative dielectric constant and conductivity, respectively, and the subscript j designates the air($j=1$), the lossy($j=2$), and the object ($j=3$) medium confined in the domain S . G is the two-dimensional Green's function[7] satisfying the half space boundary conditions at $x=0$, radiation condition at $x = \pm\infty$, and the time harmonic dependence $e^{j\omega t}$ is suppressed.

Two line sources of transmitting and receiving separated by half a wavelength moves along the interface for the excitation and the measurement of the scattered fields, as shown in Fig. 1. The measured fields, $u(y)$, which are calculated by the method of moments, scattered from the penetrable object lossy medium(of one wavelength by one wavelength having $\varepsilon_3 = 25\varepsilon_0$, $\sigma = 0.01$ S/m) are shown in Fig. 2(a), ($\varepsilon_2 = 10\varepsilon_0$, $\sigma_2 = 0.005$ S/m). The measured field $u(y)$ in Fig 2(a) shows a strong interference pattern of $u_h + u_o$ near the top of the object and approaches a constant as y departs far away from the object since u_o in eq. (1) becomes negligible.

One may take the Fourier transform of $u(y)$ as the spatial frequency spectrum along y ,

$$U(\beta) = \int_{-\infty}^{\infty} u(x, y : x_s, y_s) e^{j\beta y} dy \quad (4)$$

which is shown in Fig. 2(b). Spectral amplitudes of the spatial frequency β is peaked at the zero frequency and decreases as β increases. The spectral component of frequency zero is due to the dc part of $u(y)$ in y , i.e., the direct coupling of T/R antenna elements in the absence of the object. Since the separation of T/R antennas is a constant, u_h in eq. (1) becomes a constant for any measurement point and its Fourier transform gives the zero frequency spectrum.

By filtering out the zero frequency spectral component or the direct coupling between T/R antennas including the fields reflected from the ground interface, one may reconstruct the object from the measured scattered fields

u_o via eq. (3). Since eq. (3) is a nonlinear integral equation in solving ε_3 and σ_3 , one may discretize the object and apply the iterative inversion method[8], where a cost function is defined as the squared magnitude of the difference fields between the measured and the calculated from the assumed distributions of ε_3 and σ_3 as

$$f = \frac{1}{2} \sum_{i=1}^F \sum_{m=1}^M |U_o^M(\varepsilon_n, f_i, d_l, \beta_m) - U_o^C(\varepsilon_n^k, f_i, d_l, \beta_m)|^2, \quad (5)$$

where f_i and β_m are, respectively, the i -th frequency, and m -th spectral component. F and M are the total number of the used frequencies and the sampled spectral components, respectively, U_o^M and U_o^C are the measured and the calculated spectral coefficients of the m -th spectral component, respectively, for the original distribution of complex permittivities ε_n and the assumed set of the complex permittivity distribution at the k -th iteration step, ε_n^k .

One then minimize this cost function iteratively by updating the distribution of the complex permittivity profile until the original distribution of the complex permittivity is found. A stochastic SA algorithm may be combined with the steepest descent LM algorithm and this hybrid algorithm (HSALM)[8] optimizes the process minimizing the cost function. If the minimization by LM algorithm traps in one of the local minima of the cost function, HSALM switches LM to SA to find another permittivity distributions corresponding to the lower cost functional and let it switch to LM again to minimize the cost function to reach a deeper minimum and repeats until the global minimum is found.

3. Numerical Results and Conclusions

Fig. 3 shows the reconstruction of a homogeneous square dielectric cylinder mentioned previously. For the calculation of the scattered fields, u_o , the object is discretized into 4 cells of their cell size, $0.5\lambda_2$ by $0.5\lambda_2$ for the inversion, where λ_2 is the wavelength in the lossy background medium. Fields at 8 locations of the T/R antenna of its separation distance $0.5\lambda_2$ along the interface over $4\lambda_2$ interval, as shown in Fig. 2(a), are used for the reconstruction. When 1 percent Gaussian error(or noise) is assumed in the measured total fields, the noise fields are distributed almost uniformly, as shown in Fig. 2(a), while the noise in the spectral components are distributed mainly in the higher order spectral components, as shown in Fig. 2(b). This noise may be filtered out by eliminating the higher spatial-frequency component in $|\beta| > k_2$, which is the regularized process of the illposedness[8] without any additional regularized term in the cost function.

By estimating the size of the object from the

measured data in Fig 2(a) by $L = 4\lambda_2$, one may determine the sampling interval $\Delta\beta = 0.25 k_2$ and six spatial frequencies are available to be used if the above regularized process is implemented. For the reconstruction of the object shown in Fig. 3, two temporal frequencies and four sampled spatial frequency components are used and obtain the root mean square error of the reconstruction, 3.7 percent for the permittivity distribution and 11.0 percent for the conductivity distribution when one percent Gaussian noise is added to the total field u .

References

- [1] D.J.Daniel, "Short Pulse Radar for Stratified Lossy Dielectric layer measurement", IEE Proc. Pt. F, vol. 127, No.5, Oct. 1980, pp.384-388
- [2] A. Z. Botros, A. D. Olver, L. G. Cuthbert, and G. Farmer, "Microwave Detection of Hidden Objects in Walls", Electron. Lett., vol. 20, No. , April 1984, pp.379-380
- [4] David A. Hill, "Near-field Detection of buried dielectric objects", IEEE Tran. GRS-27, No. 4, July, 1989, pp.364-368
- [5] Luen C. Chan, D.L. Moffatt, Leon Peters, JR, "A characterization of subsurface Radar Targets", Proceedings of the IEEE. vol. 67, No. 7, July 1979, pp.991-1000
- [6] D.K., Park, and J.W. Ra, "Decoupled planar Dipoles for subsurface CW interface radar", Micro. and Opt. Tech. Lett., vol. 7, No. 8, June 5, 1994, pp.367-370
- [7] A. Sommerfeld, "Partial Differential Equation", New York:Academic Press, 1949
- [8] Park, C. S, Park, S.K., and Ra, J.W., "Moment method and iterative reconstruction of two-dimensional complex permittivity by using effective modes with multiple sources in the presence of noise", Radio Science, vol.31, Num.6, pp.1877-1886, Nov., 1996

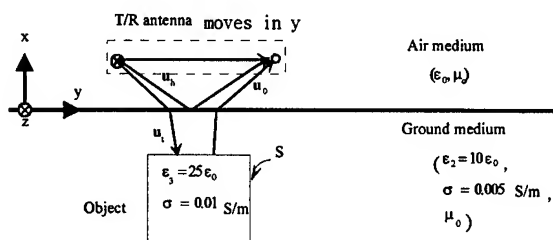


Fig. 1 T/R antenna in the air region in presence of the penetrated object in the lossy half plane

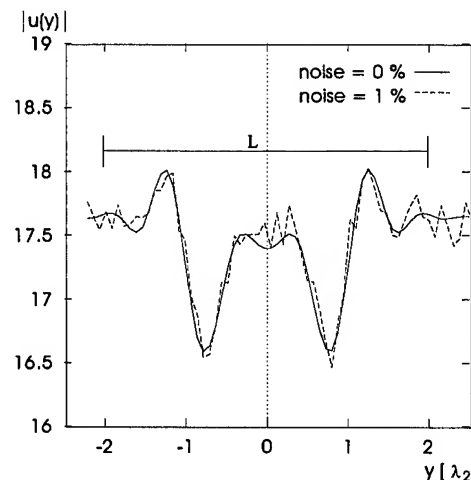


Fig. 2(a) Magnitude distribution of the measured fields along the interface along y in λ_2

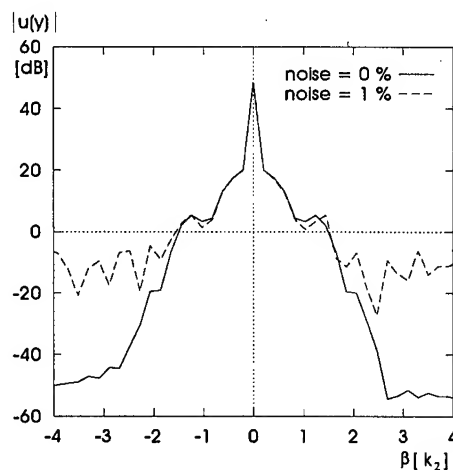


Fig. 2(b) Spectral amplitudes versus the spatial frequency β in k_2

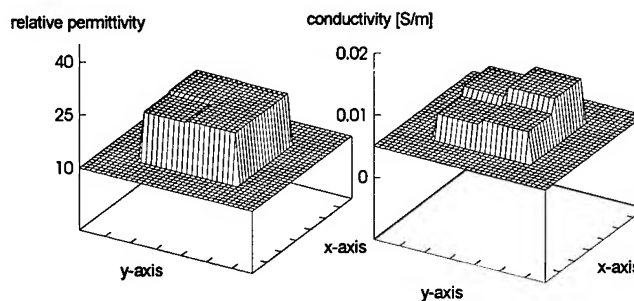


Fig. 3 Reconstruction of the permittivity and the conductivity of the buried object

Selection of an Optimum Patch for an Area-Based Stereo Matching Algorithm

Taejung Kim* and Soon Dal Choi**

Satellite Technology Research Center

Korea Advanced Institute of Science and Technology

373-1 Kusung-Dong, Yuseong, Taejeon, Korea

* Tel) +82-42-869 8629, Fax) +82-42-869-0064, tjkim@krsc.kaist.ac.kr

**Tel)+82-42-869 8611, Fax)+82-42-869-0523, sdchoi@satrec.kaist.ac.kr

Abstract – This paper describes an approach to reduce the execution time of an area-based stereo matching technique by defining a patch (or window) carefully. It will be shown that conventional way of defining a patch contains redundancy and that a patch defined otherwise improves the performance in terms of coverage and speed while accuracy degradation is nominal. This paper also describes an attempt of defining optimal patch for stereo matching.

INTRODUCTION

One of the most important and widely used techniques for extracting 3D information from imagery is stereo matching technique. This technique is traditionally classified as feature-based and area-based stereo matching. Area-based stereo matching, compared to feature-based one, delivers more accurate results but requires more computation time. This has caused area-based stereo-matching difficult to be applied to any real-time applications. Several techniques has been proposed to reduce this time requirement, such as coarse-to-fine approach or the use of feature-based stereo matching as an initial estimate of matching.

This paper describes a number of experiments undertaken in order to reduce the execution time of an area-based stereo matching algorithm, proposed by Otto and Chau [1]. This algorithm defines initially a rectangular-shaped window (or patch) with a predetermined size around the points being considered for matching. A patch has grid on it so that adaptive least squares correlation (ALSC) matching is applied on grid points of a patch. Once one loop of ALSC is completed, the shape of patch changes and brightness value and its gradient in horizontal and vertical direction on grid points needs to be recalculated. With this revised patch, the next loop of ALSC proceeds.

Conventionally, grid is defined as one pixel-wide on a patch in horizontal and vertical directions. However, the next section will show that this convention causes redundant computation and hence increases execution time. The next section will describe experiments carried out with several grid patterns. The following section will describe an approach to define an optimal patch based on an assumption that areas around the center of a patch is more important than areas around rim.

PROBLEM OF CONVENTIONAL PATCH

Let's consider a configuration of grid points on a patch superimposed on image coordinates as shown in figure 1.

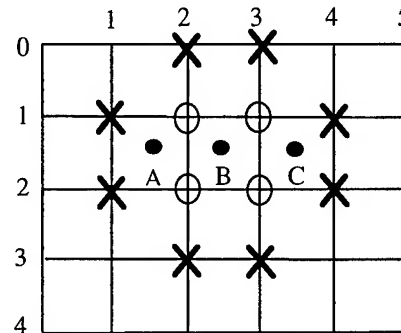


Figure 1. Configuration of grid points and image points.

In the figure, points A, B, C represent grid points within a patch. On these points stereo matching is carried out and therefore the brightness value and its gradient on these points should be calculated. The rectangular squares represent image points with coordinates as numbered. Let's consider point B first of all. In order to get the brightness value, $g(x,y)$, of the point B through bilinear interpolation, one need to consider the brightness value of pixels (1,2), (1,3), (2,2) and (2,3) as indicated with circles in the figure. To calculate brightness gradients, $dg(x,y)/dx$, and $dg(x,y)/dy$, of the point B, one needs first to calculate brightness gradients of the four surrounding points, (1,2), (1,3), (2,2) and (2,3), and next calculates the brightness gradients of the point B by bilinear interpolation. Therefore additional 8 points indicated as crosses in the figure should be considered. In total, for brightness value and brightness gradients of point B, brightness value of adjacent 12 pixels are considered.

Now let's consider for the point C. As before, 12 pixels adjacent to the point C are considered, of which seven are overlapping, i.e., have already been considered with the point B. For the point A, another 12 pixels are considered, of which again seven are overlapping. Moreover, the four points, (1,2), (1,3), (2,2), (2,3), surrounding the point B have all been considered with the points A,B, and C. The more grid points such as the ones above and below the point B are considered, the more the number of pixels are overlapping.

Table 1. Stereo matching results with various grid patterns

Patch Size	1 pixel wide grid pattern ("Grid1")			2 pixel wide grid pattern ("Grid2")			3 pixel wide grid pattern ("Grid3")		
	matched points	execution time (s)	No. of grid on patch	matched points	execution times (s)	No. of grid on patch	matched points	execution times (s)	No. of grid on patch
9	27	4.60	81	8	2.44	25	3	0.26	9
13	34	8.35	169	29	3.29	49	17	2.32	25
17	46	8.04	289	40	3.67	81	17	2.36	25
21	47	10.20	441	44	4.42	121	31	3.05	49
25	47	13.90	625	45	4.95	169	38	4.10	81
29	47	20.40	841	47	4.89	225	38	4.18	81
33	44	29.89	1089	47	6.16	289	44	4.14	121
37	43	44.67	1369	48	7.88	361	47	4.16	169

From the observations so far, it may be understood that a patch with one pixel wide grid pattern may not be necessary for stereo matching. This will be tested in the following section.

EXPERIMENTS WITH SEVARAL GRID PATTERNS

In order to test effects of grid pattern of patches on stereo matching, experiments were carried out with three different grid patterns. One was the conventional grid pattern, i.e. the grid defined as one pixel wide on the patch ("Grid1" from now on). Other one was the one defined as two pixel wide ("Grid2"). The third one was defined as three pixel wide ("Grid3"). With each grid pattern, stereo matching was applied onto 50 manually selected seed points. Since ALSC stereo matching is known to be very dependent on the size of patches, the same experiments were carried out several times with different patch size. Table 1 summarizes the results.

For each experiments the table analyzes the results in three aspects: the number of matched points (out of 50 seed points), execution time and the number of grid points on a patch. First of all, let's compare stereo matching results among the experiments with "Grid1". From the table, it is possible to reconfirm that patch size is very crucial factor for stereo matching. Smaller patch size has smaller coverage than the large one. However, it can be noticed that, if patch size is too large, stereo matching results start deteriorating. This seems because ALSC starts including too "far" for estimation. It is also possible to note that execution time is not directly proportional to the number of grid points. Although larger patch requires more computation for estimation, larger patch at the same time could lead quicker convergence of estimation.

Let's now compare the results from "Grid1" and "Grid2". When patch size is small, coverage of "Grid2" was quite smaller than that of "Grid1". This is because there were not enough grid points for accurate least squares estimation. As the patch size became larger, the coverage recovered quickly. For the patch size of 33 pixels, the stereo matching results from "Grid2" has no difference with the results from "Grid1"

in terms of coverage. For a given patch size, the execution time taken for two pixel wide grid was notably small compared to the conventional one. This comparison is based on the results from the same patch size. However as shown in the table, "Grid1" and "Grid2" of the same patch size have different number of number of grid pattern. Comparison based on the number of grid points seems more appropriate. The patch size of 13 pixels of "Grid1" has the same number of grid points as the patch size of 25 pixels of "Grid2" and the patch size of 17 pixels of "Grid1" as the patch size of 33 pixels of "Grid2". The table show that stereo matching with "Grid2" offers much better results compared to "Grid1" of the same number of grid points. Stereo matching results from "Grid2" have larger coverage, which means that through two pixel wide grid pattern, it has been possible to have effects of defining "wider" patch. The faster execution time means, at the same time, ALSC with "Grid2" converges more quickly.

The number of grid points of a given patch size was further reduced by defining a grid pattern with three pixel wide. With this, stereo matching was applied. Execution time was further reduced. For the same number of grid points, results from "Grid3" offers better results than those from "Grid2" in terms of coverage and speed. It can be noticed that more larger patch size are needed for "Grid3" in order to get improved performance and patch size larger than 37 pixels seems necessary. However, this size is where the stereo matching performance with "Grid1" started deteriorating as the patch started including too far.

The performance of stereo matching was compared in terms of accuracy. An assumption was made that the matching results from "Grid1" would be accurate ones. This was made partly due to the difficulty of acquiring accurate matching truth in image pixel coordinates. Accuracy was assessed by comparing matching results of "Grid2" and "Grid3" with the results from "Grid1". Table 2 shows the results of accuracy comparison. In the first column, the difference between the matching results from "Grid1" and "Grid2" was averaged in x and y direction and in distance.

The table shows that as the patch size increases the accuracy of "Grid2" improves. At the patch size of 33 pixel the average positional difference is 0.04 pixel, which is well below error tolerance limit of most of the image analysis systems. The next column of the table gives the accuracy of "Grid3". It seems that the accuracy of "Grid3" seems a little bit insufficient. This could mean that grid pattern of three pixel wide is too sparse.

From the table 1 and 2, it is possible to conclude that patch with one pixel wide grid pattern is unnecessary and the "Grid2" used in the experiments offers much better performance.

Table 2. Accuracy of different grid pattern

Patch size	Grid 1 - Grid 2			Grid 1 - Grid 3		
	Δx	Δy	Δ	Δx	Δy	Δ
9	0.078	0.053	0.103	0.266	0.686	0.812
13	0.093	0.060	0.124	0.138	0.201	0.286
17	0.059	0.063	0.093	0.135	0.196	0.282
21	0.053	0.058	0.088	0.179	0.119	0.238
25	0.046	0.033	0.064	0.176	0.162	0.256
29	0.097	0.076	0.143	0.241	0.221	0.363
33	0.028	0.027	0.042	0.109	0.113	0.168
37	0.026	0.027	0.042	0.098	0.142	0.180

SELECTION OF AN OPTIMAL PATCH

In the previous section, it was shown that by defining a patch with two pixel wide grid pattern better stereo matching results could be obtained. This imposes a possibility of defining grid pattern for a patch to have optimal stereo matching results. The analysis for this could be very sophisticated deserves comprehensive research. This section describes, as an example, a simple approach to find an optimal patch.

It would be reasonable to assume that when matching a point, the region adjacent to the point contains more information for matching than the region further apart. With this assumption a patch can be defined such that grid is defined narrower in the center and wider in the rim of a patch. This idea was tested. A new patch with grid of varying width was defined using the function of shown in figure 2.

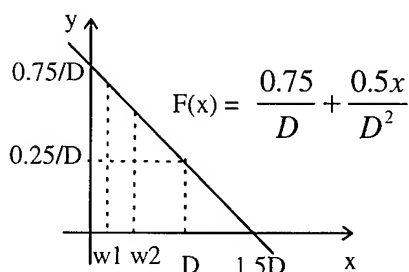


Figure 2. Function of grid sampling frequency

In the figure, $F(x)$ defines the function of grid sampling frequency. This sampling frequency function was defined as a linear function for simplicity. Grid width can be defined as the distance between the points which divides $F(x)$ into equal areas, i.e.,

$$\int_0^{w1} F(x)dx = \int_{w1}^{w2} F(x)dx, \text{ and so on.}$$

The origin represents the center of a patch and 2D is set to a patch size. Coefficient value of $F(x)$ was defined such that grid width could be between 1 pixel and 3 pixels. The number of grids was set equal to that of "Grid2". With these, new grid pattern was defined and stereo matching was applied. Table 3 summarized the results. Table 3 shows that coverage and speed has been improved compared to the results from "Grid2" and accuracy remains similar.

Table 3. Stereo matching results of new optimum patch

Patch size	New grid pattern			Grid1 - new grid		
	Matched Point	Time	No. of grid	Δx	Δy	Δ
9	16	1.93	25	0.090	0.065	0.123
13	33	2.70	49	0.098	0.077	0.141
17	46	2.73	81	0.073	0.066	0.111
21	46	3.47	121	0.042	0.065	0.084
25	48	3.41	169	0.047	0.054	0.080
29	49	3.87	225	0.105	0.093	0.162
33	49	5.44	289	0.034	0.052	0.069
37	47	7.20	361	0.038	0.062	0.079

CONCLUSIONS

This paper describes an approach to reduce the execution time of stereo matching by selecting a patch carefully. It was shown that by defining a patch with two pixel wide grid, stereo matching performance was improved in terms of coverage and speed. Also an optimal patch was defined based on the assumption that areas around the center of a patch contains more information for matching than areas in the rim and this can be modeled as a linear function. Results shows that performance was further improved.

The idea of defining optimal patch needs further analysis with more general modeling functions such as Gaussian distribution functions and with experiments using various type of stereo pairs.

REFERENCES

- [1] G.P. Otto and T.K. Chau, "A Region-Growing Algorithm for Matching Terrain Images", *Image and Vision Computing*, 7(2):83-94, 1989

Visualization of Satellite derived Time-series Datasets using Computer Graphics and Computer Animation

Robert E. Meisner, Michael Bittner and Stefan W. Dech
Deutsche Forschungsanstalt für Luft- und Raumfahrt (DLR)
Deutsches Fernerkundungsdatenzentrum (DFD)
Oberpfaffenhofen, D-82234 Wessling, Germany
Tel. +49 8153 28 1371
Fax. +49 8153 28 1445
e-mail: Robert.Meisner@dlr.de

Abstract -- The German Remote Sensing Data Centre (DFD) of the German Aerospace Research Establishment (DLR) is operationally generating remote-sensing based timeseries-datasets. These datasets can be used for example for environmental, climatological and atmospherical research. Bearing in mind the enormous amount of data already generated at DLR from today's missions, even with a comfortable search-engine like ISIS (provided by DLR) it is a major problem to identify those datasets most suitable for a specific research task. Looking into the future, data-quantities will even increase with new missions like ENVISAT. Therefore, it appears essential to provide the user-community with efficient tools to explore and evaluate these timeseries-datasets.

Visualization forms the most efficient way to explore the contents of vast data quantities and to identify the subsets showing the phenomena of interest in a relatively short time. Synthesis with secondary remote sensing data for visualization offers the possibility of multidimensional data exploration. Finally, visualization is essential for the presentation of a projects purpose and its results.

Data gaps in time-series form a problem in visualization as they are prohibitive for stable movement in computeranimation. For this reason different interpolation techniques have been developed primarily for atmospheric sensors and now prove to be a valuable tool for interpolation of other remote sensing datasets.

A video presentation showing examples of films created at DLR will be given.

ANIMATION PURPOSES

Visualization will not substitute a scientists detailed analysis and quantification, but it can lead to a faster and easier way of quantifying and understanding dynamic phenomena in remote sensing data [8].

Exploratory Visualization

Exploratory Data Analysis (EDA) as an efficient tool for exploring the contents of large data quantities has been postulated in 1980 by the work of Tuckey [7] and includes the explicit use of visualization techniques. In 1990 DiBiase

expanded this approach for remote sensing datasets saying, that computer-assisted visualization techniques will be the only effective way to explore the enormous data sets amassed by the new generation of earth observing satellites for example like NASA's „Earth Observing System“ (EOS) Program (approx. 1250 GB/day).

Confirmatory Visualization

After a question has been raised, the scientist turns from exploratory to confirmatory visualization. This is especially true for verification and analysis of model results [4]. Studying complex phenomena for confirming a hypothesis which is based on theoretical or empirically derived knowledge gets easier with graphical visualization. The use of computeranimation for confirmation is especially useful in the field of dynamic spacial systems, as they are usually found in the earth sciences [8].

Synthesis and Presentation

Visualization of remote-sensing data or research results often requires the combination of data from different sources and of different formats (synthesis). For presenting the data or the results to the scientific community visualization offers the chance to transfer complex information in an efficient and transparent way thus being scientifically correct as no information has to be dropped for ease of understanding. Presenting the same information to a non professional audience of e.g. politicians, requires convincing visualizations to transfer the usefulness and necessity of such research projects [4]. Professional presentation and communication in science is essential, as the competition is increasing and a research report not only has to be substantial and coherent but also convincing [4].

TIME SERIES DATASETS

The German Remote Sensing Data Centre (DFD) is operationally receiving and processing a variety of satellite data through its European and global receiving stations. For example NOAA-AVHRR data has been received since the early 80's. Multichannel Sea Surface Temperatures (MCSST) and Normalized Difference Vegetation Indices (NDVI) as well as image subsets have been operationally processed daily since 1993 (for more information see Dech ,

[3]). GOME data has been processed to global and polar ozone maps since June of 1996. Amongst others, all the datasets mentioned are offered to the user community through DLRs comfortable search engine, the „Intelligent Satellite Information System“ (ISIS) (for more information on ISIS see www.dfd.dlr.de). Processing of the datasets includes the generation of time-series animations and the generation of compressed video sequences at the end of the production chain. This is helpful especially, if exploration and confirmation of data is done over computer-networks. It is faster, cheaper and easier to transfer a compressed video-sequence instead of hundreds of single images to identify time ranges and areas of interest.

ANIMATION ENVIRONMENT

Different approaches have been made to fulfill the requirements of an easy to use and fast system for the analysis of remote sensing data [5]. These systems are mostly based on expensive hardware and specially developed software. At the DFD Computer animation are used to visualize time-series datasets which can assist in analyzing large data amounts and in detecting highly dynamic phenomena. The standard production pipeline for computer animation from **modeling** over **animation** to **rendering** has been adapted to the requirements of remotely sensed datasets (see Fig. 1). At the modeling end a special interface from DFDs image processing system for georeferenced data to the animation software allows easy data transfer between systems. This ensures the ability to import different layers into the animation system. The possibility to import the scientific data as wireframe 3-D models or as texturemaps ensures maximum flexibility at minimum effort. After data import, modeling is completed manually. Animation itself including design (camera attitude, length, changes) and scene composition is applied in the way most suitable for emphasizing certain aspects.

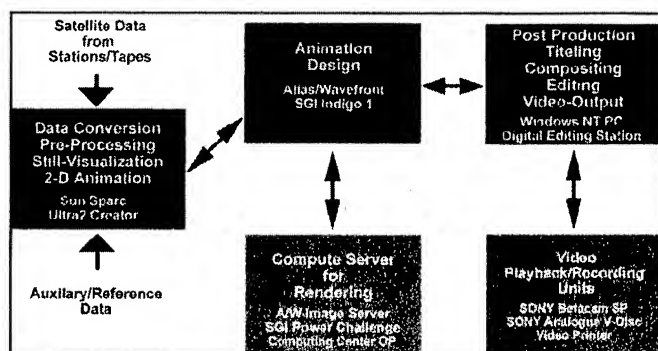


Fig. 1: Layout of Animation System at DLR/DFD.
Red = Custom designed, Gray = Standard systems

TIME-SERIES ANIMATION

Among the datasets processed at DFD are Sea Surface Temperature (SST), Normalized Difference Vegetation Index (NDVI) and Global Ozone Monitoring Experiment (GOME) time series. Due to the measurement characteristics of e.g. GOME or the weather conditions e.g. in NDVI data (cloudcover) gaps occur in the datasets. For animation these gaps have to be filled without losing detail in the information contained. For this purpose sophisticated interpolation techniques have been developed.

Selective Mean Filter

For small gaps in datasets which are not subject to intensive changes in space like e.g. Sea Surface Temperature data, a selective mean filtering method is used for filling data gaps. Depending on size and location of the gaps a mean box filter of approx. 40×40 pixels is used to fill the holes and to eliminate mixed pixels along the shore. Though this method can not be used for highly dynamic data, because they exhibit steep gradients over short distances, it gives good results for sea surface temperature analysis. The advantages of ease of application and little computing time can balance some inaccuracy coming along with the method. Inbetweening for the animation process is done using linear interpolation over time.

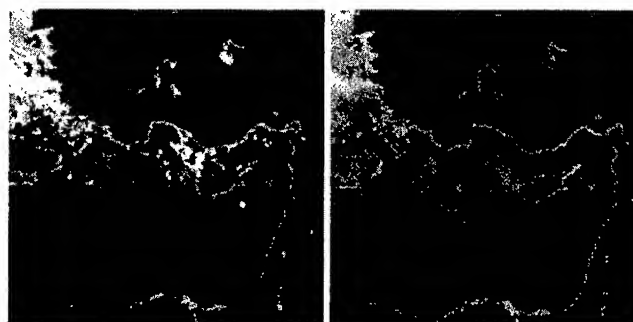


Fig. 2: Selective Mean Filter applied to Sea Surface Temperature of the eastern Mediterranean (Week 52, 1996), Cold in yellow, warm in red.

Harmonic Analysis (HA)

As mentioned above, some data sets are not suited to be treated by local interpolation techniques. For example, the global ozone distribution in the Earth's atmosphere or vegetation information is highly variable in time and space. In consequence, GOME's daily global coverage is too coarse to allow for proper generation of global ozone maps using only a finite number of 'nearest-neighbor' points. Therefore, an interpolation scheme based on sinusoidal functions (harmonics) was developed modeling the ozone distribution in between the measured data points. This technique is based on spectral analysis concepts modeling the longitude dependency of ozone concentration. Roughly speaking, the

approach begins with a binning of daily GOME data into latitude segments. Each zonal data series is then modeled by a linear combination of harmonic functions (see equation 1) by means of the least-squares technique.

$$y(\lambda) = \sum_{i=1}^N A_i \sin(\omega_i \lambda - \phi_i) \quad (1)$$

Deconvolution of the power spectrum leads to determination of optimum frequencies ω_i , amplitudes A_i , and phases ϕ_i for the N functions. (Due to physical reasons depending on atmospheric dynamics characteristics some constraints are added to the technique which are beyond the scope of this paper and will not be discussed here.) After all functions have been determined, the model allows reproduction not only of original data points but also derivation of data estimates y at each desired longitude λ . It should be noted that the technique does not depend on equally spaced input series.

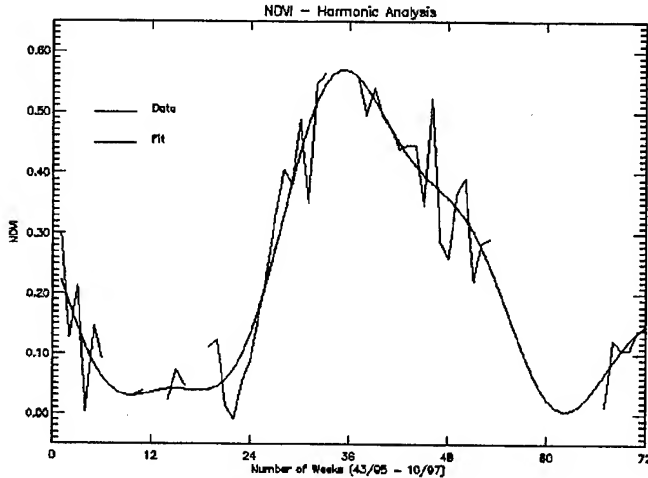


Fig. 3: Harmonic Analysis for one pixel of a time-sequence of NDVI data (black line) where the red line represents the fit

The approach has proven robustness and reliability and is therefore used operationally at DLR-DFD. For a more detailed description of the HA refer to Bittner et al. (1997) and references therein.

HA has also been applied to NDVI time-series data for Central Europe for the period of mid 1994 to mid 1996. Fig. 3 shows a typical time-series for one pixel in a 72 week period. The red line represents the fitted data, where data gaps have been filled depending on measurements taken before and after the gap. Fig. 4 shows the resulting dataset for week 20 in 1995.

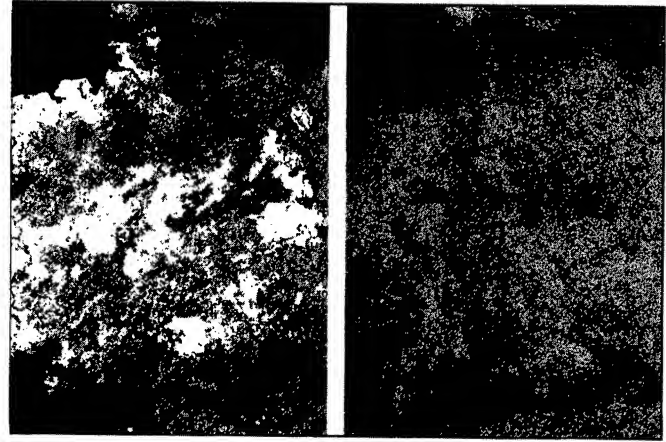


Fig. 4: NDVI Data of Central Europe from Week 20, 1995, before (left) and after (right) harmonic analysis ($N=4$), yellow = little vegetation, green = dense vegetation, white = cloud covered.

KALMAN FILTER (KF)

Several data sets rely on systems that show considerable changes not only in space but also in time. Kalman filtering allows to consider both, time and space dependency of data sets. The philosophy of the KF approach is that the (not necessarily observable) state \vec{x}_k ($n \times 1$ -vector) of a system can be derived from its earlier states \vec{x}_{k-1} via:

$$\vec{x}_k = \Phi_{k-1} \vec{x}_{k-1} + \vec{w}_{k-1} \quad (2)$$

The ($n \times n$)-matrix Φ_{k-1} contains the system characteristics. \vec{w}_{k-1} ($n \times 1$ -vector) represents the innovative input and is assumed as white noise. Equation 2 thus contains the temporal dynamics of the system. The actual measurements \vec{y}_k (1×1 -vector) are obtained through:

$$\vec{y}_k = H_k \vec{x}_k + \vec{v}_k \quad (3)$$

The ($1 \times n$)-matrix H_k defines the relationship between the statevector \vec{x} and the measurements \vec{y} . \vec{v} (1×1 -vector) accounts for the measurement error. Using recursive algorithms it is possible to derive the statevector from the measurements. For a more detailed description of the KF see, for example, Dailey [2].

In case of the GOME data processing it is assumed, analogous to the HA approach, that the state of the atmospheric ozone distribution at time s can be modeled for each latitude bin by a linear combination of trigonometrical functions (note, that in contrast to eq. (1), a Fourier sequence is used!):

$$y_s(\lambda) = A_0 + \sum_{m=1}^M [A_m \cos(m\lambda) + B_m \sin(m\lambda)] \quad (4)$$

The state vector is given by the Fourier-coefficients:

$$\vec{x} = (A_0, B_1, A_1, \dots, B_M, A_M).$$

The matrix

$$H_k = (1, \sin \lambda_k, \cos \lambda_k, \dots, \sin(M\lambda_k), \cos(M\lambda_k))$$

contains the corresponding sinusoidal functions.

Taking into account the measuring characteristics of the GOME sensor and the dynamics of ozone concentration, it is highly desirable to be able to generate full cover ozone maps from the coarse measurement given by GOME (see Fig. 5, left image). Temporal interpolation of the data in combination with a spatial representation of the atmosphere represented by a model approach allows the generation of accurate ozone maps on an hourly basis (see Fig. 5).

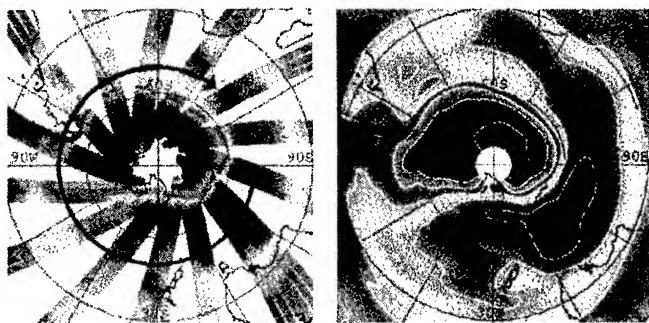


Fig. 5: GOME data as measured on September 16th, 1996 and Kalman Filtered Dataset as from 12:00 on the same day, low ozone concentration is coded in dark blues.

ANIMATION TECHNIQUES

Based on these time datasets, 2-D and 3-D Animation techniques are used, where objects, viewing angel, length, illumination can be animated (changed). For the special purpose of time-series dataset animation, the surface of the models (e.g. the globe) changes over and therefore has to be animated. This technique also referred to as texture animation or rotoscoping, allows to show the behavior of measured data in natural spatial and temporal distribution. At the DFD these techniques are mainly used for the animation of weather data, ozone distribution, vegetation development and sea surface temperature dynamics.

SUMMARY

Computer animation can help in reducing the vast amount of data to be explored from current and future remote sensing satellites. Special algorithms for data interpolation allow a constant and stable development in animations and make them easier to interpret and understand. As model

approaches are used and time dependent interpolation techniques are applied, results given by these interpolation techniques maintain data accuracy and significantly enhance interpretation possibilities. The techniques described here for animation of time-series data can be applied to any time-series dataset no matter if used for animation, interpretation or classification. Current research is evaluating this interpolation method for the generation of a base dataset for land-use classification based on vegetation datasets containing gaps due to cloud coverage. With these techniques used in the field of scientific visualization the quality of such animations will be significantly enhanced.

ACKNOWLEDGMENTS

The authors express their appreciation to Mr. Thomas Ruppert and Mrs. Heidelotte Craubner for their contributions to this work.

REFERENCES

- [1] Bittner, M., S.W. Dech, R.E. Meisner, and T. Ruppert, Generating GOME Level 3 Data Products at DFD, Technical Report, DFD-DLR, Oberpfaffenhofen, D-82234 Wessling, Germany, 1997
- [2] Dailey, R., Atmospheric Data Analysis, Cambridge University Press, New York, 1993
- [3] Dech, S.; Meisner, R.; Tungalagsaikhan, P.: Operational Generation of AVHRR-Based Level-3 Products at the German Remote Sensing Data Centre: Status and Perspectives, Proceedings of IGARSS '97, submitted.
- [4] DiBiase, D.: Visualization in the earth sciences, In: Earth and Mineral Sciences, Pennsylvania State University, Vol. 59, No. 2, 1990, S. 13 - 18.
- [5] Hasler, A. F.; Palaniappan, K.; et al.: A high performance Interactive Image SpreadSheet, in: Computers in Physics, Vol. 8, No. 4, June 1994, pp. 325-342.
- [6] Meisner, R.; Dech, S.: An advanced technique for Meteosat Cloud Animation, in: Computer Animation '95, IEEE Comp. Soc. Press, USA, 1995, pp. 190-197.
- [7] Tuckey, J.W.: We need both exploratory and confirmatory, In: The American Statistician, Vol. 34, No.1, 1980, pp. 23-25.
- [8] Wilmott, C.J.: Evaluation of model performance, in: Spatial Statistics and Models, D. Reidel, Dordrecht, The Netherlands, 1984.
- [9] Wolff, R. Yaeger, L.: Visualization of Natural Phenomena, Springer, New York, USA, 1993.

Super computing of 10-years HRPT data set for analyses of AVHRR-derived SSTs

Hiroshi Kawamura*, Futoki Sakaida** and Jun-Ichi Kudo***

*Center for Atmospheric and Oceanic Studies, Faculty of Science, Tohoku University, Sendai, 980 Japan

Tel:+81-22-217-6745/Fax:+81-22-217-6748/kamu@caos-o.geophys.tohoku.ac.jp

**Ocean Mechanical Engineering Chair, Kobe University of Mercantile Marine, 1-1, 5,

Fukae-Minamimachi, Higashi-Nada-ku, Kobe 658, Japan

***Computer Center, Tohoku University Sendai, 980 Japan

Abstract--In order to analyze the AVHRR(Advanced Very High Resolution Radiometer) SST(Sea Surface Temperature) images with full spatial resolution for wide oceans for 10-years, a processing system is developed using a super computer, high-density cassette media, and a high-speed data transfer system in the computer center of the Tohoku University. The system enable us to retrieve 0.01-degree gridded MCSSTs of 4000x4000 pixels in 15-minutes.

INTRODUCTION

One of the difficulties in terms of the satellite remote sensing for global environment is daily-increasing huge data set provided by a number of earth observation satellites. The polar-orbiting imager sensor, AVHRR onboard the NOAA series satellite, observe the global earth surface, and transfer the observation data of about 600-1000-Mbyte to the local ground station everyday. Since the AVHRR sensor has been operated from 1979, many local receiving stations archive AVHRR data set for more than 10-years. The data set is promising tools to monitor the local environment for decades.

On the contrary, algorithms to retrieve physical parameters are advanced day by day. In order to retrieve the parameters for a long period using the most reliable algorithms, recalculation of the archived huge data set is desired

The aim of present study is to develop a system to process the huge AVHRR data set for 10-years, applying the reliable advanced algorithms. The developed system enables us to test the algorithm using daily AVHRRs in a long term, and produce the various types of AVHRR parameters for 10-years.

HRPT ARCHIVE AND SST RETRIEVAL

The NOAA-HRPT data were received since 1988, and archived in the Center for Atmospheric and Oceanic Studies, Tohoku University[1],[2]. The receiving station was closed in June, 1996, and the new station has been opened at the university computer center described in the next section. The HRPT data to be processed using the developed system are now transferred from the old archive in the optical disk to the computer center, which will be ended in March, 1998.

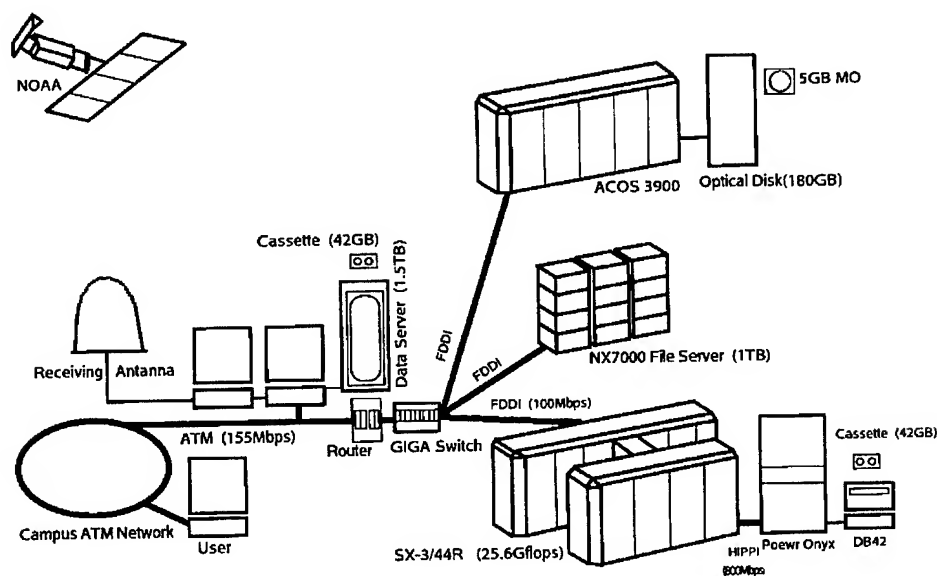
Sakaida and Kawamura[3] produced the higher spatial resolution sea surface temperature(HIGHERS) data for study of the ocean south of Japan. The grid size is 0.75 degree, and the processed area is from (19.925N, 126.75E) to (36.05N, 149.25E). The numbers of longitudinal and latitudinal grid points are 301 and 216, respectively. In order to produce the HIGHERS data set, MCSST coefficients were examined and developed[4][5], and new cloud detection scheme suitable for the processed area was developed[3]. Validation of HIGHERS using the in situ observation data from a mooring buoy shows that the rms error is 0.51C and the bias is 0.2C[3].

In the new processing system for the 10-years SST retrieval, the modified HIGHERS algorithm is used. All the software is transferred to the super computer, and modified to be applicable in the new hardware system.

HARDWARE SYSTEM

In the present study, we use computer resources for general users in the computer center of the Tohoku University. The center serves for staffs and students of the universities distributed in Japan. Fig.1 shows the outline of NOAA data

Figure 1 Outline of the NOAA-HRPT data processing. Daily HRPT data reception and the image data generation for image data base are made by a system connecting to the receiving antenna. SST retrieval from 10-years AVHRR archive is made by the system formed by SX3/44R super computer, Power Onyx and DB42 Data recorder.



processing system. The super computer, SX3/44R(25.6Gflops and 4Gbyte main memory) is used for the processing. The HRPT data is stored in DB42(42Gbyte/cassette), and the cassette reader is connected to SG/Power Onyx. The HIPPI, which has 800Mbyte/s transfer rate, connect SX3 and the Onyx. The HRPT archive is performed by the Data Server connected to the HRPT receiving system shown in the left in Fig.1. The cassettes are carried to be set in the DB42 cassette reader connected to the Power Onyx for super computing. In future, all the data transfer is to be made through the computer network shown in Fig.1.

A-HIGHERS

By using the archived and now being received AVHRR data from 1988 to 1997, we produce MCSST data set for the oceans around Japan. The processing area is a square of 20-40N and 120-160E. The spatial resolution is 0.01degree. Each AVHRR scene is processed and mapped on the processing area with the equal gridded pixels of SST value. Therefore, each image consists of 4001x4001pixels with the cloud and ancillary information. The volume of processed image is about 60-Mbyte. Then, they are compressed to reduce the data volume. The clouds are screened through seyerall tests, and MCSST algorithm tuned against the buoy

SSTs obtained in the oceans around Japan. Since the new products are a successor of the HIGHERS data set[3], we call them Advanced AVHRR-based higher spatial resolution Sea Surface Temperature(A-HIGHERS).

Several tests show that the processing time in SX3/44R is about 15-minutes, which will be reduced through software tuning and development of the computer system in future. One-year SST field with 0.01-degree spatial resolution for a 40-degree square could be processed in 10-20 days.

An example of the A-HIGHERS image is shown in Fig.2. The cloudy and land pixels are masked in black. Japanese islands are centered in the image, and the upper-left part is the Eurasian continent. SST values in the open oceans are indicated by the color bar at the bottom of Fig.2.

Fig.3 shows a part of the full A-HIGHERS scene shown in Fig.2. Since the data keep the highest spatial resolution of AVHRR data, the oceanic features appearing in the frontal regions are well visualized in the image. Efficiency of the cloud elimination is also demonstrated in Fig.3

COCLUSION

By using computer resources for general users at the university computer center, we have developed the system to process full scenes of the locally-received AVHRR within 15-minutes. The achieved capability in the A-HIGHERS

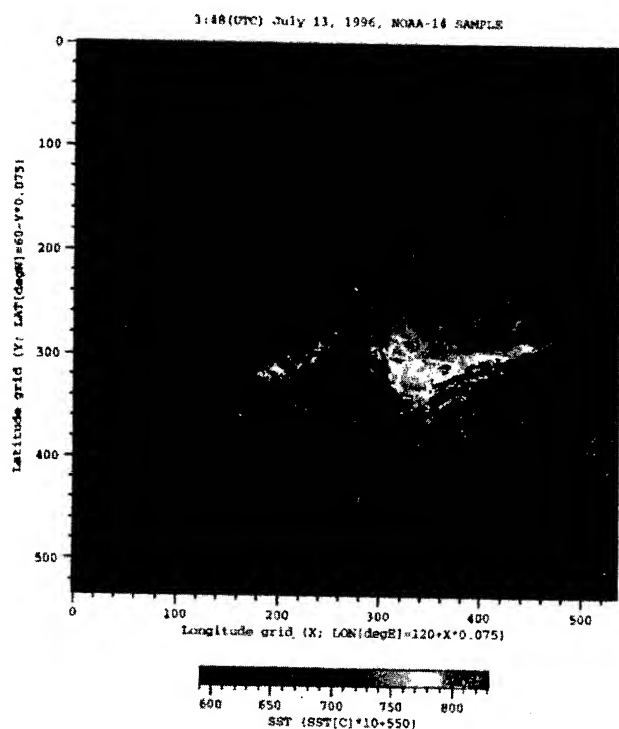


Figure 2. An example of the A-HIGHERS image.
The AVHRR scene was taken at 3:48UTC on 13 July, 1996.

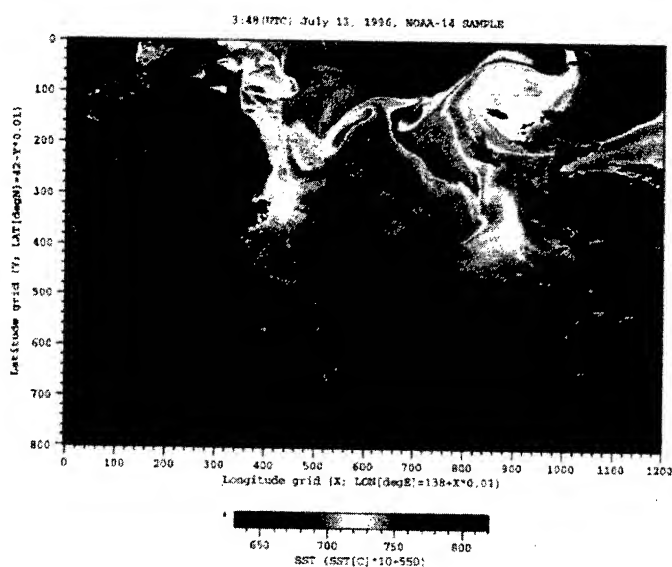


Figure 3 A part of A-HIGHERS full scene shown in Fig.3. SST pattern in the north-western Pacific ocean off the eastern Japan is presented. The red region is covered by the water from the Kuroshio, and the blue area is the Oyashio region. The imaged region is oceanographically called "Confluence Zone", because of the complicated nature associated with the two strong western boundary currents and eddies.

processing is favorable for analyses of detailed structure in the oceans around Japan for 10-years. The processing speed will be shortened in future by software tuning and development of the computer hardware.

ACKNOWLEDGMENTS

This study was supported by the international cooperative research program on GOOS (Global Ocean Observing System). The authors acknowledge supports from the computer center of the Tohoku University and NEC cooperation

REFERENCES

[1]H.Kawamura, S.Kizu, F.Sakaida and Y.Toba(1993): The NOAA-HRPT data receiving system in the Center for Atmospheric and Oceanic Studies in the Tohoku University. Tohoku Geophysical Journal (Science Reports

of the Tohoku University, Series 5), 34, 89-102.

[2]H.Kawamura, F.Sakaida and S.Kizu(1993): The AVHRR data processing system in the Center for Atmospheric and Oceanic Studies in the Tohoku University. Tohoku Geophysical Journal (Science Reports of the Tohoku University, Series 5), 34, 103-114.

[3]F.Sakaida and H.Kawamura(1996): HIGHERS—The AVHRR-based higher spatial resolution sea surface temperature data set intended for studying the ocean south of Japan, J.Oceanogr., 52, 441-455.

[3]F.Sakaida and H.Kawamura(1992): Accuracies of NOAA/NESDIS sea surface temperatures estimation technique in the oceans around Japan, J.Oceanogr., 48, 345-351.

[4]F.Sakaida and H.Kawamura(1992): Estimation of sea surface temperatures around Japan using the Advanced Very High Resolution Radiometer (AVHRR)/NOAA-11. J. Oceanography, 48, 179-192.

ONLINE ACCESS TO WEATHER SATELLITE IMAGERY THROUGH THE WORLD WIDE WEB

W. Emery
CCAR Box 431
Univ. of Colorado
Boulder, Co., 80309

Abstract

Both Global Area Coverage (GAC, 4 km) and High Resolution Picture Transmission (HRPT, 1 km) data from the Advanced Very High Resolution (AVHRR) are made available to Internet users through an online data access system. Created as a "testbed" data system for the National Aeronautics and Space Administration's (NASA's) future Earth Observing System Data and Information System (EOSDIS), this testbed provides an opportunity to test both the technical requirements of an online data system and the different ways in which the user community would employ such a system. Initiated in Dec., 1991 the basic data system experienced 5 major evolutionary changes in response to user requests. Features added with these changes were online browse, user subsetting, dynamic image processing/navigation, a stand-alone data storage system and movement from an X-windows GUI interface to a WWW interface. Over its lifetime the system has had as many as 2,500 registered users. Recent additions include a realtime 7-day, northwestern U.S. normalized difference vegetation index (NDVI) composite, a GAC SST composite, a daily image of Colorado and an NDVI image for North America.

Introduction

The primary goal of this EOSDIS testbed system was to explore how users would respond to having access to online satellite data as a guide to the future development of EOSDIS. Originally only AVHRR-HRPT data were available on the testbed data system but later the Global Area Coverage (GAC) AVHRR data were added. Most recently we have added realtime products to test the interest in ready-made products. In this paper we will briefly discuss the history of this testbed data system discussing the evolutionary changes in the system carried out to satisfy user needs. User statistics show how people use such a system and what features serve best the general user community. We will discuss the major system changes such as the recent shift to a world-wide web (WWW) interface.

The Initial System

We first thought to create a system that would make available a fixed size AVHRR image centered on Boulder, Colorado. An 8 state region surrounding Colorado was extracted from the daily AVHRR overpass, processed to retain the 1 km resolution of the direct readout AVHRR data and placed on the data system storage. The Testbed used a simple alpha-numeric interface that listed the image files on the data system. These original 8-state images were relatively small (640 X 655 pixels) resulting in network file transfer volumes that were quite modest. We soon realized that many potential users did not have access to some of the basic tools needed to work with these digital AVHRR images. We then made available over the data system our processing software to manipulate and view the AVHRR images.

The most frequent request that we received from users was to provide data from areas that were within our antenna reception circle but were not included on the 8-state images. In response we increased the size of the images to about 4 megabytes which not only stressed the storage of the Testbed system but also placed high demands on the network transfer of these larger images. It was clear that if we could somehow develop an online browse capability we could save considerably on the need for data to be shipped over the network. We decided that using a client-server system we could mount smaller subsampled browse images which were then displayed on the user's workstation/computer. This worked well with UNIX machines and on MAC's and PC's running some type of x-windows emulator. Each browse image included land boundaries, rivers, lakes and state boundaries to ease identification. After the introduction of this online browse feature there was a noticeable drop in the number of images ordered by the users.

Image Subsetting

After going to the larger images and instituting online browse users began to ask for the ability to subset these large images that they were getting over the network. What users really wanted was only a small part of each image and not the whole thing. Thus, we were stressing our processing system and the network to provide the

users with a lot of image data that they did not want. We realized that the ideal system would allow the users to define online that portion of the image that they were interested in, extract, process and deliver only that part of the image. This led to a big change in the Testbed which introduced on-the-fly navigation of the portion of the AVHRR image requested by the user. This is a form of "user-specified" automatic subsetting. Before browsing the user must first go through a search procedure to define the image(s) of interest. The new Web interface provides the user with a series of maps to define the center of the region of interest. A search is then initiated with this position and a list of files is then returned. By hitting the display button the user is presented with a browse image of the full AVHRR overpass or GAC orbit. The user must then choose a box size (by specifying the range) around this center location. The user can then choose any or all of the 5 AVHRR channels followed by the specification of the image resolution and image size (256, 512, or 1024 squared) and the projection type.

The Growth and Evolution of the Testbed System

The Testbed opened in mid-Nov., 1991 with no users as shown here in Fig. 1. Initially the user community grew up to about 400 monthly logins when the first browse was introduced. The maximum peak in September, 1992 was just after the introduction of the online subsetting system.

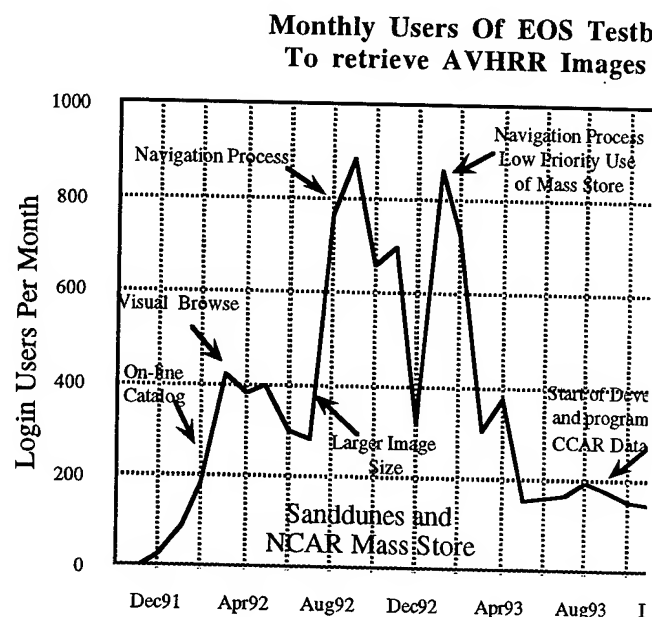


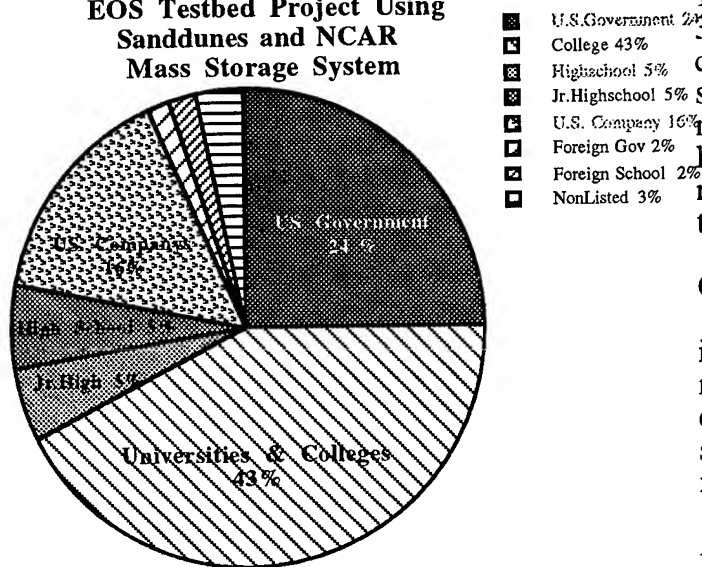
Fig. 1 Daily logins to the EOSDIS Testbed system.

The large drop in users in April 1993 was due to the fact that with a low priority on the NCAR mass store data was not being retrieved for the system or for the users. This led to the development of a stand alone system.

The User Community

The users of the original system, called Sanddunes and located at NCAR, can be separated into a number of general groups (Fig. 2).

Type of Users For Original EOS Testbed Project Using Sanddunes and NCAR Mass Storage System



Number of Type of Users

Fig. 2 Users of the first phase of the EOSDIS Testbed (Dec. 91 to Aug. 93)

The largest segment of the user community (43%) consisted of U.S. universities and colleges. In later years this dropped below 30% as the number of home users increased from 0.0 to 25%. Surprisingly government agency users made up the second largest group (24%) which later fell to 12%. Private U.S. companies comprised the next largest group (16%) and it was interesting to discover the variety of uses that people made of these online data.

The Stand Alone System

The stand alone system required an independent mass storage system. We could not afford any of the expensive systems and instead purchased a 120 tape Exabyte jukebox with a generous discount from Exabyte Corp. We could also not afford any of the commercially available file management software systems and therefore decided to write our own. An added problem was the lack of driver software for the 120 jukebox particularly for the DEC Alpha workstations we had acquired to run the Testbed. Fortunately our new system performed even better than expected. One real advantage of the new system was its speed in being able to process and deliver the requested images. This is demonstrated the time

per image taken to complete the processing of the AVHRR images for the different phases of the Testbed system. The initial system took up to 20-35 min to retrieve and process images. By comparison the average of 5 min for the new system is very fast. This time includes the file retrieval from one of the 120 Exabyte tapes, loading the file to disk, processing the image as requested by the user and storing the results on the FTP site.

Conclusions

A stand-alone data system using a WWW interface is able to deliver both data products and raw data using only the network for communications. The implementation of such a system requires a lot of original programming to make the units work together.

Acknowledgments

This project was initially funded by the Advanced Information Science Research Program (AISRP) of the National Aeronautics and Space Administration (NASA). Subsequent funding was provided by the ESDIS project at the Goddard Space Flight Center as part of its EOSDIS prototyping efforts.

Operational Generation of AVHRR-Based Level-3 Products at the German Remote Sensing Data Centre: Status and Perspectives

Stefan W. Dech, Robert E. Meisner, and P. Tungalagsaikhan

with contributions from Gerhard Gesell, Thomas Popp, and Werner Thomas

Deutsche Forschungsanstalt für Luft- und Raumfahrt (DLR), Deutsches Fernerkundungsdatenzentrum (DFD)

Oberpfaffenhofen, D-82234 Wessling, Germany

Tel. +49 8153 28 2885 / Fax. +49 8153 28 1445 / Email: Stefan.Dech@dlr.de

Abstract -- The German Remote Sensing Data Centre (DFD) of the German Aerospace Research Establishment (DLR) has been operating a ground segment for High Resolution Picture Transmission (HRPT) data acquisition, archiving, and distribution since the early 1980's. The station's visibility covers all of Europe. DFD started with the generation of thematic level-3 AVHRR value-added products consisting of Multichannel Sea Surface Temperatures (MCSST) and Normalized Difference Vegetation Indices (NDVI) in March 1993 [4]. Additionally, calibrated and registered 5-channel image subsets in two areas have been generated for supporting user-specific applications since 1994 [4]. The status of the current level-3 product generation chain as well as corresponding processing algorithms are presented. Perspectives to improve the existing products in terms of channel 1 and 2 radiometric optimization by implementing of a pre-operational atmospheric correction scheme developed by [10], as well as possibilities to correct the solar channels for anisotropic reflectance with respect to different surfaces are shown. Further, new level-3 products such as geophysical cloud parameters derived using the APOLLO [14] algorithm are presented. Also, first results from various algorithm tests are presented to define an operational land surface temperature (LST) product by estimating surface emissivity based on NDVI time profiles.

PRODUCT OVERVIEW

Currently, four different thematic level-3 data products are operationally generated. They are all based on up to six daily HRPT acquisitions.

Multichannel Sea Surface Temperatures (MCSST)

MCSST products are generated daily based on three consecutive night and afternoon NOAA-14 passes each. Daily composites are derived using maximum temperature as criteria for multiple cloudfree pixels. Weekly and monthly composites are calculated by synthesizing the daily composites using the average temperature. Examples of MCSST products are given in Fig. 1.

Normalized Difference Vegetation Index (NDVI)

NDVI products are generated from three consecutive NOAA-14 afternoon passes, which are processed to a daily maximum value composite (MVC). From these, weekly and monthly synthesis maximum value products are derived. An example for an NDVI MVC is given in Fig. 2.

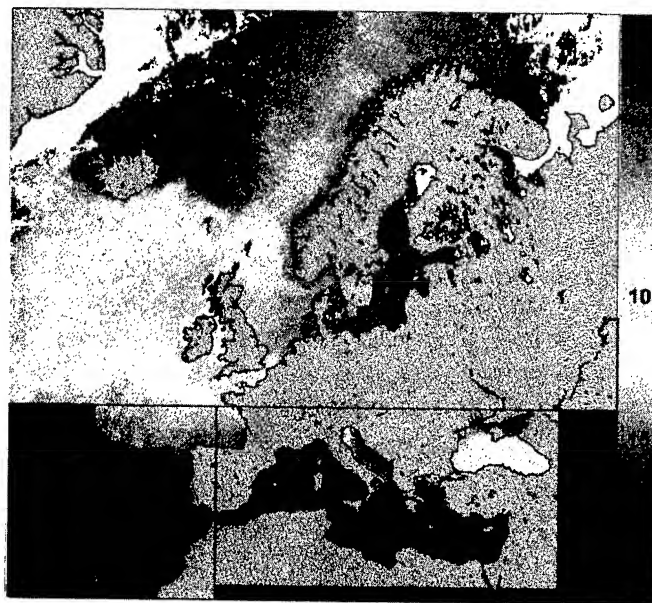


Fig. 1: MCSST Maximum value composite of March, 1997. The three different map projections are indicated by the rectangles

Thematic image subsets („Central Europe“, CE, and „Northern Baltic“, NB)

One five-channel NOAA-14 image subset in standard Mercator projection is created daily for two areas. The first covers central Europe and allows user-specific applications. The second covers the northern Baltic Sea and is dedicated to sea-ice detection and analysis. It is only provided during the ice season between December and May. The data sets are navigated, calibrated, registered and scaled to a user-friendly 8-bit data format.

MCSST AND NDVI DATA PROCESSING

Calibration

Channels 1 and 2 are calibrated into technical albedo values as described by NOAA [7]. For retrospective NOAA-11 AVHRR processing, time-adjusted calibration coefficients provided by [16] are applied. For the NOAA-14 AVHRR, monthly updated post-launch coefficients given by [13] are applied. The thermal channels 3, 4, and 5 are calibrated into radiances and then into brightness temperatures by inverting the Planck function. The non-linearity between counts and radiances is taken into account. Reference data from the internal black body and space are taken every 100 lines.

Navigation

To achieve maximum quality, a mixture of unsupervised and interactive steps is applied. For automatic pre-navigation, WDB-II coastline and river data are used as reference in conjunction with daily updated „two-line“ elements. Appropriate coastline areas with significant features are selected in 1deg×1deg boxes and checked for cloudiness by applying several spectral tests [15]. For the remaining cloudfree boxes, a cross correlation algorithm between the satellite image chips and the reference coastline is used. Based on the yielding vector array the satellite's yaw, pitch, and roll angles are adjusted. The result of this procedure is interactively controlled for every pass and corrected manually where necessary.

Cloud Detection

Apart from accurate navigation, precise cloud detection is of major interest for the overall quality of the later time synthesis. For cloud detection over land, an operational procedure has been developed by [4]. The scheme applied over oceans was developed by [2]. All tests consist of spatial, spectral, and satellite/sensor geometry parameters. In order to achieve maximum quality and operability, the applied method is a mixture of first-guess processing and interactive adjustments of the resulted cloud masks: The latest interactively defined thresholds for a certain pass type (e.g. central pass, noon) are taken for the next first-guess processing of a corresponding pass geometry and time. The resulting cloudmask is controlled interactively and thresholds are adjusted accordingly.

Generation of MCSST and NDVI

To derive MCSST values, a „split window“ algorithm [9] based on the brightness temperatures in AVHRR channels 4 (T4) and 5 (T5) is applied:

$$MCSST = A \times T4 + B \times (T4 - T5) + C \times (T4 - T5 \times \sec(\text{sza}) - 1) + D \times \sec(\text{sza}) - 1 + E$$

The sensor and day/night specific coefficients A, B, C, D, and E have been empirically derived from buoy comparisons and are provided by NOAA/NESDIS. NDVI values are calculated using the equation below, where *Red* stands for albedo values in channel 1 and *Nir* for those in channel 2:

$$NDVI = (Nir - Red) / (Nir + Red)$$

Registration into map projections

MCSST and NDVI values are remapped using „nearest neighbor“ resampling into standard Mercator or stereographic projections respectively, with a geometrical resolution of 1.1 km at the center of each map. Currently, three different MCSST maps (Mediterranean, North Atlantic, and East Atlantic) and one NDVI map (entire Europe) are generated. Further details are given by [4].

Composites (time synthesis):

Weekly and monthly MCSST maps are derived based on daily maximum value composites (MVC) which consist of

up to six passes depending on the region using the average temperature at every pixel's position. Daily, weekly and monthly NDVI composites are created using the MVC technique as default. Special products with different synthesis parameters, such as 10-day composites, can also be generated on user request.

Product availability and access

All MCSST, NDVI, CE, and NB products are generated daily and are available with a delay of one day except after weekends and holidays through DFD's Intelligent Satellite Information System (ISIS). ISIS software can be installed on PC or workstation and can be downloaded free of charge from the Internet (<http://isis.dlr.de>).

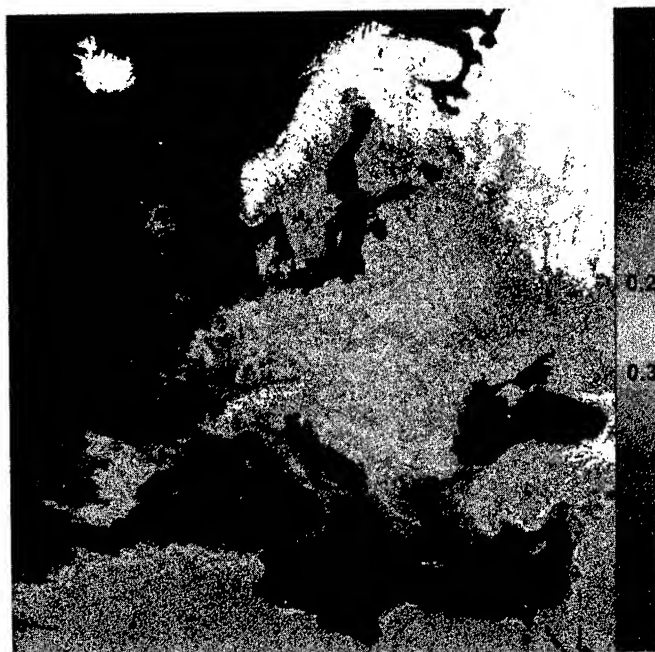


Fig. 2: NDVI maximum value composite of March, 1997

IMPROVEMENTS AND NEW PRODUCTS

One of the potential limitations of the above MCSST and NDVI products is the absence of corresponding thematic information such as satellite and sun zenith angles, time reference and a separate cloud mask for every pixel in a given synthesis product. Beside the scientific necessity to provide this additional information assimilable with the global 1 km data sets [5], costs for data storage and corresponding thematic information are currently being evaluated and solutions are being proposed.

Pure MCSST night synthesis

Based on the needs in some oceanographic research fields, it is planned to provide a pure night synthesis of three consecutive NOAA-14 acquisitions. However, all single MCSST scenes are additionally available in an off-line archive and can be composed to meet specific requirements, such as night synthesis or 10-day composites.

Development of a Land Surface Temperature (LST) product

As a fundamental, thermodynamic quantity in the energy exchange between the surface and the atmosphere, land surface temperature (LST) is one of the most important parameters required for many applications in climate-, land use- and environmental studies. Using AVHRR thermal data, such information can be derived. Generally, there are two main problems in deriving accurate LST using measurements from space: (a) correcting for the multiple atmospheric effects along the path between surface and sensor, and (b) for the surface emissivity effect related to the land surface character (e.g. bare, vegetated, or mixed).

Work on the definition of a pre-operational LST pathfinder product has begun. Currently, we have implemented and compared different existing LST algorithms based on split-window techniques [17], [11], [12], and [18]. All of the above make use of the differential absorption effect in the two AVHRR infrared bands 4 and 5 to account atmospheric water vapor absorption and other gases. For estimating the surface emissivity (ϵ) the relationship given by

$$\epsilon = 1.0094 + 0.047 \ln(NDVI)$$

was used [19]. Assuming that emissivity does not vary strongly within one week, weekly NDVI MVCs served as input data. Because no corrections on NDVI have been performed in order to avoid negative influences caused by day-to-day variations in atmospheric and angular viewing conditions, a spectrum analysis method (Harmonic Analysis) for reducing such effects was applied. An example of this method is given in Fig. 3. From resulting weekly NDVI composites in connection with a land cover classification for a test area in Germany, a land surface emissivity database, which consists of weekly emissivity values, was built. It is intended to come up with a first LST „pathfinder“ product on a daily basis over central Europe before the end of 1997.

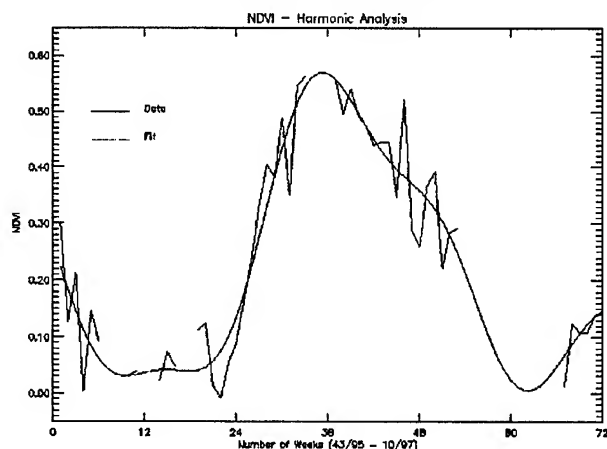


Fig. 3: NDVI time profile before (black) and after (red) application of Harmonic Analysis.
Pixel coordinates: 49°39.8287 N / 08°50.2385 E.

Atmospheric correction of the solar channels

Currently, no atmospheric correction for channels 1 and 2 is applied. To obtain accurate surface albedo and NDVI values from cloudfree pixels, the „Exact Atmospheric Correction“ method (EXACT) developed by [10] will be implemented for channels 1 and 2. This technique uses a dark field method over automatically selected dark dense vegetation pixels to extract the horizontal distribution of the aerosol content within one scene. Having obtained this most critical parameter in the solar spectral range, top of the atmosphere radiances (TOA) can be converted into surface albedo values with an inversion scheme. Radiative transfer calculations with a numerically exact treatment of multiple scattering and anisotropic reflection models underlying both the aerosol extraction and the albedo inversion. EXACT has been validated by comparing Landsat Thematic Mapper (TM) data to ground based albedometer measurements and spatially integrated TM data to AVHRR results. The accuracy was found to be better than 0.01, if the difference of bandwidths between AVHRR and TM channels is taken into account [10]. The EXACT prototype has been completed, however, operational application needs to be implemented. Once this atmospheric correction becomes available multitemporal analysis of AVHRR level-3 surface data will be enhanced.

Correction for anisotropic reflection in the solar channels

Recent studies, e.g. by [3] and [8], have shown that neglecting the anisotropic reflection properties of natural land surfaces may lead to significant errors in satellite-derived albedo and NDVI. Therefore, a remarkable improvement of the NDVI level-3 products could be achieved by the implementation of an algorithm to correct AVHRR data for anisotropic reflection effects on an operational basis. Such an algorithm could be based on a model which is able to simulate the BRDF of the underlying ground as a function of the viewing geometry. This model should account for topographic effects in the calculation of an anisotropically corrected NDVI. The impact of complex terrain is such that even for moderately high sun zenith angles between 30 and 60 degrees, shadowing and shading effects may reduce the NDVI by about 20% [17]. Studies on operational BRDF correction are in preparation.

Cloud products using the APOLLO algorithm

In addition to MCSST and NDVI values, physical cloud parameters will be generated by means of the „AVHRR Processing scheme Over cLOUDs, Land and Ocean“ (APOLLO), first developed by [14]. These cloud parameters consist of total cloud coverage which can be split into low-, mid- and high-level as well as thin ice-clouds. Further, based on parameterized relations, clouds optical depth, liquid/ice-water-path and IR-emissivity are derived from channel 1 reflectance [6]. Cloud top temperature, corrected for the atmosphere above the cloud, is also provided. The products will be generated daily for large parts of Europe beginning in

mid 1997. That is a complete AVHRR overpass received at DLR which is processed up to the result of the cloud detection in sensor projection (level 2). Level-3 products will be defined in adequate map projections. These products will mainly contribute to the generation of a European cloud climatology in the frame of an investigation of DLR's Institute for Physics of the Atmosphere (NE-PA): It is planned to process 15 years of data within three years from now. Low time resolution as compared to ISCCP will be highly compensated by the 1.1 km spatial resolution. This will allow to investigate regional climatic trends. This approach is also a further step towards a quantitative physical exploitation of AVHRR data on an operational basis over Europe.

CONCLUSION

The necessity and acceptance of operational thematic AVHRR-derived level-3 products for near real-time and retrospective applications is demonstrated by more than 10.000 external data transfers from DFD's archive between March 1995 and December 1996. As indicated in this paper, both improvements (additional information, MCSST night synthesis, atmospheric and BRDF corrections) as well as the definition of new operational level-3 data products (LST and cloud products) are foreseen for the near future. However, the realization not only depends on the scientific necessity, but also highly on the capacities available to realize the presented goals, as all products are accessible free of charge through DFD's electronic interface ISIS.

ACKNOWLEDGMENTS

The authors express their appreciation to M. Bittner, N. Hermann, A. Holz, C. Preußner, and T. Ruppert for their valuable contributions to this paper.

REFERENCES

- [1] Becker, F. and Z.L. Li, „Towards a local split window method over land surface“, *Int. J. Rem. Sens.*, Vol. 3, pp. 369-393, 1990.
- [2] Bernstein, R.L., „Sea Surface Temperature Estimation Using the NOAA-6 Satellite Advanced Very High Resolution Radiometer“, *J. Geophys. Res.*, Vol. 87, No. C12, pp. 9455-9465, 1982.
- [3] Cihlar, J., Manak, D. and N. Voisin, „AVHRR Bidirectional Reflectance Effects and Compositing“, *Rem. Sens. Environ.*, Vol. 48, pp. 77-88, 1994.
- [4] Dech, S.W., „Operational AVHRR-Based Derivation of MCSST and NDVI Products at the German Remote Sensing Data Centre“, *Proc. of the 7th Met. Satellite Data User's Conf.*, Winchester, UK, Eumetsat-Publications, Darmstadt, Germany, pp 595-599, 1995.
- [5] Eidenshink, J.C., and J.L. Faundeen, „The 1 km AVHRR global land data set: first stages in implementation“, *Int. J. Rem. Sens.*, Vol. 15, pp. 3443-3462, 1994.
- [6] Kriebel, K.T., Saunders, R.W. and G. Gesell, „Optical Properties of Clouds Derived from Fully Cloudy AVHRR Pixels“, *Beitr. Phys. Atmos.*, No. 62, pp. 165-171, 1989.
- [7] Lauritsen, L.N., Porto, G.J., and W. Frank, „Data Extraction and Calibration of TIROS-N/NOAA Radiometers“, *NOAA Technical Memorandum NESS-107*, 1979.
- [8] Lee T.Y. and Y.J. Kaufman, „Non-Lambertian Effects on Remote Sensing of Surface Reflectance and Vegetation Index“, *IEEE Trans. Geosci. Rem. Sens.*, Vol. GE-24, pp. 699-708, 1986.
- [9] McClain, P.E., Pichel, W.G., and C.C. Walton, „Comparative Performance of AVHRR-Based Multichannel Sea Surface Temperatures“, *J. Geophys. Res.*, Vol. 90, C6, pp. 11587 - 11601, 1985.
- [10] Popp, T., „Correcting, atmospheric masking to retrieve the spectral albedo of land surfaces from satellite measurements“, *Int. J. Rem. Sens.*, Vol. 16, No. 18., pp. 3483-3508, 1995.
- [11] Prata, A.J. and C.M.R. Platt, „Land surface temperature measurements from the AVHRR“, *Proc. 5th AVHRR data users' meeting*, Tromso, Norway, pp. 433-438, 1991.
- [12] Price, J.C., „Estimation surface temperature from satellite thermal infrared data a simple formulation for the atmospheric effect“, *Rem. Sens. Environ.*, Vol. 13, pp. 353-361, 1984.
- [13] Rao, C.R.N., and J. Chen, „Post-launch calibration of the visible and near-infrared channels of the Advanced Very High Resolution Radiometer on the NOAA-14 spacecraft“, *Int. J. Rem. Sens.*, Vol. 17, pp. 2743-2747, 1997.
- [14] Saunders, R.W. and K.T. Kriebel, „An Improved Method for Detecting Clear-Sky and Cloudy Radiances from AVHRR-Data“, *Int. J. Rem. Sens.*, 9, pp. 123-150, 1988.
- [15] SeaSpace Corp. (Ed.), *TeraScan User's Manual*, Version 2.4., San Diego, California, USA.
- [16] Teillet, P.M., and B.N. Holben, „Towards operational radiometric calibration of NOAA AVHRR imagery in the visible and near-infrared channels“, *Can. J. Rem. Sens.*, Vol. 20, No. 1, pp. 1-10, 1994.
- [17] Thomas W., „A Three-Dimensional Model for Calculating Reflection Functions of Inhomogeneous and Orographically Structured Natural Landscape“, *Rem. Sens. Environ.*, Vol. 59, pp. 44-63, 1997.
- [18] Ulivieri, C., Castronovo, M.M., Francioni, R. and A. Cardillo, „A split window algorithm for estimating land surface temperature from satellites“, *Cospar*, Washington DC, USA, 27 Aug.- 5 Sept., 1992.
- [19] Van de Griend, A.A. and M. Owe, „On the relationship between thermal emissivity and the normalized difference vegetation index for natural surfaces“, *Int. J. Rem. Sens.*, Vol. 14, pp. 1119-1137, 1993.

Incorporating Remotely-sensed Land Surface Parameters in a Land Surface Parameterization

K.W. Oleson, P.S. Thames, W.J. Emery
University of Colorado, Campus Box 431, Boulder, CO. 80309
303-492-1241, Fax: 303-492-2825, oleson@frodo.colorado.edu

Abstract -- Sensitivity studies are conducted with a land surface parameterization (LSP) to investigate the impact of remotely-sensed land surface parameters (leaf area index (LAI), roughness length, albedo) on modeled surface fluxes. The incorporation of albedo and LAI in the LSP are found to significantly modify the simulated surface fluxes.

INTRODUCTION

The land surface interacts with the atmospheric circulation through surface fluxes of radiation, heat, moisture, and momentum. There are land surface properties that govern the magnitude and direction of these fluxes, properties of primary importance include albedo, roughness length, and surface resistance (moisture availability) [1]. Traditionally, typical values of these parameters have been established by scientists in the field, grouped according to a general ecosystem classification system, and then extrapolated temporally and spatially using survey-based landcover type maps for use in land surface parameterizations (LSPs) (e.g., as in the Biosphere-Atmosphere Transfer Scheme (BATS); [2]). One of the disadvantages of this approach is that the spatial/temporal variability of these parameters is neglected. A case in point is the specification of leaf area index (LAI). LAI in BATS is prescribed as a function of the prognostic deep (1 meter) soil temperature, varying between minimum and maximum LAI values prescribed for a given landcover type. This ignores other factors which may influence the spatial/temporal variability of LAI (e.g., soil moisture, community development, disturbance, nutrient availability, etc.).

The goal of the work described here is to investigate the impact of a more realistic description of the spatial/temporal variability of the land surface in BATS using land surface parameters from the International Satellite Land Surface Climatology Project Initiative I (ISLSCP I) [4].

A six-month (April-September) regional climate model simulation of the 1988 drought in the US using the NCAR RegCM2 coupled to BATS at 60 km resolution has recently been completed [3]. Atmospheric conditions necessary to force BATS in a stand-alone (SA) mode were extracted from RegCM2 output over a sub-domain roughly encompassing the Upper Mississippi River Basin (UMRB) (30°N-44°N latitude, 87°W-102°W longitude). Initial and boundary conditions were prescribed identically from the RegCM2 run (e.g., soil texture and color, land cover type). A six-month SA BATS control simulation was run (denoted as CON).

ISLSCP INITIATIVE I LAND SURFACE PARAMETERS

ISLSCP Initiative I was undertaken to provide climate modelers with global datasets useful for initialization, forcing, and validation of LSPs [4]. Of particular value to this study

are the surface boundary conditions datasets, including the fields of albedo, roughness length, and LAI. Methods used to derive these land surface parameters from a normalized difference vegetation index (NDVI) dataset can be found in [5]. The data are on a 1° by 1° equal-angle grid.

Monthly fields of albedo, roughness length, total LAI, and greenness fraction were extracted for March-October, 1988. These were linearly interpolated between the fifteenth day of each month to yield daily values as in [5]. Albedo was further interpolated to half-hourly to approximate its diurnal variation with solar zenith angle and modified for snow cover using the BATS parameterizations [2]. The resultant fields were then assigned to the 60km gridcells using a nearest neighbor approximation.

COMPARISON OF BATS TO ISLSCP I PARAMETERS

It is important to note that the ISLSCP I land surface parameters have been derived under the assumption that each 1° by 1° gridcell is 100% covered by green vegetation. Thus, the derived LAI is an area-averaged value. The ISLSCP I roughness length and albedo for each gridcell are modeled using LAI as an input and hence reflect the same assumptions used in deriving LAI.

On the other hand, BATS assumes that the gridcell is divided into bare soil and vegetated fractions. Surface fluxes are calculated for each fraction and then added proportionally. Seasonal variations of LAI and fractional vegetation cover are approximated as varying between cover type dependent maximum and minimum values based on the deep soil temperature. The albedo is calculated based on the albedos of soil and vegetation weighted by their fractional cover. The roughness length for the vegetated fraction is specified by cover type and is invariant in time.

Also of note is the fact that the ISLSCP I methods use an AVHRR-based landcover dataset to assign cover type specific parameters that are required to derive the land surface parameters [6]. The RegCM2 experiment and thus the CON simulation use the AVHRR-derived 1km EROS Data Center product [7]. ISLSCP I data was used as model input only for gridcells where the two datasets agreed on landcover type.

Table 1 offers a comparison between ISLSCP I and CON land surface parameters for June, 1988. CON LAI values are area-averaged and are calculated based on the fractional vegetation cover predicted by BATS. CON roughness length values are those prescribed by BATS for the vegetated fraction of the gridcell. Greater variability in LAI for all landcover types is evident in the ISLSCP I data as compared to the CON values. In particular, the variability in ISLSCP I cropland LAI, which makes up 75% of the landcover in this region, is quite large, indicating significant influences from climate effects, human activities, or natural variability. The ISLSCP I

roughness lengths exhibit variability only for mixed woodland. CON roughness lengths have no variability since they are simply prescribed by cover type. The mean roughness values from ISLSCP I are higher than the CON values for all cover types. ISLSCP I albedos generally have a larger range of values than the corresponding CON values. The ISLSCP I albedos for mixed woodland and evergreen needle leaf are quite a bit lower than the CON.

SA SIMULATIONS USING ISLSCP I PARAMETERS

We present results from a 6-month SA simulation in which the three ISLSCP I land surface parameters were incorporated into BATS (denoted as MOD). Vegetation cover fraction is set to 100% consistent with the ISLSCP I assumption. Results from additional sensitivity studies are described where necessary to help assess the role of each parameter in modifying the surface fluxes.

Monthly averages of CON minus MOD (CON-MOD) net radiation, and sensible and latent heat fluxes are shown in Table 2. The differences in cropland albedo drive the monthly variation in the average change in net radiation per gridcell (CHNG in Table 2) from slightly negative in April to strongly negative in June to slightly positive in September. The trend from April to June is caused by a faster rate of increase in CON albedo compared to ISLSCP I albedo. In July-September, the CON albedo remains fairly constant while ISLSCP I cropland albedo increases. The ISLSCP I albedos increase in July-September because there is an increasingly larger proportion of dead leaves which are assigned higher visible leaf reflectances than green leaves. By September, the average ISLSCP I cropland albedo is higher than the CON albedo resulting in a positive CON-MOD net radiation. The lower ISLSCP I albedos for mixed woodland, evergreen needle leaf, and grassland result in a consistently negative CON-MOD net radiation for those gridcells for all months. Therefore, the overall impact of the ISLSCP I parameters on net radiation is an increase for the region for all months except September.

The average change in latent heat flux per gridcell is quite large in April-May and less than 10 W/m^2 for the remaining months. The MAX and MIN values indicate there is a great deal of spatial variability in these changes. In April-May, the MOD simulation is predicting less latent heat, particularly in the northern part of the region. A breakdown of the

evaporation into components of ground evaporation, leaf intercepted evaporation, and transpiration indicates that differences in ground evaporation are driving this behavior. As noted previously, the vegetation fractional cover in the MOD simulation is set to 100% consistent with the ISLSCP I assumption, while the CON cover in April-May was 50-60%. The 100% vegetation cover is inhibiting ground evaporation which is the primary mode of evaporation in April-May.

By June, the CON simulation is estimating 70-80% cover and the CON-MOD ground evaporation differences are smaller. Transpiration differences are now of equal importance in the overall evaporation. The net transpiration for the region in June is higher in the MOD simulation and balances the lower MOD ground evaporation so that the average change in latent heat per gridcell is less than 1 W/m^2 . There are two factors which contribute to this behavior. First, the mean LAI for the ISLSCP I mixed woodland, the second most dominant cover type in this region, is higher than the CON mean LAI in June (Table 2). From the results of supplementary sensitivity studies conducted with various values of LAI, we found that BATS will generally predict higher rates of transpiration for higher values of LAI if moisture is available in the rooting zone. Thus, the MOD mixed woodland transpiration is generally higher than the CON transpiration.

Second, we also found from the LAI sensitivity studies that lower values of LAI can actually result in increased transpiration if the rooting zone soil moisture is near the wilting point. Lower LAI means that more precipitation reaches the ground and can recharge the surface and rooting zone soil layers. The higher soil moisture can be used by the vegetation to increase transpiration. In June, the driest month of the simulation in terms of precipitation forcing, a number of the cropland gridcells are near the wilting point in the CON simulation. The mean ISLSCP I cropland LAI is significantly lower than the mean SA CON LAI, particularly in June (Table 1). The lower LAI for these gridcells in the MOD simulation thus allows for an increase in soil moisture and thus an increase in transpiration in the region. In June then, the decreased MOD ground evaporation is nearly balanced by an increase in transpiration.

In July-September, the CON-MOD ground evaporation remains about the same as in June. The CON-MOD transpiration becomes less negative with each month resulting in a positive CON-MOD latent heat flux overall. The CON soil moisture is recharged due to higher precipitation.

Table 1. June, 1988 ranges and means of green LAI in m^2/m^2 , roughness length in meters (Rough), and albedo in % (Alb.) from SA CON simulation and ISLSCP I for gridcells in the UMRB. Cover types are mixed woodland (MW), cropland (C), grassland (G), and evergreen needle leaf (EN). Values in parentheses for Alb. are the BATS albedo assuming 100% vegetation cover.

Data Source	Cover Type	LAI Range	Mean LAI	Rough Range	Mean Rough	Alb. Range	Mean Alb.
SA CON	MW	4.5-4.7	4.6	0.80	0.80	16.2-17.1	16.7 (15.0)
ISLSCP I	MW	3.2-7.2	5.0	1.08-1.16	1.14	8.8-9.8	9.6
SA CON	C	4.5-5.1	4.8	0.08	0.08	19.5-21.5	20.7 (20.0)
ISLSCP I	C	1.5-6.0	2.1	~0.13	0.13	15.1-22.0	17.2
SA CON	G	1.5-1.6	1.6	0.05	0.05	21.0-21.5	21.2 (20.0)
ISLSCP I	G	0.4-0.8	0.6	~0.12	0.12	15.2-17.2	17.0
SA CON	EN	~4.7	4.7	1.00	1.00	15.8-16.1	15.9 (14.0)
ISLSCP I	EN	4.5-5.8	5.1	~1.20	1.20	~7.7	7.7

Consequently, higher soil moisture in the MOD simulation does not have as much influence on the transpiration.

The CON-MOD sensible heat flux differences are generally of the opposite sign as the latent heat flux differences but are somewhat higher in magnitude. This is a direct consequence of the differences in net radiation discussed previously. Most of the increased net radiation in the MOD simulation is transferred to the atmosphere in the form of sensible heat.

To ascertain the influence of roughness lengths in modifying the surface fluxes, separate 6-month sensitivity experiments were run using the ISLSCP I roughness lengths in place of the CON roughness lengths. Monthly averages of sensible and latent heat fluxes were computed and compared to

the same averages for the CON simulation. The maximum monthly difference in the surface fluxes for any gridcell was less than 3 W/m². The average change per gridcell was less than 1 W/m². The most significant change in heat fluxes was associated with the grassland gridcells, which had the greatest prescribed change in roughness length of any cover type. This change caused a 3 W/m² increase in latent heat and a corresponding change of opposite sign in sensible heat for grassland gridcells in April only. Changes in other months were less than 1 W/m². Based on this we concluded that the differences between ISLSCP I and CON roughness lengths did not have appreciable effects on the simulated surface fluxes under the conditions of this study.

Table 2. Monthly averages of CON-MOD net radiation, sensible heat flux, and latent heat flux (in W/m²). MAX and MIN are the largest and smallest values of CON-MOD among all gridcells. CHNG is the average CON-MOD difference per gridcell.

Month	Net Radiation			Latent Heat			Sensible Heat		
	MAX	MIN	CHNG	MAX	MIN	CHNG	MAX	MIN	CHNG
April	2.1	-11.8	-1.9	54.1	-1.0	32.0	-9.1	-49.1	-33.5
May	0.1	-19.7	-5.4	47.0	-13.8	24.6	-1.4	-50.5	-29.8
June	0.8	-25.8	-12.5	46.6	-24.8	-0.9	10.6	-51.4	-12.1
July	3.9	-23.9	-9.9	42.2	-17.0	2.3	5.3	-41.9	-11.5
August	6.3	-15.6	-4.7	52.3	-22.0	6.5	10.2	-50.8	-10.0
September	19.8	-15.0	0.4	43.1	-29.2	9.0	14.8	-46.8	-8.2

FUTURE RESEARCH

There are several disadvantages to using the ISLSCP I land surface dataset for this regional modeling study. First, the spatial resolution is about twice as coarse as what is required. Second, the differences between the landcover datasets used in RegCM2 and in the ISLSCP I procedures means that only about 60% of the gridcells in this region can be modeled using the ISLSCP I parameters. Additionally, in the future we desire to contrast the land surface conditions in the UMRB in 1988 (a relatively dry year) with conditions in 1993 (a relatively wet year). ISLSCP I data is only available for 1987-88. Therefore, we are currently in the process of deriving a US land surface dataset for 1993 and 1988 at a 60km spatial resolution by applying ISLSCP I techniques to Pathfinder AVHRR Land (PAL) data. RegCM2 simulations are also planned to assess the impact of changes in the surface fluxes on the atmospheric circulation.

ACKNOWLEDGMENTS

The authors gratefully acknowledge the financial support of NASA's Earth Observing System (EOS) program as part of one of its InterDisciplinary Science (IDS) teams (Principle Investigator R. Dickinson). We also thank S. Los for answering questions pertaining to the ISLSCP I dataset.

REFERENCES

[1] P.J. Sellers, "Biophysical models of land surface processes," in *Climate System Modeling*. K.E. Trenberth, Ed., New York: Cambridge University Press, 1992, pp. 451-490.

[2] R.E. Dickinson, A. Henderson-Sellers, and P.J. Kennedy, "Biosphere-atmosphere transfer scheme (BATS) version 1e as coupled to the NCAR community climate model," NCAR Technical Note, TN-387+STR, 1993.

[3] A. Seth and F. Giorgi, 1997. "A regional climate model study of the role of soil moisture in the extreme events of 1988 and 1993 in the central United States." *Proceedings, Thirteenth AMS Conference on Hydrology*, February 2-7, 1997, Long Beach, Calif.

[4] P.J. Sellers et al., "The ISLSCP Initiative 1 global datasets: Surface boundary conditions and atmospheric forcings for land-atmosphere studies," *Bull. Amer. Meteor. Soc.*, vol. 77, pp. 1987-2005, September, 1996.

[5] P.J. Sellers et al., "A revised land surface parameterization (SiB2) for atmospheric GCMs. Part II: The generation of global fields of terrestrial biophysical parameters from satellite data," *J. of Clim.*, vol. 9, pp. 706-737, April, 1996.

[6] R.S. DeFries and J.R.G. Townshend, "NDVI-derived land cover classifications at a global scale," *Int. J. Remote Sens.*, vol. 15, pp. 3567-3586, 1994.

[7] T.R. Loveland, J.W. Merchant, D.O. Ohlen, and J.F. Brown, "Development of a land-cover characteristics database for the conterminous U.S.," *Photogramm. Eng. Remote Sens.*, vol. 57, pp. 1453-1463, November, 1991.

A STUDY OF THE EFFECT OF SWELL IN SCATTEROMETER WIND MEASUREMENTS USING ERS SAR WAVE MODE DATA

Dayalan Kasilingam, I-I Lin, Victor Khoo and Lim Hock

Centre for Remote Imaging, Sensing and Processing
National University of Singapore
Lower Kent Ridge Rd.
Singapore, 119260.

Tel: (65) 771-5173; FAX: (65) 775-7717; e-mail: crsdpk@leonis.nus.sg

Abstract: Coincident and nearly co-located SAR wave mode data and scatterometer data are used to study the effect of swells in the ERS scatterometer measurements. It is shown that the speckle power in the SAR wave mode spectrum is a good measure of the mean radar backscatter from the ocean surface. The wind dependence of the speckle power is compared with the scatterometer winds with and without the effects of swell. It is shown that the speckle power increases in the presence of swell. The swells travelling in the azimuth direction have a greater impact on the speckle power than range travelling swells. It is argued that the wind speed dependence of the SAR speckle power enables the SAR to be used as a high resolution wind mapper.

In addition to the scatterometer, the ERS satellite also has a synthetic aperture radar (SAR) which when operating in the wave mode, provides two-dimensional spectra of the images of the ocean surface. In many of these spectra, characteristics of long wavelength swells are clearly identifiable. The SAR wave mode data is a useful tool for identifying the presence of swells. The speckle power in the SAR spectrum may also be used as a measure of the mean backscatter from the ocean surface. This property along with its ability to identify swells makes the SAR wave-mode extremely useful for studying the effects of swell on radar backscatter from the ocean surface. This paper presents the results from a study of coincident and nearly co-located SAR wave mode data and scatterometer data from the ERS satellite.

INTRODUCTION

In scatterometry, radar backscatter measurements from the ocean surface are used to estimate the wind speed and wind direction. These measurements are possible because the radar backscatter from the ocean surface is a function of the sea surface roughness which in turn depends on the wind speed and direction. The scatterometer aboard the ERS satellite has three beams which measure the NRCS in three different azimuth directions. The NRCS measurements are then inverted using the CMOD4 model [1] to obtain the wind vector - wind speed and direction.

Studies of the scatterometer wind estimates have found that in many cases, the estimates of the wind vector are in error because of the effects of oceanic phenomena which are not related to the local winds [2]. It has been shown that long wavelength swells modulate the backscatter process through hydrodynamic interaction with the small scale roughness of the ocean surface [3]. The swell also modulates the backscatter process by tilting the scattering elements [3]. Swells are generally not related to the local wind conditions, but do affect the backscatter from the ocean surface. It has been suggested that these effects of swells could be a source of error in predicting the wind vector using scatterometer measurements.

METHODOLOGY

Fig. 1 shows a SAR wave mode spectrum obtained from the ERS-1 satellite. The image spectrum consists of a 12x12 array of data points representing the SAR spectrum in wavelength and wave direction, respectively. In this spectrum, a swell travelling at 45° to the range direction is clearly discernible. In addition to the swell power, the spectrum consists of speckle power due to the 'white-noise' like nature of speckle in the SAR image. The speckle power, if properly separated from the energy from modulating sources, can be used as a measure of the mean backscattered power from the area under observation.

In this project, an algorithm is developed for identifying swells and also for estimating the mean speckle power in SAR wave mode data. A swell is detected, if the spectral level exceeds a pre-determined threshold at wavelengths shorter than a specified cut-off wavelength. The latter cut-off wavelength enables one to separate modulation due to swell like features from low wavenumber energy due to mesoscale variations and other large scale phenomena. The swell direction is identified by the direction of the peak of the swell spectrum.

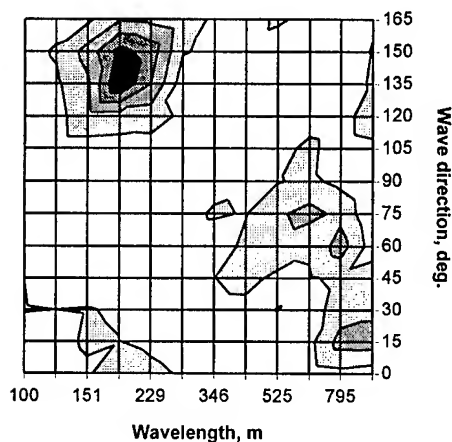


Figure 1 - SAR wave-mode spectrum from ERS-1 satellite. Range direction is given by 90°. Spectrum shows a 200m swell propagating at 45° to range.

The speckle power is calculated by integrating the power over all wavenumbers. The power due to long wave modulation is removed from this total power. However, the contribution to the total power due to long wave modulation is found to be small. It can be shown that the mean backscattered power will be dispersed across the image spectrum due to the random nature of speckle. Thus, by calculating the speckle power in the image spectrum, one is able to estimate the mean backscattered power.

RESULTS AND DISCUSSION

Coincident and nearly co-located SAR and scatterometer data are obtained from the ERS-1 satellite in the Indian ocean and the western Pacific ocean. The longitude and latitude information from a given pass are used to identify the corresponding data sets. Co-located data is found by estimating the distance between the SAR and scatterometer data for a given satellite pass. Only scatterometer and SAR wave-mode data sets which were closer than 2 km apart were used in this study.

Since the center beam of the scatterometer is aligned in the same direction as the SAR, the NRCS measurements from this beam may be compared with the SAR speckle power. The co-location criteria would automatically make the incidence angles approximately the same. Fig. 2 shows the averaged NRCS measured by the center beam of the scatterometer plotted against the averaged speckle power in the SAR wave mode spectra. The speckle power shows a linear dependence on the NRCS. This supports the hypothesis

that the speckle power is a good indicator of the mean backscattered power.

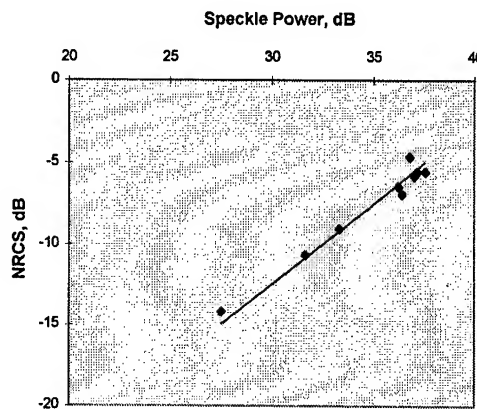


Figure 2 - The averaged NRCS measured by the center beam of the ERS-1 scatterometer plotted against the averaged total speckle power in the nearly co-located, wave-mode spectra from the SAR. The solid line indicates the best linear fit.

Fig. 3 shows the averaged speckle power plotted as a function of the wind speed. The wind speed information is obtained from the scatterometer. As a function of wind speed, the speckle power clearly shows a trend similar to those predicted by the CMOD4 model [1]. This further confirms the hypothesis that the SAR speckle power is a measure of the mean backscattered power.

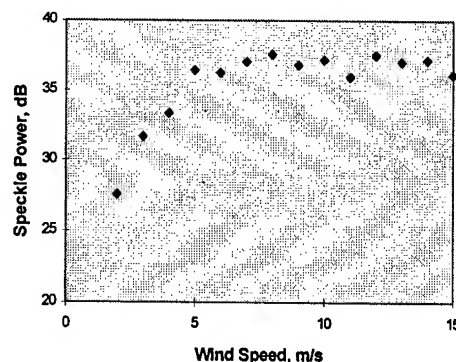


Figure 3 - Averaged speckle power in the wave-mode spectra of the ERS-1 SAR plotted against the wind speed from nearly co-located scatterometer measurements.

Fig. 4 shows the speckle power as a function of the wind speed for wave data with and without swells. The speckle power in the presence of swell is clearly higher than the speckle power without swells. This is consistently true at all wind speeds. The averaged NRCS measured by the center beam also showed a similar trend. This appears to suggest that swells tend to increase the backscattered power from the ocean surface.

Since in-situ measurements of the near-surface wind vector are not available, the scatterometer-derived wind are used in this study. This approach may appear to be circular in the sense that if the NRCS is affected by swells, then the scatterometer estimates will also be inaccurate. However, such an effect will only increase the wind speed estimates of the scatterometer. If this correction is applied to the wind speed estimates, then the separation between the two data sets in fig. 4 is likely to be greater.

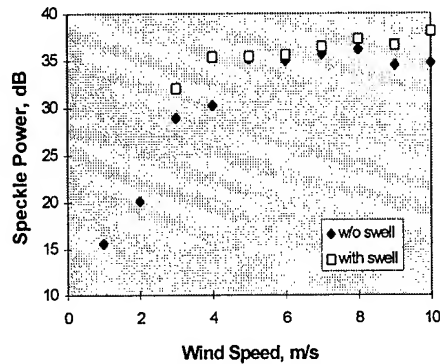


Figure 4 - Averaged speckle power in the wave-mode spectra of the ERS-1 SAR plotted against the wind speed from nearly co-located scatterometer measurements for cases with swell and without swell. The averaged speckle power in the presence of swell is consistently higher than the cases without swell.

Fig. 5 shows the speckle energy as a function of the wind speed for cases where swells have been identified. Two separate data sets are generated for swells which travel generally in the range direction and those that travel generally in the azimuth direction. Swells whose peaks are in the 45° to 135° directional range are classified as range travelling swells and the rest are classified as azimuth travelling swells.

Surprisingly, the azimuth travelling swell appear to have a greater impact on the speckle energy than range travelling swells. Most models show that the tilt modulation and hydrodynamic modulation are greatest for range travelling waves and are the least for azimuth travelling waves. However, a closer examination of the scatterometer measurement process shows that azimuth travelling waves affect the scatterometer measurements in such a way that the wind speed estimates may be underestimated. This is because the scatterometer uses three beams. If one observes a range travelling wave in the SAR wave-mode data, it means that the side beams are both equally affected by the swell. However, if one observes a azimuth travelling wave it mean that one side beam will be looking generally in the swell

direction and the other against the swell direction. Thus, the two beams are affected in different ways, resulting in a greater discrepancy in the wind speed estimates.

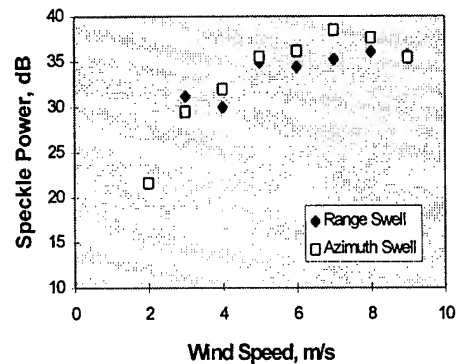


Figure 5 - Averaged speckle power in the wave-mode spectra of the ERS-1 SAR plotted against the wind speed from nearly co-located scatterometer measurements for cases with swell in the range and azimuth directions. The averaged speckle power for swells in the azimuth direction consistently higher than for swells in the range direction.

CONCLUSION

Based on the co-located ERS scatterometer and SAR wave-mode data, it is concluded that the presence of swell tends to increase the mean radar backscatter from the ocean surface. It is argued that this will lead to errors in the wind vector estimates of scatterometers. It is also shown that azimuth travelling swells have a greater impact on the backscatter power than the range travelling swells. It is concluded that there is a need to develop scatterometer models that account for non-wind dependent extraneous factors such as swell.

REFERENCES

- [1] Stoffelen, A. and D. Anderson, 'Characterisation of ERS-1 scatterometer measurements and wind retrieval', Proc. Second ERS-1 Symposium, Hamburg, October, 1993.
- [2] Rufenach, C., 'A new relationship between radar cross-section and ocean surface wind speed using ERS-1 scatterometer and buoy measurements', Intl. J. Remote Sensing, 3629-3647, 1995.
- [3] Kasilingam, D.P. and O.H. Shemdin, 'The validity of the composite surface model and its application to the modulation of radar backscatter', Intl. J. Remote Sensing, 2079-2104, 1992.

SAR IMAGING OF THE OCEAN SURFACE: NONLINEARITIES SIMULATION AND ESTIMATION

R. Garello & J.M. Le Caillec
Télécom Bretagne, Dpt ITI, BP 832
29285 Brest Cedex, France

Abstract— This paper summarizes the most important results obtained by the 2D simulations of the decomposition of the SAR ocean imaging process over the Volterra models. These models allow a quite simple nonlinearities analyze from the point of view of nonlinear energy quantification but also for the phase coupling detection (i.e. nonlinearity detection) by using Higher Order Spectrum (HOS) tools.

INTRODUCTION

Sea surface observation by a spaceborn SAR (Synthetic Aperture Radar) is known to contain some distorting phenomena which might prevent an immediate use of the SAR image for sea surface analyze. In a strict definition sense, the transfer system between the sea surface and the SAR image is nonlinear [3]. However, from a practical point of view, the interesting quantity remains the amount of nonlinear energy contained in the SAR spectrum and hence the ability to approximate the SAR process by a linear system. This first problem of nonlinear system decomposition and nonlinear energy quantification is studied in the first section. The second section deals with higher order statistics which are used to detect, localize and theoretically quantify nonlinearities in the observed signal (i.e. the SAR image). Results concerning nonlinearity decomposition and analysis are summed up and discussed in the third section. A discussion about the Volterra models inversion concludes this paper.

NONLINEARITIES DECOMPOSITION

The closest nonlinear relationship between the sea surface and the SAR image given by Hasselmann, although allowing a straightforward theoretical calculation of the SAR spectrum and bispectrum [3],[2], is rather unfit for an inverse transform. On the others hand, Volterra models are a polynomial decomposition of general nonlinear systems. For instance the Second Order Volterra Model (SOVM) is made up of a linear kernel and a quadratic one, the output signal Fourier coefficients $\tilde{Y}(k)$ can be written as regard of the input signal Fourier coefficients by:

$$\tilde{Y}(k) = H_1(k) \cdot \tilde{X}(k) + \sum_{k_1} H_q(k_1, k - k_1) \cdot \tilde{X}(k_1) \cdot \tilde{X}(k - k_1) \quad (1)$$

The second part of 1 is the quadratic kernel which implies the "creation" of energy by quadratic interactions

between two waves of the original spectrum. In fact two kind of quadratic interactions are generated, the constructive ones are centered about twice the sea spectrum dominant wavenumber and the destructive ones around the continuous component (for a complete discussion see [5]) Under the gaussianity assumption of the input data (in our case the surface), the output data spectrum of the SOVM is then the sum of a linear and a quadratic spectra.

$$S(k) = S_{lin}(k) + S_{qua}(k) = |H_1(k)|^2 \cdot E\{|\tilde{X}(k)|^2\} + \sum_{k_1} |H_q(k_1, k - k_1)|^2 \cdot E\{|\tilde{X}(k_1) \cdot \tilde{X}(k - k_1)|^2\} \quad (2)$$

A natural nonlinearity criterion is consequently the amount of nonlinear energy (i.e. the sum of $S_{qua}(k)$ over the spectrum support), and it is this criterion which has been chosen in order to classify (with regard to their "nonlinearity") the simulated SAR images and to decide if they were produced or not by a linear process. In order to detect these nonlinearities, higher spectrum tools are presented in the next section.

NONLINEARITIES ANALYSIS

Nonlinearities of a transfer function induce a linear relationship between the original waves and their quadratic interactions. A field of application of the higher order spectra (and more especially in our case of the bispectrum) is the detection of this relation by detecting the phase coherence (between several independent signal realizations). If we assume a decomposition of the Fourier component as $\tilde{X}(k) = \zeta(k) \cdot e^{j \cdot \varphi(k)}$ with $\varphi(k)$ a phase uniformly distributed over $[0, 2\pi]$. The bispectrum defined as the mathematical expectation of the Fourier coefficient triple product (3)

$$B(k_1, k_2) = E\{\tilde{X}(k_1) \cdot \tilde{X}(k_2) \cdot \tilde{X}^*(k_1 + k_2)\} = E\{\zeta(k_1) \cdot \zeta(k_2) \cdot \zeta^*(k_1 + k_2)\} \cdot E\{e^{j(\varphi(k_1) + \varphi(k_2) - \varphi(k_1 + k_2))}\} \quad (3)$$

is null if the three phases are independent meanwhile if the linear relationship $\varphi(k_1) + \varphi(k_2) = \varphi(k_1 + k_2)$ is assumed then the bispectrum is non null. Still under the gaussianity assumption the bispectrum of a SAR image can be theoretically calculated (see [2]), however a direct use of this expression is impossible due to its analytic complexity and its 4 dimensional support. For a SOVM two phase coupling phenomena can be distinguished, the Primary Phase Coupling Phenomena (PPCP) which occurs

between two original waves and their quadratic interactions

$$B(k_1, k_2) = H_1(k_1) \cdot H_1(k_2) \cdot H_q^*(k_1, k_2) \cdot E\{| \tilde{X}(k_1) |^2 | \tilde{X}(k_2) |^2\} \quad (4)$$

and the Second Phase Coupling Phenomena (SPCP) which imply mainly both constructive and destructive interactions (for an exhaustive review see [5]).

$$B(k_1, k_2) = \sum_{k_j} H_q(-k_2 + k_j, k_2 + k_1 - k_j) \cdot H_q(k_j, k_2 - k_j) \cdot H_q^*(k_j, k_2 + k_1 - k_j) \cdot E\{| \tilde{X}(k_j - k_2) |^2 \cdot | \tilde{X}(k_j - k_2 - k_1) |^2 \cdot | \tilde{X}(k_j) |^2\} \quad (5)$$

In order to quantify the nonlinearities, a useful quantity is the bicoherence defined as [1]:

$$P(k_1, k_2) = B(k_1, k_2) / \sqrt{S(k_1) \cdot S(k_2) \cdot S(k_1 + k_2)} \quad (6)$$

and which can be seen as a normalized bispectrum. Without any assumption the squared bicoherence is equal to

$$P^2(k_1, k_2) = \frac{(E\{\zeta(k_1) \cdot \zeta(k_2) \cdot \zeta_q(k_1 + k_2)\})^2}{E\{\zeta(k_1)^2\} \cdot E\{\zeta(k_2)^2\} \cdot E\{\zeta(k_1 + k_2)^2\}} \quad (7)$$

and consequently not interesting. However under a gaussianity assumption and by using the relationship $\zeta_q(k_1 + k_2) = |H_q(k_1, k_2)| \cdot \zeta(k_1) \zeta(k_2)$ verified the output SOVM Fourier coefficients, the squared bicoherence is the ratio of the nonlinear energy over the total energy. A nonlinearity index, i.e. a measure of the nonlinearity criterion defined in section 2, can be derived by summation of the squared bicoherence over the whole bispectrum support (bicoherence index). However, when no phase coupling is present, the variance of the bicoherence estimation induces strong bicoherence values which do not allow a robust nonlinearity detection. In order to take into account the bicoherence variance problem, an alternative index has been proposed in [4] by considering the modified bicoherence

$$PM(k_1, k_2) = E\left\{ \frac{\tilde{X}(k_1) \cdot \tilde{X}(k_2) \cdot \tilde{X}^*(k_1 + k_2)}{|\tilde{X}(k_1)| \cdot |\tilde{X}(k_2)| \cdot |\tilde{X}^*(k_1 + k_2)|} \right\} \quad (8)$$

and by defining the aberration index as the sum of the relative error between the theoretical distribution (under the gaussianity assumption) for a signal without phase coupling and the measured distribution of the modified bicoherence. In case of phase coupling the measured distribution presents some aberrations, especially in the tail of the distribution and consequently a strong relative error.

The nonlinearity analysis is divided into three main parts, i.e. a nonlinearity detection, localization and quantification. The nonlinearity detection can be achieved with the nonlinearity indexes. The localization is obtained with the bicoherence tables, which are the summation of the bicoherence along the axis. For given wavenumber k_1 , the bicoherence cross table is a measure of the ratio of the total energy in phase (i.e. for all wavenumbers, the sum of which being equal to k_1) over the total energy at this wavenumber. The multiplication of the cross bicoherence table by the spectrum gives theoretically the nonlinear energy amount (see [5]).

RESULTS AND DISCUSSION

Sea spectra have been simulated from a JONSWAP spectrum by generating a Rayleigh random variable, the variance of which being equal to spectrum value, in order to determine the Fourier component magnitude and the phase is generated by a random variable uniformly distributed over $[0, 2\pi]$. The sea surface is finally calculated by a inverse Fourier transform of these DFT coefficients. As previously said our goals were to use a closed nonlinear system in order to estimate the amount of nonlinear energy on simulated images, to localize the nonlinearities in these images and to validate the nonlinearity detection tools presented in section 2. The second and third order Volterra models have been simulated, (the analytic kernel are related in [6]) with different sea surface (swell or wind seas) with different significant wave heights, different direction of propagation (0° , 30° , 60° , 90° , the reference axis being the range axis) and for different wavelengths. In a similar way, SAR images have been also simulated either by the velocity field computation and all pixel moved proportionally to their velocity or by a direct computation of the sea surface using the Hasselmann's formula [3]. For these four methods, the azimuth smearing has been simulated by a linear azimuthal low-pass filter in the frequency domain in order to retrieve a spectral decrease equal to $e^{-k_x \cdot \rho_{dd}(0)}$ in the azimuthal direction, $\rho_{dd}(0)$ being the displacement autocorrelation function. The azimuth smearing is a nonlinear process, which can be modeled by a linear process and does not generate spectral components by interaction. From a pure spectral point of view several items are interesting.

-A good spectral agreement for all sea surfaces is found between the four simulation methods proving especially that a SOVM is efficient to described correctly the SAR process and consequently yields a good approximation of the SAR process. The nonlinear kernel implies destructive components localized in an azimuthal strip closed to the low frequencies. In the SAR process, constructive quadratic interactions do not exist because they are not generated in the linear mode and are removed by the azimuth smearing in the quadratic mode.

-The SAR process is almost bimodal due to fast changes from a linear mode to a quadratic one. Both kernels provide the same energy amount for in-between angle (45°) and for high significant wave heights. The figure 4 relates an example of an hybrid spectrum which the sum of two equivalent spectra (a linear and a quadratic one). This example includes the two main distortions due to the SAR process nonlinearity. A "rotation" of the linear spectrum due to the azimuth smearing (fig 2) and the quadratic component generation near the continuous component. Both distortions explain the final SAR spectrum of fig. 4. This characteristic bimodal behavior can be explained mainly by two complementary phenomena

i.e. a growing amount of quadratic energy and a decrease of linear energy (due to the azimuth smearing) when the wave direction turns to the azimuth axis. However even in linear mode, about 30 % of the energy is due to quadratic components proving so that even if the linear kernel spectrum gives the shape of the SAR spectrum, it does not describe completely this spectrum.

-The nonlinearity detection with indexes provides satisfying results for general 2D SOVM. However, for models derived from the SAR process, due to the azimuth smearing, few components present phase coupling relationship. Hence the bicoherence index gives similar results for simulated SAR images and for linear spectrally equivalent images. The aberration index provides rather good results with disjoint confidence interval for the SAR process (and allows a robust nonlinearity detection). Unfortunately, this index decreases when the nonlinearity increases (always due to the small number of components with phase coupling relationship). Highest index values are obtained for wave traveling in the range direction (i.e. in a linear mode), the phase coupling occurring between two original waves (in the range direction) and their quadratic interactions (in the azimuth direction).

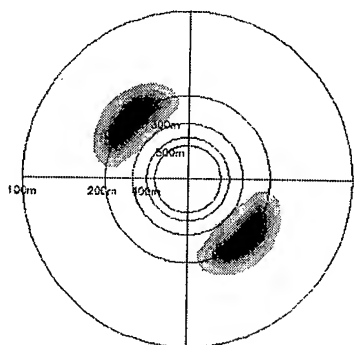


Figure 1: Original sea spectrum

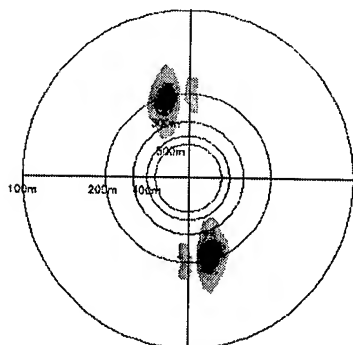


Figure 2: Linear kernel spectrum

CONCLUSION

A prime idea in order to retrieve the sea spectrum is to eliminate the quadratic components to firstly deduce a linear spectrum assumed to be as close as possible to the original sea spectrum. Although this assumption is

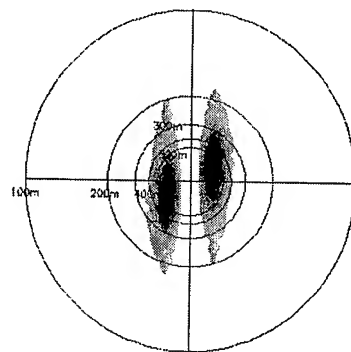


Figure 3: Quadratic kernel spectrum

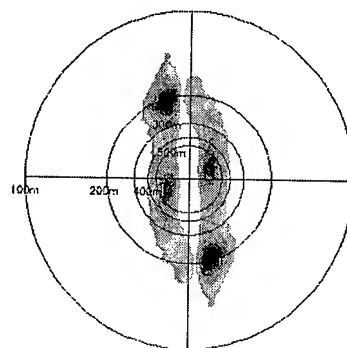


Figure 4: Complete SAR spectrum

right, the quadratic component elimination is not a so good idea, because these components contain the information destroyed by the azimuth smearing in the linear kernel. Consequently, the best method, to process the image, would be to "deconvolute" the information coded by the quadratic kernel to retrieved the lost information.

ACKNOWLEDGMENT

This work was supported by the MAST-III (MORSE) programme of the EC, the contract # MAS3-CT95-0027. The authors would like to thank Dr Bertrand Chapron, IFREMER, for his advices.

REFERENCES

- [1] D.R. Brillinger. An introduction to polyspectra. *Ann. Math. Statist.*, 36:1351-1374, 1965.
- [2] R. Garelo, J-M. Le Caillec, and B. Chapron. Estimation of the phase content of sar images of the ocean using 2D bispectrum estimation. *Proc. of IGARSS*, I:612-614, 1995.
- [3] K. Hasselmann and S. Hasselmann. On the nonlinear mapping of an ocean wave spectrum into a synthetic aperture radar image spectrum and its inversion. *J. Geophys. Res.*, 96:10713-10729, 1991.
- [4] J-M. Le Caillec and R. Garelo. Phase coupling detection using a finite number of realizations and non independent phases. *Proc. of Tencon digital signal processing applications*, II, 1996.
- [5] J-M. Le Caillec, R. Garelo, and B. Chapron. Two dimensional bispectral estimates from ocean sar images. *Nonlinear Processes in Geophysics*, 3:196-215, September 1996.
- [6] J-M. Le Caillec and R. Garelo. Study of the second order approximation of the velocity bunching in the SAR imaging process using the bispectrum. *Proceedings of IGARSS*, I:612-614, 1996.

Observation of Internal Waves in the Andaman Sea by ERS SAR

Werner Alpers

Institute of Oceanography, University of Hamburg

Tropelwitzstr. 7, D-22529 Hamburg, Germany

Phone: +49 40 4123 5432 Fax: +49 40 4123 5713 E-Mail: alpers@ifm.uni-hamburg.de

Heng Wang-Chen and Lim Hock

Centre for Remote Imaging, Sensing and Processing

Faculty of Science, National University of Singapore

Lower Kent Ridge Road, Singapore 119260

Phone: +65 772 2622 Fax: +65 775 7717 E-Mail: phylih@leonis.nus.sg

Abstract -- The Andaman Sea of the Indian Ocean is known to be a site in the world's ocean where extraordinarily large internal solitons are encountered. Synthetic aperture radar (SAR) images of the ERS-1/2 satellites acquired by the receiving station in Singapore reveal that the large internal solitons previously detected by in-situ oceanographic measurements in the western approaches of the Strait of Malacca between Phuket (Thailand) and the northern coast of Sumatra (Indonesia) are generated at shallow banks in the western part of the Andaman Sea. When propagating onto the shelf of the Malayan Peninsula, their spatial separation decreases and their shape becomes irregular, but they remain solitons of depression.

INTRODUCTION

Since long seafarers approaching the Strait of Malacca have noticed that in the Andaman Sea, between the Nicobar Islands and the north east coast of Sumatra (Fig. 1), often bands of strongly increased surface roughness, also called ripples or bands of choppy water, occur.

Osborne and Burch [1] showed by analyzing in-situ collected oceanographic data that these visually observed roughness bands are caused by internal solitons which can be described by the Korteweg - de Vries equation. Their measurements showed that the time interval between the first solitons in the packets is typically 40 minutes and the amplitude (crest-to-trough distance) of the foremost internal soliton typically 60 m, i.e., warm water from above is pushed down by the internal soliton by 60 m.

Occasionally, sea surface manifestations of internal solitons have also been identified in the Andaman Sea on satellites images acquired in the visible band, e.g., by the Landsat satellites [1], and SPOT satellites. However, no systematic investigations of internal solitons could be carried out with these optical satellite images because they can be acquired

only sporadically when there are no clouds present and when the sun elevation angle is favourable.

A large number of spaceborne synthetic aperture radar (SAR) images of the Andaman Sea have recently become available from the ERS receiving station in Singapore. These ERS SAR images allow, for the first time, to study systematically the spatial distribution of internal solitons in the Andaman Sea and thus obtain information on their generation and propagation characteristics. For our investigation we had available a total of 385 ERS-1/2 SAR scenes of the Andaman Sea each covering an area of 100 km x 100 km.

GENERATION AREAS

Fig. 1 shows a SAR strip inserted into a map of the Andaman Sea which covers an ocean area of approximately 900 km x 100 km. It shows an exceptional wealth of strong sea surface manifestations of internal solitary wave packets. From the curved shape of these patterns one can estimate the position of their focal points. If we assume that the internal solitary wave packets have their origin at these focal points, then one can identify at least three generation areas, which are marked in Fig. 1 by A, B, and C. At position A a reef rises up to a depth of 30 m below the sea surface, at position B there is a seamount that rises up to a depth of 481 m, and at position C there is a submarine bank whose shallowest point is at a depth of 88 m. We conjecture that the internal solitons develop from a disturbance generated by the interaction of the baroclinic tide with shallow topographic features in the western section of the Andaman Sea.

Fig. 2 shows a blow-up of the southern section of the ERS-2 SAR strip shown in Fig. 1 (part of frame 3465). Visible is a ring-shaped pattern that has its focal point at the crosspoint of the two bright lines inserted in this SAR image. This focal point is located at 6°40'N 95°47'W, which is the position of the shallowest point of the Dreadnought Bank, which has a depth of 241 m. This image suggests that a secondary internal solitary wave packet is generated by the interaction of strong internal soliton(s) having the origin farther west.

This work was funded by the National University of Singapore and the Deutsche Agentur für Raumfahrtangelegenheiten (DARA) under contract 50 EE 9413.

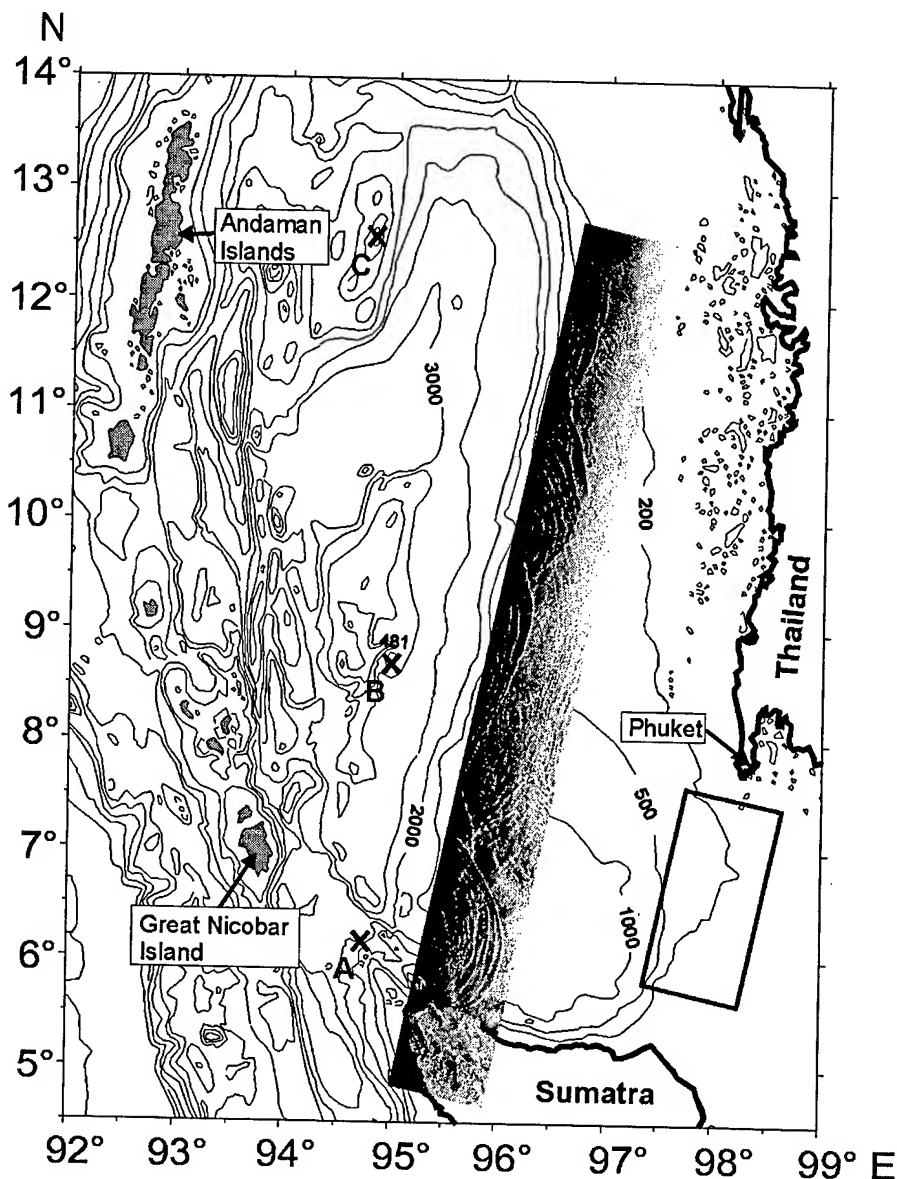


Fig. 1: A 900 km long and 100 km wide ERS-2 SAR strip inserted into a map of the Andaman Sea which was acquired on Feb 11, 1997, at 3:59 UTC. Visible are sea surface manifestations of several internal solitary wave packets originating from three different locations which are marked by A, B, C. The inserted rectangle denotes the location of the SAR strip shown in Fig. 3.

INTERACTION WITH THE SHELF

Fig. 3 shows another ERS-2 SAR strip whose location is inserted in the map of Fig. 1 and which is centered over the 200 m depth line of the western shelf of the Malayan Peninsula. Visible are sea surface manifestations of two major internal solitary wave packets, where one is located west and the other one east of the 200 m depth line. We interpret them as being generated in the same area in the western Andaman Sea, but separated in time by one tidal cycle. The internal solitary wave packet located east of the 200 m depth line has interacted with the shallow bottom topography of the shelf and thus is strongly disturbed, which results in an irregular rough-

ness pattern. This is also evident from the variation of the normalized radar cross section (NRCS) along the scan line A-B inserted in Fig. 3, which is plotted in Fig. 4. However, like the roughness pattern of the internal solitary wave packet located west of the 200 m depth line, also the roughness pattern of the solitary wave packet located east of the 200 m depth line starts with a line of increased surface roughness in front, i.e., with a line of increased normalized radar cross section (see Fig. 4). Thus the front line of the leading soliton is associated with a convergent surface current which implies that the internal solitons east of the 200 m depth line are also solitons of depression [2].

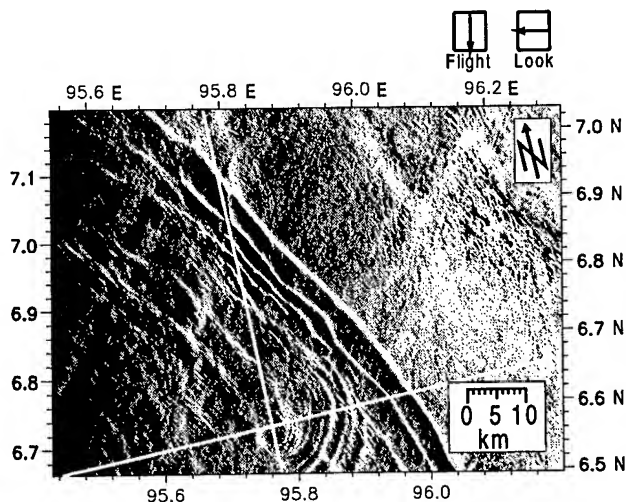


Fig. 2: Enlargement of the southern section of the ERS-2 SAR strip shown in Fig. 1. The focal point of the circular wave pattern is located at the shallowest point of Dreadnought Bank.

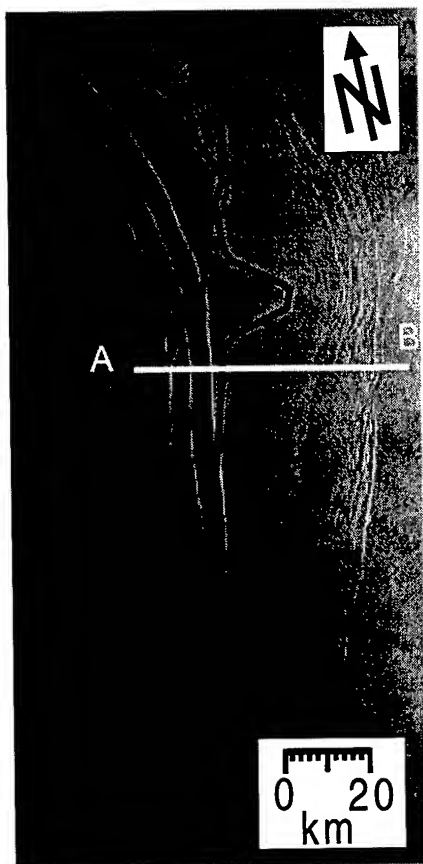


Fig. 3: SAR image of a 200 km x 100 km large section of the Andaman Sea acquired by the ERS-2 satellite on April 15, 1996, at 3:51 UTC. It shows sea surface manifestations of internal solitary wave packets west and east of the 200 m depth line.

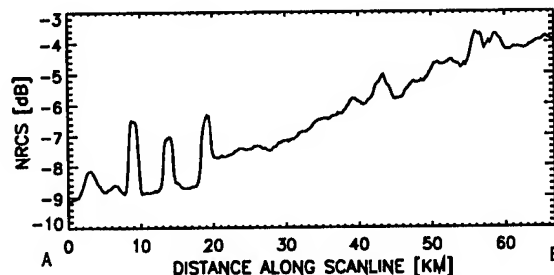


Fig. 4: Variation of the normalized radar cross section (NRCS) along the line A-B inserted in the image of Fig. 3.

Another noteworthy feature visible on the ERS SAR image shown in Fig. 3 is the surface roughness pattern associated with the interaction of two internal solitons. Phase shifts in the roughness pattern can be clearly delineated in regions where the internal solitons cross each other. Such phase shifts are predicted by soliton theory [3].

CONCLUSIONS

ERS SAR images of the Andaman Sea are an excellent means to study the spatial distribution and the form of the sea surface manifestation of internal solitons in the Andaman Sea. From them information on their generation and propagation characteristics can be derived. The analysis of 385 ERS-1/2 SAR images of the Andaman Sea has revealed that the internal solitons propagating westwards have their origin at shallow areas in the western section of the Andaman Sea where they are probably generated by the interaction of the baroclinic tide with shallow bottom topographic features. When solitary wave packets encounter the shallow waters of the western shelf of the Malayan Peninsula, they become heavily disturbed and the separations between the solitons in the wave packet decreases, but they remain solitons of depression.

ACKNOWLEDGMENT

This investigation was carried out while W. Alpers was a visiting scientist at the Centre for Remote Imaging, Sensing, and Processing (CRISP) of the National University of Singapore. We thank ESA for providing the ERS SAR data which were processed at CRISP.

REFERENCES

- [1] A.R. Osborne and T.I. Burch, "Internal solitons in the Andaman Sea", *Science*, vol. 208, 1980, pp. 451-460.
- [2] W. Alpers, "Theory of radar imaging of internal waves", *Nature*, vol. 314, No.6008, 1985, pp. 245-247.
- [3] G.B. Whitham, "Linear and nonlinear waves", John Wiley & Sons, Inc., USA, 1974.

Study of Gulf Stream Features with a Multi-Frequency Polarimetric SAR from the Space Shuttle

F. Askari¹, S. R. Chubb¹, T. Donato¹, W. Alpers², S.A Mango¹

¹Remote Sensing Division
Naval Research Laboratory,
Washington, D. C. 20375-5351, U. S. A.

² Institute of Oceanography, University of Hamburg
22529 Hamburg, Germany

Telephone: 202.767.5270, FAX: 202.767.3303, EMAIL: askari@ccf.nrl.navy.mil

Abstract -- We use simulations of radar cross-section, based on wave-current interaction calculations, to investigate the origin of a prominent enhancement in L-band, HV polarization radar return that was observed in imagery of the northern boundary of the Gulf Stream (GS) during the first Shuttle Radar Laboratory (SRL-1) mission. The calculations of surface roughness are based on a 1-dimensional surface current model that closely resembles a current convergence that was observed in in situ current measurements, taken at both sides of the Stream at the time SRL-1 imaged the GS boundary. In agreement with trends observed in the imagery, significant enhancements in L-band HV polarization cross-section occur in the neighborhood of the GS boundary, relative to comparable VV polarization cross-section signatures at X-, C- and L- band. This occurs despite the fact that the magnitude of the L-band HV cross-section is significantly reduced relative to the comparable X-, C-, and L-band VV cross-sections. These results indicate that the associated L-band HV enhancement occurs from tilt-induced modulation in the radar backscatter, which preferentially alters the *relative* modulation in L-band HV backscatter in regions where considerable variation in surface slope takes place. We also provide an overview of a number of additional sub-mesoscale features associated with the Gulf Stream that were present in the image of the GS boundary.

INTRODUCTION

Previously[1,2] we have identified and characterized a number of radar signatures from prominent sub-mesoscale features in radar imagery from the northern boundary of the Gulf Stream. We have done this using in situ measurements and fully-polarimetric SAR imagery at L-, C-, and X- band taken during the SRL-1 mission. These signatures resulted from variations in image intensity caused by separate thermal and velocity fronts at the Gulf Stream boundary, a weed line south of the boundary, and imprints of atmospheric cellular convective cells within the Stream. The unstable atmospheric forcing in the vicinity of the thermal front is conducive for

producing large modulations at higher radar frequencies. However, the largest variations in image intensity at this front occur at L-band with (HV) polarization. Because this result can not be explained from the atmospheric forcing conditions on both sides of the Stream, it is plausible that the associated signature can only have occurred through wave-current interaction effects. In this paper, we investigate this possibility by using in situ current measurements and radar image simulations, based on full spectrum wave-current interaction calculations[3]. We find, in agreement with the trends that are present in the imagery, that the relative modulation in L-band HV backscatter is significantly enhanced in the immediate vicinity of the boundary of the GS. However, we also find that the L-band HV radar cross section (RCS) is two orders of magnitude lower in value than the comparable RCS values for L-, X-, and C- band.

GULF STREAM BOUNDARY IMAGERY

Details of the ground truth and SRL imagery are presented in [1,2]. The present work focuses on imagery collected during Datatake 134 (DT134), of SRL-1, which occurred on 17 April 1994 over the north edge of the Gulf Stream. At the time of the SRL over-flight, ground truth information was being obtained aboard the R/V Cape Hatteras. Fig. 1 shows the L-band HV polarization DT134 SRL image, which is similar to a comparable image shown previously[1]. As can be seen in Fig. 1, there are a number of prominent sub-mesoscale features, which (from the available ground truth information) we are now able to identify. These features are labelled (with arrows) in Fig. 1. They include 1. the "Weed Line," in the southern portion of the Fig., where the radar backscatter is markedly reduced; 2. a prominent, bright-line, which occurs at the "Thermal Boundary" of the GS, 3. the R/V Cape Hatteras, and 4. the "Velocity Front," located in the northern portion of the Fig.. Also, readily identifiable in the Fig. is a region (surrounding, and above and below the "Weed Line") of granularly-shaped features (within the GS) that result from the sea surface manifestation of

atmospherically-induced, sub-mesoscale convective instabilities. The focus of the remainder of the paper is the origin of the signature from the "Thermal Boundary."

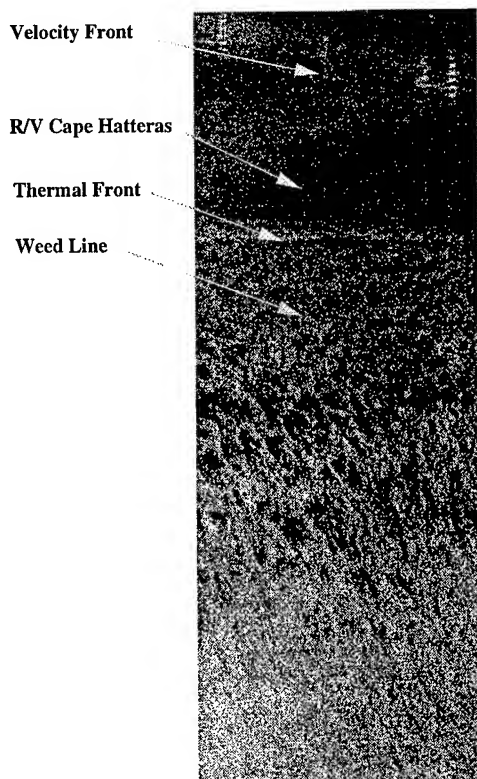


Fig. 1: L-Band SIR-C/XSAR image with HV polarization from 17 April 1994, centered at 36°42.8' N, 73°42.5'W. Resolution is 72 m x 75 m in "range" (horizontal) and "azimuth" (vertical) directions. Locations of "Weed Line", R/V Cape Hatteras, "Thermal Front", and "Velocity Front," as determined by shipboard measurements are marked by arrows

THERMAL FRONT GROUND TRUTH

In Table 1, we have tabulated the key environmental parameters that were measured on different sides of the GS near the time of the SRL-1 over-flight. Here, U^* refers to the friction velocity (defined by the square root of the local drag coefficient multiplied by the wind speed). As expected there was a large difference in the currents on the two sides of the Stream. What is somewhat surprising is that the northward current component differs by only ~ 0.16 m/s in the

Stream from its value to the north of the GS, while the eastward component is ~ 7 m/s greater in value inside the Stream. In fact, the flight path of the shuttle during the overflight was approximately directed to the southeast, so that the bright line associated with the "Thermal Front" in Fig. 1 is parallel to a line that points in the northeast-southwest direction. In fact, consistent with earlier studies of bright linear features at the GS boundary[4], the ground truth information reveals that the predominant currents (and current gradients) are directed perpendicularly to this line. This allows us to model the currents using a one-dimensional current convergence, similar to previous studies[4], as discussed in the next section.

MODELLING

Using a procedure similar to [4], RCS simulations are derived by applying the Composite Backscatter (CB) model using the wave height spectral density F values that are derived from wave-current interaction calculations. These wave-current calculations are based on calculations of the wave action density $N(\mathbf{r}, \mathbf{k}, t) \equiv \omega_o(\mathbf{k})/k F(\mathbf{r}, \mathbf{k}, t)$ as a function of two-dimensional wave-vector \mathbf{k} , at locations \mathbf{r} on the ocean surface, where $\omega_o(k) \equiv (gk + T/\rho k^3)^{1/2}$, $k \equiv |\mathbf{k}|$, ρ =density of sea water, T =surface tension) is the intrinsic angular frequency. Because the currents are directed predominantly along the southeast-northwest direction, it is possible to pick a coordinate system in which the y-component of the currents is $V \equiv V(y)$, and the x-component vanishes. Then, in analogy with earlier GS modelling [4], we use a current model of the form

$$V(y) = -\frac{\delta V}{2} \tanh\left[\frac{y}{\delta y}\right] + V_o. \quad 1$$

Consistent with the ground truth measurements, $\delta V = 0.621$ m/s, $V_o = 1.41$ m/s, and the value $\delta y = 100$ m was inferred from the SRL-1 imagery. The wave action density is derived using

$$\nabla_{\mathbf{k}} \omega \cdot \nabla_{\mathbf{r}} N - \mathbf{k}_y \left[\frac{\partial V}{\partial y} \frac{\partial N}{\partial \mathbf{k}_y} \right] = -\beta \frac{N}{N_o} (N - N_o),$$

where $\omega = \omega_o + \mathbf{k}_y V$, and β and N_o , respectively, are the Plant growth rate and Bjerkaas-Riedel equilibrium wave action density that were used previously[3,4].

MODEL/SRL-1 COMPARISON

Fig.2 shows plots of the radar image intensity along lines extending through the front for X- and C- band with VV polarization, and L- band with VV and HV polarization. As can be seen from the plot, the L HV radar intensity shows an appreciable rise (~ 2 - 3 dB) relative to its value outside the GS (to the left in the plot) at the front. In the comparable X-, C-, and L-band VV plots, there is imperceptible variation in radar intensity. Fig. 3 shows the result of applying the CB model to the current structure discussed above. Here we

also find that the maximum relative variation in intensity occurs with L-band with HV polarization. But we also find the associated values of the RCS are two orders of magnitude lower than those that occur with X-, C-, or L- band with VV polarization. Because the HV scattering coefficients in the CB model vanish in the absence of tilt, these modelling results suggest that the sharp change in currents at the boundary of the GS induces variations in tilt, which induce the relative variations in the HV return that are responsible for the relative change in L HV intensity to be larger than the comparable variations with VV polarization.

Table 1: In Situ Measurements: Average Values

Wind Speed:	3.35 +/- 0.72 m/s	
Wind Direction:	198 +/- 45°	
Air Temperature:	16 +/- 1.3°	
Parameter	Cold Side	Warm Side
Sea Surface Temperature	14.1°	23.5°
Salinity	31.0 PSU	36.19 PSU
Density	1023.07 kg/m ³	1024.700 kg/m ³
Current Speed	0.8 m/s	1.5 m/s
Current Direction	55°	65°
U*	0.014	0.0 17

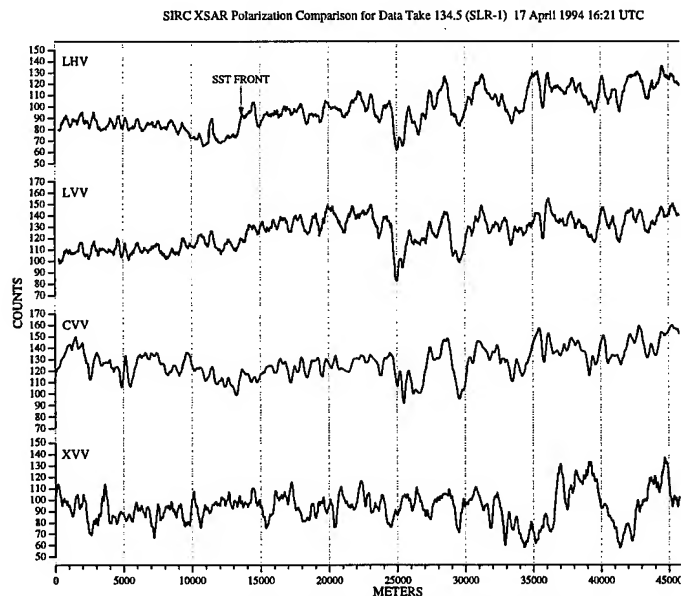


Fig. 2: Plots of relative Radar Intensity for L-band HV (top) and VV (second from top) polarizations (labelled LHV and LVV) and for CVV and XVV, as labelled. The location of the "Thermal Front" is marked with the arrow and the label "SST Front." Relative intensity is expressed using an integer byte scale (labelled "Counts"), extending between a minimal value corresponding to Count=0, to a maximum value (Count=255).

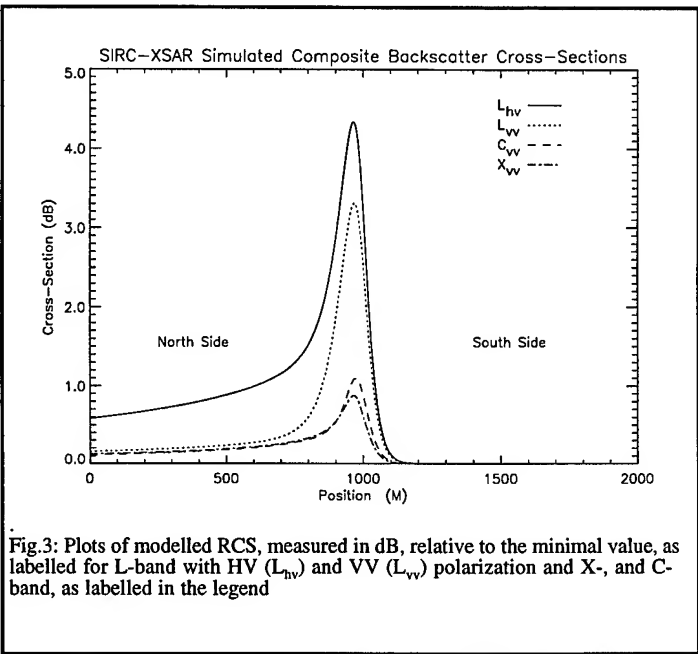


Fig.3: Plots of modelled RCS, measured in dB, relative to the minimal value, as labelled for L-band with HV (L_{hv}) and VV (L_{vv}) polarization and X-, and C-band, as labelled in the legend

REFERENCES

- [1] S. A. Mango et al., IGARSS'95 Digest, vol 2, 1325 (1995).
- [2] G. R. Valenzuela, et al., IGARSS'94 Digest, vol 3, 1728 (1994).
- [3] S. R. Chubb, A. L. Cooper, R. W. Jansen, and C. Y. Shen, IGARSS'96 Digest, vol 2, 902 (1996).
- [4] [1]R. W. Jansen, T. L. Ainsworth, R. A. Fusina, S. R. Chubb, and G. R. Valenzuela, IGARSS'94 Digest, vol 1, 460 (1994).

EFFECT OF AZIMUTH BANDWIDTH SPREADING ON SAR IMAGING AND SAR INTERFEROMETRY OVER THE OCEAN

Baosen Zhou* and Dayalan Kasilingam**

*Department of Electrical and Computer Engineering
University of Massachusetts, Dartmouth
North Dartmouth, MA 02747.

**Centre for Remote Imaging, Sensing and Processing
National University of Singapore
Lower Kent Ridge Rd.
Singapore, 119260.

Tel: (65) 771-5173; FAX: (65) 775-7717; e-mail: crsdpk@leonis.nus.sg

Abstract: Radar backscatter measurements over the ocean, from a L-band, tower-based radar are used to study the effect of bandwidth spreading on SAR imaging systems and SAR interferometry. The coherent radar measurements are put through a SAR simulator to generate the image of the radar footprint on the ocean surface. This simulated SAR image is analyzed for resolution and phase coherence. It is shown that as the SAR integration time is increased from near zero, the resolution will improve initially. However, increasing the integration time beyond the scene coherence time will have little impact on the resolution. It also shown that in SAR interferometry, increasing the integration time degrades the phase resolution. Optimum values of integration times and interferometric time delays are suggested for SAR imaging and along-track interferometry, respectively.

INTRODUCTION

In synthetic aperture radar (SAR) imaging of the ocean surface, the azimuth resolution of the images are generally degraded due to the limited temporal coherence of the backscattered signal [1]. This limited temporal coherence is generally defined in terms of a scene coherence time which is a function of the radar frequency and the sea state. The coherence time is shorter for the higher radar frequencies and for higher sea states. It is generally accepted that the azimuth resolution of SAR images of the ocean surface is determined by the scene coherence time rather than the azimuth integration time.

In SAR interferometry, the limited coherence results in phase noise [2]. This reduces the effective phase resolution in interferometry. In along-track interferometry, if the time delay between the two images is comparable to the coherence time, the phase difference measurements may be highly unreliable.

The coherence time may be measured by measuring the bandwidth of the backscattered signal from the ocean surface. The coherence time is loosely defined as the reciprocal of the bandwidth. The spreading of the azimuth bandwidth may be due to many different factors. Three factors have been identified as being the primary contributors towards the loss of coherence. First there is the lifetime of the short waves. Since the backscatter from the ocean surface is dependent on the short scale roughness of the ocean surface, the temporal properties of this short scale roughness will determine the temporal coherence of the backscattered signal [3].

In addition to this effect, there is also Doppler spreading due to the intermediate and long scale surface wave orbital velocities [1]. These velocities will smear the image in the azimuth direction. However, only the contribution from surface waves which are not resolvable by the SAR will contribute towards the bandwidth spreading. The contribution due to the longer waves which may be resolved appear as a simple azimuth shift instead of azimuth smearing [1]. Another factor that causes bandwidth spreading is the effect of orbital acceleration of long surface waves. This effect is observed when the integration time is comparable with the long surface wave periods.

These three factors will influence the resolution of the SAR image in different ways. This dependence will be a function of the azimuth integration time and in the case of the along-track SAR interferometry, a function of the time delay between the two images. Thus, there is a need to identify and understand the factors that contribute towards the spreading of the backscatter bandwidth. In this paper, the effect of limited temporal coherence on SAR images and SAR interferometry is studied using backscatter measurements from a L-band, tower-based radar.

APPROACH

A L-band radar (1.2 GHz) was used to make radar backscatter measurements from the ocean surface off the coast of San Diego, California. The radar incidence angle was about 30° and the footprint on the ocean surface was approximately $3\text{m} \times 4\text{m}$. Coherent backscatter measurements were obtained at various sea states. Time sequences of these measurements are used in a SAR simulator to simulate the image of this portion of the ocean surface. The simulated SAR image is then analyzed to study the effects of limited temporal coherence on the SAR imaging process.

The imaging parameter that influences the azimuth resolution most is the azimuth integration time. Varying the integration time will provide insights into the effect of the different mechanisms that limit the temporal coherence of the backscattered signal. The study is extended to along-track interferometry by simulating two different images separated by a time delay. The phase difference between the signal may be used to estimate the orbital velocities and the current of the ocean surface at a given location. Phase difference from simulated images are used to study the impact of limited temporal coherence on phase resolution. In addition, the effect of integration time on phase resolution is also investigated by generating images at different integration times.

RESULTS AND DISCUSSION

Fig. 1 shows the simulated SAR images of the portion of the ocean surface. In fig. 1(a), the integration time is 1s. The image appears to be shifted from its actual location which is at 1.2s. This shift is the well-known azimuth shift due to the Doppler frequency shift of the backscattered signal from a moving target. In addition, the image resolution is found to be significantly larger than the expected resolution of 20ms. This is because the azimuth resolution is limited by the scene coherence time even though the design resolution is supposed to be considerably smaller. Long wave orbital acceleration effects appear as ripples around 1.2s in fig 1(a). These effects only appear when the integration time is comparable with the long wave periods.

Fig. 1(b) shows the same image when processed with an integration time of 200ms. Clearly, the resolution of this image is no worse than that of fig. 1(a). In this case, the integration time is comparable to the scene coherence time. Fig. 1 appears to indicate that the effective integration time is of the order of 200ms. If the integration time is considerably longer than this coherence time, then the effective azimuth resolution will not be affected by the integration time.

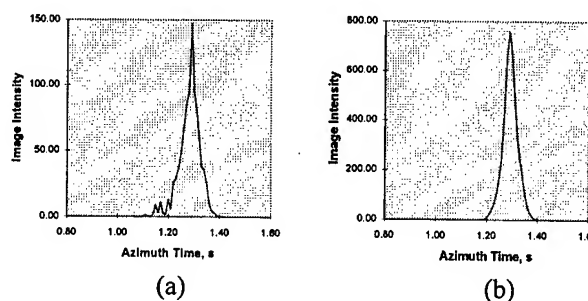


Figure 1 - Simulated SAR images using L-band radar measurements from a portion of the ocean surface for integration times of (a) 1s and (b) 200ms.

Fig. 2 shows the effective azimuth image width as a function of the integration time. Initially when the integration time is increased, the image width will decrease. However, beyond about 200ms the increase in integration time tends to produce a slight increase in the image width. This effect levels out at much longer integration times. At very short integration times, *i.e.* when the integration time is shorter than the coherence time, the azimuth resolution is determined primarily by the integration time. The minimum of the image width occurs when the integration time is comparable to the coherence time. Fig. 2 seems to suggest that the effective integration time for this sea state is approximately 200ms. The slight increase in image width beyond 200ms occurs when the acceleration effects start contributing towards the spreading of the bandwidth. The long wave acceleration effects are greatest at long integration times, because the smearing due to the change in azimuth shift will be proportional to the product of the acceleration and the integration time.

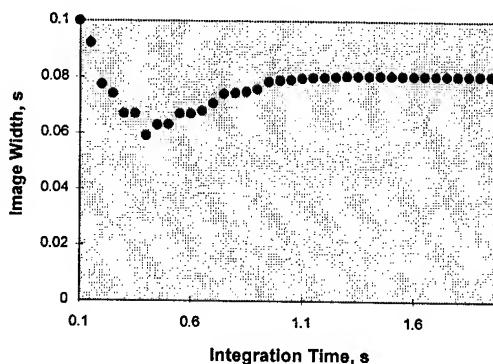


Figure 2 - The averaged azimuth width of the simulated SAR images for different integration times.

Fig 3 shows the phase difference between two simulated SAR images of the same patch of the ocean surface plotted as a function of the azimuth time. The phase difference is

measured at image pixels for two different time delays of 10ms and 50ms. The phase difference appears to vary linearly with the azimuth location. Since the azimuth location is proportional to the effective Doppler velocity of the scattering element and the phase difference between the images is also proportional to this velocity, the phase will have a linear dependence on the azimuth location.

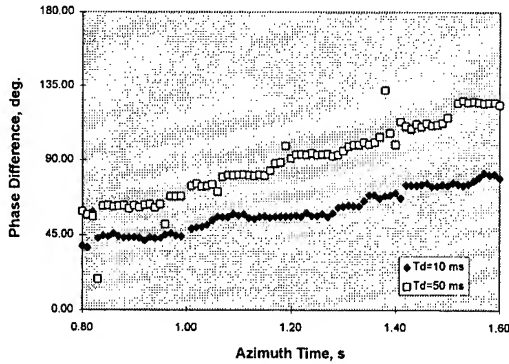


Figure 3 - Phase difference between image pixels for two simulated SAR images delayed by 10ms and 50ms.

The linear dependence on the azimuth location is stronger for a time delay of 50ms compared to that of 10ms, since the measured phase difference is proportional to the product of the velocity of the scattering element and the time delay. However, more importantly, it can be observed that the spread in the phase is significantly more for 50ms compared to that for 10ms. This is because for the 50ms time delay, the backscattered signal is less coherent than for the 10ms time delay.

Fig. 4 shows the estimated phase error calculated from the phase spread at different time delays. Clearly, as the time delay is increased beyond about 20ms the phase error increases rapidly. For delays greater than 20ms, this error could be prohibitively high and no useful phase information may be extracted from the two images. Fig. 4 appears to suggest that for reliable phase measurements, the time delay should be 20ms or less for this particular sea state.

Fig 5. shows the phase error as a function of the integration time. The delay between the images is set at 10ms. Increasing the integration time appears to increase the phase error. This due to the fact that over longer integration times, more of the signal used in the azimuth compression process is uncorrelated to the signal from the other image. Only a small fraction of the overlapping region will be coherent. Thus, the phase error appears to increase with increasing integration time.

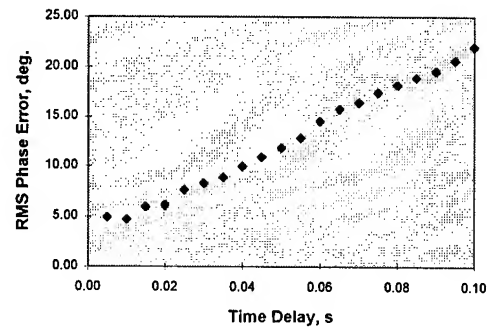


Figure 4 - The rms. phase error of the phase difference measured between two simulated SAR images plotted as a function of the time delay.

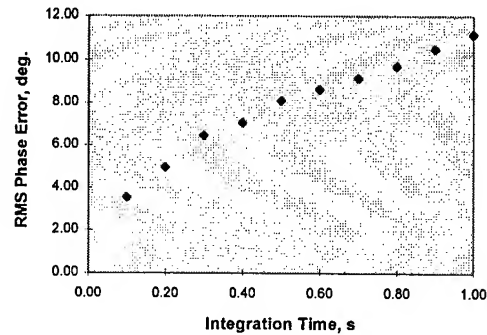


Figure 5 - The rms. phase error of the phase difference measured between two simulated SAR images plotted as a function of the integration time.

CONCLUSION

The simulations support the premise that in most cases, the SAR azimuth resolution is determined by the effective scene coherence time. It is shown that in along track interferometry, the rms. phase error increases with the time delay between the two images and also with increasing integration times. It is concluded that integration times longer than the coherence time is not desirable and that the time delay between interferometric pairs should be less than a tenth of the coherence time.

- [1] Kasilingam, D.P. and O.H. Shemdin, J. Geophys. Res., 13837-13848, 1988.
- [2] Shemer, L. and M. Marom, Intl. J. Remote Sens., 3021-3029, 1993.
- [3] Kasilingam, D.P. and O.H. Shemdin, Intl. J. Remote Sens. 2079-2104, 1992.

A QUANTITATIVE STUDY OF TROPICAL RAIN CELLS FROM ERS SAR IMAGERY

I-I Lin*, Dayalan Kasilingam*, Werner Alpers**, Tian Kuay Lim***, Hock Lim*, Victor Khoo*

*Centre for Remote Imaging, Sensing and Processing (CRISP), Faculty of Science,
National University of Singapore, Lower Kent Ridge Road, Singapore 119260

Tel: 65-7727908 Fax: 65-7757717 Email: crslinii@nus.sg

I**Institute of Oceanography, University of Hamburg

***Meteorological Service Singapore

ABSTRACT

This paper investigates the backscatter signatures of an ERS-2 SAR image of tropical rain cells. The particular type of rain cell studied is a squall line. By comparing with simultaneously acquired ground-based weather radar data, possible attenuation effects from the rain column in the atmosphere are investigated. The rainfall rate is estimated from the attenuation signature in the SAR imagery. Comparison between the estimated rainfall rate and weather radar rainfall rate shows consistency. Wind speed associated with the squall line is also estimated based on the CMOD4 scatterometry model. The estimated wind speed pattern appears to be in agreement with the observed squall line structure. Possible errors in the wind estimation due to effects of rain are suggested. Further study is required to validate these initial results.

1. INTRODUCTION

Following the initial investigation of tropical squall lines in the SAR imagery by Kasilingam et al. (1997), this paper discusses some possibilities in analysing the backscatter signatures quantitatively. A ERS-2 SAR image (figure 1) of a squall line south of Singapore is studied. Features including a gust front, an area of updraft convergence, regions of mottled structure, and attenuation regions by rain column in the atmosphere are suggested and identified with the aid of co-located ground-based weather radar data (Kasilingam et al, 1997). In this study, the attenuated backscatter signatures are investigated further and the associated rainfall rate is estimated based on the attenuation relationship for C band radar by tropical rainfall (Atlas et al, 1991). In addition, the SAR backscatter signatures are used to estimate wind speed across the squall line. This possibility in estimating wind speed in the SAR imagery using scatterometry models has received considerable attention in the recent literature (Alpers and Brummer, 1994; Horstmann et al, 1997). Given wind direction, the wind speed can be estimated from the single backscatter measurement of SAR. This concept of using SAR as a high resolution wind mapper has shown to be useful in providing detail wind structures of specific mesoscale atmospheric phenomena and is applied here in revealing detail wind structure of tropical squall lines.

2. ATTENUATION SIGNATURES

As suggested by Kasilingam et al (1997), certain regions of reduced backscatter in the SAR image (figure 1) are likely to be caused by the attenuation of the rain column.

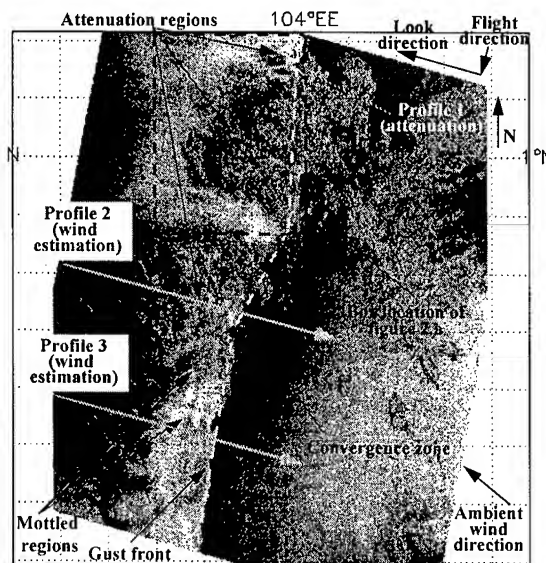


Figure 1: ERS-2 SAR imagery of a squall line at the coast of Singapore acquired on September 22, 1996, at 03.24 UTC.

Possible supportive indicators include firstly, a comparison with weather radar data and these regions are found to be correlated with heavy rainfall (typically > 50 mm/hr). Secondly, by comparing with a clear day SAR image, some islands obscured in the squall line image are identified and it is suggested that the effect of attenuation causes such obscuration (Melsheimer et al, 1996; Kasilingam et al, 1997). Figures 2.a and 2.b illustrate the situation in greater detail. A subset of the SAR image in figure 1 is displayed in colour (figure 2.a) and compared with the co-located weather radar data (figure 2.b). Increasing rainfall rates correlate to decreasing radar backscatter. In addition, the attenuated patterns (e.g., the circled region of heavy rain core in figure 2.a) are found to be displaced in the radar look direction when compared with figure 2.b. This displacement is also indicative that the attenuated patterns originate from the rain column in the atmosphere.

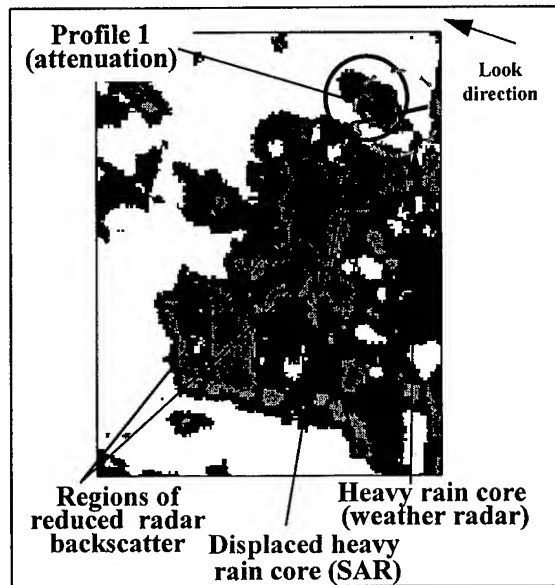
3. ESTIMATION OF RAINFALL RATE

As in figures 2.a and 2.b, a region of heavy rain core is identified (circled in the figures) in both SAR and weather radar images. Using weather radar image as a reference of the actual rain core location, this range

displacement (d) can be used to calculate the effective thickness (h) of the rain column since

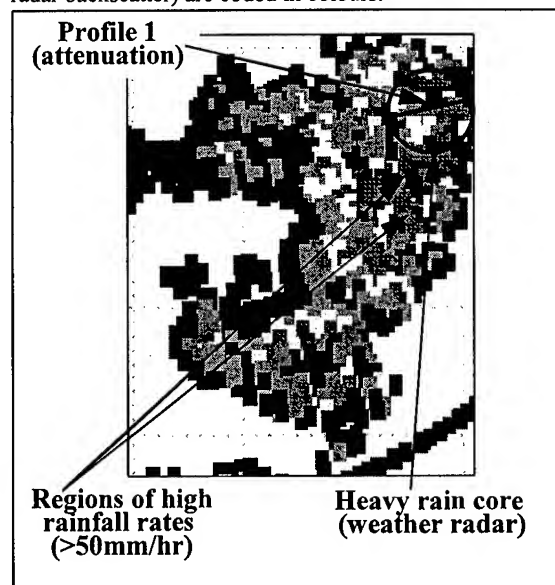
$$\frac{d}{h} = \tan(23.5^\circ) \quad (1)$$

where 23.5° is the nominal incidence angle at the centre of the ERS SAR image. The displacement is found to be 1.973 km and the effective thickness of the rain core is thus given as $h = d / \tan(23.5^\circ) = 4.54 \text{ km}$.



■ lower attenuation ■ higher attenuation

Figure 2.a: A subset of the ERS SAR imagery in figure 1 is shown and different levels of attenuation (reduced radar backscatter) are coded in colours.



■ < 0.25 mm/hr ■ < 25.0 mm/hr ■ < 125.0 mm/hr
 ■ < 12.5 mm/hr ■ < 50.0 mm/hr ■ > 125.0 mm/hr

Figure 2.b: Co-located weather radar data of figure 2.a,

regions of higher rainfall rates ($> 50 \text{ mm/hr}$) are correlated with reduction of radar backscatter in figure 2.a.

The calculated effective thickness is then incorporated in the attenuation relationship for the rainfall rate estimation. The attenuation relationship for C band radar is adopted from Atlas et al (1991). This relationship was derived specifically for tropical rainfall where a wide range of data sets (rain gauge and C band weather radar data from Darwin, Australia) were used in the derivation. The attenuation as a function of rainfall rate is given as

$$A = 0.0085 \times 2h \times R^{1.08} \quad (2)$$

where A is the attenuate NRCS (Normalised Radar Cross Section) in dB, R is the estimated rainfall rate, h is the effective thickness of rain column. The effective thickness h is multiplied by 2 as the attenuation is two-ways. The attenuate NRCS A is calculated with reference to the NRCS of the neighbouring no rain region. Using (2), rainfall rate is estimated along profile 1 in figure 1 (also shown in figure 2.a). The calculated rain fall rate is compared with the corresponding weather radar rainfall rate along the same profile (figure 3). It is shown that the two data sets are agreeable. Towards the two ends of the profile (corresponding to very low rainfall rate in weather radar, $< 0.25 \text{ mm/hr}$), the attenuation-estimated rainfall rate is not valid since the attenuation effects is very small under such light rain condition.

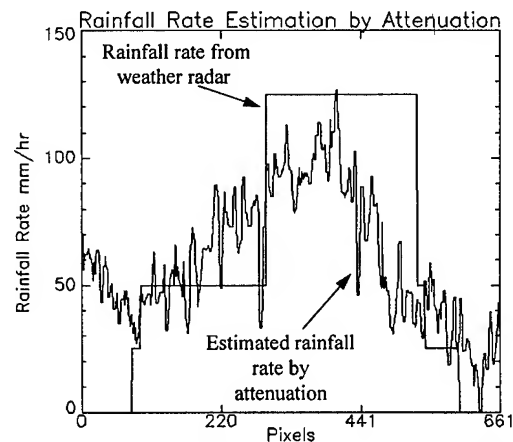


Figure 3 : Comparison between rainfall rate estimated by attenuation in the SAR image and rainfall rate from weather radar along profile 1. The discrete distribution of the rainfall rate from weather radar is that the whole range of rainfall rate was binned into 6 levels for data storage purpose.

4. ESTIMATION OF WIND SPEED

A conceptual meteorological model (Houze et al., 1989) of a squall line is illustrated in figure 4. Descending rear inflow sloping downwards towards the gust front of the squall line is observed. This information together with

routine weather charts aid us in determining the wind direction. At the rear side of the gust front, the wind direction is inflowing towards and perpendicular to the gust front (figure 1). After the determination of wind direction, the SAR image intensity was converted to the NRCS and was averaged over 2 km for noise reduction. The effect of incidence angle across the range was also accounted for so that the wind speed will neither be overestimated at the near range nor underestimated at the far range (Horstmann et al, 1997). The wind speed is then estimated using the inverse CMOD4 scatterometry model (Stoffelen and Anderson, 1993). Estimation along profiles 2 and 3 (figure 1) across the squall line was performed and the result for profile 2 is illustrated in figure 5.

In general, wind-modulated NRCS exhibits uniform and gradual changes and the corresponding wind speed increases from around 3 to 6 m/s (figure 5). However, in the rain region (e.g. the mottled regions in figure 1), the scattering and attenuation effects of rain column from the atmosphere together with the effect of rain impinging on the ocean surface (Melsheimer et al, 1996; Kasilingam, 1997) adds variability to the NRCS signature and thus the wind speed. Such variability shows possible errors in wind speed estimation as part of the NRCS is caused by rain and not wind. Passing the gust front, the wind speed exhibits a sharp decrease. In Kasilingam et al (1997), this region of sharp decrease is interpreted as a convergence zone where strong low level convergence of air results in the absence of a horizontal wind component.

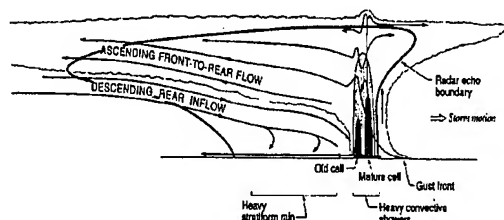


Figure 4: Conceptual model of a squall line in a vertical cross section, adopted from Houze et al. (1989).

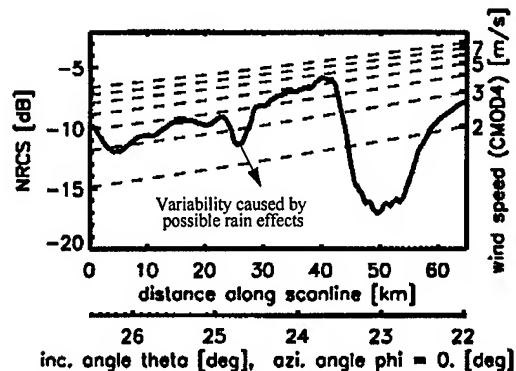


Figure 5: Wind speed estimation using the CMOD 4 model along profile 2.

5. CONCLUSION

In this research, SAR backscatter signature is used to estimate the rainfall rate and wind speed associated with a squall line. It is found that the estimated rainfall rate is consistent with the weather radar rainfall rate which suggests the possibility of deriving rainfall rate of tropical rain cells from the SAR imagery. Possible errors in wind speed estimation due to rain effects are suggested. Future work involves further validation with ground truth data and error estimations.

6. REFERENCE

Alpers, W., and B. Brummer, "Atmospheric boundary layer rolls observed by the Synthetic Aperture Radar aboard the ERS-1 satellite", *Journal of Geophysical Research*, vol. 99, pp. 12,613-12,621, 1994.

Atlas, D., D. Rosenfeld, and D. B. Wolff, "On C-band attenuation by tropical rainfall in Darwin, Australia using climatologically tuned Ze-R relations", Special Edition #20, *Journal of Applied Meteorology*, 3rd International Conference on Precipitation Modelling, Texas A&M University, College Station, Texas, 20-22 February, 1991.

Horstmann, J., W. Koch, W. Rosenthal, and S. Lehner "Wind fields from ERS SAR, compared with a mesoscale atmospheric model near to the coast", *Proceedings of the 3rd ERS Symposium*, 17-21 March 1997, Florence, Italy.

Houze, R. A., S. A. Jr. Rutledge, M. I. Biggerstaff, and B. F. Smull, "Interpretation of doppler weather radar displays of midlatitude mesoscale convective systems", *American Meteorological Society*, vol.70, no.6, pp. 608-619, 1989.

Kasilingam, D., Lin, I-I, H. Lim, V. Khoo, W. Alpers, and T. K. Lim, "Investigation of tropical rain cells with ERS SAR imagery and ground-based weather radar" *Proceedings of the 3rd ERS Symposium*, 17-21 March 1997, Florence, Italy.

Melsheimer, C., W. Alpers, and M. Gade, "Investigation of multifrequency/ multipolarisation radar signatures of rain cells, derived from SIR-C/ X-SAR data, *Proc. 1996 Int. Geosci. and Remote Sens. Symposium (IGARSS)*, 1370-1372, 1996.

Stoffelen, A., and D. Anderson, "Characterisation of ERS-1 scatterometer measurements and wind retrieval", *Proceedings of Second ERS-1 Symposium - Space at the service of our Environment*, Hamburg, Germany, ESA publication, SP-361, October 1993.

7. ACKNOWLEDGEMENT

We thank the Meteorological Service Singapore and C. Melsheimer, P. Brandt, and A. Michelsen of the University of Hamburg for data provision and technical supports.

Experimental Investigation of Doppler Spectra of Microwave Signals Backscattered by Sea Slicks¹

M.B.Kanevsky, S.A.Ermakov, E.M.Zuikova, V.Yu.Karaev,
V.Yu.Goldblat, I.A.Sergievskaia, Yu.B.Shchegol'kov
Institute of Applied Physics, Russian Academy of Sciences
46, Ulyanova St., 603600, Nizhny Novgorod, Russia
Tel.: +7 8312 384528, Fax : +7 8312 365976
e-mail: kanevsky@hydro.appl.sci-nnov.ru

J.C.Scott and N.Stapleton
Defence Research Agency, Winfrith Technology Centre
Winfrith Newburgh Dorset DT2 8XJ, UK

ABSTRACT — Doppler spectra obtained using an X-band radar have been used to study artificial slicks. The radar was deployed on a platform in the Black Sea to image slicks which were artificially laid in the sea nearby. The radar viewed the slicks at about an angle of 20° incidence. The Doppler spectra obtained from slick covered regions showed strong shifts of the mean Doppler return towards higher frequencies compared with that obtained from non-slick areas. The change in Doppler spectra can be explained if the relative contributions to the radar backscatter from Bragg and specular scatterers changes in the slick covered areas compared with that in non-slick areas. The experimental results are found to be in good agreement with theoretical predictions.

INTRODUCTION

The appearance of slicks in remotely-sensed satellite imagery due to presence of organic films on the sea surface requires urgent investigation if the imagery is to be used to address ecological problems. The main radar response to a slick covered sea surface is a reduction in the observed backscatter. This reduction results from damping of ambient surface wind-waves by the film [1-3]. However, it is desirable to have additional means of detecting whether the surface is covered by a slick to reduce the level of false slick detections. One way is to use Doppler information. As far as we know the radar Doppler spectrum measured in the presence of surfactant films has not been studied in field conditions.

Radar backscatter at incidence angles large enough (larger than 30°) is known to be principally due to Bragg waves, which, for X-band radars are centimetre-scale waves. At low incidence angles (less than 10°) radar backscatter is better described by using the Kirchhoff (quasi-specular) approximation. Specular returns from the sea surface to the radar are determined by long surface waves. At low to moderate incidence angles of order 20° (at which satellite SARs operate) Bragg and specular scattering can be comparable, so that the Doppler spectrum can be determined by the velocities of both the short centimetric waves and by longer waves. One can thus expect that if relative contributions to the radar backscatter from the two mechanisms is changed it results in a shift of the mean Doppler frequency. In particular, if slow centimetric waves are suppressed by slicks the backscatter can be mostly specular and the Doppler returns will mainly correspond to phase velocities of long waves. This effect was studied theoretically in [4], and the Doppler spectrum of radar signals was found to be quite sensitive at low to moderate incidence angles.

This paper contains an experimental confirmation of the mentioned theoretical prediction.

THEORY

In Fig. 1 taken from [4] the calculated Doppler spectra of X-band radar signals backscattered from the sea surface without slicks (curve 1) is shown together with spectrum obtained for a slick covered surface (curve 2) at wind

¹ The work was supported by the Russian Foundation of Basic Research (projects 96-05-65087, 96-05-79080, 96-05-64697, 96-02-17501) and the Defense Research Agency, Winfrith Technology Centre, UK (project SSWD1/113)

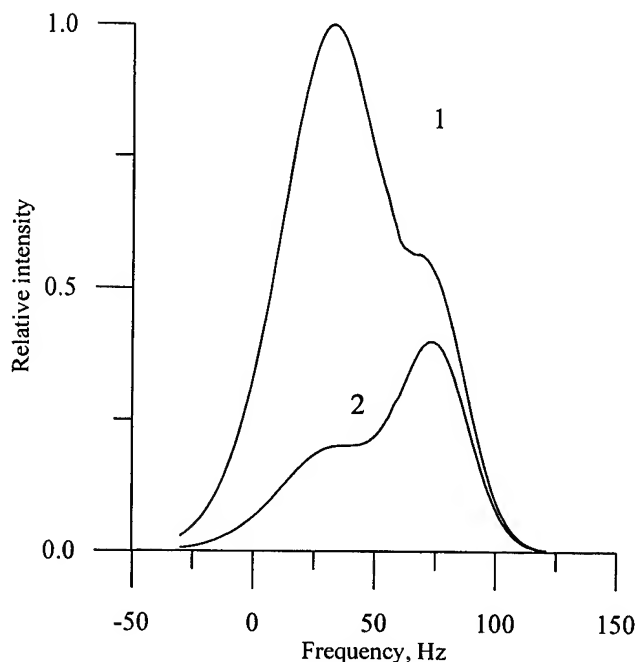


Fig.1. The X-band radar Doppler spectra for undisturbed windsea (1) and windsea disturbed by slicks (2) at wind speed 6m/s (JONSWAP sea spectrum model).

speed 6 m/s. Note the contrast between the slick and non-slick regions is around 4 dB. It is assumed that the observation was made from a stationary platform in the upwind direction at an incidence angle close to 20° . Each of these spectra consists of two spectral components due to Bragg and quasispecular scattering mechanisms. The component spectra are displaced relative to each other, as indicated in Fig. 1 by the two local maxima in the curves 1 and 2. Damping of the Bragg waves in the slick leads to a reduction of Bragg-like returns in the Doppler signal and hence a shift of the measured mean Doppler to higher frequencies as specular scattering events dominate. In non-slick areas the return is dominated by Bragg-like scattering events.

EXPERIMENT

The expected increase in mean radar Doppler frequency from slick areas was verified in experiments with artificial slicks on the Black Sea in 1996.

The experiments were carried out from the Oceanographic Platform of the Marine Hydrophysical Institute located about 0.5 km to the south of the Crimean coast, the Platform coordinates are $34^\circ 1' E$; $44^\circ 24' N$. The water

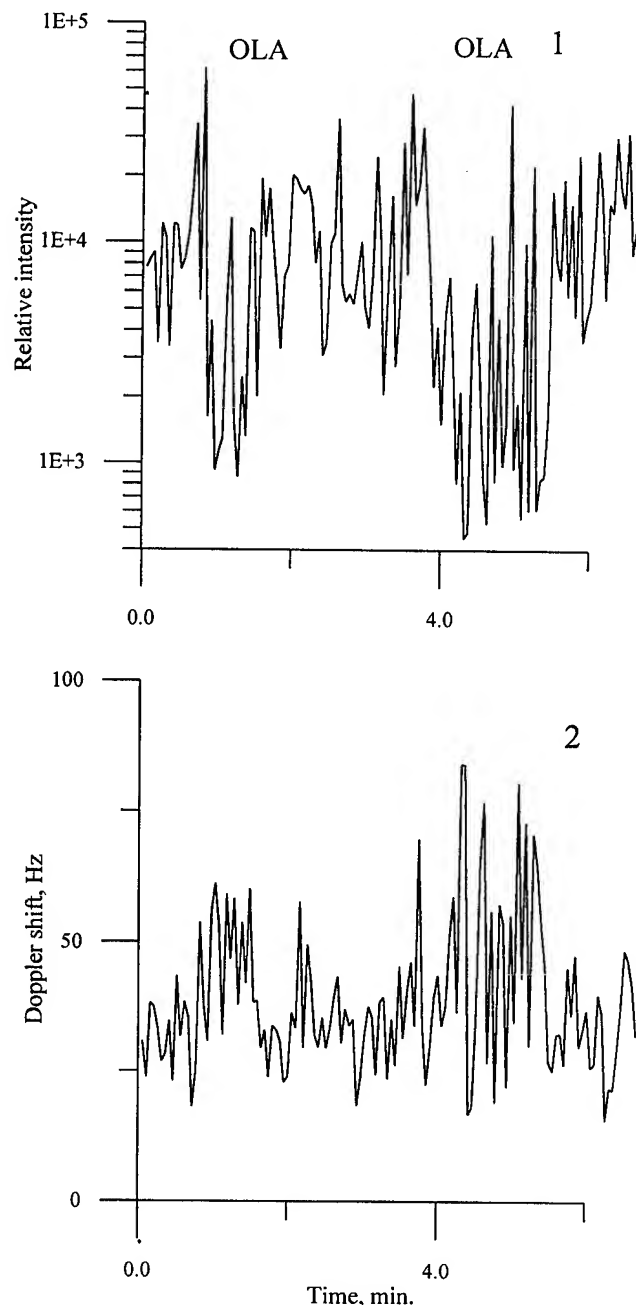


Fig.2. The relative intensity of the radar signal (curve 1) and mean Doppler frequency (curve 2).

depth near the Platform is 30 meters. A coherent X-band scatterometer was used in the experiments, the radar wavelength is 2.56cm. The incidence angle in the experiments on 3rd June 1996 was 18° , the wind velocity was about 5 m/s, wind direction 70° , and the radar look

direction was 90° . Two artificial slicks of oleyl alcohol (OLA) were deployed from a rubber boat.

The intensity of the radar signals (curve 1) and the mean Doppler frequency (curve 2) obtained in the experiment are shown in Fig.2. It is seen that the Doppler shift increases in both the slicks. The mean Doppler shift is about 30-35 Hz outside the slicks and about 50-55 Hz in the slicks. When comparing Figures 1 and 2 one can conclude that the observed Doppler shifts are in good agreement with theory. In case of space-borne radar the effect considered will not be so appreciable. Nevertheless, one can expect this effect to be detectable in as much as the Doppler shift can be estimated with high accuracy, in particular, for SEASAT SAR 1.4 Hz accuracy was reached [5].

CONCLUSIONS

The theoretically predicted effect of increasing mean Doppler frequency of microwave radar signals backscattered from sea slicks at incidence angles close to 20° has been confirmed experimentally. This effect can be considered as an additional means of confirming the presence of slicks on the sea surface over and above any decrease observed in radar backscatter.

REFERENCES

- [1] J.C. Scott, "Surface films in oceanography, in ONRL Workshop Proceedings- Role of surfactant films on the interfacial properties of the sea surface", ed. F.L.Herr, and J.Williams, ONR Rep.C-11-86, pp.187-213, U.S.Office of Naval Research, Arlington, Va, 1986.
- [2] W. Alpers, and H.Huehnerfuss, "The damping of ocean waves by surface films: A new look at an old problem", J.Geophys. Res., vol.94 (C5), pp.6251-6266, 1989.
- [3] S.A. Ermakov, S.G. Salashin, and A.R.Panchenko, "Film slicks on the sea surface and some mechanisms of their formation", Dyn. Atmos. Oceans, vol.16 (3-4), pp.279-304, 1992.
- [4] M.B.Kanevsky, V.Yu.Karaev, "The Microwave radar signal Doppler Spectrum and the Problem of ocean surface slicks detection", Proc. IGARSS'96, pp.1493-1495, 1996.
- [5] F. Li, D Held, and J.Curlander, "Doppler parameter estimation techniques for spaceborn SAR with application to ocean current measurement", Proc. IGARSS'82, pp.7.1-7.5, 1982.

Probing the Ultimate Capabilities of Radar Interferometry for Deformation with Low Gradient: a new mission?

DIDIER MASSONNET

FREDERIC ADRAGNA

Centre National d'Etudes Spatiales

18 Avenue E. Belin, 31401 Toulouse cedex 04, France

Phone: (33) 5 61-27-34-18 Fax: (33) 5 61-27-31-67

Didier.Massonnet@cnes.fr

Frederic.Adragna@cnes.fr

The use of radar interferometry for measuring geophysical ground deformation was demonstrated using the large displacement field generated by a major earthquake. This study has been quickly followed by others where the amplitude of the phenomena was lower, whether caused by smaller earthquakes or by volcanic activity. At the same time two quests were initiated in parallel: the first aimed at interpreting properly this new signal, the second, more technology oriented, aimed at pushing the limit of the method down to the artifact level while trying to observe phenomena characterized by low gradients of deformation such as post-seismic evolution. Here we discuss the prospects of extending the use of radar interferometry to a whole class of phenomena it did not explore so far. Such phenomena include post-glacial rebound, interseismic deformation, tidal loading over large areas as well as large and deep earthquakes. Some of these have their amplitudes maximized with time, which raises the question of long term coherence and the parallel issue of the proper satellite mission required to seize this opportunity. Tidal loading, a cyclic phenomenon, may be maximized by stacking adequate image pairs. The deformation field of deep earthquakes can be discriminated against noise by the consistency in the signal of adjacent radar tracks. Eliminating the artifactual phenomena: orbit adjustment, radar clock drift, meteorological phenomena... is demanding as we show in several example, but outlines the requirements of a dedicated, cost-effective radar satellite which could grasp the heritage of ERS, perfect some technical aspects and drop the unnecessary design margins. The simulation of the new specifications using existing ERS data on well known sites allows a very safe and reliable prediction of the performances.

DOMAIN OF VALIDITY OF INTERFEROMETRY

Radar interferometry has brilliantly demonstrated its capability to grasp many types of ground displacements. Initial experiments also helped define more precisely the limits of the technique, which are best understood on a

diagram featuring the typical extend of the phenomena versus the amplitude of the deformation. The extend of the phenomena are comprised between the size of a pixel or, more likely, ten pixels (in order to be able to recognize typical morphological signatures) and the width of the radar swath. Although adjacent swaths can be used, as we have done for the study of a big earthquake in Chile, the typical extend ranges from 100 m to 100 km. On the other hand, the amplitude must be above a threshold of about 2 mm (for C-band measurement), but which may be more safely put around one centimeter if we are pessimistic about our ability to separated contributions from the atmosphere. The upper amplitude limit is rather a slanted line, because the main limiting factor is the gradient of deformation, which must not exceed one fringe per pixel, or a typical 10^{-3} . We know examples, such as the vicinity of the fault rupture in an earthquake, where this limit was exceeded. In some cases, the limit can be artificially by-passed. Such is the case of small surface ruptures, which can be assessed using the property of invariance along a closed profile. Another limit may "cut the lower right corner" of the diagram, since small amplitudes extending over a swath may easily be blurred by improper "orbital tuning" or specific instrumental artifacts. The resulting five-sided area defines the possibilities of radar interferometry and all the current and past experiments can be placed within it.

OPTIMAL FEATURES FOR A NEW MISSION

The analysis of missions to be covered allows to break them into two categories. The first category is made of missions which would be covered by almost any spaceborne radar. It includes the studies which do not require exceptionally long time intervals or exceptional coverage. For instance, volcanology involves a small number of targets, typically less than 500. These targets doesn't need to be observed on the long term, but may occasionally require observations as frequent as possible. Any single satellite such as J-ERS, ERS-1/2 or ENVISAT can perform. The same applies to

glaciology, where the preservation of surface seems to forbid any long term observation. The optimal system features for studies on glaciers may be either a short orbital cycle (typically three days) coupled with a pointing capability for full coverage or a twin system similar to what ESA has done with the tandem mission. Artificial displacement fields (subsidence, soil swelling) generally cover a small surface and must be observed with typical yearly coverage. Improving the use of planned satellites can be achieved by distributing interferometric software and training people on them. A task we have begun at CNES.

The second category involves open scientific problems, such as interseismic or preseismic activity, or the dispatching of displacement and constraint on active areas, as well as topic where the underlying science is well understood, but lacking appropriate geodetic measurement. The questions raised by these missions are different from the first ones and require a specific system which:

- 1) allows a very long time interval for detailed mapping of very slow phenomena,
- 2) offers the global coverage and provides multiple acquisitions (in order to fully discriminate between atmospheric phenomena and ground displacements) on adjacent tracks (in order to observe large scale phenomena such as deep earthquakes or post-glacial uplift),
- 3) is freed from all the artifacts which would put the mission in jeopardy. That is: equipped with a more stable oscillator and thus a much better discriminating power for low gradient displacement fields; controlled much more tightly on its orbit, in order to minimize topographic residuals, even if one may expect global topography of good quality to be available in a few years,
- 4) achieves a satisfactory cost-effectiveness.

The first requirement implies being compatible with ERS1/2 archive. Even if one may argue on the choice of C-band, of the 35 day orbital cycle or of the 23 degrees incidence angle which we are used to with ERS1, this system creates a *de facto* standard. It provided full coverage of the planet in the first half of the 90's, let us imagine what we can achieve with an ERS compatible system launched in 2005 and still operating in 2010. Such a system would be capable of observing 15 years of deformation on areas where long term C-band coherence is possible, by combination with 1995 ERS archive. From our experience, such areas are much more common than anticipated if one accepts less than perfect coherence, which is what the real world is made of. An L-band system launched at the same date would not achieve the same accuracy before 2050, assuming that L-band is four times less sensitive to small displacements, with the same

signal to noise ratio. Similarly, another C-band system (i.e. not on the same orbit) would have to re-create the archive. From the long term point of view, RADARSAT is not very late by comparison to ERS. However, its archive is much more heterogeneous (due to the multiple operating modes) and may never achieve a homogenous planetary coverage. An X-band system, almost twice as sensitive as a C-band system under the above assumption, would create its archive in 2005 and would rival the "ERS follow-on" system in 2015. It would be the best system after this date. However, we are much less experienced with coherence in X-band systems than we are with C-band systems.

The second requirement is heavily influenced by the first since the orbital cycle must be 35 days and, therefore, the swath width has to be at least 80 km for full coverage. One should aim at a global coverage of land surfaces combined with an on-board recording for reliability. Besides, if such a mission was decided, the first action would be to make the ERS archive safer and, probably, to gather the archive at a single place. Having a systematic on-board recording of all land surfaces may demand some technical trade-off in terms of dynamic range of the data and, possibly, in terms of range resolution. On board azimuth frequency band selection could also be envisioned.

The third requirement is basically to strengthen the specifications for the stability of local oscillator and for the track repetition, the latter especially if the range resolution is decreased, which hardens the "interferometric condition".

The fourth requirement would be fulfilled only if a ERS compatible radar can be embarked on a small platform. The ERS concept is relatively simple (no off-pointing) and is the best candidate for low-cost redesign.

PRELIMINARY DESIGN WORK

Deriving a new mission based on ERS-1 offers many advantages. The simulation of the results is straightforward and can be based on real data, degraded appropriately. The results of these simulations is very reliable.

In an attempt to reduce power and telemetry requirements, we tested ERS1 imagery assuming that the power was 40 W on average (rather than 400), that the resolution was only 50% of that of ERS, and that data compression was used in the form of "azimuth presumming", where only half of the azimuth spectrum was recorded (after proper on-board selection). These degraded images provided the same visual quality on test sites such as Mount Etna or Landers, once put on a 100 m grid. In this regards, ERS-1 design is well above the minimum requirement of image quality.

In 1995, CNES studied a dedicated system based on the above assumptions. The radar is built on an existing C-band solid state source, expected to be very reliable and long-lived, SPOT4 solid state memory are used as well as 50 Mbit/s SPOT telemetry channel. The system can be embarked on the PROTEUS generic platform for small payloads (the same platform which will carry TOPEX-POSEIDON follow-on, called JASON). The accepted quality trade-off is minimized when the data of the new satellite are mixed with old ERS1

data, which have a much higher signal to noise ratio.

For distributing the data of such a system, one may imagine a systematic combination of the data with the one of the previous orbital cycle, the one about one year old and one of the oldest ones available (from ERS1). Since interferograms are much smaller than the data they originate from, results on specific areas could be systematically distributed electronically.

Reduction of the Phase-Unwrapping Drawbacks by the Three-Antenna Interferometric SAR System

G.Corsini, M.Diani, F.Lombardini, G.Pinelli

Department of Information Engineering - Faculty of Engineering
University of Pisa, Via Diotisalvi 2 - 56126 Pisa - Italy

Ph. +39 50 568511 - Fax +39 50 550560 - E-mail: gcorsini@radar.iet.unipi.it

Abstract - One of the most critical steps of SAR Interferometry for elevation mapping is the phase-unwrapping procedure. This paper analyzes the reduction of the phase-unwrapping drawbacks obtainable by using a recently proposed three-antenna SAR interferometer and a statistically optimal processor to estimate directly the interferometric phase with reduced ambiguity. A simulation of realistic scenarios is carried out. The performance analysis shows that the new technique significantly outperforms the conventional one, especially for high-relief terrains.

INTRODUCTION

Synthetic aperture radar interferometry (InSAR) is a well-established technique to obtain high resolution maps of the terrain height, by using the phase difference (interferometric phase) between the signals received by two antennas separated by a distance (baseline) along the cross-track direction [1],[4]. The terrain height can be derived from the interferometric phase by means of simple geometric relationships [1]. However, the phase is measured in the range $[-\pi, \pi)$, while the terrain height is related to the absolute interferometric phase, so the phase must be unwrapped before the phase to height conversion [4].

Phase unwrapping is one of the most critical steps of the conventional InSAR technique. In fact, the interferometric phase can be unwrapped to within a constant, so at least one *ground reference point* is necessary [4]. Then, the *phase aliasing* in steep areas [2] causes unwrapping errors and significant degradation of the height estimates. Moreover, phase unwrapping is complicated by phenomena related to the observational geometry such as *foreshortening* and *layover*. Finally, around the condition of complete foreshortening, the two received signals are fully decorrelated (the baseline equals the critical baseline [1]) so no useful information can be retrieved (*blind angles*).

Most of the phase unwrapping drawbacks can be reduced or avoided by using a recently proposed three-antenna SAR interferometer and a statistically optimal (maximum likelihood) processor which combines the data at three phase centers, to retrieve directly the interferometric phase with reduced ambiguity [3].

In the following sections, after recalling the three-antenna InSAR acquisition system and the related maximum likelihood (ML) phase estimator, we analyze the actual performance achievable by this new system, by making use of a statistical model that simulates most of the operative conditions of the system on a given scene and including the unwrapping procedure in the processing chain. In particular,

we show as the phase unwrapping drawbacks can be reduced, mainly thanks to the unambiguous phase range magnification. The analysis is performed in terms of the rms height error achievable by the conventional and the three-antenna InSAR system; to highlight the dependence of the performance on the terrain steepness, the analysis is carried out scaling by a variable factor s the height of the DEM used in the simulation to model the scene [2]. It is shown that the advantages of the new system over the conventional one are significant and increase with the terrain steepness.

THE THREE-ANTENNA SYSTEM AND ML DATA PROCESSOR

The system is a single-pass conventional airborne interferometer with the addition of a third antenna in asymmetric position between the two other ones, as shown in Fig.1 (one antenna both transmits and receives, the other two only receive). θ , ξ , H and r are the look angle, the baseline tilt angle, the platform altitude and the slant-range distance, respectively. The position of the additional antenna is defined by the asymmetry factor p defined as the ratio between the shortest available baseline and the over-all baseline B .

Since the ambiguity problems of interferometric SAR systems are governed by the baseline-to-wavelength ratio, the baseline diversity in the three-antenna system can be used either to increase the unambiguous phase range or to estimate the absolute phase, depending on the SAR system parameters and observational geometry. It can be shown that the unambiguous range magnification (*URM*) with respect to the conventional range (2π radians) is $1/p$ for $p = 1/n$ with n integer number[3].

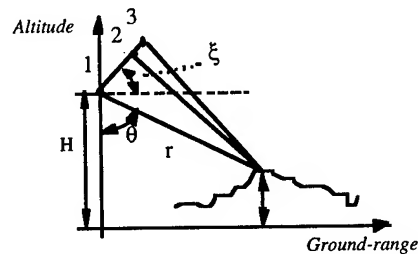


Fig.1: The three-antenna interferometric system

With the resulting *reduced phase aliasing*, the accuracy of the height estimate can be improved, especially for steep terrain. Moreover, thanks to the high correlation of the

signals received by the two closest antennas, the three-antenna InSAR system can operate also when complete decorrelation occurs in the conventional system [5].

Therefore, the *range of blind angles is reduced* and the areas without useful information shrink. Finally, the proper fusion of the information available at the three phase centers allows a general *improvement of the phase estimate accuracy* with respect to the conventional system [3].

To optimally process the data acquired by the three antennas the ML estimator is employed [3]. We choose $\varphi = \varphi_{13}$ as the interferometric phase sensed by the three-antenna system. We consider the three complex SAR images obtained by processing the echoes from the three two-way phase centers. As usual in SAR interferometry to reduce the statistical variations of the phase at expense of spatial resolution [1], we apply a multilook processing. The complex amplitudes of the pixels, corresponding to the same area on ground, observed in the three SAR images are arranged in the pixel triplets $[\tilde{P}_1^{(w)}, \tilde{P}_2^{(w)}, \tilde{P}_3^{(w)}]^T$ where $\tilde{P}_k^{(w)}$ is the pixel in the k -th image for the look $w=1, \dots, N$ with N number of independent looks.

According to the statistical model proposed in [3],[5], which is an extension of [1], the pixel triplets are complex Gaussian random vectors with hermitian covariance matrix $\tilde{\Gamma}$. Normalizing to unit power, the diagonal terms of $\tilde{\Gamma}$ are equal to 1 while the off-diagonal elements (i, j) are:

$$\gamma_{i,j} = \exp\{j\varphi x_{i,j}\} \alpha(Bx_{i,j}) SNR / (SNR + 1) \quad (1)$$

where SNR is the signal-to-noise ratio, $x_{i,j} = 1, 1-p$, and p for $(i,j) = (1,3), (1,2)$ and $(2,3)$ are the pertinent baseline fractions, and α is the corresponding spatial correlation factor [1], that is a function of the pertinent baseline, of the range, of the azimuth terrain slopes τ_r, τ_a , of the range and azimuth resolutions R_r, R_a and of r, θ, ξ and λ [1].

For the N pixel triplets corresponding to a multilook cell, the interferometric phase φ is derived by computing the ML estimate [3]:

$$\begin{aligned} \max_{\varphi \in [-\pi/p, \pi/p]} & \\ (\rho_{12} - \rho_{23}\rho_{13}) \text{Re}\{\exp[-j\varphi(1-p)] \sum_{w=1}^N P_1^{*(w)} P_2^{(w)}\} + & \\ (\rho_{13} - \rho_{12}\rho_{23}) \text{Re}\{\exp[-j\varphi] \sum_{w=1}^N P_1^{*(w)} P_3^{(w)}\} + & \\ (\rho_{23} - \rho_{12}\rho_{13}) \text{Re}\{\exp[-j\varphi p] \sum_{w=1}^N P_2^{*(w)} P_3^{(w)}\} & \end{aligned} \quad (2)$$

where $\rho_{i,j}$ are the moduli of the signal correlation coefficients $\gamma_{i,j}$ expressed in eq. (1). The coefficients $\rho_{i,j}$ in the estimator (2) depend on unknown parameters (local slopes, look angle and SNR); they can be directly estimated by the acquired data with little loss as reported in [5], so making the algorithm autoadaptive.

SIMULATION ANALYSIS

A simple simulator of the three-antenna system has been developed bypassing the complicated and time consuming generation of the unfocused (raw) SAR images. The components of the phase for the corresponding pixels in the three focused SAR images due to the observational geometry are generated with low computational load starting from the radar and platform parameters and the topography of the illuminated scene. This latter information is obtained by a Digital Elevation Model (DEM) of the area. Then, the interferometric noise component of the complex pixel triplets is generated with the proper correlation structure, exploiting the Cholesky decomposition of the correlation matrix $(\rho_{i,j})_{i,j \in \{1,2,3\}}$ as shown in [3].

The parameters of the statistical model are evaluated taking account of azimuth and range local slopes, of the variable look angle that affect the spatial correlation [1], of the scattering coefficient as a function of the local grazing angle and of the variable illuminated area that determine the SNR. To express the scattering coefficient, we resort to a general land clutter model presented in [6], which is a function of the local grazing angle, of λ and of terrain typology. Moreover, the simulator accounts also for the joint effects of topography and viewing geometry such as foreshortening and layover.

After the reduced-ambiguity interferogram generation, the expected phase of a topographically flat earth (FEP) can be subtracted by the interferometric phase before unwrapping. For the phase-unwrapping procedure, we use the completely automatic algorithm proposed in [7] which detect and avoid anomalous phases in the interferogram. Then, the FEP can be added up again and the phase in converted into height. The areas without phase informations are interpolated. Finally, the reconstruction errors are computed. The simulation procedure for the conventional system is analogous.

A performance analysis of the three-antenna airborne SAR interferometer and a comparison with the conventional system (with the same over-all baseline) on realistic scenarios has been carried out by means of the proposed simulator.

First, for a reference DEM covering an area of $3.25\text{Km} \times 3.25\text{Km}$ placed in Tuscany - Italy, we evaluate the performance of the two systems in terms of rms height error on the reconstructed DEM. For the three-antenna InSAR system, the asymmetry factor p is 0.2, so an $URM=5$ is obtained. The Digital Elevation Model (DEM) of this area is shown in Fig.2; the altitude varies from 0 to 185m. The system parameters (similar to the TOPSAR interferometer) are: overall baseline 2.75m, $\lambda=6\text{cm}$ (C-band), θ (mid swath)=35°, $\xi=60^\circ$ (30° off-vertical), $H=4\text{Km}$, $R_r=7.2\text{m}$, $R_a=6.25\text{m}$, $N=8$ look (2 rg., 4az.), nominal SNR (mid swath, hilly terrain)=12dB.

After that, we analyse how the achieved reduction of phase aliasing and the fringe widening in conditions near to complete foreshortening improve the height estimates after the phase unwrapping procedure, for different degrees of steepness. This is obtained by scaling the reference DEM for a factor scaling s variable between 1 and 2.5.

In Fig.3, the maps of the completely decorrelated areas for the conventional and the three-antenna InSAR system are superimposed one upon another. The black areas are completely decorrelated for both the systems, while the white areas are completely decorrelated only for the conventional system. The areas without useful informations for the three-antenna system are significantly reduced: the range of blind angles has shrunk and the operational capability of the new system is extended with respect to the conventional one.

In Fig.4 the interferograms without the FEP obtained by the conventional system and the new system for the DEM scaled by a factor 2.5 are presented. The advantages in terms of fringe width of the new system with respect to the conventional one are evident.

The rms height error (m) and the number of completely decorrelated cells of the investigated DEM, with size of $25 \times 25m$, are reported in Tab.I for the conventional InSAR and the three-antenna InSAR ($p=1/5$) system. The number of cells of the DEM is 16900. With the three-antenna system the areas without useful informations shrink by a factor ranging from 2.5 to 19.

The rms height error of the conventional system is higher for increasing scaling factor. This is due to the unwrapping errors that arise starting from $s = 1.5$ and become dramatic for $s = 2.5$. The height accuracy of the three-antenna system is higher than the conventional one for $s = 1$ thanks to the data fusion effect that produces better phase estimates. Then, the height error slightly increases with the scaling factor and some unwrapping errors arise only for $s = 2.5$. The accuracy gain of the three-antenna system results to be from 1.3 to 5.9; the last value is related to a situation in which the conventional system operation is very degraded while the new system still performs well.

With higher URM, the phase can be not wrapped at all, so the phase to height conversion can be performed without unwrapping and possibly, without the knowledge of ground reference points. As an example, for $s = 2.5$, we have obtained a non wrapped interferogram without FEP with $p = 1/15$ ($URM = 15$). The resulting height accuracy is slightly lower than with $URM = 5$ (4.1m), but it is still very better than the conventional system.

Table I: rms height error and number of decorrelated cells for conventional InSAR and 3-antenna InSAR ($p=1/5$)

	$s = 1$	$s = 1.5$	$s = 2$	$s = 2.5$
2 ant.	1.8 ; 9	4.6 ; 56	4.8 ; 275	21.8 ; 438
3 ant.	1.4 ; 2	1.7 ; 3	2.3 ; 32	3.7 ; 176

CONCLUSIONS

The reduced ambiguity three-antenna airborne InSAR system with ML data processor has been simulated in realistic conditions. An analysis of given scenarios has been carried out including the unwrapping in the height error budget. Results show that the system can produce height maps significantly more accurate than the conventional system, mainly through the reduced phase aliasing.

REFERENCES

- [1] E.Rodriguez, J.M.Martin, "Theory and Design of Interferometric Synthetic Aperture Raiders," IEE Proc. Pt-F, Vol.139, No.2, April 1992, pp.147-159.
- [2] J.O.Hagberg, L.M.H. Ulander, "On the Optimization of Interferometric SAR for Topographic Mapping," IEEE Trans. on Geoscience and Remote Sensing, Vol.31, No.1, January 1993, pp.303-306.
- [3] F.Lombardini, "Absolute Phase Retrieval in a Three-element Synthetic Aperture Radar Interferometer," Proc. 1996 CIE International Conference of Radar, Beijing, P.R. China, 8th-10th October 1996, pp.309-312.
- [4] R.Goldstein, H.A.Zebker, C.Werner, "Satellite Radar Interferometry: Two Dimensional Phase Unwrapping," Radio Science, Vol.23, No.4, Jul.-Aug.1988, pp.713-720.
- [5] P.Lombardo, F.Lombardini, "Multi-baseline SAR Interferometry for Terrain Slope Adaptivity," Proc. IEEE 1997 National Radar Conference, Syracuse, NY, U.S.A., 12-15 May 1997.
- [6] W.C.Morchin, "Airborne Early Warning Radar," Artech House, 1990.
- [7] G.Pinelli, M.Diani, G.Corsini, F.Berizzi, "A Method to Reduce the Phase Undersampling Effects in Airborne InSAR", Proc. of the Third International Remote Sensing Conference and Exhibition, Copenhagen, Denmark, 7-10 July 1997.

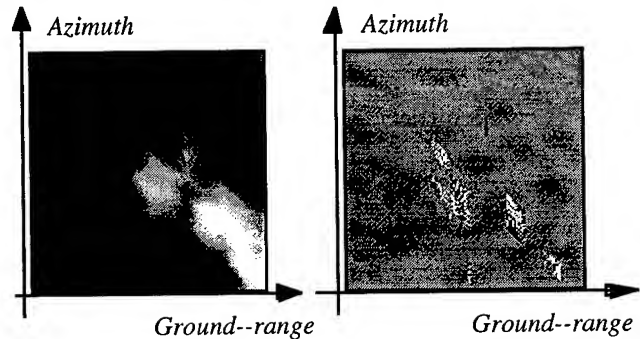


Fig.2: Original DEM

Fig.3: Decorrelated Areas, $s=2.5$ (white: Conventional InSAR, black: 3-antenna InSAR, $p=1/5$)

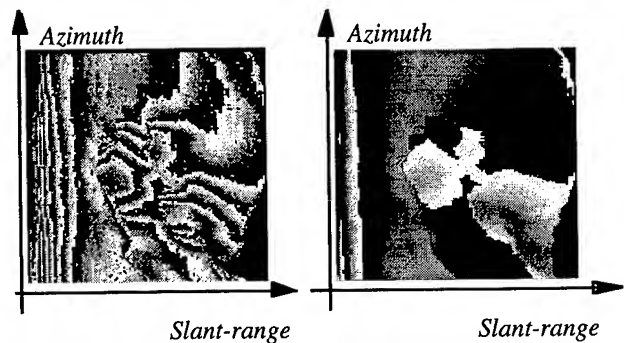


Fig.4: Interferograms obtained with the Conventional InSAR (left) and the 3-antenna InSAR, $p=1/5$ (right), for $s=2.5$

A Comparison of Interferometric Radar Surface Velocity Measurements to Subsurface Current Structure

Delwyn Moller, David L. Porter*

Stephen Frasier, Robert E. McIntosh

Microwave Remote Sensing Laboratory

University of Massachusetts, Amherst, MA 01003

* Applied Physics Laboratory

The Johns Hopkins University, Laurel, MD 20723-6099

T: 413.545.0779 / F: 413.545.4652 / moller@alex.ecs.umass.edu

Abstract—

Remote sensing of the ocean surface using interferometric SAR (INSAR) is of significant interest due to its potential for surface current measurements over large areas. INSARs use the phase difference between colocated SAR images separated by a small time lag to infer surface Doppler velocities, and hence wave orbital velocities and currents. It is not clear, however, how representative INSAR measurements may be of actual currents in the water column.

This paper presents comparisons between surface Doppler velocity measurements and subsurface water currents. Imagery from an X-band, focused phased-array radar is analyzed to yield both "interferometric" surface velocities and subsurface current estimates derived from dispersion characteristics of the imagery. The radar-derived velocities, combined with coincident Acoustic Doppler Current Profiler (ADCP) measurements are used to generate a vertical profile of current in the water column. Case studies are presented under varying environmental conditions for which the vertical structure alters considerably. The sensitivity of X-band interferometric measurements to wind-drift and the near-surface current structure is revealed.

I INTRODUCTION

In recent years the innovation of along-track Interferometric Synthetic Aperture Radar (INSAR) has provided the potential for imaging of ocean-surface currents [1]. INSARs employ two SAR antennas spatially separated in the along-track direction. Each receive the backscattered signal yielding separate complex SAR images. Through the motion of the platform, it is possible to coregister the two images. When co-registered the SAR images are separated by a time lag equal to the antenna separation divided by the platform velocity, and the covariance of the two images is the interferogram. The magnitude is akin to a conventional SAR image while the phase contains Doppler velocity information.

INSAR is a relatively recent technique and to date quantitative comparisons of interferometric velocity measurements with environmental data have been limited, [2], [3], [4]. Such comparisons are not straightforward given the large coverage of INSAR systems and the difficulty of making near-surface current measurements.

This work was supported by the Office of Naval Research (Remote Sensing) under grant N00014-95-1-0832

In a manner similar to INSAR, the FOCUSED Phased Array Imaging Radar (FOPAIR) [5] utilizes a pulse-pair technique applied to successive images to infer the scene velocity. FOPAIR is an X-band, high-resolution imaging radar consisting of a single transmit horn and a sequentially sampled, 64-element receive array. By scanning the receive array very rapidly, one obtains a near-instantaneous snapshot of the ocean surface complex backscatter, and the covariance of successive temporal images yields Doppler velocity information. Because the array synthesis time is much less than the ocean-decorrelation time, FOPAIR imagery is not degraded by scene decorrelation effects.

In this paper, the similarity in velocity measurement techniques of the FOPAIR and INSAR systems is exploited to compare interferometric velocity measurements with in situ data. In particular, FOPAIR surface measurements are compared with Acoustic Doppler Current Profiler (ADCP) current measurements. In addition, near-surface currents are estimated from the dispersion characteristics of the surface waves in FOPAIR imagery. The combination of ADCP and radar subsurface and surface velocities yields a vertical profile of current in the water column. These profiles reveal how surface velocity measurements correspond to the subsurface behavior.

II RADAR CURRENT MEASUREMENTS

A Doppler velocity, v , measurement is derived from the phase of the interferogram:

$$v = \frac{\lambda_r}{4\pi\Delta t} \arg \langle I(t)I^*(t + \Delta t) \rangle, \quad (1)$$

where λ_r is the radar wavelength, $I(t)$ is a complex image collected at time t , and Δt is the delay between successive images. To extract a mean surface velocity that is independent of wave orbital velocity, the interferogram phases are temporally and spatially averaged. A surface current is extracted from the mean surface by correcting for the phase-speed of the Bragg-resonant waves. To have confidence in the Bragg correction, the data displayed in this paper are for up and down-wind conditions only. We adopt the convention that positive velocities are approaching and negative velocities are receding.

In addition to surface radial velocity measurements, FOPAIR has sufficient temporal and spatial resolution to measure subsurface currents by the Doppler shift of the long-waves from the still water dispersion relation. When no current is present, linear gravity waves have a characteristic frequency,

$$\omega_0 = \sqrt{g|k|\tanh(|k|d)}, \quad (2)$$

where k is the wavenumber of the modulating wave, g is gravity and d is the water depth. However, this behavior is modified in the presence of a current, U , to become:

$$\omega = \omega_0 + U \cdot k. \quad (3)$$

Equation 3 states that, in the presence of a current U , a modulating wave of wavenumber k will be advected in the direction of the current, thereby causing a frequency shift. Stewart and Joy [6] showed how wave phase-speed is influenced by the vertical current structure and in particular how measurements derived from a particular frequency can be assumed to represent the current at depth,

$$d = \lambda/4\pi. \quad (4)$$

To extract subsurface current information using (3), FOPAIR imagery is transformed into wavenumber/frequency space via a 3-dimensional Fourier transform [7]. In this manner, a volume comprising a time-series of images is transformed into a volume where the dimensions are k_x , spatial frequency in the x-direction, k_y , spatial frequency in the y-direction and temporal frequency, f . The power-velocity cross-spectrum often shows most clearly the wave dispersion pattern and so it is in this product which is used for current estimation.

In Fig. 1, several constant-frequency slices of the coherence-spectrum are shown for a day when the radar was looking across a strong tidal current. The horizontal axis is k_x (m^{-1}), and the vertical axis is k_y (m^{-1}). The dotted line shows the still-water dispersion relation while the solid line is the result of a least-squares fit of (3) to the wave-energy. The currents derived from the least-squares fits were approximated from (3) to be at mean depths of 0.50, 0.35 and 0.29 meters.

III VERTICAL CURRENT PROFILES

This section presents vertical current profiles for three cases. These examples include the upwind/cross-current case already introduced, a case where the radar is looking downwind/down-current, and finally a downwind/up-current case.

Fig. 2 shows a current profile for the case where the radar was looking upwind and across a strong tidal current. The wind was about 5 m/s during this acquisition. The series of vectors plots on the left-hand-side illustrate the evolution of the current with depth. Additionally,

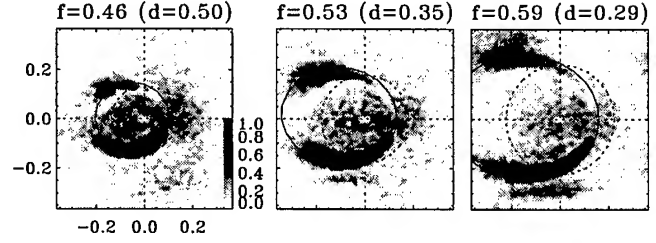


Fig. 1. Frequency slices of the power-velocity cross-spectra (10 minute average) showing the distortion of the dispersion relation due to current.

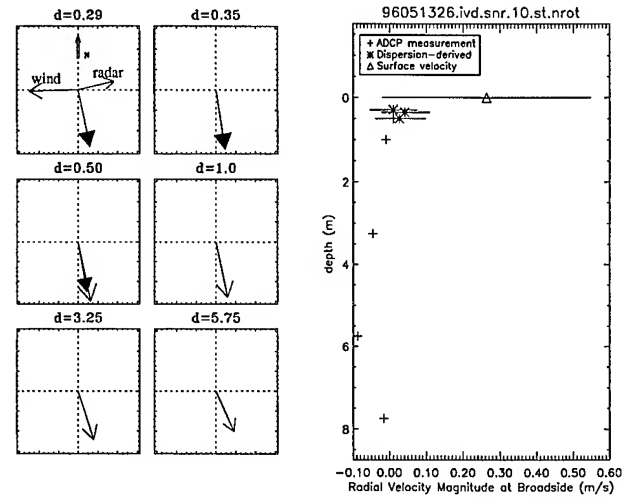


Fig. 2. Vertical profile of current structure when the radar is oriented up-wind and cross-current. a) The series of vectors show the evolution of sub-surface current with depth. Solid arrows: radar-derived vectors. Non-solid arrows: ADCP measurements. b) Current evolution in the radar-broadside direction.

the radar look-direction and wind direction are indicated in the near-surface plot ($d=0.29m$). The subsurface currents, shown by the solid arrows at depths of 0.29, 0.35 and 0.50 meters, are those derived from the dispersion characteristics of Fig. 1. The ADCP measurements are demonstrated by the line-arrows at 0.50, 1.0, 3.25 and 5.75 meters depth. The two instruments agree well.

Because the surface velocity is a radial measurement, for comparative purposes the current magnitudes at radar broadside are plotted in the right-hand-side of Fig. 2. In the radar broadside direction the subsurface velocities are very low since the radar is looking across the main tidal flow. The effects of wind-drift on the surface current is clearly reflected in the positive shift of the surface current as compared with the subsurface measurements.

A second example is given in Fig. 3 where the radar was oriented down-wind, and down-current. The wind was strong at approximately 10m/s. The three dispersion-derived subsurface estimates are illustrated by the solid arrows at depths of 0.41, 0.49 and 0.61 meters. ADCP

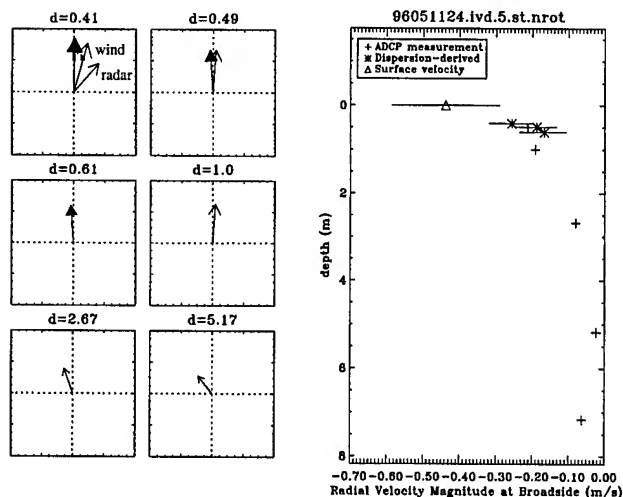


Fig. 3. Vertical profile of current when the radar is oriented downwind and down-current. a) The series of vectors show the evolution of sub-surface current with depth. Solid arrows: radar-derived vectors. Non-solid arrows: ADCP measurements. b) Current evolution in the radar-broadside direction.

currents are shown by the line-arrows for depths of 0.49, 1.0, 2.67 and 5.17 meters. Again, the ADCP and radar vectors compare favorably, and a counter-clockwise rotation of the current direction with depth can be observed.

In the radial velocity profile of Fig. 3, the near-surface evolution demonstrates wind-induced current penetrating into the water column due to the strong wind.

A final example, under light winds of approximately 2m/s opposing the tidal current, is shown in Fig. 4. For this case, only two sub-surface currents were extracted from the dispersion characteristics and they are shown at depths of 0.34m and 0.48m. At a depth of 0.48m, the radar current is smaller and slightly rotated with respect to the ADCP current, but the disparity falls within the error bars for the radar vector estimate. The evolution of the current with depth differs from the previous examples. In this case the current magnitude measured by the ADCP increases slightly from the 1.7m to the 4.2m measurements. In the previous examples, the current measurements have decreased monotonically with depth. This behavior is also observed in the radial velocity profile. In this profile, there is very little difference between the surface-current and the near-surface currents.

IV CONCLUSIONS

Several examples of vertical current profiles were presented under different environmental conditions and radar orientations. For each of these cases, the subsurface radar-derived currents and ADCP measurements compared well. In the first two examples, the influence of the wind on the surface current is pronounced. This is

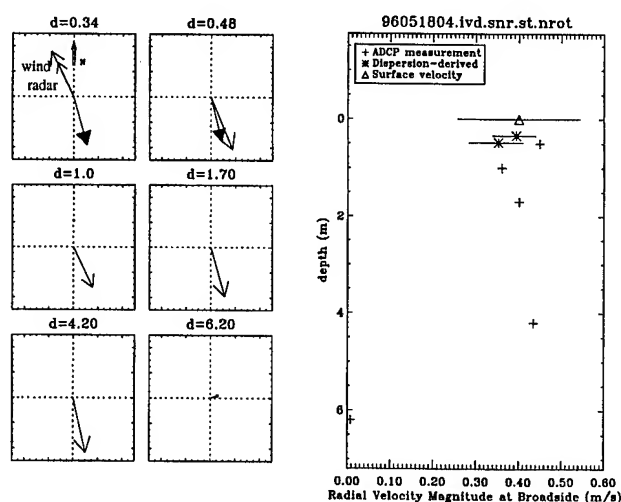


Fig. 4. Vertical profile of current structure when the radar is oriented down-wind and up-current. a) The series of vectors show the evolution of sub-surface current with depth. Solid arrows: radar-derived vectors. Non-solid arrows: ADCP measurements. b) Current evolution in the radar-broadside direction.

not so in the third example where the wind opposes the tidal flow. In this case the entire profile is not monotonically decreasing with depth.

A future study will compare surface current vectors, extracted from consecutive orthogonal acquisitions, with subsurface current vectors. For these vectors, comparisons with data from coincident INSAR overflights are also planned. Through direct comparison between the INSAR and FOPAIR measurements, effects of scene-decorrelation on interferometric surface-velocities will be studied.

REFERENCES

- [1] Goldstein, R. M., Barnett, T. P., and Zebker, H. A. Remote sensing of ocean currents. *Science*, 246:1282-1285, 1989.
- [2] Thompson, D.R. and Jensen, J.R. Synthetic aperture radar interferometry applied to ship-generated internal waves in the 1989 Loch Linnhe experiment. *Journal of Geophysical Research*, 98(c6):10259-10269, 1993.
- [3] Ainsworth, T.L., Chubb, S.R., Fusina, R.A., Goldstein, R.M., Jansen, R.W., Lee, J., and Valenzuela, G.R. INSAR imagery of surface currents, wave fields, and fronts. *IEEE Transaction on Geoscience and Remote Sensing*, 33(5):1117-1122, 1995.
- [4] Graber, H.C., Thompson, D.R., and Carande, R.E. Ocean surface features and currents measured with synthetic aperture radar interferometry and HF radar. *Journal of Geophysical Research*, 101(C11):25813-25832, 1996.
- [5] McIntosh, R.E., Frasier, S.J., and Mead, J.B. FOPAIR: A focused phased array imaging radar for ocean remote sensing. *IEEE Transaction on Geoscience and Remote Sensing*, 33(1):115-124, 1995.
- [6] Stewart, R. H. and Joy, J. W. HF radio measurements of surface currents. *Deep-Sea Research*, 21:1039-1049, 1974.
- [7] Frasier, S.J. and McIntosh, R.E. Observed wavenumber-frequency properties of microwave backscatter from the ocean surface at near-grazing angles. *Journal of Geophysical Research*, 101(C8):18391-18407, 1996.

The use of man-made features for long time scale INSAR

Stefania Usai

Delft Institute for Earth Oriented Space Research (DEOS)
Delft University of Technology, Thijsseweg 11, 2629 JA Delft, the Netherlands
phone: +31 15 278 2565, fax: +31 15 278 3711 E-mail: usai@geo.tudelft.nl

Abstract — From a series of interferograms spanning 3 and 1/2 years, a sample of features has been extracted which appear to have constantly high coherence for the whole time interval. These features, mainly of anthropogenic nature, have then been studied in order to assess whether they can be used for long time monitoring of slow deformation processes in almost completely decorrelated areas. For this purpose, both the coherence and the phase stability of the features have been checked along the time series.

INTRODUCTION

It is well-known that a strong limitation for time range applicability of repeat-pass differential SAR interferometry is temporal decorrelation. Therefore, we still cannot perform longterm studies of slow deformation processes like land subsidence and plate tectonics, in spite of the availability of SAR images over several years. However, even on very long time spans, highly coherent features are still present, mainly man-made features. The aim of this work is to investigate whether or not these highly coherent structures could be used for long time-scale monitoring of slow deformation processes. As a first step, a time series of interferograms has been generated, which constitutes

the database, spanning different time intervals between 1-day up to 3 1/2 years. The details and some remarks about the construction of such time series are shown. A sample of features showing high coherence on long time scale has then been selected, and their coherence has been studied along the whole series. For a subset of these features the phase stability has also been checked by means of the differential technique.

THE 1992-1996 TIME SERIES

The database is a time series of interferograms of the area around the city of Groningen, in the northern part of The Netherlands. The area is well known for its land subsidence, caused by the extraction of natural gas: the rate of land subsidence is up to 1 cm/yr. Fig.1 shows the interferograms generated, and their baseline components, column 5 contains the interferogram serial numbers, which are used as reference in the plots.

ANALYSIS OF THE COHERENCE

The coherence is estimated on a 2×10 window, the coherence and phase images are 2×10 multilooked. Fig.2 represents the coherence images on the shortest (tandem pair, no.9) and on the longest (about 3 1/2 years, no.1) time interval considered. Only those pixels having coherence higher than 0.8 in the coherence image no.1 were considered. Of this set of pixels, a subset has been considered, located in the area of the city of Assen (low left in the coherence images of fig.2), which contains a statistically significant number of such pixels. Fig.3 represents the coherence of these points as results in all the interferograms: each column represents an interferogram of the series, each horizontal line contains the values of the coherence for a given point. From fig.3 it is evident that interferogram no.8 presents a generally lower coherence: therefore, it has been excluded from the series in the second part of the work, the study on the interferometric phase. For more details about the construction of the time series and the results of the study on the coherence, see [2].

master	slave	B _{par}	B _{perp}	days	no
16-3-96	17-3-96	-17	24	1	9
16-3-96	11-2-96	36	212	34	8
16-3-96	20-4-96	50	145	35	7
16-3-96	21-4-96	18	79	36	6
16-3-96	6-1-96	-109	-129	70	5
16-3-96	20-8-95	-62	-272	209	4
16-3-96	19-8-95	-26	-190	210	3
16-3-96	15-10-92	5	25	1248	2
16-3-96	10-9-92	43	52	1283	1

Figure 1: The Groningen dataset. The 5th column shows the time span in days, the 6th the serial number of the interferogram

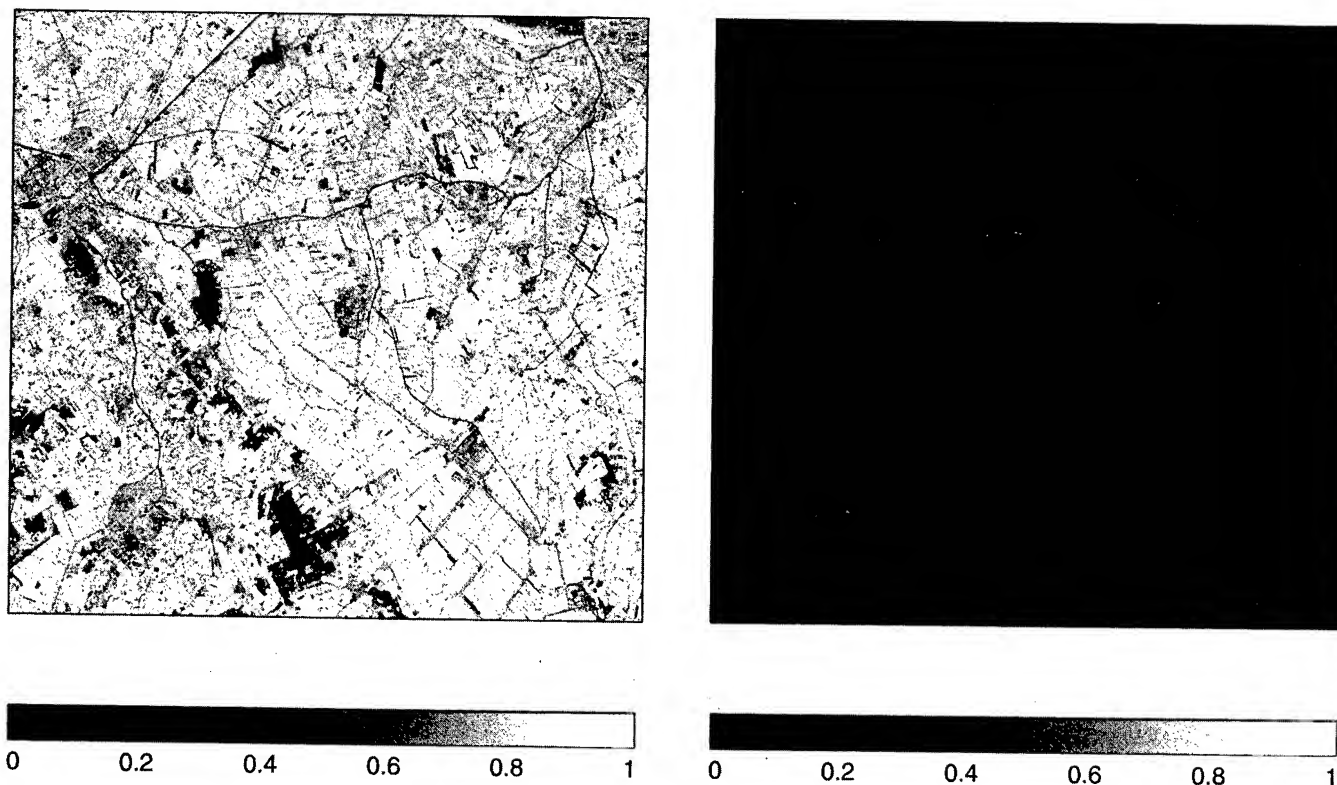


Figure 2: Coherence images respectively in the interferograms no. 9 (16-3-96/17-3-96) and no.1 (16-3-96/10-9-92)

ANALYSIS OF THE PHASE

The second step of the analysis consisted in checking whether those features showing constantly high coherence along the time series do maintain also phase stability in time. For this test, the area of Assen was particularly suitable, not only for the high concentration of features,

but also because it is the only city in the area which is not subject to land subsidence. The test consisted in applying the differential INSAR technique [1] along the time series. The interferograms no.1,2,5,6,7,9, have been considered for this purpose. From the set of pixels used for the study on the coherence (126 pixels), only those maintaining coherence above 0.8 in all the 6 interferograms were selected. They turned out to be 42. In each interferogram, the "spatial" phase difference of each pixels with respect to a reference pixel (which is the same in all interferograms) has been computed. For each of these differences, the value in interferogram no.7 has been taken as reference value and rescaled and subtracted from the corresponding phase difference value in all the other 5 interferograms. The "temporal" phase difference computed in this way, is shown in fig.4. Every line is the "spatial" phase difference between one pixel and the reference pixel plotted along the time series. From fig.4 it seems that most of the pixels considered do maintain phase stability on long time scale. From the same figure, it is also evident that the differential phases in interferogram no.2 has been undergone some disturbing effects (maybe bad meteorological conditions) which has affected the phase of many points. This is also evident from fig.5, where the standard deviations of all data within an interferogram has been plotted. Since interferogram no.6 differs from the reference interferogram no.7 of only one day, it seems reasonable to assume that for the most pixels the area represented is not changed

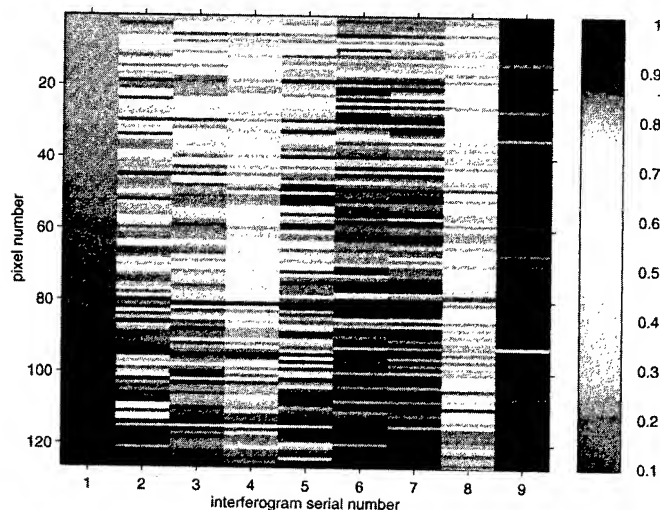


Figure 3: Coherence values for each point of the dataset and for each interferogram

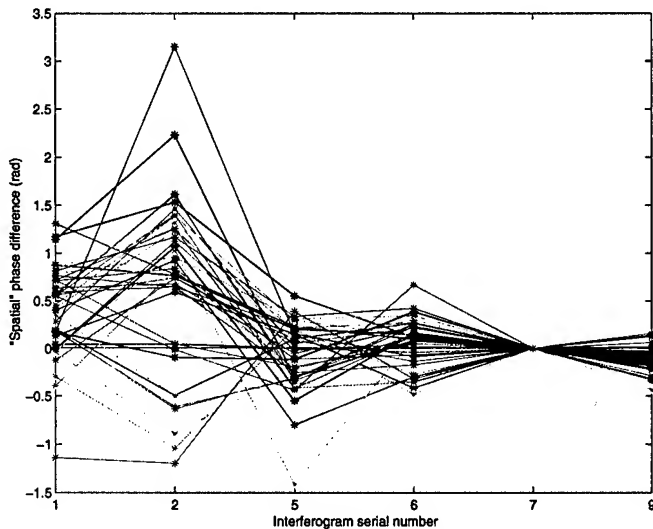


Figure 4: Differential phase values along the time series for constantly highly coherent pixels (Interf. no.7 has zero values because is taken as reference interferogram)

intrinsically, i.e. that a pixel represents an identical area in no.6 and no. 7. With this assumption, the standard deviation of the pixels in interferogram no.6 should represent occasional external disturbances of the backscattering from the pixels, due for example to different meteorological conditions, or to the presence of different scattering sources. The standard deviation in no.6 can thus be taken as representative of the "noise" of the computed differential phase measurements. From this standard deviation, with a simple error propagation it is possible to derive the standard deviation as a function of the perpendicular baseline, also represented in fig.5. Note that the "theoretical" values derived from the value in no.6, are generally lower than the standard deviations as determined from the data.

CONCLUSIONS

A time series of 9 interferograms has been generated covering time spans up to 3 and 1/2 years. Even on such a long time span, highly coherent features could be identified. The analysis of these features in the whole series permitted the identification and the exclusion of an interferogram showing significantly lower coherence than the others. A subset of constantly highly coherent pixels located in an urban area not subject to land subsidence has then been examined in order to assess the degree of phase stability of these features with respect to other factors than effective ground deformations. Most of these features turned out to be very stable even on the longest time span considered. However, reducing the time series only to those interferograms having baselines shorter than the baseline of the reference one, has limited the time series to

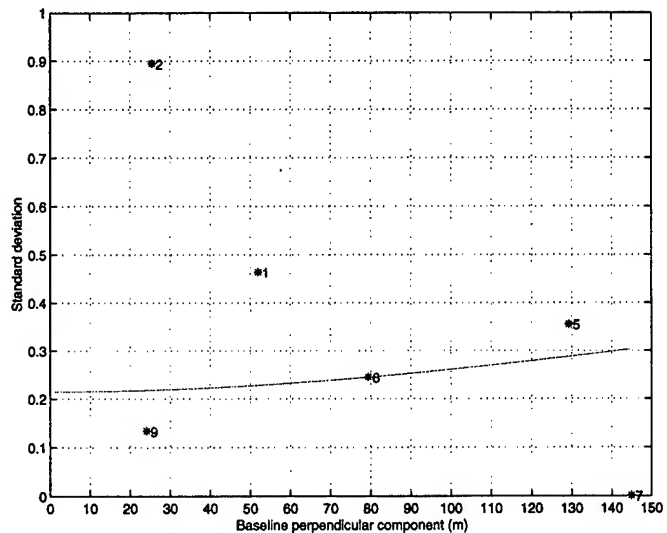


Figure 5: Standard deviations of the differential phases for each interferogram. The line is the "theoretical" standard deviation as derived from the value in interferogram no.6, the * are the computed values from the data.

6 elements. Moreover, in one of the interferograms the differential phase values turned out to be generally affected by some disturbing effect. It is evident that, in order to have more clear results, the time series should contain a large number of interferograms. This would make easier the identification of "bad" interferograms and at the same time the exclusion of such interferograms wouldn't impoverish significantly the time series. Finally, it has to be stressed that these are the first attempts to assess whether phase information coming from very small structures, whose reflection is limited to one or few more pixels, can be used for extending the time range applicability of the INSAR technique. In this sense, the results presented are an encouragement to perform more refined tests to study the interferometric characteristics of such features.

ACKNOWLEDGMENTS

...to P.Visser and R.Scharroo of DEOS for providing the ERS precise orbits.

REFERENCES

- [1] H.A. Zebker, P.A. Rosen, R.M. Goldstein, A. Gabriel and C.L. Werner, "On the derivation of coseismic displacement fields using differential radar interferometry: The Landers earthquake," *JGR*, vol. 99, no. B10 pp. 19617-19634, october 1994.
- [2] S. Usai and R. Hanssen, "Long time scale INSAR by means of high coherence features," *Proc.3rd ERS Symposium*, Florence, Italy, March 1997, available at <http://florence97.ers-symposium.org:80/>.

The Effect of Scattering from Buildings on Interferometric SAR Measurements

D. L. Bickel, W. H. Hensley, and D. A. Yocky

Sandia National Laboratories

Albuquerque, NM 87185-0537 USA

Telephone: 505-845-9038, Facsimile: 505-845-9888

Email: dlbicke@sandia.gov, whhensl@sandia.gov, dayocky@sandia.gov

Abstract

The determination of elevation models of buildings using interferometric synthetic aperture radar (IFSAR) is an important area of active research. The focus of this paper is on some of the unique scattering mechanisms that occur with buildings and how they affect the IFSAR height measurement and the coherence. We will show by theory and examples that the various data products obtained from IFSAR can be used to aid in interpreting building height results. We will also present a method that we have used successfully in mapping buildings in Washington D. C.

Introduction

IFSAR has become an important technology in providing digital elevation models (DEMs). Some advantages of IFSAR include all-weather capability and the promise of rapid-turnaround products by automated techniques. The latter is particularly important in the areas with buildings and other man-made structures.

Urban areas and other areas with buildings present great challenges for IFSAR processing. These challenges include height discontinuities, a large dynamic range of the image, layover, shadowing, multipath reflections, multiplicative noise from sidelobes, areas of low coherence, and so on. Natural terrain can exhibit these problems as well, but they are typically not as severe nor as prevalent as in urban areas.

Another issue is that the buildings can be relatively small, and thus require fine resolution. Finer resolution leads to image processing and signal-to-noise ratio (SNR) issues.

In the following sections, we will briefly touch on some of the problems presented above. In most of this paper, we will focus on the challenges presented by layover, and the role that the coherence plays in this area.

Scattering Example

Figure 1, an example image of the U. S. Capitol building, to illustrates some of the scattering issues encountered in SAR

images of buildings. The large dynamic range is apparent in the image. The building is dominated by areas of very bright isolated targets in close proximity to areas of no return. For IFSAR this implies that the multilook operation results in using pixels whose contribution is predominantly noise. Ideally, the multilook window size could be reduced for areas of high SNR.

Layover is an obvious problem in this image. The intense returns from the dome layover on top of the steps of the Capitol building. This makes retrieval of the height information from the steps very difficult. What may be less apparent is that the return from the steps can distort the height information of the dome. This issue, previously referred to as the "front-porch" effect in [1], will be discussed more later.

Many examples of shadowing are obvious in Figure 1. Less obvious is the presence of multipath near the edges of the building and around the dome and rotunda.

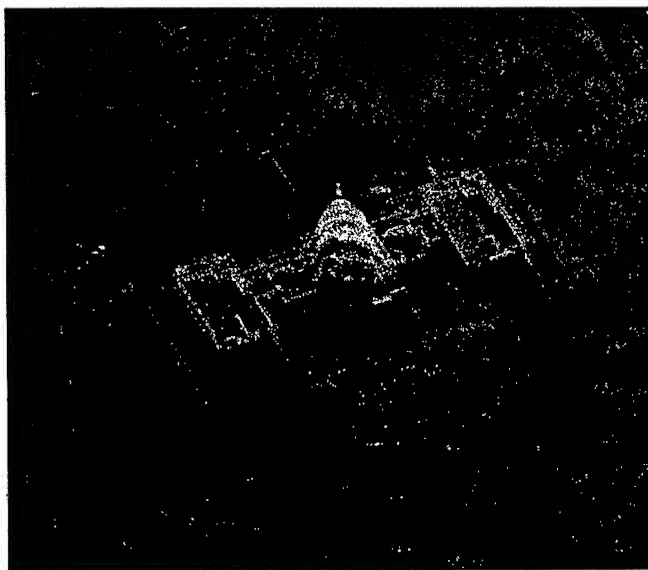


Figure 1: Example Image of the U. S. Capitol from the SNL Twin-Otter IFSAR Platform (near-range at top of image)

Issues in Reprojection for Orthorectification

The geometry of the measurements of IFSAR are in a (slant) range-Doppler plane projection. Typically, the results of the IFSAR measurements are reprojected into a top-down-looking geometry. A problem is presented in the reprojection, because the slant range may contain several samples from different parts of the side of the building located at several different heights. Figure 2 illustrates this problem. For the building, several heights are appropriate for the side of the building, ranging from the ground to the top of the building. The question becomes, which height is the appropriate height to use in the DEM? For terrain, we have chosen the height that corresponds to the maximum coherence [1]. For buildings, the DEMs are more presentable if they use the top of the building. Very often in buildings the height that corresponds to the maximum coherence does not correspond to the top of the building. In fact, the opposite is often true, due to the common presence of the strong dihedral return off of the front of the buildings. To find the top of the building, we must choose the maximum height given a reasonable coherence function. This idea can be thought of as an extension of the famous Golden Gate bridge example in [2].

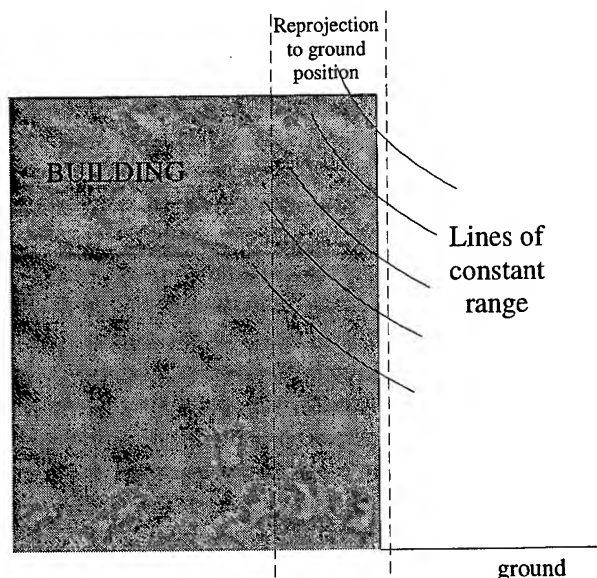


Figure 2: Multiple samples of side of building

Coherence and Layover of Buildings

IFSAR systems are built with the assumption that there is only one height sample per range-Doppler bin. In the case of layover, this assumption is invalid. In Figure 3, the front of the building is illustrated with the typical two competing samples at the top and the bottom of the building. As will be shown, the height determined by the IFSAR can be anywhere

from the top to the bottom of the building, within the range shell shown in the figure. The location within the range shell is determined by the ratio of the return from the top of the building to that of the bottom of the building. If the backscatter coefficients for the top and the bottom of the building are similar, the result is that the front edge of a building is shortened and pulled forward creating a false "front-porch" on the building.

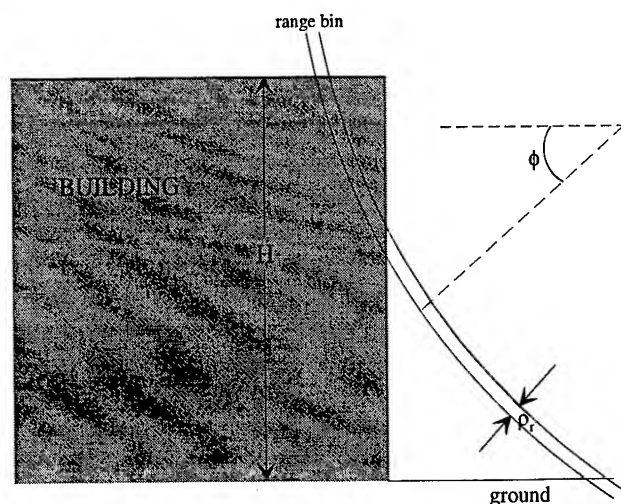


Figure 3: The effect of layover on IFSAR

The effects of layover in terms of estimated height as well as coherence can be explained by the van Cittert-Zernike theorem [3], [4]. In the case where several simplifying assumptions have been made, the normalized complex coherence can be shown to be:

$$\mu = \frac{\sin(\pi \cdot X)}{\pi \cdot X} \cdot \left\{ \beta \cdot \exp\left[\alpha \cdot \left(\frac{H}{2}\right)\right] + (1 - \beta) \cdot \exp\left[\alpha \cdot \left(-\frac{H}{2}\right)\right] \right\} \quad (1)$$

where:

$$X = \frac{2 \cdot \rho_r \cdot \tan \phi}{r_0 \cdot \lambda}$$

$$\beta = \frac{I_{\text{roof}}}{I_{\text{roof}} + I_{\text{ground}}}$$

$$\alpha = \frac{4 \cdot \pi \cdot B}{\lambda \cdot r_0 \cdot \cos \phi}$$

B - is the orthogonal component of the baseline
 I_{roof} , I_{ground} - intensity of return from roof and ground respectively

λ - is the wavelength of the radar

r_0 - is the range to the target

ρ_r , ϕ , H - as shown in Figure 3

From equation (1), we can deduce a couple of things. First, the height of the building will be biased to the stronger return area. If the roof has the stronger return, we will tend to estimate the roof height. The converse is true for brighter ground returns. Equation (1) proves the statement that we made earlier; namely, that if the ground and roof returns are similar, we will get a height in between.

Second, the magnitude of the coherence also contains geometry information in it. As an example, if β goes to 0.5, then the magnitude of the coherence is modulated by a cosine function whose frequency is determined by the height of the building. Hence, the coherence can be used as an indicator of problems due to layover. This phenomenon is strongly related to the volume-scattering effect discussed in [5] and other articles. Figure 4 shows an example of this drop in coherence for the Hirschhorn museum in Washington D. C.

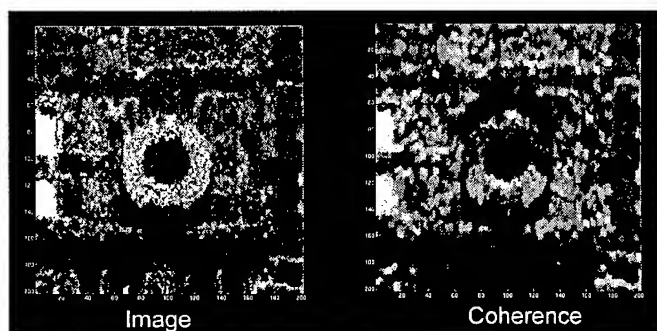


Figure 4: Backscatter and Coherence Images of the Hirschhorn Museum

The implication of equation (1) is that we can take advantage of the of the coherence to detect areas where we are receiving information from more than one target within the same range-Doppler bin. We found that we could use this coherence drop in generating the DEM of the Washington D. C. mall area. We did this by flying our IFSAR on opposite sides of the mall and registering the images. We then chose each height pixel value based upon the highest coherence. By doing this, we chose returns from the side which was least affected by layover. This reduced the problems that we had from the smeared-out fronts of the building resulting from the "front-porch" effect. Figure 5 shows the resulting height map.

Conclusions

In conclusion, we have discussed a number of challenges that commonly arise in attempting to form DEMs of buildings using IFSAR. We dwelled on the issues which crop up from the slant range geometry of IFSAR and layover effects. We

presented some ideas of how the IFSAR data could be used to avoid, or at least identify, the layover problems.



Figure 5: DEM of Washington D. C. Mall Area

Acknowledgments

This work was supported by the United States Department of Energy under Contract DE-AC04-94AL85000. Sandia is a multiprogram laboratory operated by Sandia Corporation, a Lockheed Martin Company, for the United States Department of Energy.

References

- [1] G. R. Burkhart, et al., "Elevation Correction and Building Extraction from Interferometric SAR Imagery", *Proceedings of the IGARSS'96*, Lincoln, NE., May 1996, Vol. 1, pp. 659-661.
- [2] H. A. Zebker and R. M. Goldstein, "Topographic Mapping from Interferometric Synthetic Aperture Radar Observations", *J. of Geophys. Res.*, 91(B5), pp. 4993-4999, April, 1986.
- [3] E. Rodriguez and J. M. Martin, "Theory and design of interferometric synthetic aperture radars", *IEE Proceedings-F*, Vol. 139, No. 2, April, 1992, pp. 147-159.
- [4] J. W. Goodman, *Statistical Optics*, John Wiley & Sons, 1985.
- [5] J. O. Hagberg, et al., "Repeat-Pass SAR Interferometry Over Forested Terrain", *IEEE Trans. On Geoscience and Remote Sensing*, Vol. 33, No. 2, Mar., 1995, pp. 331-340.

Quality Assessment of Coherence Between 35-day and Tandem Modes in ERS-1/2 Interferometric Studies

Nicolas STUSSI, Soo Chin LIEW, Kuldip SINGH, Leong Keong KWOH, Hock LIM
Centre for Remote Imaging, Sensing and Processing, CRISP,
National University of Singapore,
Lower Kent Ridge Road, 119260 Singapore, Republic of Singapore
Tel: (65) 772 80 29, Fax: (65) 775 77 17, E-mail: crsns@leonis.nus.edu.sg, Url: <http://www.crisp.nus.sg>

Abstract -- In this paper, we assess the quality of the coherence component γ derived from both tandem and repeat pass interferometric pairs. We first analyse the behavior of the coherence for various window sizes (number of looks). Results show that coherence is very sensitive to window size. A compromise between window size and resolution have to be found in order to better estimate the coherence. We present the first results of simulations using a simple statistical model for the coherence in order to evaluate the noise.

Moreover, we investigate the suitability of 35-day repeat pass for landuse classification. Repeat pass interferometry (35 days) is not appropriate for this application. Nevertheless, a combinaison of γ derived from tandem pair, and the $\Delta\gamma$ obtained from both tandem and repeat pass pairs should give useful information for land-use classification.

INTRODUCTION

It has been demonstrated that coherence component derived for interferometric processing can give useful information for discriminating different landcover types. For these studies, tandem is more appropriate [4,5] than 35-day repeat pass. In this paper, we analyse the quality of the coherence. Noise in the coherence image is analysed and temporal decorrelation is also investigated for the two acquisition modes.

ESTIMATION OF THE COHERENCE

The degree of coherence γ for each pair (s_1, s_2) of co-registered complex values s_1, s_2 is given by

$$\gamma = \frac{\langle s_1 s_2^* \rangle}{\sqrt{\langle s_1 s_1^* \rangle \cdot \langle s_2 s_2^* \rangle}} \quad (1)$$

where the bracket $\langle \dots \rangle$ represents an ensemble average, which is estimated by the spatial average over a finite-size window (N samples):

$$\langle s_1 s_2^* \rangle = \frac{1}{N} \cdot \sum_{i=1}^N s_{1,i} \cdot s_{2,i}^* \quad (2)$$

A first study was conducted to assess the quality of the estimation of the coherence. Coherence value highly

depends on the number of complex samples N (eq. 2) used for the ensemble average (i.e. number of looks).

A tandem interferometric pair ERS-1/2 of Singapore (acquired in May 1996) is used for this study. Coherence image obtained for 2x8 window (number of pixels in range and azimuth direction) appears to be very noisy (fig. 1). This image can be compared with Fig. 2 obtained for a 5x20 window. The latter appears sharper, with a better contrast.



Fig. 1: Coherence image of Singapore (Tandem pair, May 1996)
window size (r,a) = (2,8)



Fig.2: Coherence image of Singapore (Tandem pair, May 1996)
window size (r,a) = (5,20)

In order to analyse the statistical distribution of the noise, we first estimate the coherence level over the ocean, for which γ is expected to be very low due to a complete decorrelation of the radar signal. Fig. 3 represents a series of histograms of the coherence obtained for various window sizes. Notice that the degree of coherence is very sensitive to the number of looks. A better estimation of γ is then obtained for large window, for which the standard deviation appears to be smaller.

Four main classes relating to different degrees of coherence are then considered: ocean (complete decorrelation of the

signal), forest (low coherence), grasslands (middle range values) and built-up areas (high coherence).

Fig. 4 shows the variations of the estimated γ for various window sizes. This graph shows that the coherence level is generally overestimated for small window sizes, and tends to decrease when the window size increases.

For expected low coherence (ocean and forest), γ decreases slowly over a large range of values. For high coherence values, γ drops rapidly for small window sizes and asymptotically tends towards a constant level $\gamma^{(\infty)}$.

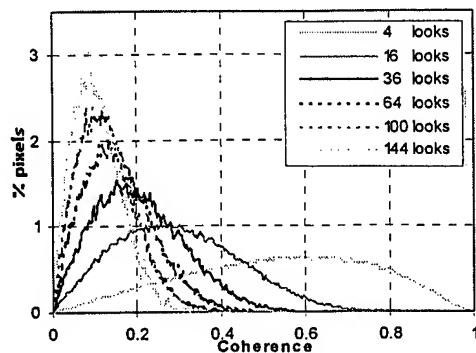


Fig. 3: Histograms of coherence over ocean for different window sizes. Tandem pair (May 96), Singapore

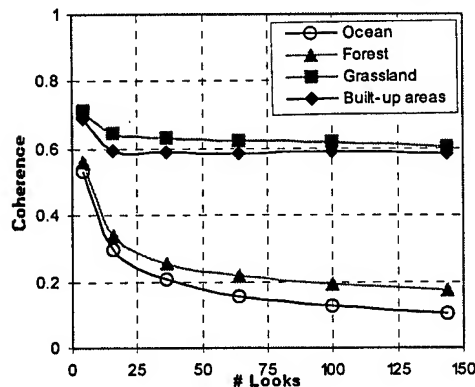


Fig. 4: Coherence as a function of number of looks for different classes. Tandem pair (May 96), Singapore

A compromise between window size and resolution have to be found in order to have a good estimation of the coherence without a loss of spatial resolution. A window size of 3x12 appears to be appropriate for tandem interferometric pair.

STATISTICAL MODEL FOR COHERENCE

We present in this paper a statistical model for the coherence. Complex values s_1 and s_2 of the two images of the interferometric pair are now considered as:

$$\begin{cases} s_1 = g + n_1 \\ s_2 = g + n_2 \end{cases} \quad (3)$$

Where g is the signal component; n_1, n_2 are the noise components, assumed to be normally distributed for the

real and imaginary parts separately. Coherence $\gamma^{[N]}$ computed over N pixels is then (4):

$$\gamma^{(N)} = \frac{\left| \sum_{i=1}^N (g + n_{1i}) (g + n_{2i}) \right|}{\sqrt{\left(\sum_{i=1}^N (g + n_{1i}) (g + n_{1i}) \right) \left(\sum_{i=1}^N (g + n_{2i}) (g + n_{2i}) \right)}}$$

$$\text{When } N \rightarrow \infty, \text{ we have: } \gamma^{[N]} \rightarrow \frac{\langle g \cdot g^* \rangle}{\langle g \cdot g^* \rangle + \langle n \cdot n^* \rangle} \quad (5)$$

Simulated coherence $\tilde{\gamma}^{[N]}$ and standard deviation $\tilde{\sigma}_\gamma^{[N]}$ are then computed for various window sizes using different g values over a large number of samples (5000 samples). Fig. (5) shows the comparison between simulation and observation.

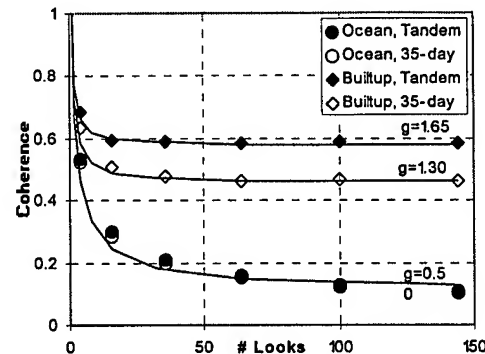


Fig. 5: Simulation of coherence for different numbers of looks and comparison with observation.

For high coherence value (built-up areas), simulation fits very well with observation. Nevertheless, simulated $\tilde{\sigma}_\gamma^{[N]}$ appears smaller than the observed $\sigma_\gamma^{[N]}$. This is due to heterogeneity of the coherence over built-up areas in the image.

For ocean, we observe a systematic error in the curve. The simulated coherence values are higher for a small number of looks, and lower for a large number of looks. This behavior needs to be investigated further in order to improve the statistical model.

TEMPORAL DECORRELATION

We next analyse the effect of temporal decorrelation between tandem and 35-day repeat passes. Both interferometric pairs should have similar baseline values (B_p, B_n). Moreover, small (B_p, B_n) are considered (typically from 50m to 300m) in order to reduce the effect of baseline decorrelation [2].

Coherence for 35-day repeat pass is analysed for four main landcover classes. Fig (6) shows clearly the drop of coherence for grassland compared to results obtained for tandem pass (Fig. 4). This is mainly due to changes in landuse and weather condition (moisture content) over one cycle. Moreover, γ_{forest} tends to be closer to γ_{ocean} . This

implies that radar signal over forest is completely decorrelated after one cycle (35 days). Coherence over built-up areas remains high, despite a small decrease of γ of around 0.15.

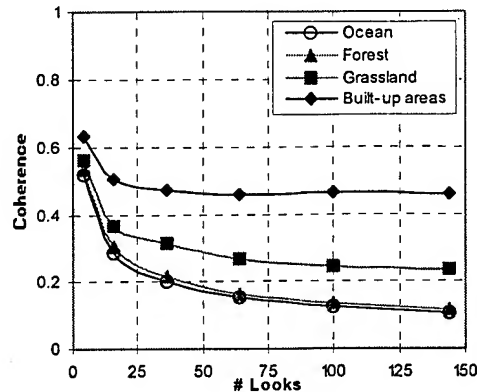


Fig. 6: Coherence as a function of number of looks for different classes .35-day repeat pass (April/May 96), Singapore

Statistical distribution of coherence for tandem and 35-day repeat passes are compared for different landcover types in order to evaluate the suitability of each acquisition mode for land-use classification.

Fig. (7) and fig. (8) show the histograms of coherence for forest and grassland using tandem and 35-day repeat pass modes respectively. We can see that the histogram of coherence for grassland is shifted to the left, corresponding to a overall decrease of coherence with 35-day repeat pass. Moreover, the width of the histogram is wider for the 35-day repeat pass.

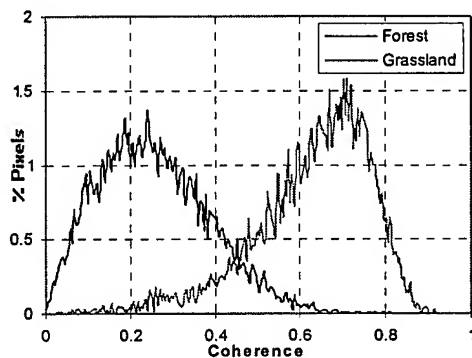


Fig. 7: Comparison of histogram of coherence for forest and grassland for tandem pass

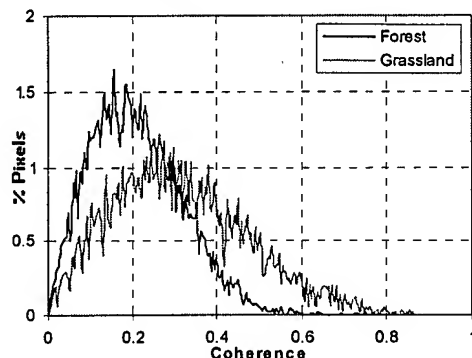


Fig. 8: Comparison of histogram of coherence for forest and grassland for 35-day repeat pass

From fig. (8), we can see clearly that the histograms of forest and grassland (tandem pass) are well separated. On the contrary, the two histograms are significantly overlapped for the 35-day repeat pass (fig. 9).

These results are consistent with those obtained in [4] over tropical forest. For this reason, we can conclude that coherence derived from 35-day repeat pass can not be used as a useful parameter from landcover classification [4,5,6]. Nevertheless, the variation of coherence ($\Delta\gamma$) between γ_{tandem} and $\gamma_{35\text{-day}}$ can be used as an other discriminator which can be taken into account for landcover classification [6].

DISCUSSION / CONCLUSION

We have demonstrated that coherence value is very sensitive to the window size (number of looks). A compromise between window size and resolution have to be found (3×12 for tandem). The simulations presented in this paper give good results for high coherence value, but a systematic error exists for low coherence values. The statistical model will be investigated further.

Moreover the temporal decorrelation greatly affects the complex radar signal. In order to have a better estimation a γ with 35-day repeat pass, the window size should be increased slightly (typically to 4×16). As previously presented in [4] and [5], tandem pair appears to be more suitable for landuse classification. Moreover, a combinaison of γ_{tandem} derived from tandem pair, and the $\Delta\gamma$ obtained from both tandem and repeat pass pairs should give additional useful information for land-use classification.

REFERENCES

- [1] U. Wegmuller and C. L. Werner, "SAR Interferometric Signatures of Forest", *IEEE Trans. Geosci. Remote Sensing*, Vol. 33, no. 5, 1995, pp 1153-1161.
- [2] H.A. Zebker and J. Villasenor, "Decorrelation in Interferometric Radar Echos", *IEEE Trans. Geosci. Remote Sensing*, Vol. 30, no. 5, 1992, pp 950-959.
- [3] F. Gatelli, A. M. Guarnieri, F. Parizzi, P. Pasquali, C. Prati and F. Rocca, "The Wavenumber Shift in SAR Interferometry", *IEEE Trans. Geosci. Remote Sensing*, Vol. 32, no. 4, 1994, pp 855-864.
- [4] N. Stussi, L.K. Kwok, S.C. Liew, K. Singh, H. Lim, "ERS-1/2 Interferometry: Some Results on Tropical Forest", *FRINGE 96*, Zurich, Switzerland, October 1996.
- [5] N. Stussi et al., "Landcover Classification using ERS SAR/INSAR Data on Coastal Region of Central Sumatra", *3rd ERS Symposium*, March 17-21, 1997, Florence, Italy
- [6] N. Stussi et al., "Landcover Classification using ERS SAR/INSAR Data over Tropical Areas", *IGARSS'97*, August 3-8, 1997, Singapore

Combination of Linear and Circular SAR for 3-D Features

H. Rudolf, D. Tarchi and A. J. Sieber

Advanced Techniques, SAI JRC 21020 Ispira (Va), Italy
Tel/Fax: +39 332 785986/5772, E-mail: hans.rudolf@jrc.it

Abstract An economic and fast change of an existing radar system with a linear synthetic aperture into a system with 3-D capabilities will be presented. For actual and future fields of radar in remote sensing, such as high precision mine detection, highly accurate vegetation measurements and interferometric SAR applications the importance of resolution in the third dimension is growing fast. Until now a such a radar required an expensive phased array antenna, a costly narrow-beam scanning system, or a combination of both of them. In order to overcome these problems, the combination of an existing linear SAR outdoor system (LISA) with a circular aperture for vertical resolution led to a fast and economic additional 3rd dimension feature. A test experiment has been performed to validate the system and the implemented SAR processor. The very promising results are presented here.

I INTRODUCTION

From the very beginning of radar technology, resolution in the third dimension was considered an important feature of radar systems. This requirement was for example crucial in finding height, distance and angle of enemy airplanes. The first solutions produced the resolution in elevation the same way the resolution in azimuth was obtained. A steered antenna with a very small beamwidth was scanning in azimuth and elevation. Progress in electronic devices and signal processing allowed later the use of phased array antennas that can be steered also in azimuth and elevation. With the arise of remote sensing applications, interest in the third dimension was lost, as it was concentrated first on SAR technology and later on interferometry. Spaceborne SAR systems inherently did not allow resolution other than range and cross-range. The SAR principle has also been applied for other applications, one major step was the use of circular rather than linear antenna movement [1, 2]. Still resolution in three dimensions lacked these systems.

In the recent past, interest in tridimensional radar images was risen again with the emerge of different applications as, for instance, abandoned anti-personal mine searching, where the exact localisation of the objects is an essential feature of the desired sensor. Exact localisation means not only the locus in x- and y-direction, but

also the depth. The resolution in depth also enhances the sensitivity of such a sensor, as the backscattered signal of the mine is now separated from the reflection of the ground. Efforts have been made in the last few years to suit the SAR principle for tridimensional measurements. Solutions for laboratory measurements are ready [3], but for out-door use the need to scan in two dimensions prohibited the vast use of this principle.

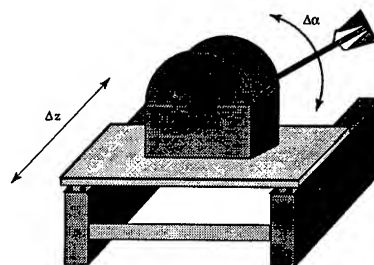


Figure 1: Combination of linear and circular scanning capabilities to realize a 3D SAR geometry.

In this paper we describe the implementation of a SAR portable system combining linear and circular scanning capabilities designed for in-field measurements in near and medium range.

After a detailed description of the system (section II) and of the different software tools implemented for data processing (section III) results of a test measurement performed on a tridimensional artificial target are presented (section IV). Finally, section V is devoted to the concluding remarks.

II COMBINED SAR

As stated in the introduction, there is a need for a simple, hence economic radar system for out-door use with 3D capabilities. By combining the linear and the circular SAR principle a system fulfilling this demand has been created. The basis of the presented radar sensor is the LISA system developed at the European Microwave Signature Laboratory (EMSL). The linear aperture is realized by a structure of rails of 5 meters length with a movement precision of less than 0.5 millimeters. Despite this high

mechanical accuracy, this system is designed for outdoor use, also under severe weather conditions.

Without enlarging the whole structure and with little changes on the control software a circular aperture has been added to this system. This has been achieved mounting the antenna system at one end of a metallic arm whose second end is fixed to a vertically mounted rotation table (fig. 1). The length of the arm is manually adjustable up to a maximum of about 2 m while the fine sampling along the vertical aperture is guaranteed by the accuracy in positioning of the rotation table which is better than a tenth of a degree. Due to this geometry we get not only a synthetic aperture in horizontal, but also in vertical direction, hence resolution in all three dimensions.

The advantages of this approach are obvious, drastically reduced costs compared to any phased array antenna, the easy change of ubiquitous linear SAR systems and therefore immediate operability.

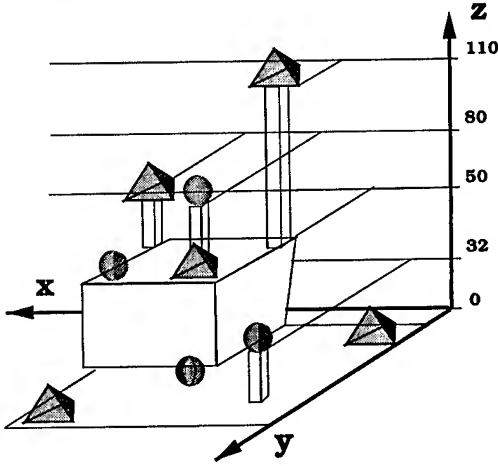


Figure 2: Target configuration for the test experiment

The microwave part is all done, as in the LISA system, by a Hewlett-Packard Network-Analyzer (HP 8753D) with included microwave source. The implemented frequency-range is presently limited by the antennas, nevertheless it covers a band from 500 MHz to 6 GHz. For high frequency operations a Hewlett-Packard Network-Analyzer HP 8510 is available, allowing a maximum frequency of 26.5 GHz. Either of these solutions allows full polarimetric coherent measurements. The RF-signal is amplified in order to measure also at large distances. As antenna set is available either a set of quadridged horn antennas or a log-periodic antennas covering the whole frequency range. System features are summarized in table I.

The calibration of the system is performed with the use of a full polarimetric procedure based on the measurement in near range of three reference targets (disc and dihedral in two different positions) [4]. The application of the calibration coefficients for target at larger distances is then achieved by introducing an appropriate range correction factor.

Table 1: System Parameters.

Trans. Mode	CW
Freq. Range	0.5 GHz - 6 GHz (26 GHz Optional)
Max. Power	ca. 55 dBm
Polariz.	HH,VH,HV,VV
Linear Range	5 m
Repeatability	.5 mm
Circular Range	270 deg.
Repeatability	.05 deg.
Computer	HP workst.

Both mechanic and electronic operations are controlled by a powerful Hewlett Packard RISC-Workstation (HP 9000/777) via a dedicated acquisition software program allowing to perform fully automated measurements in SAR mode.

III DATA PROCESSING

Besides the control operations during measurements, the workstation is also hosting dedicated software programs for data processing and SAR images focusing, making the system fully autonomous during long in-field campaigns. The processing applied to the raw data first concerns basic steps as the computation of calibration coefficients from the calibration measurements, application of calibration coefficients to the measured data and time domain gating in order to isolate the range-slice of interest.

Then data is processed in order to obtain a tridimensional SAR image. The SAR processor is a modified version of the Near-Field SAR Processor developed for the EMSL experimental conditions [5]. It is a phase preserving processor which accurately accounts for the measurement geometry and for the near-field phase distortion effects. In fact when the dimension of the target under test is electrically large in comparison to the distance between target and antenna, the spherical illuminating wavefront must be taken into account. For distant targets this correction is of course less important.

The resulting SAR image is in a right handed cartesian reference system with x-axis parallel to the displacement direction of the antenna system and y-axis parallel to the horizontal position of the arm. Spatial resolutions are given by the three following relationships for the x, y and z axis respectively [1, 5]:

$$D_x = \frac{c}{2X_a f} \sqrt{\left(\frac{X_a}{2}\right)^2 + R_0^2} \quad (1)$$

$$D_y = \frac{c}{2B_f \sin \theta} \quad (2)$$

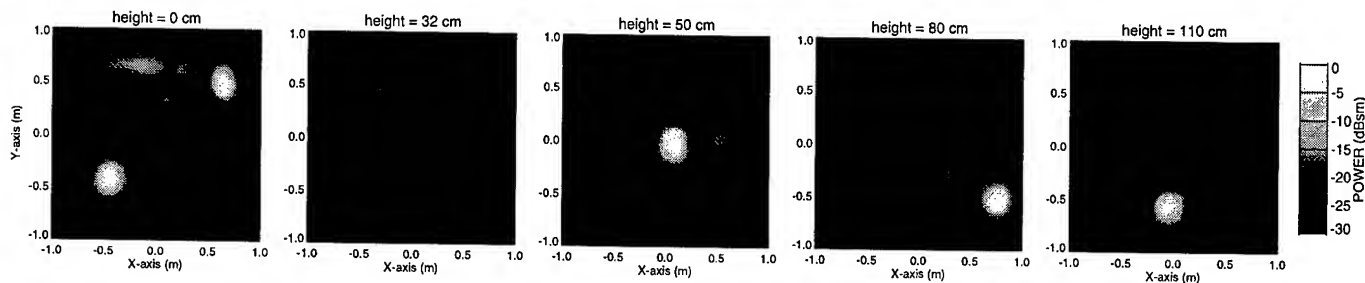


Figure 3: Five cuts at different heights of the 3D SAR image (power) corresponding to the planes where objects have been placed. The scale is normalized to the maximum inside the whole data cube.

$$D_z = \frac{c}{5fl\sin\frac{\gamma}{2}} \quad (3)$$

where X_a is the total displacement in cross-range, B_f is the frequency bandwidth, f is the center frequency, c is the speed of light, θ is the incidence angle, l the length of the arm, γ the is the 3-dB beamwidth of the antennas and R_o the distance between antenna and target.

IV TEST EXPERIMENT

For the evaluation of the validity of the above described method, a test experiment has been performed using an artificial target made up of metallic spheres and trihedrals arranged in the tridimensional configuration shown in fig. 2. All the objects lie in five planes at different heights and are contained within a cube whose side is about 1.1 m.

The target has been placed at a distance of about 10 m from the antenna system. Table II summarizes the parameters of the performed measurement.

Table 2: SAR Measurement Parameters.

Linear (span/step)	2.6/.02 m
Circular (span/step)	42/1.2 deg
Frequency (start/stop/step)	4.5/6./0.005 GHz
Arm length	1.5 m
Polarization	HH

Fig. 3 shows five cuts at different heights of the resulting 3D SAR image (power) corresponding to the planes where objects have been placed. The illuminating wavefront is coming from the positive y axis and the power scale is normalized to the maximum value inside the reconstructed data cube. By inserting the measurements parameters listed in tab. II in eqs. 1-3 spatial resolutions of the image turn out to be about 10. cm, 10. cm and 20. cm for x,y and z axis respectively.

In the cuts of fig. 3 responses from trihedrals and spheres are clearly recognizable as the bright and weak hot spots respectively, due to the large difference in RCS,

and are exactly corresponding to the spatial locations of the real objects.

V CONCLUSION

The reported results validate this novel approach to tridimensional radar imaging. The additional information about the third dimension is being added without major intervention in existing linear SAR systems. The implemented microwave hardware with the network analyzer guarantees a maximum freedom for the choice of the electric parameters. The additional information of the third dimension enhances also the resolution of the sensor in case the target is camouflaged by other objects in the same plane. Typical applications of such a system can be highly accurate vegetation measurements, high precision measurements on man made targets, such as cars, exact location of objects in the space and last but not least mine detection.

REFERENCES

- [1] H. Klausling, "Untersuchung der Realisierbarkeit eines Radars mit synthetischer Apertur durch rotierende Antennen." MBB-Publikation, MBB-UA-1150-89-Pub, OTN-029299, 1989.
- [2] A. Broquetas, R. De Porrata, Ll. Sagués, "A Circular Synthetic Aperture Radar System for Ground-Based Applications." Proceedings of 1st EMSL User Workshop, EUR Report 17326EN, Part II, 1997.
- [3] A. J. Sieber, "The European Microwave Signature Laboratory." EARSel Advances in Remote Sensing, Vol. 2, No. 1, pp. 195-204, January 1993.
- [4] W. Wiesbeck and D. Kähny, "Single reference, three target calibration and error correction for monostatic, polarimetric free space measurements", *Proc. IEEE*, vol. 79, pp. 1551-1558, Oct. 1991.
- [5] J. Fortuny and A. J. Sieber, "Fast Algorithm for a near-field synthetic aperture radar processor", *IEEE Trans. Antennas Propagat.*, 42, 1458-1460, 1994.

Results of the Mt. Etna Interferometric E-SAR campaign

M. Coltelli⁽¹⁾, G. Fornaro⁽²⁾, G. Franceschetti^(2,3), R. Lanari⁽²⁾, A. Moreira⁽⁴⁾,
G. Puglisi⁽¹⁾, E. Sansosti⁽²⁾, R. Scheiber⁽⁴⁾, M. Tesaro⁽³⁾

⁽¹⁾ Istituto Internazionale di Vulcanologia (I.I.V.)

National Research Council (CNR)

piazza Roma, 2 I-95100 Catania, Italy

Tel.: +39-95-448084 Fax.: +39-95-435801 email: geo@iiv.ct.cnr.it

⁽²⁾ Istituto di Ricerca per l'Elettromagnetismo e i Componenti Elettronici (I.R.E.C.E.)

National Research Council (CNR)

via Diocleziano, 328 I-80124 Napoli, Italy

Tel.: +39-81-5707999 Fax.: +39-81-5705734 email: fornaro@irece1.irece.na.cnr.it

⁽³⁾ Dipartimento di Ingegneria Elettronica

University of Naples "Federico II",

via Claudio, 21 I-80125 Napoli, Italy

⁽⁴⁾ Institut fuer Hochfrequenztechnik

German Aerospace Research Establishment (DLR)

P.O.Box 1116, D-82234 Wessling, Germany

Tel.: +49-81-53282360 Fax.: +49-81-53281449 email: alberto.moreira@dlr.de

Abstract -- The paper is aimed to the presentation of the first interferometric results of the E-SAR system obtained by processing raw data relative to an area of extreme interest from the geologic and volcanic point of view: the Mt. Etna test site. A comparison between the resulting SAR DEM and an existing photogrammetric one is also included.

1. INTRODUCTION

The E-SAR is a SAR system mounted onboard a Dornier DO 228 aircraft and available at the DLR. The system is operative in the P, L, C and X-Band [1]. Starting from the 1995 an interferometric mode extension of the X-Band system has been included.

In the frame of a collaboration between the DLR, the I.R.E.C.E. and the I.I.V. an interferometric campaign of the E-SAR system in the south of Italy has been planned and realized in July 1996. Main scope of this campaign was the study of the Mt. Etna which is of high geological and volcanic importance. Additionally the campaign represents also a first test of the capabilities offered by the interferometric X-Band E-SAR system of the DLR.

A large amount of data, including L-Band polarimetric and optical one [2], was acquired in two areas located around the Etna volcano: the one considered in this paper is centered on the three summit craters.

A set of 11 corner reflectors were positioned on the Mt. Etna: 4 of them lie in the area we investigated. The positions of the corner reflectors were measured via high precision GPS receivers by researchers of the I.I.V. and provided in the UTM reference system with an accuracy of

5cm. The presence of corner reflectors allows to have useful tie points in the calibration and geocoding procedure.

2. OVERVIEW OF DATA PROCESSING

The E-SAR X-Band interferometric system has a bandwidth and a sampling frequency of 100 MHz, a pulse repetition frequency of 2 KHz (1KHz for each channel); the look angle varies from 30° to 60°, the baseline is of 1.65m and a tilt angle of 77°. The resulting pixel spacing is of 1.5m in slant range and of 8cm in azimuth for a nominal aircraft velocity of 80m/s.

The dimensions of the imaged area in the narrow swath mode is of 128k by 2k which results in about 10 Km in azimuth by 4 Km in ground range. For this experiment only 64k by 2k were processed from the raw data. A presuming of 4 has been applied to reduce the data to 16k by 2k.

The presumed data have been processed by using an extended chirp scaling SAR processing algorithm [3] whose phase purity were prior assessed on simulated data to be below 1° of differential phase error.

Motion Compensation (MoCo) is of extreme importance in airborne SAR processing; with this regard it is important to note that severe motion errors (due to the high aircraft instabilities) were present on the selected data: figs.1 and 2 show the plots of the vertical and horizontal displacements together with the velocity, roll, pitch and heading variations.

These motion errors were compensated during the raw data focusing operation with respect to two parallel tracks: a more detailed discussion about this problem can be found in [4].

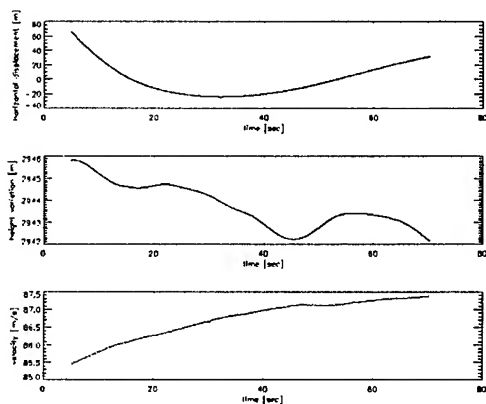


Fig.1: Horizontal, vertical and velocity variations.

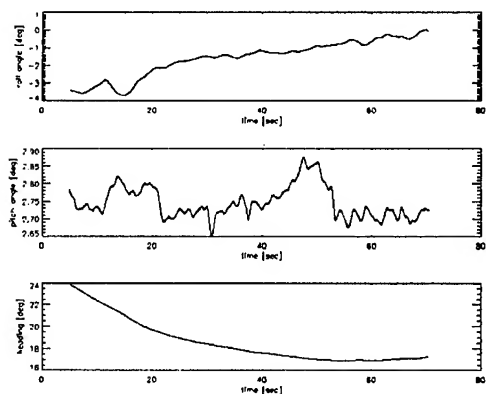


Fig.2: Roll, pitch and heading variations.

Three corner reflectors were included in the processed data and clearly visible in the focused images. Anyway one of them is located at the beginning of the data where strong motion errors were present in horizontal and heading variation (see figs.1 and 2). We considered it not reliable for further use due to the errors induced by the flat earth assumption in the MoCo step and the high variation of the Doppler Centroid along the azimuth direction.

Following the SAR focusing step, the phase difference (interferogram) was generated by complex multilooking 4 pixel in azimuth direction; further average was applied to reduce the data amount to 1k by 1k with a 5.2m (azimuth) and 4.25m (ground range) pixel spacing.

The interferogram was unwrapped via a weighted least square algorithm [5] and geocoded by using only one of the 2 remaining corner reflectors: namely the one positioned in the center of the scene.

3. RESULTS

This section is aimed to the presentation of the obtained results. In fig.3 are shown the interferometric fringes after the flat earth component removal. It is clear the absence of the roll angle variation after the motion compensation with respect to two parallel reference tracks. Clearly visible is

also the decorrelated area present in near range due to the fixed range delay and the very steep scene topography (1000m height variation).



Fig.3: Interferometric fringes

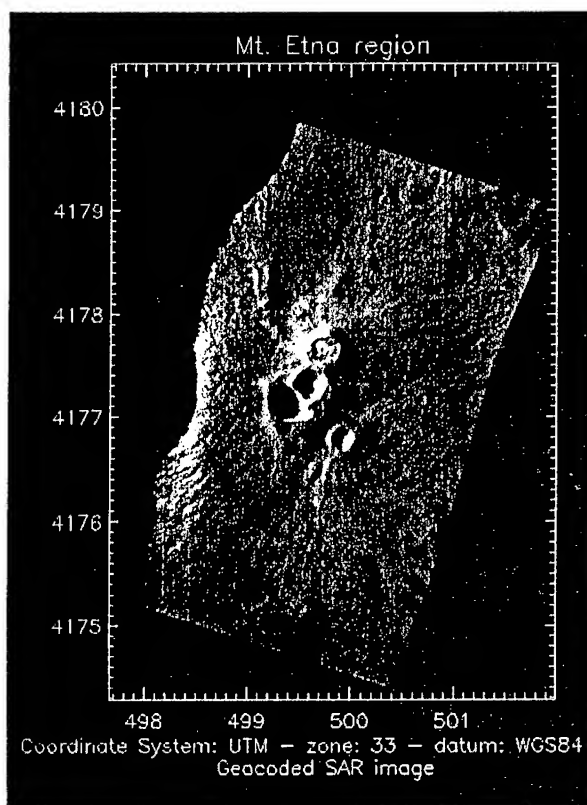


Fig.4: Geocoded SAR Image.

In fig.4 it is presented the geocoded SAR image in the UTM reference system while in fig.5 it is shown a suggestive 3-D view of the obtained DEM combined with the geocoded multilook SAR image. The height error on the corner

reflectors not used in the geocoding step is of 5m and -8m; this latter refers to the critical corner reflector at the beginning of the track.

The reconstructed SAR DEM is on a 5m by 5m grid and has been compared with an existing one obtained via a photogrammetric technique in an 25m UTM grid with 5m height accuracy. The comparison has been carried out in terms of mean and standard deviation of the error by resampling the reconstructed SAR DEM on the 25m pixel spacing grid. The numerical results on the whole image (10.5 km²) are of -8.7m mean error and 9m standard deviation. The same evaluation, once that the decorrelated

area corresponding to the summit craters (see fig.3) has been cut away from the measurement, gives a mean error of -8m and a standard deviation of 7.9m. It is worth to note that the obtained results must be also interpreted together with the phase errors induced by the MoCo of the severe flight instabilities [4].

ACKNOWLEDGMENTS

The authors wish to thank Ralf Horn for performing the kinematic GPS processing and Dr. Stefan Buckreuz for the useful discussion about the motion compensation problem.

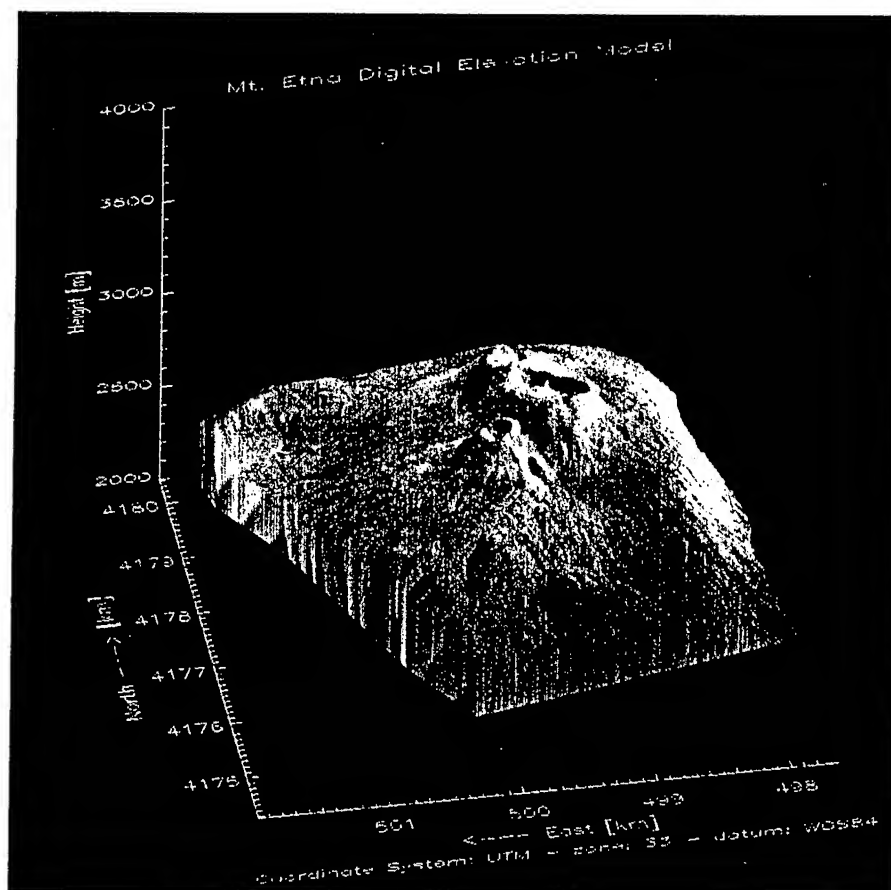


Fig.5: 3-D view of the obtained DEM combined with the geocoded SAR image

REFERENCES

- [1] R.Horn, 'The DLR Airborne SAR Project E-SAR', *Proc. of IGARSS Symposium*, Lincoln, Nebraska, 1996.
- [2] R.Horn et al., 'Mount Etna Case Study: A Multisensor View', *Proc. of IGARSS Symposium*, Singapore, 1997.
- [3] A.Moreira, Y.Huang, 'Airborne SAR Processing of Highly Squinted Data Using a Chirp Scaling Approach with Integrated Motion Compensation', *IEEE Trans. on Geosci. Remote Sens.*, vol. 32, pp.1029-1040, September 1994.
- [4] E.Sansosti, R.Scheiber, G.Fornaro, M.Tesauro, R.Lanari, A.Moreira, 'On the Motion Compensation and Geocoding of airborne-Interferometric SAR data', *Proc. of IGARSS Symposium*, Singapore, 1997.
- [5] G.Fornaro, G.Franceschetti, R.Lanari, D.Rossi, M.Tesauro, 'Finite Element Method for interferometric SAR phase unwrapping', *EUROPTO-SPIE*, pp.238-249, Taormina, 1996.

Detecting Change in Equatorial Regions of Brazil Using Medium Resolution Satellite Imagery

Chad F. Emmett. Department of Geography, 674 SWKT, Brigham Young University,
Provo, Utah 84602. Email: chad_emmett@byu.edu. Phone: (801) 378 - 7886.

Ryan R. Jensen, Perry J. Hardin, and David G. Long. Microwave Earth Remote Sensing Group,
676 SWKT, Brigham Young University, Provo, Utah 84602
Email: perry_hardin@byu.edu. Phone: (801) 378-6062

I. INTRODUCTION

Currently there is an extended international effort to monitor the change in global rain forest and equatorial woodlands. Because of government incentives, land reform, and general population pressures, the natural vegetation in these regions is being replaced by an anthropogenic agricultural mosaic.

Because of frequent cloud cover in these regions, active microwave imagery such as the ERS-1 SAR is preferred over high-resolution visible and near infrared spaceborne sensors for monitoring landscape degradation. Nevertheless, because rain forest and savanna vegetation cover such vast regions, AVHRR and its derivative vegetation indices are frequently used for medium or low-resolution monitoring where comprehensive high-resolution imaging would create unmanageable data volumes, or would be cost prohibitive. Areas showing significant change then become targets for data acquisition with higher resolution sensors such as SPOT or Landsat. In a few cases, expensive airborne sorties may be warranted.

While the cloud cover problem has always been the plague of visible and near-infrared remote sensing in equatorial regions, other problems exist. For example, many types of vegetation, such as primary equatorial forest and its older, degraded, secondary forest counterpart, frequently display very little difference in near-infrared or visible wavelength reflectance. Furthermore, conversion of forest, woodland, and grassland to agriculture is frequently slow and patchy in character. From a remote sensing perspective, this creates mixed pixels which are difficult to classify into a specific vegetation class with any certainty based on visible and near infrared data alone.

Over the past few years, reconstructed scatterometer and radiometer imagery has been used for equatorial forest inventory. This paper presents results of a project to monitor large-area changes in the natural Brazilian landscape which is apparent between 1978 and 1996. The 1978 image originates from the Seasat-A scatterometer (SASS), whereas the 1996 image is reconstructed from recent 1996 NASA (NSCAT) imagery.

II. LAND CONVERSION IN BRAZIL

Deforestation in Brazil is the result of many complex and interrelated processes. The most often cited causes include commercial logging, cattle ranching, farming, gold digging, and road building, but these causes fail to reflect the larger and more complex issues facing the government and people of Brazil which lead to deforestation. Issues of drought, soil fertility, poverty, rapid population growth, rural to urban migration, land reform, foreign debt, energy needs (including hydroelectric and charcoal), and territorial security have all had an influence on the changing use of land in Brazil's rain forest region [1].

Concerted efforts by the Brazilian government in the 1960s and 1970s to develop Amazonia illustrate the interrelated causes of deforestation. Smith (1982) offers three general causes: 1) Geopolitical reasons motivated Brazil to increase settlement in Amazonia to prevent loss of territory and resources to neighboring states and to effectively incorporate the territory into national society. 2) Demographic and economic challenges in the more densely populated coastal regions and in the less developed and drought ridden northeast region prompted the government to view Amazonia as a "safety valve" for Brazil's overpopulated cities and economically depressed regions. 3) The rich resource potential of Amazonia offered Brazil the hope of decreasing its foreign debt and thereby moving into the ranks of the world's more developed countries. To obtain these benefits, Brazil moved its capital to inward oriented Brasilia, launched an extensive road building project which sent soldiers to border states and brought settlers, miners and ranchers to frontier territories such as Rondonia [2].

III. DATA

Satellite scatterometers are active microwave radar instruments originally designed to measure the radar backscatter of the ocean's surface under all-weather conditions. Between June and October of 1978, the Seasat-A scatterometer (SASS) was able to obtain nearly continuous global coverage at a spatial unit cell resolution of 50km until a catastrophic short-circuit in the satellite's electrical system terminated subsequent data acquisition. The two SASS antennas (one on each side of the instrument) were arranged

at two different azimuth angles. As the satellite orbited, a resolution element on the surface of the Earth was observed first by the forward looking antenna and then by the aft antenna a minute or two later. This produced two sets of co-located, nearly simultaneous observation pairs from two different azimuth angles. The result of this arrangement is a set of vectors – multiple σ_0 measurements made of each cell over an irregular 50-km by 50-km along-track / cross-track sampling grid. By utilizing the overlap in these measurements, SASS data collected over the 99 day period was reconstructed into a single, enhanced resolution image [3]. A reconstructed image for central South America is shown in Figure 1.

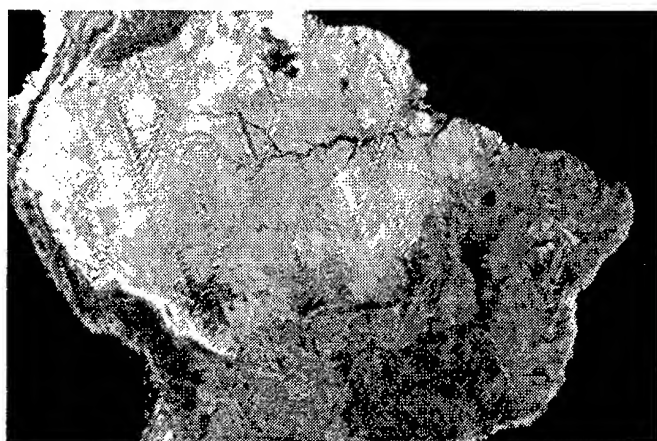


Figure 1: Reconstructed SASS image, 1978.

Launched in August, 1996, the NASA scatterometer (NSCAT) was also designed to measure ocean wind vectors. As discussed elsewhere [4], NSCAT is heavily based on SASS with significant improvements to enhance backscatter measurement accuracy at a spatial resolution of 25 km. Although designed primarily as an ocean-wind instrument, NSCAT data is also collected over land. Resolution enhancements similar to those applied to SASS permit image cell sizes approaching 8 km. An NSCAT composite, covering nearly the same seasonal time period as the SASS composite is shown as Figure 2.

IV. METHODS

In performing change detection with satellite imagery, three methods are popular. The first is simple image subtraction – the image pixels are subtracted on a cell-wise basis, creating an image of difference between the two represented time periods. Alternatively, the two images can be ratioed on a cell-wise basis, and then subjected to a logarithmic transform. The third method involves simple linear regression. The later-date image becomes the dependent variable, while the pixels in the early image are the independent variable. A regression equation is created which best predicts the later-

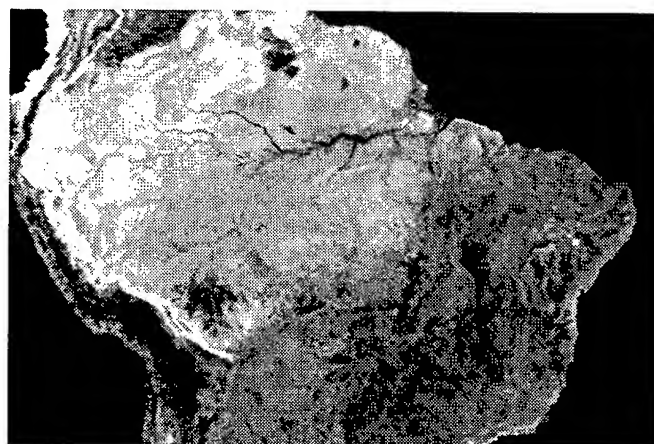


Figure 2: Reconstructed NSCAT image, 1996.

date image values from the early-date values. The residuals remaining after the fit, when displayed on a pixel-by-pixel basis, become the image of change.

In this study, all three methods were performed to detect large-area change between 1978 and 1996. Since the results produced by the three methods were nearly identical, only the simple image differencing product was used for interpretation.

Primarily because of noise in the reconstructed SASS image, the resulting difference image was quite noisy. To remove the noise, an overall difference image mean and standard deviation were calculated. Only those pixels with differences above or below two standard deviation units were considered as representing substantial change. These pixels were replotted on the 1996 NSCAT image and interpreted. Figure 3 shows those areas of change.

IV. INTERPRETATION

Several trends are easily seen in the image. While most of the Amazon basin appears unchanged, some areas, especially along the frontiers, have clearly been altered. These regions are represented by a "1" on the image. As mentioned previously, several Brazilian government policies encourage this deforestation. One example shown on Figure 3 is in the state of Rondonia, located in the southwestern section of Brazil's Amazon. Brazil Road - 364 was constructed in 1964 to allow more access to the Amazon Basin. BR-364 was widely used in the late 1970s and 1980s as the only means for people of different states to enter Amazonia. As a result, the state of Rondonia has undergone massive deforestation along the road and its side-roads. This same trend can be seen in the states of Para and Maranhao in the southeast corner of Brazil's Amazon. These locations generally contain submountainous transitional wet closed forests. When cultivated intensively, they rapidly lose native fertility after

three or four seasons. If erosion and compaction of the cultivated area is not too severe, the land reverts to a secondary forest or woodland. Otherwise, the land converts to a wasteland of shrubs, grasses, and noxious weedy species. Cattle ranching has also caused environmental damage in these regions.

Large amounts of change are also evident along Brazil's eastern coast. In these cases, it is the classic Brazilian Atlantic Forest which is suffering from clearance. As coastal states such as Espirito Santo, Bahia, Alagoas, and Pernambuco undergo rapid urban and rural population growth, land-use conversion from forest is inevitable. Example locations are labeled in the image with a "2".

States such as São Paulo and Rio de Janeiro show little change because most of their spatial growth preceded the 1978 Seasat-A flight.

VI. REFERENCES

1. P.M. Fearnside. Deforestation in Brazilian Amazonia: The Rates and Causes of Forest Destruction. *The Ecologist*. 19 (6) 214-218 (Nov/Dec 1989).
2. H. Smith. *Rain Forest Corridors: The Transamazon Colonization Scheme*. (Berkeley: University of California Press, 1982)
3. D.G. Long, P.J. Hardin, and P.T. Whiting. Resolution Enhancement of Spaceborne Scatterometer Data. *IEEE Trans. Geosc. and Remote Sensing*. 31 (3) 700 - 715 (1993).
4. F.M. Naderi, M.H. Freilich, and D.G. Long. Spaceborne Radar measurement of wind velocity over the Ocean: An Overview of the NSCAT Scatterometer System. *Proc. IEEE* 79 (6) 850 - 866 (1992).

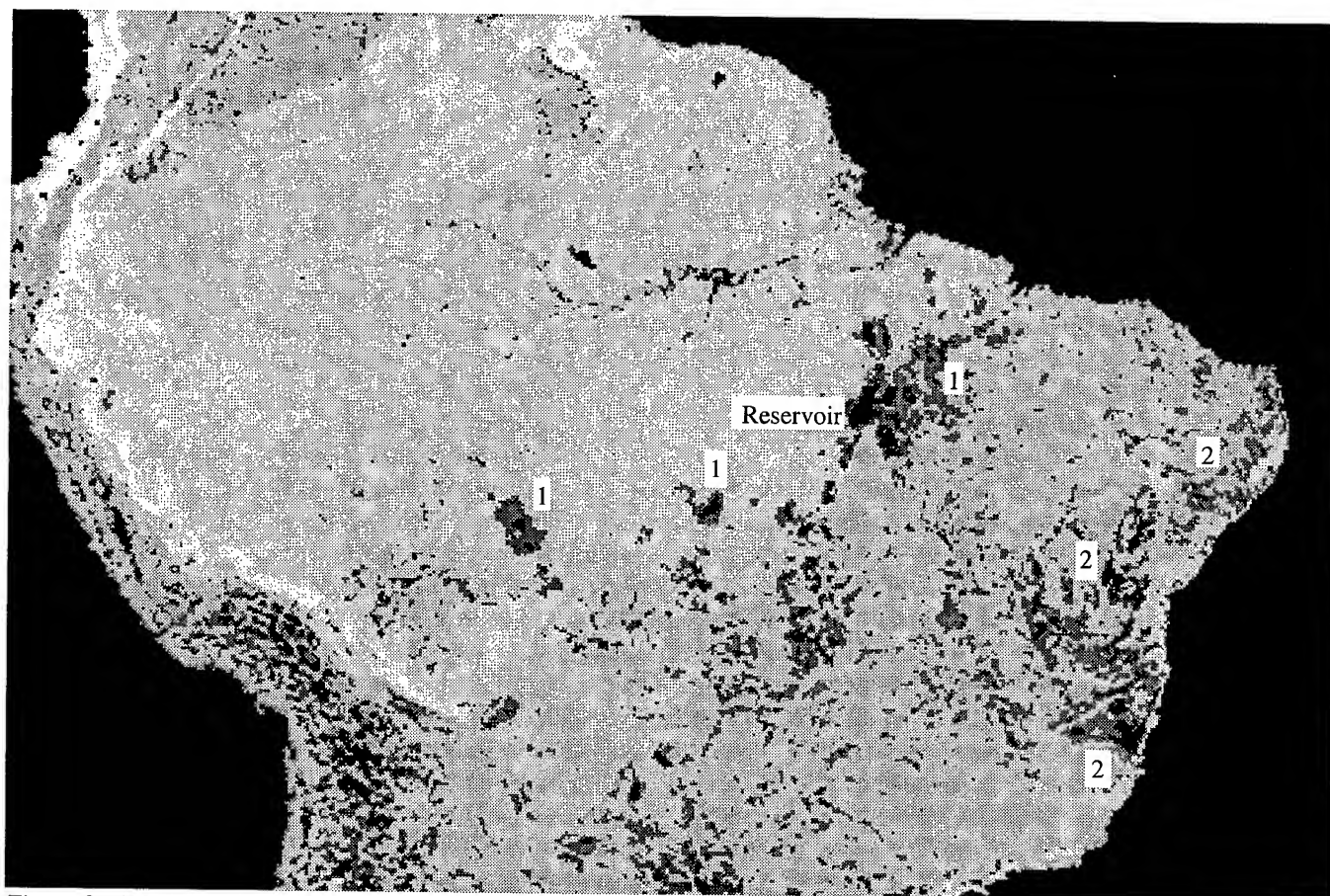


Figure 3. Areas of change within the study area. Areas of severe change in backscatter between the two dates show up as black. Areas of moderately severe change show up as dark gray patches. The areas of change are cast on the 1996 NSCAT image. Areas of apparent change in the Andes Mountains are an artifact of seasonality and the imaging process.

DEFORESTATION MONITORING IN TROPICAL REGIONS USING MULTITEMPORAL ERS / JERS SAR AND INSAR DATA

Florence Ribbes, Thuy Le Toan, Jérôme Bruniquel, Nicolas Floury
CESBIO, 18 av. E. Belin, bpi 2801, Toulouse Cedex 4, FRANCE
Tel : +33 561 55 85 12 - Fax : +33 561 55 85 00 - e-mail : ribbes@cesbio.cnes.fr

Nicolas Stussi, Soo Chin Liew
CRISP, National University of Singapore, Lower Kent Ridge Road, Singapore 119260
Tel : +65 772 80 28 - Fax : +65 775 77 17 - e-mail : crsns@leonis.nus.sg

Upik Rosalina Wasrin
SEAMO BIOTROP, Jl Raya Tajur Km 6, PO Box 116, Bogor, Indonesia
Tel : +62-251 371 654 - Fax : +62-251 371 656 - e-mail : biotrop@indo.net.id

ABSTRACT

The paper presents a study to assess the use of SAR data to map and monitor deforestation in Sumatra, a region characterized by rapid depletion of the rain forest.

Two approaches, for forest/non forest mapping, will be compared :

- 1- Temporal change approach using ERS and JERS data
- 2- Interferometric approach using coherence images from the ERS interferometric pairs

The results obtained from both approaches and both sensors will be determined by comparing the results with SPOT HRV data.

1- INTRODUCTION

In Indonesia, tropical rain forest is one of the major natural resources, covering about 60 % of the total area. Much of the existing forests have been destroyed, mainly by shifting cultivation, logging and above all, by the increasing number of people involved in agricultural activities. Therefore the magnitude of deforestation and its consequence on natural processes need to be evaluated.

In such regions under frequent cloud cover, SAR data present optimal means for regular observations. With SAR data (ERS-1/2, JERS-1) the backscatter intensity of tropical forest has stable value and the contrast between forest and other surfaces depends on the backscatter values of the non forested area, which are highly variable. Thus the use of a single SAR image is not relevant. One approach was developed using the temporal variation of backscatter intensity to map forest covers [1]. Recently, interferometric information have been used for land cover classification [2] [3].

The aim of this paper is to assess and compare ERS and JERS multitemporal intensity change and interferometric approaches.

2 - STUDY SITE AND DATA ACQUISITION

The site under study is situated in Indonesia in Sumatra island. It is located in South-Sumatra near the city of Kuayagung. It is a flat area with current active deforestation where most of the primary forest have been converted to secondary forest or plantation (mainly oil palm but also coconut or rubber). This site includes as well young tree plantations (oil palm) and short vegetation like shrubs mainly in swampy region. Two ERS PRI data have been acquired in April and May 96 and one ERS-1/2 SLC pair in May 96. Two as JERS-1 image have been acquired in June and September 96. Finally, one SPOT HRV of May 96 was also available.

3 - THE APPROACHES

The Temporal Change Approach

In this approach, the temporal change in backscatter intensity of ERS and JERS data is considered.

At C and L-band, the backscatter signal comes from the volume scattering from the foliage (leaf and stem) of the upper part of the canopy, L band penetrating more deeply into the medium. Previous backscatter modeling studies on coniferous forests have shown that for a forest canopy of more than 50 t/ha for C-band and 100 t/ha for L band, σ^0 reaches a stable value which does not change significantly with time. Thus σ^0 over dense forest present the particularity to be very stable in space and in time (-7 ± 1 dB for ERS-1 and -10 ± 1 dB for JERS-1). For less dense canopies, in terms of biomass, (<50 t/ha for C band and <100 t/ha for L band), the radar signal results from both the tree backscatter and the underlying soil or undergrowth vegetation. The resulting value depends on the development of the canopy and the conditions of the underground layers, which is strongly dependent on weather conditions. Thus, this category of canopy will have a temporal variation, especially between dry and wet seasons, mainly due to changes e.g. in soil moisture and underlying vegetation conditions. For low canopies (crops), the backscatter results from the volume and surface scattering, leading to variable radar backscatter and variable temporal change.

To distinguish forest from non forest it is necessary to have a maximum contrast between the temporal changes of forested and non forested area. This can be achieved if the delay between two acquisitions is sufficient for significant changes in non forested areas. The optimum time interval depends on the seasonal and meteorological conditions. In most cases, the 1 day interval tandem acquisition or 3 days interval is not sufficient. Optimal configuration would be the shortest possible interval between one acquisition during the dry season and one acquisition during the wet season.

The methodology consists in the three different following steps :

1. Speckle reduction filtering : in order to provide a sufficient equivalent number of looks, appropriate temporal and spatial filtering processes are applied to the 3 looks SAR data [5].
2. Temporal image ratioing : after filtering, the intensity values of two images are divided, pixel by pixels for change detection.
3. Forest/non forest Map : a threshold corresponding to a variation of less than 1dB is used over the ratio image to map forested areas.

The Interferometric Approach

In this approach, the module of the degree of coherence ρ , which is the correlation between two images acquired under slightly different geometrical configuration is considered.

The main sources of decorrelation include spatial or temporal decorrelation. The spatial decorrelation includes the difference in the geometry of observation between the two acquisitions. The temporal decorrelation, which is the most important in the case of ERS-1/2 repeat pass interferometry can be due either to environmental effect (e.g. effect of wind on leaves or branches) or to vegetation growth.

In terms of degree of coherence, bare surfaces present a high degree of coherence, if they do not undergo any modification in their characteristics (geometry, dielectric, vegetation regrowth) between the two acquisitions. Volume scatterers such as leaves or branches are more sensitive to structure variations due to vegetation growth or wind effect. In the case of repeat-pass interferometry, these scatterers have a high probability to move between acquisitions. Thus the volume scattering from vegetation corresponds to a low degree of coherence. In a previous study, ρ as a function of forest biomass has been analyzed over the temperate Landes forest [4]. High temporal coherence is obtained for clear cuts and open fields whereas it decreases with stand age.

The observations can be interpreted using the knowledge of the scattering mechanisms. In the region where the soil contribution is dominant, the degree of coherence is high. On the other hand, the region where most of the backscatter comes from the volume contribution shows a low degree of coherence. In the intermediary region, the degree of coherence decreases with stands age/biomass, with a slope depending on soil/vegetation parameters. The optimum time interval is such that the contrast between the degree of coherence of forest and other surfaces could be maximized. The shortest time interval must be the best. However, depending on the study site and the seasonal, meteorological conditions, 35 days interval can provide good forest/non forest discrimination.

In tropical regions, the vegetation (crop, forest regrowth) growth is such that in 35 days the coherence over non forested area would be too low to be distinguished from the forested area [4]. For forest/non forest mapping the time interval should be defined so that the coherence of non forest areas remains high. Thus the shortest (1-3 days) repeat pass acquisition is more appropriate to use interferometric coherence.

After the coherence image creation, a threshold, as established with the experimental data, corresponding to a coherence of less than 0.4 is used over the coherence image to map forested areas.

5 - RESULTS

Fig. 1a shows the ERS image of April 96 and fig. 1b, the ERS image of May 96. Area n°1 corresponds to dense forest, area n°2 to non forest, mainly young oil palm plantation, area n°3 to mature oil palm plantation and area n°4 shows an example of swampy-non forested area. Fig. 1c present JERS image acquire in June 96 and fig. 1d present JERS image acquired in July 96.

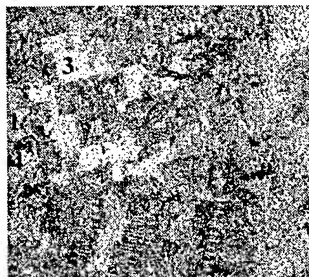


Fig. 1a : ERS image-13/04/96

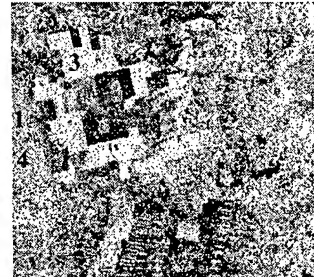


Fig. 1b : ERS image-18/05/96



Fig. 1c : JERS image-01/06/96



Fig. 1d : JERS image-28/08/96

Ratio images have been realized with the ERS SAR images (fig. 2a), and with JERS SAR images (fig3b). The coherence image have been calculated from the 1 day ERS repeat pass images of 17 May and 18 May 96 (fig. 2c).

The resulting ratio images appear in gray tones. Areas with low temporal change have dark tones, whereas areas with a high temporal change present bright tones for a positive change (σ^0 increasing between 2 acquisition) and black tones for negative temporal change (σ^0 decreasing between the 2 acquisitions).

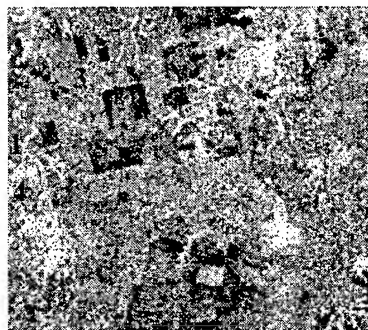
On the resulting coherence image bright tones correspond to high coherence whereas dark tones correspond to low coherence.

Area n°1 (dense forest) has a low temporal change in C and L band and a low coherence. The backscattered intensity correspond to a saturate value and the coherence, a lowest value, both not affected significantly by changes in ground conditions, since the forest backscatter results from volume contribution.

On the contrary, for area n°2 (young oil palm plantation) both C and L band temporal change and coherence are high because soil contribution is important. However the young oil palm plantation are better delineated with L-band and interferometry.

Area n°3 (mature oil palm plantation) is quite similar to area n°2 (low temporal change and low coherence) because of no soil contribution. However the backscattered intensity of the mature oil palm plantation is higher than that of the forest, due, mainly, to their leaf size which are large compared to the wavelength. This permits to distinguish them from dense forest.

Area n°4 presents a low temporal change on C band but a high temporal change at L band and a clearly high coherence. This swampy area, which is non forest, would be considered as forest with the ratio approach at V band and as non forest with L band and with interferometry, because the σ^0 has not changed between April and May 96 for most of the area on ERS images.



This illustrates particularly well the problem of non optimum acquisition dates. April and May are situated in the same season (dry). Therefore, the moisture conditions remain the same for the 2 acquisitions as well as the sparse vegetation of this area.

A previous study has already been lead on this site with 2 images acquired in December 93 (wet season) and August 94 (dry season) [2]. Fig. 3a presents the ERS image of December 93 and fig 4b the resultig ratio image. We can see that area n° 4 is no longer considered as forest because it has a high temporal change. The mapping result is largely improved. Even areas of young oil palm plantation (area n° 2) are better delineated. This shows that the dates of acquisition are crucial for the temporal change method.

For both methodology the use of intensity value for non mountainous area provide additional discriminations : e.g. forest / mature oil palm. For L-band SAR data the discrimination brought by the intensity is more significant than for C-band SAR data.

CONCLUSION

A comparison between Temporal Change approach and Interferometric approach have been assessed.

The criteria for forest / non forest discrimination are as follows :

For INSAR data, forest classes are described by a coherence lower than 0.4. The optimum conditions are reached with a small temporal interval as the results are affected by changes of non forest conditions. If the delay between 2 acquisitions is too long the characteristics of non forested area will change and their coherence will decrease, lowering the discrimination with forested area.

For ERS and JERS SAR intensity, dense forest classes area described by a temporal change lower than 1 dB. Optimum

conditions are reached when using at least one dry and on wet seasons because the results are improved by the change of non forest conditions.

At C and L-band, the intensity of backscattered signal from bare soil surfaces depends on the soil parameters (moisture, roughness). Consequently, bare soil surfaces can present a large range of responses. These possible variations of the soil responses may impede the forest / non-forest discrimination because of the possible confusions between some vegetated and non-vegetated areas. These confusions are less important with JERS-1 SAR data as the wave penetrates more deeply into the cover. However, optimum acquisition date are needed in the case of temporal change approach in order to improve the contrast between forested surfaces and non forested surfaces. On the contrary, the degree of coherence of a bare surface or surface with low vegetation cover is, in most cases, higher than the degree of coherence characterizing forested areas, and this independently of the soil moisture and roughness parameters. This is why the coherence gives more robust results for forest / non forest mapping than the ratio. However the results obtained from intensity temporal change can be largely improved by using optimum acquisition dates.

Further investigations at various geographical locations are needed to validate the results and to quantify the accuracy of both methodology in order to define thresholds to be used in most conditions.

REFERENCES

- [1] Le Toan T., Ribbes F., Floury N., Rosalina Wasrin U. « Use of ERS-1 SAR Data for Forest Monitoring in South Sumatra ». Proceedings of the TREES ERS-1 94 final workshop, JRC, ISPRA, Italy, Feb. 1995.
- [2] Wegmüller U., Werner C.L., Nuësch D., and Borgeaud M. « Land-surface analysis using ERS-1 SAR interferometry ». ESA Bulletin, n°81, pp. 30-37, Feb. 1995.
- [3] Stussi N., Kwok L. K., Liew S. C., Singh K., Lim H. « ERS-1/2 Interferometry: Some Results on Tropical Forest », FRINGE 96, Zurich, Switzerland, September 1996.
- [4] Floury N., Le Toan T., Souyris J.C., Singh K., Stussi N., Hsu C.C., Kong J.A. « Interferometry for Forest Studies », FRINGE 96, Zurich, Switzerland, September 1996.
- [5] Bruniquel J. and Lopes A., « Multi-variate optimal speckle reduction in SAR imagery », International Journal of Remote Sensing, vol. 18, No. 3, pp. 603-627, 1997

Reconstructed Imagery for Equatorial Monitoring Combining AVHRR with Reconstructed NSCAT

Perry J. Hardin, David G. Long, and Ryan R. Jensen. Microwave Earth Remote Sensing Group
Brigham Young University, Department of Electrical and Computer Engineering, 459 CB,
Provo, Utah 84602. Email: perry_hardin@byu.edu Phone: (801) 378-6062

I. INTRODUCTION

Despite engineering advances and global political changes which have both improved spaceborne image resolution and made those products available to civilian researchers, there continues to be an interest in medium-resolution imagery. This interest has been manifest in disciplines as diverse as sea-ice mapping, snow cover studies, regional vegetation monitoring, weather imaging, climate change modeling, and sea surface temperature determination.

Since 1993, researchers have developed methods of using multi-pass data over a single region to reconstruct higher-resolution images from the lower resolution instrument data. For example, images approaching 12 km in resolution have been constructed with Seasat-A scatterometer (SASS) scatterometer's native 50km measurements. Using a similar technique, the resolution of ERS-1 scatterometer imagery has been improved from 50km to 33km. Special Sensor Microwave Imager (SSM/I) data have also been reconstructed to much higher resolutions than the original single-pass data provided.

The availability of reconstructed imagery raises several questions. First, does reconstructed imagery provide any advantage over the ubiquitous Advanced Very High Resolution Radiometer (AVHRR) imagery for global monitoring? What are the advantages and disadvantages of each reconstructed image type? What kind of geophysical information does each provide? Only continuing research will answer these complex questions. In this paper, emphasis will be placed on comparisons between contemporary AVHRR and the latest reconstructed NASA Scatterometer (NSCAT) data sets for monitoring vegetation in equatorial areas. We will demonstrate that AVHRR data combined with NSCAT provides better equatorial forest differentiation than AVHRR data used alone.

II. AVHRR AND THE GLOBAL VEGETATION INDEX PRODUCTS

The AVHRR instruments that flew on polar orbiters NOAA-7, NOAA-9, and NOAA-11 were primarily five-channel radiometers capable of continuously scanning the earth with 1-km resolution. While these 1-km data were available for large portions of the earth, AVHRR global area coverage (GAC) data were resampled to 4km resolution and stored on-board the satellites for later transmission to Earth receiving stations. Channels used by the instruments included the following spectral ranges; Band 1) 0.58 to 0.68 μm , Band

2) 0.725 to 1.10 μm , Band 4) 10.30 to 11.30 μm , and Band 5) 11.50 to 12.50 μm .

Early work [1] demonstrated that vegetation indices derived from NOAA polar orbiter sensors such as AVHRR are extremely useful for monitoring vegetation on a continental scale. Several vegetation indices used with AVHRR are reported in the literature. One of the simplest, designated in this research as IR / R is defined as:

$$\text{IR/R} = \text{Band 2} + \text{Band 1}.$$

In contrast, the normalized difference vegetation index (NDVI), derived from AVHRR channels, is defined as

$$\text{NDVI} = (\text{Band 2} - \text{Band 1}) / (\text{Band 2} + \text{Band 1}).$$

For most applications, NDVI is preferred to IR/R because it helps mitigate the effects of viewing aspect, terrain slope, and changes in illumination [2].

The AVHRR image data set used in this study was the *Experimental calibrated monthly global vegetation index from NOAA AVHRR reprocessed from Kevin Gallo's biweekly GVIs*. The lineage and processing of this data are complex, but are described completely in the *NGDC Key to Geophysical Records Documentation No. 28*. In order to make the data approximately comparable to the NSCAT data, the monthly image for September 1990 was used. This image is shown in Figure 1.



Figure 1: AVHRR NDVI image, September 1990.

III. NSCAT IMAGE RECONSTRUCTION

NSCAT measures σ_0 over a wide range of incidence angles, at several azimuth angles, and with both horizontal and vertical polarization. The wide swath enables frequent observation of targets. By combining data from multiple passes with the SIRC algorithm [1], enhanced resolution images of the surface backscatter can be made with an effective resolution of 8-10 km. Primarily, the SIRC algorithm provides images of σ_0 at a 40° incidence angle (A). The algorithm also provides an image of the slope of σ_0 versus incidence angle (B). The latter is useful in understanding the scattering mechanisms responsible for the

observed backscatter and in discriminating between various land cover types. A reconstructed NSCAT A (vertical polarization) image for the tropical portions of the world is shown in Figure 2.

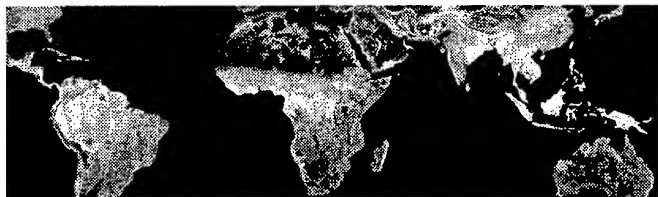


Figure 2. NSCAT image for September, 1996

IV. INTEGRATION AND COMPARISON METHODOLOGY

The goal of the integration process was to determine how well the combined AVHRR and NSCAT images could discriminate between equatorial vegetation types. The experiment utilized the Matthew's Global Vegetation data set [3]. This mapped data set consisted of 19 global vegetation classes for continental Africa with a spatial resolution of 18 km at the equator [4].

The pixels corresponding to the 19 Matthew's vegetation classes were first extracted from the NDVI and NSCAT imagery. Only those pixels which had both good NDVI and normalized backscatter (A) values were used. This extraction and weaning produced a total of 69174 valid image pixels for the Africa study area.

Since the NDVI and A units of measurement were different, each of the 69174 NDVI and A values were standardized to unitless Z-scores. With this standardized data, a mean was then calculated for each of the 19 classes. The distance between all possible pairings of the 19 different centroids was next determined in this standardized measurement space. This measurement between centroids was performed: 1) along the standardized NDVI axis, 2) along the standardized A NSCAT axis, and 3) between the centroids in two dimensional Euclidean space determined by the two axes. The improvement in separation between the centroids when the NSCAT A data was added to the AVHRR data was expressed as a percentage of the standardized AVHRR distance value. Northern hemisphere data was analyzed separately from the southern hemisphere data.

V. RESULTS AND SUMMARY

Figure 3 is a scatterplot of the 19 vegetation class group centroids in normalized space. No account is taken of hemisphere. In general, classes in the upper right corner represent equatorial forests. The centroids then grade into droughty classes toward the lower left hand corner. The correlation between the NDVI values and backscatter is obvious, indicating that the mechanism for backscatter at

NSCAT's Ku-band frequency is highly dependent on canopy density or vegetation vigor.

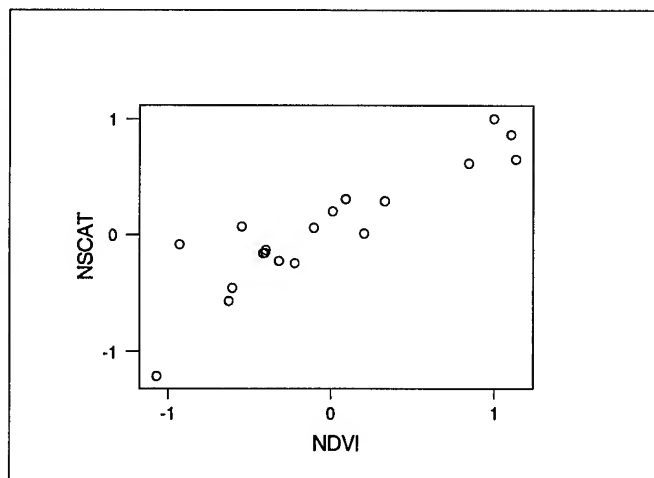


Figure 3. Correlation between NDVI and NSCAT backscatter values for the 19 classes in Africa

Tables 1 and 2 show the results of the discrimination experiments for the northern and southern hemispheres respectively. For both hemispheres, the average centroid distance between the classes is higher with the NDVI imagery than with the NSCAT imagery. Of the 34 classes represented in the two charts, there are only seven cases where average distance between class centroids are greater in the NSCAT data.

Despite the fact that NDVI alone has classes with wider mean centroid separation, in most cases the addition of NSCAT data provides a significant improvement in separation between the classes. The greatest improvement is in the southern hemisphere grassland categories, and in the southern hemisphere tropical evergreen rainforest class. Generally speaking, the improvements are most substantial in the dry-season (southern hemisphere). See Figure 4. This strong pattern seems to suggest that the greatest advantage of NSCAT would be in discriminating between vegetation with very low vegetation canopy densities, or when classification tasks are required during dry seasons.

VII. REFERENCES

1. J.D. Tarpley, S.R. Schneider, and R.L. Money, "Global vegetation indices from NOAA-7 meteorological satellite," *J. Climatol. and Appl. Meteorol.* 23: 491 - 494 (1984).
2. K.B. Kidwell. NOAA Polar Orbiter Data User's Guide. NOAA/NESDIS. Washington, D.C. (1986).
3. Matthews, E. "Global vegetation and land use: New high-resolution data bases for climate studies." *J. Climatol. and Appl. Meteorol.* 22: 474 - 487 (1984).
4. E. Matthews. Vegetation, Land-use, and Seasonal Albedo Data Sets: Documentation of Archived Data Tape. NASA Technical Memorandum #86107. (1984).

Class name	Descriptives				Average Centroid Distance			Percent improvement
	actual mean NDVI	actual mean A	standard. NDVI	standard. A	NDVI alone	A alone	NDVI and A	
1. Tropical evergreen rainforest, mangrove forest	0.41	-6.61	1.27	1.10	1.28	1.01	1.64	28.9
2. Tropical / subtropical evergreen seasonal broadleaved forest	0.41	-6.75	1.26	1.05	1.26	0.96	1.60	27.5
6. Evergreen broadleaved sclerophyllous forest, winter rain	0.11	-10.01	-0.55	0.07	0.86	0.48	1.05	21.7
9. Tropical / subtropical drought-deciduous forest	0.48	-7.79	1.71	0.69	1.68	0.67	1.83	8.8
12. Xeromorphic forest / woodland	0.13	-10.55	-0.40	-0.13	0.80	0.52	0.99	23.5
13. Evergreen broadleaved sclerophyllous woodland	0.22	-9.11	-0.09	0.33	0.78	0.52	0.98	25.9
15. Tropical / subtropical drought-deciduous woodland	0.27	-8.76	0.39	0.46	0.86	0.56	1.06	22.7
17. Evergreen broadleaved shrubland / thicket	0.16	-10.78	-0.31	0.07	0.78	0.48	0.95	22.6
18. Evergreen needleleaved or microphyllous shrubland / thicket	0.10	-11.40	-0.63	-0.57	0.90	0.84	1.26	39.9
19. Drought-deciduous shrubland / thicket	0.10	-12.42	-0.63	-0.66	0.90	0.92	1.31	46.0
21. Xeromorphic shrubland / dwarf shrubland	0.21	-11.25	0.01	-0.06	0.77	0.49	0.95	23.6
23. Tall / medium / short grassland with 10-40% tree cover	0.35	-8.57	0.91	0.49	1.06	0.57	1.24	16.4
24. Tall / medium / short grassland with < 10% tree cover	0.40	-8.03	1.18	0.67	1.20	0.66	1.41	16.9
25. Tall / medium / short grassland with shrub cover	0.18	-11.41	-0.14	-0.16	0.76	0.54	0.96	26.1
26. Tall grassland, no woody cover	0.39	-7.60	1.15	0.79	1.18	0.74	1.41	20.2
27. Medium grassland, no woody cover	0.17	-10.39	-0.21	-0.06	0.76	0.49	0.94	22.9
28. Meadow, short grassland, no woody cover	0.05	-9.78	-0.93	0.02	1.12	0.48	1.29	14.9
29. Forb formations	0.05	-10.54	-0.93	-0.08	1.12	0.50	1.29	15.1
30. Desert	0.03	-14.27	-1.08	-1.21	1.25	1.43	1.95	54.8

Table 1: Discrimination comparison -- northern Africa.

Class name	Descriptives				Average Centroid Distance			Percent improvement
	actual mean NDVI	actual mean A	standard. NDVI	standard. A	NDVI alone	A alone	NDVI and A	
1. Tropical evergreen rainforest, mangrove forest	0.31	-7.23	0.62	0.89	0.84	1.03	1.36	60.8
2. Tropical / subtropical evergreen seasonal broadleaved forest	0.32	-8.83	0.71	0.39	0.92	0.57	1.11	21.2
6. Evergreen broadleaved sclerophyllous forest, winter rain								
9. Tropical / subtropical drought-deciduous forest	0.19	-10.81	-0.11	-0.13	0.38	0.35	0.55	44.3
12. Xeromorphic forest / woodland								
13. Evergreen broadleaved sclerophyllous woodland	0.21	-9.73	0.03	0.10	0.45	0.36	0.61	35.1
15. Tropical / subtropical drought-deciduous woodland	0.18	-9.79	-0.13	0.10	0.37	0.36	0.56	51.3
17. Evergreen broadleaved shrubland / thicket	0.29	-10.40	0.53	0.04	0.77	0.35	0.90	17.2
18. Evergreen needleleaved or microphyllous shrubland / thicket								
19. Drought-deciduous shrubland / thicket	0.11	-11.53	-0.61	-0.45	0.54	0.52	0.78	44.1
21. Xeromorphic shrubland / dwarf shrubland	0.10	-10.77	-0.67	-0.22	0.59	0.37	0.75	26.5
23. Tall / medium / short grassland with 10-40% tree cover	0.17	-9.79	-0.21	0.10	0.36	0.36	0.56	54.8
24. Tall / medium / short grassland with < 10% tree cover	0.14	-10.00	-0.37	0.24	0.42	0.45	0.67	61.6
25. Tall / medium / short grassland with shrub cover	0.11	-11.15	-0.56	-0.33	0.51	0.42	0.70	36.6
26. Tall grassland, no woody cover	0.17	-10.19	-0.21	-0.01	0.36	0.34	0.53	47.9
27. Medium grassland, no woody cover	0.17	-11.00	-0.23	-0.30	0.37	0.41	0.59	61.5
28. Meadow, short grassland, no woody cover	0.18	-10.92	-0.15	-0.26	0.37	0.38	0.57	56.8
29. Forb formations								
30. Desert	0.06	-13.62	-0.90	-1.26	0.81	1.27	1.53	89.3

Table 2: Discrimination experiment -- southern Africa. Shaded classes were not found in the Southern Hemisphere.

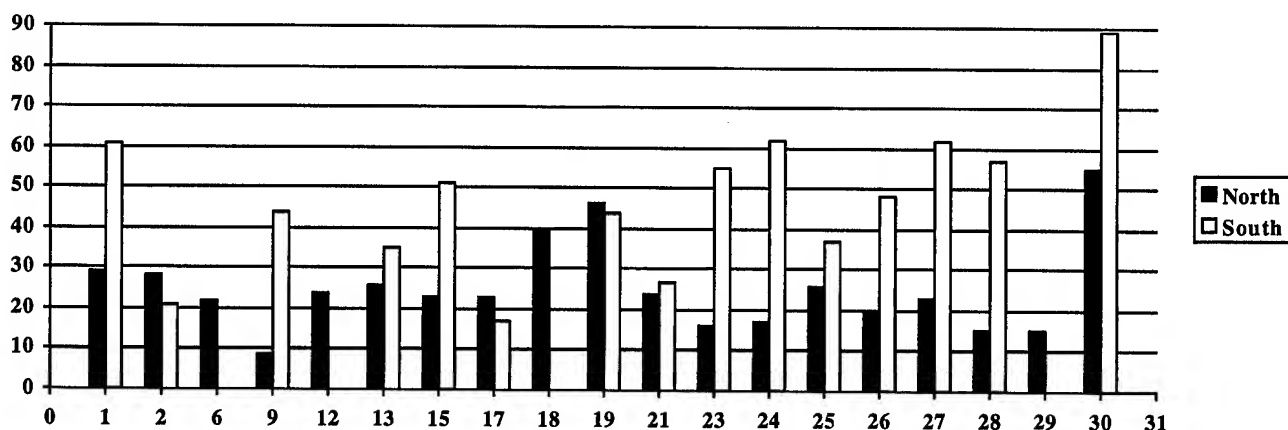


Figure 4. Improvement in centroid distance provided by addition of NSCAT data to NDVI data. The x axis shows the class number (See Table 1 for class name). The y axis is percentage improvement.

BRDF BEHAVIOR OF A TROPICAL FOREST SURVEYED FROM SPACE

Gastellu-Etchegorry J.P.^{*}, Demarez V.^{*}, Trichon V.^{**}, Ducrot D.^{*}, Zagolski F.^{***}

Centre d'Etudes Spatiales de la Biosphère^{*}
CNES/CNRS/UPS
18 Av; Edouard Belin, 31401 Toulouse cedex 4
Tel: (33) 5 61 55 61 30; Fax: (33) 5 61 55 85 00
Email: gastellu@cesbio.cnes.fr

Laboratoire d'Ecologie Terrestre^{**}
CNRS/UPS
BP 4403
31045 - Toulouse cedex (France)
Fax: (33) 5-61-55-85-44

CARTEL^{***}, Université de Sherbrooke
Québec, J1K2R1 (Canada)
PRIVATEERS, N.V.
St Marteen (Dutch Antillas)

ABSTRACT

Survey of tropical forest evolution and functioning with remote sensing is hampered by the variability of their BRDF (bi-directional reflectance distribution function); e.g. automatic classifications may be totally erroneous if view and illumination conditions are not taken into account. We used a new radiative transfer model (DART [1], Discrete Anisotropic Radiative Transfer) to analyze BRDF behavior of a tropical forest plot in Central Sumatra, Indonesia. Simulations stressed that BRDF anisotropy, especially for low sun zenith angles (θ_s), may be large enough to make difficult the study of forest evolution with satellite data time series. Variations were up to 30% for VIS (visible), 20% for NIR (near infrared) and 25% for SWIR (short wave infrared), for viewing zenith angles (θ_v) smaller than 25°. Larger variations occurred in the hot spot configuration and for variable sun zenith angles θ_s : up to 50% for VIS, 30% for NIR, 40% for SWIR, whereas local topography and diffuse atmospheric radiation (SKYL) had a much smaller influence. On the other hand, variations due to a 50% cover degradation were 14% for VIS, 23% for NIR and 18% for SWIR at nadir and $\theta_s=35^\circ$.

INTRODUCTION

Many works already proved the great potential of remote sensing for studying forest structural characteristics [2] and functioning processes through the determination of a quantity such as PAR absorption [3]. However, results are often disappointing because relationships and classification procedures valid for a study area may not be valid for another study area, or even with the same study area under different vegetation conditions or different illumination or viewing configurations. This importance is clearly stressed by the fact that canopy albedo may be underestimated by as much as 45% if it is computed with nadir reflectance only [4]. This strong BRDF variability is directly associated with forest cover architecture. However, this is usually difficult to explain and predict with empirical studies only. Here, we studied this variability with a modeling approach, through BRDF and image simulations with the DART model. This operates on realistic discrete 3-D scene representations (trees, grass, water and soil, with anisotropic atmosphere,

topography,...). We used the 6-S model to simulate atmospheric effects on satellite images.

The study area is a tropical rain forest plot (101° 47'E, 1° 37'S, altitude \approx 250m) in Central Sumatra, Indonesia. Major forest structural parameters (tree height, crown diameter, etc.) used in this study were measured by Trichon [5]: botanical identification and tree dimension and location, for all trees with a diameter of 10cm or more, topographic map, etc. Density and species richness are high since 750 trees were recorded belonging to 267 species (*Shorea conica*, *Pouteria malaccensis*, *Palaquium oxleyanum*, *Elateriospermum tapos* and *Pimelodendron griffithianum*, etc.). Total basal area reaches 37m², the maximum height of the trees is 51m. Except a recent gap important perturbations were old enough to be healed. Use of hemispherical photographs led to mean values of 5.3 for the LAI (leaf area index) and 2.8% for the canopy openness. However, these values hide a strong spatial heterogeneity of the forest structure.

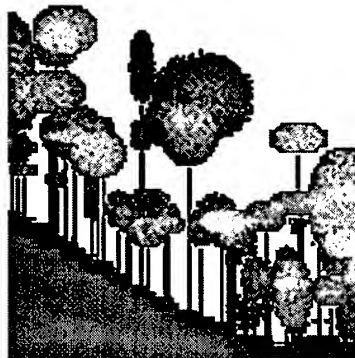


Figure 1:

Schematic profile of part of the tropical forest plot. Topography consists roughly in two marked ridges, pronounced slopes, and a depression where a small stream runs. Maximum altitude difference is 52m.

Which acquisition conditions and extent of forest degradation are necessary to detect tropical forest changes from space? This was studied with a BRDF sensitivity analysis to spatial resolution (10m \rightarrow 100m), view and illumination directions, SKYL and topography in three spectral domains (VIS, NIR, SWIR). These were compared to those from simulations with different (0% \rightarrow 50%) deforestation levels (clearing of larger trees, random clearing, constant or variable leaf biomass).

BRDF AND IMAGE SIMULATIONS

Only major results of this work [6,7] are reported here. Simulations were conducted with SKYL=0.3/0.24/0.089, foliar albedo $\omega_f=0.24/0.96/0.70$ and understorey reflectance $\rho_{und}=0.02/0.20/0.15$, for simulating the VIS/NIR and SWIR.

DART simulated images (Fig. 2) illustrate the important variability of forest BRDF with view direction and spatial resolution of analysis. Canopy structure is clearly the main cause of this variability. Reflectance (Table 1) is maximal in the hot spot configuration ($\rho_{VIS}=0.073$, $\rho_{NIR}=0.55$, $\rho_{SWIR}=0.29$) and minimal along directions between nadir and specular configurations ($\rho_{VIS}=0.027$, $\rho_{NIR}=0.33$, $\rho_{SWIR}=0.12$).

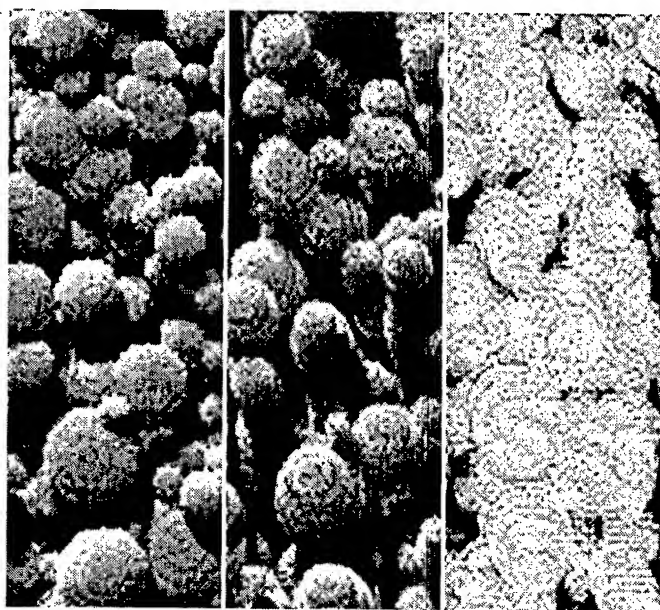


Figure 2: DART images of tropical forest. Red region. Sun zenith: $\theta_s=145^\circ$. (a) Nadir ($\rho \approx 2.8\%$), (b) off nadir ($\theta_v=35^\circ$, $\phi_v=20^\circ$: $\rho \approx 2.3\%$), and (c) hot spot ($\rho \approx 7.2\%$).

NDVI is pretty stable with spatial resolution and strongly anisotropic. Its minimal ($\approx 76\%$) in the hot spot direction and maximal ($\approx 88\%$) in the specular direction [6]. For some directions it has a local maximum variability at 30m resolution. This may indicate that optimal spatial resolution for tropical forest studies may be direction dependent.

A problem is to assess to which extent BRDF variation associated with tropical vegetation evolution can be masked with canopy BRDF anisotropy associated with variable remote sensing configurations. For that we compared forest BRDF anisotropy (10m to 50m spatial resolution of analysis, with/without SKYL, relief and atmosphere) with the BRDF variation (standard deviation) of a tropical forest simulated with 0% to 50% deforestation levels (Fig. 3).

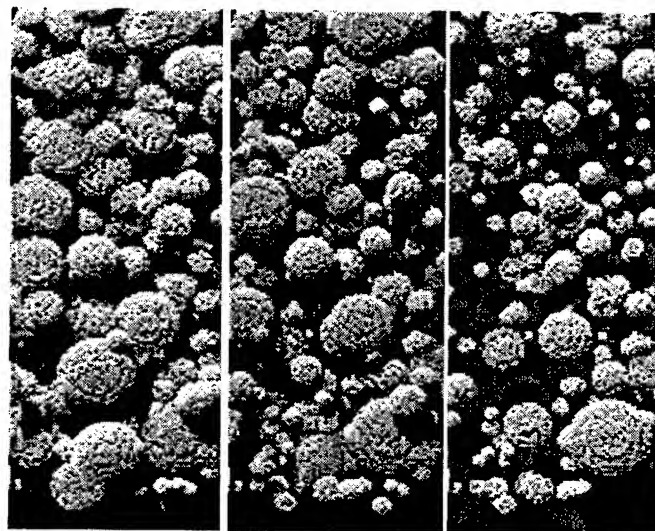


Figure 3: DART TOA VIS images. a) 0% ($\rho \approx 6.5\%$), b) 20% ($\rho \approx 6.4\%$), c) 50% ($\rho \approx 6.2\%$) deforestation. $\theta_s=35^\circ$, $\theta_v=0^\circ$.

BRDF anisotropy is very strong (Tab. 2), especially for large sun zenith angles: 30% for VIS, 20% for NIR and 25% for SWIR for $\theta_v < 25^\circ$ and $\theta_s=35^\circ$. Variations are much larger in the hot spot configuration and for variable θ_s : 50% for VIS, 30% for NIR, 40% for SWIR, whereas the influence of local relief and SKYL is weak. These variations are larger than those due to forest change; e.g. at $\theta_v=0^\circ$ and $\theta_s=35^\circ$, BRDF variation due to a 50% deforestation is 14% for VIS, 23% for NIR and 18% for SWIR. BRDF anisotropy is all the more large that ω_f is low, i.e. for VIS, and SWIR to a lesser extent.

CONCLUSION

This work shows that forest reflectance variation associated with forest cover change can be totally masked due to variable acquisition configurations, especially in the VIS. In that case, SWIR seems to bring more useful information than VIS. Moreover, it is less disturbed by atmospheric effects. Finally, this work stresses the capability of physical modeling to study forest BRDF behavior, which is essential for knowing the range of radiometric classes in classification processes.

Acknowledgment: this work was possible with the support of French Space Center (CNES contract No 95/0368), and the help of F. Blasco, head of LET, S. Lafont and Y. Laumonier.

References:

- [1] Gastellu-Etchegorry J.P., Demarez V., Pinel V., Zagolski F., 1996, Modeling radiative transfer in heterogeneous 3-D vegetation canopies, *Rem. Sens. Env.*, 58:131-156.
- [2] Peterson D.L., Spanner M.A., Running S. and Teuber K.B., 1987, Relationship of thematic mapper simulator data to leaf area index of temperate coniferous forests, *Rem. Sens. Env.*, 22:323-341.

		Visible		Near infrared		SWIR		NDVI		NIR-SWIR NIR+SWIR	
	θ_v	No atm.	Top atm.	No atm.	Top atm.	No atm.	Top atm.	No atm.	Top atm.	No atm.	Top atm.
P ₁	-50	0.0417 0.005	0.0964 0.002	0.45 0.125	0.336 0.062	0.184 0.033	0.135 0.017	0.83 0.02	0.554 0.066	0.419 0.0279	0.426 0.0278
	-35	0.0733 0.02	0.108 0.0109	0.551 0.141	0.438 0.112	0.292 0.084	0.243 0.067	0.765 0.0017	0.604 0.063	0.307 -0.0017	0.286 -0.01
	0	0.03 0.0043	0.0647 0.0031	0.326 0.074	0.294 0.062	0.128 0.023	0.115 0.0192	0.831 0.018	0.639 0.0598	0.436 0.028	0.437 0.0232
	35	0.0267 0.00217	0.0687 0.0019	0.369 0.07	0.319 0.065	0.121 0.018	0.11 0.015	0.865 0.022	0.0645 0.0624	0.506 0.0344	0.487 0.03
	50	0.0284 0.002	0.0832 0.002	0.391 0.07	0.345 0.07	0.128 0.02	0.12 0.016	0.864 0.0196	0.611 0.0691	0.506 0.0255	0.483 0.032
P ₂	-50	0.0313 0.002	0.08 0.002	0.412 0.082	0.341 0.068	0.143 0.017	0.128 0.016	0.858 0.0221	0.619 0.052	0.484 0.0383	0.454 0.0345
	-35	0.0322 0.004	0.0722 0.003	0.406 0.093	0.341 0.072	0.147 0.024	0.13 0.02	0.853 0.02	0.65 0.056	0.468 0.0317	0.447 0.028
	35	0.0321 0.005	0.072 0.003	0.409 0.113	0.341 0.08	0.144 0.03	0.127 0.024	0.854 0.0217	0.651 0.054	0.479 0.0357	0.457 0.0268
	50	0.0328 0.005	0.081 0.003	0.425 0.119	0.346 0.08	0.147 0.03	0.129 0.023	0.856 0.0189	0.62 0.05	0.486 0.0271	0.456 0.0269

Table 1:

Top of the atmosphere (TOA) and canopy reflectances (ρ_{VIS} , ρ_{NIR} , ρ_{SWIR}) and spectral indices of a tropical rain forest, in the principal (P₁) and perpendicular (P₂) planes.

Reflectance variations due to a 50% forest cover clearing of larger trees are shown. Obviously, associated figures strongly depend on the optical and structural characteristics of vegetation which grows after deforestation. Here, in a first approximation, we assumed time invariant understory characteristics.

	Spatial resolution (10m→50m)	Directional effects $\theta_v \leq 23^\circ$, $\theta_s = 145^\circ$ $\theta_s > 120^\circ$, $\theta_v = 12^\circ$		SKYL	Relief	Deform.(50%) ($\theta_v = 0$, $\theta_s = 145^\circ$)	Atmos. ($\theta_v = 0^\circ$)
		$\theta_v \leq 23^\circ$ (60% → 30%)	$\theta_s > 120^\circ$ (140%)				
ρ_{VIS} (≈3%)	30% → 17% (60% → 30%)	30% (140%)	50%	<5% (20%)	≈3% (3.3%)	14% (27%)	≈110% (47%)
ρ_{PIR} (≈35%)	25% → 12% (35% → 12%)	20% (75%)	30%	<3% (8%)	≈3% (1.7%)	23% (26%)	≈10% (21%)
ρ_{MIR} (≈13%)	28% → 15% (45% → 20%)	25% (130%)	40%	<2% (1.2%)	≈2% (1.2%)	18% (29%)	≈10% (17%)

Table 2:

Tropical forest BRDF standard deviation (SD) with resolution (10m→50m), view ($\theta_v \leq 23^\circ$, $\theta_s = 145^\circ$) and sun ($\theta_s > 120^\circ$, $\theta_v = 12^\circ$) directions, SKYL and relief. BRDF SD due to deforestation (50%) and atmosphere is shown for nadir. BRDF SD at hot spot are between brackets.

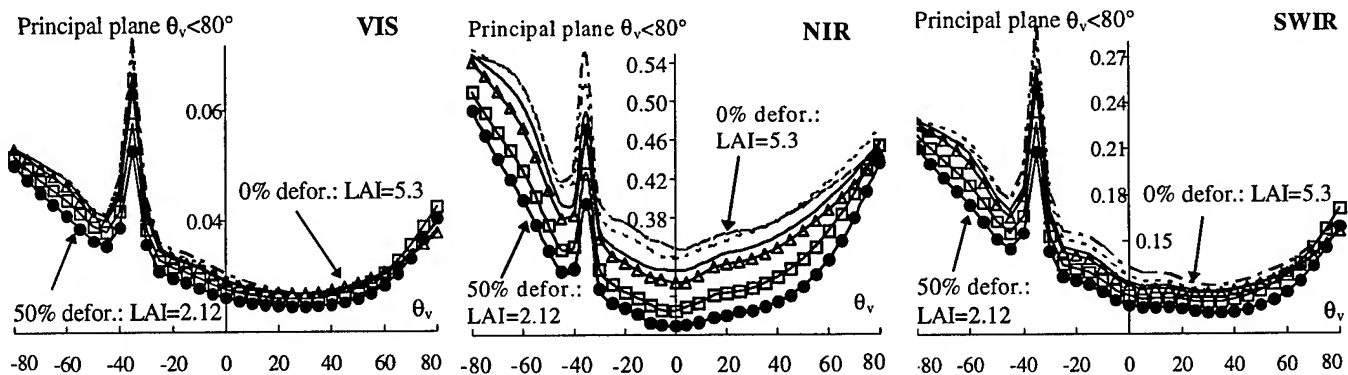


Figure 4: Forest VIS, NIR and SWIR BRDF for 0% (- - -), 10% (- -), 20% (—), 30% (—△—), 40% (—), 50% (—●—) deforestation.

- [3] Asrar G., Myneni R.B., Choudhury B.J., 1992, Spatial heterogeneity in vegetation canopies and remote sensing of absorbed photosynthetically active radiation: a modeling study, *Rem. Sens. Env.*, 41:85-103.
- [4] Kimes D.S., Sellers P.J., 1985, Inferring hemispherical reflectance of the Earth's surface for global energy budgets from remotely sensed nadir or directional radiance values, *Remote Sens. Environ.*, 18:205-223.
- [5] Trichon V., 1996, Hétérogénéité spatiale des structures en

forêt naturelle de basse altitude à Sumatra, Indonésie, PhD, Paul Sabatier University.

- [6] Gastellu-Etchegorry J.P. and Trichon V., 1997, A modeling approach of PAR environment in a tropical rain forest in Sumatra, *Ecological Modeling*, in press.
- [7] Gastellu-Etchegorry J.P., Trichon V., Ducrot D., Demarez V., Laumonier Y. and Lafont S., 1997, Suivi de la végétation tropicale, Rapport CNES (No95/0368).

Remote Sensing and GIS Tools to Support Vegetation Fire Management in Developing Countries.

Stéphane P. Flasse, Pietro Ceccato, Ian D. Downey
Environmental Science Department, Natural Resources Institute, Central Avenue,
Chatham maritime, Kent, ME4 4TB, UK
Tel: +44-1634-880088, Fax: +44-1634-880066/77, Email: stephane.flasse @ nri.org

Mahmud A. Raimadoya
Indonesia Tropical Forest Management Project (ITFMP),
Mangala Wanabakti Building Block VII 6th FloorJ1., Gato Subroto, Jarkarta 10270, Indonesia
Tel: +62-21-5731815, Fax: +62-21-5701109, Email: mud@server.indo.net.id

Pedro Navarro
Ministero del Ambiente y Recursos Naturales (MARENA),
Servicio Forestal, Managua, Nicaragua, Tel., Fax.
Tel: +505-2-631956/72, Fax: +505-2-331277

ABSTRACT

Fire is involved to some extent in clearance of vegetation for agriculture, logging access, settlement and poaching. When used inappropriately, fire events may adversely affect ecosystems and alter atmospheric conditions. In developing countries resources to monitor fire activities are usually limited (e.g., staff, material, budget), and little information is generally available at regional and/or national level. Earth observation remote sensing and GIS technologies are the most practical and feasible means to efficiently monitor biomass burning events at regional and global scale. NRI is conducting ongoing research and operational work to provide developing countries with tools to carry out timely, integrated vegetation fire management. Various low cost techniques are used: vegetation status and active fires are monitored through direct reception of NOAA-AVHRR data, and production of thematic information is carried out by the integration of fire information with local environmental knowledge. This paper describes areas of research and current tools used in Indonesia and Nicaragua to support natural resources managers. It illustrates the usefulness of direct reception of satellite data to forestry departments and associated line agencies, and underlines the challenges that have to be overcome in developing countries.

INTRODUCTION

Although fire is a useful and efficient tool for environmental management such as forest clearance, field preparation, regrowth for livestock and reduction of fire hazard, its misuse can have adverse consequences [1]. Areas of concern vary from natural resource sustainability and biodiversity

conservation to destruction of commercial wood and threats to village welfare. As a result, there is increasing pressure from international, national, regional and local communities to manage vegetation fires. However, developing countries are often challenged by a lack of means to monitor fire on a national scale. This paper describes NRI's experience in providing developing countries with local reception of satellite data and its integration into GIS in order to improve fire management effectiveness.

FIRE MANAGEMENT IN DEVELOPING COUNTRIES

In many of the more developed countries, fire management has been a common practice for years. In many other countries, although fires have occurred for millennia, concern has increased recently due to changes in fire patterns and the growing scarcity of natural vegetation. For example, the increasing number of large destructive forest fire events is believed to interfere with biodiversity and productivity (of both vegetation and fauna) or with sophisticated 20th century life as in the case of large smoke plumes disturbing aviation, (e.g., [2], [3], [4]). In addition, recent studies on global climate change have also increased pressure on countries to control gas emissions to the atmosphere (e.g., [5], [6]). As a consequence, there is high pressure for fire management.

Management of fire consists of activities designed to control the frequency, area, intensity or impact of fire within a local or regional environment. The first step to effective fire management is to know and to understand the climatic, environmental and social factors which influence fire and its impacts. In order to know and understand a fire issue in a country or in a specific region, one must:

- **document** the events (where and when does it burn?) over the years
- **gather fire information**, information related to the fire events (e.g., what and how much is burned, why was fire set, local customs, population density, meteorology, vegetation status)
- **gather ancillary information** (e.g., roads and river network, administrative boundaries, protected areas, concessions, villages, fire towers, fire fighting units).

Only the comparison of fire occurrence, within a season, between seasons, and within 'context' allows resource managers to identify trends, to understand practices and needs, to prioritise problems, and to formulate environmental management policies. In turn, the policies must be implemented by allocating the right resources, and their success must be evaluated.

While comprehensive analysis of fire data can only improve understanding and enable better management decisions to be made, such an approach may be a real challenge for a budget constrained government in a developing country, especially one with more problems than capacity to intervene. Such governments, constrained by often outdated and ineffective institutions, and pressed by increasing rates of environmental change together with growing demands for accountability and competence through enhanced political and environmental awareness, need assistance to help them improve management of their natural resources and environment. Decrepit observation networks, poor communications, underpaid and demoralised staff and urban-oriented political systems do not improve prospects. Under such circumstances, unless the need for fire control is inescapably obvious to all (and it very rarely is) then it is most unlikely that systematic, reliable data on fires over large remote areas are most unlikely to be collected, processed, assimilated, or acted upon.

As a consequence, the basic information required to analyse the situation (e.g., time and location of fires) is often the primary challenge: there is a need to find sustainable and reliable ways of documenting events to allow the scarce fire management resources to be used most efficiently.

DIRECT ACCESS TO FIRE INFORMATION

The most practical, feasible and relatively objective and cost effective means, by far, to quantify and monitor these fire events at national to regional scales is to utilise Earth remote sensing and GIS technologies (e.g., [7], [8]). Clearly, the major benefit of remote sensing is that it permits the observation of large areas of territory, on a regular basis. Its monitoring capabilities can be used to aid in the identification

of fire events as well as vegetation status and land surface temperature which are useful in the assessment of fire risk assessment.

However, it is essential that appropriate information is available directly where it can best be used. This may appear obvious, but examples exist, even in industrialised countries, which suggest that it is not working (e.g., [9]). This is a challenge NRI is actively addressing with the implementation of local reception of satellite data and the appropriate tools to create useful information from the received data [10].

Typically, this is an iterative learning process for fire management using remote sensing and GIS tools. Initially, one simply uses the tools to detect fires daily, and observes their spatial distribution on a map. Through repeated use across several fire seasons, one becomes more familiar with the data, and wants to analyse statistics in more details such as:

- proportion of fires within the forest
- correlation between fire occurrence and population density
- relation between fire occurrences and vegetation status
- relation between fire occurrences and meteorological conditions.

Progressively, one gets motivated by the different possibilities. If at the beginning a simple approach of fire event documentation is established, increasingly more elaborate strategies can be developed to inform concessions, forestry departments, and ministries, regularly, as the capacity of these institutions to absorb and act on this information increases over time. However, sustainable integration of new tools and information takes time. Can existing institutions actually cope?

DEVELOPMENT AND UPTAKE OF TOOLS

In order to support the rapid uptake of new fire management tools and information, NRI works at two main levels: in-country projects and adaptive research. In-country projects usually lead the adaptive research. The latter consists of building methods and tools that can be used operationally without sophisticated inputs from the user. Usually new methods are developed and/or existing ones are adapted to match reality. Simple user interfaces are also implemented in the local language to allow technicians to run these tools operationally and to ease the training of new staff.

In the area of fire monitoring, NRI has developed a contextual fire detection algorithm [11] to improve the reliability of automated fire detection from NOAA AVHRR data. Compared to previous multiple threshold techniques, where thresholds need constant updates according to time and space, the contextual approach allows the automatic detection of fires with minimum input from the user [12]. The algorithm was

developed in support of the IGBP-DIS Global Vegetation Fire Product and has been found to work reliably in the Central African Republic, Madagascar, Indonesia, and Nicaragua. The algorithm forms the basis of operational fire detection projects in Indonesia and Nicaragua.

The remote sensing data processing tools are implemented under the IDL software package into customised stand-alone modules. Very straightforward interfaces are added, translated into local languages. They consist of a few buttons that enable the processing of images as well as the display of primary fire maps and the extraction of fire locations.

Iterative learning is progressing in Indonesia and Nicaragua, resulting in increased demand for development of additional tools to analyse the data. Though most sites now have various GIS packages, NRI develops and implements simple prototype tools and interfaces, based on standard database software (i.e. MS Access) to allow users to produce pre-defined charts and fire reports efficiently and operationally. Currently, some countries have reached enough experience to begin looking at the assessment of fire risk using remote sensing data. Following this evolution, NRI is currently working on implementation of locally operational fire risk assessment tools. Examples of fire monitoring in Indonesia and Nicaragua are given below.

EXAMPLES

Indonesia

Operational fire monitoring over the Indonesian archipelago faces many challenges. Indonesia comprises an area of some 1.9 million km² and much is inaccessible and remote. Fire occurrence is highly variable, both spatially and temporally, but it is recognised officially that just for 1994, 5 million hectares of forest land were destroyed by fires [13]. In 1994 media attention focused on the problem of smoke from forest and agricultural fires. The ensuing air pollution caused serious local health hazards and severe restrictions to air and marine traffic. Fire issues are now addressed by the Indonesian National Coordination Team on Land and Forest Fire Management.

In 1993, a NOAA receiver was installed by NRI at the Overseas Development Administration-ODA's Indonesia-UK Tropical Forest Management Programme (ITFMP) office in Palangkaraya, Central Kalimantan. The fire monitoring system routinely captures AVHRR data of Kalimantan from any of the NOAA satellites as they pass overhead. Maps of probable fire locations are produced within 30 minutes of satellite overpass, using NRI's contextual fire detection software and simple interface. Co-ordinates of suspected fires

are also produced and transmitted to the Ministry of Forestry in Jakarta. Several projects in Indonesia are now co-ordinating their effort to best manage wildfires over the whole country. So far four NOAA systems (Jakarta-2, Palembang and Palangkaraya) are working on daily basis, and several others have been planned in order to give most provinces direct access to fire information.

After several fire seasons, the NOAA fire information is beginning to be combined with supplementary information in a GIS. At the local scale, this provides an early-warning tool in fire suppression, and at the national scale, temporal fire maps combined with supplementary vegetation maps can locate possible deforestation fronts, helping to raise political awareness, or to direct extension programmes to promote alternative land use. Work is still needed to realise the potential fully. The most important aspect will be to improve the dissemination and uptake of the fire information and by forging better links with end-users.

Nicaragua

A collaborative project between ODA and the Ministerio del Ambiente Y Recursos Naturales (MARENA) in Nicaragua commenced in May 1995. Nicaragua has prepared a National Forest Action Plan and attaches high priority to fire prevention and control. Nevertheless, base data are often lacking. One objective of the project is to identify fires in forested areas and seasonal changes in forest cover as observed by satellite. Complex social, economic and institutional issues associated with fire and the use of real-time satellite information are being broached with a view towards sustainable monitoring and optimal utilisation of the information for better decision making.

During the December 1995 - May 1996 fire season, for the first time, daily information and monthly summaries on fire activity for the whole of Nicaragua were produced by MARENA, and transmitted to provincial forestry offices. These were in the form of fire maps and lists fire coordinates referenced to topographic map sheets. Even though daily reports could not be acted on immediately, the analysis of the fire season using this new type of information has clearly shed a completely new light on the problem, provoking surprise and encouraging motivation to utilise the information nationally and regionally. Initially, these powerful new data can be contentious as they highlight the existing under capacity of institutions and resources. But progressively, as staff (from technicians to minister level) are informed, trained and involved, it is being recognised that the information offers the potential to make better decisions on fire policies and to increase awareness of the situation. Preparations for the next

fire season operations are in hand including the design of new specialised local data reports to help operational management at local level.

CONCLUSIONS

Comprehensive information on the spatio-temporal dynamics of fire is essential, for both scientific study of the impact of fire on the environment and formulation of fire management policies.

The methodology developed at NRI provides direct access to real-time data continually transmitted from NOAA satellites, via low-cost, robust satellite receiver stations, and appropriate information extracted by customised tools and automated analysis procedures. This directly contributes to the information necessary for the implementation of operational programmes for fire management at local, national and regional levels. Once actions to manage fire problem have been taken, impact assessments can be performed through the same methodology to determine whether or not fire is still a problem. This in-country approach increases uptake of new tools and information and improves local capacity to the benefit of fire managers and decision makers.

ACKNOWLEDGEMENT

This work is supported by the UK Overseas Development Administration.

REFERENCES

- [1] W. J. Bond, and B. W. van Wilgen, "Fires and Plants", Population and Community Biology Series 14, Chapman & Hall, London, 1996, 263p..
- [2] D. Mueller-Dombois, and J. G. Goldammer "Fire in tropical ecosystems and global environmental change: an introduction" in Fire in the Tropical Biota. Ecosystem Processes and Global Challenges, J. G. Goldammer, Ed. Springer-Verlag, Berlin, 1990, pp.1-10.
- [3] M. Abensperg-Trau, and A. V. Milewski "Abundance and diversity of termites (isoptera) in unburnt versus burnt vegetation at the Barrens in Mediterranean Western Australia". Australian Journal of Ecology, vol. 20, 1995, pp. 413-417.
- [4] United Nation Economic Commission for Europe/Food and Agricultural Organisation, International Forest Fire News, No 14, January 1996.
- [5] J.-P. Lacaux, H. Cachier, and R. Delmas "Biomass burning in Africa: an overview of its impact on atmospheric chemistry" in Fire in the Environment. The Ecological, Atmospheric, and Climatic Importance of Vegetation Fires, P. J. Crutzen and J. G. Goldammer, Eds. Wiley, Chichester, 1993, pp. 159-192.
- [6] D. A. Lashof "The contribution of biomass burning to global warning: An integrated assessment" in Global Biomass Burning. Atmospheric Climatic, and Biospheric Implications, J. S. Levine, Ed. The MIT Press, Cambridge, 1991, pp. 441-444.
- [7] Y. J. Kaufman, A. Setzer, C. Justice, C. J. Tucker, M. G. Pereira, and I. Fung, "Remote sensing of biomass burning" in Fire in the Tropical Biota. Ecosystem Processes and Global Challenges, J. G. Goldammer, Ed. Springer-Verlag, Berlin, 1990, pp.1-10.
- [8] D. A. Prevedel, "Project Sparkey: A strategic wildfire monitoring package using AVHRR satellites and GIS" Photogrammetric Engineering and Remote Sensing, vol. 61, 1995, pp. 271-278.
- [9] R. C. G. Smith, "Australian Vegetation Watch". Final report RIRDC/DOL-1A. Remote Sensing Application Centre, WA Department of Land Administration, and CSIRO, 1994, 113p.
- [10] J. B. Williams, and L. J. Rosenberg "Operational reception, processing and application of satellite data in developing countries: theory and practice" in Annual Conference of the Remote Sensing Society, Chester College, 1993, pp.76-83.
- [11] S. P. Flasse, and P. Ceccato "A contextual Algorithm for AVHRR fire detection", International Journal of Remote Sensing, vol. 17, 1996, pp. 419-424.
- [12] H. Eva, and S. Flasse "Contextual and multiple-threshold algorithms for regional active fire detection with AVHRR data", Remote Sensing Reviews, vol. 14, 1996, pp. 333-351.
- [13] Wildfire, June 1995

Identifying and Monitoring Change in Wetland Environments Using SAR

Anthony K Milne

The University of New South Wales

Sydney, NSW 2050, Australia

Phone: 61 (02) 9385 2731 Facsimile: 61 (02) 9385 3733 E-mail: t.milne@unsw.edu.au

The potential of synthetic aperture radar (SAR) to map the distribution of wetlands, forests and woodlands and to monitor long term developments in these ecosystems, as well as to contribute to an understanding of global change, depends on the ability of science to unravel the relationships that exist between microwave backscatter, surface conditions and the physical characteristics of trees and forests.

Four major research programs are currently being undertaken in tropical Northern Australia incorporating the analysis of SIR-C/X SAR; ERS 1/2; RADARSAT and AIRSAR data along with Landsat TM and SPOT imagery. These are:

- Investigating the Backscatter Properties and Dynamics of Australian Tree Types and Forests (with Dong and Forster).
- Monitoring Change in Coastal Wetlands, Forests and Woodlands in Northern Australia Using RADARSAT (with Finlayson).
- Characterisation of Vegetation and Land Surfaces on Intertidal Flats in Northern Australia using Radar (with Adam and King).
- Remotely Sensed Indicators of Habitat Heterogeneity and Biological Diversity: Kakadu World Heritage Region, Northern Australia (with Imhoff and Sisk).

WETLAND INVESTIGATIONS

The variable resolutions and swath widths of RADARSAT together with its repeat coverage capability provide a significant enhancement and new dimension to studies already in progress, namely, the ability to undertake regional mapping on a scale not previously possible and over several time periods. The aims of this study are to:

- (1) Map the extent of coastal wetlands across Northern Australia based on wet season/dry season imagery.
- (2) Monitor seasonal changes in the temporal and spatial patterns of inundation in selected river basins in order to delineate freshwater from tidal wetlands areas.

- (3) Contribute to the structural characterisation of vegetation types found in the Alligator Rivers Region catchment.
- (4) Monitor and assess changes in wetland environments over time, including wetland loss and degradation as well as the extent and success of wetland conservation practices.
- (5) Develop routine operational procedures for the ongoing monitoring of wetlands and tropical savanna woodlands in Northern Australia.
- (6) Continue and extend the modelling of radar backscatter characteristics of Australian tree types.

THE STUDY AREAS

A. Northern Australia

The area chosen for investigation is referred to as the 'top end' of the Australian continent and includes north-eastern Queensland, the Northern Territory and north-west Western Australia.

Seasonally and intermittently inundated floodplains occur along most of the coastal draining rivers of the 'top end' (Finlayson et al, 1991). Common to this monsoon-influenced coastal region is a dry season from April to November and a wet season from December to March. Although considerable variation in the onset and duration of rainfall occurs across the region, total precipitation declines from north to south along both the western and eastern coastlines of the Australian continent.

While the individual stream systems draining to the north-west, north and north-east of the continent are smaller than many of their counterparts in southern Australia, together these river systems account for approximately two-thirds of the total continental run-off.

In most of these catchments which drain from an upland escarpment and interior plateau towards the coast, stream flow is seasonal but prolonged throughout the dry season, especially in the lower reaches by reverse drainage from floodplains, lakes, billabongs and waterholes with water

stored from the wet season. Collectively these systems which retain and then release water or which are permanently flooded after the wet season are referred to as freshwater wetlands as opposed to the saltwater and tidal wetlands of the coastal littoral.

The ecosystems developed in these floodplain environments are complex, dynamic and resilient, often undergoing annual changes in water depth ranging from being completely dry to being covered for 3-4 months by 2-3m of water. Vegetation communities present include forests, woodlands, scrub and heath, shrublands, sedge and grasslands and extensive macrophytic floating and submerged herblands, all of which relate and respond to the hydrologic regimes of either permanent or seasonal inundation.

In addition to plants, these freshwater wetlands are important breeding grounds and refuges for micro- and macroscopic animal species (Finlayson op cit).

While many freshwater wetlands in Northern Australia have been relatively undisturbed by human activities in the past, increasingly they are coming under threat from saltwater intrusion, invasion by exotic weeds, degradation by feral animals, increased pollution from agriculture and pastoralism and from the effects of tourism and recreation use.

To date there is no regional map showing the distribution and extent of wetland environments in Northern Australia. Also, there is an absence of data to indicate the proportion of the coastal lowland areas which remain flooded all year round as opposed to the proportion which dry out. Determining the spatial pattern of wetlands and the sequence of floodplain draining and drying out is an important first step to investigating the hydrologic, geomorphic and ecological processes operating in these ecosystems.

B. Alligator Rivers Region (12°30'S, 132°30'E)

For the potential of SAR in the study of wetlands to be realised, careful examination of radar backscattering from ecologically important and representative wetlands needs to be undertaken. To facilitate this, the Alligator River region located in the Northern Territory has been chosen as the major laboratory site to examine the detailed relationships between backscatter, inundation cycles and wetland environments.

The region comprises the catchments of the East Alligator, South Alligator and West Alligator Rivers which contain approximately 195,000 ha of freshwater floodplains. Over

225 plant species have been found on the floodplain with their presence and distribution varying annually with water depth and period of inundation being key determining factors (Finlayson 1993).

This region has been chosen for three reasons:

- the conservation importance of wetlands found in the Alligator Rivers region has been recognised with the listing of Kakadu National Park which falls within the region as a World Heritage Area on the basis of the natural heritage value of its freshwater wetlands and floristic diversity;
- this is one of the few sites in Northern Australia that has ongoing research programs in aquatic biology, plant biology and physiology, environmental chemistry and geomorphology;
- complementary data sets covering the region, including ERS-1, JERS-1, SIR-C/XSAR; AIRSAR; TM and SPOT, are already available.

METHODOLOGY OVERVIEW

The investigation has been broken down into a number of sequential stages and sub-projects as follows.

1. Regional mapping of wetland areas in Northern Australia will be achieved by using RADARSAT SCANSAR data. Eight images annually will be calibrated, registered together and interrogated in an attempt to derive a map of the distribution of wetlands across Northern Australia. Comparison of wet and dry season images will also be undertaken in an attempt to try and distinguish between tidal and freshwater wetland environments.

Imagery from at least four contiguous swaths (depending on orbital paths) will be needed to map the full extent of wetlands across Northern Australia.

Regional mapping of the wetlands of Northern Australia will be carried out in all three years of the project.

2. Detailed mapping of the Alligator Rivers Region wetland environments using all datasets. Hydrologic, geomorphic and ecological field and reference data is being acquired after the end of the wet season to coincide with the recession of floodwaters. Successive stages in the drying of the floodplain will be monitored and the changing environmental conditions identified and compared to changes in the backscatter return recorded on successive images.

3. Closely related to (2) will be the determination of specific wetland processes associated with:

- (a) hydrology - monitoring the seasonal pattern of floodwater recession; measurement of sediment and biological loads.
- (b) geomorphic changes - examining the interface between freshwater and tidal estuary areas over a 6-9 month period to determine if headwater extension of saltwater streams is occurring into freshwater floodplains.
- (c) characterisation of vegetation found within the
 - (i) tidal mangroves
 - (ii) coastal salt marshes and mud flats
 - (iii) seasonally inundated floodplain, lakes and waterholes
 - (iv) macrophytic distributions
 - (v) adjacent abutting upland woodlands and forests

4. Regional mapping and the monitoring of hydrologic, geomorphic and ecological patterns and processes will be repeated and extended in the years 1998 and 1999. The timing and sequence of RADARSAT data requests will be adjusted in years 2 and 3 of the study based on the spatial and temporal patterns observed in the landscape in year 1.

In year 2 the research will focus on the characterisation, field sampling and the measurement of biomass in selected vegetation habitats as well as determining changes in the pattern of inundation and recession of floodwaters.

5. A GIS relational database will be established at the Environmental Research Institute of the Supervising Scientist (ERISS) in Kakadu National Park to incorporate the results of the ongoing hydrological, geomorphic, ecological and biochemical studies related to the management of wetlands. Image processing and analysis of RADARSAT will be undertaken at the Centre for Remote Sensing and GIS at the University of New South Wales and transferred to the ERISS database.

6. In year three a regional map of the wetlands of Northern Australia will be published incorporating RADARSAT data and planimetric information derived from other sources.

Sequential maps of floodplain inundation levels for the Alligator Rivers Region for the three years will be assessed and absolute and relative changes in the

hydrologic, geomorphic and ecological characteristics of the wetland environment examined and described. Strategies for assessing and verifying longer term changes in the wetland environment will be developed.

The methodology developed for producing the sequential mapping of individual wetland catchments in the Alligator Rivers Region will be applied to the Ord River drainage basin in Western Australia and other ecological catchments across Northern Australia..

CONCLUSIONS

The first set of RADARSAT data was acquired in November 1996 and is currently being analysed along with AIRSAR data acquired in the same month. This end of dry season imagery will also be compared with late wet season RADARSAT data recorded in March 1997.

The study is innovative in that it attempts to relate radar backscatter to specific biophysical and environmental parameters. As seasonal change brings different soil-boundary-plant conditions, so backscatter can be expected to change. The objective of this study is to take measured environmental changes and relate these to received backscatter.

SELECTED REFERENCES

- [1] Y. Dong, B.C. Forster, A.K. Milne, and C. Ticehurst, "The Applications of Wavelet Transform for Speckle Suppression in Radar Imagery," Proceedings IGARSS '97, Singapore
- [2] C.M. Finlayson, "Vegetation Changes and Biomass on an Australian Monsoonal Floodplain," in *Wetlands and Ecotones: Studies in Land-Water Interactions*, B. Gopal, A. Hillbricht-Ilkowska, and R.G. Wetzel, Eds, National Institute of Ecology, New Delhi, 1993, pp157-171.
- [3] M. Imhoff, T.Sisk, A., Milne, G. Morgan, and T. Orr, "Remoteley Sensed Indicators of Habitat Heterogeneity and Biological Diversity: A Preliminary Report," 5th JPL Airborne Geoscience Workshop, vol. 3. January 1995, JPL Publication 95-1, Pasadena, pp17-21.
- [4] A.K. Milne, and P. Hausknecht, "Evaluation of MOMS-02 Data in Mapping Coastal Wetlands in Northern Australia," Proceedings 8th Australasian Remote Sensing Conference, Canberra, 25-29 March 1996, pp-175-184.

Terrain Elevations From InSAR Incorporating Ground Control Data

Majid Mirbagheri, John C. Trinder, & Bruce C. Forster

School of Geomatic Engineering and
Centre of Remote Sensing and GIS

The University of New South Wales, Sydney 2052, Australia

Tel: 61-2-9385 4197 / Fax: 61-2-9313 7493 / Email: M.Mirbagheri@technologist.com

ABSTRACT

Interferometric SAR (InSAR) techniques permit the production of elevation maps of an area through interpretation of interference fringes between two SAR images of the same region. However, uncertainty in orbit determination causes an absolute height error of the order of several hundred meters. It is a systematic error which affects every point in the image, but can be removed using known heights of a few control points in a given image scene. A model is developed to calculate absolute terrain elevation incorporating ground control points. The computation procedure is based on stereo radargrammetric mapping of overlapping SAR images, incorporating expressions for elevation based on the fringe information. The model uses second order polynomials for orbital position and first order polynomials for satellite velocity.

INTRODUCTION

Interferometry Synthetic Aperture Radar (InSAR) is a technique that uses two or more SAR images over the same area to extract high resolution digital terrain data.

Zebker et al [1] analysed ERS-1 data collected over Alaska and southwestern US. They indicated that generating maps with relative errors less than 5 m RMS was possible in some regions. Because of orbit uncertainties, tie points are required to reduce absolute height errors to a similar magnitude. They found that about 6 tie points per 40 by 40 km scene with at least 5 m RMS height accuracy are needed to reduce systematic map height errors of the order of 1 km to below 5 m RMS.

A general formulation for InSAR which relates pixel height to phase difference is [2]:

$$\varphi = \frac{2\pi}{\lambda} (B_x \sin \theta - B_y \cos \theta)$$

$$h = H_0 - \rho \cos \theta \quad (1)$$

An alternative method based on mixture of radargrammetry and InSAR is developed (Fig. 1). The Doppler and range equations for each orbit (radargrammetry), and the range difference as a function of phase difference (InSAR), can be treated as observation equations. Then, to obtain absolute height, ground control points will be incorporated as another set of observations. A combined solution is therefore developed to consider all the necessary observation equations.

METHODOLOGY

Observation equations for Doppler frequency, range, and phase

The returns from a ground target are shifted in frequency by an amount proportional to the relative velocity between the satellite and target (Doppler effect; 2a-b). The range equation gives the distance between the sensor and a ground target point (2c-d). The range difference between two sensors and a target is related to phase difference of returns to sensors (φ) and is given by (2e).

$$F_{D1} = \frac{2(\dot{S}_1 - \dot{P}) \cdot (S_1 - P)}{\lambda |S_1 - P|} \quad (2a)$$

$$F_{D2} = \frac{2(\dot{S}_2 - \dot{P}) \cdot (S_2 - P)}{\lambda |S_2 - P|} \quad (2b)$$

$$r_1 = |S_1 - P| \quad (2c)$$

$$r_2 = |S_2 - P| \quad (2d)$$

$$|P - S_1| - |P - S_2| = \frac{\lambda \varphi}{4\pi} \quad (2e)$$

or;

$$F_1 = F_{D1} - \frac{2(\dot{S}_1 - \dot{P}) \cdot (S_1 - P)}{\lambda |S_1 - P|} = 0$$

$$F_2 = F_{D2} - \frac{2(\dot{S}_2 - \dot{P}) \cdot (S_2 - P)}{\lambda |S_2 - P|} = 0$$

$$F_3 = r_1 - \sqrt{(P_x - S_{1x})^2 + (P_y - S_{1y})^2 + (P_z - S_{1z})^2} = 0 \quad (3)$$

$$F_4 = r_2 - \sqrt{(P_x - S_{2x})^2 + (P_y - S_{2y})^2 + (P_z - S_{2z})^2} = 0$$

$$F_5 = \sqrt{(P_x - S_{1x})^2 + (P_y - S_{1y})^2 + (P_z - S_{1z})^2} - \sqrt{(P_x - S_{2x})^2 + (P_y - S_{2y})^2 + (P_z - S_{2z})^2} - \frac{\lambda \phi}{4\pi} = 0$$

Where, \dot{S}_1 , \dot{S}_2 , S_1 , S_2 , F_{D1} , F_{D2} , r_1 , and r_2 are the velocity and the position of the sensor, Doppler centroid frequency, and the range value for image 1 and image 2, respectively. P and \dot{P} are the position and velocity of the target point, respectively.

To determine the position and velocity of the sensors, we firstly need to calculate time for each pixel and secondly to propagate the nearest statevector for that time. Time of acquisition of pixel (T_p) can be derived by using the following equation;

$$T_p = T_0 + T_{off} + I/PRF \quad (4)$$

where T_0 is the parameter of raw-data-start-time, T_{off} is the parameter azimuth-offset, I is the azimuth line number containing the target of interest and PRF is the pulse repetition frequency. These parameters are provided in the header data file in each image. Statevectors (also provided by the header data file) can be determined by interpolation, using a low order interpolator. The calculations showed that in this case, second order polynomials for orbital position and first order polynomials for satellite velocity are the most suitable interpolators. Therefore;

$$S_{1x} = a_{1x} t_{1p}^2 + b_{1x} t_{1p} + c_{1x}$$

$$S_{1y} = a_{1y} t_{1p}^2 + b_{1y} t_{1p} + c_{1y} \quad (5a)$$

$$S_{1z} = a_{1z} t_{1p}^2 + b_{1z} t_{1p} + c_{1z}$$

$$\dot{S}_{1x} = \dot{a}_{1x} t_{1p} + \dot{b}_{1x}$$

$$\dot{S}_{1y} = \dot{a}_{1y} t_{1p} + \dot{b}_{1y} \quad (5b)$$

$$\dot{S}_{1z} = \dot{a}_{1z} t_{1p} + \dot{b}_{1z}$$

$$S_{2x} = a_{2x} t_{2p}^2 + b_{2x} t_{2p} + c_{2x}$$

$$S_{2y} = a_{2y} t_{2p}^2 + b_{2y} t_{2p} + c_{2y} \quad (5c)$$

$$S_{2z} = a_{2z} t_{2p}^2 + b_{2z} t_{2p} + c_{2z}$$

$$\dot{S}_{2x} = \dot{a}_{2x} t_{2p} + \dot{b}_{2x}$$

$$\dot{S}_{2y} = \dot{a}_{2y} t_{2p} + \dot{b}_{2y} \quad (5d)$$

$$\dot{S}_{2z} = \dot{a}_{2z} t_{2p} + \dot{b}_{2z}$$

The ancillary data provided with the images is used to compute the coefficients of the polynomials. The intention would be to obtain range information by interpolation of the first, the centre, and the last range of pixel range provided by the standard SAR images of the same region. Therefore, the velocity, and the position of sensors and the range for each image can be treated as observation in the model of least squares solution. Another observation in the model is the unwrapped phase measurements at each point.

From this nonlinear system of equations we need to solve the unknown coordinates of P by a least-squares algorithm. Equations (3) and (5) are linearized and in accordance with the approach described by Mikhail [3]:

$$A_i V_i + B_i \Delta_i = f_i \quad (6)$$

Where Δ_i is the vector of corrections to the approximate solution \bar{P} , V_i is the vector of residuals to the observations vector:

$$\Delta_i = (\Delta P_x, \Delta P_y, \Delta P_z)^T \quad (7)$$

$$V_i = (V_{S_{1x}}, V_{S_{1y}}, V_{S_{1z}}, V_{\dot{S}_{1x}}, V_{\dot{S}_{1y}}, V_{\dot{S}_{1z}}, V_{S_{2x}}, V_{S_{2y}}, V_{S_{2z}}, V_{\dot{S}_{2x}}, V_{\dot{S}_{2y}}, V_{\dot{S}_{2z}}, V_{r_1}, V_{r_2}, V_{\phi})^T \quad (8)$$

A_i is the coefficient matrix of partial derivatives in terms of the observations, and B_i is the coefficient matrix of partial derivatives in terms of the unknown ground coordinates.

For n points observed, the complete collection of observation equations will be;

$$A_{5n,15n} V_{15n,1} + B_{5n,3n} \Delta_{3n,1} = F_{5n,1} \quad (9)$$

Observation equations for ground control points

Observation equations for known ground coordinates are added to the model. The unknown parameters are expressed in terms of a correction and an approximate value;

$$P_x = P_x^0 + \Delta P_x$$

$$P_y = P_y^0 + \Delta P_y \quad (10)$$

$$P_z = P_z^0 + \Delta P_z$$

Note that approximate values are denoted by the superscript "0" and corrections to unknown parameters are denoted by

the prefix “ Δ ”. On the other hand let, $\overset{00}{P}_x, \overset{00}{P}_y, \overset{00}{P}_z$ be the ground coordinates of point P determined previously, and V_{px}, V_{py}, V_{pz} , are the residuals associated with $\overset{00}{P}_x, \overset{00}{P}_y, \overset{00}{P}_z$ respectively, such that the ground coordinates of point P can be expressed as follows;

$$\begin{aligned} P_x &= \overset{00}{P}_x + V_{px} \\ P_y &= \overset{00}{P}_y + V_{py} \\ P_z &= \overset{00}{P}_z + V_{pz} \end{aligned} \quad (11)$$

Rearranging terms and putting the (10) and (11) into matrix form yields;

$$\begin{bmatrix} V_{px} \\ V_{py} \\ V_{pz} \end{bmatrix} - \begin{bmatrix} \Delta P_x \\ \Delta P_y \\ \Delta P_z \end{bmatrix} = \begin{bmatrix} \overset{0}{P}_x - \overset{00}{P}_x \\ \overset{0}{P}_y - \overset{00}{P}_y \\ \overset{0}{P}_z - \overset{00}{P}_z \end{bmatrix} \quad (12)$$

These Equations can be written as a single matrix equation as follows;

$$V'_{3,1} - \Delta'_{3,1} = C'_{3,1} \quad (13)$$

To keep the model as general as possible, it is assumed that measured values are available for ground coordinates of all points. The complete set of observation equations for the ground coordinates of m points is therefore;

$$\begin{bmatrix} V'_1 \\ V'_2 \\ \vdots \\ V'_m \end{bmatrix} - \begin{bmatrix} \Delta'_1 \\ \Delta'_2 \\ \vdots \\ \Delta'_m \end{bmatrix} = \begin{bmatrix} C'_1 \\ C'_2 \\ \vdots \\ C'_m \end{bmatrix} \quad (14)$$

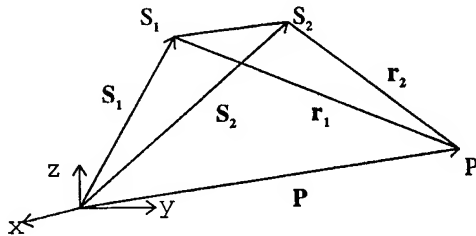


Figure 1. Radar stereo intersection

which may also be written as;

$$V'_{3m,1} - \Delta'_{3m,1} = C'_{3m,1} \quad (15)$$

Combined solution

Equations (9) and (15) can be combined and written together as;

$$\begin{aligned} AV + B\Delta &= F \\ V' - \Delta' &= C' \end{aligned} \quad (16)$$

which can be expressed as a single matrix equation as;

$$\begin{bmatrix} A & 0 \\ 0 & I \end{bmatrix} \begin{bmatrix} V \\ V' \end{bmatrix} + \begin{bmatrix} B & 0 \\ 0 & -I \end{bmatrix} \begin{bmatrix} \Delta \\ \Delta' \end{bmatrix} = \begin{bmatrix} F \\ C' \end{bmatrix} \quad (17)$$

ie.

$$\overline{A} \overline{V} + \overline{B} \overline{\Delta} = \overline{F} \quad (18)$$

In order to solve the normal equation of the above equations, equal weights for all observations are assumed. Tests are yet to be determined using real data.

CONCLUSIONS

For deriving elevations using InSAR, accurate orbit data should be known. Existing accuracy of orbit determination is not sufficient to obtain absolute height within reasonable limits, and thus ground control data is necessary to reduce errors to an acceptable level. The model described to calculate absolute terrain elevation, is based on radargrammetric mapping, phase information obtaining from InSAR and ground control data.

REFERENCES

- [1] Zebker H. A., Werner C. L., Rosen P. A. & Hensley S., "Accuracy of topographic maps derived from ERS-1 interferometric radar," IEEE Transactions on Geoscience and Remote Sensing, Vol. 32, No. 4, pp 823- 836, 1994.
- [2] Li F. K., & Goldstein R. M., "Studies of multibaseline spaceborne interferometric synthetic aperture radars," IEEE Transactions on Geoscience and Remote Sensing, Vol. 28, No.1, pp. 88-97, 1990.
- [3] Mikhail E. M., "Observation and Least Squares," IEP-A Dun-Donnelly publisher, 1976.

Improved digital elevation models via multi-baseline interferometric SAR

J. Homer and I.D. Longstaff

Department of Electrical and Computer Engineering
The University of Queensland, Brisbane, Qld 4072 Australia,
and Cooperative Research Centre for Sensor Signal
and Information Processing
Ph: +61 7 3365 3683, Fax: +61 7 3365 3684,
Email: homerj@elec.uq.edu.au

Zhishu She

Department of Electrical and Electronic Engineering
The University of Adelaide, Adelaide, SA 5005 Australia,
and Cooperative Research Centre for Sensor Signal
and Information Processing

Abstract – This paper presents an extension to interferometric SAR (InSAR), known as multi-baseline InSAR. The technique is based on the use of $N > 2$ SAR imaging flight paths to synthesise an aperture in the normal-to-slant-range (nsr) direction. This leads to the generation of digital elevation models with improved ground-range resolution and elevation accuracy as well as the ability to resolve scatterers in the nsr direction.

INTRODUCTION

Spaceborne SAR imaging systems, via the technique of interferometric SAR (InSAR), offer an effective approach to generating large scale digital elevation models (DEMs) with horizontal resolution and elevation accuracy sufficient for many applications. The horizontal resolution of the DEM is determined by the slant-range (sr) and azimuth (az) resolution of the two SAR images used to generate the interferogram based DEM, while the elevation accuracy is determined largely by the SNR of the interferogram. A number of applications, however, are emerging — such as topographically corrected hyper-resolution airborne acquired imagery — which require better quality (horizontal resolution and elevation accuracy) DEMs than spaceborne InSAR can currently provide. This paper examines an extension of standard InSAR, known as multi-baseline InSAR, which combines $N > 2$ SAR images acquired from $N > 2$ flight paths. In particular, the technique uses the flight paths to synthesise an aperture in the normal-to-slant-range (nsr) direction. The result is spatial resolution in this direction. This, coupled with the resolving power of single-pass SAR imagery in the sr direction, leads to improved ground-range resolution. Furthermore, the combination of the $N > 2$ SAR images leads to an improvement in the phase SNR of the 'multi-baseline' image as compared to the SNR of a single-baseline interferogram. An improvement in DEM elevation accuracy results. A third important feature is the ability to separately resolve scatterers which are located within the same sr - az resolution but are displaced in the nsr direction ... that is, the ability to generate true 3-dimensional images.

The next section presents background theory to the multi-baseline InSAR technique and quantifies the capabilities of this technique. Following this we present a procedural outline to the technique and then discuss some results obtained from application of the technique to a series of SAR images acquired by the ERS-1 satellite operating in repeat-pass mode.

THEORY

The multi-baseline InSAR technique is based on synthesis of an aperture in the nsr direction from $N > 2$ SAR imaging flight paths. Fig. 1 illustrates a possible flight path configuration for multi-baseline InSAR — the flight paths are directed into the page. The synthesised aperture generates a focussed beam-pattern in the nsr direction. The $3dB$ width of this beam, which is a measure of the resolution in the nsr direction, is given by: $\rho_n = \frac{R_0 \lambda}{2L_n}$, where $L_n = nsr$ synthesised aperture length, $\lambda =$ radar carrier frequency wavelength and $R_0 = sr$ distance of terrain from synthesised aperture.

The presence of resolving power in the nsr direction, in conjunction with the resolving power in the sr direction, leads to a ground-range resolving power exceeding that resulting from the sr resolving power alone. That is, the multi-baseline InSAR imaging system provides better ground-range resolution than a single-pass SAR imaging system. This improvement has been explained by analysis of the 2-D $sr - nsr$ point spread function [1] and by analysis of the ground reflectivity wavenumber spectrum [2]. The latter, which provides a better understanding of the multi-baseline InSAR procedure outlined later, is discussed briefly below.

For a given local terrain region, an imaging flight path samples a particular band of the wavenumber spectrum — centred on $k_g = 4\pi f_c \sin(\theta - \alpha)/c$ and having a width of $\delta_f k_g = 4\pi F \sin(\theta - \alpha)/c$, where θ is the local radar look angle, α is the angle the terrain makes with the horizontal, f_c is the radar carrier frequency, and F is the radar bandwidth. The ground-range resolution of the image is $\rho_g = 2\pi/\delta_f k_g$. A shift from one flight path to another, which results in a change $\delta\theta$ in the local radar look angle, consequently leads to a shift of the sampled wavenumber band by $\delta_\theta k_g = 4\pi f_c \cos(\theta - \alpha)\delta\theta/c = 4\pi f_c \cos(\theta - \alpha)B_n/(R_0 c)$, where B_n is the component of the flight path baseline in the nsr direction. Two images, related by the nsr baseline $B_n = R_0 \delta\theta$, therefore, sample a total wavenumber bandwidth of $\delta k_g = \delta_f k_g + \delta_\theta k_g$. Coherent summation leads to an image with improved ground-range resolution. This improvement, however, is conditional on: $\delta\theta < F \tan(\theta - \alpha)/f_c$, that is $B_n < R_0 F \tan(\theta - \alpha)/f_c \triangleq B_{crit}$. Failure of this condition corresponds to $\delta_f k_g < \delta_\theta k_g$, that is separation of the two wavenumber bands.

The above reasoning can be extended to a series of N imaging flight paths. The achievable improvement in ground-range resolution is determined by the total nsr baseline or nsr aperture length L_n spanned by the series:

$$\rho_g/\rho_{g,N} = 1 + L_n/B_{crit}. \quad (1)$$

Furthermore, this improvement is conditional on adjacent flight path having an nsr baseline $B_n < B_{crit}$.

The nsr synthesised aperture, being sampled, may generate an nsr beam-pattern with large grating lobes. Such grating lobes cause imaging ambiguities in the nsr direction of multi-baseline InSAR generated 3-D imagery. Knowledge of the flight path baselines enables the location and strength of such grating lobes to be determined. This then enables one to determine an upper limit on the nsr dimension of the 3-D imagery or to apply deconvolution techniques to reduce the effect of the nsr grating lobes.

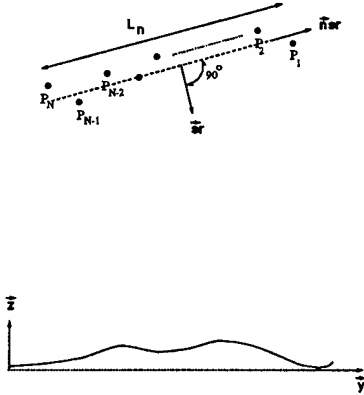


Figure 1: Multi-baseline InSAR flight path configuration.

PROCEDURE

Consider N SAR images acquired from N flight paths. Assume the nsr baselines of adjacent flight paths satisfy $B_n < B_{crit}$. The application of the multi-baseline InSAR technique involves the following procedure.

1. Co-registration of the N SAR images.
2. Interpolation of each image by at least $L_n/B_{crit} + 1$ and indexing of each image according to the flight path indexing system indicated in Fig. 1.
3. For each pair of SAR images F_i, F_{i+1} generate a phase difference image ϕ_i .
4. For a given local region, say a 16×16 pixel sized window which is zero padded to a size of 64×64 , determine the dominant phase slope in the sr direction, $\delta\phi_i$, via application of a 2-D FFT and identification of the dominant sr component within the FFT.
5. Obtain the following least squares based estimate for the local terrain angle α

$$\alpha = \theta - \arctan \left[\frac{\sum_{i=1}^{N-1} B_{n,i}^2}{\sum_{i=1}^{N-1} \delta\phi_i B_{n,i}} \right], \quad (2)$$

where $B_{n,i}$ is the nsr baseline corresponding to the SAR image pair F_i, F_{i+1} . This estimate is based on the relationship: $\delta\phi_i = \delta\theta k_{g,i}/\sin(\theta - \alpha) = 4\pi B_{n,i}/(\lambda R_0 \tan(\theta - \alpha))$. The accuracy of the terrain slope estimate α increases linearly with N — indicating the improvement in elevation accuracy achievable with multi-baseline InSAR.

6. Determine the local sr phase slope relative to image F_1 : $\delta\phi_{i,1} = \sum_{m=1}^{i-1} \delta\phi_m$, where $\delta\phi_{1,1} = 0$. Remove this relative local sr phase slope from the corresponding windowed region in image F_i :

$$\bar{F}_i(k) = F_i(k) \exp(j\delta\phi_{i,1}k), \quad (3)$$

where k is the sr index. This leads to all N images being locally phase aligned along the dominant ground plane defined by (2).

7. Sum the images to produce a single complex valued image: $G = \sum_{i=1}^N \bar{F}_i$. This image, which is focussed on the dominant ground plane defined by (2), is characterised by improved ground range resolution according to (1).

8. In general, the pixel phase values within image G will not be zero due to the presence of scattering sources located off the dominant ground plane as well as due to noise. To determine the radar backscattering strength of such sources within a given $sr - az$ pixelised terrain region, which we index by (k, l) , the following DFT based summation is applied to each set of pixels corresponding to (k, l) :

$$G_t(k, l) = \sum_{i=1}^N \bar{F}_i(k, l) \exp\left(\frac{j4\pi B_{n,1,i+1}t}{pL_n}\right). \quad (4)$$

The parameter t is an index for the nsr direction, where $t = 0$ corresponds to the dominant ground plane defined by (2); the nsr cell size is ρ_n/p , thus $p \geq 1$ is an interpolation factor; and $B_{n,1,i+1}$ is the nsr baseline of flight paths P_1 and P_i , where $B_{n,1,1} = 0$. As discussed previously, the maximum range $-T \geq t \geq T$ which avoids grating lobe imaging ambiguities, can be pre-determined by using the known set of baselines to simulate the expected nsr beam-pattern. To reiterate: the value of $G_t(k, l)$ indicates the backscattering strength of reflectors located in the 3-D $sr - az - nsr$ cell indexed by (k, l, t) .

9. Orient the 3-D image $G_t(k, l)$ according to the dominant local terrain angle of (2).

10. Repeat Steps 4-9 for all windowed regions across the images.

RESULTS

The capabilities of the multi-baseline InSAR technique have been tested using nine SAR image data sets, acquired by the ERS-1 satellite over Bonn, Germany during the period of 2 – 29 March 1992. The flight paths provide an nsr synthesised aperture

length of $L_n = 1686m$. This, together with the following typical imaging parameter values of ERS-1: $\lambda = .0567m$, $R_0 = 800,000m$, $W = 15.55MHz$, $\theta = 23^\circ$, leads to an nsr resolution cell size of $\rho_n = 26.9m$, a ground-range resolution of $\rho_g = 9.17m$ and a ground-range resolution enhancement of $\rho_g/\rho_{g,N} \approx 2.7$.

The ability of the multi-baseline InSAR technique to produce a focussed nsr beam-pattern with these data sets is demonstrated in the multi-baseline interferogram of Fig. 2. This image was generated by forming single-baseline interferograms from all 36 possible image pairs, phase aligning these interferograms on a given pixel, and then summing them. Note that the focussed fringe evident in the interferogram fades out in various locations across the image. This fading tendency, which is typical of most regions in this series of data sets, is most likely caused by temporal decorrelation amongst the images. Accordingly, temporal decorrelation may be the major limiting factor in the applicability of multi-baseline InSAR to a series of repeat-pass SAR images.

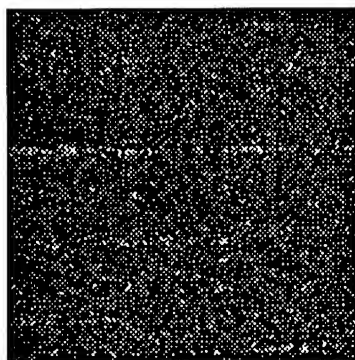


Figure 2: Multi-baseline InSAR interferogram ... showing focussed fringe.

The multi-baseline InSAR procedure outlined above was applied to a number of regions within the image series. A grey scale image output by Step 9 for a single azimuthal bin, containing 30 range bins, and which includes a corner reflector, is shown in Fig. 3. The vertical, horizontal axis of this image corresponds to the sr , nsr directions, respectively with pixel sizes $0.988m, 2.24m$, respectively. The highlighted diagonal in the image corresponds to the zeroth DFT component, that is to image G of Step 7. The cells above and below the diagonal indicate the strength of scattering sources in corresponding locations off the dominant ground plane.

The presence of grating lobes in the nsr direction is evident in Fig. 3. This is emphasised in the corresponding intensity mesh plot of Fig. 4(a). In general the effects of these grating lobes need to be removed before conducting any quantitative analysis of the 3-D imagery. Fig. 4(b) shows a plot of the pixel intensities along the highlighted diagonal in Fig. 3. Included also in Fig. 4(b) is the corresponding in-

tensity plot for one of the single-pass SAR images F_i . The multi-baseline image shows approximately 2.5 times better ground range resolution, which is in good agreement with the predicted value of 2.7.

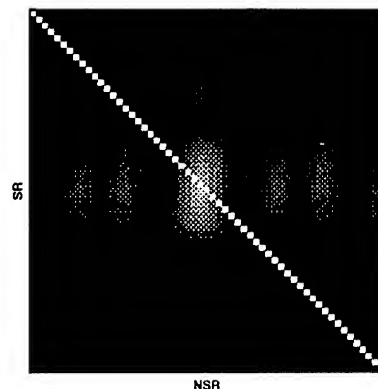


Figure 3: Grey scale multi-baseline SAR image ... imaged region contains a single corner reflector.

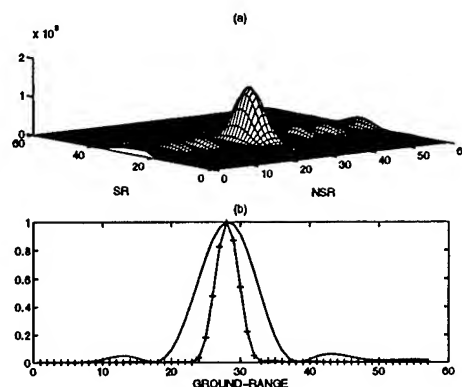


Figure 4: (a) Intensity mesh plot corresponding to Fig. 3, (b) Intensity plot corresponding to the highlighted diagonal in Fig. 3. The plot in (b) without the superimposed '+' corresponds to the pixel intensities of a single-pass SAR image along the same terrain transect.

REFERENCES

- [1] J. Homer, I.D. Longstaff, G. Callaghan, "High resolution 3-D SAR via multi-baseline interferometry", *Proceedings 1996 Int. Geosci. Remote Sens. Symp. (IGARSS96)*, 27-31 May 1996, Lincoln, USA, pp796-798.
- [2] F. Gatelli, et al., "The Wavenumber Shift in SAR Interferometry", *IEEE Trans.. Geosci. Remote Sens.*, Vol. 32, 1994, pp. 855-865.

SAR Data Processing for Interferometry Using a Personal Computer

Makoto Omura*, Katsuaki Koike, Koichiro Doi and Shigeru Aoki

* Department of Applied Science, Kochi Women's University

5-15, Eikokuji-cho, Kochi 780, Japan

Fax: +81-888-24-6579 / E-mail: omura@cc.kochi-wu.ac.jp

Abstract -- We have constructed a processing system for SAR interferometry using a personal computer. Several images were processed from raw signal data acquired by ERS-1 and JERS-1. An initial interferogram was successfully obtained from ERS-1 SAR image pair. Therefore, the constructed system was proved to be useful. Such a system on a personal computer will contribute to the SAR interferometry in a large range of geoscience.

data type which are regenerated from raw signal data. To make images of complex data type, much CPU time and large storage capacity are needed as compared with a processing for visible – reflective infrared satellite images. It was difficult to analyze SAR interferometry data without using workstations with high performance. More economical and flexible systems are required to carry out SAR interferometry easily. For this reason, we have constructed a processing system for SAR interferometry using a personal computer.

INTRODUCTION

SAR interferometry is useful to monitor changes in surface topography. SAR interferometry requires images of complex

PROCESSING SYSTEM

The personal computer consists mainly of CPU (Pentium

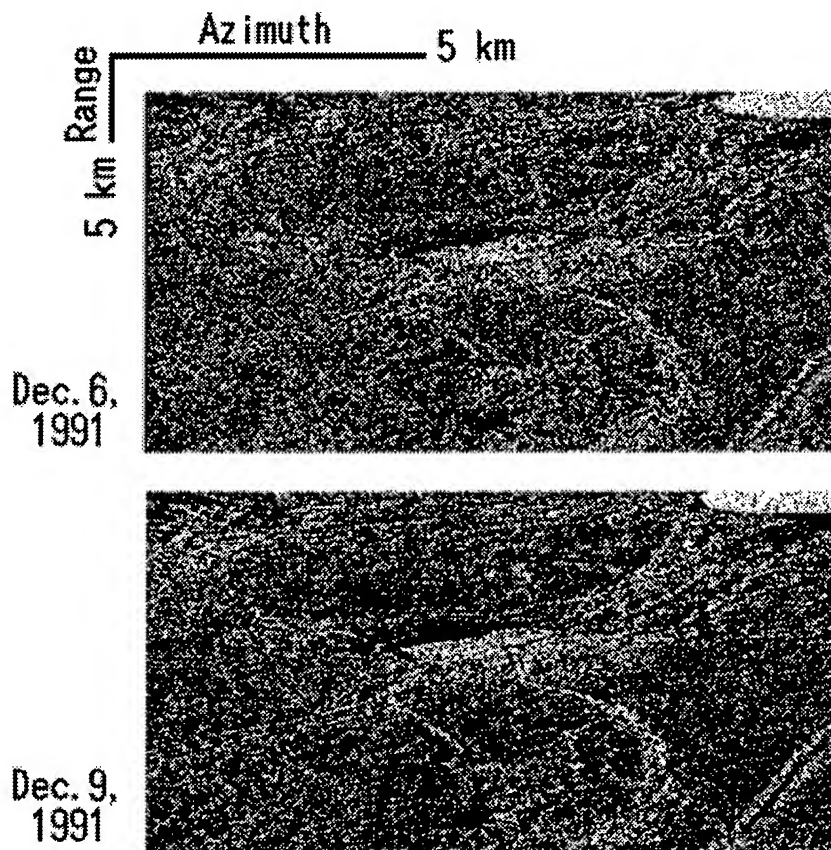


Fig. 1. SAR images by ERS-1 on Dec.6 (top) and Dec.9 (bottom),1991.

Sea ice images of the area to the west of Syowa station, Antarctica. ©ESA 1991

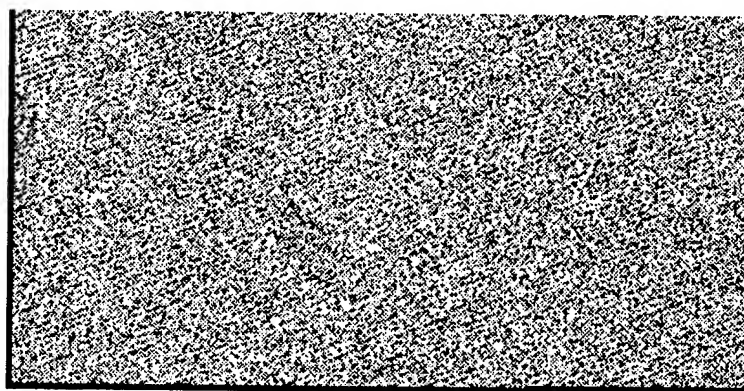


Fig. 2. An initial interferogram generated from ERS-1 SAR images in Fig.1.
Co-registration were carried out semi-automatically. Data: ©ESA 1991.

166 MHz: Intel Co.), RAM (128 MB), two internal hard discs (1.6 GB and 4.3 GB), an external hard disc of removable type (1 GB), and CD-ROM drive. Now, it becomes easier to prepare personal computers with the equivalent performance of the system used in the present study.

Two kinds of data processing software working on our system are products of Atlantis Scientific Systems Group Inc.. One is ERGOvista SAR PROCESSOR (EV-SAR ver.4.10) [1] working under MS-DOS (Microsoft Co.), the other is ERGOvista for Remote Sensing (ver.4.3) [2] working under Windows3.1/95 (Microsoft Co.). The former processor supports ERS-1, JERS-1 and other SAR sensors. The latter software allowed us to analyze and enhance images including those of complex data type.

PROCEDURE

An applied procedure is rather simple, because image generated in the present study covering limited area with dimensions of 10 - 20km. We applied proper functions of the software. Typical procedures to generate an initial interferogram are as follows;

- (1) Obtaining complex type image by using the SAR processor from raw signal data (on CD-ROMs). Suppose that a master image is image-A and another one is image-B. Both images are cut from full scene of the same observed area, but acquired on different day.
- (2) Co-registration between image-A and image-B by using ERGOvista for Remote Sensing. After manual assigning about 10 control points, the polynomial transformation coefficients are automatically calculated so as to get the best fitting between images. In this case, image-B are transformed into image-B' which is co-registered with image-A.
- (3) Calculating conjugate complex image-B'' from image-B'

by applying a function of the software.

- (4) Multiplying image-A by image-B'' to obtain an initial interferogram by using a function of the software.

EXAMPLES OF SAR IMAGE PROCESSING

We are analyzing data for a part of the Antarctica observed by ERS-1 and two active volcanic areas (Unzen and Kuju volcanoes) in southwest Japan by JERS-1.

Two ERS-1 SAR intensity images are shown in Fig.1. These two images acquired at Syowa station, Antarctica. Temporal interval is 3 days and baseline length is about 100m in the present pair. An initial interferogram (Fig.2) was successfully obtained from the pair of the images. Careful co-registration is very important to obtain a good interferogram. On the other hand, it was difficult to obtain interferograms from JERS-1 SAR data pairs selected in the present study. The difficulty may arise from longer baselines (about 2 km or longer). The system required CPU time of about 5.5 hours to generate a full scene complex image.

The present results strongly suggested that the system can be used in studies for monitoring movements of ice sheets and changes in topography related to eruptions and landslides.

CONCLUSION

The constructed system by using a personal computer was proved to be useful for SAR interferometry, because the initial interferogram was successfully generated from the ERS-1 SAR image pair. Such a system is easy to update to the latest one. The system by using a personal computer will contribute to the popularization of SAR interferometry in a large range of geoscience.

ACKNOWLEDGMENTS

We thank Dr. H. Kimura of Gifu University, Japan, for his comments to select the ERS-1 SAR image pair. We are also indebted to Mr. R. Kouda of Geological Survey of Japan for his comments on the software for SAR data processing.

A part of the present study was carried out as the Corroborative Research Program of the National Institute of Polar Research.

ESA has a ownership of ERS-1 SAR data.

MITI and NASDA have a ownership of JERS-1 SAR data.

REFERENCES

- [1] Atlantis Scientific Systems Group Inc., EV-SAR Ver.4.10 ERGOvista SAR Processor User's Manual, 1994.
- [2] Atlantis Scientific Systems Group Inc., ERGOvista Version 4.3 Command Directory, 1995.

Fault Model of the 1995 Neftegorsk, Northern Sakhalin, Earthquake based on Crustal Deformation Detected by JERS-1/SAR Interferometry

Hiroyuki Nakagawa, Mikio Tobita, Satoshi Fujiwara, Shinzaburo Ozawa, Koh Nitta, Masaki Murakami, Makoto Murakami, Masanobu Shimada* and Paul A. Rosen**

Geographical Survey Institute

Kitasato-1, Tsukuba-shi, Ibaraki-ken, 305, Japan

TEL:+81-298-64-4832/FAX:+81-298-64-1802/e-mail:hnakagaw@gsi-mc.go.jp

* National Space Development Agency of Japan

1-9-9, Roppongi, Minato-ku, Tokyo, 106, Japan

** Jet Propulsion Laboratory

4800 Oak Grove Drive, Pasadena, CA 91109, USA

Abstract -- A large ($M_w=7.0$) earthquake occurred on May 27, 1995 at the northern part of Sakhalin Island. We detect crustal deformations around seismic fault by synthetic aperture radar (SAR) interferometry using JERS-1 (Japanese Earth Resources Satellite-1) data. The result is consistent with field surveys on the part of the fault. A pair of adjacent peaks of uplift is detected at the southern edge of the seismic fault where geodetic observation is difficult because of inconvenient transportation. Using this crustal deformation data, we construct a fault model by a non-linear least squares method. Our model is in agreement with seismic wave study. It can reproduce the characteristic deformation features detected by SAR interferometry. Our study shows that SAR interferometry is a unique geodetic tool to obtain spatially dense information which could not be obtained by other techniques.

INTRODUCTION

On May 27, 1995, a large (momentum magnitude 7.0) earthquake occurred at the northern part of Sakhalin Island. This earthquake brought us important information about the tectonics on eastern side of the Japan Sea. Field workers reported that a right-lateral, strike-slip seismic fault was exposed on the surface. It runs NNE as long as 35km and the maximum lateral displacement is about 8.1m [1]. After the earthquake, GPS (global positioning system) observations were performed around northern part of the fault. Comparing them with trilateration surveys in 1990, it was found that typical crustal displacement is 3.5m northward and 1m uplift around the west side of the fault [2]. But the whole picture of the crustal displacement was hard to detect.

We report the detection of the crustal deformations associated with this earthquake by synthetic aperture radar (SAR) interferometry and the construction of a fault model using this result.

ANALYSIS METHODOLOGY

SAR interferometry

JERS-1 (Japanese Earth Resources Satellite-1) is the only satellite with L-band SAR (wavelength is 23.5cm) available at the present. When SAR interferometry is performed, L-band SAR is more robust than C-band in terms of spatial and temporal decorrelation [3]. We used JERS-1 data acquired one month before (April 28) and two weeks after (June 11) the mainshock to detect crustal movements associated with the earthquake.

We followed standard SAR processing to get single look complex data. From them we computed a raw interferogram with fringes due to both topography and crustal deformation. To remove topographic fringes there are two major methods. One is that the topographic fringes are simulated by digital elevation model (DEM) and removed from the raw interferogram. The other is that another pair without crustal deformation is used to estimate topography directly. We adopted the former one using 30-arc second mesh (approximately 1km) DEM distributed through the Internet by Earth Resources Observation Systems Data Center of U.S. Geological Survey. This mesh scale is small enough for our work because the interferometric baseline is short, the topography is relatively flat, and crustal deformation is large.

Seismic fault modeling

We constructed a fault model by a non-linear least squares method. The observable is the crustal displacement of 800 points around the fault, picked up from the SAR interferometry result. As a starting model, we used a fault system consisting of four subfaults with the same strike angles and the dip angle of subfaults was fixed to 87 degrees, which was estimated from the seismic wave study [4]. The three of them in northern part have the same width and depth, whereas the southernmost subfault has different width and depth from the remainders. After estimating this model, we improved it by dividing these subfaults into more and estimated slip distribution. The geometry of the fault parameters is shown

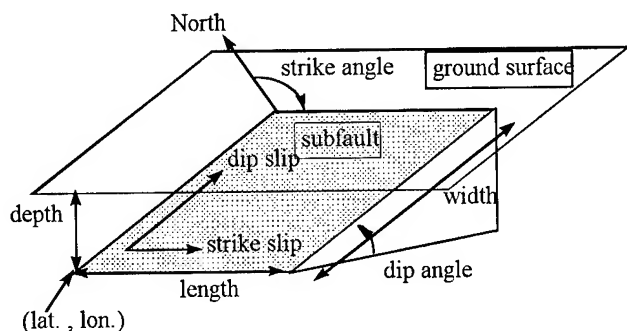


Fig.1 The geometry of the model fault parameters

in Fig.1.

RESULTS

SAR interferometry

The result of SAR interferometry is shown in Fig.2. We obtained reasonably good interferometric correlation. The baseline component perpendicular to the radar looking direction is about 260m. One cycle of interferometric phase



Fig.2 Crustal deformations of the 1995 Neftegorsk earthquake detected by JERS-1/SAR interferometry (April 28, 1995 - June 11, 1995). A color wheel shows one cycle of interferometric phase change (11.8 cm). A solid black line in the image shows the fault exposed on the surface.

change shown by the color wheel means displacement of 11.8cm. Because the mainshock fault runs nearly parallel to the JERS-1 satellite orbit and side-slip motion along the fault does not have the component in the radar look direction, the interferogram is not very sensitive to the horizontal displacement. Therefore, the interferogram shows mainly vertical displacement.

The result indicates about 1m subsidence on the eastern side of the north end of the fault and 30~45cm uplift all over the western side of the fault, which is consistent with GPS observations by Takahashi et al (1995) [2]. The interferogram also shows the crustal displacement in southern part of the fault where geodetic observation is difficult because of inconvenient transportation [2]. Characteristic fringes are shown on the eastern side of the southern end of the seismic fault. A pair of adjacent peaks of uplift clearly appears. The northern one reaches more than 70cm.

Seismic fault modeling

The position of the estimated optimal model is located near the actual seismic fault appeared on the surface. It is noteworthy that, to explain the fringe pattern in the south part, the model fault must extend more to the south than the observed fault. This result indicates that underground seismic fault extends more to the southward than observed on surface, which is also suggested by the distribution of the aftershocks.

Then we divided these subfaults into 2 or 3 and estimated slip distribution maintaining the optimal configuration from the least-squares fitting above. The slip distribution shows about 2m slip in southern part and about 4m in northern part. This is in agreement with the seismic wave study by Kikuchi (1996) of the larger rupture of northern parts [4].

Fig.3 shows a simulated interferogram calculated from our fault model. It can reproduce the characteristic displacement feature in eastern side of the fault, subsidence at the northern part and uplift on the southern part. It also shows twin-peak uplift at the southern end of the fault.

CONCLUSIONS

The crustal deformation of the Neftegorsk earthquake on the southern part of the seismic fault was not well known. By JERS-1/SAR interferometry we obtain specially dense crustal deformation data of the earthquake around seismic fault. The result shows about 1m subsidence on the eastern side of the north end of the fault and 30~45cm uplift on the western side of the fault, which is consistent with the field surveys. Moreover, a pair of adjacent peaks of uplift of over 70cm was clearly detected at the southern edge of seismic fault.

Using the result of SAR interferometry, we constructed a fault model by a non-linear least squares method. Our model

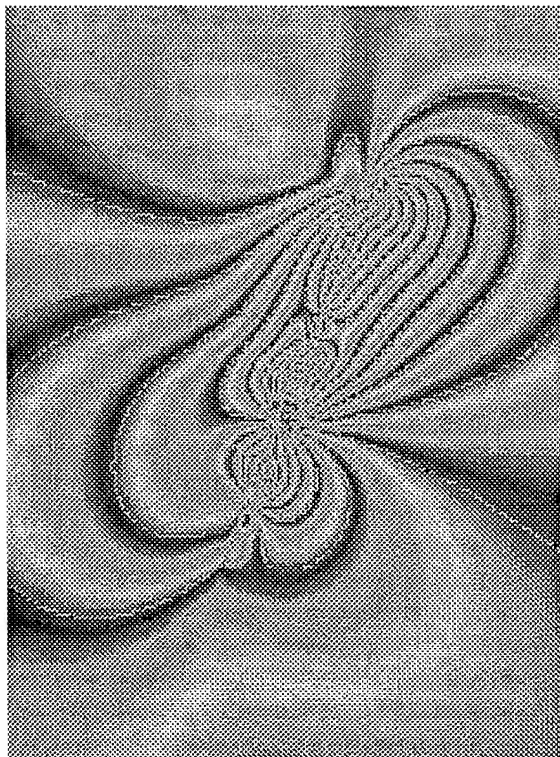


Fig.3 Simulated SAR interferogram from our seismic fault model. A color wheel shows one cycle of interferometric phase change (11.8 cm).

can reproduce the characteristic features of crustal displacement such as the contrast between northern and southern part in eastern side of the fault and the uplifts in southern end of the fault. The slip distribution of the model is in agreement with other study of seismic wave.

Our study shows that SAR interferometry is a unique

geodetic tool to acquire spatially dense information on crustal displacement.

ACKNOWLEDGMENTS

The SAR data used in this study were provided by National Space Development Agency of Japan (NASDA). Ministry of International Trade and Industry (MITI) and NASDA retains the ownership of the original SAR data.

REFERENCES

- [1] T. Shimamoto, M. Watanabe, Y. Suzuki, A. I. Kozhurin, M. I. Strelizhov, and E. Rogozhin, "Surface Faults Associated with Neftegorsk Earthquake," *J. Geol. Soc. Japan*, vol. 101, No. 7, pp.XIX-XX, July 1995 (in Japanese)
- [2] H. Takahashi et al, "The Crustal Movement of Northern Part of the Seismic Fault associated with the North Sakhalin Earthquake in 1995," in "Research study of the 1995 north Sakhalin earthquake and its damage," the report of the subsidy for science study No.07300009, Ministry of Education, Science, Sports and Culture, 1996, pp27-36 (in Japanese)
- [3] H. A. Zebker and J. Villasenor, "Decorrelation in Interferometric Radar Echoes," *IEEE Trans. Geosci. Remote Sens.*, vol. 30, No. 5, pp. 950-959, September 1992
- [4] M. Kikuchi, "Mechanism Analysis by teleseismic body waves," in "Research study of the 1995 north Sakhalin earthquake and its damage," the report of the subsidy for science study No.07300009, Ministry of Education, Science, Sports and Culture, 1996, pp37-44 (in Japanese)

Synthetic Aperture Radar Image Reconstruction Algorithms Designed for Subsurface Imaging.

Peter T. Gough,

Department of Electrical and Electronic Engineering,
University of Canterbury,
Private Bag 4800,
Christchurch, New Zealand.
64 (3) 364-2297, FAX 64 (3) 364 2761.
gough@elec.canterbury.ac.nz

Bobby R. Hunt

Department of Electrical and Computer Engineering,
University of Arizona,
Tucson, AZ 85721
USA
(520) 621-6178, FAX (520) 621-8076
hunt@ece.arizona.edu

Abstract: The standard image reconstruction algorithm for most SAR systems is either the wavenumber algorithm mainly used for exact wide bandwidth imaging or a version of the chirp scaling algorithm if computational efficiency is important. When it is desired to image a subsurface layer, these reconstruction algorithms can be modified to emphasize a subsurface layer at the expense of the surface layer. The key to the modified algorithm is a reduction of the wavelength used in the reconstruction process by a predetermined amount where the amount of the reduction depends on the depth and the dielectric constant of the soil. Some simulated results shows the effectiveness of the modified algorithm.

SAR IMAGING OF SURFACE TERRAIN.

Let us first layout the notation and the image reconstruction algorithm used to image the surface of the earth using SAR. The general geometry can be seen in Fig.1.

Recorded data in terms of Slant Plane Coordinates

First we need to project the ground plane (x, y) onto the slant plane (r, y) and also define the combined real aperture impulse response in terms of slant range r .

$$ss(t, u) = \int_y \int_r ff(r, y) \cdot a(t; r, y - u) \odot_t p \left[t - \frac{2}{c} \sqrt{r^2 + (y - u)^2} \right] dr dy \text{ for } r \geq h \quad (1)$$

and the origin of coordinates here is the center of the aperture to be synthesized.

The Transfer Function

Taking the 2-D Fourier transform from t and u to ω and k_u gives us

$$\begin{aligned} SS(\omega, k_u) &= P(\omega) A(k_u) \int_y \int_r ff(r, y) \\ &\cdot \exp(-j\sqrt{4k^2 - k_u^2} \cdot r) \cdot \exp(-jk_u y) dr dy \\ &= P(\omega) A(k_u) \int_y \int_r ff(r, y) \\ &\cdot \exp(-jk_r r) \cdot \exp(-jk_y y) dr dy \end{aligned} \quad (2)$$

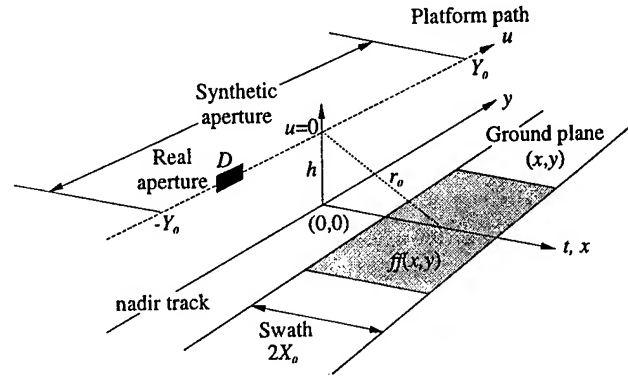


Figure 1: Generalized geometry for strip-map SAR

where $k_r = \sqrt{4k^2 - k_u^2}$ and $k_y = k_u$. Now the SAR transfer function (2) can be most elegantly expressed as

$$SS(\omega, k_u) = P(\omega) A(k_u) \cdot S\{FF(k_r, k_y)\} \quad (3)$$

where the Stolt mapping $S\{\cdot\}$ is a coordinate transformation from k_r and k_y into ω and from k_y into k_u .

Image Reconstruction

The basis of most precise SAR image reconstruction techniques is the inversion of the transfer function given in (3). To reconstruct the diffraction-limited image, we can use either inverse filtering or matched filtering but for really well controlled side lobes, we can apply external window filtering using any one of a number of well-known window functions $WW(k_r, k_y)$. This leads to the simplest of all the reconstruction algorithms with the proviso that it assumes we have *very* precise grid to grid interpolators available. This algorithm has been variously called the Stolt-mapping, wavenumber, seismic migration algorithm [1], [2], [3] and [4].

$$\widehat{FF}(k_r, k_y) = WW(k_r, k_y) \cdot S^{-1}\{SS(\omega, k_u)\} \quad (4)$$

where the inverse Stolt coordinate mapping is given by $k_r = \sqrt{4k^2 - k_u^2}$ and $k_y = k_u$ (and here we have assumed interpolators of very high precision are available). Thus

the diffraction limited image in slant range coordinates is given by

$$\widehat{ff}(r, y) = \mathcal{F}_{k_r, k_y}^{-1} \{ \widehat{FF}(k_r, k_y) \}. \quad (5)$$

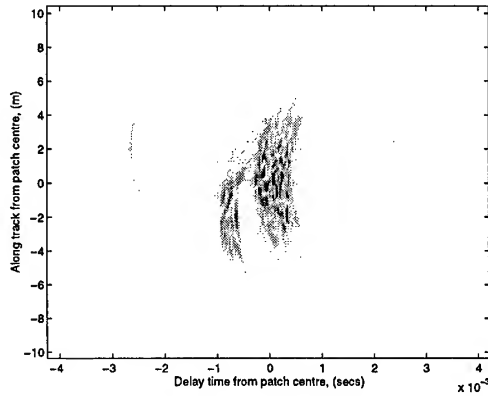


Figure 2: Raw echo data of two extended targets and a retro-reflector all on the surface.

SAR IMAGING OF SUBSURFACE TERRAIN.

Here we first make the assumption that the wavelength, dielectric constant and incidence angle are all sufficient to give some ground penetration. There is some experimental evidence that skin depths of some meters is possible [5]. Mathematically we consider the ground surface reflectivity function to be replaced by a ground volume reflectivity function $ff(x, y, z)$ where the attenuation due to absorption in the soil is included in the reflectivity function. First we must project this function onto the slant range coordinates and now the detected echoes are given by

$$ss_z(t, u) = \int_z \int_y \int_x ff(r, y, z) \cdot a(t; r, y - u) \odot_t p \left[t - \frac{2}{c} \sqrt{r^2 (1 - (z/r) \tan \phi_\epsilon \sin \phi)^2 + (y - u)^2 (1 - (z/r) \tan \phi_\epsilon \sin \phi)^2} - \frac{2\sqrt{\epsilon_r}}{c} \cdot \frac{z}{\cos \phi_\epsilon} \right] dr dy dz \quad (6)$$

where ϕ_ϵ is given by Snell's Law and the angle of the incident beam to the normal of the earth's surface at the center of the swath ϕ as well as the relative dielectric constant of the earth's subsurface ϵ_r (here assumed constant for all $z < 0$). Specifically,

$$\sin \phi_\epsilon = \sin \phi / \sqrt{\epsilon_r}$$

Now taking the 2-D Fourier transform gives

$$SS_z(\omega, k_u) = A(k_u) P(\omega) \int_{z \geq 0} \mathcal{S}_z \{ FF(k_r, k_y, z) \} \exp \left(-jk\sqrt{\epsilon_r} \frac{z}{\cos \phi_\epsilon} \right) dz \quad (7)$$

where the coordinate transformation $\mathcal{S}_z\{\cdot\}$ of k_r and k_y into ω and k_u is given by

$$\omega = \frac{c}{2(1 - (z/r) \tan \phi_\epsilon \sin \phi)} \sqrt{k_r^2 + k_y^2}$$

$$k_u = k_y$$

Thus the Stolt mapping $\mathcal{S}_z\{\cdot\}$ for the volume reflectivity case has a very slight dependence on the depth z , (as well as on the angle of incidence ϕ and on the dielectric constant ϵ_r) and we cannot change the order of transformation and integration. Thus $SS_z(\omega, k_u)$ is composed of many overlays in depth (the integral over z) and it is difficult, but not impossible, to image a layer at one depth without clutter from that at another using $SS_z(\omega, k_u)$ as input and worse, isolate anything at depth from the very much stronger surface scatter.

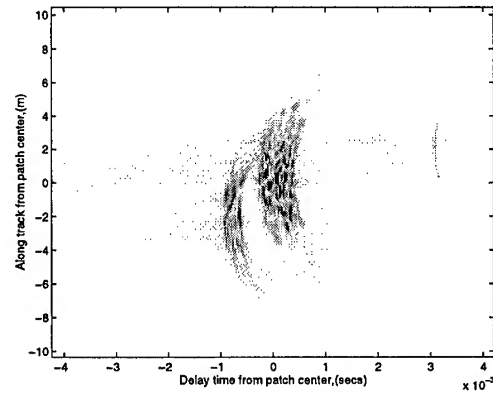


Figure 3: Raw echo data of two extended surface targets and a buried retro-reflector.

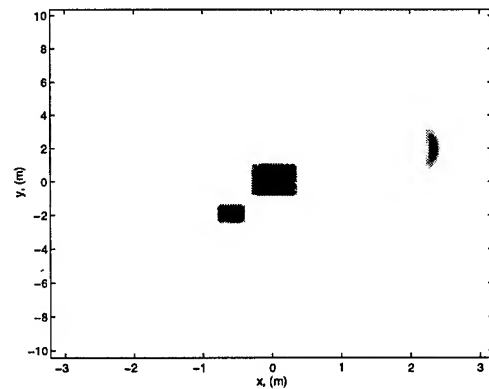


Figure 4: Image reconstructed from previous raw data. Note the buried retro-reflector appears in the wrong place and is blurred.

GROUND PENETRATING IMAGE RECONSTRUCTION ALGORITHM.

So given that we have measured $ss_z(t, u)$ and then computed $SS_z(\omega, k_u)$, the modified wavenumber image reconstruction algorithm is as follows:

$$\widehat{FF}(k_r, k_y, z) = WW(k_r, k_y) \cdot S_z^{-1} \{ \exp(jk\sqrt{\epsilon_r}z / \cos \phi_\epsilon) \cdot SS_z(\omega, k_u) \} \quad (8)$$

where the inverse depth-dependent Stolt mapping from ω and k_u into k_r and k_y is given by

$$\begin{aligned} k_r &= \sqrt{4(1 - (z/r) \tan \phi_\epsilon \sin \phi)^2 k^2 - k_u^2} \\ k_y &= k_u \end{aligned}$$

and where again we have assumed that interpolators of very high precision are available. If the depth parameter in (8) is set to zero, the equation collapses to (4) describing the normal surface imaging reconstruction algorithm.

SIMULATED RESULTS

To show subsurface focusing is possible, we first simulated (using MATLAB) two square extended targets on the surface and a retro-reflector a small distance in front of and to the side of these targets by some 2m. With the retro-reflector on the surface, the raw echoes (demodulated to baseband) are shown in Fig.2. Using this as input, the standard wavenumber algorithm happily reconstructs a true image (not shown).

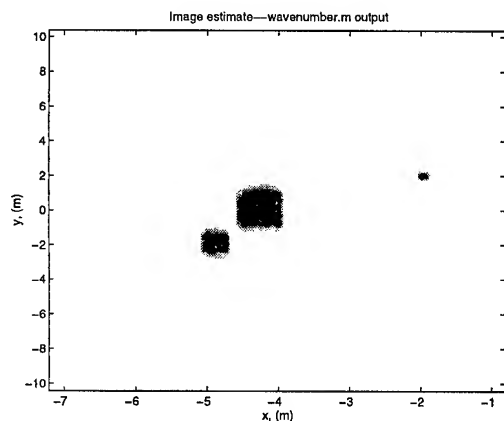


Figure 5: Image reconstructed using subsurface focusing. Note the retro-reflector appears in the correct location (the x ordinate has been moved) and the surface clutter is in the wrong location and also defocussed

Now with the retro-reflector in the same x and y location but buried to some appropriate scaled depth, the raw data shows the effect of the extra delay time necessary for the radiation to pass between the surface and the

retro-reflector and return: this is shown in Fig.3. The consequence of this extra, almost fixed time delay, is that the echo from the retro-reflector has the wrong phase curvature for the total delay time and it is this slight difference that we are exploiting in our proposed algorithm. When the normal surface reconstruction algorithm is applied to this raw data, the surface squares are still well resolved but the buried retro-reflector is quite blurred as is shown in Fig.4. Note that the complex nature of the extended targets produces an image with a typically speckled appearance. (This is a single look image.)

Now using the same data as input with our modified algorithm and focussed on the appropriate depth, the retro-reflector is now quite well focussed and at the right position in x as shown in Fig.5. The square targets now constitute surface clutter and are somewhat blurred and in completely the wrong position. (Note the x ordinate of the image has been moved to illustrate the effect of the surface clutter). It is clear from this image, if nothing else, that ways must be found to nullify or reduce the surface clutter to produce clear images of the earth's sub-surface.

CONCLUSIONS

Although it will always be difficult to image the sub-surface of the earth from satellite-borne SAR, it is possible to increase the prospect of a useful image by using an appropriately modified wavenumber algorithm. The specific modification (which turns out to be a slight reduction of the wavelength used in the image reconstruction algorithm) improves the focus of sub-surface reflectors at the expense of surface clutter.

References

- [1] M. Soumekh. *Fourier Array Imaging*, Prentice-Hall, Englewood Cliffs, NJ, 1994.
- [2] R. Bamler. A comparison of range-Doppler and wavenumber domain SAR focusing algorithms. *IEEE Trans. Geosci & Remote Sens.*, **GE-30**(4), 1992, pp.706—713.
- [3] C.Y. Chang, M. Lin & J.C. Curlander, SAR processing based on the exact two-dimensional transfer function, *Int. Geosci. & Remote Sens. Symp.*, **1**, 1992, pp. 355—359.
- [4] C. Cafforio, C. Pratti & F. Rocca. SAR focussing using seismic migration techniques, *IEEE Trans. Aero. Elect. Syst.*, **27**(2), 1991, pp. 194—207.
- [5] C. Elachi, L.E. Roth, & G.G. Schaber, Spaceborne radar subsurface imaging in hyperarid regions, *IEEE Trans. Geosci & Remote Sens.*, **GE-22**, 1984, pp.383—388.

ON THE PROPER POLARIMETRIC SCATTERING MATRIX FORMULATION OF THE FORWARD PROPAGATION VERSUS BACKSCATTERING RADAR SYSTEMS DESCRIPTION

Ernst Lüneburg¹, Shane R. Cloude² and Wolfgang-M. Boerner³

1. German Aerospace Research Establishment, DLR, Oberpfaffenhofen, Bavaria, D-82230 Wessling, Germany,
T/F: +[49](8153)28-2343/1135, e-mail: ernst.lueneburg@dlr.de
2. Applied Electromagnetics, St. Andrews, Scotland, KY16-9UR, UK,
T/F: +[44](1334)47-7598/5570, e-mail: scloude@fges.demon.co.uk
3. University of Illinois at Chicago, UIC-EECS/CSN, m/c 154, 900 W. Taylor St., SELW-4210, Chicago, IL / USA
60607-7018, T&F: +[1](312)996-5480, e-mail: wolfgang.m.boerner@uic.edu

Abstract: Jones matrices and Sinclair matrices are 2×2 complex matrices that determine forward (transmission) and backward scattering, respectively. Under a unitary change of polarization basis they transform by ordinary unitary similarity and by unitary consimilarity, respectively, forming equivalence classes with common invariant polarimetric features. In most applications the Jones matrices T are normal and, thus, have orthogonal eigenvectors; whereas, Sinclair matrices S are symmetric and have orthogonal coneigenvectors. For forward scattering the term homogeneous is used in this case. Recently, inhomogeneous Jones and Sinclair matrices characterized by non-orthogonal eigenvectors and coneigenvectors have attracted attention. The present contribution considers some characteristics of these matrices. In particular it is shown that the graphical field-of-value representation of inhomogeneous Jones matrices leads to an interesting characterization of the degree of inhomogeneity, often characterized by the (cosine of the) angle between the normalized eigenvectors. Applications of the resulting theorems to both optical (transmission) and radar (backscattering) polarimetry are demonstrated, together with identifying the inherent mathematical intricacies and physical complexities which are integral to radar and optical polarimetry.

INTRODUCTION

Radar polarimetry is the merging of the technological concept of radar (radio detection and ranging) and of the fundamental property of transversality of electromagnetic waves [1]. It started about 50 years ago with the pioneering works of Sinclair, Deschamps, Kennaugh, Graves, et al.. This early work culminated in the famous 1970 Ph.D. thesis of J. Richard Huynen. In the last two decades the importance of radar polarimetry in problems of remote sensing with real and synthetic aperture radar, inverse scattering, radar meteorology, target recognition and classification, clutter suppression and target decomposition was fully recognized [2,3].

During the past several years, however, it also became

evident that the full appreciation of polarimetric methods [4], especially in remote sensing, is hampered by a lamentable lack of understanding of basic polarimetric concepts obscuring the inherent polarimetric structures of radar responses [5]. This is related to the problem of properly defining polarization states for electromagnetic waves travelling in opposite directions, the definition of co- and cross-polarized components and the correct form of polarization basis transformations of coherent scatter matrices [6,7].

This contribution is concerned primarily with a comparison of radar polarimetry and optical polarimetry, where conventional radar polarimetry is restricted to the monostatic backscatter case and optical polarimetry is the forward scattering (transmission) case. But with the recent advent of multi(mono+bi)static radar implementation and with the rapid advancement of Interferometric Polarimetric SAR imaging, a solid understanding of the intricacies of bistatic scattering matrix theory which was derived primarily from the monostatic polarimetric radar theory becomes of utmost relevance. For the sake of simplicity mainly deterministic targets are considered that can be described by the complex 2×2 Sinclair S versus Jones T matrices, respectively [1,4], and we refer to [1] for more detailed references.

Radar polarimetry was developed in the early 1950's. It was apparent from the beginning that methods and results of the already well-established optical polarimetry could not be applied directly to the case of radar polarimetry. Recent investigations [5,6,7] indicate that radar backscattering and/or bistatic scattering are best described by an antilinear scatter operator whereas optical forward scattering polarimetry is ruled by a linear operator.

The difference in the nature of the appropriate scatter operator leads to fundamentally different transformation formulae for the Sinclair matrix S and the Jones matrix T under unitary changes of polarization bases: $S \rightarrow U^T S U$ (consimilarity) versus $T \rightarrow U^{-1} T U$ (similarity) where U is a unitary transition matrix. This behavior has important consequences for the theory of optimal polarizations as well as for copolar and crosspolar power transfer properties and

leads to remarkable and distinctive characteristic features of radar polarimetry and optical polarimetry which have unfortunately not always been treated properly [8].

The extension to the incoherent case is straightforward and it is treated in related studies on polarimetric target feature sorting [9], polarimetric target feature classification [10] and to polarimetric optimization of interferometric coherence [11] as summarized in [12,13].

TRANSMISSION VERSUS SCATTERING

In consideration of the scattering of electromagnetic waves from a finite target or from the earth, the coordinate systems used must be carefully defined. Consider [1: Fig. 5-2a/b] showing a transmitter (transmitting antenna), target, and receiver (receiving antenna). The receiver, in general, is not located at the transmitter, requiring a general bistatic coordinate system description [7]. A wave incident on the target from the transmitter is given by the transverse components E_{x1} and E_{y1} in the right-handed coordinate system $x_1y_1z_1$ with the z_1 axis pointed at the target. Coordinate system $x_2y_2z_2$ is right-handed with z_2 pointing away from the target toward a receiver. Two coordinate systems labeled $x_2y_2z_2$ are shown in [1: Fig. 5-2b] to emphasize that the receiver may be located anywhere and that z_2 points toward it from the target, where it is necessary and convenient for bistatic scattering to introduce the 'plane of scattering', spanned by k_{incident} and $k_{\text{scattered}}$. In [1: Fig. 5-2b] the unit vectors x_1 , x_2 and x_3 with $x_3 = -x_2$, lie in this plane; while y_1 , y_2 and y_3 are perpendicular to it. The $x_3y_3z_3$ coordinate system would coincide with the transmitter system $x_1y_1z_1$ if the transmitter and receiver were co-located. The wave reflected by the target to the receiver may be described in either the transverse components E_{x2} and E_{y2} or by the reverse components E_{x3} and E_{y3} . Both conventions are used, leading to different matrix formulations. The incident and transmitted or reflected (scattered) fields are given by two-component vectors; therefore, the relationship between them must be a 2×2 matrix. If the scattered field is expressed in $x_3y_3z_3$ coordinates, known as the Back-Scatter Alignment, BSA, convention [1,4], the fields are related by the Sinclair matrix, thus

$$\begin{bmatrix} E_{x3}^s \\ E_{y3}^s \end{bmatrix} = \frac{1}{\sqrt{4\pi r_2}} \begin{bmatrix} S_{x3x1} & S_{x3y1} \\ S_{y3x1} & S_{y3y1} \end{bmatrix} \begin{bmatrix} E_{x1}^i \\ E_{y1}^i \end{bmatrix} e^{ijk_2} \quad (1)$$

and if the scattered field is in $x_2y_2z_2$ coordinates known as the Forward Scatter Alignment, FSA, convention [1,4-8], it is given by the product of the Jones matrix with the incident field, thus

$$\begin{bmatrix} E_{x2}^s \\ E_{y2}^s \end{bmatrix} = \frac{1}{\sqrt{4\pi r_2}} \begin{bmatrix} T_{x2x1} & T_{x2y1} \\ T_{y2x1} & T_{y2y1} \end{bmatrix} \begin{bmatrix} E_{x1}^i \\ E_{y1}^i \end{bmatrix} e^{ijk_2} \quad (2)$$

In both equations the incident fields are those at the target, the received fields are measured at the receiver, and r_2 is the distance from target to receiver. The Sinclair matrix is most used for backscattering, but is readily extended to the bistatic scattering case depicted in [1: Fig. 5-2b]. If the name scattering matrix is used without qualification, it normally refers to the Sinclair matrix. In the general bistatic scattering case, the elements of the Sinclair matrix are not related to each other, except through the physics of the scatterer. However, if the receiver and transmitter are co-located in the monostatic or backscattering situation and if the medium between target and transmitter is reciprocal, without Faraday rotation, the Sinclair matrix is symmetrical. The Jones matrix is most used for the forward transmission case. If the coordinate systems being used are kept in mind, the numerical subscripts can be dropped. A more succinct treatment of forward propagation versus backward scattering coordinate system and matrix formulations is given in Lüneburg [5-8] associating the similarity transformation of 'Optical Polarimetry' with the first and the consimilarity transformation of 'Radar Polarimetry' with the latter, respectively [1-3,12].

It is clear that in the bistatic case, the matrix elements for a target depend on the orientation of the target with respect to the line of sight from transmitter to target and on its orientation with respect to the target-receiver line of sight. In the forms (1) and (2) the matrices are absolute matrices, and with their use the phase of the scattered wave can be related to the phase of the transmitted wave. If this phase relationship is of no interest the distance phase term can be neglected, and one of the matrix elements can be taken as real. The resulting form of the Sinclair matrix is called the relative scattering matrix. In general the elements of the scattering matrix are dependent on the frequency of the illuminating wave.

In a next step, a careful distinction of incoming and outgoing wave polarization spaces is introduced in [1,5-7] where the introduction of the time reversal operator, defined by Lüneburg [6,7] leads quite naturally to the concept of an antilinear radar backscatter operator which is distinct from the optical forward propagation operator. This procedure restores logic consistency and it does remove misconceptions related to the radar, the voltage and the power transfer equations which were derived from simplified linear network systems approaches. Back-scatter (reflection) versus Forward-scatter (transmission) matrices have fundamentally rather different representations under changes of orthonormal polarization bases. The concepts of (unitary) consimilarity

for backscattering versus ordinary (unitary) similarity for forward scattering are properly addressed and identified. In mathematical terms, the definition of the state of polarization for the backscattered wave relies on the time reversal operation which is a discrete anti-unitary operator [7]. This choice applies also to radar polarimetry, and it is perfectly adapted to the fact that an antenna possess one and only one polarization for transmission and reception; i.e., it must satisfy topologically the SO3 group rotation rules [1,5-7,12].

CONCLUSIONS

Radar polarimetry is not a mixture of scattering behavior and network performance as some people still believe. The fundamentals of radar backscatter polarimetry can now be derived without reference to the voltage equation. In our opinion there exist fundamental differences between optical (transmission) and radar (backscattering) polarimetry described by a linear and an antilinear operator, respectively, each one with its own characteristic representations.

The famed pioneers of radar polarimetry like Sinclair, Deschamps, Kennaugh, Graves, and Huynen had at their time the great insight and imagination of what radar polarimetry should be. But without having the correct advanced mathematics of antilinear transformation they had to use the crutch of the voltage and power transfer equation and a more elementary approach to optimization in order to explain their ideas. Fortunately, they had chosen and indicated the correct path to proceed which was adopted also in [9-12], whereas some truly unfortunate violations are reported in [8].

REFERENCES

- [1] W-M. Boerner, H. Mott, E. Lüneburg, C. Livingstone, B. Brisco, R. Brown, J.S. Paterson (Authors); S.R. Cloude, E. Krogager, J.S. Lee, D.L. Schuler, J.J. van Zyl, D. Randall and P. Budkewitsch (Contributing Authors), *POLARIMETRY IN REMOTE SENSING - Basic and Applied Concepts*, Chapter 5 (90 p.) in R.A. Reyerson, ed., *The Manual of REMOTE SENSING*, 3rd Edition, ASPRS Publishing, Bethesda, MD, 1997.
- [2] W-M. Boerner, et al., eds., *Direct and Inverse Methods in Radar Polarimetry*, Proc. NATO-ARW-DIMRP'88, Bad Windsheim, FR Germany, m Sept. 18-24, 1988, NATO ASI Series C: Math & Phys. Scie., Vol. C-350, Kluwer Acad. Publ. Co., Dordrecht, Holland: 1,938 pages) 1992 Feb. 15.
- [3] W-M. Boerner, Polarimetry in Wideband Interferometric Sensing and Imaging of Terrestrial and Planetary Environments (Invited Keynote Address, Vol. 1, pp. 1-38) in J. Saillard, E. Pottier, S.R. Cloude, (eds.), *Proceedings of the Third International Workshop on Radar Polarimetry*, JIPR-3, 1995 March 2-23, IRESTE, U.Nantes, La Chantrerie, Bretagne, France, Vol. 1&2.
- [4] H. Mott, *Antennas for Radar and Communications: A Polarimetric Approach*, John Wiley & Sons, New York, NY, 1992.
- [5] E. Lüneburg and W-M. Boerner, The Backscatter Operator in Radar Polarimetry, Its Con-eigen-value/vector and Con-similarity Representations, and Its Applications, in print, AEÜ, Vol.50 (1996), (PIERS'94 ESA, Noordwijk, NL, 1994 July 11-15).
- [6] E. Lüneburg, Principles of Radar Polarimetry, *IEICE Transactions on Electronics (Special Issue on Electromagnetic Theory)*, Vol. E78C, No.10, pp.1339-1345, Oct. 1995.
- [7] Lüneburg, E., 1996, Radar Polarimetry: A Revisitation of Basic Concepts in 'Direct and Inverse Electromagnetic Scattering', S.R. Cloude and A.W. Serbest (eds.), Pitman Research Notes in Mathematics, Series No.361, 257-273, Addison-Wesley Longman Co., 1996.
- [8] Lüneburg, E., 1997, Comments by E. Lüneburg on 'The Specular Null Polarization Theory, *IEEE Trans.. GRS*, 35(4), 2 p. (correspondence), July 1997.
- [9] E. Krogager, *Aspects of Polarimetric Radar Imaging*, D.Tech.Sci. Thesis, Technical University of Denmark, Lyngby, DK, 1993 (also see conference/symposium papers in PIERS, IGARSS, NATO-ARW/AGARD Proceedings; e.g., E. Krogager and W-M. Boerner, On the importance of utilizing Polarimetric Information in Radar Imaging and Classification, *AGARD SPP Symposium on "Remote Sensing: A Valuable Source of Information"*, Toulouse, France, 1996 April 22-25, AGARD Conference Proceedings 582, pp.17.1 to 17.13, Oct. 1996.).
- [10] S.R. Cloude and E. Pottier, An Entropy/ α -parameter Based Classification Scheme for Land/Sea Applications for the Interpretation of POL-SAR Data Takes, *IEEE Trans. GRS*, Vol. GE-35, No.1, Jan. 1997, pp.68-78.
- [11] Cloude, S.R. and K.P. Papathanassiou, Polarimetric Optimization in Radar/SAR Interferometry, *Electronic Letters*, 33(8), in print, Sept. 1997.
- [12] H. Mott and W-M. Boerner, eds., *Wideband Interferometric Sensing and Imaging Polarimetry*, SPIE-AM-PSC: WISIP, 1997 July 28-29, San Diego Convention Center, SPIE Proc., Vol. 3120, Fall 1997.

Determination of Propagation Parameters from Fully Polarimetric Radar Data

V. Santalla del Rio, Y.M.M. Antar*

Dpt. Tecnologías de las comunicaciones. Universidad de Vigo. 36200 Vigo, Spain.

*Dpt. of Electrical and Computing Engineering.

Royal Military College of Canada. Kingston, Ontario Canada K7K 5L0.

1 Abstract

The polarization characteristics of the electromagnetic waves, as related to its interaction with targets, is an important aspect in remote sensing applications. This polarization information is usually contained in either the scattering matrix or the covariance matrix depending on the target under consideration. Often, propagation effects are normally not considered in obtaining them. In clear-air conditions this a reasonable assumption, but when rain, or any other type of precipitation, exists in the ray-path, depolarization of the waves may not be negligible anymore. The anisotropy that precipitation media present causes this depolarization and that could greatly affect the scattering or covariance matrix measurements. Consequently, the real target information may be hidden in those measured matrices and it could be necessary to apply different algorithms to correct for depolarization effects prior to target information extraction. Depolarization effects can be determined and accounted for if the characteristic polarizations of the medium and their respective propagation constants are known. It is found that for precipitation media that generally present reflection symmetry these polarizations are linear and orthogonal. Then it is shown that differential attenuation can be obtained from copolar power measurements and differential phase shift from copolar correlation measurements. Considering the statistics of these covariance matrix elements and temporal correlation between successive pulses from the target, statistics of propagation parameters are analyzed.

2 Introduction

In radar operation, especially when polarization related information is going to be used for target classification or identification, propagation effects can greatly affect the final results. Correction for these effects becomes necessary before any information can be extracted. Different algorithms, based on different polarization measurements and assumptions on the medium have been developed [1], [2], [3], [4].

We will first consider reflection symmetry in pre-

cipitation media since the analysis of different types of hydrometeors [5] indicate the existence of this property in most cases. From this assumption characteristic polarizations and their differential attenuation and differential phase shift will be studied. Then, propagation effects will be included in the covariance matrix formulation and separation of target and propagation parameters will be discussed. Finally, some important statistical considerations on propagation parameters estimation, that will allow comparison between different algorithms, are presented.

3 Covariance matrix for hydrometeors

Consider the following two assumptions, that have been generally adopted in most studies on precipitation media:

- a) independent distributions of dropsizes and canting angle
- b) symmetrical canting angle distribution

Then, it can be shown [5] that the covariance matrix can be expressed in the form

$$C_{\alpha\beta} = \begin{bmatrix} |\overline{S_{\alpha\alpha}}|^2 & 0 & \overline{S_{\beta\beta} S_{\alpha\alpha}^*} \\ 0 & 2|\overline{S_{\alpha\beta}}|^2 & 0 \\ \overline{S_{\alpha\alpha} S_{\beta\beta}^*} & 0 & |\overline{S_{\beta\beta}}|^2 \end{bmatrix} \quad (1)$$

where linear polarization basis (α, β) is assumed, with one of the polarization vectors orthogonal and the other parallel to the plane of symmetry. This expression of the covariance matrix directly shows the existence of reflection symmetry for this class of media.

4 Propagation parameters

In obtaining the previous expression for the covariance matrix, propagation effects were not considered. There always exist two polarizations, in general not linear neither orthogonal, that propagate through the medium without suffering depolarization, these are called characteristic polarizations.

As a consequence of reflection symmetry, the dielectric tensor of the medium has the general form

$$[\epsilon] = \begin{bmatrix} \epsilon_{\alpha\alpha} & 0 & \epsilon_{\alpha z} \\ 0 & \epsilon_{\beta\beta} & 0 \\ \epsilon_{z\alpha} & 0 & \epsilon_{zz} \end{bmatrix} \quad (2)$$

where it has been assumed that propagation is in the z direction, and therefore, it directly follows that the characteristic polarizations of a medium with reflection symmetry are linear and orthogonal, more explicitly, they are the two linear polarizations parallel and orthogonal to the plane of symmetry of the medium. Based on this, the electric field at point C after propagating from point B can be expressed as

$$\begin{bmatrix} E_\alpha \\ E_\beta \end{bmatrix}_C = P(\alpha\beta) \begin{bmatrix} E_\alpha \\ E_\beta \end{bmatrix}_B = \quad (3)$$

$$\frac{e^{-\gamma R}}{R} \begin{bmatrix} e^{-\Delta\gamma R/2} & 0 \\ 0 & e^{\Delta\gamma R/2} \end{bmatrix} \begin{bmatrix} E_\alpha \\ E_\beta \end{bmatrix}_B \quad (4)$$

where:

$$\gamma = (\gamma_1 + \gamma_2)/2$$

$$\Delta\gamma = \gamma_2 - \gamma_1$$

γ_1 and γ_2 are the propagation constants corresponding to the characteristic polarizations and R is the distance between B and C .

Hence, the backscattered field can be expressed as

$$\begin{bmatrix} E_\alpha \\ E_\beta \end{bmatrix}_c = P^t(\alpha\beta) \begin{bmatrix} S_{\alpha\alpha} & S_{\alpha\beta} \\ S_{\alpha\beta} & S_{\beta\beta} \end{bmatrix} P(\alpha\beta) \begin{bmatrix} E_\alpha \\ E_\beta \end{bmatrix}_i \quad (5)$$

where it becomes clear that the measured scattering matrix is

$$P^t(\alpha\beta) \begin{bmatrix} S_{\alpha\alpha} & S_{\alpha\beta} \\ S_{\alpha\beta} & S_{\beta\beta} \end{bmatrix} P(\alpha\beta) \quad (6)$$

To obtain the covariance matrix that includes propagation effects, second order moments of the measured scattering matrix as given in (6) are calculated. So the measured covariance matrix is

$$A \begin{bmatrix} |S_{\alpha\alpha}|^2 e^{-2Re(\Delta\gamma R)} & 0 & \overline{S_{\beta\beta} S_{\alpha\alpha}^*} e^{-2jIm(\Delta\gamma R)} \\ 0 & 2|S_{\alpha\beta}|^2 & 0 \\ \overline{S_{\alpha\alpha} S_{\beta\beta}^*} e^{2jIm(\Delta\gamma R)} & 0 & |S_{\beta\beta}|^2 e^{2Re(\Delta\gamma R)} \end{bmatrix} \quad (7)$$

where

$$A = \frac{e^{-4Re(\gamma)R}}{R^4} \quad (8)$$

Now, if the medium can be considered homogeneous, at least for some range gates, along the propagation path, comparison of covariance matrices for consecutive range gates will allow determination of both parameters, differential attenuation and differential phase shift. In particular the differential phase shift can be extracted from the correlation between copolar powers obtained with the characteristic polarizations of the media

$$Im(\Delta\gamma R) = \frac{1}{2} \angle(\overline{S_{\alpha\alpha} S_{\beta\beta}^*} e^{-2jIm(\Delta\gamma R)}) - \angle(\overline{S_{\alpha\alpha} S_{\beta\beta}^*} e^{-4jIm(\Delta\gamma R)}) \quad (9)$$

and differential attenuation can be extracted from each one of the copolar powers measured at same polarizations,

$$Re(\Delta\gamma R) = \frac{1}{2} \ln \frac{|S_{\alpha\alpha}|^2 e^{-2Re(\Delta\gamma R)}}{|S_{\alpha\alpha}|^2 e^{-4Re(\Delta\gamma R)}} \quad (10)$$

5 Statistics of propagation parameters

As we have just seen, propagation parameters are estimated from covariance matrix elements. Therefore, these should also be estimated and the statistics of propagation parameters will be determined from the statistics of the covariance matrix elements. Usually the sample covariance matrix is taken as the covariance matrix estimator, since in the case of uncorrelated samples of the scattering matrix it provides the maximum likelihood estimator of the covariance matrix. The sample covariance matrix elements are obtained by direct promediation of the products of the elements of successive measured scattering matrices.

The time series corresponding to each element of the scattering matrix is considered a polarimetric channel. The three polarimetric channels that we have in the case of monostatic radar and reciprocal medium can be statistically modelled as a 3-dimensional complex Gaussian stationary and ergodic process [6], [7] with a determined temporal correlation function, in many cases considered Gaussian.

Let $S = [S_1 \ S_2 \ S_3]^t$ be a 3n-dimensional vector where $S_i = [s_1^i, \dots, s_n^i]^t$, $i = 1, 2, 3$ is an n-dimensional vector that contains n samples of a particular element of the scattering matrix. Since it was assumed that the data follows a complex Gaussian stationary process the probability density function of S is

$$p(S) = \frac{1}{\pi^{3n} |C_S|} \exp\{-S^t C_S^{-1} S\} \quad (11)$$

where,

$$C_S = C \otimes \Upsilon \quad (12)$$

C represents the covariance matrix, \otimes indicates Kronecker product and

$$\Upsilon = \begin{bmatrix} 1 & \rho_1 & \dots & \rho_n \\ \rho_1^* & 1 & \dots & \rho_{n-1} \\ \vdots & \vdots & \ddots & \vdots \\ \rho_n^* & \rho_{n-1}^* & \dots & 1 \end{bmatrix}$$

is the normalized autocorrelation matrix.

By marginalizing and integrating (11) distributions of the products $S_i^t S_j^* = \sum_k s_k^i s_k^{j*}$ can be obtained. We are interested in the distributions of those products representing the copolar power and the copolar correlation.

From further analysis, it was found that the copolar power Y distribution is

$$p(Y) = \sum_{k=1}^n \frac{nC_k}{\sigma\lambda_k} \exp\left\{-\frac{ny}{\sigma\lambda_k}\right\} \quad (13)$$

where

$$C_k = \left\{ \prod_{j=1, j \neq k}^n (1 - \lambda_k^{-1} \lambda_j) \right\}^{-1} \quad (14)$$

λ_k , $k = 1, 2, \dots, n$ are the eigenvalues of the normalized autocorrelation matrix, and $\sigma = |S_{\alpha\alpha}|^2$ or $\sigma = |S_{\beta\beta}|^2$.

Unfortunately, it has not been possible to find closed-form expressions for the probability density function of the copolar correlation phase. However, the mean and variance can be calculated from

$$E[\Phi] = \int \arctg\left(\frac{Z^I}{Z^R}\right) p(Z^R, Z^I) dZ^R dZ^I \quad (15)$$

$$E[\Phi^2] = \int \arctg^2\left(\frac{Z^I}{Z^R}\right) p(Z^R, Z^I) dZ^R dZ^I$$

where Z^R and Z^I are the real and imaginary part of the integrated copolar correlation term and $p(Z^R, Z^I)$ its joint probability density function, which can be calculated as the Fourier transform of

$$\Phi(U^R, U^I) = \prod_{k=1}^n \left\{ 1 + \frac{\lambda_k^2}{4} \sigma_\alpha \sigma_\beta (1 - k^2) (U^{R2} + U^{I2}) - j\lambda_k \sqrt{\sigma_\alpha \sigma_\beta} k (U^R \cos \phi + U^I \sin \phi) \right\}^{-1} \quad (16)$$

where the copolar correlation $\overline{S_{\alpha\alpha} S_{\beta\beta}^*}$ has been expressed as

$$\overline{S_{\alpha\alpha} S_{\beta\beta}^*} = \sigma_\alpha \sigma_\beta k e^{j\phi}$$

$$\text{with } \sigma_\alpha = |S_{\alpha\alpha}|^2 \quad \sigma_\beta = |S_{\beta\beta}|^2$$

$$k = |\overline{S_{\alpha\alpha} S_{\beta\beta}^*}| / (\sigma_\alpha \sigma_\beta) \text{ and } \phi = \angle \overline{S_{\alpha\alpha} S_{\beta\beta}^*}$$

Now the mean and variance of the the differential attenuation and the differential phase shift can be calculated.

$$\begin{aligned} E[Re(\Delta\gamma R)] &= \frac{1}{2}(E[Z(R)] - E[Z(2R)]) \\ E[Re^2(\Delta\gamma R)] &= \frac{1}{4}(E[Z(R)^2] + E[Z(2R)^2]) \\ E[Im(\Delta\gamma R)] &= \frac{1}{2}(E[\Phi(R)] - E[\Phi(2R)]) \\ E[Im^2(\Delta\gamma R)] &= \frac{1}{4}(E[\Phi(R)^2] + E[\Phi(2R)^2]) \end{aligned} \quad (17)$$

where $Z = \ln Y$ and $Z(R)$, $\Phi(R)$ ($Z(2R)$, $\Phi(2R)$) indicate those variables were obtained from a range gate at a distance R ($2R$).

This way, independence between variables from different range gates is assumed. It is important to

note that statistics of propagation parameters obtained through other algorithms can be obtained based on statistics of variables Z and Φ . In doing so it should be taking into account that the stochastic process defined by those variables at different ranges are not stationary.

6 Conclusions

From the assumption of reflection symmetry it is found that characteristic polarizations of precipitation media are linear and orthogonal, also being parallel and perpendicular to the plane of symmetry of the medium. Considering that propagation effects are included in the covariance matrix formulation. It is shown how differential attenuation can be extracted from copolar power measurements and differential phase shift from copolar correlation. Some statistical considerations on the propagation parameter estimates were made. these results should be useful in propagation studies and in identifying targets in precipitation.

References

- [1] G. McCormick and A. Hendry, "Principles for the radar determination of the polarization properties of precipitation," *Radio Science*, vol. 10, pp. 421-434, 1975.
- [2] J. Hubbert, V. Chandrasekar, and V. Bringi, "Processing and interpretation of coherent dual-polarized radar measurements," *Journal of atmospheric and Ocean. Technology*, vol. 10, pp. 155-164, 1993.
- [3] D. Bebbington, R. McGuinness, and A. Holt, "Correction of propagation effects in s-band circular polarisation diversity radars," *IEE Proc. Part H*, vol. 134, pp. 431-437, 1987.
- [4] V. Ziegler, E. Luneburg, and A. Scrotch, "Weather radar polarimetry: path integrated differential phase shift optimum polarization and the elliptical ef-basis," *Journal of Electromagnetic Waves and Applications*, vol. 9, pp. 309-325, 1995.
- [5] V. Santalla, A. Pino, and Y. Antar, "Polarimetric radar covariance matrix algorithms and applications to partially polarized waves," in *IGARSS95*, (Firenze, Italy), 1995.
- [6] K. Tragl, "Doppler correction for scattering matrix measurements of random targets," *Eur. Trans. on Telecom.*, vol. 2, pp. 43-49, 1991.
- [7] F. Ulaby and M. Dobson, *Handbook of radar scattering statistics for terrain*. Norwood, MA: Artech House, 1 ed., 1989.

A low-cost polarimetric radiometer for real time Stokes parameter measurement

Janne Lahtinen and Martti Hallikainen

Helsinki University of Technology, Laboratory of Space Technology

Otakaari 5 A, 02150 Espoo, Finland

Phone: +358-9-451 4778 / Fax: +358-9-451 2898 / Email: lahtinen@ava.hut.fi

Abstract - The HUT 36.5 GHz polarimetric radiometer is described. It is modified from a conventional two-channel radiometer, and it is capable of measuring all four Stokes parameters simultaneously. The third and fourth parameters are calculated by correlators which are based on commercial analog multipliers. The modification problem in general is also discussed. Calibration equipment is under construction, and its function is briefly described.

INTRODUCTION

In recent years there has been growing interest on passive polarimetric microwave measurements, especially for determining wind vector [1, 2]. Helsinki University of Technology (HUT) / Laboratory of Space Technology started investigations on this subject in 1995 in order to build a polarimetric radiometer as a part of the non-imaging subsystem of the HUTRAD radiometer system [3]. The aim was to have a reliable low-cost system capable of simultaneous measurement of all Stokes parameters.

HUTRAD is a multifrequency radiometer system with dual polarized profiling (6.8 - 94 GHz) and imaging (93 GHz) channels. It has a modular structure in order to guarantee easy maintenance and to allow modifications.

As the construction of the HUTRAD system had the priority in Laboratory of Space Technology the polarimetric radiometer project was divided into two parts. The first phase consisted of the preliminary design of the polarimetric radiometer as well as the construction of the conventional 36.5 GHz receiver for HUTRAD, including a modification option. The second phase consists of the receiver modification into a polarimetric radiometer and the design and construction of the calibration system. The first phase was completed in the winter of 1996-1997 and the second phase was launched after the measurement campaigns in March 1997. Because of the modular structure of HUTRAD there were no crucial difficulties in the modification.

HUTRAD is mounted onboard the Skyvan SC7 research aircraft of Laboratory of Space Technology [4]. The aircraft is specially modified for remote sensing purposes and allows several sensors to be flown simultaneously.

INSTRUMENT DESIGN

A block diagram of the HUT polarimetric radiometer is shown in figure 1. The radiometer is a Dicke type, superheterodyne receiver and the antenna has separate outputs for vertical and horizontal polarizations. In the RF-block the lower sideband is filtered out making the device a single sideband (SSB) receiver. Dicke switching is used to minimize the influence of internal noise and gain fluctuation.

In the modification a correlation block was installed, providing amplification, filtering and correlation of the vertical and horizontal IF-signals. Complex correlation produces the third (T_U) and fourth (T_V) Stokes parameters. The third parameter is obtained by in-phase correlation. For the fourth a pre-correlation 90° phase shift is required. The error caused by differences in signal propagating times is minimized using a delay line in one of the correlator channels. The channels are equalized within one correlation length $l_c = v_p / B$ [5], where v_p is the phase velocity of the signal and B the bandwidth. The phase differences in different channels are equalized using a phase shifter in the RF-block. That is not absolutely necessary, the influence of phase difference can be corrected with calibration. However, it increases the sensitivity and facilitates the data processing.

The heart of the HUT polarimetric radiometer receiver are correlators that multiply the vertical and horizontal signals. The obtained DC-component is proportional to the phase difference (δ) between the signals. The correlators of HUT polarimetric radiometer are based on commercial analog multipliers. This restricts the bandwidth, though, and a band of 100 - 500 MHz was chosen already in the original HUT polarimetric radiometer specifications. In the performed tests

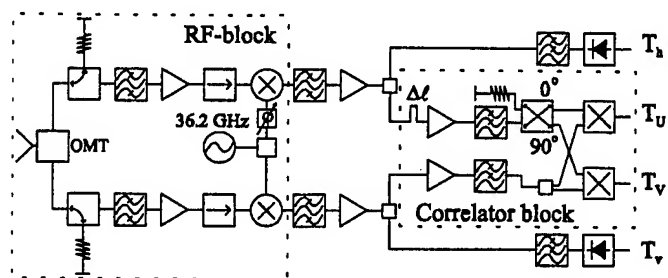


Figure 1. Block diagram of the HUT polarimetric radiometer.

the built correlators have proven to be time and temperature stable, amplitude response being within ± 1.5 dB and phase response within $\pm 5^\circ$ over this frequency band. It was also noted that the performance decreased rapidly for frequencies above 500 MHz. The transfer function of the correlators is presented in (1),

$$U_{out} = \frac{|T_v||T_h|}{\alpha} [\cos(\delta) + \beta], \quad (1)$$

where U_{out} is the output voltage, α and β (offset) are constants. The correlation channels are very sensitive to noise generated by local oscillator impedance mismatch. This influence is removed in the Dicke switching mode.

The choice of the IF-frequency forced to pay special attention to electromagnetic shielding, due to the very powerful radio and TV broadcast and link signals at this band. These could cause interference and, in the worst case, damage the equipment. The radiometer case is electromagnetically sealed to prevent electromagnetic interference. Supply voltages are filtered and control signals galvanically isolated.

The technical characteristics of the HUT polarimetric radiometer are presented in Table 1. Due to one long waveguide the measured noise temperature is 370 K higher in vertical channel than the theoretical value for which waveguide attenuations were not taken into account.

Table 1. Technical characteristics of HUT polarimetric radiometer

Center frequency	36.5 GHz
Bandwidth	400 MHz
Channels	T_v, T_h, T_u, T_v
Measurement mode	simultaneous
Theoretical noise temperature (SSB) (vertical / horizontal)	1200 / 1200 K
Theoretical sensitivity ($\tau = 0.5$ s)	0.11 K
Measured noise temperature (SSB) (vertical / horizontal)	1570 / 1210 K
Measured sensitivity ($\tau = 0.5$ s) (vertical / horizontal)	0.29 / 0.25 K
Antenna beamwidth	4°

MODIFICATION IN GENERAL CASE

A conventional two-channel radiometer can be modified into a four-channel polarization radiometer at low cost, although some requirements have to be fulfilled. First of all, the frequency of the correlated signals can not be arbitrarily high. The experience collected during the HUT polarimetric radiometer project shows that the used commercial analog multipliers have constant phase and amplitude response up to 500 MHz. With careful design and realization even 1 GHz may be achieved [6]. Mixers have been used up to 2 GHz [7]. Considering the recent technological level of analog multipliers, the use of mixers is recommended above 500 - 700 MHz.

The correlation module can be added to the basic configuration easily. Power dividers have to be added in the IF-block, though, as can be seen in Figure 1. Mechanically the most complicated and laborious task is the implementation of the phase shifter in the RF-block. This is the case at least at millimeterwave frequencies where waveguides have to be used. In the case of originally separate local oscillators a common local oscillator and a power divider have to be installed. The last requirement is that the size of the antenna has to be small enough due to a metal wire grid needed for calibration. Radiometers using separate antennas for vertical and horizontal polarizations can neither be modified

APPLICATIONS

The brightness temperature of a target has a polarized component if the target has a periodic surface or its inner scatterers are not randomly oriented.

Presently the most promising application for polarimetric radiometers is the wind vector measurement. This is easy to understand when the significant application potential in meteorology is considered. There are also some other potential applications. Plowed fields give a polarized signal [8] and the detection of wave concentration areas is crucial for the safety of ships. Some schistoseous rock types should give a polarized signal because of their orientation. If so, their classification could be possible.

CALIBRATION

Our polarimetric radiometer is calibrated with a polarized blackbody load presented in [5]. Hot and cold absorption loads are equipped with a rotating polarization grid. In order to provide a large temperature difference between the loads, the use of liquid nitrogen was chosen for the cold load and ambient temperature for the hot load. The principle of the calibration equipment is presented in Figure 2.

Different angles between grid wire orientation and antenna polarization basis will be used. Therefore, calibration

coefficients can be calculated from a priori knowledge of the grid behavior [9].

PRESENT STATUS

The polarimetric radiometer project was started in 1995. The first phase of the project was completed with the completion of the HUT polarimetric radiometer system in winter of 1996-1997. By April 1997 the modification into a polarimetric radiometer was carried out and the first uncalibrated data have been obtained. Final adjustments and the construction of the calibration equipment are in progress.

CONCLUSION

A conventional two-channel radiometer was modified into a polarimetric radiometer. The modification was taken into account already in the design of the regular receiver, but a similar modification can be carried out also if this is not the case. However, there are some restrictions. The correlated signal frequencies have to be below certain limits. If commercial analog multiplier-based correlators are used as in the HUT polarimetric radiometer, the absolute upper limit is about 1 GHz. The best results will be obtained with considerably lower frequencies. The antenna has to have outputs for two polarizations and the size must not be very large.

The material cost due to modification itself was small, 7% of the total material cost of the radiometer receiver. The preparation for modification in the first phase of the project increased the component cost also by about 7%. The cost of a calibration equipment depends considerably on the size and manufacturing method of the metal wire grid.

ACKNOWLEDGMENTS

The authors would like to acknowledge the help and ideas of H. Valmu, O. Koistinen and I. Mononen.

REFERENCES

- [1] H. S. Yueh et al., "Polarimetric measurements of sea surface brightness temperatures using an aircraft K-band radiometer," *IEEE Transactions on Geoscience and Remote Sensing* vol. 33, no. 1, pp. 85-92, 1995.
- [2] A. J. Gasiewski, D. B. Kunkee, "Polarized microwave emission from water waves," *Radio Science* vol. 29, no. 6, pp. 1449-1466, 1994.
- [3] M. Hallikainen et al., "Airborne 14-channel microwave radiometer HUTRAD," *Proceedings of IEEE IGARSS '96*, pp. 2285-2287, Lincoln, Nebraska, USA, 1996.
- [4] M. Hallikainen et al., "The Helsinki University of Technology remote sensing aircraft," *Proc. of the First International Airborne Remote Sensing Conference*, pp. 637-644, Strasbourg, France, 1994.
- [5] A. J. Gasiewski, D. B. Kunkee, "Calibration and applications of polarization-correlating radiometers," *IEEE Transactions on Microwave Theory and Techniques* vol. 41, no. 5, pp. 767-773, 1993.
- [6] Analog Devices, "Special linear reference manual," Chapter 2, Analog multipliers/dividers, 1992.
- [7] S. Padin, "A wideband analog continuum correlator for radio astronomy," *IEEE Transactions on Instrumentation and Measurement* vol. 43, no. 6, pp. 782-785, 1994.
- [8] S. V. Nghiem, M. E. Veysoglu, J. A. Kong, R. T. Shin, "Polarimetric passive remote sensing of a periodic soil surface: microwave measurements and analysis," *Journal of Electromagnetic Waves and Applications* vol. 5, no. 9, pp. 997-1005, 1991.
- [9] W. G. Chambers, T. J. Parker, A. E. Cosley, "Freestanding fine-wire grids for use in millimeter- and submillimeter-wave spectroscopy," in *Infrared and Millimeter Waves*, K. J. Button, Ed., vol. 16, pp. 77-106, 1986.

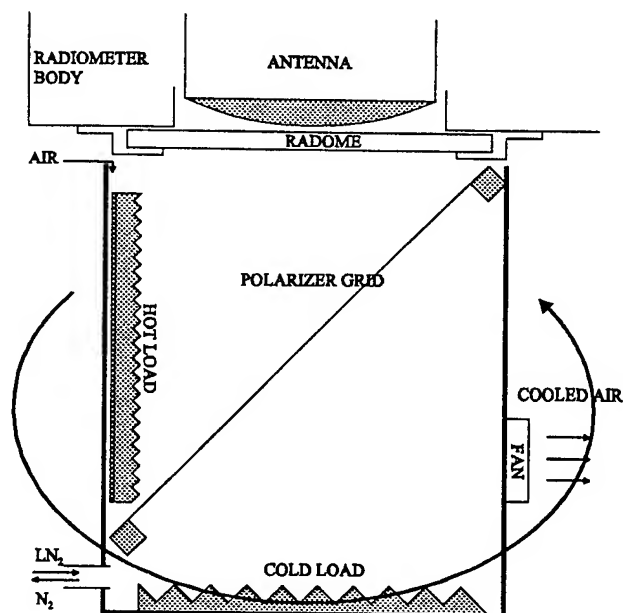


Figure 2. The principle of HUT polarimetric radiometer calibration equipment

Volume Scattering Properties of Glass Particles as a Function of Size and Absorption Coefficient

Christopher L. Betty, Adrian K. Fung, and Saibun Tjuatja
Wave Scattering Research Center
Department of Electrical Engineering
The University of Texas at Arlington
P.O. Box 19016 Arlington, Texas 76019
Phone: 817-272-3422 FAX: 817-272-3443

Abstract -- The albedo and nadir incident polarized BRDF were measured at $\lambda=633$ nm for five different Schott glasses. Measurements were acquired using a polarized goniometer and a Minolta spectrophotometer. The Schott glass samples were in the form of particles which were obtained by crushing Schott glass plates with known absorption coefficient and index of refraction. The particles were sieved into five different particle size distributions (i.e., bin sizes). A total of 25 different absorption coefficient-bin size combinations were obtained. Data is reported in the form of albedo and depolarization ratio as a function of absorption coefficient and mean bin size. Comparisons are made between albedos measured using the spectrophotometer and those approximated by averaging directional reflectance data over all view angles in the principle plane. It is shown that a close relationship exists between albedo and nadir only backscatter measurements and hence *it is possible to estimate albedo with a single measurement at nadir*. Also, an empirical factor relating depolarization ratio to individual particle diameter and absorption coefficient is developed which serves as a convenient way to estimate depolarization ratio.

INTRODUCTION

Retrieval of information from remotely sensed data relies on an understanding of the scattering process and the ability to use this understanding to obtain useful information about the scene of interest. Remotely sensed data can convey three basic types of information: 1) directional reflectance information, 2) wavelength-dependent spectral information, and 3) polarization information.

Most soils have shown to exhibit directionally anisotropic scattering characteristics meaning that their reflected intensity is dependent on both the source incident and receiver view angles [1-4]. The spectral fingerprint associated with a materials atomic and molecular composition is unique and, if it contains sufficient structure, can be used for identification. Polarization has not been extensively used because the method requires either the use of a polarized source or the sample to be illuminated at or near the Brewsters angle. Active laser based systems have used polarization to distinguish between broadleaf tree species [5] and in the lab [6] used it to study multiple scattering.

In order to fully understand and best utilize the qualifying/quantifying phenomenon, regardless of the type of information being used (i.e., directional reflectance, wavelength-dependent, or polarization information), it is necessary to first understand the roles associated with the physical and electromagnetic properties of the scattering medium. Most scattering media can be categorized into two basic groups: 1) volume scattering media and 2) surface scattering media.

Volume scattering media, such as most soils, are characterized as having albedos which are dominated by contributions from radiation multiply scattered from within the volume. This paper is primarily concerned with volume scattering media and, more specifically, how particle size and absorption coefficient influence the level, polarization state, and directional distribution of the reflected radiation.

This paper documents the results of a controlled laboratory investigation into the scattering properties of 25 different volume scattering media. Results are presented in the form of BRDF, albedo and depolarization ratio. A comparison is made between the measured albedo and an approximation using a single nadir-only backscatter measurement. Also, an empirical factor relating depolarization ratio to individual particle diameter and absorption coefficient is developed.

SAMPLE PREPARATION

A total of 5 different Schott glasses were used to obtain 25 different particle bin size-absorption combinations. The NG series Schott glass was purchased in the form of unpolished filter squares and crushed into small particles using a mortar and pestle and sieved into 5 different size distributions. The 5 particle size distributions along with its letter of designation (A-E), index of refraction (n), and absorption coefficient (α) for each of the samples is listed in table 1. Throughout the remainder of this paper the specific samples will be referred to by the Schott glass type followed by the size distribution letter of designation (i.e., NG5C).

Table 1. Particle constants.

Schott glass type	α (mm ⁻¹)	n
NG12	0.04	1.49
NG11	0.23	1.50
NG5	0.44	1.50
NG4	0.71	1.51
NG3	0.89	1.51
Size distribution	mean size	
<63 μ m	60	E
63 μ m <d< 150 μ m	106	D
150 μ m <d< 250 μ m	200	C
250 μ m <d< 500 μ m	375	B
500 μ m <d< 2000 μ m	1250	A

EXPERIMENTAL SET-UP

Polarized bidirectional reflectance measurements were acquired with the laser based ($\lambda=633$ nm) goniometer. The system utilizes three rotary tables to control the two receive angles (elevation and azimuth) and the incident elevation angle. The sample is illuminated with linearly polarized radiation. The radiation scattered into the receiver is separated into a like-polarized and a cross-polarized component using a polarizer. Two silicon over InGaAs sandwich type detectors are used to measure the intensity associated with each polarization. The laser beam diameter at the target is 1 cm for normal incidence. The field of view of the instrument is 3.5° which corresponds to a view diameter of 20 cm at the target.

Hemispherical albedo measurements were acquired using a Minolta CM-2002 spectrophotometer equipped with an integrating sphere. The instrument is calibrated using a BaSO₄ calibration standard. The instrument was set to include specular scatter.

MEASUREMENTS

The 25 Schott glass samples were utilized to obtain polarized bidirectional and hemispherical (albedo) reflectance measurements as a function of particle size (i.e., diameter) and absorption coefficient. All data reported in this paper is the result of horizontally polarized illumination and all depolarization ratios were obtained at nadir for nadir incidence.

RESULTS

The albedo as a function of particle size for the 5 different Schott glasses is shown in Fig.1. The y-axis represents the albedo and has units of % reflectance and the x-axis corresponds to the mean of the particle size ranges. Each curve represents constant absorption coefficient. All curves

show an increase in albedo with decreasing particle size and/or decreasing absorption coefficient. The curve for the least lossy particles (NG12) shows signs of saturating at a maximum albedo for smaller particle sizes. The remaining 4 curves are still increasing at the smallest particle size but it is assumed that if smaller particles were used these curves would also saturate at some maximum level. As particle size increase the albedo decreases and the curve, corresponding to the lossiest particles (NG3), appears to saturate at a minimum albedo.

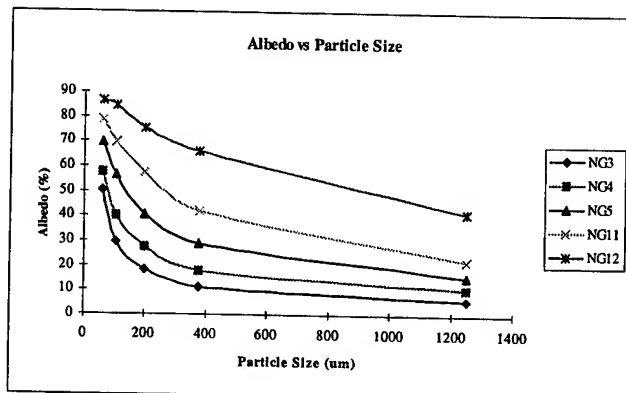


Fig.1. Albedo as a function of particle size for 5 different Schott glasses. Absorption coefficients (mm⁻¹) are: $\alpha_{NG3}=0.89$, $\alpha_{NG4}=0.71$, $\alpha_{NG5}=0.44$, $\alpha_{NG11}=0.23$, $\alpha_{NG12}=0.04$.

The % depolarization ratio (χ) as a function of particle size for the 5 different glasses is shown in Fig.2. For these curves the χ used is that for nadir incidence and reception.

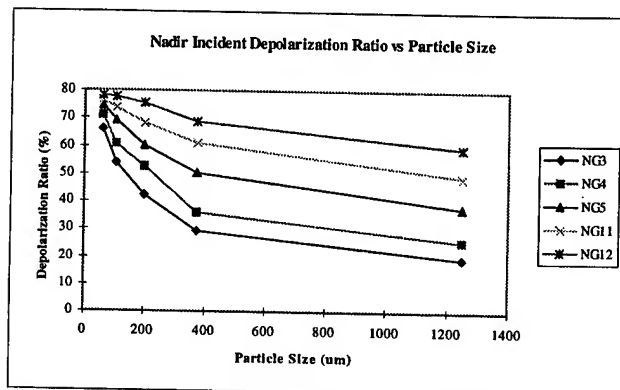


Fig.2. Nadir incident depolarization ratio (%) as a function of particle size for 5 Schott glasses. Absorption coefficients (mm⁻¹) are: $\alpha_{NG3}=0.89$, $\alpha_{NG4}=0.71$, $\alpha_{NG5}=0.44$, $\alpha_{NG11}=0.23$, $\alpha_{NG12}=0.04$.

Albedo (i.e., hemispherical reflectance) measurements require integrating spheres to capture all of the reflected radiation but a close correlation between nadir-only backscatter measurements and albedo is shown in Fig.3. The nadir-only estimate is obtained by multiplying the nadir

incident-nadir receive BRDF by π to convert to reflectance. For constant incident and azimuth angle the BRDF can be approximated by

$$f_r = \frac{\Phi_r}{\Phi_i \cos \theta_r \omega_r} \quad [\text{sr}^{-1}] \quad (1)$$

where Φ_r is the reflected flux [W] within the solid angle of the receiver (ω_r) located at (θ_r) which is measured by the detector and Φ_i represents the incident flux.

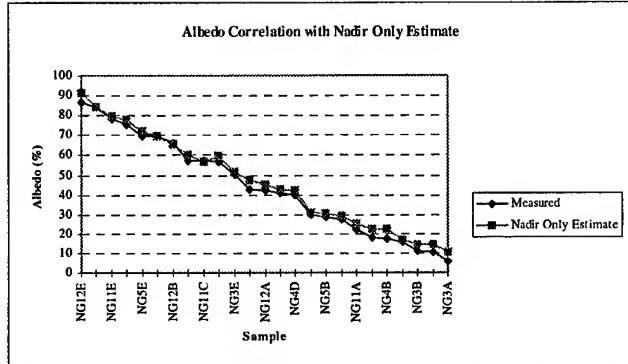


Fig.3. Comparison between albedo measured with minolta spectrophotometer and that estimated from a nadir-only reflectance measurement (avg. % err =11 %).

It was discovered that χ correlates well with the empirical factor 10^{-K} where K is the total extinction of light by a particle of diameter (d), internal transmittance (τ_i), and reflectance factor ($P(\lambda)$). The total extinction is calculated using the Bouguer-Lambert law as

$$K = 1 - P(\lambda)\tau_i(\lambda)^{\frac{d}{t}} \quad (2)$$

where t is the reference thickness at which τ_i was measured. The reflectance factor, $P(\lambda)$, accounts for reflectance losses and is given by

$$P(\lambda) = \frac{2n(\lambda)}{n^2(\lambda) + 1} \quad (3)$$

where λ is the incident wavelength and $n(\lambda)$ is the refractive index of the particle. The absorption coefficient (α) listed in Table 1 and used in many of the preceding curves is the reference absorption coefficient and is given by $\alpha(\lambda) = (1 - \tau_i(\lambda)) / t$ where $\lambda = 633$ nm.

Fig.4 shows the relationship between the empirical factor 10^{-K} and depolarization ratio for all samples. Note that the overall slope of the two curves is about the same but there is some trend for disagreement for depolarizations greater than about 0.6. For example, in the series NG3E-NG4E the level of the two curves is closer for the smaller particles "E" than for the larger particles "D", "C", and "B". Nevertheless, the average error between the two curves is 8% which is within the estimated margin of error of $\pm 10\%$ associated with the depolarization measurements.

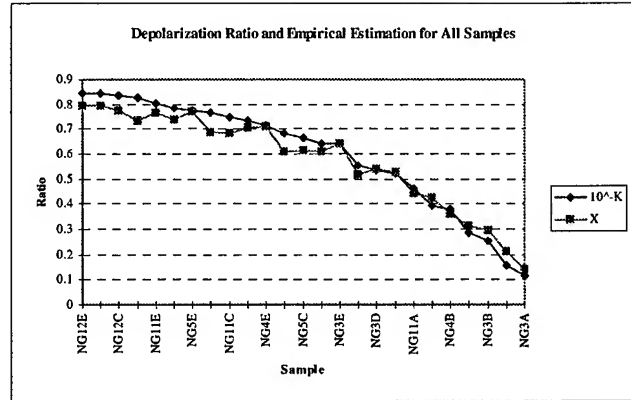


Fig.4. Correlation between empirical factor 10^{-K} and depolarization ratio for all samples.

CONCLUSIONS

The albedo and depolarization ratio are directly and consistently related to the absorption coefficient and particle size for volume scattering media which vary in appearance from black to white. For the particle size - absorption coefficient combinations used in this paper it was found that: 1) albedo increases with decreasing particle size and absorption coefficient; 2) the depolarization ratio is related to total particle absorption via the empirical relation 10^{-K} ; and 3) a single directional reflectance measurement taken at nadir can be used to accurately predict a medium's albedo.

REFERENCES

- [1] Deering, D.W., T.F. Eck, and J. Otterman (1990), Bidirectional Reflectances of Selected Desert Surfaces and Their Three-Parameter Soil Characterization, *Agricultural and Forest Meteorology*, 52:71-93.
- [2] Deering, Donald W., Thomas F. Eck, and Toby Grier, (1992), Shinnery Oak Bidirectional Reflectance Properties and Canopy Model Inversion, *IEEE Transactions on Geoscience and Remote Sensing*, Vol. 30, No. 2, pp. 339-348.
- [3] Irons, J.R., R.A. Weismiller, and G.W. Petersen, (1989), "Soil reflectance", in Theory and applications of Optical Remote Sensing, G. Astar, Ed., John Wiley and Sons, New York, pp. 66-106.
- [4] Irons, James R. (1993), Solar Radiation Scattered by Soils, Ph. D. Dissertation, The University of Maryland.
- [5] Kalshoven, James E. and Philip W. Dabney (1993), Remote Sensing of the Earth's Surface with an Airborne Polarized Laser, *IEEE Transactions on Geoscience and Remote Sensing*, Vol.31, No. 2, pp. 438-446.
- [6] Gibbs, D. P. (1992), Measurement and Model Comparisons of Polarized Bidirectional Reflectance, Ph. D. Dissertation, University of Texas at Arlington.

Modeling of Extremely Heterogeneous Radar Backscatter

H. J. Müller

DLR - German Aerospace Research Establishment

NE-HF - Institute for Radio Frequency Technology

82230 Oberpfaffenhofen, P.O.Box 1116, Germany

Phone: +49-8153-282321 Fax: +49-8153-281449 Email: hj.mueller@dlr.de

Abstract – A new class of G-distributions has been proposed to characterize the statistical properties of multi-look processed SAR data over the wide range of homogeneous, heterogeneous and extremely heterogeneous backscattering of terrain classes. The probability density function was derived as a product of a gamma distributed complex speckle variable and the generalized inverse Gaussian distribution for terrain backscatter. The latter is the outcome of a compound Poisson process which describes statistically the underlying physical scattering process. A particular case of the G-distribution is the K-distribution. Another limiting case is the called here G^0 -distribution, which is able to model extremely heterogeneous clutter, such as that of urban areas, that cannot be properly modeled with K-distribution. As the G-distribution is scaleable it can be standardized by normalizing the SAR data with the mean intensity. The other two parameters, which are responsible for shape and spread of the distribution, are estimated by the method of moments where the negative moments are generated by inverse transformation of the normalized SAR data.

INTRODUCTION

The variations of pixel intensities in high resolution SAR images are more heterogeneous the more the spatial variations of the observed terrain classes are at scale of the radar resolution cell. Over forests these variations are related to the spatial nonuniformity of tree density and height. In the case of urban areas the extreme heterogeneity is coming from man-made structures as buildings, roads, bridges etc. and their sizes, shapes, orientations and the nature of building material mainly determine the texture.

Satellite and airborne SAR data retrieved from heterogeneous terrain don't obey the Gaussian statistics, i.e. they are non-Rayleigh in amplitude. In this case the K-distribution, first applied and interpreted on radar data [4] in 1976 and successfully extended to multi-look processed and polarimetric SAR data [5,6], agrees reasonably well for measurements as over forests but fails for stronger heterogeneous media with finer resolution. The known theoretical derivations of distributions suitable for radar returns ignore the possibility to combine the positive form of a distribution with its inverse that is coming from inverse sampling of data. First this was done in [1] applying the generalized inverse Gaussian to SAR data, with particular success for extremely heterogeneous clutter, when a negative shape parameter is accepted.

ORIGIN OF THE DISTRIBUTION

Intensity measurements of radar backscatter from a random scatterer show exponential behaviour. Within a radar resolution cell many scatterers contribute their parts in all to the total backscatter intensity of a cell. Now, the sum of exponential intensities from a number of independent random scatterers has a gamma density $f_X(x) \sim x^{\mu-1} e^{-\lambda x}$. This theorem is well proved in [3]. From clutter cell to clutter cell the intensity is not stationary, it fluctuates the more the reflecting media are inhomogeneous. As the fluctuations are treated in the same manner as the composed scatterers in a cell, i.e. they are gamma distributed $f_Y(y) \sim y^{\nu-1} e^{-\gamma y}$ in all the illuminated area, a mixed or composite model, where the mean of a gamma density is smeared by another gamma density, can be represented by

$$f_Y(y|x)f_X(x) \sim x^{(\nu-\mu)-1} \exp\left(-\frac{\gamma}{x} - \lambda x\right)$$

The joint density of a conditional and an unconditional density generate the kernel of the general inverse Gaussian on the right side of the upper relation with three parameters when setting $\nu - \mu = \alpha$. The norming constant of the new distribution class can be gained by integration on the interval $0, \infty$ (see Gradshteyn/Ryzhik's 'Table of Integrals, Series and Products', no: 3.471.9 resp. 3.478.4).

$$\int_0^\infty x^{\alpha-1} \exp\left(-\frac{\gamma}{x} - \lambda x\right) dx = 2 \left(\frac{\gamma}{\lambda}\right)^{-\alpha/2} K_\alpha(2\sqrt{\gamma\lambda}) \quad (1)$$

The basic as well as the extended properties of this distribution are summarized in [2]. There is mentioned that this function was found by constructing mixtures of Poisson distributions and developing the generalized hyperbolic distribution as a mixture of normal distributions. Special cases are the Gamma ($\gamma = 0, \alpha > 0$), the inverted Gamma ($\lambda = 0, \alpha < 0$), the inverse Gaussian ($\alpha = -1/2$) and its reciprocal ($\alpha = 1/2$) and the hyperbola distribution with $\alpha = 0$ or $\alpha = 1$.

If we replace the both scaling parameter γ and λ by

$$\omega = 2\sqrt{\gamma\lambda}, \quad \sigma = \sqrt{\gamma/\lambda}, \quad \gamma, \lambda > 0$$

we get the alternative form of the generalized inverse Gaussian:

$$p_{GIG}(x) = \frac{\sigma^{-\alpha}}{2K_\alpha(\omega)} x^{\alpha-1} \exp\left(-\frac{\omega}{2} \left(\frac{\sigma}{x} + \frac{x}{\sigma}\right)\right) \quad (2)$$

ω is called 'concentration' parameter by Jørgensen [2], whereas σ is a scaling parameter.

MULTIPLICATIVE MODEL

In [1] the multiplicative model between radar speckle and terrain backscatter is developed for complex, amplitude and intensity data and discussed in detail. Speckle noise appears due to interference phenomena between the incident and reflected coherent signals. Complex speckle is usually assumed to have a bivariate normal distribution. Multilook intensity speckle appears by taking the average over n independent samples leading to the already known gamma-distribution:

$$p_{\Gamma}(x) = \frac{n^n}{\Gamma(n)} x^{n-1} e^{-nx} \quad x, n > 0$$

In case of polarimetric data the complex Wishart distribution replaces the gamma distribution as investigated in [8] and is to combine with the inverted Wishart following the ideas of this paper.

In a similar procedure as before the joint density of fluctuating speckle and terrain backscatter is the integral over a conditional gamma density and an unconditional density function of the generalized inverse Gaussian.

$$f(x) = \int_0^{\infty} p_{\Gamma}(x|y) p_{GIG}(y) dy \quad y \geq 0 \quad (3)$$

Setting the scale parameter in (2) to the mean intensity, $\sigma = \langle x \rangle$, the distribution will be normalized due to the radar cross section because the latter is defined as the ratio of the backscatter intensity to the transmitted intensity per unit area. Replacing the integration variable y in (3) also by normalized data we obtain the G-distribution for normalized intensity data with $x_n = x / \langle x \rangle$

$$f(x_n) = \frac{n^n}{\Gamma(n)} \frac{1}{K_{\alpha}(\omega)} x_n^{n-1} \left(1 + \frac{2n}{\omega} x_n\right)^{(\alpha-n)/2} \times K_{\alpha-n} \left(\sqrt{\omega(\omega + 2nx_n)}\right) \quad \omega, x > 0, \alpha = \text{real} \quad (4)$$

If $\gamma \rightarrow 0$ the G-distribution converges to K-distribution, if $\lambda \rightarrow 0$ the G-distribution converges to G^0 -distribution with negative shape parameter ($\alpha < -1$) as demonstrated in [1].

PARAMETER ESTIMATION

The moments of the joint density of independent random variables are given by the product of the moments of the individual densities.

$$E(X_n^r) = E(X_{\Gamma}^r) E(X_G^r)$$

For normalized intensity data of the G-distribution the moments of r -th order and corresponding moments of the inverted data are given:

$$\langle x_n^{\pm r} \rangle = \frac{\Gamma(n \pm r)}{\Gamma(n)} \frac{K_{\alpha \pm r}(\omega)}{K_{\alpha}(\omega)}$$

Together with the relations

$$K_{-\alpha}(\omega) = K_{\alpha}(\omega)$$

$$K_{\alpha+1}(\omega) = \frac{2\alpha}{\omega} K_{\alpha}(\omega) + K_{\alpha-1}(\omega)$$

and $\langle x_n \rangle = 1$ and the abbreviations

$$a = \frac{n}{n+1} \langle x_n^2 \rangle, \quad b = \frac{n-1}{n} \langle x_n^{-1} \rangle, \quad c = \frac{n-2}{n} \frac{\langle x_n^{-2} \rangle}{\langle x_n^{-1} \rangle}$$

$$\omega\eta = 2\gamma, \quad \omega/\eta = 2\lambda$$

we get a linear equation system for the shape and the scale parameters

$$-\hat{\alpha} - \hat{\gamma} + a\hat{\lambda} = 1$$

$$\hat{\alpha} + b\hat{\gamma} - \hat{\lambda} = 0$$

$$\hat{\alpha} + c\hat{\gamma} - \hat{\lambda}/b = 1$$

This equation system can easily be solved by standard software tools.

SPECIAL CASE

In case of $\lambda = 0$ the generalized inverse Gaussian is reduced to the inverted gamma distribution and the G-distribution converges to G^0 .

$$f(x) = \frac{n^n \Gamma(n - \alpha)}{\Gamma(n) \Gamma(-\alpha)} \frac{x^{n-1}}{\gamma^{\alpha} (\gamma + nx)^{n-\alpha}} \quad (5)$$

With formula for moments $\langle x^r \rangle = \left(\frac{\gamma}{n}\right)^r \frac{\Gamma(-\alpha-r) \Gamma(n+r)}{\Gamma(-\alpha) \Gamma(n)}$ we obtain for the mean intensity $\langle x \rangle = \gamma/(-\alpha - 1)$ and for the shape parameter

$$\alpha = -1 - \frac{n \langle x^2 \rangle}{n \langle x^2 \rangle - (n+1) \langle x \rangle^2}$$

Normalizing the density variable by mean intensity and setting $\alpha = |\alpha|$ we get the remarkable short version of G^0 -distribution (note there is no Bessel function in equation (6)):

$$f(x_n) = \frac{n^n \Gamma(n + \alpha) (\alpha - 1)^{\alpha}}{\Gamma(n) \Gamma(\alpha)} \frac{x_n^{n-1}}{(\alpha - 1 + nx_n)^{n+\alpha}} \quad (6)$$

The G^0 -distribution fits excellently high resolution SAR data about extreme heterogeneous terrain as it is shown in [1] for different urban areas in X-, C-, L- and P-band, in different resolutions, looks and polarisations. The α values for 1-look data in X, C and L over urban areas are lying between -0.9 and -1.3. The α values in P-band for 1 and 4 looks are measured between -1.6 and -2.0.

AMPLITUDE PLOTS

The equations (4) and (6) are derived for normalized intensity data. Applying the transformation $f(x_n) = 2x_n f(x_n^2)$ one gets the equations for amplitude data normalized by square root of mean intensity. Fig.1 and Fig.2 show the 2-dimensional planes of amplitude values against the shape parameter α resp. against the concentration parameter ω . The looknumber and the second parameter are arbitrarily fixed. Fig.3 is a plot of the G^0 distribution depending only on one parameter.

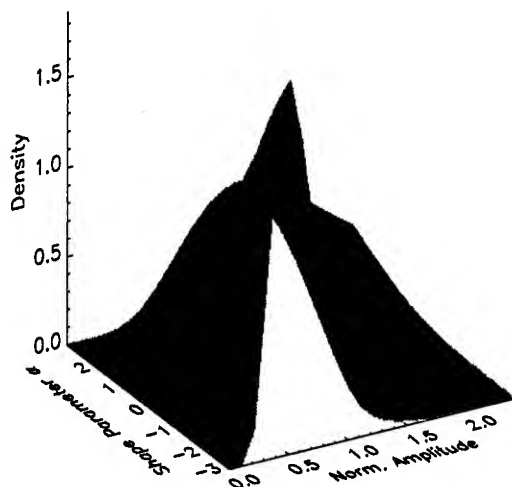


Figure 1: G-Density, Concentration Param. $\omega=2$, 4 Looks

3

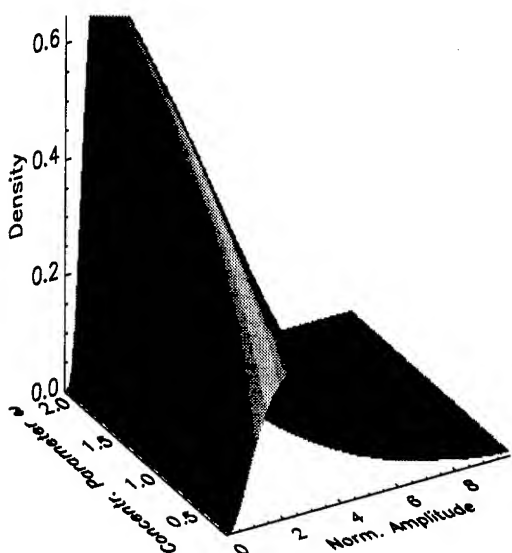


Figure 2: G-Density, Shape Parameter $\alpha=1.5$, 2 Looks

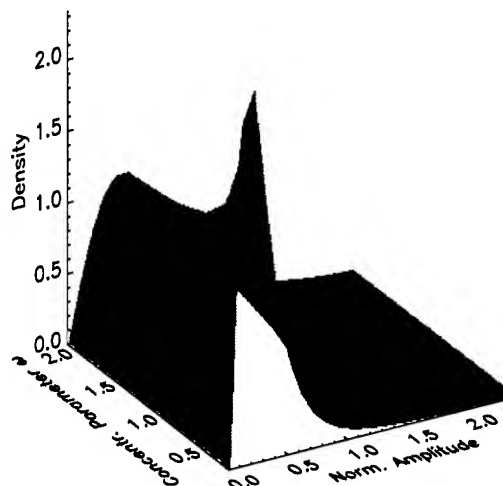


Figure 3: G^0 -Density, 1 Look

REFERENCES

- [1] A.C.Frery, H.J.Müller, C.C.F.Yanasse, S.J.S.Sant'Anna, "A Model for Extremely Heterogeneous Clutter", IEEE Trans.Geosc.Rem.Sens., vol. 3, May 1997
- [2] B.Jørgensen, Statistical Properties of the Generalized Inverse Gaussian Distribution, in Lecture Notes in Statistics, Chap. 9, Springer-Verlag, 1982
- [3] W.Feller, An Introduction to Probability Theory and Its Applications, vol. I + II, J.Wiley, 1971
- [4] E.Jakeman, P.N.Pusey, "A Model for Non-Rayleigh Sea Echo", IEEE Trans.Ant.Prop., vol. AP24, no. 6, pp. 806-814, November 1976
- [5] E.Jakeman, R.J.A.Tough, "Generalized K Distribution: a Statistical Model for Weak Scattering", J.Opt.Soc.Am.A, vol. 4, pp. 1764-1772, September 1987
- [6] J.K.Jao, "Amplitude Distribution of Composite Terrain Clutter and the K-Distribution", IEEE Trans.Ant.Prop., vol. A32, pp. 1049-1062, October 1984
- [7] S.H.Yueh, J.A.Kong, J.K.Jao, R.T.Shin, L.M.Novak, "K-Distribution and Polarimetric Terrain Radar Clutter", J.Electro.Waves Applic., vol. 3, no. 8, pp. 747-786, 1989
- [8] J.S.Lee, K.W.Hoppel, S.A.Mango, A.R.Miller, "Intensity and Phase Statistics of Multilook Polarimetric and Interferometric SAR Imagery", IEEE Trans.Geosc.Rem.Sens., vol. 32, pp. 1017-1027, 1994

ELECTROMAGNETIC SCATTERING AND FRACTAL ANALYSIS OF BARE SOIL SURFACES.

S. Rouvier¹, E. Bachelier¹, P. Borderies¹, I. Chênerie², J.C. Souyris^{3*}, T. Le Toan³, M. Borgeaud⁴

¹ DERM0, 2 Av. E. Belin, BP 4025, 31055 Toulouse Cedex, France
Ph : 33 05 62 25 27 18 e-mail : borderies@oncert.fr

² AD2M Université Paul Sabatier, 118 Route de Narbonne, 31062 Toulouse Cedex
Ph : 33 05 62 25 27 14 e-mail : chenerie@oncert.fr

³ CESBIO, 18 Av. E. Belin, BPI 2801, 31055 Toulouse Cedex, France
Ph : 33 05 61 55 85 84 e-mail : souyris@cesbio.cnes.fr

⁴ ESA, ESTEC-XEP.P.P Box 299, 2200 AG Noordwijk, The Netherlands
Ph : 31 71 565 4830 e-mail : maurice@xe.estec.esa.nl

ABSTRACT

A data base of 400 soil profiles has been analysed from the fractal point of view. Fractality of the profiles is demonstrated and compared with usual statistical descriptions. Electromagnetic computation through FDTD is introduced.

I/INTRODUCTION

Over the past few years, the assessment of Synthetic Aperture Radar (SAR) data for the estimation of moisture and/or roughness over bare soil surfaces has been the subject of numerous studies. However, only a theoretical approach based on Maxwell's equations can yield both qualitative and quantitative understanding of the interaction between the electromagnetic wave and the rough surface.

A concurrent challenging issue to the improvement of soil scattering calculation is related to the soil surface description, which is required as an input of the modeling. There is still a need for new types of representations, particularly to account for the multiscale effects, or for the fluctuations of local statistics. For example, the use of Ultra Wide Band (UWB) pulse for buried targets detection, or the assessment of multifrequency spaceborne radar data, need a multiscale characterization of rough surfaces.

Within this frame, relevancy of fractals as descriptors of bare soil has been already assessed over some agricultural surfaces [1]. Conjointly, fractal analysis of scattered fields have been shown to be a pertinent tool for soil features retrieval in the case of metallic profiles [2]. The overall objective of this paper is to extend these preliminary analysis on several aspects.

First, the investigation of fractal properties over bare soils is currently extended to a much larger data basis made of 400 roughness profiles (Meedle Zeeland data set used for the OBSESS ESA project). Then fractal properties will be

investigated in relation with the usual statistical stationary description (correlation length). Finally, scattered field calculation will be introduced to dielectric profiles, using a Finite Differences in the Time Domain (FDTD) method, which permits to account for the multiscale aspect of these profiles rigorously.

II/ MEEDLE ZEELAND DATA SET : ROUGHNESS ANALYSIS

Meedle Zeeland data set includes 400 roughness profiles, acquired in early 1994 during the three day repeat orbit of ERS1 (C band and VV polarization) over the agricultural area of Meedle Zeeland (South-West of the Netherlands). The measurements were collected using a 1.5 m laser profiler capable of measuring with an horizontal resolution of 0.5 mm, a vertical resolution of 0.1 mm, and a vertical range of approximately 10 cm. Hence each profile is characterized by 3000 points, which according to previous studies, permits an efficient fractal analysis.

Part of roughness parameters statistical study can be summarized in three tables (see Figures 1, 2 and 3), dealing with statistics of three roughness indicators : rms height, fractal dimension and correlation length. For each parameter, mean value and variance are plotted for each field of the data set. Fields have been classified into three classes, according to their way of tillage. Agricultural practices include ploughed fields, sowed fields and severely slaked fields (also said "smooth", because they have suffered from standing water on the surface). Eight fields are included in the data set, numbered 4, 5, 9, 10 for the first class, 14, 16, 17 for the second one and 19 for the last one.

• Rms heights statistics (Fig.1)

Rms heights describe vertical statistics of each profile. They are ranging from 10 to 50 mm, and, as expected,

indicate a decreasing trend from ploughed soils to sowed ones, and then to severely slaked soils. Among the ploughed fields, fields 9, 10, 16, 17 correspond to older and older plough, inducing a decreasing rms height. The last one corresponds to the order of magnitude of sowed ones.

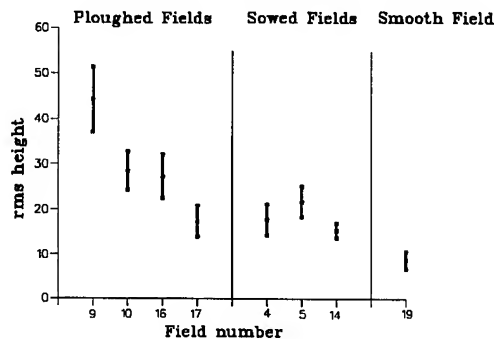


Fig.1 : Rms height (mm) statistics for Meedle Zeeland data set.

• Fractal dimension statistics (Fig.2)

Fractal dimension is a descriptor of horizontal variations of soil roughness. It is derived using counting box method [4] and works on vertically normalized curves, which implies that it has to be considered in connection with the rms height. The orders of magnitude which are considered here range from 1 m (acquisition length) to 1 mm (sampling), and are supposed to account for all scattering phenomena involved in most microwave SAR. Obviously, fractal properties will be investigated on this scale extent only, which means on a windowed spatial frequency spectrum.

Results indicate that all the regression curves obtained are linear, demonstrating the fractality of the various profiles. For the whole data set, the fractal dimensions extracted were found to range from 1.3 to 1.5. Sowed fields are characterized by higher fractal dimensions than ploughed or smooth fields which behave similarly on this point of view. Fractal dimension statistics allow to divide fields under study in two classes :

- ploughed and severely slaked soils
- sowed soils

We see that using conjointly the two statistics will permit to distinguish the three classes without ambiguity.

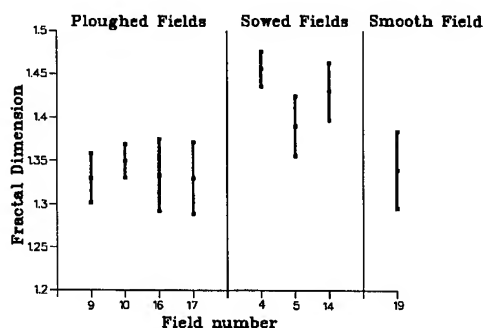


Fig.2 : Fractal dimension statistics for Meedle Zeeland data set.

• Correlation length statistics (Fig.3)

Assuming the stationarity of the roughness profile, and the exponentially-like behaviour of the correlation function, we extract the correlation length which also characterizes horizontal variations of soil roughness, like fractal dimension. The correlation length was shown to be a poor descriptor of soil roughness [3], due to the non stationarity of experimental soil profiles. This result is confirmed by the investigation of the Meedle Zeeland data set. As a matter of fact, correlation length statistics poorly discriminate the three kinds of fields.

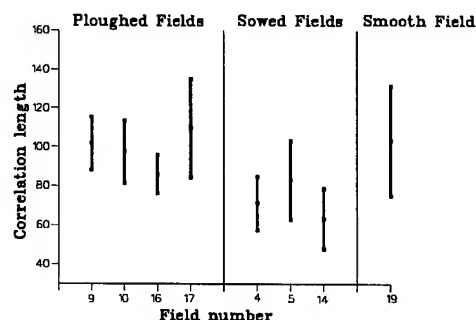


Fig.3 : Correlation length (mm) statistics for Meedle Zeeland data set.

III/ DISCUSSION:

a/ *Physical interpretation* : we could see that fractal dimension divides the fields in two classes. Figures 4 and 5 give a normalized sample of each set. These curves show that even if ploughed fields look more rugged because of higher rms height, when they are normalized they appear smoother, at least from the counting box point of view.

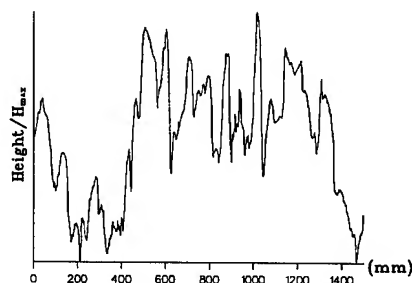


Fig 4 : Normalized sample of the field number 4 (sowed).

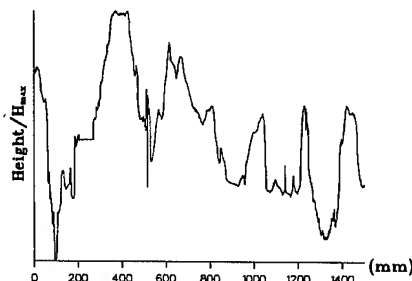


Fig.5 : Normalized sample of the field number 9 (ploughed).

Ploughed fields predominantly contain large blocks with a fairly smooth envelope, whereas sowed ones include blocks of very variable size.

b/ *Dispersion of horizontal descriptors* : Though fractal dimension and correlation lengths are very distinct concepts referring respectively to non-stationary and stationary processes, we found interesting to compare dispersion experimentally obtained for this data set.

Dispersions given for the two horizontal roughness parameters L and D are summarized in Table 1. Indeed correlation lengths appear to be much more dispersed (up to 50%) than fractal dimensions (up to 6%).

Field n°	$\Delta D/D$	$\Delta L/L$
ploughed fields		
9	4%	34%
10	3%	33%
16	6%	23%
17	6%	46%
sowed fields		
4	3%	38%
5	5%	48%
14	5%	48%
smooth field		
19	6%	55%

Table 1 : dispersions for the two horizontal roughness descriptors L and D.

Roughness analysis of Meedle Zeeland data set allows to conclude that the couple {fractal dimension, rms height} appears to be a pertinent descriptor of soil roughness. Three classes of cultivation practices have been discriminated, consisting in ploughed fields, sowed fields, and severely slaked fields. This is an experimental proof of fractal dimension relevancy for soil roughness description.

III/ FDTD METHOD FOR SCATTERED FIELD COMPUTATION

Though fractal characterization of soils is interesting by itself, implications on electromagnetic scattering has to be further investigated, in particular from the microwave SAR point of view in terms of backscattering coefficient. The objective here is first to derive this coefficient versus fractal dimension and also to investigate what is the effect of statistical description (fractals or exponential law for example) on this result. For this purpose, we use FDTD method, which allows handling any kind of profile.

In implementing this method, we divided computational space in the free space part and the soil part, respectively above and below the interface, which may be a sample of the

data base, as well as the output of a statistical generator. The near field computation algorithm is described in [5]. Absorbing boundary conditions are matched to respectively both media assumed homogeneous at their neighborhood. The classical Huygens surface, which in free space classical FDTD computations separates the scattered field zone from the inner total field zone, is here truncated when it crosses the interface. Integration of the tangential fields along that truncated surface provides an approximation of the scattered far field, and subsequently the back scattering coefficient. Computations are done in the time domain, the incident field being a pulse, and results in the frequency domain are deduced with FFT over a wide frequency band.

Some comparisons have been done to establish the validity of this approach. In particular, an excellent agreement is obtained for the far field in the case of canonical scatterers when comparing with exact or analytical methods. We also computed the backscattering coefficient of exponential profiles over several angles (20 to 50 degrees), using a Monte Carlo approach, and results are consistent with those expected from asymptotic methods.

These computations are currently extended to the Meedle Zeeland data base as well as fractal or exponential profiles generated through the parameters extracted in this paper.

This work has been supported by ESA-ESTEC under contract 12008/96/ND/NB

REFERENCES

- [1] S. Rouvier, P. Borderies, I. Chenerie, J.C. Souyris, T. Le Toan, N. Floury, "Fractal analysis of ploughed soils profiles and application to electromagnetic scattering of soils", IGARSS'96, IEEE, Lincoln, Nebraska, USA, 27-30 May 1996.
- [2] S. Rouvier, P. Borderies, I. Chenerie, "Ultra wide band electromagnetic scattering of a fractal profile", Radio Science, Vol 32, n°2, pp. 285-293, March-April 1997.
- [3] J. Costes, I. Chenerie, T. Le Toan, N. Boutier, J. Lemorton, "On the statistic characterization of random rough surfaces for electromagnetic scattering", PIERS 94, Noordwijk, The Netherlands, 11-15 July 1994.
- [4] K. Falconer, Fractal geometry mathematical foundations and applications, John Wiley, New York, 1993.
- [5] M. Jauregui, P. Borderies "Modelling and processing of ultra wide scattering of buried targets", EUREL international conference on the detection of abandoned land mines, Edimburgh 1996.

*Presently at CNES,QT/SH/SR,BPI811,18A.E.Belin,31055,Toulouse,Fr.

Semi-Rough Surface Scattering And Its Fading Effects For Active Microwave Sensors

Ji Wu, Jingshan Jiang and Liwei Wang
MIRIT, Center for Space Science and Applied Research
P.O.Box 8701, Beijing 100080, P.R. China

Tel.: +86 10 6255 9944-3417, Fax: +86 10 6257 6921, e-mail: wuji@sun20.cssar.ac.cn

Abstract - Ground scattering to a microwave incident wave is usually considered as a non-coherent process when the ground surface is rough in terms of wavelength. However, situation do exist where the composed field at the receiving antenna aperture is coherent when the ground surface is smooth or rough but with a non-uniformly distributed random phase. In this paper, the authors have calculated the coherent phenomenon and shown the fading effects exist for both nadir and off-nadir looking situations. To distinguish from conventional considerations, we introduced the semi-rough surface concept for the uniformly distributed random phase situations.

I. INTRODUCTION

The measurement principle of ground scatterometer is based on non-coherent power summation (noise model) of many independent measurement samples. The assumption of this model is that the phase distribution of each independent samples are uniformly distributed. In practice, when the ground surface is rough, i.e.

$$\Delta r > \frac{\lambda}{4} = 2\Delta h \cos \theta$$

$$\text{or } \Delta h > \frac{\lambda}{8 \cos \theta} \quad (1)$$

where Δr is the path difference between the waves reflected from the top and the bottom of

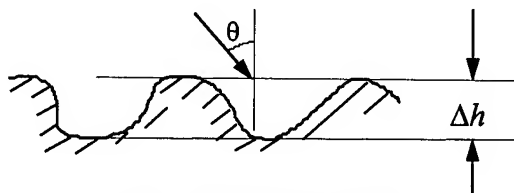


Fig.1 Definition of Δh

the rough surface and Δh is the maximum irregular height of the surface as show in Fig. 1. (1) is called the Rayleigh criterion [1].

It is normally assumed that other irregular height between Δh and 0 are uniformly distributed which will certainly cause a uniformly distributed random phase distribution. However, this is only an idea case and in practice, the distribution of the irregular height may not be uniformly distributed not mention the volume scattering. For non-uniformly distributed random phase, regardless its physical roughness, we call it the semi-rough surface. In Section II, two methods are used to calculate the semi-rough surface fading effect while the sensor is looking downwards (nadir looking). In Section III, the sidelooking situation (off-nadir looking) is considered which is the most used case in practice. The numerical results are summarized and discussed in the Conclusions.

II. FADING CALCULATIONS AND ITS EFFECTS FOR NADIR LOOKING

Last year, the authors have analyzed the normal incident situation with small disk model as described in [2]. Although it is a demonstration type, it has already given the periodical fading phenomenon caused by coherent summation of composed field at the receiving antenna aperture. In this paper, we give more precise calculation result using the Kirchhoff approximation

$$E_2 = \frac{1}{4\pi} \iint_S \frac{2R}{r^2} e^{j2\pi r} \mathbf{k}_1 \cdot \mathbf{n} dS \quad (2)$$

where E_2 is the scattered field at the direction of the incident wave. \mathbf{k}_1 is the vector wave number,

\mathbf{n} is the norm of the localized surface. E_2 is then carried into the backscattering coefficient σ^0 calculation according different platform altitudes. Fig.1-4 shown the variations of σ^0 versus platform altitude and ground surface roughness. Each value in the figure is an average of 50 independent samples. It is clearly seen that the fading effect is enhanced while the surface is changing from rough to smooth. The period of the fading is previously given in [2] and emphasized here again,

$$T = \frac{\cos(\theta_{0.5}/2)}{2 [1 - \cos(\theta_{0.5}/2)]} \lambda \quad (3)$$

where $\theta_{0.5}$ is the half power beam width of the receiving antenna. Another point we should stress here is that the fading will remain the same characteristics for very large platform altitude.

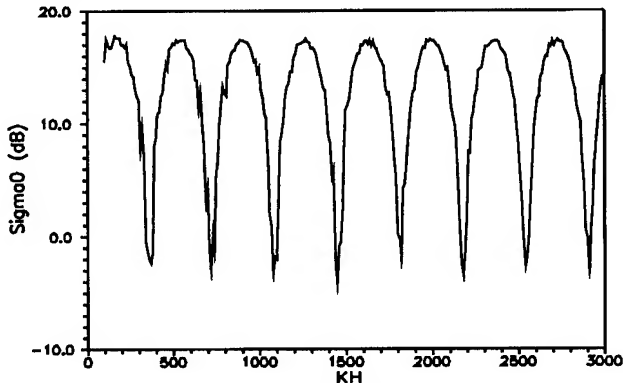


Fig.1, Smooth surface with $\Delta\phi < 36$ degrees, $\theta_{0.5}=15^\circ$

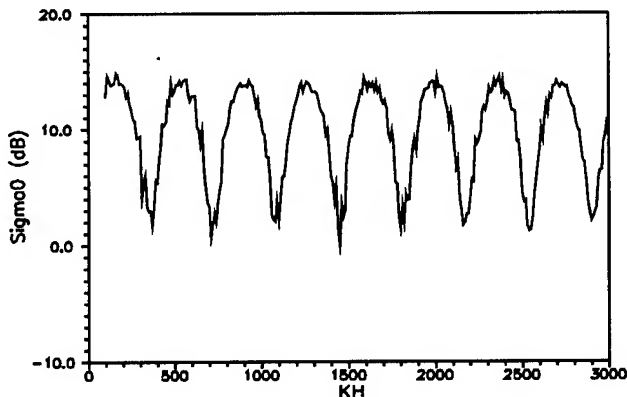


Fig.2, $\Delta\phi < 90$ degrees, $\theta_{0.5}=15^\circ$

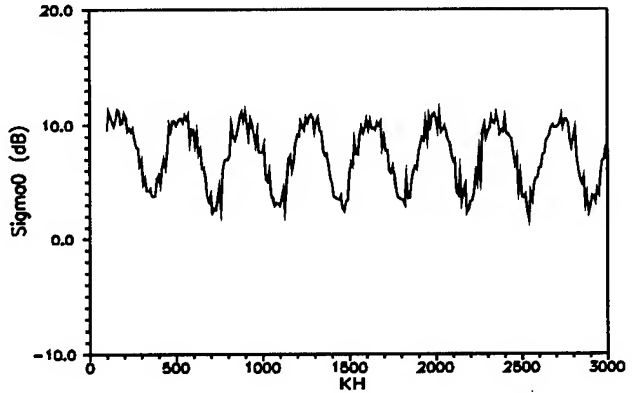


Fig.3, $\Delta\phi < 120$ degrees, $\theta_{0.5}=15^\circ$

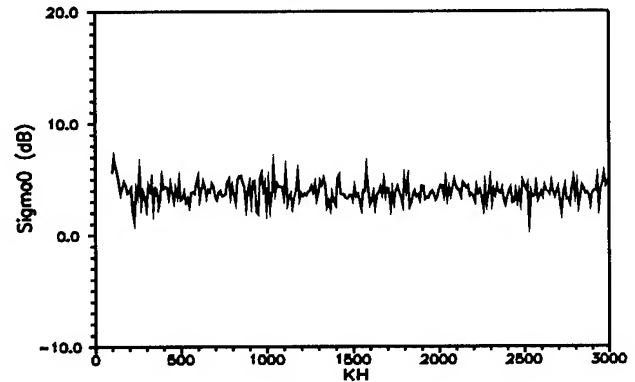


Fig.4, $\Delta\phi < 240$ degrees, $\theta_{0.5}=15^\circ$

It is to be understood that the fading is caused by the non-uniformly distributed random phase. While the platform altitude is increasing, the areas in the coverage providing the positive and negative phase are changing alternately. Since the edge of the coverage is coincident with the border of the Fresnel zone, the fading period can be calculated by summing the positive and negative Fresnel zone in the coverage area. Fig.5 shown the net area after the cancellation of the positive and negative Fresnel zones for different

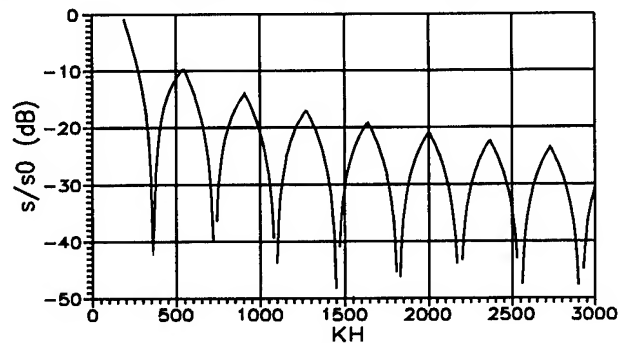


Fig.5, Net area after Fresnel zone cancellation

platform altitude. It is seen that the net area of the Fresnel zones can present the fading effect very well.

III FADING EFFECTS FOR OFF-NADIR LOOKING CASES

In practical measurements, for example a ground-based scatterometer, the wave incident angle is not limited to the nadir direction but any possible incident angles. In these situations, the fading will become very complicated since the edges of the Fresnel zones in the coverage area are not circles anymore.

It has been discussed in [2] that in off-nadir situations the fading is a composition of many frequencies from the Fresnel zone point of view. We then first use the area calculation program to calculate the net area after the cancellation of the positive and negative Fresnel zone. The result is shown in Fig.6.

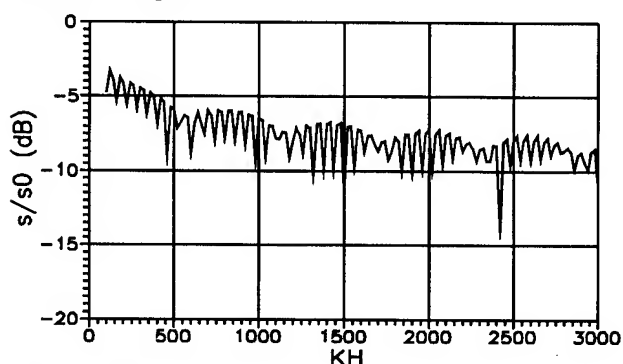


Fig.6, Net area of Fresnel zone when $\theta_{inc} = 20^\circ$

It is seen that the fading is effected by many frequencies. The dominate frequency is much faster than in the nadir looking cases.

To be closer to the practical situations, we have calculated the same fading effects by using the Kirchhoff approximation. The result is shown in Fig.7 and 8.

It is seen that the fast fading effect shown in Fig. 6 become not clear due to the random phase and the average of 50 samples. However, it is discovered that for smooth surface and large incident angle, σ^0 is seriously effected at low altitude. This effect should be taken into account for ground based measurements.

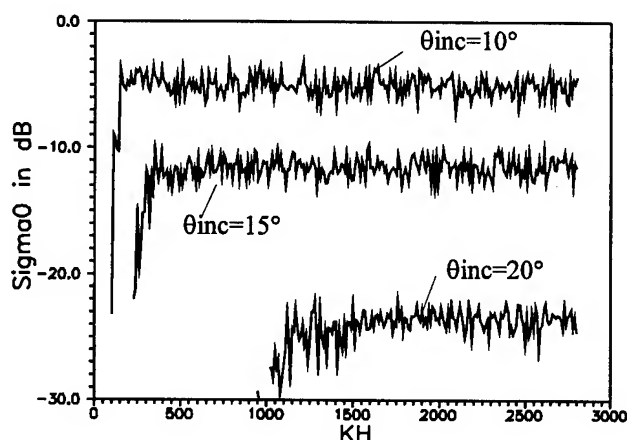


Fig.7, Effect with different incident angles

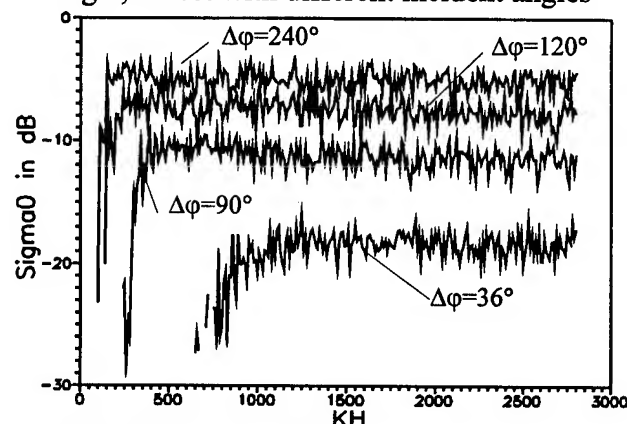


Fig.8, Effect with different surface roughness

IV CONCLUSIONS

The fading effects caused by non-uniformly distributed random phase are discussed. No matter it is nadir or off-nadir looking, the fading effect are all existence. For the nadir looking situation, the fading is very typical and with a predictable fading period related to the half power beamwidth of the receiving antenna. For the off-nadir looking cases, the fading is not strong enough, therefore it can be almost neglected except that for low altitude measurement, for example ground-based measurement. For uniformly distributed random phase, there is no fading effects.

REFERENCES

- [1] P.Beckmann and A. Spizzichino, The Scattering of Electromagnetic Waves From Rough Surfaces, Artech House, MA, 1987
- [2] Ji Wu and Jingshan Jiang, "Near-field effect of extended targets on absolute calibration of microwave sensors, IGARSS'96

Empirical and Theoretical Backscattering Behavior as a Function of Roughness for Arid Land Surfaces

Agnès REMOND (1) & Jean-Paul DEROIN (2)

(1) BRGM DR /GIG, 3 ave. C. Guillemin,
45060 Orléans Cedex 02

e.mail : a.remond@brgm.fr - fax : (33) 2 38 64 33 61

(2) BRGM SGR Haute Normandie, 10 rue Sakhorov
76130 Mont Saint-Aignan

ABSTRACT

A study was carried out to assess the potential of using satellite images to identify a parameter that could characterize land surface condition - i.e. soil roughness, a factor that strongly influences radar backscattering from semi-arid land surfaces.

A simple setting in terms of roughness - the flat Atar desert, Mauritania - was used for data extraction from an ERS-1 image, and two methods were defined for measuring the statistical parameters of roughness (standard deviation of heights and correlation length) from photographs of the ground. Analysis of these parameters showed that a close relationship exists between correlation length and standard deviation of heights for regs and that a single parameter enables us to describe roughness.

Theoretical models (Small Perturbation Model, Integral Equation Model and Geometrical Optics Model) were then used to establish data sets simulating ERS-1 backscattering coefficients for the different roughness surfaces. Based on the statistical parameters extracted from photographs, good agreement is observed between the modeled backscattering and the recorded backscattering from ERS-1 data. The relationship between the two statistical parameters was then used to simulate several surfaces, with the backscattering behavior being studied through theoretical models. The results show backscattering as a function of the standard deviation of heights and define the possibilities and limitations for extracting roughness parameters.

1. Introduction

The study of radar backscattering from natural surfaces can be approached in two ways. One method consists in multiplying the acquisitions under various configurations so as to provide statistical results between the backscattering and the looked for descriptive variable [1]. The second method uses theoretical models to study the evolution of the backscattering coefficient in relation to this variable. It is the second approach that was used in the present study to examine the theoretical behavior of the backscattering coefficient in relation to the roughness of arid land surfaces.

2. Study Area

2.1 Site description

The study sites are located in the Atar desert region of Mauritania (20°30' N, 13°00' W). The geological surfaces are water-borne deposits, sandy eolian deposits, smooth or gravelly reg, and rock slabs. The different regs comprise a) a flat cover of contiguous centimeter-size rock fragments, b) rocks spread over the surface giving to a texture of medium roughness, and c) very rough oversized boulders.

2.2 Statistical roughness parameters

The nature of the land surface was determined by quantifying and qualifying parameters, such as the maximum and mean heights of the rough spots, and the lithological nature of each site. Estimation of the statistical roughness parameters was done from photographs giving a detail of approximately $\frac{1}{2} \text{ m}^2$ [2]. A first theoretical roughness profile was estimated using the mean size of the rocks and the mean distance between two rocks. A second theoretical profile was obtained from the actual distribution of the rocks on the photograph. The statistical parameters, standard deviation of heights (s) and correlation length (l), were extracted respectively from these two profiles.

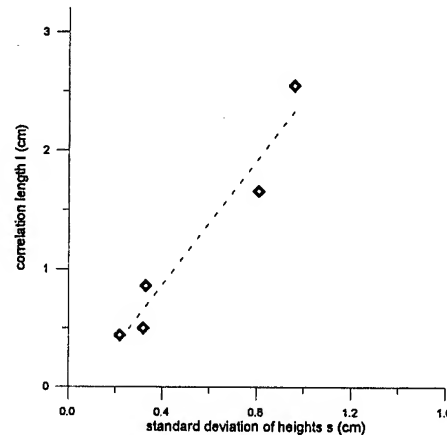


Fig.1

Coherent estimations of the standard deviation of heights (s) obtained for the reg surfaces gave values varying from 0.22 cm to 2.1 cm, and showing a logical increase with the general roughness. The results for the correlation length (l) were more random and only the values of less than 3 cm appeared probable.

Once the 's' and 'l' parameters had been extracted, it was seen that the correlation length was approximately equal to twice the standard deviation of heights (Fig.1). This in spite of the fact that the two statistical parameters were obtained by different methods.

3. SAR backscattering

3.1 ERS-1 data

The radar data used in the study were extracted from an ERS-1 image acquired on 09/11/93 (orbit 12120; frame 3195). The data were geocoded and calibrated so as to obtain a backscattering coefficient for each of the study sites.

3.2 Backscattering models

Theoretical backscattering models [3,4] enable a backscattering coefficient value (σ^0) to be obtained from the characteristics of both the sensor and the target. Three models were used: Geometric Optical Model (GOM), Small Perturbation Model (SPM) and Integral Equation Model (IEM). The five study areas are reg surfaces ($s < 0.96$ cm). The choice of model was based on the value of the standard deviation of heights. The dielectric constant of these environments was taken as equal to 6 F/m, the correlation function being exponential. The same site was used for one or several modelings and the results were compared with the ERS-1 data.

3.3 Empirical and theoretical backscattering

In the first instance, the 's' and 'l' values obtained from the theoretical profiles were used for modeling a first backscattering coefficient (Fig.2).

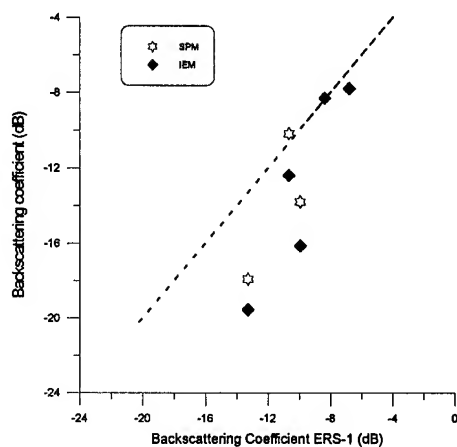


Fig.2

With a backscattering coefficient below -10 dB for ERS-1 ($s < 0.32$ cm), the SPM and IEM models underestimate the backscattering coefficients by as much as 6.3 dB for IEM and 4.5 dB for SPM. Above this value, IEM gives good results with a deviation of less than 1 dB from the ERS-1 data. One can thus consider that these two models are capable of

modeling the backscattering of the ERS-1 satellite under the conditions of the study.

In the second instance, a correlation length value equal to twice that of the standard deviation of heights was used for modeling a second backscattering coefficient.

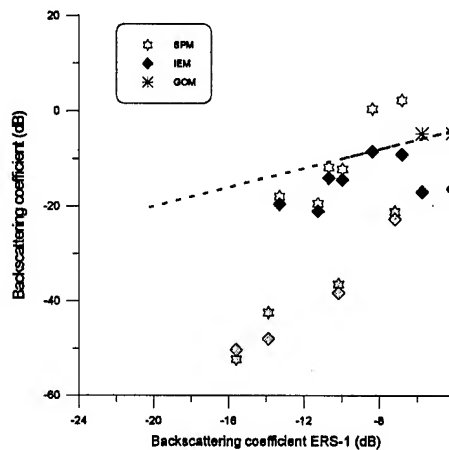


Fig.3

Two categories of results are distinguished (Fig.3).

- some of the modeling gives mediocre results (gray points) with a difference of at least 1.5 dB between the ERS-1 data and the modeled coefficients. The corresponding surfaces are very smooth regs ($s < 0.18$ cm).

- the rest of the modeling (white points, black points, stars) carried out for rougher surfaces ($s = 0.2$ to 1.9 cm) gives good results. Here it is possible to reproduce the ERS-1 data by selecting one of the three models. Thus, for a standard deviation of heights between 0 and 0.3 cm, the mean deviation between SPM values and the ERS-1 data is 4.02 dB; for values between 0.8 and 0.9 cm, the deviation between IEM and ERS-1 data is 1.16 dB; finally, for an 's' value greater than 1.84 cm, GOM reproduces the ERS-1 data with a mean deviation of 0.8 dB.

The application of correlation length values linearly dependent on the standard deviation of heights results in very satisfactory modeling for most of the regs. For $s > 0.25$ cm, we noted that the equation " $l = 2*s$ " improves the results of the SPM, IEM and GOM backscattering models. Moreover, this equation enables rapid modeling of the backscattering coefficient for surfaces where the correlation length is unknown.

4. Theoretical backscattering behavior

Using the assumption that " $l = 2*s$ ", we simulated the response of three backscattering models (SPM, IEM, GOM) as a function of the standard deviation of heights (Fig.4). With the SPM model for a standard deviation of heights of less than 1 cm, the relationship obtained between σ^0 and 's'

can, without ambiguity, be approximated by a logarithmic equation (correlation coefficient = 0.99). Similarly, with the IEM model the coefficient σ° increases rapidly with 's' for values below 0.75 cm, then gently decreases. Approximation by a logarithmic law for 's' values between 0 and 1 cm gives a correlation coefficient of 0.96. Finally, with the GOM model a simplification of the equations (where σ° is proportional to s^2/l^2) imposes an invariant backscattering regardless of the value of 's'.

The logarithmic approximations are:

$$\sigma_{SPM}^\circ = 15.28 * \log(s) - 2.03 \quad \text{for } 0 < s < 1 \text{ cm}$$

$$\sigma_{IEM}^\circ = 13.67 * \log(s) - 2.31 \quad \text{for } 0 < s < 1 \text{ cm}$$

$$\sigma_{GOM}^\circ = -4.65 \text{ dB.}$$

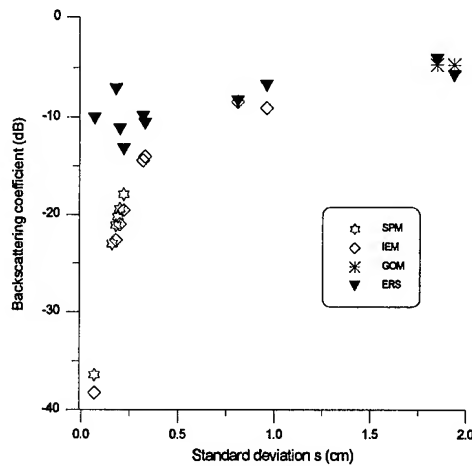


Fig.4

In conclusion, the theoretical backscattering coefficient increases rapidly with the standard deviation of heights up to 0.25 cm, after which the increase becomes more subdued. The coefficient of ERS-1 shows a similar evolution [2], albeit with a much gentler dynamics. Theoretically, it is feasible to extract the standard deviation of heights from the backscattering. Nevertheless, for standard a deviation of heights of less than 0.25 cm, it is not possible to use the logarithmic equations defined above. Moreover, their asymptotic shape leaves one to assume that high standard deviations of heights cannot be discriminated.

Conclusion

Several studies were made to characterize the roughness of regs as well as to approach the validity of the determinist backscattering models and the theoretical study of this backscattering according to the roughness. It appears that the statistical parameters of roughness can, for certain regs, be deduced from simple measurement and field photographs. Moreover, the correlation length, which is difficult to calculate, can be approximated by twice the standard deviation of heights, thus avoiding long and not very

accurate calculations. For relatively rough surfaces ($s > 0.25$ cm) the SPM, IEM and GOM models give, with this simplification, good results in specific validity fields. Finally, the theoretical evolution of backscattering from reg surfaces shows a logarithmic evolution with the standard deviation of heights. This indicates that it may be possible, for certain values of 's', to extract the roughness directly from the backscattering coefficient, whereas for other values it would be impossible.

Acknowledgments

The ERS-1 images were provided by the European Space Agency within the framework of the pilot project PP2-F6 "Radar and Geology in Arid Regions". The work was cofunded by the *Centre National d'Études Spatiales* (CNES) within the AVAL SAR program. Logistic support for the field operations was provided by the *Détachement Militaire d'Assistance Technique* (DMAT) in Atar and access to the test site was facilitated by the Mauritanian Office of Geological Research (OMRG) in Nouakchott. The study is part of the BRGM Research Division Project P01 "Perspectives for the Use of New Sensors in the Earth Sciences". This BRGM publication No. 97018 was translated from French by the BRGM *Service Traduction*.

References

- [1] A.K. Fung, "Microwave scattering and emission models and their applications" Artech House, 1994.
- [2] J.P Deroin, A.Company and A.Simonin, "An empirical model for interpreting the relationship between backscattering and arid land surface roughness as seen with the SAR", *IEEE Trans. on Geoscience and Remote Sensing*, vol. 35, no. 1, pp. 86-92, 1997.
- [3] Y. Oh, K. Sarabandi and F.T. Ulaby, "An empirical model and an inversion technique for radar scattering from bare soil surfaces", *IEEE Transactions on Geoscience and Remote Sensing*, vol. 30, no. 2, pp. 370-381, 1992.
- [4] F.T. Ulaby, R.K. Moore and A.K. Fung, "Microwave remote sensing", vol. 2, Artech House Inc., Norwood (USA), 1982.

Simulation of Unpolarized Scattering in Synthetic Aperture Radar Images

K. Tomiyasu
Lockheed Martin Corp.
P.O. Box 8048, Rm. 37D85
Philadelphia, PA 19101-8048 USA
Tel (610) 531-5740, FAX (610) 644-8521

Abstract - With fully polarimetric synthetic aperture radar (SAR), images have been produced from co-polarized, cross-polarized and unpolarized (randomly polarized) scattered signals. From these images, considerable information on scene classification is revealed. Unpolarized scattering is simulated by pairs of scatterers that are orthogonally polarized and located at the limits of range and azimuth resolutions. Sample calculations show that perhaps 10 to 30% of unpolarized scattering is possible.

Quad-pol scattering entails frequency and angle ensemble averages of orthogonal polarimetric signals scattered from a pixel, defined by the SAR range and azimuth resolutions. Typically, the pixel dimensions are many times the radar wavelength, and a pixel contains numerous scattering centers. It is assumed that for each scattering center its reflected amplitude, reflected phase, and reflected polarization components can be random variables, but remain constant within the SAR integration period.

INTRODUCTION

The immense value of quad-pol techniques for interpreting SAR images has been demonstrated. Co-polarized, cross-polarized, and unpolarized (random polarization) SAR images of the San Francisco region have revealed considerable information on scene classification [1]. Subsequent effort on unpolarized scattering has been reported [2]. There is a polarization similarity between SAR image scattering using quad-pol techniques and radiation from stellar sources.

STOKES' PARAMETERS

Stellar response is characterized by Stokes parameters which entail time ensemble averages of two orthogonally polarized complex signals. The parameters are given by:

$$I = \langle E_v^2 \rangle + \langle E_h^2 \rangle$$

$$Q = \langle E_v^2 \rangle - \langle E_h^2 \rangle$$

$$U = \langle 2E_v E_h \cos \delta \rangle$$

$$V = \langle 2E_v E_h \sin \delta \rangle$$

$$\% \text{ Polarized} = \frac{\sqrt{Q^2 + U^2 + V^2}}{I} \times 100$$

INTERFEROMETRY WITHIN AZIMUTH BIN

There are two integration variables which contribute to unpolarized scattering. The first is the radar line-of-sight viewing angle. This angular range is dictated by the azimuth resolution, and the integration is performed by varying the angle in many small steps. This can be shown from the basic approximate equation for azimuth resolution:

$$\begin{aligned} \delta_{az} &= \text{Azimuth Resolution} \\ &= \frac{\lambda/2}{\theta} \end{aligned}$$

Where λ = Radar Wavelength

θ = Viewing Angle

INTERFEROMETRY WITHIN RANGE BIN

The second variable is radar frequency. Dictated by the range resolution, there is a finite bandwidth, and the integration is performed by varying the frequency in many small steps. Interferometry occurs within a range bin governed by the bandwidth of the radar pulse as illustrated here:

$$\Delta R = c \frac{\tau}{2} = \text{Range Resolution, } c = \text{Light Velocity}$$

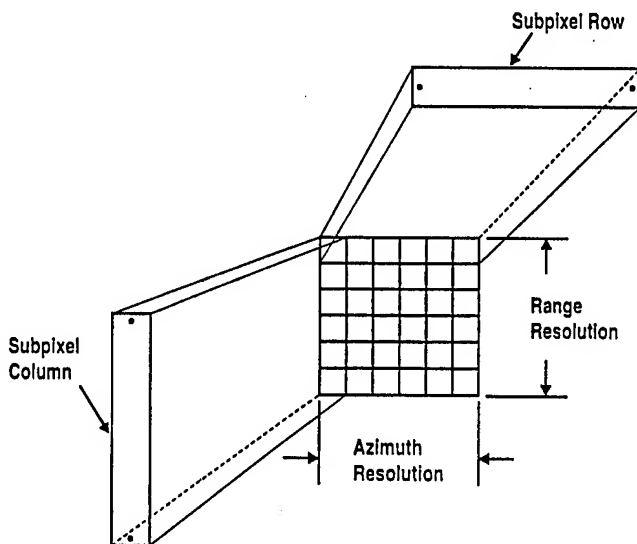
$$\tau = \text{Pulse Length} = 1/\text{Bandwidth}$$

$$\Delta R = \frac{0.5 c}{f_u - f_L} = \frac{0.5}{\frac{1}{\lambda_u} - \frac{1}{\lambda_L}}$$

$$\frac{\Delta R}{\lambda_u} - \frac{\Delta R}{\lambda_L} = 0.5 \text{ Wavelength}$$

GENERALIZED FORMULATION

To demonstrate the unpolarized scattering phenomenon, a pixel is subdivided into numerous subpixel rows and columns. Each subpixel row is parallel to the azimuth dimension. Its length is equal to the azimuth resolution, and its width could be one-half the radar wavelength. Each column is parallel to the range dimension, its length is equal to the range resolution, and its width may be one-half the radar wavelength. One pixel of a scene image with many subpixel rows and columns is illustrated below.



The generalized equations for the scattering in two orthogonal coordinates is given below:

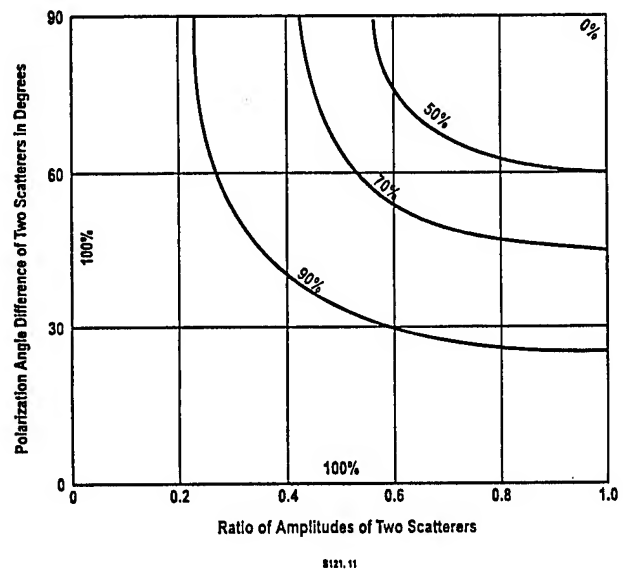
$$E_v = \sum_{\sigma} \rho_{\sigma}(x, y, z) e^{j\phi_{\sigma}} \cos \theta_{\sigma} \exp \left[j \frac{4\pi}{\lambda} r_{\sigma}(x, y, z) \right]$$

$$E_h = \sum_{\sigma} \rho_{\sigma}(x, y, z) e^{j\phi_{\sigma}} \sin \theta_{\sigma} \exp \left[j \frac{4\pi}{\lambda} r_{\sigma}(x, y, z) \right]$$

Where σ = All Scatterers
 ρ = Reflected Amplitude of Scatterer
 ϕ = Reflected Phase of Scatterer
 θ_{σ} = Polarization Orientation Angle
 r = Range to Scatterer
 λ = Wavelength

ANALYSIS

A two scatterer configuration located at the extremities of a subpixel was assumed. The ratio of the reflected amplitudes of two scatterers is one variable. The second variable is the angle difference of the polarization orientation of the two scatterers. The following graph illustrates the degree of polarization as a function of these two parameters.



The analysis has shown that the extent of the radar viewing angle can cause unpolarized scattering from scatterers in a row, but not from a column. The spread in radar frequency can cause unpolarized scattering due to interferometric effects from scatterers in a column, but not from a row.

The two-scatterer response was found to be totally unpolarized when the two amplitudes are equal and the polarization angles differ by 90°. The central region of the graph may indicate the

response of a typical terrestrial scene, and this would imply that the average response would be about 90 to 70% polarized, or about 10 to 30% unpolarized. [2]

Trans. Geosci. Remote Sensing, vol. 26, pp. 774-789, November 1988.

REFERENCES

- [1] D.L. Evans, T.G. Farr, J.J. Van Zyl and H.A. Zebker, "Radar polarimetry: Analysis tools and applications," IEEE

S.L. Durden, J.J. Van Zyl, and H.A. Zebker, "The unpolarized component in polarimetric radar observations of forested areas," IEEE Trans. Geosci. Remote Sensing, vol. 28, pp. 268-271, March 1990.

A Vegetation Classification Scheme Validated by Model Simulations

P. Ferrazzoli, L. Guerriero, G. Schiavon

DISP — Università "Tor Vergata" — Via di Tor Vergata — I-00133 Roma — Italy
ferrazzoli@utovrm.it, guerriero@utovrm.it, schiavon@disp.utovrm.it

Abstract — The capability of multifrequency polarimetric SAR to discriminate among nine vegetation classes is demonstrated using both experimental data and model simulations. The experimental data were collected by the multifrequency polarimetric SAR at the Dutch Flevoland site and the Italian Montespertoli site. Simulations are carried out using the vegetation model developed at Tor Vergata University.

INTRODUCTION

In the recent years, several experiments have been carried out to investigate the potential of Synthetic Aperture Radar (SAR) in remote sensing of vegetation.

In particular, several statistical classification works have been made, indicating that SAR systems have a good capability in discriminating among various classes over agricultural and forest sites. A critical review of significant results is shown in [1]. Some papers [1], [2], indicate that a statistically valid classification algorithm must be accompanied by a good knowledge of the interactions between electromagnetic waves and vegetation elements of various shape, dimensions and orientations. Theoretical electromagnetic models are useful to this scope. In fact, model simulations can guarantee that the separability between two classes, eventually noted in some radar data, is reliable since it finds explanation in marked differences of scattering behaviour; the latter, on their sides, are due to different plant geometries. Therefore, when an algorithm tested on a site is validated by model simulations, we have confidence in the achievement of valid results also in other sites. After validations over various sites are carried out, reliable classification results should be obtained also after a gradual reduction in the dimensions of the training set and, in a near future, fully unsupervised algorithms could be developed.

Classification works based on SAR data and supported by models are described in [1]–[3]. In this paper, we investigate the SAR discrimination capability by analyzing the experimental data collected by the polarimetric AIRSAR at the Dutch Flevoland site (MAESTRO-1 experiment, 1989) and at the Italian Montespertoli site (MAC-Europe campaign, 1991). Nine classes, corresponding to vegetation present in at least one site, are considered. The experimental data are interpreted with the aid of the microwave vegetation model developed at Tor Vergata University [4], [5]. For each class, experimental data and

model simulations are shown, both indicating that there are some combinations of frequency and polarization for which that class shows a behaviour appreciably different from that of the others. This ensures a reliable classification capability. On the basis of this analysis, a simple hierarchical scheme is proposed. The results presented in this paper can support the development of reliable classification algorithms, which will be ready for operational use after testing over several sites.

MATERIALS AND METHODS

Experimental data

In this paper, we use experimental data collected over forests and agricultural fields by AIRSAR, which is a fully polarimetric radar operating at P (0.45 GHz), L (1.2 GHz) and C (5.3 GHz) band. It is well known, since it has overflowed several sites worldwide and the results have been analyzed by several scientists. We use the AIRSAR data obtained over the Dutch Flevoland site in summer 1989 and over the Italian Montespertoli site in summer 1991. We analyze the polarized backscatter coefficient σ° measured at P, L and C band and at HH, HV, VV, RR (circular copolar), RL (circular crosspolar), 45C (45° copolar), 45X (45° crosspolar) polarization, for a total of 21 features (3 frequencies \times 7 polarizations). We will use the σ_{FPQ}° symbol, where F indicates the band (P, L or C) and PQ indicates the polarization (HH, HV, VV, RR, RL, 45C or 45X).

The Flevoland site included fields of potato, sugarbeet, corn, alfalfa and bare soils. The Montespertoli site included small forests, olive groves and fields of sunflower, corn, sorghum, colza, alfalfa, wheat and bare soils.

The model

The agricultural and arboreal vegetation samples present in the two sites have been grouped into classes; each class includes one or more vegetation species, according to the scheme which will be described later. For each class, model simulations have been carried out, aimed at demonstrating that one or more AIRSAR features allow separability of that class from the others, due to some specific properties of its radar signature. We have used the polarimetric vegetation model developed at Tor Vergata University. Details about the model and comparisons with experimental data are given in [4]–[6].

Classes definition

We have subdivided the vegetation samples present in the

*Work partially supported by ASI, Agenzia Spaziale Italiana. Information on Flevoland site provided by University of Wageningen (NL).

two sites into 9 classes. The classes selection has been based on sound differences of electromagnetic scattering behaviour. To this aim, we have adopted the well established subdivision among surface scattering, dihedral scattering and volume scattering [2]. Moreover, we have applied the concepts described in [7], where the roles of biomass and plant density N (m^{-2}) are discussed.

We have finally defined the following classes:

- senescent corn (large vertical stems, partial defoliation, dihedral effects);
- forest (low N , high biomass);
- olive grove (low N , low biomass);
- potato (intermediate N with ramification, high biomass);
- developed sunflower and sugarbeet (intermediate N and wide leaf, high biomass);
- early stage sunflower, corn and sorghum (intermediate N and wide leaf, low biomass);
- colza (high N and small stems, high biomass);
- alfalfa and drying wheat (high N and small stems, low biomass);
- bare soil (surface scattering).

DISCRIMINABILITY RESULTS

Some senescent and partially defoliated corn fields were present at Flevoland site. Experimental data and model simulations show that a discriminant property of these fields is the high depolarization that vertical stems produce for a linear 45° incident wave polarization; the effect is particularly evident at L band.

Forests, olive groves and potato fields may be discriminated from other classes and one another, since are characterized by extended ramifications, producing high depolarization. Figure 1 shows the modeled trends of σ_{PHV}° and σ_{LHV}° for canopies of randomly oriented equal cylinders as a function of cylinder radius for a branch biomass of 0.2 kg/m^2 and 1 kg/m^2 . An increasing trend is observed at P band, while at L band the trend is not monotonic, but shows a minimum at ~ 2 cm. Figure 2 shows a scatterplot of field averaged σ_{PHV}° vs. σ_{LHV}° . Forest, olive grove and potato classes are well discriminable in this figure. A comparison between the results of Figure 1 and those of Figure 2 suggests the following interpretation. The dense Montespertoli forests contain several branches whose dimensions are spread in a wide range, so that they produce high HV backscatter at both P and L band. Potato secondary stems have small radii, so that σ_{LHV}° is higher than σ_{PHV}° . Olive groves are sparse, with few branches (and inclined trunks) per m^2 and their dimensions are such to produce a σ_{PHV}° higher than σ_{LHV}° .

A further separation between wide leaf crops and crops with small cylindrical elements may be performed using C band data in circular polarization. Figure 3 shows theoretical trends of σ_{CRL}° and σ_{CRR}° for the two kinds of canopies. For bare soils

and wide leaf crops $\sigma_{CRL}^{\circ} > \sigma_{CRR}^{\circ}$, while for small cylinders $\sigma_{CRL}^{\circ} \sim \sigma_{CRR}^{\circ}$. The experimental data of Figure 4 confirm this result.

Finer subdivisions between higher and lower biomass fields may be made using σ_{LHV}° for wide leaf crops and σ_{CHV}° for colza, wheat and alfalfa. Finally, bare fields may be separated since they show low values of $\sigma_{LHV}^{\circ}/\sigma_{LVV}^{\circ}$ and $\sigma_{CHV}^{\circ}/\sigma_{CVV}^{\circ}$, as the surface models indicate.

APPLICATIONS

A simple hierarchical algorithm has been developed, based on the results described in the previous Section. The basic structure is similar to that proposed in [7] for Montespertoli data. Some modifications have been introduced and further validations come from inclusion of MAESTRO-1 data and comparisons with model simulations. When the algorithm is applied to the fields observed during MAESTRO-1 and MAC-Europe flights, the following percentages of correct classification are obtained. All fields: 62.5 % at 3×3 pixel level, 91.6 % at per-field level. Developed vegetation only: 82.0 % at 3×3 pixel level, 95.8 % at per-field level.

REFERENCES

- [1] M. C. Dobson, L. E. Pierce, and F. T. Ulaby, "Knowledge-based land-cover classification using ERS-1/JERS-1 SAR composites" IEEE Trans. Geosci. Remote Sensing, vol. 34, pp. 83–99, 1996.
- [2] J.J. Van Zyl, "Unsupervised classification of scattering behavior using radar polarimetry data", IEEE Trans. Geosci. Remote Sensing, Vol. 27, pp. 36–45, 1989.
- [3] A. Freeman, B. Chapman, and M. Alves, MAPVEG Software User's Guide, JPL Document D-11254, 1993.
- [4] P. Ferrazzoli, and L. Guerriero, "Radar sensitivity to tree geometry and woody volume: a model analysis", IEEE Trans. Geosci. Remote Sensing, vol. 33, pp. 360–371, 1995.
- [5] M. Bracaglia, P. Ferrazzoli, and L. Guerriero, "A fully polarimetric multiple scattering model for crops", Remote Sensing Environ., vol. 54, pp. 170–179, 1995.
- [6] P. Ferrazzoli, and L. Guerriero, "Interpretation and model analysis of MAESTRO-1 Flevoland data", Int. J. Remote Sensing, vol. 15, pp. 2901–2915, 1994.
- [7] P. Ferrazzoli, S. Paloscia, P. Pampaloni, G. Schiavon, S. Sigismondi, and D. Solimini, "The potential of multifrequency polarimetric SAR in assessing agricultural and arboreal biomass", IEEE Trans. Geosci. Remote Sensing, vol. 35, pp. 5–17, 1997.

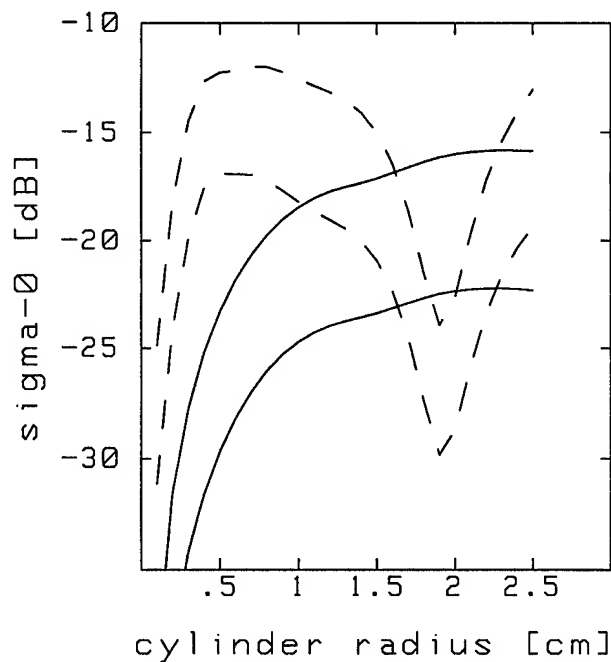


Fig. 1. Modeled σ_{HV}^0 for a canopy of cylinders (branches) vs. cylinder radius at P band (continuous line) and L band (dashed line). Branch biomass: 1 kg/m² (upper lines), 0.2 kg/m² (lower lines).

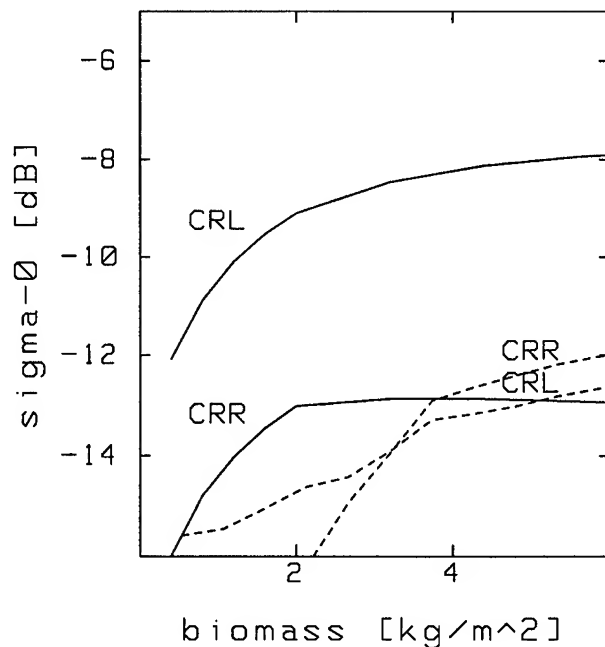


Fig. 3. Modeled σ_{CRL}^0 and σ_{CRR}^0 for wide leaf crops (continuous line) and small stem crops (dashed line) as a function of biomass.

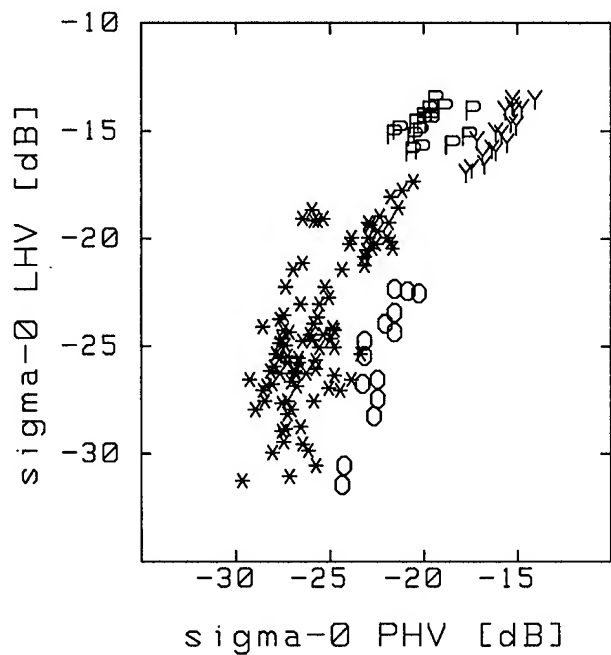


Fig. 2. Experimental (field average) σ_{LHV}^0 vs. σ_{PHV}^0 for forest (Y), olive grove (O), potato (P) and other fields (*).

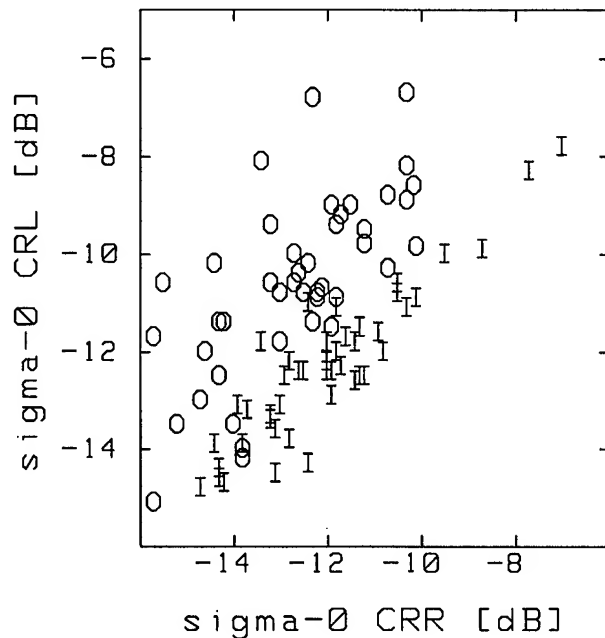


Fig. 4. Experimental (field average) σ_{CRL}^0 vs. σ_{CRR}^0 for wide leaf crops and bare soils (O) and for small stem crops (I).

The Role of Frequency and Polarization in Terrain Classification Using SAR Data

M. Craig Dobson, Leland E. Pierce, Fawwaz T. Ulaby

The University of Michigan, Radiation Laboratory

Ann Arbor, MI 48109-2122 USA

Tel.: +1 313-647-1799, Fax: +1 313-647-2106, email: dobson@eecs.umich.edu

Abstract -- The expected accuracies of land-cover classification are evaluated for existing and potential orbital SAR systems. Land-cover classifications are compared for ERS-1, JERS-1, SIR-C and X-SAR. In addition, SIR-C/X-SAR data from a largely forested test site in northern Michigan are used to simulate the expected performance of potential orbital SAR systems such as Envisat, PALSAR and LightSAR. The classification approach uses orthorectified and filtered SIR-C/X-SAR data overlain with known polygons subdivided into spatially independent training and testing populations. For each potential sensor configuration, the relevant feature vectors are subsampled for a portion of the image and used to generate unsupervised clusters. These clusters are then assigned to the known classes of the training population using maximum likelihood criteria with equal probabilities. Contingency tables are produced for the testing population using minimum distance criteria. The classification results show that longer wavelengths (such as L-band) are of greatest value for discriminating general land-cover classes on the basis of biomass and roughness since there is a greater dynamic range relative to these attributes. Shorter wavelengths (C-band or X-band) are more sensitive to smaller scattering elements such as foliage and small stems and are therefore of importance in discriminations related to crown-layer architecture (i.e., leaf size and shape). The best results are achieved when classification is based upon multiple frequency data.

INTRODUCTION

Remote sensing of terrain using SAR is rapidly maturing in a time period characterized by diminishing resources and political will to launch new systems of high complexity and cost. A frequently asked question is what are the trade-offs in SAR system parameters with respect to performance for a given application. In terrain classification for example, what are the relative merits of polarimetry or of one frequency versus another and what is the additive value of cross-polarization. The answers to such questions have obvious and important consequences with respect to system design and cost.

At present, such questions are often answered at an intuitive level with little substantive backing. Although a large number of excellent studies have been done using both

airborne and orbital SAR for terrain classification, these studies have sought optimal performance using all available feature vectors to perform the classification. As such, they quantify performance of the given SAR system for a given scene or scenes, but they do not provide the comparative information needed to address these types of questions. Although some studies have reduced the total number of feature vectors via discriminant or principal components techniques, they have not yielded comparative performance measures by which to evaluate or optimize system design criteria.

This study uses polarimetric SIR-C/X-SAR data of the ecology supersite located in the Upper Peninsula of Michigan to examine and compare the terrain classification performance of various SAR design scenarios. These scenarios include: (1) single-frequency polarimetry at L- and C-bands, (2) dual-polarized and single-frequency SAR at L- and C-bands (i.e., both like-polarizations or cross-polarization with one like-polarization), (3) dual-frequency and single-polarization SAR, and (4) 'traditional' single-frequency and single-polarization SAR (i.e., the currently orbiting ERS-1/2, JERS-1 and Radarsat). These scenarios include those considered for Envisat, PALSAR and LightSAR.

METHODOLOGY

The input SAR data are standard products: ERS-PRI, JERS-Level 2.1, and SIR-C/X-SAR single-look scattering matrix. These are orthorectified using a DEM derived from USGS 1:100,000 digital line graphs and amplitude corrected for the area term given by the local angle of incidence. The effects of fading are reduced via application of spatial filtering which also reduces the 'effective' spatial resolution to approximately 70-m [1].

Classifications of ERS and JERS data using a supervised, hierarchical decision tree has been previously reported [2,3]. The ERS and JERS data were acquired in August 1992. The SIR-C/X-SAR data were acquired in October 1994 at a 31° angle of incidence. For the SIR-C/X-SAR data we use an unsupervised clustering algorithm [4] and then assign these clusters back to *a priori* known classes using polygons of 'training' data. The clusters are based upon a 10% sample of the image data and a seed file of cluster

centers. The relabeling is optimized using the confusion matrix generated for the training data to identify and eliminate clusters with ambiguous class definition. The final classification rules are applied to a spatially independent set of 'testing' data by using minimum distance rules to assign pixels to clusters and class names. The process is performed sequentially at three levels of cluster aggregation.

Level 1 considers aggregation of the clusters into classes of: surfaces (water or soil), short vegetation (less than about 2-m in height and 2.5 kg/m² of dry biomass) and tall vegetation. Level 2 further subdivides the tall vegetation class on a community basis into: upland conifers (red pine, jack pine, white pine), lowland conifers (larch, white spruce, black spruce and Northern white-cedar) and deciduous forest (aspen and northern hardwoods). At Level 3, the forest categories are split into finer, near species-level, associations: red pine, jack pine, spruces, N. White-cedar, aspen and hardwood.

CLASSIFICATION RESULTS

At this time, final results are available for sensor configurations of frequency and polarization representing the ERS SAR, JERS-1 SAR, the combination of ERS/JERS, SIR-C and SIR-C/X-SAR [5]. These results are given in Table 1 and assume that all classes have equal probability of occurrence. Preliminary results (not on independent testing population) indicate that the other configurations (i.e., for PALSAR, Envisat and LightSAR) yield intermediate classification accuracies.

The single frequency/polarization SAR systems yield generally poor results, especially at more detailed levels of discrimination. L-band is found to be superior to C-band alone; this is largely the consequence of a greater dynamic range in backscatter and the sensitivity to greater levels of above-ground biomass than at higher frequencies. The best classification results are achieved when there is frequency and polarization diversity.

The simulated results should be interpreted as approximations of actual system performance since no attempt was made to either select SIR-C angles of incidence equivalent to that of an existing SAR nor to optimize angles of incidence for a proposed SAR system. Only SIR-C/X-SAR data at a 31° angle of incidence is used. Never the less, Table 1 shows that the classification results for the simulated and actual JERS/ERS composite classifications are very similar at Level 1. The simulated and actual results are found to diverge for Level 2. Presumably, the differences found relate either to the change in season (i.e., phenologic and moisture differences) or to the incidence angle diversity present in the actual JERS/ERS composite data.

Table 1. Unbiased overall classification accuracy of various sensor configurations. Results are for 'testing' population. An "*" indicates that results are simulated from SIR-C data.

Configuration	System	Classification Accuracy (%)	
		Level 1	Level 2
L-hh	JERS	97.7	65.9
C-vv	ERS	74.9	63.5
C-hh	*Radarsat	TBD	TBD
L-hh,hv	*PALSAR	TBD	TBD
C-vv,hv	*Envisat	TBD	TBD
L-quad	*LightSAR	TBD	TBD
L-hh + C-vv	JERS/ERS	98.6	93.7
L-hh + C-vv	*JERS/ERS	98.8	83.1
L-hh + C-hh	*JERS/Radarsat	98.7	68.8
L-hh + C-vv,hh	*JERS/ERS/ Radarsat	99.7	78.0
L-quad + C-hh,hv	*LightSAR	TBD	TBD
L-quad + X-vv	*LightSAR	TBD	TBD
L- + C-quad	SIR-C	99.0	90.0
L- + C-quad + X-vv	SIR-C/X-SAR	99.3	97.8

Another issue to consider is that classifications based upon multifrequency or multipolarization composites derived from two or more SAR systems are inherently multitemporal classifications as well since the probability of simultaneous observation is near zero for non-polar regions. This can either enhance or reduce classification accuracy since the backscatter from most terrain classes is well known to be time dependent [5,6].

REFERENCES

- [1] W. Hagg and M. Sties, "Efficient speckle filtering of SAR images," Proc. IGARSS'94, Pasadena, CA, vol. 4, pp. 2140-2142, 1994.
- [2] M.C. Dobson, F.T. Ulaby, L.E. Pierce, "Land-cover classification and estimation of terrain attributes using synthetic aperture radar," Rem. Sens. Env., vol. 51, no. 1, pp. 199-214, 1995.
- [3] M.C. Dobson, L.E. Pierce, F.T. Ulaby, "Knowledge-based land-cover classification using ERS-1/JERS-1 SAR composites," IEEE Trans. Geosci. Rem. Sens., vol. 34, no. 1, pp. 88-99, 1996.
- [4] J.T. Tou and R.C. Gonzalez, Pattern recognition Principles, Addison-Wesley, 1974.

- [5] L.E. Pierce, K.M. Bergen, M.C. Dobson and F.T. Ulaby, "Multi-temporal land-cover classification using SIR-C/X-SAR imagery," submitted to IEEE Trans. Geosci. Rem. Sens., 1997.
- [6] K. Bergen, M.C. Dobson, L.E. Pierce and F.T. Ulaby, "Effects of within-season dielectric variations on terrain classification using SIR-C/X-SAR," IGARSS'97, Singapore, 1997.

Mapping Vegetation Structure For Biodiversity Analysis Using Synthetic Aperture Radar

Marc L. Imhoff¹, Anthony K. Milne, Thomas D. Sisk, William T. Lawrence, and Kym Brennan

¹NASA Goddard Space Flight Center, Greenbelt, MD 20771, USA; Phone 301-286-5213,
FAX 301-286-0239, email: mimhoff@ltpmail.gsfc.nasa.gov

Abstract -- An integrated remote sensing/field ecology project was carried out to link the use of synthetic aperture radar (SAR) and other remotely sensed data to studies of landscape spatial heterogeneity and bird community ecology as a first step toward applications in predicting biodiversity. P-, L-, and C-band SAR data were collected over a section of the South Alligator River in Kakadu National Park in Australia's Northern Territory as part of the Joint NASA/Australia DC-8 AIRSAR data acquisition campaign in 1993 and the NASA/PACRIM AIRSAR deployment in 1996. The SAR data were analyzed with field data integrating vegetation structure and floristics with bird abundances across a heterogeneous study site that spanned several abrupt habitat edges. Results indicate that SAR data are able to discern structural differences relevant to bird habitat quality within floristically homogeneous stands, while multispectral sensors successfully identified floristic differences among habitat types.

INTRODUCTION

As part of the NASA/JPL/PacRim AIRSAR campaign we explored the use of remote sensing technology to further our understanding of how species diversity and population density are affected by edge effects, habitat heterogeneity, and landscape composition. The primary focus of this study is an investigation of the ability of SAR to provide useful information on vegetation structure for the purpose of mapping bird habitats. We tested the hypothesis that SAR responds to vegetation structure in predictable ways, based on wavelength and the degree of consolidation of living plant tissue. Past research has shown that SAR is linked to vegetation structure and that the ratio of the vegetation surface area to vegetation volume (SA/V) may be a useful measure of structural consolidation [1]. If SAR can discriminate among vegetation structural types, and this information is layered onto floristic data from TM and other sensors, the potential for high resolution mapping of animal habitats, over large areas, is immense.

SITE DESCRIPTION AND REMOTELY SENSED DATA

A study area was identified in the Northern Territory of Australia, where abrupt structural and floristic edges are sustained by edaphic conditions near the South Alligator River in Kakadu National Park (12.5 deg. S Lat. / 132.5 deg. E. Long.). The area has a tropical hot-wet / hot-dry climate with 85-95% of its 1400 mm of precipitation occurring between December and March. Maximum daily temperatures are + 30 deg. C all year. It is characterized by a flat estuarine flood plain, with freshwater billabongs, paleosol (laterite) uplands and sandstone ridges and outcrops scattered throughout. The area is under considerable stress with conflicting uses serving as a national park, world heritage area, and a producer of uranium for the world energy market. The site is characterized by two primary floristic types; a paperbark (*Melaleuca cajuputi*) stand located on wet lowland soils, which diminish in stature as they approach the upland, and a mixed woodland composed of Eucalypts and other broadleaf species. There are two structural edges in the *Melaleuca* forest; one where the perennially flooded soil line is located (denoted as Edge A) and another midway toward the uplands. A distinct floristic edge occurs at the upland boundary, defined by the furthest extent of flooding in the wet season where the *Melaleuca* woodland abruptly terminates and is replaced by mixed woodland species. The floristic edge is denoted as Edge B.

P-, L-, and C-band SAR data were collected over the study sites. The habitat edges run roughly east-west in orientation across radar range of about 5 degrees (52-57 deg. incidence angle). The edge structural gradient changes in a north-south direction which is the azimuth direction of the radar and therefore not subject to the large changes in incidence angle.

METHODS

Field data on vegetation structure, floristic composition, and bird abundances were collected simultaneously during the same season of the AIRSAR flights. The data were collected along 10 transects 1 km in length established at random intervals running orthogonally to the habitat edges (parallel to the flight line). The southernmost census point was established 200 m south of the edge between the wet

Melaleuca and dry *Melaleuca* woodland (Edge A). Each of the ten transects spanned Edge A and a second edge (Edge B) between the dry *Melaleuca* woodland and open mixed *Eucalypt* woodland. Subdivision of the transects along lines parallel to the habitat edges allowed for the generation of 9 zones for the derivation of bird, vegetation, and SAR statistics.

Community-wide indices of bird diversity were calculated. Species richness is used to measure alpha diversity (diversity at the species level) at regular intervals along the habitat gradient. The Jaccard index of similarity is used to measure beta diversity, the degree of turnover in species composition between two adjacent points along the gradient. Additional analysis focused on abundance patterns for individual bird species. Abundance, represented by the number of detections per point count, was plotted against the position of the point along the habitat gradient.

Vegetation data were collected using the point-center-quarter method. The data collected included: species, stem diameter (dbh), height, height to live crown, crown dimensions in 3 dimensions, and stocking density. Estimates for crown components, such as branch length, diameter, and number of branches were made using photographic methods on selected trees. Bulk densities (wood) for the various species were derived and used to compute biomass values from bole and branch volume. Leaf area index (LAI) was estimated using hemispherical canopy photography at each PCQ point. Statistics are reported for floristic composition and vegetation structure, including mean stems density, dbh, height, biomass, and the ratio of vegetation surface area to volume (SA/V) for each of the 9 zones. Structural differences between zones were determined using a mean difference unpaired t-test ($\alpha=0.05$) where the hypothesized difference is 0.

The SAR backscatter statistics were calculated for the 9 zones and is reported as σ^0 in dB (m^2/m^2). SAR channels showing highest correlations with structural parameters were selected. C-band was used to define leaf parameters, L-band, branch parameters, and P-band, stem parameters. These selected channels were further tested to determine if significant differences in the backscatter were being observed between zones for those channels. Statistical comparisons of backscatter between zones was made using a Z-test ($\alpha = 0.01$, $N \geq 200$).

RESULTS AND DISCUSSION

Statistical analysis of the vegetation field data clarified the structural and floristic changes in our edges. All three SAR bands (C-, L-, and P-) had channels bands (C-HV, L-VV, and P-VV) that responded predictably with changes in the identified habitat relevant vegetation structural features. The mean SAR backscatter showed statistically significant

changes at Edge A, and again at Zone 5 where there were significant structural changes (despite the near monospecific composition of those *M. cajuputi* stands (Z-tests $\alpha \leq 0.01$)). C-HV responded strongly to LAI in all zones, and backscatter changed significantly at Edge A and at Zone 5, where LAI also showed statistically significant changes. C-HV did not show a significant change in backscatter at Edge B, and neither did LAI change significantly. Because the data were collected in the dry season, the leaf area present in all zones was quite low (below $1.5 \text{ m}^2/\text{m}^2$) reducing the possibility of signal saturation. At Edge B, the SAR backscatter again responded strongly to the only significant structural change occurring at Edge B, crown volume, and subsequently branch SA/V (Fig. 1).

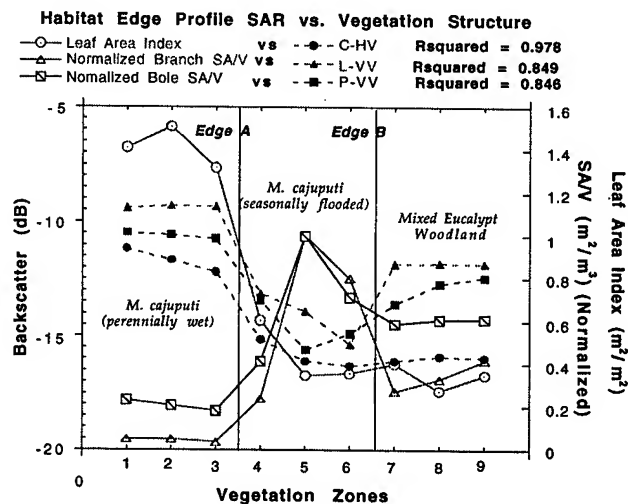


Figure 1. SAR response to vegetation structure and biomass along the habitat gradient or zones. All changes in structural parameters except stem density were significant across edge A, and at Zone 5 despite their nearly monospecific composition ($p < 0.01$, T-test). Few structural changes were statistically significant across edge B except notably Branch SA/V. The SAR channels shown responded significantly (Z-test $\alpha=0.01$) to changes in crown parameters at Edge A, Zone 5, and Edge B.

Over the ten-day census period, 1449 positive identifications were made of birds representing 58 species. Of these, 21 were detected more than 20 times. The mean number of bird species (alpha diversity) detected in the nine vegetation zones ranged from 6 to 8.4, with high variation within zones. The key factors in this case are not how many, but which species are present in the different vegetation types.

The lemon-bellied flycatcher (*Microeca flavigaster*) responded primarily to floristics (Fig. 2a). It was associated with habitats dominated by both *Melaleuca* species, and abundance did not change significantly at the structural edge (Edge A)

between the wet and dry *Melaleuca* woodland. At Edge B, where vegetation structure did not change markedly but where the *Melaleuca*-dominated woodland was replaced by the mixed woodland dominated by *Eucalypts*, the species declined significantly ($p < .05$, G-test). The brown honeyeater (*Lichmera indistincta*) occurred abundantly throughout the study site (Fig. 2b), and its density did not differ markedly in the different vegetation communities. Its significant increase at Edge B ($p < .05$) suggests that structural aspects of its habitat may be important, a hypothesis supported by the small peak in abundance in Zone 5 where a structural shift occurred within the dry *Melaleuca*. The yellow oriole (*Oriolus flavocinctus*) appears to be strongly associated with wet *Melaleuca* forests (Fig. 2c). Within this habitat it occurred with greater frequency at the edge. This species appears to be responding strongly to both floristic and structural elements, generating a more complex edge-associated response.

At this site, and in many heterogeneous landscapes, the within-habitat variation of community metrics is high, relative to between-habitat variation. These composite indices often are not very informative, making it difficult to extract messages relevant to conservation planning [2]. Some species, illustrated here by the lemon-bellied flycatcher, respond strongly to floristics. Such responses may be driven by food availability, cover, perching or nesting sites, and other factors related to the species composition of the plant community. Other species, such as the brown honeyeater, appear to key on edges and other structural and/or spatial aspects of the habitat. Many species show detectable responses to both floristics and structure and, like the yellow oriole, show more complex patterns of abundance associated with vegetation type, structure, and spatial characteristics of the landscape. The overlaying of SAR data with floristic information (Fig. 2) illustrates the differing degree to which structural data may help explain changes in bird abundance across the study site. Lemon-bellied flycatcher and yellow oriole, both canopy species, decline in abundance as L-band backscatter, presumably indicative of canopy and branch architecture, increases in the dry *Melaleuca* woodland. Both species are rare in the floristically distinct mixed *Eucalypt* woodland, despite the rebound in canopy architecture in Zones 7-9. Abundance of brown honeyeater (Fig. 2b), a generalist found in all vegetation layers, does not track L-band or any SAR channel. This study demonstrates that the relative importance of these factors differs among species, suggesting that knowledge of both factors is essential for understanding avian community organization.

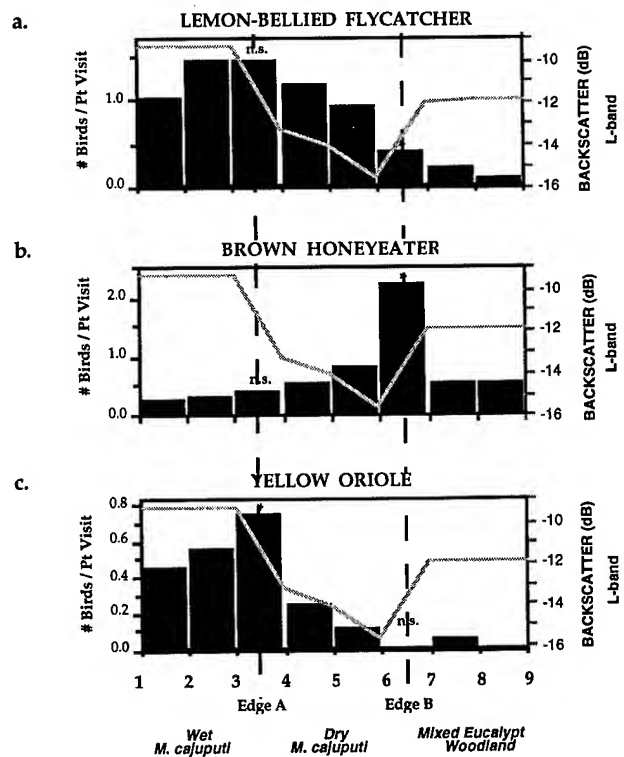


Figure 2. Changes in the abundances of three bird species across a habitat gradient ranging from wet *Melaleuca* woodland (zones 1-3), through dry *Melaleuca* woodland (zones 4-6), to mixed *Eucalypt* woodland (zones 7-9.)

CONCLUSION

Our results confirm that SAR data is capable of discerning vegetation structural changes that can be significant contributors to avian habitat quality. The combination of SAR and multispectral data may provide the foundation for a new generation of remote sensing tools for mapping spatial patterns in the distribution of wildlife habitats. These maps, when combined with species-level ecological data, should permit better predictions of the distribution and abundance of multiple focal species in heterogeneous landscapes.

REFERENCES

- [1] M. Imhoff, "A theoretical analysis of the affect forest structure on synthetic aperture radar backscatter and the remote sensing of biomass", IEEE TGARS 33(2): pp. 341- 352, 1995.
- [2] T. Sisk, C. Margules, Habitat edges and restoration: methods for quantifying edge effects and predicting the results of restoration efforts, In Nature Conservation III: the restoration of degraded ecosystems, (Saunders and Hobbs, Eds.), Surrey Beatty & Sons, Sydney, pp. 57-69, 1992.

Comparative Assessment of Multisensor Data for Suitability in Study of the Soil Salinity using Remote Sensing and GIS in the Fordwah Irrigation Division, Pakistan

Iftikhar Ahmed¹
Haja H. Andrianasolo²

¹**Pakistan Space & Upper Atmosphere Research Commission (SUPARCO)**
Satellite Ground Station, P.O. Box 1271, Islamabad-44000, Pakistan
Tel: (92-51) 421 263, Fax: 495 909, E-mail: isb01183@paknet1.ptc.pk

²**Space Technology Application and Research (STAR), Asian Institute of Technology (AIT)**
P.O. Box 4, Klong Luang, Pathumthani 12120, Thailand
Tel: (66-2) 516-0110-44, Fax: 524-5597, E-mail: haja@ait.ac.th

Abstract -- Assessment of soil salinity and its various factors in time and cost effective manner to reclaim the saline area is one of the prime requirements in the progress and development of an agriculturally dependent country. Remote Sensing (RS) and Geographic Information System (GIS) technologies are emerging as indispensable tools in the study and mapping of dynamic phenomenon having spatial and temporal characteristics. This study presents practical application of RS data in integration of GIS in assessment of soil salinity and some of its physical factors. Approximately 788 sq. km. of salt-affected area in an irrigated regime of southern Punjab, Pakistan was selected for the study. The Landsat Thematic Mapper (TM) and SPOT Multispectral (XS) data have been compared qualitatively and quantitatively using Digital Image Processing and statistical techniques to study their usefulness in soil salinity mapping. The locations of variables in two dimensional feature space were also assessed to achieve higher degree of accuracy in classification. The SPOT XS data have been found more helpful than Landsat TM in study of the salinity at semi-detailed level as it provided finer details of various thematic variables. The extent and intensity of the salinity were corroborated through a 6-day detailed ground survey of the area. The highly saline areas (mostly in crust form) were mapped using Satellite RS Data. However, it was found difficult to have an accurate qualitative differentiation between moderately saline and other highly reflective eroded material due to their close correlation in reflectance behavior. A global decrease in all salinity classes since 1960 has been observed due to various measures of reclamation. Only 1.68% new area is found affected by the salinity during last two decade.

INTRODUCTION

Pakistan, having fertile lands, suitable climate and ample sources of water, is basically an agricultural country. Like many other countries, Pakistan is facing problems of salinity and water logging which affects crop growth and yield.

"At least 20% of the total irrigated land of the country is affected by salinity" [1]. Saline soils are largely confined to areas with extensive irrigation systems and waterlogging. A fraction of these salt-affected soils are the result of natural processes but major portion of such degraded soils can be attributed to the changes brought due to human intervention by way of introduction of irrigation, use of saline water or caused by other development work leading, ultimately, to accumulation of salts in soil. Unscientific and improper use of irrigation water is also highly detrimental to the fertile land and one of the main physical constraints in accelerating the water logging and soil salinity problem.

Since the country's economic development is directly based on agriculture, reclamation of saline areas is always on priorities of the Government. Resource planners are always eager to explore the efficient and economical methods to bring more unproductive areas under cultivation. Considering the potential of Remote Sensing (RS) and Geographic Information System (GIS) technologies which provide flexible, and more accurate means to monitor, map, and manage the resources in time and cost effective manner, this study was conducted to examine the applicability of these technologies in assessment of soil salinity. It demonstrates a methodology to study the usefulness of multisensor data using statistical and Digital Image Processing (DIP) techniques in mapping of the salt-affected soils. GIS techniques have been used to study various factors which contributes to salinity e.g. soil type, soil texture, surface cover, waterlogging and Water Table Depth (WTD). Historical salinity data, collected by the Pakistan Water and Power Development Authority (WAPDA) in 1960 and 1977 was used to study the changes in salinity status.

STUDY AREA

The study area, covering approximately 788 sq. Km, is located in the Bahawalnagar and Bahawalpur districts of southeast Punjab, Pakistan between Cholistan Desert and the

Sutlej River. It is within the command area of Fordwah Canal off-taking at Sulemanki Headwork. The study area falls within Latitudes from 29° - 41' to 29° - 58' N and Longitudes from 72° - 25' to 73° - 11' E.

METHODOLOGY

An integrated approach was adopted using Satellite Remote Sensing (SRS) data, GIS, and statistical techniques for the assessment of soil-salinity and its various physical factors.

A questionnaire, aiming to facts gathering about the history, severity and possible reasons of the salinity in the area, was prepared to assist towards farmer interviews. An extensive field survey was conducted to gain first hand information regarding the extent and severity of the salinity. Initial Image Analysis exercise and unsupervised classification approach on geometrically corrected Landsat Thematic Mapper (TM) Image (bands 2,3 and 4) of November 19, 1993 and SPOT Multispectral, XS, Image of March 5, 1995 yielded the locations of representative salt-affected sampling sites of the study area. Both images were classified using Maximum Likelihood approach of Supervised Classification Technique. Two indices, namely, Vegetation Index (VI) and Brightness Index (BI) were created using SPOT XS band 2 (XS2) and band 3 (XS3) to achieve maximum differentiations between various surface features. Following formulas were used to generate the indices:

$$VI = (XS3 - XS2)/(XS3 + XS2) \quad (1)$$

$$BI = \text{SQRT}(XS2^2 + XS3^2) \quad (2)$$

A color image was created using BI, XS2 and VI and later classified to obtain surface salinity classes as per WAPDA's salinity classification criteria (Table-1) based on variations of soils's Electrical Conductance of Saturation Extraction (ECe).

Table-1: Surface Salinity Criteria

Salinity Class	ECe(mmho/cm at 25°C)	Salt on soil	Crop Growth
Salt Free (S1)	<4	not visible	unaffected
Slightly Saline (S2)	4-8	slightly visible	uneven or patchy
Moderately saline (S3)	9-15	fairly visible	very patchy
Strongly Saline (S4)	>15	wide spread	nil or poor

Spatial data (Soil Series, Soil Texture, WTD in 1960 and 1994, and Surface Salinity in 1960 and 1977) in form of maps [2] were converted into thematic layers and stored in a GIS database for overlay analysis and cross referencing.

RESULTS

Visual Interpretation techniques on data of both sensors provided benchmark information about spectrally and spatially separable thematic variables. Extracted information were found helpful during field data collection phase.

Digital Image Processing and Classification

Five thematic variations namely waterlogged areas, high moisturized regimes, vegetation, open/fallow land and saline areas were identified and selected as training samples across all the three band-data of both sensors.

Measures of central tendency, and dispersion of selected training samples provided adherence to the classification phase. Assessment of variable locations in two dimensional feature space known as scatterplot also provided a higher level of confidence and control on study of the classified thematic variables. Training samples from fallow/open and saline areas were found well separable in all 3 selected bands of the TM data. Other thematic variables were not accurately distinguishable because their radiance values in bands 2 and 3 were in close proximity of each other. Statistical and graphical evaluation of variables on the SPOT XS data provided a well differentiation among all thematic categories except vegetation and waterlogged areas which were found intermixed in bands 1 and 2.

Supervised classification technique provided separation and refinement among classes. Since the XS bands 1, 2, and 3 utilize, almost same wavelengths as in TM bands 2, 3, and 4, spectral response of various features are also similar.

Classification on TM image could not provide as perfect differentiation between fine high reflective eroded material like silt, sand and surface salinity as on SPOT XS image. The SPOT XS classified image presented a clear distinction between salinity and the sand having short height bushy/grassy cover. On the other hand both classes were found intermixed in resultant classification of TM data. Maximum spectral and spatial separation among the surface features along with their minor details has been found as main characteristic of SPOT XS data in which Landsat TM lacks. Better resolution of SPOT XS than Landsat TM is certainly one of the main reasons for this difference but the other important factor is the range of the radiance values in each band of the data. None of the TM band has the maximum reflectance value above 56. On the other hand SPOT XS channels have the maximum reflectance values

200 which provide better separation among the classes. The SPOT XS data also provided more details of soil salinity in agricultural area of heterogeneous nature than Landsat TM.

It was observed that both indices provided better differentiation than the original bands among the surface features particularly between high salinity and fine eroded material, less vigorous and more vigorous vegetation and moisture and dry open areas. Classification on the image, formed using indices, provided well distribution of four salinity classes (S1..S4). It was observed that moderately saline areas (S3) are not separable from the other highly reflective features like sand, silt and dry open areas. Similarly slightly saline areas (S2) are not differentiable from non-saline areas (S1) due to presence of vegetation or crops.

Integration of Remote Sensing and GIS

Some of the salinity factors were assessed qualitatively and quantitatively through cross referencing of various GIS thematic maps with SPOT XS classified image. It was noticed that there is no direct relation of salinity with soil series and soil texture. Major portion of saline areas were found as part of dominant soil series and soil texture. An inverse correlation was found between salinity and drainage of the soil. It was observed that nearly 85% of saline area (moderately and slightly) have been reclaimed during 1960-1995 due to improvement in soil drainage conditions. WTD in the study area had been gradually decreased due to various measures from 151-245 centimeter to 310 centimeter during 1977-1994. Difference in Elevation/relief of the area with its surrounding was also found an important constraint attributed to salinity.

It was observed that soil reclamation and degradation processes are taking place side by side but at far different rates. Nearly 62% of the salt-affected areas had been reclaimed during 1960 and 1977. Table-3 presents the statistics of changes in salinity situation during 1960-1977.

Table-3: Changes in Salinity Conditions from 1960 to 1977

Unchanged		Improvement		Deterioration	
Salinity Class	%	Change From/to	%	Change From/to	%
S1	93.15	S2/S1	57.47	S1/S2	21.22
S2	2.90	S3/S1	13.26	S1/S3	29.24
S3	2.46	S4/S1	19.66	S1/S4	16.21
S4	1.50	S4/S2	2.92	S2/S3	29.54
-	-	S4/S3	6.68	S2/S4	03.79
Total ^A	48.19	-	36.49	-	6.37

^A Total percentage of whole study area

CONCLUSION

Based on Ground Truth Survey, information collected through interviews of farmers, application of GIS, image analysis and statistical techniques on SRS data enabled the authors to conclude that:

- poor drainage of the soil, elevation differences in the area, acute shortage of irrigation water and rain in some of the areas, poor quality of the ground water in most of the areas and some negligence are the main reasons of salinity in the study area.
- This study presents the usefulness of SRS data in conjunction with other supporting data in assessment of soil salinity at semi detailed level. The SPOT XS provided better results than the Landsat TM in identification of fine details of thematic variables due to its higher resolution and wider ranges of radiance values.
- Data of both sensors are found not helpful in differentiating moderately saline areas from high reflective eroded material.
- Integrated approach of RS and GIS has been found to be useful in assessment of the relationships between salinity and some of its physical factors.

RECOMMENDATIONS

Following are the recommendations for future research:

- SRS data may be selected of dry season to obtain clear differentiation between various salinity classes.
- Other bands of Landsat TM may also be studied to assess its full potential against SPOT XS.
- As the soil characteristics are changed with time, soil samples from each test site may be chemically examined.

REFERENCES

- [1] B. Baerends, Z.I. Raza, M. Sadiq, M.A. Chaudhry, and J.M. Hendrickx, "Soil Salinity Survey with an Electromagnetic Induction Method", Proceeding of the INDO-PAK Workshop on "Soil Salinity and Water Management", Islamabad, Pakistan, pp. 201, 1990.
- [2] WAPDA, "Soil Salinity Survey Atlas", 1981, Lahore, Pakistan.

Title: Development Results of TRMM Precipitation Radar

Kouki Oikawa, Toneo Kawanishi, Hiroshi Kuroiwa, Masahiro Kojima
National Space Development Agency of Japan

2-4-1 Hamamatsu-cho Minato-ku, Tokyo 105-60 Japan

Phone: +81-3-3438-6354, Fax: +81-3-5401-8703, E-mail: oikawa.kouki@nasda.go.jp
and Toshiaki Kozu

Communications Research Laboratory, MOPT
4-2-1 Nukui-kitamachi Koganei, Tokyo 184 Japan

Abstract -- Precipitation radar (PR) has been developed by National Space Development Agency of Japan (NASDA) in cooperation with Communication Research Laboratory (CRL). PR was integrated onto Tropical Rainfall Measuring Mission (TRMM) Satellite and TRMM satellite system test is ongoing by NASA. Throughout the various tests of PR, it was confirmed that PR satisfies its requirements.

INTRODUCTION

PR is a first space-borne rain radar and a key instrument of TRMM which is a joint U.S./Japan space program to measure global rainfall distribution from space mainly for global climate studies [1]. TRMM satellite is scheduled to be launched by Japanese H-II rocket from Japan in 1997, on an inclined (35°) and low altitude (350 km) orbit.

The major objectives of PR are (1) to provide 3-dimensional rainfall structure, (2) to achieve quantitative measurement over land as well as over ocean, and (3) to improve the accuracy of TRMM Microwave Imager (TMI) measurement by providing the rain structure information.

In order to accomplish the above mentioned objectives of PR, various tests of PR protoflight model have been conducted.

In the following sections, development results such as major system parameters, protoflight test results as well as calibration scheme of PR are outlined.

SYSTEM CHARACTERISTICS

System Characteristics and Parameters

PR is a 128-element active phased array system, operating at 13.8 GHz band and uses a frequency agility technique to obtain 64 independent samples (N_S) with a single PRF of 2776 Hz. The transmitter/receiver (TX/RX) mainly consists of 128 Solid State Power Amplifiers (SSPAs), Low Noise Amplifiers (LNAs) and PIN-diode phase shifters (PHSs). To achieve low antenna sidelobe levels (i.e., to suppress sidelobe-coupled surface clutter), SSPA output powers and LNA gains are weighted to achieve the Taylor distribution ($SL = -35$ dB, $n = 6$) with a 1 dB quantization. Thus, SSPAs are classified into 17 groups with output power from 24.4 dBW to 40.4 dBW and LNAs are also classified into 17 groups with their gain from 17.6 dB to 33.6 dB. The phase shifter is a 5-bit PIN-diode type and can control the antenna beam direction by changing the phase code in 11.25° step.

During the PR observation mode, PR performs a cross-track scanning of $\pm 17^\circ$ in 0.71° step. There are 49 observation angle bins in one scan (0.6 sec) and the swath width is 215 km. 32 pairs of $1.6 \mu s$ pulses are transmitted to each angle bin.

Major system parameters of PR are summarized in Table 1.

Operation Mode

PR has seven operation modes as described below.

Observation Mode is normally used for rain observation in the cross-track scan over $\pm 17^\circ$ (215 km swath).

External Calibration Mode is used to perform the PR calibration with an Active Radar Calibrator (ARC) which is placed on the ground calibration site in Japan. Cross-track and along-track antenna pattern of the PR can also be measured in the External Calibration mode.

Internal Calibration Mode is used to measure the Input-Output transfer function by an internal calibration loop. There is a 32-staged and 2.6 dB-stepped automatic attenuator in the loop which changes the returned signal level for the internal calibration.

Stand-by mode is used to load the phase codes by command and to verify the loaded phase codes by science telemetry. Re-loading of the phase codes is necessary

Table 1 Major system parameters of PR

Frequency	13.796, 13.802 GHz
Sensitivity	≤ 0.7 mm/h at rain top
Swath width	215 km
Observable range	Surface to 15 km
Horiz. resolution	4.3 km (nadir)
Range resolution	250 m
Antenna type	128-ele. WG Planar array
Beam width	$0.71^\circ \times 0.71^\circ$
Antenna aperture	2.1 m x 2.1 m
Scan angle	$\pm 17^\circ$ (Cross track scan)
Transmitter/Receiver	
Type	SSPAs and LNAs(128chs.)
Peak power	600 W (antenna interface point)
Pulse width	$1.6 \mu s \times 2$ ch. (Transmitted pulse)
PRF	2776 Hz
Dynamic range	≥ 70 dB
N_S	64
Data rate	93.5 kbps (max)
Mass	465 kg
Power	250 W

whenever PR is turned on. This mode is also used to temporally stop the RF radiation to avoid interference with ground stations.

Analysis Mode is used for checking the aliveness of the LNAs by activating each LNA sequentially, using reflected sea surface echo.

Health Check Mode is used for checking the ROM and RAM status of PR. Whenever PR is turned on, PR is set into this mode.

PR is turned off in the safety mode. This mode is used when TRMM satellite is in contingency situation.

Radar Echo Collection

The radar echo sampling is performed over the range gates between the sea surface and the altitude of 15 km for each observation angle bin. For nadir incidence, the "mirror image" is also collected up to the altitude of 5 km. In addition, "over-sample" echo data are partially collected for surface return echoes (for scan angles within $\pm 9.94^\circ$) and for rain echoes (for scan angles within $\pm 3.55^\circ$ up to the height of 7.5 km). These over sampled data will be used for precise measurements of surface return echo level and melting layer structure. Fig. 1 shows a rain echo collection scheme.

Calibration Scheme

Accurate calibration of PR is important to establish the clear interface condition between Level-1 and higher level algorithms, thereby assuring accurate and stable rain products [2]. To eliminate estimation error from PR component data base, PR has some calibration functions.

System Noise monitor: In every observation angle bin (total 49), four "echo-free" range bin data are inserted into the science telemetry as a system noise data.

SSPA Output Monitor: Each SSPA has a power monitor and the monitor data is inserted into the science telemetry.

Panel Temp. Telemetry: As to the components which

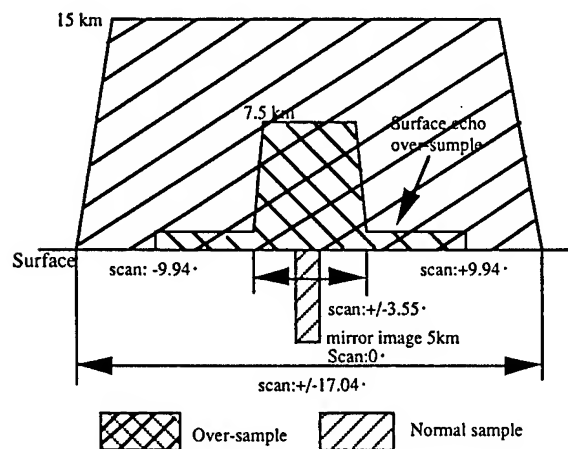


Fig. 1 Rain echo collection scheme

change their gain, loss and so forth due to temperature, calibration is made using ground test data and measured temperature on orbit. For this calibration, panel temperature data is inserted into the house keeping (HK) telemetry.

Internal Calibration: Log amplifier was adopted to convert the radar echo into the video signal. when the linearity and log gradient of the log amplifier is changed on orbit, it will be an estimation error of the received radar echo power. To eliminate this estimation error, the internal calibration mode is selected.

Log Amp. Noise: Bias value of the log amplifier is changed by its temperature. Therefore, the video voltage is monitored in every one scan (0.6 sec) terminating the input port of the log amplifier (no input signal). This bias data is inserted into the science telemetry.

External Calibration: In the case that an absolute gain of PR system is estimated using ground test data of each component, bias error may be involved in the estimated value. On the other hand, system performance may be degraded gradually as a long term change. To calibrate these errors, ARC which is placed on the calibration site in Japan will be used during external calibration mode.

MAJOR TEST RESULTS

Various system tests of PR protoflight model including thermal vacuum test and vibration test were performed successfully at Tsukuba Space Center of NASDA. In this section, major test results of the protoflight test are presented.

Sensitivity

PR sensitivity showed 0.5 mm/h of rain detection capability in the worst temperature condition, which satisfies the specification of 0.7 mm/h.

Antenna Pattern

Along track TX/RX patterns and cross track TX/RX patterns were measured in 49 observation angle bins in a far field measurement. Fig. 2 shows one of the test data of the antenna pattern (cross track at nadir).

Electric field distribution measurement on each slot of the antenna was also performed. Using amplitude and phase distributions of the TX/RX which was measured in thermal vacuum test, the antenna patterns for both hot and cold temperature were calculated and evaluated. It was confirmed that beam width specification (0.71° at nadir, 0.74° at $\pm 17^\circ$) and peak side lobe specification (-27 dB) were satisfied.

Input-Output Characteristics

Fig. 3 shows one of the test data of Input-output characteristics. It was confirmed that test data satisfies the specification of input-output linearity.

Internal Calibration

One of the test data of the internal calibration is shown in fig. 4. Output counts show quantized data after A/D conversion. It was confirmed that internal calibration result had a good stability.

SSPA Output Power Monitor

Each SSPA output power data which was acquired by power monitor telemetry and hard-line test was compared with estimated value as shown in Fig. 5. It was confirmed that output power monitor telemetry could be used for status monitor of SSPA and PR calibration on orbit.

LNA Aliveness

LNA aliveness test in analysis mode was performed. One of the test result is shown in Fig. 6. It was confirmed that analysis mode could be used for LNA aliveness check on orbit.

CONCLUSIONS

The PR protoflight test was successfully completed and it was confirmed that PR had a quality as a flight instrument of TRMM satellite. PR calibration method mentioned in the paper could be used on orbit operation. PR was integrated onto TRMM satellite in June 1996 and TRMM system test is almost finished in NASA/GSFC. Throughout TRMM system test, it was also confirmed that PR performance was maintained.

ACKNOWLEDGMENT

The authors would like to thank all the people of NASA TRMM project for their support and cooperation. We also would like to thank the staff of Toshiba corporation and NEC for their contribution to the PR development.

REFERENCES

- [1] J.Simpson, ed.,: A Satellite Mission to Measure Tropical Rainfall. Report of the Science Steering Group. NASA/GSFC, 1988.
- [2] T.Kozu, T.Kawanishi, K. Oshimura, M. Satake, and H.Kumagai, "TRMM Precipitation Radar: Calibration and Data Collection Strategies", IGARSS '94, Aug., 1994.

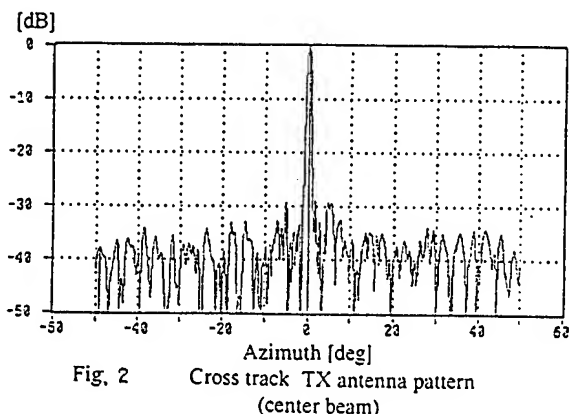


Fig. 2 Cross track TX antenna pattern (center beam)

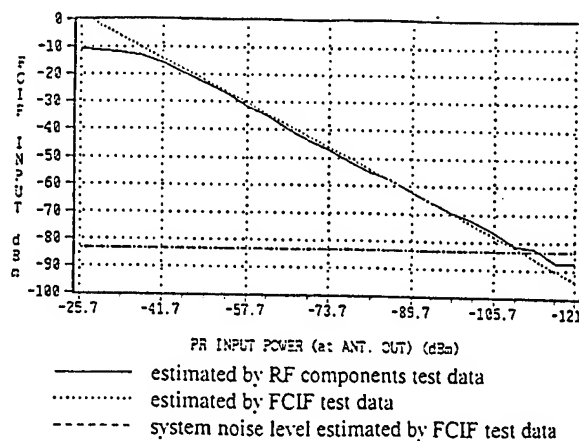


Fig. 3 Input-output characteristics

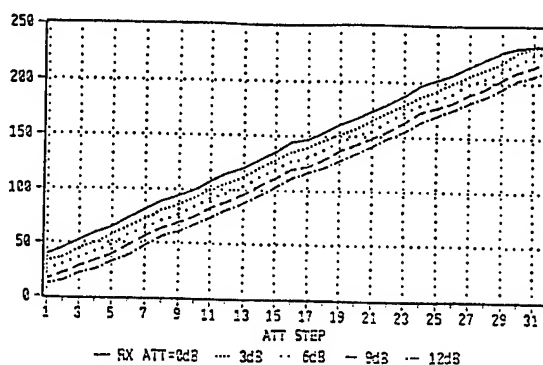


Fig. 4 Internal calibration test result

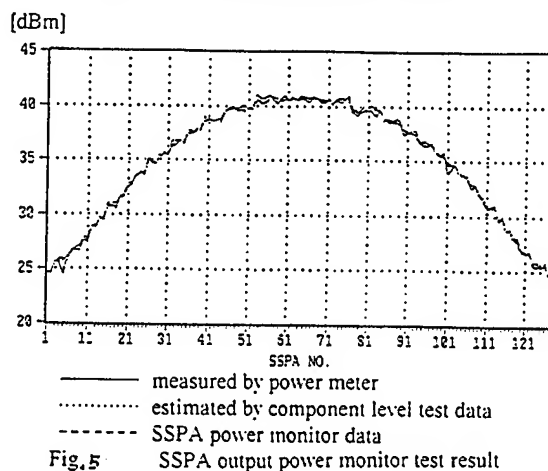


Fig. 5 SSPA output power monitor test result

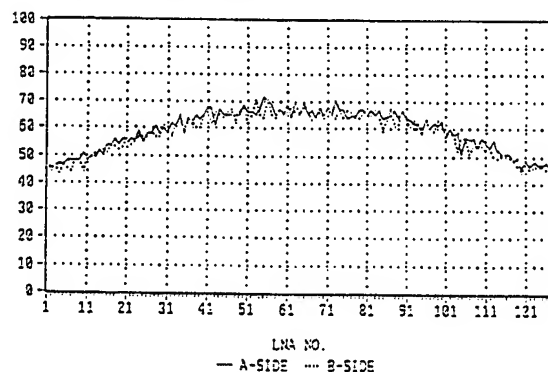


Fig. 6 LNA aliveness test result

Rain Type Classification Algorithm for TRMM Precipitation Radar

Jun AWAKA*

Hokkaido Tokai University

Minami-ku, Minami-sawa 5-1-1-1, Sapporo 005, Japan

awaka@de.htokai.ac.jp

Toshio Iguchi, Hiroshi Kumagai, and Ken'ich Okamoto

Communications Research Laboratory

Abstract – A TRMM Precipitation Radar (PR) standard algorithm for classifying precipitation types is designated as the algorithm 2A-23. This algorithm classifies precipitation type into three categories: stratiform, convective, and other. In the case of convective precipitation, a further examination is made to determine whether it is warm rain or not. The algorithm 2A-23 also detects bright band and determines the height of bright band when it is detected.

OBJECTIVES

Main objectives of the Tropical Rainfall Measuring Mission (TRMM) Precipitation Radar (PR) standard algorithm 2A-23 are as follows:

- Detection of bright band (BB)
- Determination of the height of BB when it exists
- Classification of rain type into three categories
- Determination of warm rain

In 2A-23, two algorithms are installed for classifying precipitation type; they are called respectively as a vertical profile method (V-method) and a horizontal pattern method (H-method). Both methods classify precipitation into three categories: stratiform, convective, and other. Since the results are different for two methods, a merged precipitation type is written in the output file of 2A-23. A strategy for the merge of precipitation type is explained later.

VERTICAL PROFILE METHOD

The V-method tries to detect the existence of bright band (BB) first. When BB is detected, the precipitation is basically classified as stratiform. Then the V-method goes on to the detection of convective precipitation, which is characterized by a strong radar echo. When the precipitation type is neither stratiform nor convective, it is classified as other type.

The detection of BB is carried out using the following spatial filter:

*Supported by NASDA through TRMM JRA contract.

$$\begin{pmatrix} -1 & -1 & -1 \\ 2 & 2 & 2 \\ -1 & -1 & -1 \end{pmatrix} \quad (1)$$

where the row indicates the direction of antenna scan angle and the column the range direction. Since adjacent three antenna scans of data are applied to the spatial filter, it can detect BB which usually extends somewhat uniformly in the horizontal direction.

The above spatial filter is based on the following second derivative of Z factor with respect to the range from the satellite,

$$\frac{\partial^2 Z}{\partial r^2} \simeq -\{-Z(r - \Delta r) + 2Z(r) - Z(r + \Delta r)\}/(\Delta r)^2 \quad (2)$$

where r stands for the range, and Δr stands for the range resolution (=0.25 km in the case of TRMM PR).

When the output of the spatial filter satisfies certain conditions, it is concluded that the bright band (BB) is detected. The followings are main conditions for the existence of BB:

- (1) Near the height of BB, the output of the spatial filter exceeds a given threshold,
- (2) Above the height of BB (Hbb), the value of Z decreases appreciably,
- (3) The height Hbb must appear almost at the same height,
- (4) The height Hbb must be within the BB window region, which is estimated from a climatological surface temperature.

In the above, the spatial filter is applied to the real value of Z, but not to the dB value of Z, in order to detect the maximum value of Z in its vertical profile. With conditions (2) and (3), we can discriminate the BB peak and a fictitious peak of convective precipitation, which occurs due to a strong attenuation on the radar signal of TRMM PR (whose frequency is 13.8 GHz) when the precipitation type is convective.

When BB is detected, it is straight forward to compute the height of BB using the information about range and local zenith angle.

After the detection of BB, the V-method goes on to the classification of precipitation type. Outline of the determination of precipitation type is as follows:

- (a) Stratiform: BB exists, and Z below BB is less than 40 dBZ.
- (b) Convective: (i) BB exists but Z below BB is strong enough (≥ 40 dBZ) to be convective, or (ii) BB does not exist, and the maximum value of Z along the range exceeds certain threshold.
- (c) Other: Not stratiform and not convective.

Note that the stratiform type of precipitation classified by the V-method crucially depends on the detection of BB; if the BB detection fails, the V-method automatically classifies the precipitation type either convective or other.

Since the V-method examines the vertical profile of Z, it can also detect the warm rain, which may belong to convective precipitation. The conditions for the warm rain are as follows:

- (α) The storm top of warm rain is lower than the estimated height of freezing level.
- (β) The warm rain, i.e. warm convective, is isolated from stratiform or cold convective precipitation.

Note that the convective precipitation is sub-classified as warm convective and cold convective, and the warm convective is regarded as the warm rain.

HORIZONTAL PATTERN METHOD

The H-method is basically based on the University of Washington convective/stratiform separation method [1], which has been developed by Prof. Houze group for analyzing data obtained by ground based radars. The original Houze method examines the horizontal pattern of Z factor on a plane at a constant height (nominally 2 km above the sea level) with a 2 km horizontal resolution. Since the horizontal resolution of TRMM PR is about 4.3 km, the original Houze method needs to be modified for the analysis of TRMM PR data. Examining Z factor on a horizontal plane at a given height also needs to be changed because TRMM PR observes rain in the latitude region ranging from -35° to 35° . The following modifications to the original Houze method are made for analyzing TRMM PR data:

- (a) Instead of the horizontal pattern of Z at a given height, the horizontal pattern of the maximum Z along the range for each antenna scan angle below the estimated height of freezing level (minus 1 km margin) is examined. In other words, let $Z_{\max}[i]$ stand for the maximum Z along the

range below the estimated height of freezing level (minus 1 km margin), where $[i]$ indicates the i -th antenna scan angle. The H-method examines the horizontal pattern of $Z_{\max}[i]$ for the classification of precipitation.

- (b) Parameters are adjusted so that the 2 km resolution data and the 4.3 km resolution data produces almost the same results.

Except for the above two modifications, the H-method is essentially the same as the Houze method [1], that is, the classification of convective precipitation is made first by detecting the convective core and by determining the precipitation type adjacent to the convective center. When the precipitation is not convective, it is basically classified as stratiform unless the echo is weak enough to be classified as other type of precipitation; other type of precipitation by H-method consists of very weak echo only, which may possibly be a noise.

MERGE OF PRECIPITATION TYPES

Though the classification of precipitation type is made by two different methods, only a merged precipitation type is written in the output file of 2A-23. Table 1 summarizes the merge of precipitation types.

Table 1 Merge of precipitation types

V-method	H-method	merged type
stratiform	stratiform	stratiform
stratiform	other	stratiform
other	stratiform	stratiform
stratiform (BB certain)	convective	stratiform
convective	convective	convective
other	convective	convective
convective	other	convective
convective	stratiform	convective
stratiform (BB not so certain)	convective	convective
other	other	other

The rule for the merge shown in Table 1 can be summarized as follows:

- (1) When it is stratiform by one method and is stratiform or other by the other method, the merged precipitation type is stratiform.
- (2) When it is convective by one method and is convective or other by the other method, the merged precipitation type is convective.
- (3) When it is convective by the V-method but is stratiform by the H-method, the merged precipitation type is convective.
- (4) When it is stratiform by the V-method, which means that BB is detected, but is convective by the H-method,

the merged precipitation type is stratiform or convective depending on the level of confidence in the BB detection.

(5) When it is other by both methods, the merged precipitation type is other.

The reason for case (3) is as follows: The meaning of stratiform by the H-method is simply that the radar echo below the estimated height of freezing level (minus 1 km margin) is not strong enough to be convective. But since the V-method classifies it as convective, the radar echo above the estimated height of freezing level (minus 1 km margin) is strong enough to be convective, and there is not a clear BB peak. Since there is a strong radar echo in the upper region, it is convective.

Because of the merge of precipitation types, the algorithm 2A-23 is stabilized. The reason is as follows:

When the V-method classifies the precipitation type as other, the radar echo is not strong enough to be convective. This means that the type of precipitation is (i) really other, (ii) actually stratiform but 2A-23 fails to detect BB, or (iii) convective if its location is adjacent to the convective center. The merged precipitation type is stratiform when the type by the H-method is stratiform, and is convective when the type by the H-method is convective, the latter of which corresponds to (iii). Let us focus our attention in cases (i) and (ii), i.e. the case when it is other by the V-method but is stratiform by the H-method. The merged precipitation type in this case is stratiform means that the H-method covers the failure of detecting BB by the V-method. Because of this cover, the algorithm 2A-23 can now safely fail to detect BB when the BB peak is not clear. There may be a high chance of mis-classifying the real other type (i) wrongly as stratiform (ii). But this mis-classification, if it occurs, may not have a large impact to the users of 2A-23, because the precipitation rate is small, and attenuation effect is also small.

The merge of precipitation types enables us to make a straightforward comparison between the 2A-23 results and the Houze group's 2A-54 results, the latter of which are obtained by ground based precipitation radars. This direct comparison between the results of 2A-23 and 2A-54 is very important for the validation of 2A-23.

TEST OF 2A-23

Pre-launch test of the algorithm 2A-23 has been made using (1) synthetic test data [2], (2) the Communications Research Laboratory (CRL) dual-wavelength airborne radar data [3], and (3) the Jet Propulsion Laboratory (JPL) Airborne Rain Mapping Radar (ARMAR) data [4].

Among the above test data, only the synthetic data are three dimensional. The airborne test data are two dimensional, and the airborne test data are used for the test of

V-method which includes the detection of BB. Since the H-method needs three dimensional data, the whole test of 2A-23 is made using the synthetic test data.

The test results show that there is a good agreement between V-method and H-method for the classification of convective type precipitation. This occurs because the both methods characterize the convective precipitation by a strong radar echo. There also is a good agreement between the stratiform precipitation classified by the H-method and stratiform-other precipitation combined by the V-method.

A reliability of the merged precipitation type is also written in the output file of 2A-23: the reliability is indicated by a non-negative number depending on the agreement between the result by V-method and that by H-method. This number, expressing the reliability level, is small when the reliability is high, and the number increases as the level of reliability decreases.

SUMMARY

The parameters in the algorithm 2A-23 are tuned using several test data, and the results are satisfactory as far as the test data are concerned. But the final parameter tuning must be made using the actual TRMM PR data. There is also a room for improving the algorithm, in particular in the detection of BB by the V-method because the BB detection strongly depends on the actual profile of Z observed by TRMM PR.

ACKNOWLEDGMENT

J. A. is very grateful to Prof. R. Houze and his staff, Ms. S. Brodzik and Dr. S. Yuter, for making available their computer code of TRMM algorithm 2A-54, for providing J. A. with the parameters of H-method, and for fruitful discussions.

REFERENCES

- [1] M. Steiner, R. A. Houze, Jr., and S. Yuter, "Climatological characterization of three-dimensional storm structure from operational radar and rain gauge data", *J. Appl. Meteor.*, vol. 34, pp. 1978-2007, 1995.
- [2] H. Y. Yeh, N. Prasad, R. Meneghini, W. K. Tao, J. A. Jones, and R. F. Adler, "Model-based simulation of TRMM spaceborne observations", *J. Appl. Meteor.*, vol. 34, pp. 175-197, 1995.
- [3] H. Kumagai, R. Meneghini, and T. Kozu, "Preliminary results from multiparameter airborne rain radar measurement in the western Pacific", *J. Appl. Meteor.*, vol. 32, pp. 431-440, 1993.
- [4] S. L. Durden, E. Im, F. K. Li, W. Ricketts, A. Tamer, and W. Wilson, "ARMAR: An airborne rain-mapping radar", *J. Atmos. Ocean. Tech.*, vol. 11, pp. 727-737, 1994.

Rain Profiling Algorithm for the TRMM Precipitation Radar

Toshio Iguchi¹, Toshiaki Kozu¹, Robert Meneghini², and Ken'ichi Okamoto¹

¹Communications Research Laboratory

Nukui Kitamachi 4-2-1, Koganei, Tokyo 184, Japan

Phone: +81-423-27-7551, Fax: +81-423-27-6666, E-mail: iguchi@crl.go.jp

²NASA/Goddard Space Flight Center, Code 975

Greenbelt, Maryland 20771

Abstract – This paper describes an outline of the algorithm that estimates the instantaneous profiles of the true radar reflectivity factor and rainfall rate from the radar reflectivity profiles observed by the Precipitation Radar (PR) onboard the TRMM satellite. The major challenge of the algorithm lies in the correction of rain attenuation with the non-uniform beam filling effect. The algorithm was tested with synthetic data and the result is shown.

INTRODUCTION

The TRMM (Tropical Rainfall Measuring Mission) radar team has been developing several standard algorithms which will be used to generate standard TRMM products from the TRMM Precipitation Radar data. Among these algorithms, the level 2 standard algorithm that retrieves the instantaneous vertical profiles of rainfall and attenuation corrected radar reflectivity factor is designated as 2A-25 in the TRMM project. The algorithm reads the measured vertical profiles of reflectivity factor (Z_m) from 1C-21 and estimates the true reflectivity factor (Z_e) at each radar resolution cell. The rainfall rate is then calculated from the estimated true reflectivity factor. The major challenges in the algorithm lie in the corrections for the effects of rain attenuation and non-uniform beam filling (NUBF). Another important element in the algorithm is the identification of precipitating particles, because the phase state and the drop size distribution affect the relations between reflectivity and attenuation and between reflectivity and rainfall rate.

The attenuation due to heavy rain comes from the use of a relatively short wavelength (2.2 cm, 13.8 GHz) for the precipitation radar. The surface reference method, which attributes the decrease of apparent surface return power to the propagation loss, is used to determine the correction needed. As long as the rain is horizontally uniform, this method generally works well when the attenuation is significant. When the rain is not uniform, however, the actual surface return may be significantly different from that expected with the same amount of rain distributed uniformly. Consequently, the NUBF may become a source of serious bias in estimating the vertical rain structure of horizontally non-uniform rain. Since the TRMM precipitation radar has a large footprint size of 4 km, the NUBF

may affect the attenuation estimates at storm edges and within convective storms. In order to compensate for the NUBF effect, we need to know the variation structure of rain within the footprint. Since it is impossible to obtain a structure more detailed than the radar resolution, we estimate its statistical variances inside a footprint from variations of radar reflectivities and surface attenuations of larger scales in the vicinity of the footprint.

PROCESSING FLOW

A simplified flow chart of the 2A-25 algorithm is shown in Fig. 1. It first opens the three input files (1C-21, 2A-21, and 2A-23) and two output files (2A-25 and verification file) given in the command line. It also inputs the parameters used in the program such as initial coefficients for k - Z relationship from the parameter files. The input data are read scan by scan. Within the scan, data in each angle bin (each radar beam) are processed independently except in the estimation of NUBF effect.

The range bins for processing in 2A-25 are first defined according to the storm top range bin, the earth ellipsoid, the actual surface range bin, and the surface clutter by the antenna main lobe.

The attenuation correction is carried out assuming a power law between the true radar reflectivity factor Z and the specific attenuation coefficient k : $k = \alpha Z^\beta$. β may change from one angle bin to another depending on the rain type, but is assumed constant for each angle bin (radar beam). α varies according to the rain type, the relative height from the estimated freezing level, and the absolute altitude from the earth ellipsoid in order to take into account the dependence of k - Z relationship on the drop size distribution, and the phase state and temperature of precipitating particles.

The NUBF effect is estimated from the normalized standard deviation of the 9 path-integrated attenuations (PIA) in 3×3 radar beams with the beam in question at the center [1]. To calculate such a quantity, it is necessary to read one scan ahead of the scan that is to be processed. The path-integrated attenuation for non-uniformity calculation is estimated by using the hybrid of the Hitschfeld-Bordan and surface reference methods [2]. The hybrid method is used to avoid a large relative error when the

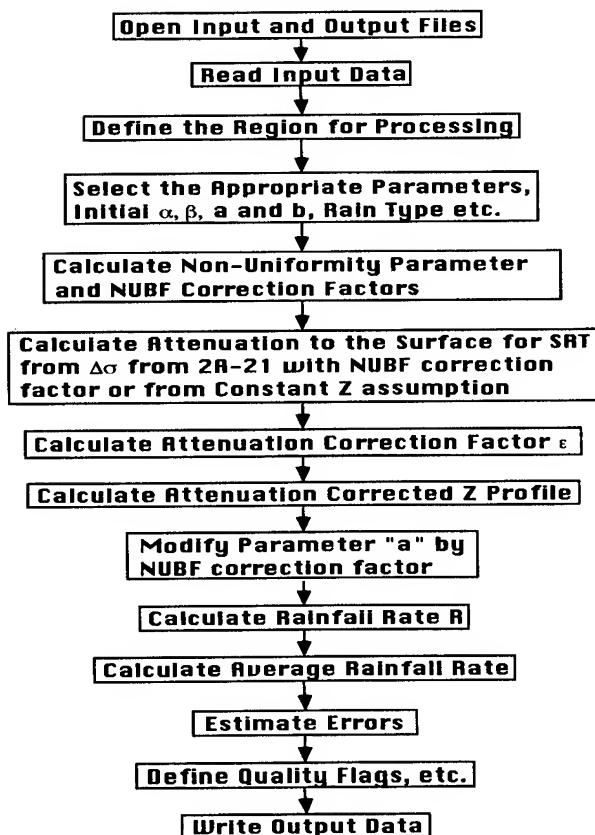


Fig. 1. Simplified flow chart of 2A-25.

total path attenuation is small. If the surface reference from 2A-21, i.e., the decrease of the apparent surface cross section ($\Delta\sigma^0$), is not available, or not reliable, the attenuation that is consistent with the rate of decrease in the measured reflectivity factor (Z_m) with range near the surface for a constant true reflectivity is calculated. In other words, the attenuation is calculated assuming that the apparent decrease of Z_m with range can be totally attributed to the rain attenuation. If the measured reflectivity profile is increasing with range near the surface, the attenuation is set to 0. This assumption of constant Z_e near the surface may not be a scientifically justifiable assumption, but is adopted as a better-than-nothing basis [3]. In fact, it not only prevents the Hitschfeld-Bordan solution from unstable divergence, it quite often gives rather reasonable profiles [4]. Moreover, the case in which the surface reference is not reliable occurs mostly when the path attenuation is not significant. In such a case, the attenuation correction by the hybrid method is not significantly affected by the estimate of the path attenuation given either by the surface reference or the constant- Z_e -near-surface assumption, because the hybrid method weighs more on the attenuation estimates from the radar returns themselves than the independent estimates in the calculation of attenuation correction.

Once the non-uniformity at radar resolution is obtained, the NUBF correction factors for PIA and Z - R relation are calculated. The NUBF correction factor for PIA is multiplied by the surface reference $\Delta\sigma^0$ from 2A-21. This corrected surface reference, if reliable, is used in the hybrid method to obtain the attenuation corrected reflectivity factors. If it is not reliable, the constant- Z_e -near-surface assumption is again used.

As described above, the hybrid method is used twice. In the first instance, the PIA for each beam is estimated by retrieving the Z profile without taking the NUBF effect in the surface reference into account. Using the PIA estimates thus obtained, the NUBF correction factors are calculated. The surface reference is then modified by the NUBF correction factor. The hybrid method is applied with this modified surface reference in the second instance, and the attenuation corrected Z_e profile is calculated.

The rainfall rate R is calculated from the attenuation corrected reflectivity factor Z_e by using a power law: $R = aZ_e^b$. In this equation, the parameters a and b are determined according to the rain type, the relative height from the estimated freezing level, and the absolute altitude from the earth ellipsoid in order to take into account the dependence of Z - R relationship on the drop size distribution, the phase state and temperature of precipitating particles, and the pressure effect on terminal velocities. The proportional coefficient a is further multiplied by the NUBF correction factor for Z - R relationship to compensate for the non-uniform rain distribution within the resolution cell.

From the rainfall rate at each range bin, the average rainfall rate between 2 and 4 km is calculated. The path integrated rainfall rate from the top of the storm to the bottom is also calculated.

Since the attenuation correction including the NUBF correction is considered to be the major source of error in 2A-25, errors in the estimates at the farthest range bin are largest in most of the cases. 2A-25 provides very rough estimates of errors for Z_e and R near the surface. The error estimates are rough because only the linearized infinitesimal error propagation formulas are used and because the error bounds for many of the parameters used in the algorithm are not well known. In the error calculation, the uncertainties are assumed not only in the initial values of α , β , a , and b , but also in the data from input files such as Z_m , $\Delta\sigma^0$, the estimates of the freezing height, and the classification of rain type.

2A-25 also outputs several other parameters, which include the PIA estimates and their variations, the NUBF correction factors, the weight used in the hybrid method, the k - Z and Z - R coefficients, the bin numbers of the rain top, bright band etc. in the output of 2A-25, and the quality and other status flags.

TEST WITH SYNTHETIC DATA

The algorithm was tested with TRMM PR synthetic data which was created numerically from a TOGA/COARE storm model. The synthetic data includes the surface scattering, non-uniform beam filling effects, different types of precipitating particles (rain, snow, graupel, and hail), and fluctuation noise due to the finite number of sampling. An advantage of the synthetic data is the fact that the truth is available. Fig. 2 (a) shows the measured reflectivity factor Z_m vs. the true reflectivity factor at 1.5 km above the surface. Note that Z_m in the figure does not exceed 45 dBZ because of attenuation. Fig. 2 (b) shows the retrieved reflectivity factor Z_e by 2A-25 for the same data set. Although there are still some points which are not well compensated for attenuation, the overall performance is satisfactory. It is worthwhile to note that any parameters such as k - Z parameters assumed in the creation of the synthetic data are not known to the algorithm developer of 2A-25. The deviations from the diagonal line in Fig. 2 (c) indicate the attenuation corrections made in 2A-25. It is apparent from the figure that the hybrid method works well and that almost no attenuation corrections are made for light rain regardless of the surface reference.

CONCLUSIONS

The performance test of the 2A-25 algorithm with synthetic data gives encouraging results. Since we have no experience with space borne weather radar, some unexpected situation might happen with real data. Because the 2A-25 algorithm uses many adjustable parameters in it, we need to develop a strategy for tuning the parameters after launch and a method for testing the algorithm itself in order to find inherent problems if there are any.

REFERENCES

- [1] Kozu, T., and T. Iguchi, "A preliminary study of non-uniform beam filling correction for spaceborne radar rainfall measurement," *IEICE Trans. Commun.*, E79-B, pp. 763-769, 1996.
- [2] Iguchi, T., and R. Meneghini, "Intercomparison of single frequency methods for retrieving a vertical rain profile from airborne or spaceborne radar data," *J. of Atmos. Oceanic Technol.*, 11, 1507-1516, 1994.
- [3] Marzoug, M., and P. Amayenc, "A class of single- and dual-frequency algorithms for rain-rate profiling from a spaceborne radar. Part I: Principle and tests from numerical simulations," *J. of Atmos. Oceanic Technol.*, 11, 1480-1506, 1994.
- [4] Amayenc, P., J. P. Diguët, M. Marzoug, and T. Tani, "A class of single- and dual-frequency algorithms for rain-rate profiling from a spaceborne radar. Part II: Tests from airborne radar measurements," *J. of Atmos. Oceanic Technol.*, 13, 142-164, 1996.

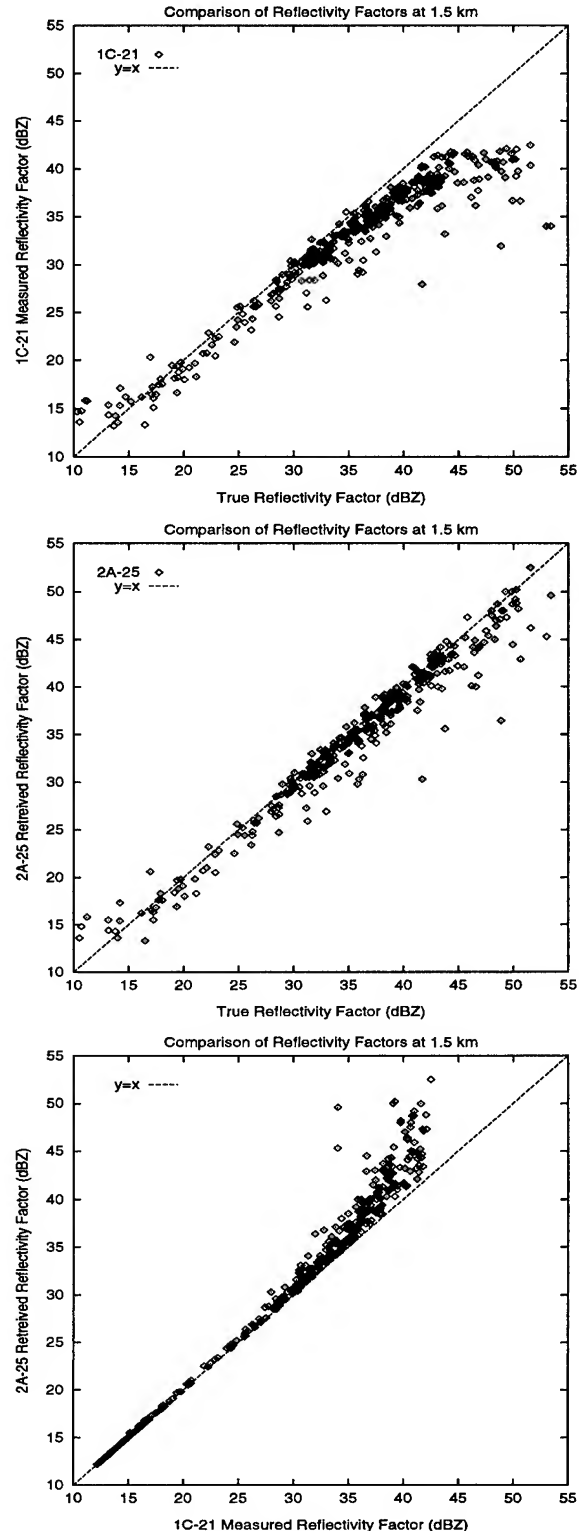


Fig. 2. Comparison of Z_m and Z_e against true Z at 1.5 km above the surface. The upper panel (a) shows the measured reflectivity factor from 1C-21. The middle panel (b) shows the same data set after the attenuation correction by 2A-25. The amount of correction made in 2A-25 can be seen in the panel (c).

Effect of Non-Uniform Beam-filling on TRMM PR Rainfall Measurements

S. L. Durden, Z. S. Haddad, A. Kitiyakara, and F. K. Li
Jet Propulsion Laboratory, California Institute of Technology
JPL 300-235

4800 Oak Grove Dr.

Pasadena, CA 91109 USA

ph: (818)354-4719, fax: (818)393-3077, email: sdurden@jpl.nasa.gov

Abstract -- We investigate effects of non-uniform beam-filling on TRMM PR rain retrieval using data from the NASA/JPL Airborne Rain Mapping Radar (ARMAR) acquired during TOGA COARE in early 1993. Our approach is to simulate TRMM PR observations using the ARMAR data and compare the radar observables and retrieved rain rate from the simulated PR data with those corresponding to the high-resolution radar measurements.

INTRODUCTION

The Tropical Rainfall Measuring Mission will include a Precipitation Radar (PR) for rainfall measurement. Because the 4.3 km diameter of the PR footprint is larger than the size of many convective cells, it is possible that rainfall estimates may be biased. Such biases in radar retrieved rain rate due to non-uniform beam-filling (NUBF) have been found by a number of authors [1],[2],[3]. We study the statistical nature of NUBF effects using a large data set acquired by the NASA/JPL Airborne Rain Mapping Radar (ARMAR) [4] during the Tropical Oceans Global Atmosphere Coupled Ocean Response Experiment (TOGA COARE). Data from ARMAR is well-suited for such a study because it operates with the same 13.8 GHz frequency and downward-looking geometry as the TRMM PR but has substantially better spatial resolution (0.8 km at the surface). Our approach is to simulate TRMM PR observations using the ARMAR data and compare the radar observables and retrieved rain rate from the simulated PR data with those corresponding to the high-resolution radar measurements.

BACKGROUND

Algorithms for retrieving rain from spaceborne radar typically use a form of the Hitschfeld-Bordan technique, in combination with the path-integrated attenuation (PIA) measured by the Surface Reference Technique (SRT) [5], [6]. These algorithms assume uniformity of the rain rate across the antenna beam. When this is not the case, the goal must then be retrieval of the horizontally-averaged rain rate, as discussed in [2]. Unfortunately, because of non-linearity in the Z-R

relation and the relation between PIA and rain rate, the measured PIA and reflectivity profile do not correspond to the average rain rate profile. Consequently, if NUBF is present, the radar measurements and the resulting retrieved rain rates can be biased.

DATA ANALYSIS TECHNIQUE

To quantify the effects of NUBF, we simulate TRMM PR observations using ARMAR TOGA COARE data. First, the ARMAR data is resampled to a uniform Cartesian grid. Second, a multi-dimensional Gaussian function is convolved with the resampled data. The Gaussian is chosen so that it approximates both the range resolution and the two-way antenna pattern. The simulation procedure does not explicitly include attenuation since the attenuation experienced by a simulated PR bin is essentially the same as the attenuation already experienced by the ARMAR measurement.

For the analysis of NUBF effects we consider only data at nadir and do not add thermal or fading noise so that the results depend only on NUBF effects. Furthermore, only the 2-D simulation is used, so that the simulated TRMM PR data has the PR resolution along-track and the ARMAR resolution across-track. In this case all averaging uses ARMAR data acquired at the same scan angle, so no assumptions about surface wind speed and backscatter models are needed.

The errors due to NUBF effects are found by comparing "true" and "apparent" radar observables: the SRT-derived PIA, the near-surface reflectivity (altitude 0.5 km), and the rain-top reflectivity (4 km). The "apparent" radar observables are taken directly from the output of the simulation. In addition to the radar observables, corresponding rain rates are also compared. The apparent path-averaged rain rate (PARR) is derived from the apparent PIA using a k-R relation. The apparent rain rate at 4 km is derived from the apparent reflectivity using a Z-R relation; attenuation is neglected. The apparent rain rate at 0.5 km altitude is derived by normalizing the apparent reflectivity by the apparent SRT-derived PIA, as done in both the kZS algorithm [6] and the alpha-adjustment method used

in the TRMM algorithm [5]. The resulting, corrected reflectivity is then converted to rain rate using a Z-R relation. The k-R and Z-R relations are not adjusted based on the measured PIA. This approach follows the kZS algorithm [6].

Derivation of the "true" radar observables, corresponding to the horizontally-averaged rain rate, requires the high-resolution rain rate. We first perform vertical averaging of the ARMAR data to the PR range resolution so that the errors found in this study are due solely to horizontal variability of the rain. The high-resolution rain rates are then retrieved from these data and averaged over the PR footprint, using precisely the same antenna pattern as for the reflectivity data in the PR simulator. Once the horizontally-averaged rain rates have been computed, the "true" radar observables are computed using the radar equation and k-R and Z-R relations.

RESULTS

Table 1 shows the mean, standard deviation, minimum, and maximum of NUBF errors ("apparent" minus "true") over all of TOGA COARE. These statistics are based on the 1397 simulated PR footprints with a true PARR of more than 2 mm/h. While the means and standard deviations of the errors in all quantities are relatively small, the distributions have long tails, i.e., there are some cases with very large errors. The range between minimum and maximum error is always much larger than the standard deviation. Also, for some quantities the errors are only positive or only negative. The PIA and PARR errors are always smaller than the true; i.e., the TRMM PR would always underestimate PIA and PARR. The greatest underestimation is 12 dB for the PIA and 21 mm/h for the PARR. Previous studies using simulated data and smaller sets of real radar data have also noted underestimation of the PIA [1],[2],[3]. If we compute the average PARR over all 1397 footprints, we find that the average using the apparent PARR is underestimated by 4%.

The reflectivity and rain rate at 4 km altitude are always overestimated. Since attenuation is neglected in retrieving the rain at 4 km, these results are characteristic of rain retrieval using a Z-R relation. Previous authors have also noted overestimation due to the non-linearity of the Z-R relation (e.g., [1],[2]). When comparing the TOGA COARE average rain rates using both the high-resolution rainfall and the rainfall from the simulated TRMM PR, we find an overestimation by 3%, similar to the findings of Amayenc et al. [2] for the Z-R algorithm.

The near-surface reflectivity errors are both negative and positive, extending from -12.3 dB to +10.5 dB. The mean is very close to zero, and the distribution is fairly symmetric about the mean. Both underestimation and overestimation of the near-surface reflectivity are possible due to the presence of the competing effects of the Z-R relation, causing overestimation, and the attenuation, causing underestimation. The near-surface rain rate errors are more negative than positive and there are a few cases with negative errors as large as -79 mm/h. The maximum positive error is much smaller at approximately 18 mm/h. The average rain rate at the surface, computed over all 1397 footprints, is underestimated by 11%, similar to the findings in [2] for the kZS algorithm at 35 GHz. The reason that the near-surface rain rate is typically underestimated even though the near-surface reflectivity error has zero mean is that the rain rate is derived by correcting the reflectivity by the PIA, which is always underestimated. Thus, the PIA error causes the non-zero mean error, i.e., the bias in the near-surface rain rate.

Fig. 1 shows a scatter plot of the PIA measurement errors versus the standard deviation of the high resolution PIA within the footprint. The two quantities are correlated (correlation coefficient $r = -0.77$). We also examined the relation of other quantities to the high-resolution measurement variability. The error in the 4 km altitude reflectivity is correlated with the standard deviation of the high resolution 4 km altitude reflectivity ($r = 0.86$). The near-surface reflectivity error is not correlated with the PIA standard deviation. Its mean remains close to zero even for large PIA standard deviation. However, the absolute value of the error does increase with increasing PIA standard deviation.

ACKNOWLEDGMENT

The research described here was performed by the Jet Propulsion Laboratory, California Institute of Technology, under contract with the National Aeronautics and Space Administration. Support from the NASA TRMM Science program is gratefully acknowledged.

Table 1: Statistics of NUBF Errors

	Mean	SD	Min	Max
PIA (dB)	-0.2	0.8	-11.7	0.0
PARR (mm/h)	-0.4	1.5	-20.6	0.0
Rain-top Z (dBZ)	0.3	0.5	0.0	4.7
Rain-top R (mm/h)	0.1	0.1	0.0	2.3
Near-surf Z (dBZ)	0.0	0.8	-12.3	10.5
Near-surf R (mm/h)	-1.0	5.5	-78.7	18.1

REFERENCES

- [1] K. Nakamura, "Biases of rain retrieval algorithms for spaceborne radar caused by nonuniformity of rain," *J. Atmos. Oceanic Technol.*, vol. 18, pp. 363-373, 1991.
- [2] P. Amayenc, J. P. Diguët, M. Marzoug, and T. Tani, "A class of single-frequency algorithms for rain-rate profiling from a spaceborne radar. 2. Tests from airborne radar measurements," *J. Atmos. Oceanic Technol.*, vol. 13, pp. 142-164, 1996.
- [3] T. Kozu and T. Iguchi, "A preliminary study of non-uniform beam-filling correction for spaceborne radar rainfall measurement," *I.E.I.C.E. Trans. Comm.*, vol. E79B, pp. 763-769, 1996.
- [4] S. L. Durden, E. Im, F. K. Li, W. Ricketts, A. Tanner, and W. Wilson, "ARMAR: An airborne rain mapping radar," *J. Atmos. Oceanic Technol.*, vol. 11, pp. 727-737, 1994.
- [5] T. Iguchi and R. Meneghini, "Intercomparison of single-frequency methods for retrieving a vertical rain profile from airborne or spaceborne radar data," *J. Atmos. Oceanic Technol.*, vol. 11, pp. 1507-1516, 1994.
- [6] M. Marzoug and P. Amayenc, "A class of single-frequency algorithms for rain-rate profiling from a spaceborne radar. 1. Principle and tests from numerical simulations," *J. Atmos. Oceanic Technol.*, vol. 11, pp. 1480-1506, 1994.

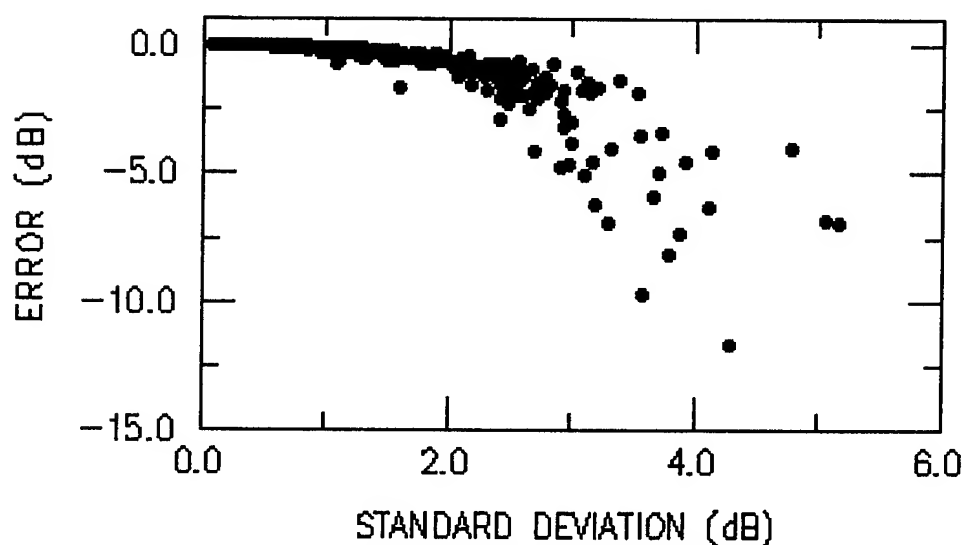


Figure 1. Scatter plot of the PIA error ("apparent" minus "true") versus the standard deviation of the high resolution PIA within the footprint.

Bayesian Fusion of TRMM Passive and Active Measurements

Ziad S. Haddad, Stephen L. Durden and Eastwood Im
Jet Propulsion Laboratory, California Institute of Technology
4800 Oak Grove Drive, Pasadena, CA 91109-8099, USA

Telephone: 818 354 1218 – Fax: 818 393 5285 – Email: zsh@AlbertoVO5.jpl.nasa.gov

Abstract – a Bayesian method was adopted to combine the instantaneous measurements of the Tropical Rainfall Measuring Mission (TRMM)’s radar and radiometer ([4]). The method makes multiple estimates of the rain-rate profile using the radar reflectivities assuming various plausible values for the drop size distribution (DSD) shape parameters, then selects those parameter values which produce estimates that are most consistent with the passive observations. The resulting estimates are expressed directly in terms of the DSD parameters, thus allowing one to calculate any rain-related quantity, such as rain rate profile, precipitating liquid water profile, etc. The Bayesian approach also allows one to calculate the “error bar” associated with each estimate.

MATHEMATICAL APPROACH

Combining the simultaneous measurements of a microwave radar and a passive radiometer observing the same event can help resolve the ambiguities inherent in single-instrument attempts at rain retrieval: indeed, the fine resolution of the radar measurements should compensate for the corresponding ambiguity in the radiometer measurements (e.g. in detecting the freezing level), while the robustness of the radiometer measurements should reduce the error which the radar can make when estimating integrated quantities (errors that are due mostly to the significant dependence of the radar backscatter on the unknown hydrometeor size).

We chose a Bayesian approach to implement such a combined algorithm in the case of TRMM, the Tropical Rainfall Measuring Mission ([5]). The advantage of such an approach is that it gives as much importance to the measurements of the radar and of the radiometer as their respective intrinsic ambiguities warrant, while avoiding all ad hoc shortcuts that might introduce large biases in the rain estimates.

Starting with the idea advocated some time ago by J. Weinman ([7]) and H. Kumagai ([3]) of estimating the “high resolution” rain profile using the spatially detailed radar reflectivities, while constraining

this estimation to be consistent with the (independent) estimate of the total attenuation derived from the passively-measured brightness temperatures, we adopt a two-step procedure: first, since the radar-rain relations depend mostly on the drop size distribution (DSD) parameters \vec{D} , we use the radar reflectivities $Z(h)$ to perform a radar-only rain-profile estimate $R_{\vec{D}}(h)$ as a function of height h , for every possible set of values of the DSD parameters \vec{D} . The second step consists of deriving from each radar-only profile $R_{\vec{D}}(h)$ and from the radar-estimated freezing level h_{ice} the expected brightness temperature $T_i(\vec{D}, h_{ice})$ at the various microwave frequencies represented by the index $i = 1, \dots, M$. The next two sections describe how these two steps are implemented individually. To combine the results of these steps, we try to determine the probability that the rain rates at altitudes h_1, \dots, h_N are R_1, \dots, R_N , given the measured radar reflectivities $Z(h)$ and brightness temperatures T_i :

$$\begin{aligned} \mathcal{P}(R_1, \dots, R_N, \vec{D} | Z(h), T_1, \dots, T_M) \\ = \mathcal{P}(T_1, \dots, T_M | R_1, \dots, R_N, \vec{D}, Z(h)) \\ \cdot \mathcal{P}(R_1, \dots, R_N, \vec{D} | Z(h)) \\ \cdot \mathcal{P}(T_1, \dots, T_M | Z(h))^{-1} \end{aligned} \quad (1)$$

The last term is a constant C as far as our unknowns R_1, \dots, R_N, \vec{D} are concerned. Applying Bayes’s rule again to the middle term we obtain

$$\begin{aligned} \mathcal{P}(R_1, \dots, R_N, \vec{D} | Z(h), T_1, \dots, T_M) \\ = \mathcal{P}(T_1, \dots, T_M | R_1, \dots, R_N, \vec{D}, Z(h)) \\ \cdot \mathcal{P}(R_1, \dots, R_N | \vec{D}, Z(h)) \cdot \mathcal{P}(\vec{D} | Z(h)) \cdot C, \end{aligned} \quad (2)$$

with C that constant which makes the integral of the right-hand-side with respect to R_1, \dots, R_N, \vec{D} equal to 1. If we had explicit expressions for the terms in the right-hand-side of (2), all we would need to do to obtain optimal estimates \hat{R}_i of the rain rates at the various altitudes h_i given the combined data would be to evaluate the mean of R_i . We shall write down such explicit expressions in the next two sections, then return to (2) to derive the corresponding estimate of the rain rate.

PASSIVE MODEL

The first version of the TRMM combined algorithm ignores the higher passive frequencies, and uses for the 10.7 GHz brightness temperature the forward model

$$T_1(\bar{D}, h_{ice}) = T_A - (T_A - T_0)e^{-\alpha'(\bar{D}) \int R(h)^{\beta(\bar{D})} dh} \quad (3)$$

where αR^β is the attenuation coefficient in dB/km corresponding to a rain-rate of R mm/hr (both of whose factors α and β depend on the DSD parameters), $\alpha' = \alpha c$, and T_A , T_0 and c are regression coefficients obtained from careful forward simulations ([6]) comparing the integrated attenuation at 14 GHz (the TRMM radar frequency) with the 10.7 GHz radiance within the same field of view. The integral in the exponential is taken over the entire rain column.

By analogy with the low-frequency case, we postulate the following empirical form for the brightness temperature at an arbitrary microwave frequency f :

$$T_f(\bar{D}, h_{ice}) = T_A + (\tau - T_A + T_0)e^{-\alpha'(\bar{D}) \int R'(h) dh} - \tau e^{-\rho \alpha'(\bar{D}) \int R'(h) dh} \quad (4)$$

where the coefficients T_A , T_0 , τ , α' and ρ must be determined for the given band, freezing level and drop size distribution, and where $R'(h)$ is no longer the rain rate itself but rather an ad-hoc "attenuated" version

$$R'(h) = R(h)e^{-\gamma_f \int_h^{h_t} R(h') dh'} \quad (5)$$

In (5), h_t denotes the top of the storm, and γ_f is a coefficient to be determined. To determine values for the coefficients γ_f , T_A , T_0 , τ , α' and ρ appropriate for a given frequency f , simulations with a given \bar{D} and h_{ice} are used to produce pairs $(T_f, \int R')$, where R' is computed with several trial values of $\gamma > 0$: since the problem of estimating the values of the 5 remaining parameters ($T_A, T_0, \tau, \alpha', \rho$) that best fit the simulated data is quite difficult, we simplify it by noting that

- T_0 can be approximated by the average radiance when $\int R' \simeq 0$,
- T_A can be approximated by the apparent asymptotic radiance when $\int R' \rightarrow \infty$,
- and if T_m denotes the maximum radiance in the given population and R_m the corresponding value of $\int R'$, then τ , α' and ρ must satisfy

$$\frac{\tau \rho}{\tau + T_0 - T_A} = e^{(\rho-1)\alpha' R_m} \quad (6)$$

$$\tau = \frac{T_A - T_m}{1 - \rho} e^{\rho \alpha' R_m} \quad (7)$$

a system which determines α' and τ in terms of ρ .

In this fashion, each ρ between 0 and 1 determines the "best-fit" parameters completely, and the ρ producing the smallest overall residual r.m.s. error between (4) and the simulated radiances is retained. The individual r.m.s. uncertainty $\sigma(T)$ as a function of the brightness temperature is recorded for future use.

Fig. 1 shows an example of simulated data at 36.6 GHz with a 4-km freezing level, together with the fit that was achieved using the approach above. This case was chosen specifically because it was theoretically among the most difficult to treat ($T_A < T_0 < T_m$).

RADAR MODEL

In [1], we described a bayesian approach to estimate, given \bar{D} and $Z(h)$, the mean rain profile $R_{\bar{D}}(h)$ (given the noise in $Z(h)$ and given other unknown factors affecting the accuracy of the model). In fact, the extended Kalman filter which was used also produces an approximation of the variance $\delta(R)^2$ of its estimates.

There remains to define the DSD parameters \bar{D} . In [2], we defined "normalized" versions D'' and s'' of the mass-weighted mean drop diameter and of the relative drop diameter variance, "normalized" in the sense that the mean-drop-diameter's and relative-drop-diameter-variance's empirically observed correlations with the rain-rate R and with one another were factored out to produce mutually uncorrelated parameters. Thus the DSD was assumed to have the shape of a Γ -distribution with parameters specified by $\bar{D} = (R, D'', s'')$. The first version of the TRMM combined algorithm does indeed use these parameters. They are, however, unsatisfactory, for the main reason that the Γ -distribution model seldom fits measured DSD samples very well. To remedy that problem, and short of using the binned drop diameters themselves as parameters (of which there would then be far too many), we have chosen to apply the Karhunen-Loève decomposition to the variables B_1, \dots, B_{20} representing the number of drops whose diameters lie in twenty contiguous intervals covering the positive real numbers (B_{20} is open-ended), and retaining the 3 eigenvariables with the largest variance, while setting the values of the remaining 17 eigenvariables equal to their sample mean (which is justified since they vary much less significantly from DSD sample to DSD sample than the first 3). A detailed description of this

procedure and the resulting parametrization and radar-only retrieval will be described in an upcoming paper.

COMBINED MODEL

Let us write \mathcal{G}_Σ for the 0-mean Gaussian density function with variance Σ^2 . Returning to (2), we need to calculate the mean of that function in order to obtain our optimal estimate \hat{R}_i of the rain rate at altitude h_i . Using the results of the previous two sections, this can be approximately accomplished by the integral

$$\hat{R}_i = \int R_{\bar{D}}(h_i) \left(\prod_{i=1}^M \mathcal{G}_{\sigma(T_i)}(T_i - T_i(\bar{D}, h_{ice})) \right) \mathcal{P}(\bar{D}) d\bar{D} \quad (8)$$

Similarly, the m.s. uncertainty Σ_i^2 in this estimate can be approximated by

$$\Sigma_i^2 = \int \delta(R_{\bar{D}}(h_i))^2 \left(\prod_{i=1}^M \mathcal{G}_{\sigma(T_i)}(T_i - T_i(\bar{D}, h_{ice})) \right) \cdot \mathcal{P}(\bar{D}) d\bar{D} - \hat{R}_i^2 \quad (9)$$

In (8) and (9), we have replaced $\mathcal{P}(\bar{D}|Z)$ by " $\mathcal{P}(\bar{D})$ " to simplify the notation. In practice, the radar reflectivities do allow one to discriminate between stratiform and convective rain, and the a priori distribution of \bar{D} is chosen accordingly (see [2] for the case of the Γ -distribution model).

ACKNOWLEDGMENT

This work was performed at the Jet Propulsion Laboratory, California Institute of Technology, under contract with the National Aeronautics and Space Administration.

REFERENCES

- [1] Z.S. Haddad, E. Im, S.L. Durden and S. Hensley. "Stochastic filtering of rain profiles using radar, surface-referenced radar, or combined radar-radiometer measurements". *J. Appl. Meteor.*, vol. 35, no. 2, pp 229-242. 1996.
- [2] Z.S. Haddad, D.A. Short, S.L. Durden, E. Im, S. Hensley, M.B. Grable, and R.A. Black. "A new parametrization of the rain drop size distribution". *I.E.E.E. Trans. Geosci. and Remote Sensing*, in press.

- [3] H. Kumagai, R. Meneghini, and K. Nakamura, "Combined analysis of airborne single-frequency radar and multi-frequency radiometer observations in the TRMM-1 experiment", *Proc. 26th Intl. Conf. Radar Meteor.*, pp 696-698. 1993.
- [4] C. Kummerow, B. Barkstrom, W. Barnes, H. Christian, K. Okamoto, and J. Shiue. "The TRMM instrument package", submitted to *Bull. Amer. Meteor. Soc.*, 1996.
- [5] J. Simpson, R.F. Adler, and G. North, "A proposed Tropical Rainfall Measuring Mission (TRMM) satellite", *Bull. Amer. Meteor. Soc.*, vol. 69, pp 278-295, 1988.
- [6] E.A. Smith, F.J. Turk, M.R. Farrar, A. Mugnai, and X.W. Xiang. "Estimating 13.8 GHz path integrated attenuation from 10.7 GHz brightness temperatures for TRMM Combined PR-TMI precipitation algorithm", submitted to *J. Appl. Meteor.*, 1995.
- [7] J.A. Weinman, R. Meneghini, and K. Nakamura, "Retrieval of precipitation profiles from airborne radar and passive radiometer measurements - comparison with dual-frequency radar measurements", *J. Appl. Meteor.*, vol. 29, no. 10, pp 981-993, 1990.

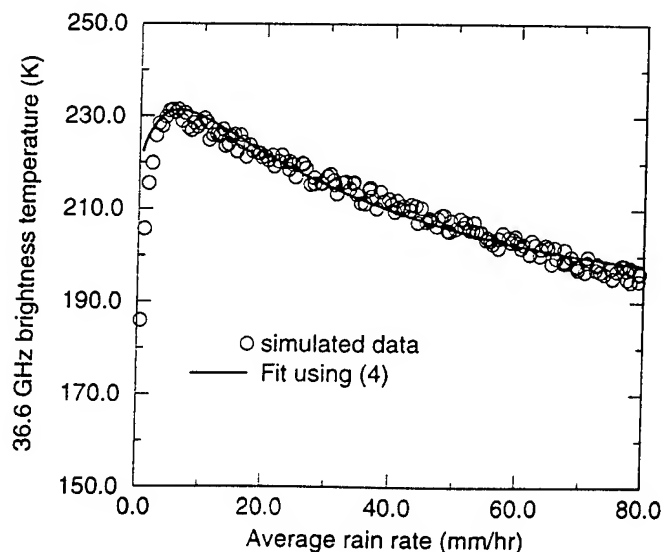


Figure 1: example of the passive model fit

Simultaneous observation of a rain event using the MU radar and an airborne Doppler radar for simulating TRMM ground validation

Toru Sato, Ruichun Peng, Hiroshi Hanado(*) and Hiroaki Horie(*)

Department of Electronics and Communication, Kyoto University

Kyoto 606-01, Japan

(*)Kashima Space Research Center, Communications Research Laboratory

Hirai, Kashima, Ibaraki 314, Japan

Corresponding Author: T. Sato

Phone: +81-75-753-5960, Fax: +81-75-751-8201

E-mail: tsato@kuee.kyoto-u.ac.jp

INTRODUCTION

The largest advantage of space-borne measurements is in its global coverage, especially in the tropical area, where most of the rainfall occurs. TRMM (Tropical Rainfall Measuring Mission) satellite[1] will be the first one which installs a precipitation radar (hereafter referred to as PR)[2] on board, and will be launched in 1997. It is expected to provide essential information in understanding the global water circulation. However, since the planned radar is a single-frequency, single-polarization, and non-Doppler one, the retrieval of rain intensity from the echo intensity data requires careful interpretation based on sophisticated algorithms which incorporate with peripheral ground validation data.

The MU (Middle and Upper atmosphere) radar of Kyoto University and CAMPR (CRL Airborne Multi-Parameter Radar) of Communications Research Laboratory are expected to play important roles in the Japanese ground validation programs for TRMM (Tropical Rainfall Measuring Mission) satellite to be launched in 1997.

MU RADAR MEASUREMENTS

The MU radar, which is a powerful VHF Doppler radar, has an advantage of being able to measure the rain dropsize distribution compensated for the vertical air motion. It operates at 46.5 MHz with peak output power of 1 MW. The antenna is an active phased array of 475 Yagi antennas, with the diameter of 103 m. Its electronically steerable antenna beams can cover the footprint size of the TRMM PR almost simultaneously by multiple beam positions with the vertical and time resolutions of 150 m and 1 minutes, respectively. Although it can provide an accurate profile of a rain event, it serves only when it rains during a TRMM overpass of the MU radar site, which is expected to occur roughly once per month.

At the frequency of the MU radar the Rayleigh scattering from raindrops are received with similar intensity as the turbulence echo under precipitating conditions. It is thus possible to estimate accurate DSD compensated for the background atmospheric motion.

We have developed a special observation scheme for TRMM

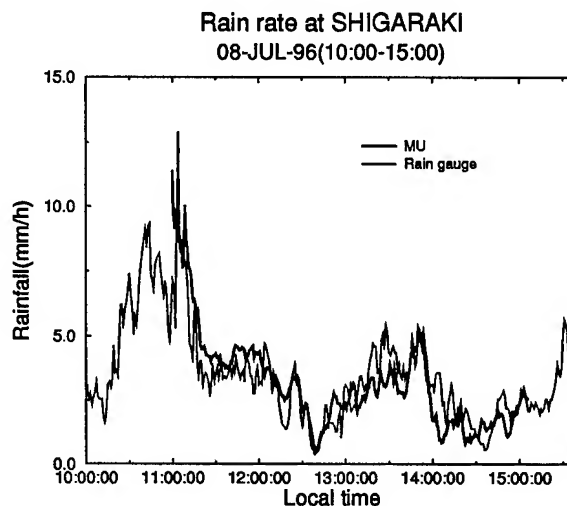


Figure 1: Rainfall rate measured on July 8, 1996 by the MU radar (thick line) and the rain gauge located at the MU radar site (thin line).

PR ground validation. In this mode 19 beam directions are evenly distributed over the TRMM PR footprint size of about 4 km at 3-km height. These 19 beam directions are switched electronically at the pulse interval of 400 μ s in a cyclic manner. Doppler echo power spectra are computed at a height interval of 150m for each beam direction every 10 seconds, and averaged for 1 minute. Rain dropsize distribution is estimated from the observed spectra by fitting the theoretical spectra assuming the gamma distribution. Background wind and spectral broadening due to atmospheric turbulence are automatically compensated for by simultaneously fitting the atmospheric component.

Fig. 1 compares the rainfall rate derived from the DSD averaged for the height range of 2-3 km with that of the drop-counter type rain gauge located at the MU radar site. It is confirmed that the measurements agree well within the random error of the MU radar measurement of about 0.7mm/h, which is estimated from the statistical fluctuations of the measured Doppler spectra.

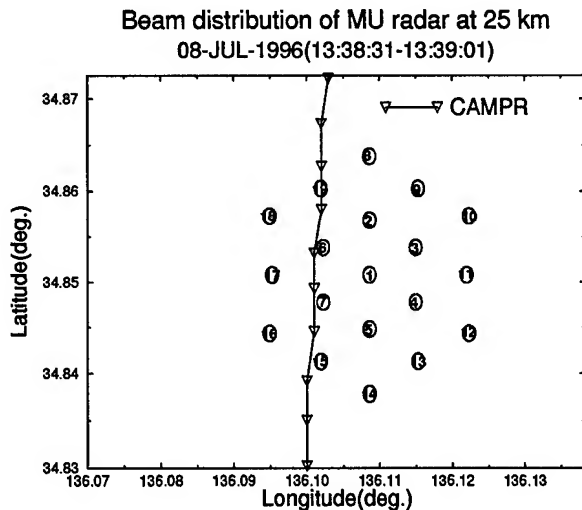


Figure 2: An example of the flight path of CAMPR over the MU radar site on July 8, 1996.

CAMPR MEASUREMENTS

The airborne Doppler radar CAMPR operates at the same frequency of 13.8 GHz as TRMM PR with peak output power of 2 kW. It has a slotted waveguide antenna, whose beam is scanned in a plane perpendicular to the flight direction. Two orthogonal linear polarizations can be utilized. The range resolution is selected from 75 m, 150 m, and 300 m. CAMPR is installed on a Beechcraft B-200 airplane, whose maximum cruising altitude is about 8 km.

It is planned to underfly TRMM when it is expected to observe interesting rain events, and thus will provide validation data with an order higher frequency than the MU radar. It can also be used as a 'transfer standard' by flying over multiple ground based radars. The combination of the MU radar and CAMPR will thereby constitutes an ideal complementary pair for the TRMM PR ground validation.

COMPARISON OF TWO RADARS

Simultaneous observation of a rain event with these two radars was first made successfully during 12:50–14:00 JST on July 8, 1996. The rain condition is a weak stratiform rain with 1–7 mm/h intensity as shown in Fig. 1. The airplane flew over the MU radar 7 times during this period. Fig. 2 shows one of the flight path. The radar beam of CAMPR was scanned in a plane perpendicular to the flight direction. Triangles denote the nadir point at the beginning of each scan of CAMPR beams, and circles with numbers indicate the MU radar beams at 2.5 km height. The beam spot size at this height is about 200 m for the MU radar, and 300 m (along track) \times 600 m (cross track) for CAMPR.

While the accuracy of the rainfall rate estimated from the MU radar data is well understood, the rainfall rate estimated from CAMPR data depends on the processing algorithm, whose accuracy is hard to justify. Here we compare the vertical and horizontal distributions of the radar reflectivity factor Z since they can be more directly derived from the observed data, and thus easier to make quantitative comparison. Figs. 3 and 4 shows the horizontal distributions of Z -factor measured by the two radars and averaged for the height range of 2–3 km. It should be noted that the shaded polygons are enlarged than the actual size of the beams, which are described above, for the illustrative effect. The large circle on these figures denote the footprint size of TRMM PR at 2.5 km. It is found from the figures that the Z factors observed by the two radars not only agree in their values, but also consistent in the horizontal gradient in the east-west direction.

Fig. 5 compares the Z factors for all seven paths of the flight. Each point represents the case where a MU radar beam falls within 400 m from a CAMPR beam. The dashed curves indicate the range of random errors in the estimated Z factors. This figure shows a good agreement within the range of random errors theoretically expected for the two radars.

As clearly shown in Figs. 3 and 4, strong horizontal variation of the rain intensity is observed inside the footprint size of TRMM PR even under the fairly stable stratiform condition. We can use the data of this experiment to simulate TRMM PR data with a special emphasis on the NUBF (Non-Uniform Beam-Filling) effect, which arises from the non-linearity of the Z -R relation.

It is possible to correct for the NUBF effect if the standard deviation of the rain inside the TRMM PR beam is obtained. Analysis of this data together with numerical simulations showed that the correction factor for the NUBF effect is a smooth and single-valued function of the standard deviation of the Z factor inside the simulated TRMM PR beam.

The more important and more difficult factor is the relation of the inhomogeneity inside and outside the beam size because only the inhomogeneity of the Z factor across the beams can be measured directly from TRMM observations. The simulation using the present data suggests that the standard deviation of Z factors among the synthesized TRMM PR beams is about twice larger than that inside a TRMM PR beam. It is thus important to accumulate such data under various rain conditions and for different latitudes.

SUMMARY

Result of the first simultaneous measurement of a rain event by two of candidate ground validation radars for TRMM Precipitation Radar was presented. It was found that the Z factors measured by the ground-based MU radar and the airborne CAMPR agreed well within the accuracy range of the measurements. They also showed the existence of fairly strong horizon-

Horizontal distribution of Radar Reflectivity
2.0 - 3.0 km height
08-JUL-1996 13:38:24.08 - 13:39:13.00

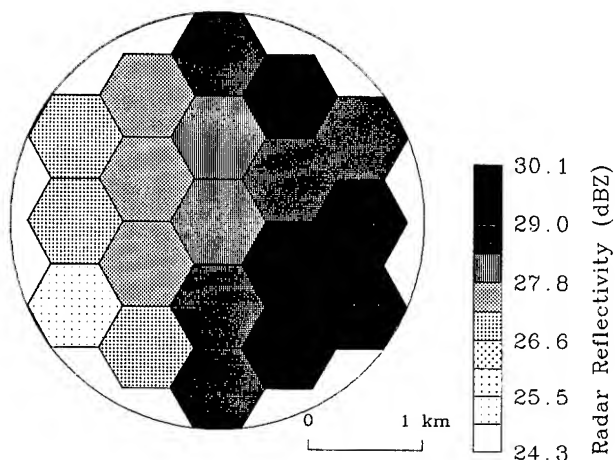


Figure 3: Horizontal distribution of the radar reflectivity factor at 2-3 km height measured by the MU radar.

Horizontal distribution of Radar Reflectivity
2.0 - 3.0 km height
08-JUL-1996 13:38:26 - 13:39: 2

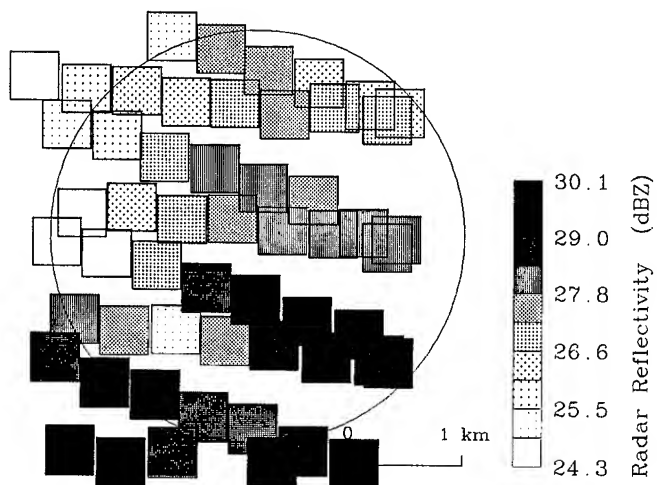


Figure 4: Horizontal distribution of the radar reflectivity factor at 2-3 km height measured by CAMPR.

Comparison between MU and CAMPR
08-JUL-96 at SHIGARAKI

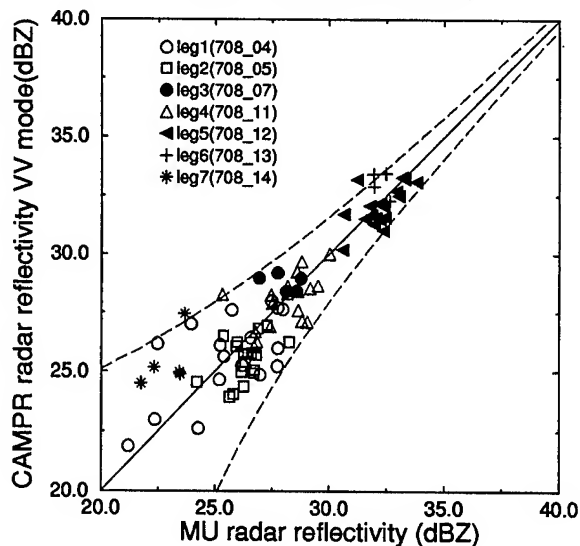


Figure 5: Comparison of the radar reflectivity factors measured by the MU radar and by CAMPR.

tal variation of the rain intensity inside the TRMM PR footprint size, suggesting the importance of NUBF effect in the signal processing of the TRMM PR.

REFERENCES

- [1] J. Simpson, R. F. Adler, and G. North, "A proposed Tropical Rainfall Measuring Mission (TRMM) satellite", *Bull. Amer. Meteor. Soc.*, **69**, 278-295, 1988.
- [2] K. Nakamura, K. Okamoto, T. Ihara, J. Awaka, and T. Kozu, "Conceptual design of rain radar for the tropical rainfall measuring mission", *Int. Satellite Comm.*, **8**, 257-268, 1990.
- [3] T. Sato, T. Teraoka, and I. Kimura, Validation and ground truth for TRMM precipitation radar using the MU radar, *IEICE Trans. Commun.*, Vol. E79-B, No. 6, pp. 744-750, 1996.

Radar Measurements from Papua New Guinea and Their Implications for TRMM PR retrieval algorithms

D.N.Ladd, C.L.Wilson and M.Thurai

Rutherford Appleton Laboratory, Oxon, UK
Tel: +44 1235 445770, e-mail: m.thurai@rl.ac.uk

ABSTRACT

The retrieval algorithms for the TRMM Precipitation Radar are depend on several parameters. Amongst them are (a) the coefficients relating to reflectivity-rainfall relationships and (b) the melting layer heights. A radar installed at Lae in Papua New Guinea, together with a co-located distrometer has provided statistical information on both these parameters. They are given in terms of the type of precipitation events, broadly classified as stratiform and convective events.

INTRODUCTION

In 1995, the Rutherford Appleton Laboratory (RAL, UK) developed a 3 GHz vertically pointing Doppler radar for monitoring precipitation in the tropics [1]. After numerous tests and calibrations in the UK, the Radar was shipped to Papua New Guinea and installed at University of Technology at Lae. It started its continuous campaign in December 1995. Vertical profiles of co-polar and cross-polar reflectivity, together with the Doppler spectra were recorded for 6 months. We report here examples of measurements and some statistically derived parameters which are of relevance to the proposed algorithms for retrieving rainfall rates from the TRMM PR measurements [2]. Also installed at Lae is a Joss distrometer belonging to RAL. Both the radar measurements and the Joss data are reported in this paper.

CALIBRATIONS

On deployment, it was assumed that the external calibration of the radar was as determined from the tests in the UK. The Joss-distrometer alongside the radar provides the ground level drop-size distribution, which was used to compute the radar reflectivity at 3GHz. Figure 1 shows these values as time series and compares them with the measured radar reflectivity at a height of 1 km. At the beginning of the event there appears some discrepancy, but, thereafter, very good agreement between the two is obtained. To achieve the best correlation, the distrometer derived reflectivity had to be time shifted by 100s, which corresponds approximately to the fall velocity of the drops. This implies that their size distribution is preserved as the particles fall from 1 km to the ground.

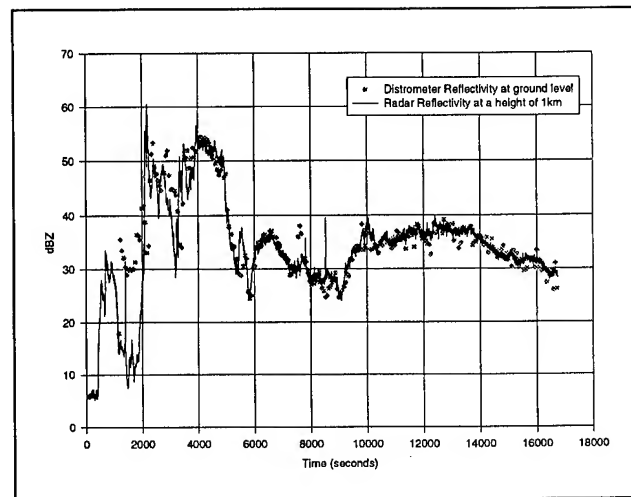


Figure 1. dBZ comparisons as time series.

TIME SERIES EXAMPLES

The radar data were classified into two cases: stratiform and convective. The criteria used to distinguish between the two is based on the presence or absence of a clear bright-band enhancement in the co-polar reflectivity as well as the occurrence of significant updrafts in convective events. Figures 2 and 3 illustrate typical examples of convective and stratiform events.

The stratiform case (Fig. 2.) shows the clear presence of the melting layer at a height of 4.5 km, which corresponds to the 0°C isotherm. The peak in the reflectivity (dBZ) is due to the strong echoes from the water-coated melting snowflakes, whilst the peak in the cross-polar reflectivity (LDR) results from the combined effect of three factors, viz. (a) the asymmetry of the melting process, (b) the large difference between the dielectric constants of ice and water, and (c) the rotation and tumbling of the particles as they fall. The Doppler mean velocities show a rapid increase as the low-density snowflakes melt and form water droplets of a much higher density, the latter falling at a much higher speed, caused by the variation in air drag resulting from the differences in particle size and density. The narrow height over which particle melting occurs can therefore be identified by the rapid increase in fall velocity. Finally, the spectral

width shows a corresponding increase in rain. The clear change is due to snowflakes falling with similar velocities, while raindrops tend to fall with a large range of velocities, resulting in larger spectral widths.

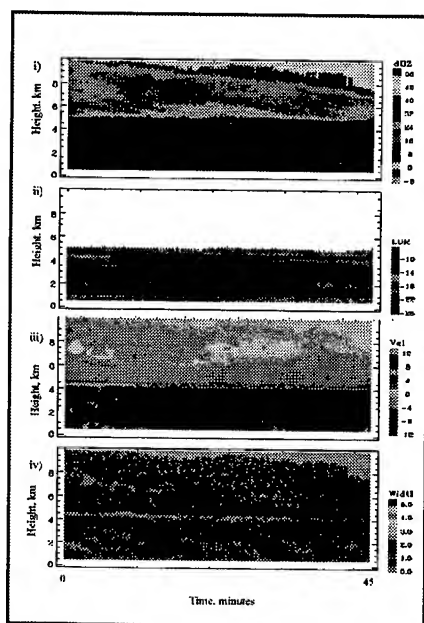


Figure 2. Stratiform Event, i) dBZ, ii) LDR, iii) Doppler mean velocity, iv) Doppler spectral width.

By contrast, the convective event (Fig. 3.) provides no evidence of a melting region in dBZ but enhancements seen in the latter half of the LDR plot indicate regions where melting may be occurring. The figure also shows regions of severe updrafts (indicated by negative mean velocities) along with areas of strong turbulence (shown by the large values of spectral width).

DISTROMETER DATA

From the data logged over the six month period, 62% of events were classified as stratiform, 19% convective and 19% 'mixed' events. The simultaneously recorded distrometer data were classified in accordance with the radar classification. Figure 4 shows the reflectivity (dBZ) versus rainfall rate (R), both computed from the Joss-derived DSD. Two parallel lines are obtained, with the intercept of the best-fit line for the stratiform case lying lower than that of the convective classification. For the same radar reflectivity, the convective events have a higher rain rate than the stratiform events. This is in qualitative agreement with the results from recent studies by Tokay & Short (1996), conducted in a tropical oceanic climate [3] but opposes some previous studies from temperate and mid-latitude regions. The integration time used in this study is 60 seconds, and to avoid sampling errors rainfall rates of less than 0.1mm/hr were

excluded from calculations. The Z-R relationships are $Z=132R^{1.36}$ for stratiform events where $R>0.1\text{mm/hr}$ and $Z=93R^{1.36}$ for convective events where $R>1.0\text{mm/hr}$ (NB. $Z=107R^{1.33}$ if $R>0.1\text{mm/hr}$).

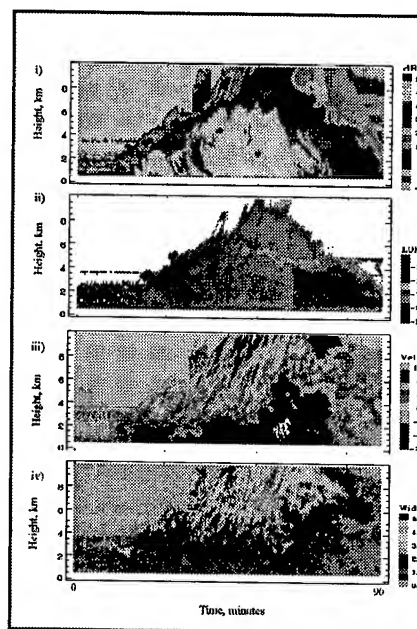


Figure 3. Convective Event, i) dBZ, ii) LDR, iii) Doppler mean velocity, iv) Doppler spectral width.

The recorded convective events in all cases show that they are very often followed by stratiform rain of less intense rainrate. In the case of stratiform rain there were no cases where rain rate exceeded 20mm/hr; in fact, in most cases, the rain rate for stratiform events is less than 10mm/hr, while in convective events it is usually greater than this value. The convective cases also have a larger spread of data points; this may need classification into two further categories: deep and shallow convection, while the data from the stratiform events shows significantly less spread.

Table 1 compares the power law coefficients for all the relevant best-fit relationships with those derived from other studies. As found in previous tropical studies, convective events - for a given rainfall rate - generally show lower mean diameter (D_0) than stratiform events. For example, for a rain rate of 10 mm/hr stratiform events tend to have D_0 typically of the order of 0.16mm whilst the convective events exhibit typically 0.12mm. The D_0 -R relationships imply that the apparent size distribution for convective events is biased towards drops with smaller diameters. This could be partly due to drop break up which one would expect to occur more in convective storms. It should be noted however that the D_0 -R relationship for the convective cases showed large deviations from the best-fit line.

MELTING LAYER HEIGHT

Finally, the cross-polar and Doppler information from the radar data were used to determine the height of the melting layer for all stratiform and convective events. Figure 5 shows the statistics of the heights so derived. The stratiform events have a narrow distribution of melting layer heights, with nearly 80% of these events having a melting layer height of 4.5km above the ground. The convective events have a broader distribution ranging from 3-8km above the ground. Only 40% of the convective events logged in Lae showed the presence of a melting layer while all the stratiform events contained a melting layer.

SUMMARY

Stratiform and convective events in Lae differ markedly in their characteristics. Both the reflectivity - rainfall rate relationships as well as the melting layer height statistics have been obtained. These were derived from a combination of radar measurements and a co-located Joss distrometer. Also obtained are other parameters pertinent to TRMM PR retrievals such as coefficients relating to specific attenuation-reflectivity relationship at 13 GHz and information on the mean drop diameter. They agree qualitative with a previously published study in the tropics.

REFERENCES

- [1] J. Eastment, M. Thurai, D. Ladd, I. Moore, "A Vertically-Pointing Radar to Measure Precipitation Characteristics in the Tropics," *IEEE Transactions on Geoscience and Remote Sensing*, 1995, Vol. 33, No. 6, pp. 1336-1340.
- [2] K. Okamoto and T. Kozu, "TRMM Precipitation Radar Algorithm," *IGARSS*, 1993, Tokyo, Japan, Vol. 2, pp. 426-428.
- [3] A. Tokay and D. Short, "Evidence from Tropical Raindrop Spectra of the Origin of Rain from Stratiform versus Convective Clouds," *Journal of Applied Meteorology*, Vol. 35, 1996, pp. 355-371.

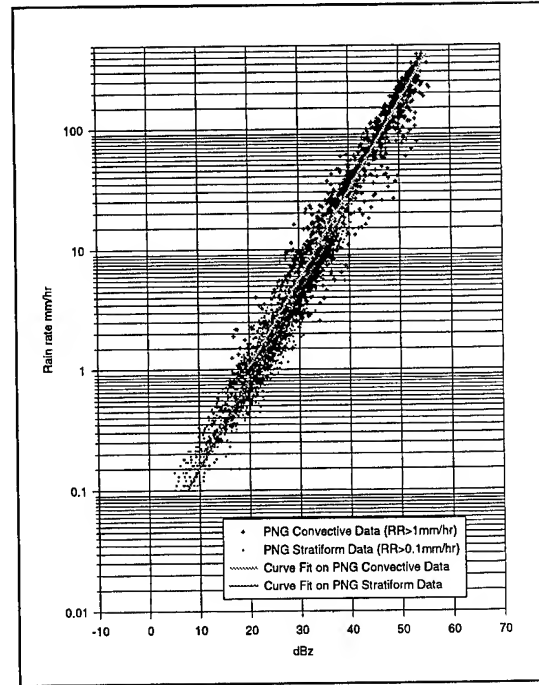


Figure 4. Z-R relationship for both convective and stratiform events.

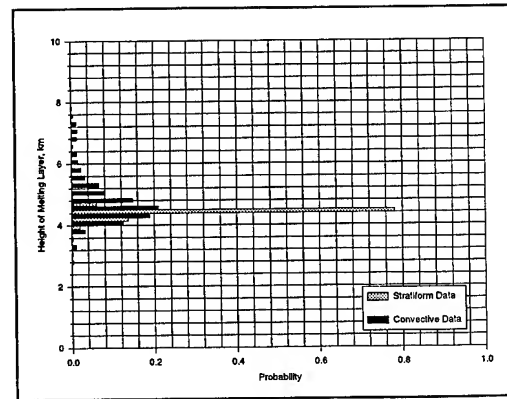


Figure 5. Melting layer distribution for stratiform and convective events.

Table 1. Comparison of power law coefficients for best-fit relationships.

Study	Event	Limits of R	Z-R	D_0 -R	γ -Z for 13 GHz	b
RAL, PNG (1997)	Stratiform	$R > 0.1 \text{ mm/hr}$	$Z = 132R^{1.36}$	$D_0 = 0.113R^{0.14}$	$\gamma = 0.000075Z^{0.88}$	1.33
	Convective	$R > 1.0 \text{ mm/hr}$	$Z = 93R^{1.36}$	$D_0 = 0.095R^{0.15} *$	$\gamma = 0.000142Z^{0.83}$	1.48*
Marshal Palmer (1948)	Stratiform		$Z = 200R^{1.6}$		$\gamma = 0.000398Z^{0.75}$	
Tokay & Short (1996)	Stratiform	$R > 0.1 \text{ mm/hr}$	$Z = 367R^{1.30}$	$D_0 = 0.133R^{0.13}$		1.30
	Convective	$R > 0.1 \text{ mm/hr}$	$Z = 139R^{1.43}$	$D_0 = 0.093R^{0.19}$		1.44

* These results were derived using only the major convective events logged in PNG.

The Dual Beam Airborne Technique as a Tool for Validation of the TRMM Rain Radar Retrieval

Jacques Testud and Stéphane Oury

Centre d'Etudes des environnements Terrestre et Planétaires (CETP)

10-12 avenue de l'Europe, 78140 Vélizy (France)

tel: 331-39 25 47 76 - fax: 331- 39 25 47 78 - email: testud@cetp.ipsl.fr

Abstract -- TRMM will be the first space observation platform with a precipitation radar (PR) on board. A key issue in the data processing of the PR is the correction for attenuation. In the standard algorithm, this correction is made using a K-Z power law relationship as $K = a Z^b$ where a is adjusted using the ocean surface as a reference target. This paper argues that a dual beam airborne Doppler radar as ELDORA-ASTRAIA should be of great interest in the validation of TRMM. Attenuated reflectivities sampled from two viewing angles may be processed following the "stereoradar analysis", or the new "dual beam algorithm" (proposed in this paper) to derive the unattenuated reflectivity Z , specific attenuation K , rainfall rate R , and the associated K-Z relationship at the ELDORA-ASTRAIA frequency (9.3 GHz). All this information greatly useful to validate TRMM is obtained with the flexibility of an airborne platform.

INTRODUCTION

The Tropical Rainfall Measurement Mission (TRMM) will be the first satellite to associate on the same platform active and passive instruments to measure rain. The satellite is scheduled to be launched next November 1997. Validation of TRMM is anticipated from ground based radars and airborne experiments. The purpose of this paper is to point out the interest of dual beam airborne radars in the experiments dedicated to TRMM validation.

The recent development of airborne or spaceborne meteorological radar systems [1] [2] [3], has stimulated the interest for the problem of attenuation correction, since on an airborne or a spaceborne platform, one is constrained to operate at higher frequency than on the ground, in order to reduce the size of the radar antenna. Several algorithms have been developed and tested on real data. Some of them are derived from the Hitschfeld and Bordan algorithm, with addition of an "external" constraint (use of the ocean surface as a reference target for the radar, use of a passive radiometer at the same frequency) in order to ensure numerical stability [4] [5]; others do not make any assumption on the K-Z relationship, or on the type of hydrometeors, but use a two-parameter approach, considering dual frequency [6], or dual beam [7] radar techniques. In this last category, falls the stereoradar technique developed in [7] in the framework of the scientific exploitation of ELDORA-ASTRAIA, a dual beam airborne Doppler radar developed in common by NCAR and CETP [1]. The stereoradar technique is a very powerful technique since it allows to derive simultaneously the Z and K fields,

without making any assumption on a K-Z relationships. However, this technique requires a complex treatment that is not easy to apply extensively (i.e. to large data set). The object of the present paper is the development of a new algorithm for a dual beam radar, much simpler than the stereoradar analysis, which presents the great advantage that it can be applied to any dual beam data set.

If dual beam airborne radars are used in validation experiments for TRMM, the present "dual beam" algorithm seems a good candidate for data analysis since its simplicity allows to easily perform the processing of large data set that will be required for such purpose.

PRINCIPLE OF THE DUAL BEAM ALGORITHM

Sampling strategy with the dual beam airborne radar

The sampling strategy with ELDORA-ASTRAIA is the following: the two radar antennas (in the aircraft tail) rotate about an axis collinear to the aircraft fuselage. One antenna is looking fore at $+20^\circ$ from the plane perpendicular to the rotation axis, and the other aft at -20° . The combination of the rapid scan of the antenna (at a rate of 120 to 240 $^\circ$ /s), and of the aircraft motion at 120 m/s, provides a three dimensional sampling of the attenuated reflectivities Z_1 and Z_2 (subscripts "1" and "2" refer to the fore and aft antenna, respectively). At each point of space, the sampling by the two antennas is not simultaneous, but the time shift is nevertheless small (one minute at 10 km range, increasing linearly with range). Thus the basic approximation of the dual beam data processing is to neglect any storm evolution (storm advection, if any, may nevertheless easily be taken into account).

The Hitschfeld and Bordan algorithm [8]

The starting point of our new algorithm is [8] whose principle is recalled hereafter. The observed radar reflectivity (attenuated) Z is expressed as a function of the true reflectivity Z_0 ($\text{mm}^6 \text{m}^{-3}$) and of the specific attenuation K (in dB/km) as:

$$Z = Z_0 \cdot 10^{-0.2 \left[\int_0^r K(s) ds \right]} \quad (1)$$

The basic assumption of [8] is that the specific attenuation K may be related to Z_0 through a power law relationship as: $K(Z_0) = a Z_0^b$. Introducing this relationships in (1), and differentiating with respect to r yields a differential equation in Z_0 whose solution is expressed as:

$$Z_0 = \frac{Z}{(1 - aI)^{1/b}} \quad (2)$$

$$\text{with: } I(r) = 0.46b \int_0^r Z^b ds \quad (3)$$

In a K-Z relationships for rain, scattering calculations show that coefficient b is poorly sensitive to the variability of the drops size distribution, as opposed to coefficient a whose sensitivity is quite significant. It may be shown that a varies as $N_0^{(1-b)}$ ($b=0.8$ at 9.3 GHz). Also a radar calibration error would modify the "apparent" value of a to be used to estimate K (a 1dB radar calibration error induces a modification of the apparent a of 0.8 dB).

(2) emphasizes the uncertainty in a as the major cause of divergence of the Hitschfeld and Bordan algorithm (occurring when aI is close to 1).

The dual-beam algorithm

The present dual beam algorithm considers the Hitschfeld and Bordan's solution. But in the K-Z relationship, it specifies b , and leave a free (this parameter is adjusted by the algorithm). In other terms, we write:

$$Z_{0i} = \frac{Z_i}{(1 - aI_i)^{1/b}} \quad i = 1, 2 \quad (4)$$

where Z_{0i} and Z_{02} are the "corrected" reflectivities from the fore and aft beam, and where integrals I_1 and I_2 run along the fore and aft beam, respectively. Setting that the two estimates of the corrected reflectivity should be identical in (4) [$Z_{01} = Z_{02}$], allows to derive parameter a as:

$$a = \frac{Z_1^b - Z_2^b}{Z_1^b I_2 - Z_2^b I_1} \quad (5)$$

Alternatively, we may eliminate a between the two equations (4) and determine Z_0 as:

$$Z_0 = \left(\frac{Z_1^b I_2 - Z_2^b I_1}{I_2 - I_1} \right)^{1/b} \quad (6)$$

Meanwhile, an estimate of the specific attenuation K may be also derived as:

$$K = \frac{Z_1^b - Z_2^b}{I_2 - I_1} \quad (7)$$

It is worth noting that if there is a calibration error c in Z_1 and Z_2 , the Z_0 estimate in (6) is multiplied by c (the calibration error is conserved through the algorithm), the a estimate in (5) is multiplied by c^{-b} , but the K estimate in (7) is unaffected by the calibration error.

TEST WITH REAL DATA

We use presently data collected during TOGA-COARE, a field experiment devoted to air-sea interaction over the warm pool of the West Pacific, and in which were operated

ELDORA-ASTRAIA on the NCAR Electra aircraft, and two other airborne Doppler radars on two NOAA P3's using the same strategy as ELDORA-ASTRAIA. We have selected a data set from one of the NOAA radar (on board the P3-42), collected on February 9th, 1993 between 16:33 and 16:44 UT. During this period the aircraft flew an approximately straight trajectory along a squall line.

The choice of this data set was mainly dictated by the fact that it allows to define the boundary conditions needed to perform the stereoradar analysis. The stereoradar analysis operate the Z_0 retrieval on a quite different principle, and without making any assumption on the K-Z relationships or on the type of hydrometeors. So it may be used to validate our new algorithm. The consistency between stereoradar and dual-beam analysis appears in Fig.2 which displays a scatter plot between their respective retrievals. The standard deviation is about 2 dBZ, instead of 6 dBZ when comparing the attenuated reflectivities Z_1 and Z_2 (Fig. 1).

Another interesting product of the dual beam analysis is the estimation of the a coefficient of the K-Z relationships from (8). After correction of the radar calibration error (-4.5 dB), the a coefficient as determined by the dual beam algorithm is shown in Fig.3. The dispersion of the values is relatively small about an average value of a equal to 0.66×10^{-4} . A very good agreement is obtained with the a value derived from in-situ microphysical probes and scattering calculations (determined as 0.65×10^{-4}).

Finally Fig.4 shows that the average K-Z relationship for these data set departs from that predicted for a Marshall-Palmer DSD, but fits well that deduced from the airborne microphysical probe.

CONCLUSION

Dual beam airborne Doppler radar is a developing tool for observation of deep convection or non precipitating clouds. Four systems are already operating at X-band (9.3 GHz), ELDORA ASTRAIA, the two systems on the NOAA P3 aircrafts, and the EDOP radar on the NASA ER-2. Two other systems are in project at the Japanese CRL (Communication Research Laboratory) (14 GHz radar, dual beam) and in our laboratory (94 GHz, dual beam). In the data processing of all these radars, one is faced with the problem of correcting the radar reflectivity for attenuation.

The new algorithm developed in this paper is almost as simple as the Hitschfeld and Bordan algorithm from which it is derived. The availability of Z-data from two viewing angles at each point of space allowed us to formulate an algorithm very stable, and in which the a coefficient of the K-Z relationships ($K=aZ^b$) automatically adjusts.

The main interest of this algorithm is:

- (i) it may be applied extensively because of its simplicity;
- (ii) it provides a K-estimate not subject to the radar calibration error;
- (iii) it provides an estimate of the a coefficient that may be used either to calibrate the radar by comparison to microphysical in situ probe, or to diagnose variations in the

properties of the drops size distribution, if the radar is well calibrated.

REFERENCES

- [1] Hildebrand, P.H., C.A. Walther, C. Frush, J. Testud, and F. Baudin, "The ELDORA/ASTRAIA airborne Doppler weather radar: Goals, Design, and First Field Test", *Proc. of IEEE*, **82**, (12), 1873-1890, 1994.
- [2] Kozu T., K. Nakamura, R. Meneghini, and W. Boncyck, 1991: "Dual parameter measurement from space: a test result from an aircraft experiment", *IEEE Trans. Geosci.Remote Sens.*, **29**, 690-703.
- [3] Hemsfield G., Bidwell S., Caylor J., Ameen S., Nicholson S., Boncyk W., Miller L., Vandemark D., Racette P., Dod L., 1996: "The EDOP radar system on the High-Altitude NASA ER-2 Aircraft", *J. Atmos. Oceanic Technol.* **13**, 795-809.
- [4] Iguchi T. and Meneghini R., 1994: "Intercomparison of single frequency methods for retrieving a vertical rain profile

from airborne or space borne data", *J. Atmos. Oceanic Technol.* **11**, 1507-1516.

[5] Marzoug M. and P.Amayenc, 1994: "A class of single and dual frequency algorithms for rain rate profiling from a spaceborne radar". *J. Atmos. and Ocean, Technol.* **11**, 1480-1506.

[6] Iguchi T. and Meneghini R., 1995: "Differential Equations for Dual Frequency Radar Returns", *Proc. of the 27th Conference on Radar Meteorology*, Vail, 9-13 October 1995, 190-192, 831pp

[7] Kabèche, A., and J. Testud, "Stereoradar meteorology : a new unified approach to process data from airborne or ground-based meteorological radars", *J. Atmos. and Ocean, Technol.* **12**, (4), 783-799.

[8] Hitschfeld and Bordan, 1954: "Errors inherent in the radar measurement of rainfall at attenuating wavelengths", *J. Meteor.*, **11**, 58-67.

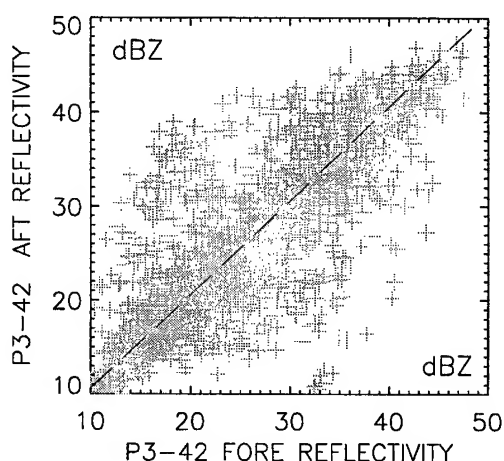


Fig.1: Scatter Plot of the apparent reflectivity from the aft antenna, against that from the fore antenna

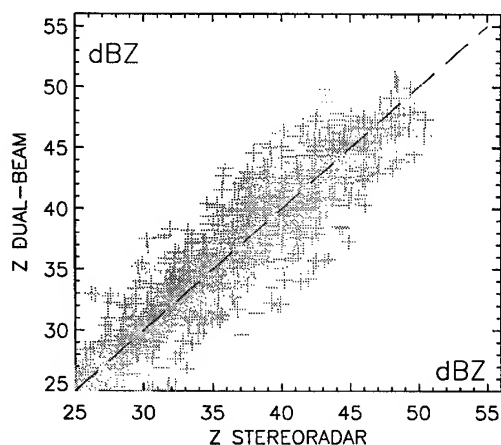


Fig.2: Scatter plot of the reflectivity retrieved from the dual beam algorithm against that retrieved from the stereoradar analysis

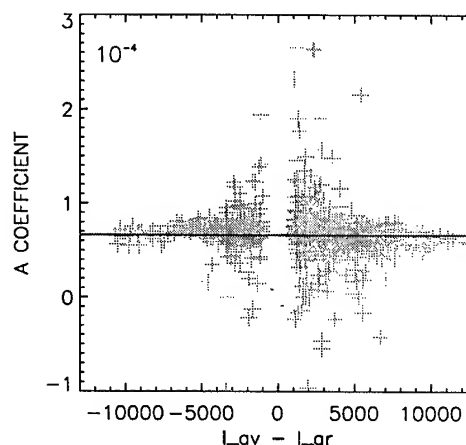


Fig.3: Scatter Plot of the a coefficient as a function of the integral difference I_1-I_2 .

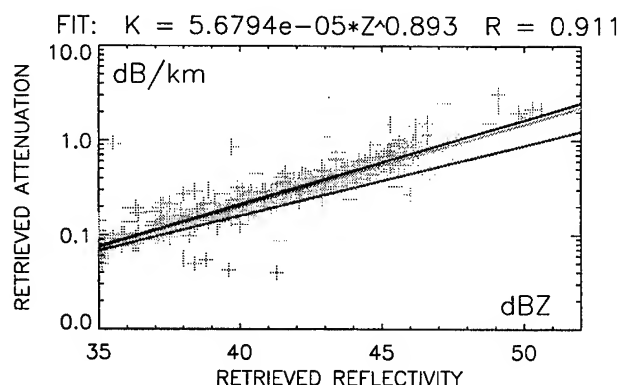


Fig.4: Scatter Plot of the retrieved specific attenuation K as a function of the "dual beam" reflectivity Z . The lowest straight line corresponds to the K - Z power law for a M-P DSD. The next one up is derived from microphysical probes. The upper one is the best fit of the scatter plot

A Comprehensive Data Management and Fusion System for Multi-Band Imaging Systems and Associated Data

Thomas Cooley, Ph.D., Lisa Standley and Jan Erickson
Nichols Research Corp.
Albuquerque, NM 87106
Phone: (505) 846-2986
Fax: (505) 846-0033
email: tcooley@zia.nrcabq.com

ABSTRACT

In order to optimally discriminate military targets from the background, it is necessary to compare and fuse remote sensing data from multiple sources including high-resolution panchromatic imagery data, modest resolution Multi-Spectral Imagery (MSI) data and modest to coarse resolution Hyper-Spectral Imagery (HSI) data. The data fusion involves radiometric calibration, geocoding, and topographic relief correction of the remote sensing data, integration of these data with multiple Geographic Information System (GIS) files, and analysis of the fused data with discrimination algorithms. These operations and the subsequent analysis require complex software components. These software components require expertise to correctly perform the data fusion operations. With an additional requirement of near-real-time processing, automation of data management and processing become essential. Both data integrity and a controlled log of what processing has been performed on each set of data for standard processing and experimental development processing are important for data traceability.

A data management and fusion system has been devised to control all of the image data and correlative data resulting from atmospheric measurements and ground truth measurements. The integration of several standard commercial and non-commercial tools into the data system enables the user to access dependable GIS and/or spectral processing algorithms.

INTRODUCTION

As anyone who has had to process large volumes of data which are typically stored in relatively small flat files can attest, the painful process of keeping track of filenames, directories and what settings an instrument was on during a particular measurement can be a painful experience. Structured data formats alleviate some of the difficulties in keeping track of header or meta information. However, careful attention is still required for file naming conventions generally created for a specific application. Because we are faced with the task of real-time processing of the data collected from a host of sensors including imagers, point

spectrometers, and atmospheric instrumentation, a systematic approach is required to control all of the data and processing. The processing of the data includes application of discrimination algorithms, archiving the data and comparing the data in myriad ways. An added complication is that the processing must be done on a variety of platforms depending on the end users' needs.

Our system incorporates familiar commercial and government products which can be employed by those users familiar with a particular software package. This also prevents unnecessary development of processing techniques when existing software is available which is proven in its particular specialty. Erdas Imagine™ is an excellent example of this: it is a commercial software package which has been developed and validated with particular attention to GIS applications. Orthorectification of images to a Digital Elevation Map (DEM) can be done painlessly within Erdas but the development and validation cost of this particular capability would be significant if Erdas were not used.

APPROACH

In order to achieve the kind of data management, control, and selected fusion needed, we have designed a toolkit that links the available processing algorithms with a database.

We have invested in a commercial UNIX-based database software package as the backbone of the processing system. This eliminates the difficulties associated with storing flat files and controls and records all of the processing performed on a particular piece of data. The toolkit manages all the stored data, including header and meta information, and provides standard naming conventions instead of requiring the user to perform this function. We are also able to perform queries on the data contained in the database.

From the toolkit, the user can access a variety of commercial, civil, and government algorithms which can be applied to appropriate problems. Custom algorithms can also be developed and tested against standard algorithms within the toolkit and database structure. Figure 1 illustrates the overall approach to the data management and fusion system. The algorithms can be accessed through each tool's user interface for experimental and development purposes. Once the steps are determined for a particular application through

experimentation, the algorithms can then be employed directly, combining multiple algorithms into a single step for the user by linking to the tools' applicable algorithm libraries and providing a single user interface for any required input.

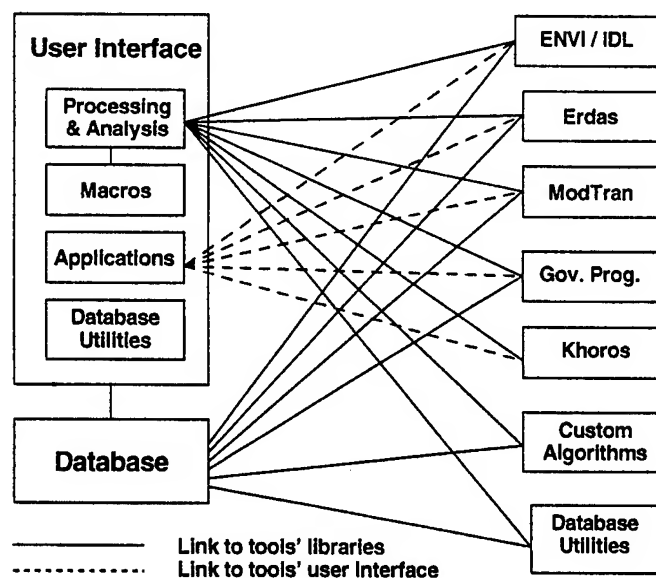


Figure 1: Block Diagram of Toolkit structure

We have created a database schema to control all of the sensor data, processed data, processing information, and any additional information that is available. This allows us to use an object-oriented information structure for relating dissimilar data in a single database. The image data is stored in files that are controlled by the database. The data files have a common data file hierarchy and follow a naming convention imposed by the toolkit. These data files can be accessed through the toolkit and the database and can be exported outside of the control of the database into common data formats to be used in other stand-alone programs.

Because the characteristics of various targets of interest and other surfaces are well understood and available in myriad databases, we have designed to allow hooks from the toolkit into phenomenology databases. This will permit us to use the best information available for the application of identification algorithms. A no less important set of data which is made available to the user is a record of Ground Control Points (GCP) which are necessary for geocoding data. Historical GCP are kept in the database along with the uncertainty inherent in obtaining the GPS geolocation.

Most important to the scientific user is the ability to test various algorithm approaches on the wealth of data available without spending undue time shuffling files. The commercial package ENVI/IDL™ from Research Systems, Inc. is included as a central package for both data analysis and algorithm development.

FUSING REMOTE SENSING AND GIS DATA

Several steps are required to fuse remotely sensed data into a GIS. They include: data acquisition and archiving the raw data, data correction/calibration and atmospheric correction, georeferencing and archiving the reduced data. From this point, the reduced data can be analyzed to identify objects of interest which are defined by the end user.

By using a GIS system, it is possible to overlay any number of sensor or historical data at the same location. Additionally, other GIS information may be available to the database including DEMs, landcover raster data, or other raster data which is geocoded. Point measurements of atmospheric and surface characteristics can also be geocoded and referenced to the image data.

When trying to georeference data at the scale of $\approx 1\text{km}$, the uncertainties of the geocoding are not difficult to ignore because the accuracy of GCPs is generally well within that range. Problems arise very rapidly in georeferencing one dataset to another with remote sensing images that have Ground Sample Distances (GSD - the pixel to pixel distance) less than 10 meters. Many point targets we are interested in being able to detect are sub-resolved in a pixel. Thus, the uncertainty of the georeferencing must be taken into account and, when appropriate, dataset to dataset referencing is required for accurate data fusion. This is not a desirable consequence but is necessitated by the errors inherent in establishing quality GCPs and georeferencing myriad data to the same location.

Geocoding point data is accomplished by creating an information object which is referenced to a particular point and a radius of 2σ , where σ is the uncertainty in the geolocation of that point. When the database is queried for a particular point all point objects and image data within the margin of uncertainty are made available to the user for inclusion in the current action. The user is then free to choose which objects and images he wishes to include in the information producing data fusion. This principal applies to time as well as location. Because time of data collection does not have significant uncertainties associated with the collections, an acceptable time window can be used in a query.

STANDARD PRODUCTS

As we are preparing this data management and algorithm development tool for specific satellite systems, we are preparing for those standard products which we know will be expected from those systems. In the case of the satellite imaging products, we have set forth a set of general processes which are applied to new data which is summarized in Figure 2.

Many end users are simply interested in obtaining a georectified image product which has had any sensor defects removed and which has had a reasonable atmospheric

correction applied to the image to produce a clear image once displayed.

Other standard processing capabilities we are including in the toolkit but which are not considered essential for most end users include:

- DEMs from stereo image pairs. The software package Orthomax™, which is an add on module to Erdas Imagine™, is able to generate DEMs from stereo image pairs.
- Change detection using available image data.
- Image mosaicking.
- Pan sharpened MSI/HSI images.

FUTURE WORK

As we continue to expand the capabilities of this toolkit, we anticipate new end user product needs and will create the ability to deliver the desired products.

Central to our effort is the need to meet the end users' requirements in a robust yet intuitive way. We believe this approach can be applied to the variety of sensors which we are required to include in the fusion process.

ACKNOWLEDGMENTS

Our thanks goes to the Air Force Phillips Laboratory at Kirtland AFB for their funding support.

REFERENCES

- [1] Goodenough, D. G., et. al., "Intelligent Data Fusion for Environmental Monitoring," IGARSS 95, pp. 2157-60.
- [2] ERDAS IMAGINE Production Reference Manuals, Ver. 8.2, 1995.
- [3] ENVI USER'S GUIDE, Research Systems, Inc., © Better Solutions Consulting, Ver. 2.6, January 1997.

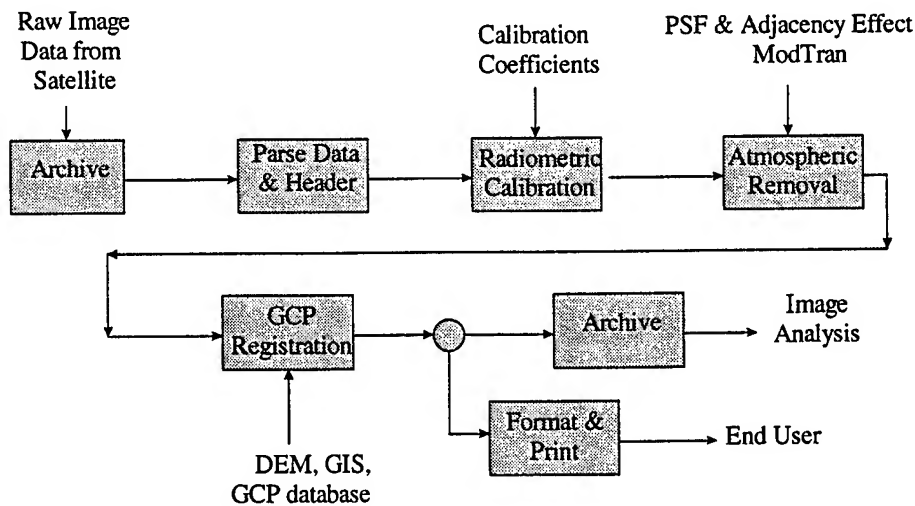


Figure 2: Data flow for satellite image data

An MSOM Framework for Multi-Source Fusion and Spatio-Temporal Classification

Weijian Wan and Donald Fraser

School of Electrical Engineering, University College, The University of New South Wales,

Australian Defence Force Academy, Canberra, ACT 2600, Australia.

EMail: wwan@evans.ee.adfa.oz.au or d-fraser@adfa.oz.au

ABSTRACT — This paper presents a unified neural network framework, known as MSOM, for multi-source data fusion and spatio-temporal classification. MSOM was originally developed as a classifier-design framework [2] and is now extended for joint scene-modeling (i.e., jMSOM) attempting to “fully” exploit the potential of multi-source data of spectral and categorical features as well as their spatio-temporal attributes in a compound fashion. Difficulties of high dimensionality, disparate statistical and geometrical characteristics, and joint spatio-temporal modeling are addressed. Experiments with a bitemporal set show significant improvement by jMSOM over its SOM or GMLC counterparts and any of its sub-models if only part of data sources is used.

INTRODUCTION

Multi-source sensors and computerized maps have provided ever-improved data for applications. The most straightforward yet simplest approach to multi-source fusion is the stack-vector method, by which we incorporate all sources of spectral and geographic features as well as associated spatio-temporal attributes into a single vector. This allows a joint modeling of all features involved to exploit the full the potential of data for various needs. However, modeling of a joint vector is extremely difficult due to high dimensionality, complex geometric and statistical characteristics of disparate sources, and sophisticated spatio-temporal operations. There have been many efforts in the past on the idea of decomposition of joint vector into tractable sub-vectors on a source-specific basis and composition of decision outcomes at a later stage. But, according to Shannon's rate-distortion theory (a foundation for vector quantization), decomposition loses significant information, particularly those mutual dependencies between various sources and between input and output. Thus, it is really not a matter of the stack-vector but of the modeling techniques.

In this paper, we propose a neural framework for joint modeling. It is based on our work with MSOM, i.e., Multiple Self-Organizing Maps [2]-[3], an extension of the Kohonen SOM [1]. In the following sections, we shall briefly analyze the virtues of MSOM and then present a further extension of MSOM for scene modeling to show that MSOM is adequate for multi-source classification.

MSOM vs. SOM

The major difference between MSOM and SOM is the multiple-map architecture in MSOM (Fig. 1) rather than the

single-map in SOM. This substantially improves the discrimination capacity of SOM in terms of effectively generating and maintaining a partition of data space into sensible clusters, whose distributions are explicitly represented and approximated by sub-maps based on sample frequency (Fig. 2). So, the MSOM is not only a clustering method which can discover underlying structures in clusters but also an associative memory which jointly associates all of the input features in a mutually-conditioning yet mapping fashion.

According to the principle of minimization of mean-squared errors (MSE), we can theoretically demonstrate that the MSOM is able to achieve, in the process of SOM-like neighborhood learning, a good compromise between minimization of *global* MSE over the whole map of multiple sub-maps and of *local* MSE over each sub-map in both generalization and specialization terms. Thus, MSOM is a “true” yet empirical Bayesian learning scheme under MSE. In addition, the SOM/MSOM is efficient and effective in processing and representation of high-dimensional data with disparate statistical and geometric characteristics if sufficient prototype units and sub-maps are used. The complexity and computation increase is linear. This means the MSOM is appropriate for modeling of the stack-vector.

Moreover, based on the MSOM concept and in conjunction with Kohonen LVQ and Hecht-Nielsen CPN (i.e., feedforward CPN and augmented CPN, or fCPN and aCPN), we have proposed a range of MSOMs (Fig. 1) from purely supervised and unsupervised (sMSOM and uMSOM) to two hybrid MSOMs (i.e., fMSOM and aMSOM). In principle, MSOM can work well with all sorts of sample situations, where each class may have only one labeled sample for class assignment or none at all. Descriptions and experiments of these models are detailed in [3] (Fig. 2).

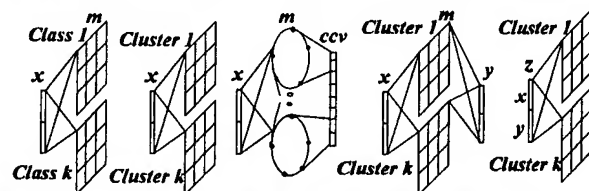


Fig. 1 MSOMs' Schematic Architectures



Fig 2 a) SOM; b) uMSOM (clusters); c) sMSOM; d) 1D uMSOM

It is worth noting that the input of aMSOM is a special stack vector $Z = (X, Y)$ which augments both the input X and output Y (coded as label vectors) as its input. The result is a mutually-conditioned mapping formed by aMSOM between all sources within and between X and Y for hybrid mapping and classification (e.g., $Y = F(X)$). This is the foundation of the joint MSOM (jMSOM) since we can virtually fuse all data sources including coded labels and other categorical data as well as their coded spatio-temporal features in Z and use aMSOM to form a compound mapping between all the sources in and between X and Y for spatio-temporal classification.

FEATURE SET AND MODEL DESIGN

Let us consider the issues of feature-set and model design. Firstly, for categorical data we use a technique, known as the label-vector coding, to convert labels into geometrically meaningful unit-vectors (i.e., 1 out of M classes). Secondly, we calibrate all features with reference to the unit metric according to their weights in the whole set (e.g., the label vectors need to be adjusted in length and centered). Because of continuity of adjacent bands a neighboring operation over the hyperspectral domain may be used.

On spatial modeling we propose a new method to extract co-occurrence context vectors (namely, CCV), which contain frequency-based interpixel dependencies over a 3×3 neighborhood on both X and Y spatial domains. For X , a 1D uMSOM is trained at first as a front-end (Figs. 1c and 3) to linearly and sequentially quantize the data space. It is then used to produce the CCV of X into the stack vector for joint modeling (Fig. 4). Also, during the modeling while jMSOM is in training, the spatial context of 3×3 over both X and Y is maintained and manipulated in a recursive and relaxation manner over both X and Y spatial domains. Finally, jMSOM is crafted to make temporal modeling a flexible option. Temporal training sets are treated as prototypic sampling points over a regressive, predictive or periodical modeling domain. New temporal sets, whether with labels or not, are allowed to insert or update jMSOM, or input to jMSOM for output on an interpolative, predictive basis (Fig. 4).

So far, all major issues for joint modeling of multi-source data have been addressed covering categorical coding, and hyperspectral, spatio-temporal modeling (see [3] for details). Due to space, we only discuss joint spatio-temporal modeling in more detail, here.

SPATIO-TEMPORAL MODELING

For simplicity, let us consider a bitemporal model with X_1 and X_2 as input and Y_1 and Y_2 as output (labels). Let X_{1c} , X_{2c} be the CCV of X_1 , X_2 , and Y_{1c} , Y_{2c} for Y_1 , Y_2 , respectively. Let Z be $(X, Y) = (Z_1, Z_2)$, where $X = (X_1, X_{1c}, X_2, X_{2c})$ and $Y = (Y_1, Y_{1c}, Y_2, Y_{2c})$, or $Z_1 = (X_1, X_{1c}, Y_1, Y_{1c})$

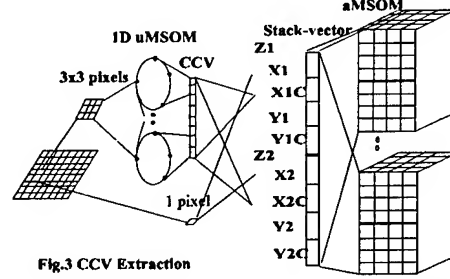


Fig.3 CCV Extraction

Fig.4 Joint MSOM: Spatio-Temporal

and $Z_2 = (X_2, X_{2c}, Y_2, Y_{2c})$. Generally, jMSOM can take any part of Z as input dependent on the availability of samples (e.g., (x_1, y_1) for supervised mapping or (x_1, x_2) for unsupervised) to form a compound model and output any part of Z , afterwards. This is another virtue of MSOM. From $f(Z)$, we can derive many sub-models with any combination of sources, e.g., $f_1(X_1, Y_1)$, $f_2(X_1, Y_2)$, etc. And we can get a feedforward mapping (e.g., $Y_1 = F_1(X_1)$) from any of sub-models. But, it is understood that only those which were sufficiently associated by consistent training pairs are statistically sensible to produce outcomes (e.g., $f_1(X_1, Y_1)$ normally sensible but $f_2(X_1, Y_2)$ perhaps not)

Operations of jMSOM: The first one is training, which is a 2-step procedure., and the second is relaxation labeling. In training, firstly a 1D MSOM front-end is trained with x without supervision over the temporal X on a pixelwise basis in order to derive the CCV. Secondly, jMSOM is trained with supervision on a neighboring basis by use of temporally labeled samples, (x_1, y_1) or (x_2, y_2) , to incorporate and associate X and Y as well as the CCV fields of X and Y until this process is stabilized. Then, entering the relaxation labeling, jMSOM (re)generates labels (y_1, y_2) over the whole scene and refines itself further in a recursive, relaxation mode. Afterwards, jMSOM is used to produce (y_1, y_2) or either of them. New temporal sets with or without labeled outputs can be added by expanding Z and be used to produce interpolative or extrapolative outcomes.

Analysis of Spatio-Temporal Modeling: In the light of MRF and Bayesian estimation, with extraction of CCVs jMSOM forms spatial sub-models (e.g., $f(X_{1c})$ over X_1 , $f(Y_{1c})$ over Y_1) in conjunction with the formation of the pixelwise models (e.g., $f(X_1)$, $f(Y_1)$) to explore the global inter-pixel dependencies over local contexts of X and Y . Later on, through further recursive updating over the spatial domains of X and Y , jMSOM (re)generates spatial compositions of homogeneous objects via those spatial models in the presence of the overall model. This is a parallel, global context expanding process over X and Y , in which all sub-models are updated to explore more consistent spatial dependencies on a robust basis of statistical relaxation. In this context, although sharing the same principle as Besag's

ICM, jMSOM is fully and mutually conditioned rather than sequentially decomposed and, thus, is superior to ICM (see [3]). The same effect takes place over the time domain, where hybrid temporal conditionings can be generated.

EXPERIMENTS

Experiment Design: We have carried out many experiments on artificial and real data to show the performance of all MSOMs. In particular, we did unsupervised classification with uMSOM on the Jasper Ridge data (152 bands used) and a number of multi-source sets with GIS attributes ([2], [3]). In this section, experiments on a bitemporal TM set, known as Purdue TIP JUL2/SEP2 (referred as J2/S2 or X_1/X_2 , hereafter) with ground truth and training sites are given. Only 5 bands were used. It was noted that the selection of the sites was somehow mistaken (e.g., Fig. 4: the sixth site from S2 bottom) and appears not representative (see Table 2). The methods compared were GMLC (Gaussian MLC), jMSOM (6 maps of 4x4 units) and jSOM (1 map of 10x10). Let jMSOMf denote the full model $f(Z)$ using all spatio-temporal contexts. Whereas, jMSOMa, $f(X_i, Y_i)$, is the raw model using no context, jMSOMd, $f(X_i, X_{ic}, Y_i)$, with X context, jMSOMl, $f(X_i, Y_i, Y_{ic})$, with Y context, and jMSOMt with temporal context. Note that, to evaluate every aspect of jMSOM, all sub-models were trained under the same conditions, under which all context fields (totaling 34 dimensions) were used but filled with null values if a field was uninterested. So, the results only show relative performances of sub-models but real ones of the full model.

Summary of Results: Using the KIA metric (Overall or Class KIA), Tables 1/2 show that jSOM/MSOMa outperform MLC if only raw data is used. All jSOM/MSOMd and jSOM/MSOMl outperform jSOM/MSOMa, indicating the effectiveness of CCVs over either data or label domains. jSOM/MSOMt outperform jSOM/MSOMa indicating the usefulness of temporal dimension in this set. jSOM/MSOMf using all spatio-temporal contexts substantially outperform all of sub-models by OKIAs. This shows the effectiveness of joint modeling by jMSOM. Moreover, MSOM always outperforms SOM in extraction of class-specific discrimination information measured by CKIAs although sometimes jSOMf appears better than jMSOMf in OKIAs. Other experiments further show that jMSOMf can extract almost all discrimination information provided by samples. If using only the training sites (6% of truth with mistakes), 70.37/72.85% on J2/S2 are achieved. Whereas, with the same net settings, by use of the truth (all correct), 98.23/98.84% (100% expected) are reached. This finally shows that by incorporating all sorts of disparate and high-dimensional features jMSOM has a substantial storage and discrimination capacity to form hybrid subjective and objective mappings from labeled and unlabeled samples.

Table 1. jMSOMf outperforms others (see Table 2 for *)

OKIA (%)	J2	S2
GMLC	44.81	48.89
jSOM/MSOMa	52.87/52.81	52.78/53.39
jSOM/MSOMd	55.32/56.40	53.54/54.68
jSOM/MSOMl	58.32/60.14	53.18/57.76
jSOM/MSOMt	67.00/65.10*	67.72/63.03*
jSOM/MSOMf	70.37/72.85	69.59/68.36*

Table 2. Site selection on J2/S2 appears erratic (see * in particular). jSOMt/f cannot classify J2 well between Wheats and Alfalfa/Oats but jMSOMt/f can (c/f. Fig. 5).

CKIA (%)	Corn	Soybn	Wheats	Al/Oats	OKIA
GMLC, J2	33.93	43.93	64.38	73.64	44.81
GMLC, S2	79.35	32.20	53.07	14.88*	48.89
jSOMt, J2	80.73	73.97	17.98^	51.97^	67.00
jMSOMt, J2	79.09	70.56	41.88	31.58	65.10
jSOMf, J2	90.4	70.54	28.54^	57.13^	70.37
jMSOMf, J2	93.76	70.62	54.75	36.33	72.85

CONCLUSION

We believe we have successfully set up a framework of a unified nature for multi-source fusion. Based on the statistical sustainable technology of self-organization and nonparametric representation, the jMSOM provides a suitable solution to the problem of multi-source data fusion and spatio-temporal classification.

Acknowledgment: The TIP set was supplied by Prof. D. Landgrebe, Purdue. The first author was supported by ADCSS and ADFA scholarships.

REFERENCES

- [1] Kohonen, T. Self-Organizing and Associative Memory. 3rd Edition, Springer-Verlag, 1989.
- [2] Wan W. and Fraser, D. MSOM papers. IJCNN'93, 1993. ACNN'94, 7ARSC, IGARSS'94, 1994.
- [3] Wan, W. An MSOM Framework For Classification and Scene Analysis. Ph.D. Thesis, UNSW, 1995.

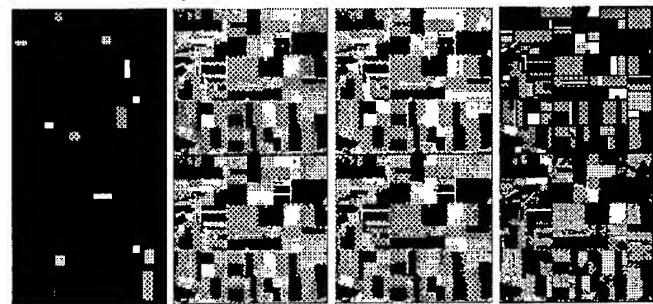


Fig. 5 First 3 columns for J2/S2: training maps (6% of truth), classification maps by jMSOMf/jSOMf. Last: the truth at top and a cluster map of 6 by the same jMSOMf.

Urban Land Use Mapping with Multi-Spectral and SAR Satellite Data Using Neural Networks

Jukka Heikkonen¹, Ioannis Kanellopoulos², Aristide Varfis³, Alan Steel² and Karen Fullerton²

1. Laboratory of Computational Engineering, Helsinki University of Technology,
Miestentie 3, FIN-02150 Espoo, Finland

tel: +358-9-4514829, fax: +358-9-4514830, e-mail: Jukka.Heikkonen@hut.fi

2. Space Applications Institute, Environmental Mapping and Modelling Unit,
tel. +39-332-785115, fax: +39-332-789803, e-mail: ioannis.kanellopoulos@jrc.it

3. Institute for Systems, Informatics and Safety,
Joint Research Centre, Commission of the European Communities,
I-21020 Ispra (VA), Italy.

Abstract – Statistical, textural and Gabor features were extracted from integrated multi-temporal multi-spectral TM data and ERS-1 SAR imagery for urban land use mapping. The computed features are first normalised using the SOM algorithm and then a decision tree algorithm is applied for feature selection. The classification procedure was carried out with a multi-layer perceptron, trained with the resilient back-propagation algorithm. Our results demonstrate the potential of the proposed methodology.

1. INTRODUCTION

The derivation of urban land use classes from remote sensing requires the use of context information in order to transform a land cover description based on the physical surfaces present in a pixel into a description that is suitable for statistical or socio-economic analysis.

To derive the best possible urban land use products Synthetic Aperture Radar (SAR) imagery from ERS-1 was used together with multi-temporal, Landsat TM data. By using combined imagery from the optical and microwave part of the spectrum improved land use products can now be generated [1,2,3] and previous work has demonstrated that significant gains in classification accuracy of urban areas [1,3] may be obtained compared to the use optical imagery alone.

In the experiment reported here a multi-layer perceptron neural network is used for the classification, trained with the resilient back-propagation algorithm [4] with weight decay regularisation. Furthermore, in order to recognise complex land use classes in the satellite imagery, different feature extraction and feature selection methods were applied, to extract structure and context information from the remotely sensed data and subsequently choose the most significant features for classification purposes.

2. STUDY AREA AND SATELLITE DATA USED

The study area chosen for this experiment lies on the western side of Portugal in the vicinity of the city of Lisbon and covers an area of approximately 80 x 80 km. There is a

considerable variety of ground cover in this area and includes, besides the urban area, extensive zones of arable agriculture, forestry, grasslands, vine, fruit and rice plantations. A detailed field survey was carried out within the test site to provide ground truth data for training and verifying the performance of the classifiers. For the purposes of this study additional reference data from urban areas were identified using stereo aerial photographs. All the reference data were labelled according to "CLUSTERS", a hierarchical land use statistical nomenclature from the European Statistical Office.

The input data used to carry out the urban mapping were co-registered Landsat TM multi-spectral images from two different dates (January 1991 and June 1991) SAR data from ERS-1 (March 1992). Fortunately for most of the experimental area the landscape relief was very flat and there were no severe distortions of the SAR imagery.

Speckle Filtering of the SAR Data

Before the SAR data could be used in the classification process it was necessary to remove the speckle noise, inherent in the image, by an appropriate filtering procedure. The filtering process we chose for this experiment was based on the multi-channel least squares modelling technique [4]. In this method a multi-dimensional regression is performed between a reference image, with better noise characteristics and the image to be corrected. In our case the TM image was used as the reference for the procedure. Other filtering techniques were also applied to the SAR data, but the regression filter resulted in sharper edges and better retained local spatial variations within the image[1,2].

3. FEATURE EXTRACTION AND SELECTION

Feature extraction methods were employed to extract context and structural information from the remotely sensed imagery. Ideally the features extracted should facilitate the discrimination of the land use classes, by providing a compact feature space for each class. This means that the within class variation of the features is small, whereas the variation of features between different classes is high. The following basic feature groups were extracted:

- 1) statistical features showing the intensities and intensity variations of pixels,
- 2) textural features, based on spatial gray level co-occurrence matrices [5], which provide information on local spatial variations within a certain neighbourhood in the imagery,
- 3) Gabor features, capture first order (i.e. local radiance values), second order (i.e. edge continuations) and higher order correlations (i.e. homogeneous textures).

In all the above feature extraction methods the features are computed within a local moving image window $W(x,y,c)$ of different sizes and orientations.

The statistical features extracted were the mean, standard deviation as well as skewness and kurtosis which give information on the distribution of pixel intensity values within the window W .

In previous work [3] we demonstrated that textural features, as defined by Haralick *et al.* [5], extracted from ERS-1 SAR imagery can greatly increase the discrimination of certain land cover classes and in particular urban areas. Therefore for the purpose of this work textural features, as defined in [5], were also extracted, based on the gray level co-occurrence matrices. The following textures were computed, energy, entropy, correlation, inertia and local homogeneity, resulting in a total of 50 textural features for each $W(x,y,c)$.

The Gabor filters are spatial sinusoids localised by Gaussian window, and they are defined in 2-D spatial domain with the impulse response, centred at the origin [6]. To extract the Gabor features each image window $W(x,y,c)$ is convolved with Gabor filters of different widths and orientation.

The resulting features were normalised in order to simplify the feature selection and the training of the neural network classifiers. The normalisation of the feature vectors is achieved by vector coding, in which the feature vectors are compared to a set of code vectors and replaced by their best matching code vectors. Kohonen's Self Organising Map [7] was used to encode the feature values.

After feature extraction the dimensionality of the feature space has increased considerably, taking also into account the multi-spectral, multi-temporal satellite data used in the experiments (a total of 13 channels). This not only makes the design and training of the classifier difficult but it may also reduce the accuracy by which the class statistics can be estimated. Therefore a feature selection procedure is applied. We have used a tree structured classifier based on the "Classification and Regression Trees" algorithm [8]. This is an iterative recursive procedure that splits the feature space into smaller and smaller parts by dividing the feature space into homogeneous class spaces. Starting with the whole feature space mapped to the root node, the tree is grown until a certain predefined number of features has been applied for splitting the feature space.

4. THE RPROP ALGORITHM

To carry out the urban land use mapping the Resilient back-propagation (RPROP) algorithm [4] was used for training the multi-layer perceptron (MLP) neural network classifier. In this method only the sign of the partial derivative $\partial E/\partial w$ is used to determine the direction of the weight update, in contrast to other gradient-descent algorithms that use the size of the partial derivative in the weight update. Furthermore a weight decay regularisation is used to eliminate the overfitting of the training set and therefore to improve generalisation by encouraging smooth network mappings. The composite error function used is:

$$E = \sum (t_i - o_i)^2 + 10^{-a} \sum w_{ij}^2 \quad (1)$$

where o_i is the output of the network, t_i is the desired output, w_{ij} is the weight between two nodes in layers i and j and α is the weight decay parameter. The RPROP algorithm works in "batch mode learning" i.e. the weights are updated after the presentation of the entire training set to the neural network.

5. EXPERIMENTAL RESULTS

The "CLUSTERS" nomenclature is divided into four hierarchical levels. In the first level there are the following six land cover/ land use classes: 1. Man-made areas, 2. Utilised agricultural areas, 3. Forests, 4. Bush or herbaceous areas, 5. Surfaces with little or no vegetation and 6. Wet surfaces. In the second level these 6 broad categories are sub-divided into 16 classes, at the third level become 35 and finally 64 in the fourth level. However many of the classes in levels 3 and 4 were not identifiable from the images and therefore they were not considered in the classification scheme. The resulting nomenclature consists of 6, 15, 26 and 33 classes in the four levels respectively. The urban classes that are present at the fourth level are: 1. Continuous/dense residential areas, 2. Continuous residential of medium density, 3. Suburban residential, 4. Discontinuous, 5. Collective, 6. Road transport, 7. Rail networks, 8. Airports, 9. River and maritime transport, 10. Extractive industries 11. Sport facilities and 12. Leisure areas.

In the feature extraction process a total of 4835 features were obtained for feature selection. The statistical and Gabor features were computed using window sizes of $W = 3, 5, \dots, 15$ pixels. The textural features were obtained using $W = 7, 11, 15$.

The entire set of the extracted features was then normalised with feature maps of 128 units, and using the tree structured feature selection method, 5, 10, 15, 20 and 25 features were used.

The selected datasets were then used to train the RPROP MLP neural networks for each hierarchical level of the nomenclature scheme. To determine the value of the decay parameter α in equation (1), a cross-validation approach was employed. The value of α which provided the best average

classification accuracy at each level with K features selected was then selected to train the neural network. The value of α in most cases was 2.25. Table 1 summarises the classification results in each level of the CLUSTERS scheme. The best classification accuracies achieved were 95.9 % for level 1 with 15 features used, 79.3% for level 2, when 25 features were used. This was also the case for levels 3 and 4 with overall classification accuracies 85.3% and 67.4% respectively.

The man-made areas were classified with an accuracy of 99.6 % in the first level. In the second level there are 5 man-made land use classes including residential areas, industrial activities, technical and transport infrastructure, extractive industries and land developed for recreational purposes. The total classification accuracy achieved for these 5 classes was 76.9%. There is a significant spread of classification accuracies between the 5 classes ranging from only 52% for the 'industrial or commercial activities' class to 85.8% for residential areas and 91.4% for 'land developed for recreational purposes'. Finally in the fourth level the accuracies are generally low ranging from 92% for the 'extractive industries' class, to 33% and 37% for the 'technical infrastructure' and 'road network' classes. At this level however, the low accuracies were expected since many of the classes have similar characteristics.

6. CONCLUSIONS

In this paper we have shown that there are significant gains to be made by using a multi-sensor approach to urban land use mapping and feature extraction methods that can provide context and structural information. Different man-made classes were mapped using a highly complex land use classification scheme. Additional gains could be made by investigating alternative feature selection methods or neural network architectures for classification.

Table 1: Classification results (%) in CLUSTERS scheme

No. of Features	Level 1 6 classes	Level 2 15 classes	Level 3 26 classes	Level 4 33 classes
5	89.9	66.1	80.4	63.9
10	94.3	73.6	82.7	65.2
15	95.9	76.7	82.3	67.1
20		77.6	84.9	66.8
25		79.3	85.3	67.4

The overall accuracy could also be improved by studying the possibility of integration of other sources of information as input layers in the classification process, or using these in a post-classification process. Such sources may be ancillary information from a Geographical Information System such as a Digital Terrain Model or a road network. Furthermore the potential of the new generation very high resolution satellite data such as IRS-1C, should be evaluated for urban land use mapping.

REFERENCES

- [1] G. G. Wilkinson, I. Kanellopoulos, W. Mehl and J. Hill, "Land cover mapping using combined Landsat thematic mapper imagery and ERS-1 Synthetic Aperture Data Imagery", Proc. 12th PECORA Memorial Conference, 'Land Information from Space Based Systems', Sioux Falls, South Dakota, 24-26 August 1993, Am. Soc. For Photogrammetry and Rem. Sensing, pp. 151-158, 1994.
- [2] G. G. Wilkinson, S. Folving, I. Kanellopoulos, N. McCormick, K. Fullerton and J. Mégier, "Forest Mapping from multi-source satellite data using neural network classifiers - An experiment in Portugal", Remote Sensing Reviews, vol. 12, pp. 83-106, 1995.
- [3] I. Kanellopoulos, G. G. Wilkinson and A. Chiuderi, "Land cover mapping using combined Landsat TM imagery and textural features from ERS-1 SAR imagery", in Image and Signal Processing for Remote Sensing, Proc. SPIE 2315, pp. 332-341, 1994.
- [4] M. Riedmiller and H. Braun, "A direct adaptive method for faster backpropagation learning: The RPROP algorithm", Proc. Of the IEEE Int. Conf. On Neural Networks, pp. 586-591, 1993.
- [5] V. T. Tom, "A synergistic approach for multi-spectral image restoration using reference imagery", Proc. IGARSS'86 Symposium, Zurich, ESA SP-254, ESA Publications Division, pp. 559-564, 1986.
- [6] R. Haralick, K. Shanmugam and I. Dinstein, "Textural features for image classification", IEEE Trans. On Systems Man Cybernetics SMC-3, pp. 610-621, 1973.
- [7] J. Daugman, "Complete Discrete 2-D Gabor transforms by neural networks for image analysis and compression", IEEE Trans. On ASSP, vol. 36, no. 7, pp. 1169-1179, 1988.
- [8] T. Kohonen, Self-Organization and Associative Memory, Springer-Verlag, Berlin, 1989.
- [9] L. Breiman, J. H. Friedman, R. A. Olshen and C. J. Stone, Classification and Regression Trees, Chapman & Hall, 1984.

Multisource and Multitemporal Data in Land Cover Classification Tasks: the Advantage Offered by Neural Networks

Alessandra Chiuderi
Space Applications Institute
Agriculture Information Systems Unit
Joint Research Centre of the European Commission
21020 Ispra (Varese) Italy
e-mail: alessandra.chiuderi@jrc.it

Abstract – This paper addresses the problem, within the MARS (Monitoring Agriculture with Remote Sensing) project, of land cover classification and acreage assessment based on remotely sensed images in case of lack of optical input data due to cloud cover. An alternative strategy, based on the exploitation of Multi-source and Multi-temporal data by means of a feed-forward Neural Network (NN) is proposed and discussed. The results reported in the following show that NNs not only provide a useful tool for data fusion but also an extremely powerful mean for early and reliable acreage assessment.

INTRODUCTION

The work presented here has been carried out within the MARS (Monitoring Agriculture with Remote Sensing) Project ([1]) of the Joint Research Centre of the European Commission, one of the widest projects in terms of Remote Sensing (RS) applications. The aim of MARS project is to provide decision support to the European Commission as far as agricultural policies are concerned.

In particular, one of the purposes of MARS is to rapidly, timely and accurately forecast and estimate the production of the twelve principal cultures in Europe. As production (P) can be considered as the product of area (A) times yield (Y),

$$P = A \times Y \quad (1)$$

production forecasts require at the same time a model for yield forecasting ([2]) and an accurate area estimation methodology.

Within this context, LANDSAT and SPOT images of 60 selected European sites are acquired during the period April-September together with the corresponding ground surveys. The cloud-free images are successively classified by means of a semi-automatic procedure, refined by photo-interpretation and finally passed through a statistical module to provide information at a global European level. The accuracy of land cover classification based on RS images is therefore fundamental for the overall reliability of this complex estimation process.

Unfortunately, for some Northern European countries, most of the optical-infrared images are rejected due to cloud

cover: for some sites only one acceptable image in terms of cloud cover is available during the whole growing season.

This lack of information on land use may therefore seriously compromise the possibility of providing reliable information on crop growth, health, acreage and consequently production for all the cultures in these areas.

Independently on cloud related problems, it is well known that the use of multi-temporal and/or multi-source data substantially improves land cover classification accuracy. In [3] the integrated use of LANDSAT and SPOT for one of the MARS sites located in Spain (Valladolid) showed that even for those areas where cloud cover does not represent a problem, the combination of two different optical-infrared sensors can dramatically increase classification accuracy.

The aim of the study presented in this paper is to show that the integration of optical images with microwave data, not only improves classification accuracy but also allows to fill in the lack of information caused by clouds and makes it possible to provide useful information on acreage estimation.

MATERIALS AND METHODS

Despite all statistics, 1996 has been a sunny year for the area of Driffield, North East England; therefore for the experiments presented here four images acquired by SPOT and four images acquired by ERS-1 were available. This allowed us to test the performances of our classification algorithm under various assumptions of data availability.

The data

All images were acquired during 1996 growing season which spans between April and September.

In Tab. 1 the acquisition calendar as well as the notation employed in what follows for each combination data source/date is reported.

SPOT images, preprocessed by the software GRIPS [4], result in 2000 lines by 2000 pixels. ERS-1 PRI images were calibrated, fully corrected, georeferenced by a 50m DEM and finally resampled and co-registered to SPOT. All ERS-1 processing is part of the automated process TSAR by NRSC (UK). Filtering of ERS-1 images has been performed by using the GG-Map filter ([5]).

The ground survey was carried out within the Action 6 activity of the MARS project during the summer 1996. For the experiments presented here, 9 land cover classes were identified: grassland, oat, spring barley, forest, winter barley, winter wheat, urban, moorland, water.

Table 1 Acquisition calendar and notation employed

Month	Date	SPOT	ERS-1
April	04-04-96	S1	
May	14-05-96	S2	
	24-05-96		E1
June	09-06-96		E2
	16-06-96	S3	
	28-06-96		E3
July	14-07-96		E4
August			
September	16-09-96	S4	

The experiments

All the experiments reported in this paper have been carried out on data sets extracted from the available images based on the aforementioned ground survey.

For each selected data set, several multi-layer feed forward neural networks, trained by means of the Error Back Propagation algorithm ([6]), were tested; the results reported in the next section refer to the best architecture in terms of average omission precision.

The training set employed for all the experiments presented in this paper is composed of 12984 pixels, whereas all the results refer to a test set composed of 6492 pixels.

RESULTS AND DISCUSSION

The first set of experiments was carried out on each SPOT data set separately: the results were extremely bad except for S3. Class 2 (Oat) was completely misclassified and all classes showed a very poor omission/commission accuracy. As far as S3 is concerned, the results, not particularly accurate, are reported in Tab.2. These results were obtained by a NN having 3 input nodes, 15 hidden nodes and 9 output nodes. This table and all the following ones, share the same structure: in parenthesis the input data set employed according to the notation introduced Tab. 1 and the results availability date.

It is important to emphasize at this point that a traditional classifier (maximum likelihood) can deal with only one data source at the time, whereas NNs allow us to exploit all the data sets available in order to improve as much as possible classification accuracy.

S3 can be considered as a key date for land cover classification in this area due to growing and harvesting calendars: it is important therefore to stress that the combination S1, S2, E1 (Tab. 3) not only provides an early

and reliable classification, but also deals with the lack of information arising from unavailability of S3.

Moreover, S3 was acquired on June 16th, this means that before that date, no kind of reliable assessment could be made on acreage estimation, if we were forced to use a single source data set.

Table 2. Classification accuracy (S3, June)

Class	Commission (%)	Omission (%)
Grassland	31.13	34.74
Oat	60.43	47.77
Spring barley	66.32	69.07
Forest	76.62	78.05
Winter Barley	42.97	55.25
Winter Wheat	69.37	49.95
Moorland	67.07	78.38
Urban	75.51	62.82
Water	98.62	93.97
Overall (%)	66.73	

By using a NN, on the contrary, if only two optical images are available (namely S1 and S2), it is possible to combine them and to produce as from May classifications showing an overall accuracy of 82.69%; a further improvement is also possible by adding a ERS-1 image (E1) which raises the overall accuracy to 83.18% as shown in Tab. 3. The best resulting NN architecture employed in this case was composed by 7 input nodes, 18 hidden nodes and 9 output nodes.

Table 3. Classification accuracy (S1-S2-E1, May)

Class	Commission (%)	Omission (%)
Grassland	87.50	79.21
Oat	72.32	67.35
Spring barley	84.72	78.80
Forest	91.34	92.02
Winter Barley	84.83	70.12
Winter Wheat	71.61	84.09
Moorland	80.71	89.28
Urban	81.89	75.21
Water	96.04	95.28
Overall (%)	83.18	

In June, if all optical images are available, NNs allows us to obtain a reliable land cover classification by exploiting either the multi-temporal optical data source (S1, S2, S3), or the full data set (S1, S2, E1, E2, S3).

Some more interesting combinations can be considered in order to cope with the unavailability of one (or more) optical images due to cloud cover. If only S3 is available, the combination E2, S3, E3 (possible at the end of June) provides the results reported in Tab. 4 which are slightly more accurate than the ones reported in Tab.2 on S3 alone, in particular for

the identification of classes 6 (Winter Wheat) and 1 (Grassland). The best performing NN in terms of average omission precision was in this case composed of 5 input neurons, 2 hidden layers of 8 and 14 nodes respectively and 9 output nodes.

Some interesting results can also be obtained in July: according to the acquisition calendar, the last ERS-1 image (E4) is available for our purposes at this time.

Table 4. Classification accuracy (E2-S3-E3, June)

Class	Commission (%)	Omission (%)
Grassland	66.77	56.01
Oat	65.30	49.65
Spring barley	59.30	55.01
Forest	68.30	82.79
Winter Barley	58.74	41.05
Winter Wheat	64.39	71.16
Moorland	60.37	63.64
Urban	73.82	86.08
Water	99.33	92.04
Overall (%)	69.07	

Assuming that S1 is missing but S2 and S3 are available, a NN having 10 input nodes (corresponding to S2, E1, E2, S3, E3, E4 respectively), 18 hidden nodes and 9 output nodes was trained for 200 iterations. The results obtained for this data set are reported in Tab. 5. In this experiment, besides the satisfactory overall accuracy of 84.58%, each class is well identified as shown by both the omission and commission accuracies reported in the table.

Table 5. Classification accuracy (S2-E1-E2-S3-E3-E4, July)

Class	Commission (%)	Omission (%)
Grassland	78.48	78.68
Oat	88.03	70.79
Spring barley	80.70	88.63
Forest	90.02	91.15
Winter Barley	74.79	78.28
Winter Wheat	82.32	81.57
Moorland	86.74	82.29
Urban	80.19	83.87
Water	99.45	94.36
Overall (%)	84.58	

Finally, just as a confirmation of the power of data fusion in terms of land cover classification accuracy, a NN was trained on all the available data set. The best resulting network, in this case, was composed by 16 input channels (corresponding to the 8 data sources available), 22 nodes in the hidden layer and the usual 9 nodes corresponding to the 9 land cover classes. For the complete data set, the overall accuracy reached 90.50% whereas the average omission

precision and average commission precision rated 90.13% and 90.44% respectively.

CONCLUSIONS

The aim of the studies presented in this paper is twofold: on one side to cope with and overcome the problems arising from lack of optical infrared data due to cloud cover within an automatic land cover classification scheme, and the necessity to provide early and accurate area estimates on the other side.

The experiments reported here, based on the use of Neural Networks show that the combination of two optical and one microwave image can provide early and very satisfactory results as from the month of May of the current growing season.

Furthermore, the accuracy of the classification can be strongly increased, if four microwave images are available, as happens in mid July.

Moreover, in the case that only one optical image is available due to cloud cover, the addition of microwave data can still improve the overall classification accuracy.

ACKNOWLEDGMENTS

The author would like to thank Ioannis Kanellopoulos (Joint Research Centre SAI-EMAP) for kindly providing the NN software employed for the simulations described in this paper, Richard Kidd and Carmelo Attardo (Joint Research Centre, SAI-AIS) for providing the data employed.

REFERENCES

- [1] F. J. Gallego, J. Delincé, C. Rueda: "Crop area estimates through remote sensing: stability of the regression correction" Int. J. Remote Sensing, 1993, Vol 14, N. 18, pp. 3433-34459
- [2] P.Vossen: "Forecasting National Crop Yields of E.C. Countries: the Approach Developed by the Agriculture Project".Proc. of The Application fo Remote Sensing to Agricultural Statistics, Belgirate, 1991. EUR 14262 EN (92) Pg. 159 - 176
- [3] A. Chiuderi "Integrating LANDSAT and SPOT images to improve land cover classification accuracy" pg. 365-368
- [4] C. Casteras, G. Doyon, E. Martin, V. Rodriguez: "Corrections Geometrique et atmospherique - Manuel Utilisateur" CISI-Geo Design, CCR (Ispra), RSO/DOT-CGA-MU, Ed. 2 (1994).
- [5] Nezry, E, 1993, The Refined Gamma-Gamma MAP Speckle Filter, EEC Expert Contract n. EARS 92-0004-FR, pp74, 1 June 1993
- [6] P.D. Wasserman: *Neural Computing, Theory and Practice*, Van Nostrand Reinhold, 1989, New York

Combining Structural and Spectral Information for Discrimination Using Pulse Coupled Neural Networks in Multispectral and Hyperspectral Data

James H. Cooley
Consultant
3833 South 8th Street
Arlington, VA 22204
Phone: (703) 892-5354
email: jcooley@us.net

Thomas W. Cooley, Ph.D.
Nichols Research Corp.
Albuquerque, NM 87106
Phone: (505) 846-2986,
Fax: (505) 846-0033
email: tcooley@zia.nrcabq.com

ABSTRACT

The emerging field of dynamic neural networks motivated by recent biological understanding of the way in which the brain encodes discrimination information in a time signal from a large, multi-layered image suggests an approach to fusing data. Pulsed Coupled Neural Networks (PCNNs) have shown a robust ability to segment a single spectral band image into segments for terrain categorization but have not proven to be very robust in structural identification. However, linking fields of PCNNs can easily be configured for scale and/or rotation invariance. Using a variation on the Eckhorn [1] pulsing neuron model, a PCNN is constructed to reduce the structural information with the spectral information of a coarse resolution Hyperspectral image. The configuration of the linking network is studied to try to yield meaningful pulsing signals that can be combined for enhanced segmentation or discrimination.

INTRODUCTION

Imaging spectroscopy promises to yield significant improvements in the ability of a sensor to discriminate targets of interest from the background over Multi-Spectral Imaging (MSI) techniques that are characterized by such satellite systems as SPOT and Landsat. With the advent of space-based imaging spectroscopy, or sometimes called Hyper-Spectral Imaging (HSI), in the NASA Lewis satellite, new problems arise. Foremost is the transportation of image data from the satellite to the ground for analysis. Due to the extremely high data rate of the Lewis primary payload, the HSI imager, a single scene cannot be downloaded in one pass. Our long term objective is to develop techniques to reduce the volume of data generated by such a system and distill it into the desired information for downlinking to a ground station.

John Johnson of MICOM has been a significant proponent of the utility of Pulsed Coupled Neural Network (PCNN) technology and has published several articles that articulate well the framework from which the current work is derived including the Eckhorn model of the pulsing neuron [2,3].

The current research has been motivated by the initial results of PCNN and the looming problem of reducing data

into information which falls under the rather broad umbrella of data fusion [4].

APPROACH

PCNN models are interesting for two primary reasons. First, it has been demonstrated that a purely analog pulsing neuron can be built in silicon and has the promise to deliver very rapid computations at the focal plane level such that a set of standard data reduction processes can be implemented in parallel just behind the focal plane sensor. Second, they are biologically based on the signals produced in the human brain and specifically have been shown to reduce the volume of data transmitted between the eye and the brain by preprocessing at the focal plane level in the eye. PCNNs have been used to perform image segmentation with remarkable results and they also can be easily designed to have the desirable properties of scale and rotation invariance based on the neuron to neuron linking configuration (see [2] for more information).

The simple model of a pulse-coupled neuron we use in our modeling is outlined in Figure 1. It has a feeding input, which is given by F and represents the optical input from the focal plane detector, linking inputs from source n denoted L_n , an internal neuron energy U given by:

$$U = F \cdot (1 + \beta \cdot \sum_{i=1,n} L_i) \quad (1)$$

The f_{Step} function coupled with the $f_{\text{Threshold}}$ function has the effect of generating an output pulse when the op-amp like input matches the reference. The reference input to the step function has been described as a leaky integrator which is modeled with an exponential decay with time until reset by the pulsing step function. To date, the linking signals have been largely (if not exclusively) assumed to be spatially neighboring neurons which cause their neighboring neurons to fire. Our approach is to use this same basic spatially linked neuron model but under three different cases which vary the fusion process to identify possible target areas. The three cases we considered are summarized below where we denote the input data from the spectral-spatial 'hypercube' as \overline{M}_λ ,

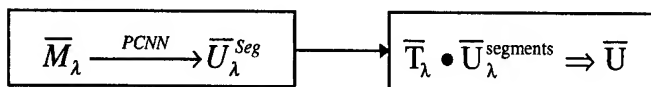
\bar{T}_λ is the spectral signature of the target, and \bar{U} is the output segmented spatial map which can be directly related to the probability of a target at each pixel segment.

Case 1:



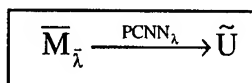
The simplest implementation to find a segmented target region which has both known spectral and spatial features is to find the inner product of the hypercube with the expected characteristics of the target which produces a 2-d matrix of the target probability in each pixel represented by \bar{M}_Σ and then apply a segmentation algorithm such as the PCNN.

Case 2:



Alternatively, we may consider performing the segmentation process first due to the speed of the eventual implementation at the focal plane level, and then take the inner product of those image segments with the target spectral signature to produce the segmented target probability.

Case 3:



A variation on case two is to identify those spectral bands which have the most separation between the target and background and link those bands in an appropriate way to generate a single band segmented target probability which is a 'good estimate' of what we would find if we performed all of the calculations of case 1 or 2. The estimate may be checked against the full spectral signature of the target for those target regions as in case 2. In case 3, the difference in the principal components of the target and background regions can be used as the linking input into the estimated probability \tilde{U} .

A simulated data set is constructed from ground-truth reflectance measurements, resampled to 80 bands and built into a simple 'ground' structure. Each of these cases is applied to the 40x40 pixel image of simulated data shown in Figure 2, where the spectral signature of the target and decoy have small spectral differences and the background has modest spectral differences from the target and decoy signatures.

RESULTS

Our results indicate that the application of case 3 produces sufficiently accurate results for the tremendous savings in required computations.

Case 1 was applied to the test data and the internal energy \bar{U} of the array of neurons after the first firing is shown in Figure 3. The second pulsing neuron firing is shown in Figure 4. The second firing is selected because it demonstrates the characteristic expanding wave of neuron firing of the PCNN model used. The inner product of target spectra with segmented image bands for Case 2 with noise of 20% of signal is shown in Figure 5. The target is difficult to distinguish from the decoy in this case due to the imperfect segmentation to generate a hypercube of neuron energies.

Case 3 gave promising results as it found the target well and did not confuse the decoy structures even in the case of significant noise. Figure 6 shows the internal energy of neurons for Case 3 with noise of 20% of signal after first firing. Four bands of feeding input and one band of the nearest neighbors were linked into a single neuron to produce this internal neuron energy image.

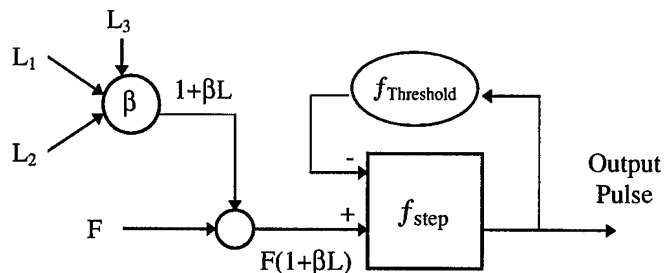


Figure 1 -- Pulse-coupled neuron model

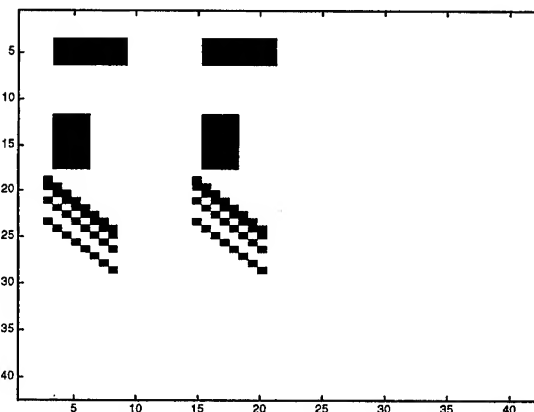


Figure 2 -- Test image with the Target structures on the left and decoy structures on the right over a solid background.

ACKNOWLEDGMENTS

Our thanks go to the Air Force Phillips Laboratory at Kirtland AFB.

REFERENCES

- [1] Eckhorn, R., et al. "Feature linking via synchronization among distributed assemblies: Simulations of results from cat visual cortex," *Neural Computation*, Vol. 2, pp. 293-307 (1990)
- [2] Johnson, John L., "Pulse-coupled neural nets: Translation, rotation, scale, distortion, and intensity signal invariance for images," *Applied Optics*, 1994, Vol. 33, pp. 6239-6253.
- [3] Johnson, John, L., PULSE-COUPLED NEURAL NETWORKS, March 1994, Technical Report RD-WS-94-1, U.S. Army Missile Command, Redstone Arsenal, Alabama.
- [4] Broussard, R.P. & Rogers, S.D., "Physiologically motivated image fusion using pulse coupled neural networks," *SPIE Conference on Applications of Artificial Neural Networks*, 1996, Orlando, FL, Vol.2760, pp. 372-383.

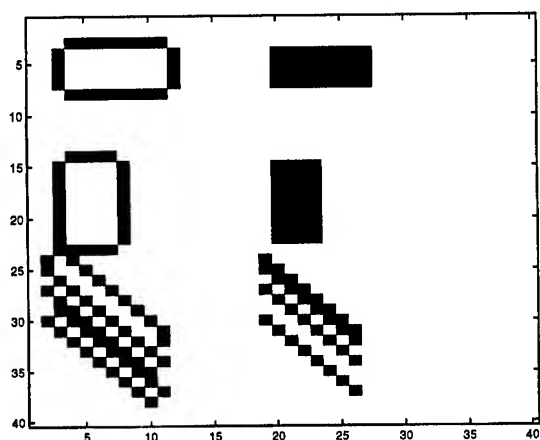


Figure 3 -- Internal neuron energy for Case 1 with noise of 20% of signal after first firing (black indicates regions which have fired and reset)

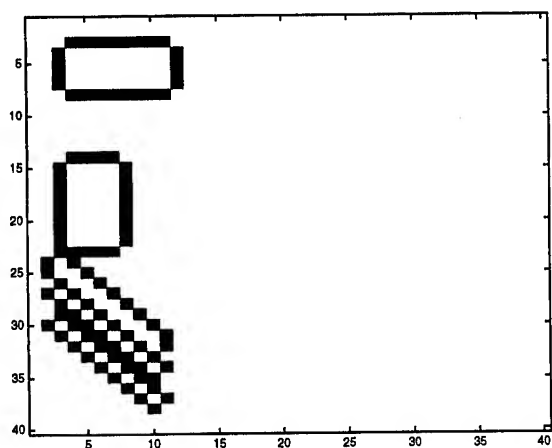


Figure 4 -- Second firing of neurons for Case 1 without noise. The white pixels are firing and will trigger their neighboring pixels to fire during the next time step if their internal energy is sufficiently high.

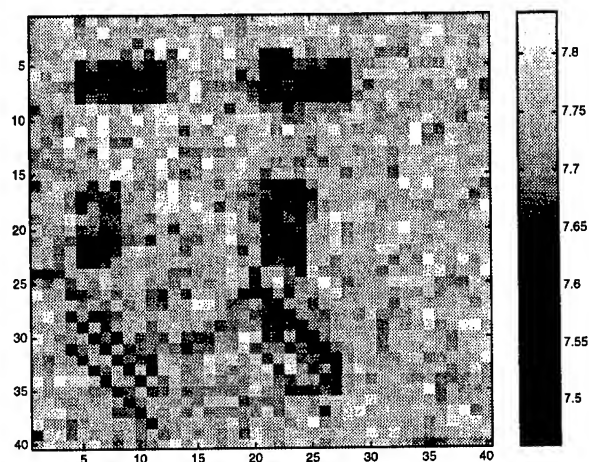


Figure 5 -- Inner product of Target spectra with segmented image bands for Case 2 with noise of 20% of signal.

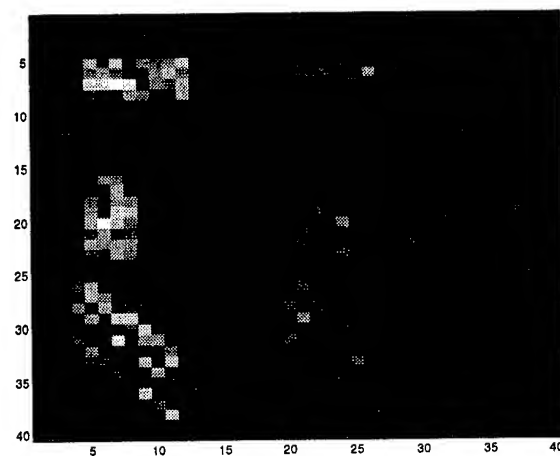


Figure 6 -- Internal energy of neurons for Case 3 with noise of 20% of signal after first firing. Due to the noise many of the target pixels are bright indicating that they will fire in the next time step.

CLASSIFICATION OF HYPERDIMENSIONAL DATA USING DATA FUSION APPROACHES¹

Jon Atli Benediktsson and Johannes R. Sveinsson

Engineering Research Institute
University of Iceland
Hjardarhaga 2-6, 107 Reykjavik, Iceland

ABSTRACT

Statistical classification methods based on consensus from several data sources are considered with respect to classification and feature extraction of hyperdimensional data. The consensus theoretic methods need weighting mechanisms to control the influence of each data source in the combined classification. The weights are optimized in order to improve the combined classification accuracies. Decision boundary feature extraction is considered as a preprocessing method in the data fusion. Consensus theory optimized with neural networks outperforms all other methods in terms of test accuracies in the experiments.

1. INTRODUCTION

The purpose of this paper is to discuss new classification approaches for hyperdimensional data and give experimental results in classification of AVIRIS (Airborne Visible-Infrared Imaging Spectrometer) data from Iceland 1991. The AVIRIS sensor has 224 data channels and generates a vast amount of data. A problem with using conventional multivariate statistical approaches for classification of hyperdimensional data such as the AVIRIS data is that these methods rely on having nonsingular class-specific covariance matrices for all classes. However, estimates of class-specific covariance matrices may be singular in hyperdimensional cases when limited training samples are available. To overcome this problem statistical methods based on consensus theory will be applied. Such methods have shown potential in classification of data from multiple sources [1]. In order to apply consensus theoretic methods in classification of hyperdimensional data, the data need to be split into several "data sources." The data sources can, e.g., be data from a specific spectral range. Each data source is of lower dimension than the original data, and, therefore, the singularity problems with the multivariate classification approaches will be overcome.

Here we also investigate using decision boundary feature extraction to lower the dimensionality of the data sources even further. When the consensus theoretic approaches are applied, the discriminative information from the individual data sources needs to be weighted or optimized.

In this paper optimized consensus theory is discussed and applied in classification of hyperdimensional data. First, consensus theory is reviewed in Section 2. Then, weight selection schemes in consensus theory are discussed in Section 3. Decision boundary feature extraction is briefly reviewed in Section 4. Finally, experimental results are given in Section 5.

2. CONSENSUS THEORY

Several consensus theoretic combination formulas (consensus rules) have been proposed [1]. Probably the most commonly used consensus rule is the linear opinion pool (LOP) which has the following (group probability) form for the information class ω_j if n data sources are used:

$$C_j(Z) = \sum_{i=1}^n \lambda_i p(\omega_j | z_i) \quad (1)$$

where $Z = [z_1, \dots, z_n]$ is a compound vector consisting of observations from all the data sources, $p(\omega_j | z_i)$ is a source-specific posterior probability and λ_i 's ($i = 1, \dots, n$) are source-specific weights which control the relative influence of the data sources. The weights are associated with the sources in the global membership function to express quantitatively the goodness of each source [1].

The linear opinion pool, though simple, has several weaknesses [1]. Another consensus rule, the logarithmic opinion pool (LOGP), has been proposed to overcome some of the problems with the linear opinion pool. The logarithmic opinion pool [1] can be described by

$$L_j(Z) = \prod_{i=1}^n p(\omega_j | z_i)^{\lambda_i} \quad (2)$$

¹This research is supported in part by the Icelandic Research Council and the Research Fund of the University of Iceland.

Table 1: Training and Test Samples for Information Classes in the Experiment on the AVIRIS data.

Class #	Information Class	Training Size	Test Size
1	Andesite Lava from 1991	1659	1511
2	Andesite Lava from 1980	1182	1162
3	Andesite Lava from 1970	978	922
4	Old Unvegetated Andesite Lava	2562	2444
5	Andesite Lava with Sparse Moss Cover	1008	1008
6	Andesite Lava with Moss Cover	528	495
7	Andesite Lava with Thick Moss Cover	2863	2733
8	Lichen Covered Basalt Lava	1674	1023
9	Rhyolite	202	202
10	Hyaloclastite	2062	1979
11	Scoria	275	275
12	Lava Covered with Tephra and Scoria	350	350
13	Volcanic Tephra	1654	1608
14	Snow	528	484
15	Firn and Glacier Ice	242	216
Total		17767	16412

or

$$\log(L_j(Z)) = \sum_{i=1}^n \lambda_i \log(p(\omega_j|z_i)). \quad (3)$$

3. WEIGHT SELECTION SCHEMES

The weight selection schemes in consensus theory should reflect the goodness of the separate input data sources, i.e., relatively high weights should be given to data sources that contribute to high accuracy. There are at least two potential weight selection schemes. The first scheme is to select the weights such that they weight the individual stages but not the classes within the stages, e.g., use heuristic measures which rank the data sources according to their goodness. These heuristic measures might be, e.g., stage-specific classification accuracy of training data, overall separability or equivocation [1].

The second scheme is to choose the weights such that they not only weight the individual stages but also the classes within the stages. This scheme consists of defining a linear or non-linear function

$$Y = f(X, \Lambda) \quad (4)$$

where X contains source-specific posteriori discriminative information and Λ corresponds to the source-specific weights in (1) and (3). In our application, f will be estimated by a neural network.

4. DECISION BOUNDARY FEATURE EXTRACTION

In [2] it was shown that discriminantly informative features and discriminantly redundant features are related to and can be extracted from the decision boundary. Also, by considering the *effective decision boundary* only, the number of features can be significantly reduced while achieving

almost the same classification accuracy. Here it is of interest to see how well the consensus theoretic classifiers perform when decision boundary feature extraction is applied to the individual data sources.

5. EXPERIMENTAL RESULTS

The test area is the region surrounding the volcano Hekla in Iceland. Hekla is one of the most active volcanos in Iceland. It sits on the western margin of the Eastern volcanic zone in South Iceland. Hekla is a ridge, built by repeated eruptions on a volcanic fissure and reaches about 1500 m elevation and about 1000 m above the surroundings. AVIRIS data from the area were collected on June 17th 1991, which was a cloud-free day in the area covered. Fifteen information classes were defined in the area, and 34179 samples were selected from the classes [3],[4]. Approximately 50% of the reference samples were used for training, and the rest were used to test the data analysis algorithms (see Table 1).

The data were assumed to be Gaussian distributed. In order to use the consensus theoretic algorithms, the data had to be subdivided into two or more independent "data sources." The correlations between the spectral channels were computed and based on them it was determined that three data sources should be used in the consensus theoretic classification. Data source number one consisted of 53 data channels, data source number two of 52 data channels and data source number three of 50 data channels. The individual data sources were DBFE transformed and the transformed data channels that accounted for about 99% accumulated eigenvalues were used as the data sources in the consensus theoretic classification. After the DBFE transformation, data source number 1 consisted of 36 channels, data source number 2 of 38 channels and data source number 3 of 34 channels. Thus, by applying the DBFE as a preprocessing method, the individual data sources were reduced by 6 to 17 data channels.

The information classes were modeled by the Gaussian distribution for all the data sources. The classification accuracies for the data sources using the ML approach are listed in Table 2. There it can be seen that the DBFE transformation strongly affected the classification accuracies for all the sources.

The training classification accuracies were used to select a *heuristic* weighting for the LOGP and LOGP-DBFE. The *heuristic* weights were selected as 0.45 for source number one, 0.4 for source number two, and 0.35 for source number three.

Several different classification methods were applied on the original data (157 data channels) [3],[4] and compared to the LOGP and LOGP-DBFE. The statistical classification methods were the Minimum Euclidean distance (MED) and the Gaussian ML method [5]. These methods

Table 2: Overall Training and Test Accuracies for ML Classification Methods Applied to the individual original and DBFE transformed data sources for the AVIRIS Data Set.

Method	Training Accuracy	Test Accuracy
Source # 1 (53 channels)	98.2%	86.2%
Source # 2 (52 channels)	95.7%	75.2%
Source # 3 (40 channels)	90.9%	68.7%
Source # 1 (DBFE) (36 channels)	69.1%	67.4%
Source # 2 (DBFE) (38 channels)	59.2%	53.7%
Source # 3 (DBFE) (34 channels)	47.2%	42.2%
Number of Samples	17767	16412

were also compared to conjugate gradient perceptron with 40 hidden neurons (CGP40) and conjugate gradient perceptron with no hidden layer (CGP0). The summarized training and test classification results are listed in Table 3. There it can be seen that the ML approach outperformed all other methods in terms of classification accuracies of training data. On the other hand, the neural network and consensus theoretic classifiers were more successful in terms of test accuracies. The LOGP methods showed excellent improvement in terms of test accuracies when compared to the single source classifications in Table 2. The LOGP optimized with the CGP0 achieved the highest test accuracies in this experiment and outperformed the ML classifier by more than 10%. The LOGP optimized with CGP40 also achieved excellent test accuracies but this approach was much slower in training than the one that used CGP0. The classification accuracies obtained by using equal and heuristic weights were also very good for the LOGP. In contrast, the LOGP-DBFE accuracies were significantly lower than their LOGP counterparts. Such results were expected after obtaining the low accuracies in Table 2. The results in this experiment indicate that feature extraction may not be appropriate when consensus theoretic classifiers are applied for data fusion.

6. CONCLUSION

The results presented here demonstrate that consensus theoretic classification methods are desirable alternatives to conventional classification methods when hyperdimensional data, such as AVIRIS data, are analyzed. Consensus theory overcomes two of the problems with the conventional ML method. First, using a subset of the data for individual data sources lightens the computational burden of a multivariate statistical classifier. Second, a smaller

Table 3: Summarized Overall Training and Test Accuracies for the Classification Methods Applied to the AVIRIS Data Set.

Method	Training Accuracy	Test Accuracy
ML (157 channels)	100.0%	82.2%
MED (157 channels)	68.0%	62.2%
CGP40 (157 channels)	95.7%	85.4%
CGP0 (157 channels)	90.1%	78.9%
LOGP (Equal Weights)	99.7%	93.0%
LOGP (Heuristic Weights)	99.7%	93.0%
LOGP (Optimized with CGP40)	94.3%	91.0%
LOGP (Optimized with CGP0)	97.4%	93.9%
LOGP-DBFE (Equal Weights)	74.8%	70.6%
LOGP-DBFE (Heuristic Weights)	74.6%	71.9%
LOGP-DBFE (Optimized with CGP40)	80.2%	79.8%
LOGP-DBFE (Optimized with CGP0)	79.3%	79.1%
Number of Samples	17767	16412

data set should also help in providing better statistics for the individual sources when the same number of samples are used as for the original data. Here, the individual data sources were reduced further by using DBFE feature extraction. However, the results using DBFE were much lower in terms of accuracies than the results obtained on the untransformed data.

7. REFERENCES

- [1] J.A. Benediktsson and Philip H. Swain, "Consensus Theoretic Classification Methods," *IEEE Transactions on Systems Man and Cybernetics*, vol. 22, no. 4, pp. 688-704, July/August 1992.
- [2] C. Lee and D.A. Landgrebe, "Feature Extraction Based on Decision Boundaries," *IEEE Transactions on Pattern Analysis and Machine Intelligence*, vol. 15, no. 4, pp. 388-400, April 1993.
- [3] J.A. Benediktsson, K. Arnason, A. Hjartarson and D.A. Landgrebe, "Classification and Feature Extraction with Enhanced Statistics," *Proceedings of IGARSS'96*, pp. 414-416, Lincoln, Nebraska, May 27-31, 1996.
- [4] J.A. Benediktsson and J.R. Sveinsson, "Optimized Classification of Data from Multiple Sources," *Proceedings of Norsig'96*, pp. 75-78, Espoo, Finland, September 24-27, 1996.
- [5] J.A. Richards, *Remote Sensing Digital Image Analysis*, 2nd Edition, Springer Verlag, New York, N.Y., 1993.

Determination of the Dominant Spatial Modes of Terrestrial Snow Cover Over North America Using Passive Microwave Derived Data

E. LeDrew¹, C. Derksen¹, and B. Goodison²

¹Waterloo Laboratory for Earth Observations ²Climate Research Branch,

Department of Geography

University of Waterloo

Waterloo, ON, Canada, N2L 3G1

Phone: (519) 888-4567 Ext. 2689

Fax: (519) 888-6768

email: chris@glenn.uwaterloo.ca

Climate and Atmospheric Research Directorate,

Atmosphere Environment Service,

4905 Dufferin Street,

Downsview, ON, Canada, M3H 5T4

email: Barry.Goodison@ec.gc.ca

Abstract -- Passive microwave derived measures of snow water equivalent (SWE) provide an excellent means of monitoring snow cover because of a broad spatial resolution, daily orbital coverage, and all weather imaging capabilities. Combining analysis of this remotely sensed data with gridded atmospheric pressure and temperature data will allow improvement in our understanding of the complex interactions between seasonal terrestrial snow cover and overlying atmospheric systems. This study utilizes one winter season of Special Sensor Microwave/Imager (SSM/I) passive microwave SWE imagery and National Meteorological Center (NMC) gridded atmospheric data to examine an analysis methodology which utilizes both principal components analysis (PCA) and canonical correlation analysis (CCA) to link surface and atmospheric processes. The short time series was limited by data availability, but is still useful for isolating the strengths and weaknesses of the methodology, which can be applied in the future to the ever increasing time series of SWE imagery. Results show a meridional circulation pattern is linked to periods of snow accumulation, while a zonal circulation pattern corresponds to persistent snow ablation.

INTRODUCTION

The climatic and hydrologic significance of seasonal terrestrial snow cover makes the identification of the dominant modes of snow cover, and linkages to corresponding atmospheric conditions, an important venture. Snow cover has been shown to have considerable local and regional influence on energy exchange through both a high surface albedo and low thermal conductivity [1], and also influences the thickness of overlying air masses. A lack of spring snow cover is significant through the induction of rapid air temperature warming [2]. Unfortunately, the effects of snow cover, or lack of it, at a hemispheric scale are difficult to establish as snow distribution is influenced by large-scale circulation patterns that vary considerably over synoptic time-scales. To compound matters, while snow cover has established seasonal patterns, a single weather event can extend snow lines extensively and modify snow water equivalent [2].

Consistent temporal and spatial snow cover datasets are therefore desired to improve the understanding of climatic feedbacks and linkages. Remote sensing technology can contribute to this need.

Passive microwave technology has improvements over conventional optical remote sensing systems because of all weather, and cloud penetrating imaging capabilities. In this study, we utilize the first release of Special Sensor Microwave/Imager (SSM/I) passive microwave brightness temperatures at a geographic projection which allows snow cover analysis of a study area which has been ground validated. The purpose is to use a short time series of available data to explore a methodology which can later be applied to a multiyear time series. In this study a two step method to identify and isolate relationships between patterns of snow water equivalent and the atmosphere is incorporated. First, rotated principal components analysis (PCA) was used to mathematically simplify the time series of data for each variable. Associations between upper atmospheric patterns and snow cover data were then identified through canonical correlation analysis (CCA) of the derived principal component loadings.

DATA

SSM/I Derived Snow Water Equivalent Data

Northern Hemisphere snow water equivalent (SWE) imagery was derived from SSM/I (Special Scanner Microwave Imager) data available in the EASE (Equal Area SSM/I Earth) Grid projection provided by the National Snow and Ice Data Center, Boulder. Passive microwave data were used for the study as they provide excellent temporal (daily) and adequate spatial (approximately 25 km pixel centres) coverage for snow investigations. From the EASE-Grid projection, a study area encompassing a large portion of the Canadian Prairies and the American Great Plains (approximate area of 1.5 million km², or 30 by 80 = 2400 pixels) was selected (Fig. 1) as this region is frequently subjected to transitional snow events of short ground duration. The Canadian Atmospheric Environment Service dual frequency algorithm was used to derive SWE from passive

microwave brightness temperatures. This algorithm utilizes the vertically polarized 19 and 37 GHz channel brightness temperatures and was developed in conjunction with field work performed in the Canadian Prairies [3].

Data were combined into 17 five day averaged images (pentads) between January 16 and April 9, 1988. A five day temporal resolution was selected to construct a time series of acceptable synoptic sensitivity, while ensuring orbital coverage. The study time period was limited due to the shutdown of the SSM/I sensor between December 2, 1987 and January 15, 1988, while the study area was clear of snow by April 10, 1988. Ascending orbits were used for analysis as brightness temperatures are recorded in the morning and thereby lessen the influence of melt.

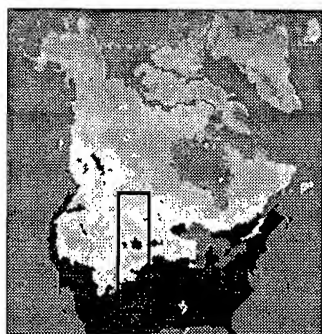


Fig. 1. Prairie study area.

National Meteorological Center Grid Point Upper Atmospheric Circulation Data

Atmospheric data from the National Meteorological Center (NMC, now National Center for Environmental Prediction, NCEP) were used in the analysis. These data are projected onto a 1977 point octagonal grid, with equally spaced data points when viewed polar stereographically. Grid points over the entire North American continent including the Arctic Archipelago and Greenland were used for the principal components analysis to ensure an adequate number of data points created a statistically robust PCA procedure. The North American continental area has a 323 point NMC data coverage (19 by 17). Pentads of 700 millibar (mb) geopotential height (700H) and temperature (700T), 500 mb geopotential height (500H), and 500-700 mb thickness (THK) were created.

METHODOLOGY

Principal Components Analysis

PCA is a technique used to mathematically transform an original data set into a reduced set of uncorrelated variables to represent the majority of the information presented in the original data. This set of uncorrelated variables simplifies time series data analysis by representing the entire data set in a smaller number of images which

proportionally explain the variance within the original time series data. PCA was performed on the SSM/I snow water equivalent and NMC upper atmospheric pentads using SAS, a statistical analysis software package. These data were orthogonally transformed using the varimax rotation method.

Each PCA input matrix was composed of columns for each time series pentad, while SSM/I pixels or NMC grid points comprised the rows. For example, the input matrix for the SWE data was 17 columns by 2400 rows. PCA was performed using a correlation matrix approach as opposed to a covariance matrix as discussion has shown this method to be advantageous in synoptic climatological applications [4]. The first three components for each variable were subjectively retained for CCA analysis. In all cases, variance explained by component 3 was just below or greater than 10% while the variance explained by component 4 dropped to near 1% making this an obvious cutoff. While tests for component selection do exist [4], components can fail selection tests and still track a geophysical process that occurs through the presence of noise and therefore, can still be relevant [5].

Canonical Correlation Analysis

In essence, CCA replaces a series of linear regressions of each pattern in one variable set with those of another by a single procedure that considers multiple variables in each of the two data sets. CCA was performed on the rotated principal component loadings of snow cover and each atmospheric variable, producing a series of canonical scores. These scores indicate the strength or weakness of the relationship between the dominant patterns of SWE and related atmospheric circulation patterns. CCA was only performed on the retained component loadings so the first three SWE components were correlated against the loadings from the first three atmospheric components. The SAS statistical analysis software package was used to perform the CCA.

RESULTS

Results of the PCA (Table 1) for the SWE data indicate that the first three components combine for over 90% of the variance in the original data. After these first three components, variance explained drops below an acceptable level and predominantly expresses data noise. Results of the PCA of the atmospheric data indicate that the majority of the variance in all of the upper atmospheric data can be also be explained by the first three principal components (Table 1).

SWE PC1 characterizes snow cover maximum, PC2 isolates snow cover minimum, while PC3 shows a transitional state. The first atmospheric components all characterize a zonal circulation pattern, while PC2 shows meridional flow.

Canonical Correlation Analysis

Space limitations do not allow for presentation of extended CCA results, but cross loadings, or correlations between original variables (in this case, SWE) and the canonical variates of the opposite set (atmospheric variables), and are given for all combinations of SWE and atmospheric data in Table 2.

Results of the CCA indicate strong positive associations between a meridional atmospheric circulation pattern at both the 500 and 700 mb geopotential height levels with ridging over the western cordillera and SWE component 1 which is the pattern of snow cover maximum. This meridional pattern allows for the penetration of systems of Arctic and North Pacific origin over the central plains and is clearly the pattern of greatest moisture advection. 700T component 2 also cross loads strongly to SWE component 1 and the time series data that loads highly to 700T component 1 shows generally colder air temperatures over the majority of the study area than characteristic conditions that load strongly to 700T component 2.

CCA cross loadings also reveal a relationship between the zonal pressure and temperature distribution pattern as characterized by the first components of 500H, 700H, and 700T, and snow cover minimum (SWE component 2). This zonal pattern constrains Arctic air masses and associated temperatures in the north allowing moderating temperatures and snow ablation to dominate the study region under predominantly westerly air flow.

CONCLUSIONS

In this paper we have restricted the analysis to the first two spatial modes in the aerological and SWE data to demonstrate the feasibility of the approach for examining snow cover processes at the synoptic scale. The results of the first two components are logical and consistent. A meridional flow over the Great Plains is associated with

the pattern of maximum extent in the snow water equivalent, whilst a zonal flow is associated with minimum extent. These two modes are the major components in the variance fields.

More insight into the nature of the linkages must await further analysis of several years of data which will allow lag analysis to be applied with confidence. The intent is to develop a climatology of atmosphere - snow water equivalent comparable to that which exists for atmosphere - sea ice variability and change. The constraint is the validation of the SWE algorithms for which we have confidence only over the Great Plains.

ACKNOWLEDGMENTS

Thanks to Joe Piwowar, Mike Wulder, and Kevin Misurak for assistance with data preparation.

REFERENCES

- [1] J. Walsh "Snow cover and atmospheric variability," Am. Scient., vol. 72(1), pp. 50-57, 1984.
- [2] T. Davies, "Snow cover -- atmosphere interactions," International Association of Hydrological Sciences Publication 223 (Symposium at Yokohama 1993 -- Snow and Ice Covers: Interactions with Atmosphere and Ecosystems), pp. 3-13, 1994.
- [3] B. Goodison, "Determination of areal snow water equivalent on the Canadian Prairies using passive microwave satellite data," in Proceedings, IGARSS'89, vol. 3; pp. 1243-1246, 1989.
- [4] J. Overland, and R. Preisendorfer. "A significance test for principal components applied to a cyclone climatology," Mon. Weath. Rev., vol. 110(1), pp. 1-4, 1982.
- [5] R. Preisendorfer and T. Barnett. "Significance tests for empirical orthogonal functions," Fifth Conference on Probability and Statistics in Atmospheric Society, pp. 169-172, 1977.

Table 1. Percent variance explained by retained principal components.

Component	SWE	500H	700H	THK	700T
1	42.6	27.3	33.1	29.2	36.8
2	40.2	22.4	21.4	26.5	33.9
3	9.6	12.6	13.78	16.8	11.3

Table 2. CCA cross loadings.

	SWE1	SWE2	SWE3		SWE1	SWE2	SWE3
500H1	-0.52	0.52	-0.02	700H1	-0.64	0.34	0.21
500H2	0.86	0.19	-0.09	700H2	0.69	0.02	0.26
500H3	-0.15	-0.31	-0.32	700H3	0.05	0.28	-0.37
THK1	0.75	0.24	0.03	700T1	-0.59	0.22	-0.12
THK2	-0.55	0.17	0.17	700T2	0.85	0.02	0.05
THK3	-0.58	-0.06	-0.06	700T3	-0.73	0.23	0.07

Microwave Measurements of Sea Ice in the Kara and Laptev Sea

Klaus-Peter Johnsen, Andrei Darovskikh¹, Georg Heygster, Andreas Wiesmann²
Institute of Environmental Physics, University of Bremen, D-28334 Bremen, Germany

¹Arctic and Antarctic Research Institute, St. Petersburg, Russia

²Institute of Applied Physics, University of Bern, Switzerland

Tel.: +49 421 218-2584, Fax: -4555, E-mail: johnsen@diana.physik.uni-bremen.de

Abstract - Radiometric measurements made during the Arctic-expedition ARK 12 of R.V. Polarstern in the Kara and Laptev Sea which took place from 12th July to 23th September 1996 are obtained using three Dicke Radiometers from the University of Bern (Switzerland) mounted on a sledge operating at 11, 21 and 35 GHz and measuring in horizontal and vertical polarization with incidence angles between 20 and 70 degrees. The observed brightness temperatures show a strong correlation with the snow thickness. The size of the snow grains is also important. Some examples of the data set are compared to a combined radiative transfer-strong fluctuation theory approach using a layer model describing the sea ice and calculating the emissivities of both polarizations.

INTRODUCTION

Remote sensing of the polar regions has significantly increased our understanding of sea ice extent and variability [8]. Sea ice is a mixture of ice crystals, brine and air and forms a complex structure depending on the conditions of growth. The concentration of brine and air has the major influence on the dielectric constant of ice. The most important parameters of the snow are the sizes of the snow grains, the density and the content of free water as shown theoretically [1,3]. Different snow grain sizes or contents of free water effect the degree of volume scattering within the snow. The upper layers of the sea ice determine the scattering.

Increasing free water content in the snow decreases the scattering contribution to the emissivity because the penetration depth decreases. This also decreases the gradient ratio GR(37h,19h) defined as

$$GR(37h,19h) = \frac{T_B(37h) - T_B(19h)}{T_B(37h) + T_B(19h)}. \quad (1)$$

Reference [9] has compared the gradient ratio of the SSM/I and snow thicknesses measured at different sites over Antarctic sea ice and has shown that it decreases also with increasing snow depth.

Our ground based measurements of the brightness temperature of snow over old ice in the Siberian Arctic show a clearly defined increase of the brightness temperature with the snow thickness within the first 25 cm of the snow cover. This is explained by absorption in the snow.

MEASUREMENT SITES AND CONDUCTION OF RADIOMETER MEASUREMENTS

The microwave instrumentation used during the ARKTIC 96 experiment consisted of three portable, linearly polarized Dicke radiometers at frequencies of 11, 21 and 35 GHz. The radiometer antennas are rectangular standard gain horns at 21 and 35 and a Picket-Horn at 11 GHz, respectively. The radiometers were mounted on a sledge which easily allowed variation of incidence angle from 10 to 180 degrees and change of polarization.

During the entire duration of the expedition snow covered the ice-floes. We used level parts of old ice floes to obtain clearly defined brightness temperatures. Thus, the error of the incidence angle is low, approx. 2° which results in a small error in the measured brightness temperature (approx. 0.5 K). The incidence angle was 50° to allow comparison with satellite data (SSM/I: 51.7°).

To calibrate the radiometers before and after every profile measurement a blackbody as hot load and the sky as cold load were used. Samples were taken to analyse the sizes of the snow grains, the temperature and the salinity. The sky temperature was calculated from measurements at two different incidence angles based on the assumption of a plane-parallel atmosphere according to the tipping-curve-method [2] to calibrate the radiometers.

Measurements of brightness temperatures and snow depths were taken at profiles of different length. Here we present two longer profiles with 74 and 100 points every 53 cm with different snow properties. The first was carried out on the 2nd of September at 132° 49.4' E and 78° 49.2' N (station 246), the second on the 3rd of September at 132° 39.9' E and 78° 27.0' N (station 247) in the Laptev Sea. The floe diameter was approximately 3–5 km at station 246 and 6 km at station 247. No melt ponds were visible [4].

Polarization Differences

The polarization differences decrease with greater snow thickness (Fig. 1). This can be explained qualitatively by the isotropic geometry of snow grains compared with the ellipsoidal brine pockets in the ice. Thus the snow acts as a depolarising medium. If the snow thickness is greater, the influence of the underlying ice layer on the brightness temperature decreases. The penetration depth for the higher frequency (35 GHz) is lower than for the lower frequency, thus

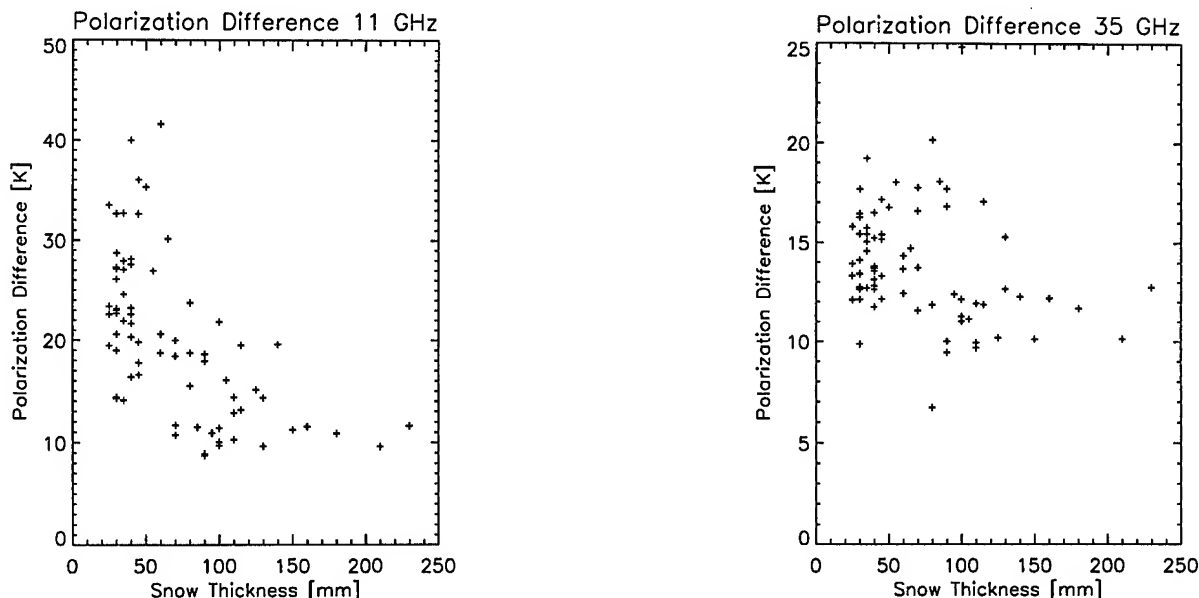


Figure 1: Polarization Differences for the measurements at the frequencies 11 and 35 GHz from the 3rd of September 1996, measured on an old ice floe in the Laptev Sea at $132^{\circ} 49.4' E$ and $78^{\circ} 49.2' N$ (station 247)

the depolarizing influence of the snow is greater for higher frequencies. At lower snow thicknesses, the polarization difference is also lower for higher frequencies. For greater snow thicknesses the difference between the polarization differences of two frequencies decreases (the polarization differences are approximately 10 K for 230 mm snow thickness) because the influence of the underlying ice layer is very small.

Gradient ratio versus snow thickness

Fig. 3 shows that in the Siberian Arctic the gradient ratio $GR(35h,21h)$ increases with the snow depth. In contrast to this, [9] obtained from Antarctic measurements a linear regression decreasing with $GR(37h,21h)$:

$$H_{\text{snow}} = 1.5 - 953GR(37h, 19h). \quad (2)$$

If we neglect the slight differences in the frequencies of the GR, a possible, qualitative explanation of this discrepancy could be different contributions of scattering and absorption in the snow to the emitted signal: while our measurements were taken in the Arctic summer with temperatures between -4 and $-2^{\circ} C$, where the free water content of the snow increases the emissivity, the measurements of [9] were taken in the Antarctic with lower temperatures where the influence of the free water content is smaller. Comparison of the scattering contributions of the measurements from the 2nd and 3rd of September as calculated with the strong fluctuation theory [3] show that the gradient ratio decreases if the scattering increases. See Fig. 2 for the comparison between the measurements and the results of the strong fluctuation theory.

CONCLUSIONS

The passive microwave measurements on second year ice in the Siberian Arctic at 11, 21 and 35 GHz during summer can qualitatively be explained by absorption of the snow. This causes an increase of the emissivity, brightness temperature and the gradient ratio calculated from the 35 and 21 GHz horizontal polarized channels (Fig. 3) with the snow thickness.

Calculations with the strong fluctuation theory [3] have shown that an increasing free water content decreases the volume scattering in the snow and increases the brightness temperature. We conclude that the free water content at station 246 was very low (model value: 0 %) while at station 247 it reached approximately 0.5 %.

Altogether our measurements in the Siberian Arctic have shown two effects which increase the brightness temperature T_B (increasing snow thickness and increasing free water content) while the volume scattering in dry snow decreases T_B .

The situation observed during the summer of 1996 in the study area with a remaining snow cover of up to 30 cm thickness is rather unusual compared with long-term climatological records [6]. Given the importance of the snow cover for the surface energy balance as well as the thickness evolution of level ice [5], the disappearance or persistence of the snow at the sea ice surface during summer may be of wider interest. Such snow cover effects may at least in part be retrieved from passive microwave data based on the demonstrated effects of the snow on the surface emissivity.

REFERENCES

- [1] A.Stogryn. A study of the microwave brightness temperature of snow from the point of view of strong fluctuation theory. *IEEE Tr.Geosc.and Rem.Sens.*, GE-24:220-231,

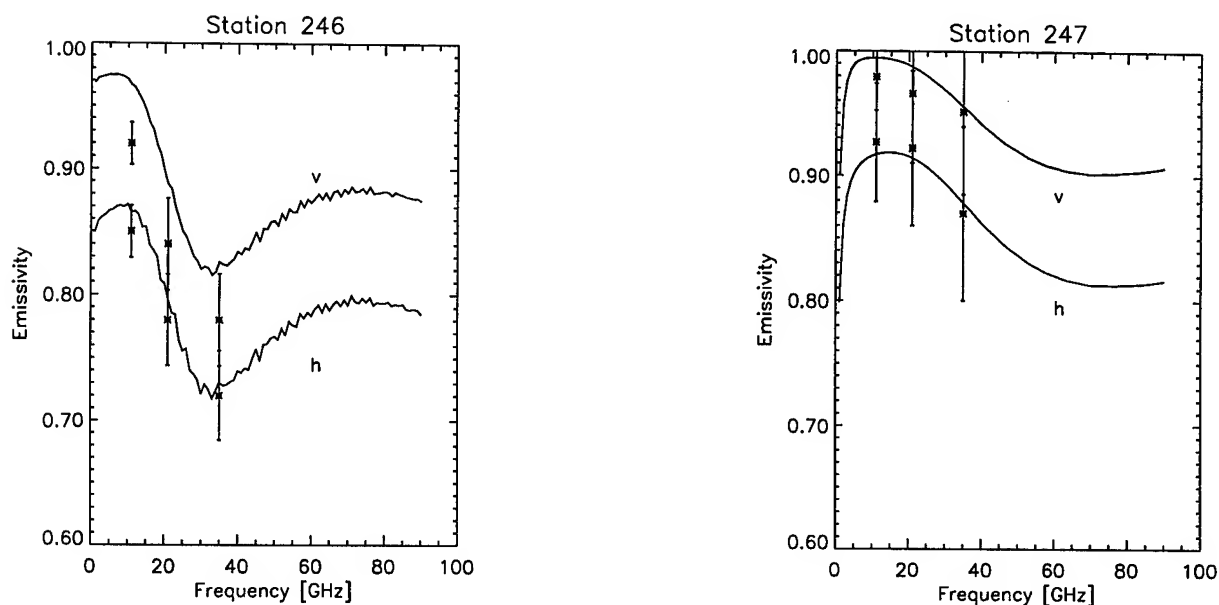


Figure 2: Emissivities calculated with the strong fluctuation theory for the microwave measurement of the stations 246 and 247 (2nd and 3rd of September, resp.). The parameters are taken from the samples. v: vertical polarization, h: horizontal polarization.

- 1986.
- [2] C.Maetzler. Ground-based Observations of atmospheric radiation at 5, 10, 21, 35 and 94 GHz. *Radio Science*, 27(3):403–415, 1992.
 - [3] R.Fuhrhop T.C.Grenfell G.Heygster K.-P.Johnsen P.Schlüssel M.Schrader C.Simmer. A combined radiative transfer model for sea ice, open ocean, and atmosphere. *Submitted to Radio Science*, 1997.
 - [4] M. Lensu C. Haas F. Cottier C. Friedrich J. Weissenberger K.Abrahamsson A. Ekdahl A. Darovskikh and K.-P. Johnsen. *Arctic '96: Polarstern Ice Station Report*, volume M-214. Helsinki University of Technology, 1996.
 - [5] G.A.Maykut. The surface heat and mass balance. In N. Untersteiner, editor, *The geophysics of sea ice*, pages 395–463. Martinus Nijhoff Publ., Dordrecht (NATO ASI B146), 1986.
 - [6] K.-P.Johnsen A.Darovskikh A.Wiesmann H.Eicken and C.Haas. Ground-based microwave radiometer measurements over snow-covered sea ice in the Siberian Arctic. *Submitted to Polarforschung*, 1997.
 - [7] I.P.Romanov. *Ice cover of the Arctic Basin*. St.Petersburg, 1993.
 - [8] W.B.Tucker D.K.Perovich A.J.Gow W.F. Weeks M.R.Drinkwater. Physical properties of sea ice relevant to remote sensing. In F.D.Carsey, editor, *Microwave Remote Sensing of Sea Ice Geophysical Monograph*, volume 68. 1992.
 - [9] T.Markus and D.J.Cavaliere. Snow depth distribution over sea ice in the southern ocean from satellite passive microwave data. In M. Jeffries, editor, *Submitted to AGU Antarctic Research Series*. American Geophysical Union, 1996.

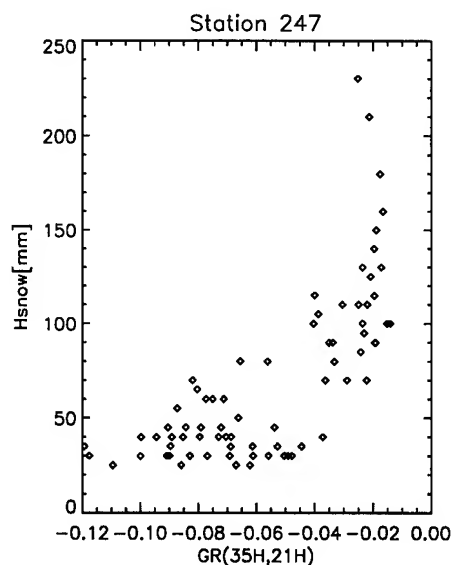


Figure 3: Gradient ratio versus snow thickness for the radiometric measurements from the 3rd of September (station 247)

First Realtime Use of RADARSAT SAR Imagery for Ship Navigation in Antarctica

P. Danduran[†], M. C. Mouchot[†], R. Garelo[†] D. Fleury[†], I. Thépaut[‡]

[†]Ecole Nationale Supérieure des Télécommunications de Bretagne, Dpt. ITI

Technopole de Brest-Iroise - BP 832 - 29285 Brest Cedex - France

Tél: (+33) 2 98 00 10 94, Fax: (+33) 2 98 00 10 98

E-mail: {Patrice.Danduran, MC.Mouchot, Rene.Garelo}@enst-bretagne.fr

[‡]Institut Français pour la Recherche et la Technologie Polaires

Technopole de Brest-Iroise, BP 75 - 29285 Plouzané Cedex - France

Tél: (+33) 2 98 05 65 04, Fax: (+33) 2 98 05 65 55

E-mail: Isabelle.Thepaut@ifrtp.ifremer.fr

Abstract – In polar regions, navigation strongly depends on ice conditions which can be defined by ice types and ice concentration. For a long time, satellite imagery, specially AVHRR and SAR data, has been providing such information. Henceforth, until now the availability of SAR images for ship navigation in Antarctica was not sufficient for this data to be used in a realtime approach. However, due to its onboard recorder, the Canadian satellite, RADARSAT, can acquire images over Antarctica on a regular basis. The experiment presented in this paper investigates its potential for ship routing to Antarctica and, in particular, towards the Dumont d'Urville French Polar Station.

INTRODUCTION

Every year, from October to March, the French Polar Institute (Institut Français pour la Recherche et la Technologie Polaires - IFRTP) needs to convoy staff and material by ship down to the Dumont d'Urville French Polar Station (Antarctica). In order to optimize its route, the polar vessel "*L'Astrolabe*" requires information about ice types and ice concentration. Satellite imagery allows us to retrieve this kind of information using various sensors in several acquisition modes [1], [2], [3]. Due to ice variability over the area, the acquired information is obsolete after a period of about one day. It is then mandatory to be able to process the acquired information and forward it to the ship in this time frame.

In the northern hemisphere, SAR imagery has been used for a long time to monitor ice conditions and, thus, to help ship navigation. In the southern one, the space-time coverage provided by the ERS-1 and JERS-1 satellites did not permit such intensive use of SAR data. In particular, the area of Dumont d'Urville (65° 40' S, 140° 01' E) was not covered by these satellites due to the lack of an operational receiving station. Therefore, the IFRTP decided to use AVHRR imagery because of its daily coverage over the area of interest. A receiving station was then installed on the premises of the Polar Station. However, since the launch of the Canadian satellite,

RADARSAT, in late 1995, users have at their disposal a more complete radar coverage of Antarctica. That is the reason why the IFRTP decided to investigate the eventual realtime use of RADARSAT images.

RADARSAT CHOICE

Until now and in order to optimize the route of its polar vessel "*L'Astrolabe*", the IFRTP has been using images acquired by the spaceborne AVHRR radiometer (NOAA satellites). This kind of data allows the retrieval of ice temperature. However, AVHRR sensors suffer from several disadvantages. Firstly, in comparison to SAR, they provide coarse pixel resolution of about 1 km at nadir but exceeding 3 km for the highest incidence angles. In addition, acquisition wavelengths, from visible to thermic infrared, do not allow the AVHRR sensor, unlike to SAR, to acquire data during cloudy days or bad illumination conditions [4]. For instance, among the 34 AVHRR images received from the IFRTP during October only 6 can be used. Moreover, although they possess a less wide swath than AVHRR data (500 km versus 2800 km), SAR provide a much better pixel resolution.

Our goal was then to investigate the potential of SAR imagery compared to AVHRR data. As previously mentioned, RADARSAT was chosen instead of ERS-1 or JERS-1, which do not provide an adequate space-time coverage. On the other hand, their use can not be considered because of their limited swath range and also of their lack of tape-recorder. Concerning the acquisition mode, the SCANSAR Wide, which has a 100 m pixel resolution, was preferred to the other ones due to its larger swath range (500 km). This one is sufficient to adequately cover the whole area of interest.

EXPERIMENT DESCRIPTION

The experiment took place the 10th and 11th December 1996. It consisted of acquiring SAR data over the Dumont d'Urville Polar Station, retrieving the data at the ENSTB (Ecole Na-

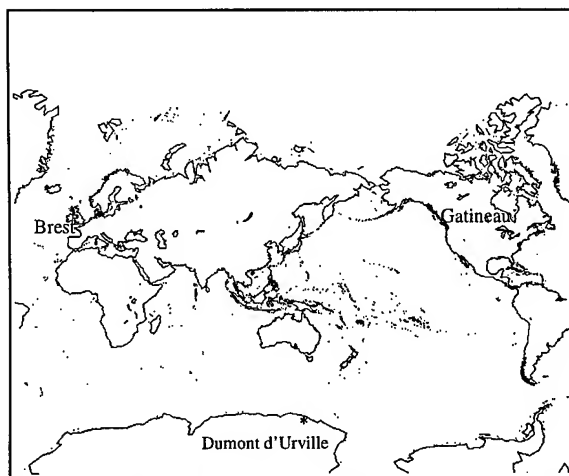


Figure 1: Geographical locations

tionale Supérieure des Télécommunications de Bretagne in Brest, France) which was mandated, by the IFRTP, for the data processing, and then processing and supplying it to the polar vessel "L'Astrolabe" on route to the Dumont d'Urville Polar Station.

By request to RADARSAT International, the data was recorded on board and downloaded to the Gatineau Receiving Station. Six hours after the acquisition by the satellite we started retrieving the image from a ftp server at Gatineau Receiving Station (Canada). In order to minimize the consequences of a ftp connection loss while retrieving the data, the image was split into 5 scenes. This choice made it possible to begin the image processing before receiving the whole data. For each scene, a text file, including georeferencing data, was available. The entire image size was 95 megabytes because the SCANSAR Wide images are supplied at a 50 m pixel resolution. Table 1 and table 2 show the schedule planned for the experiment. Figure 3 shows the acquired image

The retrieving step is strongly dependent of the ftp transfer rate which can vary according to the time of the day. The best transfer rate we obtained was about 3 megabytes per 10 mn,

Planned Schedule	Operation Description
10:38 (10.12.1996)	Image acquisition and storing on the RADARSAT tape-recorder
Acq. + 04:00 (10.12.1996)	Data transmission to Gatineau Receiving Station
Acq. + 06:00 (10.12.1996)	Data processing at Gatineau Receiving Station
about 17:30 (10.12.1996)	Images downloaded to the ftp server of RADARSAT

Table 1: Planned Schedule (Acquisition part).

Planned Time	Operation Description
50 mn per scene	Retrieval of the 5 scenes
30-40 mn per scene	Processing of the 5 scenes (Segmentation and classification)
20-30 mn per scene	Choice and selection of areas of interest
about 15 mn	Images created and sent to the IFRTP

Table 2: Planned Schedule (Processing part).

i.e. about 1 hour for each scene. In addition, several problems, which delayed the retrieval of the images, occurred during the experiment. For instance, we encountered several connection losses and, as previously mentioned, the transfer rate was very low. However, as the ship was not present in the area of interest when we received the image, we decided to transfer the data two days later according to the schedule of the polar vessel.

Before being processed, the 5 scenes were georeferenced using the associated text files. Then, each of them was resampled in order to obtain a 100 m pixel resolution. This permitted the data volume to be divided by 4. Because the acquisition was made at a 50 m pixel resolution, it did not have any consequences for an eventual information loss.

The classification process consists of two steps [5]. The first one provides a segmentation in thousands of regions grouping the pixels according to an homogeneity criterion (σ/μ). This criterion is used in such a way that it describes the local homogeneities of the image. However, among the obtained regions some may have similar characteristics. Therefore, we must use a second criterion, based on the variance σ^2 , to group regions which represent the same ice type. The image was classified into 8 classes according to this criterion. Figure 4 shows the obtained classified image.

The classification process described in this section gave, as a result, a 25 megabytes georeferenced image from which areas of interest for the polar vessel "L'Astrolabe" were extracted. This selection reduced the data to a 9 megabytes georeferenced image which was compressed using "pkzip". Depending on the images the compression rate can vary from 76% to 85%. The resulting 2.5 megabytes georeferenced image was supplied to the IFRTP and transmitted to the ship using an

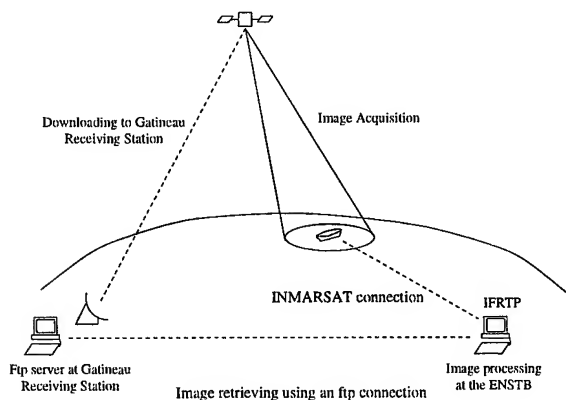


Figure 2: Experiment Scheme.



Figure 3: RADARSAT SAR image acquired on December 10, 1996, at 10:38 UTC over the Dumont d'Urville Polar Station. It shows approximately a 500 km x 500 km area and is centered at 66° 55' S, 143° 59' E.



Figure 4: Classification obtained for the image presented in Fig. 3.

INMARSAT connection. On board, the image was decompressed using "pkunzip" and then visualized. Regarding the time taken for the complete experiment, it strongly depends on the internet and INMARSAT transfer rates. For example, a 19 megabytes scene takes at least 50 mn to be retrieved whereas the INMARSAT transfer rate between the IFRTTP and the ship is about 40 mn for a 2.5 megabytes file. We have also taken into account the processing time, that is about 40 mn for a 19 megabytes file. This includes resampling, georeferencing, segmentation and subsampling. Finally the whole tasks took about 10 hours due to the above mentioned problems.

CONCLUSIONS

The experiment described in this paper demonstrated that sea ice information retrieved from RADARSAT data, once the SAR image is acquired, can be supplied within such a time frame allowing its use for ship navigation in Antarctica i.e. less than one day. Even if the obtained classification was not completely satisfactory, the main difficulty remains to acquire the SAR image during the presence of the ship in the area of interest. In the presented experiment, the polar vessel "L'Astrolabe" reached the area to be imaged by the satellite 3 or 4 days later than expected due to departure delays. When the critical sea ice conditions regions were then reached, the acquired SAR data was no more reliable in comparison to real ice conditions. Operational use of RADARSAT data should then allow more flexibility in the planed acquisition schedule in order to better fit the hazard of ship navigation.

ACKNOWLEDGMENTS

The authors would like to thank all RADARSAT staff at Gatineau Receiving station, specially for their help and

disponibility during the retrieving of the images. We also would like to thank Alain Cavané from the IFREMER (Institut Français pour la Recherche et l'Exploitation de la MER in Brest, France) and Michel Fily from the LGGE (Laboratoire de Glaciologie et Géophysique de l'Environnement in Grenoble, France) for their help concerning the interpretation of the images.

REFERENCES

- [1] B. Ramsay, T. Hirose and al. "Potential of RADARSAT for Sea Ice Applications", Canadian Journal of Remote Sensing.
- [2] B. A. Burns, M. Schmidt-Gröttrup, and T. Viehoff "Methods for Digital Analysis of AVHRR Sea Ice Images", IEEE Transactions on Geoscience and Remote Sensing, Vol. 30, n 3, May 1992.
- [3] J. C. Comiso and R. Kwok "Summer Arctic Ice Concentrations and Characteristics From SAR and SSM/I Data", Proceedings of First ERS-1 Symposium - Space at the Service of our Environment, Cannes, France, 4-6 November 1992.
- [4] D. M. Nazarenko, D. J. Lapp and K. F. Link "Antarctic Satellite Remote Sensing: An information Source for Research and Operational Activities", ISPRS, Commission VII, Rio de Janeiro, 26-30 September 1994.
- [5] A. J. Sephton, L. M. Brown, J. T. Macklin, K. C. Partington, N. J. Veck "Segmentation of Synthetic Aperture Radar Imagery of Sea Ice", International Journal of Remote Sensing, 1994, Vol. 15, n4.

ICEWATCH - REAL-TIME SEA ICE MONITORING OF THE NORTHERN SEA ROUTE USING SATELLITE RADAR TECHNOLOGY

O. M. Johannessen, S. Sandven, L. H. Pettersson, K. Kloster, T. Hamre, J. Solhaug
Nansen Environmental and Remote Sensing Center, Edvard Griegsvei 3a, N-5037 Solheimsvik, Norway
Tel: + 47 55 29 72 88, fax: + 47 55 20 00 50

A. M. Volkov, V. Asmus, O. E. Milekhin, V. A. Krovotyntsev
NPO Planeta, 7 B. Predtechenskii street, Moscow 123 242, Russia
Tel/fax: + 7 095 299 4210

V. D. Grischenko, V. G. Smirnov
Arctic and Antarctic Research Institute, 38 Bering str. 199397 St. Petersburg, Russia
Tel: + 7 812 352 1520 Fax: + 7 812 352 2652

L. P. Bobylev, V. V. Melentyev, V. Alexandrov
Nansen International Environmental and Remote Sensing Center, Korpusnaya Str. 18, 197042 St. Petersburg, Russia
Tel: + 7 812 230 78 37, fax: + 7 812 230 79 94

ABSTRACT

ICEWATCH is the first joint project in earth observation between Russian Space Agency (RKA) and European Space Agency (ESA). The overall objective of the project is to implement satellite monitoring by combined use of ESA ERS SAR, RKA Okean SLR and other remote sensing data to support ice navigation in the Northern Sea Route (NSR), offshore industry and environmental studies. ERS-1 SAR images have been used in ice monitoring of the NSR in several demonstration campaigns since 1991. The experience from use of SAR data onboard Russian icebreakers to assist in ice navigation is very positive although ERS-1 can only provide data in selected parts of the NSR with a limited swath width of 100 km. In the ICEWATCH project a concept for integrating ERS SAR data in the Russian ice monitoring service is demonstrated where Okean SLR data are included. The system is currently tested in pilot demonstration phase before it is planned to become operational. In addition to data acquisition and interpretation techniques for data integration, ice classification and data transmission techniques have been tested. Also user requirements have been investigated, suggesting that there are many new and potential users of SAR ice information in the NSR. In future other radar satellites will also be used such as ESA ENVISAT which will be launched in 1999. The first results of ICEWATCH were presented at the Second ERS Applications Workshop in London in December 1995 [1].

2. BACKGROUND

The NSR is the sailing route along the coast north of Russia between the Barents Sea and the Bering Strait. In ICEWATCH we have concentrated the studies to the western part of the NSR which includes the Barents and Kara Sea (Fig. 1). The ice conditions in this region restrict

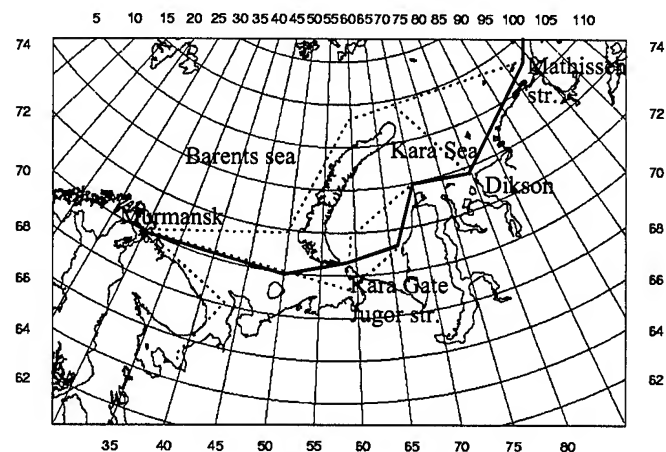


Figure 1. Map showing alternative sailing routes in the western part of the Northern Sea Route, between Murmansk, Dikson and Mathiessen Strait. The bold line is the most frequently used route if ice conditions permit.

sea transportation which requires ice class vessels as well as icebreaker assistance throughout the year. In summer there is traffic in the whole sailing route, whereas in winter it is mainly the western part which is used serving the ports on the Yenisei River. An extensive ice monitoring and forecasting service has been built up in Russia over the last 50 years to serve the sea transportation and icebreaker operations in the NSR. The service is based on data collection from ice stations, coastal stations, vessels, aircraft and satellites. But use of spaceborne SAR has not been a routine part of this service.

The Nansen Environmental and Remote Sensing Center in Bergen, Norway first demonstrated use of ERS-1 SAR data for near real-time ice mapping in the NSR in August 1991,

only a few weeks after the launch of the ERS-1 satellite. SAR derived sea ice maps were then sent by telefax to the French polar vessel *L'Astrolabe* during her voyage through the Northeast Passage from Norway to Japan [4]. Since 1993 SAR ice monitoring demonstrations have been carried out by the Nansen Centers in Bergen and St. Petersburg on several Russian icebreakers. In all these demonstration experiments, a scientist from the Nansen Center in St. Petersburg stayed onboard the icebreakers and analyzed the SAR images in cooperation with the captain and ice pilots [2] and [3]. In addition to supporting ice navigation these experiments also had scientific objectives to study various ice processes and phenomena and their SAR signature. Several hundred ERS SAR scenes have been obtained showing the different stages and conditions of ice in the NSR. Fig. 2 shows an example of an annotated SAR image of different young and new ice types from the freeze-up season in the southern Kara Sea. The ICEWATCH project started officially in August 1995 after signature of agreement between ESA, Russian Space Agency and the participating institutes.

3. PROJECT TASKS

The six major tasks in ICEWATCH are 1. Study of ERS SAR backscatter characteristics of different ice types in the NSR; 2. Implementation and improvement of methods and algorithms for processing, classification and interpretation of radar data; 3. Development of techniques for combined processing and use of ERS SAR and Okean SLR data; 4. Development of a scheme for polar ice radar monitoring, including study of user requirements, infrastructure and necessary equipment installation; 5. Application demonstration of radar ice monitoring for Murmansk Shipping Company icebreakers including cost benefit assessment; and 6. Recommendation for a real-time operational information system using satellite radar data.

Task 1: Radar backscatter studies of sea in the NSR.

Examples of ERS SAR images were analyzed and interpreted for a number of characteristic ice conditions in the NSR. The ERS images demonstrated good capability to distinguish between the main ice types in the NSR such as multiyear ice, firstyear ice, young ice and new-frozen ice. Different classes, forms and features of ice can also be identified such as fast ice, drifting ice, river ice, shear zones, leads, polynyas, ice topography (ridges and hummocks) and ice edge processes. However, in many cases the SAR backscatter data are ambiguous and it is difficult to classify ice the types correctly without additional data. This is particularly the problem for identification of various stages of young ice and firstyear ice, for quantification of surface roughness and to distinguish ice and open water during melt conditions. In spite of some

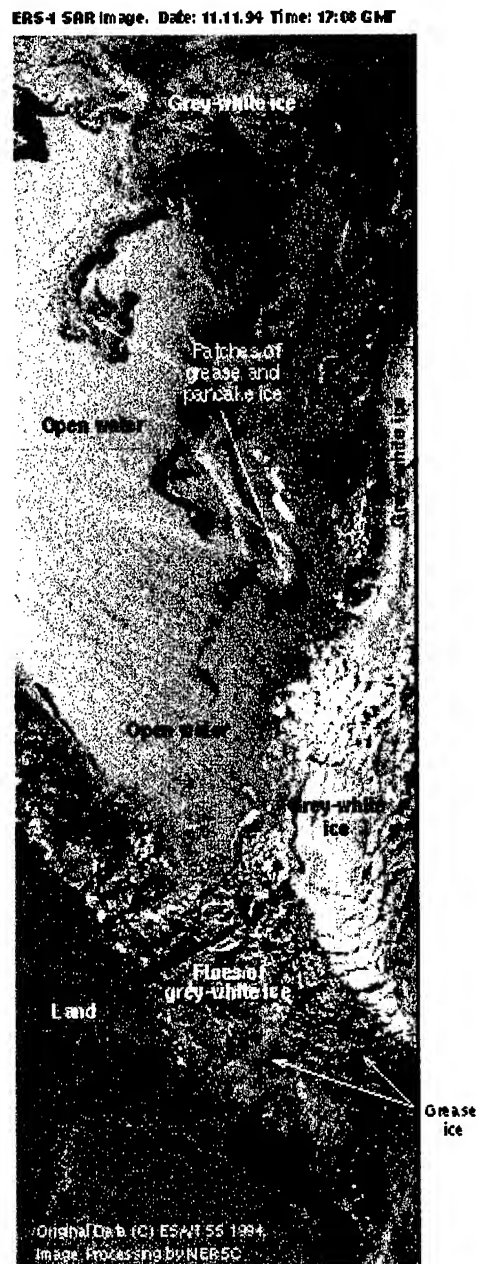


Figure 2. Example of ERS SAR image from southern Kara Sea (11. November 1994) in the beginning of the ice season. The image is shown with annotation of ice types and colour code (green: land, blue: open water, various grey shades: various stages of new and young ice).

limitations, the ERS SAR has proven to be a very useful instrument which can provide quantitative data on most of the important ice parameters except ice thickness. The ERS SAR backscatter values for various ice types were compared

to simultaneous OKEAN Side Looking Radar (SLR) data (Table 1).

Table 1. Okean-01 SLR parameters

Wavelength	3.2 cm
Polarization	VV
Swath width	450 km
Resolution	1.8 km along track 0.8-2.0 km across track
Orbit altitude	600 - 650 km
Incidence angle	20° - 50°

The main results of Task 1 was that state-of-art methods in radar ice classification was reviewed and exchanged, and that ERS SAR ice classification was tested and assessed positively by Russian ice experts.

Task 2: Methods and algorithms for processing, classification and interpretation of radar data.

In Task 2 ERS SAR data and Okean SLR data were exchanged among the project partners, and methods for radiometric and geometric corrections as well as algorithms for derivation of ice parameters were documented. SAR and SLR data were displayed in common map projection (polar stereographic projection). Both ERS SAR and Okean SLR data showed similar backscatter properties of multiyear, firstyear and young ice/new-frozen ice for the cases which have been studied.

Task 3: Techniques for combined processing and use of ERS SAR and Okean SLR data.

ERS SAR and Okean SLR data will have different but complementary roles in and ice monitoring system. Okean SLR stripes obtained within one week can be merged into a mosaic which can cover most of the sea ice in the NSR, as is shown by the SLR mosaic in Fig. 3. The SLR mosaics show the main features of the ice pack such as ice edge location, coastal polynyas, firstyear ice and multiyear ice at a resolution of 1.5 km which is sufficient for the regional ice mapping.

The main role of ERS SAR data is to cover smaller, selected areas with detailed images of the sea ice which are needed in practical applications such as ice navigation. With 100 m resolution in the ERS SAR images, most of the ice features important for navigation can be detected. ERS SAR coverage maps can be superimposed on the SLR mosaics and the most interesting areas for SAR coverage can be selected, as shown in Fig. 3.

Most of the technical preparations for combined use of ERS SAR and Ocean SLR data, such as radiometric and geometric corrections, choice of map projection, etc. were made in Task 2. The main effort in Task 3 was therefore to analyze several examples of SAR and SLR images which were obtained near simultaneously over the same area and

assess how combined use of SAR and SLR data can be optimized for better ice classification and ice mapping.

Task 4. Scheme for polar ice radar monitoring, including study of user requirements

In order to design a system for polar ice monitoring it is essential to know the requirements from the main user categories, both from established users and new or potential users. A number of such users were contacted and asked about their requirements for ice information. More than 50 users were found who considered ERS SAR images to be useful in their activities.

The operational users are first of all Murmansk Shipping Company's icebreaker fleet, other shipping companies operating in ice-covered seas and the Russian HydroMet Service. Oil companies and offshore industry currently need consulting services, but will become operational users when they start offshore operations. Consulting services are also required from engineering companies, consulting companies and transport institutions. Scientific users include universities, marine research institutions and other and environmental research institutes.

Task 5: Demonstration of real-time transmission of SAR images to icebreakers.

An important part of the ICEWATCH project is to develop methods for near real-time distribution of the high resolution, 100 m, ERS SAR images and maps to icebreakers operating in the NSR. Digital transfer of compressed images in near real-time have been successfully tested using the INMARSAT - A service. For example, on January 25 - 26 1996 the icebreaker Taymir was sailing from Dikson to Bely Island (70° - 80° E) in 100 % ice. With a PC and modem connected to the INMARSAT station onboard, ERS-1 SAR images were received 5 hours after the satellite overpass (Fig. 4). In the image areas of rough ice and hummocks (brighter signature) could be clearly distinguished from smooth undeformed ice (darker signatures). Based on this information the icebreaker changed its course and selected a much quicker and safer sailing route. Occasional use of SAR data like this is interesting for demonstration of new technology, but there is a number of requirements which need to be satisfied before the SAR monitoring technology can become an operational tool, such as: selection of SAR coverage in strategic areas, real-time access to SAR data, data ordering procedure, interpretation of SAR images, quantitative ice parameters from SAR, linking ERS data to the Russian ice monitoring services, transmission of ice maps and images to ships and other end users.



Figure 3. Okean Side Looking Radar (SLR) mosaic from 4 stripes obtained from 16 to 21 May 1996. The mosaic is superimposed on a polar stereographic projection with land contours. The Okean SLR images have a resolution of about 1.5 km. The two white rectangles indicate where ERS SAR images were obtained at the same time as the SLR image

Task 6. Recommendation of a near-real time operational information system using satellite radar data.

It is suggested to implement an operational radar ice monitoring system which will be included in the general Russian ice monitoring service. It will use Okean SLR data for large scale surveying and ERS SAR data for detailed observations in specific key area, which are identified as difficult for the navigation. It is recommended to obtain weekly coverage of SLR for the whole Northern Sea Route, and 6 - 10 ERS SAR stripes of 2--5 scenes per week covering key areas in prioritized order as shown in Table 3:

With one Okean satellite and one ERS operational satellite it is only possible to implement a limited operational system for the next 2 - 3 years. From 1999, with wide-swath ENVISAT SAR data available, and possibly also the new Russian SAR satellite Resurs Arctica, the system can be fully operational using SAR data every day. This system also requires a SAR receiving station in Russia in order to have full SAR coverage of the NSR. The system will provide SAR and SLR products which will be distributed to a selection of users in near real time: such as icebreakers, the headquarters of Murmansk Shipping Company, and ice centers in Dikson and AARI. Offline products will be made available for offshore industry and environmental agencies.

The system will be open to include also other users who need radar ice information.

Table 2. Priority areas for ERS SAR coverage

Area	Season of priority	Main users
White Sea	December - June	Ship traffic
Pechora Sea	December - June	Oil and gas exploration
Kara Gate and Jugor strait	March - July	ship traffic
Yamal coast, Belyi island, Ob estuary	March - August	Ship traffic, environmental monitoring
Yenisei estuary	March - July	Ship traffic
Vilkitsky and Mathiessen str.	June - August	Ship traffic
New Siberian islands	July - October	Ship traffic
Long strait	July - October	Ship traffic

4. CONCLUSION

SAR derived ice information has proven to be essential in ice monitoring of the NSR, both for navigation and off-shore operations. Near real-time use of SAR data onboard Russian icebreakers can improve the ship velocity considerably if the data are obtained over the critical areas at the right time. The main limitation of ERS data is that only selected parts of the NSR can be covered. A synergetic use of ERS SAR and Okean SLR data is considered to be the optimal scheme for real time ice monitoring. The SLR data will be used for regional mapping every week, whereas the ERS SAR data will be used only in the most critical areas where high resolution ice information is needed. A future operational monitoring system will first be based on ERS SAR and Okean SLR data. Later, ENVISAT ASAR data will be included, which will enable a much better SAR coverage in the NSR.

4. ACKNOWLEDGMENT

The project has been supported by European Space Agency, Russian Space Agency the Norwegian Research Council and Murmansk Shipping Company.

REFERENCES

- [1] Johannessen, O. M., S. Sandven, and V. Melentyev. ICEWATCH - Ice SAR Monitoring of the Northern Sea Route. Proceedings of the Second ERS Applications Workshop, London, UK, 6 - 8 December 1995. ESA SP-383, pp.291 - 296, 1996



Figure 4. ERS SAR image of 26 January 1996. The image was transmitted to the icebreaker Taymyr in near real-time and was used by the captain to change the sailing route due to difficult ice conditions. The ship track with time markers are superimposed on the image. Copyright ESA/TSS 1996.

- [2] Johannessen, O. M., L. H. Pettersson, S. Sandven, V. V. Melentyev, M. Miles, K. Kloster, L. P. Bobylev, M. Stette, Å. Drottning and K. Ya. Kondratyev. Real-time sea ice monitoring of the NSR using ERS-1 satellite radar images. Terra Orbit Technical Report no.1/94, Bergen, July 1994, 33 pp.
- [3] Johannessen, O. M., S. Sandven, K. Kloster, M. Miles, V. V. Melentyev and L. Bobylev. A Sea Ice Monitoring system for the NSR using ERS SAR data. NERSC Technical Report no. 103, September 1995, 50 pp.
- [4] Johannessen, O.M. and S. Sandven,. ERS-1 SAR ice routing of "L'Astrolabe" through the Northeast Passage. NERSC technical report no. 56, February 1992b.

Sea ice concentration in response to weather systems in the Weddell Sea: Comparison between SSM/I data and model simulations

Holger Fischer¹ and Christoph Oelke²

¹ Alfred Wegener Institut (AWI) für Polar- und Meeresforschung, Columbusstr., D-27568 Bremerhaven, Germany
Tel: +49 471 4831 523, Fax: +49 471 4831 425, e-mail: hfischer@awi-bremerhaven.de

² International ACSYS Project Office, Norwegian Polar Institute, P.O. box 5072 Majorstua, N-0301 Oslo, Norway
Tel: +47 22 95 96 13, Fax: +47 22 95 96 01, e-mail: oelke@npolar.no

Abstract – This study compares sea ice concentrations derived from Special Sensor Microwave/Imager (SSM/I) data with results from a dynamic-thermodynamic sea ice model forced by daily means of air temperature and wind. The analyses focus on two regions with different ice characteristics and concentrations in the eastern and western Weddell Sea (Antarctica) for the austral winter period June to July 1992. Additional synoptic observations, surface and radiosonde measurements from a *R. V. Polarstern* cruise are used for validation. Fluctuations of wind and air temperature are found to be equally important for rapid changes of sea ice concentrations on a daily time scale. The typical reduction of SSM/I-derived sea ice concentration is in the range of 5–10% for transient cyclones, but simulated ice concentrations are reduced by 5%.

INTRODUCTION

Southern Ocean sea ice is highly variable in extent and concentration, on seasonal to daily time scales. Open water areas within the sea ice cover and thin ice, both control the exchange of heat and momentum between ocean and atmosphere, affecting water mass formation and the oceanic circulation. During austral winter with less minor incoming solar radiation, the fraction of open water contributes significantly to sea ice production, even at ice concentrations between 95 and 100%. The ice cover dynamics, causing opening and closing of leads, are strongly connected to synoptic-scale weather systems [6, 7]. This study investigates SSM/I-derived and simulated changes of ice concentration due to atmospheric weather effects for different areas in the Weddell Sea.

MODEL CONFIGURATION

Sea ice model

The dynamic-thermodynamic sea ice model has a spatial resolution of 0.5625° (zonal) and 1.6875° (meridional) on a polarstereographic grid covering the Weddell Sea region from 70°W to 40°E. The model simulates the conditions of the year 1992, restarting from a 6-year run (1986–1991). Rheology in the model is approximated by a viscous-plastic concept [4]. The parametrization of thermodynamic processes include an additional snow layer on

the ice according to previous sea ice model studies [3]. The oceanic heat flux is kept constant at 3 W/m².

Forcing data

The standard sea ice model is forced by atmospheric data from analyses of the European Centre for Medium-range Weather Forecasts (ECMWF). Alternatively, air temperature and wind data are used from the numerical weather prediction model of the United Kingdom Meteorological Office (UKMO) [2]. A mix of both forcing data sets was used for additional simulations. Daily averages of air temperature and wind vectors from both, the ECMWF and the UKMO, are interpolated on the model grid. Ship measurements of air temperature and wind from *R. V. Polarstern* are used for model verification. Cloud coverage and oceanic currents are climatologically represented.

OBSERVATIONAL DATA AND STUDY AREA

Total sea ice concentrations were derived from Special Sensor Microwave/Imager (SSM/I) brightness temperatures using the NASA Team algorithm [1]. The algorithm tie-points [7] define brightness temperatures of the pure surface types (open ocean, first-year ice and multiyear ice). The analysed data represents averaged values over 7–8 hours from multiple satellite orbits.

During austral winter, the Weddell Sea ice cover typically consists of ice pack with concentrations close to 100% in inner regions. Large areas of the eastern Weddell Sea (box no. 1 in Fig. 1) are covered with first-year ice which does not survive the summer melt. In the western Weddell Sea, however, sea ice is strongly deformed by dynamic processes and often older than one year (box no. 2 in Fig. 1). In addition sea ice concentrations are studied along a *R. V. Polarstern* cruise track crossing the Weddell Sea in June/July 1992, with further information on synoptic atmospheric conditions [5]. The integrated water vapor content (W) and the cloud liquid water path (LWP) are calculated from radiosonde ascents [7], representing the atmospheric conditions, especially for transient cyclones.

RESULTS

The simulated ice concentrations for June and July 1992 for an area of 500 × 500 km in the eastern Weddell Sea

are in good agreement with the SSM/I-derived concentrations (Fig. 2). Maximum differences between simulated and observed values are less than 10% for this typical first-year ice area. Decreasing ice concentrations at the end of June (around day 180) correspond to the passage of a low pressure system. W and LWP over sea ice are derived from SSM/I data using the difference method of [7]. For strong low pressure systems with an increase in LWP of 0.5 kg/m^2 and W of 13 kg/m^2 a typical decrease of 5 to 10% in total ice concentration occurs using SSM/I data including atmospheric corrections. This is similar to the concentration differences obtained from the simulations with mixed atmospheric forcing data. For the western Weddell Sea (box no. 2) the simulated ice concentrations are generally higher than those observed (Fig. 3) showing less variations. During the passage of two low pressure systems (days 198–210), simulated ice concentrations decrease by about 5%, but the satellite-derived concentration decrease by less than 15%. Differences resulting from application of the two forcing data sets and from the atmospheric correction of SSM/I-derived concentrations are in the range of 3 to 4%, which agrees with results for the first-year ice regions (Fig. 2).

The observed and simulated ice concentrations along the cruise track of *R. V. Polarstern* (Fig. 4) are averaged for an area of $100 \times 100 \text{ km}$ around the actual ship position. In general, the simulated ice concentrations vary less than the satellite derived concentrations, but both time series reveal highly consolidated pack ice. At the end of the time series, observed and simulated ice concentrations decrease significantly, caused by passing atmospheric low pressure systems as seen from synoptic weather observations (Fig. 4b and c). Simulations with ECMWF, UKMO or mixed forcing data reveal ice concentration changes of less than 5% for this period. Air temperature changes seems to be at least as important as changes in wind. Observed ice concentration is reduced by up to 5%, if an atmospheric correction is applied [7].

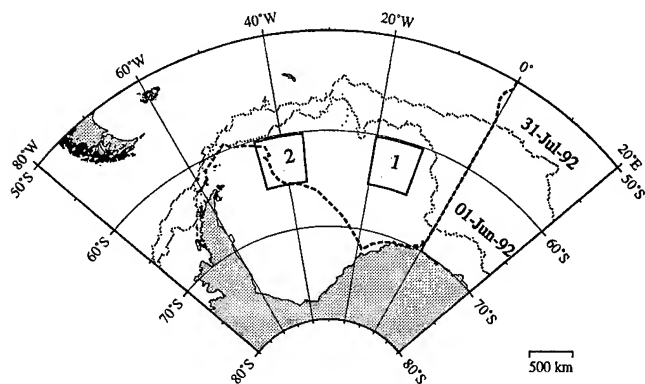


Figure 1: Study areas 1 and 2 in the Weddell Sea. The ice edge (15% concentration) on 1 June and 31 July 1992 (dotted lines), and the cruise track of *R. V. Polarstern* for the same period (thick dashed line) are also shown.

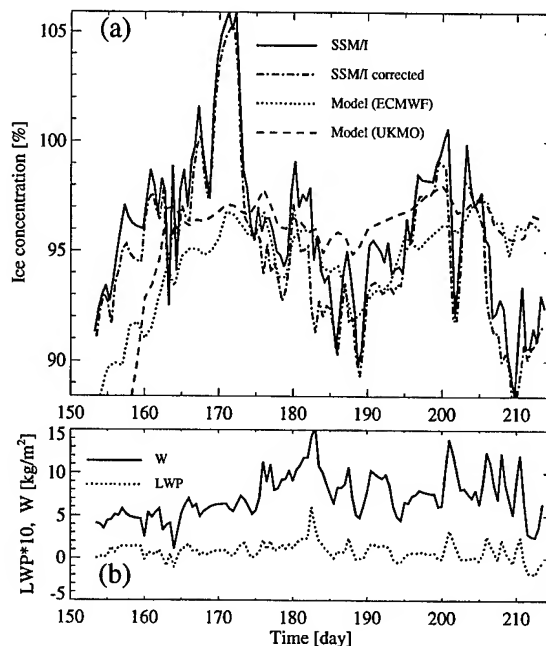


Figure 2: Simulated and observed sea ice concentration for the eastern Weddell Sea (area no. 1 in Fig. 1) for June/July 1992 (a). W and LWP, derived from SSM/I data, are shown for the same period (b).

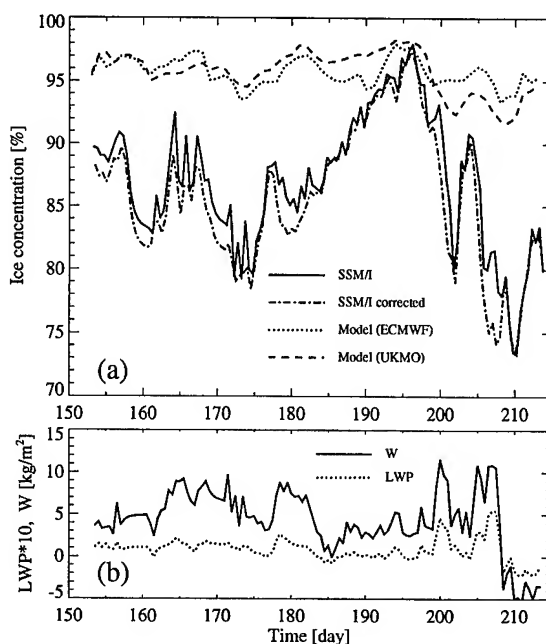


Figure 3: Same as Fig. 2, but for area no. 2 (see Fig. 1).

The strong winds of a low pressure system passing the northwestern Weddell Sea reduce the ice concentration by more than 10% in the marginal ice zone, and by up to 5% north of 65°S . Due to a better resolution, SSM/I data generally pronounces the wind effects on sea ice concentration (Fig. 5).

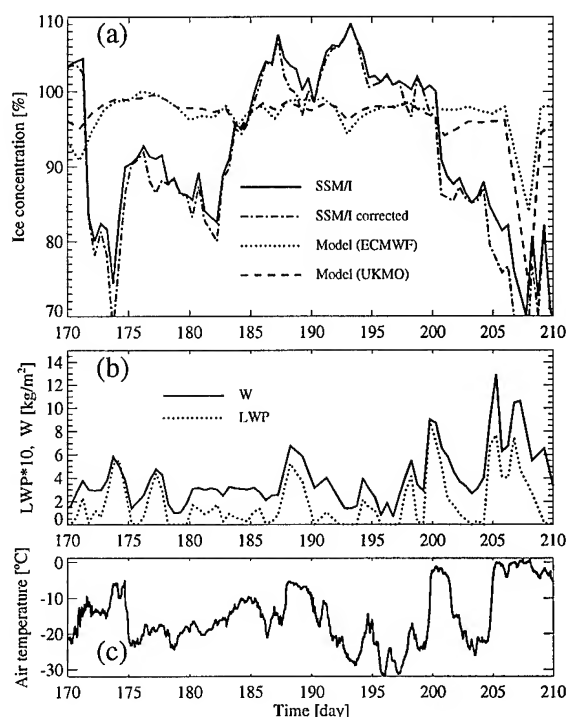


Figure 4: Sea ice concentration along the track of *R. V. Polarstern* from 20 June to 28 July 1992 in the Weddell Sea, averaged over an area of 100×100 km around the ship's position (a). W and LWP are shown from analysed radiosonde ascents (b), and air temperatures (c) are 10-minute samples measured on-board the ship.

CONCLUSIONS

Variations of atmospheric conditions cause changes in observed and simulated ice concentration of about 5% for Antarctic sea ice. These changes, which are lower in previous Arctic studies [6], are strongly related to transient low pressure systems. The differences between observed and simulated ice concentrations, especially in areas of multiyear sea ice, might originate from the sea ice model, the forcing data and/or the SSM/I algorithms.

However, variations of surface emissivity and the effects of atmospheric water vapor and cloud liquid water can cause changes in SSM/I-derived ice concentrations, which are of the same order of magnitude as those caused by air temperature and wind fluctuations in model simulations. The results show that atmospheric conditions over sea ice have to be accurately considered in order to predict climate-induced trends for the Antarctic sea ice cover.

ACKNOWLEDGMENTS

Thanks are due to ECMWF and UKMO for providing their data. We thank S. Leonard (British Antarctic Survey) and M. Kreyscher (AWI) for their help in preprocessing the model forcing data.

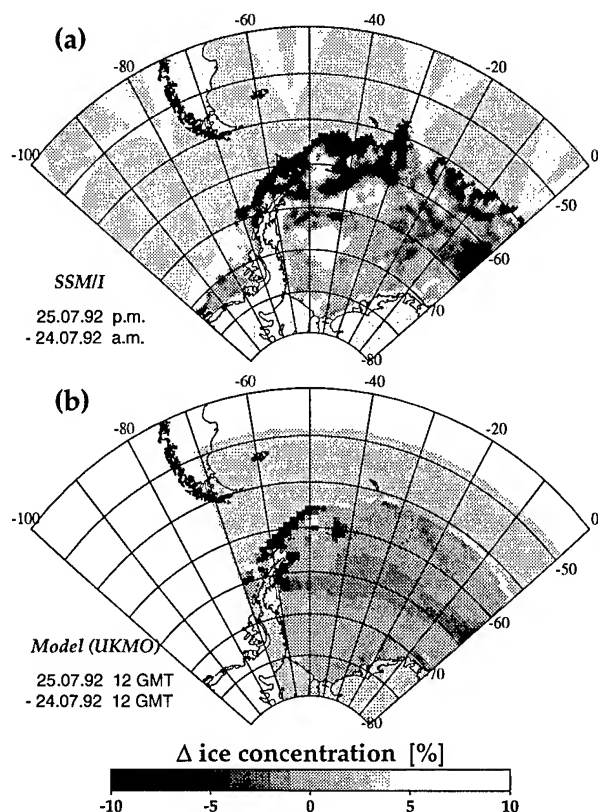


Figure 5: Differences of ice concentration between 25 July and 24 July 1992 from uncorrected SSM/I data (a) and from the model simulation with UKMO forcing (b).

REFERENCES

- [1] Cavalieri, D.J., et al., "Aircraft active and passive microwave validation of sea ice concentration from the DMSP SSM/I", *J. Geophys. Res.*, 96, 21989–22008, 1991.
- [2] Connolley, W.M. and Cattle, H., "The Antarctic climate of the UKMO unified model", *Antarctic Science*, 115–122, 1994.
- [3] Fischer, H. and Lemke, P., "On the required accuracy of atmospheric forcing fields for driving dynamic-thermodynamic sea ice models", In: *The Polar Oceans and their role in shaping the global environment*, Geophysical Monograph 85, AGU, 373–381, 1994.
- [4] Hibler, W.D., III., "A dynamic thermodynamic sea ice model", *J. Phys. Oceanogr.*, 815–846, 1979.
- [5] Lemke, P. (Editor), "The Expedition ANTARKTIS X/4 of *R. V. Polarstern*", *Reports on Polar Research*, 140, 1–90, 1994.
- [6] Maslanik, J.A., Fowler, C., Heinrichs, J., Barry, R.G., and Emery, W.J., "Remotely-sensed and simulated variability of Arctic sea-ice concentrations in response to atmospheric synoptic systems", *Int. J. Remote Sensing*, 16, 3325–3342, 1995.
- [7] Oelke, C., "Atmospheric signatures in sea-ice concentration estimates from passive microwaves: modelled and observed", *Int. J. Remote Sensing*, 18, 1113–1136, 1997.

Design and Development of an Operational Sea Ice Mapping System for Meteorological Applications in the Antarctic.

R.N.Williams, P.Crowther

Department of Computing, University of Tasmania,

PO Box 1214, Launceston, Tasmania, Australia, 7250

Phone: 61 (3) 63243480 Fax: 61 (3) 63243368 Email: R.Williams@appcomp.utas.edu.au

and S.F.Pendlebury

Bureau of Meteorology, Tasmania and Antarctica Regional Office

GPO Box 727G, Hobart, Tasmania, 7001

Abstract -- A semi-automated sea ice mapping system has been developed for use by meteorologists responsible for providing information to Antarctic shipping on current sea ice conditions in the vicinity of the Antarctic stations at Casey, Davis and Mawson. The system uses AVHRR images from NOAA satellites and processes these images to identify areas of cloud, open water and sea ice. It further analyses sea ice regions to determine concentrations of sea ice found within these regions. The system is currently being used on a trial basis, at the Bureau of Meteorology in Hobart, to evaluate its effectiveness, prior to installation at the Casey station later in 1997.

INTRODUCTION

One of the responsibilities of the Australian Bureau of Meteorology's Antarctic Meteorological Centre (AMC) located at Casey, Antarctica, is to provide information on sea ice conditions in East Antarctic waters, particularly in the vicinity of the three Australian stations at Casey, Mawson and Davis. When the AMC is closed during the Antarctic winter this responsibility is transferred to the Bureau's Tasmania and Antarctica Regional Office in Hobart. The sea ice information is derived from Advanced Very High Resolution Radiometer (AVHRR) data received directly from NOAA satellites via a High Resolution Picture Transmission station at Casey. An expert sea ice interpreter views each image and then draws a sea ice map, by hand, showing the sea ice regions depicted in the image and indicating the concentration of sea ice within these regions. When the map has been completed, it is transmitted, together with some written interpretive comments, to ships currently operating in the vicinity of these stations.

Currently, the manual process being carried out is relatively slow and labour intensive; a significant disadvantage when the analysis task is one of many tasks in a busy operational centre. Moreover, symbolically representing varying ice concentrations is a difficult task if done manually. ICEMAPPER is a computer program which has been developed, as a collaborative project

between the Department of Computing and the Bureau of Meteorology, in an effort to at least partially automate the mapping process. Development has progressed from the prototype system described at IGARSS'96 [1] to an operational system which is currently being trialled on a real-time basis. Images are transmitted to Hobart from the reception facility at Casey, processed by the system, and retransmitted to the AMC for independent examination.

SYSTEM DESIGN AND OPERATION

Details of the prototype design and implementation were reported in [1] and the operational system is relatively similar in overall design, but with a range of enhancements designed to improve the useability of the system in an operational setting. Although the design is similar to that of the prototype system, the operational system is a completely new implementation based on the Interactive Data Language (IDL). IDL was used because it enabled us to produce a cross-platform system with a very user-friendly graphical user interface and with many image-based operations optimised for maximum execution speed.

The ICEMAPPER system accepts calibrated or uncalibrated AVHRR images and can apply an initial classification procedure in order to identify the various regions depicted in the images. The classification procedure uses a set of rules to assign each pixel to a specific class according to the values associated with that pixel in the five wavelength bands sampled by the AVHRR sensor on the satellite. The rules used to perform this classification have been derived from information obtained from published research papers [2,3], together with details given by practising meteorologists involved in manual analysis of AVHRR images for sea ice map production [4].

Since a completely reliable technique for classifying AVHRR images in polar regions is not yet available, the system operates in a semi-automated mode. The rules performing the initial classification incorporate a number of movable thresholds. These thresholds are set at specified default levels, but can be altered by the user if required. In operational use, the system loads the five-band AVHRR

image currently being analysed and calibrates the image into albedos and brightness temperatures if required [5]. It then attempts an initial classification using the default threshold values. If the meteorologist using the system is satisfied with the result, it is transmitted to the appropriate recipient, with extra interpretive comments provided by the meteorologist. If, however, the meteorologist feels that the sea ice map is not accurate, he or she can alter the thresholds being used in the rules in order to improve the result. If a satisfactory result can be produced in this way, the final map will be transmitted to the users and the modified threshold values used to produce that map will be recorded, together with the map and a variety of other ancillary details (such as time of year) which may be relevant.

As well as using it as an operational tool, we intend to carefully analyse the details recorded by the system to see how the rule thresholds vary with time of year and other factors. We hope to incorporate information obtained in this way into later versions of the system, reducing the need for operator interaction in the future and to provide a sound base for related scientific work involving the automated processing of many images.

INITIAL MAP CREATION

The initial ice map is created by considering each pixel of the image in turn and classifying it as belonging to one of the following internationally recognised categories [6]:-

- open water - less than 1 tenth ice concentration.
- very open ice - ice concentration of 1 to 3 tenths.
- open ice - ice concentration of 4 to 6 tenths.
- close ice - ice concentration of 7 to 8 tenths.
- very close ice - ice concentration of about 9 tenths.
- compact ice - ice concentration of 10 tenths.
- cloud over ice - thin cloud through which ice is visible.
- high cloud - colder cloud composed mostly of ice.
- low cloud - warmer cloud composed mainly of water.

The above classification is achieved by applying a set of rules to the corresponding pixel values within the five bands in the AVHRR image. A typical rule looks like this:-

```
IF time-of-day = daytime
AND btemp3 - btemp4 < D34
AND SST - btemp4 < DHI
AND albedo1 < ALI
THEN class = open water.
```

where btemp3 and btemp4 are the brightness temperatures recorded in the specified pixel in bands 3 and 4 respectively, albedo1 is the albedo value recorded in the pixel in band 1, SST is the anticipated sea surface temperature at that

location at that time of year (as obtained from climatology records) and D34, DHI and ALI are thresholds which are given default values for the initial ice map creation process.

THRESHOLD MODIFICATION AND RECORDING

In those cases where the initial ice map that ICEMAPPER produces is deemed inaccurate the expert using the system will then choose the "Modify Threshold" option, whereupon a dialog box will appear, showing a number of slider bars, each corresponding to one of the thresholds being used within the rules producing the pixel classifications. As well as showing the slider bars, the dialog box also displays a number of diagrams to remind the expert user of the effect that altering the different thresholds will have on the final classification. This facility helps the user to adjust the thresholds in the most effective way to produce the desired sea ice map. It may take several iterations for the expert user to produce a satisfactory map, although experience so far suggests that in most cases a satisfactory map can be produced within two or three iterations.

Once a satisfactory map has been produced the expert can record salient details about the process that has just been carried out. These details include the name of the image being analysed, the name given to the ice map produced, the final values of the thresholds used, the satellite id, the year, the day of year, the time of day and finally any comments that the expert wishes to have recorded in relation to this particular analysis.

SYSTEM TESTING

The IDL version of the ICEMAPPER system has been tested on nineteen images taken over the 1996/97 Antarctic summer season and in about half of the tests circumstances allowed processing to be carried out in near real time. The AVHRR images were received at the AMC at Casey and were relayed to the Bureau of Meteorology regional office at Hobart. There the sea ice image interpreter used the system to create an initial ice map, using the default threshold values. The initial map was then compared by the human expert with individual grey scale images of the various AVHRR bands for the situation under consideration. The system thresholds were adjusted where necessary to improve the initial ice map. If the adjusted map was considered accurate by the expert the result was transmitted back to the meteorologists at Casey base for comment and critical analysis. If, however, it proved impossible to create a satisfactory map even after modifying the thresholds, the classification attempt was deemed to have failed and this would be recorded within the threshold records file.

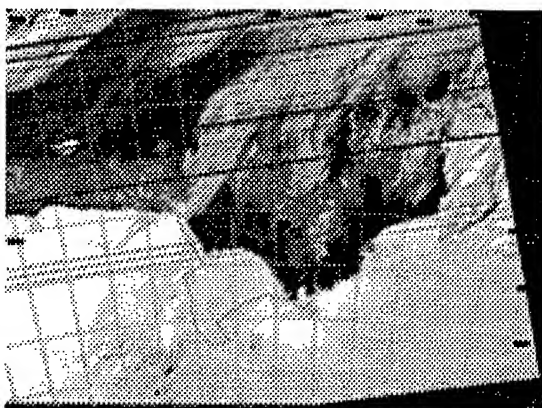


Figure 1 - Visible light image (AVHRR band1).
(light - high albedo, dark - low albedo)

Of the nineteen images processed, none were completely successfully classified on the first attempt, but all were able to produce satisfactory ice maps with modified thresholds within several iterations, suggesting that the technique is basically sound but that the default thresholds need to be set at slightly different values than the ones currently being used.

Figure 1 shows the visible light (band1) image of one of the test cases and is a scene depicting a region along the East Antarctic coastline between Mawson and Davis stations. Figure 2 shows an ice map produced for this image, using modified threshold values. This map was deemed accurate by the expert sea ice interpreter and by the meteorologist, at the AMC Casey, to whom it was sent.

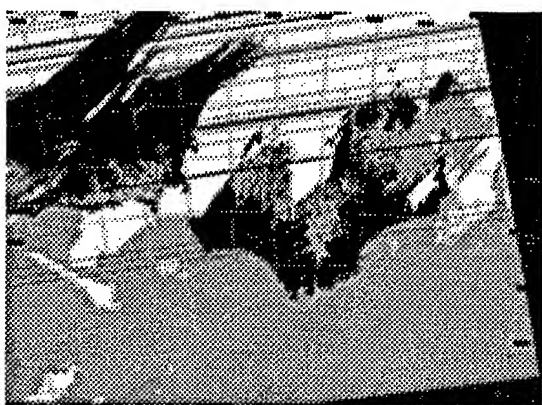


Figure 2 - Ice map created from the scene in Fig 1.
(grey - ice, white - cloud, black - open water)

CONCLUSIONS

The performance of the ICEMAPPER system over the last eight weeks of the 1996/7 summer season indicates that the system will be a very useful tool when it is put into operational use during the 1997/8 summer season. For all nineteen images tested to date, a satisfactory ice map has been produced within several iterations, resulting in a very significant reduction in time and effort on the part of the expert sea ice image interpreter. The estimated average time required for the interpreter to produce a satisfactory map using ICEMAPPER was 10 minutes, whereas the production of an ice map by hand takes an average of approximately 60 minutes.

ACKNOWLEDGMENTS

We wish to thank Dr Kelvin Michael, Dr Robert Massom and Mr Neal Young (all from the Antarctic CRC) as well as Dr Beth Ebert (Bureau of Meteorology, Melbourne) for contributing sea ice interpretive knowledge to the ICEMAPPER system. Also Justin Baker and Dr Robert Dahni (Bureau of Meteorology, Melbourne) provided us with valuable information on McIDAS file formats and on the IDL runtime system respectively. The work reported in this paper was partly supported by a research grant from the Antarctic Science Advisory Committee.

REFERENCES

- [1] R.N.Williams and J.Hartnett, "A prototype sea ice mapping system using a geographical information system and expert knowledge", Proc. IGARSS'96, Lincoln, Nebraska, pp 1111-1113, May 1996.
- [2] R.Massom and J.Comiso, "The classification of Arctic sea ice types and the determination of surface temperature using advanced very high resolution radiometer data.", Journal of Geophysical Research, vol.99, no.C3, pp. 5201-5218, 1994.
- [3] T.F.Lee, S.Atwater and C.Samuels, "Sea ice - edge enhancement using polar-orbiting environmental satellite data.", Weather and Forecasting, vol.8, no.3, pp. 369-377, 1993.
- [4] E.Ebert, private communication, April 1992.
- [5] K.Kidwell, NOAA Polar Orbiter Users Guide, NOAA-NESDIS, Washington, 1991.
- [6] The Danish Meteorological Institute, "International Ice Symbols - the Egg Code", Denmark, 1985.

Microwave Scattering From a Slightly Rough Surface of a Medium Possessing a Finite Large Dielectric Constant, and Applications to an Air-Water Scattering.

G.M. Nedlin⁺, S.R. Chubb, and A.L. Cooper.

Remote Sensing Division, Naval Research Laboratory, Washington, D.C. 20375-5351, USA
phone: (202)767-7075, FAX:(202)767-3303, e-mail: nedlin@neptune.nrl.navy.mil

Abstract -- A theory for electromagnetic scattering from a slightly rough surface is developed that is based on application of an effective boundary condition. The theory generalizes previous approaches that apply only to the infinite dielectric constant ($\epsilon \rightarrow \infty$) limit to cases of finite but large ϵ . Also, the theory yields the known results by J.Wright. In a particularly important case of scattering from the ocean, the backscatter cross-section is dramatically different from that calculated for $\epsilon \rightarrow \infty$ over a wide range of incident angles, for both vertical and horizontal polarization.

INTRODUCTION

Since a ratio of the dielectric constants of water and air, $|\epsilon_w/\epsilon_a|$ is large, a "perfect conductor" approximation (PCA), $\epsilon_w = \infty$, is used commonly in air-water electromagnetic scattering (see, e.g., [1,2] and references there). PCA reduces a two-media (air and water) wave propagation problem to a single (air) medium problem, with a boundary condition of vanishing of a tangential component of electric field on a water surface. This paper goes beyond the PCA, to account for an effect of a finite, although large, ϵ_w . While an "air-water" terminology is used throughout the paper, a general problem considered is a derivation of a scattering cross-section (CS) from a slightly corrugated surface (SCS), separating two substances when a subsurface medium ("water") has a dielectric constant ϵ_w much larger than that (ϵ_a) of an "incident wave" medium ("air"). In such a case, a two-media problem can also be reduced to a single-medium ("air") problem by considering another effective boundary condition [3]. SCS implies that $k\zeta' \ll 1$, where ζ' is a characteristic height of a corrugation. $k = \omega/c_a$ and c_a are the electromagnetic wave number and velocity in the air. This is a linearized theory (LT), i.e., the scattered field is proportional to a corrugation. The CS is derived for a general case of a spatially non-uniform surface, when an ensemble average of heights correlator (EAHC), for two points located at x_1, x_2 , depends both on a "separation" $x = (x_1 - x_2)$, and "location" $X = 1/2(x_1 + x_2)$ of the pair. This incorporates both short- and long-range statistical-dynamical features of a water surface. In this paper we present the results for a backscatter cross-section (BCS) only. Our result for BCS is consistent with the BCS calculated by J.W. Wright [4]. The BCS is proportional to a Bragg Fourier-transform of EAHC, with regard to a variable x , averaged (with regard to location X) over the water surface. For the case of an actual air-water scattering, BCS is expressed also via the averaged, over a water surface, local wave action

$N(p, X)$, thus providing a direct relationship between a BCS and statistical-dynamical features of waves on the water surface.

SURFACE CURRENTS AND SCATTERED FIELD.

General.

A scattered electromagnetic field $(\mathbf{E}, \mathbf{H})(\mathbf{r}_o)$, at a point \mathbf{r}_o in the air is a superposition of the fields $(\mathbf{E}_{e,m}, \mathbf{H}_{e,m})$ due to vector-potentials \mathbf{A}_e and \mathbf{A}_m , generated, respectively, by effective electric and magnetic "surface currents", \mathbf{J}_e and \mathbf{J}_m

$$\mathbf{A}_{e,m}(\mathbf{r}_o) = (4\pi)^{-1} \int dS(\mathbf{r}) \mathbf{J}_{e,m}(\mathbf{r}) \exp(ik|\mathbf{r}_o - \mathbf{r}|) / |\mathbf{r}_o - \mathbf{r}|, \quad (1)$$

$$\mathbf{J}_e(\mathbf{r}) = \mathbf{n}(\mathbf{r}) \times \mathbf{H}(\mathbf{r}), \quad \mathbf{J}_m(\mathbf{r}) = -\mathbf{n}(\mathbf{r}) \times \mathbf{E}(\mathbf{r}).$$

Here \mathbf{r} is a point on the surface, and $\mathbf{n}(\mathbf{r})$ is an "outward" unit vector normal to the surface at this point. In a wave-zone ($k r_o \gg 1$), a magnetic field of a scattered wave

$$\mathbf{H}(\mathbf{r}_o) + \mathbf{H}_m = ik \{ (\kappa_{sc} \times \mathbf{A}_e) + \eta_a^{-1} (\kappa_{sc} \times (\kappa_{sc} \times \mathbf{A}_m)) \}. \quad (2a)$$

$\eta_{a,w} = (\mu_{a,w}/\epsilon_{a,w})^{1/2}$, and $\kappa_{sc} = \mathbf{r}_o / r_o$ is the unit "scattering vector". For a backscatter, $\kappa_{sc} = -\kappa_{in} = (\sin\theta, 0, \cos\theta)$, where κ_{in} and θ are the unit propagation vector and an incident angle of an incident wave, and xz - is an incident plane. When Fraunhofer's approximation condition is satisfied,

$$\mathbf{H}_e = (ik/(4\pi r_o)) \exp(ikr_o) \int dx \exp(-ikx \sin\theta) (\kappa_{sc} \times \mathbf{J}_e(\mathbf{x})) \exp(-ik\zeta(\mathbf{x}) \cos\theta), \quad (2b)$$

$$\mathbf{H}_m = -\eta_a^{-1} (ik/(4\pi r_o)) \exp(ikr_o) \int dx \exp(-ikx \sin\theta) (\kappa_{sc} \times (\kappa_{sc} \times \mathbf{J}_m(\mathbf{x}))) \exp(-ik\zeta(\mathbf{x}) \cos\theta).$$

Here $z = \zeta(\mathbf{x})$ is an equation of a water surface (with a zero mean value of ζ), and \mathbf{x} is a vector in x,y -plane. In LT below, $dS = dx dy = dx$, and $\exp(-ik\zeta \cos\theta) = 1 - ik\zeta \cos\theta$.

Large ϵ Reflector ($|\epsilon_w/\epsilon_a| \gg 1$).

When $|\epsilon_w/\epsilon_a|$ is large, a scattering problem can be reduced to that of a single-medium problem, with the subsurface medium property incorporated into an effective boundary condition (BC), $\mathbf{E}_{tan} = \eta_w(\mathbf{n} \times \mathbf{H})$, [3] for the tangential $(\mathbf{E}_{tan}, \mathbf{H}_{tan})$ field components on a surface (Σ) . In the following, we introduce, for all \mathbf{H} -fields, $\mathbf{b} = \eta_a \mathbf{H}$. Thus,

$$\mathbf{b} = \eta_a \mathbf{H}_e + \eta_a \mathbf{H}_m = \mathbf{b}_e + \mathbf{b}_m, \quad \mathbf{j} = \eta_a \mathbf{J}_e = \mathbf{n}(\mathbf{r}) \times \mathbf{b}(\mathbf{r}), \quad (3)$$

⁺ Supported by the Consortium for Oceanographic Research and Education (CORE)

and the BC becomes

$$E_{\tan} = \alpha(n \times b) \big|_z, \quad \alpha = (\eta_w / \eta_a) \equiv (\epsilon_a / \epsilon_w)^{1/2}, \quad |\alpha| < 1. \quad (4)$$

(where $\alpha=0$ corresponds to PCA). From Eqs.(4) and (1), $J_m(r) = -\eta_w(n(r) \times J_e(r))$, and fields in Eq.(2) can be expressed in terms of electric surface current j alone.

$$b_e = (ik/(4\pi r_0)) \exp(ikr_0) \int dx \exp(-ikx \sin \theta) (\kappa_{sc} x j(x)) (1 - ik\zeta(x) \cos \theta), \quad (5)$$

$$b_m = \alpha(ik/(4\pi r_0)) \exp(ikr_0) \int dx \exp(-ikx \sin \theta) (\kappa_{sc} x (\kappa_{sc} x (n \times j(x)))) (1 - ik\zeta(x) \cos \theta).$$

SURFACE CURRENT j .

Eqs. (5) relate the scattered field to current j , i.e. to yet unknown tangential component of a total E -field on a surface. We derive here a closed integral equation for a field on a surface and then transform it into equation for j .

On-Surface Field Equations (OSFE).

It can be shown that the Stratton-Chu derivation [5] for the fields outside the surface can be generalized to derive a system of the integral equations for the fields on the surface,

$$b(r) = 2b_{in}(r) + 2 \int dS(r') \{ ((n \times b_{tan}) \times \nabla' f) - ik(n \times E_{tan})f - (i/k)(n \cdot (\nabla_{tan} \times E_{tan})) \nabla' f \}, \quad (6a)$$

$$E(r) = 2E_{in}(r) + 2 \int dS(r') \{ ((n \times E_{tan}) \times \nabla' f) + ik(n \times b_{tan})f + (i/k)(n \cdot (\nabla_{tan} \times b_{tan})) \nabla' f \}, \quad (6b)$$

$$f = f(\rho) = \exp(ik\rho)/(4\pi\rho), \quad \rho = |r - r'|$$

In OSFE Eqs. (6), both points r and r' are on the same ("water") surface. b_{in} and E_{in} are the incident fields; E, b and n in the integrals are evaluated at r' . A (\cdot) , in ∇' , means that the derivatives are with regard to the variable r' . The RHS in Eq. (6) is twice the RHS in the Stratton-Chu equations (in the latter, r is outside the surface). The terms $(n \cdot b)$ and $(n \cdot E)$ in Eq.(6) are replaced, from the Maxwell equations, by $-(i/k)(n \cdot (\nabla_{tan} \times E_{tan}))$ and $(i/k)(n \cdot (\nabla_{tan} \times b_{tan}))$, respectively, showing explicitly that RHS in Eq. (6) (as well as in the Stratton-Chu equation) involves the tangential field components and their tangential derivatives only.

Large ϵ Medium and Equation for j .

In this case, Eq. (6a) becomes (by utilizing BC Eq. (4))

$$b(r) = 2b_{in}(r) + 2 \int dS \{ (j \times \nabla' f) - i\alpha k(n \times j)f - i(\alpha/k)(n \cdot (\nabla \times j)) \nabla' f \}, \quad (7)$$

and can be transformed into a closed integral equation for j , when cross-multiplied $(n \times \cdot)$ by n . In LT, it is convenient to work with the explicitly two (x, y) -component vector $(\delta j^t$ below). Consider $n = -\nabla\zeta + e_z$ ($e_{x,y,z}$ are unit vectors along x, y, z -axes, $\nabla\zeta(x, y)$ is a two (x, y) -component gradient). Also,

$$b = b^o + \delta b^t, \quad j = j^o - \nabla\zeta \times b^o + \delta j^t, \quad \delta j^t = (e_z \times \delta b^t), \quad (8)$$

where $j^o = (e_z \times b^o)$. Here and below, a superscript (o) is for the quantities calculated for a flat surface ($\zeta=0, n = e_z$), while a superscript (ζ) is for the quantities proportional to ζ . The incident field $b_{in}(r)$ is linearized also,

$$b_{in}(x, y, \zeta(x)) = b_{in}^o(x) + \delta b_{in}^t; \quad \delta b_{in}^t = -ik\zeta(r) \cos \theta b_{in}^o(x), \quad \text{and} \quad (9)$$

$$b_{in}^o(x) = \eta_a H_{in}^o \exp(-ik \sin \theta x), \quad b^o(x) = \eta_a H^o \exp(-ik \sin \theta x).$$

$H_{in}^o, E_{in}^o, (H^o, E^o)$ are the complex amplitudes of the incident (total) fields (on a surface $z=0$), and

$$H^o = 2H_{in, \tan}^o g_p(\theta) + \alpha \sin(2\theta) \eta_a^{-1} E_{in, y}^o. \quad (10)$$

For a horizontal polarization (HP; $E_{in}^o = e_y E_{in, y}^o$), $g_p = (1 + \alpha \cos \theta)^{-1} \equiv 1 - \alpha \cos \theta$. For a vertical polarization (VP; $H_{in}^o = e_y H_{in, y}^o$), $g_p = \cos \theta / (\cos \theta + \alpha)$, and, particularly, $H^o \rightarrow 0$ and $E_{tan}^o \rightarrow 2E_{in, \tan}^o$ when $\theta \rightarrow \pi/2$, while, for PCA, $H^o = 2H_{in}^o, E_{tan}^o \rightarrow 0$. Thus, PCA breaks, for VP, at grazing angles, $\cos \theta < \alpha$. Also, a scattered field below contains

corrections to PCA, which are proportional to $\alpha/(\cos \theta + \alpha)$ (rather than to α), for VP, and not small at grazing angles.

Equation for δj^t is obtained by cross-multiplying $(e_z \times \cdot)$ of Eq.(7). A linearized equation for δj^t is

$$\delta j^t - \alpha \delta L^o(\delta j^t) = 2e_z \times \delta b_{in}^t - L^o(\nabla\zeta \times b^o) + M^o. \quad (11)$$

$$L^o(A)(x) = -2 \int dx' A_z(x') (x' - x) \rho^{-1} \partial f / \partial \rho; \quad \delta L^o(\delta j^t)(x) = 2i \int dx' \{ k \delta j^t(x') f(\rho) - k^{-1} (\nabla \times \delta j^t(x'))_z (e_z \times (x' - x)) \rho^{-1} \partial f / \partial \rho \}.$$

The term $M^o = 2 \int dx' j^o(x') (\zeta(x') - \zeta(x)) \rho^{-1} \partial f / \partial \rho$ doesn't contribute to BCS.

BACKSCATTER FIELD AND CROSS-SECTION.

Eq. (11) is an integral equation, with a kernel depending on $(x' - x)$. It has been solved by a Fourier transform (FT), and a backscatter field b has been calculated by Eqs.(3,5,8).

$$b = (-k^2/(\pi r_0)) \exp(ikr_0) \chi(2k_H) \eta_a \{ F_H H_{in, \zeta}^o e_\zeta + F_V H_{in, y}^o e_y \}, \quad (12)$$

$$F_H = \cos^2 \theta (1 - 2\alpha \cos \theta), \quad F_V = (1 + \sin^2 \theta) [\cos \theta / (\cos \theta + \alpha)]^2 \quad (13)$$

$\chi(p) = \int dx \exp(-ip \cdot x) \zeta(x)$ is a FT of a roughness ζ , and $k_H = (k \sin \theta, 0, 0)$. $e_\zeta = \kappa_{sc} e_y$ is a unit vector along a magnetic field, for a horizontally (E) polarized wave. The BCS (per unit solid angle) $\sigma = d\sigma_{eff}/d\Omega$, where $d\Omega$ is a solid angle supported by a radar (as seen from a reflector), and $P_{sc} d\Omega r^2 = P_{in} d\sigma_{eff}$. P_{in} (P_{sc}) is an absolute value of a Poynting vector in an incident (scattered) wave. Therefore, $\sigma = (P_{sc} r^2)/P_{in} = (r_0 |b|/\eta_a |H_{in}^o|)^2$, and the BCS $\sigma_{HH} (\sigma_{VV})$, for a horizontal (vertical) polarization are

$$\sigma_{HH} = (k^4/\pi^2) \langle |\chi(2k_H)|^2 \rangle |F_H(\theta, \alpha)|^2, \quad (14a)$$

$$\sigma_{VV} = (k^4/\pi^2) \langle |\chi(2k_H)|^2 \rangle |F_V(\theta, \alpha)|^2, \quad (14b)$$

where $\langle \dots \rangle$ stands for an ensemble average. BCS can be expressed also in terms of the heights correlator (HC)

$$\Phi(x, X) = \Phi(-x, X) = \langle \zeta(X + x/2) \zeta(X - x/2) \rangle. \quad (15)$$

It can be shown that $\langle \chi(p) \chi^*(p) \rangle = S \bar{\psi}(p)$, where S is a total area, and $\bar{\psi}(p)$ is a FT of the HC, averaged over X ,

$$\bar{\psi}(p) = \int dx \cos(p \cdot x) \bar{\Phi}(x); \bar{\Phi}(x) = \bar{\Phi}(-x) = S^{-1} \int dX \Phi(x, X). \quad (16)$$

Thus Eqs. (14) become

$$\sigma_{HH}/S = (k^4/\pi^2) \bar{\psi}(2k_H) |F_H(\theta, \alpha)|^2, \quad (17a)$$

$$\sigma_{VV}/S = (k^4/\pi^2) \bar{\psi}(2k_H) |F_V(\theta, \alpha)|^2. \quad (17b)$$

Note that an angular variation of BCS is determined both by $F_{H,V}(\theta, \alpha)$ and also by $\bar{\psi}(2k_H)$ (because $k_H = k \sin \theta_{in}$), and further applications depend on particular features of $\bar{\psi}(p)$. Particularly, for actual air-water scattering, when a surface roughness is due to capillary-gravity surface waves (CGSW), it can be shown that

$$\bar{\psi}(p) = 2\pi^2 (p/\omega(p)) \{ \bar{V}(p) + \bar{V}(-p) \}, \text{ where } \bar{V}(p) = S^{-1} \int dX N(p, X),$$

$\omega(p)$ is a CGSW frequency, and $N(p, X)$ is a local value of a wave action.

On the other hand, the effect of a finite ϵ ($\alpha \neq 0$) of a scatterer is described completely by $F_{H,V}(\theta, \alpha)$ alone, i.e., by Eqs.(13). Actual BCS ($\alpha \neq 0$, in Eq. (17)) differs significantly from BCS calculated in PCA ($\alpha = 0$). As illustrated on Fig.1 below, a difference is well pronounced over a whole range of incident angles, and for both VP and HP, for the realistically large ϵ . Note, particularly, that BCS vanishes at near-grazing angles ($\theta \rightarrow \pi/2$), for both HP and VP (rather than for HP only, in a PCA [2]).

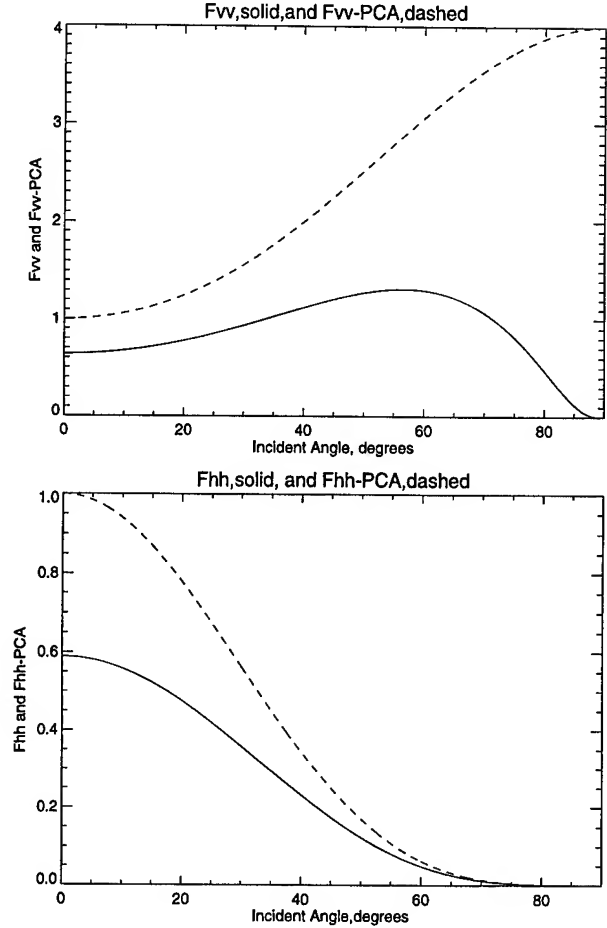


Fig. 1. $F_{VV} = |F_V(\theta, \alpha)|^2$ and $F_{HH} = |F_H(\theta, \alpha)|^2$ as calculated for air-sea scattering ($f=10$ GHz, $\epsilon/\epsilon_0=55+i37$), the solid curves. The dashed curves are for F_{VV} and F_{HH} , for a perfect conductor approximation (PCA, $\alpha=0$).

CONCLUSIONS

We have developed a linearized theory of electromagnetic scattering from a SCS of a substance with a large dielectric constant. It is shown particularly that a radar BCS differs significantly from the BCS calculated in PCA, and that BCS vanishes at near-grazing angles for both VP and HP.

REFERENCES

- [1] D. Holliday, G. St-Cyr, and N.E. Woods, "A radar ocean model for small to moderate incidence angles", *Int. J. Remote Sensing*, vol. 7, pp. 1809-1834, 1986.
- [2] D. Holliday, "Resolution of a Controversy Surrounding the Kirchhoff Approach", *IEEE*, vol. AP-35, pp. 120-122, 1987.
- [3] L.D. Landau, E.M. Lifshitz and L.P. Pitaevskii, *Electrodynamics of Continuous Media*, 2d ed., Pergamon Press, 1984, p. 300
- [4] J. W. Wright, "Backscattering from Capillary Waves", *IEEE*, vol. AP-14, pp. 749-754
- [5] J.A. Stratton, *Electromagnetic Theory*, McGraw-Hill, 1941, pp. 464-470.

VALIDATION OF WAVE MODEL USING ERS ALTIMETER AND SAR WAVE MODE DATA

Ruixue Zhang***, Tian Kuay Lim**, Dayalan Kasilingam*, I-I Lin* and Victor Khoo*

***DSO National Laboratories, 20 Science Park Drive, Singapore 118230

Tel: (65)-7727268, Fax: (65)-7759011, Email: zruixue@dso.org.sg

**Meteorological Service Singapore, P.O. Box 8, Changi Airport Post Office, Singapore 918141

Tel: (65)-5422863, Fax: (65)-5425026, Email: mssltk@pacific.net.sg

*Center for Remote Imaging, Sensing and Processing, Faculty of Science, National University of Singapore 119620

Tel: (65)-7723220, Fax: (65)-7757717

ABSTRACT

A second generation ocean wave model of Meteorological Service Singapore (MSS) is validated in two ways, theoretically and by using field data. The results of theoretical validation show that the wave growth rate and spectrum are in agreement with expected parameters. The field data is chosen between 16-21 Nov., 1995, which corresponding to the North East Monsoon period. The wave model is driven by the 10m surface wind of MSS Numerical Weather Prediction (NWP) model. The Significant Wave Height (SWH) of the wave model is compared with the SWH ERS altimeter data. In general, it is found that the two data sets are in agreement, the SWH of the wave model is found to be higher than the altimeter SWH in high wave region and lower in low wave region. Qualitative comparisons between SAR wave mode data and the wave model spectra are also made. SAR wave mode spectra reflect the peak frequency detected in wave model outputs. From the evolution of SWH with time, it is shown that the wave model is capable in predicting the wave pattern in response to the North East monsoon phenomena.

1. INTRODUCTION

This paper presents the results of a preliminary study on the validation of MSS wave model. Traditionally, reliable wave measurements from open ocean areas are very limited. Due to the lack of observation data, some wave models are not properly validated. The launches of the ERS-1 and ERS-2 satellites have made altimeter wave height measurements available in near real time. This makes it possible to compare the SWH from the MSS ocean wave model and the SWH from the altimeter to assess the performance of the wave model.

2. THE WAVE MODEL

The wave model used in the current study is the operational wave model of MSS. It is a revised second generation model developed by the Meteorological Research Institute, Japan. It runs on a rectangular grid on the Mercator projection. The model domain is from 50°N to 45°S and from 40°E to 180°E. It produces a full two

dimensional wave spectrum at 22 frequency bands from 0.04Hz-0.25Hz and 16 directional sectors on a 127km grid.

The evolution of the surface wave is governed by transportation equation:

$$\frac{\partial F}{\partial t} + C_g \cdot \nabla F = S_{net} = S_{in} + S_{nl} + S_{ds} \quad (1)$$

where F is the two-dimensional wave spectrum, C_g the group velocity, S_{net} the sum of the input S_{in} by wind, the non-linear transfer S_{nl} and the dissipation term S_{ds} .

The propagation part is a combination of the finite difference and "jumped" methods. The reference spectrum similar to Pierson-Moskowitz (PM) spectrum is:

$$F(\sigma, \theta) = \frac{\alpha g^2}{\sigma^5} \frac{\sigma_p}{\sigma_{pm}} \exp\left(-1.25 \left(\frac{\sigma_p}{\sigma}\right)^4\right) \cos^2(\theta), \quad (2)$$

where σ is the angular velocity, θ the wave direction, $\alpha=0.0081$, $\sigma_{pm} = \frac{8.5962}{U_{19.5}}$ is the PM spectrum, $U_{19.5}$ is the wind speed at 19.5m height.

The wave growth is governed by Toba's stochastic growth equation [1]:

$$\frac{d\sigma^{*-2}}{dt} = 1.838 \times 10^{-3} \left[1 - \text{erf}(4.59 \times 10^{-2} \sigma^{*-1}) \right], \quad (3)$$

where the variables with suffix * at the upper right are non-dimensionalized by the friction velocity u_* and the gravity acceleration, g .

Input to the wave model is the wind at 10m height given by the MSS Numerical Weather Prediction (NWP) model. The region of interest is in South East Asia of 90°E-145°E, 10°S-40°N. The real data validation period is from 16 Nov. to 21 Nov., 95, during the North East monsoon. Strong winds are observed which correspond

to higher sea state prevalent over most of the region. The wave model was run from 14 Nov., 95 to 21 Nov., 95, two days in advance to let the model spin up.

3. RESULTS

(i) Theoretical validation

The wave model is calibrated against stationary, uniform wind, fetch limited wave growth measurements. The stationary, homogeneous wind field with wind speed $U_{10}=20\text{m/s}$ blows orthogonally offshore. The initial wave energy at time $t=0$ is zero. The model is run with wind speed of $U_{10}=20\text{m/s}$ and run until a stationary state is reached for the entire area.

Fig. 1 shows the growth of wave spectra for the transient stages of growth resemble the Pierson-Moskowitz spectra corresponding to different wind speeds. The SWH at the fully developed equilibrium stage is 8.95m, which is comparable to the WAM model results [2].

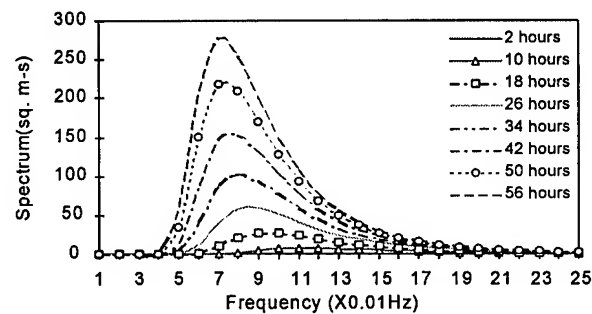


Fig.1 The growth of wave spectra with respect to wind duration for wind speed of 20m/s.

Fig. 2 illustrates the non-dimensional peak frequencies evolution with non-dimensional time. It is found that the peak frequencies of model output match those of Toba’s wave growth theory well. Propagation and fetch tests also show the wave model performs well.

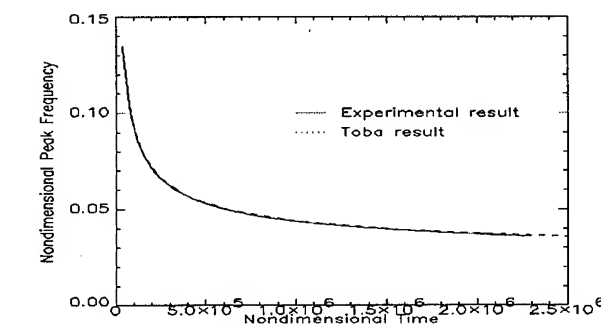


Fig.2 Change of the non-dimensional peak frequencies with non-dimensional time. The solid line refers to the model values, dotted line the Toba theoretical values.

(ii) Real data validation

A typical wind field during North East monsoon is shown in Fig. 4. It is the wind field at 03 hour, 16 Nov., 1995 generated by MSS NWP model. It is seen that the winds are strong over South China sea. These stronger than normal wind will cause rough sea states. The cold air from north China will push southward along the north east wind . This kind of weather system is called cold surge. The cold air which meets the warm air in the tropical area will form a circulation, which leads to rainfall.

The wave model is run during this cold surge period. It is found that the SWHs increase and the wave direction moves southward as wind field becomes stronger. Fig.5 presents the SWH field at the same time mentioned above. It is found that model responds to the monsoon wind field well.

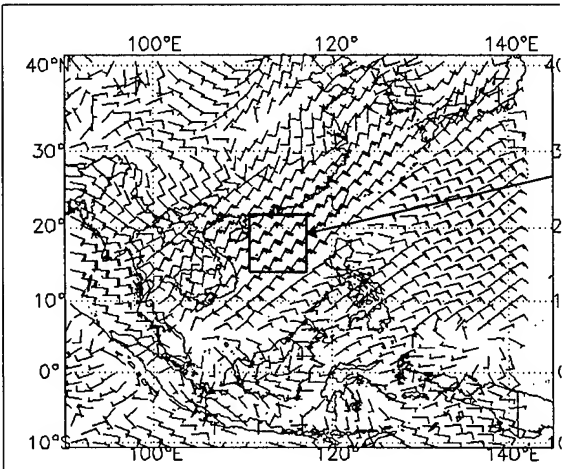


Fig. 4 The wind field at 03UTC 16 Nov., 1995.

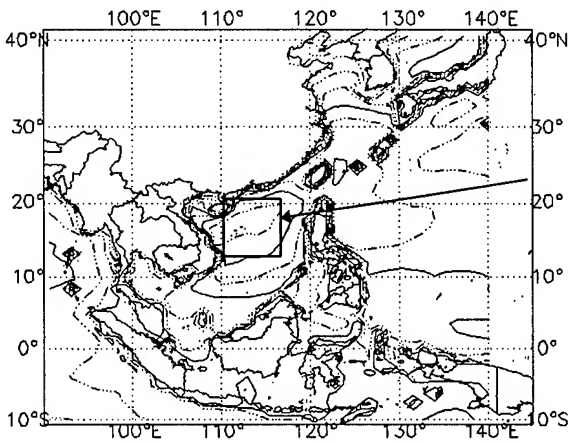


Fig. 5 The SWH distribution at 03UTC 16 Nov., 1995

Detailed comparison between altimeter SWH and the SWH of wave model generally shows good agreement. Examples are given in Fig. 6 and 7. The wave model data

are chosen approximately at the same time of that ERS passes, the SWHs of the wave model are chosen as the spline interpolation of the nearest four grid points to altimeter track points. It is seen that they agree well. In the low sea states, altimeter data give higher SWHs for lower waves than the wave model. In higher sea states the altimeter SWHs are lower than the wave model. The root mean square of the first data set is 0.75m, the second 0.67m. It is found that there are some points of altimeter SWH are much larger than wave model SWH, which corresponds to the reading of altimeter near coastline. While wave model gives higher wave height for the open sea. Fig. 8 show the difference between the wave model SWH and the altimeter SWH along the orbits. At the same time, it is found that altimeter SWHs are all larger than 0.4m, it implies that for very low sea states altimeter is unable to give the accurate values.

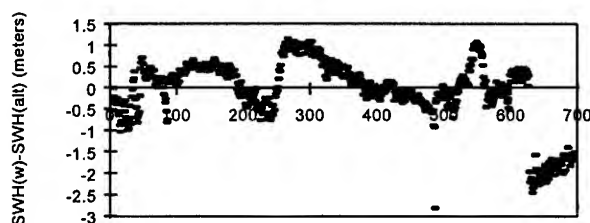


Fig. 6 The difference of wave model SWH and altimeter SWH on 03UTC 17 Nov., 1995

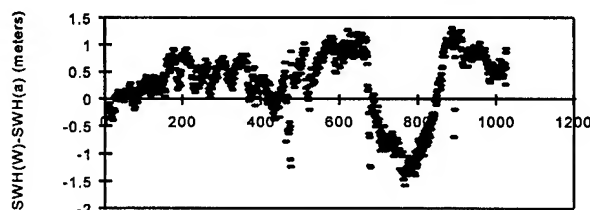


Fig. 7 The difference of wave model SWH and altimeter SWH on 15UTC 17 Nov., 1995

SAR wave mode data are qualitatively compared with wave spectra. Fig. 9 and 10 show the spectra contour. Because of the 180° ambiguity, the spectra over the other 180° are symmetric. It is found that the peak frequencies are in agreement. The directions require further investigation.

4. CONCLUSIONS

From the results shown above, it is found that the wave model responds well to the forcing of atmosphere. It is able to predict the cold surge process. The comparison between SWHs shows that wave model produces higher wave height than the observations of altimeter in open sea. As for the area near coastline, wave model generates the low values compared to the altimeter. This suggests that the model description of waves along coastline needs further study.

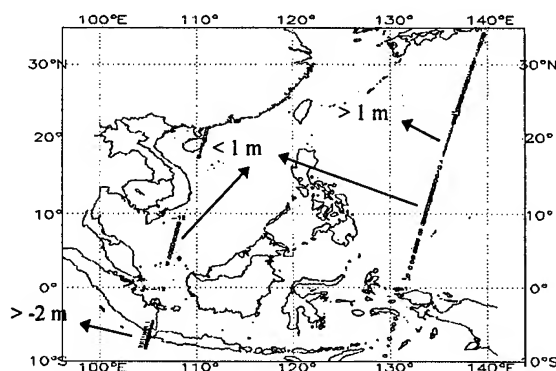


Fig. 8 The difference between the wave model SWH and the altimeter SWH along orbits at approximately 03UTC 17 Nov, 95.

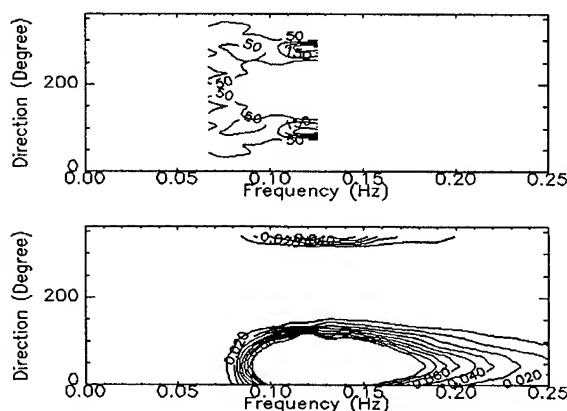


Fig. 9 The spectra obtained from SAR(upper plot) and wave model (lower plot) at approximately 03UTC 17 Nov,1995 at the location 118.44°E,20.25°N

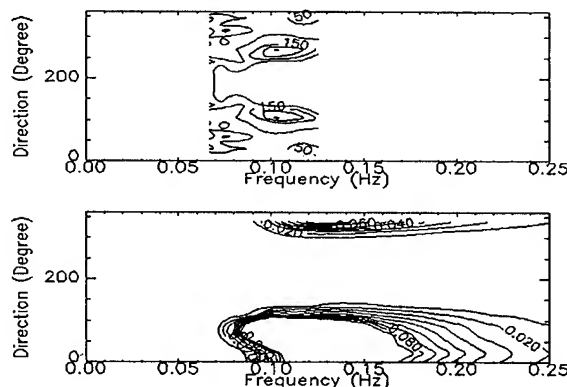


Fig. 10 The spectra obtained from SAR(upper plot) and wave model (lower plot) at approximately 03UTC 18 Nov,1995 at the location 113.4°E,21.0°N

REFERENCES

- [1] Toba, Y.,(1978): Stochastic form of the growth of wind waves in a single-parameter representation with physical implications. J. Phys. Oceaogr., 8, 494-507.
- [2] Technical report.No.4, 1992. WAM model cycle 4 (revised version).

Studying the monsoon circulation in the Indian Ocean using altimeter data.

Vibeke E. Jensen, Paul Samuel, Ola M. Johannessen*
Nansen Environmental and Remote Sensing Center,
Edvard Griegs vei 3a, N-5037 Solheimsviken, Norway;
Phone +47-55 29 72 88, Fax +47-55 20 00 50, Vibeke.Jensen@nrsc.no

ABSTRACT

The oceanic variability in response to the monsoon system in the northern Indian Ocean was for the first time studied using the three altimeters Geosat, ERS-1 and Topex/Poseidon. The Root Mean Square, computed from the sea surface height anomalies indicates values of 15–17 cm in highly energetic areas such as the Somali Current, and 13–15 cm in the western part of the Bay of Bengal. As the most prominent variations occur, and because most *in situ* observations are from these areas the investigation was focused on these two areas.

Complex Principal Component analysis was applied to the gridded SSH anomalies and the results indicate that the annual signal is strongest when the monsoon period is at its peak, and the semi-annual time series seems to be related to the onset and decay phase of the SW and NE monsoon. CPCA analysis of the Topex/Poseidon data indicates characteristic periods of 40–50 days which are probably related to earlier observations in the study area of mesoscale variability generated by the horizontal shear in the velocity field. Westward propagating waves are identified from the annual and semi-annual modes, and they are observed to have a westward propagating speed of 13 km/d at the equator, with decreasing speed away from the equator.

Mesoscale eddies with diameters between 250–1000 km and maximum amplitudes up to 45 cm are observed during the monsoon periods. The propagation and life time of eddies in the study area are in good agreement with those reported in previous investigations using *in situ* data and numerical models.

1 INTRODUCTION

The circulation patterns in the Indian Ocean, forced by the reversing southwest (May to August) and northeast (October to January) monsoonal winds, represent a unique oceanographic problem that has been the subject of a number of investigations. The South West (SW) monsoon is normally observed over the Arabian Sea from May to August and the North East (NE) monsoon from October to January.

Significant mesoscale variability has also been observed in the northern Indian Ocean and a number of eddies have been examined by previous investigators. Satellite altimetry is particularly suited for studying mesoscale variability and has been used in the Southern Indian Ocean.

However, so far the extensive data set from ERS-1 and Topex/Poseidon altimeters have not been used jointly in the Indian Ocean circulation. Therefore the main objective of our investigation was to gain an improved understanding of the oceanic variability in response to the monsoon system in the northern Indian Ocean using altimeter data.

The altimeter data used and the method of processing are described in Section 2. In Section 3 the details of the SSH variability field from the altimeters is examined, and the temporal and spatial characteristics obtained from Complex Principal Component Analysis (CPCA) are presented. In Section 4 results pertaining to the propagation and life time of eddies are presented, and in Section 5 a discussion and conclusion is given.

2 ALTIMETER DATA PROCESSING

The altimeter data used in the study are from the Geosat (17 days repeat period, 01.11.86 – 01.09.89), the ERS-1 (35 days repeat period 01.04.92 – 31.12.93) and the Topex/Poseidon (10 days repeat period, 01.01.93 – 10.08.95) missions. The first 10 cycles of Topex/Poseidon data are not used in this study, because of attitude problems with the satellite. The data were processed using standard repeat track analysis to obtain SSH anomalies.

For each data point, Root Mean Square (RMS) of the SSH were computed. The SSH anomalies are also interpolated to a regular space-time grid using a simple exponential weighting scheme. Geosat data are gridded on a $1.0^\circ \times 1.0^\circ$ spatial grid at 8 days intervals, ERS-1 on a $0.5^\circ \times 0.5^\circ$ spatial grid at 15 days time intervals and Topex/Poseidon on a $2.0^\circ \times 2.0^\circ$ spatial grid at 5 days intervals. These grid spacings and intervals were chosen in order to properly present the spatial and temporal sampling characteristics of the different satellite missions.

*Also at Geophysical Institute, University of Bergen, Norway.

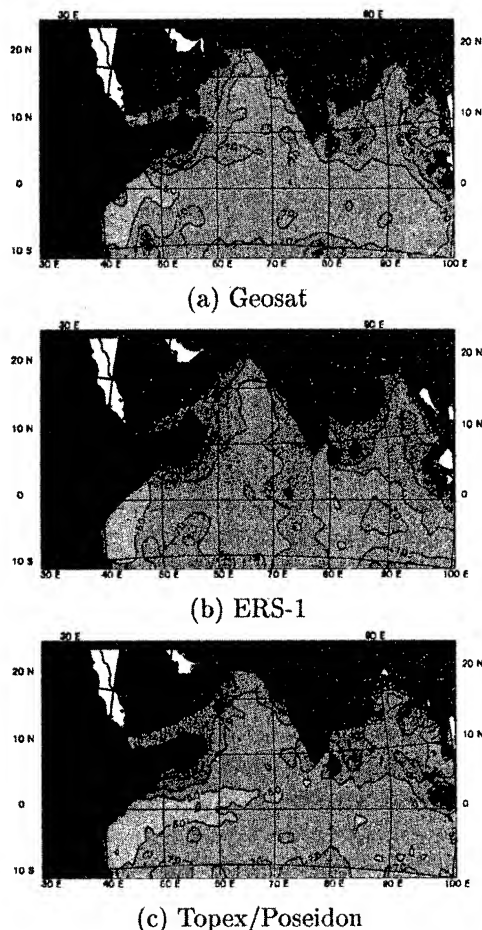


Figure 1: RMS Sea Surface height anomaly distribution. Units in cm.

3 SPATIAL AND TEMPORAL VARIABILITY

3.1 Root Mean Square variability

Root Mean Square (RMS) of the SSH provides an indication of the distribution of mesoscale variability in the study area. Over most of the study area the RMS variability is low, less than 7 cm (Figure 1). High RMS variability is observed in highly energetic areas such as the Somali Current area (15–17 cm), and along the western part of the Bay of Bengal (13–15 cm). High variability is also observed along 10° S at 45°–50° E and at 75°–82° E (11–13 cm) and in the eastern part of the Bay of Bengal (9–11 cm).

There is a close relationship between the areas of greatest SSH variability and the major currents, the Somali Current, East Indian Coastal Current and Southern Equatorial Current, and higher variability is most prevalent in the western parts of the oceans.

As an overall assessment the distribution of RMS height in the Indian Ocean seems to be consistent for the three data sets. In general the ERS-1 shows more extended areas with high variability (9–11 cm), which is particularly seen over the Chagos Laccadive Ridge (north-south ridge, extending between 73°–78° E).

Other areas with high RMS distribution are around 78° E, 10° S where the Southern Equatorial Current is found and around 47° E, 10° S which is in the area of the East African Counter Current. Geosat indicates values of 11–13 cm in these areas, while the other two altimeters show values of 7–9 cm. In the eastern part of the Bay of Bengal values of 13–15 cm are shown for all three altimeters.

3.2 CPCA

Phase and amplitude time series extracted from CPCA of the first two modes for Geosat and Topex/Poseidon is shown in Figure 2.

Dominant modes for both the data sets have a clear annual period as seen in the phase plots Figure 2a and 2c. The phase plot for the Geosat first mode shows a clear annual signal while for Topex/Poseidon there is some leakage from shorter periods. Both the data sets indicate that the annual signal has maxima around January and July, with small variations from year to year, possibly related to variability in the onset of the monsoon.

The amplitude time series (Figure 2b and 2d) indicate when the annual signal is strongest. For Geosat the strongest is January 1989 and also relatively strong in January 1987 and 1988, May 1988 and 1989. The amplitude time series for Topex/Poseidon mode one (Figure 2d) suggests that this mode actually contains two signals, the annual signal and a signal with a period of approximately two months. As mentioned earlier, this is also evident in the corresponding phase plot (Figure 2c). The fact that the two signals are combined in one mode suggests that they are correlated. Several investigators have observed oscillations with a 40–60 days period in the western Indian Ocean using *in situ* data and numerical models and explain these oscillations as caused by horizontal shear (barotropic instability) which generate eddies at a period of 40–50 days. This signal is possibly not resolved by the 17 days repeat period of Geosat, explaining the absence from Figure 2a and 2b.

The phase time series of the second mode for Geosat (Figure 2e) show a clear semi-annual period with maxima in May, August and November, February. This mode therefore appears to be related to the onset and decay phase of the SW and NE monsoons.

4 MESOSCALE EDDIES

Closer inspection of the gridded SSH anomaly data set showed evidence of several mesoscale eddies. Figure 3 shows the location and rotation of the most persistent eddies observed from the three data sets. We observed eddies to be more dominant during the monsoon periods, and the two areas, the Somali Current area in the Arabian Sea (30°–61° E, 0°–20° N) and the western part of the Bay of Bengal (75°–95° E, 0°–20° N) examined, indicate eddies with a maximum amplitude up to

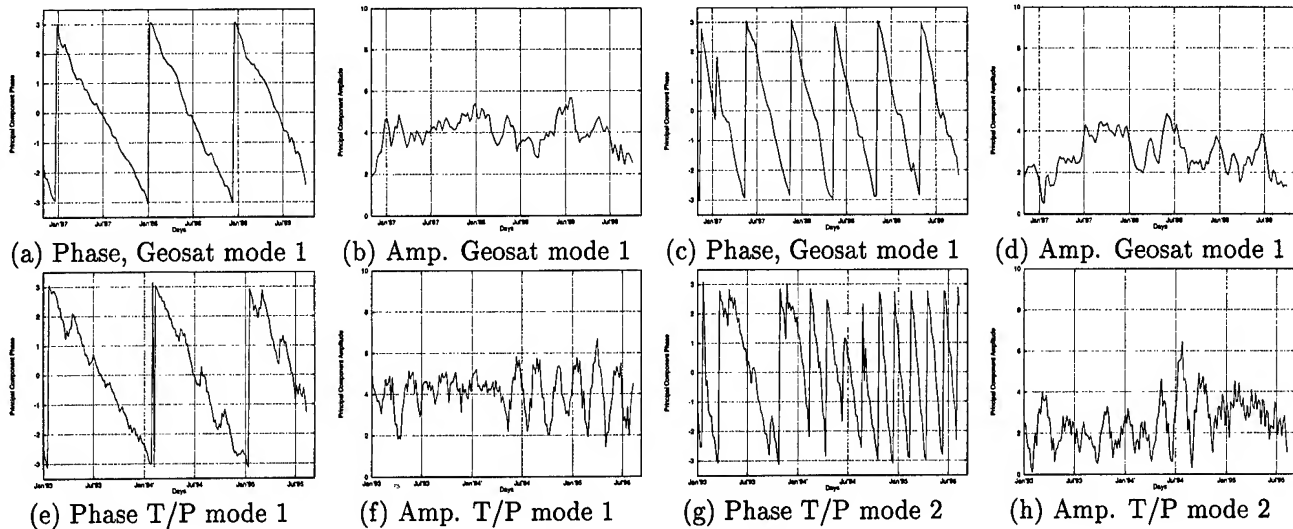


Figure 2: Temporal characteristics for first and second Geosat and Topex/Poseidon SSH CPCA mode. The amplitude is in cm, and the phase is from $-\pi$ to $+\pi$.

45 cm in July/August and December/January, with a spatial scale ranging between 250–1000 km. The typical life cycle of these eddies is illustrated by examining consecutive time steps of the gridded Geosat, ERS-1 and Topex/Poseidon data in the area of the Somali Current.

5 DISCUSSION AND CONCLUSION

For the first time SSH data from three altimeter missions are used to study mesoscale variability in the Arabian Sea and the Bay of Bengal. The correlation between the three altimeters is very good. The Root Mean Square of the SSH anomalies indicates where the high energetic areas are. This formed the basis for the further investigation. Using CPCA analysis we were able to study the temporal and spatial characteristics of the monsoon periods. The annual period based on Geosat data indicate maxima in January and June, indicating the time when the monsoon is most intense. The semi-annual period indicate maxima in May, August and November, February, and appears to be related to the onset and decay phase of the SW and

NE monsoons. Topex/Poseidon indicate oscillations caused by horizontal shear which generate eddies at a period of 40–50 days. A reconstruction using the annual and semi-annual mode for Geosat and Topex/Poseidon was done to describe the varying physical attributes of propagating features. From this an anticyclonic movement is observed during the 1987/88 NE monsoon from the Geosat data in the Somali Current area and the Bay of Bengali Westward propagating features, possibly Rossby waves are also identified from the CPCA, along equator with speeds of 13 km/d. Along 4° – 10° N speeds up to 6 km/d are observed, and between 5° S and equator they travel with a speed of 7 km/d. This indicate a decrease in speed away from equator.

Mesoscale eddies are located, and the propagation, spatial range, amplitude and life time of these are observed during the monsoon periods. These results compare well with previous investigators who have used altimeter measurements. The dimensions of the eddies and the horizontal movement are within the expected range of the observations and model simulations. The correlation between the three altimeter data sets used in this investigation is also very good. Small variations occur, due to the satellites different temporal and spatial sampling and due to different errors and corrections.

Inspite of few investigations in especially the Bay of Bengal investigating the sea surface variability, our results confirms and strengthen previous results using other techniques.

REFERENCES

Jensen, V.E, P. Samuel, and O.M Johannessen, Studying the monsoon circulation in the Indian Ocean using altimeter data , *submitted to Journal of Geophysical. Research*, 1997.

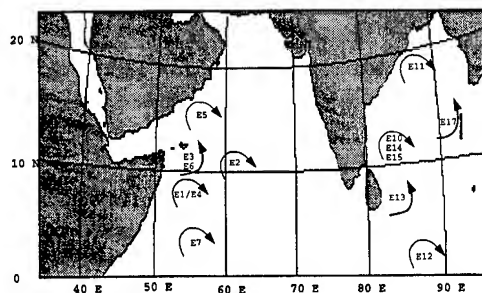


Figure 3: Overview of the location and rotation for eddies observed in the Indian Ocean using altimetry data.

Efficient Simulation of SAR Interferometric Raw Signal Pairs

Giorgio Franceschetti ^{1,2}, *IEEE Fellow*, Antonio Iodice ¹,
Maurizio Migliaccio ³, *IEEE Member*, Daniele Riccio ¹, *IEEE Member*

¹ Università di Napoli Federico II, *Dipartimento di Ingegneria Elettronica*, Via Claudio 21, 80125 Napoli, Italy
☎ +(39)-81-7681111, fax. +(39)-81-5934448 email: riccio@diesun.die.unina.it , iodicea@irece1.irece.na.cnr.it

² Consiglio Nazionale delle Ricerche, *I.R.E.C.E.*, Via Diocleziano 328, 80124 Napoli, Italy
☎ +(39)-81-5704945, fax. +(39)-81-5705734 email: francesc@irece1.irece.na.cnr.it

³ Istituto Universitario Navale, *Istituto Teoria e Tecnica delle Onde Elettromagnetiche*, Via Acton 38, 80133 Napoli, Italy
☎ +(39)-81-5513976, fax. +(39)-81-5521485 email: migliaccio@nava1.uninav.it

Abstract -- An efficient SAR raw signal simulator of across-track interferometric pairs is here presented. It is based on the Physical Optics evaluation of the scattering contributes and it is efficiently implemented via an analytic formulation of the SAR system transfer function. A certain number of meaningful examples are also presented and discussed.

INTRODUCTION

Across-track SAR interferometry (IFSAR) is used to generate high resolution DEMs of the scene under survey from a SAR image pair [1-4]. Within this framework it is certainly very useful to benefit of an IFSAR raw signal simulator. In fact, simulation is helpful for experimentation of processing procedures (focusing, registration, phase unwrapping), system design and mission planning. Furthermore, IFSAR simulation can be exploited to better understand the physical phenomena involved in SAR interferogram formation.

In this paper a novel across-track raw signal IFSAR simulator is presented and discussed. It includes an electromagnetic model of surface backscattering and a two-dimensional formulation of the SAR system transfer function (STF). The electromagnetic model is based on a facet description of the surface, and the backscattered fields are evaluated by using the Physical Optics (PO) solution and the Kirchhoff approximation [5]. PO is also applied in order to analytically evaluate the correlation coefficient between the fields received by the two antennas [2-4] in terms of the geometry of the problem and facet characteristics [6]. The presented two dimensional formulation leads to an efficient

simulation since it can be carried out in the Fourier domain [5].

A set of meaningful examples relevant to some canonical scenes show the potentialities of the simulator. Its effectiveness is assessed by comparing theoretical [2-4, 7] and simulated results. In particular, this has been done with reference to the correlation coefficient and the phase difference probability density function (pdf) measured on the interferograms obtained from the simulated raw signals. We show that geometrical consistency is achieved, and the baseline decorrelation effect is correctly simulated both in the mean and in the distribution sense.

The paper is organized as follows: first a description of the simulator is given, then some examples are illustrated and finally conclusions are drawn.

THE SIMULATOR

In this Section we briefly outline the rationale of our simulator of interfereometric raw signal pairs, see the block scheme in Fig.1.

Since we are dealing with a SAR raw signal simulator for extended three-dimensional scenes [8], we need to electromagnetically model the signals backscattered at the two antennas. As a consequence, an electromagnetic model, depending on the impinging electromagnetic wave, i.e., wavelength, local incidence angle, polarization, and on the scene geometric and physical characteristics must be embodied into the simulation scheme.

In the proposed version of our simulator no time-varying effect on the backscattered field is taken into account. Accordingly, the model is that of two parallel travelling

antennas. The scene is described by means of certain rastered basic characteristics: the elevation map, the permittivity and permeability map, the microscopic roughness map.

In order to evaluate the electromagnetic field scattered at the two antennas the PO solution of the Kirchhoff scattering integral is considered [5]. The scene is modelled in terms of planar facets, large in terms of the incident wavelength, perturbed by a microscopic roughness. The roughness perturbation enters into the electromagnetic model by introducing a randomness into the backscattered field, usually described by means of a Rayleigh amplitude and uniform phase distributions [9]. This is represented in Fig.1 by the pdf block. The PO model allows to evaluate the power of the field received at the two antennas ($E(|\gamma|^2)$ in Fig.1) and to determine the backscattered fields correlation coefficient (ρ in Fig.1). The latter can be evaluated by following an approach similar to that of Ref. [6], thus getting:

$$\rho = \exp[j2k(R_1 - R_2)] \exp\left[-\frac{1}{2} \left(\frac{4\pi\sigma \sin\vartheta B_\perp}{\lambda R}\right)^2\right] \cdot \text{sinc}\left\{\pi\Delta y \left[\frac{2\cos(\vartheta - \beta)B_\perp}{\lambda R \cos\beta}\right]\right\} \cdot \text{sinc}\left\{\pi\Delta x \left[\frac{2\tan\alpha \sin\vartheta B_\perp}{\lambda R}\right]\right\}, \quad (1)$$

where σ is the facet height profile standard deviation, R_1, R_2 are the first and second antenna - facet centre range, R is the average antenna - facet centre range, ϑ the average look angle, B_\perp the baseline component perpendicular to the look direction, Δx and Δy are the facet dimensions, and α, β the tilt angles of the mean plane along x and y directions, respectively.

Once the backscattered field has been evaluated for the first antenna (γ_1 in Fig.1) the backscattered field at the second antenna (γ_2 in Fig.1) must be determined by taking into account the field correlation. This is depicted in Fig.1 by the conditional pdf block (c-pdf in Fig.1).

Details on the backscattered field at the two separate antennas can be found in [9], whereas the decorrelation model is illustrated in [5] and is based on the background provided in [7].

Once the two reflectivity maps have been computed, they are Fourier-transformed and multiplied by the SAR STF (see the STF blocks in Fig.1), evaluated as in Ref. [9]. A modified kernel Fourier Transform method [10] is used, so that range migration, range curvature and variations of focus

depth are automatically included. This procedure is efficient, amenable of modular extension, and compares favourably with other available techniques. Finally, it is important to note that, as shown in Ref. [5], only two facets per resolution cell are needed to get the correct correlation on the final complex image pair. This makes the simulation procedure even faster and memory saving.

RESULTS

In this section some meaningful simulation examples relevant to some canonical scenes are illustrated. In these simulation runs, the ERS-1 SAR system parameter have been used. We recall that theoretical analytical expressions of the complex image pair correlation coefficient and of the phase difference pdf are available only in the case of a flat (possibly tilted) scene [2,3,7]. Therefore, we simulated the interferograms of a flat scene using different values of the baseline length: 50, 100, 200, 400 m; then we measured the correlation coefficient and the phase difference distribution of these data, in order to compare them with the theoretical ones. The single-look interferogram relevant to a 50 m baseline length is shown in Fig. 2; measured and theoretical correlation coefficients are listed in Table I. Theoretical correlation coefficients are evaluated using the following expression [2, 3]:

$$\rho_i = 1 - \frac{2R_r B_\perp}{\lambda R \tan\vartheta}, \quad (2)$$

wherein R_r is the slant range resolution. We stress that ρ_i is the correlation coefficient between the two final complex images, and does not at all coincides with the correlation coefficient ρ between the two backscattered fields that appears in Eq. (1).

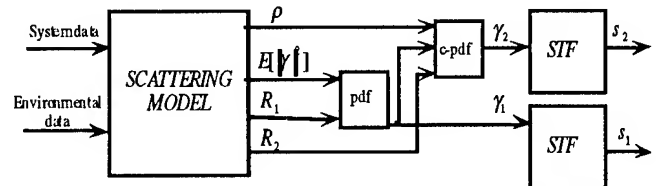


Fig. 1: Block scheme.

Measured phase difference distributions and theoretical pdfs relevant to a 100 m baseline length are plotted in Fig. 3. Theoretical pdfs are computed as in Ref. [7]. All results show a good agreement between simulations and theory, therefore sustaining the employed simulation procedure. Besides, high efficiency is achieved; in fact, simulation of a 2048x2048 pixel ERS-1 raw signal pair requires about 13' CPU time on an IBM RISC 6000 computer.

CONCLUSIONS

An efficient simulator of SAR interferometric raw signal pairs has been presented. The rationales underlying such a simulator have been illustrated as well as a set of meaningful examples relevant to some canonical scenes. The subjective and objective analysis of these examples strongly support the consistency of our simulator both on a geometrical and physical basis.

TABLE I

Baseline [m]	Measured ρ_i	Theoretical ρ_i
50	0.955	0.957
100	0.910	0.914
200	0.811	0.828
400	0.609	0.656

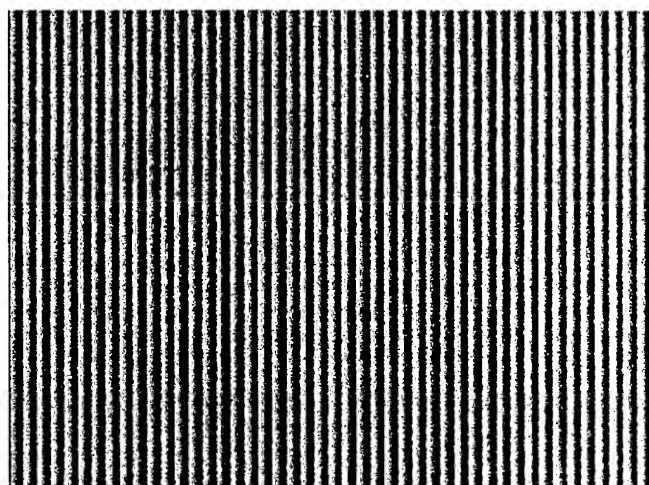


Fig. 2: Single-look interferogram of a flat scene.

REFERENCES

- [1] F.K.Li and R.M.Goldstein, "Studies of Multibaseline Spaceborne Interferometric Synthetic Aperture Radars", *IEEE Trans. Geosci. Remote Sensing*, GE-28, 88-97, 1990.

- [2] H.A.Zebker and J.Villasenor, "Decorrelation in Interferometric Radar Echoes", *IEEE Trans. Geosci. Remote Sensing*, GE-30, 950-959, 1992.
- [3] E.Rodriguez and J.M.Martin, "Theory and Design of Interferometric Synthetic Aperture Radars", *IEE Proc.-F*, 139, 147-159, 1992.
- [4] F.Gatelli, A.Monti Guarnieri, F.Parizzi, P.Pasquali, C.Prati and F.Rocca, "The Wavenumber Shift in SAR Interferometry", *IEEE Trans. Geosci. Remote Sensing*, GE-32, 855-865, 1994.
- [5] G.Franceschetti, A.Iodice, M.Migliaccio and D.Riccio, "A Novel Across-Track SAR Interferometry Simulator", *submitted*.
- [6] G.Franceschetti, A.Iodice, M.Migliaccio and D.Riccio, "The Effect of Surface Scattering on IFSAR Baseline Decorrelation", *J. Electro. Waves Applic.*, 11, 353-370, 1997.
- [7] D.Just and R.Bamler, "Phase Statistics of Interferograms with Applications to Synthetic Aperture Radar", *Applied Optics*, 33, 4361-4368, 1994.
- [8] G.Franceschetti, M.Migliaccio and D.Riccio, "The SAR Simulation: an Overview", *Proc. IGARSS'95*, Firenze, Italy, 2283-2285, 1995.
- [9] G.Franceschetti, M.Migliaccio, D.Riccio and G.Schirinzi, "SARAS: A Synthetic Aperture Radar (SAR) Raw Signal Simulator", *IEEE Trans. Geosci. Remote Sensing*, GE-30, 110-123, 1992.
- [10] G.Franceschetti, R.Lanari and E.S.Marzouk, "Efficient and High Precision Space-Variant Processing of SAR Data", *IEEE Trans. Aerospace Electr. Syst.*, AES-31, 227-237, 1995.

This work has been partly conducted under the Italian Ministry of the University and Scientific Research, M.U.R.S.T. 40% "Telerivamento dell'ambiente: modelli e sperimentazione" sponsorship.

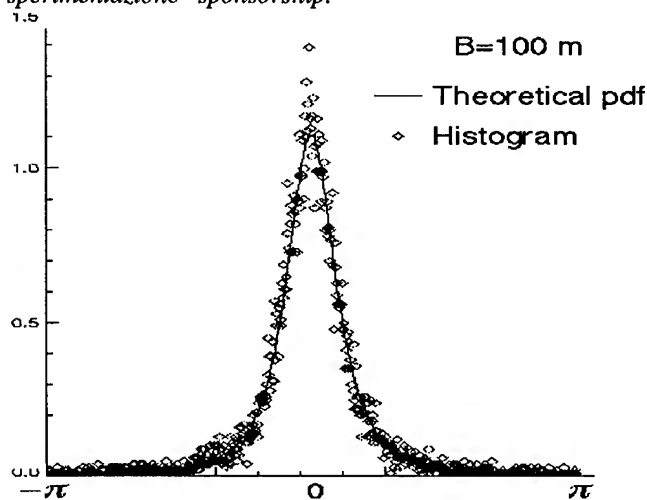


Fig. 3: Phase difference distribution and theoretical pdf.

Simulator for Repeat-Pass Satellite InSAR Studies

Wei Xu, Ian Cumming

Department of Electrical and Computer Engineering, University of British Columbia

2356 Main Mall, Vancouver, B.C. Canada V6T 1Z4

Tel: (604) 822-4162, Fax: (604) 822-5949, Email: weix@ee.ubc.ca

Abstract — An Interferometric Synthetic Aperture Radar (InSAR) simulator has been developed for testing and optimizing InSAR processing algorithms. With the help of the InSAR simulator, the errors introduced by the InSAR processing algorithms can be isolated and quantitatively detected. The InSAR simulator takes one SAR complex image, and uses a geometry model and noise/error models to create a second image as would be collected from a second SAR antenna. Examples of the application of each module are given, illustrating the performance of the InSAR simulator and the generation of realistic SAR interferograms.

1 INTRODUCTION

There are many open research topics in SAR interferometry. These vary from optimization of the processing algorithms to developing new applications of interferometry. All of the algorithms and applications need a performance verification. While no SAR image pairs with controlled error and known ground truth are available, a simulator seems to be the most practical tool for measuring algorithm accuracy. The InSAR phase values are subject to a number of error sources [1–3]. Examples of the errors are receiver noise, processing errors, phase aliasing caused by steep terrain or excessive phase noise, temporal decorrelation, and baseline speckle. Errors embedded in the input parameters are also passed on to the resultant interferogram. They are errors in the estimated satellite orbit and baseline and other registration errors.

We have developed an InSAR data simulator which creates a second (slave) complex image from a given (master) complex image, in which the slave image contains a controlled subset of the noise sources listed above. A real SAR image can be used as the master complex image. This makes the simulated SAR interferogram as realistic as possible. It is possible to turn each error source on and off independently, as well as to control the magnitude of each error independently. The InSAR simulator is written in ANSI C under the UNIX operating system with a convenient I/O interface. An additional function of the InSAR simulator is to evaluate the effect of satellite and radar parameters on InSAR results.

2 SATELLITE GEOMETRY MODEL

Parallel orbits are assumed at this stage for simplicity. In such case, the baseline length and elevation angle are fixed throughout the whole scene, the azimuth and range

displacements are separated. It is sufficient to assume the earth surface and satellite motion are flat in the azimuth direction for simplicity.

The geometry of an InSAR system is shown in Fig. 1, where O is the center of the earth; A is the master SAR antenna at time $t=0$; A' is the slave SAR antenna at time $t=0$; R is the radius of the earth assumed locally spherical in the range direction; H is the altitude of the master SAR antenna; B is the baseline at time $t=0$; ω is the elevation angle of the baseline; V is the motion direction of the master and slave SAR antenna, and it is defined as the direction of the x axis when the SAR is left looking or its opposite direction when the SAR is right looking; Ω is the local off-nadir angle. The positions of the master SAR antenna (x_a, y_a, z_a) and the slave SAR antenna (x'_a, y'_a, z'_a) as functions of time t are

$$x_a = tV; \quad y_a = 0; \quad z_a = R + H \quad (1)$$

$$x'_a = tV; \quad y'_a = B_c; \quad z'_a = R + H + B_s \quad (2)$$

where V the projection of V on the x axis, and B_s, B_c are

$$B_s = B \sin \omega; \quad B_c = B \cos \omega. \quad (3)$$

Given the coordinates in the slave image (x', r'_s) and DEM, the coordinates in the master image (x, r_s) can be obtained by:

$$x' = x + x_0 \quad (4)$$

$$r'_s = \sqrt{r_s^2 + B^2 - 2Br_s \sin(\Omega - \omega)} \quad (5)$$

where x_0 is slave image shift in azimuth and

$$\cos \Omega = \left(r_s^2 + 2R(H - h)^2 - h^2 \right) / (2(R + h)r_s) \quad (6)$$

$$\sin(\Omega - \omega) = \cos \omega \sqrt{1 - \cos^2 \Omega} - \sin \omega \cos \Omega \quad (7)$$

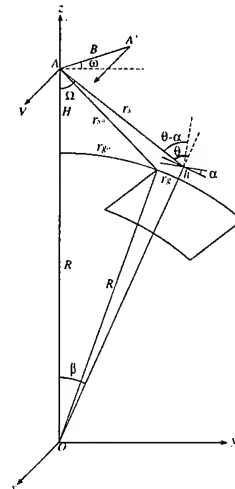


Fig. 1 Geometry of an InSAR system

This work is sponsored by the Canada Centre for Remote Sensing, Macdonald Dettwiler and Associates and the Natural Sciences and Engineering Research Council (NSERC).

3 INSAR DISPLACEMENT MODEL

3.1 Displacement in azimuth direction

The displacement in the azimuth direction is simple and constant throughout the whole scene.

$$x = x' + x_0 \quad (8)$$

As the multiples of sample interval, d_{az} can be removed by shifting the line in the master SAR image, the range of x_0 can be restricted to one sample interval $[0, 1)$.

For a pixel (x', r'_s) in the slave complex image, its backscattering coefficient $\sigma'_b(x', r'_s)$ is calculated from the corresponding point in the master complex image. If (x', r'_s) is not on the grid in the master complex image, an 8-point *sinc* interpolator is used for azimuth interpolation.

3.2 Displacement in range direction

Let r_{s1} and r_{s2} have their corresponding value of r'_{s1} and r'_{s2} satisfies

$$r'_{s1} \leq r'_s < r'_{s2} \quad (9)$$

Then the approximate value of r_s for the given r'_s is obtained by the following linear interpolation

$$r_s = r_{s1} + (r'_s - r'_{s1})(r_{s2} - r_{s1})/(r'_{s2} - r'_{s1}) \quad (10)$$

An 8-point *sinc* interpolator is used for range interpolation.

4 INSAR PHASE SHIFT MODEL

The noise-free backscattering coefficient $\sigma'_b(x', r'_s)$ for the slave image can be calculated from the noise-free backscattering coefficient $\sigma_b(x, r_s)$ for the master image by applying the range-dependent phase shift

$$\sigma'_b(x', r'_s) = \sigma_b(x, r_s) e^{-j \frac{4\pi}{\lambda} (r'_s - r_s)} \quad (11)$$

5 INSAR NOISE MODELS

5.1 Multiplicative speckle noise

Multiplicative speckle noise can be used to simulate temporal and baseline decorrelation. Let the SAR images with multiplicative noise be $\sigma_{bm}(x, r_s)$ and $\sigma'_{bm}(x', r'_s)$, then

$$\sigma_{bm}(x, r_s) = \sigma_b(x, r_s)(1 + n_m(x, r_s)) \quad (12)$$

$$\sigma'_{bm}(x', r'_s) = \sigma'_b(x', r'_s)(1 + n'_m(x', r'_s)) \quad (13)$$

where n_m and n'_m are independent Gaussian random processes with zero mean and standard deviation determined by the temporal and baseline decorrelation. With (11) we have

$$\sigma'_{bm}(x', r'_s) = (1 + n_{mm}(x', r'_s)) \sigma_{bm}(x, r_s) e^{-j \frac{4\pi}{\lambda} (r'_s - r_s)} \quad (14)$$

$$n_{mm}(x', r'_s) = (n'_m(x', r'_s) - n_m(x, r_s)) / (1 + n_m(x, r_s)) \quad (15)$$

Assuming that $E\{|n_m|^2\} = E\{|n'_m|^2\}$, we have $E\{|n_{mm}|^2\} = 2E\{|n_m|^2\} = 2(1/\rho_m - 1)$.

5.2 Additive receiver noise

Let the SAR image with both multiplicative noise and additive receiver noise be $\sigma'_{bma}(x', r'_s)$ and $\sigma_{bma}(x, r_s)$

$$\sigma_{bma}(x, r_s) = \sigma_{bm}(x, r_s) + n_a(x, r_s) \quad (16)$$

$$\sigma'_{bma}(x', r'_s) = \sigma'_{bm}(x', r'_s) + n'_a(x', r'_s) \quad (17)$$

where n_a and n'_a are independent Gaussian random processes with zero mean and their standard deviation can be determined by the noise level of the SAR image. With (14) we have

$$\sigma'_{bma}(x', r'_s) = (1 + n_{mm}(x', r'_s)) \sigma_{bma}(x, r_s) e^{-j \frac{4\pi}{\lambda} (r'_s - r_s)} + n_{aa}(x', r'_s) \quad (18)$$

$$n_{aa}(x', r'_s) = n'_a(x', r'_s) - n_a(x, r_s)(1 + n_{mm}(x', r'_s)) e^{-j \frac{4\pi}{\lambda} (r'_s - r_s)} \quad (19)$$

Assuming that $E\{|n_a|^2\} = E\{|n'_a|^2\}$, we have $E\{|n_{aa}|^2\} = 2E\{|n_a|^2\}$.

6 TEST AND DEMONSTRATION RESULTS

A real complex SAR image and an artificial DEM shown in Fig. 2 a is used to test and demonstrate the functions of the InSAR simulator. A simulated SAR interferogram with phase shift only is shown in Fig. 2 b. Only round-off errors occur in this experiment.

A simulated SAR interferogram with baseline decorrelation multiplicative speckle noise is shown in Fig. 7 a. Various scaled multiplicative speckle noise is added in the simulation. The resultant phase error as a function of the equivalent correlation coefficient is shown in Fig. 3. A simulated SAR interferogram with additive noise is shown in Fig. 7 b. Various additive noise is added in the simulation. the resultant phase error as a function of the SNR coefficient is shown in Fig. 4.

A simulated SAR interferogram with a large azimuth displacement (0.5 pixel) is shown in Fig. 7 c. With various azimuth shifts, the resultant phase error as a function of the azimuth displacement is shown in Fig. 5. The phase error

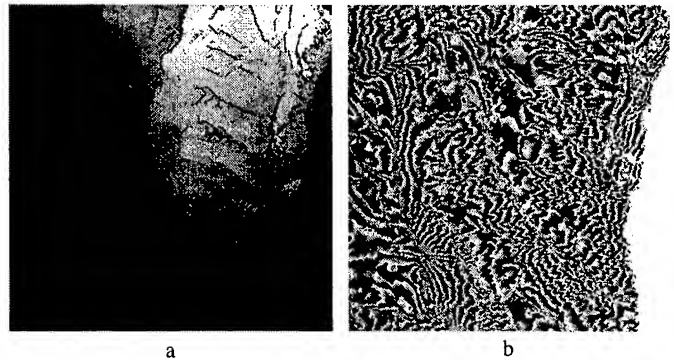


Fig. 2 a) DEM; b) A simulated SAR interferogram without noise and displacement

without azimuth displacement is caused by range interpolation error. A simulated SAR interferogram with a large range displacement (about 0.5 pixel of average displacement) is shown in Fig. 7. With various range displacements, the resultant phase error as a function of the average range displacement is shown in Fig. 6.

The test experiments shows that the simulator is reliable for the following reasons: both average absolute phase error and

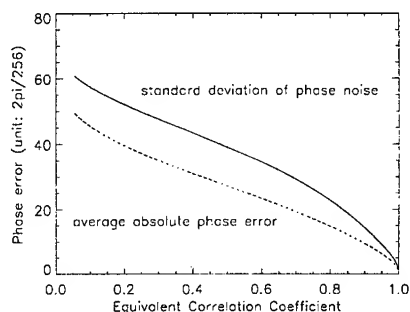


Fig. 3 Phase error as a function of the correlation coefficient

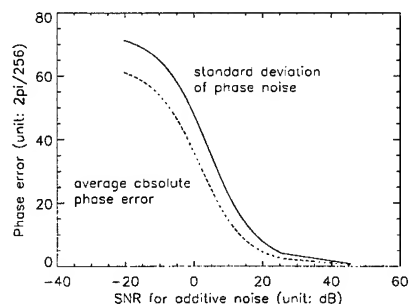


Fig. 4 Phase error as a function of the SNR for additive noise

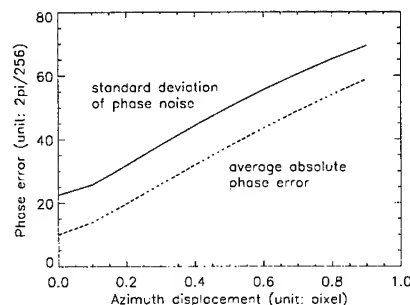


Fig. 5 Phase error as a function of the azimuth displacement

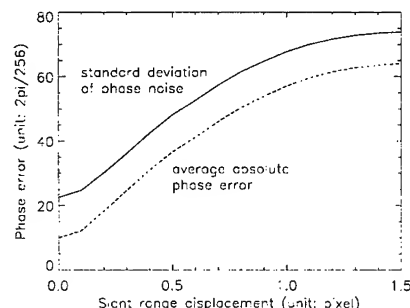


Fig. 6 Phase error as a function of the range displacement

the standard deviation of phase noise should be zero when there is no noise or displacement; the average absolute phase error should be $\pi/2$ and the standard deviation of phase noise should be $\pi/\sqrt{3}$ when the noise or displacement dominates the data.

7 CONCLUSIONS

The flexibility and accuracy of the InSAR simulator has been demonstrated by the examples. It can generate very realistic SAR interferograms, and quantitatively controllable errors can be added into the output to simulate various error and noise sources in a real InSAR system, and to test the performance of InSAR processing algorithms.

REFERENCE

- [1] Fuk K. Li and R. M. Goldstein. Studies on Multibaseline Spaceborne Interferometric Synthetic Aperture Radar. *IEEE Trans. Geosci. Remote Sens.*, 28(1):88-97, Jan. 1990.
- [2] Howard A. Zebker, Charles L. Werner, Paul A. Rosen, and Scott Hensley. Accuracy of Topographic Maps Derived from ERS-1 Interferometric Radar. *IEEE Trans. Geosci. Remote Sens.*, 32(4):823-836, July 1994.
- [3] D. R. Stevens, I. G. Cumming, A. L. Gray, and M. R. Ito. Airborne Interferometric SAR: Terrain Induced Phase Errors. In *IGARSS'93*, pages 977-979, Tokyo, Japan, 1993.

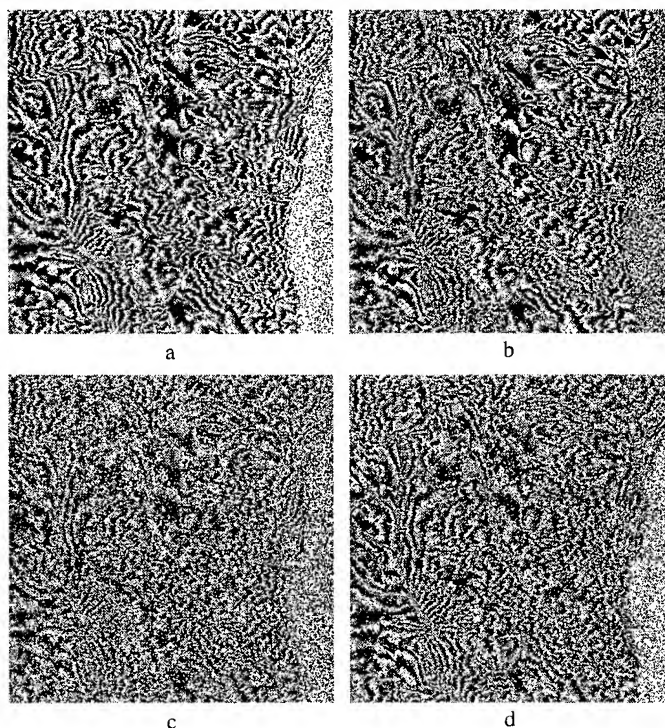


Fig. 7 Example simulated SAR interferograms with a) baseline decorrelation; b) additive noise; c) azimuth displacement; d) range displacement

Optimization of SAR Interferogram by Using Coherence Information

Chinatsu YONEZAWA and Shoji TAKEUCHI

Remote Sensing Technology Center of Japan

Roppongi First Bldg., 8F, 1-9-9, Roppongi, Minato-ku, Tokyo 106, JAPAN

TEL: +813-5561-8777, FAX: +813-5561-9542, E-mail: chinatsu@restec.or.jp

Abstract-- The authors tested the applicability of coherence information for optimizing SAR (Synthetic Aperture Radar) interferogram. The purpose of the optimization in this study is to improve the smoothness of the topographic fringe in SAR interferogram, which results in better fringe for unwrapping.

Coherence information was computed as the complex correlation coefficient between two SAR complex data. To optimize the interferogram, the maximum coherence value was searched in 3 x 5 window around the initial registered position between two data and then the phase difference was obtained from the pixel pair that has the maximum coherence.

This optimizing method was attempted for several SAR complex data pairs. The effect of the optimization was found in some pairs. It was found that the increase of the coherence due to the optimization was one of the important factors for the improvement of the smoothness.

1. INTRODUCTION

Interferometric SAR has been highlighted as one of the promising techniques for a topographic mapping and a production of DEM (Digital Elevation Model). SAR interferogram is generated as a wrapped pattern of phase differences between two single-look SAR complex data. Therefore it should be followed by unwrapping to produce the DEM and the smoothness of the interferogram is quite important to achieve the unwrapping successfully. One of the key issues to get the smooth interferogram is that the optimal registration is achieved between the two SAR data.

The cross correlation of SAR intensity has been generally used for the registration in order to obtain the optimal coincidence of land cover patterns. However, it is difficult to insure the optimum at the areas where any distinctive feature does not exist. Coherence is another useful information for the registration because it has been proved to be highly correlated to the smoothness of the interferogram[1]. However, it should be also considered that the primary factor to affect the coherence is the stability of phase differences and not the coincidence of land cover and also that the coherence is much affected by the change of phase differences due to the topographic fringe.

Therefore, a practical approach to achieve the optimal registration is to use the coherence as a supplemental

information after the initial registration is performed by using the intensity. The authors tested the effect of the coherence for a post-processing to optimize the registration and to improve the smoothness of the SAR interferogram.

2. METHOD OF OPTIMIZATION

2.1 Test Data and Initial Registration

The optimization method was attempted to six data pairs observed by JERS-1 and one data pair by ERS-1.

The raw data in a single data pair were compressed in the range and azimuth direction using ERGOvista SAR processor, and the pair of single-look complex (SLC) data were obtained after the compression. The power and intensity images were generated from the SLC data. First, fifteen to sixteen tie points were selected by visual inspection of the two power images. Then the initial coordinate of the tie points were redefined by searching the cross correlation between the two intensity images by 31 x 61 window size in 61 x 121 searching area surrounding the initial coordinate. The slave image was registered onto the master image using 1st or 2nd order polynomial transformation.

2.2 Generation of Topographic Fringe

The initial interferogram was generated by extracting the phase differences between the SLC data pair after the initial registration. To obtain the topographic fringe, the orbital fringe (flat surface fringe) was removed from the initial interferogram. The optimal orbital fringe frequency was obtained manually referring to the calculated value from baseline length. On the topographic fringe, three pixels in range and nine in azimuth (JERS) or two pixels in range and ten in azimuth (ERS) were averaged and then smoothed by three by three moving window.

2.3 Calculation of Coherence

The coherence is calculated as the complex correlation coefficient in a small corresponding patch as follows;

$$\rho = \frac{|E(c_1 c_2^*)|}{[E(c_1 c_1^*) E(c_2 c_2^*)]^{1/2}} \quad (2.1)$$

where c_1 and c_2 are the corresponding complex values of the two SLC data, * means the complex conjugate, and $E(\)$ denotes statistical expectation. As correspondence to averaging and smoothing window size on the topographic fringe, nine pixels in range and twenty-seven in azimuth (JERS) or six pixels in range and thirty in azimuth (ERS) were adopted for the corresponding patch size. The orbital fringe was removed in the process of coherence calculation.

2.4 Re-registration by Pixel-wise Optimization Using Coherence

The optimizing procedure for re-registration of initially registered SLC data pair is as follows. First, the coherence in the small corresponding patch is calculated by shifting the corresponding position by three pixels in range and five in azimuth surrounding the initial registered position. Next, the position where the maximum coherence is obtained is defined as the optimal corresponding point. Then, the optimal corresponding point is redefined by the majority operation in a block with 10 to 100 times areas of the coherence patch size. This majority operation is performed to avoid the instability of the corresponding position. Finally, the phase difference is extracted again from the optimized pixel pairs to generate the optimized topographic fringe.

3. RESULT OF OPTIMIZATION

3.1 Visual Evaluation of the Optimization

The effect of the optimization was investigated by visual inspection of the interferograms before and after the optimization. In some data pairs, obvious improvement of the smoothness was found partially in the interferogram. One of the examples is shown in Plate 1. The test site is Mt. Fuji and a part of the whole image is shown here. The transformation for the initial registration is 1st order. In Plate 1, the smoothness of the fringe at the center and the right parts including the top of Mt. Fuji is improved by the optimization, while, the smoothness is almost unchanged at the left part of the image. It seems that the areas where the fringe is already smooth enough does not change so much even after the optimization. In addition, there are some noisy areas where no improvement is achieved by the optimization.

3.2 Quantitative Index of the Smoothness

For the quantitative index of the smoothness of the topographic fringe, negative absolute residual values were

extracted from the topographic fringe. The residues are calculated for phase unwrapping and non-zero residue indicates the existence of singular point for phase continuity. The sum of the negative absolute residual value in a small window was calculated over the whole interferogram image. 30 x 30 was adopted for a window size here. The better the fringe is, the more the index becomes.

3.3 Relation between the Improvement of Smoothness and the Change of Coherence by Optimization

The relation between the improvement of the smoothness and the change of the coherence by the optimization was investigated quantitatively. Fig.1 shows the relations between the changes of the smoothness index and the average coherence value in the window by optimization in the data pair for Mt. Fuji, same data pair shown in Plate 1. The transformation for the initial registration is 1st order. In Fig.1, more than three hundreds windows are selected automatically.

From Fig.1, the increase (improvement) of the smoothness index is correlated to the increase of the coherence in general. However, in some sample windows, the smoothness index decreases after the optimization. It means no improvement or getting worse to the continuity of the fringe and in these windows, the increase range of the average coherence value by the optimization is less than about 0.1.

It is supposed that the potential value of the coherence is somewhat limited due to land cover conditions and topographic features because the coherence is affected not only by the registration accuracy but also by the land cover and the topography. For the verification of this fact, the average coherence values before and after optimization were compared between the data pairs transformed by 1st order and 2nd order polynomials for the initial registration. In Fig.2, twelve examples of window are selected manually from the data pair for Mt. Fuji. There are seen the differences of coherence between the two transformations before the optimization, but the coherence after the optimization show almost same value. This result suggests that the optimization procedure using the coherence brings actual effect when the coherence value is much less than its potential value because of insufficient registration at the initial registration using the intensity.

4. CONCLUSION

The above experimental results verify that the optimization using coherence information is effective for the areas where the registration by intensity information is inaccurate. It is very difficult to judge whether the initial registration is enough or

not and to predict the increase of the coherence by the optimization. Even if the improvement is achieved only when the coherence increases more than a certain degree, it is worth to attempt the optimization after the initial registration. The result of this study also supports the close relationship between the coherence and the smoothness of the interferogram, and the importance of the coherence information for generating a smooth interferogram.

ACKNOWLEDGMENTS

We would like to thank NASDA and ESA for providing the JERS-1 and ERS-1 SAR data for this study.

REFERENCE

- [1] S. Takeuchi, "A Case Study for Applying Interferometry in Tropical Regions Using JERS-1/SAR" (Japanese), Proceedings of the 20th Japanese Conference on Remote Sensing. May, 1996.



Topographic fringe pattern before the optimization.



Topographic fringe pattern after the optimization.

Plate1 Examples of topographic fringe pattern before and after the optimization. (JERS-1/SAR at Mt. Fuji)

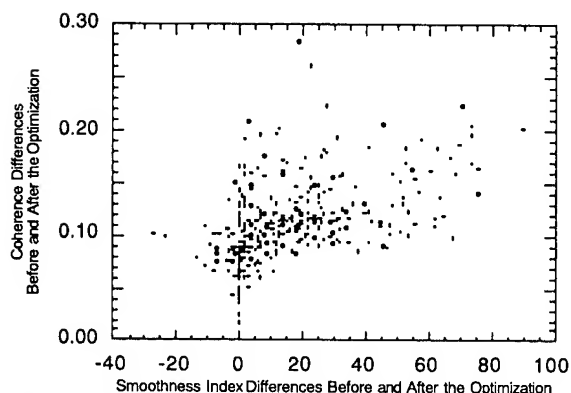


Fig.1 Average coherence value differences vs. smoothness index differences before and after the optimization. The test data are JERS-1/SAR data at Mt. Fuji.

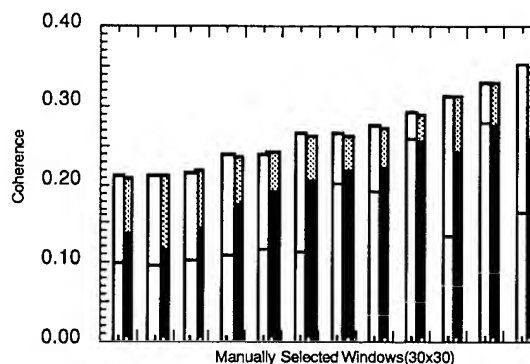


Fig.2 Average coherence values in some 30 x 30 windows on the interferogram for Mt.Fuji. Blue columns show 1st order and red columns show 2nd order polynomial transformation respectively for the initial registration. The mesh pattern means increased value by the optimization.

Decorrelation Induced by Interpolation Errors in InSAR Processing

Richard Bamler¹ and Ramon Hanssen²

¹German Aerospace Research Establishment (DLR), German Remote Sensing Data Center Oberpfaffenhofen
D-82234 Wessling, Germany phone: +49 8153 28 2673, fax: +49 8153 28 1420 E-mail: Richard.Bamler@dlr.de

²Delft Institute for Earth Oriented Space Research (DEOS) Delft University of Technology
2600 GA Delft, the Netherlands phone: +31 15 278 2565, fax: +31 15 278 3711 E-mail: hanssen@geo.tudelft.nl

Abstract — Interpolation is required in interferometric SAR processing for co-registration of complex signals. Straightforward system theoretical considerations provide objective figures of merit, like interferometric decorrelation and phase noise, for interpolators. Theoretical and simulation results are given for nearest neighbor, piecewise linear, 4-point and 6-point cubic convolution kernels.

INTRODUCTION

The first step in SAR interferogram processing is often the resampling of one complex SAR image u_1 to map it onto a second image u_2 to within an accuracy of about a tenth of a resolution element.

Although the implementation may be different, resampling can be viewed as consisting of two steps:

1. reconstruction of the continuous signal from its sampled version by convolution with an interpolation kernel $i(x, y)$, and
2. sampling of the reconstructed signal at the new sampling grid.

This paradigm holds even in many cases, where the convolution (step 1) is not obvious. For example, nearest neighbor and Lagrange-type interpolation of equidistantly sampled data can be considered as a convolution with particular kernels. The choice of the interpolation kernel (especially its length) requires a trade-off between interpolation accuracy and computational efficiency. This paper shows that straightforward system theoretical considerations give objective criteria for choosing or designing interpolation kernels.

THEORY OF INTERPOLATION ERRORS

Fig. 1 shows (for the 1-D case) how the Fourier transform $I(f)$ of a kernel $i(x)$ acts as a transfer function on the periodically repeated signal power spectral density $|H(f)|^2$. The two classes of errors to be considered are: the distortion of the useful spectral band $|f| \leq \frac{B}{2}$, and the insufficient suppression of its replicas $|f - nf_s|_{n \neq 0} \leq \frac{B}{2}$,

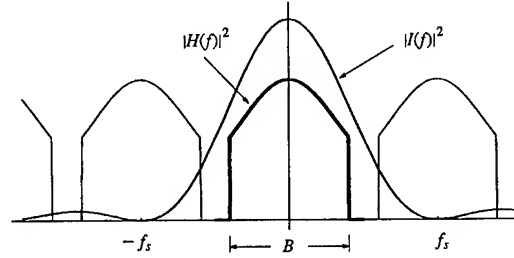


Figure 1: Fourier transform $I(f)$ of interpolator $i(x)$ acting on the replicated signal spectrum

where f_s is the sampling frequency. Hence, the interpolated signal will not be strictly lowpass limited and the subsequent new sampling creates aliasing terms. If in the resampling process all inter-pixel positions are equally probable, the aliasing terms are superposed incoherently and can be treated as noise with a signal to noise ratio of

$$\frac{S}{N} = \frac{\int_{-B/2}^{+B/2} |H(f)|^2 |I(f)|^2 df}{\sum_{n \neq 0} \int_{nf_s - B/2}^{nf_s + B/2} |H(f - nf_s)|^2 |I(f)|^2 df} \quad (1)$$

In the following we will quantify interpolation errors in terms of interferogram decorrelation and associated phase noise. We assume that the original data u_1 has been sampled at least at the Nyquist rate and that the sampling distance after resampling is similar to the original one.

Consider a perfect and noise free interferometric data pair of coherence $\gamma = 1$, before interpolation. Both of them have passed the SAR imaging and processing system described by a transfer function $H(f)$. Signal u_1 additionally suffers from the interpolation transfer function $I(f)$, and alias noise n . It can be derived from [1] and [2] that for circular Gaussian signals (i.e. for distributed targets) the coherence of such a system is given by

$$\gamma = \frac{1}{\sqrt{1 + \frac{N}{S}}} \cdot \frac{\int |H(f)|^2 I(f) df}{\sqrt{\int |H(f)|^2 df \cdot \int |H(f)|^2 |I(f)|^2 df}} \quad (2)$$

These equations are readily extended to two dimensions.

If both $H(f_x, f_y)$ and $I(f_x, f_y)$ are separable, we find:

$$\gamma = \gamma_x \cdot \gamma_y. \quad (3)$$

The phase noise resulting from $\gamma < 1$ is known to be (in the L -Look case):

$$\sigma_\phi^2 = \int_{-\pi}^{+\pi} \phi^2 \text{pdf}(\phi) d\phi, \quad (4)$$

where

$$\text{pdf}(\phi; \gamma, L) = \frac{\Gamma(L + 1/2)(1 - \gamma^2)^L \gamma \cos \phi}{2\sqrt{\pi}\Gamma(L)(1 - \gamma^2 \cos^2 \phi)^{L+1/2}} \quad (5)$$

$$+ \frac{(1 - \gamma^2)^L}{2\pi} \cdot {}_2F_1(L, 1; 1/2; \gamma^2 \cos^2 \phi). \quad (6)$$

EXAMPLES FOR INTERPOLATORS

The interpolators and their spectra evaluated here are (assuming unity sample grid distance)[3][4]:

- Nearest neighbor:

$$i(x) = \text{rect}(x) = \begin{cases} 0, & |x| > \frac{1}{2} \\ \frac{1}{2}, & |x| = \frac{1}{2} \\ 1, & |x| < \frac{1}{2} \end{cases} \quad (7)$$

$$I(f) = \text{sinc}(f)$$

- Piecewise linear interpolation:

$$i(x) = \text{tri}(x) = \begin{cases} 0, & |x| > 1 \\ 1 - |x|, & |x| < 1 \end{cases} \quad (8)$$

$$I(f) = \text{sinc}^2(f)$$

- 4-point cubic convolution ($\alpha = -1$):

$$i(x) = \begin{cases} (\alpha + 2)|x|^3 - (\alpha + 3)|x|^2 + 1, & 0 \leq |x| < 1 \\ \alpha|x|^3 - 5\alpha|x|^2 + 8\alpha|x| - 4\alpha, & 1 \leq |x| < 2 \\ 0, & 2 \leq |x| \end{cases}$$

$$I(f) = \frac{3}{(\pi f)^2} [\text{sinc}^2(f) - \text{sinc}(2f)] + \frac{2\alpha}{(\pi f)^2} [3\text{sinc}^2(2f) - 2\text{sinc}^2(f) - \text{sinc}(4f)]. \quad (9)$$

- 6-point cubic convolution ($\alpha = \frac{-11}{12}, \beta = \frac{2}{12}$):

$$i(x) = \begin{cases} (\alpha + \beta + 2)|x|^3 - (\alpha + \beta + 3)|x|^2 + 1, \\ \alpha|x|^3 - (5\alpha - \beta)|x|^2 + (8\alpha - 3\beta)|x| - (4\alpha - 2\beta), \\ \beta|x|^3 - 8\beta|x|^2 + 21\beta|x| - 18\beta, \\ 0, \end{cases} \quad (10)$$

for ($0 \leq |x| < 1$), ($1 \leq |x| < 2$), ($2 \leq |x| < 3$), and ($3 \leq |x|$) respectively.

Table 1 lists the theoretically derived coherence and 1-look phase noise introduced by the first three of these interpolators for one and two dimensions; ERS range signal parameters have been used for both dimensions with uniformly weighted spectrum and oversampling ratio of $f_s/B = 18.96\text{MHz}/15.5\text{MHz} = 1.223$ (in real systems, azimuth oversampling is slightly higher than in range).

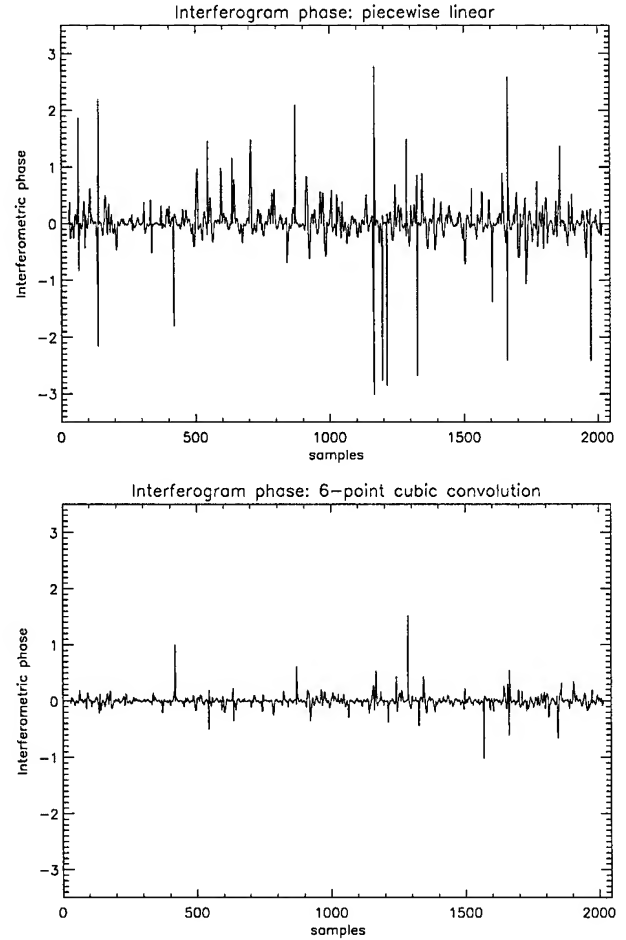


Figure 2: Phase errors from simulated interferograms using piecewise linear and 6-point cubic convolution interpolation.

Often, SAR data are oversampled by a higher factor before an interferogram is computed, be it either to avoid undersampling of the interferogram or as a consequence of baseline dependent spectral shift filtering. In these cases the requirement on the interpolator is relaxed [5].

EXPERIMENTAL RESULTS

One-dimensional complex circular Gaussian random sequences have been generated and low pass filtered to an oversampling ratio of 12.23. This signal is used as a reference u . Undersampling by 1/10 gives a test signal u_s that reflects ERS conditions. The test signal u_s is then interpolated using the kernels under investigation, yielding an estimate \hat{u} of the reference signal.

The four interpolation kernels *nearest neighbor*, *piecewise linear*, *4-point cubic convolution* and *6-point cubic convolution* are created using (7), (8), (9) and (10). For every kernel the interferometric phase error $\phi = \arg[\hat{u} \cdot u^*]$, the phase error histogram, the total coherence and the

Table 1: Theoretically and empirically derived influence of different 1-D and 2-D interpolators on interferogram coherence and phase noise (phase standard deviation without multi-looking)

	1-dimensional				2-dimensional	
	coherence		phase std. [deg]		coherence	phase std. [deg]
	theory	exp	theory	exp	theory	theory
nearest neighbor	0.9132	0.9135	37.4	35.4	0.8345	48.7
piecewise linear	0.9773	0.9783	21.4	19.3	0.9551	28.5
4-point cubic convolution	0.9949	0.9953	11.3	10.1	0.9898	15.2
6-point cubic convolution	—	0.9975	—	7.2	—	—

standard deviation of the interferometric phase error are evaluated. Single experiment results of the interferometric phase error are shown in fig. 2. It can be seen that the variation of the interpolated signal decreases considerably as the kernel contains more sample points. The total coherence and the standard deviation of the interferometric phase are studied using averaged values from 500 simulation loops. The results are given in table 1, to allow comparison with the theoretical findings.

Fig. 3 shows the mean standard deviation of the phase as a function of the coherence for the four kernels. The simulation results pretend to be slightly better than the theory. This, however, is an artifact of the used simulation method: only ten subpixel positions have been interpolated, and every one out of ten samples is error-free.

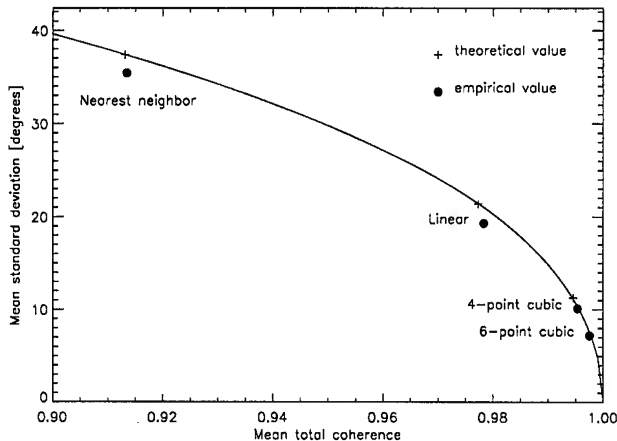


Figure 3: Mean standard deviation phase as a function of coherence for the 1-D case, the four kernels

DISCUSSION OF THE RESULTS

The spurious spikes in the interferogram, as shown in fig. 2, appear at those positions in the signal where the amplitude is extremely low. The signal to noise ratio at these interpolation points is therefore dominated by the interpolation noise. This makes a sudden phase jump at low amplitude areas likely to occur. Due to the small am-

plitude, multi-looking suppresses these spikes, and considerably diminishes the phase noise.

The interpolation kernels used here can be referred to as Parametric Cubic Convolution (PCC)[4]. The parameters α and β for the 4-point and 6-point kernels chosen here have proved to be close to optimal for this particular configuration. Optimization for specific purposes can be performed by evaluating (1).

Interpolation errors are due to the aliasing of repeated signal spectra and the cut-off of the signal spectra's corners. Hence, the choice of an optimal interpolator will always depend on the correlation properties of the signal. However, a subjective recommendation can be given for ERS conditions, where temporal decorrelation dominates the interferogram quality anyway. In these cases, a 4-point cubic convolution with $\alpha = -1$ proved to be sufficient. For high resolution applications of high coherence single-pass interferometers, where multi-looking is not desirable, longer interpolation kernels like the optimized 6-point cubic convolution presented here are recommended. A more detailed version of this paper will be given in [5].

REFERENCES

- [1] Dieter Just and Richard Bamler, "Phase statistics of interferograms with applications to synthetic aperture radar," *Applied Optics*, vol. 33, pp. 4361–4368, 1994.
- [2] M Cattabeni, A Monti-Guarnieri, and F Rocca, "Estimation and improvement of coherence in SAR interferograms," in *Proc. IGARSS'94*, pp. 720–722, 1994.
- [3] Robert G Keys, "Cubic convolution interpolation for digital image processing," *IEEE Trans. ASSP*, vol. ASSP-29, pp. 1153–1160, Dec. 1981.
- [4] Stephen K. Park and Robert A. Schowengerdt, "Image reconstruction by parametric cubic convolution," *Computer Vision, Graphics and Image Processing*, vol. 23, pp. 258–272, Sept. 1983.
- [5] Ramon Hanssen and Richard Bamler, "Evaluation of Interpolation Kernels for SAR interferometry," *Submitted to IEEE Tran. Geosc. & Remote Sens.*, Jan. 1997.

An Interferometric SAR Processor Avoiding Phase Ambiguities

Klaus Schmitt, Werner Wiesbeck

Institut für Höchstfrequenztechnik und Elektronik (IHE)

University of Karlsruhe

Kaiserstrasse 12, D-76128 Karlsruhe

Telefon: +49 721 608 2522 Fax: +49 721 691865 e-mail: ihe@ihewap.etec.uni-karlsruhe.de

Abstract -- One of the key problems in SAR interferometry is the determination of the absolute phase of a scatterer by unwrapping the calculated phase difference of two SAR images. Since the phase difference is a function modulo 2π software algorithm are used to perform a phase unwrapping to obtain an unambiguous phase and thus the corresponding height information. This paper presents a procedure using two different transmit frequencies to enlarge the unambiguous range for height determination. Measurements performed in an anechoic chamber are used to test the processing. Using this procedure it is not only possible to resolve the height of a surface but also of single scatterers in space or in urban areas with steep slopes.

INTRODUCTION

SAR interferometry is becoming a standard tool for the generation of digital elevation models of the earth surface. Two two-dimensional complex SAR images of the same scene, acquired from two neighboring receiving antennas, are used to generate an interferogram. It is produced by subtraction of the phase of the two images. The phase difference is a measure for the difference in the propagation time and contains therefore the height information. A problem arises from the fact that the phase difference is ambiguous and therefore the desired result, the height, too. To remove this, phase unwrapping algorithms are often used. These algorithms are in principle not necessary if the unambiguous range for the wanted height information is large enough. The unambiguous range depends on the transmit frequency as well as the geometry for the antenna sensor. Thus the ambiguous free range can be increased by changing the transmit frequency [1] as well as the position of the receiving antennas [2]. In the following the two frequency interferometry is presented which uses a second frequency to perform an unambiguous height mapping.

NEAR FIELD ALGORITHM FOR LINEAR SAR

A typical geometry for a linear SAR is shown in Fig.1. The scatterer is located in the (x,y) -plane. The antenna at position (x_a, y_a) is moving on a straight line parallel to the x -axis. Assuming that the distance r_0 between the antenna and the target is not much larger than the dimension of the target itself, the scatterer is illuminated by a spherical wave. Neglecting the antenna pattern of the transmitting and receiving an-

tenna, the interesting two-dimensional reflectivity density function $I(x,y)$ in the (x,y) -plane can be determined by:

$$I(x,y) = \frac{4}{c^2} \int \int_{x_a f} E(f, x_a) \Psi(f, x_a, x, y) df dx_a \quad (1)$$

Here c is the speed of light, $E(f, x_a)$ the backscattered signal as a function of frequency f and antenna position x_a and $\Psi(f, x_a, x, y)$ an operator to focus the signals, which can be expressed for a linear SAR configuration as follows:

$$\Psi(f, x_a, x, y) = \frac{y_a}{x_a^2 + y_a^2} \left(\frac{r}{r_0} \right)^2 f e^{j 4\pi \frac{r}{c} (r-r_0)} \quad (2)$$

In (2) the distance between antenna and scatterer is defined by:

$$r(x_a, x, y) = \sqrt{(x-x_a)^2 + (y-r_0 \sin \theta)^2 + H^2} \quad (3)$$

taking the spherical wavefront at the scatterer into account. A fast implementation of this algorithm is described in [3].

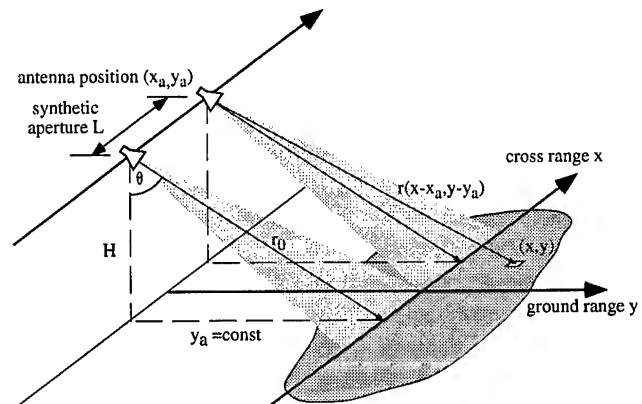


Fig 1: geometry of a linear synthetic aperture radar

TWO FREQUENCY INTERFEROMETRY

Using a reconstruction algorithm following (1) a three dimensional object can only be resolved in two dimensions. The third dimension can be determined by an interferometric approach. Therefore one transmitting and two receiving anten-

nas are used, where the two receiving antennas are separated by the distance B , called baseline, as shown in Fig. 2. Thus two complex SAR images can be processed. From these two images an interferogram of the object of interest can be generated by calculating the phase difference $\Delta\phi(x,y)$ on a pixel by pixel basis of the images [4].

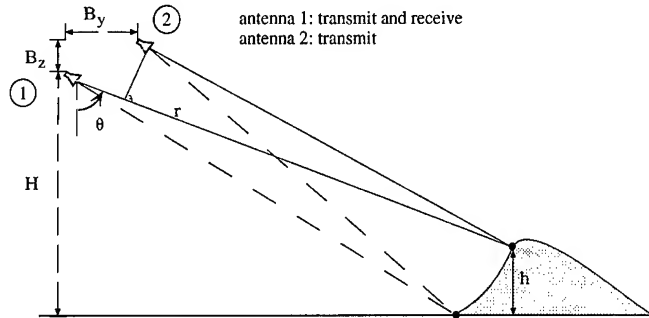


Fig. 2: geometry of an interferometric SAR

The phase difference $\Delta\phi$ contains information on the path difference between both antennas and the scatterer. From Fig. 2 it can be seen that the phase difference is a function of the transmitted wavelength λ , the baseline B and the looking angle θ .

$$\Delta\phi = \frac{2\pi}{\lambda} [B_y \sin\theta - B_z \cos\theta] \quad (4)$$

With the knowledge of λ and B , the angle θ can be calculated and then also the height h as wanted third dimension:

$$h = H - r \cos\theta \quad (5)$$

There are different possibilities to resolve the phase ambiguities. The most common approach is the phase unwrapping using different algorithms to obtain the absolute phase. Another approach is the two frequency interferometry, which will be explained in the following. From (4) it can be seen that for a specified height h or angle θ respectively the phase difference is only a function of frequency assuming that the baseline is fixed. For a lower frequency the unambiguous range is increased resulting in a lower resolution. A rough estimation for a practical airborne SAR shows that a useful transmit frequency has to be in the MHz region depending on the flight height and the wanted unambiguous phase range. Obviously it is impossible to take the measurements directly at such a low frequency. Another possibility is to perform the measurement at two neighboring frequencies and evaluating the difference frequency. This approach is visualized in Fig. 3.

In the upper part of Fig. 3 the phase response is shown as a function of path length difference for the transmit frequency f_1 and f_2 . Over that range both frequencies have several phase discontinuities and thus unwanted ambiguities. Working with the frequency difference $f_2 - f_1$ (bottom of Fig. 3) it can be

seen that this leads to an unambiguous range over the whole path length difference and the direct estimation of the absolute phase is possible. To keep the resolution of the higher frequency the interferogram at this frequency is evaluated. The difference frequency is only used to resolve the ambiguities.

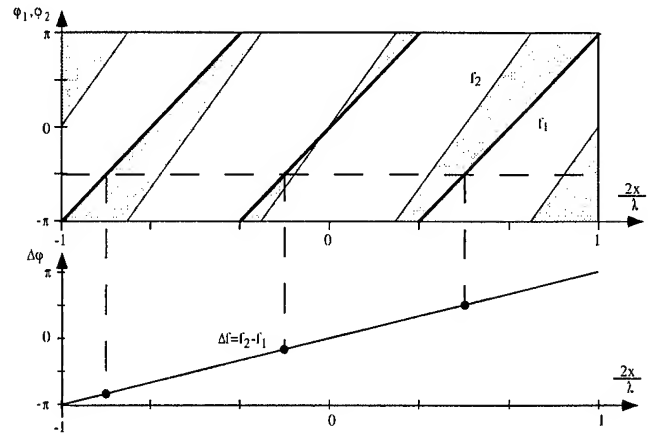


Fig. 3: Increased unambiguous range at lower frequencies

4. MEASUREMENT RESULTS

In contrast to airborne and spaceborne SAR systems an anechoic chamber is an ideal possibility to test SAR processors, since most of the disturbances are not existent. All other distortions are systematic and can easily be eliminated by system calibration. As measurement set-up a typical indoor measurement configuration for RCS measurements based on a vector network analyzer was used. The measurements were performed in the stepped frequency mode from 26.5-40 GHz using broadband horn antennas for transmitting and receiving. The object was moved stepwise on a straight line by a line scanner. As measurement object an array of metallic spheres were chosen which were positioned on a plane tilt by 25° simulating a discrete height profile of point scatterers.

In contrast to the phase unwrapping approach the two frequency interferometry can also be used to determine the absolute phase of discrete scatterers. Two interferograms were produced at 30 GHz and 37 GHz using a bandwidth of 6 GHz each. In Fig. 4 the phase ambiguities at 37 GHz can clearly be seen. They are resolved by evaluating the difference frequency at 7 GHz resulting in an absolute phase as shown in Fig. 5. From the absolute phase the height of each sphere can easily be calculated on a pixel by pixel basis. The resulting height profile is shown in Fig. 6 and agrees well with the real arrangement.

As outlined in [1] and [2] the influence of noise is the most critical point in this processing. The errors in the two original interferograms are compounded in the interferogram at the difference frequency, resulting in degraded fringes. Although the influence of noise in an anechoic chamber is

smaller than in airborne or spaceborne systems, this problem will be investigated in the future work.

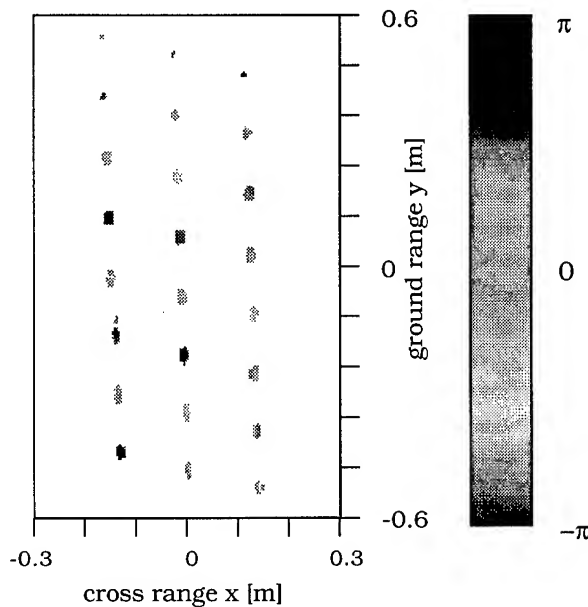


Fig. 4: interferogram of an array of spheres at 37 GHz

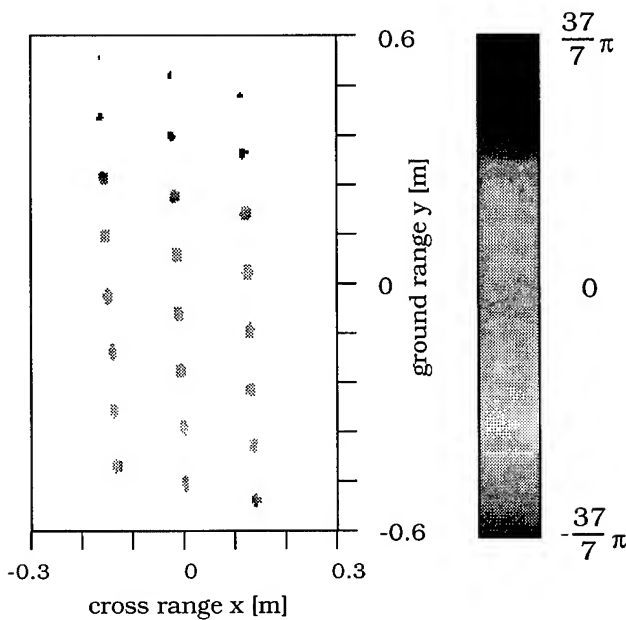


Fig. 5: interferogram of an array of spheres at 7 GHz

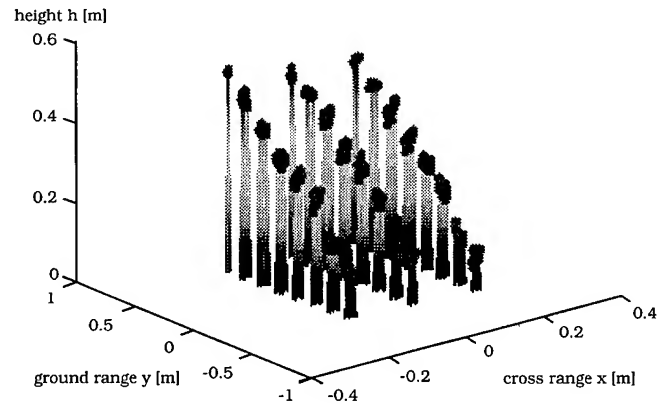


Fig. 6: height profile of an array of spheres

CONCLUSION

Using the two frequency interferometry it is possible to resolve the phase ambiguities common in the interferometric processing. This approach can not only be applied to smooth surfaces but also to steep ones like in urban areas or to discrete scatterers as well. The main unsolved problem of this processing is still the error propagation of the noise effects.

REFERENCES

- [1] S. Madson, H. Zebker, "Automated Absolute Phase Retrieval in Across-track Interferometry", Proceedings of the International Geoscience and Remote Sensing Symposium, 1992, pp. 1582-1584
- [2] W. Xu et al., "Phase-unwrapping of SAR Interferogram with Multi-frequency or Multi-baseline", Proceedings of the International Geoscience and Remote Sensing Symposium, 1994, pp. 730-732
- [3] J. Fortuny, A. J. Sieber, "Fast Algorithm for a Near-Field Synthetic Aperture Radar Processor", IEEE Transactions on Antennas and Propagation, Vol.42, No.10, 1994
- [4] L. Graham, "Synthetic Interferometer Radar for Topographic Mapping", Proceedings of the IEEE, Vol.62, No.2, 1974

A New Technique for Noise Filtering of SAR Interferogram Phase Images

J.S. Lee¹, K. P. Papathanassiou², T. L. Ainsworth¹, M.R. Grunes¹ and A. Reigber²

¹Remote Sensing Division, Code 7263, Naval Research Laboratory
Washington DC 20375-5351, USA Tel: (202) 767-2004, Fax: (202) 767-5599
Email: lee@imsy1.nrl.navy.mil, toma@imsy1.nrl.navy.mil

²DLR, Deutsche Forschungsanstalt fuer Luft und Raumfahrt, D-82234
Oberpfaffenhofen, Germany. Tel: +49-8153-2822367, Fax: +49-8153-281135
Email: Kostas.Papathanassiou@dlr.de, Reigber@ohffo1.hf.op.dlr.de

Abstract – This paper addresses the noise filtering problem for SAR interferogram phase images. The phase noise is characterized by an additive noise model, and a filtering algorithm based on this noise model was developed by filtering noise along fringes. In addition, this filter adaptively adjusts the amount of filtering according to the coherence. The effectiveness of this filter is demonstrated using SIR-C/X-SAR multi-pass generated interferograms.

INTRODUCTION

Cross-track radar interferometry has been successfully applied to measure surface topography and to monitor topographic displacements over time. Digital elevation maps are generated by phase unwrapping interferogram phase images. It has been shown that phase noise has a hypergeometric probability distribution [1], and that the noise standard deviation depends on the coherence and the number of looks used in processing. The presence of noise reduces the accuracy of the derived digital elevation model and hinders phase unwrapping.

The phase noise is characterized by an additive noise model rather than the multiplicative one found in SAR amplitude and intensity images. An adaptive noise filter is developed based on the additive noise filter [2].

The effectiveness of this filter is verified using interferograms generated from multi-pass SIR-C/X-SAR L, C and X-band data of Mt. Etna, Italy [3]. Comparisons with a box-filter, a median filter and an adaptive 2-D Gaussian filter are also made.

NOISE CHARACTERISTICS

It is well known that the speckle effect in the interferogram generates noise in the phase image. To reduce the noise problem in phase unwrapping, multi-look processing is frequently implemented by averaging neighboring pixels:

$$z = \sum_{i=1}^n y_1(i) y_2^*(i)$$

where $y_1(i)$ and $y_2(i)$ are the pair of complex one-look images and n is the number of looks. The noise standard deviation of

z depends on n and the magnitude of the correlation coefficient (or coherence), defined as

$$\rho = \frac{E[y_1 y_2^*]}{\sqrt{E[|y_1|^2] E[|y_2|^2]}} = |\rho_c| e^{i\psi}$$

It should be noted that multi-looking processing will not improve the coherence, but will reduce the standard deviation of ψ .

Based on circular Gaussian statistics, Lee *et al.* [1] derived the probability density function for single-look and multi-look phase distributions

$$p_\psi(\psi) = \frac{\Gamma(n + \frac{1}{2})(1 - |\rho_c|^2)^n \beta}{2\sqrt{\pi} \Gamma(n)(1 - \beta^2)^{n+1/2}} + \frac{(1 - |\rho_c|^2)^n}{2\pi} F(n, 1; \frac{1}{2}; \beta^2)$$

where $\beta = |\rho_c| \cos(\psi - \theta)$, θ is the location of the peak of the distribution, and F is a Gauss Hypergeometric function. Based on this distribution, the standard deviation as a function of n and $|\rho_c|$ is plotted in Fig. 1. It shows that the standard deviation decreases as $|\rho_c|$ and n increase.

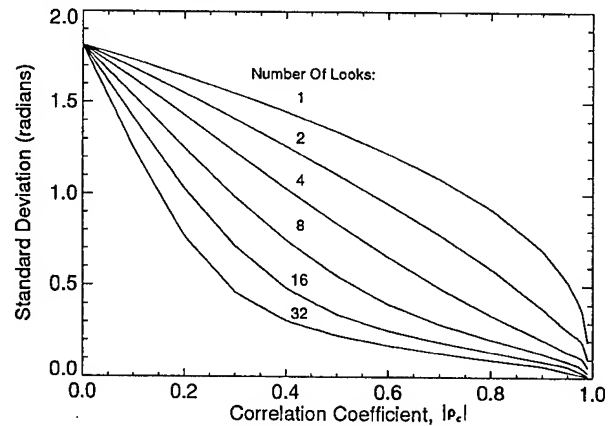
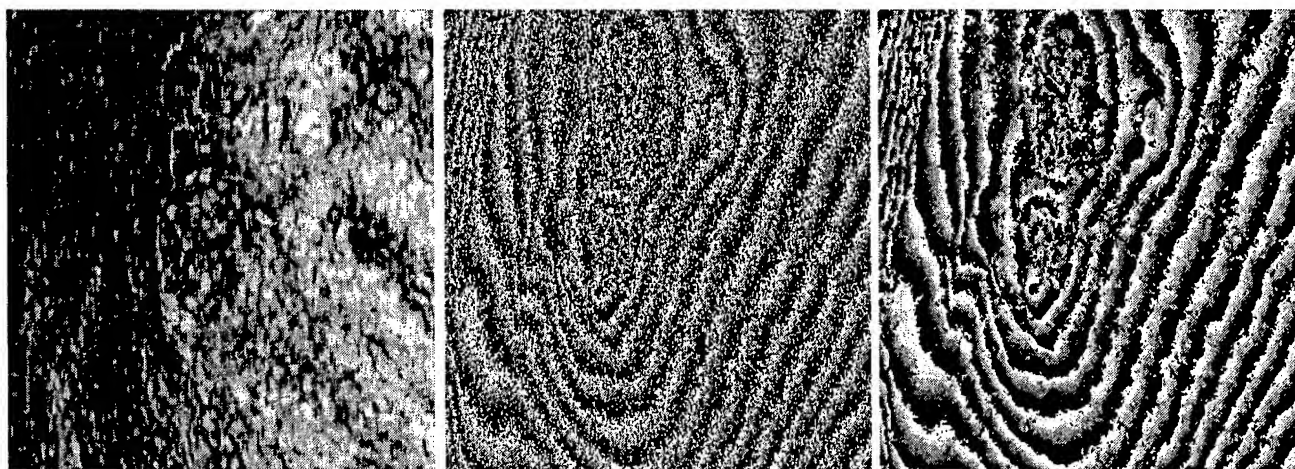


Fig. 1 Standard deviation of phase noise as a function of $|\rho_c|$ and the number of looks.

Additive Noise Model

Since ψ distribution is symmetrical about θ , θ is the mean. The standard deviation is independent of θ . Consequently, ψ can be characterized by an additive noise model:

$$\psi_z = \psi_x + v \quad (1)$$



(a) Coherence map (b) Original 1-look phase image (c) Phase noise filtered once
Fig. 2 Phase noise filtering for a section of 386x412 pixels; (a) the Coherence map, (b) the one - look phase image after flat - earth removal, and (c) the result of applying the filter. The noise reduction is quite evident.

where ψ_z is the measured value, ψ_x is to be estimated and v is the noise, with mean 0 and standard deviation σ_v , as shown in Fig. 1.

Verification of Noise Model:

The X-band 1-look phase image of Mt. Etna and its coherence map are used for illustration. The coherence is low with 70% of the pixels below 0.6. A section of the interferogram (386x412 pixels) is shown in Fig. 2b. The noise level is high and fringes are tightly packed in some areas. It would be difficult to find large flat areas with constant $|\rho_c|$. For each pixel, we utilized 16 directions of 3x9-window as shown in Fig. 3, and use the statistics of the window that has the minimum variance. The mean and variance are computed in the 3x9 window using phases unwrapped with respect to a centered value. The centered value is the argument of a 3x3 centered average of $e^{i\psi}$.

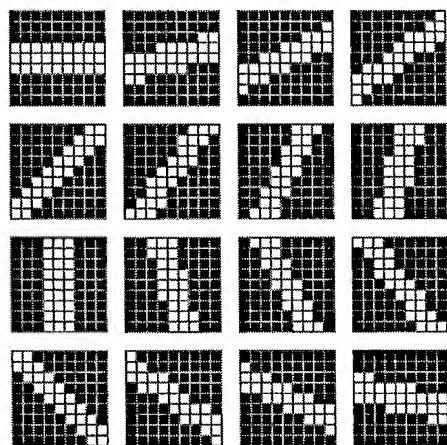


Fig. 3 Sixteen directional masks for phase noise filtering. Only the white pixels are included in the computation.

Four scatter plots of standard deviation vs. mean for $|\rho_c|$ in the intervals of [0.1- 0.2], [0.4- 0.5], [0.6- 0.7] and [0.7- 0.8] are shown in Fig. 4. The additive noise characteristics are evident. The horizontal line fit for each plot is also shown. The averaged standard deviation for each plot is somewhat lower than the 1-look σ_v curve in Fig. 1,. This is because the use of the minimum variance window lowers the estimation of the standard deviation.

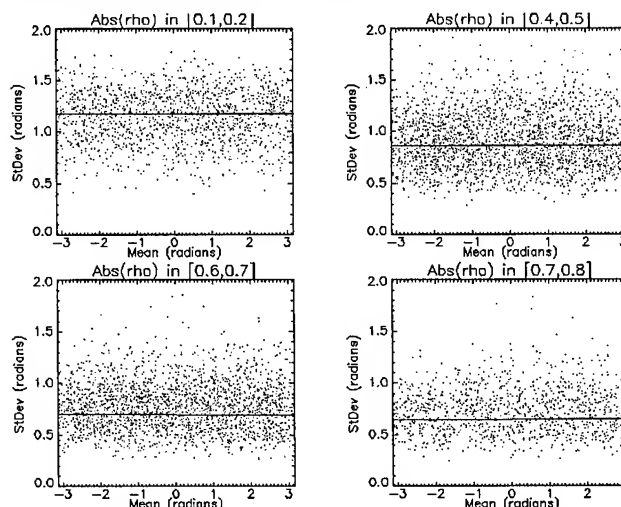


Fig. 4 Verification of the additive noise characteristic of the phase image. Scatter plots of standard deviation (SD) vs mean show constant SD suggesting additive noise characteristics.

PHASE NOISE FILTERING

Based on the additive noise model (1), the local statistics filter [2] is applied. The estimated phase is

$$\hat{\psi}_x = \bar{\psi}_z + \frac{\text{var}(\psi_z) - \sigma_v^2}{\text{var}(\psi_z)} (\psi_z - \bar{\psi}_z) \quad (2)$$

$\bar{\psi}_z$ and $\text{var}(\psi_z)$ are the local mean and standard deviation, and σ_v is the noise standard deviation given in Fig. 1.

The following additional considerations were built into this noise filtering algorithm:

- The coherence map is used to obtain the noise standard deviation for adaptive noise filtering to provide more smoothing for low coherence areas and vice versa.
- Since the phase image is a modulus of 2π , pixels in the moving window were phase unwrapped within $(-\pi, \pi)$ of the average of the center 3×3 pixels.
- Non-square windows are used to smooth noise along fringes. Sixteen directional windows (Fig. 3) are used. Some windows have less than 27 pixels.
- For each pixel, variances are computed in all 16 windows, and the window with the minimum variance is used for the filtering. The use of directional window is more effective in noise smoothing than a square window, because the directional window contains more homogeneous phase pixels.
- The phase standard deviation σ_v is computed as follows: a) the pixel's correlation coefficient is obtained from the coherence map, b) σ_v is obtained using a look-up table. The table was created in advance using the curve in Fig. 1 for a specified number of looks.
- When applies Eq. (2) in the selected directional window, $(\text{var}(\psi_z) - \sigma_v^2)$ may become negative. If so, it should be set to zero to ensure that the weight is between 0 and 1.

This filter can be repeatedly applied. For example, this filtering algorithm can be applied again to the filtered phase image using a value σ_v from a curve in Fig. 1 corresponding to a larger number of looks.

EXPERIMENTAL RESULTS

The 1-look X-band interferometric phase image of 900×3400 pixels was filtered, and the result of the small section in Fig. 2(b) is shown in Fig 2(c). Comparing these two images, the noise reduction is fairly significant, and the fringes are much better defined. The high noise level of the 1-look interferogram phase image makes phase unwrapping nearly impossible without filtering. We applied a least square phase unwrapping algorithm [4] to a twice filtered phase images, and the result is shown in Fig. 5. It is known that least square methods underestimate the height. Iterative unwrapping the filtered phase difference between the original phase and the initial solution can reach the full height. The use of this adaptive filter in the iterative phase unwrapping would accelerate convergence.

The effectiveness of this algorithm was judged by the reduction of the number of residues and preservation of phase gradient. This filter reduces the number of residues drastically by 90% for this X-band Mt. Etna image. The results of the Gauss-filter [5] is similar,

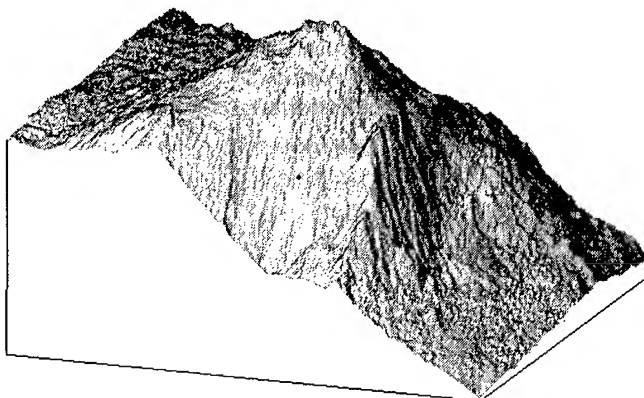


Fig. 5 Phase unwrapped image by a least square method using twice filtered data.

but the preservation of the phase gradient and orientation of the fringes is not as good, especially in low coherence areas.

We also compared results with median filter and the boxcar filter. Results (not shown) indicated the superiority of this filtering algorithm in preserving fringes and in noise reduction.

CONCLUSION

A new technique has been developed to filter the interferogram phase image. It uses 16 directional masks to adaptively filter phase noise along the fringes. The statistics of phase images has also been investigated and found that the noise can be characterized with an additive noise model. Experimental results demonstrated the algorithm's effectiveness.

ACKNOWLEDGMENT

This work done by US researchers was supported by Office of Naval Research (ONR) under 6.1 and 6.2 funding.

REFERENCES

- [1] J.S. Lee et al., "Intensity and phase statistics of multilook polarimetric and interferometric imagery," *IEEE Trans. Geoscience and Remote Sensing*, vol. 32, no. 5, September, 1995.
- [2] J.S. Lee, "Digital image enhancement and noise filtering by use of local statistics," *IEEE Trans. on Pattern Analysis and Machine Intelligence*, vol. 2, no. 2, 165-168, 1980.
- [3] R. Lanari, et al., "Generation of digital elevation models by using SIR-C/X-SAR multifrequency two-pass interferometry: The Etna case study," *IEEE Trans. GRS*, Vol. 34, No. 5, 1097-1114, Sep. 1996.
- [4] T. Ainsworth, "Interferometric SAR phase unwrapping using selected boundary conditions," (in preparation).
- [5] D. Geudtner, M. Schwabisch, and R. Winter, "SAR-Interferometry with ERS-1 data," *Proceedings of PIERS'94*.

Toward Consistent Global Physiognomic Vegetation Mapping Using ERS/JERS SAR Classification

Josef M. Kelldorfer, M. Craig Dobson, Fawwaz T. Ulaby

Radiation Laboratory, EECS Department,

The University of Michigan, Ann Arbor, MI 48109-2122, USA

Phone: +1 (313) 764-0501, Fax: +1 (313) 647-2106

e-mail: josefk@eecs.umich.edu homepage: <http://www.eecs.umich.edu/~josefk>

ABSTRACT

Recent research identified a small number of vegetation characteristics that are essential to describe parameters needed for global atmosphere-biosphere models. Efforts to derive some of these characteristics from satellite remote sensing focussed on the use of AVHRR NDVI datasets, and global land cover characteristics data bases were produced. The usefulness of this dataset is hampered by the fact, that low spatial resolution of the AVHRR data results in the necessary definition of mixed herbaceous/shrub/tree classes, where the % mixture of these basic physiognomic classes are unknown. Radar is known to be very sensitive to vegetation physiognomy and biomass. In a study at the University of Michigan the potential of the existing orbital SAR imaging systems JERS-1 and ERS-1/2 for vegetation mapping has been investigated. Both sensors have mapped the global land masses within a period of four years. Using the complimentary characteristics of frequency (L-, C-Band) and polarization (hh, vv), a classification scheme was developed to produce vegetation maps at a scale of ca. 1:200,000 with classes based on physiognomic characteristics of vegetation. The approach uses unsupervised clustering techniques and class assignment based on radar signatures, hence consistent, automatic classification is possible. The combination of the high spatial resolution of JERS/ERS SAR composites and the high temporal resolution of the AVHRR based datasets could be the winning combination to describe vegetation distribution and vegetation dynamics.

1. INTRODUCTION

Models to describe exchanges of energy, water, and carbon dioxide between the atmosphere and biosphere require global scale information about the states of both the atmosphere and biosphere. While atmospheric parameters have a long history of measurements, biospheric parameter estimates over the land surface are sparse. The link between the most important vegetation characteristics and land surface parameters needed for atmosphere/biosphere models are summarized in Tab. 1 [1].

Efforts in the past years to use satellite remote sensing data to generate datasets of global vegetation distribu-

Table 1: Land surface characteristics required to calculate parameters used in atmosphere-biosphere models of water, energy, and carbon dioxide exchange [1].

Land Surface Parameter	Land Surface Characteristic Required to Calculate Parameter Field
Absorbed Radiation	Seasonality (evergreen, deciduous), leaf type (broadleaf, coniferous)
Albedo	Woodiness (trees/shrubs, herbaceous plants, bare ground)
Canopy Conductance	Photosynthetic pathway (C_3 , C_4), disturbance type (e.g. cultivation)
Roughness	Woodiness, leaf type
Photosynthesis and transpiration	Photosynthetic pathway, woodiness, plant longevity (annual, perennial)
Net primary production	Woodiness, seasonality, photosynthetic pathway, disturbance type
Carbon and nutrient dynamics	Woodiness, disturbance type, plant longevity

tion and dynamics resulted in the generation of AVHRR-based monthly maximum NDVI maps, currently available for Africa, North and South America. The usefulness of this dataset for the characterization of vegetation dynamics as well as estimation of continuous distributions of vegetation's functional properties is out of question and is partly achieved through the high temporal resolution of the AVHRR sensors. However, attempts to use this dataset for the identification of basic physiognomic vegetation classes show deficiencies, when analyzed on a regional scale [2]. Tab. 2 shows classification accuracies achieved in five test sites in the US when comparing vegetation classes from the USGS Land use/Land cover (LULC) data from 1979, based on Ultra High Altitude Photography (UHAP), classification from the Land Cover Characteristics (LCC) prototype dataset from 1990 and classification from the preliminary release of the "North America Land Cover Characteristics Data Base" from 1993 [3].

To facilitate comparison, vegetation classes from the different datasets were translated to the vegetation characteristics *woodiness* (tree, shrub, herb) and *leaf type/seasonality* (deciduous broadleaf, evergreen needle-leaf). The percentages in Tab. 2 represent % coverage of

these vegetation characteristics in five test sites throughout the US [4]. Generally, discrepancies between the classifications can be seen to be great, even at the simplified level herbaceous/shrub/tree. Also, mixed categories had to be introduced to represent unresolvable class mixtures, esp. within the LCC data. This is partly due to the effective low spatial resolution of $3 \times 2 \text{ km}^2$ of the multitemporal NDVI datasets [5].

Hence, the information content from the multitemporal NDVI datasets in particular and the AVHRR data in general for observation of global vegetation dynamics needs improvement in distinction of basic vegetation categories.

2. VEGETATION MAPPING WITH SYNTHETIC APERTURE RADAR

Experiments like the shuttle imaging radar (SIR) missions or airborne synthetic aperture radar (SAR) campaigns and research over the last decades has demonstrated, that SAR data is well suited for vegetation classification and characterization [6]. With the past and future launch of earth remote sensing radar satellites (ERS, JERS, RADARSAT, ENVISAT, LIGHTSAR, PALSAR) global, multi-temporal datasets of SAR imagery are now available to the earth science community. The strengths of using SAR data for regional- to global-scale vegetation mapping can be summarized as follows:

- SAR sensors can be calibrated to a very high degree of accuracy ($<1\text{dB}$), allowing stable comparison of backscattering values over time and space,
- the strong dependency of radar backscatter on structural and dielectrical attributes of terrain relate directly to vegetation physiognomic characteristics like growth form (*woodiness*) and leaf morphology (*leaf type*),
- independence from atmospheric conditions (cloud cover) guarantee the availability of multi-seasonal (vegetation phenological stages) datasets for identification of the land surface characteristics *seasonality* (deciduous, evergreen) and *plant longevity* (annual, perennial).

The major constraints in using SAR data for vegetation classification are:

- Calibration depends on the availability of high resolution Digital Elevation Models in mountainous terrain to correct for incidence angle dependent backscatter changes,
- dependency of the radar backscatter on soil and (intercepted) plant moisture changes,
- dependency of the radar backscatter signal on soil roughness.

Since the dependencies on soil moisture and roughness vary with frequency, there is a general potential to overcome the last two constraints by using the appropriate

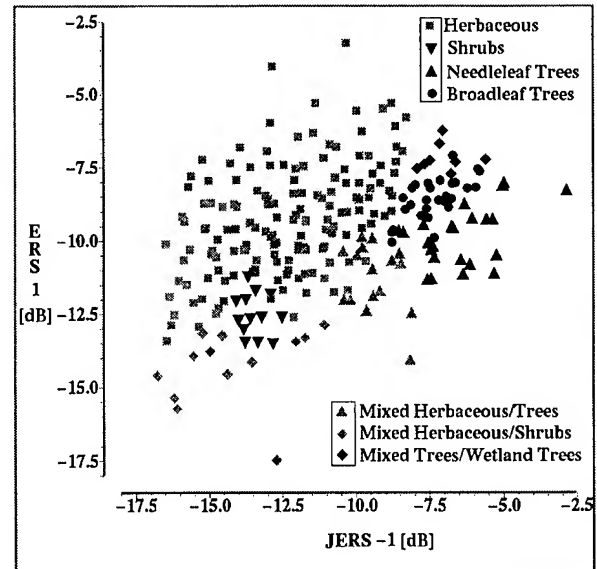


Figure 1: Distribution of cluster centers generated with ISODATA in five test sites from different eco-regions; class assignment was based on measured ERS/JERS signatures using the minimum euclidian distance [4].

wavelength combination for surface characterization. For example, a bare soil might appear rough at C-Band (5cm wavelength) with strong backscatter towards the sensor, whereas the longer L-Band (ca. 23cm) measurements are still dominated by specular scattering away from the sensor. Another example would be the differences in penetration through vegetation. Whereas longer wavelength still penetrate herbaceous vegetation and are sensitive to soil moisture, this might not be the case for a shorter wavelength (e.g. X-Band).

3. THE MULTI-ECOREGION ERS/JERS EXPERIMENT

In a study conducted at the University of Michigan, composites of ERS-1 (C-band, vv-polarization) and JERS-1 (L-band, hh-polarization) were investigated for their use for vegetation mapping in various biomes throughout North- and Southamerica. Goal of the study was to develop a classification algorithm with which

- vegetation structural classes are identified, and
- no scene dependent training is necessary, leading to a classification protocol, based on calibrated radar-signatures and their derivatives (e.g. textural parameters).

Using ca. 150 polygons distributed in the five test sites, radar backscatter measurements from vegetation were compared within the framework of the proposed "Standard for Vegetation Classification" [7]. It was found, that different vegetation types can be distinguished, and that separation of vegetation structural classes based on

Table 2: Comparison of the distribution in % of several simple physiognomic vegetation classes in five LTER/SIR-C/X-SAR sites derived from various classification sources. The size of each test site analyzed here is approx. $50 \times 50 \text{ km}^2$, which is the gridcell size of most global climate models (GCM). The test sites are Cedar Creek (CE), Jornada (JO), Kellogg (KE), Konza (KO), Raco (RA). See text for explanation of classification sources.

Classification Source	USGS LULC 1979					USGS LCC 1990					USGS LCC 1993					ERS/JERS 1993				
LTER/UofM test site	CE	JO	KE	KO	RA	CE	JO	KE	KO	RA	CE	JO	KE	KO	RA	CE	JO	KE	KO	RA
Herbaceous	72	5	83	97	8	14	5	3	73	13	16	13	21	87	0	55	51	42	84	8
Woody: Shrub	0	0	0	0	0	0	64	0	0	0	0	83	0	0	0	1	27	1	4	0
Woody: Tree	28	1	17	0	89	31	2	10	0	59	4	3	41	3	71	38	3	51	7	89
-Tree: Needleleaf	5	0	0	0	45	0	0	0	0	0	4	3	40	0	56	5	1	17	1	58
-Tree: Broadleaf	10	0	15	0	12	21	0	9	0	18	0	0	0	0	0	30	1	26	5	14
-Tree: Mixed	13	1	2	0	32	10	2	1	0	41	4	0	1	3	15	3	1	8	1	16
Mixed Herbaceous/Tree	0	0	0	0	0	55	1	86	25	23	80	0	36	8	15	4	1	5	2	2
Mixed Herbaceous/Shrub	0	93	0	2	0	0	28	0	0	0	0	0	0	0	0	2	16	1	2	1

backscatter signatures is possible and site independent. A developed hybrid "unsupervised clustering/minimum distance class assignment" technique showed overall classification accuracies for the testing part of the polygons of >80% [4]. Fig. 1 shows the distribution of the classified cluster centers in a ERS-1/JERS-1 scattergram. Tab. 2 shows the percentages for vegetation cover types in the five test sites resulting from this classification process. These estimates are partly very close to the USGS LULC estimates (KO, RA) and help resolving mixed categories (JO). Discrepancies exist and show the necessity to use multi-temporal data sets, which was not done for the test sites at this stage. Using multi-temporal ERS/JERS SAR imagery certainly helps solving signature ambiguity between corn and forest in particular, as experienced in the agricultural test sites (CE, KE), and is needed for the distinction of *leaf longevity* and *seasonality* vegetation characteristics in general.

4. CONCLUSIONS

Efforts to derive some important vegetation parameters needed for global atmosphere-biosphere modelling are so far focussed on AVHRR monthly maximum NDVI values. The usefulness of these datasets is limited by the regional inaccuracies and ambiguities in classification of basic vegetation classes. Since 1991 several earth orbiting radar satellites have been launched, providing global coverage for SAR signature based classification of vegetation. Despite the fact of guaranteed multi-temporal image availability (cloud penetration) and site-independent high system calibration accuracies, uninfluenced by sun-illumination changes and atmospheric conditions, the higher spatial resolution of SAR image composites enables distinction of classes, where AVHRR based classifications are restricted to mixed categories.

The synergism between SAR derived basic vegetation cover maps with high spatial resolution and the observance of vegetation dynamics with temporally high re-

solving AVHRR satellites seems to be the winning combination. The globe is mapped with JERS-1, ERS-1/2 and RADARSAT data, and the only gap for ERS-1/2 in the Siberian forest will be closed as of summer '97 with the deployment of the German Mobile Receiving station. Hence - the data is there, it is upon the science community to use them.

5. REFERENCES

- [1] R. S. DeFries, et al., "Mapping the land surface for global atmosphere-biosphere models: Toward continuous distributions of vegetation's functional properties," J. of Geophysical Research, vol. 100, 1995, pp. 20867-20882.
- [2] M. C. Dobson, F. T. Ulaby, and L. E. Pierce, "Land-cover classification and estimation of terrain attributes using Synthetic Aperture Radar," Remote Sensing of Environment, vol. 51(1), Jan. 1995, pp. 199-214.
- [3] T. R. Loveland, et al., "Western hemisphere land cover: Progress toward a global land cover characteristics database," in Proceedings Pecora 13, US Geological Survey, in press, 1996.
- [4] J. M. Kellndorfer, M. C. Dobson, and F. T. Ulaby, "Multi-ecoregion vegetation mapping using combined ERS/JERS SAR imagery," in Proc. Third ERS Symposium "Space at the service of environment", ed. European Space Agency, in press, 1997.
- [5] D. J. Meyer, "Estimating the effective spatial resolution of an AVHRR time series," Int. J. of Remote Sensing, vol. 17(15), Oct. 1996, pp. 2971-2980.
- [6] M. C. Dobson, et al., "Estimation of forest biophysical characteristics in northern Michigan with SIR-C/X-SAR," IEEE Trans. Geo. Remote Sensing, vol. 33(4), Jul. 1995, pp. 877-895.
- [7] Federal Geographic Data Committee, Vegetation Subcommittee, "FGDC Vegetation classification and information standards," Jun. 1996.

Effect of Environmental Temperatures on SAR Forest Biomass Estimates.

K.J. Ranson¹ and G. Sun²

¹Code 923, NASA/GSFC, Greenbelt, MD 20771 USA,
TEL: 301-286-4041, FAX: 301-286-1757, e-mail: jon@taiga.gsfc.nasa.gov

²Univ. of Maryland, Code 923, NASA/GSFC, Greenbelt, MD 20771 USA
TEL: 301-286-2485, FAX: 301-286-0239, e-mail: guoqing@aspen.gsfc.nasa.gov

Abstract -- This paper discusses the observed effects of temperature conditions on estimates of forest biomass in a portion of the Canadian boreal forest. Biomass estimation equations were developed from relationships between SAR backscatter and measured forest biomass for several forest stands. Separate relationships were developed for SAR images acquired under widely different temperature conditions. The biomass estimates obtained from the different images were compared. Differences in observed backscatter behavior and biomass results are discussed.

Table 1. SIR-C data acquisition information.

Date	Data Take	GMT	Illumination Angle
April 15	100.2	13:52	43.40
April 17	148.4	12:49	46.8
Oct. 4	68.2	14:43	39.32
Oct. 6	100.12	14:04	43.6

STUDY SITE

The two SIR-C/XSAR missions took place during April and October of 1994. Several studies have been conducted to use satellite SAR data to characterize the boreal ecosystem in terms of forest type classification and biomass estimation [e.g., {1,2}], and growing season length [Way et al, 1997]. Since it is well known that radar backscatter is greatly influenced by temperature through changes in the surface dielectric constants [Way et al. 1990, Ahern 1993, Rignot and Way, 1994] it is important to quantify these effects. Our goal for this study was to determine the what effects, if any, changes in environmental temperature have on SAR data analysis for biomass and forest type.

SIR-C/XSAR DATA

The SIR-C/X-SAR missions were successfully conducted during April 9-19, 1994 and September 30-October 10, 1994. The instrument was fully polarimetric in L and C bands and had a single VV polarization in X-band. The mission was a cooperative experiment between NASA, the German Space Agency, and the Italian Space Agency. SIR-C/X-SAR was launched on space shuttle Endeavour and acquired multiple data takes covering over 6% of the Earth's surface including a variety of land, ocean and polar ice targets. The SIR-C/X-SAR design includes bandwidths of 10, 20, and 40 MHz with the 40 MHz bandwidth providing better resolution. The SIR-C images used in this study were acquired with a bandwidth of 20MHz and processed with 12 looks providing a nominal resolution of 25 m. Four images were used in this analysis representing a wide range of environmental conditions. Table 1 summarizes the data take parameters. XSAR were available but were included in this analysis

The image data discussed in this paper covers the eastern portion of the BOREAS Southern Study Site (SSA) 53° 53' N, 104° 45' W). The vegetation in this area is classified as mixed boreal forest. On well drained soils the predominant species is jack pine (*Pinus banksiana*). Poorly drained sites support black spruce (*Picea mariana*). Mixed stands of aspen (*Populus tremuloides*), balsam poplar (*Populus balsamifera*) and white spruce (*Picea glauca*) are found on well drained glacial deposits. Deciduous trees were without leaves during both missions. Localized logging for paper pulp and fence posts is common within the area. The fen areas are composed mostly of sedge (*Carex spp.*) vegetation with discontinuous cover of tamarack (*Larix spp.*) or swamp birch (*Betula pumila*). Periods of freezing and above freezing temperatures were experienced during both time periods within the Southern Study Area (SSA) of the Boreal Ecosystem-Atmosphere Study (BOREAS) test site.

WEATHER VARIABILITY

Meteorological conditions were recorded within the area covered by SIR-C images as part of the BOREAS project. Fig. 1 shows the average above canopy air temperature, average soil temperature (10 cm depth and total precipitation recorded over 15 min. intervals during the SIR-C missions. Fig. 1 illustrates the variation in temperature and precipitation during the SIR-C/XSAR missions. During April there were no major precipitation events and soil temperatures were gradually warming, but stayed close to 0°. Air temperature was widely varying throughout the mission period with freezing occurring on days 99, 100, 105 and 109. The SIR-C data used here was acquired on days 105 and 107 as indicated by the vertical lines in Fig. 1. During the October mission, there was significant precipitation on days 275 and 282, with soil temperatures consistently above 5°. Air temperatures were warmer than in April with

freezing occurring on days 277, 280 and 284. Vertical lines at days 277 and 279 indicate the SIR-C data used here. Table 1 lists the 15-minute average meteorological conditions acquired during the SIR-C data takes.

EFFECT ON BACKSCATTER

Fig.2 presents backscatter acquired for the four days for five forest cover types. Mature forest stands of aspen, black spruce and jack pine were selected along with a young stand of pine and an open fen covered with low vegetation. Backscatter exhibited the greatest dynamic range on April 15 under frozen conditions. Standard deviations (not shown) were also much greater on this day. This is in contrast with the other days that exhibited less variation. Backscatter from the forest stands decreased due to freezing, especially in LHV where a decrease of up to 9dB for young jack pine was observed. Fen backscatter decreased except for a 3 db increases in CVV and 1 dB increase in LVV. The October data varied less than the April days, despite a near freezing conditions and the possibility of frost or dew on the trees on Oct. 4.

EFFECT ON BIOMASS ESTIMATION

Relationships between SAR data and measured biomass were developed using biomass data for 15 forest stands in the vicinity of the meteorological station. The stands were also selected on the basis of uniformity to reduce errors from image registration. Radar data was extracted from the SIR-C images and used to develop an empirical equation using stepwise linear regression. The biomass equations selected are listed in Table 3 for the four images. In addition, the SAR derived biomass and field biomass were compared and the results shown in Table 3 as the intercept and slope of the best fit line.

The consequences of freezing conditions on estimation of biomass can be seen in Table 3. The April 15 data yielded the poorest results for biomass estimation (low r^2 and large root mean square error (RMSE)). However, the results developed from October 6 data under warm air temperatures and warm soil temperatures had the largest negative bias. The best results were obtained from the October 4 data where the soil temperatures were warm, but the canopy temperatures were near freezing. There was also possible dew or frost during this acquisition.

SUMMARY AND CONCLUSIONS

Four data sets acquired under different meteorological conditions were examined. The SIR-C backscatter was found to be lowest when the trees and background were frozen in agreement with other studies [3, 5]. The biomass estimates were also affected by temperature with greater errors observed when both trees and ground were frozen. From Table 2 there is not an obvious conclusion that can be drawn regarding temperature effect and biomass mapping from these data. Biomass estimation equations are different for each date (Table 3). The LVV channel was most important for the April 17 data given the large negative coefficient (i.e, b_2 in Table 3). A possible reason for this may be the presence of high dielectric fluid in the trees from spring sap flow.

The implication of this work is that care should be taken when trying to apply biomass equations developed on one date to other dates with different environmental conditions.

REFERENCES

- [1] J. Ranson, S. Saatchi and G. Sun, "IEEE Trans. Geosci. Remote Sens, vol. 31, pp.668-680, 1995.
- [2] J. Ranson, G. Sun, R. Lang, O. Kilic, N. Chauhan and R. Cacciola, "JGR-Atmospheres, (in press)
- [3] J. Way, R. Zimmerman, E. Rignot, K. Mac Donald, R. Orem "Winter and spring thaw as observed with imaging radar at Boreas " JGR-Atmospheres, in press.
- [4] J. Way et al., The effect of changing environmental conditions on microwave signatures of forest ecosystems:preliminary results of March 1988 Alaska aircraft campaign," Int. J. Remote Sens., vol. 11, pp. 1119-1144, 1990.
- [5] F. Ahern, D. Leckie and J. Drieman, Seasonal changes in relative C-band backscatter of northern forest cover types," IEEE Trans. Geosci. Remote Sens, vol. 31, pp.668-680, 1993.
- [6] E. Rignot and J. Way, "Monitoring freeze-thaw cycles along north-south transects using ERS-1 SAR," Remote Sens. Environ. vol. 49, pp. 131-137, 1994.

Table 2. Meteorological measurements acquired around the time of SIR-C data acquisitions.

Date	GMT	Air Temp (°C)	Canopy Temp (°C)	10 cm Soil Temp (°C)	Rel. Hum (%)	Solar Rad. (w/m ²)
April 15	14:30	-2.7	-4.0	0.03	87.8	197.2
April 17	13:45	6.8	2.6	0.03	47.8	61.9
Oct. 4	14:45	0.10	-0.1	4.5	100	75.6
Oct. 6	14:00	5.1	4.3	6.3	82.5	51.2

Table 3. Coefficients for biomass estimation equations Intercept and slope values are from regression of predicted and measured biomass.

Biomass Estimation Equation					Predicted vs. Measured Relationship			
(Biomass ^{1/3} = b ₀ + b ₁ *LHV + b ₂ *LVV)					Intercept	Slope	r ²	RMSE
April 15	4.2625	0.1201	-0.0306	0.81	2.3300	0.7617	0.50	4.10
April 17	2.6312	0.2569	-0.3251	0.73	1.7741	0.7932	0.72	2.73
Oct. 4	4.0178	0.2042	-0.1211	0.80	0.7233	0.8739	0.72	2.88
Oct. 6	4.9087	0.1754	0.0199	0.79	2.5375	0.6655	0.68	2.96

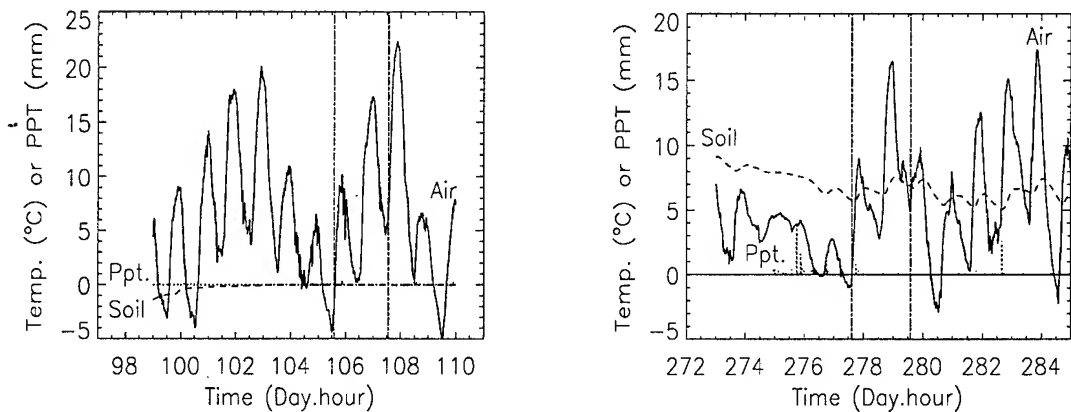


Fig.1. Air temperature, soil temperature (10 cm depth) precipitation at BOREAS site for periods of April (right) and October (left) 1994 SIR-C/XSAR missions.

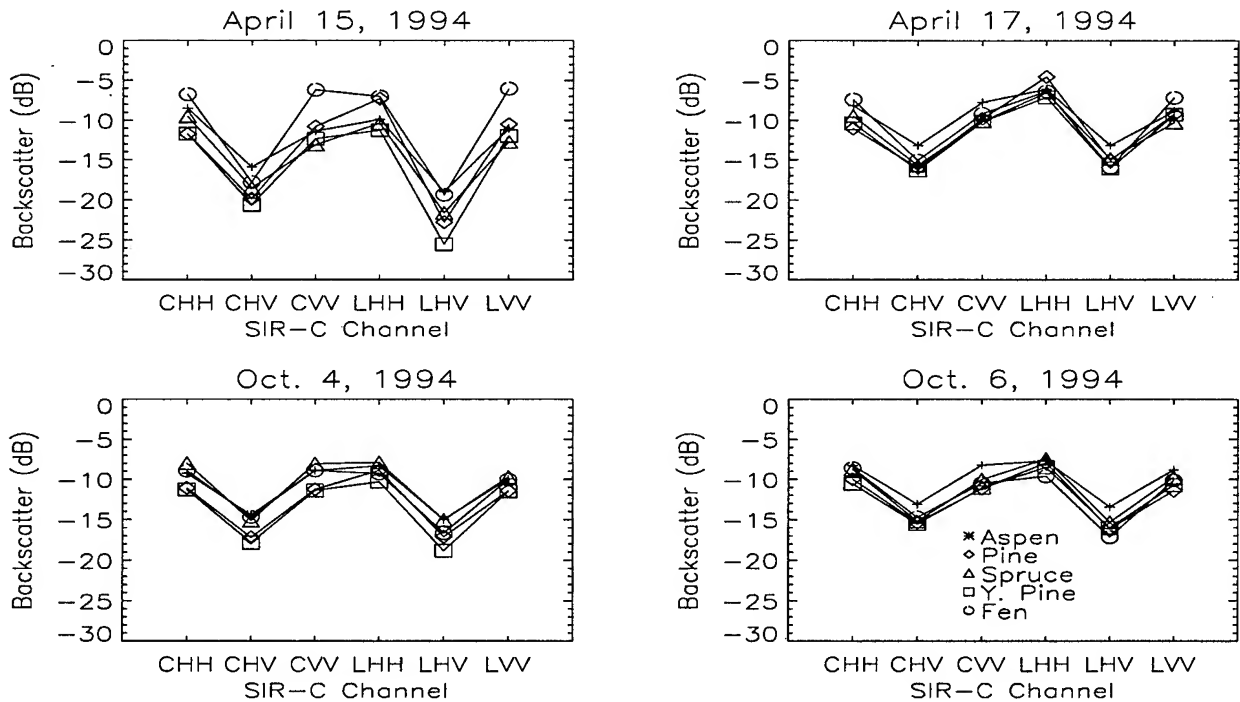


Fig.2 SIR-C backscatter measured for five forest cover types during four data takes.

The ERS-1 Central Africa Mosaic: a New Role for Radar Remote Sensing in Global Studies of the Tropical Ecosystem

J.P. Malingreau (1), G.F. De Grandi (1), M. Leysen (1,3), P. Mayaux (1), M. Simard (1, 2)

(1) European Commission Joint Research Centre - Space Applications Institute

Monitoring Tropical Vegetation 21020 Ispra (VA) Italy

Tel.: +39 332 789823 Fax: +39 332 789073 Email: gianfranco.degrandi@jrc.it

(2) Centre de Recherche en Geomatique, Universite' Laval, Quebec, CANADA

(3) VITO Flemish Institute for Technological Research

Boeretang 200 B-2400 Mol Belgium, Tel.+ 32 14 33 58 85, E-mail leysenm@vito.be

ABSTRACT

The Central Africa Mosaic project - CAMP - is an attempt to bring space-borne SAR remote sensing into an entirely new perspective for global studies of the tropical ecosystem. The new approach hinges around the concept of multi-resolution information extraction, whereby using a high resolution radar sensor one can obtain information both at large geographical scale and at fine spatial detail; the access point to the data hierarchy - or the level of detail needed - is driven by the thematic application. CAMP consists of more than 450 ERS-1 SAR scenes, which were acquired on demand and in a short time frame (two months) over the entire Central African continent by the ESA Libreville ground station and correlated by the German PAF at DLR. The project is carried out by the European Commission Space Applications Institute MTV unit at Ispra and within the R/D activity of TREES (Tropical Ecosystem Environment Monitoring by Satellites). In this communication the basic concepts underlying the CAMP project are first summarized; aspects related to the thematic interpretation, the data processing and new initiatives for large scale radar maps are then discussed with emphasis on peculiarities of the CAMP approach.

INTRODUCTION

In the context of the TREES 94 ERS-1 Study a novel approach for large (continental) scale mapping of the tropical forest using radar remote sensing was proposed by the JRC SAI MTV (Monitoring Tropical Vegetation) unit. TREES (Tropical Ecosystem Environments monitoring by Satellites) is a project funded in the current phase by the European Commission. The new approach called for the assemblage on demand and in a short turn around time of a vast amount of high resolution radar imagery from the Synthetic Aperture Radar instrument on-board the ESA ERS-1 satellite to obtain thematic information over the whole bio-geographical domain of Central Africa at several scales and with unprecedented completeness, spatial resolution and quality. A demonstration and test bed for the new concept was put together in MTV at the end of 1995, and was henceforth referred to as the TREES ERS-1 Central Africa Mosaic Project (CAMP). A detailed description

of the project can be found in [1]. In this communication we want to highlight those aspects that make CAMP the seed for an entirely new role of radar remote sensing in global studies of the earth ecosystems. This catalytic action spans a gamut of issues, from the introduction of new processing and analysis paradigms, such as the multi-resolution processing on demand, to the thematic aspects, to the spin off of new initiatives for continental scale radar maps of the tropical forest.

We will at first summarize the basic concepts that underpin the CAMP approach, and will then give an overview of the above mentioned points in the project evolution.

CAMP FUNDAMENTALS

The fundamental concepts underlying the CAMP approach can be summarized as follows:

- change of scale
- multiresolution
- geometric precision and consistency
- richness in information content

First of all CAMP introduces a major change in scale with respect to the conventional use of radar imagery. While typical coverage in conventional studies is in the order of 10^4 Km^2 , the CAMP radar map is extended over an area of several 10^6 Km^2 , which implies an increase of 2 orders of magnitude. However the concept of scale alone would be meaningless if it were not associated with the concept of resolution. Actually large scale coverage of the tropical ecosystem was already obtained in the past within the TREES project using the 1 km resolution AVHRR sensor. But it is indeed the scale-resolution product that gives to the CAMP approach a distinctive connotation. The availability of a large number of images at high spatial resolution over a large area - which is assured by the all-weather imaging capability and the radiometric stability of the SAR space-borne sensor - allows for the information extraction and analysis at the scale which is locally (in a spatial sense) more suitable for a certain thematic goal. In other words if suitable processing techniques are used to keep the full bandwidth-resolution product, it is possible to generate from the original high resolution data set products that best match the analysis

requirements for a certain location and a certain application. In terms of image processing techniques this links to the multi-resolution decomposition concept.

Second important characteristic is the high geometric precision and consistency of the CAMP data set over a large geographic area; this point, in conjunction with the sensor's resolution (30m) and the signal sampling rate (12.5m) makes the CAMP data set an ideal candidate for cartographic applications. The only limiting factor in this respect is the influence of topography on the geometric accuracy of the radar signal.

Finally the richness in information content is one of the most striking assets of the ERS-1 CAMP mosaic. From the first analyses made on a visual inspection basis, a series of features related to the TREES main thematic goal (deforestation) have already emerged and indicate that these large scale radar maps can indeed pave the way to a re-assessment of our knowledge about the rain forest ecosystem. A related aspect is the mixture in the same data set of temporal and spatial variations of the ecosystem. This is due to two reasons. The acquisition time frame (two months) where changes can be expected both in the ecosystem, and in the meteorological conditions. Second the geographical area covered by the mosaic straddles the equator, and therefore there is an intrinsic seasonal reversal in the ecosystem. Time and spatial effects must therefore be taken in due account in the thematic analysis, and can of course also be exploited for monitoring the time evolution on short term (within the acquisition time of a single mosaic) or using truly multi-temporal acquisitions.

THEMATIC ANALYSIS

The CAMP imagery reveals a series of features which are of most relevance in the framework of tropical forest mapping and in particular of the TREES project objectives. The preliminary results are also of high interest for global vegetation monitoring, a major objective of the International Global Change Research Program (IGPB). The mosaic represents, indeed, a unique and uniform cross section of important tropical biomes from the savannah and dry forest in the north, through the entire rain forest domain and again through seasonal formations south of the equator (savannah and edge of the Miombo Woodland). The design of this Central Africa mosaic is such that, since it crosses the equator it contains at the same time dry and rainy season acquisitions with a gradient of wetness in between. This allows a range of observations to be made with respect to the occurrence or to the lack of seasonal contrasts between various vegetation formations.

The high potential in terms of information extraction is demonstrated for example in Fig. 1. Unexpectedly, the ribbon of secondary forest formations following the older road network of Zaire is visible in the SAR microwave return signal by contrast with the surrounding primary forest. These forest "galleries", correspond to the pattern of land management which since



Fig. 1 - Thematic analysis: ribbon of secondary forest following an old road network in Zaire.

colonial time has essentially followed the road communication system.

A formidable data base is progressively being built within the CAMP project, and by the new initiatives that will be briefly outlined next. The problem of information extraction is a challenging one. In a first phase the analysis was mainly conducted on a visual interpretation level and on sampled areas, primarily to assess the potential of the new approach. Results from this type of analysis are for instance reported in [1]. From this baseline, two different avenues were also started under the coordination of the SAI MTV. On one side new image processing and radar science techniques were taken into consideration in order to optimize the information content retrieved from the underlying signal [3].

On the other side research has been initiated to bring the CAMP thematic interpretation to the full breadth of the spatial extent and the thematic diversity which is by definition inherent to a global scale exercise. This ambitious goal can only be achieved pulling together the expertise and the work force of many laboratories and investigators, who can span the gamut of applications where the CAMP remote sensing data source have a relevant fall out. To this purpose, the SAI MTV is organizing a network of interested research partners who will work on several aspects of the mosaic thematic interpretation.

DATA PROCESSING

The CAMP processing chain has been recently revised with respect to the 1994 prototype in view of the evolution and expansion of the project. A completely new paradigm - mul-

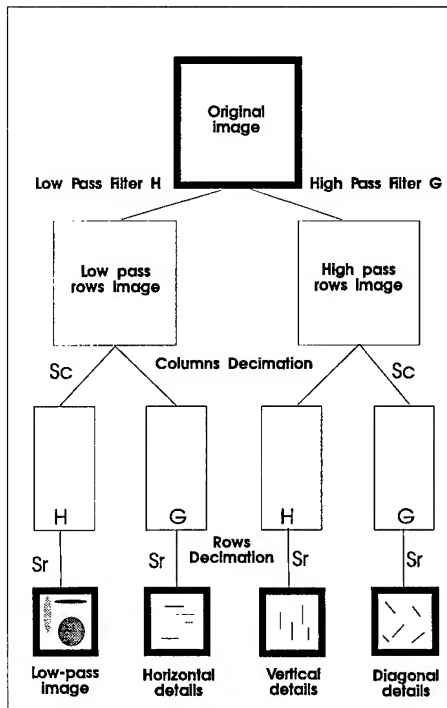


Fig. 2: Block diagram of the wavelet multiresolution decomposition algorithm.

ti resolution decomposition using the wavelet transform - has been introduced. This is indeed a computational solution which is strictly bound to one of the intrinsic characteristics of the CAMP high resolution - large scale approach. The basic theory behind this approach was developed by Stephane Mallat [2]. Details on the JRC MTV implementation can be found in [3].

The mathematical properties of the multiresolution wavelet decomposition match the requirements of the CAMP data processing under several points of view. The wavelet pyramid gives the possibility of generating approximations of the original radar imagery at several dyadic scales. The detail signals between two approximations can be interpreted as texture measures at that scale. The wavelet representation can be used to implement a sub-band image coding scheme, which is quite attractive for the CAMP image distribution on low bandwidth media. Last but not least the existence of fast discrete wavelet transform algorithms makes this approach ideal for high data volume. A block diagram of the chain is shown in Fig. 2.

CAMP EVOLUTION

CAMP also acted, in our opinion, as a catalysts in the international remote sensing community, to promote the onset of new international projects, that start from, but capitalize and expand upon, the same concepts brought forth by the first prototype over Central Africa. Along this line we cite here the following initiatives [4]:

1. A new blanket acquisition over Central Africa using the ESA ERS-1 and ERS-2 sensors, performed in January-February 1996, and meant to explore seasonality and change detection aspects.
2. The Global Rain Forest Mapping Project, an initiative by the Japanese space agency NASDA that foresees a truly global coverage of the tropical ecosystem including the Amazon basin, Central and West Africa, and South East Asia. The JRC MTV is principal investigator and processing centre for the Africa part of the project.
3. An approved JRC MTV proposal to the Canadian ADRO program, which foresees two full coverages of the Central Africa site between 6 S - 9 N, 8 E - 32 E using the ScanSAR wide swath low resolution mode.

CONCLUSIONS

From the inception of the idea, back in 1994, up to now, CAMP has grown to maturity, bringing a novel approach in radar remote sensing for studying global scale problems of the earth ecosystems from the conceptual stage deep into the implementation phase. On one side new blanket acquisitions performed by the ESA ERS-1 and ERS-2 sensors, the Japanese JERS-1 and the Canadian RADARSAT are bringing new dimensions into the project and enriching our information budget on the tropical forest. On the other side new techniques in data processing and in radar science, and new experience gained in the thematic interpretation are paving the way for an ever increasing exploitation of the thematic content of these continental scale radar data sets.

REFERENCES

- [1] G.F. De Grandi, J.P. Malingreau, M. Leysen, "The ERS-1 Central Africa Mosaic: A New Perspective in Radar Remote Sensing for the Global Monitoring of Vegetation", submitted to IEEE Trans. on GARS, 1997.
- [2] S.G. Mallat, "A Theory for Multiresolution Signal Decomposition: the Wavelet Representation", IEEE Trans. on Pattern Analysis and Machine Intelligence, vol. 2 no. 7, July 1989.
- [3] M. Simard, F. De Grandi, K. Thomson, M. Leysen, "Sensitivity Analysis of ERS-1 SAR Signal to Multiscale Structures of the Tropical Forest by Means of the Wavelet Transform", Proc. of the 3rd ERS Symp., Florence, 1997
- [4] G.F. De Grandi, J.P. Malingreau, M. Leysen, Y. Rauste, M. Simard, P. Mayaux, "Wither Radar Global Mapping of the Tropical Forest", New Avenues form the TREES ERS-1 Central Africa Mosaic", Proc. of the 3rd ERS Symp., Florence, 1997.

Land Cover Type and Forest Biomass Assessment in the Colombian Amazon

Dirk H. Hoekman and Marcela J. Quiñones

Wageningen Agricultural University

Dept. of Water Resources, Nieuwe Kanaal 11, 6709 PA Wageningen, The Netherlands

tel:+31-317-482894, fax:+31-317-484885, email:dirk.hoekman@users.whh.wau.nl

Abstract. Results of an analysis of AIRSAR data of the Colombian Amazon (province Guaviare) acquired during the 1993 AIRSAR South American deployment of NASA are discussed. Research is focused on the potential of AIRSAR radar images to classify land cover types, such as primary and secondary forest, recently cut forest, pasture, savanna and bush, taking into account the influence of incidence angle and speckle level. Also the relation between backscatter and biomass level is studied. Very good classification results were obtained using combinations of two channels. High correlation between biomass and backscatter were found for many channels. The use of (partial) polarimetry and circular polarizations furthers results.

1. INTRODUCTION

The present world-wide concern about environmental changes and the high rate of deforestation underlines the urgent need for reliable inventory and monitoring systems for surveillance, management and law enforcement. In tropical forest areas deforestation processes take place due to colonization processes and timber exploitation. Conversion of natural forests into grasslands, croplands, forest plantations and secondary vegetation are some of the typical changes in land cover. In such areas data on land cover change and land degradation processes are needed. However, in the extensive and poorly accessible tropical rain forest environment, nearly all remote sensing monitoring techniques fail because of cloud cover. Spaceborne radar may offer good possibilities because it can cover these areas with sufficient temporal frequency. The advent of high resolution multi-frequency and polarimetric radar systems may advance the possibilities for monitoring considerably.

This paper focuses on the results of the AIRSAR-93 campaign in San José del Guaviare, Colombia. Airborne radar data were acquired by the NASA/JPL multi-frequency fully polarimetric AIRSAR (POLSAR) system at 31 May 1993. More detailed system specifications can be found in literature [5]. The data were processed on the JPL frame processor version 3.56., which includes absolute calibration. Pixel spacing of the imagery is 6.66 m in range and around 8.20 m in azimuth. The number of looks per pixel is 16. The incidence angle varies from about 20° to 60°.

The San José del Guaviare site (2.5° N, 72.5° W) in Colombia is an expanding settlement area near the edge of the Amazon forest, the area can be divided in two main

landscape units: the upland and the alluvial plain. Colonization activities have been occurring since the late 40's. Due to these processes, extensive parts of the area have been deforested and converted into cropland, pastures or secondary re-growth. Part of the remaining forest is under human influence, meaning that valuable trees have been extracted. [1].

2. METHODOLOGY

For the classification analysis six land cover types occurring in the area were used (primary forest, secondary forest, recently cut areas, pastures, natural savannas and bush lands). Field observations on vegetation and terrain characteristics were made for 123 training areas in the 45-60° inc. angle range (identified on the AIRSAR total power image), representing all the cover types. The training areas were classified according to one of the six cover classes. After field checking, another 835 polygons (representing the six land cover classes) were digitized over 5 consecutive scenes of the AIRSAR images, covering the whole incidence angle range, according to the land cover map [1] and aerial photography collected in 1990. Images were corrected to ground range and Stokes matrix parameters were extracted and averaged for each of the digitized polygons. Linear and circular, cross and like polarization backscatter values were calculated for the C-, L- and P-band, and were expressed in gamma values ($\gamma = \sigma^0 / (\cos \theta_i)$) in dB.

Additionally, polarimetric phase information was studied by using the normalized complex correlation between the HH- and VV-channels, which can be expressed in elements of the Stokes scattering operator as:

$$\rho = \langle S_{hh} S_{vv}^* \rangle / \left(\langle S_{hh} S_{hh}^* \rangle \langle S_{vv} S_{vv}^* \rangle \right)^{1/2} \quad (1)$$

A data base of 835 samples (of at least 50 pixels) with 18 γ channels and 6 ρ (real and imaginary parts) channels was created and used as an input file for the classifications. A maximum likelihood classification algorithm with Bayes criterion was applied to classify the data set. Results are presented in percentages of well classified samples.

For the estimation of (total above-ground wet) biomass field data was collected over 13 plots of primary forest and 10 plots of secondary forest. Measurements on trunk diameters, total height and height to the first living branch were used to compute biomass from two different allometric equations, resulting in two biomass estimations per plot. The first uses trunk diameter and total tree height and was calibrated with data from tropical rain forests in Central- and South-America, Africa and S.E. Asia [2]. The

second uses trunk diameter and height to the first living branch and was calibrated for the (Colombian) Amazon to estimate trunk biomass [4]. The biomass data computed according the latter method is believed to yield more realistic figures, especially in the lower biomass range. The computation of basal area from trunk diameters is straightforward and was also used in this research. Details on the field data collection can be found in [3].

3. RESULTS

The first classification attempt was made using a single channel for the classification of all six cover types, over the whole incidence angle range. The best result was recorded for the L-HV channel with 85% classification accuracy, but when restricting the cover classes to the main 4 (primary forest, secondary forest, recently cut areas and pastures) the results improved to 89% for the same channel. The remaining analyses were made using only these 4 cover classes, considering these are the ones of main interest for monitoring purposes. The influence of the incidence angle over the classification accuracy was studied using the polygons of the 4 selected cover types (775 fields). Some classification results for the combination of two channels within different incidence angle ranges are presented in table 1. Results indicate that the classification is better for the range of 45-50° inc. angle, with many results close to 100%. Figure 1 shows the clustering of the samples of the four cover types, when combining the γ values of the C-VV and P-LL channels for that inc. angle range.

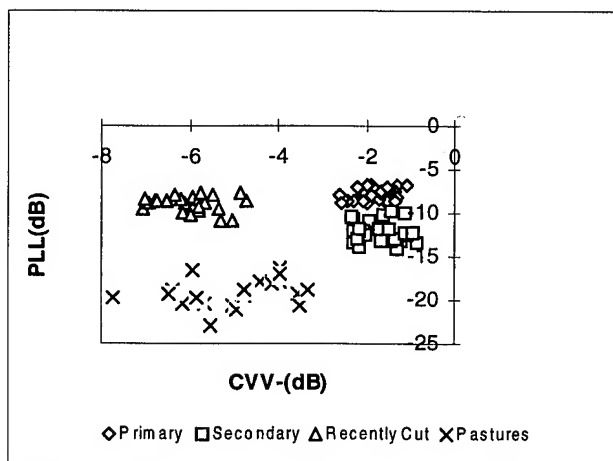


Figure 1. Scatter plot of field averaged values in C-VV and P-LL for four land cover classes.

Table 1. Classifications accuracy percentages for the combination of C-band with VV polarization with all L- and P-band linear and circular, cross and like polarizations, for the incidence angle range of 20-60, 30-35 and 45-50. For the latter range the effect of speckle is simulated for a 1 dB and 2 dB level.

C vv	L hh	L hv	L vv	L rr	L rl	L ll	P hh	P hv	P vv	P rr	P rl	P ll
20-60	89	93	87	92	90	92	95	96	94	96	97	96
30-35	91	97	94	96	93	96	95	98	94	96	95	98
45-50	96	99	97	97	98	98	99	100	98	100	98	100
45-50 1 dB	82	86	76	83	82	84	93	95	95	96	95	95
45-50 2 dB	63	71	57	64	61	63	77	81	72	79	71	77

The effect of speckle in the classification results was analyzed for the set of samples in the 45-50° inc. angle range. Accuracy decreases when higher speckle values (dB) are added (table 1), but still can be in the order of 80% for a 2 dB speckle level.

Partial polarimetric data (γ -HH, γ -VV and ρ only) was used for the single frequency band classification of the four cover types. The percentages were 78% for C-band, 91% for L-band and 94% for P-band. Figure 2 shows the complex correlation values ρ ($=\text{Re}[\rho]$, $\text{Im}[\rho]$), for primary forest and pastures, for C-, L- and P-band. The primary forest shows a distinctive pattern, indicating that single bounce (odd) scattering mechanism is dominating in the C-band while diffuse scattering is dominating in the L- and P-bands. Between L- and P-band it can be observed that there is a difference in the phase of ρ , indicating that the polarimetric phase difference (PPD) for P-band is higher than for L-band.

High Pearson correlation coefficients between forest biomass and radar values were found. The highest value found for L-band was $r = 0.89$ for the L-LL combination and for P-band $r = 0.93$ for the P-RL combination (table 2). It is noted that biomass itself is not easy to determine and good correlation coefficients within a single class (e.g. secondary forest) not necessarily mean that estimates can be made without good prior classification. Using the partial polarimetric information of the C-band, it can be seen that the correlation is better than the ones calculated for the single polarization C-bands. This result is interesting considering that the new ASAR system on ESA's ENVISAT will provide this partial polarimetric information, showing some potential for biomass classifications and mapping.

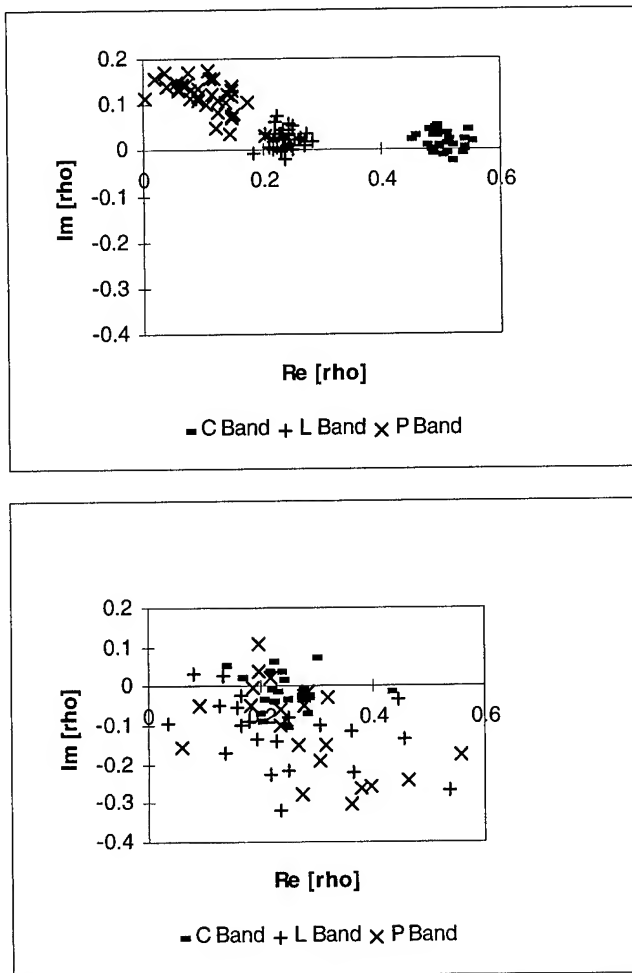


Figure 2. Normalized complex correlation of HH and VV channels for three frequency bands, for primary forest (a) and pastures (b).

Table 2. Pearson correlation coefficients, calculated between biomass, basal area and radar data for different channels. 1=Log10(BIO1), 2=Log10(BIO2), 3=BA. BIO1 and BIO2 are biomass values estimated with two different allometric equations. BA, Basal area calculated from field data.

	C vv	C rl	L hh	L hv	L ll	P hh	P hv	P vv	P rr	P rl	P ll	C pol
1	54	59	86	86	89	91	91	93	92	93	92	69
2	51	56	84	84	87	89	88	91	89	91	90	67
3	56	60	87	88	89	91	90	92	91	93	91	72

4. CONCLUSIONS

The capabilities for the classification of four land cover types, using single bands and combinations of two bands, were excellent (higher than 92%, in most of the cases), considering the fact that contemporaneous field observations were not available and that the differences between some classes are not distinct but gradual. It is important to point out that the best classification results, for most of the two band combinations were found when

combining any C-band channel with the ones of the P- and L-bands. In addition in many of the combinations, the good classification percentages between primary and secondary forest will constitute an important aspect in the establishment of monitoring systems in the Amazon region. It is also interesting to note that the combinations of the C-VV and P-LL band gave some of the best classification results, meaning that the circular polarization P-LL could be the one implemented in satellite radar systems, overcoming the problem of Faraday rotation encountered for linear polarizations of the long wavelengths.

On the other hand biomass appears not to be the single main explaining factor in the description of backscatter. Results indicate that forest structural and physiological parameters as well as soil moisture and roughness parameters can also have influence.

ACKNOWLEDGMENTS

NASA is acknowledged for provision of AIRSAR data and execution of the AIRSAR South American Deployment. Financial support was provided by the Netherlands Remote Sensing Board (BCRS) through project 3.3/AO-06: "AirSAR93 of Tropical Rain Forests" of the National Remote Sensing Program. Logistic support was provided by the Tropenbos foundation through Tropenbos - Colombia. In Colombia support was also provided by the Corporación Colombiana para la Amazonia -(SINCHI) and ITC. Martin Vissers (WAU) is acknowledged for general support in data processing and data management.

REFERENCES

- [1] Andrade, A and A. Etter, 1987, Levantamiento ecologico del área de colonización de San José del Guaviare, Corporación de Araracuara, Proyecto DAINCO-CASAM, Bogotá.
- [2] Brown, S., A.J.R. Gillespie, and A.E. Lugo, 1989, Biomass estimation methods for tropical forests with applications to forest inventory data, Forest Science, Vol.35, pp.881-992.
- [3] Hoekman, D.H., J.J. van der Sanden and W. Bijker, 1996, radar remote sensing of tropical rain forests: The AIRSAR-93 campaign in guyana and Colombia, BCRS report 96-02, Delft, The Netherlands
- [4] Sicco Smit, G. , 1994, Personal communication
- [5] Van Zyl, J.J., R. Carande, Y. Lou, T. Miller and K. Wheeler, 1992. 'The NASA/JPL three-frequency polarimetric airsar system'. In: Proceedings of IGARSS'92; International Space Year: Space Remote Sensing. Houston, May 26-29 1992, Volume I, pp.649-651.

Radar Monitoring System for Sustainable Forest Management in Indonesia

Dirk H. Hoekman

Wageningen Agricultural University

Dept. of Water Resources, Nieuwe Kanaal 11, 6709 PA Wageningen, The Netherlands

tel: +31-317-482894, fax: +31-317-484885, email: dirk.hoekman@users.whh.wau.nl

Abstract -- The year 2000 is considered as the final year for the obligation to reach sustainable forest management for timber production. To support management and to verify proper execution of guidelines and legislation, appropriate observation tools should be available. Current observation techniques suffer too much from severe cloud cover. The Indonesian Ministry of Forestry and the Tropenbos Foundation coordinate research into the utility of advanced radar techniques. In this paper some of the information needs and first research results are given.

1. INTRODUCTION

The present awareness and concern about global environmental changes, such as high rates of deforestation, brings governments and international organizations to develop effective measures for a better management of our environment. Deforestation rates are especially high in the vast tropical rain forest areas. At the same time these areas are acknowledged as an important factor in the global hydrological and biochemical cycles, as an important genetic reservoir and as a potential permanent source of production for the benefit of many people. For these reasons the government of Indonesia has decided to take strong measures in support of sustainable forest management.

For management of these areas the availability of up-to-date information is imperative. Severe cloud cover is the main obstacle for timely acquisition of information while the pronounced topography of the terrain and the vastness of the area, fragmented over many islands, poses additional problems. The major part of the Indonesian land surface area, i.e. 143 million ha or 75%, has the status of forest land. According to the National Land Use Law of 1992, 65 million ha is designated as production forest, 49 million ha as protected forest and 30 million ha as conversion forest. The production forest is used by some 500 concession holders to produce timber. Information is needed by the government to verify proper execution of rules developed for sustainable management and to evaluate the (long term) effects of these measures.

According to international agreements the year 2000 is considered as the final year for the obligation to reach sustainable forest management for timber production [1, 2]. An independent organization will be established in Indonesia to certify timber for the international market (the so-called 'eco-labeling institute'). It should verify proper execution of national rules and compliance with the guidelines of the International Tropical Timber Organization (ITTO). According to ITTO Indonesia, together with Ghana and possibly Malaysia belong to the

few countries still on schedule to meet these guidelines. One of the key problems is the practicability of policy and legislation. Proper execution of rules or guidelines can only be evaluated according certain criteria. And only those criteria that can be tested accurately and timely over these large areas are appropriate. Current remote sensing techniques for acquiring information, such as aerial photography and spaceborne optical imaging, suffer too much from cloud cover. Advanced airborne and spaceborne radar techniques are, however, very promising in this respect. For this reason the Indonesian Ministry of Forestry, in cooperation with the Tropenbos Foundation, has initiated a research project to achieve proper introduction of these new mapping and monitoring tools. In this paper some of the first conclusions will be presented. After indicating the main information needs (section 2) and the research approach (section 3), some first result showing the utility of radar for monitoring indicators of sustainable management will be presented (section 4). Finally (section 5), some considerations will be given on the problem of how to realize an *operational* monitoring system, meeting information needs and providing data in a fully transparent way, before the year 2000.

2. INFORMATION NEEDS

Making an assessment of information needs is an evolutionary process rather than a straightforward procedure. Certain types of information are easier to obtain than others in terms of cost or timeliness. This strongly depends on the existing infrastructure and available technology. The technological "state-of-the-art" is changing, improving capabilities. At the same time new policies develop, generating new information needs. Within the current study these considerations are taken into account.

An inventory was made of current and foreseen information needs and current difficulties to acquire this information [3]. Within the Ministry of Forestry (MOF) the Directorate for Forest Inventory and Land Use Planning (INTAG) is responsible for mapping and monitoring Indonesia's forests and for scrutinizing information delivered by forest concession holders. The major challenge for the Indonesian forestry community, however, is the need to fully implement a monitoring system for the verification of indicators of sustainable forest management, before the year 2000. The MOF Agency for Forestry Research and Development (Litbang) is responsible for the development and validation of suitable criteria.

Current Indonesian guidelines for sustainable forest management depend on certain local forest and terrain characteristics. These can be summarized very briefly as follows. A 'production forest' is a forest area which has a merchantable timber volume in excess of 20 cubic meter per ha, in which no clearcuts are allowed. Only trees with a diameter of at least 50 cm can be harvested. To avoid erosion additional limitations are applicable for cutting on moderately steep slopes (the so-called 'limited production forest') and no cutting is allowed on slopes in excess of 38 degrees (i.e. 'protected forest'). Also in buffer zones along rivers, lakes and protected forests cutting is not allowed as an additional measure to protect watersheds. In so-called 'non-production forest' areas and production forest areas with less timber than 20 m³ per ha cutting is only allowed after enrichment planting or when reforested after clearcutting.

The MOF considers remote sensing, and especially radar remote sensing, as the best practical approach to collect and/or verify such information in such large quantities. It would, for example, be very useful if information on the degree of crown cover opening, skid roads, timber road construction, logging of individual trees (as have been marked previously on tree position maps) and erosion could be acquired routinely. The large scale of the data needed (in the order of 1:20,000), the large area (at least a considerable fraction of all production forests), the large distances in Indonesia and the high temporal frequency (once or twice yearly) would, of course, still require a large degree of effort.

3. RS RESEARCH PROGRAM

Integration of data acquisition techniques, exploiting the high temporal resolution of satellite radar, the somewhat higher spatial resolution of optical satellite systems and their different information contents, in addition to airborne survey with either photographic or advanced radar techniques would provide a versatile basis for forest monitoring [4]. The development of an 'end-to-end' system, tuning information needs within the available infrastructure, new sensors, observation and processing strategies, training of qualified staff, etc., would then be the next step.

The key problem is to decide how to complement existing facilities with one (or more) airborne radar system(s) or, possibly, advanced optical instruments. To date radar remote sensing technology offers many new and unique observation possibilities, such as the use of the P-band, polarimetry, interferometry and very high spatial resolution (higher than 1 m). The latter could be introduced in forest practice very easily as an all-weather alternative for aerial stereo photography. Many of these possibilities still need to be studied systematically and in much more detail. The use of long wave (P- or L-band) systems may be useful to obtain specific classification results and for assessment of forest timber volume or forest re-growth classes.

Therefore, within the MOF-Tropenbos project, several airborne radar campaigns have been planned at study sites in the provinces East-Kalimantan and Jambi. The first one,

the Indrex-96 campaign, funded by the European Space Agency (ESA) and carried out under the auspices of INTAG and ESA, already has been executed in the period July-August 1996. The main objective is to generate a useful data set to study the utility of very-high resolution and/or interferometric systems at C- and X-band. Participation to NASA's PacRim follow-on campaign is tentatively planned for 1999.

4. MONITORING INDICATORS OF SUSTAINABLE MANAGEMENT

From the discussion in section 2 it follows that information is needed on slope limits (e.g. the 38° limit) and timber volume limits (e.g. the 20 m³ limit) to determine the local type of management required. To verify proper execution of guidelines information is needed on items such as the position and size of trees that were extracted, on the degree of canopy closure, on the characteristics of skid trails and timber roads that were constructed and, where needed, on reforestation.



Figure 1. Detail of a Dornier C-band SAR image with 0.8 m resolution acquired during the ESA/Indrex-96 campaign at the East-Kalimantan test site in July 1996. A 100 m x 100 m test plot is indicated for which all trees have been measured.

Since information at the tree level is required the use of very high resolution radar images is imperative. Characteristics of such images can be illustrated from the Indrex data set. Figure 1 shows a 4-look 0.8 m resolution C-band non-interferometric image. Even though the resolution is very high, it is still difficult to identify all large crowns in the canopy. This is partly due to shading, radar foreshortening and radar overlay. Other image fragments

show that large gaps in the canopy, which result from harvesting a number of closely spaced trees, can be observed clearly and can be compared with naturally occurring gaps in undisturbed primary forest. Main roads can be observed well. Even 5-year old timber roads and skid trails can be identified. Within one year after their construction the detectability would even have been much better because, in the mean time, the canopy may have largely overgrown these timber roads and skid trails abandoned 5 years ago. A 6-look 1.5 m resolution C-band interferometric image fragment from another area is shown in figure 2. This image seems to fulfill the information needs better. The recognizability of tree crowns is much improved, tree positions are not displaced by (radar) parallaxes and information on slopes can be extracted. Other essential information, like the degree of crown cover, seems to be covered as well.

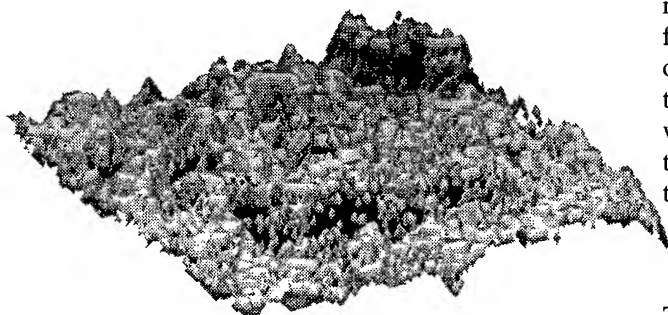


Figure 2. Detail (size 150 m square) in perspective view of a Dornier interferometric C-band SAR image with 1.5 m resolution acquired during the ESA/Indrex-96 campaign at the East-Kalimantan test site in July 1996. (Note that this image is just a 'quick-look' product. The final quality will be much improved.)

Of course much work remains to be done on the selection of optimum parameters for such images; for example, the minimum number of looks and the minimum spatial resolution required, the height accuracy required and the wave parameters: frequency, polarization and incidence angle. Moreover, algorithms to derive height should be developed as well as new algorithms to deal with very high resolution three-dimensional radar data. The availability of robust automated interpretation procedures is of great importance because of the enormous data volumes to be handled in short periods. The total area to be covered by such a system may possibly be up to 40 million ha per year [3]. The total amount of raw data to be acquired would be in the order of 15 Terabyte. After SAR processing the total yearly amount of data to be interpreted and archived would still be huge. Even for pixel sizes of 2 m squared, using only 2 bytes per pixel (to code backscatter level *and* height) it would already be 200 Gigabyte.

5. CONCLUSIONS AND RECOMMENDATIONS

Several types of information needs could be identified, which require specific approaches and have different

strategies of implementation [3]. For mapping and fire monitoring currently available airborne radar systems would suffice (up to a map scale of 1:50,000). For monitoring indicators of sustainable management the technology is available to realize a system before the year 2000. Such a system would at the same time advance certain mapping possibilities (up to a scale of 1:25,000 to 1:10,000).

Satellite systems can direct airborne surveys to places of interest, thus avoiding unnecessary operations. Airborne and spaceborne radar systems are mere elements of an operational 'end-to-end' information system. Proper care should be taken to develop such an 'end-to-end' system, which also requires well-trained and educated staff, availability of interpretation algorithms and sufficient processing capabilities.

The role of the research is crucial: it is the basis for proper selection of instruments, development of conceptual approaches, remote sensing data interpretation methodologies, education and training. It would also allow for the development of 'advanced' products with new types of radar. Research efforts need more support, for example to realize more airborne radar campaigns and more field work campaigns in Indonesia. Only then, full advantage of the possibilities of advanced radar remote sensing techniques can be taken.

ACKNOWLEDGMENTS

The Indonesian Ministry of Forestry, the Tropenbos Foundation, the Wanariset research station, APHI, PT Mapindo Parama, University of Gadjah Mada, CIFOR, EU-IFSSP, ITC, IBN-DLO, European Space Agency, Dornier Space Systems, Fokker Space, Netherlands Aerospace Laboratory and FEL-TNO are acknowledged for their contributions to the ongoing research activities. The European Space Agency, the Netherlands Remote Sensing Board and the Netherlands Ministry of Economic Affairs are acknowledged for their substantial financial contributions during the first phase of the project.

REFERENCES

- [1] Achmed Sumitro (Dean Faculty of Forestry, Gadjah Mada University), 1993, The Indonesia's preparedness toward target year 2000 for sustainable forest management.
- [2] Lammerts van Bueren, E.M. and E.M. Blom, 1997, Hierarchical framework for the formulation of sustainable forest management standards, The Tropenbos Foundation, Wageningen, The Netherlands.
- [3] Hoekman, D.H., 1997, Radar monitoring for sustainable forest management in Indonesia, Seminar on "radar technology for sustainable forest management", 3 April 1997, Jakarta.
- [4] Herman Hidayat (Director, Pt Mapindo Parama), 1994, Forest inventory and monitoring over production forest areas in Indonesia.

Tabular Summary of SIR-C/X-SAR Results: Synthetic Aperture Radar Frequency and Polarization Requirements for Applications in Ecology and Hydrology

Christiane C. Schmullius¹ and Diane L. Evans²

¹German Aerospace Research Establishment (DLR), Institute for Radio Frequency Technology
P.O. Box 11 16, D-82230 Wessling, Germany, Email: chris.schmullius@dlr.de
Phone: +49.(0)8153.28-2337, Fax: +49.(0)8153.28-1449

²Jet Propulsion Laboratory, California Institute of Technology, M/S 180-703,
4800 Oak Grove Drive, Pasadena, CA 91109, Email: Diane.L.Evans@jpl.nasa.gov

Abstract -- The Spaceborne Imaging Radar-C, X-Band Synthetic Aperture Radar (SIR-C/X-SAR) was the first multifrequency and multipolarization SAR system to be launched into space. SIR-C is a two-frequency radar which simultaneously acquires polarimetric C-band (5.8 cm wavelength) and polarimetric L-band (23.5 cm wavelength). X-SAR operates at X-band (3.1 cm wavelength) and vertical polarization (VV). SIR-C/X-SAR was carried in the cargo bay of the Space Shuttle Endeavour in April and October 1994, imaging over 300 sites around the Earth and returning 143 terabits of data. SIR-C/X-SAR data have been used to validate algorithms (developed from earlier aircraft data) which produce maps of vegetation type and biomass, snow, soil and vegetation moisture or the distribution of wetlands. A polarimetric X- and L-band radar is suggested as a result of this overview for future SAR sensors.

INTRODUCTION

The advancement of knowledge in the field of radar remote sensing accomplished in the last two years as well as the verification of earlier findings since the two successful SIR-C/X-SAR missions is tremendous. Results clearly show the increased value of using multiparameter and interferometric capabilities to characterize Earth's surface and vegetation cover and to generate geophysical products compared with optical sensors or single-channel radars alone [1,2].

This overview paper presents the current status of optimal SAR parameters for various key issues within the disciplines of Ecology and Hydrology. SIR-C/X-SAR investigators, who presented their results during the Science Team Meeting at the University of California, Santa Barbara in February 1996, were asked to participate in this effort. Two tables summarize the current SAR requirements for ecology and hydrology. A full paper with an extended reference list and also including summaries on geological and oceanography applications is in press [3].

TABLE LAYOUT

The two tables summarize current SAR requirements for ecology and hydrology, evaluated by SIR-C/X-SAR investigators. The research topics were chosen using [4] and [5]. Many investigators had worked with polarimetric C-, L- and P-band (68 cm) data acquired by the NASA AIRborne Synthetic Aperture Radar (AIRSAR) prior to the SIR-C/X-SAR missions. P-band proved to be very useful for many applications and has therefore been added to the tables. X-band HH and cross-polarized results were retrieved from past scatterometer and airborne experiments

(e.g. AGRISCATT, MAESTRO-1).

hh and *vv* stand for horizontal and vertical co-polarization, *x* means cross-polarization. Boxes were combined, where no specific polarisation was mentioned. Boxes are empty, where no information was given.

The dot size is a prioritization:

•: Important; ◐ or ◑: Important but only one of the polarizations is required; ◐◐ or ◑◑: polarimetry is required, but only one of the two frequencies; ∙: helpful; -: not mandatory; □: no information.

ECOLOGY

Monitoring global vegetation is of major importance to understand the Earth's climate and to detect possible changes. Imaging radar provides a unique tool for mapping the often cloud covered tropical and boreal ecosystems. Beyond mapping vegetation types, multiparameter SAR data allow the calculation of biomass with accuracies of 25 kg/m²[6] or monitoring of tropical floodplain inundation to aid in the understanding of biogeochemical processes [7]. Table 1 summarizes which SAR parameters have been most important for each of the eight research topics. An elaborated analysis of radar remote sensing for ecological applications can be found in [8]. Backscattering from vegetation is influenced by the volumetric water content in a canopy and the distribution of water molecules which depends on the canopy geometry. Therefore, vegetation mapping is a combination of both and requires cross-polarized multifrequency data. Table 1 illustrates the importance of multiple wavelengths for ecological applications. Cross-polarization aids in the description of the vegetation type and the constituents of a canopy.

The requirements can be summarized as follows:

- mapping and monitoring requires a combination of X- or C-band with L- or P-band;
- L-band or P-band are essential for forest/non-forest discrimination;
- modelling forest biomass requires cross-polarized L- or P-band;
- mapping of inundated areas requires HH-polarized L- or P-band;
- best crop classification results are gained with X- and L-band, second best: C- and L-band;
- L-band is the single most important band for agricultural remote sensing.

HYDROLOGY

The hydrological cycle, as one of the Earth's climate generators, has two components: 1) the ocean-continent water and energy exchange due to the global circulation, and 2) the continent-internal energy-water interactions, which change in response to land surface management practices. Soil moisture is an environmental descriptor that integrates much of the land surface hydrology. Only microwave data have demonstrated the ability to quantitatively measure soil moisture under a variety of topographic and vegetation cover conditions [9]. Temporal changes in the distribution and volume of glaciers and ice sheets are good indicators of climate trends. Seasonal snow cover and alpine glaciers are the largest contributors to the ground-water recharge in many parts of the world. Multiparameter radar data have shown sensitivity to snow wetness with an absolute error of 2.5% by volume at a 95% confidence interval [10]. Good agreement was found for the mass balance estimated with SIR-C/X-SAR data and the field measurements carried out at two Alpine glaciers [11]. Table 2 lists the current SAR requirements for hydrological and glaciological applications. The table illustrates the need for long wavelengths for soil moisture mapping. Polarimetric data are necessary for snow and ice volume estimations. Short wavelengths are required to map snow and ice extent

The requirements can be summarized as follows:

- P-band is best choice for soil moisture mapping, because of penetration through the vegetation layer;
- polarimetric L-band is needed to model the volumetric water content of snow;
- polarimetric X- or C-band is required to map the snowpack extent;
- best discrimination of mountain glaciers with cross-polarized X- and L-band or X- and P-band;
- polarimetry and multifrequency are required for ice mapping.

RECOMMENDATIONS

This review paper serves as an overview of the current user requirements for future SAR systems. It is obvious from Tables 1 and 2 that polarimetry and multifrequency allow the most beneficial results for monitoring the Earth's environment. A polarimetric X- and L-band radar is suggested for future SAR sensors. This recommendation is in accordance with the "strawman SAR mission scenario" proposed by the Science Panel for the Space Studies Board of the National Research Council to NASA's Office of Mission to Planet Earth [5].

ACKNOWLEDGMENTS

This work was initiated by the International SAR Working Group and could have not been accomplished without the input of many SIR-C/X-SAR investigators and their publications. Parts of this work have been included in two studies for the European Space Agency: "Next Generation SAR Instrument" and "Combination of SAR and Optical Spectroradiometer Data in Aggregated Models".

REFERENCES

- [1] Stofan, E., Evans, D., Schmullius, C., Holt, B., Plaut, J., van Zyl, J., Wall, S. and J. Way, 1995, Overview of results of Spaceborne Imaging Radar-C, X-Band Synthetic Aperture Radar (SIR-C/X-SAR). *IEEE Transactions on Geoscience and Remote Sensing*, **33:4**, 817-828.
- [2] Evans, D., Plaut, J. and Stofan, E., 1997, Overview of the Spaceborne Imaging Radar-C/X-Band Synthetic Aperture Radar (SIR-C/X-SAR) Missions. *Remote Sensing of Environment*, in press.
- [3] Schmullius, C. and D. Evans, 1997, Synthetic Aperture Radar Frequency and Polarization Requirements for Applications in Ecology, Geology, Hydrology, and Oceanography - a Tabular Status Quo after SIR-C/X-SAR. *Intern. Journal Remote Sensing*, in press.
- [4] Earth Observing System, 1984, Synthetic Aperture Radar Instrument Panel Report. *NASA*, Vol. IIf.
- [5] Evans, D. (Ed.), Apel, J., Arvidson, R., Bindschadler, R., Carsey, F., Dozier, J., Jezek, K., Kasischke, E., Li, F., Melack, J. Minster, B., Mouginis-Marks, P., and van Zyl, J., 1995, Spaceborne Synthetic Aperture Radar: Current Status and Future Directions - A Report to the Committee on Earth Sciences, Space Studies Board, National Research Council. *NASA Technical Memorandum* 4679.
- [6] Dobson, M.C., Ulaby, F., Pierce, L., Sharik, T., Bergen, K., Kelndorfer, J. Kendra, J., Li, E., Lin, Y., Nashashibi, A., Sarabandi, K., and P. Siqueira, 1995a, Estimation of Forest Biophysical Characteristics in Northern Michigan with SIR-C/X-SAR. *IEEE Transactions on Geoscience and Remote Sensing*, **33:4**, 877-895.
- [7] Hess, L., Melack, J., Filoso, S., and Y. Wang, 1995, Delineation of inundated area and vegetation along the Amazon floodplain with the SIR-C Synthetic Aperture Radar. *IEEE Transactions on Geoscience and Remote Sensing*, **33:4**, 896-904.
- [8] Kasischke, E., Melack, J., and M. C. Dobson, 1997, The use of imaging radars for ecological applications - a review. *Remote Sensing of Environment*, in press.
- [9] Hall, F., Townshend, J. and T. Engman, 1995b, Status of remote sensing algorithms for estimation of land surface state parameters. *Remote Sensing of Environment*, **51**, 138-156.
- [10] Shi, J. and J. Dozier, 1995, Inferring Snow Wetness Using C-Band Data from SIR-C's Polarimetric Synthetic Aperture Radar. *IEEE Transactions on Geoscience and Remote Sensing*, **33:4**, 905-914.
- [11] Rott, H., Nagler, T. and D.-M. Floricioiu, 1996, Snow and glacier parameters derived from single channel and multiparameter SAR. *Proceedings of the International Symposium on Retrieval of Bio- and Geophysical Parameters from SAR Data for Land Applications*,

Toulouse, France, 10-13 October 1995 (Toulouse, France: CNES), pp. 479-488.

Table 1: Optimal SAR Parameters for Ecological Applications

Disci- pline	Research Topic / Operational Application	X			C			L			P		
		h h	v v	×	h h	v v	×	h h	v v	×	h h	v v	×
E C O L O G Y	Vegetation Mapping	•	•	•	•	•	•	◐	◑	•	◐	◑	•
	Biomass Estimation	•			•			•	•	•	•	•	•
	Canopy Geometry	•	•	•	•	•	•	•	•	•	•	•	•
	Monitoring Flooded Forests	-	-	-	-	-	-	•	•	•	•	•	•
	Non-forested Wetlands	•	•	•	•	•	•	•	•	•	•	•	•
	Crop Monitoring	◐	◐	◐	◑	◑	◑	•	•	•	-	-	-
	Tundra Monitoring	•	•	•	•	•	•	•					
	Frozen/Thawed Vegetation	◐	◐	◐	◑	◑	◑	•					

Table 2: Optimal SAR Parameters for Hydrological and Glaciological Applications

Disci- pline	Research Topic / Operational Application	X			C			L			P		
		h h	v v	×	h h	v v	×	h h	v v	×	h h	v v	×
H Y D R O	Soil Moisture / Texture	-	-	-	•	•	•	•	•	•	•		
	Salinity Mapping	-	-	-	-	-	-	•	•	-			
	Soil Surface Roughness	•	•	•	•	•	•	•	•	•	•	•	•
	Land-Water Boundaries/Flooding	-	-	-	•	•	-	•	•	-	•		
	Snowpack Extent	◐	◑	•	◐	◑	•	•	•	•	-	-	-
	Snow Wetness / Water Equivalent	•	•	•	•	•	•	•	•	•			
I C E	Mountain Glaciers	◐	◑	•	•	•	•	◐	◑	◐	◑	◑	◑
	Sea Ice Discrimination	◐	◑	•	◐	◑	•	◐	◑	•	-	-	-
	Ice Sheets and Shelves	◐	◐	◐	◑	◑	◑	◐	◑	•	◐	◑	•
	Iceberg Monitoring	◐	◑	•	◐	◑	•	-	-	-	-	-	-

Airborne Millimeter-wave Radiometric Observations of Cirrus Clouds

J. R. Wang and P. Racette

Laboratory for Hydrospheric Processes

NASA Goddard Space Flight Center, Greenbelt, MD 20771, U.S.A

Tel: 301-286-8949/FAX: 301-286-1762/e-mail: wang@sensor.gsfc.nasa.gov

ABSTRACT

This paper reports the first radiometric measurements of cirrus clouds in the frequency range of 89-325 GHz from a high-altitude aircraft flight. The measurements are conducted with a Millimeter-wave Imaging Radiometer (MIR) on board the NASA ER-2 aircraft over a region in northern Oklahoma. Aboard the same aircraft are a cloud lidar system and a multichannel radiometer operating at the visible and infrared wavelengths. The instrument ensemble is well suited for identifying cirrus clouds. It is shown that the depressions in brightness temperatures associated with a few intense cirrus clouds occur at all frequency channels of the MIR. Estimates of total ice water path of the cirrus clouds are derived from comparisons of radiative transfer calculations and observed brightness depressions.

INTRODUCTION

Remote measurements of cirrus clouds have mostly been made in the visible and infrared regions of the electromagnetic wave spectrum [1]. Observations in the microwave and millimeter-wave regions were limited to ground-based radars [2]. At aircraft altitudes, there are measurements [3] over storms in which the brightness temperatures (T_b) in the frequency range of 90-220 GHz are ≤ 150 K. The modest decreases in T_b values at millimeter wavelengths expected from radiative transfer modeling of cirrus clouds [4], to the best of our knowledge, have not been observed and reported.

The following gives a brief description of MIR observations of cirrus clouds in the frequency range of 89-325 GHz [5]. The measurements were made over northern Oklahoma during the SUCCESS (SUBsonic aircraft; Contrail and Cloud Effects Special Study) mission of April-May 1996. The MIR was on board the NASA ER-2 aircraft, which was flown at an altitude of about 20 km and generally above the tops of most clouds. Data from two other instruments aboard the same aircraft, the Cloud Lidar System (CLS) and the MODIS (Moderate-resolution Imaging Spectrometer) Airborne Simulator (MAS), were used to help identify the presence of cirrus clouds. Three events of cirrus clouds are discussed in the following; they are among the most intense ones observed by the MIR during the mission.

OBSERVATIONS

The data reported in this paper were acquired on April 16, 1996 when the aircraft made 12 repeated passes over the same region in northern Oklahoma along the 36.6°N latitude line and between the two endpoints defined by the longitude lines of 95.9°W and 98.5°W. Figure 1 shows the backscatter profiles from the CLS and brightness temperatures $T(11 \mu\text{m})$ measured by the thermal infrared channel (11 μm) of the MAS over a straight 135-km path with two endpoints at geographic locations of (36.6°N, 97.5°W) and (36.6°N, 96.0°W). Four plots (A, B, C, and D) in the figure represent four consecutive measurements over the same path. The endpoint at (36.6°N, 97.5°W) always begins from the left side of each plot; thus, the time axes in plots (A) and (C) run from right to left. The top portion of each plot gives the heights of cloud layers and surface (~ 0 km) as detected by the CLS, which appear to be closely correlated to the $T(11 \mu\text{m})$ values measured by the MAS displayed in the bottom portion of the plot. In each of the plots (A), (B), and (C), there is a region where the values of $T(11 \mu\text{m})$ are < 250 K. In this region the CLS fails to observe the return signals from the surface; the region is covered with dense cirrus clouds that totally attenuate the lidar signals. In the fourth pass over the region between 1938-1949 UTC, shown in plot (D), $T(11 \mu\text{m})$ are ≥ 250 K, suggesting the presence of thin cirrus clouds only.

The corresponding variations of $T_b(\nu)$'s at frequency ν from the MIR for the same four consecutive passes are shown in Figure 2. Only the $T_b(\nu)$ values from six channels at 150, 220, 183.3 \pm 3, 183.3 \pm 7, 325 \pm 3, and 325 \pm 8 GHz are plotted in order to maintain the simplicity of the figure. The two horizontal dotted lines in each plot, at $T_b(\nu)$ values of 225 K and 250 K, provide a reference of $T_b(\nu)$ variations for the 183.3 GHz and 325 GHz channels, respectively. The two vertical dotted lines in plots (A), (B), and (C) identify the areas of dense cirrus where the CLS fails to observe signal return from the surface; in these areas a strong depression in $T_b(\nu)$'s are observed at all six channels. This depression in $T_b(\nu)$ displays a frequency dependence characteristic of wave scattering by ice particles: the higher the frequency of observations the stronger the $T_b(\nu)$ depression [4]. At the location of the strongest $T_b(\nu)$ depression in plot (C), for example, the changes in $T_b(\nu)$'s from their nominal values

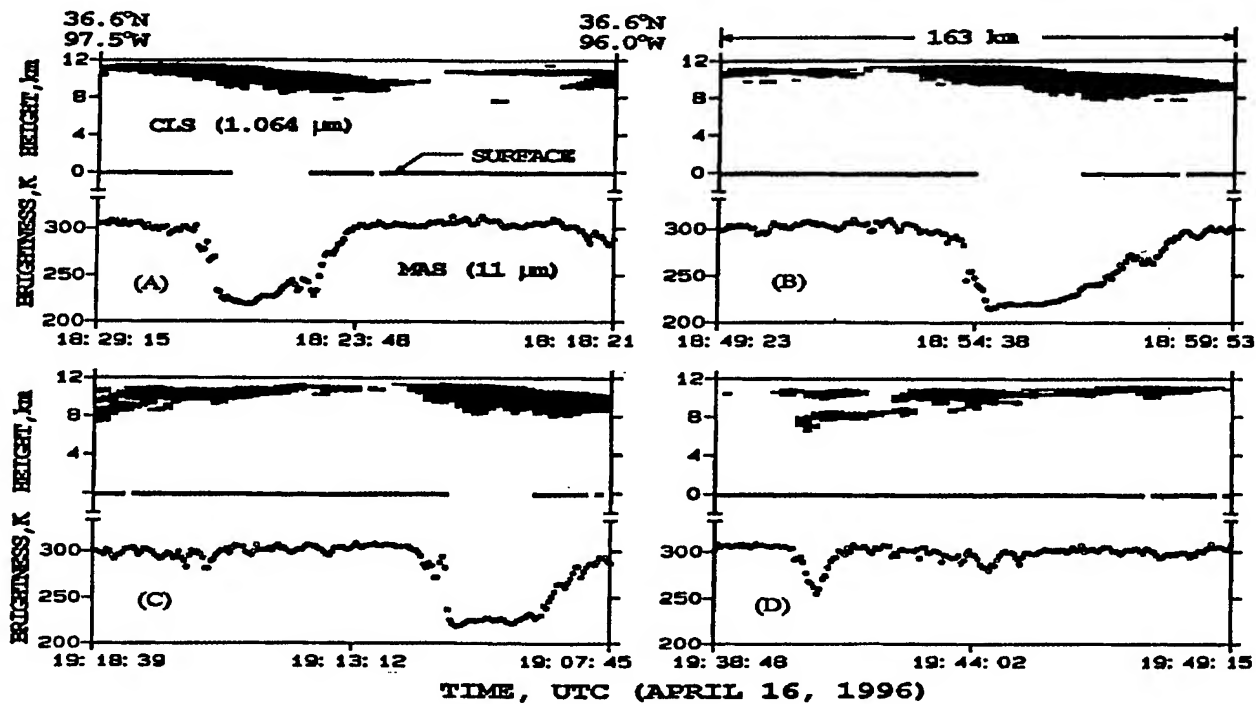


Figure 1. Variations of lidar backscatter and 11 μm brightness from four ER-2 aircraft passes over the same region in northern Oklahoma.

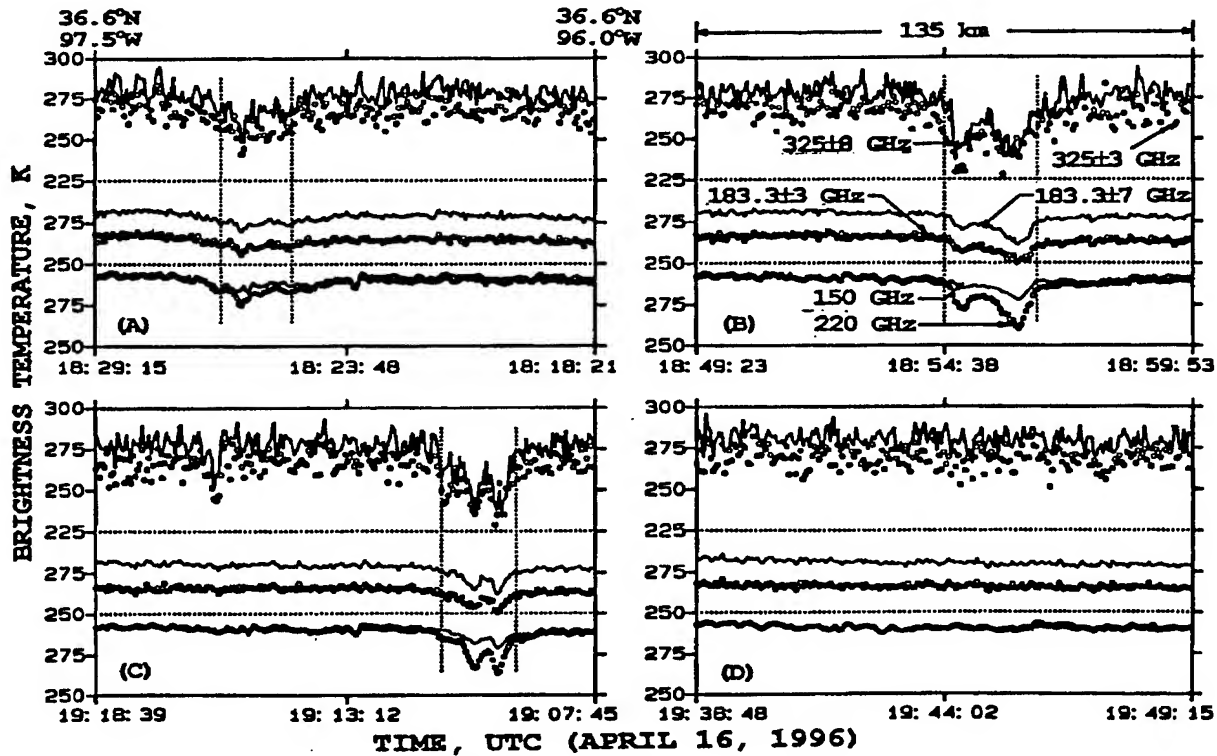


Figure 2. Brightness temperature variations observed by the MIR at six frequencies from the same four ER-2 aircraft passes described in Figure 1

are about 12 K, 15 K, 30 K, and 35 K at frequency channels of 150, 183.3 ± 7 , 220 and 325 ± 8 GHz respectively.

COMPARISON WITH CALCULATIONS

The measured brightness depressions, $\delta T_b(\nu)$'s, are compared with the results of radiative transfer calculations for estimation of cloud parameters as shown in Figure 3. Here the smooth curves adopted from Gasiewski [4] give the dependence of $\delta T_b(\nu)$ on cloud density at $\nu = 89, 166, 220$, and 340 GHz. Notice that some of these calculations are not made at the exact frequencies as those of the MIR, but they are close enough for a valuable comparison with the MIR measurements. The values of $\delta T_b(\nu)$ at $\nu = 89, 150, 220$, and 325 ± 8 GHz from areas of largest depressions in Figure 2, A, B and C, are plotted on the curves of 89, 166, 220 and 340 GHz in Figure 3.

The $\delta T_b(\nu)$ values observed at $\nu = 89, 220$, and 325 GHz from the second and third passes, as represented by open and solid circles in Figure 3, give an estimated cloud density of about $0.05\text{--}0.06 \text{ g/m}^3$. The $\delta T_b(\nu)$ values at $\nu = 150, 220$ and 325 ± 8 GHz from the first pass around 1826 UTC give a cloud density of about 0.025 g/m^3 , which is much lower than $\sim 0.046 \text{ g/m}^3$ implied by the value of $\delta T_b(89)$. Clearly, calculated results do not match the observed values of $\delta T_b(89)$ for all three selected periods and yield cloud densities that are consistent with estimations at other frequencies. These discrepancies suggest the need of refining the radiative transfer calculations with realistic inputs of surface and atmospheric parameters.

CONCLUSION

Three cases of intense cirrus clouds observed by the MIR during the SUCCESS mission are presented in this paper. Although theoretical calculations [4] have shown cirrus clouds to have a measurable frequency response in the millimeter-wave region, the strong brightness depressions described in this paper provide the first conclusive evidence of cirrus cloud radiometric signatures in the frequency range of 89–325 GHz. The brightness depressions are found to be highly frequency dependent; for the three cases examined here, the brightness depression could be as large as 12 K at 150 GHz and 35 K at 325 ± 8 GHz. The largest brightness depressions at several selected frequencies from each of the three cases are compared with the results of radiative transfer calculations for an estimation of cloud density. The estimated cloud density ranges from about 0.025 to 0.06 g/m^3 , which is equivalent to 50–120 g/m^2 of ice water path, based on a 2-km cloud layer assumed in the

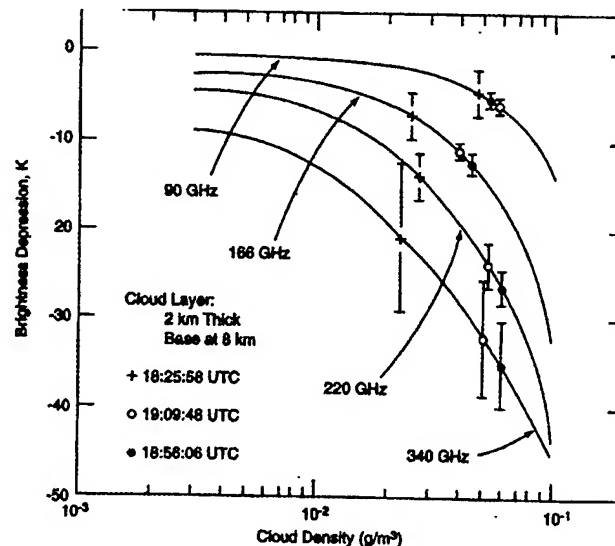


Figure 3. Variations of measured and model-calculated brightness depressions with cloud density.

calculations. There are some discrepancies in the cloud density estimation from brightness depressions at different frequencies, which are likely due to the input of generalized surface and atmospheric parameters in the radiative transfer calculations. More realistic characterization of input parameters pertaining to the site environment are required to bring about a better agreement between measurements and calculations, and a more reliable estimation of ice water path.

REFERENCES

- [1] J. D. Spinhirne and W. D. Hart, "Cirrus structure and radiative parameters from airborne lidar and spectral radiometer observations: the 28 October 1986 FIRE study," *Mon Wea. Rev.*, **118**(11), 2329–2343, 1990.
- [2] S. Y. Matrosov, T. Uttal, J. B. Snider, and R. A. Kropfli, "Estimation of ice cloud parameters from ground-based infrared radiometer and radar measurements," *J. Geophys. Res.* **97**(D11), 11567–11574, 1992.
- [3] J. R. Wang, J. Y. Zhan, and P. Racette, "Storm-associated radiometric signatures in the frequency range of 89–220 GHz," *J. Atmos. Ocean. Tech.*, **14**(1), 13–31, 1997.
- [4] A. J. Gasiewski, "Numerical sensitivity analysis of passive EHF and SMMW channels to tropospheric water vapor, clouds and precipitation," *IEEE Trans. Geosci. Remote Sens.*, **30**(5), 859–870, 1992.
- [5] P. Racette, R. F. Adler, J. R. Wang, A. J. Gasiewski, D. M. Jackson, and D. Zacharias, "A millimeter-wave imaging radiometer for cloud, precipitation and atmospheric water vapor studies," *J. Atmos. Ocean. Tech.*, **13**(3), 610–619, 1997.

Application of Space Lidar to the Remote Sensing of Clouds and Aerosols

David M. Winker
NASA Langley Research Center
MS/475, Hampton VA USA 23681
757 864-6747 / 757 864-2671 (fax) / d.m.winker@larc.nasa.gov

Abstract -- Clouds and aerosols have important influences on the climate and remote sensing from space is required to assess their effects on a global scale. Current capabilities to observe clouds and aerosols using passive satellite sensors are limited, however. The Lidar In-space Technology Experiment, flown on the space shuttle in September 1994, demonstrated the application of space lidar to the study of clouds and aerosols. Lidar technology has now matured to a point where satellite lidars are feasible. Space lidar will provide new measurement capabilities and provide improved detection and characterization of the role of aerosol and cloud in global climate.

INTRODUCTION

The nature of the role played by clouds in altering radiative fluxes at the surface and within the atmosphere is now recognized as one of the largest uncertainties in predicting global climate change. Clouds scatter incoming solar radiation and absorb upwelling thermal radiation from the Earth's surface. The net effect is to alter the atmospheric heating profile, which can then influence the large scale circulation of the atmosphere [1,2]. Complex interactions between precipitation, convection, and radiation determine the nature of the effects of clouds on the atmosphere. These interactions are poorly understood due to our current limited capabilities to remotely characterize clouds. Therefore, the nature and magnitude of cloud radiative feedbacks, which modify the sensitivity of the climate system to changes in the concentrations of greenhouse gases, remain undetermined.

In addition to various regional environmental impacts, anthropogenic aerosols are now believed to be significantly impacting global climate, through the absorption and scattering of incoming solar radiation [3,4]. The magnitude of greenhouse warming which has been predicted may in fact be mitigated by increases in aerosol due to human activities [5]. Thus the sensitivity of climate to increasing levels of greenhouse gases cannot be understood without understanding the effects of aerosols on the Earth radiation budget. Passive sensors have limited abilities to observe key characteristics which required to understand the role of clouds and aerosols in climate. This paper will briefly discuss the application of space lidars to these problems.

LITE

The Lidar In-space Technology Experiment (LITE) was flown on space shuttle mission STS-64 in September 1994 to demonstrate the feasibility of space lidar and explore applications of space lidar to atmospheric studies [6]. An orbital inclination of 57 degrees provided observation of a wide variety of tropical and mid-latitude cloud and aerosol phenomena during the 11 day mission

The ranging nature of lidar provides unambiguous height information and improved detection of optically thin cloud and aerosol. More realistic assessments of cloud distribution in the vertical, and particularly the occurrence of cloud layering, are critical to the accurate calculation of radiative heating in the atmosphere. Data from LITE such as the example shown in Fig. 1 illustrate the ability of lidar to

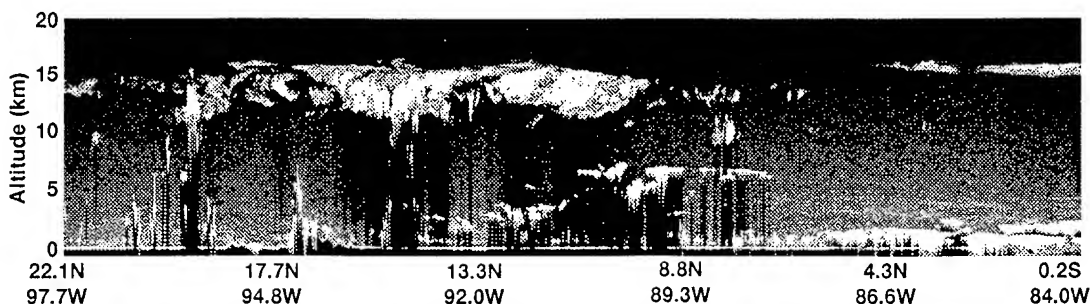


Figure 1. LITE raw backscatter signal at 532 nm over the eastern tropical Pacific. A pair of anvil clouds is seen between 10 and 15 km to the left of center. To the right is a layer of thin cirrus overlying marine stratus. Although the lidar signal is completely attenuated in deep convective clouds and boundary layer clouds, most upper level clouds are penetrated.

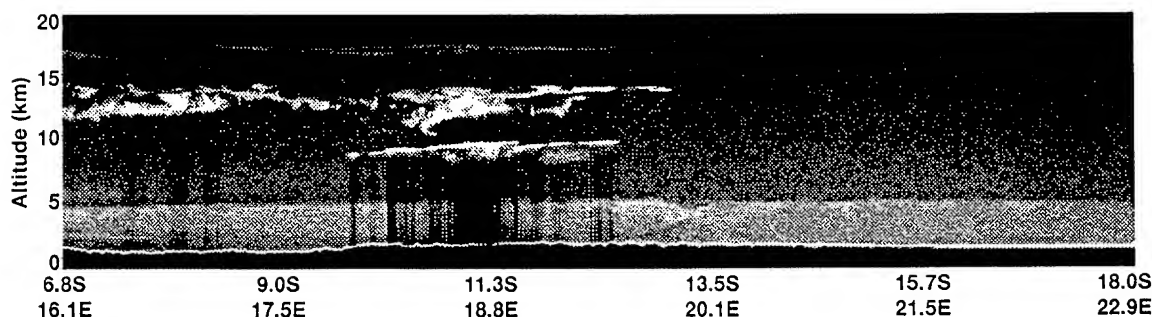


Figure 2. LITE raw backscatter signal at 532 nm over southwest Africa. A deep layer of biomass smoke (light gray) extending from 0 to 5 km is observed beneath multiple layers of thin cirrus (white) between 8 and 17 km.

penetrate upper level clouds to observe the structure of multilayer cloud systems [7].

Current uncertainties in the global production and distribution of aerosols are due in part to the difficulty of monitoring aerosols from space using passive sensors. Variations in aerosol optical properties and surface brightness produce uncertainties in passive retrievals of aerosol properties, especially over land where many important sources of aerosol are located. The high sensitivity provided by lidar allows improved identification of aerosol sources and observation of the dispersion of the aerosol. Data from LITE shown in Fig. 2 illustrate the ability to observe aerosol even beneath thin cirrus clouds. The statistics in Table 1 indicate the ability of lidar to penetrate cloud and observe underlying aerosol.

Table 1. Cloud cover and penetration statistics between 57N and 57S derived from LITE.

cloud fraction	77%
fraction of profiles reaching surface	72%
fraction of cloudy profiles reaching surface	60%

THE FUTURE FOR SATELLITE LIDAR

LITE employed a flashlamp-pumped laser. The longer lifetime and higher efficiency of diode-pumped lasers permit the development of lidars with multi-year lifetimes on small satellite platforms. The Vegetation Canopy Lidar (VCL) was recently chosen to be the first mission developed for the NASA Earth System Science Pathfinder Program (ESSP). VCL is a type of laser altimeter and uses relatively low pulse energy lasers. Higher energy lasers, suitable for atmospheric lidars, will soon be proven and ready for space missions.

To solve the outstanding problems of the role of clouds and aerosols in climate, lidar observations will have to be integrated with observations from other satellite sensors, as

well as from networks of surface instruments. Lidar has inherently high vertical resolution but it is nearly impossible to achieve horizontal resolution and coverage comparable to passive imaging sensors. The most advantageous way to use future space lidars is to fly them in conjunction with passive sensors, either on the same satellite platform or on separate satellites flying in coordinated orbits. The PICASSO (Pathfinder Instruments for Cloud and Aerosol Spaceborne Observations) mission is under development to place a high-power lidar on a small polar-orbiting satellite for global studies of cloud and aerosol. Like all active instruments, lidar performance improves as the orbit altitude decreases. Therefore PICASSO is proposed to fly in the same inclination as the EOS PM satellite but at a lower altitude. Availability to the PM instruments of coincident lidar data will allow improved retrievals of cloud and aerosol properties.

Some important quantities, such as aerosol absorption, are difficult to measure remotely, while others, such as size-resolved aerosol composition, are impossible to measure from space. Integration of space observations with data from surface networks will be required to understand problems such as the climate forcing due to anthropogenic aerosol [8, 9]. As an example, one aspect of understanding the impacts of human activities on the environment is the determination of source strengths of sulfur emissions from urban and industrialized areas. Many plumes of aerosol originating from urban areas were observed by LITE. In a recent study, the mass flux of sulfate in an aerosol plume originating from Taipei, Taiwan was estimated from LITE observations [10]. This estimate required assumptions on the intrinsic optical properties of the aerosol and on the rate of conversion from sulfur dioxide to sulfate. Nevertheless, this study points to the eventual ability to globally map anthropogenic emissions of sulphur by integrating space lidar observations with optical and chemical data from surface networks.

Future space lidars will have additional observational capabilities beyond those of LITE. Differences in the size and shape of ice crystals and water droplets strongly effect how a given amount of cloud water affects the radiation budget. The lidar backscatter from spherical water droplets

retains the degree of linear polarization of the incident light, while the backscatter from ice crystals is depolarized. Therefore a polarization-sensitive receiver can be used to discriminate between ice clouds and water clouds [11]. This is particularly important in the upper troposphere, where enhanced layers can be mistaken for layers of thin cirrus, and in the middle troposphere where mixed phase clouds are found.

The retrieval of aerosol optical depth from backscatter lidar signals is an underconstrained problem in that there are more unknowns than measurements required to solve for them. The problem is dealt with in practice by assuming an extinction to backscatter ratio for the aerosol. This introduces significant uncertainties into the derived optical depth values and better accuracy is required to understand the issue of aerosol forcing of climate. The high spectral resolution lidar (HSRL) technique [12] allows direct measurement of aerosol extinction. The spectral broadening of backscatter from molecules is much greater than from aerosols, due to differences in their velocity spectrum. Use of a laser with a linewidth on the order of 50 MHz and high resolution filters in the receiver allow the signal return from molecules and aerosols to be discriminated and measured separately. Aerosol extinction can then be derived directly from the attenuation of the molecular return signal within the aerosol layer. Advances in the technology for space qualified lasers will provide laser sources with the characteristics required for HSRL systems within a few years.

REFERENCES

- [1] B. A. Weilicki, R. D. Cess, M. D. King, D. A. Randall, and E. F. Harrison, "Mission to Planet Earth: Role of Clouds and Radiation in Climate," *Bull. Amer. Meteorol. Soc.*, vol. 76, pp. 2125-2153, 1995.
- [2] D. A. Randall, Harshvardhan, D. A. Dazlich, and T. G. Corsetti, "Interactions among radiation, convection, and large-scale dynamics in a general circulation model," *J. Atmos. Sci.*, vol. 46, pp. 1943-1970, 1989.
- [3] R. J. Charlson, S. E. Schwartz, J. M. Hales, R. D. Cess, J. A. Coakley, J. E. Hansen, D. J. Hofmann, "Climate forcing by anthropogenic aerosols," *Science*, vol. 255, pp. 423-430, 1992.
- [4] B. Santer, E. Anyamba, T. Barnett, and T. Wigley, "Detection of climate change and attribution of causes," In *Climate Change 1995: The Science of Climate Change*. Cambridge: Cambridge U. Press, 1996, pp. 406-443.
- [5] S. E. Schwartz and M. O. Andreae, "Uncertainty in climate change caused by aerosols," *Science*, vol. 272, pp. 1121-1122, 1996.
- [6] D. M. Winker, R. H. Couch, and M. P. McCormick, "An overview of LITE: NASA's Lidar In-space Technology Experiment," *Proc. IEEE*, vol. 84, pp. 164-180, 1996.
- [7] D. M. Winker, "Observations of the vertical distribution of cloud using space lidar," In *Preprints of the AMS 9th Conference on Atmospheric Radiation* (Long Beach, CA, February 2-7, 1997), 1997, p. 422-425.
- [8] J. A. Ogren, "A systematic approach to in situ observations of aerosol properties," in *Aerosol Forcing of Climate*, Charlson and Jeintzenberg, eds., New York: Wiley, 1995.
- [9] NRC Panel on Aerosol Radiative Forcing and Climate Change, *Aerosol Radiative Forcing and Climate Change*. Washington, DC: National Academy Press, 1996, 161 pp.
- [10] R. M. Hoff and K. G. Strawbridge, "LITE observations of Anthropogenically Produced Aerosols," in *Advances in Atmospheric Remote Sensing with Lidar*, Ansmann, Neuber, Rairoux and Wandinger, Eds., New York: Springer Verlag, 1997, pp. 145-148.
- [11] K. Sassen, "The polarization lidar technique for cloud research: A review and current assessment," *Bull. Amer. Meteor. Soc.*, vol. 72, pp. 1848-1866, 1991.
- [12] C. J. Grund and E. W. Eloranta, "University of Wisconsin High Spectral Resolution Lidar," *Opt. Eng.*, vol. 30, pp. 6-12, 1991.

Ground-based Validation of the EOS Multi-angle Imaging SpectroRadiometer (MISR) Aerosol Retrieval Algorithms and Science Data Products

James E. Conel, William C. Ledebøer, Stuart H. Pilorz, John V. Martonchik, Ralph Kahn, Wedad Abdou,
Carol Bruegge, Mark C. Helmlinger, Barbara J. Gaitley
Jet Propulsion Laboratory, California Institute of Technology
4800 Oakgrove Dr., MS 169-237, Pasadena, CA 91109
(818)354-4516/ (818)393-4619/ jconel@jpl.nasa.gov

Abstract -- A plan for the ground-based validation of MISR aerosol retrieval is outlined. Activities occur in two phases: (1) pre-launch, work is focused on technique development and MISR algorithm validation using conventional ground-based methods and a MISR simulator (AirMISR) operating from the ER-2 aircraft to simulate MISR on-orbit observations. (2) Post-launch, the validation program relies on ground campaigns, underflights with the MISR simulator and the use of local measurements of aerosol loading and properties and irradiance measurements derived from the AERONET and ISIS networks.

INTRODUCTION

We outline a ground-based program for validation of aerosol recovery algorithms and post-launch science data products from the Multi-angle Imaging SpectroRadiometer (MISR). The ground optical measurements program employs conventional instrumentation for measurement of diffuse sky spectral radiances and irradiances and direct spectral solar radiances, and a new sphere scanning radiometer (downwelling and upwelling spectral radiances) for estimation of the surface bidirectional reflectance factor (BRF). Interpretation of the atmospheric measurements in terms of aerosol microphysical properties is carried out using inversion methods and algorithms available from the literature and developed over the past 20 years or so by numerous investigators. Here an attempt is made to combine various methods to secure estimates of all of the aerosol physical properties important in the MISR retrieval process independently of assumptions made in the MISR retrievals. An aircraft simulator (AirMISR) is under development for use on the ER-2 aircraft platform to provide near-TOA multi-angle radiance measurements at MISR wavelengths of ground targets over the entire range of instrument view angles. AirMISR will replace the Advanced Solid State Array Spectrometer (ASAS) which operated from the lower altitude C-130 aircraft platform, and which has heretofore acted as the MISR simulator. The simulator data will be used to provide estimates of the retrieved optical depths and aerosol properties according to the MISR retrieval strategy for comparison with results of ground measurements. Radiative closure is checked by comparison of measured sky radiances with those calculated for the retrieved aerosol model using a radiative transfer code.

We provide herein descriptions of MISR and the MISR experiment, the MISR aerosol recovery strategy, the field instrumentation, and the field-based aerosol recovery algorithms.

DEFINITION OF TERMS

The process of validation implies here intercomparison of aerosol properties derived from MISR-simulator or MISR measurements using MISR procedures, with aerosol properties derived from ground-based measurements and conventional interpretation or inversion methods. Implied in all present validation studies is a comprehensive analysis of experimental uncertainties. This suggests a second possibly independent definition of validation, also sought here, as the complete understanding of the uncertainties (both systematic and random error) in each experimental path.

Validation field experiments consist of overflights of a chosen target by the MISR simulator duplicating the overpass of MISR on orbit in azimuth, direction, and local time of overpass. Simultaneously, field measurements of atmospheric and surface reflectance properties are carried out in the target area. Where possible, comparisons of radiatively retrieved aerosol properties from the ground will be compared with direct aerosol measurements, either ground-based or from aircraft.

MISR EXPERIMENT OVERVIEW

MISR is scheduled for launch on the EOS AM-1 platform in mid-1998. MISR will provide radiometrically calibrated, stable radiance measurements coregistered at nine view angles ($\pm 70.5^\circ$, $\pm 60^\circ$, $\pm 45.6^\circ$, $\pm 26.1^\circ$, 0°) and four wavelengths (443, 555, 670, and 865 nm) globally over a 360 km swath of the Earth's surface on each pass. The fundamental cross-track pixel size at the surface is 275 m for all off-nadir pixels and 250 m in the nadir camera. From these 36 multi-angle and multispectral observations, estimates of atmospheric aerosol abundance and composition, surface bidirectional reflectance properties, cloud top heights and albedo of cloud layers, surface and cloud albedo together for mixed scenes, and the surface albedo alone in cloud-free areas will be obtained. Such data will be employed for improved determinations of the effects of aerosol burden on atmospheric heating and cooling via constraint of the global aerosol budget, for identification of sources and sinks of aerosols, for surface and atmospheric radiation balance through measurement of the surface and TOA albedos, and for improved classification of surfaces and surface architecture via specification of the spectral BRF.

From the perspective of timing of ground-based validation campaigns or MISR simulator underflights, at northern mid-latitudes, the expected MISR on orbit overpass

time is about 10:15 A.M. local time at a heading of about 190°.

MISR AEROSOL RETRIEVAL STRATEGY

The principal MISR aerosol science data product is the column aerosol optical depth, reported at a wavelength of 555 nm, together with aerosol type and with spatial sampling of 17.6 km globally. These retrievals are carried out for all cloud-free areas. The MISR-based retrieval of aerosol amount and aerosol type are carried out by minimizing residuals between the observed radiances on orbit and radiances precalculated from a radiative transfer model.

A collection of mixtures globally representative dry aerosol components and characteristic sizes together with an adsorbed water component driven by atmospheric RH, is assumed in an aerosol climatology data base used in the aerosol retrieval. The generic pure particle types assumed in the aerosol climatology are: (1) sulfate/nitrate, (2) mineral dust, (3) sea salt, (4) urban soot, (5) biomass burning particulates, (6) near surface fog, and (7) thin cirrus. For each of these, the particle size distribution is taken as log-normal except for fog and mineral dust, which are assumed to follow power laws. A characteristic radius, size limits, real and imaginary refractive indices (sometimes variable with wavelength), and particle shape are specified. All particles are assumed spherical except for dust (prolate/oblate spheroids) or cirrus (fractal facet geometry).

Three retrieval pathways are specified for surface reflectance to separate surface-reflected and path radiance components: (1) dark ocean or lake waters, (2) dense dark vegetation (DDV), and (3) heterogeneous land. Reflectance characteristics of surface types (1) and (2) are specified from selected standard DDV BRF models. The retrieval path for type (3) utilizes spatial variations in the surface reflectance (hence heterogeneous) to develop an Empirical Orthogonal Function (EOF) representation of the angular variation of the scene reflectance, which is employed to separate surface-reflected and path radiance components. Subsequently, for all pathways the procedure is to match observed radiances with calculated radiances for different models in the climatology tables using the path radiance (zero surface reflectance) alone. These procedures are explained in detail in [1].

ALGORITHM AND PRODUCT VALIDATION

MISR validation activities are divided into two phases: (1) pre-launch, focused on accumulation of instrumentation, development of methodology, and field exercises aimed at algorithm validation; (2) post-launch, focused on validation of the on-orbit instrument calibration and upon product validation using field experiments coordinated with overflights together with observations from automated networks of sunphotometers including AERONET [2] and radiation instruments of the ISIS network [3].

Field Instruments and MISR Aircraft Simulator AirMISR

The principal field instruments used for retrieval of aerosol optical depth and microphysical properties and for determination of surface BRF are described:

CIMEL Sky and Sun Photometer: The CIMEL CE 318-3 is an automated instrument capable of long term monitoring of both direct solar irradiance and diffuse sky irradiance in the solar almucantar and principal plane, and can operate over extended numbers of days unattended. It is the principal instrument of the so-called AERONET aerosol monitoring network [2] and will therefore play an important role in post-launch MISR as well as MODIS product validation. Observations at resolution of 10 nm are made by filters at wavelengths of 300, 340, 380, 440, 670, 870, 940, and 1020 nm. The data form principal input to software [4] for columnar aerosol features. A data transmission system through geostationary satellites feeds field information to computers at Goddard Spaceflight Center.

Reagan Sunphotometer: The so-called Reagan sunphotometers (manufactured by J. A. Reagan, University of Arizona) automatically track the sun and record direct solar irradiance. These data can be used for determination of atmospheric total spectral optical depth and for the separation of it into molecular, ozone, water vapor and aerosol optical depth components based on the so-called Langley method. The ten filter channels (7-17 nm width) recorded are near 380, 400, 440, 520, 610, 670, 780, 870, 940 and 1030 nm.

MultiFilter Rotating Shadowband Radiometer: The Multifilter Rotating Shadowband Radiometer (MFRSR), [5], provides automated, unattended recording and separation of total-horizontal, direct-normal, and diffuse-horizontal irradiances. The instrument forms one component of the ISIS radiation network [3]. Six narrowband filter channels (each 10 nm) are located at 415, 500, 610, 665, and 862 nm, and a broadband unfiltered channel covering about 300-1000 nm. These data provide aerosol optical depths, water vapor column abundance, plus direct measurement of surface spectral irradiance for comparison with MISR-calculated quantities. The data are used with theoretical models (e.g., [6], [7], [8]) for estimation of a regional Lambertian surface reflectance and bulk aerosol complex index of refraction and also to retrieve aerosol optical depth.

Portable Apparatus for Rapid Acquisition of Bidirectional Observations of the Land and Atmosphere (PARABOLA III): This sphere-scanning radiometer has a long previous history in a different mechanical configuration as PARABOLA I [9]. PARABOLA III measures the complete distribution of radiance at a site from both sky and ground hemispheres in 5° fields-of-view. These data are used in the defining equation for boundary energy conservation to estimate the bidirectional reflectance factor (BRF, see [10]). PARABOLA III has bands near 443, 551,

650, 861, 948, 400-700 (PAR), and 1655 nm. In addition to BRF, PARABOLA III will provide high dynamic range radiance measurements in all sky azimuths 5° apart, including zenith to horizon data. These latter measurements provide independent data sets not included in the inverse problems for recovery of phase function and size distribution, and are therefore useful in aerosol closure experiments.

ASD/GER Spectrometers: Two spectrometers are employed in field operation. The purpose of these instruments is to place the sparse aerosol optical depth and the surface reflectance determinations by MISR in context with data of higher spectral resolution extending over a broader spectral range. Both instruments cover the approximate spectral range from 350-2700 nm with a resolution of ~ 10 nm and a spectral sampling interval of about 2 nm. The ASD instrument is devoted to rapid measurement of surface hemispherical directional reflectance while the GER focuses on recovery of high resolution optical depth of the atmosphere using the Langley method (described below).

AirMISR: AirMISR has been fashioned from a spare MISR camera and mounted on a gimbal to rotate on an axis perpendicular to the direction of aircraft motion. Images simulating MISR viewing are built up for each MISR view angle and wavelength line by line in pushbroom fashion through forward motion of the aircraft. The instrument resides in the nose of the ER-2. At 20 km altitude above the surface, the IFOV of the AirMISR camera of 0.36 mrad provides a ground footprint ranging from 7-22 m along track. The full image size can vary depending on view angle and the programmed time line of dark current observation, slew, and dwell for image acquisition. For example one extreme acquisition time line (14.96 minutes total elapsed time) generates images ranging from about 11 km on a side at nadir to 25.5 km (along track) \times 32.9 km (across track) at the extreme view angles of $\pm 70^\circ$. The resulting flight lines can be quite lengthy to get the complete angular range, for example in the above, beginning and ending 90.5 km to either side of the target point.

Calibration and Intercomparison of Instruments

Field Instruments: Because of inherent changes in instrument behavior over time and also because of the small disparities in wavelength between channels of all field instruments already described, these instruments are regularly calibrated and intercompared. The Langley method [11] for determination of instrument V_0 is utilized and other approximate transformation formulas between responses are developed. Calibrations are carried out at high altitude mountain sites by observing the sun (to experience maximum expected dynamic range) under stable clear sky conditions. It is expected that the inherent problem of atmospheric variability with air mass will always be present, but minimized for such sites. In addition the spectral

response functions of channels on all instruments are determined in the laboratory using a monochromator with slit width set for 1-2 nm. The calibration of water vapor channels is always determined relative to other channels in the laboratory. Histories of instrument calibration are kept to track performance changes with time.

Vicarious Calibration of AirMISR and MISR: Vicarious calibration of instruments in-flight is synonymous with use of the so-called reflectance-based method [12]. The calibration of MISR and evaluation of possible instrument drift over time is crucial to the long-term success of detecting secular changes in aerosol and surface characteristics of the Earth-atmosphere system. The vicarious calibration pathway is independent of preflight or on-board calibration modes. The vicarious method employs a radiative transfer code (RTC) to predict top-of-atmosphere radiance above a natural target surface. The surface reflectance and the atmospheric optical depth plus an aerosol model and water vapor abundance are used to constrain the code. The aerosol model itself is constrained by ground-based or, where possible, by direct sampling of aerosol properties. The RTC-calculated radiance is compared to that predicted at the sensor for the target area given a laboratory or on-board estimate of the calibration. It is expected that dry lake beds in remote desert environments at moderate altitude (~ 5000 feet) will be employed to minimize atmospheric interference. An example site is Lunar Lake, NV.

Principal Algorithms

Primary elements of the MISR aerosol validation activity are: (1) verification of the aerosol optical depths and types retrieved by this novel multi-angle method, (2) establishing independently the appropriateness of the local aerosol climatology selected by MISR for the retrieval(s) (3) providing estimates of uncertainty for the retrieved quantities.

Method of Aerosol Optical Depth Retrieval: The total optical depth retrieved using the Langley method [11] from sunphotometer observations of the direct solar irradiance in the ~ 400 -1000 nm region consists of components due to aerosols, molecular (Rayleigh) scattering, ozone and water vapor. The molecular scattering optical depth is estimated from measurement of the atmospheric pressure. The difference between the total and Rayleigh scattering optical depths is termed the residual optical depth. Except for the water vapor absorption band itself (~ 940 nm), continuum or band absorption elsewhere by water vapor is neglected. The aerosol optical depth in the 940 nm band is obtained by interpolation(extrapolation) between (from) residual optical depth components in adjacent bands. The ozone columnar and aerosol optical depths are retrieved together using a technique developed in [13]. This method avoids the assumption, often employed, of a power law form for the aerosol spectral optical depth variation.

Microphysical Properties of Aerosols, SKYRAD.pack: SKYRAD.pack is a code developed by Nakajima *et al.* [4] for remote estimation of columnar equivalent aerosol volume size distribution, single scattering phase function, aerosol optical depth, and single scattering albedo. (This code has kindly been made available to us by Prof. Nakajima). The measured input data required are those supplied by the CIMEL sunphotometer, namely direct solar and diffuse sky radiances as measured in the solar almucantar, and (optionally) spectral optical depth derived from the direct solar irradiance measurement. An iterative scheme is utilized in which the observed radiance distribution in both the almucantar and principal plane is compared to that calculated with a radiative transfer code. For the iteration, initial guesses must be supplied for the aerosol complex refractive index, radius limits on the particle size distribution, the surface spectral albedo, and initial ratio of sky radiance to direct solar irradiance, obtained from the observations. When direct and diffuse solar radiation observations are employed together with optical depth measurements, the detectable radius interval for aerosol particle size retrieval is determined to be about 30-10000 nm.

Estimation of surface albedo and complex refractive index: A statistical method developed by King and Herman [6] and King [7] is used to estimate the optimal values of the ground albedo and effective index of absorption of atmospheric particulates. The method compares the ratio of the diffuse to direct transmitted solar irradiance to radiative transfer computations of these quantities and is therefore suited to analysis of MFRSR observations [5]. The ratio is sensitive to optical depth, particle size distribution and absorption index, and ground albedo, and is insensitive to other radiative transfer parameters, e.g., the real part of the refractive index, vertical distribution of the atmospheric particulates. Both optical depth and size distribution are inferred from the spectral measurements of the directly transmitted solar irradiance. Comparisons of the observed and calculated ratios allows the inference of effective values of the absorption coefficient and a weighted average albedo over the entire area which affects the transfer of radiation. An advantage of using the diffuse-direct ratio is that absolute calibration of the instrument is not needed.

Inversion of spectral optical depth for size distribution: While size distribution estimates will be obtained from the SKYRAD.pack inversions, we will in addition employ the inversion technique on spectral variation of aerosol optical depth developed in [14] and [15] for use with our other direct beam sunphotometers, as well as high resolution spectral optical depth retrievals from the GER spectrometer, which not only potentially increases the number of bins in the size distribution but also the retrievable particle size range.

PARABOLA III measurements: Both the upward and downward radiance measurements from PARABOLA III as a function of sun zenith angle are combined together in an algorithm developed by Martonchik [10] to estimate local surface BRDF by iterative solution of an integral equation

describing reflected light energy at the surface. This procedure explicitly accounts for the presence of directional diffuse light, which cannot ordinarily be accounted for by simple bidirectional measurements with field instruments.

Method of Combining Algorithms for Aerosol Microphysical Property Estimates

The inversion algorithms described provide a significant, sometimes redundant, observational basis for recovery of the required aerosol optical depth and other MISR aerosol climatology parameters. A method of combination of these observations is comprised of the following steps:

(1) The total spectral optical depth will be obtained from direct solar irradiance measurements taken with the Reagan and CIMEL sunphotometers.

(2) The aerosol optical depths as a function of time are then calculated, reconciled, and interpolated to MISR wavelengths.

(3) Simultaneous MFRSR observations of diffuse and direct sky and solar irradiances are interpreted according to the methods of [6], [7], and [8], and estimates of "regional" surface spectral albedo and real and imaginary complex indices produced.

(4) An estimate of the "local" spectral albedo is generated from PARABOLA III observations for the currently available range of sun zenith angles. The "regional" and "local" albedo values are compared, for reasonableness. Both values may be utilized independently in subsequent calculation, but such use of the PARABOLA III measurements compromises them as an independent data set against which radiances subsequently calculated for the aerosol model can be compared.

(5) The measurements of optical depth and estimates of aerosol index and surface albedo (diffuse/direct-based) are imported to SKYRAD.pack for calculation of size distribution, phase function, and single scattering albedo.

(6) Using the derived aerosol model thus estimated, a radiative transfer code is employed to calculate the downward directed radiance as a function of position over the sky. These radiance values are compared with PARABOLA III sky radiance observations, which have not yet been employed in the calculation stream, to achieve the current result.

(7) The goodness of fit is judged by comparison of calculated and measured sky radiances. Roughly 1300 such individual PARABOLA III observations will be available for this comparison.

(8) An iterative scheme may need to be established once sensitivity analyses determine the causes of extant departures between calculated and measured quantities.

Closure Experiments and Connections with Direct Aerosol Sampling

Closure experiments are crucial in deciding on viability of retrieved aerosol and surface reflectance models adopted at experiment sites. For example, radiative closure here implies

agreement between irradiances calculated from a radiative transfer code with a specified aerosol and surface reflectance model, and values measured at the surface. We have exercised portions of the diffuse-direct irradiance procedure described above to study sensitivity of calculated downwelling spectral irradiance to model assumptions about aerosol refractive index and surface (Lambertian) reflectance to force agreement with field measured downwelling irradiance. The observations consistently fell below model-calculated irradiances by 15-20% for the initial aerosol model adopted. Agreement between model values and observations was easily achieved by increasing the imaginary index of aerosol particles from 0.005 to 0.04, for example, whereas no reasonable adjustment of the surface Lambertian reflectance proved suitable. The required value of the imaginary index is consistent with the value obtained for midcontinental aerosols of 0.04 from other analyses [16]. The results of such intercomparisons will to some extent always remain arbitrary unless the precise aerosol size and compositional model can be specified by direct observation. Details of these studies will be reported elsewhere.

Sunphotometer and Radiation Networks

Use of the so-called AERONET and ISIS networks for local validation of MISR aerosol optical depth, particulate microphysical properties and surface irradiance has been mentioned above. Observations of atmospheric optical depth from single instruments refer to line of sight values strictly applicable to the local area where inhomogeneous atmospheric conditions prevail. To assess the spatial variation of aerosol properties and assess the problems of recovery over larger domains pertinent to the MISR scale of aerosol retrieval at 10-20 km, we will employ networks of intercalibrated instruments arranged on regular grids. The use of optimal interpolation and averaging methods will be used to infer averages at these scales.

FUTURE WORK

During calendar year (CY) 1997 field experiments will be carried out where possible with AirMISR to provide important new data sets for MISR algorithm validation. Choice of field sites represents an attempt to combine together important aerosol and surface types of the MISR retrieval strategy. For CY 97 experiments are presently scheduled for the following localities: (1) Jornada Experimental Test Range, NM; Continental aerosols and heterogeneous surface reflectance, late May; (2) Lunar Lake, NV; Arid region aerosols, heterogeneous reflectance, late June; (3) Rocksprings, PA; sulfate/nitrate aerosols, heterogeneous reflectance; mid August, (4) Monterey Bay, CA; marine aerosol, deep ocean water reflectance, mid-September. In CY 1998, a schedule for aerosol observations thusfar includes the following sites: (1) Pacific northwest; biomass burning particulates over forest cover or water, (2) Florida Keys; dust aerosol over marine waters; August-September.

Connections with direct aerosol sampling on the ground, and by aircraft, as well as determining vertical distributions from such sampling and from lidar observations will be stressed. The use of network observations coordinated with field tests and overflights of AirMISR will also be sought preliminary to application systematically in post launch time.

ACKNOWLEDGMENTS

We appreciate discussions with John Reagan, University of Arizona, and Peter Hobbs, University of Washington, on the questions of radiative closure and direct aerosol measurement. The present work was sponsored by NASA under Contract to the Jet Propulsion Laboratory, California Institute of Technology

REFERENCES

- [1] D.J. Diner, et al., "Level 2 aerosol retrieval algorithm theoretical basis", JPL D-11400, Rev.B, Jet Propulsion Laboratory, 81 pp., 1996
- [2] B.N. Holben, T.F. Eck, I. Slutsker, D. Tanre, J.P. Buiss, A. Setzer, E. Vermote, J.A. Reagan, and Y.J. Kaufman, "Multiband automatic sun and sky scanning radiometer system for measurement of aerosol", Remote Sens. Environ. (unpublished).
- [3] B.B. Hicks, J.J. DeLuisi, J.A. Augustine, and D. Matt, "The NOAA Integrated Surface Irradiance Study (ISIS)--A new surface radiation monitoring network", Abstract, A.G.U. Fall Meeting, December, San Francisco, CA, 1995.
- [4] T. Nakajima, G. Tonna, R. Rao, P. Boi, Y. Kaufman, and B. Holben, "Use of sky brightness measurements from ground for remote sensing of particulate polydispersions", Appl. Opt., vol. 35, no. 15, pp. 2672-2686, 1996.
- [5] L. Harrison, J. Michalsky and J. Berndt, "Automated multifilter rotating shadow-band radiometer: an instrument for optical depth and radiation measurements", Appl. Opt., vol. 33, no. 22, 5118-5125.
- [6] M. D. King and B. Herman, "Determination of the ground albedo and the index of absorption of atmospheric particulates by remote sensing. Part I: Theory" J. Atmos. Sci., vol. 36, pp 163-173, 1979.
- [7] M.D. King, "Determination of the ground albedo and the index of absorption of atmospheric particulates by remote sensing. Part II: Application", J. Atmos. Sci., vol. 36, pp. 1072-1083, 1979.

- [8] B.M. Herman, R.S. Browning, and J.J. DeLuisi, "Determination of the effective imaginary term of the complex refractive index of atmospheric dust by remote sensing: The diffuse-direct radiation method", *J. Atmos. Sci.*, vol. 32, pp. 918-925, 1975.
- [9] D.W. Deering, and P. Leone, "Sphere scanning radiometer for rapid directional measurements of sky and ground radiance", *Remote Sens. Environ.*, vol. 19, pp. 1-24, 1986.
- [10] J.V. Martonchik, "Retrieval of surface directional reflectance properties using ground level multiangle measurements", *Remote Sens. Environ.*, vol. 50, pp.303-316, 1994.
- [11] G.E. Shaw, "Sun photometry", *Bull. Am. Meteor. Soc.*, vol. 64, no. 1, pp. 4-10, 1983.
- [12] P.N. Slater, S.F. Biggar, R.G. Holm, R.G. Jackson, R.D. Mao, Y. Moran, M.S. Palmer, and B. Yuan, "Reflectance- and radiance-based methods for the in-flight absolute calibration of multispectral sensors", *Remote Sens. Environ.*, vol. 22, pp 11-37, 1987.
- [13] D.E. Flittner, B.M. Herman, K.J. Thome, and J.M. Simpson, "Total ozone and aerosol optical depths inferred from radiometric measurements in the Chappuis absorption band", *J. Atmos. Sci.*, vol. 50, no. 8, pp. 1113-1121, 1993.
- [14] M.D. King, D.M. Byrne, B.M. Herman, and J.A. Reagan, "Aerosol size distribution obtained by inversion of spectral optical depth variation", *J. Atmos. Sci.*, vol. 35, pp. 2153-2167, 1978.
- [15] M.D. King, "Sensitivity of constrained linear inversions to the selection of the Lagrange multiplier", *J. Atmos. Sci.*, vol. 39, pp. 1356-1369, 1982.
- [16] R.J. Ball and G.D. Robinson, "The origin of haze in the central United States and its effect on solar irradiation", *J. Appl. Meteor.*, vol. 21, pp. 171-188, 1982.

LITE Aerosol Retrievals

J.A. Reagan and H. Liu

Department of Electrical and Computer Engineering

University of Arizona, Building 104

Tucson, AZ 85721-0104

Tel (520) 621-6203, Fax (520) 621-8076

<email reagan@ece.arizona.edu>

Abstract -- The Lidar In-space Technology Experiment (LITE) shuttle mission demonstrated that spaceborne lidar offers an effective means for detecting the spatial features of significant regional aerosol concentrations resulting, for example, from Saharan dust, African and South American biomass burning and anthropogenic sources. To obtain quantitative estimates from the LITE data of radiatively important aerosol optical properties such as optical depths and extinction profiles requires supplemental information about the aerosols, supplied either by modeling or from auxiliary measurements. This paper outlines techniques for retrieving these aerosol optical parameters, and presents example retrievals obtained from the LITE observations.

INTRODUCTION

The NASA Lidar In-space Technology Experiment (LITE) shuttle mission flown in September 1994 collected more than 50 hours of data. These data provide a unique global snapshot of a variety of cloud, atmospheric aerosol and surface reflectance data [1]. Firing at a 10 Hz rate with a shuttle ground-track speed of 7.4 km/s, atmospheric column profile measurements were acquired with a horizontal center to center separation of 740 m and with a vertical sampling spacing of 15 m (approximately half the vertical resolution limit set by the 2.1 MHz bandpass of the receiver electronics). The Nd:YAG laser transmitters generated doubled and tripled frequencies permitting simultaneous data collection at three wavelengths (355 nm, 532 nm and 1064 nm). Due to different beam divergences at the three wavelengths, the sampled atmospheric column diameter (through the stratosphere-troposphere) ranged between ~275 m (355 nm & 532 nm) and ~450 m (1064 nm). These diameters were small enough to often yield clean-air profiles all the way to the surface even with broken clouds present. Thus, a wealth of data were provided for investigation of global aerosol features.

A survey of the LITE data clearly reveals that spaceborne lidar offers an effective means for detecting detailed spatial features of regional aerosol concentrations. Examination of longitudinally separated orbit track segments extending from Africa across the Atlantic (Orbits 115, 116, 117 & 146 for ~10° to ~25° N latitude) reveal aerosol layers associated with the transport of dust from the interior Saharan Desert

region to the Caribbean [2]. Looking further north (~35° to ~45° N) Orbits 115-117 reveal continental haze over northeast North America apparently extending across the Atlantic to north of the Azores. Indications of large-scale biomass burning [3] can also be seen in widespread aerosol layers over south-central South America (Orbit 150 for ~20° to 30° S) and southwest African (Orbit 146 for ~5° to 15° S). Indications of urban influences are evident in urban area aerosol plumes seen around numerous urban areas on five continents [4], including locations such as the San Francisco - Los Angeles region, the general northeastern US and around Taiwan, to name a few. This paper addresses techniques for retrieving aerosol optical parameters from the LITE data and presents example results obtained for some of the above noted regional aerosol features.

AEROSOL RETRIEVAL METHODOLOGY

To outline the retrieval problem one is facing, let us start with the received lidar response. For a vertically pointing lidar, looking downward or upward,

$$V(z) = \frac{CE_0\beta(z)T^2(z)}{z^2}, \quad (1)$$

where $V(z)$ is the instantaneous lidar signal due to backscattering a distance z from the lidar, C is the lidar calibration constant, E_0 is the transmitted laser pulse energy, $T^2(z)$ is the round-trip transmission to z , and $\beta(z)$ is the unit volume backscattering coefficient at z . This equation assumes that only single scattering is important and applies for a given lidar operating wavelength, λ . For λ selected to avoid molecular absorption regions, $\beta(z)$ and $T(z)$ are due to the combined effects of air molecules (Rayleigh scattering) and atmospheric aerosols; hence, $\beta(z)$ may be expressed as

$$\beta(z) = \beta_R(z) + \beta_a(z) \quad (2)$$

where $\beta_R(z)$ and $\beta_a(z)$ are the Rayleigh and aerosol backscattering coefficients, respectively. Similarly, $T^2(z)$ is the product of $T^2(z) = T_R^2(z)T_a^2(z)$;

$$T_R(z) = e^{-\int_0^z \sigma_R(z) dz} \text{ \& \& } T_a(z) = e^{-\int_0^z \sigma_a(z) dz} \quad (3)$$

where $T_R(z)$ and $T_a(z)$ are the Rayleigh and aerosol transmission factors, and $\sigma_R(z)$ and $\sigma_a(z)$ are the Rayleigh and aerosol unit volume extinction coefficients. As with $\beta(z)$,

$$\sigma(z) = \sigma_R(z) + \sigma_a(z) \quad (4)$$

The Rayleigh factors $\beta_R(z)$ and $T_R(z)$ may be theoretically determined from the Rayleigh scattering law and knowledge of the atmospheric temperature and pressure structure. Assuming the calibration constant, C , has been determined, only $\beta_a(z)$ and $T_a(z)$ remain as unknowns. However, with these two unknowns and only one measurement, $V(z)$, at any z , certain assumptions or constraints must be implemented to yield a unique solution for $\beta_a(z)$ or $T_a(z)$.

The solution dilemma noted above is common to both lidar and radar. Following the approach of Fernald et al. [5], an analytic solution for $\beta_a(z)$ or $\sigma_a(z)$ may be obtained for the general two types of scatterers case (when both molecular and aerosol scattering are important) by requiring the aerosol extinction to backscatter ratio to be a constant, $S_a = \sigma_a/\beta_a$, with range over the height interval for which the solution is obtained. This constraint permits the aerosol number density to vary freely with range but restricts the aerosol phase function to be constant. It is a reasonable assumption for well mixed atmospheric regions, particularly if the humidity isn't too high and doesn't change greatly with range.

Using a retrieval formulation after Fernald et al. [5], the aerosol plus Rayleigh backscatter may be retrieved with a specification of S_a and S_R (which is known for Rayleigh backscatter; $S_R = 8\pi/3$) by the relation

$$\beta_a(z) + \beta_R(z) = \frac{X(z) \exp[-2(S_a - S_R) \int_{Z_c}^z \beta_R(z') dz']}{\frac{X(Z_c)}{\beta_a(Z_c) + \beta_R(Z_c)} - 2S_a \int_{Z_c}^z X(z') \exp[-2(S_a - S_R) \int_{Z_c}^{z'} \beta_R(z'') dz''] dz'} \quad (5)$$

where z is increasing downward (from the spacecraft towards the surface). Also, Z_c is a calibration height where $\beta(Z_c) = \beta_a(Z_c) + \beta_R(Z_c)$ is assumed known as at a height where $\beta(Z_c) \approx \beta_R(Z_c)$. While Z_c could be taken at a height well above any stratospheric aerosol (i.e., $Z_c > \sim 30$ km above ground), the upper troposphere ($Z_c \sim 8$ to 12 km above ground) is also generally quite clean, permitting calibration at a height where the signal is significantly higher (i.e., better signal-to-noise ratio, SNR) than in the upper stratosphere. Even limiting the analyses to low

background nighttime conditions, averaging is still required over many lidar shots to obtain good retrievals. The procedure we have found successful in processing the LITE 532 nm channel data to retrieve aerosol profiles is as follows:

LITE Data Processing Procedures

1. Preprocessing for pulse energy and electronics system gain normalization, background subtraction, shuttle altitude correction, removal of cloud saturated image segments as well as time/horizontal averaging over 100 shots (~ 70 km) and vertical averaging over 20 bins (~ 300 m) to enhance the SNR.
2. Obtain approximate upper tropospheric profile of the backscatter ratio $\beta(z)/\beta_R(z)$ using initial nominal value for the LITE calibration factor C and an assumed S_a characteristic of the free troposphere ($S_a \approx 25$). Determine $\beta_R(z)$ from atmospheric temperature and pressure data from NMC (National Meteorological Center) data incorporated in the LITE database. Find height for minimum $\beta(z)/\beta_R(z)$ ratio over height range ~ 8 to 15 km above ground and use this height as the reference calibration height Z_c . Determine the system calibration at this local minimum assuming $\beta(Z_c)$ is 1.03 ± 0.03 times $\beta_R(Z_c)$.
3. Retrieve $\beta_a(z)$ and $\sigma_a(z)$ below Z_c using the Fernald retrieval relation (eq. 5) with best estimates of S_a for the various aerosol layers between Z_c and the ground. In practice, S_a is set to 25 in the clean upper troposphere where there is no evidence of significant aerosol structure, and a climatological estimate of S_a is applied for the aerosol mixed layer normally found in the first few kilometers above the ground.
4. Choices generally made for S_a include $S_a \approx 35 \pm 15$, covering most situations, $S_a \approx 32 \pm 8$ for continental, somewhat anthropogenically influenced aerosols, and $S_a \approx 60 \pm 20$ for smoke/heavily anthropogenically influenced aerosols.

The preprocessing averaging procedure over 100 shots typically yields an rms SNR of 50 to 100 for heights between Z_c and the ground. Variation in the determined calibration factor at Z_c is typically within $\pm 2\%$ from one 100 shot averaged segment to the next. The uncertainty in the retrieval of $\beta_a(z)$ due to the assumed uncertainty in $\beta(Z_c)$ of $\pm 0.03\beta_R(Z_c)$ is typically within $\pm 15\%$. This is less than the effect of S_a not being well known/specified (e.g., $S_a = 35 \pm 15$) which can cause uncertainties easily double this amount. The effect is further magnified in the

retrieval of $\sigma_a(z) = S_a \beta_a(z)$, yielding uncertainties in $\sigma_a(z)$ that can exceed $\pm 100\%$. Hence, it is essential to use the best possible estimate of S_a in retrieving $\beta_a(z)$ and $\sigma_a(z)$.

RESULTS

Signal intensity plots of LITE raw (background subtracted) signal height profiles versus surface position, for the 532 nm wavelength channel, are given in Fig. 1 for four different interesting aerosol features. Figure 1a, a segment of Orbit 116 in the mid Atlantic, is one of a series of orbits extending from Africa to the Caribbean that revealed long distance transport of Saharan Desert dust [2]. Orbit 116 reveals significant aerosol structure extending to heights of almost 5 km, as was true for the other orbits in this series (Orbits 83, 115, 116 & 117). Data for these orbits, over the latitude range $\sim 20^\circ$ N to $\sim 30^\circ$ N, were processed to retrieve profiles of aerosol backscatter and extinction, and the extinction profiles were height-integrated to obtain the aerosol optical depth from the surface to the top of the aerosol layer. These retrieved optical depths (obtained assuming $S_a = 35$) are plotted versus latitude for the different orbits in Fig. 2. It can be seen that the optical depths are quite high, peaking at almost 0.7 for the orbits crossing onto Africa (83 & 115) and still exceeding 0.4 in the mid Atlantic. These are the highest aerosol optical depths we have yet encountered in processing the LITE data. The retrieved values may actually be smaller than the true optical depths due to multiple scattering [3], but we have yet to investigate this effect. It is important to note that these retrieved optical depths are comparable to the seasonal Equivalent Aerosol Optical Thickness (EAOT) values retrieved from NOAA AVHRR measurements in the same region as reported by Husar et al. [6].

Figures 1b & 1c show intensity plots from orbit segments over South America (Orbit 150) and the southern part of Africa (Orbit 146). Both plots reveal significant aerosol loading in the lowest few kilometers extending horizontally well over 1000 km which, based on location and time of year, is attributed to widespread biomass burning [3]. These orbit segments were processed to retrieve aerosol extinction profiles and layer optical depths based on the assumption of $S_a = 50$, which is within the range $S_a = 60 \pm 20$ suggested for smoke, but somewhat low to account for long-range transport/aging effects. The resulting aerosol optical depths ran about 0.5 for most of the Orbit 150 segment and about 0.3 for the Orbit 146 segment.

Figure 1d is an intensity plot for a segment of Orbit 24 over southern California that passed over the Edwards AFB Rogers dry lake playa and along the eastern edge of the LA urban area. Low gain surface return measurements (the dark

vertical portion of the image) were made at, north and south of Rogers dry lake for calibration purposes. As a part of this experiment, solar radiometer measurements were also made along the orbit track for a few hundred km south of Edwards AFB. These optical depth measurements, made the day before (9/10/94) and the day after (9/11/94) the nighttime Orbit 24 overpass provide optical depths for comparison with the LITE retrievals. This is shown in Fig. 3.

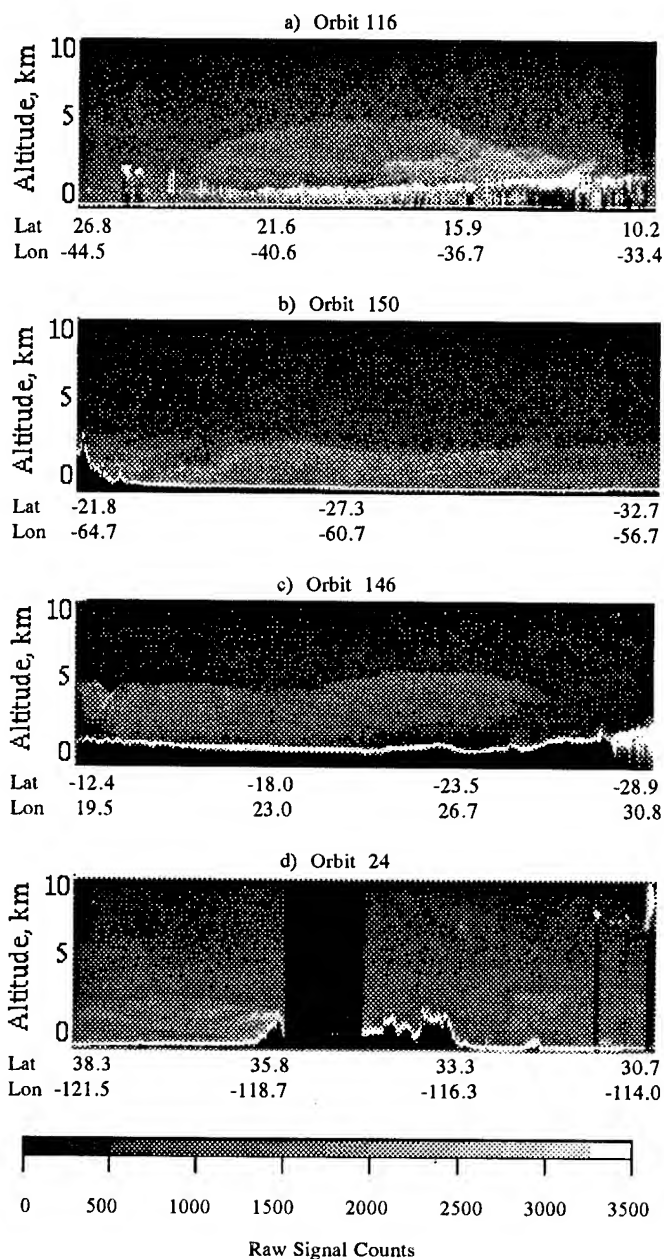


Figure 1. Intensity plots of LITE data for different orbit segments; a) Orbit 116, b) Orbit 150, c) Orbit 146 and d) Orbit 24.

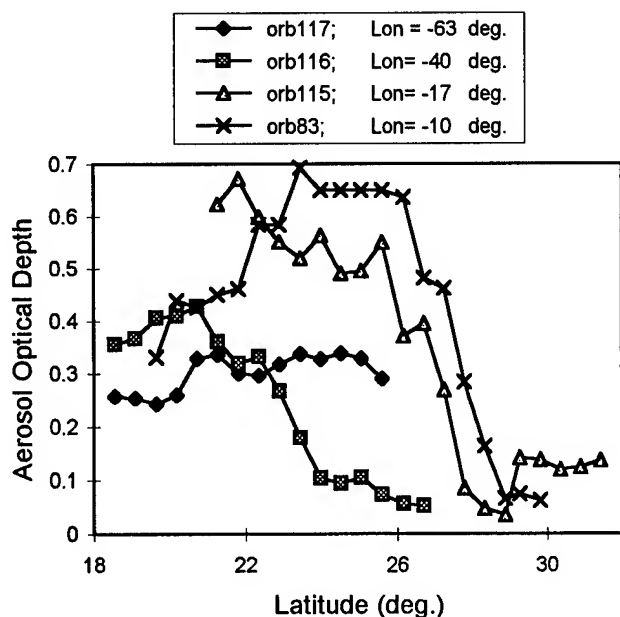


Figure 2. Aerosol optical depths retrieved from LITE measurements (532 nm channel).

The LITE retrievals are for $S_a=32$, with uncertainty bars showing the effect of varying S_a by ± 8 (25%) from this value. The radiometer optical depth retrievals include \pm one sigma error bars due to the rms uncertainty in the calibrations of the various solar radiometers used to measure optical depths during daylight hours on 9/10/94 and 9/11/94. It can be seen that the radiometer and LITE optical depths overlap within their respective uncertainty limits for the majority of the points, although some of the 9/10/94 radiometer values are clearly much larger. These larger values are within the range of temporal-spatial daily variability in aerosol optical depth that might be expected in the vicinity of an urban area. Hence, the agreement between the LITE retrievals and the ground-based solar radiometer measurements is considered to be quite good.

The results presented here are but a few of those obtained to date from the LITE data. Additional details and discussion will be given in the oral presentation of this paper. Work continues with the investigation of different retrieval approaches, including combined use of LITE data obtained with the 355 nm and 1064 nm channels.

ACKNOWLEDGMENTS

Information and assistance provided by other members of the LITE Science Steering Group and mission Validation Team are gratefully acknowledged. This work is supported by NASA Langley Research Center under contract NAS1-19953.

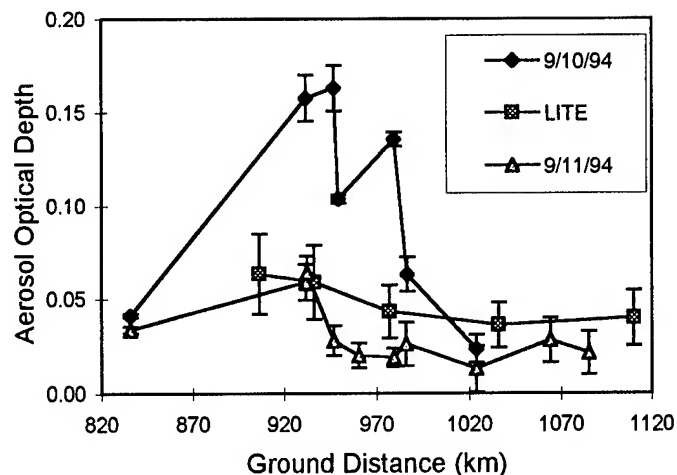


Figure 3. Solar radiometer and LITE retrieved optical depths for 532 nm.

REFERENCES

- [1] D.M. Winker, R.H. Couch, and M.P. McCormick, "An Overview of LITE: NASA's Lidar In-space Technology Experiment," *Proc. IEEE*, 84, pp. 164-180, 1996.
- [2] K.A. Powell, C.R. Trepe, and G.S. Kent, "Observations of Saharan Dust by LITE," *Advances in Atmospheric Remote Sensing with Lidar - selected papers from 18th ILRC* (A. Ansmann, R. Neuber, P. Rairoux and U. Wandinger, Eds.), Springer-Verlag, Berlin, Germany, pp. 149-152, 1997.
- [3] W.B. Grant, E.V. Browell, C.F. Butler, and G.D. Nowicki, "LITE Measurements of Biomass Burning Aerosols and Comparisons with Correlative Airborne Lidar Measurements of Multiple Scattering in the Planetary Boundary Layer," *Advances in Atmospheric Remote Sensing with Lidar - selected papers from 18th ILRC* (A. Ansmann, R. Neuber, P. Rairoux and U. Wandinger, Eds.), Springer-Verlag, Berlin, Germany, pp. 153-156, 1997.
- [4] R.M. Hoff and K.B. Strawbridge, "LITE Observations of Anthropogenically-Produced Aerosols," *Advances in Atmospheric Remote Sensing with Lidar - selected papers from 18th ILRC* (A. Ansmann, R. Neuber, P. Rairoux and U. Wandinger, Eds.), Springer-Verlag, Berlin, Germany, pp. 145-148, 1997.
- [5] F.G. Fernald, B.M. Herman, and J.A. Reagan, "Determination of aerosol height distributions by lidar," *J. Appl. Meteor.*, 11, pp. 482-489, 1972.
- [6] R.B. Husar, J.M. Prospero, and L.L. Stowe, "Satellite sensing of tropospheric aerosols over the oceans with NOAA AVHRR," *J. Geophys. Res.*, in press, 1997.

Non-Rayleigh Scattering Applied to Hydrometeor Size Estimation

Stephen M. Sekelsky and Robert E. McIntosh

Microwave Remote Sensing Laboratory, University of Massachusetts at Amherst
Amherst, MA 01003, email:sekelsky@alex.ecs.umass.edu and mcintosh@ecs.umass.edu

Warner L. Ecklund

Cooperative Institute for Research in Environmental Sciences (CIRES), University of Colorado
Boulder, CO, email:kgage@al.noaa.gov

Kenneth S. Gage

National Oceanic and Atmospheric Administration (NOAA) Aeronomy Laboratory
Boulder, CO, email:kgage@al.noaa.gov

INTRODUCTION

Multi-frequency Radar measurements collected at 2.8 GHz (S-band), 33.12 GHz (Ka-band) and 94.92 GHz (W-band) are processed using a neural network to estimate particle size distributions in ice-phase clouds composed of dry particles. The model data used to train the neural network was generated using the discrete-dipole approximation (DDA), a gamma particle size distribution function and an assumed size-density relationship, which is applied to distributions of both crystals and aggregates.

Measurements are presented from the Maritime Continent Thunderstorm Experiment (MCTEX)¹, which was held near Darwin Australia during November and December, 1995. The University of Massachusetts 33.12 GHz/94.92 GHz Cloud Profiling Radar System (CPRS) [1], the NOAA 2.8 GHz profiler [2] and other sensors were clustered near the village of Garden Point, Melville Island where numerous convective storms were observed. The 2.8 GHz radar is essentially non-attenuating over the path lengths considered and we use its cloud-top reflectivity values to remove extinction from measurements at the higher frequencies. Below we outline development of a generalized backscattering model for ice particles, describe the neural network used to retrieve particle size distribution parameters, and present results for a stratiform cloud case.

GENERALIZED SCATTERING MODEL

At millimeter-wavelengths substantial differences between measured backscatter and that predicted by the

Rayleigh approximation are observed for particles larger than a certain threshold diameter. For 95 GHz this diameter is approximately 0.1 mm but depends on the size distribution and dielectric properties of the hydrometeors observed. These differences can be measured by referencing reflectivity measured at the millimeter-wavelength to reflectivity measured at longer wavelengths. The Dual-wavelength ratio is a convenient measure of this difference and is defined by:

$$DWR_{l,h} = 10 \log \left(\frac{Z_{e,l}}{Z_{e,h}} \right), \quad (1)$$

where l denotes the lower frequency radar band and h denotes the higher frequency radar band. Equivalent radar reflectivity is given by,

$$Z_e = \frac{10^{10} \lambda^4}{\pi^5} |K_w|^{-2} \int_0^\infty \xi_b(D, n) D^2 N(D) dD, \quad (2)$$

where Z_e is normally expressed in units of $mm^6 m^{-3}$. $\xi_b(D, n)$ is the backscatter efficiency as a function of particle diameter, D , and refractive index, n . λ is the radar wavelength, and K is a dimension-less quantity related to the complex index of refraction of water. The particle size distribution, $N(D)[mm^{-1} m^{-3}]$, is a first order gamma distribution given by,

$$N(D) = N_o D \exp^{-4.67 D / D_m}. \quad (3)$$

Figs. 1a and 1b plot a model of DWR versus median diameter. The model assumes dry spherical ice particles with a size-density relationship, $\rho[g/cm^3] = 0.7/D[mm]$, given by [3]. As suggested by Klassen the range of ρ is limited so that $0.005 \leq \rho \leq 0.9 [gcm^{-3}]$. Backscatter cross-sections were calculated with the discrete-dipole

¹ The University of Massachusetts was supported by Department of Energy (DOE) Atmospheric Radiation Measurement (ARM) program grants 352095-AQ5 and DEFG02-90ER61060. NOAA Aeronomy Laboratory S-band work was supported in part by the National Science Foundation under grant ATM-9214800 and by the DOE ARM program.

NEURAL NETWORK SIZE ESTIMATOR

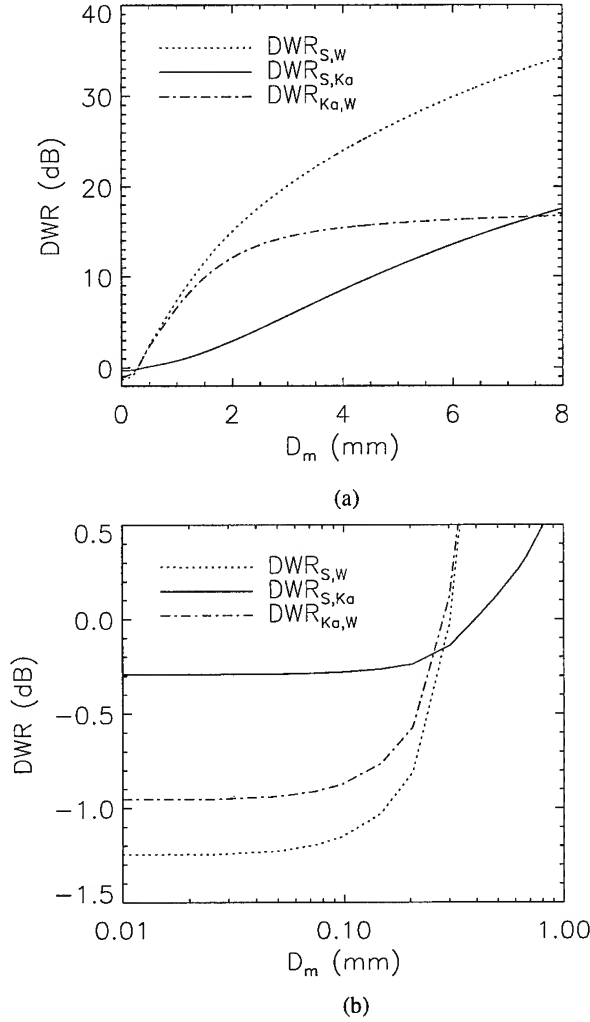


Figure 1: Dual-wavelength ratio as function of median diameter: (a) for a typical range of particle diameters encountered, and (b) for small particles.

approximation (DDA) using the DDSCAT (V5a) software package [4]. Although this method is computationally intensive it is preferred to Mie calculations because the DDA model can be easily modified to include other particle geometries.

ATTENUATION CORRECTION

The modeled data in Fig. 1b show that DWR is insensitive to particle size for median diameters smaller than approximately 0.1 mm. This feature of DWR can be exploited to calibrate reflectivity values measured at the higher frequencies. Because particles found near cloud tops often have very small diameters, DWR values measured here should equal the limiting values shown in Fig. 1b. Since the S-band data experiences negligible attenuation over the path lengths considered it is used as a reference for attenuation removal.

While a single pair of radar wavelengths can estimate particle size, combining reflectivity measurements at S-band, Ka-band, W-band permits more accurate size estimates over a larger range of particle diameters than any single pair. The neural network shown in Fig. 2 was used to combine the data. It consists of four layers: (1) a layer containing three input nodes, (2) a layer of seven hidden nodes, (3) a second hidden layer of four nodes, and (4) a layer of two output nodes.

The input vector, \bar{X} , is

$$\bar{X} = \frac{1}{100} [DWR_{S,W}, DWR_{Ka,W}, dBZ_{e,W}], \quad (4)$$

where the dual-wavelength ratio, DWR, is defined by (1). Elements of the input vector, \bar{X} , were chosen for their physical relationship to the outputs, but are equivalent to inputting the three radar reflectivities. Scaled logarithmic values are used to reduce the dynamic range of values that must be modeled by the neural network.

The output vector, \bar{Y} , includes two parameters of the gamma particle size distribution given by (3):

$$\bar{Y} = \frac{1}{100} [\log(N_o), D_m], \quad (5)$$

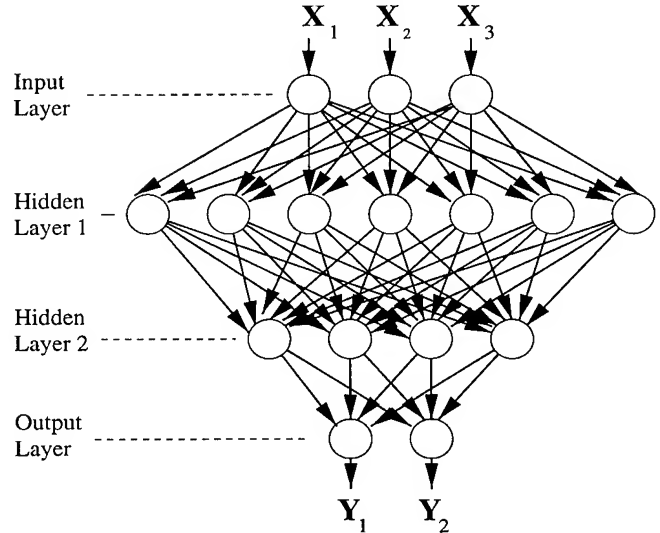


Figure 2: Neural network particle size estimator with two hidden layers.

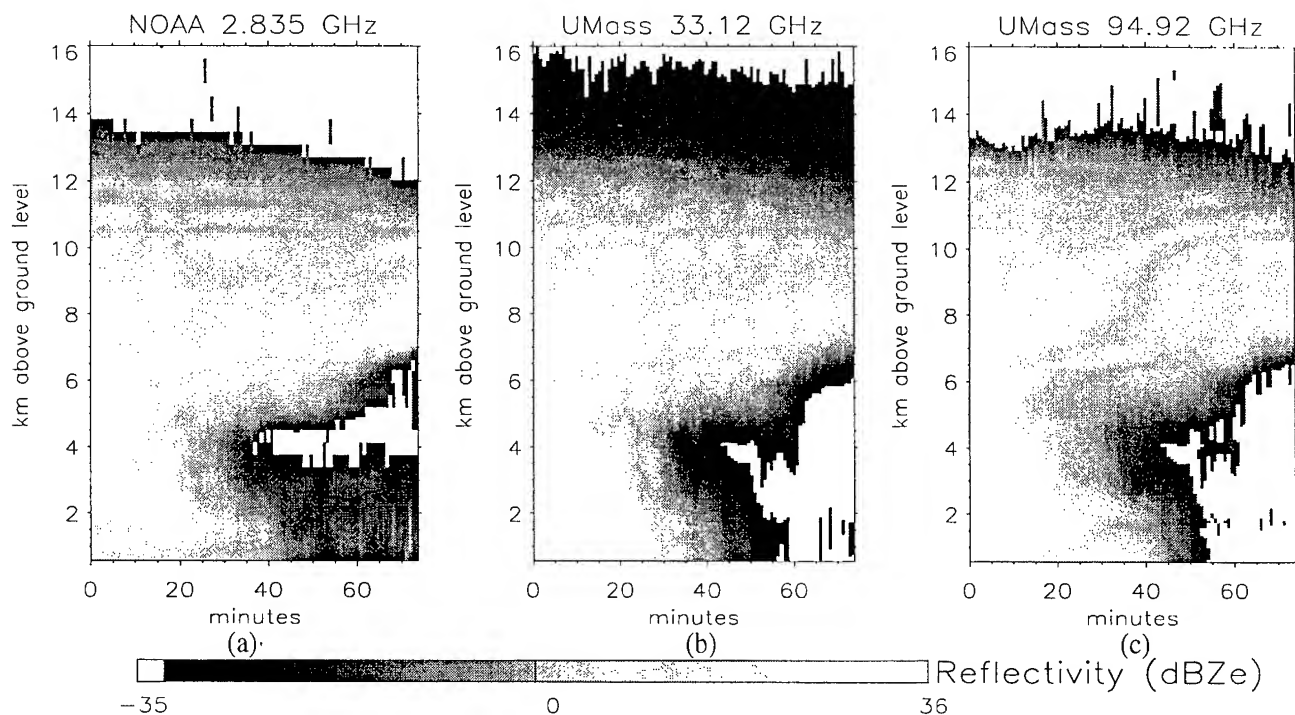


Figure 3: Radar reflectivity images of a stratiform cloud observed at S-band (2.853 GHz), Ka-band (33.12 GHz) and W-band (94.92 GHz). This dataset was measured on November 28, 1995 starting at 07:24:04 UTC. Note the common scale in units of dBZe, where $\text{dBZe} = 10\log(Ze)$.

RESULTS

Fig. 3 shows time-height images of radar reflectivity simultaneously measured at S-band, Ka-band and W-band for a precipitating stratiform cloud. The measurements in Fig. 3 were collected beginning at 07:24:04 UTC, about 2 1/2 hours after intense convection, and radar Doppler measurements show no substantial updrafts. The two radar systems were positioned side-by-side, and radiosonde estimates of horizontal winds were used to correct for differences in sampling volumes due to the different beam widths and pulse widths for CPRS and the NOAA S-band radar. The resolution of CPRS data is degraded and the resultant temporal resolution is approximately 30 seconds. To correct for attenuation effects, cloud top reflectivities were matched at the different frequencies, according to the procedure previously outlined. Zenith attenuation estimates are plotted in Fig. 4.

Neural network estimates of median particle diameter, D_m , and peak number concentration, N_o , corresponding to the measurements in Fig. 3 are shown in Figs. 5a and 5b respectively. Fig. 5c also shows total particle concentration, which is calculated by integrating (3) over all values of D . For this stratiform cloud case we note that Figs. 5a and 5b show that median particle size tends to decrease with height, while particle concentration tends to increase.

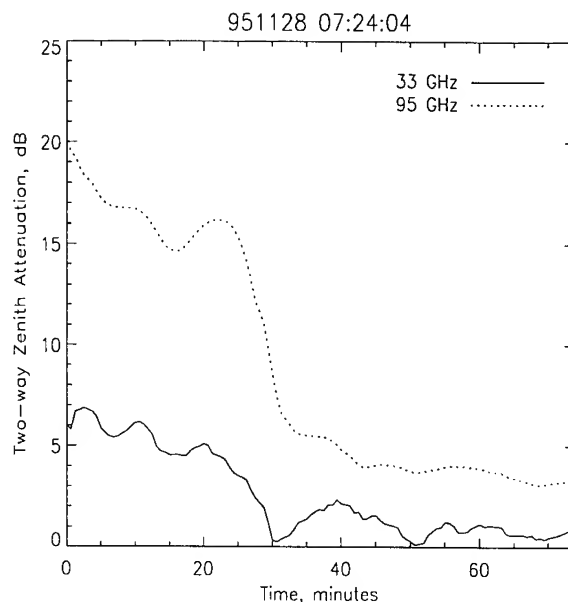


Figure 4: Zenith attenuation at 33 GHz and 95 GHz for the precipitating cloud shown in Fig. 3. Significant precipitation ends approximately 30 minutes into measurement. Note that attenuation after this time is primarily due to water vapor absorption.

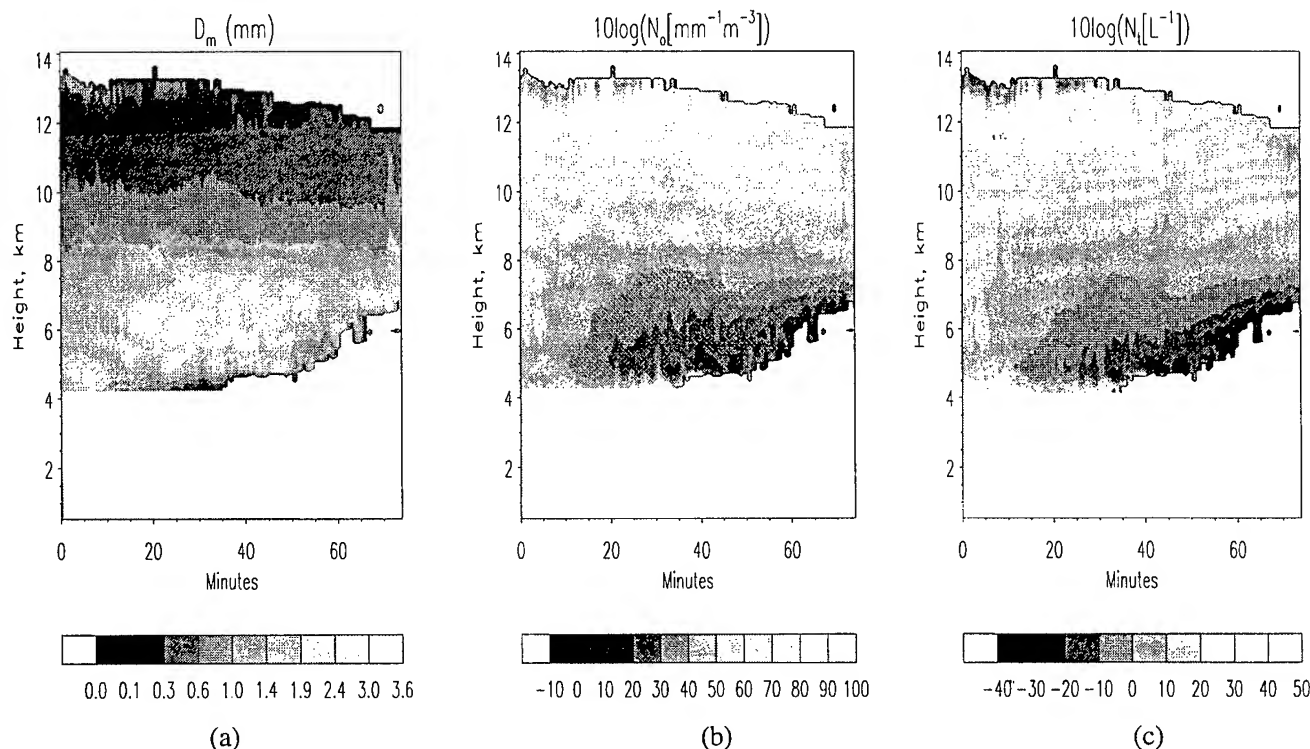


Figure 5: Neural network outputs corresponding to the data shown in Fig. 3. Estimates of size distribution parameters for a first order gamma distribution: (a) median diameter, (b) peak number concentration, and (c) total number of particles.

CONCLUSIONS

Cloud reflectivity measurements collected by multi-wavelength radars employing one or more millimeter-wavelengths can estimate median particle size, and other particle size distribution characteristics in clouds composed of dry ice particles. In contrast to techniques requiring lidar or IR radiometer measurements, the multi-wavelength radar technique described is substantially less affected by atmospheric attenuation, and works for clouds having large optical depths.

When measurements are available for more than two radar wavelengths, neural networks are a practical means for weighting the measurements and producing a single estimate of particle size distribution parameters. Using W-band (95 GHz), Ka-band (33 GHz) and S-band (2.8 GHz) radar reflectivity measurements collected during the Maritime Continent Thunderstorm Experiment (MCTEX), median particle size, D_m , and peak number concentration, N_o , are estimated for stratiform clouds, assuming a first order gamma distribution. Estimates of D_m show a characteristic decrease with height for the stratiform clouds considered.

REFERENCES

- [1] S. M. Sekelsky and R. E. McIntosh. Cloud observations with a polarimetric 33 GHz and 95 GHz radar. *Meteorology and Atmospheric Physics*, 58:123–140, 1996.
- [2] W. L. Ecklund, P. E. Johnston, J. M. Warnock, W. L. Clark, and K. S. Gage. An S-band profiler for tropical precipitating cloud studies. *Preprints, 27th Conf. on Radar Meteorology*, pages 335–336, 1995.
- [3] W. Klassen. Radar observations and simulation of the melting layer of precipitation. *Journal of the Atmospheric Sciences*, 45(24):3741–3753, Dec 1988.
- [4] B.T. Draine and P.J. Flatau. *User Guide to the discrete dipole approximation code DDSCAT (version 5a)*. Princeton Observatory Preprint, Princeton University, Dec 1996.

Modified Gamma Model For Singapore Rain Drop Size Distribution

J. T. Ong and Y. Y. Shan

School of Electrical & Electronic Engineering

Nanyang Technological University

Singapore 639798

E-mail: jtong@ntuvax.ntu.ac.sg and eyyshan@ntu.edu.sg

ABSTRACT — A modified gamma model is used to describe the rain drop size distribution in Singapore (1°21'N, 103°41'). The general expression of the moment estimates for the model is derived first. Since Joss type Distrometer RD69 is used in the measurement, the special equations for such data are then derived. The parameters for the modified gamma model are calculated for ten rainfall rates ranging from 1 mm/hr to 140 mm/hr. Using the least square fitting method, the general model suitable for all rainfall rates is obtained. The theoretical model is compared with the measured data. It shows that the derived model can be used to represent the Singapore rain drop size distribution.

INTRODUCTION

Future terrestrial or earth-satellite communication systems have to employ the increasingly higher microwave frequency bands since the existing demand for communications is already causing frequency-spectrum congestion at the lower frequency bands [1, 2]. The problems in using higher frequency bands for communication exist in that strong interactions can occur between microwaves and atmospheric hydrometeors. Such atmospheric hydrometeors can significantly degrade the communication quality. It has given rise to the need for acquiring more detailed knowledge of interactions between hydrometeors and microwaves. To obtain such knowledge, the detailed microphysical properties of hydrometeors, such as shape, size distributions, have to be known.

In the tropical and equatorial regions, since rainfall is copious throughout the year, at frequencies above 10 GHz, the attenuation of microwave signals caused by heavy rainfalls is a major problem for designing the communication systems[3-9].

From our previous papers [10-12], the plots of the Singapore rain drop size distributions eliminated the exponential and Gaussian models as possible candidate distributions. From the profiles of the measured drop size distribution, it seems that modified gamma model can be used to fit such distribution.

The general expression of the moment estimates for the modified gamma model is derived first in the paper. Then since we used Joss type Distrometer RD69 to measure the rain drop size distribution, the expression for such data is

derived in the paper. The parameters for the modified gamma model are calculated for a total of ten rainfall rates ranging from 1 mm/hr to 140 mm/hr. Using different orders of moments, there are three to five solutions of moment estimators for the modified gamma model. By the goodness of fit test, the better model for describing the Singapore rain drop size distribution can be obtained. Using the least square fitting method, the general model suitable for all rainfall rates is obtained. Finally the theoretical model is compared with the measured data.

MODIFIED GAMMA MODEL

Modified gamma model is expressed as follows:

$$N(D) = \Lambda_1 D^p e^{-\Lambda_2 D^q} \quad (1)$$

where D is the rain drop diameter (mm), $N(D)$ is the number of rain drop per cubic meter per millimetre diameter ($\text{m}^{-3} \text{mm}^{-1}$), Λ_1 , p , Λ_2 and q are parameters to be determined through measured data.

The estimates from the method of moments are obtained from equating a sufficient number of the measured moments to the corresponding theoretical moments.

The k th experimental moment is expressed by M_k

$$M_k = \frac{N_t}{n} \sum_{i=1}^n D^k \quad (2)$$

where n is the number of samples; M_k is given by the experimental data. The k th theoretical moments can be written as

$$\begin{aligned} \Omega_k &= \int_0^\infty D^k N(D) dD \\ &= \Lambda_1 \int_0^\infty D^{p+k} e^{-\Lambda_2 D^q} dD \\ &= \frac{\Lambda_1}{q \Lambda_2^{\frac{p+k+1}{q}}} \int_0^\infty y^{\frac{p+k+1}{q}-1} e^{-y} dy \\ &= \frac{\Lambda_1}{q \Lambda_2^{\frac{p+k+1}{q}}} \Gamma\left(\frac{p+k+1}{q}\right) \end{aligned} \quad (3)$$

Let

$$M_k = \Omega_k, \quad (4)$$

for simplicity, assume parameter $q = 1$, yielding

$$M_k = \frac{\Lambda_1}{\Lambda_2^{p+k+1}} \Gamma(p+k+1) \quad (5)$$

Let

$$\eta_{k,k-1} = \frac{M_k}{M_{k-1}} \quad (6)$$

then with the different m th moment, and assuming integer $m = 0, 1, 2, \dots$, integer $k > m$,

$$\begin{cases} \eta_{k,k-1} = \frac{p+k}{\Lambda_2} \\ \eta_{m,m-1} = \frac{p+m}{\Lambda_2} \end{cases} \quad (7)$$

Solving the equations, we get parameters p and Λ_2 , as follows:

$$p = \frac{k\eta_{m,m-1} - m\eta_{k,k-1}}{\eta_{k,k-1} - \eta_{m,m-1}} \quad (8)$$

$$\Lambda_2 = \frac{k-m}{\eta_{k,k-1} - \eta_{m,m-1}}$$

For Λ_1 , by solving the following two equations

$$\begin{cases} M_k = \frac{\Lambda_1}{\Lambda_2^{p+k+1}} \Gamma(p+k+1) \\ M_m = \frac{\Lambda_1}{\Lambda_2^{p+m+1}} \Gamma(p+m+1) \end{cases} \quad (9)$$

yielding

$$\frac{1}{\Lambda_1} = \frac{1}{M_k - M_m} \left[\frac{\Gamma(p+k+1)}{\Lambda_2^{p+k+1}} - \frac{\Gamma(p+m+1)}{\Lambda_2^{p+m+1}} \right] \quad (10)$$

Hence from (8) and (10), the parameters Λ_1 , Λ_2 , and p for modified gamma distribution when $q=1$ can be obtained.

RESULTS FOR JOSS TYPE DISTROMETER

Since we used Joss type Distrometer RD69 [13] to measure the rain drop size distribution, which is an impact measurement instrument, the special equation for such data has to be derived. The Distrometer is capable of measuring the drop diameters ranging from 0.3 mm to >5 mm. The total number of drops of diameters ranging from 0.3 mm to >5 mm is divided into 20 different channels for 1 minute integration time. So the k th experimental moment of D is estimated by

$$M_k = \sum_{i=1}^{20} D_i^k N_i(D_i) \Delta D_i = \frac{10^6}{ST} \sum_{i=1}^{20} \frac{n_i}{v(D_i)} D_i^k \quad (11)$$

where n_i is the number of rain drops in i th of 20 channels; integration time $T = 60$ s; the sample area $S = 5000 \text{ mm}^2$;

$v(D_i)$ is the terminal velocity of rain drop in m/s obtained from Gunn and Kinzer's [14] terminal velocity of water drop.

By the derived equations, p , Λ_1 and Λ_2 are calculated for every single rainfall rate from 1 mm/hr to 140 mm/hr, total 10 rainfall rates. Using different orders of moments, there are several solutions of moment estimators for the modified gamma model. Fig. 1 illustrates the results for rain rate at 66.88 mm/hr.

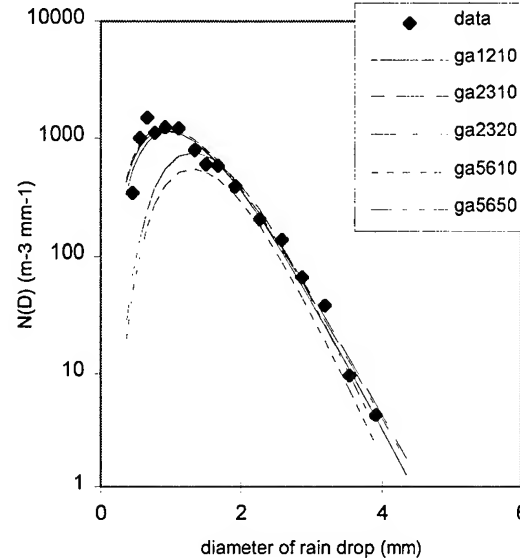


Fig. 1 Modified gamma models by different moments compared with measured data at rainfall rate 66.88 mm/hr

If a general model for all rainfall rates is needed which means that one set of parameters is suitable for all rainfall rates, the parameters p , Λ_1 and Λ_2 are related to the rainfall rate R as

$$\begin{aligned} \Lambda_2 &= \alpha R^{-\beta} \\ \Lambda_1 &= \alpha_1 R^{-\beta_1} \\ p &= \alpha_p R^{-\beta_p} \end{aligned} \quad (12)$$

By least square fitting method, the general model suitable for all rainfall rates is obtained. Since the lower moment results better fitted the measured data as observed in Fig.1, the two lower moment results, ga1210, which used the 0th, 1st, and 2nd moments to get the result, and ga2310 were selected to calculate the parameters for two general models. Table 1 lists the parameters.

Table 1 Parameters for general modified gamma model by different calculation methods

Ga	Λ_1		p		Λ_2	
	α_1	β_1	α_p	β_p	α	β
—1210	10387238	1.32397	5.98084	0.09806	10.0797	0.23443
—2310	6482957	1.23981	6.07632	0.1158	10.1169	0.24489

Finally the general models are compared with the measured data. Fig.2 illustrates the results.

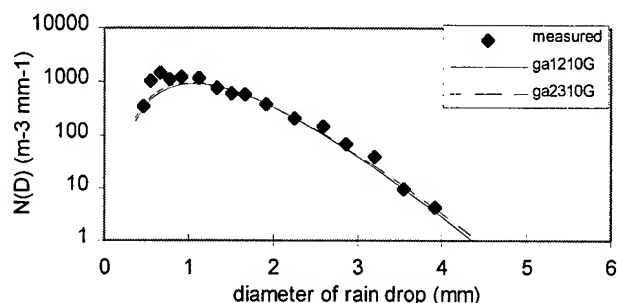


Fig. 2 Modified gamma general model compared with measured data at rainfall rate 66.88 mm/hr

It is observed that the general models obtained from the 0th, 1st, 2nd and 3rd moments can be used to describe the rain drop size distributions in Singapore. For the ten rainfall rates at 1.5, 5, 10, 23, 40, 67, 76, 100, 124 and 147 mm/hr which were used for the calculation, the modified gamma model fits the measured data very well.

CONCLUSION

The paper presented the Singapore rain drop size distribution by using a modified gamma model. The general expression for describing the rain drop size distribution by such model as well as the special expression for Joss type Distrometer were derived. The comparison between the theoretical model and the measured data showed the suitability of the modified gamma model for describing the rain drop size distributions in heavy rain rate characterised tropical regions.

ACKNOWLEDGEMENT

The authors would like to thank Associate Professor Edmund Choi from the School of CSE, NTU for making available the data used in this study.

REFERENCES

- [1] C. Gloaguen & J. Lavergnat, Attenuation due to hydrometeors at 94 GHz: experimental results and comparison with theory, IEE Proc.-Microw. Antennas Propag., Vol.143, No.1, pp.79-86, February, 1996
- [2] T. Oguchi, Electromagnetic wave propagation and scattering in rain and other hydrometeors, Proceedings of the IEEE, Vol.71, No.9, pp.1029-1078, September, 1983

- [3] L.R. Maciel & M.S. Assis, Tropical rainfall drop size distribution, International Journal of Satellite Communications, vol.8, pp.181-186, 1990
- [4] B.S. Jassal, Arun K. Verma & Lal Singh, Rain drop-size distribution and attenuation for Indian climate, Indian Journal of Radio & Space Physics, Vol.23, Iss.3, pp.193-196, June 1994
- [5] K.I. Timothy, Sanjay Sharma, M. Devi & A.K. Barbara, Tropical raindrop size distribution (RSD): prediction and modelling its effects on microwave propagation, Proceedings of 9th International Conference on Antennas and Propagation, pp.244-248, Eindhoven, The Netherlands, 4-7 April, 1995
- [6] A.R. Tharek & J. Din, Rainfall drop size distribution measurements in Malaysia, Proc. URSI comm. F 1992 Symposium Wave Propagation and Remote Sensing, Ravenscar, North Yorkshire, UK, 8-12 June, 1992, pp.1.2.1-1.2.5
- [7] G.O. Ajayi & R.L. Olsen, Measurements and analysis of raindrop size distribution in South Western Nigeria, Proc. URSI comm. F 1983 Symposium, Louvain, Belgium, June 1983
- [8] G.O. Ajayi & R.L. Olsen, Modelling of a tropical raindrop size distribution for microwave and millimetre wave applications, Radio Science, Vol.20, No.2, pp.193-202, March-April 1985
- [9] J.T. Ong, C.N. Zhu & Y.K. Lee, Ku-band satellite beacon attenuation and rain rate measurements in Singapore - comparison with ITU-R models, Proc.the 10th International Conference on Antennas and Propagation (ICAP'97), p.p. 2.153-2.156, 14-17 April 1997, Edinburgh UK
- [10] J.T. Ong, Y.K. Choo & Y.Y. Shan, Investigation on rain drop size distribution in Singapore for application in microwave systems, IEEE ICCS/ISPACS'96 Proceedings, Vol. 2 of 3, pp.907-911, Singapore, 25-29 Nov., 1996
- [11] J. T. Ong and Y. Y. Shan, "Modelling of Singapore rain drop size distribution", Proc. the 8th MINDEF-NTU Joint R&D Seminar, p.p.93-97, 21 Feb. 1997, Singapore
- [12] J. T. Ong and Y. Y. Shan, "Rain drop size distribution models for Singapore — comparison with results from different regions", Proc.the 10th International Conference on Antennas and Propagation (ICAP'97), p.p. 2.281-2.285, 14-17 April 1997, Edinburgh UK
- [13] Distromet Ltd, Distrometer RD-69 Instruction Manual, 1993
- [14] Gunn & G.D. Kinzer, the terminal velocity of fall for water droplets in stagnant air, J. Meteor., 6(1949) 243-248

Relationship between Cirrus Particle Size and Cloud Top Temperature

Qingyuan Han, Joyce Chou, and Ronald M. Welch

Institute of Atmospheric Sciences
South Dakota School of Mines and Technology
501 E. Saint Joseph Street
Rapid City, SD 57701-3995
Phone: (605) 394-2291; Fax (605) 394-6061
email: han@cloud.ias.sdsmt.edu

Abstract - The relationship between cirrus particle size and cloud top temperature is surveyed on a near-global scale. The cirrus particle size is retrieved assuming ice crystals are hexagonal columns and the cloud top temperature and the radiances in channel 1 and 3 of AVHRR used to retrieve ice particle sizes are from ISCCP product. The results show that for thick clouds over North America, the relation between cirrus particle size and cloud top temperature is consistent with a summary of this relationship based on aircraft measurement over that region for thick clouds. However, this relationship is not universal for other regions especially for tropical zone, which has been found by other *in situ* measurements.

INTRODUCTION

Cloud microphysical parameterizations have attracted a great deal of attention in recent years due to their effect on cloud radiative properties [1] and cloud-related hydrological processes in large-scale models [2]. The parameterization of cirrus particle size has been demonstrated as an indispensable component in the climate feedback analysis [3]. In parameterization schemes, relationships between cloud temperatures/optical thickness and cirrus ice crystal sizes are of critical importance because the microphysics of cirrus clouds modifies the relationship between cloud optical depth and cloud ice/liquid water path. Climate models not accounting for this relationship cannot correctly predict the temperature dependence of infrared emittance of cirrus clouds [4] and thus arrive at wrong conclusions about climate change. Many efforts have been made to investigate the cloud temperature-cirrus crystal size relationship and controversial conclusions have been reached. For example, twenty flights of aircraft measurements over North America during winter times [5,6] show that the cloud-particle mode radius increases with temperature. Similar results were found by *in situ* measurement during CEPEX at tropics [7] and by surface lidar observations [8]. However, investigations using radar measurements [9], Doppler radar

and IR radiometry [10], and millimeter-wave radar [11] found a negative correlation between ice crystal size and temperature and conclude that temperature cannot be used to

parameterize the ice crystal size as Heymsfield and Platt [6] suggested. While these data supply valuable information about this relationship, they are all regional measurements during a short time period for mostly thick cirrus clouds.

This study investigates this relationship based on the cirrus particle size data retrieved from ISCCP CX data. We found that for thick clouds ($\tau \geq 10$), similar to those found by aircraft measurements, most of the regions over the globe show positive relationships between cloud temperature and cirrus ice crystal sizes. However, if relatively thin clouds are included ($\tau \geq 3$), this correlation becomes negative for tropical areas but remains mostly positive for midlatitudes.

RETRIEVAL OF ICE CRYSTAL PARTICLE SIZE

The detailed methodology of retrieving ice crystal size is presented in another paper [12]. In that paper, the method for retrieving cirrus particle size information on a near-global scale (50°S to 50°N) using currently available satellite data from ISCCP is described. To retrieve cirrus particle size, we use a radiative transfer model that includes all major absorbing gases and cloud scattering / absorption to compute synthetic radiances as a function of satellite viewing geometry. Ice clouds are determined by cloud top temperature $T_c \leq 240\text{K}$. Shapes and orientations of ice crystals are assumed to be hexagonal columns and plates randomly oriented in the atmosphere. Although ice crystals may have complicated shapes such as bullets, rosettes, aggregates, irregular and quasi-spherical particles and show preferred orientations, it is difficult to determine which shape and/or orientation is dominant in a specific clouds by current remote sensing instruments. On one hand, we realize the possible effect of non-hexagonal particles and preferred orientations. On the other hand, we also notice that the difference of phase functions between hexagon and other irregular shapes is much smaller than that of non-spherical and spherical particles [13]. Therefore, we adopt the phase functions for hexagonal columns in the retrieval and estimate the possible effect of non-hexagonal and preferred orientation by comparing the retrieved particle sizes with *in situ* measurements. Ray tracing techniques are used to calculate phase functions for different size distributions. Five different size distributions from

Acknowledgement. We wish to thank Dr. Ou and Takano for supplying phase functions used in this study. This research was supported by NASA Grant Nos. NAGW-3922, NAGW-3788; was partially funded by DOE through the NIGEC Great Plains Regional Center at the University of Nebraska-Lincoln (DOE Cooperative Agreement No. DEFC03-90ER61010). Financial support does not constitute an endorsement by DOE of the views expressed in this paper. This research was also supported by the NASA Climate Program managed by Dr. Bob Curran.

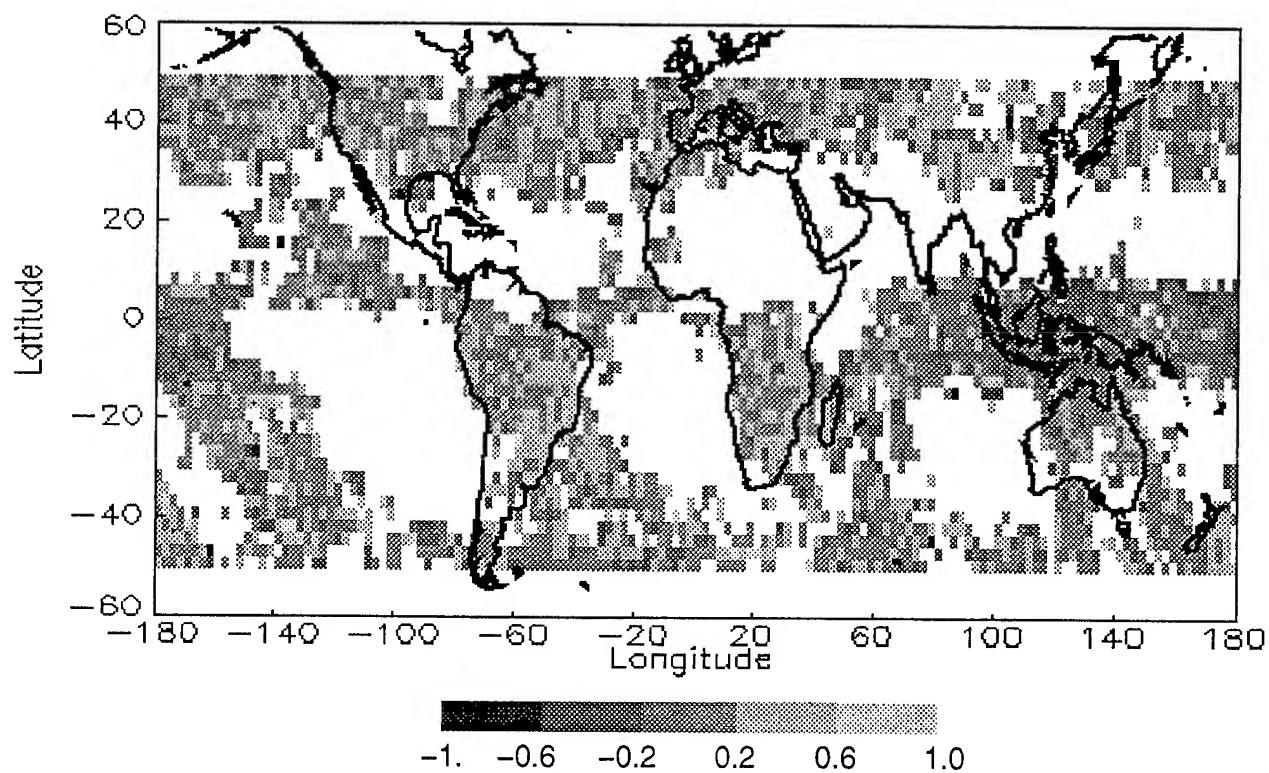


Fig. 1 Correlation (De, Tc) for Ice Cloud ($\tau \geq 10$; 8701 NOAA-9)

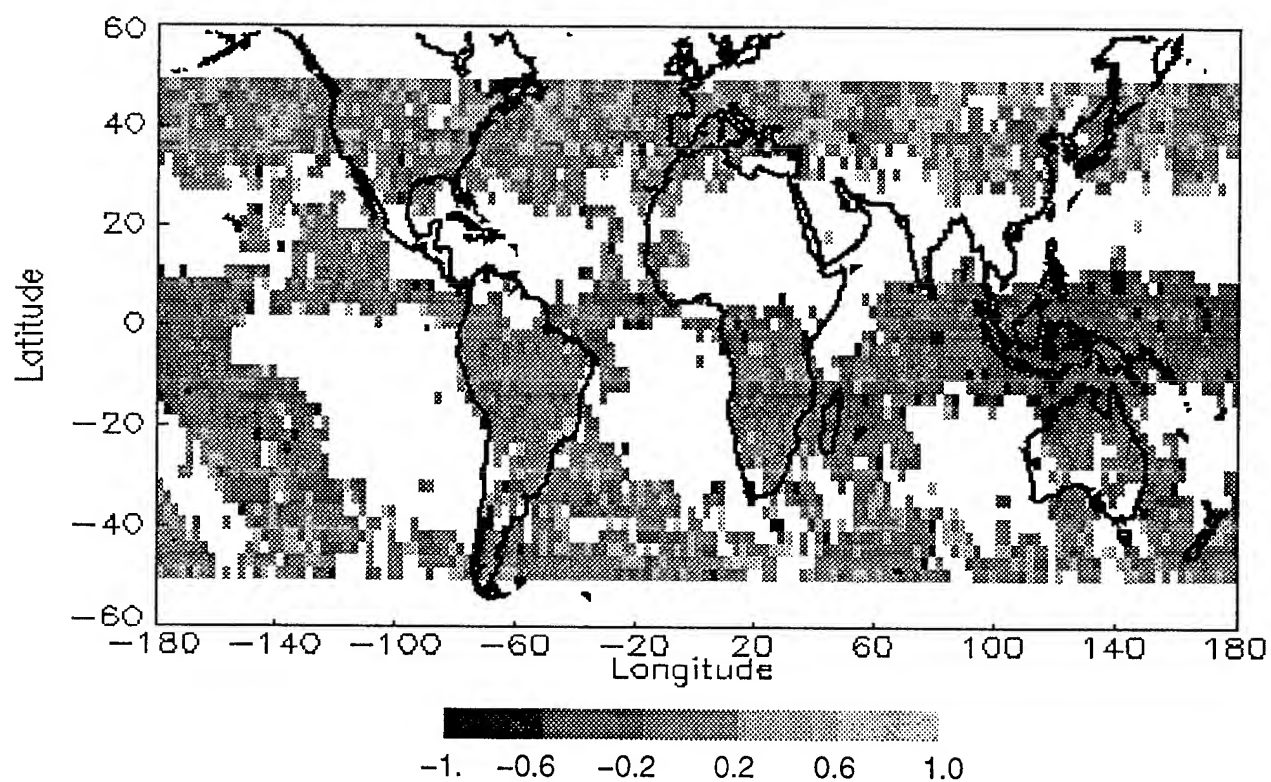


Fig. 2 Correlation (De, Tc) for Ice Cloud ($\tau \geq 3$; 8701 NOAA-9)

cirrus ($D_e=47.6 \mu\text{m}$), -40°C cirrus ($D_e=64.1 \mu\text{m}$), Nov. 1 cirrus ($D_e=75.1 \mu\text{m}$) and Cirrus uncinus ($D_e=123.6 \mu\text{m}$). Phase functions of these five size distributions for channels 1 and 3 of AVHRR are applied in the model for calculations of multiple scattering. The model results have been validated against clear sky observations and are consistent with the observed radiance range under cloudy conditions.

The results of this near-global survey show that the peak frequency of cirrus crystal effective diameter D_e for hexagons is about $60 \mu\text{m}$, the mean value corresponding to a $30 \mu\text{m}$ radius for an equivalent sphere. The survey also reveals that about 15% of the small crystal sizes are less than $23 \mu\text{m}$ in effective diameter. The geographical distribution of small crystal sizes is consistent with the results of Prabhakara et al. [14]. There are no significant differences between particle sizes of continental and maritime cirrus.

RELATION BETWEEN ICE CRYSTAL SIZE AND TEMPERATURE

Figure 1 shows the distribution of correlation coefficients between ice cloud crystal size and cloud top temperature for thick clouds ($\tau \geq 10$). Ice clouds over most of the regions show positive relation between ice crystal size and cloud top temperature, consistent with the results of Heymsfield and Platt (1984). However, this relation changes when thin clouds are included into the statistics. Figure 2 shows that for ice clouds with ($\tau \geq 3$, most ice clouds over tropical and sub-tropical regions show negative relation between ice particle sizes and cloud top temperature. The possible explanation includes different cirrus systems over tropics and midlatitudes. The strong convective motion in tropics brought large ice crystal particles up to very high and cold regions and spread out to form vast and relatively thin anvils. Further information about the underlying mechanism and possible explanations are under investigation.

REFERENCES

- [1] Stephens, G. L., 1984: The parameterization of radiation for numerical weather prediction and climate models. *Mon. Wea. Rev.* **112**, 826-867.
- [2] Fowler, L. D., and D. A. Randall, 1996: Liquid and ice cloud microphysics in the CSU General Circulation Model. Part II: Impact on cloudiness, the Earth's radiation budget, and the general circulation of the atmosphere. *J. Climate*, **9**, 530-560.
- [3] Ou, S. C., and K. N. Liou, 1995: Ice microphysics and climate temperature feedback. *Atmos. Res.*, **35**, 127-138.
- [4] Platt, C. M. R., 1989: The role of cloud microphysics in high-cloud feedback effects on climate change. *Nature* **341**, 428-429.
- [5] Heymsfield, A. J., 1977: Precipitation development in stratiform ice clouds: A microphysical and dynamical study. *J. Atmos. Sci.* **34**, 367-381.
- [6] Heymsfield, A. J., and Platt, C. M. R., 1984: A parameterization of the particle size spectrum of ice clouds in terms of the ambient temperature and the ice water content. *J. Atmos. Sci.* **41**, 846-855.
- [7] McFarquhar, G. M., and A. J. Heymsfield, 1996: Microphysical characteristics of three cirrus anvils sampled during the Central Equatorial Pacific Experiment. *J. Atmos. Sci.*, **53**, 2401-2423.
- [8] Platt, C. M. R., J. C. Scott, and A. C. Dilley, 1987: Remote sounding of high clouds. VI, Optical properties of midlatitude and tropical cirrus, *J. Atmos. Sci.*, **44**, 729-747.
- [9] Atlas, D., S. Y. Matrosov, A. J. Heymsfield, M. D. Chou, and D. B. Wolff, 1995: Radar and radiation properties of ice clouds. *J. Appl. Meteor.*, **34**, 2329-2345.
- [10] Matrosov, S.Y., D. Atlas, A.J. Heymsfield, and R.A. Kropfli, 1995: Variations of cirrus cloud particle sizes with temperature: Results of remote sensing and direct measurements. Preprints, *Cloud Physics Conf.*, Dallas, TX, Amer. Meteor. Soc., 55-58.
- [11] Brown, P. R. A., A. J. Illingworth, A. J. Heymsfield, G. M. McFarquhar, K. A. Browning, and M. Gosset, 1995: The role of space borne millimeter-wave radar in global monitoring of ice cloud. *J. Appl. Meteor.*, **34**, 2346-2366.
- [12] Han, Q.Y., W.B. Rossow, J. Chou, and R.M. Welch, 1997: A near-global survey of ice cloud properties using ISCCP, Part I: Methodology. [Submitted to *J. Climate*, Accepted]
- [13] Mishchenko, M.I., W.B. Rossow, A. Macke, and A.A. Lacis, 1996: Sensitivity of cirrus cloud albedo, bidirectional reflectance and optical thickness retrieval accuracy to ice particle shape. *J. Geophys. Res.*, **101**, 16973-16985.
- [14] Prabhakara, C., R.S. Fraser, G. Dalu, M.L.C. Wu and R.J. Curran, 1988: Thin cirrus clouds: Seasonal distribution over oceans deduced from Nimbus-4 IRIS. *J. Appl. Meteor.*, **27**, 379-399.

Quantification of the Impact of Misregistration on the Accuracy of Remotely Sensed Change Detection

Xiaolong Dai and Siamak Khorram

Computer Graphics Center, North Carolina State University

Campus Box 7106, Raleigh, North Carolina 27695 - 7106, USA

Tel: (919)515-3430 Fax: (919)515-3439 Email: xdai@unity.ncsu.edu, khorram@ncsu.edu

Abstract -- In this study, the impact of misregistration on the accuracy of change detection is quantitatively investigated using TM imagery. This simulation study focuses on two interconnected issues. First, the statistical properties of the difference images are evaluated using semivariograms when images are progressively misregistered in order to investigate the *Band Sensitivity*, *Temporal Sensitivity*, and *Spatial Frequency Sensitivity* of change detection to misregistration. The *Ellipsoidal Change Detection* technique is then proposed and used to progressively detect the land cover transitions at each misregistration stage for each image. The impact of misregistration on change detection is then evaluated in terms of the accuracy of change detection using the output from the *Ellipsoidal Change Detector*.

G, B, respectively) are shown in Fig. 1 (a) through (h).

Table 1: Characteristics of study areas and dates of images

Location	Cover type	Imaging Date	Main Changes
Bladen, NC	Forest in Carolina Bays	Winter 1988	Urban development
		Winter 1994	
Jones, NC	Pocosin in coastal plain	Winter 1988	Moisture change
		Winter 1994	
Wilson, NC	Agricultural land	Winter 1988	Land conversion to forest
		Winter 1994	
Wilmington, NC	Urban areas	Winter 1988	Urban development
		Winter 1994	

Introduction

The registration of data sets to a common spatial framework is a precursor to the use of remotely sensed data for monitoring change. If accurate registration between images is not achieved, then spurious differences will be detected [1]. The majority of current change detection techniques depend critically upon the accuracy of geometric registration of two images. However, the impact of misregistration on change detection was previously explored by few studies. Townshend *et al.* [2] provided an initial in-depth research on this topic. However, many important consequences of misregistration in quantitative terms on multitemporal data analysis, especially on the accuracy of change detection, are still unknown. Therefore, there is a need to explore and quantify the impact of misregistration on the accuracy of digital land cover change detection. Given these concerns, in this study it is designed to simulate varying degree of misregistration and to quantify their impact on estimates of true differences between the images.

Study Areas and Data Sets

Four study areas in North Carolina have been chosen in this quantification research. The data sets to be utilized are four test windows of 200×200 pixels extracted from the TM scenes of North Carolina coastal plain. Characteristics of the study areas are listed in Table 1. Their standard false color composite (FCC) images (TM bands 4, 3, and 2 as R,

This work was partially supported by the Coastal Change Analysis Program (C-CAP) of National Oceanographic and Atmospheric Administration (NOAA).

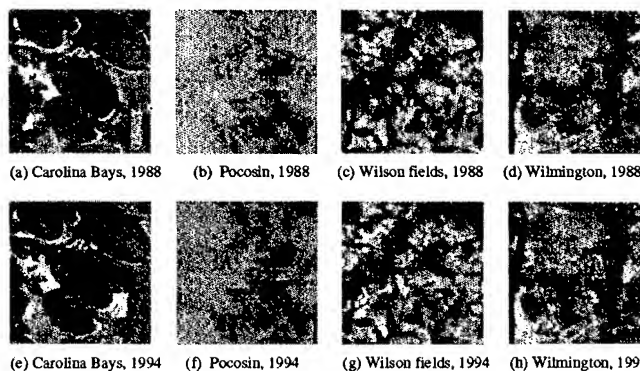


Fig. 1 Standard false color composite images of the test windows.

Quantification Methods

General Description of Quantification Methods

On the basis that the images are well registered using ground control points, the experiments are then performed to assess the consequences of progressive misregistration of the images. As the image are sequentially misregistered, the differences in changes are evaluated by both semivariance increase and actual output from change detector. In this simulation, we define the following three sensitivities of change detection to misregistration: *band sensitivity*, *spatial frequency sensitivity*, and *temporal sensitivity*. *Band sensitivity* is the difference in the responses among the TM spectral bands to misregistration. *Spatial frequency sensitivity* is defined as the difference in semivariance change as a response to misregistration. *Temporal sensitivity* is the difference in the responses of multirate images of the same

area to misregistration. We then develop and apply the *Ellipsoidal Change Detection* method to the test areas to evaluate the effects of misregistration on the accuracy of change detection.

Simulation Study by Semivariance

In order to estimate the effects of misregistration, the differences between the misregistered images can be measured by semivariances [2]. In the case of misregistering one image against another, each pixel $X(i, j)$ is compared to a corresponding pixel $Y(i + d_i, j + d_j)$, where d_i is the misregistration error from row to row, and d_j is the misregistration error from column to column. The difference between the two image gray values is measured by the semivariance (SV):

$$SV = \frac{\sum_{i=1}^R \sum_{j=1}^C \{X(i, j) - Y(i + d_i, j + d_j)\}^2}{2R \cdot C} \quad (1)$$

where C is the number of columns and R is the number of rows in the overlapped part of image.

Ellipsoidal Change Detection and False Change Analysis

To evaluate the impact of misregistration on the accuracy of change detection, a method that we call *Ellipsoidal Change Detection* is proposed and used to subjectively evaluate the impact of misregistration on change detection accuracy. In the case of multidimensional feature space, a hyperellipsoidal decision boundary between change and non-change is more representative of changes than any other kind of decision boundaries, such as hypercubic, as shown in Fig. 2. Therefore, the *Mahalanobis distance* function of n -D differenced image can be used as the discriminant function between change and non-change.



Fig. 2 Example feature space plots describing changes.

The *Mahalanobis distance*-based discriminant function for change detection can then be expressed as follows:

$$M_d = \sqrt{(x - \mu)^T \Sigma^{-1} (x - \mu)} \begin{cases} M_d < T & \text{unchanged} \\ M_d \geq T & \text{changed} \end{cases} \quad (2)$$

where x is the differenced image of six bands, μ and Σ are the mean vector and the covariance matrix of the differenced image, respectively; and T is the threshold. Since only relative amount of changes are of interest in the following experiments, the absolute value of the threshold should be

irrelevant to the results of the analysis and the impact of the different thresholds on false change analysis results can be ignored.

Based on the output from this change detection technique, a *true change* (C_t) can be defined as the amount of change detected at zero misregistration. At every misregistration point while we slide one image over another, we apply the ECD method to the overlapped areas to detect the *overall changes* (C_o) between these two misregistered images. At the same time, the true changes (C_t) can be detected over the overlapped areas using zero-misregistered images. The *true changes detected* (C_{td}) when images are misregistered are then the intersection of C_t and C_o . The *false changes added* by misregistration (C_{fa}) (false positive or commission error) can be expressed as: $C_{fa} = \{C\} \quad C \in \{C_o\} \quad \text{and} \quad C \notin \{C_t\}$. The *true changes removed* due to misregistration (C_{tr}) (false negative or omission error) can then be defined as: $C_{tr} = \{C\} \quad C \notin \{C_o\} \quad \text{and} \quad C \in \{C_t\}$. Based on these definitions, the following evaluation quantities can be defined to evaluate the effect of misregistration on the overall change detection accuracy: (1) The *percentage of true changes detected* (P_{td}) when misregistration exists: $P_{td} = C_{td} / C_o \cdot 100$; (2) The *percentage of false changes added* (P_{fa}) due to misregistration: $P_{fa} = C_{fa} / C_o \cdot 100$; (3) The *percentage of true changes removed* (P_{tr}) by misregistration: $P_{tr} = C_{tr} / C_o \cdot 100$; and (4) The *percentage of overall change increase* (P_i) caused by misregistration: $P_i = (C_o - C_t) / C_t \cdot 100$.

Experimental Results

Band Sensitivity

It is important to investigate the sensitivity of TM bands to misregistration in change detection. The six non-thermal bands of the Wilmington image are misregistered against themselves. Fig. 3 (a) shows that TM band 4 is the most sensitive band to misregistration among the six non-thermal TM bands since the slopes of the semivariance increases for TM band 4 display the steepest rise within first 3 pixels of misregistration than any other 5 non-thermal bands. This result is important since TM band 4 is widely used in vegetation studies. This result can be understood by knowing that TM band 4 is the most sensitive band to vegetation change.

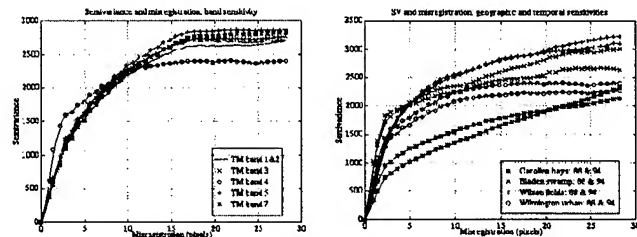


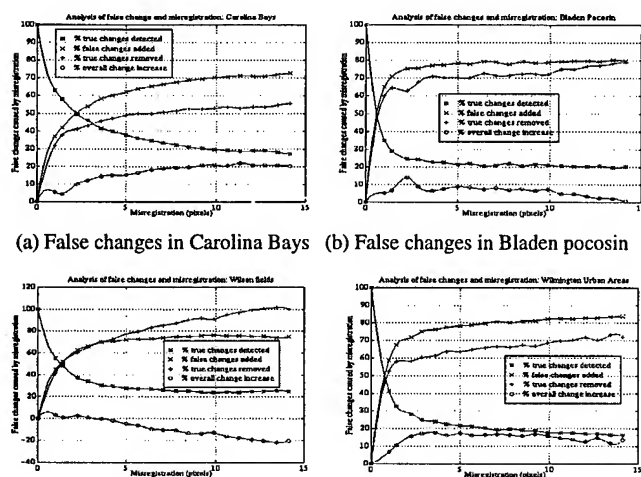
Fig. 3 (a) TM Band Sensitivity (b) Temporal S. & Spatial Freq. S.

Spatial Frequency Sensitivity and Temporal Sensitivity

Fig. 3 (b) shows the results obtained when all eight images are progressively misregistered against themselves using TM band 4. The semivariance plots show similar results in terms of the overall trends of semivariance increase with misregistration. All four pairs of plots for temporal images show that temporal images of the same areas but of different times have the same sensitivities to misregistration when the basic image structure (spatial frequency) remains the same. The moisture change patterns and spatial image structure (spatial frequency) are two important factors that affect the sensitivity to misregistration.

Analysis of False Changes Caused by Misregistration

The simulation study on semivariance increases when misregistration is present shows only general trends and combined effects of real changes on the ground and changes caused by misregistration. When misregistration exists in the data, it will introduce both additional false positive changes (commission errors) and false negative changes (omission errors) as well in the detected changes. Besides, misregistration reduces the ability of any change detector to detect the true changes and increase the probabilities to pick up additional false changes because the wrong locations are compared in the presence of misregistration. In the following experiments, we apply the ECD method to the four test areas. To simulate real applications, only TM bands 2, 3, and 4 are used in the change detection. The threshold in the Mahalanobis distance discriminant function is 2.5 for all areas to assure the comparability among results. For every area and at every point of misregistration, the total changes detected, the true changes present, false changes added by misregistration, and the true changes removed by misregistration are identified. Fig. 4 shows the experimental results of the false change analysis.



(c) False changes in Wilson fields (d) False changes in Wilmington area
Fig. 4 False change analysis using Ellipsoidal Change Detection.

From the plots in Fig. 4, we notice that, for all four study areas, the percentages of true changes detected within 1-pixel misregistration dramatically drop ranging from 35.0 to 62.5. The main contribution to this drop is the percentage of true changes removed by misregistration (omission error), which are 32.5, 60.0, 42.0, and 53.4, respectively. Since there is only slight difference between the commission error and omission error, the overall changes detected remain almost constant regardless of the amount of misregistration. It is interesting to quantitatively evaluate the required registration accuracy to achieve a specific accuracy of change detection. On average, less than 0.1934 pixel of registration accuracy should be achieved in order to detect 90% of the true changes, which means that a registration accuracy of less than one fifth of a pixel is required to achieve a change detection error of less than 10%.

Conclusions

This study is basically a simulation study of the error propagation process of misregistration in remotely sensed change detection. From these experiments, we conclude that TM band 4 is most sensitive to misregistration among the six non-thermal TM bands. All four pairs of plots for temporal images show that temporal images of the same areas but of different times have the same sensitivity to misregistration if the basic image structure (spatial frequency) remains the same. The moisture change patterns and spatial image structure are two important factors that affect the sensitivity to misregistration.

The change detection accuracy drops dramatically within the first pixel of misregistration. The true changes removed (omission error) by misregistration is the main reason why the true changes detected drop. The percentages of false change added by misregistration are slightly greater or slightly less than the corresponding percentages of true changes removed. To detect 90% of the true changes, less than 0.1934 pixel of registration accuracy should be achieved in order to detect 90% of the true changes, which means that a registration accuracy of less than one fifth of a pixel is required to achieve a change detection error of less than 10%. This research is important in evaluating and investigating the ability of remotely sensed data to detect changes in land covers.

References

- [1] Singh, A., "Digital change detection techniques using remotely-sensed data," *Int. J. of Remote Sensing*, vol. 10, no. 6, pp. 989-1003, 1989.
- [2] Townshend, J. R. G., C. O. Justice, C. Gurney, and J. McManus, "The impact of misregistration on change detection," *IEEE Trans. Geosci. and Remote Sensing*, vol. 30, no. 5, pp. 1054-1060, September 1992.

Assessing the Accuracy of High Spatial Resolution Image Data and Derived Products

Douglas Stow, Allen Hope, Stuart Phinn, Alice Brewster, and Brian Bradshaw
Department of Geography, San Diego State University, San Diego, CA 92182 USA
Phone: 619-594-5498; Fax: 619-594-4938; E-mail: stow@mail.sdsu.edu

Abstract -- We examine accuracy assessment issues for high resolution multispectral image products from theoretical and empirical perspectives. The general advantage of having greater certainty when assessing locational and attribute accuracy for high resolution image data is offset by the requirement for high precision and more expensive ground reference data. Kinematic global positioning system (KGPS) surveys provide highly precise ground reference data, as is demonstrated in this paper. The locational and attribute accuracy of orthorectified image, thematic classification, biophysical map, and land cover change products derived from a commercial airborne multispectral digital camera system was found to be high, particularly in the context of specific coastal wetland monitoring objectives.

INTRODUCTION

Given the high likelihood of abundantly available high spatial resolution image from commercial and government remote sensing systems data in the near future, there is a need to develop accuracy assessment procedures that are appropriate for such data. The requirements for and ability to assess the locational and attribute accuracy of high spatial resolution image data (which we will refer to as H-resolution data for brevity) and derivative products are likely to differ from those associated with the moderate- and coarse-resolution image data that have been predominantly utilized in the past. One of the key requirements is precise, survey accuracy reference data. Kinematic (carrier phase differential) global positioning systems (KGPSs) provide such reference data by enabling measurements of absolute horizontal and vertical locations within ± 5 cm. When suitable survey control has been established KGPS units also enable convenient logging of land surface attributes at the time of surveying. Our objectives are to address several issues pertaining to the assessment of accuracy of H-resolution multispectral remotely sensed data and derived environmental monitoring products and to demonstrate some approaches to accuracy assessment that are based on the use of KGPS for field surveys.

In order to demonstrate approaches to assessing the accuracy of H-resolution multispectral data and products, several case studies are presented that are drawn from ongoing research projects pertaining to airborne monitoring of disturbed and restored coastal wetland habitats in southern California. These studies are based on the application of H-resolution data from a commercially available multispectral digital camera system, the ADAR System 5500 [1]. Examples are from the Sweetwater Marsh Wildlife Reserve, a complex of natural and constructed coastal saltmarshes adjacent to San Diego Bay near San Diego, California, USA.

HIGH RESOLUTION IMAGE DATA

According to [2] there are plans for no less than 14 satellites that are to yield optical image data with spatial resolutions that are 10 meters or less, 8 of which will sense in more than one waveband (i.e., multispectral sensors). Currently, there are many airborne scanner, digital camera, and video systems that routinely produce multispectral image data with spatial resolutions varying from 0.5 - 5 meter resolutions. Multispectral image data from airborne sensors provide a prototype for the next generation of H-resolution satellite data, but with some differences (e.g., greater atmospheric pathlengths, narrower range of view, and more limited extent of coverage).

The utility of H-resolution data would seem to be virtually endless, though cost factors will influence the actual degree of usage. A few of the applications that stand to benefit most from such data are urban infrastructure assessment, precision agriculture, and environmental monitoring. Major advantages of H-resolution data are: (1) visual image interpretation is facilitated, (2) fine-scale features and structures may be resolved, and (3) the data can be aggregated to achieve a GRE that is most appropriate for a given landscape and image analysis approach [3]. Most image analysis strategies for H-resolution data are based on the H-resolution scene models, originally described by [4]. For the H-resolution scene model, the GRE is smaller than the features or structures that are of interest. Accuracy should be assessed within the context of application requirements and with consideration of the H-resolution model.

Several generic issues that pertain to accuracy assessment are particularly amplified for H-resolution image data and products. A common issue is distinguishing between errors of location and those associated with the attributes (i.e., thematic category or biophysical quantity) of spatial data. There is greater certainty in determining locations of features on H-resolution image data, due to the greater definition of objects within a landscape. This improves the ability to distinguish locational and attribute errors. However, another issue is that the reference data to which image-based products are assessed must be of greater certainty, precision and accuracy than the image data products. This normally means that reference data are derived from detailed ground-level samples, which can be costly and obtrusive. Finally, the type of image product should determine the manner in which accuracy is assessed. Different types of reference data are required to quantify the accuracy of image maps (i.e., orthorectified images), thematic classification maps (discrete spatial units and attributes), maps of biophysical variables (continuous spatial fields and attributes), and dynamic change

maps that are derived from multitemporal image products of any of the three data types above.

ADAR IMAGE ACQUISITION AND PROCESSING

Digital multispectral image data covering the Sweetwater Marsh Wildlife Reserve have been acquired by Positive Systems, Inc. at least once a year since 1991 using the Airborne Data Acquisition and Registration (ADAR) system. All of the examples in this paper are based on ADAR 5500 data acquired in August 1994, June 1995 and July 1996. Sixteen image frames were captured with a spatial resolution of approximately 0.75 meters and a coverage of 1150 by 750 meters.

The 1994 ADAR 5500 frames were mosaicked and orthorectified by TRIFID, Inc. to produce a near-seamless image map. The orthorectification was achieved using a bundle adjustment correction and based on 20 ground control points. Subsequent ADAR 5500 data acquired in the summers of 1995 and 1996 were also utilized in some of case studies. Image frames from these dates were spatially registered to the 1994 image mosaic. This was achieved with empirical image warping functions that were based on image control points and by mosaicking adjoining frames.

ORTHORECTIFIED IMAGE MOSAIC ACCURACY

We analyzed the locational accuracy of the 1994 ADAR orthorectified image mosaic by comparing the geographic coordinates of 30 independent GCPs that had not been used in the orthorectification process. The GCP samples were selected from the image mosaic by locating distinct image features and with consideration that the samples were evenly distributed. KGPS survey measurements were used as the reference data. GCPs were marked on hardcopy prints of the ADAR mosaic and assisted in the location of GCPs during the KGPS survey.

The root means square (RMS) error of the commercially-generated image mosaic was found to be equivalent to the size of the GRE (i.e., one pixel) or about 0.75 meters. No directional bias or spatial concentration of errors were evident. While there is minimal relief within the Sweetwater Marsh study site to cause image relief displacement, the high degree of locational accuracy exceeded contract specifications for the orthorectification. The RMS magnitude is within the range of uncertainty for co-locating GCPs on the ground and the image.

IMAGE CLASSIFICATION ACCURACY

Two different saltmarsh habitat type maps generated from the 1994 ADAR image mosaic with image classification techniques enable demonstration of thematic map accuracy for H-resolution data. In both cases, several "per-pixel" classification approaches were tested and some type of unsupervised clustering approach was deemed superior for the final mapping and accuracy assessment. Also, the KGPS system was utilized to record locational coordinates and

marsh habitat type attributes for ground-level reference data used to assess thematic map accuracy of the ADAR classification.

A saltmarsh habitat type map was generated for a natural saltmarsh (E Street Marsh) within the SMWR, as part of a study of the nesting characteristics of the Belding's Savannah sparrow (an endangered saltmarsh dwelling bird) [5]. The ADAR image classifications yielded digital maps with 0.75 m pixels categorized into three marsh habitat types, and bare/sparse and channels/standing water cover types. Based on the KGPS ground surveys and *in situ* classification of 270 reference sites, the overall classification accuracy was $86 \pm 3\%$ with a Kappa statistic of 0.75. All categories were classified with an accuracy that was over 75%.

The other thematic mapping assessment was based on a study of incorporating H-resolution digital elevation data into ADAR image classifications, in the context of monitoring restored and constructed coastal wetlands sites within the SMWR [6]. Digital elevation data and *in situ* vegetation samples were collected with the KGPS system providing horizontal and vertical positional accuracy within 3 to 5 centimeters. The KGPS survey was conducted using systematic spaced either 3 or 6 meters apart. The vegetation data was used to model the relationship of saltmarsh habitat types to elevation for each artificial marsh. Several methods of integrating the ancillary data with the imagery were tested. Based on a 163 reference samples a standard unsupervised approach with four marsh habitat type and two land cover type classes yielded an overall accuracy of $54.6 \pm 9\%$ and a Kappa statistic of 0.45. The highest accuracy ($73 \pm 6\%$, 0.64) was achieved by incorporating the H-resolution DEM using the post-classification sorting approach [7] a statistically significant increase in overall accuracy over the conventional unsupervised classification product.

VEGETATION COVER ACCURACY

We assessed the accuracy of horizontal vegetation cover proportions estimated using spectral vegetation indices and multispectral radiance values from ADAR 5500 data with calibration data from field plots. Horizontal cover of saltmarsh vegetation is a useful indicator of habitat suitability for rare, threatened and endangered bird species. Cover proportions were estimated with regression models that were calibrated and validated (from different samples) with cover estimates from ground-based measurements obtained within one week of an August 1996 ADAR overflight. The KGPS was used to survey field transect and plot locations, such that corresponding pixels could be located on the orthorectified image data.

Due to the significant difference in vertical and horizontal structure and therefore, spectral reflectance characteristics between plants in different plant assemblages that follow tidal zonation, the regression relationships were examined separately in plots from low (n=36), middle (n=66) and high marsh (n=48) areas. The optimal regression model for each of the low, middle and high marsh zones was applied to all pixels of a particular zone, based on the following equations:

Low marsh: cover = $0.376\text{NIR} - 0.127\text{Red} - 1.717$; $r^2 = 0.39$
 Mid marsh: cover = $0.0543\text{NIR} + 0.609\text{Red} - 8.919$; $r^2 = 0.57$
 High marsh: cover = $0.4227\text{NIR} - 0.225\text{Red} + 2.3$; $r^2 = 0.74$.

Accuracy assessment yielded an overall agreement of 85% between ADAR and field-derived cover estimates for all sample plots combined and a relatively low root mean square errors (RMSE) of 4%. Significantly higher RMSE resulted for estimates of individual marsh zones.

LAND COVER CHANGE ACCURACY

An operational remote sensing based monitoring application provides an excellent example of H-resolution accuracy assessment in the context of identifying detailed land cover changes in a wetland restoration site at the SMWR. An iterative unsupervised classification routine was applied independently to two registered ADAR 5500 image mosaics from summer 1995 and 1996 to identify marsh cover types. A post-classification comparison approach enabled areas of change and no-change to be identified and quantified [8]. The cross-tabulation of time sequential maps of marsh cover types indicate areas of stable habitat and areas changing towards or away from restoration objectives.

Individual image class accuracy ranged from 30% to 100% based on comparison with aggregated species cover data sampled within one square meter plots along a transect consisting of six contiguous plots. Changes (or 'no change') of dominant cover types were also compared on a transect by transect basis. The ADAR-derived estimate of 'no change' appeared to be moderately accurate when compared to the field estimates. Of the cover transition types that are important to the monitoring of the saltmarsh habitat restoration effort, changes in dense *Spartina foliosa* coincided with field estimates. This accuracy assessment was limited by slightly different ground sample points used in 1996 and an average spatial misregistration of one GRE between the two image dates..

SUMMARY

The general advantage of having greater certainty when assessing locational and attribute accuracy for high resolution image data is offset by the requirement for high precision and more expensive ground reference data. Kinematic global positioning system (KGPS) surveys provide highly precise ground reference data. The locational accuracy of an orthorectified image mosaic generated from Airborne Data Acquisition and Registration (ADAR) System 5500 image data of a salt marsh complex and urban surroundings had a root means square error (RMSE) equivalent to the size of the ground resolution element (GRE) or about 0.8 meters. We also found the accuracy of wetland vegetation and marsh habitat type maps (i.e., thematic data) generated from the ADAR image mosaic with conventional image classification techniques. Overall, classification accuracy ranged from 60 to 85 %. Vegetation cover proportions (i.e., biophysical data) were quantified using spectral vegetation indices and multispectral radiance values from ADAR data. Cover estimates from regression models were reliable when

stratified by the three major elevational zones of the coastal wetland study site. Finally, we assessed the accuracy of detailed land cover change maps derived using a post-classification comparison approach. Both change and no-change cover classes corresponded closely to field estimates.

ACKNOWLEDGMENTS

Funding for these projects was provided by the California Department of Transportation and a NASA-EOCAP grant with Positive Systems Inc. Field assistance was provided by the Pacific Estuarine Research Laboratory. Image processing assistance by Clint Garrison.

REFERENCES

- [1] D.A. Stow, A. Hope, A.T. Nguyen, S.R. Phinn and C.A. Benkelman "Monitoring detailed land surface changes using an airborne multispectral digital camera system," IEEE Transactions on Geoscience and Remote Sensing, vol.34(5), pp. 1191-1202, 1996.
- [2] A.S.P.R.S. , Land satellite information in the next decade. Conference Proceedings, September 25-28, Vienna, Virginia, 1995.
- [3] S.R.Phinn, Remote sensing and spatial analytic techniques for monitoring landscape structure in disturbed and restored coastal environments, PhD Dissertation, Departments of Geography, San Diego State University, University of California at Santa Barbara, 1997.
- [4] A. Strahler , C. Woodcock and J.Smith, "On the nature of models in remote sensing," Remote Sensing of Environment, vol.20, pp.121-139, 1986.
- [5] A. Brewster, D.Stow and L.Deysher, "Integrating multispectral digital image data, kinematic GPS and GIS to analyze the habitat preferences of the Belding's Savannah Sparrow," in Proceedings of the Second International Airborne Remote Sensing Conference, San Francisco, California, vol.2, pp. 653-660, June 24-27, 1996.
- [6] B.Bradshaw, D. Stow and A. Brewster, "High resolution digital imagery and digital terrain data for mapping southern California coastal salt marshes," in Proceedings of the Second International Airborne Remote Sensing Conference, San Francisco, California, vol.2, pp. 662-671, June 24-27, 1996.
- [7] C.F. Hutchinson, "techniques for combining Landsat and ancillary data for digital classification enhancement," Photogrammetric Engineering and Remote Sensing, vol.48, pp.123-130, 1982.
- [8] S.R. Phinn and D.A. Stow, " Monitoring a wetland restoration project based on post-classification comparison of high-resolution image data," in Proceedings of the Fourth International Conference on Remote Sensing for Marine and Coastal Environments, Orlando, Florida, vol.1, pp. 187-196, March 17-19, 1997.

An Introduction to Using Generalized Linear Models to Enhance Satellite-based Change Detection

Jeffrey T. Morisette and Siamak Khorram

Computer Graphic Center

North Carolina State University

Box 7106

Raleigh NC 27695 - 7106

Phone: (919)515-3434 / Fax: (919)515-3439/ e-mail: jtmorise@unity.ncsu.edu

Abstract -- A popular satellite-based land cover change detection technique is to use the spectral information to set up a binary "change/no-change" mask. For each pixel, if there is a big enough difference between the reflectance values for two images acquired at different times, the area represented by that pixel is considered to have changed. The different change detection methods are different in how they determine a "big enough difference". The analyst is left to choose which function of the reflectance values to use and where to set the "change" threshold. This choice is often subjective and affects the accuracy of the change detection. In our paper we explore the use of Generalized Linear Models (GLM) as a way to enhance satellite based change detection by helping determine the most appropriate function of the reflectance values to use then apply the modeling to select the threshold. The main idea is that reflectance values from satellite imagery can be incorporated into a GLM to predict the *probability of change* from one land cover to another and that this method of change detection will provide more information than current change detection methods. A major benefit of using generalized linear models is to determining the significance and most useful combinations of the spectral data for predicting changed areas.

INTRODUCTION

A standard change detection technique for large areas is to use the spectral information from two satellite images acquired at different dates. This method considers individual pixels in an image and compares them to their corresponding pixels from the other image. For each pixel, if the *difference* between the reflectance values from the two images is *big enough*, the area represented by that pixel is considered to have changed. Change detection methods vary in how they determine if the "difference" is "big enough". First there is the question of what is meant by "difference". Is it changes in infrared reflectance? Is it changes in some vegetation index? In general, the "difference" is some function of the reflectance values. For example, the difference might be a simple subtraction of the infrared reflectance for a pixel at one time from the infrared reflectance for the corresponding pixel at another time. The next question is how big is "big enough". This is the issue of choosing a threshold. If the difference is beyond the threshold then the area represented by the pixel is believed to have experienced a change in land

cover sometime between the two images' acquisition. A binary change images is created by labeling those pixels whose functional values are beyond the threshold as changed and those pixels whose functional values are less than the threshold to be unchanged. Choung [1] and Fung and LeDrew [2] have investigated the determination of optimal threshold levels. Both studies reveal an intuitive balance of errors for various threshold levels. For example, with image differencing the lower the threshold, the more non-changed pixels were classified as changed (commission errors); the higher the threshold, the better the chance of changed pixels classified as non-changed (omission errors).

In all studies that create a binary change image, the value at which the threshold is set is somewhat arbitrary. With respect to image differencing, Jensen states that "most analysts prefer to experiment empirically...thus the amount of change...is often subjective and must be based on familiarity with the study area" [3, p.269]. With respect to the application of a binary change mask, the final outcome is dependent on the quality of the mask [3, p.270] and the quality of the mask will depend on the appropriate threshold level for the mask [4]. In order to avoid the subjectivity and arbitrary nature of setting a threshold, we have worked to develop a procedure that can be used as a more analytical method for investigating which function of radiance values is most effective for determining change areas.

In this paper we introduce the use of generalized linear models (GLMs) as a way to enhance satellite based change detection. Generalized Linear Models are a broad class of regression-type models. The use of GLMs has continued to gain attention since they were introduced by Nelder and Wedderburn in 1972 [5]. Unlike standard linear regression, GLMs can be used to model binary or discrete response variables. In this paper, the main idea is that GLMs can be used to regress the binary response of "change/no-change" on the reflectance values from satellite imagery. The binary response is determined from the interpretation of air photos. The radiance values are extracted from the satellite images. The object is to describe how GLMs can be used to enhance satellite-based change detection. This will be done by describing an example change detection utilizing GLMs.

EXAMPLE

First, we collected a sample of "ground truth" or reference data. The sample was based on a set of particular ground locations. For each location we determined if the land cover had changed by interpreting the sample areas on the air photos. We do this from the digitized air photos for 1994 and from the hardcopy air photos for 1988. For each point in the sample we therefore have the land cover type for each time. For each point, if there is a different land cover type for the two time periods then the response for that point is a 1. If there is no change, the sample point will be assigned a response of 0. The next step is to relate the 0 and 1 responses from the sample points to the radiance values from the satellite data. So, for each point in the sample we obtain the satellite radiance values from Landsat TM data from 1988 and 1994 for each sample area. From this, for each sample point, we have a paired set:

*{Change determination from reference data :
Satellite radiance values from corresponding area}*

Similar to a standard regression procedure, for every point in the sample we have one response (the "Y" value) and a set of possible explanatory variable (the "X" values). Using the LOGISTIC procedure in SAS [6] we can determine which function of the radiance values does the best at discriminating between the 0's and 1's – the unchanged and changed sample areas. The objective is to find a function of radiance values that can be used to predict where changes have occurred. Once an appropriate function is found, this function will serve as a model from which to predict the probability of change for the entire satellite image. That is, we use the sample points, for which we have air photo reference data coupled with the radiance values, to develop a model to estimate the probability of change for every pixel in the image.

Fig 1 shows the empirical data in the two dimensions corresponding to the two variables that the GLMs indicated as the most significant indicators of change out of a set of 27 different functions of the radiance values. By using the empirical data and the statistical model we were able to sort through the different possible functions of radiance values and select those which proved to be the most significant for discriminating change areas. The most significant variables were the difference in tassell cap band 5 and a Euclidean distance measure of all tassell-cap bands (expressed in the equation below as "vector-tas"). The GLM procedure produces a model in this two-dimensional space. The fitted logistic model follows the equation:

$$Prob\ of\ change = \frac{e^{-4.2954 - 0.9294 \times dif - tas - band5 + 0.1551 \times vector - tas}}{1 + e^{-4.2954 - 0.9294 \times dif - tas - band5 + 0.1551 \times vector - tas}}$$

Fig 2 shows the surface produced by this model. The model can be incorporated with the image data to produce an

image in which the pixel values represent the probability of change (POC). The POC image shows one of the unique qualities of using GLM for a change detection product: there is no need to set a threshold. Instead the change detection product gives a probabilistic measure for change where values near zero represent a less likely chance of change and value near one represent a higher likelihood of change. Currently, we are research methods to utilize this continuous change product for display and modeling purposes. Fig 3 shows an image that uses the logistic model to produce a POC image. Darker areas represent a low POC with the chances increasing through the lighter colors, which represent the highest POC. Another unique quality of using GLMs is that the logistic model can also be used to estimate the variability of the estimated POC. As with any regression, the logistic model can be used to put a confidence interval on the estimates derived from the model [6]. Fig 4 shows an image representing the same ground area as in Fig 3. In Fig 4 the pixel values represent the width of the confidence interval for the estimated POC. Larger confidence intervals have brighter values. In Fig. 4 we see how the boundaries around change areas are more variable. This makes sense intuitively in that we are less certain of changes in these transitional zones. Fig 4 shows how the GLM can be used to indicate the spatial nature of the variability in the change detection estimates.

CONCLUSIONS

The GLM help to select, from a group of possible functions of radiance values, the most significant function of the radiance values. The resulting model can be used to produce a POC image as well as image which represents the variability of the estimates.

ACKNOWLEDGMENTS

Thanks to NASA's Earth System Science Graduate Student Fellowship Program for support of this research. Thanks to the U.S. National Oceanic and Atmospheric Administration Coastal Change Analysis Program for the project which supplied the data for this research.

REFERENCES

- [1] Choung, Song Hak. 1992. "Wetland Change Detection Using Landsat-5 Thematic Mapper Data in Jackson Hole, Wyoming." Ph.D. Dissertation, University of Idaho, Ulliman, Joseph J.
- [2] Fung, Tung and Ellsworth LeDrew. 1987. "Application of Principal Components Analysis to Change Detection." *Photogrammetric Engineering and Remote Sensing* 53(12):1649-58.
- [3] Jensen, John R. 1996. "Introductory Digital Image Processing: A Remote Sensing Perspective". Second ed. Upper Saddle River, NJ: Prentice Hall.
- [4] Jensen, John R., David J. Cowen, John D. Althausen, Sunil Narumalani, and Oliver Weatherbee. 1993. "An Evaluation of the CoastWatch Change Detection Protocol

in South Carolina." *Photogrammetric Engineering and Remote Sensing* 59(6):1039-46.

- [5] Agresti, Alan. "Categorical Data Analysis." New York: John Wiley and Sons.
- [6] SAS. 1990. *SAS/Stat User's Guide, Version 6, Forth Edition*. Cary NC: SAS Institute Inc.

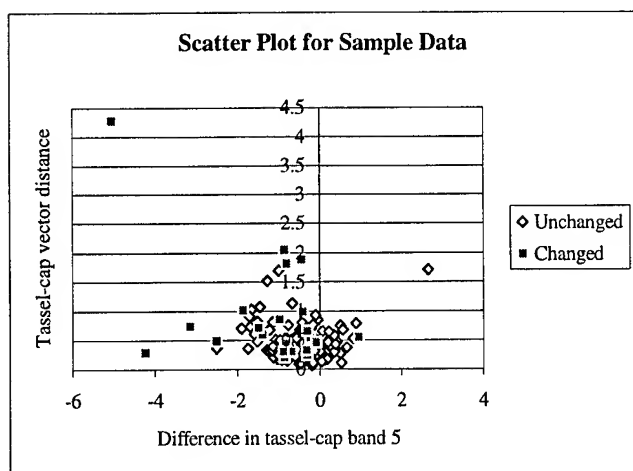


Figure 1: Distribution of empirical data

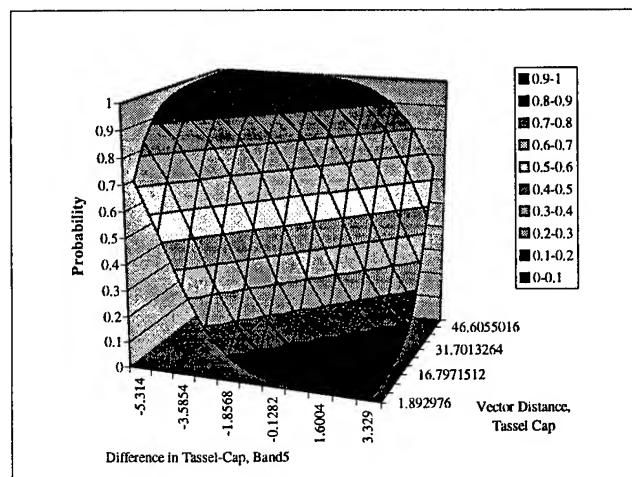


Figure 2: Model surface



Figure 3: Probability of change image



Figure 4: Variability image

IMAGE CLASSIFICATION AND PERFORMANCE EVALUATION OF IRS 1C LISS - III DATA

I. V. Muralikrishna, Member IEEE

Center for Remote Sensing, JNT University,
Hyderabad - 500 028 A. P. INDIA, Fax : +91 40 3397648

ABSTRACT

LISS-III onboard IRS 1C is very much suitable for land cover mapping. LISS-III provides improved spatial resolution compared to Landsat TM. The study aims at improvement of classification accuracy and as such a performance evaluation of IRS 1C LISS-III bands is taken up. A level II classification scheme with 12 classes has been adopted to classify data.

The LISS 1, 2 and 3 combinations provided overall classification accuracy of 93 percent because of higher spatial resolution. The inclusion of SWIR band in classification improved classification of vegetation classes but decreased overall accuracy to 76 percent.

INTRODUCTION

The improvements in spatial and spectral resolution of Remote Sensing Satellite sensors during the last decade

Table 1 SPECTRAL BAND COMPARISON

Spectral regions	LISS - III		Landsat M	
	Band No.	Wave length in microns	Band No.	Wave length in microns
- Blue		---	1	0.45 - 0.52
- Green	1	0.52 - 0.59	2	0.52 - 0.60
- Red	2	0.62 - 0.68	3	0.63 - 0.69
- Near IR	3	0.77 - 0.86	4	0.76 - 0.90
- SWIR	4	1.55 - 1.70	5	1.55 - 1.75
- Thermal		---	6	10.4 - 12.4
- Shortwave		---	7	2.08 - 2.35

has helped in accepting the satellite data for a variety of applications related to natural resources survey and environmental monitoring.

LISS-III Onboard IRS-1C is very much suitable for land cover monitoring and mapping. The LISS-III provides improved spatial resolution compared to Landsat TM. The shortwave infrared band on LISS-III provides enlarged scope for frequent monitoring of large areas for agricultural applications. When spatial detail is important the PAN and LISS-III data provide the best commercially available Remote Sensing data product. The Landsat TM provides multispectral data with 7 bands unlike the LISS-III which provides 4 bands data. A spectral band comparison of TM and LISS-III is given in Table-1.

The spatial resolution of LISS-III is 23 meters for visible and near IR bands and 70 meters for shortwave IR

band. The Wide Field Sensor - WIFS covers 774 x 774 Km area with 180 meters resolution once in 5 days. It is useful for vegetation index computation on par with AVHRR.

A study of the band allocation of LISS-III and TM suggest the scope for high correlation of bands for LISS-III data than TM. This high correlation reduces the dimensionality of data under normal circumstances.

IMAGE CLASSIFICATION

Classification of multispectral image amounts to identifying which pixels contain various spectrally distinct features. Several techniques for classification of multispectral pixels are being used from minimum distance and maximum likelihood classifiers [1] to correlation based approaches such as spectral signatures matching [2].

The present study aims at improvement of classification accuracy for which performance evaluation of LISS-III data has been carried out. The characteristic features of LISS-III and comparison with Landsat TM are given in Table-1 above. The LISS-III Spectral bands are used for computation of basic statistical parameters like mean, standard deviation and covariance matrices. The error matrices for 3 different cases are computed. The classification level adopted is level II and 12 classes have

Table 2 CLASSES IDENTIFIED

Class No.	CLASS	Class No.	CLASS
1.	Deep Water	7.	Fallow Land
2.	Shallow Water	8.	Barren Rock
3.	Agricultural Crop.	9.	Sandy Area
4.	Plantation	10.	Upland with Scrub
5.	Decidious Forest	11.	Settlement
6.	Degraded Forest	12.	Thermal Plant Area

been taken for classification. Maximum likelihood, Mahalanobis, Minimum distance and Parallelepiped classification techniques have been adopted. The standard Digital image processing software package ER MAPPER 5.0 on DEC ALPHA Workstation has been used in the study. In addition ERDAS IMAGINE software package also is used to find out any differences in the software implementation of algorithms for these two popular image processing software packages. The paper reports essentially the classification techniques and performance

Table 3 MAIN SUMMARY REPORT FOR THE TRAINING SITES GIVEN ON INPUT IMAGE

CLASS / REGION	BAND1	BAND2	BAND3
CROP	99.208	39.532	77.987
DECT-FOREST	81.698	38.346	69.013
DEEP-WATER	33.260	38.563	70.458
DEGR-FOREST	61.169	55.302	78.795
FALLOW	86.037	79.795	106.840
PLANTATION	72.104	45.146	77.443
SAND	85.300	98.000	122.500
SCRUB	93.164	86.772	112.500
SETTLEMENT	58.587	56.702	86.125
BARREN AREAS	45.680	39.000	72.600
THERMAL-PLANT	57.442	57.564	86.081
WATER	20.348	36.394	76.062

Table 4 STANDARD DEVIATION SUMMARY REPORT FOR THE TRAINING SITES GIVEN ON INPUT IMAGE

CLASS / REGION	BAND1	BAND2	BAND3
CROP	8.899	2.542	2.468
DECT-FOREST	4.968	3.028	2.709
DEEP-WATER	5.503	2.802	4.203
DEGR-FOREST	4.804	4.154	3.164
FALLOW	4.572	7.940	7.118
PLANTATION	1.479	1.282	1.239
SAND	8.870	18.673	16.761
SCRUB	2.492	4.542	3.746
SETTLEMENT	11.260	6.431	6.473
BARREN AREAS	4.819	1.384	1.871
THERMAL-PLANT	10.174	8.417	8.593
WATER	1.155	0.936	1.489

evaluation of LISS-III bands. The following classes are delineated by using appropriate Ground Truth information through training sets (Table2). The scene corresponds to part of Khammam district in Andhra Pradesh, India.

Table 3 and Table 4 show the mean summary report and standard deviation report for the three bands of LISS-III for all the three classes. A comparison of Classification efficiencies of 4 classification Algorithms namely Maximum Likelihood, Mahalonobis, Minimum Distance and Parallelpiped is presented in Tabel 5.

Out of all classified images and area summary reports it shows that the Parallelpiped algorithm resulted poor classification due to the high mean and low standard deviation for the given training sites. It assigned most of the pixels to thermal-plant class/region and to sand. The maximum likelihood enhanced algorithm, which uses the co-variance did the best nearer to the truth. The minimum distance algorithm resulted more plantation than any other algorithm for the area which is far from truth. The Mahalanobis and Minimum Distance (std. Dev.) algorithms are more or less same in giving the outputs and they are true to some extent with the ground truth.

Table 5 STANDARD DEVIATION SUMMARY REPORT FOR THE TRAINING SITES GIVEN ON INPUT IMAGE

CLASS / REGION	MAX. LIKELIHOOD	MIN. DISTANCE	MAHALA-NOBIS	PARALLEL PIPED
CROP	0.437	0.421	0.443	0.001
DECT-FOREST	4.311	2.696	3.600	0.001
DEEP-WATER	0.155	0.116	0.074	0.001
DEGR-FOREST	0.723	0.947	0.269	0.000
FALLOW	3.396	3.074	2.783	0.000
PLANTATION	1.313	6.061	0.402	0.000
SAND	0.100	0.075	0.093	9.511
SCRUB	0.400	0.393	0.273	0.046
SETTLEMENT	7.286	5.868	7.783	0.000
BARREN AREAS	0.212	0.573	0.055	0.000
THERMAL-PLANT	3.022	0.725	5.630	12.264
WATER	0.469	0.725	5.630	12.264

The band combination 1, 2 and 3 gives overall improved classification accuracy of 93 percent. The incorporation of band 4 in the place of band 1 maintains overall classification accuracy at 91 percent, (ie.,) almost at the same level but the major contribution of band 4 lies in vegetation discrimination though at a lower spatial resolution. That is, both deciduous and degraded forest areas are having classification accuracy of 96 percent while other features like fallow, settlement and scrub areas have reduced classification accuracy 76 percent. The accuracy for the classes like fallow, settlement and scrub area is 91 percent for band combinations 1, 2 and 3.

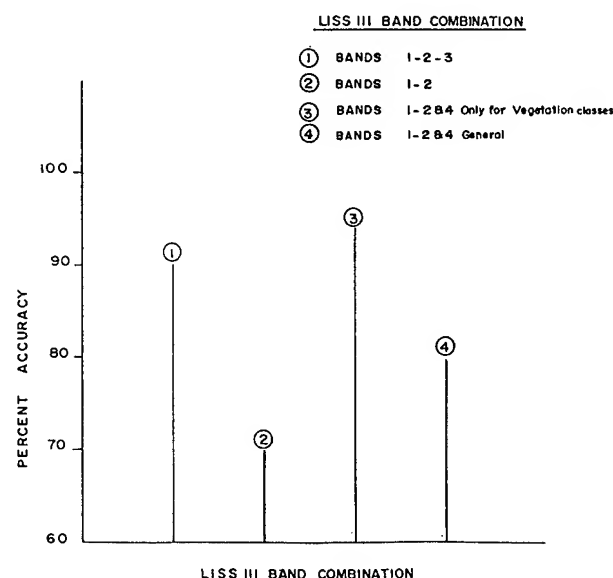


FIG. 1 : PERCENTAGE ACCURACY OF CLASSIFICATION

Fig.1

The details of gray values in Table-3 almost represent the spectral signatures of 12 features taken for classification. Fig.1 shows percentage accuracy of classification. The four vertical lines in the figure show percentage accuracies for each of the different Band Combination. The inclusion of Band 4 has resulted in improved classification accuracy of vegetated areas to almost 96 percent. But the lower spatial resolution of Band 4 decreased over all classification accuracy to less than 76 percent.

REFERENCES

- [1] P. Swain and S. Davis Ed., "Remote Sensing - The Quantitative Approach", NewYork, McGraw Hill - 1983.
- [2] A.S. Mayer, M. Martin et al, "Image Processing Software for Imaging Spectrometry Data Analysis - Remote Sensing of Environment, Vol 24, No.1, pp 201-210, 1988.

* * *

IRS - 1C Applications For Land Use/Land Cover Mapping, Change Detection And Planning

N.C.Gautam
NRSA, Balanagar
Hyderabad - 500 037. India.

ABSTRACT

Remote sensing applications using IRS -1A and IRS-1B data has successfully demonstrated the capabilities in generation of district-wise land use/land cover maps, depicting the information up to level - II on 1 : 250,000 scale which are being used as a basic input in land use planning of the 15 Agro-climatic Zones in the country. The launch of IRS - 1 C on 28 December, 1995 provided a new dimension in the application capabilities, in particular for land use/land cover mapping on various scales and levels for use by a diverse user community. An analysis has been made in the present paper on the

capabilities of Wide-field Imaging Sensor (WiFS), Linear Imaging Self Scanning Sensor - III (LISS - III), Panchromatic sensor data for land use applications. It was observed from the above studies that WiFS data is useful in extracting land use/land cover information at Level - I for use at National/Regional level applications, LISS - III data useful in extraction of information at Level - II/III for use at District/Tehsil level applications and Panchromatic data has the capability to provide information at Level - III/IV for use in Cadastral and Urban applications.

IRS-1C

Considering the need for higher spatial resolution for various applications, especially in the disciplines where the technology has a wider scope to extract information, in addition to the amalgamation of the gains

achieved so far, the IRS 1C satellite was designed and placed in the orbit in December, 1995. The details of sensors on board the satellite and application potentials are given in table 1.

TABLE - 1
SPECIFICATIONS OF IRS 1C SENSORS AND PRINCIPAL APPLICATIONS

Sensor	Ground Resolution (in mts)	Spectral Range	Application
WiFS	188	0.62-0.68 0.77-0.86	Vegetation dynamics, Disaster Mapping, Crop vigour & health monitoring, cropping pattern spectral growth profiles etc.
LISS - III	23	0.52-0.59 0.62-0.68 0.77-0.86	Crop discrimination in mixed crop regions
	70	1.55-1.70	Crop studies/Vegetation dynamics
PAN	5.8	0.50-0.75	Digital Cartography Data Base, Digital Terrain Model, Cadastral Applications/Micro Level Planning Utilities planning/Urban Applications; Updation of topographical maps

POTENTIALS OF IRS 1C SENSORS IN LAND USE/LAND COVER APPLICATIONS

Because of the limitations of scale and resolution the categories lesser than the minimum mappable units like transportation lines, canals and in land use categories where there is least separability were not delineated in the land use/land cover mapping. In order to increase the accuracy of the statistics so derived, a standard procedure

was evolved for refining the same. The availability of a wide range of data from IRS 1 C sensors has broadened the scope for its use in mapping at State/regional, district and village level. Table 2 gives the details of the level of information that is possible to be extracted from IRS 1 C data.

TABLE 2
LEVEL OF INFORMATION POSSIBLE TO BE EXTRACTED
FROM IRS - 1C SENSORS

Sensor	Scale	Minimum Mappable Unit (in mm)	Area (in ha)	Classification Level
WiFS	1:250,000	3 x 3	56.25	Level - I
LISS-III	1:25,000	3 x 3	0.56	Level II/III
PAN	1:10,000	3 x 3	0.009	Level III/IV

LAND USE/LAND COVER ANALYSIS USING IRS 1C DATA

An attempt has been made to analyze the capabilities of WiFS, LISS - III and Panchromatic data for land use/land cover applications. The natural and artificial cover embodied on the land surface offer a varying degree of response which are recorded by the

sensors placed on board satellites in the space. These responses are deciphered to derive information about the surface features based on the image characteristics like tone/colour, texture, shape, size, pattern, location, association and season during which the data is acquired.

METHODOLOGY

Operational methodology of land use/land cover mapping covering large areas using two seasons data was standardized by the Department of Space. The following steps are involved in the classification procedure.

- Data acquisition, loading, merging and georeferencing
- Ground data collection
- Training area definition, signature generation and classification

- Annotation, demarcation of administrative boundaries and cultural features.
- Generation of statistics from the classified outputs.

The process of georeferencing has been done using Survey of India (SOI) topographical maps by identifying the ground control points (GCP's) from the maps and the corresponding points on the image and finally applying the map-image transformation model. Digitization of the administrative and cultural features from the SOI maps

was done to transfer the same on the georeferenced image. Maximum likelihood algorithm available on EASI PACE image analysis software on IBM RS 6000 has been used

for classification followed by extraction of area statistics from the classified outputs.

MULTISPECTRAL CLASSIFICATION OF WiFS DATA

Multispectral classification was attempted for the State of Andhra Pradesh which is covered in parts of three WiFS scenes which were digitally mosaiced to cover the total State. A third channel on texture was derived using the Near Infra Red (NIR) band. The classification has been performed on the three Channels of Red, NIR and the texture channel of NIR. The final output contains ten land use/land cover categories of both Level - I and Level -

II. All the level I categories that are possible to be mapped from IRS 1A/1B LISS-I data could be derived using this sensor. Because of wide swath covering large areas, a synoptic view of the total State is seen. The classes of built-up land, cropland, fallow land, dense forest, open/degraded forest, barren/rocky, upland with or without scrub, waterbodies and sand were classified using this data.

MULTISPECTRAL CLASSIFICATION OF LISS - III DATA

An attempt has been made to classify LISS - III data acquired over Kaziranga National Park and environs in the eastern part of Assam State. The National park which is having a dense vegetation cover has been separated and Normalised Difference Vegetation Index (NDVI) has been applied to classify these areas/ The Maximum Likelihood algorithm has been employed to classify other

categories. Twelve land use/land cover categories were delineated and classified. The classes that resulted from the classification include settlements with plantation, cropland, seasonal fallow, tea gardens, dense vegetation, open forest, sal forest, high grasses, medium grasses, low grasses, water bodies, sand/cloud.

ANALYSIS OF PANCHROMATIC DATA FOR LAND USE/LAND COVER

It is possible to generate data on 1 : 12,500/10,000 scale using IRS 1C Panchromatic data which is of immense use in cadastral and urban applications. Because of high resolution, the land use/land cover features are sharp which enable to separate them distinctly from one another. Fusion of LISS - III and Pan data enabled to discriminate the features in a better way combining the multispectral properties of LISS - III and higher spatial resolution of Pan sensor for achieving greater contextual clarity and separability of surface features. Studies were carried out to analyze the potentials of merged data

around Hyderabad area the results of which highlighted in the identification and mapping of features like roads, bridges, residential lay outs, developments in vacant lands, cart tracks, grape gardens which are possessing a definite shape and appearing in bright red patches, farm houses etc. The results of this analysis demonstrates the use of this data, especially when merged with multi spectral data of other sensor will enable to extract information at cadastral level with a reasonably good accuracy.

CONCLUSION

The evaluation of IRS 1 C sensors has highlighted the invigorating potential of mapping land use/land cover to meet the users requirements at different levels. The availability of information at cadastral level is a major breakthrough in the application of satellite data for

microlevel planning. The varied advantage and application potential of data acquired from the payload of IRS 1 C will be of immense value for the planners and decision makers in the years to come.

Contrast Enhancement of IRS - 1C LISS Data

* I.Ramesh Babu and ** I.V.Murali Krishna Member IEEE
 * Dept. of Computer Science & Engg., Nagarjuna University,
 Nagarjuna Nagar - 522 510, A.P INDIA. Fax : + 91 866 842460
 ** Centre for Remote Sensing, JNT University,
 Hyderabad - 500 028. A.P. INDIA. Fax : + 91 40 3397648

ABSTRACT

Histogram modification technique is regularly applied to improve contrast and feature discrimination. The spectral components of any feature are mutually dependent and any histogram overlooking this aspect will not provide scope for multispectral data utilisation. The Remote Sensing Satellite IRS-1C has three sensors on board, namely, Wide Field Imaging Sensor (WIFS), LISS-III and PAN Sensor, with varying spatial and spectral resolutions. The maintenance of relative intensity levels is a major casualty in case of Histogram Equalization of low contrast images of high resolution sensor LISS-III. This results in some sort of defocussing of image for low contrast original data. An approach that is possible to apply without causing any image with patchiness is described in this paper. Basically, the idea underlying this approach is to perform three independent transformations on the gray level of any input pixel and manipulate the histogram while performing the Histogram Equalization. Thus the approach adopted in the study is supposed not to alter the spectral signature as may be possible in automated Histogram Equalization.

INTRODUCTION

The Indian Remote Sensing Satellite IRS-1C, launched in December 1995, was developed by the Indian Space Research Organisation to observe the surface of the earth. The sensors on board of the satellite are Wide Field Imaging Sensor, LISS-III a Multispectral Scanner and PAN a Panchromatic Sensor. The sensor characteristics are given in table -1.

HISTOGRAM EQUALISATION CONCEPT

The histogram of a digital image with gray levels in the range 0 to 255 is a discrete function

Table -1 IRS IC SENSORS

SATELLITE	LAUNCH	INSTRUMENTS	SPATIAL RESOLUTION	SWATH	REPEAT COVERAGE
IRC-1C	1995	LISS-III	23.5M VNIR	142 K.M	24Days
		Multispectral	70.5M SWIR	148 K.M	
		WIFS Wide Field Panchromatic	188M 5.8M	774 K.M 70 K.M	5Days 5Days

$$P = p(g_k) = \frac{n_k}{n} \quad (1)$$

where g_k is the k th gray level and n_k is the frequency pixels at gray level k and n is total number of pixels and $k = 0$ to 255 [1]. Here 'P' or 'p' gives probability of a given gray level occurrence. Generally the shape of histogram does not deal with contents of the image but it gives information about the need and scope for contrast enhancement. While defining the Histogram and Probability of gray level occurrence the analysis carried out in [1] is adopted in the present study and the salient features are mentioned before discussing actual case study.

By normalizing pixel gray levels so that they lie in the interval [0,1] we can assume that the pixel values are continuous. Here let g represent the gray levels in the image to be enhanced. $g = 0$ and $g = 1$ represent black and white respectively. For any value of g in the interval [0,1], we assume that $b = f(g)$ so that a pixel with gray level g is represented in the image as a pixel with gray level b . The inverse transformation from b to g also can be defined. Now a transformation function $b = f(g)$ is defined by modifying the appearance of an image and by controlling the probability density function of its gray levels via the transformation function $f(g)$. From elementary probability theory if probability density function $P_g(g)$ and $f(g)$ are known, the probability density function of the transformed gray levels is [1]

$$P_b(b) = \left[P_g(g) \frac{dg}{db} \right] \quad (2)$$

Here g is the level obtained from inverse transformation of $b = f(g)$ i.e., $g = f^{-1}(b)$. The value of $P_b(b) = 1$ in the interval $0 \leq b \leq 1$ suggest that the $P_b(b)$ is of uniform density in the interval of definition of the transformed variable b . This indicates that using a transformation function equal to the cumulative distribution of 'g' produces an image whose grey levels have a uniform density. In terms of enhancement this result implies an increase in the dynamic range of the pixels, which can have a considerable effect in the appearance of an image. In order to be useful for digital image processing the above concept is formulated in discrete form [1]. The probability for gray levels that take discrete values can be defined as

$$P_g(g_k) = \frac{n_k}{n} \quad (3)$$

Here $0 \leq g_k \leq 1$ and $k = 0$ to 255, $P_g(g_k)$ is probability of k th

grey level, n_k is gray level frequency and n is total number of pixels. A variation of $P_g(g_k)$ with respect to g_k is called histogram and the technique of obtaining uniform histogram is called Histogram Equalization. The discrete form of transformation $b = f(g)$ is defined as

$$b_k = f(g_k) = \sum_{j=0}^k P_j(g) = \sum_{j=0}^k \frac{n_j}{n} \quad (4)$$

Here $0 \leq g_k \leq 1$ and $k=0$ to 255 . The function $f(g_k)$ can be computed by using the above equation. In this process of Histogram Equalization, the gray levels of the image are spread out and always reach white (i.e. gray level $k = 255$). This process increases the dynamic range of gray levels and consequently produces an increase in image contrast. However in images with low contrast or with a narrow histogram, the dynamic range stretching results in isolated grains on the image. This appears like defocussed region on the image. This is also defined as patchiness [1]. For the sake of discussion in this paper this defocussing is referred to as patchiness. Essentially Histogram Equalization does not provide scope for interactive image enhancement. The method is generally capable of producing only one result namely an approximation to a uniform histogram. This sort of defocussing is found to be very significant for Remote Sensing data obtained from high resolution sensors like LISS-III. Let us digress a little here to identify the reason for this.

The sensor LISS-III is essentially a 3 band sensor in the visible and near infrared region with highly correlated band allocations. In such a case the spectral signature variations of the earth surface feature in these three bands need to be maintained also with reference to band ratio values. That is the relative intensities of the earth features are to be maintained even after enhancement of the low contrast image. The maintenance of relative intensity levels is a major casualty in case of Histogram Equalization of low contrast images of high resolution sensor LISS-III. The patchiness reported here could be due to this reason as found in the present analysis of LISS-III data through the study is not exhaustive. An approach that is possible to apply without such patchiness is described in this paper. Basically, the idea underlying this approach is to perform independent transformations on the gray level of any input pixel and manipulate the histogram while performing the Histogram Equalization.

HISTOGRAM MANIPULATION

In the conventional RGB color model each color appears in its primary spectral value of Red (R), Green (G) and Blue (B). Images in the RGB color model consist of three independent image planes, one for each primary color. When fed into an RGB monitor, these three images combine to produce a composite color image. Because of the presence of three images and because Histogram Equalization deals only

with intensity values, the obvious approach is to subject each image plane to Histogram Equalization independently. However, the intensities in all the three image planes will be altered differently resulting in change of the relative intensities between them. The net result is that the important color properties in the image such as vegetation, tones, water bodies and built-up areas when viewed on an RGB monitor. RGB monitor are found to get blurred or create patchiness. Fig.1, is raw multispectral image of LISS-III representing visible and near infrared wavelengths. The technique of Histogram Equalization is applied on this bright and low contrast image. Fig.2, is image after Histogram Equalization



Fig.1 Raw Data of IRS LISS Image



Fig.2 Histogram Equalized Image Conventional Approach

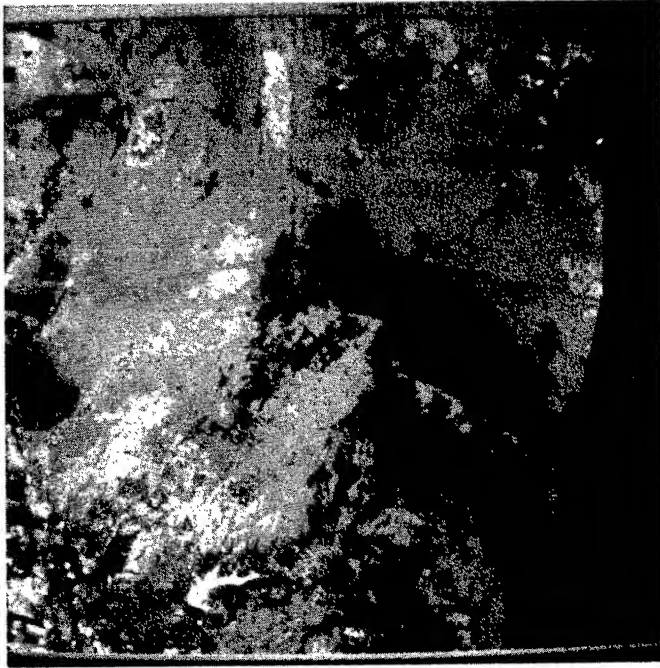


Fig.3 Histogram Manipulated Image

with bright patches in the image. Now the discrete value based transform (4) is applied to band 1 data of the sensor. Independently the band ratio values of Band 1 / Band 2, Band 1 / Band 3 are calculated. The conventional technique of Band Ratioing not only minimizes the effects of environmental factors, but also provides unique information

not available in any single band. The use of Band Ratioing is envisaged here so that the relative intensity levels of the image are maintained even after Histogram Equalization. Thus the histogram for each band of the Multispectral data is evaluated. The three bands for display in the RGB color cube are selected. The band with narrowest histogram is taken and the conventional technique of Histogram Equalization is applied as given above. The histograms for Band 2 and Band 3 are now computed respectively multiplying the Histogram Equalized Band 1 gray values with ratio values of Band 1 / Band 2 and Band 1 / Band 3. Thus the approach adopted in the study is supposed not to alter the spectral signature as may be possible in automated Histogram Equalization. Thus the modified histogram gray values are taken and are multiplied by band ratioed values derived earlier as Band 1/Band 2 and Band 1/ Band 3. Thus the three color planes of RGB systems are assigned three band data which give a multispectral image with high contrast and still maintaining the spectral variation characteristics of the original data. Fig.3, is the image obtained by combination of Histogram manipulation as described above. The contrast in the image is significant.

REFERENCES

- [1] Rafael C Gonzalez and Richard E Woods, "Digital Image Processing", Addison-Wesley Publishing Company, 1993, pp.171-185.

Angular Signatures of NASA/NOAA Pathfinder AVHRR Land Data and Applications to Land Cover Identification

Shunlin Liang (IEEE member)[†], John R. G. Townshend[‡]

[†] [‡] Laboratory for Global Remote Sensing Studies, Department of Geography

[‡] University of Maryland Institute for Advanced Computer Studies (UMIACS)

University of Maryland, College Park, MD 20742, USA

(301)-314-9299 (Fax)

[†] (301)-405-4556 (Phone), sliang@geog.umd.edu

[‡] (301)-405-4558 (Phone), jt59@umail.umd.edu

ABSTRACT -- The angular signatures of the NASA/NOAA Pathfinder AVHRR Land data set are examined by applying several widely used empirical models and by developing a new temporal angular model. These models are compared for 10 different cover types, and results show that the temporal model performs much better than other models. The coefficients of the temporal angular model are applied to classify those cover types. The classification rate with two channel inputs is about 97% based on the quadratic discriminant analysis. If a single channel is used, the thermal channels are better than the visible and near-Infrared channels.

I. INTRODUCTION

Multitemporal Advanced Very High Resolution Radiometer (AVHRR) data from the NOAA series polar orbiters have been widely used for a variety of applications on global studies. In different applications, angular information was treated as either noise or valuable signatures. Many studies are reported in the literature correcting bidirectional effects for vegetation indices. On the other hand, bidirectional reflectance data contain rich information about surface characteristics in the angular dimension. Either option requires an effective bidirectional model to characterize the angular behavior.

In this study, a temporal angular model is developed in which a temporal component is approximated by a Fourier series and an angular component is expressed by the modified Walthall model [1]. This model has been compared with some other empirical models and gives the best fit to all data points from NASA/NOAA Pathfinder

AVHRR Land (PAL) data. The coefficients are used for land cover classification.

II. MODEL DESCRIPTIONS

The existing models are suitable for signatures without any temporal variations. When we assemble data from temporal profiles, most cover types have obvious seasonal variations. Thus, we have made the coefficients of these empirical angular models a function of the observation time. When the number of observations is large enough, the model should look like

$$R(t, \Omega_0, \Omega) = f[a_i(t), \Omega_0, \Omega]$$

where $a_i(t)$ are coefficients dependent on time. In this study, the number of observations is up to 48. It is found that the following model can significantly improve model fitting

$$R(t, \Omega_0, \Omega) = g(t) f(\Omega_0, \Omega) \quad (1)$$

or

$$R(t, \Omega_0, \Omega) = g(t) + f(\Omega_0, \Omega) \quad (2)$$

where $g(t)$ is the function only dependent on time, and $f(\Omega_0, \Omega)$ is the ordinary angular model. It is found that the following model fits our data reasonably well.

The model consists of two parts: a temporal component and an angular component. The first component is represented by a low-order Fourier series, and the second component by the modified Walthall model. The temporal series $R(t, \Omega, \Omega_0)$ can

be expressed

$$R(t, \Omega, \Omega_0) = g(t) + f(\Omega, \Omega_0)$$

$$g(t) = \sum_{i=0}^N \left[a_i \cos(2\pi i \frac{t-1}{12}) + b_i \sin(2\pi i \frac{t-1}{12}) \right]$$

$$f(\Omega, \Omega_0) = c_0 + c_1 \theta_0 \cos(\phi - \phi_0) + c_2 \theta_0^2 \theta^2 + c_3 (\theta_0^2 + \theta^2)$$

where t is the month of the year. Our experiments indicated that $N=3$ is sufficient for our purposes. The temporal series $R(t, \Omega, \Omega_0)$ could be reflectance of channels 1 and 2, NDVI or brightness temperature of channels 4 and 5. Thus, the equation contains 8 coefficients to be estimated.

III. PATHFINDER AVHRR LAND DATA SET

The NASA/NOAA sponsored AVHRR Land Pathfinder data set has been created to act as a precursor for the international Earth Observing Systems (EOS) [2]. There are two problems associated with the current Pathfinder data. First, the solar zenith angles were not correctly calculated. Second, the Rayleigh scattering corrections contained errors. Processing mistakes found are currently being corrected in the University of Maryland. The four-year corrected, monthly composite dataset from 1983-1996 are used in this study.

Based on hundreds of Landsat images (primarily MSS imagery), several dozens of cover types have been confidently identified [3]. This global training data set contains over 9000 pixels. To avoid cloudy impacts, we only picked 10 cover types that have a small amount of cloud contamination. If the number of clear observations every year is smaller than a threshold, we throw that pixel away. Thus, total 2312 pixels were selected in this study for model training and validation.

IV. DATA ANALYSIS

The temporal angular model was compared with the modified Walthall model, Roujean model [4], Legendre model (the angular signatures are expanded by the associated Legendre function up to second order), and the MODIS kernel models [5].

After a series of model comparisons, it was found that the temporal angular model performs the best in all cases. Fig. 1 presents median values of the correlation coefficients between observed

and fitted data for different cover types. The MODIS kernel models perform very similar to the Roujean model.

In the following, we will demonstrate how these coefficients derived from the temporal model can be effectively used for global land cover classification.

Two classification methods are explored in this study: Linear discriminant analysis (LDA) and Quadratic discriminant analysis (QDA). To evaluate the classification accuracy, the traditional approach is to divide the training data set into two parts, one for training and one for validation [6]. If the total training size is not large enough, the alternative approach is so-called cross validation. A 10-fold cross-validation is applied in this study. The idea is quite simple, the training size is split into 10 (roughly) equally sized parts. We can then use 9 to train the classifier and test them on the tenth. The procedure is repeated 10 times and the result is averaged.

The averaged misclassification rates for different number input coefficients are shown in Fig. 2. If one channel is specified, we actually input 8 coefficients into the classifiers. From this figure, we can see that the QDA performs much better than LDA. If one channel is used, thermal channels (4 and 5) generate lower misclassification rate than the first two channels (1 and 2) probably because not much scattering occurs in the thermal channels. Although three-channel combinations (channels 1,2,4 or 1,2,5) produce the best results, it seems a two-channel combination is a good choice since a much smaller number of coefficients are required. Any two-channel combination provides about 97 percent classification rate if QDA is employed.

V. SUMMARIES AND DISCUSSIONS

Angular signatures of remotely sensed data contains rich information about surface and atmospheric characteristics. A series of semi-empirical or empirical models are fitted to the NASA/NOAA Pathfinder AVHRR Land data set. It is found that the temporal model works best for 10 cover types (some have seasonal variations and other do not). All models are found to work better in the thermal channels (4 and 5) than the visible and near-Infrared channels (4 and 5). Overall, the temporal

model performs the best. The coefficients of the temporal model are used to classify the land cover types based on the linear and quadratic discriminant analysis. If one channel is used, the thermal channels work better than the visible and near-IR channels, but the two channel combinations are better. The mis-classification rate is about 3 percent based on the quadratic discriminant analysis if any two channels are used. Employing more channels would not improve classification results significantly.

MODIS has very similar viewing geometry to AVHRR, although much more channels will be available. The algorithms for presenting surface angular patterns of AVHRR data will also be very helpful to MODIS data analysis. Long-term records of AVHRR observations will also be of value to MODIS data that need to be integrated initially with precursors data to disentangle temporal trends.

VI. ACKNOWLEDGEMENTS

The authors like to thank Dr. Ruth DeFries, Mr. R. Sohlberg and Mr. M. Hansen for their help in data processing and training dataset evaluations. This study was supported in part by the U.S. National Science Foundation under grant BIR-9318183 and NASA under grant NAS-596060.

VII. REFERENCES

- [1] Nilson, T. and A. Kuusk, "A reflectance model for the homogeneous plant canopy and its inversion," *Remote Sens. Environ.*, vol. 27, pp. 157-167, 1989.
- [2] M. E. James, and S. Kalluri, "The Pathfinder AVHRR land data set: An improved coarse resolution data set for terrestrial monitoring," *Int. J. Remote Sens.*, vol. 15, pp. 3347-3364, 1994.
- [3] R. DeFries, M. Hansen, J. R. G. Townshend, and R. Sohlberg, Global Land Cover Classifications at 8 km Spatial Resolution. Part 1: Training and Validation Data Derived from Landsat Imagery, *in prep.*, 1997.
- [4] J. L. Roujean, M. Leroy, and P. Y. Deschamps, "A bidirectional reflectance model of the earth's surface for the correction of remote sensing data," *J. Geophys.*

Res., vol. 97, pp. 20455-20468, 1992.

- [5] W. Wanner, X. Li, and A. H. Strahler, "On the derivation of kernels for kernel-driven models of bidirectional reflectance," *J. Geophys. Res.*, vol. 100, pp. 21077-21089, 1995.
- [6] Jensen, J. R., *Introductory Digital Image Processing*, 1996

Fig. 1. Comparisons of median values of correlation coefficients.

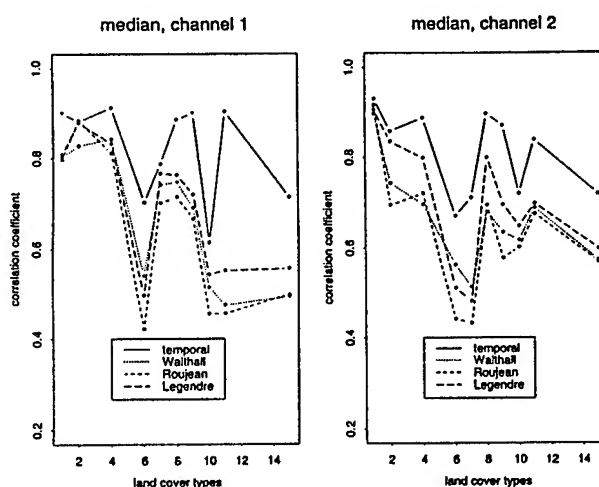
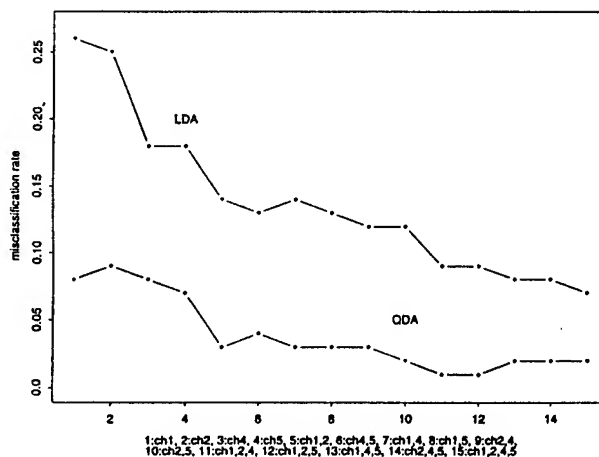


Fig.2. Misclassification rate of two classifiers with different numbers of inputs.



Spatial Assessment of Soil Properties for Agricultural Land Using Remotely Sensed Imagery, Relief Analysis and GIS

Thomas M. Selige

GSF-National Research Centre for Environment and Health

PoBox 1129; Ingolstaedter Landstrasse 1; Neuherberg; D-85758 Oberschleissheim; Germany

Tel.: +49 89 3187 2255; Fax.: +49 89 3187 3369; Email: selige@gsf.de

Abstract – This paper presents a methodological framework and has applications in sustainable land use planning and the management of agroecosystems. On examples of a mountain range in Germany airborne remote sensing and digital relief analysis have been used to improve the inventory of soil heterogeneity and to assess its impact on crop growth. A bioindicative model conception has been developed, based on cause and effect relations of soil-plant system. Soil pattern has been described using remote sensing detection and developed bioindicative transferfunctions. The detected landscape pattern has been analysed using digital relief analysis to derive local principles of soil occurrence.

INTRODUCTION

Soil is a basic natural resource for life on land. Soil can not be procreated. Lost soil is not renewable. Its functionality is difficult to recover. Based on these cognitions a global rule for human activities can be derived:

Sustainable development constrains sustainable land use
constrains sustainable soil use [1].

In heterogeneous landscapes, the high variability of crop stand and yield within most fields can be easily detected. This is mainly caused by variations in relief, soil properties and local drainage conditions and has effects on water balance and nutrient consumption. The local site resources will be utilized in a different manner. On the level of practical farm management the local distinction of soil sites has to be considered. Therefore, detailed high resolution spatial information about the site properties is required for land management to be conformable with sustainable soil use. Hence these studies follow up to the question:

Where in landscapes which soil properties do occur?

METHODOLOGY

The mountain range testsite is characterized by long extended, gently inclined hilltops, interrupted by valley cuts with steep slopes. A high diversity is characteristic for geology and soils in this area. Geology is dominated by Devonian limestones, calcites and dolomites of Zechstein, sediments of triassic bunter and quartarian deposits as well as solifluction layers and aeolian deposition of loess. The diversity of soil is related to the variety in relief and geology. The dominating soil is eutric Cambisol of different development stage. The hilltops are mainly of rendzic Leptosol. In hollows and valleys cummulic Anthosol is predominating. On

loess covered eastside slopes Luvisol has developed. The land use is arable farming of 80% cover.

An extended ground truth program to record data about the soil properties, plant development, crop stand condition and land use has been implemented. Airborne scanner overflights have been undertaken by German Space and Aircraft Establishment (DLR). The 11-channel line-scanner records wavebands of visible, near, middle and thermal infrared wavelength. By aerial photos photogrammetrically produced contour maps of scale 1:5000 have been used to derive a 12.5m resolution digital terrain model (DTM) by finite element algorithms. Digital relief analysis was based on different tools as SARA [2] and DRM [3]. All point, vector and raster data are linked to GIS.

RESULTS

soil plant interactions

To detect soil quality by remote sensing it has to be taken into account that soil is predominantly covered by vegetation and its surface is most of time not visible. Also essential soil properties can not be discerned from soil surface appearance. On the other hand it is well known that crop growth depends on soil attributes. Hence it should be able to use the phenotype of crop stand as indication of soil properties.

Penetrating the soil profile with their root system crops are discovering the availability of soil resources as water and nutrients. A well known regulatory feedback system of phytohormones exist between roots and crop stand. Because of its root system behavior plant can be used as biophysical probe. Because of the crop stand reaction it is a bioindicator for soil productive and regulatory function. Biomass is an important parameter to describe the crop stand grade. But biomass sampling on representative soil sites is time consuming.

Therefore, an estimation method has been developed to assess the crop stand. Biomass measurement and crop stand graduation by estimation were found to be highly correlated. This gives the possibility of fast and also accurate ground truth sampling.

For regions with negative water balance during growing season the availability of soil water capacity (AWC) takes an important role for plant production. Plant can only utilize the available water capacity of root zone (AWC_{rz}). This soil parameter has been recognized to be the central regulatory attribute of soil productive function. The AWC_{rz} correlates highly with the crop stand grade (Fig. 1). These results were

also discovered by investigations on recultivated open pit mining areas [4] and on the tertiary hilly landscape of Upper Bavaria [5]. The crop stand conditions have been recognized to be indicative for soil properties at specific time of growing season. The studies included winter wheat, sugar beet, winter barley and rye as suitable bioindicative crops.

remote sensing

Airborne remote sensing has been used in view of time flexibility and spatial resolution. These requirements had to be made to ensure overflights at the best indicative stage of plant development. The tessellated soil pattern with typical variability of less than 20m requires a spatial resolution of less than 5m.

Remote sensing is used to develop a monitoring system to detect the soil depend crop stand grade and to derive an assessment of soil productive and regulatory functions. Biophysical processes will be spatially quantified by analysis of the cause and effect relations between soil and plant. These relations will be used as biophysical transfer functions to calibrate remote sensing data as quantitative expression of soil condition. By this conceptional way research of biophysical processes of soil plant system can be integrated to spatial studies.

It was the task to delimitate quantitative subclasses. The regression function of figure 2 can be used to transform spectral values of the airborne detected remotely sensed imagery to spatial maps of AWC_{rz} (Fig. 3).

To improve the classification of quantitative attributes a method using singular value decomposition and key vector analysis has been developed [6]. This technique gives the opportunity to use only those channels who separate an object class from the others and allow simultaneously to derive subclasses of quantities as biomass.

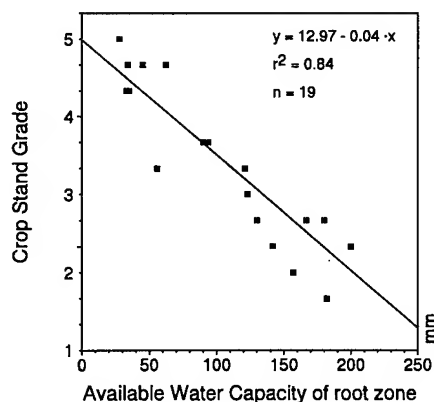


Figure 1: Crop stand grade of winter wheat in dependence of available water capacity of root zone

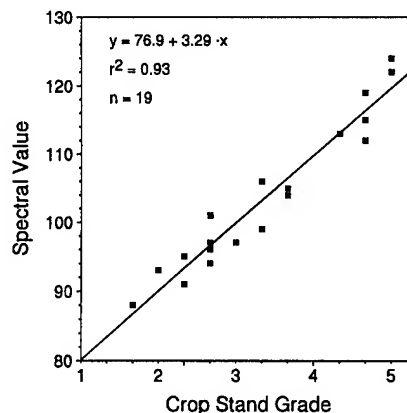


Figure 2: Relation between crop stand grade and the spectral characteristic by a combination of channel 5, 9, 10 and 11

relief analysis

Aim of the geomorphological relief analysis is to subdivide regions by the terrain shape. This is based on objective algorithms considering the process related neighborhood of sites. As important geofactor of soil formation the relief determines in many areas the spatial soil distribution. Hence follows that the integration of digital relief analysis and GIS-based modelling can improve the regionalisation of soil occurrence by digital terrain model. These first studies were focused on the delineation of complex relief units by pedologically oriented relief analysis.

The combination of weighted vertical and transversal curvature with slope has been discovered to give suitable relief units which relate to soil (Fig. 4). Between soil pattern and relief units a close conformity was found. The relief units correlate with the pattern derived from remote sensing classification. For soil related relief analysis two major tasks were ascertained to be focused on:

1. The quality of 12.5 m DTM was suitable to describe and to delineate the landscape into functional units. But the field internal subdivision of gentle inclined slopes has been detected as problem.
2. The used GIS method of overlay-intersection creates problems at uncertain boundaries of units. As more parameter are in use as less suitable this method will be.
3. The relief analysis must be calibrated by the knowledge about the soil landscape. It has to be joined with soil mapping.

Based on objective algorithms of multivariate clustering and neighborhood methods like complete-linkage it will be investigated to derive unbiased conceptional soil maps. Lateral processes and regional aspects as aeolian deposit have to be considered more. For that GIS modelling will be the used tool.

CONCLUSIONS

Three conceptional steps of research have been integrated by these studies:

1. Analysis of biophysical processes by investigation of soil-plant relations.
2. Description of functional and process related pattern by remote sensing detection and bioindicative transfer-functions.
3. Pattern analysis by pedologically oriented relief analysis to delineate complex relief-soil units.

Remote sensing contributes significantly to improve the spatial information concerning functional soil properties and also for the characterisation of arable land for extended regions. The integration of remotely sensed maps and derived maps from geomorphological analysis into land information systems has been proved to be complementary and correlate with the results produced by the various techniques. This methodology gives a broader spatial base to land information and planning systems at state authorities, local administrative unions of farmers, communities, water resource management and agricultural consultants, for to protect the natural resources of densely populated landscapes.

REFERENCES

- [1] H. Eger, E. Fleischhauer, A. Hebel and W. Sombroek, "Taking Action for Sustainable Land-use: Results from 9th ISCO Conference in Bonn," *Ambio*, vol. 25, no. 8, Stockholm: Royal Swed. Akad. Sci., 1996, pp. 480-483.
- [2] B. Kleefisch and R. Köthe, "Computerized pedological interpretation of digital relief data, [Wege zur rechnergestützten bodenkundlichen Interpretation digitaler Reliefdaten]," *Geol. Jb.*, F 27, 1993, pp.59-122.
- [3] J. Bauer, H., Rodenburg and H.-R. Bork, "Digital relief model as requirement to a deterministic matter and water flow model, [Ein digitales Reliefmodell als Voraussetzung für ein deterministisches Modell der Wasser- und Stoff-Flüsse]," *Landschafts- und Landschaftsökologie*, Vol. 10, 1985, pp. 1-15.
- [4] Th. Selige and Th. Vorderbrügge, "Root and yield as Indicators of Soil Structure," in "Root Ecology and its Practical Application," in, L. Kutschera, E. Hübl, E. Lichtenegger, H. Persson, M. Sobotik, Eds., Klagenfurt: Verein für Wurzelforschung, 1992, pp. 121-124.
- [5] M. Wehrhan and Th. Selige, "Airborne Remote Sensing to Support Precision Farming," in press.
- [6] G. Herries, Th. Selige and S. Danaher, "Singular Value Decomposition in Applied Remote Sensing," *Proc. of IEEE-Symp. on Image Process. for Rem. Sens.*, London: IEE Press, 1996, pp. 24-29.

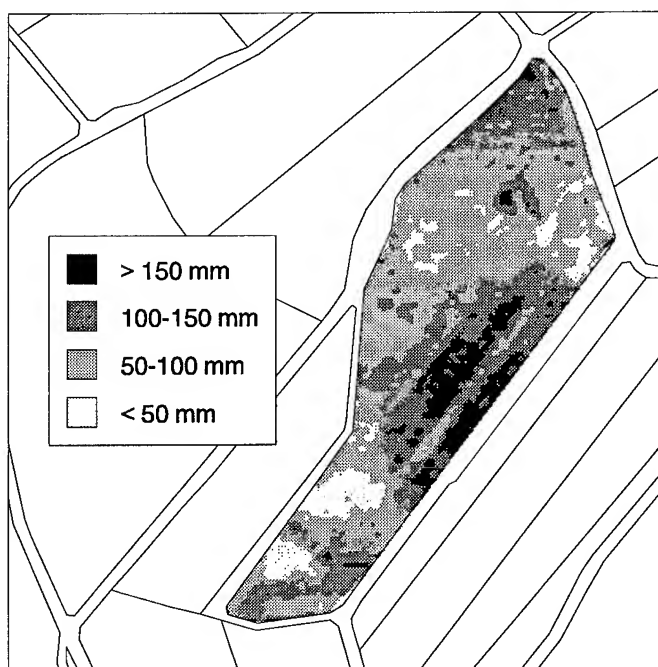


Figure 3: Classified image of winter wheat field 2409 with four classes of available water capacity of root zone (AWC_{rz})

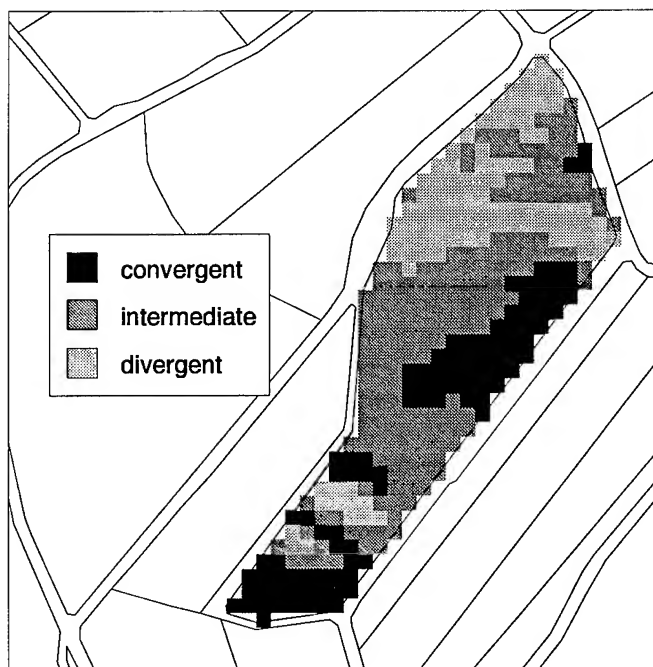


Figure 4: Delineated relief units of field 2409 using vertical and transversal curvature with slope

A MODELLING STUDY OF BRDF CANOPY AND RADIATION REGIME FOR BOREAL FORESTS

F. Zagolski ⁽¹⁾, *P. Guillevic* ⁽²⁾, *J.P. Gastellu-Etchegorry* ⁽²⁾,

C. Gaillard ⁽³⁾, *D. Deering* ⁽⁴⁾, *M. Leroy* ⁽²⁾

(1) PRIVATEERS N.V., Private Experts in Remote Sensing,
De Weaver Drive 42, Philipsburg,
St Maarten - Netherlands Antilles.
c/o 228 Gillespie street, Sherbrooke - Canada J1H-4X3.
Phone / Fax (on demand): (+1) 819-569-7632
E-mail: zagolski@interlinx.qc.ca

(2) Centre d'Etudes Spatiales de la Biosphère (CESBIO),
(CNES / CNRS / UPS)
18, Av. Edouard Belin,
31401 - Toulouse cedex 4 - France.

(3) Centre d'Applications et de Recherches en Télédétection,
Université de Sherbrooke, Sherbrooke - Canada J1K-2R1.

(4) NASA / Goddard Space Flight Center,
Greenbelt - MD 20771 - USA.

ABSTRACT: This paper presents a new radiative transfer modelling approach, for retrieving information on forest structural characteristics and photosynthetic activity, both directly through an accurate computation of 3-D Photosynthetically Active Radiation (PAR) regime, and indirectly with the simulation of remote sensing measurements. DART model was used for investigating spectral behavior and PAR environment of boreal forest in Canada. Main features of BRDF (Bidirectional Reflectance Factor Distribution) anisotropy are clearly verified. Comparison between simulated and measured (PARABOLA, CASI, POLDER) BRDFs stresses the potential of DART, but also the importance and difficulty to use accurate field data. Differences in forest architectures induce distinct PAR transmission and 3-D absorbed PAR (APAR), and their influence on canopy photosynthesis is illustrated with the coupling of the DART model with a leaf model.

INTRODUCTION

Radiation regime within forest canopies, and more especially PAR, plays an important role in relation to forest architecture and dynamic. This is particularly emphasized by the existence of its close relationship to dry matter production which is mainly dependent on incoming PAR, on the fraction of PAR intercepted (IPAR) by the foliage and on the efficiency of its use for dry matter production. Past empirical studies already proved the great potential of remote sensing for such investigations [1]. However, relationships derived from these works present often variabilities dependant on the study area or illumination or viewing configurations that makes difficult the prediction.

In this context, we used a 3-D radiatif transfer model, DART ('Discrete Anisotropic Radiative Transfer'), that

takes into account both forest characteristics and illumination and viewing configurations [2]. This model operates on realistic discrete scene representations with any heterogeneity degree. Radiation propagation is tracked with the discrete ordinate method and major electromagnetic interaction mechanisms (*i.e.*, single and multiple scattering, specular reflectance, variable sky conditions, *etc.*) of soils, leaves, trunks and water are simulated. DART provides BRDF, directional images and the within stand radiation regime (*i.e.*, IPAR and APAR).

This modelling approach was applied to boreal forest covers, in Canada. A sensitivity analysis to experimental conditions (*i.e.*, scale of analysis, illumination and viewing directions, *etc.*) was conducted with relationships between reflectances and canopy APAR. Moreover simulated boreal forest BRDFs were compared to experimental measurements (PARABOLA, CASI, POLDER). Finally, a preliminary analysis of canopy photosynthesis was conducted through the coupling of DART model with a leaf model [3].

STUDY AREA AND FIELD DATA

Test sites are located in the Southern Study Area (SSA) of BOREAS (Boreal Ecosystem-Atmosphere Study) project [4], in Canada. They are very well documented (location and tree dimensions, leaf optical properties, *etc.*). Canopy BRDFs were measured over three primary boreal forest types, Old Black Spruce (OBS), Old Jack Pine (OJP) and Old Aspen (OA), in visible (VIS) and near-infrared (NIR) region simultaneously with in-situ PARABOLA (Portable Apparatus for Rapid Acquisitions of Land and Atmosphere) instrument [5] and two airborne imaging spectrometers, POLDER (POLarization Directionality of Earth's Reflectances) [6] and CASI (Compact Airborne Spectrographic Imager) [7], at several dates in spring and summer 1994.

DART, PARABOLA, CASI AND POLDER BRDF

DART simulated BRDFs (Fig. 1) were compared both with actual canopy BRDFs, *i.e.* PARABOLA and atmospherically and geometrically corrected POLDER and CASI derived BRDFs. Moreover, in order to assess the impact of canopy heterogeneity on BRDF, we also simulated BRDF with the SAIL model [8]. Optical and structural parameters are from the BORIS data base [4] [9].

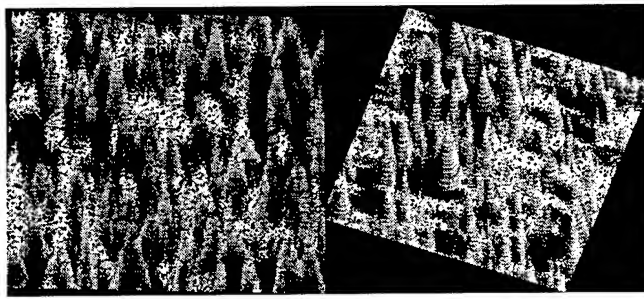


Figure 1: DART images of OBS ($\lambda=670\text{nm}$, $\theta_s=33^\circ$)

Figure 2 depicts NIR PARABOLA, POLDER, DART and SAIL BRDF of OBS. Mean VIS (NIR) reflectances are 3% (15%) for OBS, 3% (16%) for OJP, and 2% (36%) for OA.

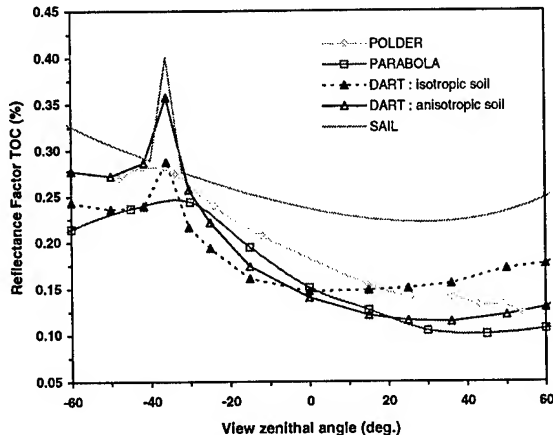


Figure 2: NIR DART, PARABOLA, POLDER and SAIL BRDF in the principal plane for OBS ($\theta_s=36^\circ$)

SAIL BRDF tend to be systematically much larger than POLDER, PARABOLA and DART BRDF [9]. In VIS (NIR) region, mean relative SAIL and PARABOLA BRDF difference is 35%, 15% and 45% (75%, 75% and 20%) for OBS, OJP and OA, respectively. These large differences originate from the neglect of canopy structure by SAIL model. This implies an overestimation of BRDF which is partly compensated with a BRDF underestimation due to smaller influence of understorey of which reflectance is larger than that of tree canopy.

Most DART and measured BRDFs present similar shapes, with a maximum for the hot-spot configuration and a minimum between nadir and specular directions (Table 1). The major shape difference occurs in the principal plane in VIS region, where, contrary to other BRDFs, POLDER reflectance decreases with increasing zenith angle in the forward direction [9]. PARABOLA and POLDER VIS (NIR) BRDF differences are around 25% (25%) for OBS, 25% (15%) for OJP, and 3% (15%) for OA. These results stress that POLDER and PARABOLA BRDF are not fully comparable. Apart from sensor accuracy, this could be explained by the fact that POLDER data are atmospherically and geometrically corrected, and PARABOLA, contrary to POLDER, sampled a single 20mx20m forest, with a much larger FOV. However, both instruments are unique and essential tools to better understand and exploit forest BRDF from space.

Table 1: Simulated and measured VIS [NIR] BRDF for OBS

	Specular	Nadir	Hot-Spot
DART	2.2% [11.7%]	3% [13.8%]	6.0% [35%]
PARABOLA	2.2% [10.8%]	3% [15.0%]	5.8% [24%]
CASI	1.5% [12.9%]	2% [16.4%]	5.0% [30%]
POLDER	1.4% [14.2%]	-	5.2% [27%]

Results showed the potential of DART to simulate accurately real BRDF. Mean relative VIS and NIR BRDF differences with POLDER and PARABOLA are around 10%. However, we stressed a constraint commonly met when comparing theoretical and actual data: unavailable and/or inaccurate field data are sufficient to explain large BRDF variability. Here, this is especially true for understorey structural and optical parameters because canopy LAI is low (≈ 2). For example, OA simulations with an anisotropic understorey, instead of an isotropic one, give much smaller BRDF relative differences with PARABOLA: 2% instead of 10%. Moreover, BORIS values of LAI and leaf optical parameters display a significant variability, depending on experimenters.

CANOPY APAR REGIME

Both local and mean PAR transmission within canopy were studied as a function of sun zenith angle. For that, we considered a $[0^\circ 80^\circ]$ range much larger than that possible at the latitude of SSA sites. Results of this analysis showed a very strong time and spatial variability of the local PAR transmission, related to the location below canopy [9]. Depending on solar zenithal angle and mean dimensions of the boreal forest cover, sun may directly illuminate understorey vegetation, which maximizes local transmission. Canopy PAR transmission does not follow the exponential law of Goudrian [10]. This implies important differences about the 3-D fAPAR distribution (Fig. 3): canopy heterogeneity increases PAR transmission, which reduces canopy APAR and increases understorey APAR.

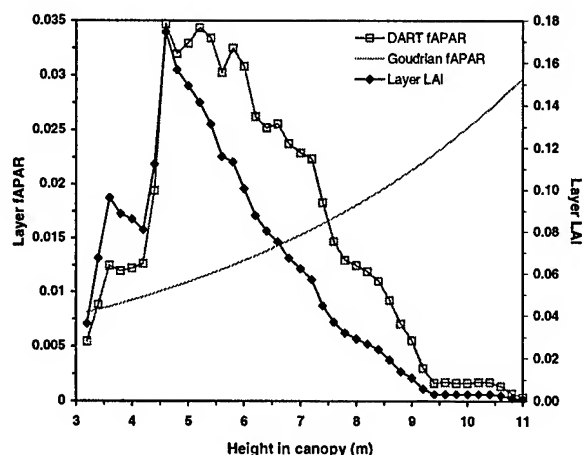


Figure 3: DART and Goudrian fAPAR canopy profiles

Canopy photosynthesis is closely related to APAR. To investigate the influence of 3-D APAR distribution we coupled the DART model with a leaf model [3] which simulates leaf photosynthesis with foliar APAR and a biochemical parameter proportional to leaf photosynthesis capacity (Rubisco catalytic carboxylating potential: V_m). The "DART-Collatz" coupling scheme is described in [9].

Preliminary results indicate that the "DART + Collatz" (Fig. 4) and "Sellers + Collatz" [10] approaches can lead to significant differences for canopy CO_2 assimilation, evaporation, conductance, etc. [9].

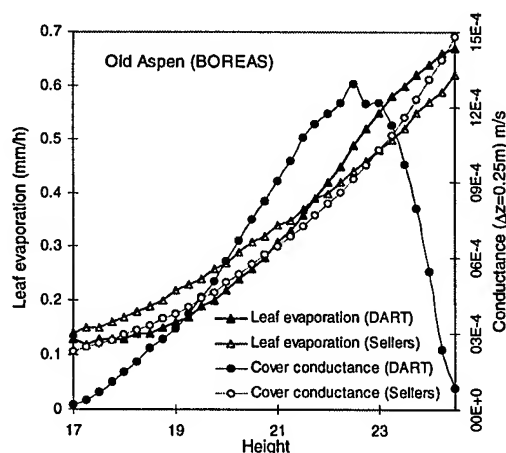


Figure 4: DART / Collatz simulation for OA

CONCLUDING REMARKS

This work stressed the importance of the 3-D forest canopy heterogeneity in relation to their BRDF, radiation regime, and finally photosynthesis activity. Moreover, we conducted a comparative analysis of DART, PARABOLA, CASI and POLDER BRDFs.

ACKNOWLEDGMENTS

We are very thankful to French Space Center (CNES contract No 95/0368) and to the BOREAS, CASI, POLDER and PARABOLA teams for this opportunity.

REFERENCES

- [1] G. Asrar, R.B. Myneni, and B.J. Choudhury B.J., 1992, "Spatial heterogeneity in vegetation canopies and remote sensing of absorbed photosynthetically active radiation: a modeling study", *Rem. Sens. Env.*, vol. 41, pp. 85-103.
- [2] J.P. Gastellu-Etchegorry, V. Demarez, V. Pinel, and F. Zagolski, 1996, "Modeling radiative transfer in heterogeneous 3-D vegetation canopies", *Rem. Sens. Environ.*, vol. 58, pp. 131-156.
- [3] G.J. Collatz, J.T. Ball, C. Grivet, and J.A. Berry, 1991, "Physiological and environmental regulation of stomatal conductance, photosynthesis and transpiration: a model that includes laminar boundary", *Agric. For. Meteorol.*, vol. 54, pp. 107-136.
- [4] P.J. Sellers, F.G. Hall, H. Margolis, B. Kelly, D. Baldocchi, G. Den Hartog, J. Cihlar, M.G. Ryan, B. Goodison, P. Crill, K.J. Ranson, D. Lettenmaier, and D.E. Wickland, 1995, "The BOREAL Ecosystem-Atmosphere Study: An overview and early results from the 1994 Field Year", *Bull. Amer. Meteor. Soc.*, vol. 76, pp. 1549-1577.
- [5] D.W. Deering, S.P. Ahmad, T.F. Eck, and B.P. Banerjee, 1995, "Temporal attributes of the bidirectional reflectance for three boreal forest canopies", *Proceedings of IGARSS'95, Firenze, Italy, July 1995*.
- [6] F.M. Br on, V. Vanderbilt, M. Leroy, P. Bicheron, C.L. Walthall, and J.E. Kalshoven, 1997, "Evidence of hot-spot directional signature from POLDER measurements", *I.E.E.E. Trans. GRS*, in press.
- [7] N.O'Neill, F. Zagolski, M. Bergeron, A. Royer, J. Miller, and J. Freemantle, 1997, "Atmospheric correction validation of CASI images acquired over the BOREAS Southern Study Area", *Can. J. of Rem. Sens.*, in press.
- [8] W. Verhoef, 1984, "Light scattering by leaf layers with application to canopy reflectance modeling: the SAIL model", *Rem. Sens. Environ.*, vol. 16, pp. 125-141.
- [9] J.P. Gastellu-Etchegorry, P. Guillevic, F. Zagolski, V. Trichon, D. Deering, S. Laffont and M. Leroy, 1997, "Modeling BRDF and radiation regime of boreal and tropical forests", *Proc. of the 7th Int. Symp. Phys. Meas. & Sign. in Rem. Sens.*, Courchevel, France, April 1997.
- [10] P.J. Sellers, J.A. Berry, G.J. Collatz, C.B. Field, and F.G. Hall, 1992, "Canopy reflectance, photosynthesis and transpiration, III. A reanalysis using enzyme kinetics electron transport models of leaf physiology", *Rem. Sens. Environ.*, vol. 42, pp. 187-216.

Estimation of Surface Reflection Parameters over Lands Using Linear Polarization Data by Airborne POLDER

Kazuya Takemata and Yoshiyuki Kawata*

Kanazawa Technical College, 2-270 Hisayasu, Kanazawa, Ishikawa 921, Japan
81-762-48-1080 ext. 2892; 81-762-48-5548 (FAX); takemata@infor.kanazawa-it.ac.jp (Internet)

*Kanazawa Institute of Technology, 1-1 Ogigaoka, Nonoichi, Ishikawa 921, Japan
81-762-48-1100 ext. 2594; 81-762-48-7753 (FAX); kawata@infor.kanazawa-it.ac.jp (Internet)

Abstract -- This paper shows the estimated results of surface reflection parameters, such as the leaf inclination distribution function (LIDF) and the mixing ratio (α) of specular to diffuse component for a vegetated area, using the observed linear polarization data at 550 nm and 650 nm over lands measured by the airborne POLDER. The main results in this study can be summarized as follows:

- 1) We found the simplified Rondeaux - Herman model for "Forest01" and "Rice Field01" is able to show similar polarization variations against zenith viewing angles in the principal plane to the observed one.
- 2) The isotropic assumption of LIDF seems to be valid. The values of α for "Forest01" are estimated to be $\alpha \sim 0.50$ and $0.20 < \alpha < 0.40$ at 550 nm and 650 nm, respectively. Those for "Rice Field01" are to be $\alpha \sim 0.50$ and $\alpha \sim 0.40$ at 550 nm and 650 nm, respectively.

INTRODUCTION

Advance earth observing satellite ADEOS was launched in August 17, 1996 by the National space development agency (NASDA), Japan. This platform satellite has eight sensors. The POLDER instrument is one of those sensors and was built by Centre National d' Etudes Spatiales (CNES) [1]. This sensor has an ability to measure both the polarized and directional solar radiation in the visible and near-infrared bands reflected by the earth-atmosphere system.

In this paper we estimated the surface reflection parameters, such as LIDF of vegetated targets and α in the radiation reflected by the targets, using the observed linear polarization data by the airborne POLDER in the La Crau area. Since the ADEOS/ POLDER data are not available yet, the analysis results on the airborne data were presented in this paper. The "La Crau campaign" was conducted in the southeast of France on June 17, 1990 [2]. In this study we consider only a subset of a large La Crau data set to estimate optical parameters for surface covers.

LA CRAU 90 CAMPAIGN DATA

The POLDER sensor acquires successively the 2-dimensional pictures (that is called framed images) of the

ground on a CCD matrix (384×288 pixels). The angular coverage of the airborne version is $\pm 51^\circ$ in the cross-track direction and $\pm 43^\circ$ in the along-track direction. The La Crau campaign was conducted in seven flight passes. The flight altitude was 6000 m, and the ground dimension for a pixel is approximately a $37 \text{ m} \times 37 \text{ m}$ [2]. Two out of those flight data sets were available to us, and our data consists of 55 sequential framed images. The measurements over La Crau area were done at three wavelengths, i.e. 550 nm, 650 nm and 850 nm. Both the reflectance and polarization data are included in the La Crau 90 campaign data sets.

ATMOSPHERE - GROUND SURFACE MODEL

For the airborne frame image data, we need to evaluate the internal radiation field. Let us assume an incident solar flux πF_0 illuminates a plane parallel atmosphere from the direction of (μ_0, ϕ_0) , where μ_0 and ϕ_0 are the cosine of the solar zenith angle θ_0 and the solar azimuth angle, respectively. In order to deal with the internal radiation field, we divide such the atmosphere into two layers at the aircraft altitude. The atmosphere above the aircraft is denoted by Layer 1 and the atmosphere below the aircraft is denoted by Layer 2. Each layer is assumed to be horizontally homogeneous atmosphere, respectively.

The incident solar flux is given by (1) in Stokes vector representation,

$$\pi F_0 = \pi [F \ 0 \ 0 \ 0]^t \quad (1),$$

where a superscript t represents the matrix transposition. The upward Stokes vector $I_u(\tau, \mu, \mu_0, \phi - \phi_0) = [I \ Q \ U \ V]^t$ at the top of the atmosphere in the direction of (μ, ϕ) can be expressed by (2) in terms of the reflection matrix of the atmosphere - ground surface system $R_{\text{atmos+surface}}$,

$$I_u(\tau, \mu, \mu_0, \phi - \phi_0) = \mu_0 R_{\text{atmos+surface}}(\tau, \mu, \mu_0, \phi - \phi_0) F_0 \quad (2).$$

As the components of the Stokes vector, I is the intensity, Q is related to the linear polarization, U to the plane of polarization, and V to the circular polarization. $R_{\text{atmos+surface}}$ can be expressed in terms of the reflection and transmission matrices of the

atmosphere, R_{atmos} and T_{atmos} , and the surface reflection matrix, R_{surface} . These reflection and transmission matrices of the atmosphere can be computed by the doubling and adding method for a given atmospheric model [3]. As for R_{surface} , we describe it in the later.

In the computation we adopted the optical parameters listed in Table 1. The refractive index of aerosol, $m = 1.5 - i0.05$ and the Junge type aerosol size distribution function with $v = 3$ are adopted. Those atmospheric parameters are deduced from the air truth data in La Crau 90 campaign [2]. And we adopted the molecular optical thickness values based on the standard model atmosphere of Lowtran6 (Midlatitude, Spring - Summer model) [4].

Table 1. Optical Parameters in the Atmospheric Model

Band[nm]		τ_{total}	f_r	ω
550	Layer1	0.092	0.699	0.711
	Layer2	0.434	0.121	0.951
650	Layer1	0.058	0.618	0.643
	Layer2	0.309	0.088	0.931

τ is the total optical thickness, f_r is molecule gas - aerosol mixing ration, and ω is the scattering albedo of the atmosphere for each layer.

For a natural surface, we assume that the surface reflection matrix consists of the diffuse and specular component. The specular component includes the polarization but the diffuse component does not. Then R_{surface} can be expressed as follows,

$$R_{\text{surface}}(\mu, \mu_0, \phi - \phi_0) = \alpha \rho_{\text{diff}} + (1 - \alpha) \rho_{\text{sp}} \quad (3),$$

where α is the mixing ratio of specular to diffuse component. In (3), ρ_{diff} and ρ_{sp} represent the diffuse and specular components in the polarized radiation by the target surface. The diffuse reflectance component, ρ_{diff} , is essentially equal to the surface albedo of Lambertian surface. Although several authors have derived theoretical models for the polarized reflectance of vegetation canopies, we shall adopt the Rondeaux and Herman's model [5],

$$\rho_{\text{sp}}(\mu, \mu_0, \phi - \phi_0) = [\pi f(\theta_n) / 2(\mu_0 + \mu)] R_{\text{sp}}(2\omega) \quad (4).$$

In addition, if the LIDF is uniform for this model, (4) can be simply written [6],

$$\rho_{\text{sp}}(\mu, \mu_0, \phi - \phi_0) = [1 / 4(\mu_0 + \mu)] R_{\text{sp}}(2\omega) \quad (5).$$

In (5),

$$\omega = 0.5 \cos^{-1} [\cos \theta \cos \theta_0 + \sin \theta \sin \theta_0 \cos(\phi - \phi_0)] \quad (8),$$

$$\theta_n = \cos^{-1} [(\cos \theta + \cos \theta_0) / 2 \cos \omega] \quad (9),$$

$$R_{\text{sp}}(2\omega) = 1/2 \times$$

$$\begin{pmatrix} \gamma_{//}^2 + \gamma_{\perp}^2 & \gamma_{//}^2 - \gamma_{\perp}^2 & 0 & 0 \\ \gamma_{//}^2 - \gamma_{\perp}^2 & \gamma_{//}^2 + \gamma_{\perp}^2 & 0 & 0 \\ 0 & 0 & -2\gamma_{//}\gamma_{\perp} & 0 \\ 0 & 0 & 0 & -2\gamma_{//}\gamma_{\perp} \end{pmatrix} \quad (10),$$

where elements are given by Fresnel's law as follows.

$$\begin{aligned} \gamma_{//} &= (\chi_i - n\chi_t) / (\chi_i + n\chi_t) \\ \gamma_{\perp} &= (\chi_i - n\chi_t) / (\chi_i + n\chi_t) \end{aligned} \quad (11),$$

$$\chi_i = \cos \omega \quad \chi_t = (1 - \sin^2 \omega / n^2)^{1/2} \quad (12).$$

In (11) and (12), n is the ratio of refractive index of the surface to that of the atmosphere, and 1.5 for a leaf surface and 1.338 for a water surface, respectively.

AIRBORNE POLDER DATA ANALYSIS

In this study we selected 2 target areas (each consisting of 5x5 pixels) which are identified by consulting the local geographic map with a scale of 1/25,000. The targets, i.e. "Forest01" and "Rice Field01", are in near the east - west flight line. The moving direction of airplane was roughly toward the sun's direction in the flight line. The solar zenith and the azimuthal angle at the time of the observation were $= 43^\circ$ and $= 104^\circ$, respectively. Only the reflectance and degree of linear polarization data of 550 nm and 650 nm were analyzed in this analysis because degree of linear polarization data at 850 nm are too noisy over the vegetation area to use.

Results at 550 nm

The theoretical reflectance and degree of linear polarization curves in the principal plane are presented for the atmospheric model with the vegetation surface of $A = 0.10$ and $\alpha = 0.50$ in Fig.1, together with observed value of "Forest01" and "Rice Field01". The reflectance is defined as $(\pi I_u / \mu_0 \pi F = I_u / \mu_0 F)$. Positive and negative signs in the zenith viewing angle correspond to cases of the surface reflection occurred in the backward and forward scattering directions, respectively. In Fig.1 we found a good agreement between the theoretical and observed values. This suggests that the assumption of uniform LIDF for the these covers is acceptable at 550 nm.

Results at 650 nm

In a similar manner at 550 nm, we estimated the parameter α at 650 nm. The theoretical reflectance and degree of polarization curve in the principal plane is presented for the model with $A = 0.10$ and $\alpha = 0.40$ for "Rice Field01" in Fig.2,

and $A = 0.10$ and $0.20 < \alpha < 0.40$ for "Forest01" in Fig.3. We found a good agreement between the theoretical and observed values in the forward scattering direction, but we have a large disagreement in the backward scattering direction. The ground polarization measurements of the vegetated surface indicate monotonous polarization decreases in the backward scattering direction [5], whereas the airborne measurements did not show such decreases. There is a possibility that the disagreement is due to atmospheric effects, but the exact cause is not obvious at present.

CONCLUSIONS

In this paper, for the first time, we have made a polarization analysis of the airborne POLDER image data over lands, introducing the combined model with the atmosphere and ground surface. Our conclusions based on this study are summarized as follows:

- 1) We found the simplified Rondeaux - Herman model for "Forest01" and "Rice field01" is able to explain observed polarization variations against zenith viewing angles in the principal plane. This suggests the isotropic assumption of LIDF is valid.
- 2) We estimated α for a vegetated area at 550 nm and 650 nm, using our atmosphere - ground surface model.
- 3) There is left to study, such as the existence of difference between the theoretical and observed degree of linear polarization values in the backward direction.

ACKNOWLEDGMENTS

We thank Prof. Herman and Dr. Deschamps at Laboratoire d'Optique Atmospherique, France and Dr. Bréon at Laboratoire de Modelisation du Climat et de l'Environnement, France for kindly providing the La Crau POLDER data. This study was supported by the aid of the Sumitomo foundation.

REFERENCES

- [1] P.M. Deschamps, F.M. Bréon, M. Leroy, A. Podaire, A. Bricaud, J.C. Buriez, and G. Séze, "The POLDER mission: instrument characteristics and science objectives", IEEE Trans. Geosci. Remote Sensing, vol.32, no.3, pp.598-615, 1994.
- [2] J.L. Deuzé, F.M. Bréon, P.Y. Deschamps, and M. Herman, "Analysis of the POLDER Airborne Instrument Observations over Land Surfaces", Remote Sens. Environ., vol.45, pp.137-154, 1993.
- [3] J.E. Hansen and L.D. Travis, "Light scattering in planetary atmospheres", Space Sci. Rev., vol.13, pp.527-610, 1974.
- [4] F.X. Kneizys, E.P. Shettle, W.O. Gallery, J.H. Jr. Chetwynd, L.W. Abreu, J.E.A. Selby, S.A. Clough, and R.W. Fenn, "Atmospheric Transmittance/Radiance : Computer code Lowtran-6", Air Force Geophys. Laboratory, Hanscom AFB, MA, Rep. AFGL-TR-83-0187, 1983.
- [5] G. Rondeaux and M. Herman, "Polarization of light

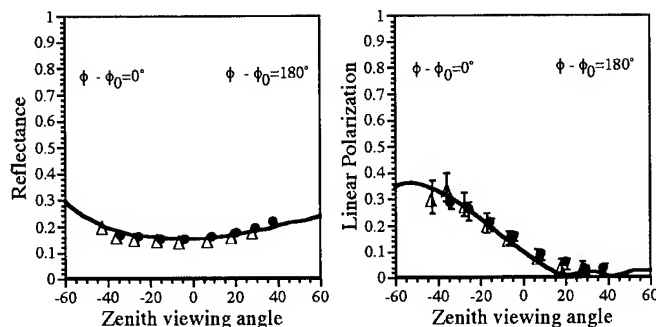


Fig.1 The reflectance and degree of linear polarization variation at 550 nm against the zenith viewing angle in the principal plane for vegetated surface covers ("Forest01":• and "Rice Field01": Δ). Lambertian surface of $A = 0.10$ and $\alpha = 0.50$ is assumed. The incident solar zenith angle $\theta_0 = 43^\circ$ is also assumed.

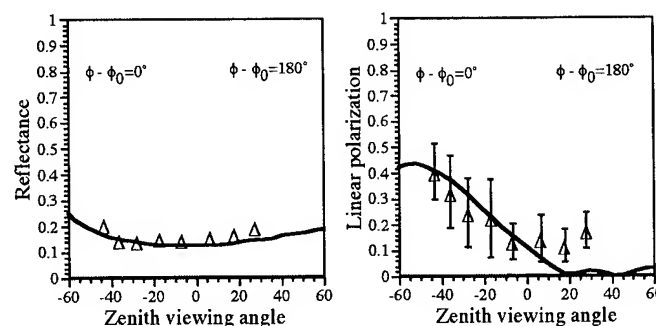


Fig.2 The same as Fig.1, except for "Rice Field01" and at 650 nm. Lambertian surface of $A = 0.10$ and $\alpha = 0.40$ is assumed.

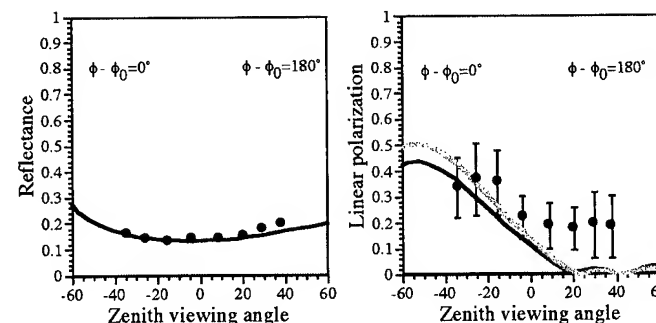


Fig.3 The same as Fig.1, except for "Forest01" and at 650 nm. Lambertian surface of $A = 0.10$, $\alpha = 0.20$ (the block line) and 0.40 (the gray line) is assumed.

reflected by crop canopies", Remote Sens. Environ., vol.38, pp.63-75, 1991.

- [6] F.M. Bréon, D. Tanré, P. Lecomte, and M. Herman, "Polarized reflectance of bare soils and vegetation: measurements and models", IEEE Trans. Geosci. Remote Sensing, vol.33, no.2, pp.487-499, 1994.

Radiometric Estimates of Grain Yields Related to Crop Aboveground Net Production (ANP) in Paddy Rice

Sukyoung Hong, Jeongtaek Lee, Sangkyu Rim, and Jaesung Shin

Remote sensing Lab., Soil Management Div., National Institute of Agricultural Science and Technology,
249 Seodungong, Kwonsungu, Suwon 441-707, Korea, Tel:+82-331-290-0246, Fax:+82-331-290-0222

Email:syhong@sun20.asti.re.kr

ABSTRACT

Crop Aboveground Net Production(ANP) is a major factor for determining the total biomass and closely related to the amount of grain production at each development state. Spectral reflectance was measured in paddy field(Ilpum var.) to interpret grain yield from satellite image using the relations between agronomic parameters such as LAI and ANP. LANDSAT TM equivalent band set was created by integrating measured spectral reflectance values to the real TM band range. We made polynomial function of spectral reflectance on two wavelength range, VIS(0.50-0.68 μm) and NIR(0.69-1.00 μm), of each development state. As a result of correlation analysis between the LANDSAT TM equivalent bands, agronomic parameters, and multi-channel vegetation indices, both ANP and LAI of paddy rice could be estimated by TM

equivalent bands and vegetation indices, functionally. Rice ANP and LAI can be estimated from spectral measurements. These estimates can then be used to forecast final grain yield.

INTRODUCTION

There have been few studies of the spectral reflectance at each development state in paddy rice related to agronomic parameters such as LAI, ANP, and grain yield in Korea.

Both LAI and ANP can be important variables explaining rice canopy status. Leaf area variations accounted for virtually all variability in canopy reflectance data[1,2]. A few attempts to predict the amounts of the aboveground dry weight of paddy rice canopies using spectral reflectance data and vegetation indices[3,4,5]. These spectral estimates of canopy biomass could also be highly correlated with final grain yield[1,6,7].

Table 1. Polynomial regression model of spectral reflectance on the visible wavelength range(0.50-0.68 μm) and the near-infrared range(0.69-1.00 μm) at each development state of paddy rice.

Growth stage	β_0^*	β_1^*	β_2^*	β_3^*	β_4^*	β_5^*	β_6^*	Coefficient of determination (R^2)
<u>VIS (0.50-0.68 μm)</u>								
Rooting	7.9384	0.3533	0.2432	-0.0431	0.0027	-0.00006		0.9971
Effective tiller	3.0020	-1.3292	1.1975	-0.2630	0.0247	-0.0011	2E-05	0.9949
Panicle differentiation	2.0675	-1.0279	1.0074	-0.2239	0.0210	-0.0009	1E-05	0.9927
Panicle formation	1.5620	-0.7042	0.6741	-0.1509	0.0143	-0.0006	1E-05	0.9912
Booting	1.2477	-0.4523	0.4890	-0.1119	0.0107	-0.0005	8E-06	0.9922
Heading(milk ripe)	1.5362	-0.6605	0.6165	-0.1356	0.0127	-0.0005	9E-06	0.9884
Green neck	1.9812	-0.5602	0.7192	-0.1633	0.0155	-0.0007	1E-05	0.9945
Yellow ripe	0.9298	0.1405	0.1991	-0.0525	0.0052	-0.0002	4E-06	0.9852
Full ripe	3.0207	-1.0930	1.0723	-0.2312	0.0217	-0.0010	2E-05	0.9963
Dead ripe	3.0417	-0.7156	0.7358	-0.1623	0.0158	-0.0007	1E-05	0.9954
<u>NIR (0.69-1.00 μm)</u>								
Rooting	9.8410	3.9516	-0.5329	0.0354	-0.0011	0.00005	1E-09	0.9816
Effective tiller	-0.1212	1.3292	1.5675	-0.2377	0.0140	-0.0004	4E-06	0.9901
Panicle differentiation	1.5205	-2.0602	2.6629	-0.3588	0.0203	-0.0005	5E-06	0.9924
Panicle formation	4.1011	-5.4755	3.0867	-0.3835	0.0210	-0.0005	5E-06	0.9888
Booting	5.0686	-6.7440	3.3710	-0.4119	0.0225	-0.0006	6E-06	0.9930
Heading(milk ripe)	1.8541	-2.0774	1.8352	-0.2388	0.0133	-0.0003	3E-06	0.9929
Green neck	0.7367	0.5209	1.3200	-0.1949	0.0116	-0.0003	3E-06	0.9907
Yellow ripe	0.8104	0.1939	0.9019	-0.1324	0.0079	-0.0002	2E-06	0.9950
Full ripe	1.0464	5.3519	-0.2650	-0.0147	0.0020	-7E-05	9E-07	0.9971
Dead ripe	4.2723	4.0227	-0.4087	0.0203	-0.0004	-3E-06	1E-07	0.9987

$$* Y = \beta_0 + \beta_1 X^1 + \beta_2 X^2 + \beta_3 X^3 + \beta_4 X^4 + \beta_5 X^5 + \beta_6 X^6$$

(X:Wavelength(μm), Y:Spectral reflectance(%), β_n :regression coefficient at given(n) order expression)

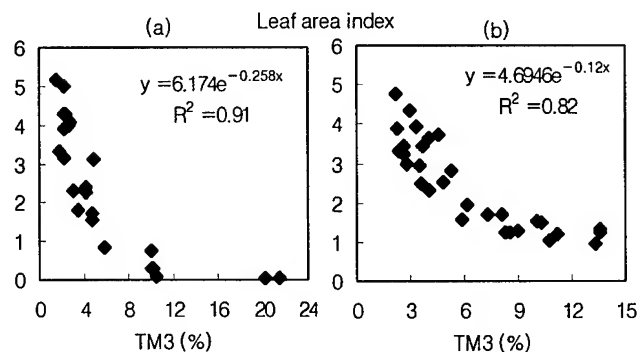


Figure 1. Regression model for estimating LAI of paddy rice with TM equivalent band before(a) and after(b) heading stage.

The investigations which will be described here are radiometric estimation of LAI, aboveground net production, and grain yield through relationship between LANDSAT TM equivalent band, multi-channel vegetation indices, and agronomic parameters.

MATERIALS AND METHODS

Spectral reflectance of paddy rice canopies (Ilpumbyeo) was measured with spectroradiometer (GER Inc. SFOV : 0.35 - 2.50 μm) *in situ* weekly or biweekly from transplanting to ripening stage. Ground truth data of rice were collected including LAI and ANP, at the same time. Statistical analysis was carried out to make out correlations between agronomic parameters, TM equivalent bands, and vegetation indices using SAS procedures.

RESULTS AND DISCUSSION

Polynomial functions of spectral reflectance at each development state on the visible wavelength range(0.50-0.68 μm) and the near-infrared wavelength range(0.69-1.00 μm)

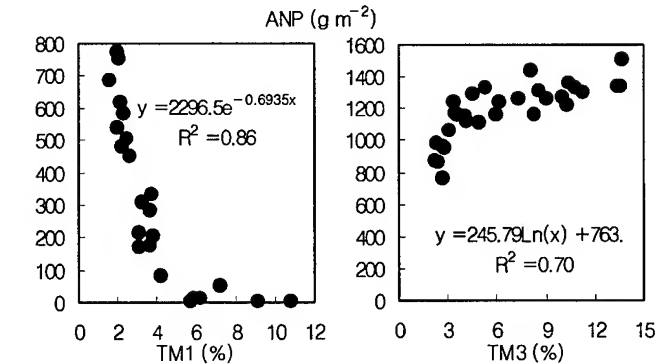


Figure 2. Regression model for estimating ANP of paddy rice with TM1 and TM3 equivalent band before(a) and after(b) heading stage.

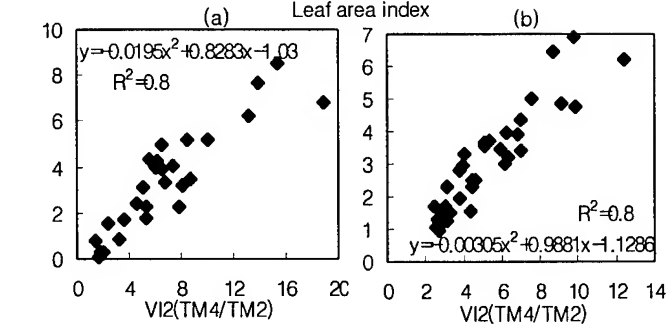


Figure 3. Regression model for estimating LAI of paddy rice with VI2(TM4/TM2) before(a) and after(b) heading stage.

were made, respectively (Table 1). Sixth order expression well explained spectral reflectance on both wavelength ranges. In the visible wavelength range(0.50-0.68 μm), each polynomial expression curve was well fitted for the spectral reflectance curve at each development state, while some mismatches in several wavelengths were shown in the near-infrared wavelength range (0.69-1.00 μm).

Correlation analysis between the LANDSAT TM equivalent bands and agronomic parameters(LAI, ANP, etc) showed that LAI and ANP of rice were highly correlated with visible range band such as TM1 and TM3 before heading stage rather than after heading stage. Regression model for estimating LAI of paddy rice with TM3 equivalent band showed that the higher LAI, the lower spectral reflectance, exponentially(Fig.1). As LAI is high, rice leaves absorb big amount of the solar radiation through phytopigments including chlorophyll a, b and carotenoids at the blue and red visible wave bands. TM1 and TM3 equivalent band value could estimate ANP before and after heading stage, respectively(Fig. 2).

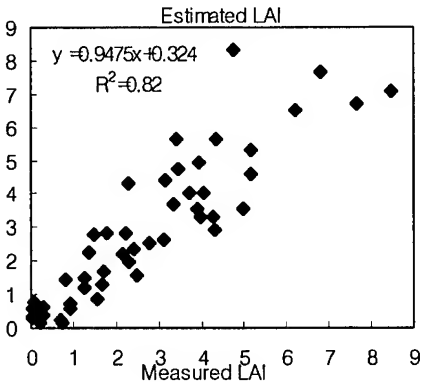


Figure 4. Relationship between measured LAI and estimated LAI with VI2(TM4/TM2) during rice growing period.

Until heading stage, TM1 equivalent value showed exponentially reverse trend toward ANP. As rice matures, the chlorophyll amount reduced slightly. As results, when the ANP increased, TM3 equivalent value increased together logarithmically.

We examined multi-channel vegetation indices and selected TM4/TM2 for estimating leaf area index. LAI was well explained with TM4/TM2 through all growing periods (Fig.3). Relationship between the measured LAI and the estimated by TM4/TM2 was shown(Fig.4). As shown in Fig. 4, LAI as one of critical parameters explaining rice canopy status could be predicted by VI2(TM4/TM2) on the basis of spectral reflectance.

Regression for grain yield with VI2(TM4/TM2) and TM3 were shown in Table 2. When the measurements from 2 developmental stages were combined, the multiple regression yield somewhat improved results. The highest correlation obtained was shown in 2 dates, booting and dead ripe, multiple regression ($R^2=0.99$) using TM3 equivalent band. Estimated grain yield by the 2 dates multiple regression model corresponded well with measured grain yield(Fig.5).

CONCLUSIONS

Rice is the most important crop in Korea. Estimation and improvement of the forecasting of rice grain yield is a very valuable objective. These fundamental investigations have shown that spectral reflectance function of each development

Table 2. Correlation of TM4/TM2 and TM3 with rice grain yield.

Rice development state at the time of radiometric field observation	TM4/TM2 versus grain yield(R^2)	TM3 versus grain yield(R^2)
<i>SIMPLE REGRESSION</i>		
P	0.85	0.81
B	0.62	0.85
H	0.95	0.67
Y	0.66	0.61
D	0.30	0.66
<i>2 DATES IN MULTIPLE REGRESSION</i>		
P	0.86	0.85
B	0.95	0.86
H	0.95	0.82
Y	0.73	0.73
D	0.96	0.81
P	0.86	0.97
P	0.86	0.97
P	0.86	0.97
B	0.66	0.91
B	0.84	0.99*
H	0.95	0.92
KEY : Development state		
P = Panicle formaiton	Date of observation	
B = Booting	August 6, 1996	
H = Heading	August 13, 1996	
Y = Yellow ripe	August 20, 1996	
D = Dead ripe	Setember 17, 1996	
	October 8, 1996	

* $R^2=0.99$ is the highest correlation obtained.

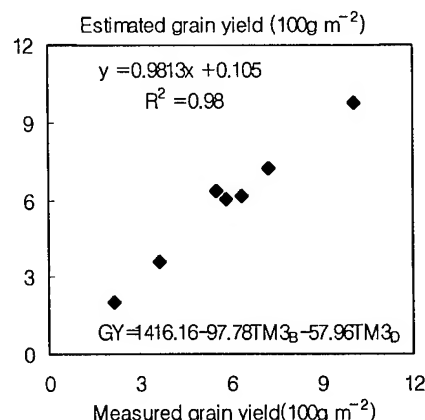


Figure 5. Relationship between measured grain yield and estimated grain yield by 2 dates multiple regression model in rice canopies. (GY = Grain yield, TM3B = TM3 equivalent band at booting stage, TM3D = TM3 equivalent band at dead ripe stage)

state can be made and rice ANP and LAI can be estimated from spectral measurements. So that, final grain yield of paddy rice in Korea can be predicted as the function of ANP.

REFERENCES

- [1] B. R. Gardner, "Techniques for remotely monitoring canopy development and estimating grain yield of moisture stressed corn," Dissertation, Univ. of Nebraska, 1983
- [2] J. T. Lee, C. W. Lee, M. K. Joo, and S. Y. Hong, "Estimation of leaf area index(LAI) using spectral reflectance of solar radiation in paddy rice field," in press
- [3] J. T. Lee, C. W. Lee, M. K. Joo, and S. Y. Hong, "Dry matter estimation for paddy rice using spectral reflectance of solar radiation," in press
- [4] M. Shibayama and K. Munakata, "A spectroradiometer for field use, II. Biomass estimates for paddy rice using 1,100 and 1,200 nm reflectance," Japan Jour. Crop Sci., Vol. 55(1), pp. 28-34, 1986a
- [5] M. Shibayama and K. Munakata, "A spectroradiometer for field use, III. A comparison of some vegetation indices for predicting luxuriant paddy rice biomass," Japan Jour. Crop Sci., Vol. 55(1), pp. 47-52, 1986b
- [6] M. Shibayama and K. Munakata, "A spectroradiometer for field use, IV. Radiometric prediction of grain yields for ripening rice plants," Japan Jour. Crop Sci., Vol. 55(1), pp. 53-59, 1986c
- [7] Y. K. Yang and L. D. Miller, "Correlations of rice grain yields to radiometric estimates of canopy biomass as a function of growth stage," J. of the Korea Soc. of Remote Sensing, Vol. 1(1), pp. 63-87, 1985

*NIAST 97-1-2-42

A Simple Model for the Estimation of Biomass Density of Regenerating Tropical Forest Using JERS-1 SAR and its Application to Amazon Region Image Mosaics

Adrian Luckman and John Baker

Remote Sensing Applications Development Unit, Natural Environment Research Council
Monks Wood, Abbots Ripton, Huntingdon, Cambridgeshire, PE17 2LS, UK
Tel: +44 1487 773381 Fax: +44 1487 773277 Email: A.Luckman@nerc.ac.uk

Abstract -- Regenerating tropical forests are important to the regional carbon balance because they represent areas of high carbon flux from the atmosphere to the land. These forests are complex in species distribution and structure so generalised models of radar backscatter are difficult to develop. However, empirical studies suggest a sensitivity of L-band SAR to the biomass density in these forests which may be employed to map and measure their growth. This paper investigates a simple empirical model representing the response of the JERS-1 SAR to the biomass density of regenerating forest in Brazil. This model was verified using independent data sources and employed to map biomass density over large regions of Amazonia from large scale JERS-1 image mosaics provided by NASDA.

INTRODUCTION

Because of the complexity of the interaction of microwave radiation with vegetation, invertible models are unlikely to be developed for any but the simplest and most homogeneous canopies. Tropical forests in particular are so variable in species and structure that a generalised radar interaction model are difficult to develop. Nevertheless, SAR backscatter at wavelengths of L-band and longer shows enough sensitivity to biomass density in various forest types to suggest that a simpler model may usefully describe forest backscatter under certain conditions. A simple model of forest backscatter used to retrieve the biomass density of regenerating tropical forest from JERS-1 would serve to quantify an important element of the regional carbon balance.

In this paper, a simple form of the water-cloud backscatter model provides the starting point for an algorithm for the retrieval of regenerating forest biomass density from L-band SAR imagery. This function was fitted to the response of the JERS-1 SAR to the biomass density of regenerating forest as measured during a field campaign to the Tapajós region of central Amazonia in Brazil. The seasonal variation in response was investigated with a sequence of images and the fitted function was verified using field and image data acquired independently at Manaus, 500km from Tapajós.

A retrieval algorithm was derived from the fitted model by inversion and quantisation into biomass density classes. The confidence limits of this retrieval scheme were investigated to find a texture and speckle tolerant threshold for image saturation with biomass density. The spatial distribution of biomass density in central Amazonia was estimated by applying the retrieval algorithm to a mosaic of 90 JERS-1

scenes compiled by NASDA and the result compared to a regeneration map derived from NOAA AVHRR data.

TEST SITES AND DATASETS

The study used field data and remotely sensed images from the Tapajós region of Pará State and the Manaus region of Amazonas State in Brazil and a mosaic of imagery covering approximately 250,000 sq. km of Amazonia (Figure 1)

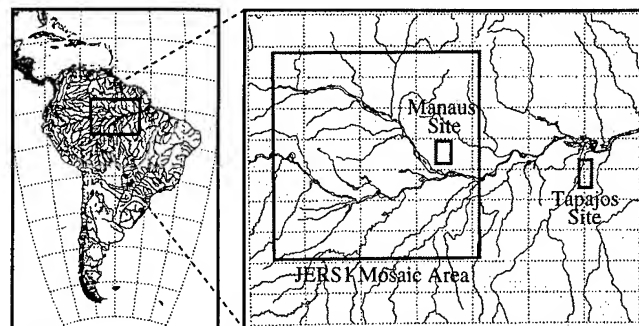


Figure 1. Study areas

During a field campaign to the Tapajós region in August 1994, fifteen plots of 10m by 50m (0.05 has) representing a suitable range of regrowth age were measured for diameter at breast height (dbh), species and tree height. Biomass density was derived by employing timber specific gravity values and published species-dependent regressions [1]. Fieldwork campaigns were carried out around the abandoned Fazendas to the north of Manaus in August 1993 and August 1995 [2]. Estimates of biomass density were derived in the same way as at Tapajós but here the sample plots were 10m by 100m.

Remotely sensed imagery included SAR data from JERS-1 and an extract from a map of land cover and regenerating forest biomass density derived from an Amazon-wide compilation of AVHRR data. To quantify the temporal variation in SAR signature, six JERS-1 coverages of Tapajós, each comprising of a consecutive pair of images, were acquired from the following dates:

Image	Date	Season
1	22/8/92	dry
2	14/2/93	wet
3	30/3/93	peak wet
4	26/6/93	dry
5	27/7/94	dry
6	10/10/95	peak dry

A single JERS-1 coverage (also a pair of images) of the Manaus test site from 1/10/93 was also acquired. Each of these individual coverages was georegistered to the UTM

projection so that image statistics could be easily extracted for areas corresponding to sample plots on the ground.

A 500km by 500km preliminary mosaic of ninety JERS-1 images from Amazonia was also employed in the study. This was acquired between February and March 1993 and processed jointly by the Japanese Ministry of International Trade and Industry (MITI) and National Space Development Agency (NASDA) [3].

As an independent source of data for the distribution of biomass within Amazonia, a map of regenerating forest derived from 1km NOAA (National Oceanic and Atmospheric Administration) AVHRR (Advanced Very High Resolution Radiometer) imagery was used [4]. For this study, only the forest/non-forest boundary and the 0-40 tonnes/ha class from the regeneration map were used.

Image regions or polygons with a minimum area of 1 ha, corresponding to the homogeneous forest areas sampled on the ground at both Tapajós and Manaus, were located by a combination of image geocoding and GPS positioning.

SIMPLE BACKSCATTER MODEL

A simple though plausible model for the relationship between biomass density and microwave backscatter from vegetation was defined as:

$$\sigma^0(\text{linear units}) = a - e^{-(bB+c)} \quad (1)$$

where B is the biomass density, a, b and c are constants and the incidence angle is assumed not to vary significantly.

This equation is based loosely on the water cloud model [5] which essentially represents the extinction of microwave radiation as it passes through a layer of vegetation made up of elements containing water. This model was fitted to each of the six JERS-1 responses by the Levenberg-Marquardt non-linear least-squares method, weighted by the standard error of the mean.

As might be anticipated due to the relatively smaller contribution from the soil backscatter, the images from the dryer parts of the seasonal cycle in general gave the greater dynamic range in backscatter between low and high biomass areas and the higher biomass densities at which saturation begins to occur. Image 4 (June) had the most favourable response but the relationship obtained with the highest confidence was the one derived from the image closest in date to the biomass sampling (Image 5, July 1994). Mature tropical forest is believed to present very stable backscattering properties [6]. The differences in saturation level between images (maximum 0.6dB) was well within the specified JERS-1 one-sigma calibration accuracy of 1.86dB [7].

The residual error in the fit of the backscatter model was adequately explained by the texture and speckle measured in the sample forest areas. Data collected independently at Manaus gave no reason to reject the backscatter model. Using the worst-case texture found at both test sites and the expected

levels of speckle, confidence limits of +0.55dB and -0.63dB (2 standard errors) were given for the estimation of σ^0 from 1 ha regions of further JERS-1 acquisitions [8].

BIOMASS DENSITY RETRIEVAL SCHEME

Based on the fitted backscatter model, a suitable scheme to estimate biomass density of regenerating forest from JERS-1 imagery was proposed:

- 1) Cross-calibrate the gain of a new image to the July 1994 data such that mature forest areas have the same backscatter level of -7.69dB.
- 2) Compensate for scattering area with the use of a DEM and knowledge of the instrument track and altitude.
- 3) Calculate the mean backscatter in homogeneous areas of regenerating and mature tropical (min 1ha). Use the model fitted to the July 1994 data to retrieve biomass density.
- 4) Calculate the confidence limits in the retrieved biomass density using the model and the expected variability in σ^0 .

By quantising the measured backscatter into bins corresponding to limited ranges of biomass density, the retrieval scheme was used to classify JERS-1 data. The size of bins was constant in the decibel scale and equal to the confidence interval calculated for worst texture and speckle based on 1 ha samples. Two further tentative classes of water, urban and flooded forest were proposed based on experience of JERS-1 data from this area and on local knowledge.

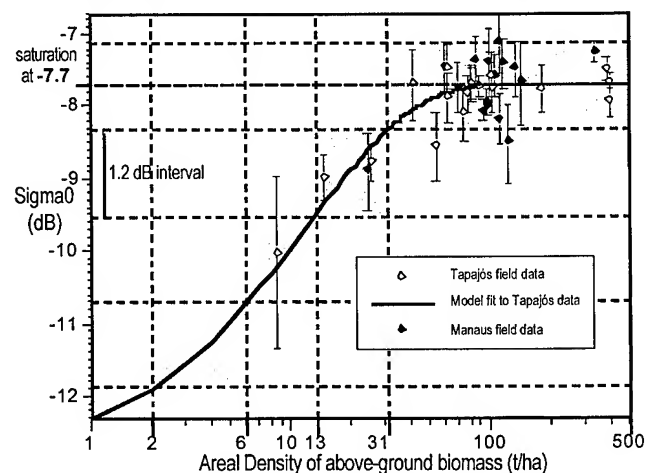


Figure 2. Biomass - backscatter responses for both test sites

Lower σ^0 Threshold	Upper σ^0 Threshold	Typical Land Cover	Regenerating Forest Biomass Density Class
noise floor	-11.9 dB	inland water	
-11.9 dB	-10.7 dB	pasture and crops	
-10.7 dB	-9.5 dB	young regrowth	6- 13 t/ha
-9.5 dB	-8.3 dB	established regeneration	13 - 31 t/ha
-8.3 dB	-7.1 dB	old regen. to primary forest	> 31 t/ha
-7.1 dB	maximum	flooded forest and urban	

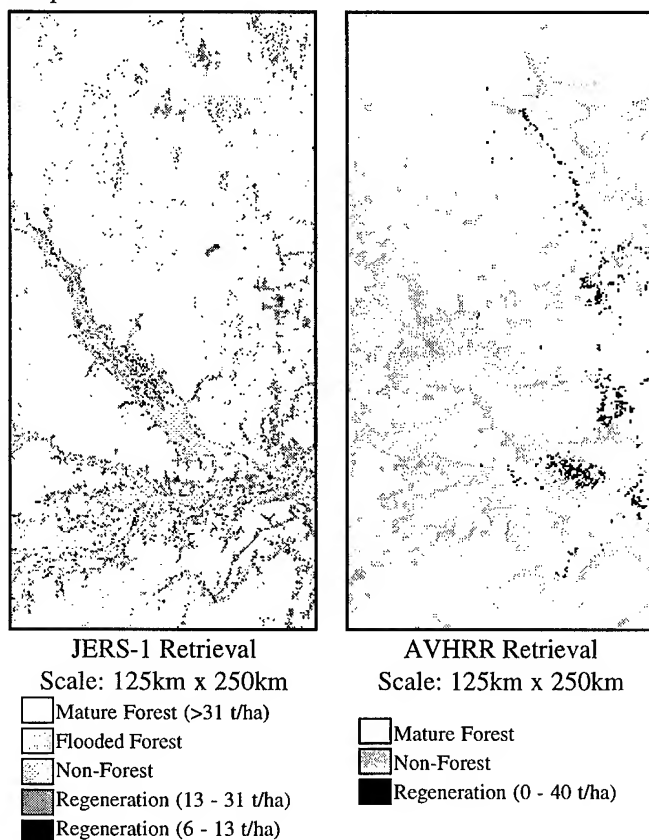
Table 1. Quantised biomass density retrieval scheme

This quantised scheme is shown in Figure 2 and Table 1 and indicates the limits of biomass density bins that may be retrieved with confidence at the 95% level.

APPLICATION TO IMAGE MOSAIC

The biomass density retrieval scheme was applied to a JERS-1 mosaic of Amazonia. The mean σ^0 was recomputed by a simple relationship from the 8-bit pixels and the retrieval scheme was applied to this value to predict the mean biomass density within each 1 ha area of forest.

Figure 3 shows the retrieved biomass density classification calculated from part of the Amazonia JERS-1 mosaic. The corresponding area of the AVHRR classification is shown for comparison.



There appears to be a general correspondence between the JERS-1 and AVHRR derived biomass density maps. The non-forest limits are similar although the AVHRR classification includes flooded forest in this category. Areas of regenerating forest appear to correspond well, especially the north of Manaus where several abandoned ranches are to be found.

DISCUSSION AND CONCLUSIONS

This study has employed JERS-1 image data from a series of dates, together with field data collected at Tapajós and Manaus in the Brazilian Amazon, to develop a semi-empirical model for the retrieval of above-ground biomass density within regenerating tropical forest. A detailed analysis of error

sources has led to a retrieval scheme with well-quantified confidence limits that has been shown to produce comparable results to other remotely sensed imagery when applied to a large-scale data set. While AVHRR can only be employed as a combination of cloud-free pixels from different days, JERS-1 images can take a high resolution snapshot of the forest in each 44 day period.

ACKNOWLEDGEMENT

This was a NERC funded TIGER programme study. The AVHRR regeneration map and field data from Manaus were provided by Richard Lucas and Miro Honzák of Swansea University. Fieldwork was in collaboration with INPE, Sheffield University and the NERC ABRACOS project with help from IBAMA, SUDAM and the Smithsonian Institute. Landsat Images were provided by INPE. JERS-1 images and mosaics were provided by NASDA.

REFERENCES

- [1] A. J. Luckman, J. R. Baker, T. M. Kuplich, C. C. F. Yanasse, and A. C. Frery, "A Study of the Relationship between Radar Backscatter and Regenerating Forest Biomass for Spaceborne SAR Instruments," *Remote Sensing of Environment*, vol. 60, pp. 1-13, 1997.
- [2] R. M. Lucas and M. Honzák, "Secondary Forests at Manaus: Data collected during a field campaign, July-August, 1993. Report to the Instituto Nacional de Pesquisas Espaciais (INPE) and the Instituto Nacional de Pesquisas da Amazônia INPA.," Department of Geography, University of Swansea 1995.
- [3] Y. Hashimoto and K. Tsuchiya, "Investigation of Tropical Rain Forest in Central Amazonia, Brazil based on JERS-1 SAR Images," *Journal of Geography, Japan*, vol. 104, pp. 827-842, 1995.
- [4] R. M. Lucas, "Integration of NOAA AVHRR and fine spatial resolution imagery for tropical forest monitoring," in *Advances in the use of AVHRR Data for Land Applications*, J. P. Malingreau and A. Belward, Eds. Dordrecht: Kluwer Academic, 1996, pp. 371-394.
- [5] E. P. W. Attema and F. T. Ulaby, "Vegetation modeled as a water cloud," *Radio Science*, vol. 13, pp. 357-364, 1978.
- [6] I. J. Birrer, E. M. Bracalente, G. J. Dome, J. Sweet, and G. Berhold, "Sigma0 Signature of the Amazon Rainforest Obtained from the Seasat Scatterometer," *IEEE Trans. Geosci. and Remote Sensing*, vol. 20, pp. 11-17, 1982.
- [7] Shimada, "Radiometric and Geometric Calibration of JERS-1 SAR," *Advanced Space Research*, vol. 17, pp. 79-88, 1996.
- [8] A. J. Luckman, J. R. Baker, M. Honzák, and R. Lucas, "Tropical Forest Biomass Density Estimation Using JERS-1 SAR: Seasonal Variation, Confidence Limits and Application to Image Mosaics," *Remote Sensing of Environment*, (Submitted), 1997.

Laser-Induced Imaging of Blue/red and Blue/far-red Fluorescence Ratios, F440/F690 and F440/F740, as a Means of Early Stress Detection in Plants

H. K. Lichtenthaler¹, N. Subhash^{1,2}, O. Wenzel¹, and J. A. Miehe³

¹ Botanical Institute, University of Karlsruhe, Kaiserstrasse 12, D-76128 Karlsruhe, Germany
(Phone: +49-721-608-3833, FAX: -608-4874; E-mail: Hartmut.Lichtenthaler@bio-geo.uni-karlsruhe.de)

² Centre for Earth Science Studies, P.B. 7250, Thiruvikkal P.O., Trivandrum - 695 031, India

³ Groupe d'Optique Appliquée, Centre de Recherches Nucléaires, F-67037 Strasbourg-Cedex 2, France

Abstract -- Green plants exhibit a blue (F440), green (F520), red (F690) and far-red (F740) fluorescence emission. These laser-induced fluorescence (LIF) signatures and ratios allow an early stress diagnosis. The fluorescence ratios blue/red (F440/F690) and blue/far-red (F440/F735) proved to be very sensitive indicators of ongoing stress events. This has been demonstrated by fluorescence emission spectra and the new fluorescence imaging technique. High-light, water and temperature stress as well as nitrogen deficiency, herbicide application, or attacks by mites, etc., can easily be monitored via increasing or decreasing fluorescence ratios and images.

INTRODUCTION

When illuminated by a UV-laser (e. g. 355 nm), green plants emit a genuine blue and green fluorescence as well as the well known red and far-red chlorophyll (Chl) fluorescence [1-4]. In green leaves the blue fluorescence is primarily emitted by the cinnamic acids of the cell walls of the chlorophyll-free epidermis cells [2, 4, 5], whereas the red and far-red fluorescences are emitted by the chlorophyll *a* in the chloroplasts of the leaves' mesophyll cells. Plants are exposed to various kinds of natural and anthropogenic, biotic and abiotic stress constraints [6]. The chlorophyll fluorescence ratio red/far-red (F690/F740) has proved to be an excellent non-destructive indicator of stress-induced changes in chlorophyll content [2, 5, 7]. The fluorescence ratios blue/red (F440/F690) and blue far-red (F440/F740), in turn, are even more sensitive to changes in the environment and to stress constraints. Both ratios, as determined via fluorescence emission spectra or via the new fluorescence imaging technique [4, 5], thus allow a very early stress detection as is demonstrated here.

MATERIALS AND METHODS

The plants used for this investigation were grown in the green house and the Botanical garden. The photosynthetic pigments (chlorophylls and carotenoids) were determined according to Lichtenthaler [8]. The fluorescence emission spectra were recorded using a conventional spectrofluorometer (LS-50, Perkin-Elmer, Germany) with a red sensitive Hamamatsu photo-multiplier using 355 nm as excitation wavelength and cut-off filters (390 nm for blue-green and 430 nm for Chl fluorescence) in order to exclude

excitation light and its second order. Fluorescence images (in the blue, green, red and far-red region) and fluorescence ratio images (blue/red, blue/far-red, red/far-red) were taken with the Karlsruhe/Strasbourg high resolution fluorescence imaging system [4, 5] with a pulsed Nd:YAG laser (355 nm, 100 kHz) as the excitation source.

RESULTS AND DISCUSSION

The fluorescence emission spectrum ($\lambda_{exc} = 355$ nm) of a green leaf exhibits a maximum in the blue region near 440 to 450 nm (termed F440 or F450), a shoulder in the green region between 520 to 530 nm (termed F520 or F530) as well as the red and far-red Chl fluorescences near 690 nm (F690) or in the range of 735 to 740 nm (termed F735 or F740) as shown in Fig. 1. The fluorescence emission of the upper leaf sides show a lower yield of blue, green and red fluorescence than that of the lower leaf sides. This is caused by a partial reabsorption of the emitted blue, green and red fluorescences by chlorophylls and carotenoids of the densely packed green palisade cells of the upper leaf half of the bifacial C3-plants such as tobacco and *Carpinus*. In contrast, the lower leaf half (spongy parenchyma) containing less green cells and many aerial interspaces, exhibit less reabsorption and a higher blue, green and red fluorescence emission. This differential chlorophyll content of both leaf halves is reflected in the lower value of the Chl fluorescence ratio F690/F735 of the upper leaf side (1.2) than of the lower leaf side (1.7).

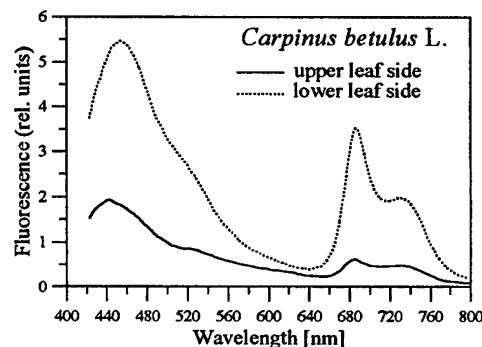


Fig. 1. Fluorescence emission spectrum of the upper and lower leaf side of a young sun-exposed *Carpinus* leaf (excitation 355 nm). The fluorescence ratios blue/red (F440/F690) and blue/far-red (F440/F735) amount to 3.3 and 3.9 when measured at the upper leaf side and 1.6 and 2.8 at the lower leaf side, respectively.

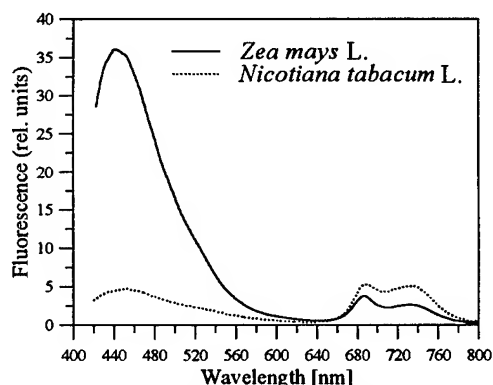


Fig. 2. Differential yield of blue-green fluorescence of a maize (*Poaceae*) and tobacco (dicot plant) leaf with 355 nm excitation. These differences are also seen between other members of the grass family (wheat, barley, rice) and dicot plants and reflect the higher content of cinnamic acids in the cell walls of the *Poaceae* than dicot plants.

In contrast to dicotyledonous plants, where the blue-green fluorescence is often lower than the red and far-red Chl fluorescence, the blue-green fluorescence yield of the grasses (*Poaceae*) is much higher (Fig. 2). Correspondingly, the fluorescence ratios blue/red and blue/far-red of maize, wheat and other *Poaceae* are much higher than that of dicot plants.

In plants with mineral deficiencies, in particular at nitrogen deficiency (lower Chl content), the blue-green fluorescence emission is higher than in normal green plants. This results in much higher values of the fluorescence ratios blue/red and blue/far-red and often higher values of the Chl fluorescence ratio red/far-red (Fig. 3).

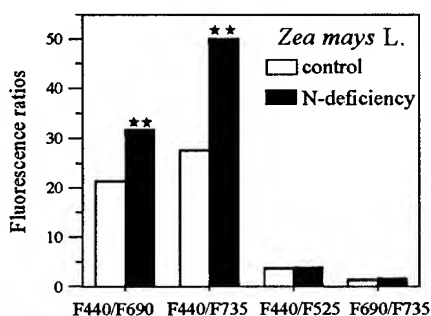


Fig. 3. Differences in the fluorescence ratios blue/red (F440/F690) and blue/far-red (F440/F735), red/far-red (F690/F735) and blue/green (F440/F525) in a green maize leaf (control) and a leaf from an N-deficient maize plant. Mean of 3 determinations. Significance: ** $p < 0.01$.

During water stress (2 weeks), combined with a short heat stress (40 °C, 6 h), the photosynthetic quantum conversion ceased at the leaf rim of tobacco leaves with a concomitant increase of the Chl fluorescence emission, whereas the blue and green fluorescences were little altered. This could be recognized after the treatment by forming the fluorescence ratio images blue/red and blue/far-red, which were several

times higher on the leaf rim than in the center leaf parts which retained the same ratios as in control leaves (Fig. 4). When after the treatment, these leaves were watered and kept at 20 to 25 °C, the photosynthetic activity was regenerated, whereas plants watered only one week later developed a broad leaf rim necrosis. The fluorescence ratios green/red (F520/F690) and green/far-red (F520/F740) exhibited somewhat lower values but showed in principle the same trends and increase as the ratios blue/red and blue/far-red. In fact, they are also very suitable early stress indicators.

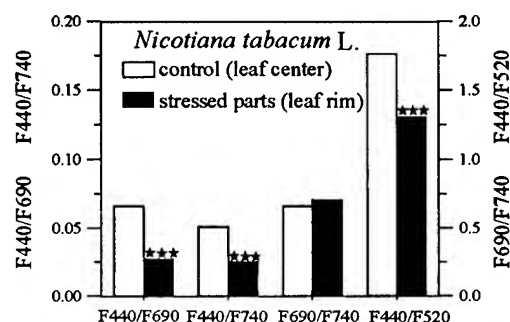


Fig. 4. Differences in fluorescence ratios blue/red, blue/far-red (left scale) and red/far-red and blue/green (right scale) between control (central leaf parts) and heat and water stressed leaf parts (lateral parts and leaf rim) of a tobacco leaf treated at 40 °C for 6h. Fluorescence imaging (n=10) with 180 pixels each. Significance: *** $p < 0.001$ [9].

After 4 week exposure of an attached *Rhododendron* leaf to full sunlight the leaf had a 30% lower Chl content as also reflected in a significant increase of the values of the Chl fluorescence ratio red/far-red (Fig. 5). The blue and green fluorescence emission had increased as compared to the shade control leaf and the red and far-red Chl fluorescence emission in the mesophyll cells was drastically reduced due to accumulation of UV-absorbing substances (e.g. flavonols) in the epidermis cells [9]. As a consequence the fluorescence ratios blue/red and blue/far-red were several times higher than in control leaves (Fig. 5). These changes in the blue/red and blue/far-red fluorescence ratios could already be detected after several days of sun exposure.

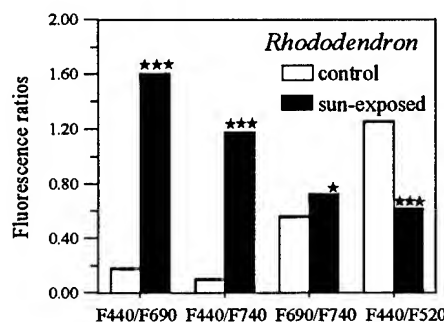


Fig. 5. Differences in the fluorescence ratios blue/red, blue/far-red, red/far-red and blue/green of a sun-exposed and shade leaf of *Rhododendron*. Fluorescence imaging (n=10) with 200 pixels each. Significance: *** $p < 0.001$; * $p < 0.05$ [9].

Early damage of bean plants attacked by mites was also detected by increases in the fluorescence ratios blue/red and blue/far-red (Fig. 6) long before visual symptoms of damage were detectable.

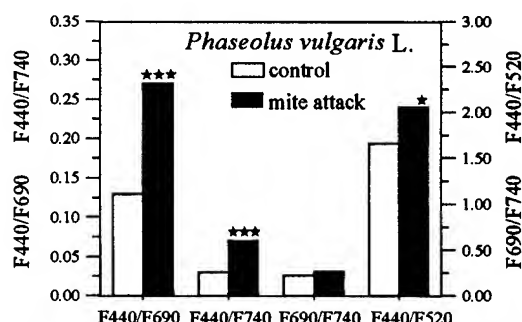


Fig. 6. Increase in the fluorescence ratios blue/red (F440/F690) and blue/far-red (F440/F740) in bean leaves attacked by mites as compared to controls. Determined via fluorescence imaging (n=10) with 200 pixels each. Significance: ***p<0.001 and *p<0.05.

Treatment and successive uptake of the herbicide diuron, which blocks photosynthetic electron transport and increases Chl fluorescence several fold, can be detected and monitored within hours or days (depending on the mode of application) by a strong decrease in the fluorescence ratios blue/red and blue/far-red (Fig. 7). Upon diuron treatment the Chl fluorescence ratio red/far-red increased up to 30%.

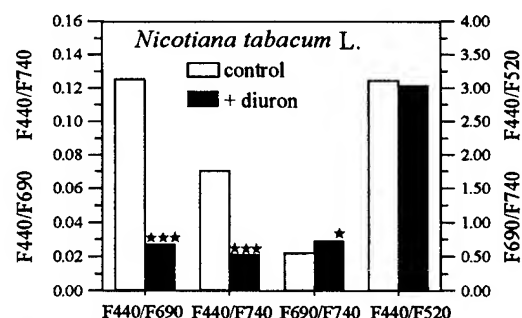


Fig. 7. Decline of the fluorescence ratios blue/red (F440/F690) and blue/far-red (F440/F740) in a green tobacco leaf treated with the herbicide diuron (10^{-5} M) via the lower leaf side. The Chl fluorescence ratio red/far-red increased by 25% as compared to the control. Fluorescence imaging (n=5) with 300 pixels each. Significance: ***p<0.001 and *p<0.05.

CONCLUSION

The fluorescence ratios blue/red (F440/F690) and blue/far-red (F440/F740) are very sensitive stress indicators of plants. Their monitoring permits a very early stress detection in plants at such a stage where countermeasures can still be taken to overcome the stress-induced changes in order to avoid severe damage to the plants. Furthermore, a stress-induced decrease in chlorophyll content is detected by significant increases of the Chl fluorescence ratio red/far-red. Although all fluorescence ratios can be determined from

fluorescence emission spectra of leaves (point data measurements), the laser-induced fluorescence imaging is much superior since it simultaneously senses the fluorescence emission of the complete leaf (i.e. several hundred leaf points) or even whole plants. This allows to detect gradients and local disturbances in fluorescence yield and ratios which are very early indicators of stress events. The Karlsruhe/Strasbourg fluorescence imaging system [4, 5] works already in the near distance of 0.5 to 10 m and can easily be further developed for remote sensing of the state of health of terrestrial vegetation.

ACKNOWLEDGMENTS

Financial support from the European Union, Brussels, within the INCO-COPERNICUS and the INTERREG II programs is gratefully acknowledged. N.S. acknowledges support under the ICTP Associateship scheme for his visit.

REFERENCES

- [1] F. Stober and H.K. Lichtenthaler, "Studies on the constancy of the blue and green fluorescence yield during the chlorophyll fluorescence induction kinetics (Kautsky effect)," *Radiat. Environ. Biophys.*, vol. 32, pp. 357-365, 1993.
- [2] F. Stober and H.K. Lichtenthaler, "Studies on the localization and spectral characteristics of the fluorescence emission of differently pigmented wheat leaves," *Botanica Acta*, vol. 106, pp. 365-370, 1993.
- [3] E.W. Chappelle, F.M. Wood, W.W. Newcomb and J.E. McMurtrey, "Laser-induced fluorescence of green plants," *Appl. Opt.*, vol. 24, pp. 74-80, 1985.
- [4] M. Lang, H.K. Lichtenthaler, H.K., M. Sowinska, P. Summ and F. Heisel, "Blue, green and red fluorescence signatures and images of tobacco leaves," *Botanica Acta*, vol. 107, pp. 230-236, 1994.
- [5] H.K. Lichtenthaler, M. Lang, M. Sowinska, F. Heisel, and J.A. Miehe, "Detection of vegetation stress via a new high resolution fluorescence imaging system," *J. Plant Physiol.*, vol. 148, pp. 599-612, 1996.
- [6] H.K. Lichtenthaler, "Vegetation stress: an introduction to the stress concept in plants," *J. Plant Physiol.*, vol. 148, 4-14, 1996.
- [7] H.K. Lichtenthaler and U. Rinderle, "The role of chlorophyll fluorescence in the detection of stress conditions in plants," *CRC Crit. Rev. Anal. Chem.*, vol. 19, Suppl. I, pp. 29-85, 1988.
- [8] H. K. Lichtenthaler, "Chlorophylls and carotenoids: pigments of photosynthetic biomembranes," *Methods Enzymol.*, vol. 148, 350-382, 1987.
- [9] M. Lang, M., H.K. Lichtenthaler, M. Sowinska, F. Heisel, J.A. Miehe, and F. Tomasini, "Fluorescence imaging of water and temperature stress in plant leaves," *J. Plant Physiol.*, vol. 148, pp. 613-621, 1996.

Over-the-Horizon Radar: Ground-Based Ocean Remote Sensing on Basin-Wide Scales

T. M. Georges

*NOAA Environmental Technology Laboratory
Boulder, CO 80303 USA
tgeorges@etl.noaa.gov*

J. A. Harlan

*Cooperative Institute for Research in Environmental Sciences
NOAA / University of Colorado
Boulder, CO 80306 USA*

Abstract — The U.S. National Oceanic and Atmospheric Administration (NOAA) has been testing high-frequency, ground-based, over-the-horizon (OTH) radars for mapping winds, waves, and surface currents over very large ocean areas. Recent results show that unambiguous surface wind direction can be mapped by combining meteorological insight with seeds from in-situ data. Vector surface currents can be mapped using two OTH radars whose coverage overlaps. A map of surface currents in the vicinity of a hurricane is an example.

INTRODUCTION

It has long been known that the “ocean clutter” that is normally discarded in military applications of high-frequency, over-the-horizon (OTH) radar contains useful information about the ocean surface. NOAA has been a principal player in exploiting the unique ocean-monitoring capabilities of OTH radar, and we have been fortunate indeed to have been given access to US Air Force and US Navy OTH radar systems, on a not-to-interfere basis, for testing and demonstrating these capabilities.

Results of recent tests show that it is feasible to map ocean-surface winds, waves, and currents over very large ocean areas. For example, we have mapped near-surface currents to ranges greater than 1,500 km, with 10- to 15-km resolution. The effects of ionospheric distortion on the sea echo, previously thought to prevent extraction of currents, can be mitigated by using land echoes as zero-Doppler references, by taking advantage of the different time scales of ionospheric motions and ocean currents, and by data editing using an objective data quality index.

These and other results of our ocean-monitoring tests can be viewed on our OTH radar web site at:

<http://www1.etl.noaa.gov/othr>. Because there is insufficient space here to show our graphical results (many of which are in color), the reader is invited to view them at our web site.

MAPPING WIND DIRECTION

Our most extensive wind-direction mapping exercise used two of the three Air Force OTH-B radars in Maine. During the 1994 hurricane season, we mapped surface wind direction over a large part of the tropical and subtropical Atlantic once a day for 40 days and delivered the products to the National Hurricane Center in near real time [1]. Our web site contains a movie of surface wind streamlines in the Atlantic coverage area for the 40 days.

Part of this data set was used to test a method for removing the left-right ambiguity in OTH radar wind directions, using an algorithm that combines meteorological insight with seeds from in-situ wind data. The results were used to analyze the interactions of tropical waves with a low-latitude polar front and the resulting effects on weather in the tropical Atlantic [2]. The OTH-B radars were also used to track several Atlantic hurricanes using their surface-wind-direction fields [3].

MAPPING RADIAL SURFACE CURRENTS

A few single-OTH-radar maps of radial surface currents were made in the vicinity of the Gulf Stream by the OTH-B radar in Maine [4]. Later, surface currents were mapped in the Florida Straits using the U.S. Navy Relocatable Over-the-Horizon Radar (ROTHR) in Virginia [5]. These currents were compared with geostrophic currents derived from satellite altimetry. Using the ROTHR radar in Texas, a radial current map was made that covers a large part of the Gulf of Mexico and the Caribbean Sea [6]. It shows details of the Caribbean

Western Boundary Current where it flows through the Yucatan Straits, makes a 180° turn in the Gulf of Mexico, then turns eastward into the Florida Straits. Bifurcations and eddies in the current cores reveal influences of bottom topography never before seen. The radar image also shows a southward counterflow through the eastern Yucatan Straits, which appears to generate wake eddies to the south of Cuba.

MAPPING VECTOR SURFACE CURRENTS

The first attempt to map vector ocean surface currents using two OTH radars was in May, 1995. The ROTHr radars in Texas and Virginia were pointed at the Florida Straits, and the two radial current maps were combined into a vector current map that showed details of the Florida Current and ancillary flows [7]. Subsequent dual-radar measurements in the Florida Straits have attempted to reveal the dynamics of the Florida Current by weekly sampling.

SURFACE CURRENTS NEAR A HURRICANE

In September, 1996, the Texas and Virginia radars were trained on hurricane Hortense, north of Hispanola. A vector surface current map reveals details of the ocean surface response to this storm, including strong currents in the right-forward quadrant of this storm that would become the storm surge at landfall. A region of surface-wind convergence coincides with a storm band revealed by airborne microwave radar, and current-map features resembling inertial oscillations in the storm wake are still being analyzed.

MAPPING UNAMBIGUOUS WIND DIRECTION

The Hortense data set was also analyzed for surface wind direction, which can be unambiguously determined when two radars are used. Dual-radar coverage in the vicinity of the storm center provided an unambiguous wind direction map there, which was extrapolated into the single-radar coverage. In addition, dual-radar data can be used to solve for a wave-directional spreading parameter, which appears to show high wave directionality where surface wind direction has not changed much for several hours.

MERGING OTH AND SATELLITE WIND DATA

To combine the wind-direction reliability of OTH radar with the wind-speed reliability of an orbiting microwave scatterometer, OTH-B wind directions measured in the Atlantic were merged with ERS-1 wind speeds during the 40-day test mentioned earlier [8]. When ambiguities are correctly resolved, scatterometer and OTH wind directions are in reasonable agreement, although there is some evidence of a bias of about 10° that could be attributed to the effects of the mean long-wave direction on the scatterometer measurement.

IN-SITU VALIDATION OF SURFACE CURRENTS

On June 14, 1995, the Texas ROTHr mapped the radial component of ocean surface current with 15-km resolution over a $230,000\text{-km}^2$ area in the Gulf of Mexico. Concurrently, an oceanographic research vessel measured near-surface currents within part of the area illuminated by the radar, providing an opportunity to compare radar-derived surface currents with in-situ sea truth. The *R/V Gyre*, operated by Texas A&M University, twice traversed the Gulf of Mexico Loop Current while measuring current vectors with a 153-kHz acoustic Doppler current profiler (ADCP). We compared radar-derived currents with spatially averaged currents in the uppermost ADCP bin (centered at 10-m depth). If only radar data exceeding a quality threshold are considered, the rms difference in the radial currents measured by the two techniques is 21 cm s^{-1} [9].

CONCLUSIONS

Ground-based over-the-horizon radars offer useful wind, wave, and current-mapping capabilities over large, fixed ocean areas on demand and can see through clouds and rain. Progress toward routine application of these radars to monitor marine meteorology and circulation will depend to a large degree on the availability of existing military OTH radars, the siting chosen for future ones, and on forming partnerships with other users of these multimission sensors. The immediate future presents opportunities to use the Navy ROTHr radar on a non-interfering basis for meteorological and oceanographic investigations in the region now being called the Intra-Americas Sea.

ACKNOWLEDGMENTS

We thank the U.S. Air Force and the U.S. Navy for providing access to their OTH radar systems at no cost to NOAA.

REFERENCES

- [1] T.M. Georges, J. A. Harlan, L. R. Meyer, and C. A. Grunden, "Ocean-surface wind directions measured by the Air Force over-the-horizon radar during the 1994 hurricane season," NOAA Tech Memo ERL ETL-246, 93 pp., 1995.
- [2] G. S. Young, J. A. Harlan, and T. M. Georges, "Application of over-the-horizon radar observations to synoptic and mesoanalysis over the Atlantic," *Weather and Forecasting*, vol. 12, pp. 44-55, 1997.
- [3] T. M. Georges, J. A. Harlan, L. R. Meyer, and R. G. Peer, "Tracking hurricane Claudette with the U.S. Air Force

- over-the-horizon radar," *J. Atmos. Oceanic. Technol.*, vol. 10, pp. 441-451, 1993.
- [4] T. M. Georges and J. A. Harlan, "Gulf Stream anomaly seen by defense radar," *EOS*, vol. 76, p. 146, 1995.
 - [5] T. M. Georges, J. A. Harlan, R. R. Leben, and R. A. Lematta, "A test of surface-current mapping with over-the horizon radar," *IEEE Trans. Geosci. Rem. Sens.*, in press, 1997.
 - [6] T. M. Georges and J. A. Harlan, "Over-the-horizon radar: Ground based ocean remote sensing on basin-wide scales," *Backscatter*, Newsletter of the Alliance for Remote Sensing, vol. 7, p. 6-8, 1996.
 - [7] T. M. Georges, J. A. Harlan, and R. A. Lematta, "Large-scale mapping of ocean surface currents with dual over-the-horizon radars," *Nature*, vol. 379, pp. 434-436, 1996.
 - [8] T. M. Georges, J. A. Harlan, and P. Chang, "Merging over-the-horizon radar with satellite oceanographic data," *Backscatter*, Newsletter of the Alliance for Remote Sensing, vol. 7, pp. 19-21, 1996.
 - [9] J. A. Harlan, T. M. Georges, and D. C. Biggs, "Comparison of over-the-horizon radar surface current measurements in the Gulf of Mexico with simultaneous sea truth," *J. Marine Sys.*, in press, 1997.

A Comparison of Surface Current Fields derived by Beam Forming and Direction Finding Techniques as applied by the HF Radar WERA

Klaus-Werner Gurgel, Georg Antonischki and Thomas Schlick

Universität Hamburg, Institut für Meereskunde, Troplowitzstraße 7, D-22529 Hamburg, Germany

Phone: +49 40 4123 5742 Fax: +49 40 4123 5713 Email: gurgel@ifm.uni-hamburg.de

Abstract – HF radar in oceanography makes use of backscattering of electromagnetic waves of 10 m to 50 m wavelength from the rough sea surface to measure surface current and ocean wave parameters. In Germany, the work on ground wave HF radar started in 1980, adopting NOAA's CODAR (COastal raDAR). Recent developments within the European project SCAWVEX (Surface Current And Wave Variability Experiment) lead to a new design called WERA (Wellen RAdar). In Spring 1996, two WERA and CODAR systems have been deployed north and south the Rhine mouth at the Dutch coast. While CODAR uses a four-element squared receive antenna array and direction finding technique for azimuthal resolution, WERA in addition can be configured to use a linear array and beam forming. As both systems have been operated simultaneously at the same location, comparisons of the surface current fields measured by the different systems and algorithms are possible. By defining an absolute quality criterion based on spectral analysis of current time series, limitations in the direction finding algorithm concerning ship traffic can be identified.

INTRODUCTION

HF radar in oceanography makes use of backscatter of electromagnetic waves of 10 m to 50 m wavelength from the rough sea surface. The backscattered signal can be analysed to derive ocean surface current and wave parameters. The basic physics have been discovered in 1955 by Crombie [1]. In Germany, the work on ground wave HF radar started in 1980 by adopting NOAA's CODAR (COastal raDAR), which had been introduced in 1977 by Barrick, Evans and Weber [2]. Recent developments within the European project SCAWVEX (Surface Current And Wave Variability Experiment) [3] lead to a new design called WERA (Wellen RAdar). As WERA uses a flexible design, different techniques for azimuthal resolution can be compared.

This paper tries to contribute to the controverse discussions on different techniques of azimuthal resolution in a HF radar, as beam forming and direction finding. It will show advantages and disadvantages on the basis of measured data. The paper does not aim to make any final decision on what to be the best algorithm or technique.

This work has been supported by the European Commission, DG XII, within the Mast-2 programme, project MAS2-CT94-0103, SCAWVEX (Surface Current And Wave Variability EXperiment).

SPATIAL RESOLUTION OF A HF RADAR

Spatial resolution of a HF radar has to be done in range and azimuth. Two different techniques can be applied to perform range resolution. The CODAR uses the travelling time of a pulse to resolve the range. WERA uses a linear frequency chirp, where the frequency shift between the transmitted signal and the received echo determines the range. The range cell depth is related to the bandwidth of the chirp. This technique is known as FMCW¹.

Common techniques for azimuthal resolution are direction finding and beam forming. The University of Hamburg CODAR uses direction finding with a 4-element array of vertical polarized antennas, which are arranged in a square. **Direction finding** is based on a known set of values (phase differences and amplitudes of the antenna signals) as a function of incident angle. To find the incident angle for a measured set of values, this function is inverted by some kind of least-squares-fit. Superposed sea echos from different incident angles are resolved in frequency domain, stating different angles to be attached to different Doppler shifts. Several algorithms and antenna configurations are possible, some of which can be found in [5], [6] and [7]. For **beam forming**, the weighted and phase shifted signals from each antenna of a linear array are summed up. The weighting function is needed to reduce side lobes, the phase shift steers the beam to the desired direction. The beam width depends on the aperture of the array. This technique gives access to the complete timeseries of sea echos at the selected area.

WERA is designed with 16 parallel operated receiver channels, which can be used to configure a 4-antenna "CODAR" array together with a 12-antenna linear array or a 16-antenna linear array. Direction finding can be applied to all antenna configurations including linear arrays. Beam forming is possible on the linear arrays. This flexibility allows simultaneous measurements with different configurations. A description of WERA and advantages and disadvantages of direction finding and beam forming are given in [4].

THE EXPERIMENT

The experiment area was selected in front of the Rhine mouth at Eurogeul, which is the main shipping channel to Rotterdam harbour. Here, the Rhine river transports about 2,000 m³/s of fresh water into the North Sea. Interaction with the tidal current leads to complex eddies

¹Frequency Modulated Continuous Wave

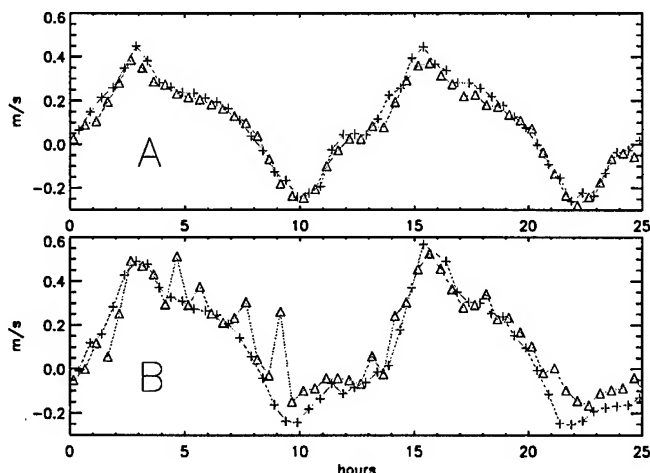


Figure 1. **Upper:** The radial component of the current velocity at location A in fig. 2 as a function of time, CODAR (Δ) and WERA (+) with beam forming. **Lower:** The same as above at location B in fig. 2. This radar cell lies within Eurogeul, which is the main shipping channel to Rotterdam harbour. Note the spikes found in the CODAR measurements.

and fronts, which are moving through the measurement area.

In Spring 1996, WERA and CODAR systems were deployed north and south of the Rhine mouth near Arendsduin and Ouddorp (Fig. 2). At each site, one CODAR and one WERA was operated in alternating time slices. This setup of the HF radars allows comparisons between both systems as well as between the different algorithms for azimuthal resolution, direction finding and beam forming.

A reduction of HF radar working range from 50 km to 30 km was observed with both systems, which may be related to reduced sea surface salinity due to the fresh water input. Also, some effects were noted, which may be induced by the heavy ship traffic.

COMPARISON OF RADIAL CURRENT VELOCITIES

Because the algorithm combining the radial components of the surface current has nonlinear effects [6], radial components measured at the Ouddorp site are compared. Data from both CODAR and WERA are available from March 17th 21:00 UTC to March 25th 19:00 UTC, which corresponds to 382 measurements in 191 hours. During this periode, the sea state was low. CODAR data have been analysed using the 4-antenna square array direction finding technique (*cod*), whereas WERA data have been analysed using the 4-antenna square array direction finding technique (*we4*), a 12-antenna linear array direction finding technique (*we12*), and a 12-antenna linear array beam forming technique (*we12b*). Potential difficulties expected in the comparisons are, that CODAR and WERA operate at slightly different range resolution (2 km compared to 1.2 km), that both systems have a different range offset, that CODAR integrates over 18 minutes and WERA integrates over 9 minutes, and that

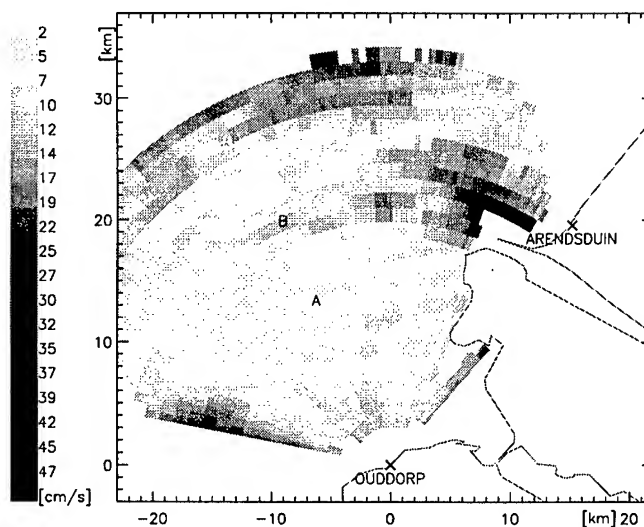


Figure 2. The spatial distribution of the mean RMS difference between the radial components of the current velocities measured by CODAR and by WERA using beam forming.

there is a time shift between the radar measurements.

Fig. 1 (upper diagram) shows two tidal cycles of the radial component of the current velocity measured at location A in fig. 2 by CODAR (*cod*) and by WERA (*we12b*). The velocities are dominated by the tidal current. Both curves show a good agreement. The RMS² difference of the complete time series is below 5 cm/s.

To compare the radars over the whole measurement area, the RMS difference is calculated for each radar cell. The result is shown in fig. 2. Up to ranges of 25 km, the RMS difference is lower than 10 cm/s. An increase of the RMS difference can be seen near the outflow of the Rhine river and extends over the Eurogeul.

Fig. 1 (lower diagram) shows the time series for a radar cell, which is located near to the Eurogeul. In the CODAR measurements, some spikes occur. These can be identified as errors, which might be caused by ship echoes.

AN INDEPENDENT CRITERION ON QUALITY

A principle problem is, that differences between instruments do not indicate which one is the better one. The common result of such a comparison is, that the instruments measure more or less the same values. An independent criterion is desired, which would help to describe data quality absolutely.

As a quality criterion, the energy of the high frequency components of the signal was selected, because spikes and discontinuities dominate the high frequency band. Such a noise value is determined for each radar cell by applying a window to the time series, calculating a FFT³, and summing up the energy of the spectral lines between perodes of 1 hour to 1.35 hours. This absolute noise value is calculated for all HF radar configurations:

²Root Mean Square

³Fast Fourier Transformation

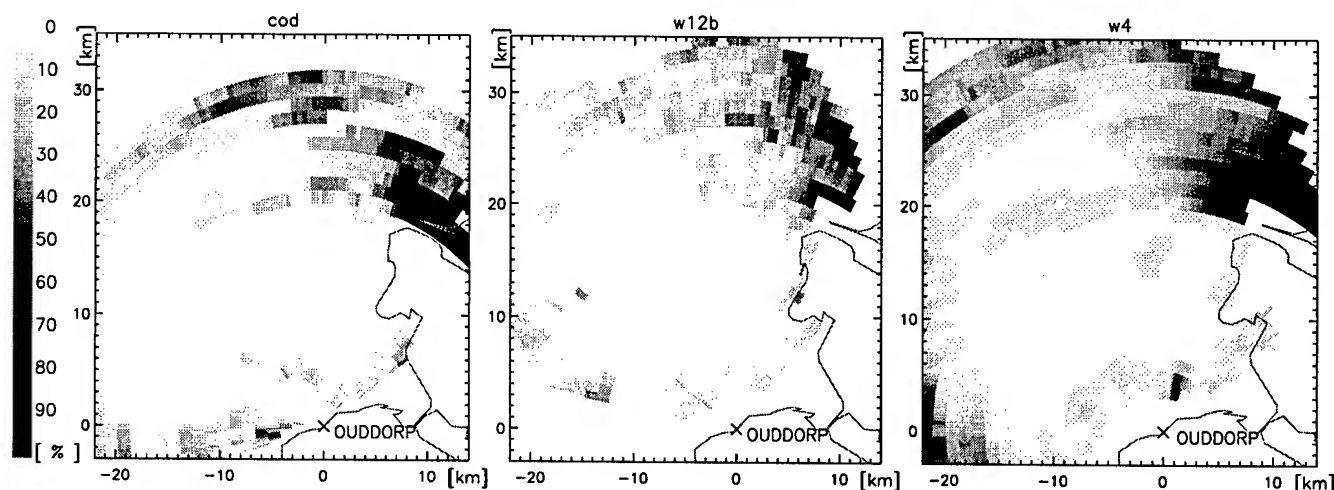


Figure 3. The spatial distribution of the amount of noise and spikes in the radial component of the surface current for different radar configurations Left: CODAR (*cod*), Middle: WERA with beam forming (*w12b*), Right: WERA with 4-antenna direction finding (*w4*)

cod, *w12b*, *w12* and *w4*. The main energy of the signal can be found around the dominant M2 tide at 12.4 hour periode.

Fig. 3 shows the noise value for the area covered by the different radar configurations. The scale is adjusted for 0.4 times the maximum observed noise of all configurations to be 100 %. CODAR (*cod*) and WERA (*w12b*) show low noise values up to ranges of 25 km. The dark patches in the CODAR results near the Eurogeul can be traced back to spikes (fig. 1). This is an indication, that the direction finding algorithm used by CODAR does not suppress ship echos as good as the beam forming algorithm used by WERA. Configuration *w4* compared to *cod* and *w12b* shows reduced performance, especially on the Eurogeul area. These problems might be caused by interaction or shading of the non multiplexed antennas. Direction finding on a linear array (*w12*, not shown here) gives even worse performance. As information perpendicular to the array is missing, the algorithm can not have a "linear" characteristic in azimuth. The increase of noise at far ranges for all radar configurations might be caused by gaps in the data, due to variations in the working range.

SUMMARY

Radial components of the surface current velocity measured by different HF radar systems and different techniques for spatial resolution were compared. It was shown, that in most cases the differences in the measurements have been below 10 cm/s. Problems occur at areas with heavy ship traffic. An absolute quality criterion was defined and it showed, that the direction finding technique is more faulty in this case. In future work, simulation studies will be used to optimize the direction finding algorithm to be more stable in such situations. The method used to compare our systems can easily be applied to other HF radars.

ACKNOWLEDGEMENTS

The authors wish to thank the other members of the HF radar group, H. H. Essen, F. Schirmer and our technician M. Hamann for building WERA, discussing results and supporting the field campaign, and the Dutch Rijkswaterstaat, H. C. Peters, J. Vogelzang, A. Wijzes and local authorities for excellently supporting the logistics and supplying topographic and oceanographic data.

REFERENCES

- [1] D. D. Crombie, "Doppler spectrum of sea echo at 13.56 Mc/s," *Nature*, vol. 175, pp. 681-682, 1955.
- [2] D. E. Barrick, M. W. Evans, and B. L. Weber, "Ocean surface current mapped by radar," *Science*, vol. 198, pp. 138-144, 1977.
- [3] L. R. Wyatt, K.-W. Gurgel, H. E. Krogstad, H. C. Peters, D. Prandle, and G. J. Wensink, "Surface current and wave variability experiments," in *Marine sciences and technologies, Second MAST days and Euromar market - Volume 1*, pp. 154-168, 1995.
- [4] K.-W. Gurgel and G. Antonischki, "Remote Sensing of Surface Currents and Waves by the HF Radar WERA," in *proceedings EEO 97*, in press, 1997.
- [5] B. L. Weber and J. A. Leise, "A four-element direction finding antenna," NOAA Tech. Memo., ERL WPL-99, U.S. Dept. Commerce, NOAA/ERL, Boulder, CO, 1982.
- [6] K.-W. Gurgel, *Flächenhafte Messung der Oberflächenströmung vom fahrenden Schiff aus*. PhD thesis, Universität Hamburg, November 1993.
- [7] B. J. Lipa and D. E. Barrick, "Least-squares methodes for the extraction of surface currents from CODAR crossed-loop data: Application at ARSLOE," *IEEE Journal of Oceanic Engineering*, vol. OE-8, pp. 226-253, 1983.

Initial Observations of Ocean Currents, Current Shears and Wind Direction Using Multi-Frequency HF Radar

Calvin C. Teague

**Space, Telecommunications and Radioscience Laboratory
Stanford University, Stanford, CA 94305-9515**

**John. F. Vesecky, Peter E. Hansen, Neil G. Schnepf, Jason M. Daida
Department of Atmospheric, Oceanic, and Space Science
2455 Hayward, University of Michigan, Ann Arbor, MI 48109-2143**

Robert G. Onstott, Ken Fischer

**Environmental Research Institute of Michigan
P.O. Box 134001, Ann Arbor, MI 48113-4001**

Daniel M. Fernandez

**Institute of Earth Systems Science and Policy
California State University, Monterey Bay, 100 Campus Center, Seaside CA 93955-8001
and CE/CS, University of California, Santa Cruz, CA 95064**

A new High-Frequency (4–25 MHz) phased-array radar, constructed jointly by the University of Michigan, the Environmental Research Institute of Michigan and Stanford University, was installed at Santa Cruz, California in July, 1996. After initial equipment checkout and antenna calibration using a transponder carried on a small boat, regular data collection started in October, 1996. Installation of a second HF radar is planned at a site south of Santa Cruz to allow resolution of current vectors. Wind and wave data from moored buoys in the radar field of view, wind sensors at several coastal sites, and current measurements from several CODARs in the Monterey Bay area also are available.

RADAR HARDWARE AND DATA PROCESSING

The radar employs a direct digital frequency synthesizer which is programmable on a pulse to pulse basis, a coded modulation waveform, a pair of omnidirectional transmit antennas, and an array of eight wideband loop receive antennas which are sequentially sampled and individually recorded. Conventional beamforming is done by software in the frequency domain, and alternative direction-finding algorithms can be applied to the recorded data. Range resolution is 3 km, and the 48 m phased-array aperture gives an angular resolution at the highest frequency of about 20°. Vertical current shear is estimated by using multiple radar frequencies which are scattered through Bragg resonance by ocean waves of different lengths, which in turn are sensitive to currents at various depths. For this experiment, the radar was programmed to operate on four frequencies between 4.8 and 22 MHz, allowing estimation of the vertical current shear

in the upper meter of the ocean surface [1], [2]. Assuming a logarithmic current profile, current is probed at depths ranging from about 1.4 m using 4.8 MHz to about 30 cm using 21.77 MHz [3].

Radar timing, frequency control and data sampling are controlled by an MC68332 microprocessor, and overall radar operation and data processing are done on a Macintosh 7100 computer. Radar data are recorded for about 13 minutes each hour, and the raw data are stored on removable disk cartridges for subsequent analysis. The raw data are processed by partitioning the time series from each frequency, range bin and antenna into several segments, and computing a Fourier transform for each segment. Beam steering is done by applying an amplitude taper and phase shift to the transforms for the 8 antennas and then coherently adding those together, followed by incoherent power summation over the various segments. Doppler shift is estimated by computing the centroid of the stronger of the approaching and receding Bragg peaks, and current is estimated by subtracting the Doppler shift due to the still-water phase velocity of the resonant waves. This procedure is repeated for each beam direction, range bin and frequency.

CURRENT ESTIMATION

Figure 1 shows an example of radar data taken at 1600 PST on 6 March 1997. The radar location is at (0,0), and the x-axis is along the coastline. The radar antenna broadside direction (y-axis) is 173°T. The plots show the received power multiplied by r^3 , where r is the range to the ocean surface, normalized by the maximum received power. The height of each

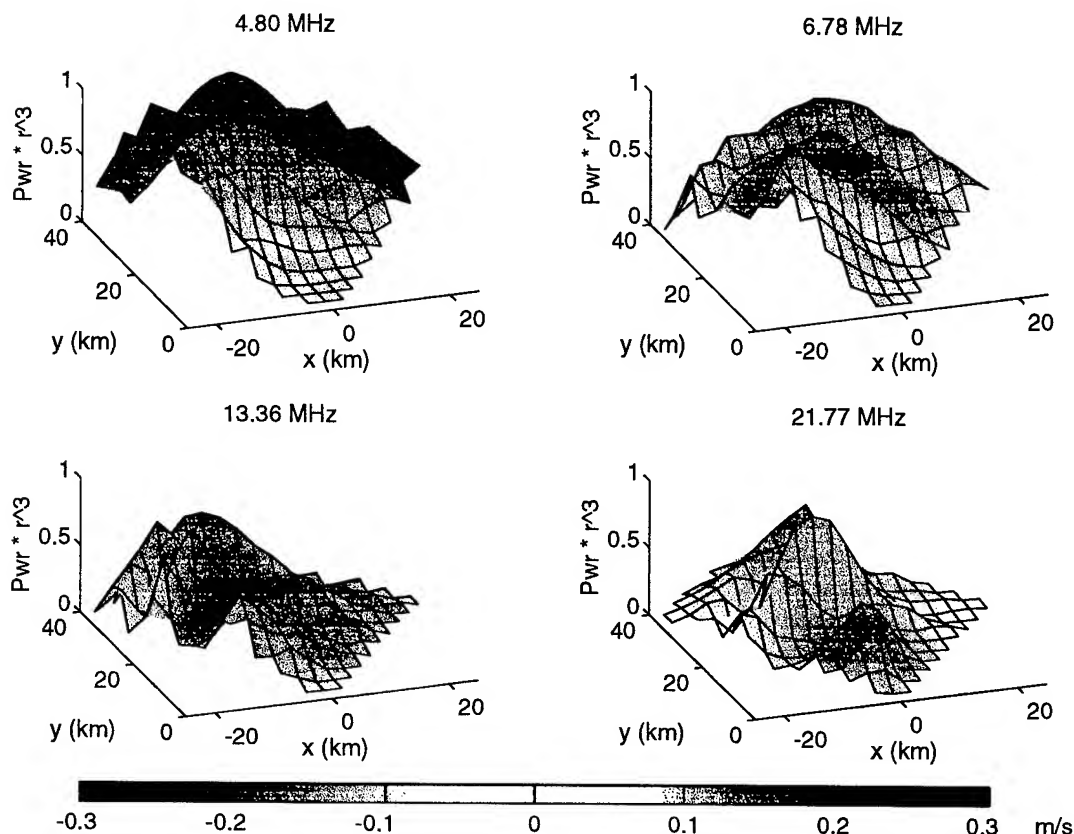


Figure 1: Plots of relative backscatter power and ocean surface current for data collected at 1600 PST on 6 March 1997. The height of the plot surface represents received radar power scaled by r^3 and normalized by the maximum power at each frequency; thus it is proportional to the normalized radar cross-section of the ocean surface at each frequency. The color of the plot surface represents the radial component of the ocean surface current inferred from the Doppler measurements. The scale at the bottom shows the current velocity color-coding ranging from -0.3 to 0.3 m s^{-1} . The radar carrier frequency is indicated above each plot.

plot thus shows the relative radar cross-section of the ocean surface at each radar frequency. The color of the surface indicates the ocean current radial velocity. For these data, the wind at the M1 buoy operated by the Monterey Bay Aquarium Research Institute (MBARI), near the center of the radar field of view, was between 9 and 11 m s^{-1} toward 120°T during the previous 2 hours. Note that the peak of the radar cross-section is generally in the direction of the wind and that it increases as a function of distance from the radar, as one would expect for fetch-limited receding waves. However, the maximum (negative) current is not necessarily in the same direction as the maximum cross-section. Also note that the most negative current is seen farthest from shore at the lowest radar frequency corresponding to a depth of about 1.4 m and moves progressively closer to shore with increasing radar frequency (depth decreasing to about 30 cm).

During the 10 day period of 6–15 March 1997 the quality of the data depends on the operating frequency and time of

day. At 4.8 MHz , the noise level shows a strong diurnal variation of almost 20 dB due to the variation in ionospherically-propagated noise which is low during the day and high at night. In addition, the 31 m ocean waves respond quickly to the local wind which typically is stronger during the afternoon than during the night, so the signal-to-noise ratio is much higher during the day. This pattern is seen to a lesser extent at 6.78 MHz . At 13.38 and 21.77 MHz the noise level shows little diurnal variation, but at 21.77 MHz the propagation loss due to a rough sea surface causes lower signals during high wind conditions, even though the ocean waves are high. The use of multiple frequencies allows some optimization of radar operation with time of day and under various wind conditions in addition to enabling an estimation of vertical current shear.

WIND DIRECTION ESTIMATION

The wind direction can be estimated by comparing the approaching and receding backscattered energy. The Bragg

peak ratios are calculated from the HF radar return echo at each of the four operating frequencies of the Santa Cruz-based high-frequency radar system. The ratios (which are typically expressed in dB) represent the comparative energies associated with resonant Bragg ocean waves that propagate away from the radar to those that propagate toward the radar. There is a strong connection between the measured Bragg peak ratios at each of these frequencies to the prevailing wind speed and wind direction. The difference in the response of the Bragg peak ratios at multiple wavelengths, however, has not been explored in past studies. For the four radar frequencies represented in this study, the corresponding Bragg resonant ocean wavelengths are: 31.3, 22.1, 11.2, and 6.9 m.

A time period was selected in March where there was a 10 day duration when the winds exhibited a cycle of strong afternoon seabreeze and much weaker winds during the evening and early morning hours. The stronger afternoon winds blew in over Monterey Bay (as measured from MBARI's M1 buoy) from the W-NW and the weaker winds' directions were variable.

Winds that developed over Monterey Bay during these afternoon time periods were very strong, with wind speeds at times in excess of 10 m s^{-1} . Radar measurements of the Bragg peak ratios are shown for this time period from a radar cell that lies in the direction of the buoy from the radar site, but was approximately 12 km closer than the buoy. This closer radar range cell was chosen because it contained a greater number of usable radar runs for the comparison. Figure 2 illustrates high correlation between the Bragg peak ratio at 13.8 MHz. Correlation was similar at 4.8 and 6.78 MHz, but the highest radar frequency of 21.8 MHz had very few usable data points at this location, so any correlation is not apparent at this radar frequency.

Although it is not shown in this plot, it is of interest to note that the Bragg peak ratios indicated a predominance toward onshore (approximately northerly) waves at the lower radar frequencies and offshore waves (especially during the daily wind events) at the 13.38 MHz frequency. The strong daily winds (which blew toward the southeast) appeared to increase the energy in the offshore waves at all of the frequencies to which the radar was sensitive, but the presence of an onshore component at the lower radar frequencies is perhaps indicative of swell propagating onshore from other locations.

The relationship between the wind speed and direction and the ocean gravity wave spectrum has been modelled with a cardioid directional spectrum (e.g. Phillips) and the wind speed and direction both affect the energy associated with the ocean gravity waves at a given angle [4]. This initial study presents some measurements that indicate the fairly large range of ocean gravity waves that respond quickly to wind forcing and points to the utility of multiple frequency high-frequency radar for the measurement of nearshore oceanic wind and wave parameters.

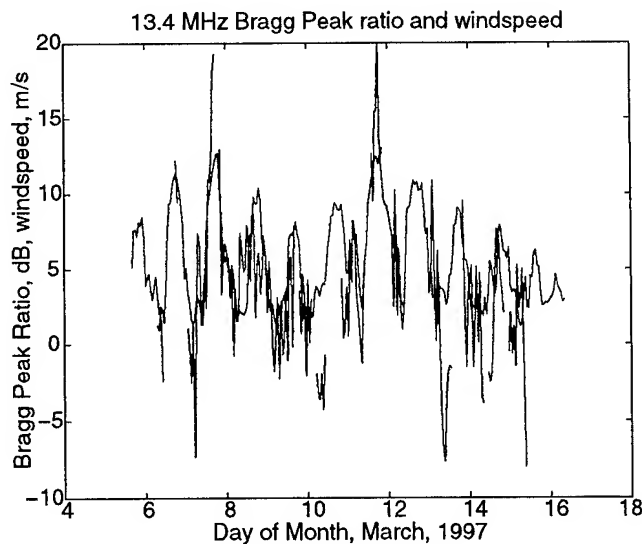


Figure 2: Bragg peak ratio (red) versus wind speed (blue) from MBARI buoy M1 for a 10 day period in early to mid March. The Bragg peak ratio (in dB) represents the energy from the receding ocean waves divided by the energy from the approaching ocean waves. The location at which the radar data were collected corresponds to a point between where the buoy is located and where the radar is stationed, and is approximately due south of the radar and about 12 km from the radar. The radar data were collected at the 13.38 MHz radar frequency, which corresponds to approximately 11 m ocean waves.

We wish to thank Francisco Chavez for use of the MBARI wind data, and Steve Davenport for making the facilities at Long Marine Laboratory available for the radar installation.

REFERENCES

- [1] Stewart, R. H. and J. W. Joy, "HF radio measurement of surface currents," *Deep-Sea Research*, 21, 1039–1049, 1974.
- [2] Fernandez, D. M., J. F. Vesecky and C. C. Teague, "Measurements of upper ocean surface current shear with high-frequency radar," *Journal of Geophysical Research*, 101, 28615–28625, 1996.
- [3] Ha, E. C., "Remote sensing of ocean surface current and current shear by HF backscatter radar," Ph.D. dissertation, Stanford Electronics Labs, Stanford Univ., Stanford, Calif., Tech. Rep. D415-1, 1979.
- [4] Tyler, G. L., C. C. Teague, R. H. Stewart, A. M. Peterson, W. H. Munk, and J. W. Joy, "Wave directional spectra from synthetic aperture observations of radio scatter," *Deep-Sea Research*, 21, 989–1016, 1974.

Observations of Near-Surface Ocean Currents at Varying Depths Using a New Multifrequency HF Radar

John F. Vesecky¹, Calvin C. Teague², Robert G. Onstott³, Peter Hansen¹, Neil Schnepf¹, Dan Fernandez⁴, Jason Daida¹ and Ken Fischer³

¹ Atmospheric, Oceanic and Space Science Dept., University of Michigan, 2455 Hayward Rd., Ann Arbor MI 48109-2143, Tel: 313-764-5151, 764-5137 (FAX), email: jfv@umich.edu

² STAR Laboratory, Electrical Engineering Dept., Stanford University, Stanford CA 94305-4055,

³ ERIM International, 3300 Plymouth Rd., Ann Arbor MI 48105

⁴ Computer Engineering Dept., University of California at Santa Cruz & California State Univ. Monterey Bay,

Abstract -- A new multifrequency (4-25 MHz) HF radar was installed at the Long Marine Lab. (University of California at Santa Cruz) on the north coast of Monterey Bay CA in July, 1996. This radar is capable of observing near-surface currents at varying depths in the top two meters of the ocean. Observations were made over a ten day period in March, 1997 during which there was a strong land-sea breeze circulation over Monterey Bay. Radial current measurements corresponding to depths of about 0.3, 0.5, 1.0 and 1.4 m were made during this period using HF radar data from four operating frequencies. Fourier analysis of these data shows that very near the surface the strongest periodic component is a diurnal one corresponding to the diurnally varying surface stress from the land-sea breeze. At deeper depths the diurnal component remains, but a semi-diurnal component grows in strength with increasing depth of the current measurement. Thus, multifrequency HF radar combined with deeper current measurements from buoys and moorings are able to investigate the upper layer of the coastal ocean where wind and tidally driven currents struggle for dominance.

OBJECTIVE and INTRODUCTION

The objective of this paper is to investigate the impact of wind stress at the ocean surface and of tidal flows on near-surface currents in the top few meters of the ocean. This work follows on investigations of surface current circulation in Monterey Bay using single frequency HF radars by Paduan and Rosenfeld [1]

A new high-frequency (4-25 MHz) phased-array radar, designed and constructed jointly by the University of Michigan, Stanford University and ERIM International was installed at Santa Cruz, California in July, 1996. After initial equipment checkout and antenna calibration using a transponder (carried on a small boat), regular data collection started in October, 1996. The radar operates on four frequencies in the HF band using vertical transmit antennas, and an array of eight wideband loop receive antennas. Range resolution is about 3 km, and the 48 m phased-array aperture gives an angular resolution at the highest frequency of about 15°. Vertical current shear is

estimated by using multiple radar frequencies which are scattered through Bragg Resonance by ocean waves of different lengths, which in turn are sensitive to currents at various depths [2 & 3]. For these observations the radar operated on four frequencies: 4.8, 6.8, 13.4 and 21.8 MHz, allowing estimation of the vertical current shear at 'effective' depths of 1.4, 1.0, 0.5 and 0.3 m respectively. The calculation of these effective depths assumes a logarithmic current profile. Further description of the radar's design features and operation is given in a companion paper by Teague et al. in these proceedings [4] and a progress report by Vesecky et al. [5].

OBSERVATIONS

The observational geometry is illustrated in Fig. 1. Radar coverage changes with the wave height of the Bragg resonant ocean waves. With a strong wind the range can be 50 km or more and with weak winds significantly less. Further information is given by references [4 & 5]. The typical resolution cell size is shown for the highest frequency of operation. In normal practice currents would be estimated on a grid that is 1/2 of this size in both range and azimuth. At lower operating frequencies standard (delay and sum) beamforming techniques produce azimuth resolution that is inversely proportional to frequency so that at the lower operating frequencies resolution cells become very large in azimuth angle -- the range cells remain the same size since the radar bandwidth is held constant. In Fig. 1 the azimuth lines are separated by 15°, corresponding to the azimuth resolution at the 21.8 MHz operating frequency. Each resolution cell will contain an estimate of the radial surface current at the four depths mentioned above. These current estimates usually vary over the range ± 0.4 m/s.

Strong Land-sea breeze circulation often dominates the surface wind field over Monterey Bay, especially during the summer. Typically sunlight warms the surface in the Salinas Valley (east of Monterey Bay) beginning at sunrise. The warm ground heats the cooler surface layer of the atmosphere and convection proceeds with rising air over the Salinas Valley. This

action in turn causes cool air over Monterey Bay to flow from the sea toward the land. By noon a circulation is

magnitudes (not power) of the Fourier components are shown in Fig. 3.

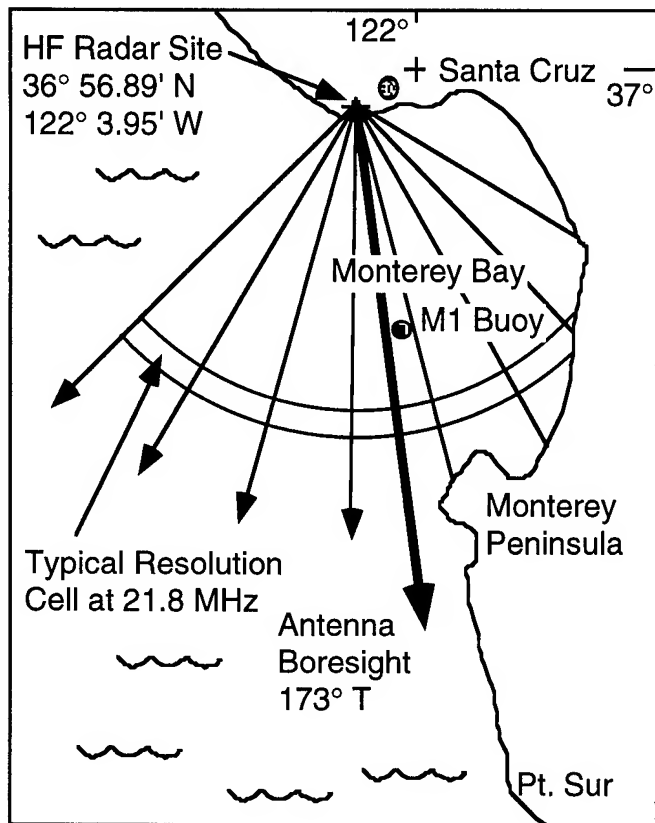


Fig. 1. Observational geometry for the multifrequency HF radar located at the Long Marine Laboratory of the University of California at Santa Cruz.

established with air flowing from sea to land near the surface and from land to sea at about a kilometer altitude. This process produces westerly surface winds of 8 to 12 m/s by about 4 pm local time. After sunset the air over the ocean cools rapidly and the process reverses due to the relatively warm sea surface at night, but is weaker. For analysis we picked March 7-17, 1997 when the land-sea breeze circulation was strong. Fig. 2 shows the wind speed fluctuations observed at the M1 buoy deployed by the Monterey Bay Aquarium Research Institute (MBARI) and shown in Fig. 1.

ANALYSIS and DISCUSSION

To accomplish our objective we assembled a ten day time series of hourly surface current estimates at each of the four radar operating frequencies. Each point in the time series was an average over 5 range bins and three 15° angle bins centered on the M1 buoy location shown in Fig. 1. This average covers a region about 10 km in radius centered on M1. Each of these four time series was Fourier transformed. The resulting

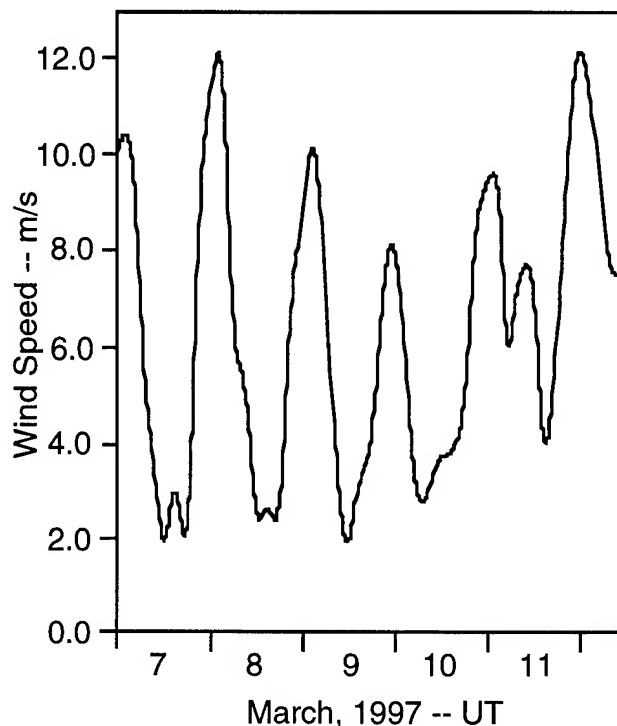
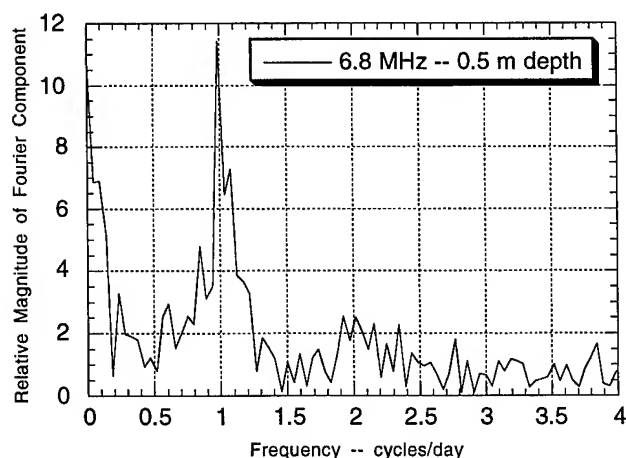
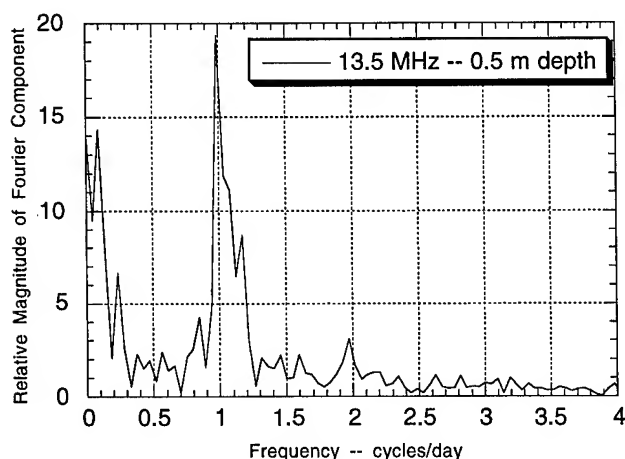
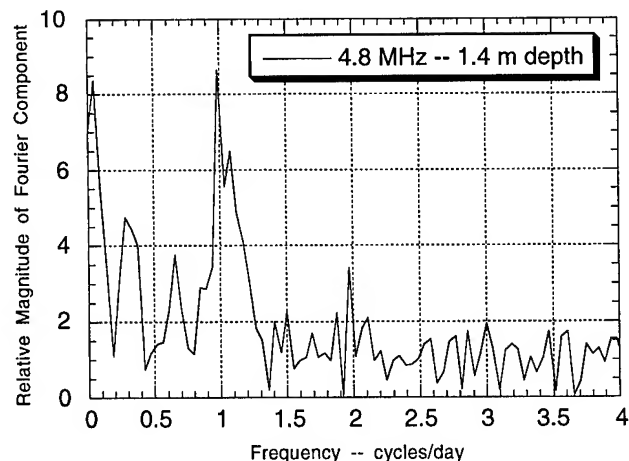
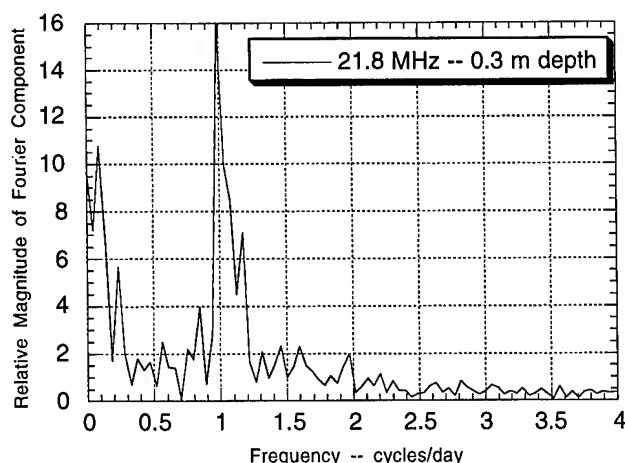


Fig. 2. Wind speed at MBARI moored buoy M1. Note the strong diurnal variation. See Fig. 1 for M1 location.

Moving from the highest operating frequency of 21.8 MHz to the lowest frequency of 4.8 MHz the effective depth of the current measurements range from 30 cm down to 1.4 m. Fig. 3 shows the dominant diurnal variation of these currents for all four depths. What Fig. 3 also shows is the relative strength of the diurnal (wind driven) and semi-diurnal (tidally driven) currents. There are of course diurnal tidal components, but the semi-diurnal tides dominate in Monterey Bay, e.g. at the Moss Landing tidal gage. At the shallow depth of 30 cm the diurnal variation at 1 cycle/day is nearly 10 times the semi-diurnal variation at 2 cycles per day. Thus, at 30 cm depth the wind stress dominates strongly in driving surface currents. Slightly deeper at 0.5 m, the 13.5 MHz observation still shows the strong diurnal wind forcing, but a semi-diurnal component is now clearly identifiable at 2 cycles/day. At a depth of 1 m (6.8 MHz observation) the diurnal component is reduced in magnitude and the semi-diurnal component has grown in strength to about 20% of the diurnal variation. Finally at 1.4 m depth the diurnal component has fallen further and the semi-diurnal component is about 30% in relative strength.



CONCLUSIONS

We find that multifrequency HF radar allows observation of the top few meters of the ocean where wind stress dominates very near the surface and tidally driven currents gain in strength as depth increases. The combination of HF radar with acoustic Doppler

Fig. 3. Spectra of radial currents at depths of 0.3, 0.5, 1.0 and 1.4 m respectively from top to bottom.

current profilers (ADCP's) on buoys or moorings provides a comprehensive view of the near surface ocean and the processes that transfer momentum and other quantities between atmosphere and ocean.

ACKNOWLEDGMENTS

Field work requires much help; we are grateful to the following: Steve Davenport (Long Marine Lab.) and Prof. Pat Mantey (REINAS project) at the University of California at Santa Cruz. Dr. Don Barrick of CODAR Ocean Sensors Ltd., and the Monterey Bay Aquarium Research Institute. The construction and operation of the radar are supported by the Office of Naval Research, Drs. Dennis Trizna and Frank Herr, technical officers.

REFERENCES

- [1] Paduan, J. D. and L. K. Rosenfeld, "Remotely sensed surface currents in Monterey Bay from shore based HF radar (CODAR)," *J. Geophys. Res.*, vol. 101, pp. 20,669-20,686, Sept. 1996.
- [2] Ha, E. C., "Remote sensing of ocean surface current and current shear by HF backscatter radar," Ph.D. dissertation, Stanford Univ., Stanford, Calif., Tech. Rep. D415-1, 1979.
- [3] Fernandez, D. M., J. F. Vesecky and C. C. Teague, "Measurements of upper ocean surface current shear with high-frequency radar," *J. Geo. Res.*, vol. 101, 28615-28625, Dec. 1996.
- [4] Teague, C. C. et al., "Initial observations of ocean currents, current shears and wind direction using multi-frequency HF radar," *IGARSS '97 Proceedings*, Picataway NJ:IEEE Press, 1997.
- [5] Vesecky, J. F. et al., "Multifrequency HF Radar Observations of Coastal Ocean Dynamics," Progress Report, Proj. 032883, University of Michigan, Jan. 1997.

Two-Dimensional Diurnal to Monthly Period Surface Currents in Monterey Bay from CODAR-Type HF Radar

J. D. Paduan and M. S. Cook

Department of Oceanography
Naval Postgraduate School
Mail Code OC/Pd
Monterey, California 93943
(408) 656-3350; (408) 656-2712/FAX
paduan@oc.nps.navy.mil

D. M. Fernandez

Earth System Science and Policy
California State University, Monterey Bay
100 Campus Center
Seaside, California 93944-8001
(408) 582-3786; (408) 482-4122/FAX
daniel_fernandez@monterey.edu

Abstract—Surface current maps from Monterey Bay, California are analyzed from a network of three CODAR-type HF radar systems for the period December 1994 and compared with previous results from summertime observations. Mean currents show a narrow, meandering poleward flow opposite to the situation in summer. At diurnal periods, motions are more rectilinear in winter than in summer, which is consistent with differences in the wind forcing. Additional evidence is provided to suggest that non-linear interactions of the mean and diurnal-period motions may affect the observed pattern of diurnal-period current ellipses.

INTRODUCTION

High Frequency (HF) radar receivers operated along an ocean coastline, or from offshore platforms, are capable of determining the speed with which surface currents approach the radar site. This measurement is possible because, at HF (3 MHz–30 MHz), resonant Bragg scatter from deep-water surface gravity waves produces a large peak in the backscatter spectrum [1]. Although Bragg scattering from the sea surface is exploited in many instruments operating in various frequency bands (e.g., microwave scatterometers), only at HF is the speed of the reflecting surfaces determined as a function of the radar wavelength, i.e., $c^2 = g\lambda/(4\pi)$, where c is the (deep water) phase speed and λ is the wavelength of the transmitted HF signal. Any observed Doppler shifts of the resonant Bragg peaks can, therefore, be corrected for the motion of the reflectors, and a Doppler shift due to the surface current underlying the waves can be extracted. This remote sensing capability was pointed out early on by [2], and an early review was provided by [3].

Monterey Bay HF Radar Network

A single HF radar installation can measure one component of flow along radial lines emanating from the radar site. In order to obtain a map of two-dimensional current flow at maximum resolution and reliability, it is

necessary to obtain measurements from at least two radars located in different places. Since 1992, we have been operating at least two HF radar installations around the shores of Monterey Bay, California [4,5]. The radar network has been composed, primarily of direction-finding HF radar systems known as the Coastal Ocean Dynamics Applications Radar (CODAR), or its modern derivative called SeaSonde. Shorter duration deployments of beam-forming phased array systems have also been conducted, including recent measurements described elsewhere in this volume.

The locations of the radars used in this study are shown in Fig. 1. In this note, we examine radar-derived surface currents from December 1994. This period was analyzed in the context of seasonal changes by [4]. Higher frequency (e.g., diurnal) fluctuations in the summer months were the focus of [5] and [6]. Here we present the monthly averaged currents for December and compare diurnal-period patterns between August and December.

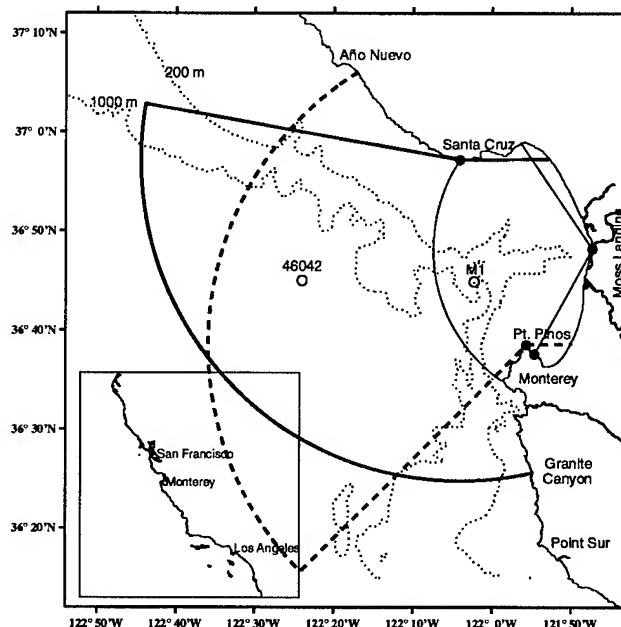


Fig. 1. Monterey Bay HF radar network with nominal coverage areas for 12.5 MHz SeaSonde antennae at Santa Cruz (heavy) and Pt. Pinos (dashed) and a 25.4 MHz CODAR antenna at Moss Landing. Mooring locations M1 and 46042 are also shown.

This work was supported by the Dean of Research, Naval Postgraduate School, and by the Office of Naval Research's physical oceanography and ocean modeling and prediction programs.

MONTHLY AVERAGED CURRENTS

The Monterey Bay HF radar network provides a unique opportunity to observe the evolution of surface current patterns on time scales from hours to months. At the longest time scales, cyclonic surface circulation throughout Monterey Bay in summer is observed to give way to anticyclonic circulation dominated by poleward currents across the mouth of the Bay [4]. Some seasonal shift in the surface currents may be expected based on the winds. Vector winds from the offshore mooring site 46042 are shown in Fig. 2 for the period August–December 1994. As

is typical of the central California coast, persistent equatorward winds are observed in summer giving way to more frequent periods of sustained poleward wind in fall and winter.

An example of the radar-derived surface currents during the period of more variable winds is shown in Fig. 3, which presents the average currents for December 1994. In this case, the equatorward flow across the mouth of Monterey Bay seen in summer [4,5] is displaced offshore by a band of poleward flow. Daily current maps during this period reveal this poleward flow setting up very quickly following reversal of the wind.

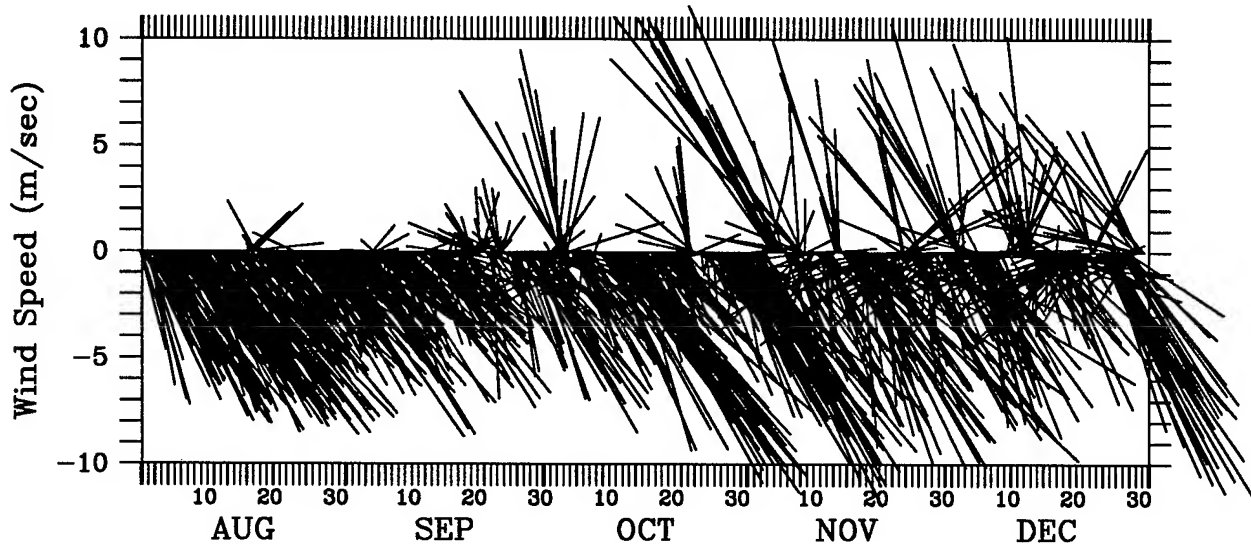


Fig. 2 Wind velocity (10-minute average every 3 hours) measured on NOAA buoy 46042 in 1994.

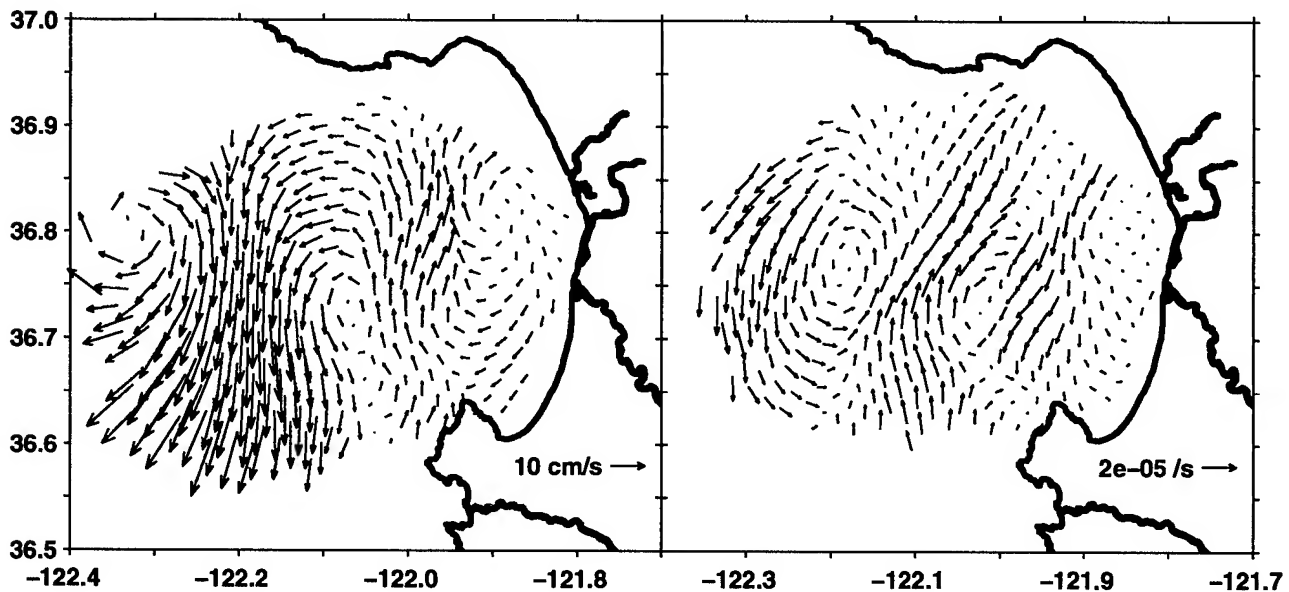


Fig. 3. Average radar-derived surface currents (left) and the non-linear advection tendency, $u_x - u_y, v_x - v_y$, (right) for December 1994.

DIURNAL-PERIOD CURRENT FLUCTUATIONS

In addition to the more slowly varying background currents, the surface currents around Monterey Bay are modulated by diurnal-period fluctuations that are related to diurnal (sea breeze) fluctuations in the winds. Harmonic analyses of the current and wind time series [7] reveal the strong coupling between wind and ~ 1 m radar-derived currents. "Tidal" ellipses at the period of the K1 diurnal tidal constituent (23.9 hr) are shown in Fig. 4 for December and, for comparison, August 1994.

Diurnal wind forcing was present throughout the period, but those oscillations were more rectilinear in December than in August. In both cases, the diurnal wind constituent was weaker at the offshore mooring site 46042 than at the M1 site near the mouth of Monterey Bay. Diurnal current motions were rotated approximately 45° to the right of the diurnal winds. Interestingly, the rectilinear focusing of the diurnal winds in December relative to August is reflected in the current ellipses, which suggests that, for these ~ 1 m currents, an Ekman-like balance is maintained with the wind, even for these high frequency motions.

The diurnal current ellipses are relatively uniform and aligned in the northwest-southeast direction. However, the spatial variations in the ellipses suggest possible coupling of the diurnal currents to the mean currents. To illustrate this possibility, we look at the non-linear accelerations:

$$u_i = -u\langle u \rangle_x - v\langle u \rangle_y; \quad v_i = -u\langle v \rangle_x - v\langle v \rangle_y,$$

where u, v are the diurnal currents, $\langle u \rangle, \langle v \rangle$ are the mean currents, and subscripts denote partial differentiation. If we assume $u = -v$, we can map the advection tendency (Fig. 3), which illustrates where in the field non-linear effects are most likely to have been important. Comparing Fig 3. and Fig 4., we see that the large ellipses near the M1 site may have been the result of non-linear interactions between the mean and diurnal currents.

SUMMARY

Time series observations from the Monterey Bay HF radar network have allowed us to begin to address the complicated issue of how winds drive surface currents in the coastal ocean. At periods of days to weeks, currents evolve to match gross features of the wind. At diurnal periods, ~ 1 m currents maintain an Ekman-like balance with diurnal wind forcing that is not found at 10 m depth. Spatial variations in the diurnal current ellipses are correlated with the largest gradients in the monthly mean currents suggesting possible non-linear contributions to the observed diurnal patterns.

REFERENCES

- [1] D.D. Crombie, "Doppler spectrum of sea echo at 13.56 Mc/s," *Nature*, vol. 175, pp. 681-682, 1955.
- [2] R.H. Stewart and J.W. Joy, "HF radar measurement of surface current," *Deep-Sea Res.*, 21, 1039-1049, 1974.

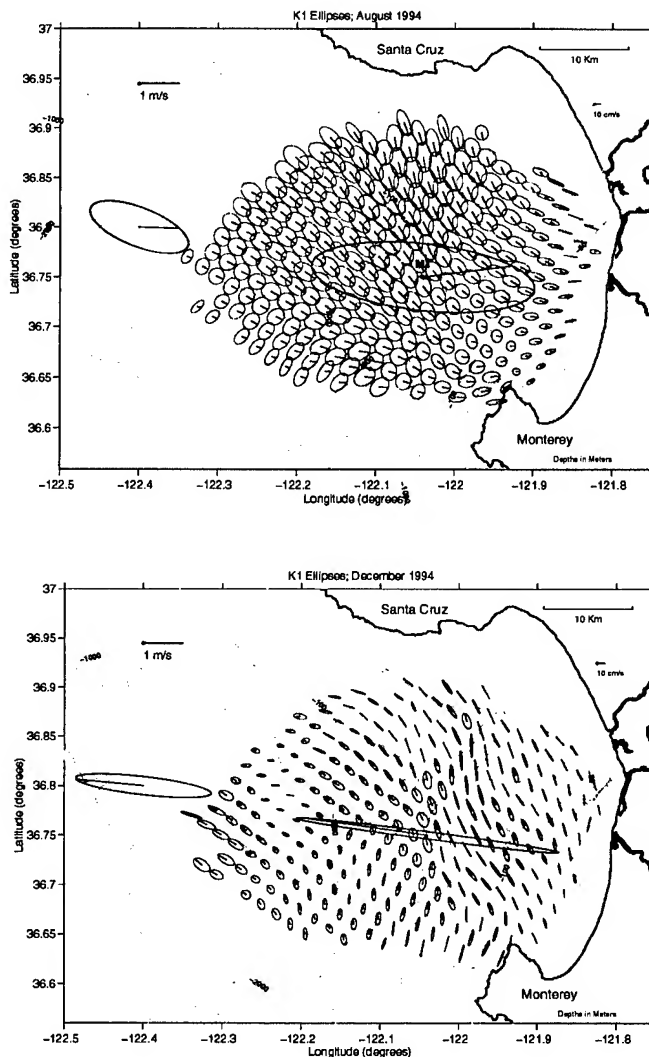


Fig. 4. Diurnal ellipses for ~ 1 m, radar-derived currents (green) and measured wind (magenta, larger) for August (upper) and December (lower) 1994. Weaker current ellipses measured at 10 m depth on the M1 mooring (red, smallest) are also shown.

- [3] E.D.R. Shearman, "Radio science and oceanography," *Radio Science*, vol. 18, pp. 299-320, May-June 1983.
- [4] J.D. Paduan and L.K. Rosenfeld, "Remotely sensed surface currents in Monterey Bay from shore-based HF radar (CODAR)," *J. Geophys. Res.*, vol. 101, pp. 20669-20686, 1996.
- [5] J.D. Paduan, E.T. Petruncio, D.E. Barrick, and B.J. Lipa, "Surface currents within and offshore of Monterey Bay as mapped by a multiple-site HF radar (CODAR) network," *Proceedings, IEEE 5th Working Conference on Current Measurement*, pp. 137-142, 1995.
- [6] J.D. Paduan and M.S. Cook, "Mapping surface currents in Monterey Bay with CODAR-type HF radar," *Oceanography*, vol. 10, in press.
- [7] G. Godin, "The Analysis of Tides," Univ. of Toronto Press, Toronto, 1972.

Coastal Near-Inertial Wave Bursts Detected by OSCR

Lynn K. Shay

Division of Meteorology and Physical Oceanography
Rosenstiel School of Marine and Atmospheric Science

University of Miami

4600 Rickenbacker Causeway

Miami, FL, 33149

(305) 361-4075 (Fax:4696)

nick@iwave.rsmas.miami.edu

INTRODUCTION

Surface current observations from High Frequency (HF) radar have revealed that not only are the low-frequency and tidal currents well resolved by the measurement, higher-frequency motions are also contained within the records such as near-inertial oscillations. These motions are associated with oscillations in the internal wave continuum and usually dominate the internal wave energy. A complicating feature in the coastal regime is oceanic frontal structure that influences inertial motions through the relative vorticity fields [1],[2]. These background vorticities may be considerably larger than in the deep ocean case due to the larger density contrast between the fresher, cooler coastal water and the more saline, warmer water masses associated with the subtropical gyre circulation.

Synoptic observations of the horizontal flow structure from High Frequency radar provides the spatial context to assess the role of coastal fronts on the near-inertial motions. Observations from an Ocean Surface Current Radar (OSCR) during the Office of Naval Research (ONR)/Naval Research Laboratory (NRL) High Resolution Remote Sensing Experiment [3], the ONR-sponsored Duck-94 experiment [4], and U.S. Coast Guard (USCG)-sponsored Ocean Pollution Research Center (OPRC) experiments and NOAA Southeast Caribbean Recruitment Studies (SEFCAR) in the Florida Keys [5] have revealed the presence of internal waves in surface current expressions. The data from the Florida Keys will be used here to demonstrate that the near-inertial motions (≈ 29 h period) were detected in surface current records acquired from an OSCAR¹.

OBSERVATIONS

As shown in Fig. 1, the HF-radar system mapped the coastal ocean currents over a $30 \text{ km} \times 45 \text{ km}$ domain at 20 minute intervals with a horizontal resolution of 1.2 km along the Florida Keys. Over a 25 day period from 18 May to 13 June 1994, about 5% of the samples were missing yielding a data return found in previous experiments [3]. An upward-looking, narrow-beam ADCP was moored in 150 m off Looe Key and provided current observations at 5 m intervals from 15 to 130 m.

¹The author acknowledges funding support from the USCG-sponsored OPRC (RD9401) and the ONR Remote Sensing Program (N00014-96-1-1101).

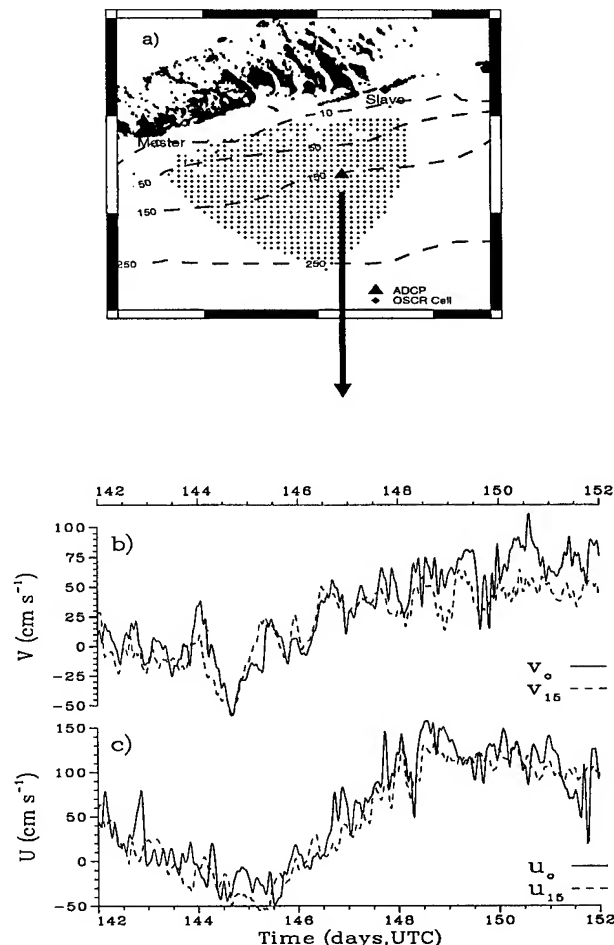


Figure 1: a) Experimental domain of OPRC/SEFCAR experiments along the Florida Keys with moored ADCP in 150 m of water off Looe Key, b) cross-shelf and c) along-shelf surface (solid) and 15 m (dash) current time series from 22 May (YD 142) to 1 June (YD 152) 1994 during OPRC-2.

The data acquired over a ten-day period from the OPRC-2 experiment indicated submesoscale vortices located along the inshore side of the Florida Current that were aligned with the 150 m isobath. Between 22 May (Yearday 142) to 27 May (Yearday 147), the along-shelf flow reversed direction as the Florida Current moved further offshore. The maximum cross-shelf component exceeded 75 cm s^{-1} whereas the along-shelf current exceeded 150 cm s^{-1} when the Florida Current was located over the mooring (Fig. 1b,c). *Rms* differences were 18 cm s^{-1} between the surface and 15 m records. Previous estimates of *rms* differences between surface and subsurface currents from HIRIS-2 were 10 to 14 cm s^{-1} due to mesoscale variability associated with low-frequency baroclinic currents of the Gulf Stream and internal waves [3],[6]. In a time-averaged sense, reference [7] suggests that at least 50% of these differences may have been due to a combination of surface wave and wind-induced currents and these baroclinic currents. Comparisons between surface and subsurface (4 m) currents from Vector Measuring Current Meters (VMCM) acquired during the CoOP and Duck94 experiments indicated *rms* differences of 7 cm s^{-1} [4]. These observations were at the uncertainty limits of resolvable processes from these instruments.

SURFACE CURRENT IMAGERY

Observed current time series were decomposed into components including the subinertial (48 h low-pass), tidal, inertial (29 h period), high-frequency (5 h period) and residual surface velocities. This decomposition uses digital filtering techniques and harmonic tidal analysis to isolate signals in the frequency bands based upon the peaks in the rotary spectra [3],[4]. Observed and decomposed surface velocities indicated structure in the surface velocity field including a submesoscale eddy-like structure (Fig. 2). Based on the observed surface current images, submesoscale vortices translated from the western part of the domain towards the eastern part at a rate of 25 to 30 km day^{-1} . This translation rate was not only above the expected envelope of low-frequency baroclinic features such as eddies and rings, but the direction of movement was opposite to coastally-trapped Kelvin waves along the east coast of basins. Subinertial flows, defined as the 48 h low-pass signals, indicated little evidence of this submesoscale feature. However, a large fraction of this signal was embedded in the near-inertial flows. The horizontal wavelength associated with this burst based on a series of least squares fits was about 30 km with velocities of up to 20 cm s^{-1} (Fig. 3). Based on the ADCP mooring data, the vertical wavelength was about 50 m. These wavelengths lie within the spectrum of near-inertial motions suggesting that a large fraction of this submesoscale variability in the surface currents was associated with near-inertial motions.

SUBINERTIAL FLOW VORTICITY

The horizontal structure of the near-inertial flows was affected by the subinertial flow vorticity which ranged between $\pm 2f$ (Fig. 4). Reference [2] showed that the vorticity associated with geostrophically-balanced currents alters the pass-band of allowable near-inertial frequencies. Here, the subinertial flow is used as a proxy for the geostrophic current to examine the role of surface current vorticity on the near-inertial flows. On

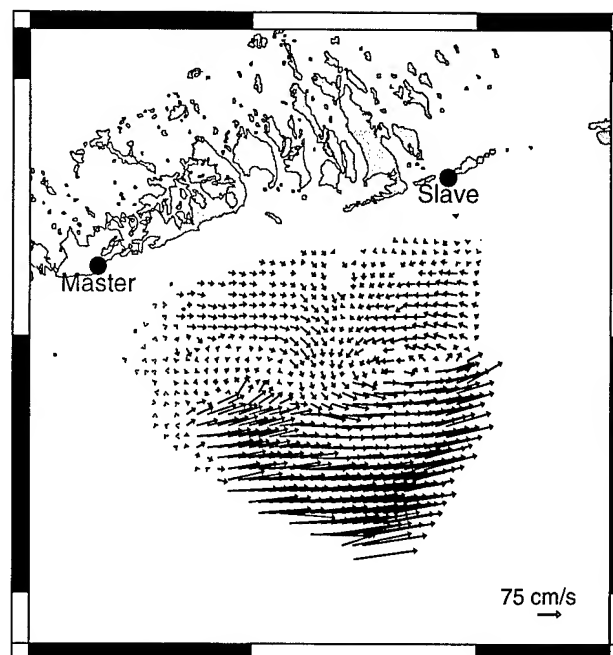


Figure 2: Observed surface flows from the OPRC-2 experiment in the Florida Keys on 25 May 1994.

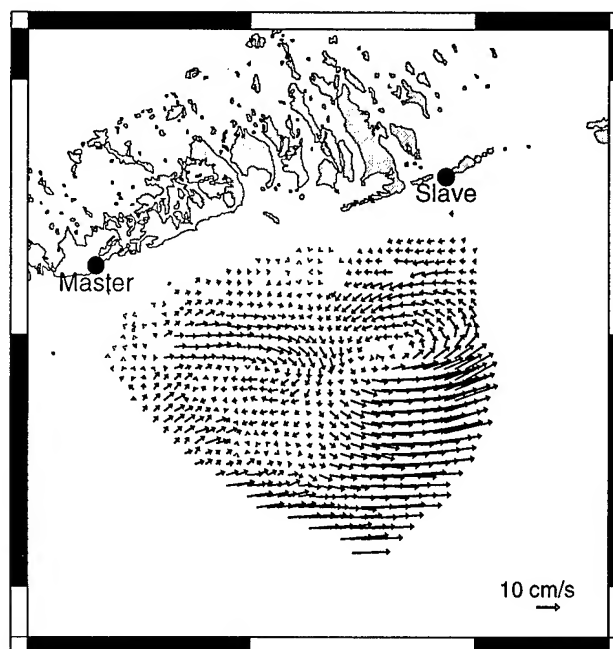


Figure 3: Near-inertial surface flows from the OPRC-2 experiment in the Florida Keys on 25 May 1994.

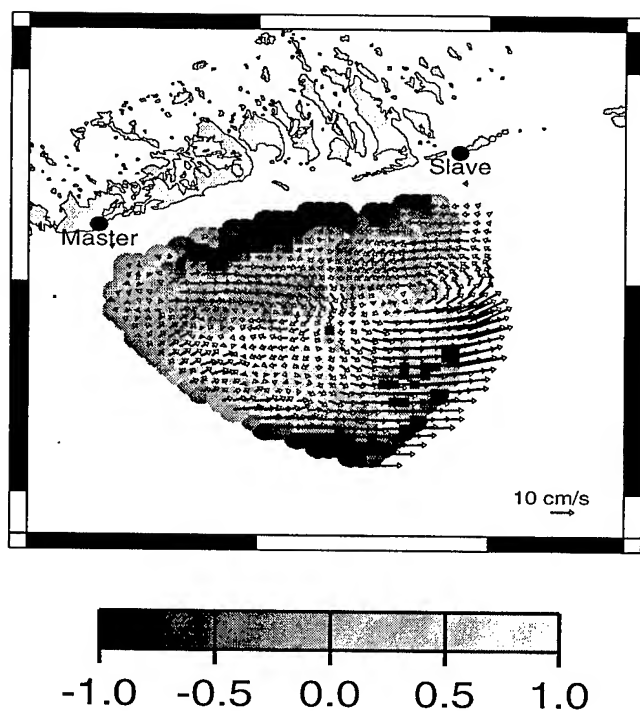


Figure 4: Near-inertial currents (arrows) superposed on the subinertial flow vorticity (color) normalized by $2f$ (f is the local Coriolis parameter) from the OPRC-2 experiment at 1800 UTC on 25 May.

25 May, the center of the submesoscale feature was located along the inshore edge of the cyclonically-rotating vorticity (> 0), and a strong convergence zone was centered in the domain. Closer to shore, the vorticity changed direction by rotating anticyclonically (< 0), which suggests that a significant fraction of the near-inertial surface current motions was trapped and advected towards the east by the subinertial flow vorticity regime. This effect is consistent with theoretical arguments applied to the deep ocean [1],[2]. Previous observations have also found spin-off eddies due to frontal instabilities as the Florida Current moves across the shelf break in this complex regime [8]. Thus, the forcing mechanism in generating these submesoscale vortices remains unclear; however, the near-inertial component did contribute to the observed flows.

SUMMARY

Emerging technological capabilities of *in situ* and remote sensing observational techniques are providing reliable, spatially-evolving snapshots of submesoscale to mesoscale oceanic flows [9]. Surface current observations from several experiments in the United Kingdom [10] as well as the HIRES, OPRC and Duck94 experiments have suggested that the HF radar-derived surface currents agree well with subsurface time series measurements. These HF-radar surface current measurements not only detect the low-frequency and tidal currents, but also internal waves including near-inertial motions. The

combined approach of subsurface profiling with high-resolution surface current images described herein provides data to resolve a spectrum of these oceanic processes.

ACKNOWLEDGMENTS

Ms. Gretzali Perez from the University of Puerto Rico who assisted in processing the observations under a summer NASA fellowship. The dedicated efforts of Duncan Ross and Jorge Martinez are sincerely appreciated. Hans Graber, Chris Boyce, Nick Peters, John Hargrove, Brain Haus and Louis Chemi were involved in the experimental setup and data acquisition efforts. Tom Lee and Liz Williams provided the ADCP data, Jean Carpenter drafted figures and Terry Faber assisted in the programming effort.

REFERENCES

- [1] C. N. K. Mooers, *Several effects of a baroclinic current on the cross-stream propagation of inertial-internal waves*, *Geophys. Fluid Dyn.*, 6, 245-275, 1975.
- [2] E. Kunze, E., *Near-inertial wave propagation in geostrophic shear*, *J. Phys. Oceanogr.*, 15, 544-565, 1985.
- [3] L. K. Shay, H. C. Graber, D. B. Ross and R. D. Chapman, *Mesoscale ocean surface current structure detected by HF radar*, *J. Atmos. and Oceanic Tech.*, 12(4), 881-900.
- [4] L. K. Shay, S. J. Lentz, H. C. Graber, and B. K. Haus, *Current structure variations detected by HF radar and vector measuring current meters*, *J. Atmos. and Ocean. Tech.*, (in press).
- [5] L. K. Shay, T. N. Lee, E. J. Williams, H. C. Graber, and C. G. H. Rooth, *Vertical structure variations in ocean currents detected by HF-Radar and an acoustic Doppler current profiler*, *J. Geophys. Res.*, (in revision).
- [6] R. D. Chapman, L. K. Shay, H. C. Graber, J. B. Edson, A. Karachintsev, C. L. Trump, and D. B. Ross, *Intercomparison of HF radar and ship-based current measurements*, *J. Geophys. Res.*, (in press).
- [7] H. C. Graber, B. K. Haus, R. D. Chapman, and L. K. Shay, *HF radar comparisons with moored estimates of current speed and direction: Expected differences and implications*, *J. Geophys. Res.*, (in press).
- [8] T. N. Lee, *Florida current spin-off eddies*, *Deep-Sea Res.*, 22, 753-765, 1975.
- [9] L. K. Shay, *Mesoscale Oceanic Flows*, *Handbook of Fluid Dynamics*, ed Richard Johnson, CRC Press, Boca Raton, FL, (in press).
- [10] D. Prandle, *The fine-structure of nearshore tidal and residual circulations revealed by HF radar surface current measurements*, *J. Phys. Oceanogr.*, 17, 231-245.

Measurement of Surface Current Fields with High Spatial Resolution by the HF Radar WERA

Klaus-Werner Gurgel and Georg Antonischki

Universität Hamburg, Institut für Meereskunde, Troplowitzstraße 7, D-22529 Hamburg, Germany
Phone: +49 40 4123 5742 Fax: +49 40 4123 5713 Email: gurgel@ifm.uni-hamburg.de

Abstract – Ground wave radar using electromagnetic waves with wavelengths between 10 m and 50 m (HF radar) can be used in oceanography to measure surface current and ocean wave parameters. In Germany, the work on HF radar started in 1980, adopting NOAA's CODAR (COastal raDAR). Recent developments within the European project SCAWVEX (Surface Current And Wave Variability Experiment) lead to a new design called WERA (Wellen RAdar). In autumn 1996, two WERA systems were deployed at the Dutch coast near Petten, south of the island Texel. For the last two days of the experiment, the new 300 m resolution mode of WERA was used to measure surface current fields. This mode revealed much more detail of a coastal jet connected to a sharp front.

INTRODUCTION

HF radar in oceanography makes use of backscatter of electromagnetic waves of 10 m to 50 m wavelength from the rough sea surface. The backscattered signal can be analysed to derive ocean surface current and wave parameters. Several HF radars have been developed all over the world and significant progress has been achieved since the discovery of the basic physics in 1955 by Crombie [1].

In Germany, the work on ground wave HF radar started in 1980. NOAA's CODAR (COastal raDAR), introduced in 1977 by Barrick, Evans and Weber [2], has been adopted, modified and deployed during numerous experiments. In 1987, the system has been extended to a ship-borne version to allow measurement of the circulation at the Arctic Front and near the ice edge in the North Atlantic [3]. Recent developments within the European project SCAWVEX (Surface Current And Wave Variability Experiment) [4] lead to a new design called WERA (Wellen RAdar).

WERA can be operated in many different modes, depending on the oceanographic requirements. Due to an advanced FMCW (Frequency Modulated Continuous Wave) technique, a range resolution between 300 m and 1.2 km can be selected. A flexible receiving antenna configuration allows beam forming and direction finding techniques, revealing high azimuthal resolution and access to second order sea echos, which can be used for deriving wave parameters. WERA has been operated in the 27 MHz and 30 MHz band, resulting in working ranges

of up to 55 km. With slight modifications, operation in other frequency bands is possible. A description of the system is given in [5].

THE EXPERIMENT

Within the SCAWVEX project, two WERA systems were deployed at the Dutch coast near Petten, south of the island Texel. Between the 29th of October and the 7th of December 1996, the radars were run every 20 minutes. The integration time of each measurement cycle was 9 minutes. The radars were operated alternately in order to avoid interfering each other. The measured data are analysed by L. Wyatt (University of Sheffield) for wave directional spectra [6] and by the University of Hamburg for surface current fields.

The land in this area lies some meters below sea level and is heavily exposed to the sea. North and south of Petten, high sand dunes form a natural protection, whereas between the dunes, a dike is protecting the land. During the last 100 years, the dunes lost sand to the sea and the dike got more and more exposed. To study the wave impact on the dike, a line of wave measuring instruments has been installed from directly in front of the dike to 8 km off the coast in north-west direction by the Dutch Rijkswaterstaat and has been operated since several years. One WERA system was set up directly on the dike at the beginning of the line of wave measuring instruments. The directional waverider buoys at 3.5 km and 8 km off the coast and an additional one 3.5 km more to the north in fig. 1 will be used to verify WERA's wave measurement capabilities.

The second WERA was set up near Voordijk, about 10 km north of Petten. This short baseline between the radars was chosen to ensure a high signal-to-noise ratio of the radar signal at the buoys' positions, which was required for the wave retrieval algorithm. This small distance reduces the accuracy of the current measurements due to geometry. The influence of narrow angles between the measured radial vector components, which are to be combined to the two-dimensional surface current vector, can be described by a factor similar to navigation systems like GPS¹. This factor describes the degrading of accuracy compared to the radial measurements and is known as GDOP². The calculation of this factor for HF radar systems is described in [7]. Fig. 1 shows the

This work has been supported by the European Commission, DG XII, within the Mast-2 programme, project MAS2-CT94-0103, SCAWVEX (Surface Current And Wave Variability EXperiment).

¹ Global Positioning System

² Geometrical Dilution of Precision

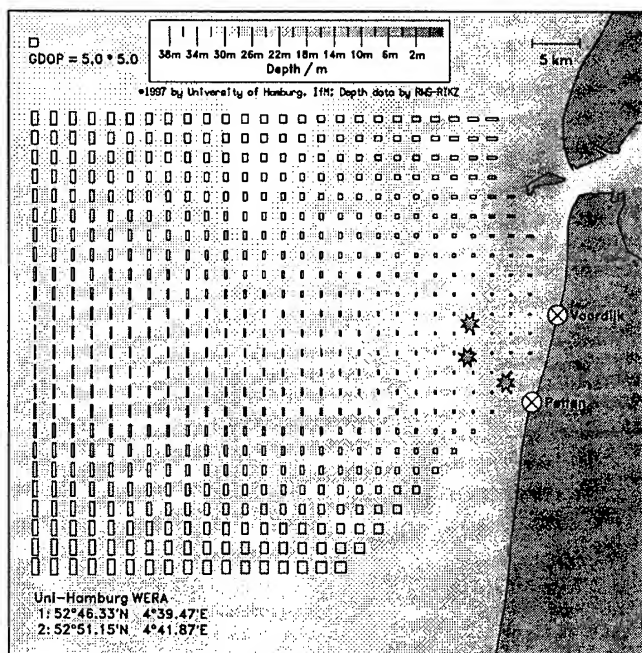


Figure 1. The measurement area off the Dutch coast. The two WERA sites are at Petten and Voordijk. The boxes show the influence of geometry on the accuracy of the measurement. The stars mark the positions of the wavebuoys used in the experiment. Bottom topography data has been supplied by Rijkswaterstaat.

spatial distribution of the GDOP. Near to the buoys, the GDOP does not exceed a factor of 2, but at narrow angles and far distances, values worse than 5 can be found for the north and east components. In this areas, the surface current calculated from the two radial components is more than 5 times less in accuracy compared to the radial components.

Bottom topography data have been supplied by the Dutch Rijkswaterstaat. The decrease in depth from the open sea to the coast is rather homogeneous except in the area between the main land and Texel, which is in the upper right in fig. 1. This depth structure allows the study of wave modification in shallowing waters. The tidal current mainly flows parallel to the coast.

SURFACE CURRENTS MAPPED BY WERA

WERA was operated with a 16-element linear receive array using beam forming for azimuthal resolution. The range resolution was set to 1.2 km, because this mode is expected to give better results for the wave spectrum estimation. For the last two days, however, resolution of 300 m was used to examine the high geometrical resolution mode of WERA. In this mode, the high amount of data constrains the working range to 38.4 km, although the signal-to-noise ratio allows ranges of up to 50 km.

During measurements with 1.2 km range resolution, surface current vectors were calculated on a $2 \text{ km} \times 2 \text{ km}$ grid. In near ranges, the actual geometrical resolution of

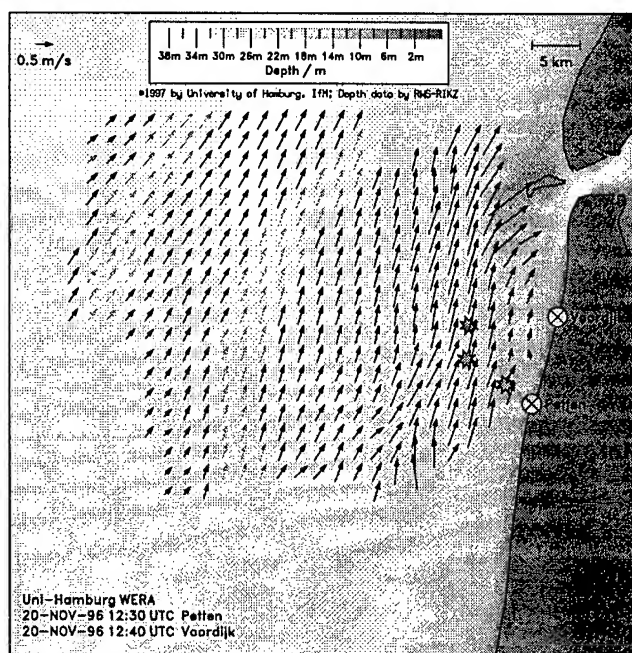


Figure 2. A surface current field mapped by WERA. Near to the coast, the current velocities are increased. The light arrows show interpolated values (interference at the Petten site).

WERA is finer, but as the azimuthal resolution decreases with range, the $2 \text{ km} \times 2 \text{ km}$ grid is adequate.

Strong HF-interference from the wave buoys have been observed at the Petten site. Three wave buoys within 300 m off the radar worked like transponders, retransmitting the radar signal with the buoys' modulation on it. As WERA is using FMCW for range resolution, some ranges have been distorted.

Fig. 2 shows a surface current field calculated from the radial components measured by the WERAs at Petten and Voordijk. In the distorted ranges from Petten, values have been calculated using the radial component measured from Voordijk and interpolating the perpendicular component from the surrounding current field.

COMPARISON OF RANGE RESOLUTION MODES

Fig. 3 shows a selected area of the current field given in fig. 2, measured in 1.2 km resolution mode. The absolute value of the surface current is encoded in colour/gray-scale to clearly mark the area of the coastal jet. The arrows indicate direction and value of the current.

During the measurement with 300 m range resolution, surface current vectors have been calculated on a $300 \text{ m} \times 300 \text{ m}$ grid. This is adequate, because the total working range is reduced and the decrease in azimuthal resolution with range is less.

Fig. 4 shows the same area as fig. 3. Again, the absolute value of the surface current is encoded in colour/gray-scale to mark the area of a coastal jet. To make the figure more clearly, arrows indicating direction and value of the current are shown every fourth column and row only. The

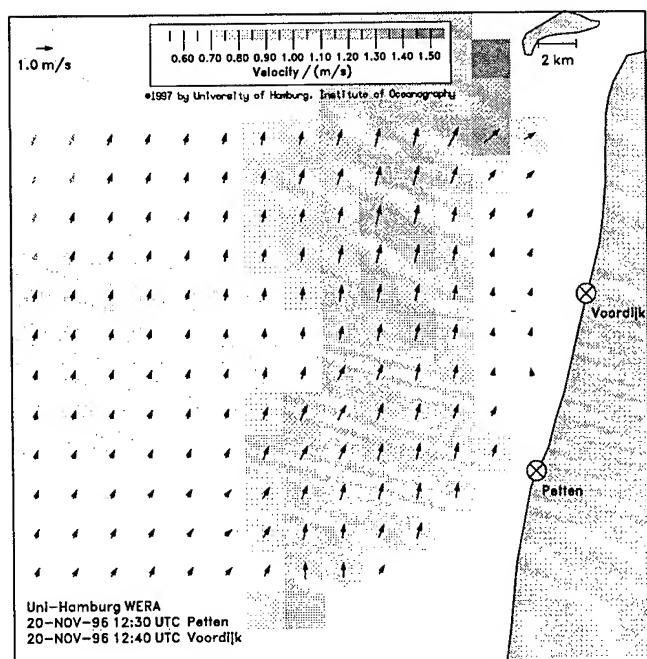


Figure 3. A selected part of the surface current field shown in fig. 2, measured in 1.2 km resolution mode. The absolute value of the surface current is encoded in a colour/gray-scale, the arrows indicate direction and value of the current. The increased current velocities near to the coast can be seen clearly in the shading.

oceanographic situation is similar to fig. 3. Some ranges of the Petten WERA are distorted by the wave buoys' interference. In this case, the gap was too wide for the interpolation technique used.

The band of high current velocity reveals more details than in fig. 3. West of the costal jet, there is a band with very low current velocities, which is not resolved in the 1.2 km mode.

SUMMARY

The HF radar WERA can be operated with different range resolutions. The 1.2 km mode reveals a good overview on the main structure of the current field at working ranges up to 50 km. A first test of the 300 m mode has shown more oceanographic details of a coastal jet associated with a front, as observed at the Dutch coast.

ACKNOWLEDGEMENTS

The authors wish to thank the other members of the HF radar group, H. H. Essen, F. Schirmer, T. Schlick and our technician M. Hamann for building WERA, discussing results and supporting the field campaign, and the Dutch Rijkswaterstaat, H. C. Peters, J. Vogelzang, A. Wijzes and local authorities for excellently supporting the logistics and supplying topographic and oceanographic data.

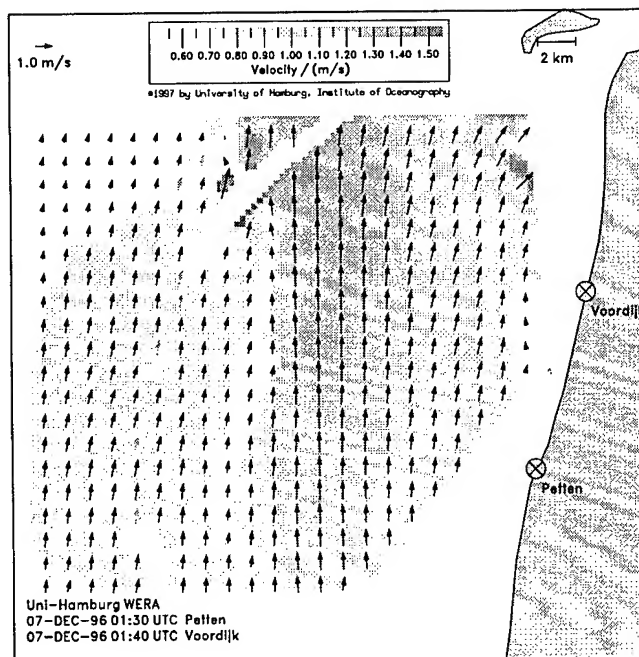


Figure 4. Surface current measured in 300 m resolution mode. The absolute value of the surface current velocity is encoded in colour/gray-scale, the arrows give direction and value of the current. An oceanographic situation similar to fig. 3 is shown. The distorted ranges from the Petten WERA are too wide to be interpolated.

REFERENCES

- [1] D. D. Crombie, "Doppler spectrum of sea echo at 13.56 Mc/s," *Nature*, vol. 175, pp. 681-682, 1955.
- [2] D. E. Barrick, M. W. Evans, and B. L. Weber, "Ocean surface current mapped by radar," *Science*, vol. 198, pp. 138-144, 1977.
- [3] K.-W. Gurgel, "Shipborne Measurement of Surface Current Fields by HF Radar," *L'ONDE ELECTRIQUE*, vol. 74, N°5, pp. 54-59, 1994.
- [4] L. R. Wyatt, K.-W. Gurgel, H. E. Krogstad, H. C. Peters, D. Prandle, and G. J. Wensink, "Surface current and wave variability experiments," in *Marine sciences and technologies, Second MAST days and Euromar market - Volume 1*, pp. 154-168, 1995.
- [5] K.-W. Gurgel and G. Antonischki, "Remote Sensing of Surface Currents and Waves by the HF Radar WERA," in *proceedings EEO 97, in press*, 1997.
- [6] L. R. Wyatt and L. J. Ledgard, "OSCR Wave Measurements - Some Preliminary Results," *IEEE Journal of Oceanic Engineering*, vol. VOL. 21, pp. 64-76, January 1996.
- [7] K.-W. Gurgel, *Flächenhafte Messung der Oberflächenströmung vom fahrenden Schiff aus*. PhD thesis, Universität Hamburg, November 1993.

Snow Accumulation on Greenland Estimated from ERS Scatterometer Data

V. Wismann¹, D. P. Winebrenner², K. Boehnke¹, and R. J. Arthern²

¹ Institute for Applied Remote Sensing, Bahnhofstrasse 54, 22880 Wedel, Germany
T : +49 (0)4103 13922; F : +49 (0)4103 7469; E : ifars@compuserve.com

² Applied Physics Lab., University of Washington, 1013 N.E. 40th Street, Seattle, Wa 98105-3521, USA
T : +1 (206)543-1393; F : +1 (206)543-1393; E : dpw@apl.washington.edu

Abstract -- Radar cross section measurements over Greenland by the scatterometer of the European Remote Sensing Satellites (ERS-1 and ERS-2) between August 1991 and March 1997 have been analysed. For large areas especially in the transition region between the percolation and dry-snow zone an almost linear decrease of up to 0.75 dB/year in normalized radar cross section was observed. This reduction can be attributed to increasing attenuation of the radar backscatter due to dry-snow accumulation on the firn of the percolation zone. A 2-layer radar backscatter model accounting for the measurement parameters of the ERS scatterometers and considering a firn layer buried by dry-snow was used to estimate the thickness of the dry-snow layer and to derive a snow accumulation rate. The spatial pattern and absolute values of accumulation rates so inferred agree well with recent synthesis of ground-based observations.

INTRODUCTION

Since August, 1991, the wind scatterometers aboard the ERS satellites of the European Space Agency (ESA) provide operationally measurements of the normalised radar cross section (NRCS) of the Earth's surface. The excellent calibration and maintenance of the instrument guarantee high quality data which, for the first time, allow a precise evaluation of the spatial and temporal variability of the NRCS of Greenland's snow and ice cover. The surface can be divided into four shell-like zones: the central dry-snow zone at high altitudes is surrounded by the percolation zone, the wet-snow zone, and the ablation zone [1]. These facies result from different diagenesis of the snow and ice cover which is determined by the amount of snow accumulation and melt and, therefore, on the local climate at the respective elevation. A large lateral shift of the borderlines between the different snow and ice facies will result even from a slight climate change due to the very gentle slope of the ice shield. Therefore, monitoring these borders can provide information on climate change.

The capability of discriminating different snow and ice facies by radar remote sensing was shown for the C-band SAR of ERS-1 [2], for the Ku-band SEASAT-A scatterometer and the C-band ERS-1 scatterometer [3,4]. In order to derive information about the snow properties the temporal and

spatial variability of the NRCS of Greenland has been investigated recently [5,6]. Here we present the results of our analysis of a very specific trend found in the scatterometer data over a large portion of Greenland.

RADAR BACKSCATTER DATA

The C-band (5.3 GHz) wind scatterometers aboard the ERS-1 and ERS-2 satellites operate at vertical polarization (VV), their three antennae are looking 45 degrees forwards, sideways, and 45 degrees backwards with respect to the satellite flight direction, the incidence angle ranges from 18 to 57 degrees, the illuminated swath is 500 km wide, the along-track and cross-track spatial resolution is 50 km, and global coverage is achieved within 3 to 4 days.

For this analysis the NRCS data obtained over Greenland between August 1991 and March 1997 are re-sampled to a grid with a resolution of 0.5° in latitude and 1° in longitude which approximately corresponds to the spatial resolution of the instrument. For 3 day intervals an average radar cross section (σ_{40}) is computed for each grid point by linear regression between the measured NRCS and their respective incidence angles. σ_{40} is the value of the regression line at 40° incidence angle.

Two typical time series plots of σ_{40} are depicted in Fig. 1 for a location in the percolation zone (a) and a second one further towards the dry-snow zone (b). The dominating signal is an almost linear decrease in radar cross section over the entire time span as indicated by the linear regression line through the data obtained before July 1995.

In July 1995 the decline in radar cross section was interrupted when the summer melting of snow reached far uphill and the dry-snow pack was transformed into firn by a melt-related metamorphism [5,6]. This episode lasted less than two weeks before σ_{40} again, tends to decrease similarly.

NRCS MODELING

Our model describing the decreasing radar backscatter at the dry-snow/percolation zone boundary is based on the following physical picture: During 1991-1995, the boundary of the dry-snow zone evidently moved downslope from its

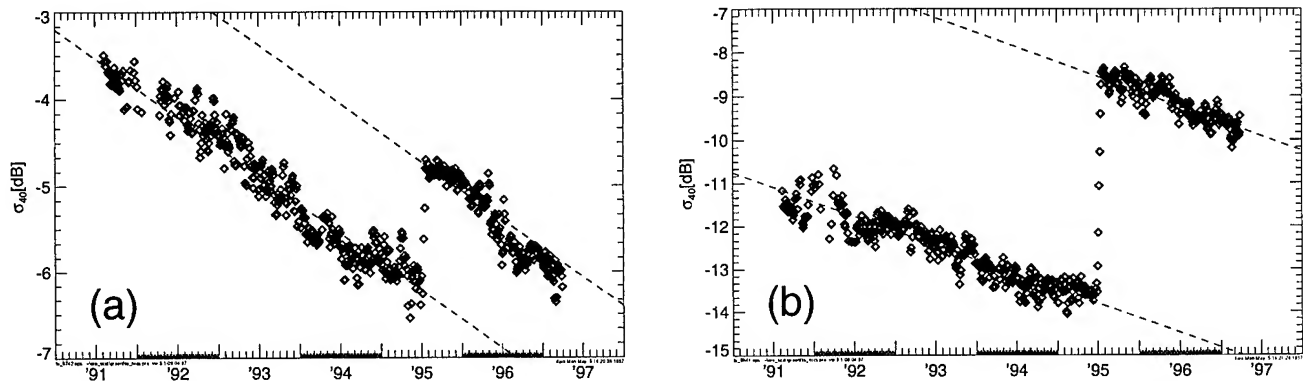


Fig. 1: Time series of the radar backscatter (σ_{40}) for two locations on Greenland at 67°N; 42°W (a) and at 68°N; 41°W (b).

previous location. Thus ice layers and pipes in the percolation zone (which cause strong backscattering) were progressively buried under several years accumulation of dry-snow which did not melt, even during summers, until 1995. Dry-snow overlying the percolation zone structure diminishes backscattering by means of at least two mechanisms. First, scattering depends on the dielectric contrast between ice structures and the surrounding snow. The ice structures are incompressible but the snow densifies as being buried, reducing this contrast. Quantitative modeling shows, however, that this effect is likely to be small. Second, propagation through the dry-snow layer to and from ice structures of the firm layer is effectively attenuated by absorption in the snow, by scattering within the dry-snow layer, and by reflection away from the ice structures of the firm as well as from the radar at internal density layer interfaces [7]. Interface reflection, in particular, leads to significantly greater effective attenuation than would otherwise be expected.

Fig. 2 shows results from a radar backscattering fading model that accounts for effective attenuation due to absorption, scattering and layering. The model parameters include radar frequency, polarization, and incidence angle (5.3 GHz, VV-polarization, and 40 degrees, respectively), together with parameters in an idealized physical model of layered dry-snow overlying the percolation zone ice structure. The overlying snow is modeled as a stack of discrete, planar layers of randomly varying thickness and density. The average density of the overlying snow is set, for this calculation, to 400 kg/m³, independent of depth. The effective permittivity of each layer is governed by its density and a size distribution of snow particles (i.e. ice, idealized as spherical). The size-distribution is log-normal with a 1 mm mean particle diameter and a logarithmic variance of 1.4. Layer density is assumed to follow a Gaussian distribution (with independence of distinct layers) and layer thickness is assumed to be exponentially distributed. The density variance is set by reference to ground-based Antarctic observations [7]; typical layer densities vary from approximately 250 to 500 kg/m³. The mean layer thickness varies depending on the snow

accumulation rate; typical values include 3 and 6 cm.

We performed Monte-Carlo simulations over an ensemble of randomly layered stacks to obtain theoretical estimates of backscatter fading as a function of snow depth overlying the percolation zone ice structure, as shown in Fig. 2. Computed fading is comparable to that observed, assuming either 3 cm or 6 cm mean layer thickness. Because the actual layer thicknesses are likely to depend on the accumulation rate itself, with larger accumulation rates associated with larger layer thicknesses, there is presently a moderate uncertainty in conversion from radar fading rate to the rate of increasing dry-snow depth. This uncertainty and the uncertainty in dry-snow density appear to be the most significant uncertainties in the conversion from radar fading rate to mass accumulation rate of snow. We expect both uncertainties to be narrowed upon a more detailed comparison of ground-based and scatterometer-inferred accumulation rates.

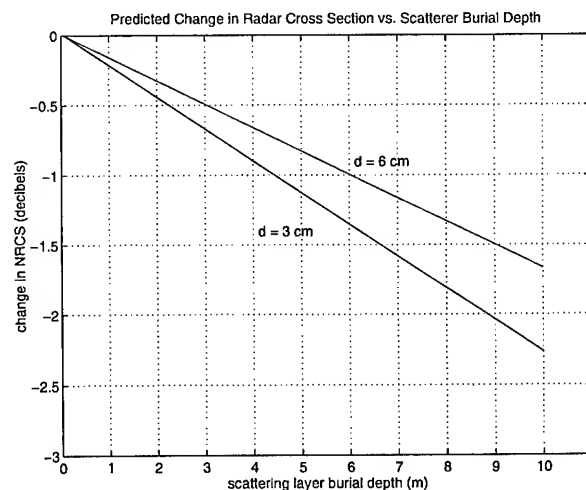


Fig. 2: Reduction of σ_{40} of firm snow as a function of the thickness of a covering dry-snow layer, for two possible values of the mean value of random layer thickness in the dry-snow layer.

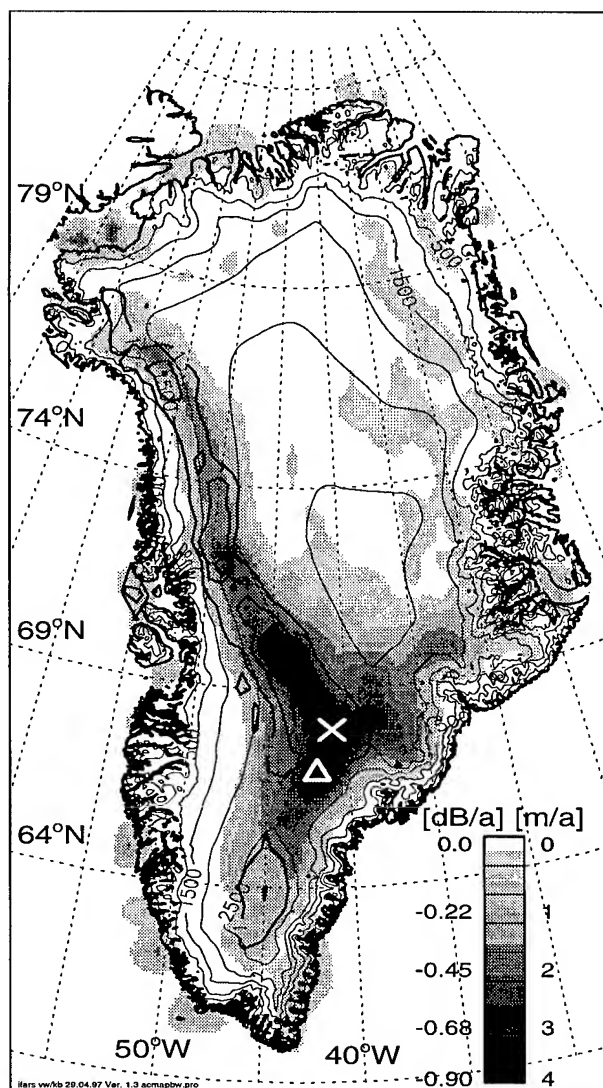


Fig. 3: Map of σ -rate which has been scaled also to an accumulation rate of dry-snow [m/a]. Superimposed are contour lines of the topography (thin lines) and of the jump in σ_{40} in July 1995 (thick lines). The locations of the σ_{40} time series in Fig. 1 at 67°N;42°W and 68°N;41°W are marked by the (Δ) and (x), respectively.

ACCUMULATION ESTIMATE

The observed decrease in radar cross section (see Fig. 1) was attributed to accumulation of the dry-snow which reduces the radar return from the buried firn layer. Since the observed decrease in σ_{40} is spatially variable and for comparison with meteorological data it is convenient to define a rate by which the radar cross section changes with time. In analogy to climatological parameters we define :

$$\sigma_{rate} = \frac{\Delta\sigma_{40}}{a}$$

which can, within the uncertainties discussed above, be transformed into an accumulation rate of dry-snow using the results of the radar backscatter fading model. Specifically, we assume for this demonstration a fading curve corresponding to 3 cm mean layer thickness, and a dry-snow density of 350-400 kg/m³ which is a good approximate of reality in Greenland [1].

A map of the averaged σ -rate for the period August 1991 to July 1995 is depicted in Fig. 3. The color bar in the figure has two scales, on the left hand side for the σ -rate and on the right hand side for the accumulation rate of dry-snow. The spatial pattern of these snow accumulation rates as well as their absolute values are in very good agreement with observations reported by Ohmura and Reeh [8]. There is a zone of high precipitation/accumulation stretching along the westward slope having one maximum around 69°N and a second maximum far in the north around 76°N 60°W. Ohmura and Reeh [8] gave precipitation rates of 500-600 mm/year for the maxima which corresponds approximately to 2 meters of dry-snow.

REFERENCES

- [1] Benson, C. S., Stratigraphic studies in the snow and firn of the Greenland ice sheet, SIPRE Res. Rep. 70, 1962.
- [2] Fahnestock, M., R. Bindshadler, R. Kwok, and K. Jezek, Greenland ice sheet surface properties and ice dynamics from ERS-1 SAR imagery, Science, Vol. 262, 1530-1534, 1993.
- [3] Long, D. G., and M. R. Drinkwater, Greenland ice-sheet surface properties observed by the Seasat-A scatterometer at enhanced resolution, J. of Glaciology, Vol. 40, No. 135, 213-230, 1994a.
- [4] Long, D. G., and M. R. Drinkwater, Comparison of enhanced resolution images of Greenland from ERS-1 and Seasat scatterometer, Proceedings of the International Geoscience and Remote Sensing Symposium, IGARSS '94, Pasadena, California, USA, 8-12 August, 2382-2384, 1994b.
- [5] Wismann, V., K. Boehnke, A. Cavanie, R. Ezraty, F. Gohin, D. Hoekman, and I. Woodhouse, Land surface observations using the ERS-1 scatterometer, Final Report Part II to the European Space Agency, ESTEC Contract 11103/94/NL/CN, 1996.
- [6] Wismann, V., and K. Boehnke, Monitoring snow properties on Greenland with ERS scatterometer and SAR, Proceedings of the 3rd ERS Symposium, Florence, Italy, March 17-21, 1997.
- [7] West, R. D., D. P. Winebrenner, L. Tsang, and H. Rott, Microwave emission from density-stratified Antarctic firn at 6 cm wavelength, J. of Glaciology, 42(140), 63-76, 1996.
- [8] Ohmura, A. and N. Reeh, New precipitation and accumulation distribution maps for Greenland, J. of Glaciology, Vol. 37, No. 125, 140-148, 1991.

Thawing Processes During Siberian Spring Observed by ERS Scatterometer and SAR

K. Boehnke, and V. Wismann

Institute for Applied Remote Sensing, Bahnhofstrasse 54, 22880 Wedel, Germany
T : +49 (0)4103 13922; F : +49 (0)4103 7469; E : ifars@compuserve.com

Abstract – From multi-temporal radar backscatter measurements obtained from the ERS scatterometers at various incidence angles, the state (frozen/thawed) of the upper layer of the soil in arctic to temperate climate regions is monitored. Sequences of SAR images are compared to the temporal signal of the scatterometer. In spring, the data of both instruments show distinct variations which can be attributed to thawing and freezing soils. From tracking a warm event in spring 1995, a high sensitivity of the radar return to the state of the snow is observed. The radar signature of dry-snow and firn varies on the same order as frozen and thawed soils (approx. 4 dB) whereas variations associated with the day-night temperature difference are not detected.

INTRODUCTION

The temporal variability of the normalised radar cross section (σ_0) encountered for bare or sparsely vegetated ground essentially depends on the dielectric properties of the soil, which in turn depends on the amount of free liquid water in the soil. Frozen soil, in this sense, behaves like dry soil and is characterised by low σ_0 values. In spring, when the amount of free liquid water increases due to snow melting and soil thawing, σ_0 also increases. This behaviour is altered significantly for a snow or water covered ground and altered moderately in the presence of a vegetation cover.

Previous investigations have shown that information on the freeze-thaw cycle of the soils can be inferred from ERS scatterometer [1,2] and ERS SAR [3] data. Here, we present results of comparing the radar signals of these instruments for three locations in northern Siberia:

- S1: centred at 71.75° N; 78.5° E,
- S2: centred at, 65.75° N; 68.5° E, and
- S3: centred at 70.75° N; 76.5° E.

For the first two locations, the observation period (spring, 1996) coincides with the tandem phase of the ERS satellites providing good scatterometer and SAR coverage, while during the observation period for S3 (spring, 1995), only ERS-1 data are available.

DATA PROCESSING

In order to compare the radar signatures of the ERS scatterometer and SAR, the incidence angle dependence of the scatterometer data must be accounted for. First, the scatterometer data are re-sampled to a grid with a resolution of 0.5° in latitude and 1° in longitude which corresponds roughly to the instrument resolution of 50 by 50 km. For three day intervals, σ_0 at an incidence angle of 23° is computed for each grid point by linear regression between the measured σ_0 and their respective incidence angles. Fig. 1 shows scatterometer measurements at different incidence angles for frozen soil (second week in May) and thawed soil (first week in July) conditions for a site in northern Siberia (S1). For both conditions the linear relationship between σ_0 and incidence angle was observed. The more modest slope in July arises from a higher degree of volume scattering and is indicative of a light vegetation cover. The SAR images were co-registered and an average radar cross section was computed for the overlapping area which is approximately the size of a scatterometer resolution cell.

In Fig. 2 the σ_0 values of the scatterometer are plotted versus the coincident SAR σ_0 values for all three test sites. On average, the σ_0 values measured by the SAR are found to be approx. 1 dB higher than the corresponding scatterometer derived values. However, due to the limited amount of data, it is not demonstrable whether there exists a mismatch in

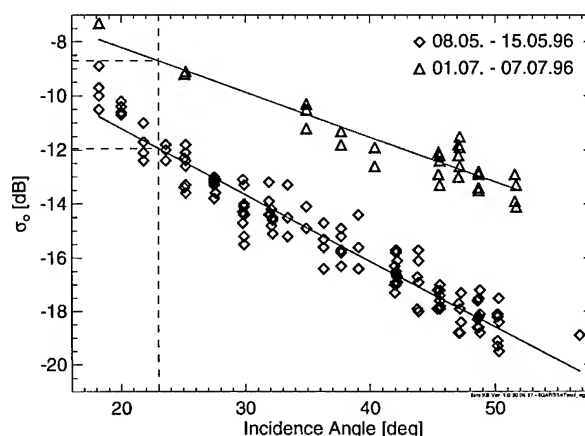


Fig. 1: Dependence of σ_0 on incidence angle for the second week in May and the first week in July, respectively. Data are from site S1 in northern Siberia. σ_0 at 23° incidence angle is calculated by linear regression.

This research was partly funded by the European Space Agency within the Earth Observation Preparatory Programme (EOPP) under ESTEC contract 11103/94/NL/CN.

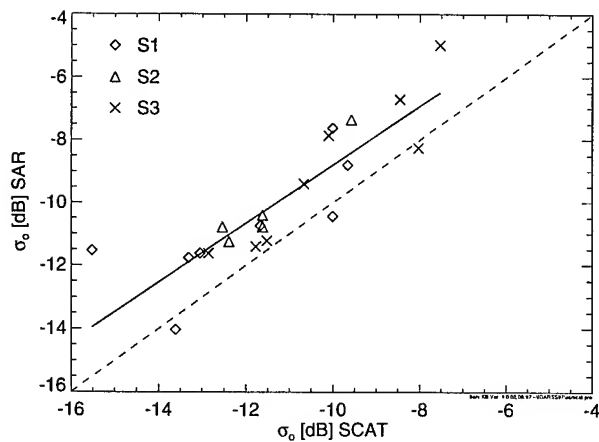


Fig. 2: Comparison of σ_0 derived from scatterometer and SAR measurements for all three test sites.

calibration of the ERS SAR and scatterometer. For this comparison, a constant offset of 1 dB is added to the scatterometer σ_0 values.

RADAR SIGNATURE COMPARISON

Fig. 3 depicts time series of σ_0 determined from scatterometer measurements at locations S1 to S3. The respective σ_0 values from sequences of SAR images are displayed as triangles and marked with letters. Common to all time series is a low σ_0 when the soils are frozen and an increase of over 4 dB when the soils thaw. There between, an additional short-term decrease in σ_0 is typical for the Siberian Tundra (Fig. 3a and c) but also visible in Fig. 3b, test site S2, situated within the sparse spruce and larch Taiga. From evaluation of the SAR images, this drop can be explained by the increasing wetness of the snow leading to an enhanced absorption of the microwaves and the subsequent low radar return from melt water ponds formed on the frozen grounds when infiltration is still blocked [3].

The low deviation of scatterometer values from ascending and descending passes as well as the similarity of SAR measurements C and D of Fig. 3b which were taken on the same day at 10:30 and 22:00 local time, respectively, indicate that day - night air temperature fluctuations have no significant effect on the radar return.

In Fig. 3c, the NCEP air temperatures [4] are included for comparison. In spring 1995 a warm event at the beginning of April initiated snow melt. However, air temperatures above freezing did not persist long enough to completely deplete the snow cover. The top layer of the snow melted but the subsequent decrease in air temperature led to the recrystallisation of the snow. This so-called *melt-related metamorphism of snow into firn* [5] led to the first strong increase in radar return from -11 to -6.5 dB - a phenomenon also observed over the Greenland Ice Shield [6,7]. At the end of May, high air temperatures transform the firn into wet

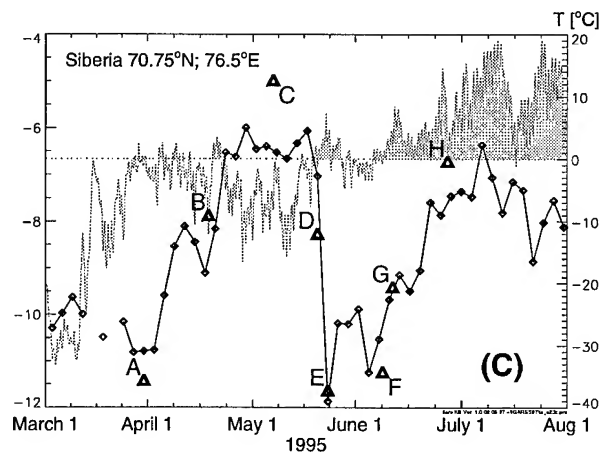
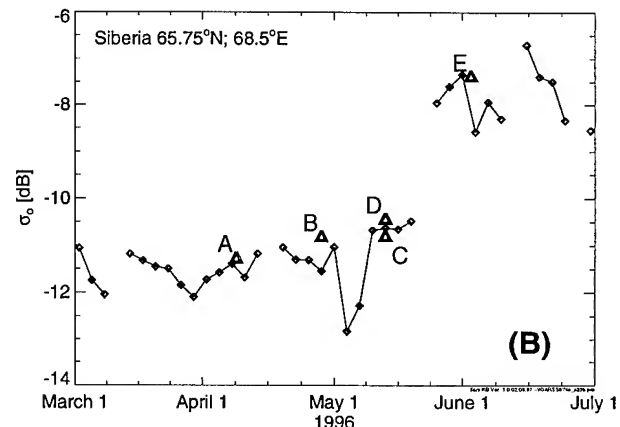
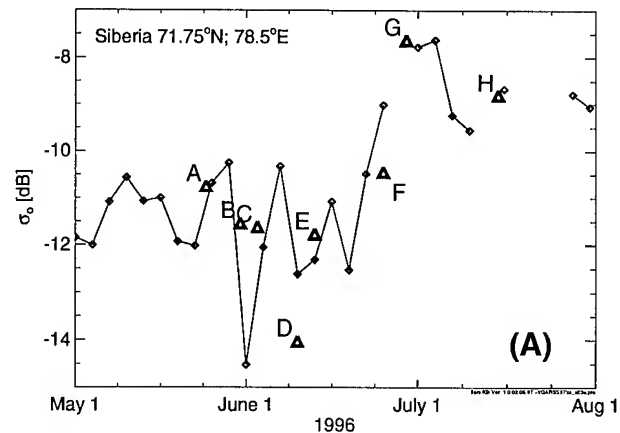


Fig. 3: Time series of σ_0 derived from ERS scatterometer data for three locations (S1 to S3 from top to bottom) in Siberia. The triangles and letters denote coincident SAR measurements. 1 dB has been added to the σ_0 values of the scatterometer (see Fig. 2). In (C), the NCEP air temperature reanalyses are included.

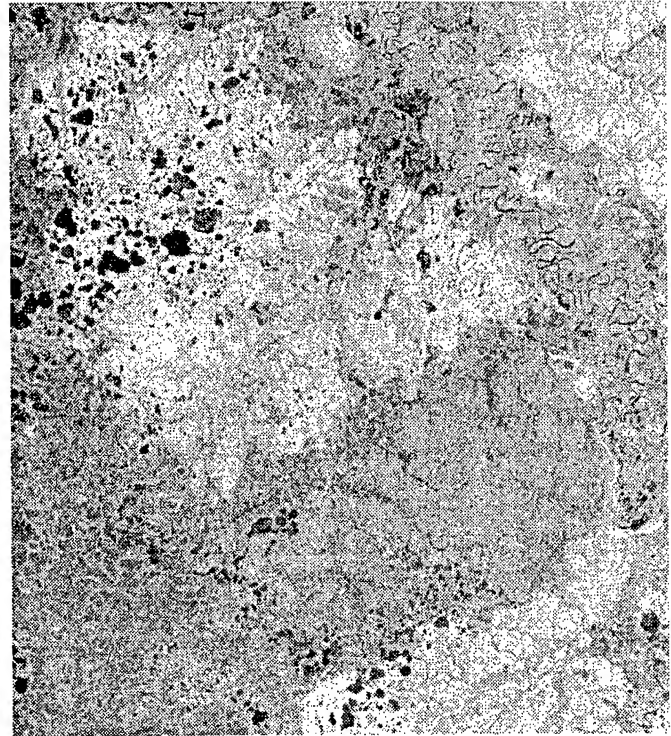
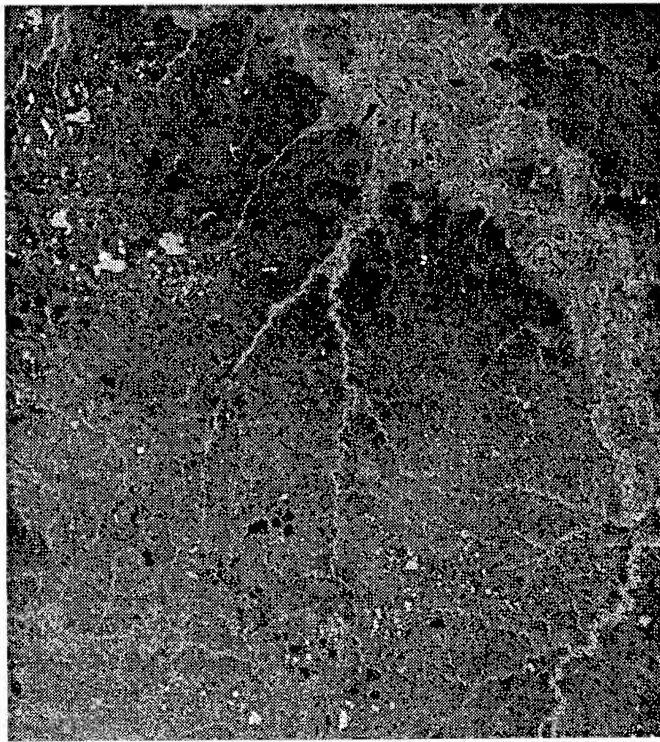


Fig. 4: ERS-2 SAR scenes of frozen ground (left; O: 5062; F: 1323; D: 08.04.96) and thawed ground (right: O: 5843; F: 2277; D: 02.06.96) at site S2 near the mouth of the river Ob corresponding to (A) and (E) in the time series of Fig. 3b, respectively.

snow resulting in a drop in σ_0 of over 6 dB. Finally, the second increase in σ_0 marks the thawing of the soils.

The spatial variability encountered within the SAR image on the left of Fig. 4 is determined by low radar return from frozen soils (including a dry-snow cover), wet snow, and open water. Higher values of σ_0 are encountered for frozen lakes and ice and firn in river beds. In June, when the soils have thawed, the signatures in the SAR image represent variations in the vegetation cover rather than soil features. All open water appears as dark patches (Fig. 4 right).

CONCLUSIONS

Coincident ERS scatterometer and SAR data of northern Siberia are examined for the strong variations associated with the snow melt - soil thaw succession in spring. Both instruments, despite their different spatial resolution, are highly sensitive to the state of the soils and the state of the snow cover. Snow, after experiencing a re-crystallisation into firn is characterised by an enhanced radar return of the same order as thawed soils, making a discrimination of these two processes more difficult. For the scatterometer, the more modest slope of the σ_0 values versus their incidence angles with the onset of vegetation growth can serve as an additional discriminator. In SAR images the inversion of the radar signature of open water can aid in the discrimination. Short-term temperature variations as they occur throughout the course of the day seem to have no significant effect on σ_0 .

REFERENCES

- [1] Boehnke, K. and V. R. Wismann, ERS Scatterometer Land Applications: Detecting the Thawing of Soils in Siberia, Earth Observation Quarterly, ESA Publication Division, 52, 4-7, 1996.
- [2] Boehnke, K. and V. R. Wismann, Detecting Soil Thawing in Siberia with ERS scatterometer and SAR, Proceedings of the 3rd ERS Symposium, Florence, Italy, Mar. 17-21, 1997.
- [3] Rignot, E. and J. B. Way, Monitoring freeze-thaw cycles along north-south Alaskan transects using ERS-1 SAR, Remote Sens. Environ., 49, 131-137, 1994.
- [4] NCEP, NCAR/NCEP reanalysis data provided through the NOAA Climate Diagnostics Center (<http://www.cdc.noaa.gov/>), 1996.
- [5] Echelmeyer, K., W. D. Harrison, T. S. Clarke and C. Benson, Surficial glaciology of Jakobshavn Isbr , West Greenland: Part II. Ablation, accumulation and temperature, Journal of Glaciology, Vol. 38, No. 128, 169-181, 1992.
- [6] Wismann, V., K. Boehnke, A. Cavani , R. Ezraty, F. Gohin, D. Hoekman and I. Woodhouse, Land surface observations using the ERS-1 windscatterometer Part II, Report for the European Space Agency, ESTEC Contract No. 11103/94/NL/CN, 59 pages, 1996.
- [7] Wismann, V., D. P. Winebrenner, K. Boehnke and R. J. Arthern, Snow accumulation on Greenland estimated from ERS scatterometer data, Proceedings of the International Geoscience and Remote Sensing Symposium, IGARSS'97, Singapore, 4-8 August, 1997, this issue.

Assessment of Scatterometer Data for Environmental Studies in Thar Desert

Haroon Stephen, Robert L. G. Schumann, Kiyoshi Honda and Keaw Nualchawee

Space Technology Applications and Research Program, Asian Institute of Technology, P.O. # 4,
Klong Luang 12120, Pathum Thani, Thailand, F: +66(0)2-524-5596 E: sta67169@ait.ac.th

Abstract -- Since summer 1991 the scatterometer aboard European Remote Sensing Satellites ERS-1 and ERS-2 have provided global radar backscatter measurements of the Earth's surface. Over the oceans, these data are used operationally for wind field retrieval. Simultaneously possible applications of these low resolution data over land surfaces were studied by numerous investigators. Due to the global coverage, the continuity of the data and the wide range of incidence angle these data have been found to provide valuable information despite the coarse resolution[1 and 2].

In this paper we analyze normalized radar cross section (NRCS) measurement obtained over Thar desert in Pakistan between May 1994 and May 1996. Spatial variations in the radar cross section are compared with vegetational and meteorological parameters. Seasonal as well as interannual variations are investigated by correlating the radar backscatter with phenological, meteorological and AVHRR NDVI data. Zonal characterization of area is made on the basis of backscatter behavior and meteorological data. The geophysical parameters of the land are reflected in the incidence angle diversity of the ERS scatterometer. It is demonstrated that valuable information can be delineated from the ERS scatterometer data over arid regions in order to provide data for environmental and especially climatic monitoring.

INTRODUCTION

The first European Remote Sensing Satellite (ERS-1) with C-band (5.3 GHz) windscatterometer on board has been observing oceans for global wind measurements since July 1991. The launch of its sister ERS-2 in April 1995 enabled the uninterrupted supply of the global normalized radar cross section NRCS data to be continued towards the turn of the century. In middle 1996, the launch of Advanced Earth Observing Satellite (ADEOS) carrying NASA Scatterometer (NSCAT) on board indicates that interest is gaining in these set of measurements. The ERS scatterometer operates at vertical polarization (VV) and provides quasi-simultaneous views using three antennae which look 45° forward, perpendicular and 45° backwards with respect to the satellite flight direction. The incidence angle varies from 25° to 59° for the fore- and aft-beam and from 18° to 47° for the mid-beam antenna. Different incidence angles and look directions provide enhanced geometric sensitivity of backscatter measurements. The two scattering mechanisms i.e. surface

and volume scattering enable different land cover identifications. The sensor illuminates a swath of 500 km wide to the right hand side of the satellite ground track. The data has an along track and cross track resolutions of 50 km which is resampled to a 25 km grid. Scatterometer acquisition is sun independent and is not hampered by clouds. The instrument achieves global coverage within 3-4 days [3].

Thar desert is situated between 65°-75°E and 25°-30°N. With a very low annual rainfall of less than 250 mm, it has a hot arid climate. The population density and human activity reduces towards the central desert. Fig. 1 shows the study area for this research, which constitutes the part of desert which lies in the territorial boundaries of Pakistan and is around 100,000 sq. km or 10% of total area of the country. In the west of the desert lies the river Indus with a wide patch of vegetation on both sides, and in the south of the desert is Arabian sea with a band of mangroves along the coast. Since agriculture is the backbone of Pakistan's economy, great attention is given to bring more area under cultivation. Canal networks are constructed for better irrigation in areas with less rain. The desert fringe provides a site where the dynamics can be investigated quantitatively for better agricultural planning and development.

The sand movement caused by wind results in dune formation and changes the topography of the area. Small amounts of unevenly distributed rains in some parts of year cause vegetational changes which are cyclic in the nature. Furthermore, the fluctuations in the discharge of the river Indus passing through the desert also affect the semi desertic part.

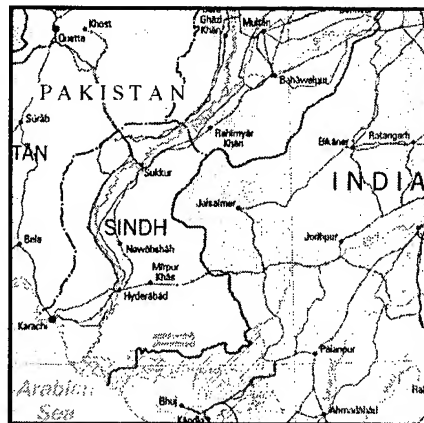


Fig. 1 Map of the study area

Being a large geographical zone in the area Thar is expected to play a vital role in the regional climatic conditions.

DATA SET

The investigations are made with meteorological and NRCS measurements obtained between May 1994 and May 1996.

Meteorological Data

From the climatic data i.e. temperature, relative humidity, evaporation and rainfall for 16 ground stations in the study area, data files containing data from May 1994 to May 1996 are prepared for each station

Radar backscatter data

Backscatter data is extracted from global NRCS dataset distributed on CD-ROM by "Centre ERS d'Archivage et de Traitement" (CERSAT), the French Processing and Archiving Facility (F-PAF). In the first part of this research, computer programs for data extraction, processing and plotting were developed using Interactive Data Language (IDL). The backscatter measurements were extracted for the 16 ground points in the form of data files. The extracted data is resampled to a 50 km grid.

Vegetation Cover Data

Atlas of Pakistan[4] and NOAA AVHRR images were studied to determine vegetation cover variations in the study area and the ground stations were categorized based upon vegetation density.

TIME SERIES ANALYSIS

Based upon study of the maps from atlas of Pakistan and AVHRR data, different zones in the study area can be characterized. The area is subdivided based upon two sets of criteria; vegetational/geographical and climatic information. The climatic zoning is as follows:

- A. Hot arid and dry (annual rainfall 125-250 mm)
- B. Hot arid and very dry (annual rainfall < 125 mm)

Since the study area constitutes the desert as well as its surrounding areas a further division is made based upon vegetation cover and geophysical parameters. The following zones were considered:

1. Desert
2. Semi Desert
3. Vegetated area by the river side
4. Undulating surface

Analysis of these two sets of zones indicate that the first two zones (1 and 2) fall in hot arid and dry climatic areas (A) and the last two zones (3 and 4) in the very dry climatic area (B).

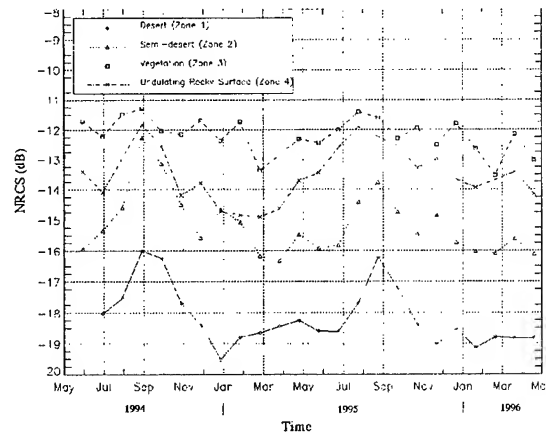


Fig. 2 Time series of 30 day mean values of backscatter for fore-beam and 40°-57° incidence angles for different zones in the desert.

The time series plots of mean monthly NRCS and mean monthly climatic data for four stations from four characteristic zones are studied for three beams and three incidence angles (18°-30°, 30°-40° and 40°-57°). Fig. 2 presents such plot for fore-beam and 40°-57° incidence angle from May 1994 to May 1995 and it clearly shows that various zones are well differentiable. This provides a possibility of zonal differentiation by means of backscatter however it remains to identify reasons for these differences.

Backscatter in the desertic zone is as low as -19.5 dB due to the uniform landform with very low vegetation, and during the period from July to September increases to a value of -16 dB, which probably results from rains taking place during this period. The decline in backscatter after the peak value is gradual as compared to the drastic rise and could possibly be due to sparse natural vegetation growth after rains.

Based upon qualitative evaluation of AVHRR data, it is noticed that the vegetation density increases towards the west and south west of central desert, gradually resulting in a semi desert transitioned to well vegetated area by the river side. The backscatter in the semi desertic zone during the dry parts of the year retains its value around -16 dB and depending upon the amount of rain could have as much as 4 dB increase. The increased vegetation density in this zone is probably the main cause of higher NRCS values. The AVHRR data showed that there exists variations in the vegetation distribution even within the zones and these inter-zonal variations were reflected in the backscatter values while comparing plots of stations within the zone. The vegetated zone is one area where surface and volume

scattering could be investigated for different incidence angles to identify various vegetation types.

Near the coast and along the west bank of river Indus lies the barren land with undulating surface. The area is sparsely vegetated and the higher backscatter could be mainly caused by the rocky surface. The fluctuations of NRCS in this area also increase in the rainy season by 3 dB, which is lesser than the semi desertic zone.

The backscatter increases in all above mentioned zones in rainy season but the range of increase reduces towards vegetated areas. The rise of about 1.5 dB takes place and the variation is very gradual.

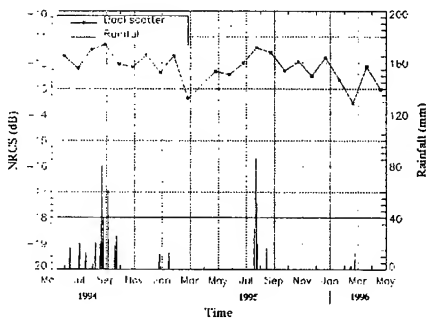


Fig. 3a Time series of 30 days NRCS for fore-beam and 40°-57° incidence angle; and daily rain in vegetated zone .

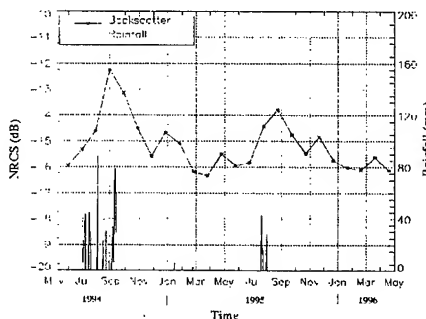


Fig. 3b Time series of 30 day NRCS for fore-beam and 40°-57° incidence angle; and daily rain in semi-desertic zone

The dependence of backscatter over rain is also investigated and shows promising results. Figs. 3a and 3b show that the peak of the NRCS occurs during rainy season. A delay of one month in backscatter peak from rainfall peak depicts the NRCS increase due to vegetational growth followed by the rain. Backscatter also increases due to increase in moisture dependent dielectric constant of the ground.

CROSS CORRELATION AND REGRESSION ANALYSIS

The cross correlation of backscatter with the available climatic parameters indicate that there is a relationship

between NRCS and temperature, relative humidity, evaporation, and rainfall and the peak of correlation occurs at various delays from one to three months. However, it can also be shown that meteorological measurements are themselves correlated and more work needs to be done for further investigation.

CONCLUSION

The potential of scatterometer to study the geophysical and climatic parameters of Thar desert were investigated. The results showed that various landforms could be distinguished from their NRCS measurements. This can potentially be used for differentiating different landforms and needs further detailed studies.

The backscatter has large dependence upon the vegetation density, which by itself is a function climatic conditions. Hence there is a potential to use backscatter measurements to develop climatic model based upon vegetational behavior. This research is still in progress and it is expected to get some more results, to show the effectiveness of scatterometer for environmental studies.

ACKNOWLEDGEMENT

The author is grateful to the following organizations for providing necessary data to conduct this research: European Space Agency (ESA) Space and Upper Atmospheric Research Commission, Pakistan. (SUPARCO) and Meteorological Department of Pakistan.

REFERENCES

- [1] Wismann, Volkmar et.al. (1996), "Land Surface Observation using the ERS-1 Windscatterometer", ESA Report No. 11103/94/NL/CN, Institute of Applied Remote Sensing, Wedel, Germany., pp. 1-57.
- [2] Wismann, Volkmar et.al. (1996), "Land Surface Observation using the ERS-1 Windscatterometer Part II", ESA Report No. 11103/94/NL/CN, Institute of Applied Remote Sensing, Wedel, Germany, pp. 11-59.
- [3] ERS-1 (1989), A new tool for global environmental monitoring in 1990's, ESA 8-10, rue Mario-Nikis, 75738 Paris CEDEX 15, France. pp 14-15.
- [4] Survey of Pakistan (1981), "Atlas of Pakistan", Survey of Pakistan, Muree road, Rawalpindi, Pakistan. pp. 51-54.
- [5] Boehnke, K.; Wismann, V. R.; (1996) ERS scatterometer land applications: Detecting soil thawing in Siberia. Earth Observation Quarterly n. 52, pp.4-7.
- [6] Wismann, V.R.; Boehnke K.; Schmullius, C.; (1995) Monitoring ecological dynamics in Africa with the ERS-1 scatterometer. Proc. IGARSS'95, Firenze, Italy, July 10-14.

OBSERVATIONS AND SIMULATIONS OF THE ERS WIND SCATTEROMETER RESPONSE OVER A SAHELIAN REGION

Pierre-Louis Frison, Eric Mougin

CESBIO (CNES-CNRS-UPS)
18 Ave. E. Belin 31401 TOULOUSE CEDEX FRANCE
frison@cesbio.cnes.fr

Pierre Hiernaux

International Livestock Research Institute
Centre Sahélien de l'ICRISAT, NIAMEY NIGER
P.Hiernaux@cgnet.com

ABSTRACT

ERS-1 wind-scatterometer data acquired over a sahara-sahelian region located in the Gourma (Mali) during the period 1992-1995, are analysed. Experimental observations show that $\sigma^0(45^\circ)$ temporal data display a marked seasonality associated with the development and senescence of annual grasses during the rainy seasons. The interpretation of the temporal σ^0 plots is performed with the assistance of a semi-empirical backscattering model combined with an ecosystem grassland model. The use of this model allows the total biomass to be estimated with a 33% error.

1. INTRODUCTION

Low resolution spaceborne scatterometers such as the instruments on board ERS-1 and ERS-2, have recently shown considerable potential for monitoring vegetation dynamics at global and regional scales (e.g. Mougin et al., 1993a; Wismann et al., 1993; Kerr and Magagi, 1993; Frison and Mougin, 1996a; 1996b). Scatterometers operate in the microwave domain and provide a measurement of the bi-directional reflectivity of the observed surface, expressed as the backscattering coefficient σ^0 . The later mainly depends on the dielectric properties of the surface (Ulaby et al., 1982). As green living plants contain a high percentage of water, it was expected that σ^0 measurements could be used to monitor biomass during the growing season. In the case of sparse vegetation like the sahelian one, σ^0 data displayed a large dynamic range between the dry and the rainy seasons, whereas little variation was observed over regions showing higher vegetation density. Furthermore, no saturation in the σ^0 values was observed even at the peak of standing biomass which occurs toward the end of the wet season. In contrast, the signal may saturate over more humid savannahs, thus leading to a lesser sensitivity of σ^0 data to the vegetation development. For all these considerations, the Sahel is retained as a study region for assessing the potentialities of the ERS-1 wind-scatterometer.

In this paper, we analyse multi-temporal ERS-1 WSC data acquired during the period 1992-1995, over a sahara-sahelian region located in the northern Gourma (Mali). We also investigate the capability of the ERS-1 WSC for retrieving herbaceous biomass.

2. EXPERIMENTAL OBSERVATIONS

The 50 x 50 km² study region located in the northern part of the Gourma region (16.7°N, 1.7°W) belongs to the bioclimatic zone defined as the sahara-sahelian transition. The landscape is characterised by gently undulating sandy soils partially covered with a low herbaceous layer and a very scattered shrub layer. For the period 1992-1995, annual rainfall ranged from 59 mm to 233 mm with a mean value of 155 mm. The phenology of vegetation is mainly determined by rainfall. Grass development starts after the first rains in June and senescence is associated with the end of the rainy season in September. During the long dry season, there is no green vegetation apart from a few shrubs. Ground data consist of measurements of the total herbaceous above-ground biomass performed at the end of the growing season. During the period 1992-1995, maximum biomass is ranging from 240 kg DM ha⁻¹ (in 1995) to 1050 kg DM ha⁻¹ (in 1994). In each sample site, the associated uncertainty on the means of biomass is about 15%. Daily rainfall data is obtained from the meteorological station of Gourma Rharous (16.9°N, 1.9°W).

Temporal profiles of the backscattering coefficient σ^0 for the period January 92 - December 95 are depicted in Figure 1. The sahara-sahelian region shows a marked seasonality associated with the development and senescence of annual grasses during the rainy season. This vegetation cycle is well depicted by the $\sigma^0(45^\circ)$ plots. Low σ^0 values are observed during the dry season (December-May) when the soil is dry and green vegetation is absent. In July, the vegetation growth is associated with an increase in the $\sigma^0(45^\circ)$ values up to a maximum occurring in either August or September. The peak in the $\sigma^0(45^\circ)$ data is followed by a prompt decrease. The yearly dynamic range is large and appears to be strongly correlated with annual rainfall; it reaches about 4.4 dB, 5.1 dB, 6.7 dB and 2.4 dB for 1992, 1993, 1994 and 1995,

respectively. In contrast, the $\sigma^0(20^\circ)$ temporal plots do not display such a characteristic signature. Overall, $\sigma^0(20^\circ)$ data show a large scatter in their values. The annual dynamic range reaches about 1 dB, 1.5 dB, 3 dB and 2 dB in 1992, 1993, 1994 and 1995, respectively.

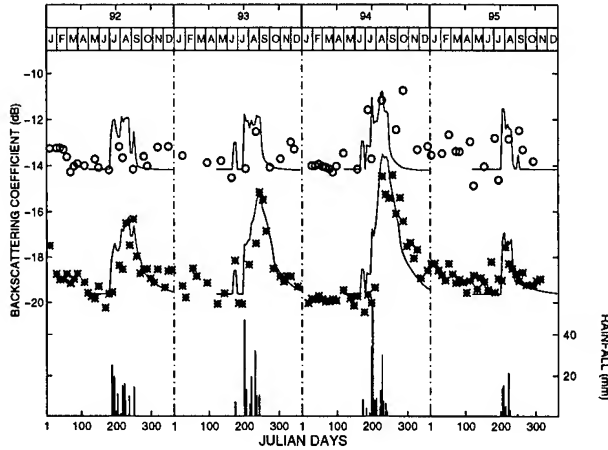


Figure 1 : Temporal variation of σ^0 at 20° (o) and 45° (*) of incidence angle and comparison with simulations (—). January 92 - December 95.

3. MODELLING APPROACH

At the scale under consideration *i.e.* at the scale of a resolution cell, the sahelian landscape is mainly seen as an integration of contributions from two components (bare soil and herbaceous vegetation). The backscattering coefficient of the observed scene, σ^0_{scene} , is thus given as the incoherent sum of the two previous components after being linearly weighted by their respective cover fractions. This simple area additive σ^0 model therefore implies that the vegetation is confined in a fraction v_c of a considered resolution cell. Hence, by assuming that there is no azimuthal dependency on σ^0 , which is a reasonable assumption (Frison and Mougin, 1996a), the backscattering coefficient σ^0_{scene} , as seen by the three antennae is written :

$$\sigma^0_{scene}(\theta_i) = (1 - v_c) \sigma^0_{bare\ soil} + v_c \sigma^0_{canopy} \quad (1)$$

where $\sigma^0_{bare\ soil}$ and σ^0_{canopy} denote the contribution of the bare soil and the vegetation canopy, respectively and where θ_i is the incidence angle.

The soil backscattering is simulated by using the Oh et al.'s model which has been validated with radar data acquired for numerous roughness and moisture conditions (Oh et al., 1994). The vegetation canopy is modelled as a collection of discrete, randomly oriented scatterers representing the vegetation components, above a rough surface. Within the

considered layer, all the scatterers are assumed to be uniformly oriented in azimuth. The leaves are modelled as elliptic discs whose axe dimensions are chosen to represent typical C_4 leaves. The backscattering coefficient of the vegetation canopy, σ^0_{canopy} , is given as the zeroth-order solution (soil scattering) and the first order solution (vegetation scattering and surface-vegetation interaction) of the radiative transfer equation (Karam et al. 1995). The backscattering coefficient is written:

$$\sigma^0_{canopy} = L^2 \sigma^0_{soil} + \sigma^0_{vegetation} + \sigma^0_{interaction} \quad (2)$$

where L is the canopy transmission factor and the terms σ^0_{soil} , $\sigma^0_{vegetation}$ and $\sigma^0_{interaction}$ denote the contributions of the soil beneath the vegetation layer, the contribution of the vegetation volume and the interaction component between the soil and the vegetation, respectively. The explicit content of $\sigma^0_{interaction}$ can be found in Karam et al. (1995). For the VV polarisation, the vegetation term has the following expression:

$$\sigma^0_{vegetation} = 4\pi \cos\theta_i n_o \langle |f_{vv}(-\hat{i}, \hat{i})|^2 \rangle \left[\frac{1 - L^2}{2\kappa_e} \right] \quad (3)$$

where κ_e is the extinction coefficient for V polarisation given by $n_o \langle \sigma_t \rangle$, σ_t is the extinction cross section, n_o is the density of scatterers per unit volume, $f_{vv}(-\hat{i}, \hat{i})$ is the scattering amplitude in the backscattering direction, L is the loss factor given by $\exp(-\kappa_e h_c / \cos\theta_i)$, and $\langle \rangle$ denotes the ensemble average over the probability density functions of orientation of the scatterers. The dielectric constant for leaves $\epsilon_{r,v}$, is computed with the dispersion Ulaby and El Rayes' model (1987). Equations (1) and (2) yields the following expression for the backscattering coefficient :

$$\sigma^0_{scene}(\theta_i) = (1 - v_c) \sigma^0_{bare\ soil} + v_c L^2 \sigma^0_{soil} + v_c (\sigma^0_{vegetation} + \sigma^0_{interaction}) \quad (4)$$

The inclination distribution of leaves is chosen to be erectophile due to the predominance of C_4 grasses. Leaf dimensions are assumed to be constant throughout the growing season. The other necessary parameters v_c and h_c are simulated by the *STEP* grassland model (Mougin et al. 1995). The number density of scatterers n_o is derived from the simulated vegetation volume fraction f_v which can be expressed as a function of the total biomass B_t , the canopy height h_c and the gravimetric water content of vegetation H_p . Soil roughness is assumed to be constant throughout the growing seasons; its value being adjusted with the σ^0 measurements acquired at the end of the first dry season (May 1992). Soil surface moisture content H_v is provided by the *STEP* model.

The evolution of the soil and vegetation parameters are fed into equation (4) to compute the variation of σ^0_{scene} throughout the four successive growing seasons. At 45° of

incidence angle, there is an overall good concordance between the simulations and measurements (Figure 1). Particularly, the annual σ^0 dynamic range is very well described by the model. At the peak of backscattering, the differences between measurements and simulations never exceed 1 dB. In contrast, there are obviously some difficulties in simulating the beginning of the growing period. Particularly, in 1992 there is a time shift of about 3 weeks between the observed increasing in the σ^0 values and the simulations. During this period, the magnitude of the backscattering mainly depends on the moisture content of the soil surface which, within a resolution cell, is highly variable. Here, it is apparent that we fail to simulate an appropriate soil moisture from the rainfall data recorded at only one meteorological station. On the other hand, when vegetation is sufficiently developed, the contribution of the soil decreases and the agreement between the experimental data and the model is good. At 20° of incidence angle, maximum observed values are pretty well simulated during the rainy seasons.

4. INVERSION

The inversion approach follows a two-step procedure. Firstly, the Oh et al.'s model is used to derive a linear relationship between $\sigma_{\text{scene}}^0(20^\circ)$ and H_v from which a maximum value of the surface soil moisture during the rainy season, is estimated. Second, a procedure which minimises the differences between the experimental data and the simulated $\sigma_{\text{scene}}^0(45^\circ)$ data is performed. This later is run with two constraints: on one hand, the soil moisture value to be retrieved must be smaller than the maximum value previously found, and on the other hand, the biomass must follow a 2-parameter logistic function simulating its temporal evolution. Results of the biomass retrieval are given in Figure 2.

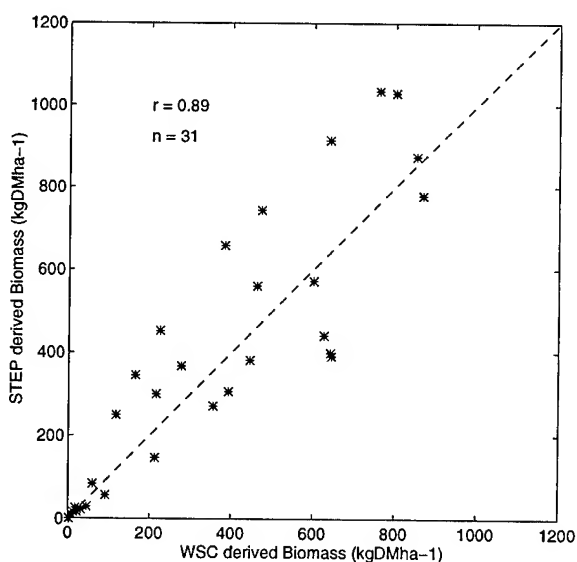


Figure 2 : Comparison between WSC-Derived Biomass and STEP-Derived Biomass. Growing seasons 92-94.

The associated error is about 33% indicating that biomass retrieval can be performed with a certain degree of confidence. Particularly, the maximum retrieved biomass equal to 500, 650 and 900 kg DM ha⁻¹ compare well with the field-estimated values equal to 400, 620 and 1050 kg DM ha⁻¹ for 1992, 1993 and 1994, respectively.

5. CONCLUSION

ERS-1 wind-scatterometer data acquired over a saharo-sahelian region located in the Gourma, Mali during the period 1992-1995, are analysed. Experimental observations show that $\sigma^0(45^\circ)$ temporal data display a marked seasonality associated with the development and senescence of annual grasses during the rainy seasons. The interpretation of the temporal σ^0 plots is performed with the assistance of a semi-empirical backscattering model combined with the ecosystem grassland model STEP. The use of this model allows the total biomass to be estimated with a 33% error.

ACKNOWLEDGMENTS

The authors thank ESA for providing us the ERS-1 scatterometer data used in the present study (project AO2.F121). This work was partly supported by the 'Pôle Espace' of the Région Midi-Pyrénées, France.

5. REFERENCES

- Attema, E.P.W., and Ulaby, F.T. (1978), Vegetation modeled as a water cloud, *Radio Science*, 13:357-364.
- Frison, P.L., and Mougin, E. (1996a), Use of ERS-1 wind scatterometer data over land surfaces, *I.E.E.E. Trans. Geosc. Remote Sens.*, 34:1-11.
- Frison, P.L., and Mougin, E. (1996b), Monitoring global vegetation dynamics with ERS-1 wind scatterometer data, *Int. J. Remote Sens.*, 17(16):3201-3218.
- Karam, M.A., Fung, A.K., Amar, F., Mougin, E., Lopes, A., Levine, D.M., and Beaudoin, A. (1995), A microwave polarimetric scattering model for a forest canopy based on vector radiative transfer theory. *Remote Sens. Environ.*, 53:16-30.
- Kerr, Y.H., and Magagi, R.D. (1993), Use of ERS-1 windscatterometer data over land surfaces. *Proceed. 2nd ERS-1 Symposium, Hamburg, 11-14 Oct., ESA SP-361*, pp. 381-388.
- Mougin, E., Lopes, A., Proisy, C., Warich, A., Frison, P.L., Lo Seen, D., and Lecomte, P. (1993a), Analysis of ERS-1 scatterometer data over land surfaces. Preliminary results. *Proceed. 2nd ERS-1 Symposium, Hamburg, 11-14 Oct., ESA SP-361*, pp. 393-397.
- Mougin, E., Lo Seen, D., Rambal, S., Gaston, A., and Hiernaux, P. (1995), A regional Sahelian grassland model to be coupled with multispectral satellite data. I. Description and validation. *Remote Sens. Environ.*, 52:181-193.
- Oh, Y., Sarabandi, K., and Ulaby, F.T. (1992), An empirical model and inversion technique for radar scattering from bare soil surfaces, *I.E.E.E. Trans. Geosci. Remote Sens.*, 30:370-381.
- Ulaby, F.T., Moore, R.K., and Fung, A.K. (1982), Microwave remote sensing : active and passive, vol. II, *Addison-Wesley Publishing Company*.
- Wismann V.R., Bochnke K., Schumllius C., (1993), Radar signatures of land surfaces measured by the ERS-1 scatterometer. *Proceed. 2nd ERS-1 Symposium, Hamburg, 11-14 Oct., ESA SP-361*, pp. 405-410.

Characterizing Earth's Surface Using Moderate Resolution 14Ghz Scatterometer Imagery: Early Results from NSCAT Construction

Perry J. Hardin, David G. Long, and Ryan R. Jensen

Microwave Earth Remote Sensing Group, 676 SWKT, Brigham Young University, Provo UT, 84602

Email: perry_hardin@byu.edu, long@ee.byu.edu. Phone: (801) 378-6062

I. INTRODUCTION

Currently there is an extended effort to measure and model global climate. Small-scale vegetation maps, some derived from satellite imagery, are important components of these models. Because of the very large continental regions involved, Advanced Very High Resolution Radiometer (AVHRR) imagery and its derivative vegetation index products with resolutions between 1 and 12 km have been the preferred source material for many of these maps. However, because of persistent cloud cover in many regions critical to global climate such as polar and equatorial areas, active microwave sensors which are sensitive to vegetation and ice variations may be better for this global mapping task than visible and near infrared sensors such as AVHRR.

Scatterometers are active microwave instruments used to measure ocean wind speed and direction. The first spaceborne scatterometer, S-193, flew as part of the Skylab mission in 1973. However, most of what we learned early about spaceborne scatterometers came from the ill-fated flight of Seasat-A. Although the mission lasted only 99 days in 1978 before being catastrophically terminated, the experience gleaned from the Seasat-A scatterometer (SASS) was sufficient to prove that satellite-based scatterometers were invaluable instruments for the study of ocean winds. The launch of ERS-1 in 1991 provided further evidence of the scatterometer's worth. The ERS-1 advanced microwave instrument (AMI), operating in wind scatterometer mode, is capable of land and sea imaging with pixel resolutions of approximately 50 km.

Launched in August 1996, the NASA scatterometer (NSCAT) was also designed to measure ocean wind vectors. However, like its SASS predecessor, NSCAT data is also acquired over land. Though collected at a resolution of 25km, resolution enhancements permit image reconstruction to image cell approaching 8 km. When reconstructed to this moderate resolution, the NSCAT data can be an important addition to AVHRR for global monitoring of cloudy regions. In other words, the scatterometer can be viewed as an active microwave instrument for land and ice imaging, as well as wind assessment.

The purpose of this paper is to report preliminary results of research designed to measure the characteristics of earth's land surface as depicted in reconstructed NSCAT imagery.

II. NSCAT AND IMAGE RECONSTRUCTION

NSCAT measures σ_0 over a wide range of incidence angles, at several azimuth angles, and with both horizontal and vertical polarization. The wide swath enables the frequent observation of targets. By combining data from multiple passes with the SIRF algorithm [1,2], enhanced resolution images of the surface backscatter can be made with an effective resolution of 8-10 km. Primarily, the SIRF algorithm provides images of σ_0 at a 40° incidence angle (designated *A*). The algorithm also provides an image of the slope of σ_0 versus incidence angle (designated *B*). While *A* images are used more frequently, *B* images may prove useful in understanding the scattering mechanisms responsible for the observed backscatter and in discriminating between various land cover types.

III. FIRST IMAGES

Figure 1 is a low-resolution reproduction of a global NSCAT composite (*A*, vertical polarization) for September of 1996. Perhaps the most striking characteristic of the image as a whole is the contrast and detail available in the absence of any significant atmospheric effect.

Figure 2 is a low-resolution reproduction of the United States and Canada. Unlike its early SASS counterpart, the major urban areas such as St. Louis, Kansas City, Chicago, Montreal and several Texas conurbations are clearly visible as bright dots or patches. The boundary between the agricultural heartland (brighter) and the shortgrass prairie (very dark) to the east of the Rocky Mountains is also clearly seen. The boundary between the Canadian taiga and agriculture is also detectable. Besides the urban areas, the brightest areas on the map (which is not an artifact of the imaging process) are the Mojave Desert and southwestern Great Basin.

This high Mojave desert backscatter is in contrast to the low backscatter from the sandy desert in Northern Africa (Figure 3). This stunning depiction of the Northern Africa surficial geology shows the areas of erg, reg, and hamada with different backscatter. The Tibesti Massif appears as a bright gray spot nearly dead-center in the image, whereas the large sand seas such as the Grand Erg Occidental appear as very dark gray patches. The transition from equatorial broadleaf forest through savanna grasslands, to the shrub steppe zone and ultimately to the north African desert is easily recognizable on the NSCAT image as a progression from white to nearly black tones.

Figure 4 is an image of Earth's north polar region. Currently there is an ongoing effort to map the extent and movement of sea ice using reconstructed NSCAT imagery. Two fundamental challenges are being addressed. First is the challenge to distinguish between rough open water and the edge of the ice which borders it. The second is distinguishing between the various phases of the sea ice itself.

Figure 5 is a reconstructed NSCAT image which includes Europe, southwest Asia, and the Mediterranean. Several urban areas are visible on the image. The non-urban tone gradations are largely due to agricultural mosaics and differences in natural vegetation. In the barren tundra areas, the different tones are likely due to moisture content of the soil.

IV. QUANTITATIVE ANALYSIS

In order to better determine the utility of reconstructed NSCAT imagery for actually discriminating between land cover classes and mapping land cover extent and change, a digital version of Matthew's vegetation type map [2] was compared to the NSCAT imagery. Summary backscatter statistics were calculated for each of the 31 vegetation classes represented in the map. The results of this simple analysis, sorted in descending order by A are shown in Table 1. As shown in the table, both ice and equatorial evergreen forest have the highest backscatter of any land cover class. Roughly speaking, backscatter decreases as the density of canopy cover decreases. There are some exceptions. Dense temperate needleleaved backscatter is relatively low compared to its equatorial equivalent.

V. SUMMARY

To a large extent, early research conducted with reconstructed SASS imagery to determine its ability to monitor vegetation at a regional scale has been confirmed by these early examinations of NSCAT imagery. While not a replacement for moderate resolution sensors such as AVHRR, reconstructed NSCAT imagery can be viewed as another primary source of geophysical data over earth's land and ice surfaces. From visual examination of imagery and simple quantitative analysis, there appears to be a relationship between normalized backscatter (A) and variables such as canopy cover, stage of crop growth, bare ground exposure, and moisture.

VI. REFERENCES

1. Long, D.G. and P.J. Hardin (1993) High resolution imaging of land/ice using spaceborne scatterometry part I: the imaging technique. *IEEE Transactions on Geoscience and Remote Sensing*. Vol. 31, No. 3, pp. 700-715.
2. Matthews, E. (1983). *Global Vegetation, Land-Use, and Seasonal Albedo* [NASA Goddard Institute for Space Studies]. Digital Raster Data on a 1-degree geographic (lat / lon) 180x360 grid. Boulder, CO: National Center for Atmospheric Research. 9 track tape, 0.8 mb.

Table 1. NSCAT backscatter summary for global land cover.

Land cover category	Mean A	Standard deviation A
Tropical evergreen forest, mangrove forest	-7.03	1.57
Ice	-7.21	3.73
Tropical / subtropical evergreen seasonal broadleaved forest	-7.41	1.64
Tropical / subtropical evergreen needleleaved forest	-7.92	1.02
Temperate evergreen seasonal broadleaved forest, summer rain	-7.94	1.19
Tropical / subtropical drought - deciduous forest	-8.01	1.78
Tall / medium / short grassland with < 10% woody tree cover or tuft-plant cover	-9.11	2.03
Xeromorphic forest / woodland	-9.18	1.53
Tropical / subtropical drought-deciduous woodland	-9.21	1.58
Tall grassland, no woody cover	-9.25	2.03
Cold-deciduous forest, with evergreens	-9.35	1.44
Tall / medium / short grassland with 10 - 40% woody tree cover	-9.45	1.92
Evergreen broadleaved sclerophyllous forest, winter rain	-9.47	1.39
Cold-deciduous forest, without evergreens	-9.71	1.16
Drought-deciduous shrubland / thicket	-9.89	2.31
Subtropical evergreen forest	-9.90	1.25
Temperate / subpolar evergreen rainforest	-9.90	1.66
Evergreen broadleaved sclerophyllous woodland	-10.00	1.67
Meadow, short grassland, no woody cover	-10.15	2.12
Forb formations	-10.15	1.83
Evergreen broadleaved shrubland / thicket, evergreen dwarf-shrubland	-10.29	2.51
Evergreen needleleaved or microphyllous shrubland / thicket	-10.41	1.31
Temperate / subpolar evergreen needleleaved forest	-10.44	1.02
Evergreen needleleaved woodland	-10.47	1.55
Medium grassland, no woody cover	-10.56	1.74
Cold deciduous woodland	-10.85	1.19
Arctic, alpine tundra, mossy bog	-11.23	1.99
Xeromorphic shrubland / dwarf shrubland	-11.24	2.56
Tall / medium / short grassland with shrub cover	-11.40	2.86
Cold-deciduous subalpine / subpolar shrubland, cold-deciduous dwarf shrubland	-12.30	1.82
Desert	-12.90	4.53

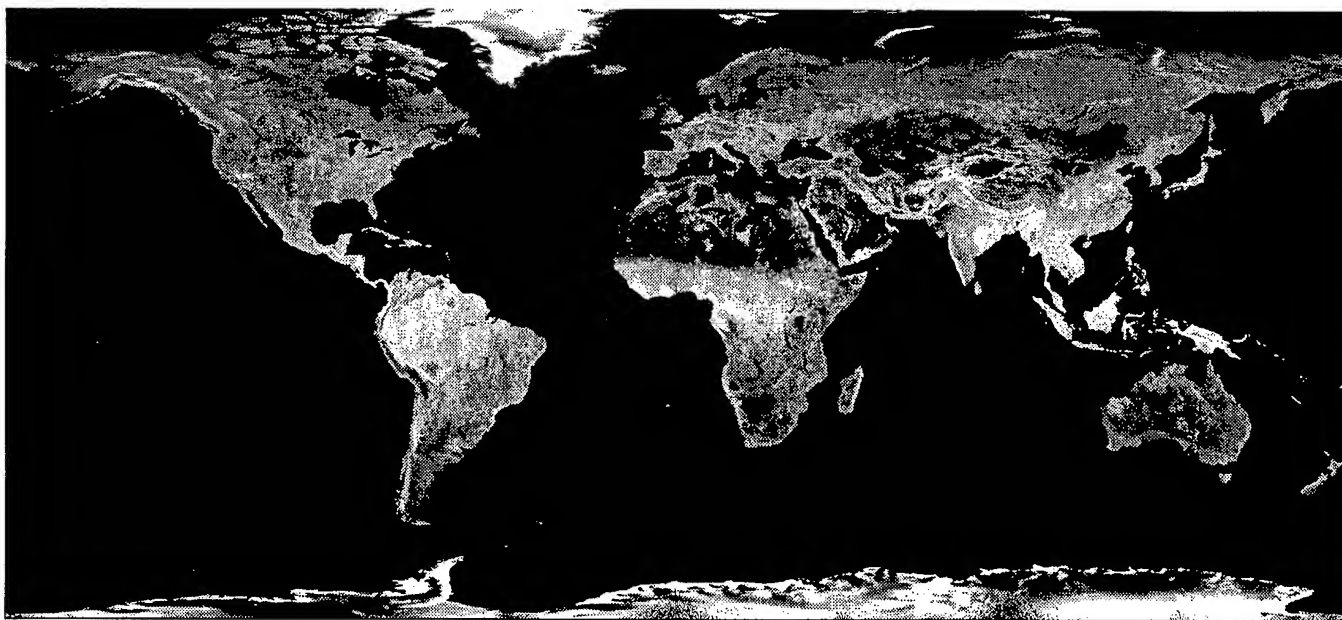


Figure 1. Reconstructed NSCAT image of the earth. September, 1996

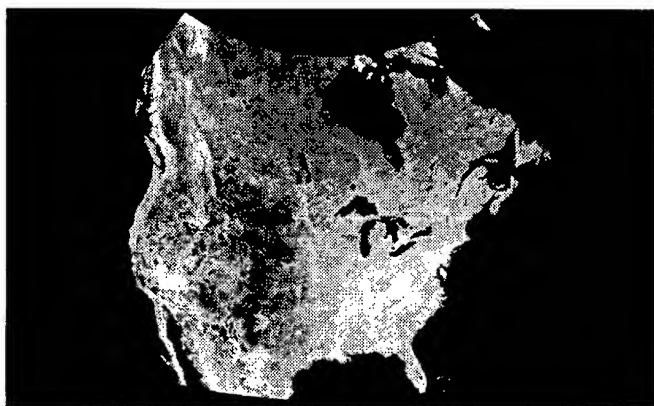


Figure 2. Reconstructed NSCAT image of the continental United States and Canada. Note the bright urban areas.

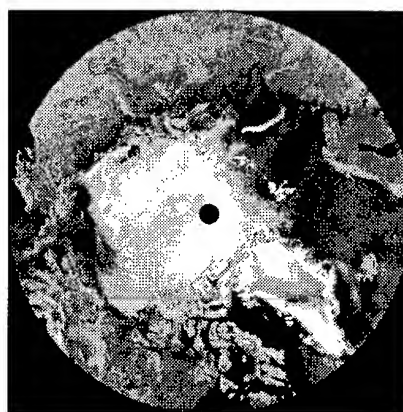


Figure 4. Reconstructed NSCAT image of the North Polar region. September, 1996

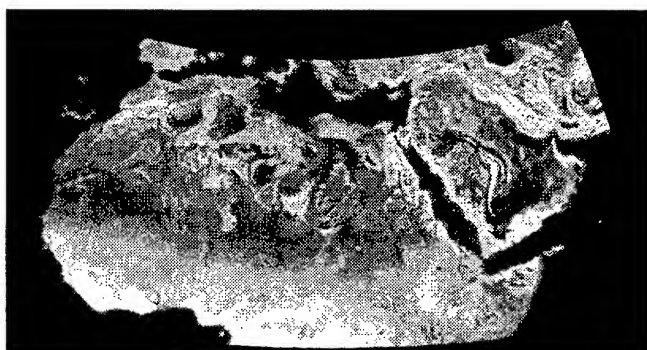


Figure 3. Reconstructed NSCAT image of North Africa, September, 1996.

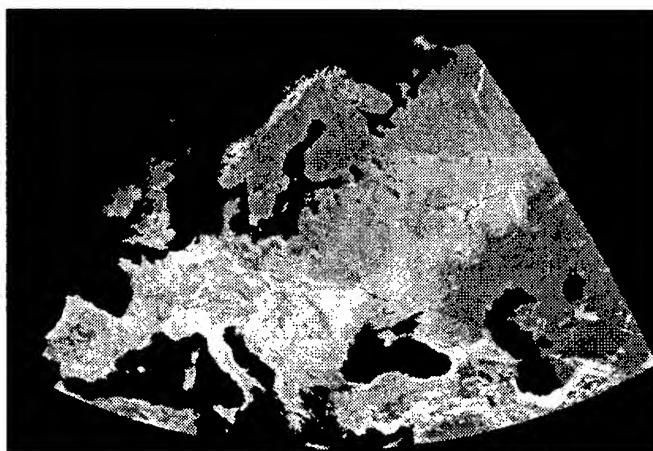


Figure 5. Reconstructed NSCAT image of Europe and Southwest Asia, September 1996.

Ice Classification in the Southern Ocean Using ERS-1 Scatterometer Data

David S. Early, David G. Long

Electrical and Computer Engineering Department, Brigham Young University
459 Clyde Building, Provo, Utah 84602
(801) 378-4383 fax: (801) 378-6586 long@ee.byu.edu

Abstract - A simple method for classifying Southern Ocean sea ice from enhanced resolution ERS-1 scatterometer images is presented. The enhanced resolution images are created with the Scatterometer Image Reconstruction (SIR) algorithm. This algorithm uses a dense, irregular sample grid created with multiple, overlapping passes of the ERS-1 scatterometer to achieve resolutions better than the nominal 50 km ERS-1 resolution. Because the scatterometer provides measurements over a range of incidence angles, the incidence angle dependence of the observed σ^o can be used as part of the classification algorithm along with the incidence angle normalized σ^o , improving the accuracy of the classification. In this study, a third parameter, the standard deviation of a measure of the anisotropy, is used to further help delineate sea ice types.

I. INTRODUCTION

The utility of the scatterometer for polar remote sensing is its rapid, repeat coverage measurements at a variety of incidence angles, which aid in the separation of ice classes. Backscatter from ice is a function of the measurement incidence angle, θ , and physical properties of the ice. In the incidence angle range $18^\circ \leq \theta \leq 60^\circ$, σ^o (in dB) is approximately a linear function of θ

$$\sigma^o(\text{dB}) = \mathcal{A} + \mathcal{B}(\theta - 40^\circ)$$

where the coefficients \mathcal{A} and \mathcal{B} depend on the ice characteristics. \mathcal{A} is the 40° incidence angle-normalized σ^o , while \mathcal{B} describes the dependence of σ^o on θ .

We use the Scatterometer Image Reconstruction (SIR) algorithm to generate enhanced resolution images of \mathcal{A} and \mathcal{B} from the nominally 50 km resolution ERS-1 AMI scatterometer measurements. The SIR algorithm effectively combines multiple passes of the scatterometer over a several day period into a single image with an effective resolution of 30 km [5].

With the aid of the SIR algorithm, a time series of enhanced resolution images of \mathcal{A} and \mathcal{B} have been produced. Each image is based on 6 days of data. These images are input to a simple classification scheme which maps the areal extent of six sea ice types. In this paper we concentrate on the details of separating multiyear ice from pancake ice in the marginal ice zone (MIZ) during the winter months. We also show the time evolution of the sea ice pack over an annual cycle.

II. SEA ICE CLASSIFICATION

Combining multiple measurements of the same location using multiple passes, *Lecomte et al.* [3] used the normalized standard deviation of the normalized difference d between the fore/aft beam measurements,

$$d = |\sigma_F^o - \sigma_A^o| / |\sigma_F^o + \sigma_A^o|,$$

as a measure of the scattering anisotropy in order to distinguish the open ocean from sea ice since sea ice scattering is isotropic while the ocean exhibits a strong azimuthal response.

While most sea ice exhibits an isotropic response [4], the normalized standard deviation can be a useful aid in classifying sea ice surface conditions. For the current application, an image of the normalized standard deviation of the anisotropy is created from the scatterometer measurements taken over the 6 day imaging interval of the SIR algorithm. For each fore-aft measurement pair, the value of d is projected onto a high resolution pixel grid matching the pixel grid used for the SIR images. The aperture weighting need not be used since it factors out and is canceled. The standard deviation of the d values for each pixel is then computed. The result is an image (known as the STD image) that reflects the average anisotropic response of the sea ice surface. Though the resulting image has lower effective resolution than the SIR \mathcal{A} and \mathcal{B} images, this imaging approach results in a somewhat higher resolution than merely binning the data. A sample STD image, where the ocean has been masked off using the detected ice edge, is shown in Fig. 2(a). In this study, we use STD images along with \mathcal{A} and \mathcal{B} images as input to a sea ice classifier.

III. ICE CLASSIFICATION

Drinkwater [1] developed a simple 5 class classifier based on the \mathcal{A} values. A summary of his reported \mathcal{A} values for each class is presented in Table I. The Smooth First Year (SFY), Rough First Year (RFY) and Iceberg classes are distinguishable using \mathcal{A} alone. However, from the \mathcal{A} value alone, it is not possible to distinguish between Multiyear (MY) and MIZ/Pancake (MIZ) ice [1].

The goal of this work is to separate the Multiyear (MY) and MIZ/Pancake (MIZ) classes. Based on scattering characteristics of each ice class, we can predict the behavior of \mathcal{B} and STD for each class. These are summarized in Table II (exact values are not crucial for this discussion).

For simplicity, since all but MY and MIZ ice are separable by \mathcal{A} value, we consider only the \mathcal{B} value and STD values for separating MY ice from MIZ ice. In the algorithm, Pixels are first classified by \mathcal{A} value. A second classification of MY pixels to separate MY and MIZ is then done. Since the \mathcal{B} and STD values for MIZ are higher than for MY ice, we select a threshold for an extended classification algorithm based on the histograms of \mathcal{B} and STD values (see Fig. 1). Using the histograms, the optimum threshold for the \mathcal{B} image data is set at -0.22. The optimum threshold for the STD value is set at

Class	Ice Type	Backscatter Range
ICE	Icebergs	$-6.0 \leq \sigma^o < 0.0$
MY	Multiyear	$-11.0 \leq \sigma^o < -6.0$
MIZ	MIZ/Pancakes	$-11.0 \leq \sigma^o < -6.0$
RFY	Rough First-year	$-14.0 \leq \sigma^o < -11.0$
SFY	Smooth First-year	$-20.0 \leq \sigma^o < -14.0$
NIL	Nilas	$-32.0 \leq \sigma^o < -20.0$

Table I

Summary of winter \mathcal{A} values for each class. Note that multiyear ice and MIZ/pancake ice have the same dB range [1]

Class	Ice Type	\mathcal{B} value	STD value
ICE	Icebergs	Mixed	Mixed
MY	Multiyear	Low	Low
MIZ	MIZ/Pancakes	High	High
RFY	Rough First-year	Mid	Mid
SFY	Smooth First-year	High	Low
NIL	Nilas	High	Low

Table II

Predicted winter \mathcal{B} and STD behavior for each class. MY and MIZ are separable.

0.03. Pixels with \mathcal{B} and STD values above the respective thresholds are classified as MIZ.

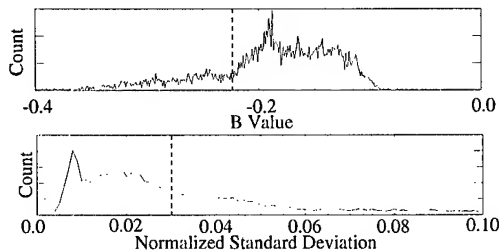


Figure 1. Histograms of \mathcal{B} and STD values. Vertical lines denote MY/MIZ thresholds.

IV. VALIDATION

For the Winter Weddell Gyre Study (WWGS) of 1992, the research vessel *Polarstern* was dispatched to enter the sea ice pack and study the surface conditions [2]. During this expedition, a ship borne C-band scatterometer made measurements of the surface conditions of homogeneous ice types, and visual observations of surface conditions were made. This is one of the limited *in situ* observations available for validation of the scatterometer data. Shortly after the ship entered the sea ice pack, a large, persistent field of MIZ/pancake ice was encountered. Later, the ship skirted around a large patch of RFY ice in the middle of the Weddell Sea.

We apply the one-dimensional (\mathcal{A}) classifier and use the \mathcal{B} and STD values to separate the MY and MIZ ice classes. Figure 2(b) shows a classified SIR image for JD 168, 1992. While the MIZ region near 0 degrees longitude is classified as MY by \mathcal{A} alone, use of \mathcal{B} and STD correctly classifies this area corresponding to the observed *Polarstern* data. Other regions in and around the sea ice pack have also been classed as MIZ ice, most notably the regions at the ice edge at 45 degrees west and 135 degrees west where we would expect the MIZ because of wave action at the ice edge. Also classed as MIZ are the ice production regions off the Ronne-Filchner ice shelf in the Weddell Sea and the ice production area off the Ross ice shelf.

As validation of the \mathcal{A} algorithm, records from the *Polarstern* show that the ship course was modified to the north to avoid a large mass of rough first-year ice in the center of the Weddell Sea [1, 2]. This feature of the ice pack is clearly represented in the classified SIR image.

While the new algorithm is an improvement over the one-dimensional \mathcal{A} classification, there are indications of some misclassification, e.g., the small amount of MIZ in the typically old ice mass at the tip of the Antarctic Peninsula. Review of images prior to and after this image show that little if any change occurs in the size and shape of this region, confirming the supposition that the area is actually MY ice since MIZ ice tends to rapidly change size and shape as the surface congeals and solidifies into SFY ice. Also, there are small MY areas in the largely MIZ ice class at 0 degrees longitude. However, since previous algorithms classified all MIZ ice, the separation of the majority of pixels in these two classes is considered

an important improvement over the one dimensional algorithm.

V. ANNUAL SEA ICE CYCLE 1995

Figure 2(c-f) shows samples from a typical annual cycle of sea ice growth and decay for 1995. These help illustrate the consistency of the classification algorithm.

Figure 2(c) shows an example of the early expansion of the sea ice sheet. A prominent feature is the relatively large quantities of MY ice both in the Weddell Sea and along the continental coast line. In the Weddell Sea, a band of rough first year ice surrounds an inner core of smooth first year ice. This is expected because the ice production begins near the continent, and as the ice ages, deforms and thickens it moves out to make room for newer ice to form off the Ronne-Filchner ice shelf.

Figures 2(d) shows the expanding sea ice pack and the gradual break up of the older ice masses. Notice the substantial reduction in the MY sea ice compared to the first image. Figure 2(e) shows a good example of a typical MIZ ice class near the ice edge at the top of the figure. Figure 2(f) shows the sea ice pack near its maximal extent.

Examination of the full set of images from 1995 shows that the classification results for the various ice classes display a spatial and temporal stability over the course of several annual cycles. The consistency of the ice classes from image to image further supports the definition of the classes while the spatial stability indicates that the classes are useful for studying dynamic motion in the sea ice pack.

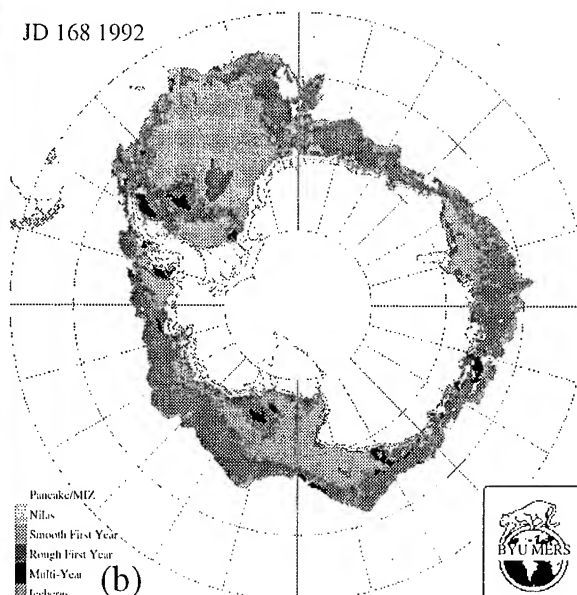
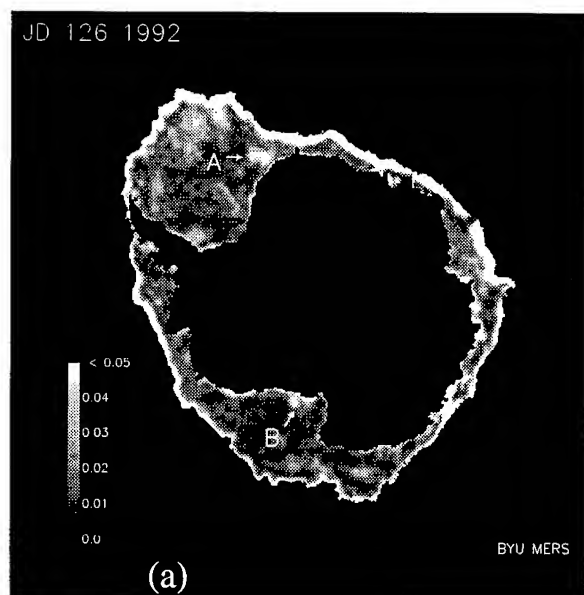
VI. SUMMARY

We have extended a simple one dimensional sea ice classifier to separate MIZ/Pancake ice from MY ice in enhanced resolution ERS-1 scatterometer images. The new algorithm uses σ° at 40° (\mathcal{A}), the incidence angle slope of σ° (\mathcal{B}), and the normalized standard deviation of anisotropy (STD) values to distinguish between the two classes.

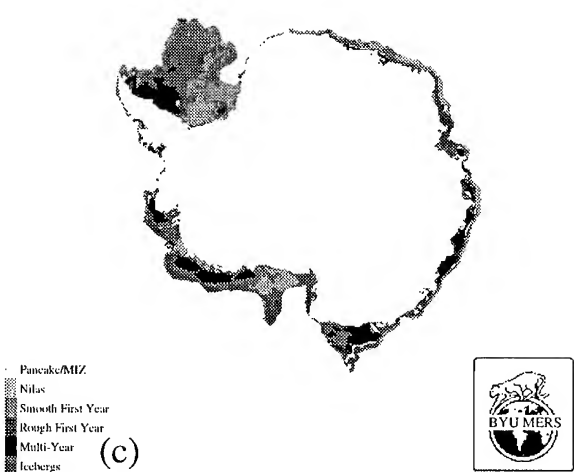
In situ observations of the sea ice pack made in 1992 were compared with classified imagery to validate the results. The result is a strong correlation between the observed sea ice conditions and the 6 ice classes used. An examination of a full year cycle of sea ice growth and decay in 1995 reveals that the various ice classes show strong spatial and temporal stability from the beginning of the ice pack expansion to the beginning the decay of the sea ice pack. The stability of the classification suggests that the images have value for study of motion in the sea ice pack.

REFERENCES

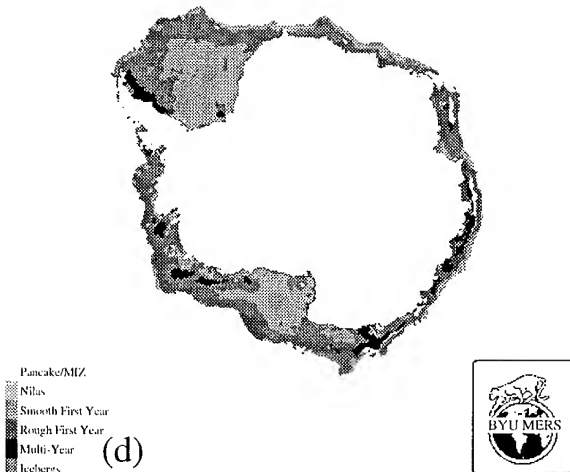
- [1] M.R. Drinkwater, "Satellite Microwave Radar Observations of Antarctic Sea Ice", in *Recent Advances in the Analysis of SAR for Remote Sensing of the Polar Oceans*, C. Tsatsoulis and R. Kwok, Eds. American Geophysical Union, In Press: Submitted October 1996.
- [2] M.R. Drinkwater and C. Haas, "Snow, Sea-ice, and Radar Observations During ANT X/4: Summary Data Report." Tech. Rep. 53, Alfred Wegener Institut, July 1994.
- [3] P. Lecomte, M. Davison, and A. Cavanie, "Ice Boundary Mapping using ERS-1 Scatterometer Data," *Earth Observation Quarterly*, no. 40, pp. 8, 1993.
- [4] D. Early and D.G. Long, "Azimuth Modulation of C-Band Scatterometer σ° over Southern Ocean Sea Ice," to appear, *IEEE Trans. Geosci. Rem. Sens.*, 1997.
- [5] D. Early and D.G. Long, "Enhanced Resolution Imaging from Irregular Samples," *Proc. IGARSS*, Singapore, 1997.



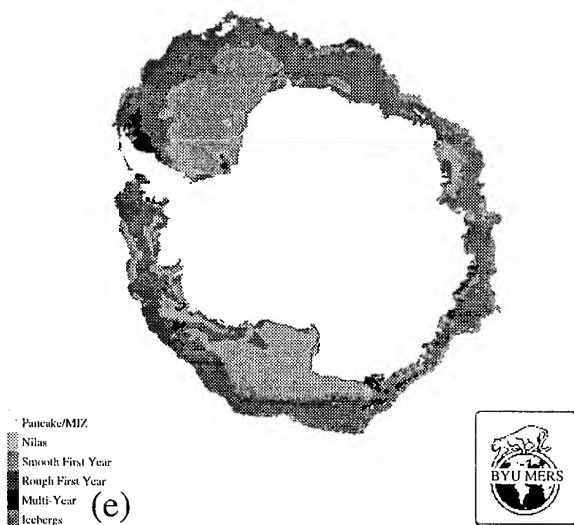
JD 063 1995



JD 099 1995



JD 144 1995



JD 270 1995

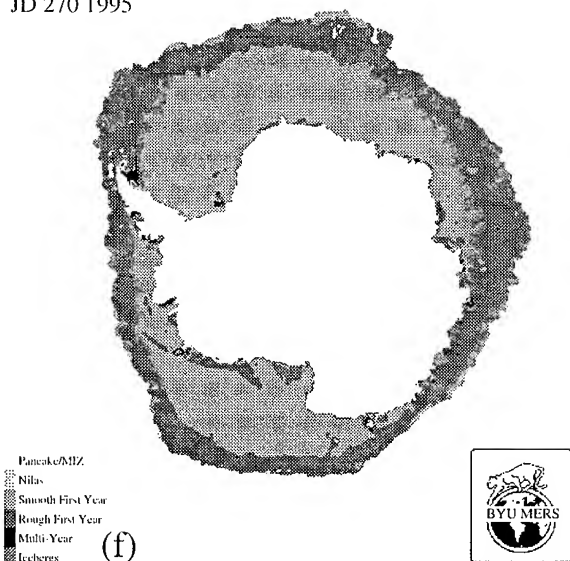


Figure 2. (a) STD image. Region A warm water upwelling. Region B new ice formation. (b) Classified image 1992. (c-f) time-series of classified images 1995.

AUTOMATED ANTARCTIC ICE EDGE DETECTION USING NSCAT DATA

Quinn P. Remund and David G. Long
Brigham Young University, MERS Laboratory
459 CB, Provo, UT 84602

801-378-4884, FAX: 801-378-6586 remundq@nscat.ee.byu.edu

Abstract— Polar sea ice plays an important role in the global climate and other geophysical processes. Although spaceborne scatterometers such as NSCAT have low inherent spatial resolution, resolution enhancement techniques can be utilized to make NSCAT data useful for monitoring sea ice extent in the Antarctic. Dual polarization radar measurements are \mathcal{A} and \mathcal{B} values are used in a linear discrimination analysis to identify sea ice and ocean pixels in composite images. Ice edge detection noise reduction is performed through region growing and erosion/dilation techniques. The algorithm is applied to actual NSCAT data. The resulting edge closely matches the NSIDC SSM/I derived 50% ice concentration edge.

INTRODUCTION

Historically, space-borne scatterometers have been employed primarily in atmospheric and oceanic studies. Rapid repeat coverage makes these instruments valuable in these applications. The low nominal spatial resolution inherent to scatterometers is acceptable for studying such large scale phenomenon. Spaceborne scatterometers have also been used to study non-ocean surface parameters (e.g. [1] [2]). However, for land and ice studies, the low resolution can limit the utility of this data.

The Scatterometer Image Reconstruction with Filter (SIRF) algorithm was developed [3] to enhance scatterometer image resolution by combining data from multiple passes of the satellite. It uses multiple σ^0 values to increase the effective resolution of the data. Over a limited incidence angle range of $[20^\circ, 55^\circ]$, σ^0 (in dB) is a approximately a linear function of θ ,

$$\sigma^0(\theta) = \mathcal{A} + \mathcal{B}(\theta - 40^\circ)$$

where \mathcal{A} and \mathcal{B} are functions of surface characteristics, azimuth angle, and polarization. \mathcal{A} is the σ^0 value at 40° incidence and \mathcal{B} describes the dependence of σ^0 on θ . \mathcal{A} and \mathcal{B} provide valuable information about surface parameters. 40° was chosen as a mid-swath value, but any interior swath angle can be used.

Polar sea ice is a critical input to global climate and geophysical models. It acts as an insulating layer between the warmer ocean and cooler atmosphere and can radically change the albedo of the Earth's surface. Hence, monitoring the extent of polar sea ice is of great interest to the remote sensing community. An automated algorithm for detecting the polar sea ice edge from NSCAT data has

been developed and shown to estimate the actual Antarctic ice edge with a high degree of accuracy. This paper describes the development and implementation of this algorithm.

ANTARCTIC NSCAT DATA

The NASA Scatterometer (NSCAT) launched in August of 1996 is a real aperture dual polarization Ku-band radar scatterometer designed to measure the normalized radar backscatter coefficient (σ^0) of the earth's surface. The two polarization \mathcal{A} and \mathcal{B} values provide four parameters that can be used to detect polar sea ice. Each of these parameters contains different information about the surface that may be useful in the discriminant analysis. This section examines the statistical properties of these variables to determine which combination provides the best basis for discrimination between ice and open ocean.

The \mathcal{A}/\mathcal{H} ratio is useful in determining the amount of volume versus surface scattering. In log space, this is equivalent to taking the difference between the V and H components. For smooth, conductive surfaces such as sea water, different reflection coefficients exist for vertically and horizontally polarized incident waves. In general, vertically polarized waves will reflect more than their horizontal counterparts. Thus, the \mathcal{A}/\mathcal{H} ratio will be positive. In volume scattering situations from dielectric surfaces with randomly oriented scatterers, such as ice with low water content, multiple reflections of the incident radiation tends to depolarize it. As a result, vertical and horizontal waves are scattered similarly and the \mathcal{A}/\mathcal{H} ratio is very close to one. Thus the \mathcal{A}/\mathcal{H} ratio is useful in discriminating between surfaces that display these scattering mechanisms.

According to the previous discussion, the ocean will generally have high \mathcal{A}/\mathcal{H} ratio values while sea ice (with low water content) will have low values. In actual \mathcal{A}/\mathcal{H} images, this is generally the case. However, in high wind conditions some ocean areas do exhibit low \mathcal{A}/\mathcal{H} ratios. The winds induce roughness on the ocean surface which depolarizes the scattering and drives the \mathcal{A}/\mathcal{H} ratio down. To minimize the effects of this error, the \mathcal{B} parameters are also used to classify the data.

\mathcal{B} Values

\mathcal{B} values represent the incidence angle dependence of σ^0 . Ice tends to be more isotropic than open water and has

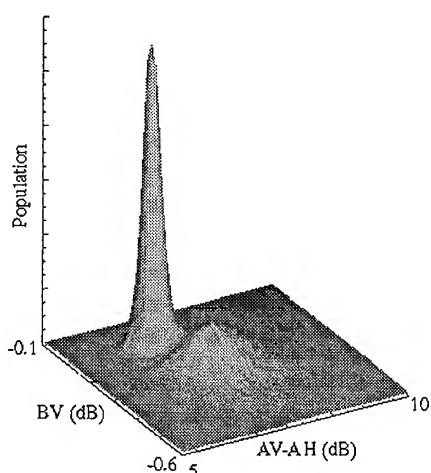


Figure 1: Two dimensional distribution of AV/AH values vs. BV values. The two modes correspond with ice and ocean pixels.

less incidence angle dependence. Ocean σ^0 is strongly dependent on incidence angle with the low incidence angles exhibiting higher σ^0 . A strong correlation exists between BV and BH . Noting that BV values are less noisy than BH due to the greater number of vertical polarization measurements, BV was chosen for the discriminant analysis in this study.

Multi-Parameter Analysis

The AV/AH ratio is combined with the BV value for each pixel in a resolution enhanced image for classification. For all non-land pixels a AV/AH ratio vs. BV two dimensional distribution is plotted in Figure 1. The two modes of the distribution correspond with sea ice and ocean pixels. Figure 2 illustrates a contour plot of the AV/AH ratio vs. BV distribution. The linear discrimination line is also plotted and is addressed in a following section. The contour level corresponds to the point at which the separate distributions begin to overlap and was used to set the linear threshold value.

ALGORITHM DESCRIPTION

Several steps are required to implement the actual ice edge detection. Initial steps (1-2) prepare the data and perform the linear discrimination. Following steps (3-4) are taken to reduce the effects of noise caused by misclassification. The general steps are as follows:

1. Generate the AV/AH ratio and BV images.
2. Produce binary threshold image through linear discriminant analysis.

3. Use region growing techniques to eliminate isolated patches of noise.
4. Use erosion and dilation techniques to reduce edge noise.
5. Apply the mask to the desired image.

Once SIRF images are generated from 6 days of NSCAT data, the difference is taken of the AV and AH images in log space to create a AV/AH ratio image. A median filter is then applied to reduce speckle in the image. The median filter was chosen since it is an edge preserving operation.

Linear Discrimination

The linear discrimination function is given by

$$BV = 0.0295(AV/AH) - 0.23$$

where BV and AV/AH are in dB. This line is plotted over the contour plot in Figure 2. For each pixel in question, the AV/AH value is used in this equation to derive a BV threshold value. If the observed BV value is greater than this threshold, the pixel is classified as ice, otherwise the pixel is considered ocean. This binary decision is performed for each pixel in the image.

Noise Removal

The linear discrimination portion of the algorithm results in a binary image illustrating the location of sea ice and ocean regions. High winds over the ocean can cause ocean pixels to be misclassified as ice for reasons previously addressed. This noise is manifested in the binary image as

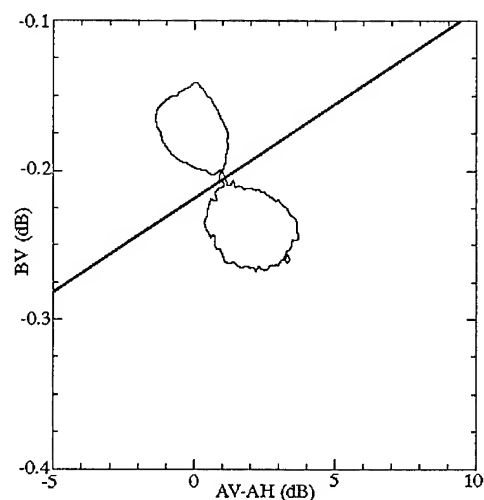


Figure 2: Contour plot of the distribution at the point where the modes intersect. The decision boundary line is plotted as well.

patches of ocean that have been classified as sea ice and patches of ice that were classified as ocean. Some of these are small isolated regions in the ocean area while others occur on or near the actual ice edge and are thus connected to the large ice region of the image. Each of these is handled separately in the noise removal step.

Region growing techniques are used to eliminate the isolated misclassification patches in the ocean. The region growing algorithm starts with a small region known to be within the ice area. It then expands this region within the ice area of the binary threshold image. The region continues to grow until it gets to the outer edge of the ice region. This eliminates all the patches of pixels misclassified as ice in the ocean. The region growing algorithm is then inverted to grow from the outer edge of the image inward until it reaches the binary threshold edge. This eliminates all the patches of pixels misclassified as ocean in the ice.

Once the region growing is complete, some residual noise exists on the edge itself as high spatial frequency edge characteristics and as small lobes attached by only a few pixels to the main body of ice. To remove this, image erosion and dilation techniques [4] are used. Two erosion iterations separate the smaller misclassified lobes from the main body. Region growing is then performed again to eliminate these separated lobes. To restore the edge (a

low pass filtered version), two iterations of image dilation are performed.

The result is a binary image depicting the location of sea ice and ocean. This is then used to mask the original resolution enhanced images.

RESULTS

The algorithm was implemented using SIRF resolution enhanced Antarctic images for the time period 1996 JD 276-281. Figure 3 shows a region of Antarctica with an ice edge derived from this algorithm plotted over the top. Another ice edge is plotted in the image that was created from thresholded NSIDC SSM/I ice concentration images. This particular edge corresponds with a 50% ice concentration. This level produced an edge had the highest correlation with the NSCAT derived ice edge.

CONCLUSIONS

NSCAT dual polarization Ku-band data in concert with the SIRF resolution enhancement algorithm can be used to effectively determine sea ice extent in the Antarctic. Linear discrimination analysis differentiates between ice and ocean pixels with a high degree of accuracy. Region growing and erosion/dilation procedures are effective in minimizing the effects of residual misclassified pixels. The resulting ice edge correlates very well with the NSIDC SSM/I derived 50% ice concentration edge.

REFERENCES

- [1] D. Long and M. Drinkwater, "Greenland Ice-Sheet Surface Properties Observed by the Seasat-A Scatterometer at Enhanced Resolution", *J. of Glaciology*, vol. 40, no. 135, pp. 213-230, 1994.
- [2] A. R. Hosseinmostafa, V. I. Lytle, K. C. Jezek, S. P. Gogineni, S. F. Ackley, and R. K. Moore, "Comparison of Radar Backscatter from Antarctic and Arctic Sea Ice", *J. of Electromagnetic Waves and Applications*, vol. 9, no. 3, pp. 421-438, 1995.
- [3] D. Long, P. Hardin, and P. Whiting, "Resolution Enhancement of Spaceborne Scatterometer Data", *IEEE Trans. on Geosci. and Rem. Sens.*, vol. 31, pp. 700-715, 1993.
- [4] J.C. Rush, *The Image Processing Handbook*, 2nd Ed., CRC Press, Boca Raton, FL, 1995.

ACKNOWLEDGMENTS

SSM/I data provided by the EOS Distributed Active Archive Center (DAAC) at the National Snow and Ice Data Center. NSCAT data provided by PO.DAAC at the Jet Propulsion Laboratory.

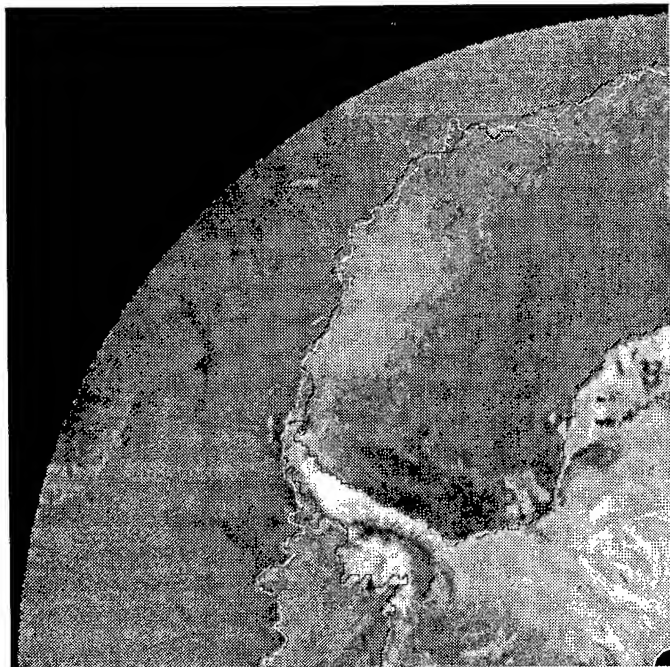


Figure 3: NSCAT SIRF enhanced *A* value vertical polarization image of a portion of Antarctica with ice edges plotted. The white edge was derived from the NSCAT algorithm while the black edge corresponds to the NSIDC SSM/I 50% ice edge.

Enhanced Resolution Imaging From Irregular Samples

David S. Early, David G. Long

Electrical and Computer Engineering Department, Brigham Young University
459 Clyde Building, Provo, Utah 84602
(801) 378-4383 fax: (801) 378-6586 long@ee.byu.edu

Abstract - This paper considers techniques for creating enhanced resolution images from irregular samples, with specific application to imaging from scatterometers. Using previously established irregular sampling theory, and developing the idea of sub-band limited Banach space, we show that frequency content in attenuated sidelobes can be recovered using resolution enhancement techniques, thus taking advantage of the high frequency content of measurements made with imperfect low pass aperture filters. We briefly compare and contrast the performance of additive ART, multiplicative ART and the Scatterometer Image Reconstruction (SIR) (a derivative of multiplicative ART) algorithms with and without noise.

I. INTRODUCTION

A theory for resolution enhancement from irregular samples is presented. The theory and techniques are illustrated for enhanced resolution ERS-1 scatterometer imagery. First, a theory of image reconstruction from irregular samples and the equivalence of the algebraic reconstruction technique (ART) and this theory are discussed. We demonstrate that reconstruction can recover sidelobe information and consider the practical use of the theory with the addition of noise to the reconstruction. We discuss scatterometer image reconstruction (SIR), a derivative of multiplicative ART tailored to reduce the influence of noise on enhanced resolution image reconstruction from scatterometer data [6].

II. SYSTEM MODEL

While this theory is developed around a model of the surface response that describes the microwave backscatter from a point, it is generally applicable. We desire to make images of the backscatter from ERS-1 scatterometer measurements. We model the radar backscatter (σ^0) from the surface as a function of location with the backscatter's incidence angle dependence suppressed.

Let $f(x, y)$ be the function that gives the backscatter from a point (x, y) on the surface. The measurement system can be modeled by

$$z = Hf + \text{noise} \quad (1)$$

where H is an operator that models the measurement system (aperture filtering and sample spacing), f is the true surface function, and z represents measurements of σ^0 made by the instrument. For resolution enhancement, we are interested in the inverse problem:

$$\hat{f} = \hat{H}^{-1}z \quad (2)$$

where \hat{f} is an estimate of f from the measurements z . The inverse of the operator H , \hat{H}^{-1} , is exact only if the measurements are noise free and H is invertible, in which case $\hat{f} = f$.

Real-life sampling usually involves a non-ideal sampler with a finite aperture which low-pass filters the data. The aperture functions may have frequency nulls that result

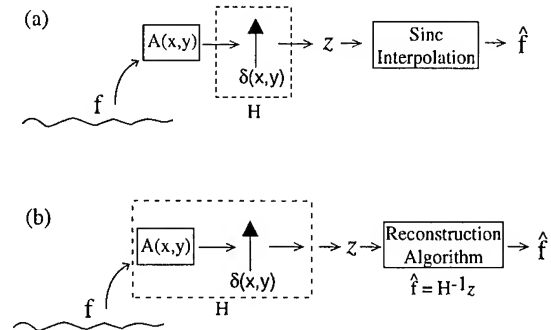


Figure 1. Block diagram illustrating sampling and signal recovery. The original surface, f , is filtered by the system aperture function, $A(x, y)$, and sampled to obtain the measurements z . In (a), the signal is uniformly sampled. The surface function is recovered using low pass filtering which inverts only the sampling. In (b), the operator inverted, denoted by H and the dotted box, includes both the aperture function and the sampling. Sampling is dense and may be irregular.

in information which can not be recovered. However if suitably sampled and processed, information in the aperture frequency response sidelobes can be recovered if the signal-to-noise ratio (SNR) is sufficiently high.

The traditional approach to sampling and reconstruction is based on the Nyquist sampling theorem which states that a band limited function can be completely reconstructed from regularly spaced samples if the sample rate exceeds the Nyquist sample rate of twice the maximum frequency in the signal. The reconstruction is done with a simple low pass filter consistent with the sampling. The filter is equivalent to using a *sinc* function as an interpolating function (see Fig. 1). When possible, the aperture function is designed to act as a prefilter to eliminate high frequency components of the signal that might otherwise cause aliasing in the reconstructed signal. Such an approach was used with the ERS-1 scatterometer design: A desired sample spacing of 25 km dictated an aperture function that filters wavelengths smaller than 50 km to minimize aliasing.

Because the aperture function is non-ideal, if the data is over-sampled at least some of the higher frequency content of the original signal can be recovered using a reconstruction algorithm which inverts both the sampling and aperture functions [see Fig. 1(b)].

III. IRREGULAR SAMPLING THEORY

In this section we consider irregular sampling and reconstruction. We are interested in irregular sampling because we can combine multiple passes of a scatterometer to achieve a closely spaced irregular sample grid [4].

Gröchenig analyzed the irregular sampling problem [1]. He presented a lemma which can be stated as follows: Let A be a bounded operator on a Banach space B such that $\|I - A\|' < 1$ (I is the Identity Operator), where $\|\cdot\|'$ denotes the operator norm on B . Then A is invertible on B and $A^{-1} = \sum_{n=0}^{\infty} (I - A)^n$. Moreover, every $f \in B$ can

be reconstructed by the iteration

$$\begin{aligned}\phi_0 &= Af \\ \phi_{n+1} &= \phi_n - A\phi_n \\ f &= \sum_{n=0}^{\infty} \phi_n\end{aligned}$$

with convergence in B. The operator A which includes the sampling and aperture functions must be bounded with $\|I - A\|' < 1$.

Gröchenig showed that if f is band limited on a Banach space and sampling is δ -dense with $\delta \cdot \omega < \ln(2)$ where ω represents the highest frequencies present in f , f can be reconstructed from its samples using this algorithm [1]. Experimental results for the ERS-1 scatterometer when several days of data are considered show that in the polar regions, the sampling sets are δ -dense with $\delta = 10$ km to 13 km [4]. The best resolution recovery is thus approximately 30 km, a value consistent with experimental results [4].

It can be shown that Gröchenig's Algorithm is functionally equivalent to the additive algebraic reconstruction technique (ART), a well-established image reconstruction technique [3]. Block additive ART can be written as [2]

$$a_{n+1}^j = a_n^j + \frac{\sum_i (s_i - p_i) h_{ij}}{\sum_i h_{ij}} \quad (3)$$

where a represents the image to be estimated, a_n is the n^{th} iterative estimate of a , j is the pixel index and i is the measurement index. The essence of this equation is that all measurements that touch a pixel a^j are summed and normalized to create the per pixel update value. Eq. (3) can be written as

$$a_{n+1} = a_n + \mathcal{H}(a - a_n) \quad (4)$$

where the a 's are now vectors with a being the 'true' image, a_n the n^{th} iterative estimate of a and $\mathcal{H} = H'H$ is an $N \times N$ matrix operator equivalent to Gröchenig's A [3]. H incorporates both the sampling and the aperture function.

While Gröchenig was primarily interested in low-pass function, we are interested in signals sampled by an aperture function with side lobes and nulls. We thus consider the sub-band limiting scheme illustrated in Fig. 2. It can be shown that such a sub-band limited space defined in Fig. 2(a) is a Banach space [3].

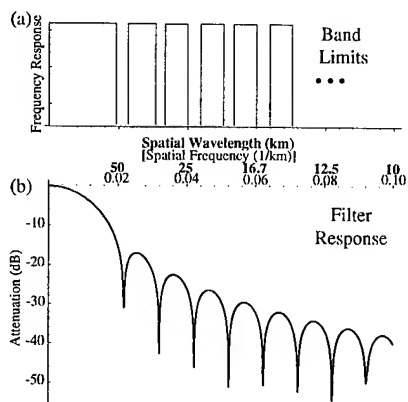


Figure 2. (a) A band limiting scheme that delimits nulls in the filter response in (b). (b) Frequency response of the ERS-1 scatterometer.

In the following discussion we assume that the sample spacing is adequate (δ -dense) for recovering the desired original and deal strictly with aperture function affects on invertibility. We define the domain of H to be $u \in B^2(\Omega')$ which consists of all functions with a sub-band limited frequency response as illustrated in Figure 2(a). The low pass characteristics of the aperture function built into the operator H indicate that certain frequencies of an arbitrary input are nulled out and therefore unrecoverable in any reconstruction. By setting the domain $B^2(\Omega')$ to be exclusively functions without those frequencies, no information is lost for $v = Hu$, though v may have attenuated frequency components. Then, $u' = H'v = H'Hu \in B^2(\Omega')$ is also in the original Banach space. Thus, $\mathcal{H} = H'H$ is a bounded operator on the sub-band limited Banach space, meeting the first requirement of Gröchenig's Lemma. Further, \mathcal{H} will be invertible on this Banach space. It follows that Eq. (4) represents a valid algorithm for the complete recovery of the original vector a within Banach space $B^2(\Omega')$. Note, however, that complete recovery is only possible if the original function is contained in the Banach space spanned by the operator inverse \mathcal{H}^{-1} , i.e., $B^2(\Omega')$. Otherwise, as discussed below, the result is an approximation of the original function.

IV. PRACTICAL APPLICATION

While \mathcal{H} is a valid operator for Gröchenig's algorithm for function which is band-limited or sub-band-limited, in application the surface function may not be sub-band limited. The original function can only be recovered in the sub-bands over which \mathcal{H} is invertible. Ideally, we would modify or reduce the space to correspond to a band-limited form. However, it is frequently impractical, from an algorithmic and computational standpoint, to reduce the problem to such a form. Instead, for practical application we use regularization of \mathcal{H} to insure its invertibility over the full space. The ART algorithms implicitly include regularization. Block additive ART is a least squares solution to the inverse problem in Eq. (2) while multiplicative ART with damping is a maximum entropy estimate in the limit [2][5]. Thus, even if the complete original function is unrecoverable, ART algorithms provide good estimates of the original function.

The Scatterometer Image Reconstruction (SIR) algorithm is a modified multiplicative ART algorithm specifically designed for scatterometer data reconstruction [4]. The SIR update has square root damping and includes a non-linearity to minimize the effects of noise and reaches the maximum entropy solution in the limit [6].

The results of additive ART, multiplicative ART and SIR are similar in the noiseless case. However, because of noise in the measurements, none of the reconstruction algorithms can be run for more than a few dozen iterations so the theoretical limits may not be reached. Nevertheless, as will be shown the algorithms provide good resolution enhancement with only limited iterations. The limited iteration results are approximations of the least squares or maximum entropy solution. Experimental data demonstrates that even highly attenuated frequency components are effectively recovered with finite iterations.

In order to illustrate and compare the ART and the SIR algorithm each are applied to a simple 1-D signal. A *sinc* function was chosen since it readily shows the frequency domain reconstruction from the various methods. The test signal is sampled with an irregular sampling grid. A rectangular aperture was chosen for convenience and its utility for demonstrating sidelobe recovery. The relationship between the spectrum of the aperture function and the test signal is illustrated in Fig. 3. The rectangular aperture for this study was chosen so that the first side

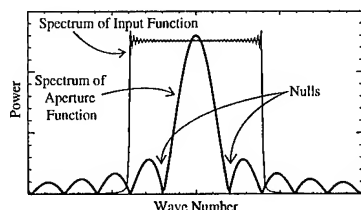


Figure 3. Illustration of the overlay of the test signal spectrum (light) with the frequency response of the aperture function (bold).

lobe of the aperture is inside the spectrum of the test signal as illustrated in Fig. 3, allowing the reconstruction of the attenuated and nulled frequencies within the side lobe to be easily evaluated. For each algorithm, a noisy case is also considered. Following the scatterometer noise model, multiplicative Gaussian noise with a K_p of 5% is added to the test signal.

Figure 4 illustrates the spectra of the output from Multiplicative ART and SIR at 25 and 100 iterations for both noiseless and noisy cases. (Both additive and multiplicative ART produce similar results for these cases.) While the noiseless case shows very good spectral recovery for just a few iterations, the performance of the ART algorithms in the presence of noise is significantly degraded. After 100 iterations the energy in the noise outside the desired band is increasing rapidly for the ART algorithm.

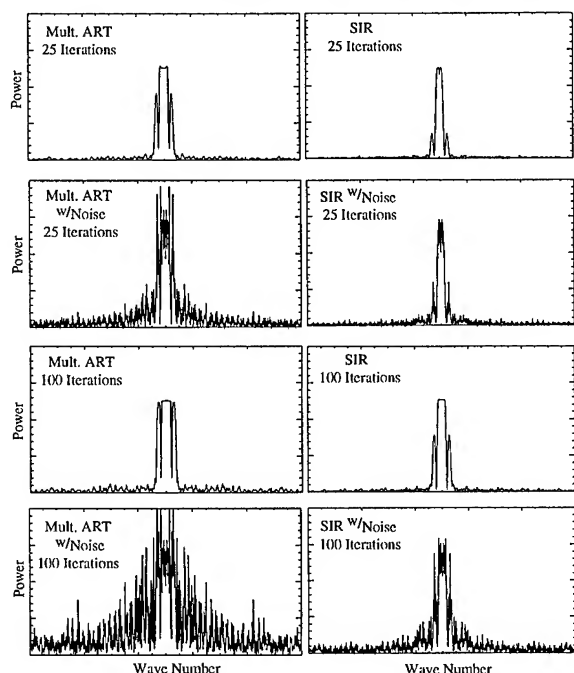


Figure 4. Spectra of multiplicative ART and SIR with noiseless and noisy measurements in the simulation.

In the noiseless case the signal is completely recovered with sufficient iterations for all of the algorithms. The poor performance of ART in the presence of noise originally motivated the development of SIR [6]. For SIR, the multiplicative scale factor is damped so that large scale factors do not overly magnify the noise at any one iteration, slowing the reconstruction but minimizing the effects of the noise. This is evident in the first sidelobe of the SIR estimate which, while enhanced, is not as noisy as it is for ART.

Figure 5 compares the error performance of the three algorithms in the simulation. To compute the total squared error shown, the output at each iteration is subtracted from the original test function and the difference squared and summed. The noisy cases for multiplicative and additive ART show greater error with increasing it-

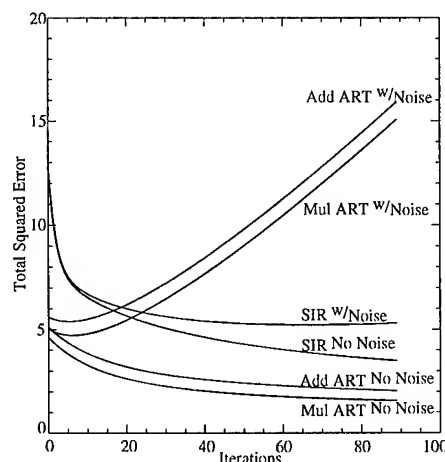


Figure 5. Cumulative squared error between the output of the algorithms for various iterations and noise.

erations after a brief initial decrease. Even though the total squared error is low in the initial iterations for the ART algorithms, a minimum number of iterations (about 30) is required to generate acceptable resolution enhancement, in which case SIR begins to perform better than the ART algorithms. SIR is also convergent to a lower total error than the ART algorithms which are nonconvergent for noisy measurements. The curves in Fig. 5 do not converge to zero because of the nulls in the aperture function. The corresponding frequencies are unrecoverable and result in some minimum error level between the original signal and the algorithm outputs. Based on Fig. 5 we conclude that SIR performs better when noise is present. Noting that the SIR algorithm also recovers the incidence angle response [6], we conclude that it is better suited for application to scatterometer data than an ART algorithm.

V. SUMMARY

Gröchenig's results suggest that a sub-bandlimited signal can be recovered from irregular samples. By using multiple passes of ERS-1 scatterometer data, an irregular δ -dense sampling grid of measurements is produced. Using a reconstruction algorithm such as ART or SIR permits resolution enhancement in excess of the Nyquist rate and the aperture function frequency response for a single pass.

REFERENCES

- [1] K. Gröchenig, "Reconstruction Algorithms in Irregular Sampling," *Mathematics of Computation*, vol. 59, no. 199, pp. 181-194, 1992.
- [2] Y. Censor, "Finite series-expansion reconstruction methods," *Proc. IEEE*, vol. 71, no. 3, pp. 409-419, March 1983.
- [3] D.S. Early and D.G. Long, "Enhanced Resolution Imaging from Irregular Samples," Submitted to, *IEEE Trans. Geosc. Remote Sens.*, 1997.
- [4] D.S. Early and D.G. Long, "Error and Resolution Characteristics of the SIRF Resolution Enhancement Algorithm," *Proc. IGARSS*, Lincoln, Nebraska, pp. 124-126, 1996.
- [5] T. Elfving, "On Some Methods for Entropy Maximization and Matrix Scaling," *Linear Algebra and its Applications*, no. 34, pp. 321-339, 1980.
- [6] D.G. Long, P. Hardin, and P. Whiting, "Resolution Enhancement of Spaceborne Scatterometer Data," *IEEE Trans. Geosci. Remote Sens.*, vol. 31, pp. 700-715, 1993.

Wind Field Models and Model Order Selection for Wind Estimation

Charles G. Brown, Paul E. Johnson, Stephen L. Richards, and David G. Long

Brigham Young University, MERS Laboratory

459 CB, Provo, UT 84602

801-378-4884, FAX: 801-378-6586 browncg@@salt.ee.byu.edu

Abstract—Traditional scatterometer wind estimation inverts the model function relationship between the wind and backscatter at each resolution element, yielding a set of ambiguities due to the many-to-one mapping of the model function. Field-wise wind estimation dramatically reduces the number of ambiguities by estimating the wind for many resolution elements, simultaneously, using a wind field model that constrains the spatial variability of the wind.

In this paper several wind field models are presented for use in field-wise wind estimation. Model accuracy, as a function of the number of model parameters, is reported for each model. This accuracy is evaluated using NSCAT JPL nudged L2.0 data.

In order to reduce the computational load, automated classification schemes are developed to select the optimal number of model parameters necessary for a given wind field. Classification is performed through hypothesis testing on raw NSCAT data and point-wise estimates.

INTRODUCTION

Radar backscatter data from NSCAT (NASA Scatterometer) are related to the near-surface ocean wind through a geophysical model function. However, due to the nature of the geophysical model function, each set of measurements yields an ambiguous set of estimates of the corresponding near-surface ocean wind in traditional point-wise estimation. An additional step is required to identify a unique solution from the very large number of possible fields. Field-wise estimation provides wind estimates for many resolution elements simultaneously by estimating the parameters of a wind field model, involving local or global optimizations on the model parameters. The accuracy of field-wise estimation increases with the number of model parameters. However, as the number of model parameters increases so does the computational expense of the optimizations.

In this paper we present several simple wind field models and evaluate the average accuracy of each model as a function of the number of model parameters. We also present two wind field classification algorithms. The first is based on radar backscatter data (σ^0), while the second uses the ambiguous point-wise estimates. The algorithms are used to classify which wind fields can be modeled by low-order models and which fields require higher-order models. This approach decreases the average number of model parameters

without significantly increasing the average modeling error. Throughout this work model accuracy is evaluated relative to NSCAT JPL nudged data, though we recognize the occasional failure of nudged data to identify the correct wind ambiguity. These failures can adversely affect the performance of our algorithm beyond that expected from simulated wind.

WIND FIELD MODELS

We consider linear wind field models applied to square regions, 600 km on each side. They are described by a matrix F in the equation $\mathbf{W}_M = F\mathbf{X}$, where \mathbf{X} is a column vector of model parameters and $\mathbf{W}_M = (\mathbf{U}^T \mathbf{V}^T)^T$, with \mathbf{U} and \mathbf{V} defined as column vectors containing the rectangular components of the wind vector cells. The model order is determined by the number of parameters in \mathbf{X} or, equivalently, the number of columns of F that are used. We evaluate several models in this section: Fourier and Legendre basis models [1], an orthogonal basis model derived using the Karhunen-Loeve transform [2], and the parameterized boundary conditions (PBC) model [3].

The matrix F of the Fourier model is constructed by sampling two-dimensional Fourier basis functions, while that of the Legendre model is created by sampling two-dimensional Legendre polynomials. The Karhunen-Loeve (KL) model, in contrast, is data driven. To create F , NSCAT JPL nudged L2.0 data was used to estimate the autocorrelation matrix for 600 km square regions, and the orthonormalized eigenvectors of the autocorrelation matrix were column-scanned to form the columns of the model matrix F . Finally, the columns of F were sorted in descending order according to the corresponding eigenvalues. The PBC model describes the field in terms of the divergence and vorticity of the pressure field along the region boundary [3].

In order to evaluate each of the models and compare their performance, the models were fit to regions of NSCAT JPL nudged data under a least-squared error constraint for each of the four models and for a range of model orders. The model based wind, $\hat{\mathbf{W}}$ is computed according to the equation $\hat{\mathbf{W}} = FF^\dagger \mathbf{W}$, where F^\dagger is the pseudo-inverse of F , and \mathbf{W} is the nudged wind field. The average errors for fits with the four models are displayed in Fig. 1 as functions of the number of model parameters used. The speed, direction, vector and normalized RMS errors between the model fit field $\hat{\mathbf{W}}$ and the nudged field \mathbf{W} show similar

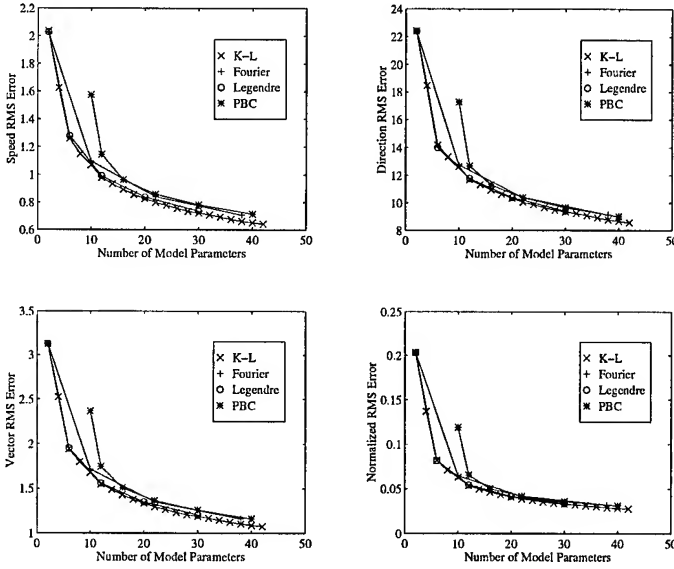


Figure 1: Average speed, direction, vector, and normalized rms error as a function of number of model parameters. These errors represent the difference between the nudged wind field, \mathbf{W} , and the least-squares model fit, $\hat{\mathbf{W}}$.

trends. Specifically that increasing the model order improves model accuracy, and that in general the choice of a particular model is not critical. Unfortunately, as the model order increases so does the computation required to estimate the wind using the model. The compromise for each field-wise estimate, then, is to minimize the number of model parameters while minimizing the model error. We propose to use different model orders for each optimization depending on the wind in the region.

MODEL ORDER SELECTION

Wind field classification algorithms can be used to select models with a minimal number of parameters while keeping the error in an acceptable range. The result increases the computational efficiency of field-wise estimation without significantly increasing the modeling error. In this section we describe two simple wind field classification algorithms that test the hypothesis that a field is poorly modeled by a low-order model. Lacking a clearly superior model using few parameters, the two algorithms described here are developed using the KL model, though adaptation to other models is straightforward.

Both classification algorithms divide wind fields into two disjoint classes based on some computable statistic of the data. Either the region is well modeled by a low-order model (designated θ_0), or it is poorly modeled by the low-order model (θ_1). Comparing a statistic, y , to a threshold, ν , provides the basis for the binary hypothesis

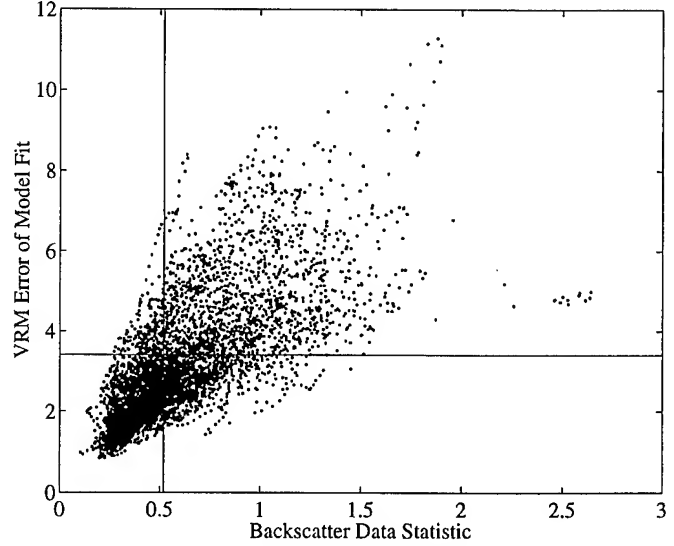


Figure 2: In general a field that is poorly fit by a 2 parameter KL model has a large value of the statistic, y , defined for the BC algorithm as the standard deviation of the normalized backscatter.

test:

$$\text{Wind Class} = \begin{cases} \theta_1 & \text{if } y > \nu \\ \theta_0 & \text{if } y \leq \nu. \end{cases}$$

The Backscatter Classification Algorithm

The backscatter classification (BC) algorithm relates the variability in the wind field to the variability in the corresponding σ^0 data, that is, the statistic for BC is computed directly from the σ^0 measurements. Selecting only smooth wind fields, so the dominant backscatter dependence is due to incidence angle, an average backscatter is computed for each beam as a function of the cross track cell. In the BC algorithm the σ^0 measurements are first normalized with respect to these averages. The statistic, y , for the BC algorithm is defined as the standard deviation of the σ^0 values of all the beams normalized by the average backscatter values.

Fig. 2 displays the relationship between the standard deviation of the normalized backscatter, y , and the vector rms (VRMS) error of the 2 parameter KL model fit to over 5000 NSCAT JPL nudged fields. The strong correlation between the statistic and the VRMS error of the 2 parameter KL model fit can be exploited to estimate the range of the VRMS error given y .

The choice of a threshold for the VRMS error of model fit identifies a field as being either well (θ_0) or poorly (θ_1) modeled by a 2 parameter KL model. The definition of “well” modeled, and the choice of the threshold, depends on the particular application. If, for example, the wind field class θ_0 is defined as wind fields that have a 2 parameter KL model fit VRMS error less than 3.4 m/s (below

the horizontal line of Fig. 2), then a threshold ν is selected from the normalized backscatter standard deviation. This selection requires a compromise between the probabilities of correctly classifying a wind field and the probabilities of misclassifying it. With the choice of $\nu = 0.52$ (selected to declare half the wind fields in θ_0 and half in θ_1), for example, the probability of correctly classifying a θ_1 wind field is 86% and the probability of incorrectly classifying a θ_0 wind field is 32%. With these thresholds (rather arbitrarily chosen) 50% of the wind fields are declared to be well modeled by just 2 parameters—in fact, the average VRMS error of these fits is 2.2 m/s, a modest increase from the 1.2 m/s error when 40 parameters are used (see Fig. 1).

The Point-wise Classification Algorithm

The point-wise (PC) algorithm classifies wind fields according to patterns in the point-wise ambiguity field, and relies on the statistics of the field directions only, regardless of the wind speed. The point-wise ambiguities are pre-processed to remove spurious ambiguities according to [4] with a probability of removing the correct ambiguity of 10^{-4} . The statistic, y , is defined for the PC algorithm as the minimum DRMS error between a mean wind field and the closest point-wise ambiguity field (minimized over all possible directions of the mean wind fields).

Fig. 3 reveals the correlation between y and the DRMS error in the 2 parameter KL model fit to over 3500 nudged wind fields. The correlation allows estimation of the range of model fit DRMS error given y . If the wind field class θ_0 is defined as wind fields that have a 2 parameter KL model fit DRMS error less than 20° , then the probability of correctly classifying a θ_1 wind field is 93% for $\nu = 14^\circ$. The probability of incorrectly classifying a θ_0 wind field is about 26%. Again, the choice of thresholds would depend on the application. The choice of $\nu = 14^\circ$ divides the declared regions in two nearly equal sized classes, and the average DRMS error of the θ_0 fields is 12° . This is a very modest increase from the 8° DRMS error resulting from the use of 40 model parameters.

CONCLUSIONS

Field-wise wind estimation profoundly reduces the number of ambiguities and reduces the computational load of scatterometer wind estimation. Examination of modeling error with four typical models reveals only minor differences. However, the average quality of the model fit is strongly influenced by the number of model parameters used. Increasing the number of model parameters

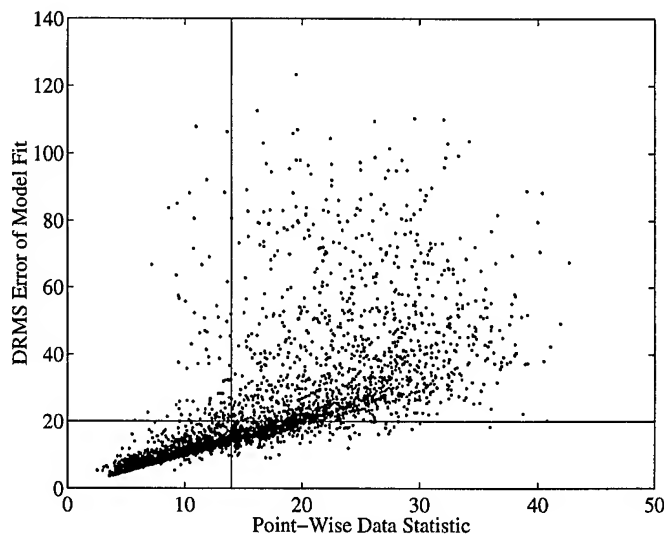


Figure 3: The DRMS error in a 2 parameter KL model fit to NSCAT JPL nudged wind fields is highly correlated with the PC algorithm statistic, y .

increases modeling accuracy; however, it also increases computational expense. Classification algorithms, such as the BC and PC algorithms presented here, can be used to decrease the average number of model parameters without significantly increasing the average modeling error. Identifying, *a priori*, fields that will be well modeled by a low-order model conserves computing resources for more difficult fields.

REFERENCES

- [1] T. E. Oliphant, "New Techniques for Wind Scatterometry," Master's Thesis, Brigham Young University, 1996.
- [2] J. Gunther and D. G. Long, "Models for the Near-Surface Oceanic Vorticity and Divergence," IGARSS, pp. 951-953, August 1994.
- [3] D. G. Long and J. M. Mendel, "Model-Based Estimation of Wind Fields Over the Ocean From Wind Scatterometer Measurements, Part I: Development of the Wind Field Model," IEEE Trans. Geosci. Remote Sensing, vol. 28, no. 3, pp. 349-360, May 1990.
- [4] T. E. Oliphant and D. G. Long, "Development of Statistical Methods for Eliminating Improbable Wind Aliases in Scatterometer Wind Retrieval," IGARSS, pp. 1715-1717, May 1996.

A NEURAL NETWORK-BASED MODEL FOR ESTIMATING THE WIND VECTOR USING ERS SCATTEROMETER DATA

Dayalan Kasilingam, I-I Lin, Victor Khoo and Lim Hock

Centre for Remote Imaging, Sensing and Processing
National University of Singapore
Lower Kent Ridge Rd.
Singapore, 119260.

Tel: (65) 771-5173; FAX: (65) 775-7717; e-mail: crsdpk@leonis.nus.sg

Abstract: A technique based on artificial neural networks is developed for describing the inversion of the CMOD4 model for estimating wind speed and direction from the scatterometers aboard the ERS satellites. Multi-layer perceptrons are trained using simulated data from the CMOD4 model. The normalized radar cross-sections (NRCS) and the respective incidence angles of the three beams are used as inputs. Separate networks are trained for the wind speed and wind direction. It is shown that the neural networks are able to learn the inverse mapping process accurately. The networks are tested with actual scatterometer measurements from the ERS-1 scatterometer. For these data sets, the output of the network appear to be more accurate than the corresponding wind vector estimates provided by the European Space Agency (ESA). It is also shown that the network can also be easily modified to include the effects of extraneous sources such as swells.

INTRODUCTION

Artificial neural networks (ANN) are well suited for describing processes that are either ill-defined or difficult to represent analytically. Frequently in remote sensing, extracting useful information from measurements requires inverting a complex, nonlinear mapping process. In most of these applications, the mapping function cannot be derived from fundamentals. Instead, one relies on empirical models based on experimental data to invert the measurements. In radar scatterometry, algorithms have been developed for extracting near surface wind speed and direction from backscatter measurements from the ocean surface. These algorithms are based on empirical models and do not necessarily reflect the physics of the measurement process. Thus, in general, it is difficult to modify these models to include extraneous effects that may also influence the backscatter process.

The radar reflectivity of the ocean surface is generally represented in terms of the normalized radar cross-section (NRCS). The ERS scatterometer measures the NRCS in three different azimuth directions. The CMOD4 model [1] is the

standard model used by the European Space Agency (ESA) to extract the wind vector from the C-band, scatterometer measurements from the ERS satellites. The CMOD4 model describes the NRCS in terms of the wind speed, direction, incidence angle and radar azimuth angle. It is highly nonlinear and impossible to invert analytically.

In this paper, a ANN-based inversion technique is developed for extracting the near surface wind vector from the ERS scatterometer. Simulations of the CMOD4 model are used to train a multi-layer perceptron (MLP) to perform the inversion process. It has to be noted that this technique performs the inversion of the CMOD4 model and does not represent a new scatterometer model. However, the technique may be adopted to any scatterometer model.

METHODOLOGY

Different topologies of neural networks were tested. The feedforward, multi-layer perceptron (MLP) with one hidden layer was selected for its simplicity. Since the training is done only once, the difficulties associated with training such a network is not an issue. In addition, the MLP also lends itself well to modifications.

It is found that the complexity required for training one MLP to estimate both wind speed and direction is significantly greater than training two networks separately for each of these parameters. Both networks consisted of five inputs - three NRCS values and two incidence angles. The two outer beams have the same incidence angle. The optimum number of units in the hidden layer was found to be ten. A single output unit generated either the wind speed or the wind direction.

At a given wind speed and direction, the NRCS values measured in two azimuth directions separated by 180° are similar. This gives rise to an ambiguity in the estimated wind direction. In this project, two separate sets of networks are trained with simulated data in the range 0° to 180° and in the range 0° to -180°, respectively. Wind vectors are obtained

from both sets. These estimates are then used in the CMOD4 model to estimate the NRCS values of the three beams. The ambiguity is resolved by choosing the wind vector that gives the best match to the measured NRCS values.

Training is done by using 5000 sets of randomly generated values of the wind speed, direction, incidence angle, azimuth angle and the corresponding NRCS values calculated from the CMOD4 model. The wind speed range is chosen to be between 3 and 20 m/s and the incidence angle is between 18° and 58° . Two separate training sets are generated by varying the azimuth angle randomly between 0° and 180° and 0° and -180° , respectively. Training is assumed to be complete when the errors reach an acceptable level.

RESULTS AND DISCUSSION

Learning is monitored by estimating the training error. The networks for estimating the wind speed reach an error of less than 0.2 m/s, after 10 million training cycles. The networks for estimating the wind direction reach an error of less than 5° after 10 million training cycles. These error levels are deemed as acceptable for the inversion process.

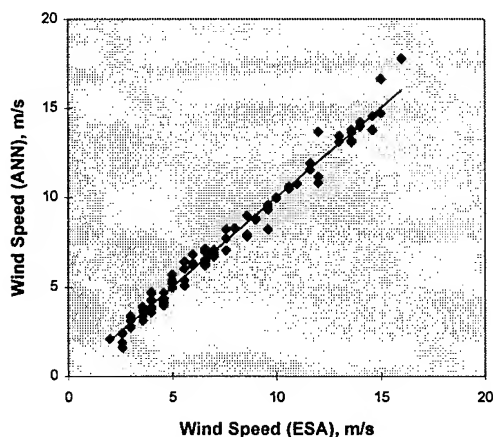


Figure 1 - Scatter plot showing the output of the neural network plotted against the ESA wind speed estimates. The solid line represents values where both estimates are equal.

Low-bit rate data from the ERS-1 scatterometer were used to test the inversion technique. The low-bit rate data consisted of the three measured NRCS values and the corresponding incidence angles and azimuth angles. In addition, the wind speed and direction which were estimated by ESA were also provided. The NRCS values and the incidence angles were used as inputs to the neural networks. 30,000 data samples covering the wind speed range from 3 to 20 m/s were inverted using the neural network. Fig. 1 shows the scatter

plot for the wind speed estimates from the neural network plotted against the wind speed estimates provided by ESA. The neural network output follows the ESA prediction accurately. The scatter is found to be minimal except at the very high wind speeds where it appears to increase.

Fig. 2 shows the average wind speed obtained from the neural network plotted against the wind speed provided by ESA. The average of the neural network output is estimated at each wind speed bin of 1 m/s. The curve seems to suggest that the neural network output is approximately 0.2 m/s less than the ESA estimates.

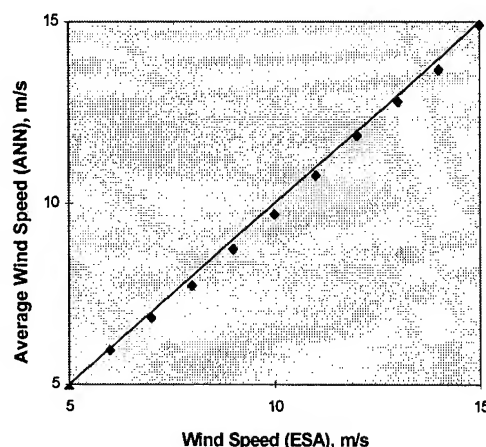


Figure 2 - Averaged wind speed output from the neural network plotted against the ESA wind speed estimate.

Fig. 3 shows the wind direction estimates from the neural network plotted against the corresponding quantity estimated by ESA. The most distinguishable feature in this plot is that there appears to be significant disagreement in the resolution of the 180° ambiguity. Work is underway to resolve this discrepancy using independent wind directional measurements. Allowing for the ambiguity, the scatter appears to be small.

To evaluate the quality of the estimates of the wind vector, the wind vector information is used with the CMOD4 forward model to estimate the NRCS of the three beams. These values of the NRCS were compared with the measured NRCS values. Fig. 4 shows the rms. errors of the calculated NRCS values as a function of the incidence angle of the center beam. The rms. error associated with the neural network output is consistently lower than that of the ESA wind vector estimates. This appears to suggest that the neural network-based technique gives a more accurate inversion of the CMOD4 model. The rms. error in the ESA estimates also appear to increase with the incidence angle, whereas the rms. error of the neural network remain reasonably flat across the range of incidence angles.

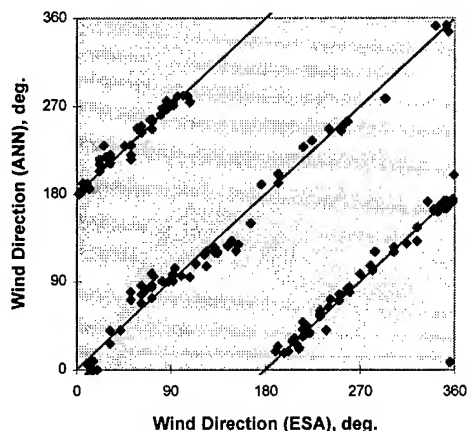


Figure 3 - Scatter plot showing the wind direction estimates from the neural network plotted against the corresponding ESA estimates. The three solid lines represent the curves where the estimates are equal and those separated by $\pm 180^\circ$, respectively.

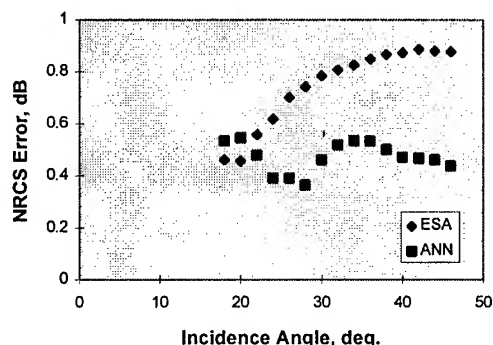


Figure 4 - Rms error in the NRCS calculated by comparing the NRCS values calculated from the CMOD4 model with the actual NRCS measurements from the ERS scatterometer. The wind vector estimates provided by ESA and the neural network were used separately as inputs to the CMOD4 model.

It has been suggested that the effect of swells on the NRCS results in error in the wind vector estimates in the tropics [2]. One of the advantages of the neural network-based technique is that it can easily be modified to include extraneous effects such as swell. In a separate study, synthetic aperture radar (SAR) wave-mode and scatterometer measurements were used to show that the presence of swell increased the NRCS of the ocean.

Estimated changes in the NRCS due to the presence of swell were incorporated in the low-bit rate data set. These modified NRCS values were used as inputs to the neural network. Fig. 5 shows the output of the neural network with and without the swells. Swells travelling the range direction and swells

travelling in the azimuth direction were treated separately. Fig. 5 shows that the wind speed estimates are higher for both cases of swell compared with the case where there was no swell. This is to be expected. However, fig. 5 also appears to suggest that azimuth travelling swell may have a greater impact on the wind speed estimates than range travelling swell.

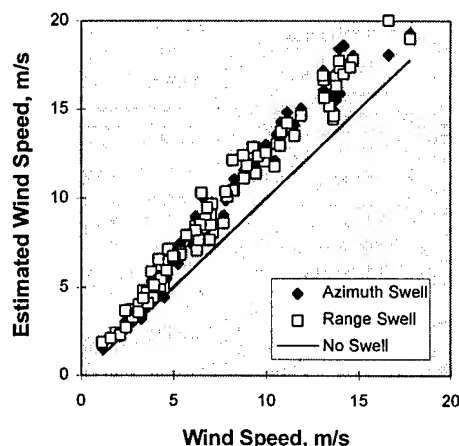


Figure 5 - Wind speed estimates from the neural network in the presence of swells. The solid line represents the wind estimates in the absence of swell.

CONCLUSION

The results indicate that the neural network is able to estimate the wind vector using the NRCS measurements from the ERS scatterometer. The results also seem to indicate that these estimates are superior to the estimates provided by ESA. It is also shown that the neural network based technique can easily be modified to include the effects of extraneous sources such as swells.

REFERENCES

- [1] Stoffelen, A. and D. Anderson, 'Characterisation of ERS-1 scatterometer measurements and wind retrieval', Proc. Second ERS-1 Symposium, Hamburg, October, 1993.
- [2] Rufenach, C., 'A new relationship between radar cross-section and ocean surface wind speed using ERS-1 scatterometer and buoy measurements', Intl. J. Remote Sensing, 3629-3647, 1995.

On a New Relationship between Radar Cross Section and Wind Speed Using ERS-1 Scatterometer Data and ECMWF Analysis Data over the Mediterranean Sea

Maurizio Migliaccio, *Member, IEEE*, Paolo Colandrea

Istituto Universitario Navale, *Istituto Teoria e Tecnica delle Onde Elettromagnetiche*, Via Acton 38, 80133 Napoli, Italy.
tel +39-81-5513976, fax +39-81-5521485, email: migliaccio@naval.uninav.it

Antonio Bartoloni, Claudia D'Amelio

Nuova Telespazio S.p.A., Via Tiburtina 965, 00156 Roma, Italy.
tel +39-6-40791, fax +39-6-40793628, email: Claudia_Damelio@telespazio.it

Abstract -- It is here presented a work in the field of wind reconstruction by means of spaceborne scatterometer. A new relationship between the radar cross section and the wind field is investigated. Its functional form has been recently suggested by some recent studies performed over the Pacific Ocean [1]. Due to its intrinsic capability to model weak wind fields is of special relevance in a closed sea, such as the Mediterranean Sea. It is here investigated the case of ERS-1 scatterometer data (C-band) and the radar cross section - wind field relationship is determined by means of the ECMWF analysis over the Mediterranean Sea.

INTRODUCTION

Remote sensing of the marine environment is matter of great interest both for the capability to provide a continuous monitoring of such an important part of our ecosystem and for forcing the oceanographic models [2-3].

Within such a framework the estimation of the wind vector field on sea surface is of particular relevance. This can be accomplished by means of different remote sensing techniques, e.g. scatterometer [4], and synthetic aperture radar [5]. In any case, the definition of a reliable radar cross section model is a key point for the accurate reconstruction of the wind vector field. Recently, an improved radar cross section model derived by Rufenach has been proposed in order to better model the sea radar cross section at low wind speed regimes [1].

The exponential model dependence on wind speed proposed by Rufenach is adopted in this paper to define a new radar cross section relationship to be used for the reconstruction of the wind vector field over the Mediterranean Sea starting from ERS-1 scatterometer data. Its calibration is based on a suitable fitting procedure performed on ECMWF analysis data over the Mediterranean Sea.

The main motivation of this work is given by the expectation that such a new relationship overcomes the intrinsic CMOD4 low wind speed regimes limitation, which indeed play a key role within the Mediterranean Sea, and performs as good as the CMOD4 for other wind regimes.

The impact of this new radar cross section model on the problem of the wind speed reconstruction is investigated on real ERS-1 scatterometer processing.

As main result of these investigations we have a positive confirmation of the validity of such new relationship although some further *ad hoc* investigations are certainly advisable.

The paper is organized as follows: first a brief background is provided, then the derivation of the new relationship between radar cross section and wind speed using ERS-1 scatterometer data and ECMWF analysis data over the Mediterranean Sea is illustrated. Then, a set of reconstructed fields is obtained to show the impact of this new relationship. Finally, some conclusions are reported.

THE BACKGROUND

The reconstruction of a wind field by means of an appropriate set of measured radar cross sections [4-5] is made possible by the use of a semi-empirical relationship which relates the σ_o 's to the wind vector. A large set of experiments and speculations, partly published in open literature, have clearly demonstrated the σ_o dependence on the electromagnetic wavelength, the incidence angle, and the directional ocean wave spectrum [2-3]. Accordingly, given an electromagnetic frequency (5.6 GHz in the ERS-1 case) it is possible to proceed to an angular-diversity based set of measurements in order to reconstruct the wind field. The reconstructed wind field is meant to be the wind field at 10 m height above the sea level in a neutrally stratified atmosphere.

A very general relationship between the radar cross section σ_o and the wind speed and direction can be casted in the following form [1]:

$$\sigma_o = f(\vartheta, U) \left[1 + \sum_{n=1}^N b_n(\vartheta, U) \cos n\varphi \right] \quad (1)$$

wherein U is the wind speed, ϑ is the incidence angle of the electromagnetic wave impinging on the sea surface and φ is the wind direction referred to the ground-projected antenna beam direction. Note also that a popular choice for N is 2 since it appears to be satisfactory for the wind reconstruction [6]. The classical form for the $f(\cdot)$ is the power-law as suggested by extensive measurement campaigns [6-7], that is:

$$f(\vartheta, U) = \chi(\vartheta) U^{\gamma(\vartheta)} \quad (2)$$

This is the functional form for the CMOD4 model currently recommended and adopted by the ESA [6-8]. More recently, a different functional form has been suggested as the result of an extended ERS-1 and buoy-based measurement campaign over the Pacific Ocean [1]. It has the following form:

$$f(\vartheta, U) = c(\vartheta) \exp[\alpha(\vartheta)U + \beta(\vartheta)U^2] \quad (3)$$

which has the implicit capability to take into account low wind regimes [1] at variance of the CMOD4 model which shows a cut-off behaviour [1]. This is the main motivation of the present work.

THE NEW RELATIONSHIP

In this Section we employ the functional form of eq.(3) and eq.(1) to derive a new relationship between radar cross section and wind speed using ERS-1 scatterometer data and ECMWF analysis data over the Mediterranean Sea.

In other words it is here illustrated the model calibration procedure which permits us to define the new relationship. Before proceeding further it is important to stress that the CMOD4 model requires the knowledge of 60 parameters whereas the exponential model calls for the estimation of 16 parameters only (6 for the $f(\cdot)$ and 10 for the $b_n(\cdot)$). This is in accordance to the adopted ϑ -expansion of the harmonic parameters [1, 6-8] as well as the ϑ -expansion of the exponential ones [1].

As a matter of fact, the first step takes care of collocating a set of σ_o 's at the same time and space of some external (to the radar system) wind field measurements. This is by no means an easy task due to the usual impossibility to have such an external fine data set. In our case, no buoy measurements were at disposal so the external data set has been obtained by the ECMWF analysis. In particular, four data set, relevant to periods of time from March 1992 to January 1993, have been considered. The whole set of data summed up to about 150,000 wind field data. Since the ECMWF analysis provides a temporal and spatial resolution of 6 hours and about 50 km an interpolation procedure must be accomplished in order to collocate the available ERS-1 σ_o measurements to the ECMWF wind field [8]. In Fig.1 is shown the number of occurrences of the wind speeds for four ϑ ranges as provided by the ECMWF analysis data set used into the calibration step. We note that for all cases we have a Rayleigh-like distribution and that the great part of the wind regimes are bounded within 10 m/sec whereas a peak is found around 5 m/sec. This can be justified by the fact that the ECMWF analysis is critical to retaining fine-scale features.

Coming back to the calibration procedure we have that as second step a (U, ϑ, φ) binning procedure must be dealt. The bin size has been chosen in accordance to the ECMWF wind field resolution. In particular a (U, ϑ, φ) bin size of 1 m/sec, 5° , 20° has been considered.

After that a bin-to-bin averaging step is performed. This step requires that a sufficient number of independent σ_o measurements fall into each bin thus the need to have a large data set of σ_o 's and external data set [8]. Then, the integration step is accomplished as follows:

$$\frac{1}{2\pi} \int_0^{2\pi} \sigma_o d\varphi = f(U, \vartheta) \quad (4)$$

wherein σ_o is the averaged value pertaining to the φ values. In practice, eq.(4) is numerically evaluated over the data at disposal. As a result an overdimensioned system into the 6 $f(\cdot)$ parameters is constructed. The system is linear as soon as eq.(4) is expressed in decibel units [1]. Applying a pseudo-inversion technique the $f(\cdot)$ parameters are determined [6-8].

Finally, reentering into eq.(1) it is possible to similarly determine the $b_n(\cdot)$ harmonic parameters [6-8].

Once that these steps have been accomplished the model parameters are determined and it is possible to establish the relationship between radar cross section and wind speed.

WIND RECONSTRUCTION

In this Section, the application of the exponential model calibrated according to the above described procedure has been used in order to reconstruct the wind over the Mediterranean Sea. The wind reconstruction procedure has been performed in accordance to what illustrated in [4] and fully tested over some reference wind data set [4]. In particular, in [4] it has been shown that such a reconstruction scheme, even without any *a priori* information, is able to reconstruct the wind field, within the customary confidence levels [4], both in the doublets and triplets case, with an high percentage of success [4].

By benefiting of the new relationship between radar cross section and wind speed many experimentation have been performed [8]. In particular, the whole January 1996 ERS-1 scatterometer data set has been investigated.

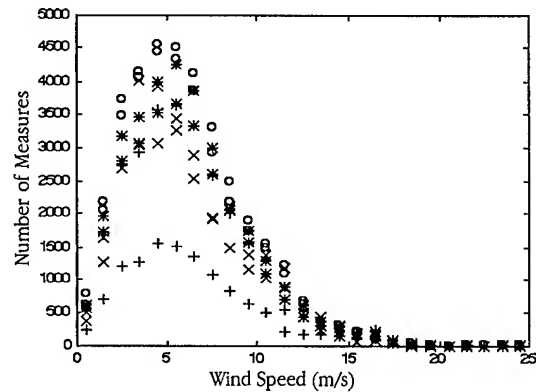


Fig.1: Relevant to the ECMWF calibration data. +: $\vartheta < 30^\circ$, *: $30^\circ < \vartheta < 40^\circ$, o: $40^\circ < \vartheta < 50^\circ$, x: $\vartheta > 50^\circ$.

In Fig.2 the reconstructed wind field relevant to January, 10 UTC 8:30:11.000 and to the Eastern Mediterranean Sea is shown. We note a dominant wind speed from N-NE and a realistic Cyprus Island downwind feature. Both in the NW part of the frame and in the Cyprus Island downwind part we have the presence of weak wind fields. The mean wind speed is of 3.680 m/sec. In order to validate the reconstructed wind field would be highly advisable to perform a comparison with some *in situ* measurements. Unfortunately, this is generally difficult or impossible. Although only indicative we can perform such a comparison again with the data furnished by the ECMWF analysis. In Fig.3 the corresponding wind field is shown. We note that the large-scale features are in good agreement with what showed in Fig.2. We note also that, as expected, the fine-scales features are not predicted by the ECMWF analysis thus showing the unique scatterometer capability to detect such wind fields. The mean wind field is of 3.597 m/sec in close agreement to what reconstructed by the scatterometer data. A comparison with a similar result based on the CMOD4 model show the cut-off phenomenon for low wind speed regimes and a good agreement for other wind regimes [8].

CONCLUSIONS

A new relationship between radar cross section and wind speed for the C-band V-polarized ERS-1 scatterometer and the Mediterranean Sea has been illustrated. A first set of experimentations showed that it behaves as good as the CMOD4 for high wind speed regimes and is able to reconstruct low wind speed regimes. Furthermore, it requires a far limited number of parameters than the CMOD4.

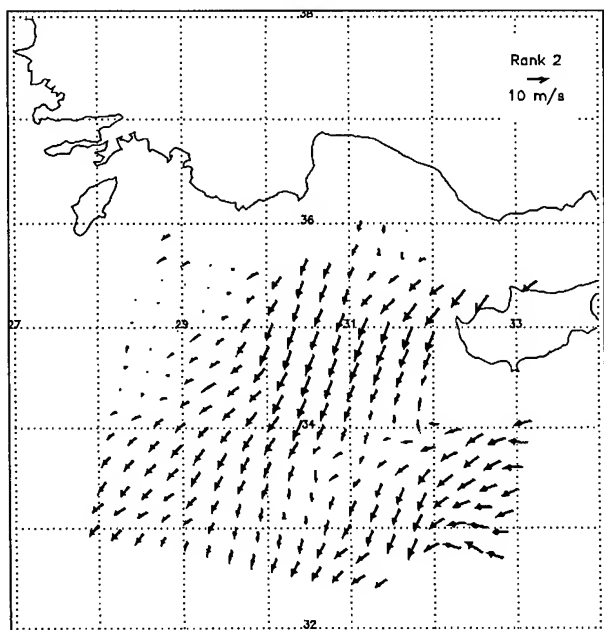


Fig.2: Reconstructed wind field.

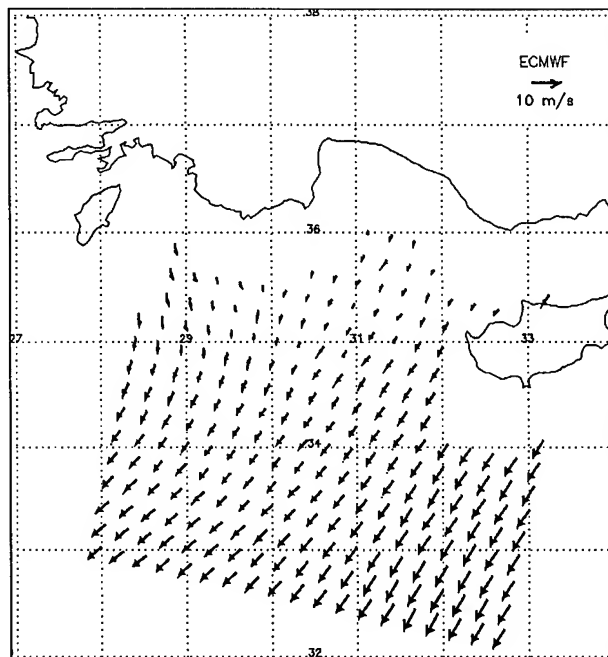


Fig.3: ECMWF analysis.

ACKNOWLEDGMENTS

The authors wish to thank the Italian Space Agency (A.S.I.) and the European Space Agency (E.S.A.) for making available the scatterometer raw data set used in this work.

REFERENCES

- [1] C.L.Rufenach, "A New Relationship between Radar Cross-Section and Ocean Surface Wind Speed Using ERS-1 Scatterometer and Buoy Measurements", *Int. J. Remote Sensing*, 16, 3629-3647, 1995.
- [2] R.K.Moore and A.K.Fung, "Radar Determination of Winds at Sea", *Proc. IEEE*, 67, 1504-1521, 1979.
- [3] M.A.Donelan and W.J.Pierson, "Radar Scattering and Equilibrium Ranges in Wind-Generated Waves With Application to Scatterometry", *J.Geophys. Res.*, 92, 4971-5029, 1987.
- [4] A.Bartoloni, C.D'Amelio and F.Zirilli, "Wind Reconstruction from Ku-Band or C-band Scatterometer Data", *IEEE Trans. Geosci. Remote Sensing*, GE-31, 1000-1008, 1993.
- [5] C.C.Wackerman, C.L.Rufenach, R.A.Shuchman, J.A.Johannessen and K.L.Davidson, "Wind Vector Retrieval Using ERS-1 Synthetic Aperture Radar Imagery", *IEEE Trans. Geosci. Remote Sensing*, GE-34, 1343-1352, 1996.
- [6] A.E.Long, "C-band V-polarized Radar Sea Echo Model from ERS-1 Haltenbanken Campaign", in *Proc. ERS-1 Geophys. Validation Workshop*, Penhors, F, 1992.
- [7] *CMOD4 Model Description*, ESA Document ER-TN-ESA-GP-1120, 1993.
- [8] P.Colandrea, "La Ricostruzione di Campi di Vento con Dati Scatterometrici dell'ERS-1", (in Italian), Istituto Universitario Navale Thesis Work, 1997.

Backscatter Variability Observed in C-Band and Ku-Band Scatterometer Data

Paul E. Johnson and David G. Long
Brigham Young University, MERS Laboratory

459 CB, Provo, UT 84602

801-378-4884, FAX: 801-378-6586 johnsonp@sage.ee.byu.edu

Abstract—The backscatter from ocean waves measured by scatterometers is primarily determined by the speed and direction of near-surface wind, while other influences (temperature, salinity, swell, etc.) appear to be secondary effects. A complete theoretical geophysical model, incorporating all influences on the backscatter, appears beyond the current state of science; empirical estimates of the wind-backscatter relationship do not incorporate non-wind influences and suffer from variability due to unmodelled parameters. Having previously developed a method of estimating this variability directly from scatterometer measurements, this paper provides an analysis of ERS-1 (C-band) and NSCAT (Ku-band) data to identify some governing factors in the value of the modeling variability.

INTRODUCTION

Empirical estimates of the geophysical model function relate the wind over the ocean surface, along with parameters characterizing the way the radar looks at the surface, to the normalized radar cross section, σ° . However, unmodelled factors affect the relationship between the wind and the radar cross section; these cause variability in the true value of the backscatter for given wind and observation geometry. Identifying the sensitivity of this variability to various parameters improves our understanding of the model function and the scatterometer measurement process, thereby enhancing wind estimation.

A simple model which describes the basic measurement process [1] is depicted in Fig. 1. The empirically determined model function maps the surface wind, along with the parameters of the scatterometer, to the model function backscatter, σ_M° . This value is perturbed by unmodelled parameters, via a zero-mean unit-variance random variable, ν_1 , to yield the true backscatter coefficient of the surface, σ_T° . The measurement of the true backscatter, σ_T° , is corrupted by thermal noise, again with a zero-mean

unit-variance random variable, ν_2 . A given measurement is modeled as $z = (1 + K_{PM}\nu_1)(1 + K_{PC}\nu_2)\sigma_M^\circ$, where ν_1 and ν_2 are assumed to be independent (i.e., the uncertainty due to unmodelled parameters is independent of the thermal noise in the communication channel), and K_{PM}^2 and K_{PC}^2 are the normalized variances for the modeling error and the communication error, respectively. The communication noise, K_{PC} , is well understood in terms of the time-bandwidth product of the measurement process, and has long been accepted in the radar community as having a multiplicative nature, corresponding to the fact that the communication noise is proportional to the signal itself [2]. K_{PM} describes the variability in the empirical model function, that is, it quantifies the uncertainty in the backscatter for given wind conditions. This variability has received little attention, though a method of estimating the value of K_{PM} from scatterometer-only data has been developed [1] and some initial investigations of the effect of K_{PM} on wind estimation have been performed [3, 4].

Here a more thorough analysis of C-band (ERS-1) and Ku-band (NSCAT) data are reported to describe the magnitude and some of the dependences of K_{PM} . In doing this, we wish to make clear that this is not a comparison of instruments or of model functions. Rather, the focus and contribution of this paper is to quantify the variability of empirical model functions and to identify a few of the parameters that affect this variability. These should be useful in improving future empirical model functions.

C-BAND ESTIMATES OF K_{PM}

First we consider the variability observed in the C-band model function. We use CMOD-FDP [5] though results should be similar for other model functions. Specifically, we consider the sensitivity of K_{PM} to wind speed, observation incidence angle, latitude, and temporal variations in various latitude bands. The estimates of K_{PM} are determined solely from ERS-1 scatterometer data by comparing the variance of the measurements to the variance of the model function driven by the retrieved wind [1].

Fig. 2 plots the estimated value of K_{PM} against the incidence angle (angle of observation) for four typical wind speeds. The error bars indicate one standard deviation above and below the mean value of the estimates. We see a very clear trend of decreasing K_{PM} with wind speed. There is also a slight increase in K_{PM} with incidence angle, and an unusual dip at 50° . It should be noted that

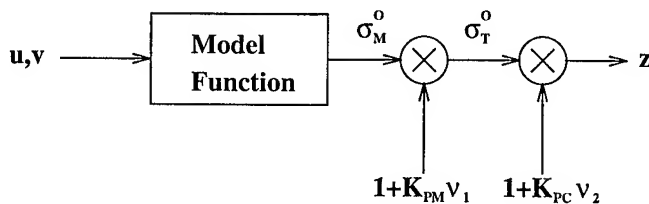


Figure 1: The model for scatterometer measurements.

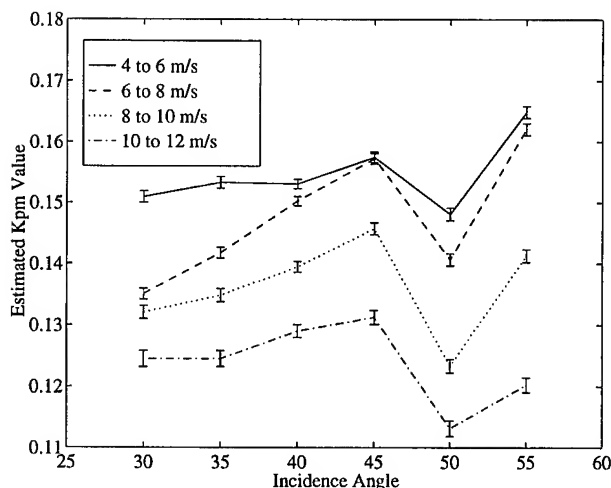


Figure 2: Estimates of the value of K_{PM} , the model function variability, based on ascending passes of ERS-1 data. The plot indicates a clear trend that K_{PM} decreases with wind speed, but has only a small dependence on incidence angle, though there is a consistent dip in the value for 50° incidence angle.

this wind speed dependence is not as clear using data from descending passes, for which we have no explanation.

Since different latitudes have different wind speed distributions, the wind speed dependence observed in Fig. 2 could be due to a latitude effect such as sea surface temperature (which would affect water viscosity) or fetch (which would affect sea state development). To consider the latitude dependence of the model function variability, Fig. 3 plots estimates of K_{PM} against latitude for the same four wind speed bins. A clear wind speed depen-

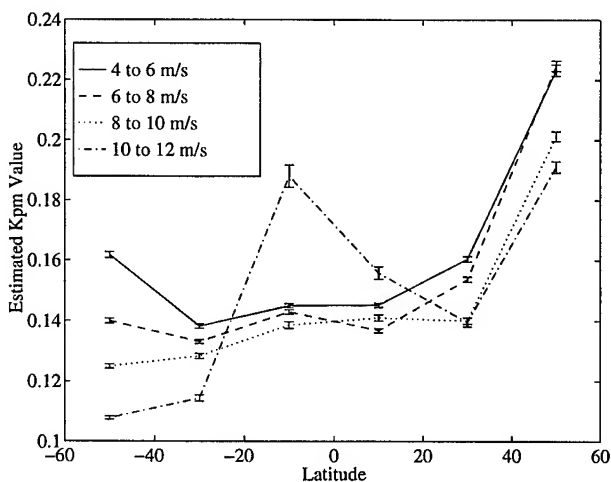


Figure 3: Estimates of the value of K_{PM} from ERS-1 data, for 20° latitude bands. Again we see a clear speed trend. We also see little latitude variation except at higher latitudes.

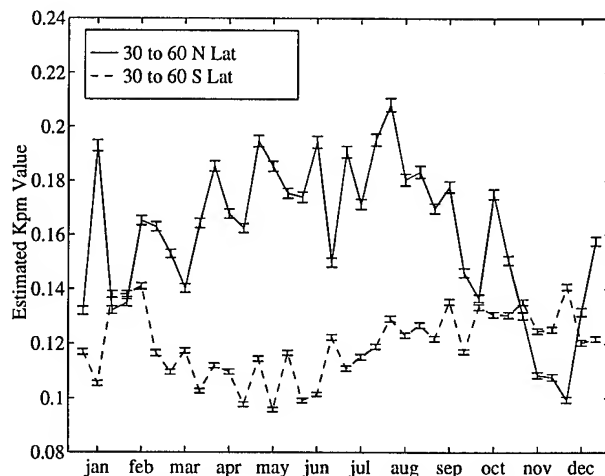


Figure 4: Estimates of the value of K_{PM} from 1993 ERS-1 ascending data, plotted against time, for two latitude bands. Each latitude band seems to have increased K_{PM} during the warmest part of the year in that latitude.

dence remains, except at low latitudes where high wind speeds are relatively uncommon and the estimation suffers from limited data.

Fig. 4 plots the estimates for one year of data collection in 1993 in two latitude bands (averaging over all wind speeds and incidence angles) in order to examine seasonal trends. Equatorial latitudes show little variation about $K_{PM} = 0.14$ and are omitted from the plot for clarity. The northern latitudes show a generally higher value of K_{PM} , which decreases considerably in the winter months. Similarly, the southern latitudes show lower values of K_{PM} during the colder months. These temporal variations in K_{PM} may be due to the different wind speed distributions of different seasons in each hemisphere.

KU-BAND ESTIMATES OF K_{PM}

In this section, the model function variability, K_{PM} , is estimated for Ku-band from NSCAT data using the new NSCAT-1 model function. While this data has many differences from ERS-1 data, the variability in the model functions often show similar trends.

Fig. 5 plots the estimated value of K_{PM} determined from NSCAT data against the incidence angle for the four typical wind speeds. As with ERS-1 data, we see a clear trend of decreasing K_{PM} with wind speed. There is also a substantial increase in K_{PM} with incidence angle, which was not observed in the C-band data. It should be noted that the Ku-band data used consists of one week of data (18 to 25 December, 1996), where the C-band data is a full year of data (1993) sampled every ten days.

The dependence of the variability on latitude is observed in Fig. 6 where estimates of K_{PM} are plotted

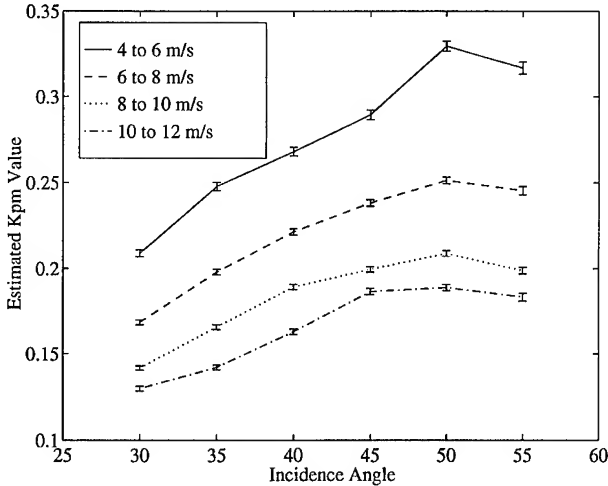


Figure 5: Estimates of the value of K_{PM} , the model function variability, based on ascending passes of NSCAT data (Ku-band). The plot indicates a clear trend that K_{PM} decreases with wind speed, and increases substantially with incidence angle.

against latitude for the same four wind speed bins. As with ERS-1 data, the plot shows slight decreases in the estimate of K_{PM} at mid latitudes, though there is less apparent variation than was seen at C-band. We also recognize the poor estimates near the equator for high wind speeds due to the relatively few data points usable in the averaging, and that using only a single week of data, in December, will affect the estimates.

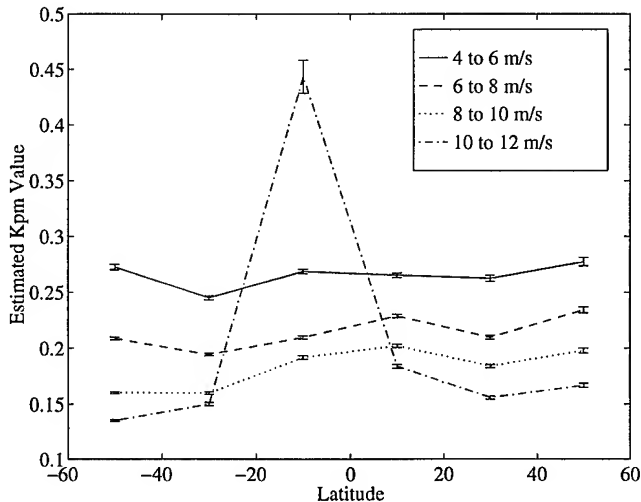


Figure 6: Estimates of the value of K_{PM} from NSCAT data, for 20° latitude bands. Again we see a clear speed trend. We also see little latitude variation except at higher latitudes.

DISCUSSION

The simple model for scatterometer measurements depicted in Fig. 1 establishes a method for estimating, directly from scatterometer measurements, the variability in empirical model functions for given wind conditions [1]. This variability has been reported here and computed for various parameter sets to identify some dependences.

The value of K_{PM} is important in wind scatterometry for several reasons. Estimates of the wind require a realistic noise estimate of the measurements. The variance of the measurements is crucial in performing maximum likelihood or maximum *a priori* estimates of the probable wind to have generated those measurements. The variability of the empirical model function, embodied in K_{PM} , contributes significantly to the total noise figure of the measurements.

Estimates of the model function variability for both C-band and Ku-band model functions presented here indicate considerable dependence on wind speed and latitude. The seasonal variations observed at C-band need to be further examined to identify if the effect depends on sea surface temperature or other parameters. As additional NSCAT data becomes available, similar temporal sensitivities will undoubtedly be observed at Ku-band. The sensitivity of K_{PM} will provide direction for further improvements in empirical model functions.

REFERENCES

- [1] P. E. Johnson, D. G. Long, and T. E. Oliphant, "Geophysical modeling error in wind scatterometry," in *Proc. IGARSS '96*, (Lincoln, NE), pp. 1721-1723, 1996.
- [2] R. E. Fischer, "Standard deviation of scatterometer measurements from space," *IEEE Transactions on Geoscience and Electronics*, vol. GE-10, no. 2, pp. 106-113, 1972.
- [3] T. E. Oliphant, "New techniques for wind scatterometry," Master's thesis, Brigham Young University, 1996.
- [4] T. E. Oliphant and D. G. Long, "Cramer-Rao bound for wind estimation from scatterometer measurements," in *Proc. IGARSS '96*, (Lincoln, NE), pp. 1724-1726, 1996.
- [5] M. Freilich and R. Dunbar, "A preliminary C-band scatterometer model function for the ERS-1 AMI instrument," in *Proceedings of the First ERS-1 Symposium*, (Cannes, France), pp. 79-84, ESA, 1993. SP-359.

An Aggregate Spectral Model for ERS-1 Wind Retrieval

Ellen Lettvin¹ and John Vesecky

AOSS Department, The University of Michigan, Ann Arbor MI 48109-2143

¹ Fellow-by-courtesy, EPS Department, Johns Hopkins University, Baltimore MD 21218
(410)516-7155, (410)466-0293, ellenl@engin.umich.edu; ellenl@gibbs.eps.jhu.edu

ABSTRACT

The wind field at the ocean surface has been estimated via radar scatterometry for nearly two decades. Approximately one decade ago, several efforts (e.g. [1]) were undertaken that investigated in detail the effect of the wind on the radar signature. These efforts were based on the use of an ocean spectral model in conjunction with a model of electromagnetic scattering. These techniques led to an improved understanding of the air/sea interface and its interrogation by radar remote sensing, but their success was hampered in part due to limitations of the ocean spectral models used in these efforts.

Ocean spectral models that are employed in scatterometer-based wind retrievals must accurately model waves on scales spanning several decades. The waves responsible for the preponderance of the radar signature are on the order of a few centimeters, but these waves are tilted, modulated, stretched and compressed by the large-scale underlying waves. Due to the numerous difficulties associated with obtaining spectral measurements at high frequencies, particularly on the open ocean, our understanding of the relevant theory and hence the modeling of ocean waves at high frequencies is still far from adequate. In addition, computational limitations still present considerable challenges to modeling of ocean waves, particularly at the smallest scales that demand high resolution. To address some of these issues, we are developing an ocean spectral model that combines *in situ* measurements of the directional wave spectrum with physically-based predictive models. This spectral model will be described below.

INTRODUCTION

We are developing an ocean spectral model intended for application to scatterometer-based wind retrieval. The primary goal of this model is to predict the ocean waves sensed by the ERS-1 scatterometer (Bragg wavelengths between 3 cm and 9 cm). The model partitions the ocean wavenumber spectrum into three different regimes, each of which is treated using a different approach. We refer to this model as an 'Aggregate Spectral Model' (ASM). An overview of the ASM is as follows: the low wavenumber regime ($0.0036 \text{ m}^{-1} < k < 0.493 \text{ m}^{-1}$) of the spectrum uses measurements obtained by buoys belonging to the National Data Buoy Center network (NDBC); for gravity waves above the spectral peak in the equilibrium range of the spectrum we use Phillips' [2] model;

for the highest wavenumber regime ($k < 210 \text{ m}^{-1}$), we use a modified form of Phillips' model derived from analysis of high-frequency buoy data acquired off Andros Island in the Caribbean Sea. Model parameters and matching criteria for the three spectral models are discussed. The three components of the ASM, as well as some justification for their use are developed in the following sections.

APPROACH

1. Low-Wavenumber Range

At the present time, the ASM employs NDBC buoy measurements to characterize the low-wavenumber portion of the spectrum although ultimately other sources will be used to characterize this regime of the spectrum. For example, altimeter-derived spectral estimates, or the WAM [3] or JONSWAP [4] models can furnish this portion of the spectrum since clearly it is necessary to apply this approach to wind retrieval on the open ocean where buoy-based spectral estimates are unavailable. Nonetheless, buoy measurements are used in this effort in order to limit the sources of error in the wind retrievals.

NDBC maintains 20 to 30 buoys along the east and west coasts of North America that are capable of measuring the directional wave spectrum between 0.03 and 0.35 Hz. These buoys record the vertical displacements of the buoy as well as angles of pitch and roll. From these quantities it is possible to estimate the angular distribution of the power spectral density of the ocean waves as a truncated Fourier series.

In this paper we use NDBC buoy 44014, which measures both meteorological data as well as the directional frequency spectrum. This buoy is located off the coast of Norfolk, Virginia ($36^{\circ} 34' 59'' \text{ N}$; $74^{\circ} 50' 1'' \text{ W}$, water depth 48 m). For the purposes of this effort we wished to exclude cases where swell was present to simplify the analyses.

2. Mid-Range

For the Equilibrium range of the spectrum, we employed the spectral model due to Phillips [2]. This model is written in wavenumber space as:

$$S(k) = \alpha u^* g^{-(1/2)} k^{-(7/2)} D(k, \theta) \quad (1)$$

where k denotes wavenumber, g denotes gravity, u^* is the friction velocity, α is a constant determined by spectral energy levels, and $D(k, \theta)$ denotes the angular distribution of spectral energy ($D(k, \theta)$ integrated over direction, θ , yields 1).

This model was initially developed in frequency space, using dimensional arguments. One of its main assumptions is that energy levels of the power spectral density are limited by wave breaking. There have been both analytical efforts and measured data that support this spectral form (e.g. [5],[6]).

Another model for the equilibrium spectrum of gravity waves is due to Banner [7]. His model, developed specifically for wavenumber data, predicts a spectrum of the following form:

$$\phi(k) \sim (ku^2/g)^{\gamma} k^{-4} D'(k, \theta) \quad (2)$$

where $\gamma = 0.09 \pm 0.09$, where D' also denotes the angular distribution of energy.

For the mid-range of the ASM (i.e. wavenumbers greater than those measured by the NDBC buoys, and less than the Bragg wavenumbers for the ERS-1 system) we use (1), with model parameters selected to ensure continuity with the low-wavenumber regime. In future analyses we will also consider application of (2) for the mid-range of wavenumbers.

3. High-Wavenumber Regime

One of the chief difficulties in modeling this regime is the paucity of high wavenumber and high frequency data collected on the open ocean. The Johns Hopkins Applied Physics Laboratory conducted an experiment in 1990 that measured the spectrum of ocean waves for frequencies up to 6 Hz [8]. We were fortunate to be given access to these data. Although the data were collected under a limited range of conditions, they nonetheless exhibited consistent behavior supporting a model based on Phillips' equilibrium spectrum appropriate to high wavenumbers.

For six days in the spring of 1990, a wave spar buoy was deployed in a test range off Andros Island that obtained measurements of the one-dimensional power spectral density. The environmental conditions (wind speed and direction, air and sea temperature, relative humidity, significant wave height, and an estimate of significant wave slope) during the experiment are summarized in the following table:

Table I: Summary of Conditions During Standard Leopard Experiment

	5/31	6/3	6/4	6/5	6/7	6/9
U (m/s)	3-4	6-8	3-5	4-5	6-9	8-10
Tair (°C)	27.2	26.5	27.5	27.3	27.5	27.4
Tsea (°C)	26.7	26.8	27.7	27.3	27.5	27.5
Humidity(%)	94	81	81	81	85	75
ϕ (deg wrt N)	150	80-115	105-145	150-160	105-120	110-115
SWHt (m)	0.12	0.44	0.16	0.10	0.87	0.92
SWSlope	0.06	0.09	0.10	0.09	0.12	0.12

We used these data to investigate the behavior of the high-wavenumber portion of the spectrum and to determine whether Phillips' model was appropriate for this regime. However, the spar buoy obtained spectral measurements in frequency space, and we needed to characterize the spectrum in wavenumber space, which presented some difficulties.

For gravity waves in deep water, the wavenumber and frequency spectra are related via the dispersion relation. For high frequency waves, however, the problem is considerably more complicated. Large-scale gravity waves perturb the dispersion relation of the high-frequency gravity waves by 'smearing' the energy over a range of frequencies. Thus, the measured frequency spectrum represents the 'true' frequency spectrum modified by Doppler shifting by the underlying waves, currents and bottom topography. Consequently, a straight-forward relationship between the frequency and the wavenumber spectra no longer exists. This problem was studied by Kitaigorodskii et al. [9] who presented an approach for estimating these effects on the frequency power spectral density and also on the dispersion relationship.

In our analysis of the Standard Leopard (SL) data, we applied the above technique. Specifically, to obtain the needed wavenumber spectra, a two-step process was required: first, we would obtain an estimate of the 'true' frequency spectrum (i.e. one in which the Doppler shifting effects had been removed); second, we would apply the dispersion relationship to obtain the wavenumber space representation. Fig. 1 presents an example of two SL wavenumber spectra: one that has undergone both of the above procedures, and one that has only undergone the second of the two procedures.

We then regressed the logarithm of the power spectral density on the logarithm of wavenumber to see how closely the power of k suggested by the SL wavenumber data agreed with the theoretical ($k^{-3.5}$) distribution. An example of such a comparison is provided in Fig. 2. In addition, we examined the results of the above regressions to determine whether or not the power of k exhibited a dependence on either friction velocity, u^* , or on the slope of the long waves, AK .

In fact, we observed a significant, monotone relationship in the SL data between the power of k and u^* , but did not observe any dependence of the exponent on AK . The specific relationship that we observed, averaging over all the SL data sets is:

$$\log(S(k)) \propto (-3.538 - 1.316u^*)(\log(k)) \quad (3)$$

where $S(k)$ denotes the power spectral density in wavenumber space. Although we suspect that AK should impact the exponent, for these particular data such a relationship was not evident. Analysis of additional data will be required to elucidate this matter. For the highest wavenumber regime,

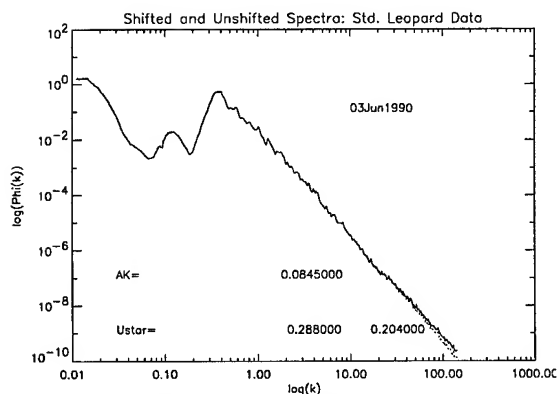


Figure 1. Comparison of Shift Correction Prior to Application of Dispersion Relation (.....) and no Shift Correction (—)

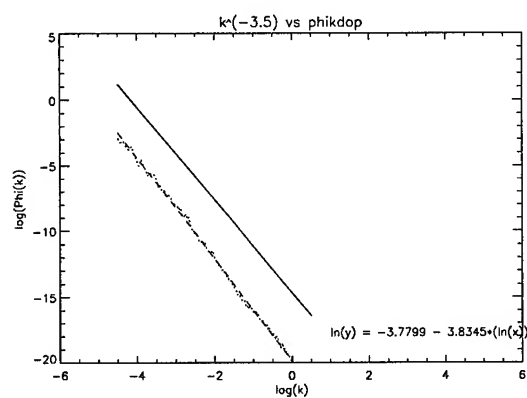


Figure 2. Comparison of Theoretical Relationship (—) and Observed Relationship Fitted by Linear Regression (.....) for SL data

the relationship given by (3) will model the power of k , and the constant will be dictated by matching with the mid-range spectrum.

REMARKS

Fig. 3 provides an example of the ASM; the low wavenumber spectrum is given by NDBC data, the mid-range is given by (1) and the high-wavenumber regime is given by (3) subject to the constraint of matching spectral levels at the point where the curves are joined. By analyzing each region of the spectrum using a model specific to that regime, the ASM is ideally suited for application to retrieval of the wind vector at the ocean surface from ERS-1 scatterometer data. It should also be noted that the behavior exhibited by the high wavenumber portion of the ASM lies between the model of Phillips (1) and the model of Banner (2). Future efforts will include comparing the ASM with other spectral models and to evaluate its behavior over a broader range of atmospheric and oceanic conditions.

The ASM addresses several of the needs particular to the problem of wind retrieval from scatterometer measurements, and takes advantage of both theoretical developments and experimental measurements. We intend to use this spectral

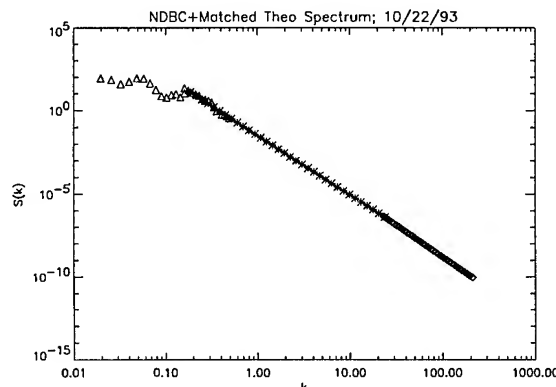


Figure 3. Illustration of ASM for 10/22/93. Triangles: NDBC data; Stars: Phillips' Model; Diamonds: High-Wavenumber Spectral Model

model to investigate the effects of long waves on the radar backscatter and thus to assess the need for incorporating these effects into wind prediction algorithms. Finally, the ASM is flexible and can readily incorporate additional innovations.

ACKNOWLEDGMENTS

Thanks are due to Owen Phillips for his helpful discussions and to Carl Nelson of Johns Hopkins Applied Physics Laboratory for providing the Standard Leopard data.

REFERENCES

- [1] Donelan M.A. and W.J. Pierson, 1987, Radar Scattering and Equilibrium Ranges in Wind-Generated Waves With Application to Scatterometry. *Jour. Geophys. Res.* **92**, No. C5. pp. 4971-5029
- [2] Phillips O.M., 1985, Spectral and Statistical Properties of the Equilibrium Range in Wind-Generated Gravity Waves. *Jour. Fluid Mech.*, **156**, pp. 505 - 531
- [3] Komen G.J. et al., 1994, Dynamics and Modeling of Ocean Waves, Cambridge University Press, New York
- [4] Hasselmann K. et al., 1983, Measurement of Wind Wave Growth and Swell Decay During the Joint North Sea Wave Project (JONSWAP). *Herausgegeben vom Deutsch-Hydrograph. Inst.*, Reihe A., no. 12.
- [5] Kitaigorodskii S.A., 1983, On the Theory of the Equilibrium Range in the Spectrum of Wind-Generated Gravity Waves, *J. Phys. Oceanogr.*, **13**, pp. 816-827
- [6] Kawai S., et al., 1977, Field Data Support of Three-Seconds Power Law and $gu*\sigma^4$ Spectral Form for Growing Wind Waves, *J. Oceanogr. Soc. Japan*, **33**, pp. 137 - 150
- [7] Banner M.L., 1990, Equilibrium Spectra of Wind Waves. *J. Phys. Oceanogr.*, **20**, pp. 966 - 984
- [8] Nelson C.V., 1990, Wave Data Summary Standard Leopard I, Sub. Tech. Dept. Rept. STD-N-727, Johns Hopkins University, Applied Physics Laboratory
- [9] Kitaigorodskii S.A. et al., 1975, On Phillips' Theory of Equilibrium Range Spectra of Wind-Generated Gravity Waves. *J. Phys. Oceanogr.*, **5**, pp. 410-420

AN INVERSION TECHNIQUE FOR ESTIMATING THE WIND-DEPENDENT SHORT WAVE SPECTRAL DENSITY FROM THE CMOD4 AND COMPOSITE SURFACE MODELS

Jiffeng Chen* and Dayalan Kasilingam**

*Department of Electrical and Computer Engineering
University of Massachusetts, Dartmouth
North Dartmouth, MA 02747.

**Centre for Remote Imaging, Sensing and Processing
National University of Singapore
Lower Kent Ridge Rd.
Singapore, 119260.

Tel: (65) 771-5173; FAX: (65) 775-7717; e-mail: crsdpk@leonis.nus.sg

Abstract: Calculations of the normalized radar cross-section (NRCS) from the CMOD4 model are inverted using the composite surface model (CSM) to estimate the short wave spectral density in the C-band region of the short wave spectrum. Simulations of the composite surface model are used to train an artificial neural network. Short wave spectral densities from a variety of short wave models are used with the CSM. The simulated NRCS from the CSM is used as the input parameter and the short wave spectral density is used as the output parameter. The properly trained neural network is then used with the CMOD4 model to generate the corresponding short wave spectra at different wind speeds. These wave spectra are compared with predictions of existing empirical wave spectral models and appear to agree well in shape. However, the actual spectral levels were quite different.

INTRODUCTION

The radar backscatter from the ocean surface is determined primarily by the short scale roughness of the ocean surface. This short scale roughness of the ocean surface is best described by the wind-dependent, short wave spectral density. Considerable effort has gone into understanding and modelling the wind dependence of the short wave spectral density [1-2]. This dependence allows one to extract information about the near surface wind vector from radar backscatter measurements.

The CMOD4 model is a model developed for extracting such wind information from the scatterometers aboard the ERS satellites [3]. The model is empirical and relates the C-band backscatter to wind speed and direction. However, it does not explicitly relate the backscatter to the short wave spectral density.

In radar imaging, the composite surface model is used to describe the image modulation observed in images of the ocean surface [4]. The composite surface model shows that the image intensity is directly dependent on the short wave spectral density. Thus, one may use the CMOD4 model along with the composite surface model to estimate the wind dependence of the short wave spectral density.

Since both models are nonlinear, the inversion of these models requires an accurate and computationally tractable technique. Neural networks are well suited for describing complex, nonlinear mapping processes. If corresponding input and output values are available, then a neural network may be trained to perform the inversion.

In this project, simulations of the composite surface model are used with a variety of short wave spectral models to train a neural network to estimate the short wave spectral density at various wind speeds. Having trained the network, calculations from the CMOD4 model are used as inputs to the network to estimate the corresponding short wave spectral densities. Since the CMOD4 model applies to C-band backscatter over a range of different incidence angles, the short wave spectral density is derived for wavelengths in the range 4.5-8.0 cm.

METHODOLOGY

The slightly rough model gives the normalized radar cross-section (NRCS) of the ocean surface as

$$\sigma_{SR} = 16\pi k_0^4 |g_{vv}|^2 P_s(k_B) \quad (1)$$

where P_s is the short wave spectral density and g_{vv} is the scattering coefficient for vertical polarization. Since the scattering process is due to the resonant interaction between

the electromagnetic waves short scales waves of comparable wavelength, the relevant short wave spectral density is determined at the resonant wavelength, which is also known as the Bragg wavelength. The Bragg wavenumber is given by

$$k_B = 2k_0 \sin \theta_i \quad (2)$$

The slightly rough model is a zeroth order model for radar backscatter from the ocean. The composite surface model accounts for the effect of long surface waves and describes the effective NRCS of the ocean surface as

$$\sigma_{CS} = \iint \sigma_{SR}(\theta, \delta, \xi) f(\tan \delta, \tan \xi) \tan \delta \tan \xi \quad (3)$$

where the NRCS of the scattering facets are averaged over all long wave tilt angles.

The CMOD4 model is an empirical model which was developed by the European Space Agency to describe the C-band NRCS of the ocean surface at various wind speeds and incidence angles. The NRCS is given by the form

$$\sigma_0 = b_0 [1 + b_1 \cos \phi + b_2 \cos 2\phi]^{1.6} \quad (4)$$

where b_0 , b_1 and b_2 are coefficients which are functions of the incidence angle and the wind speed. ϕ is the relative angle between the wind direction and the radar look direction. Calculations of NRCS from equation (4) can be compared with either equation (1) or equation (3) to estimate the wind dependent short wave spectral density of short waves in the wavelength comparable with the C-band wavelength. Comparison with (1) is linear and can be done readily. However, comparisons with (3) requires a nonlinear inversion.

A standard feedforward network is trained to perform the nonlinear inversion. The objective is to use the NRCS values from the CMOD4 model as the input to the neural network and the short wave spectral density as the output. The training set is generated by using standard forms of the short wave spectral density model in equation (3) to calculate the NRCS model as predicted by CSM. These NRCS values and the spectral density values are used as inputs and outputs, respectively, in the training process.

RESULTS AND DISCUSSION

The inversion of the SRM is linear and is used as a reference in this study. Fig. 1 shows the omni-directional, short wave spectral densities at three different wind speeds obtained by inverting the SRM. The spectra are compared with the

standard k^{-n} models used by investigators in the past. The optimum value for the exponent appears to be $n = 4.5$. This is consistent with previous models obtained from in-situ measurements of the short wave spectral density.

Fig. 2 shows the directionality of the short wave spectrum. This directionality is almost an exact replica of the azimuth angle dependence of the NRCS as predicted by the CMOD4 model. Note the directionality is sharper at the higher wind speeds.

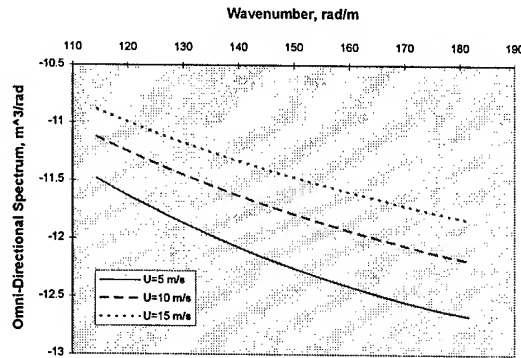


Figure 1 - Omni-directional short wave spectral density from the CMOD4 model obtained by inverting the slightly rough model at three different wind speeds.

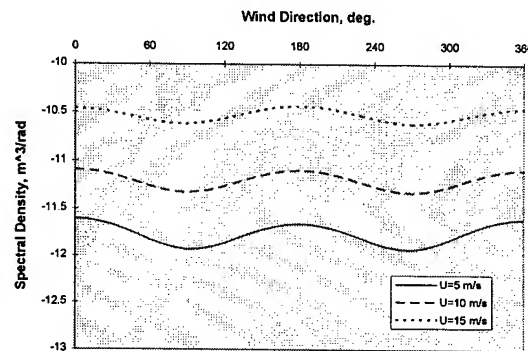


Figure 2 - Short wave spectral density from the CMOD4 model obtained by inverting the slightly rough model as a function of the wind direction at three different wind speeds.

Fig. 3 shows the omni-directional short wave spectral density obtained from the neural network which was trained to invert equation (3). The spectra appear to be slightly different from those observed in fig. 1. The wavenumber exponent in this case come out as $n = 4.2$. The apparent decrease in the steepness of the wavenumber spectrum is because the long waves the CSM takes into account the contribution of the long wave tilt. When the long wave tilt is included in the backscatter model, the effective Bragg wavenumber which contributes towards the backscatter process over a band of

short wavelengths. The 'effective' spectral density observed in fig. 1. is due to the averaging of the spectral density over this band of wavenumbers. It is necessary to 'deconvolve' this effect to estimate the actual spectral density at each wavenumber.

Fig. 4 shows the directional dependence of the spectral density. This dependence is slightly different from that observed in fig. 2. The directionality is sharper and more pronounced at all wind speeds. This may also be attributed to the deconvolution process.

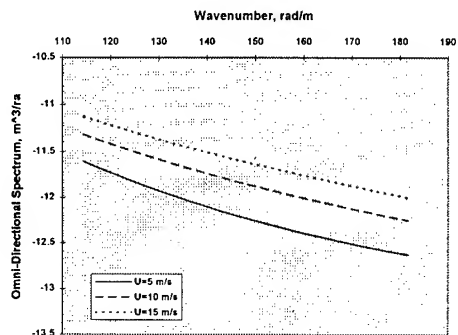


Figure 3 - Omni-directional short wave spectral density from the CMOD4 model obtained by inverting the composite surface model at three different wind speeds. The inversion is performed using neural networks.

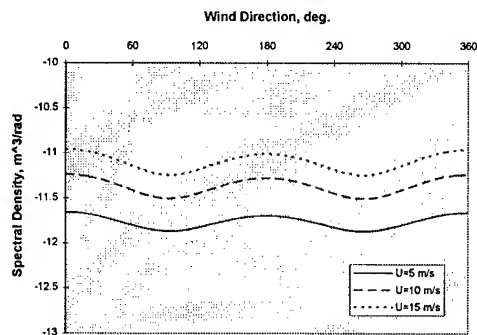


Figure 4 - Short wave spectral density from the CMOD4 model obtained by inverting the composite surface model as a function of the wind direction at three different wind speeds. The inversion is performed using neural networks.

Fig. 5 shows the wind speed dependence of spectral density of 5cm waves. Also shown is the short wave spectral density given by Glazman [1]. The shape of the wind dependence appears to be consistent with the Glazman model. However, the spectral values are significantly lower.

Figure 5 also shows that the spectral density initially increases rapidly with the wind speed and then appears to saturate at moderate wind speeds. The saturation wind speed

for these C-band waves is around 5 m/s. Around these wind speed, it may be assumed that the dissipational forces such as those due to breaking, viscous effects and wave-wave interaction are counter-balanced by the generative forces due to wind input.

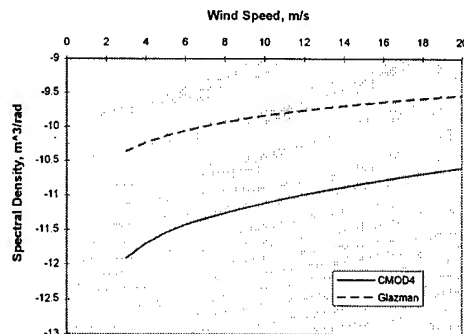


Figure - 5 Spectral density of 5cm short waves as a function of wind speed based on the CMOD4 model. Also shown are the spectral densities given by the Glazman model [1].

CONCLUSION

It has been shown that the nonlinear inversion of the CMOD4 model may be used to extract short wave spectral densities in the C-band region. The spectral densities are consistent with existing short wave spectral models. However, the predicted spectral levels appears to be lower. Further studies are needed to assess the validity of comparing the composite surface model with predictions from the CMOD4 model.

REFERENCES

- [1] Glazman, R., J. Geophys. Res., 5249-5262, 1994.
- [2] Pierson, W and L. Moskowitz, J. Geophys. Res., 5181-5190, 1964.
- [3] Stoffelen, A. and D. Anderson, 'Characterisation of ERS-1 scatterometer measurements and wind retrieval', Proc. Second ERS-1 Symposium, Hamburg, October, 1993.
- [4] Kasilingam, D.P. and O.H. Shemdin, 'The validity of the composite surface model and its application to the modulation of radar backscatter', Intl. J. Remote Sensing, 2079-2104, 1992.

The Influence of Topography on Wind over the Sea of Japan

Peiming Wu,¹ Hiroshi Kawamura^{1,2} and Fujio Kimura³

1. EORC, National Space Development Agency of Japan, 1-9-9, Roppongi, Minato-ku, Tokyo, 106 Japan

e-mail: pmwu@eorc.nasda.go.jp FAX: +81-3-3224-7052

2. Center for Atmospheric and Oceanic Studies, Faculty of Science, Tohoku University, Sendai, 980 Japan

3. Institute of Geoscience, University of Tsukuba, Tsukuba, 305 Japan

Abstract—Wind is the critical factor in determining regional weather patterns and climate. Also, winds over the ocean directly effect the exchange of heat, moisture and gases between the atmosphere and the ocean surface. In this paper, the wind distribution over the Sea of Japan is analyzed by using wind data observed by the NASA Scatterometer (NSCAT). A synoptic view of the wind fields over the Sea of Japan is provided in January 1997. Remarkable evidence of a land topography effect is shown as a convergence of the surface wind field during cold-air outbreaks. The Changbai mountains are located in North Korea upstream of the outbreak winds, and the wind field was deformed by them over the western part of the Sea of Japan. Strong northwesterly winds (westerly winds) of about 16 to 20m/s were observed off Vladivostok (the Korea Peninsula). They converge while blowing over the sea. A wind shadow, in which the wind speed is less than 8m/s, is seen downwind of the mountains and extends more than 200 km.

Numerical experiments using a three-dimensional local circulation model were performed to investigate the formation mechanisms of the outbreak-wind deformation. The results shows that the land topography is essential to form the convergence of the surface winds observed by NSCAT.

1. Introduction

Wind is the critical factor in determining regional weather patterns and climate. Wintertime air-sea interaction over the Sea of Japan is strongly enhanced by outbreaks of dry and cold air masses from the Eurasian continent. Heat and moisture released from the ocean to the atmosphere during the outbreaks significantly influence the weather and climate of Japan because of the geographical positioning of the Japanese islands and the Sea of Japan. Specifically, the released moisture results in heavy snowfall on the Sea of Japan side of the islands. Understanding the wintertime wind distribution and air-sea interaction over the Sea of Japan has been a primary subject for Japanese meteorologists and oceanographers. So far, wind data over the Sea of Japan in winter season can only be acquired from infrequent and sometimes

inaccurate reports from ships and buoys because of severe weather conditions.

The NASA Scatterometer (NSCAT) launched aboard Japan's ADEOS Satellite in August 1996 has provided ocean surface wind vectors since September 1996. The purpose of this study to use the wind data obtained by NSCAT to investigate the wind distribution and effect of upwind topography on the wind distribution over the Sea of Japan. Numerical experiments were performed to investigate the formation mechanisms of the wind convergence over the Sea of Japan.

2. Wind Data Observed by NASA Scatterometer

The NASA scatterometer (NSCAT) is one of the eight Earth observing instruments aboard Japan's Advanced Earth Observing Satellite (ADEOS). NSCAT is an active microwave radar which measures winds over the oceans by transmitting Ku band microwave pulses (13.995 GHz) and receiving backscatter signals from the ocean surface. The backscatter signals are subject to changes in direction due to surface waves. Multidirectional measurements were used to determine wind speed and direction. An improved SASS-II model function algorithm relates the backscatter signal strength to wind speed and determines the wind direction by modeling the azimuthal dependence as a truncated Fourier cosine series. The ambiguities are selected using the NWP initialization (nudging) of the median filter.

NSCAT covers a 600 km swath with an effective resolution of 25 km on either side of the spacecraft. The two swaths are separated by a gap of about 330 km directly below the satellite where no wind data is available. The data used in this study were provided by the Jet Propulsion Laboratory, NASA. The difference between NSCAT wind speeds and data buoy wind is less than 2 m/s for winds under 20 m/s. Wind speeds over 20 m/s have a standard deviation of less than 10% of the buoy wind. Wind direction has a standard deviation of less than 20.

3. Description of the Numerical Model

Numerical experiments were conducted with a three-

dimensional local circulation model. The governing equations and numerical scheme of the model are described in detail by Kimura and Takahashi (1991). The equations used are the Boussinesq hydrostatic equations, which are written in a terrain-following coordinate system. Lateral boundary data are provided with 12 hourly GANAL data made by the Japan Meteorological Agency. Initial fields of winds, potential temperature and specific humidity are evaluated from GANAL data for the model calculations.

4. Wind distribution over the Sea of Japan During Cold-air Outbreaks

The topography surrounding the Sea of Japan is shown in Fig. 1. The Changbai mountains with an altitude exceeding 1500 meters are located in North Korea. Vladivostok and its surrounding area have a very low altitude.

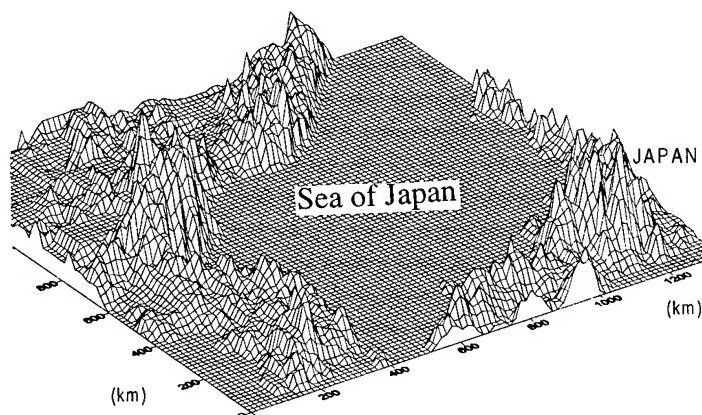


Fig. 1. Topography Surrounding the Sea of Japan.

The surface weather map at 1300 UTC 2 January 1997 shows that a surface-level high with centers of around 52N/115E and 32N/120E expanded to western parts of the Japanese Islands. A strong surface-level low was located near 42N/143E, and a strong cold front passed through the Japanese islands out to the Pacific Ocean. There is a very high pressure gradient in the area around the Sea of Japan.

Figure 2 shows the wind fields over the Sea of Japan observed by NSCAT at 1352 UTC 2 January 1997. Strong northwesterly winds (about 20m/s) were observed off Vladivostok, and westerly winds (about 16m/s) were observed off the Korea Peninsula. A wind shadow, in which the wind speed is less than 8m/s, is seen in the downwind of the mountains and extends more than 200 km. A strong horizontal wind convergence is formed in the low wind speed regions.

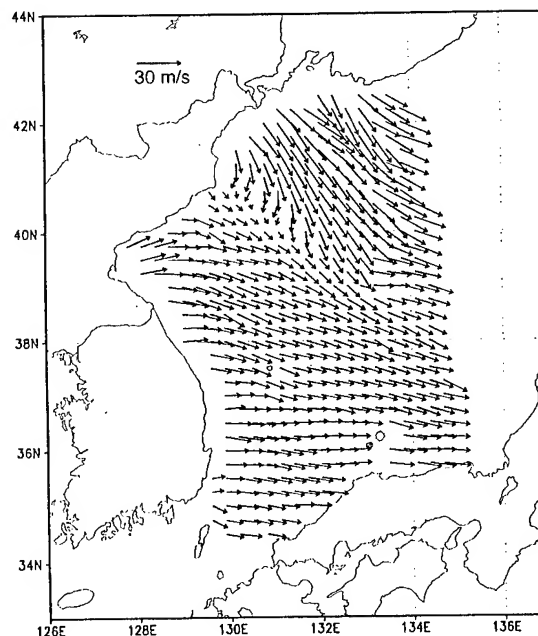


Fig. 2. Wind Observed at 1352 UTC on 2 January 1997.

Numerical experiments under different conditions have been performed to investigate the formation mechanisms of the wind convergence. Wind velocities at the $Z^*=10$ m level for 1300 UTC 2 January 1997 calculated by the model are shown in Fig. 3. The calculated wind distribution agrees well with winds observed by NSCAT (Fig. 2).

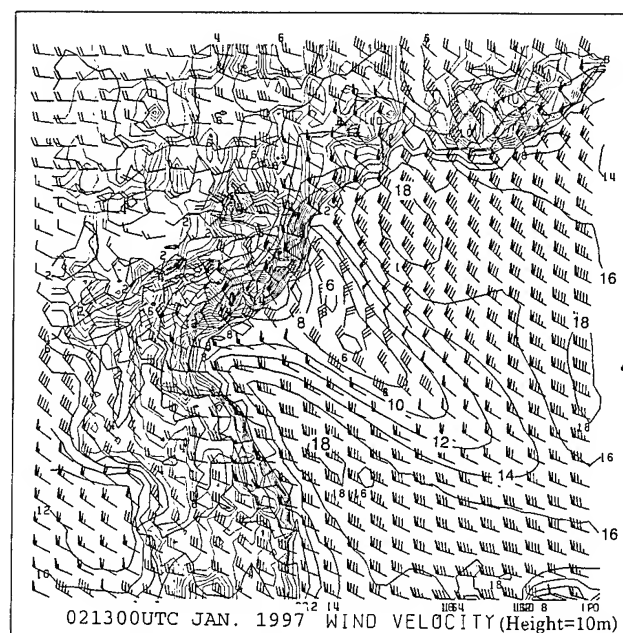


Fig. 3. Wind for 0200 UTC 2 January 1997 Calculated by Numerical Model.

Figure 4 and 5 show the mean wind vector and speed for January 1997. In January, northwesterly winds prevail over the Sea of Japan. High mean wind speed (more than 13 m/s) region are observed off Vladivostok. A wind shadow, in which the wind speed is less than 8 m/s, is seen downwind of the Changbai mountains.

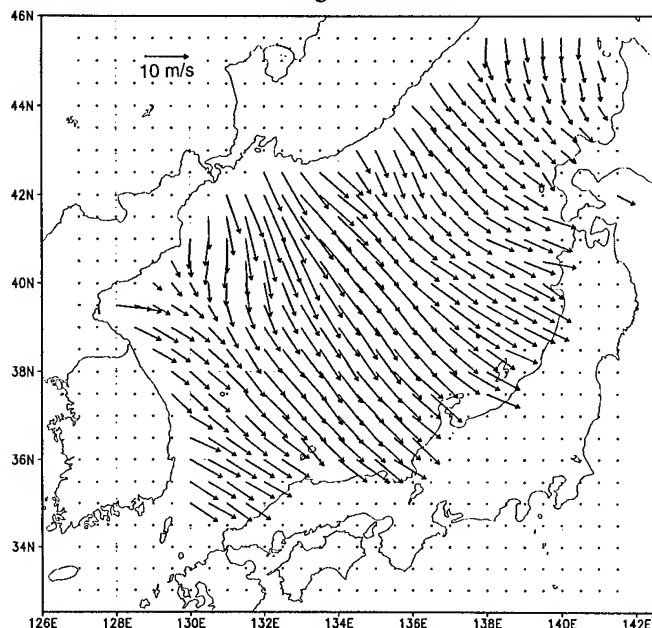


Fig. 4. Mean Wind Vector for January 1997

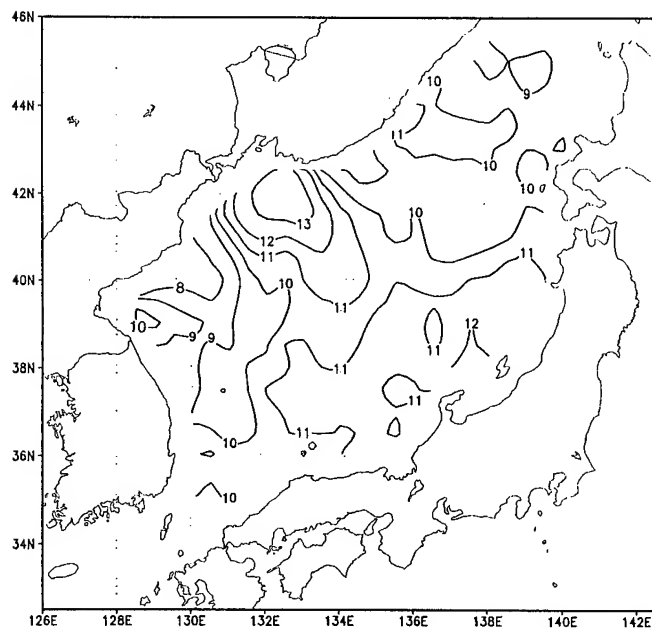


Fig. 5. Mean Wind Speed for January 1997 (m/s).

5. Remarks

So far, ocean wind information obtained from ship reports have not provided a detailed description of the

wind field over the Sea of Japan. In winter seasons, a cloud band is often observed over the Sea of Japan by satellite cloud photograph (Okabayashi and Satomi, 1971). This cloud band is strong related to the heavy snowfalls in the Hokuriku area of Honshu Island. In this paper, wind distributions over the Sea of Japan during cold-air outbreak situations were obtained. Strong northwesterly winds (westerly winds) of 15 to 20 m/s were observed off Vladivostok (the Korea Peninsula). A wind shadow, in which the wind speed is less than 8 m/s, is seen downwind of the mountains and extends more than 200 km. Strong wind convergence was formed in the low wind regions.

The wind field given by the numerical model agree well with the results observed by NSCAT. The wind convergence was formed because the northwesterly air flow was blocked by the high mountains and forced to go around them. This means that the upwind mountains play a crucial role in the formation of wind convergence. In comparison, the observed wind convergence is more than twice that of the numerical results (the figure is not shown here). The reason for this is not yet clear. It is also unclear whether the wind vector determined by the empirical model function relating the backscatter to wind still has the same accuracy under strong wind convergence conditions. This is also a subject for further NSCAT calibration and validation study.

Ocean wind is a very important factor for air-sea interaction. However, the cloud band over the Sea of Japan is not always observed when a cold air outbreak occurs. The behavior of the convective mixed layer is deeply affected by lower-boundary thermal properties (Nagata et al., 1986). Therefore, it is necessary to make a further study to examine the effect of wind and the distribution of sea surface temperature on the formation of convergent clouds.

Reference

- [1] T. Okabayashi and M. Satomi, "A study on the snowfall and its original clouds by the meteorological radar and satellite," *Tenki*, vol. 18, pp.573-581, 1972.
- [2] F. Kimura and S. Takahashi, "The effects of land-use and anthropogenic heating on the surface temperature in the Tokyo metropolitan area: a numerical experiment," *Atmos. Environ.*, vol. 25B, pp. 155-164, 1991.
- [3] M. Nagata, M. Ikawa, S. Yoshizumi and T. Yoshida, "On the formation of a convergent cloud band over the Japan Sea in winter: numerical experiments," *J. Meteor. Soc. Japan*, vol. 64, 841-855, 1986.

A Study of SAR Interferometry over Forests: Theory and Experiment

N.FLOURY, T. LE TOAN, J.C. SOUYRIS and J.BRUNIQUEL

Centre d'Etudes Spatiales de la BIOSphère (CESBIO)
CNRS-CNES-UPS
18 Ave Edouard Belin, bpi 2801, 31401 Toulouse cedex 4, France
tel: (33) 5.61.55.85.84
fax: (33) 5.61.55.85.00
e-mail: floury@cesbio.cnes.fr

ABSTRACT

Recent studies have pointed out the usefulness of interferometric data for forest mapping and their potential for the retrieval of forest parameters.

In this paper the interferometric responses of the pine forest of Les Landes are studied. A coherent model is developed for a better understanding of scattering mechanisms.

1. INTRODUCTION

The development of SAR interferometric techniques have recently made interferometric data widely available to users. Studies have recently pointed out the usefulness of interferometric data for forest mapping and their potential for the retrieval of forest parameters (biomass from coherence and height from phase difference analysis). However, the understanding of the interferometric signal is impeded by the lack of theoretical models which can predict both the amplitude and the phase of the backscattered signal.

The objective of this paper is to present a coherent backscattering model which can be applied to interferometric responses of forests.

2. SUMMARY OF EXPERIMENTAL RESULTS

Experimental analysis of ERS interferometric SAR data over the Landes test-site, in South-Western France, have been undertaken. The Landes forest, characterized by large and homogeneous stands of maritime pine over a flat topography, is well suited to methodological studies.

Interferograms have been generated using the ISAR software from ERS-1/ERS-2 SLC data for different baselines (10 m to 170 m) and time intervals (tandem to 45 days).

Coherence is shown to be decreasing as stand biomass increases [1]-[2] (Fig. 1): high coherence is obtained for bare soil surfaces and it decreases with the growing contribution of scatterers more sensitive to temporal variations in terms of their geometric properties.

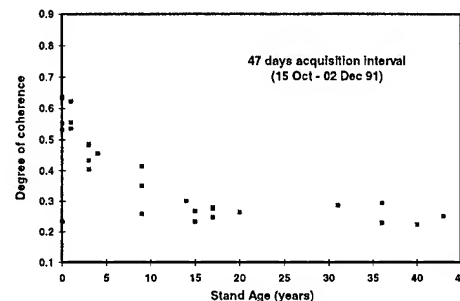


Figure 1: Example of the variations of the degree of coherence with the stand age (linked to biomass).

Over large stands, phase difference has been found to be linked with the canopy height discontinuities. When the penetration depth estimated using the MIT/CESBIO modified radiative transfer model is included, a better estimate of the canopy height from interferometric measurements is obtained [3] (Fig. 2).

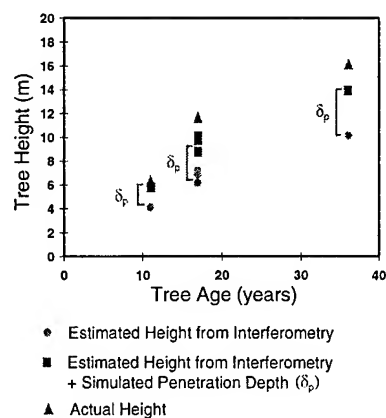


Figure 2: Estimation of the canopy height from interferometry measurements.

To provide an insight into the dependence of interferometric parameters on target structure and system configuration, a theoretical study has been carried out.

3. THEORETICAL MODELING

In this model, the backscattering is calculated by performing Monte Carlo simulations of the scattering of a medium constituted of dielectric cylinders using the Foldy-Lax multiple scattering equations.

Each cylinder (representing a trunk, a branch or a needle) is defined by its position, size, orientation and dielectric constant. These parameters can be randomly generated, can be extracted from ground truth measurements or directly derived from an architectural tree growth model.

Contributions from the soil surface (direct contribution through gaps in the canopy and contribution attenuated by the canopy itself) are given in intensity by the IEM model for copolarisation terms [4].

Previous studies [5] using radiative transfer model over the Landes forest have shown that at C-band and 23 degrees of incidence angle, the main contributions come from the crown and from the ground through the gaps; the contribution of the crown-ground interaction can be neglected.

Given an incident wave \vec{E}_p^i with the polarisation \hat{p} in the direction (θ_i, ϕ_i) , the backscattered field with the polarisation \hat{q} can be written:

$$\vec{E}_q^s(\vec{r}) = \frac{e^{ikr}}{r} \sum_j f_{qp}^j(\pi - \theta_i, \pi + \phi_i; \theta_i, \phi_i) \cdot e^{i[\vec{k}_p^i(\theta_i, \phi_i) - \vec{k}_q^s(\pi - \theta_i, \pi + \phi_i)] \cdot \vec{r}_j}$$

where j is the index of the scatterer of position \vec{r}_j , f_{qp}^j is the scattering matrix element for the j^{th} scatterer, p and q are the polarisation components (h or v) of the incident and scattered waves respectively. \vec{k}_p^i and \vec{k}_q^s are the propagation vectors of the incident and backscattered fields.

The scattering is computed using the finite cylinder approximation which assumes the induced currents in the dielectric cylinder to be the same as that of the infinitely long cylinder of the same radius [6].

The effect of attenuation of the coherent wave into the canopy is taken into account using the Foldy's approximation [7]. The incident and backscattered waves propagate in the medium along the direction (θ, ϕ) with the propagation constants:

$$k_h = k_0 - i.M_{hh}$$

$$k_v = k_0 - i.M_{vv}$$

for horizontally and vertically polarised waves, with:

$$M_{pq} = i \frac{2\pi n_0}{k_0} \langle f_{qp}(\theta, \phi, \theta, \phi) \rangle$$

where n_0 is the number density of scatterers in the medium.

The forest is defined by the statistical properties of the elements for each order of branches: number density of stems, mean value and standard deviation of the radii and lengths of stems and of the moisture content, pdfs of the insertion angles of branches and needles. Dielectric constants are computed using the Ulaby-El Rayes model [8].

The ground surface is characterized by its rms height and its correlation length. The dielectric constant is given by the Hallikainen model [9].

Each pixel of the simulated complex image is constructed from a realisation of the statistical parameters describing the medium, as shown on figure 3.

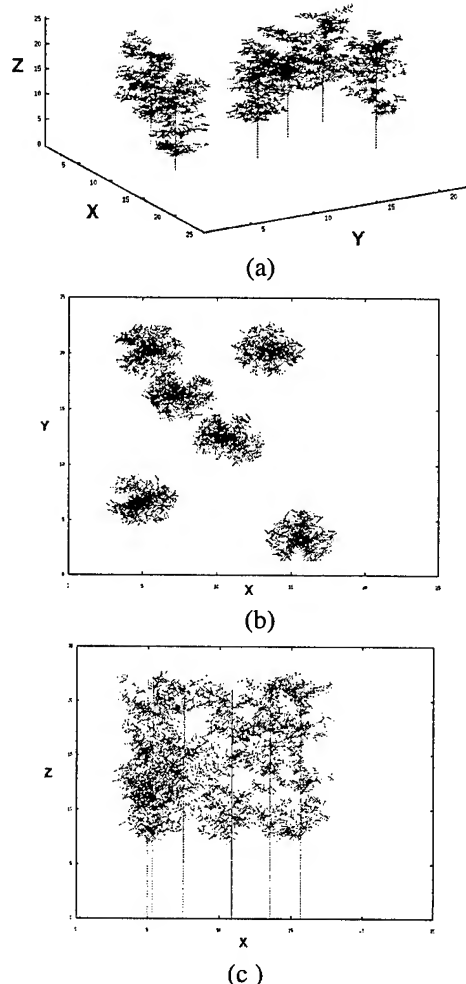


Figure 3: Realisation of a 46 years old maritime pine forest

Previous experiments [1] have shown that the interferometric degree of coherence strongly depends on the relative soil contribution in the total backscatter. At present, no coherent computation of the soil backscatter is carried out. But with some assumptions, the complex degree of coherence may be reformulated to make it dependent only on the coherent response of forest and on the intensity response of soil surface.

The complex degree of coherence is defined by:

$$\rho = \frac{\langle E_1 E_2^* \rangle}{\sqrt{\langle |E_1|^2 \rangle \langle |E_2|^2 \rangle}}$$

where E_1 and E_2 are the received complex fields for the two acquisitions. As we assume that the crown-ground interaction is negligible, we can write the backscattered complex field as:

$$E_i = E_i^{veg} + E_i^{soil}$$

where E_i^{veg} and E_i^{soil} are the complex contributions of forest and soil respectively. By developing the expression of the complex coherence and assuming that the variation in the height of forest scatterers is much larger than the wavelength, we get:

$$\rho = K_{veg} \rho_{veg} + K_{soil} \rho_{soil}$$

ρ_{veg} is computed by the coherent model, K_{veg} and K_{soil} are coefficients depending only on a combination of the backscattered intensities of ground and forest (derived from the coherent model and from IEM). If there is no temporal change of the soil surface, ρ_{soil} may be assumed equal to 1.

3. RESULTS

The first results obtained using the model address ρ_{veg} and more specifically the decorrelation effect caused by the displacement of uniformly distributed scatterers. The effect of wind may be simulated by introducing a random motion of the scatterers between the two simulated images. Figure 4 shows the variations of the degree of coherence with the rms motion of scatterers in the horizontal direction, both for C and

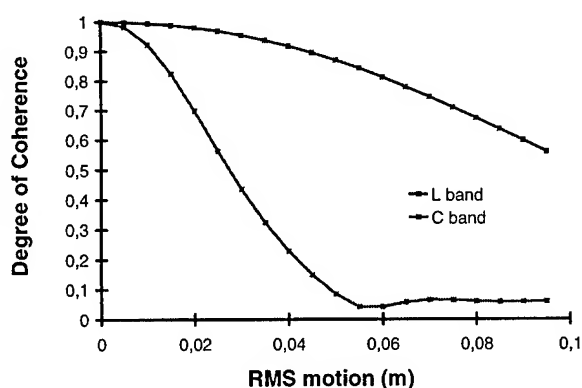


Figure 4: Dependence of correlation on random motion of scattering centers
Modelling results

L-band. The results are similar to those obtained in previous studies [10].

Current work is being carried out to include the soil contribution in order to interpret the degree of coherence derived for young stands.

5. CONCLUSION

Experiments have shown the usefulness of interferometric data for the study of forested environment. However, a theoretical model is needed (1) to identify the different scattering contributions to the interferometric signal, (2) to extend the range of validation of the first experimental results and (3) to determine the optimum configurations for the system (frequency, polarisation, incidence, baseline).

6-ACKNOWLEDGMENTS

This work has been conducted in the frame of the European Union DG XII EUFORA project and French Space Agency (CNES). Nicolas Floury receives a grant from CNES and Alcatel Espace.

7. BIBLIOGRAPHY

- [1] N. Floury, T. Le Toan, J.C. Souyris: « Relating forest parameters to interferometric data », Proceedings of IGARSS'96, pp 975-977, Lincoln, Nebraska, 27-31 May 1996.
- [2] J. Askne, G. Smith: « Forest INSAR decorrelation and classification properties », ERS Symposium on Interferometry, Zurich, September 96.
- [3] N. Floury, T. Le Toan, F. Ribbes, J.C. Souyris, K. Singh, N. Stussi, C.C. Hsu, J.A. Kong: « Interferometry for forest studies », ERS Symposium on Interferometry, Zurich, September 96.
- [4] A.K. Fung: « Microwave scattering and emission models and their applications », Artech House, Boston-London, 1994.
- [5] Souyris J.C., T. Le Toan, N. Floury, C.C. Hsu, L.F. Wang, J.A. Kong: « Microwave Remote Sensing of Natural Targets: Theory and Experiment », Advisory Group for Aerospace Research & Development meeting, Toulouse, 22-25 April 1996.
- [6] Karam, M.A., A.K.Fung, and Y. M. M.Antar, "Electromagnetic scattering from a layer of finite length, randomly orientated, dielectric, circular cylinders over a rough interface with application to vegetation", *IJRS*, Vol. 9, No. 6, 1109-1134, 1988.
- [7] L. Tsang, J.A. Kong, R.T. Shin: « Theory of microwave remote sensing », Wiley-Interscience, 1985.
- [8] F.T. Ulaby, M.A. El Rayes: « Microwave dielectric spectrum of vegetation - Part II: Dual-dispersion model », *IEEE Transactions on Geoscience and Remote Sensing*, Vol. 25, No 5, pp 550-557, September 1987.
- [9] M.T. Hallikainen, F.T. Ulaby, M.C. Dobson, M.A. El Rayes, L.K. Wu: « Microwave dielectric behavior of wet soil - Part I: Empirical models and experimental observations », *IEEE Transactions on Geoscience and Remote Sensing*, Vol. 23, No 1, January 1985.
- [10] H.A. Zebker and J. Villasenor: « Decorrelation in Interferometric Radar Echoes », *IEEE TGRS*, Vol. 30, No. 5, September 1992, pp 950-959.

An Electromagnetic Scattering Model for Tree Trunks Over a Tilted Rough Ground Plane

H. Esteban¹, J. M. López¹, M. Baquero¹, J. Fortuny², G. Nesti² and A. J. Sieber²

¹ Departamento de Comunicaciones, ETSIT, UPV
Camino de Vera s/n, 46071 Valencia, Spain

² Advanced Techniques, SAI JRC 21020 Ispra (Va), Italy
Tel/Fax: +39 332 785104/5772, E-mail: Joaquim.Fortuny@jrc.it

Abstract Remote sensing of forest canopies is dominated by the interaction between tree trunks and ground at lower microwave frequencies and/or when the crown layer is tenuous. An efficient and complete electromagnetic scattering model for tree trunks above a tilted rough ground plane has been performed and enhanced. The individual trunks are modelled as finite-length stratified cylinders, with an external corrugated bark layer. The ground plane is modelled as a rough dielectric half space underlying the cylinders. Realistic natural conditions can be simulated by properly setting the parameters of this model. Results have been computed for the mean square error of the bistatic scattering pattern, by means of a Monte-Carlo simulation.

I INTRODUCTION

Focusing on the remote electromagnetic characterization of the earth's vegetation cover, it has been shown from Vector Radiative Transfer Theory [1] that the backscattering from a typical forest canopy at lower microwave frequency and/or when the crown layer is tenuous is dominated by the ground-trunk interaction. Therefore in such cases an accurate model is composed by tree trunks above a ground plane.

It is demonstrated that the multiple scattering from cylinders overlying a dielectric half space is highly dominated by the first order solution (coherent sum of scattered fields by each cylinder as a response of the incident field), and that the interaction among cylinders is only of significance when trees are very close together [2, 3]. Then, for the realistic case of uniformly distributed tree trunks with a fractional surface on the illuminated area of the order of 0.1% occupied by trees, interaction among trees needs not to be considered. The characterization of an individual trunk-ground set has been solved using the model presented in [4], discussed and improved as in [5].

This work was supported by the contract No. 11846-96-05 F1EI ISP E between the Departamento de Comunicaciones UPV¹ and the Space Applications Institute JRC².

Once the individual trunk-ground sets are characterized, the multiple scattering is obtained by coherently summing the individual scattered fields by each trunk-ground set, each weighted by a phase factor obtained from its position. Results have been computed for the mean square error of the bistatic scattering pattern, using Monte-Carlo simulations. The influence of many variable parameters can be shown by the numerical simulations, allowing a complete study of vegetation covers.

The individual characterization of a trunk-ground set and the multiple scattering algorithm are outlined in the first part. Later, some numerical results and their discussion are explained.

II FORMULATION

II.1 Single Trunk-Ground Characterization

The characterization of an individual trunk-ground set is made by means of a scattering matrix \mathbf{S} that relates the incident and scattered fields [4] in the far field region,

$$\begin{bmatrix} E_v^s \\ E_h^s \end{bmatrix} = \frac{\exp(jk_0 r)}{r} \begin{bmatrix} S_{vv} & S_{vh} \\ S_{hv} & S_{hh} \end{bmatrix} \begin{bmatrix} E_v^i \\ E_h^i \end{bmatrix} \quad (1)$$

where fields are decomposed into a vertical and a horizontal polarization, using the FSA convention [6].

The computation of the \mathbf{S} matrix for a trunk-ground set is made in the same way as [4], but including a rough ground plane which has been characterized using a reflection coefficient matrix Γ according to the roughness of the ground. The local to the plane coefficients $\Gamma_{v'}$ and $\Gamma_{h'}$ are the coherent field reflection coefficients from a surface with a Gaussian height distribution [7]. Their expression is,

$$\Gamma_p = \Gamma_{p0} \exp(-2k^2 s^2 \cos^2 \theta_i) \quad (2)$$

where the polarization subscripts p, q are either h' or v' , the angle θ_i is both the angle of incidence and reflection, and s is the rms height of the surface. Coefficients Γ_{p0} are the Fresnel reflection coefficients [8] of a smooth surface with the same dielectric properties.

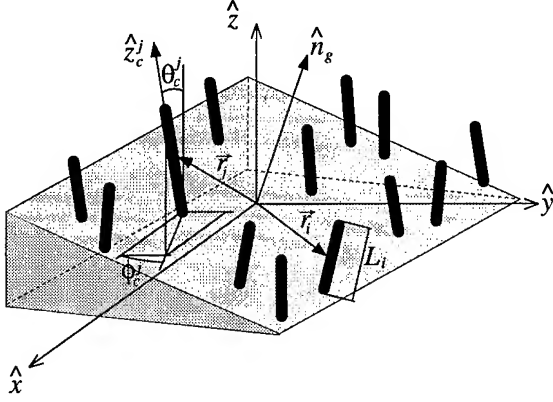


Figure 1: Multiple scattering problem arrangement

II.2 Multiple Scattering

The multiple scattering problem is illustrated in Fig.1. Multiple tree trunks are positioned over a tilted rough dielectric ground plane. Trunks length (L_j) follow a Gaussian distribution with L mean and σ_L deviation, and positions of trunks (\vec{r}_j^s) are uniformly distributed over the elliptic illuminated area of the ground surface.

The orientation of each tree j is defined by the unit vector \hat{z}_c^j , expressed as,

$$\hat{z}_c^j = \sin \theta_c^j \cos \phi_c^j \hat{x} + \sin \theta_c^j \sin \phi_c^j \hat{y} + \cos \theta_c^j \hat{z} \quad (3)$$

where θ_c^j and ϕ_c^j are elevation and azimuth inclination angles. In the Monte-Carlo simulation θ_c follows a Gaussian distribution with zero mean and σ_{θ_c} deviation, and ϕ_c is uniformly distributed in $[0, \pi]$.

The transmitting antenna is supposed to produce an elliptic beam (spot-like coverage). The lengths of the axes of the incident beam in the plane defined by \hat{k}_i are Δ_v (ground-range) and Δ_h (cross-range), respectively. This ellipse has been projected over the ground surface by means of a geometrical method.

The multiple scattering problem consists of N tree trunks. For each trunk j , its position, height and orientation together with the ground tilt and roughness is used to construct the scattering matrix \mathbf{S}_j that characterizes its interaction with the ground plane. Once all matrices \mathbf{S}_j , are computed, summation of all \mathbf{E}_j^s gives the total scattered field by the layer of tree trunks after the first interaction, providing the so called first order solution for the multiple scattering problem,

$$\begin{bmatrix} S_{vv}^M & S_{vh}^M \\ S_{hv}^M & S_{hh}^M \end{bmatrix} = \sum_{j=1}^N \begin{bmatrix} S_{vv}^j & S_{vh}^j \\ S_{hv}^j & S_{hh}^j \end{bmatrix} e^{jk_0(\hat{k}_i - \hat{k}_s) \cdot \vec{r}_j} \quad (4)$$

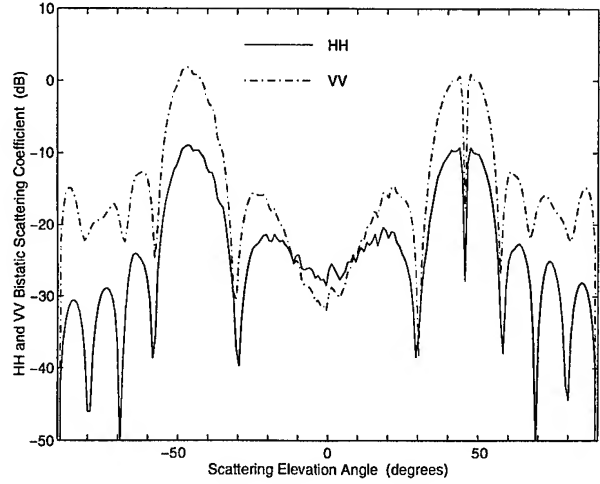


Figure 2: Simplest case. $\epsilon_c = (20 + j3)\epsilon_0$, $\epsilon_g = (15 + j5)\epsilon_0$, $\lambda = 20$ cm, $a = 1$ cm, $s = 0$, $L = 60$ cm, $\sigma_L = 0$, $\sigma_{\theta_c} = 0$, $\Delta_v = \Delta_h = 560.5$ cm, $d = 0.1\%$, $\theta_g = 0$, $\phi_g = 0$, $\theta_i = 45.55^\circ$, and $\phi_i = 0^\circ$

III RESULTS AND DISCUSSION

Numerical results have been computed using Monte-Carlo simulations with 50 realizations in order to guarantee their random features. The displayed value is the mean square error of the Bistatic Scattering Coefficient [2], defined by,

$$\gamma_{\beta\alpha}(\theta_s, \phi_s; \theta_i, \phi_i) = \lim_{r \rightarrow \infty} \frac{4\pi r^2 \left\langle |E_\beta^s - \langle E_\beta^s \rangle|^2 \right\rangle}{|E_\alpha^i|^2 A_i \cos \theta_i} \quad (5)$$

where angular brackets denote average over realizations, A_i is the illuminated area and α, β represent, respectively, the input and output polarizations.

The γ_{HH} and γ_{VV} coefficients as a function of the elevation observation angle are shown in Fig.2 for a uniform distribution of vertical homogeneous dielectric cylinders (ϵ_c) of radius a , overlying a straight smooth dielectric half space (ϵ_g). The spot coverage ground and cross range are equal, and cylinders occupy 0.1% of fractional surface. Fig.2 is the simplest case, and most values for the involved parameters have been taken from [2] for comparison. All results appeared there for the first order solution agree with the ones obtained using this method.

In the simplest case, the Bistatic Scattering Coefficient when all trunks are equal and colinear is the bistatic response of an individual trunk-ground set weighted by the array factor of N elements positioned at \vec{r}_j^s each one. Thus the mean square error of the Bistatic Scattering Coefficient is the mean square error of the array factor. Two maxima appear in the back and forward regions, a dip just in the specular direction, and there is a relation between the angular width of both maxima and the ratio

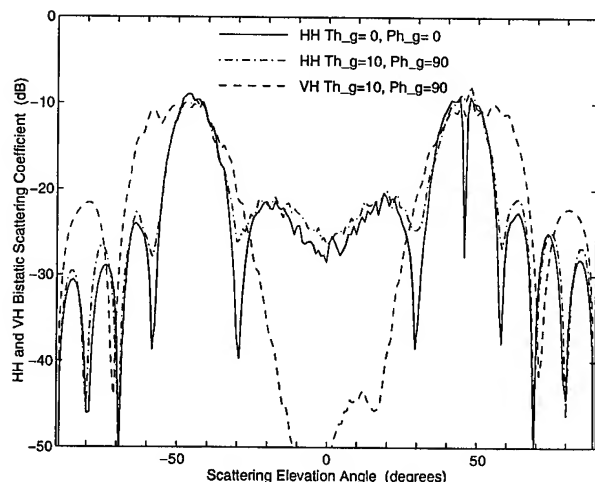


Figure 3: Effect of the ground tilt in γ_{HH} . $\theta_g = 10^\circ$, $\phi_g = 90^\circ$

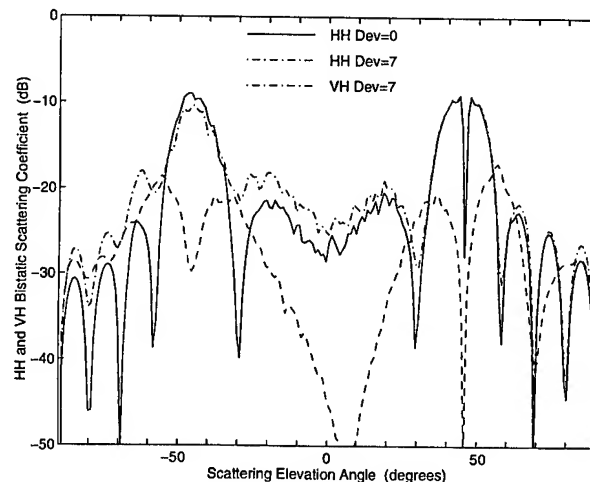


Figure 4: Effect of non-colinearity of trunks

wavelength over cylinders' average length, as shown in [2].

Many simulations have been performed to analyze the sensitivity of the bistatic scattering pattern to every involved parameter. For example, the influence of the ground tilt is presented in Fig.3. The slope of the ground plane is characterized by a directional vector \hat{n}_g , which depends on θ_g and ϕ_g (elevation and azimuth inclination angles, respectively). Fig.3 shows the response for a typical small elevation angle $\theta_g = 10^\circ$. As expected, the backscattering maximum disappears because cylinders are not perpendicular to the ground. Moreover, if the azimuth inclination ground angle ϕ_g becomes non-zero, a high cross-polarized signal appears (see VH) as it occurs for an individual trunk-ground set [4]. Another important effect is the missing dip for $\theta_s = 45^\circ$, since the true specular direction when $\phi_g \neq 0$ does not occur for $\phi_s = 0$.

Fig.4 shows the effect of the non-colinearity of trunks. The former situation (vertical trunks) is compared with that of trunks randomly oriented, with 7° of standard deviation around the vertical position. The peak in the specular direction is unchanged due to the array factor not being modified, but the backscattering peak disappears and there is a high level of cross-polarized signal due to trunks not being normal to the ground.

Other observed effects have been the dependence to the height of the ground roughness, the sensitivity to the dielectric characteristics of the trunk layers, the effect of the incidence angle, the frequency and the trunks dimensions.

IV CONCLUSION

An efficient, complete and realistic model for multiple tree trunks above a tilted rough ground plane has been presented. This model is an improved combination of the model described in [4] for a single tree trunk above a tilted

ground plane and the model for multiple vertical cylinders overlying a dielectric half space presented in [2]. An algorithm for obtaining a matrix providing the scattering in the far field zone and the first order solution was developed.

This scattering model allows a complete study of forest canopies, since many parameters can be customized and many realistic features have been added.

REFERENCES

- [1] F. T. Ulaby, K. Sarabandi, K. MacDonald, M. Whitt, and M. C. Dobson, "Michigan microwave canopy scattering model," *Int. J. Remote Sensing*, vol. 11, no. 7, pp. 1223-1253, 1990.
- [2] L. Tsang, K. Ding, G. Zhang, and J. A. Kong, "Backscattering enhancement and clustering effects of randomly distributed dielectric cylinders overlying a dielectric half space based on Monte-Carlo simulations," *IEEE Trans. Antennas Propagat.*, vol. 43, pp. 488-499, May 1995.
- [3] K. Sarabandi, P. F. Polatin, and F. T. Ulaby, "Monte-Carlo simulation of scattering from a layer of vertical cylinders," *IEEE Trans. Antennas Propagat.*, vol. 41, pp. 465-475, Apr. 1993.
- [4] Y.-C. Lin and K. Sarabandi, "Electromagnetic scattering model for a tree trunk above a tilted ground plane," *IEEE Trans. Geosci. Remote Sensing*, vol. 33, pp. 1063-1070, July 1995.
- [5] J. M. López, H. Esteban, J. Fortuny, and A. J. Sieber, "Discussion of an electromagnetic scattering model for a tree trunk above a tilted ground plane," Tech. Rep. I-96-41, Joint Research Centre. Space Applications Institute, Mar. 1996.
- [6] F. T. Ulaby and C. Elachi, *Radar Polarimetry for Geoscience Applications*. Nordwood: Artech House Inc., 1990.
- [7] R. D. D. Roo and F. T. Ulaby, "Bistatic specular scattering from rough dielectric surfaces," *IEEE Trans. Antennas Propagat.*, vol. 42, pp. 220-231, Feb. 1994.
- [8] J. A. Stratton, *Electromagnetic Theory*. New York: Mc Graw-Hill Book Company, Inc., 1941.

Effect of Temporally Varying Parameters on L- and C-Band SAR Observations of Boreal Forests

Jouni Pulliainen, Lauri Kurvonen and Martti Hallikainen

Helsinki University of Technology, Laboratory of Space Technology

Otakaari 5A, 02150 Espoo, Finland, Fax: +358 9 451 2898, email: pulliainen@ava.hut.fi

Abstract -- An analysis of L- and C-band boreal forest backscattering properties with respect to various temporally changing parameters is presented. The seasonal or weather dependent parameters investigated include the depth of soil frost, top-soil moisture, snow water equivalent, air temperature and precipitation. The effect of these parameters on σ^0 are studied for various stem volume (biomass) classes by comparing the results against a semi-empirical modelling approach. Semi-empirical modelling is also used for a forest biomass retrieval experiment. The SAR data set includes 4 JERS-1 (L-band, HH-polarization) and 19 ERS-1 (C-band, VV-polarization) images for a single test area in southern Finland. The results show that at C-band response to forest biomass is more sensitive to changes in temporally varying parameters than at L-band. The semi-empirical modelling approach was found to describe well the behavior of σ^0 when large areas are considered. Hence, the results in biomass retrieval show high accuracies (25-30% relative accuracy) when areas under investigation are larger than 20 ha.

INTRODUCTION

L- and C-band radar response to forest biomass is affected by various weather dependent or seasonally changing parameters, such as soil moisture, total water content of vegetation canopy, soil frost and snow cover. The aim of this paper is (a) to investigate how large the changes in σ^0 caused by variations of these parameters are, and (b) can information on these parameters be obtained using L- or C-band SAR data. Moreover, the issue of retrieving forest biomass information using L-band, C-band and combined L/C-band SAR data is discussed.

The presented analysis is based on the employment of a semi-empirical boreal forest backscatter modelling approach for the inversion of SAR data. The same approach has been previously used for soil moisture and forest biomass retrieval using multi-temporal ERS-1 SAR data [1].

MATERIAL AND METHODOLOGY

Study material

The SAR data include 4 JERS-1 and 19 ERS-1 SAR images for the 5000 km² Porvoo test area, southern Finland. The forest reference data set for the area covered by SAR images includes detailed ground-based measurements for 230 to 360 forest sample plots (the number varies for different images). These ground truth data give information on numerous parameters, including stem volume, height and species for different tree strata, and also, information on soil type and fertility class. Additional reference data is provided by a digital stem volume/land use map (obtained from Finnish Forest Research

Institute) produced using the same sample plot information together with a Landsat TM image. The digital map was used for a 1800 km² sized sub-area of the Porvoo test area.

The reference information on varying parameters include *in situ* soil frost depth and snow water equivalent/density observations, and additionally, hydrological model-based top-soil moisture predictions (all obtained from Finnish Environment Institute). Standard meteorological observations on air temperature and precipitation were also available.

Data processing

The employed ERS-1 SAR data set was geocoded using a topographic terrain model [1]. This enabled processing of 25m × 25m pixel-sized ERS data for the reference sample plots which have a size varying from 1 to 37 ERS-1 SAR pixels (mean σ^0 -values were determined for each sample plot). For JERS-1 data, topographically corrected geocoding was not possible. Thus, the JERS-1 SAR measurements were only compared with the digital stem volume map.

Semi-empirical modelling approach and model inversion

Assuming that the forest canopy extinction coefficient κ_e given in [ha/m³] and the volume scattering coefficient σ_v [ha/m³] are constant with respect to stem volume V [m³/ha] and assuming that their relation to the changes in volumetric water content of canopy $m_{v,can}$ can be described using a cloud model [2], σ^0 for forested terrain can be given by

$$\sigma^0(V, \theta, m_v, m_{v,can}) = \frac{\sigma_v(m_{v,can}) \cos \theta}{2\kappa_e(m_{v,can})} [1 - \exp(-2\kappa_e(m_{v,can})V/\cos \theta)] + \sigma_g^0(\theta, m_v) \exp(-2\kappa_e(m_{v,can})V/\cos \theta) \quad (1)$$

where θ is the incidence angle, m_v is the volumetric soil moisture and σ_g^0 is the backscattering coefficient of forest floor (soil and surface vegetation). The effect of m_v and θ on σ_g^0 is described by a semi-empirical model [3].

The applicability of (1) at C-band, in the case of conifer-dominated boreal forest, was demonstrated in [1]. [4] describes the method that was used to determine κ_e and σ_v from airborne high resolution ranging scatterometer data. This paper further discusses the applicability of (1) for both L- and C-band under varying environmental conditions. For JERS-1 data, the mean values of κ_e , σ_v and σ_g^0 for a single image are estimated through fitting (1) using least squares method into the stem volume-wise processed (V is known) JERS-1 SAR data. Three independent

parameters have to be determined, since values for κ_e and σ_v at L-band are not available from airborne measurements. For ERS-1 SAR data the fitting is also conducted using only the two volumetric moisture parameters: m_v and $m_{v,can}$.

The stem volume inversion experiment is also performed by fitting (1) into (multi-temporal/multi-instrument) SAR observations. This is conducted using a two-step method similar to that introduced in [1]. In the first step, if multi-channel simultaneous SAR data are not available, the method requires the use of teaching areas with a known stem volume V to estimate the water content-related model parameters (either m_v and $m_{v,can}$ or κ_e , σ_v and σ_g^o). In the second step, these parameters are used when V is estimated for the test areas.

EFFECT OF SOIL FROST AND SOIL MOISTURE TO BACKSCATTER AT C-BAND

The effect of soil frost on σ^o was investigated using an ERS-1 SAR image obtained for conditions where the top-soil was frozen (25 Nov. 1993). The observed depth of soil frost was 16 cm in open, deforested areas and 7 cm in forested areas. The air temperature was -2.3°C and the ground was covered by a thin (2 cm) dry snow layer, which only had a marginal effect on C-band signatures. The (effective) average soil and vegetation moisture for this image were estimated by fitting the semi-empirical model (1) into sample plot-wise observations. The values obtained are $m_v = 6.6\%$ and $m_{v,can} = 37.5\%$. These values are very low indicating that both the soil and vegetation are at least partially frozen (from the model point of view, frozen soil (vegetation) where liquid water is replaced by ice behaves like a very dry soil (vegetation)).

Fig. 1 depicts a comparison of the results for frozen soil (25 Nov. 1993) with those representing unfrozen conditions (6 Nov. 1993). Fig. 1 shows the sample plot-wise performed model fittings for these two dates and the corresponding mean responses for 7 classes: deforested areas and six stem volume categories. The number of ERS-1 SAR pixels per class varies from 40 to 1400 (i.e. area in hectares from 2.5 to 89). The drop of σ^o between these two dates is about 1.6 dB for forested areas and about 2.0 dB for the deforested areas. A possible reason for this difference is that the depth of frost was deeper in open areas. On 6 Nov. the conditions were dry and thus, the estimated soil moisture shows a relatively low value $m_v = 12.9\%$. Considerable precipitation did not occur between the two dates.

Fig. 1 also shows the average responses of σ^o to stem volume (biomass) for an other 8 cases representing non-frozen summer and autumn conditions (dotted lines). The soil moisture estimate obtained from SAR data varies from 12% to 34% for these observations and the canopy moisture estimate from 50% to 71%, respectively. The corresponding hydrological model-based reference predictions for the soil moisture showed a variation range from 13% to 36% (for the four month time period from June to Sept. 1993).

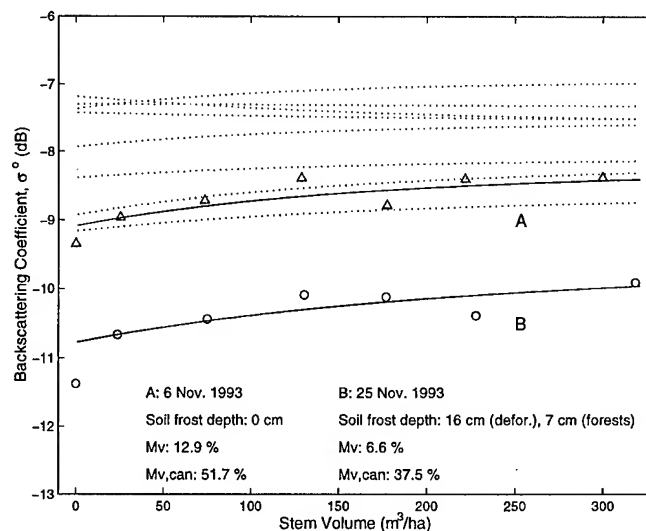


Fig. 1. Effect of soil frost on ERS-1 SAR-derived σ^o . The solid lines show the model fittings for (A) unfrozen (6 Nov.) and (B) frozen (25 Nov.) conditions, whereas the triangles and circles show the observed average responses for various stem volume classes. The dotted lines show the behavior of σ^o as a function of stem volume for other data acquisition dates representing unfrozen conditions (summer and autumn 1993).

RESPONSE OF σ^o TO BIOMASS UNDER VARYING CONDITIONS AT THE L- AND C-BANDS

The response of L-band σ^o to stem volume (biomass) was investigated using four images, two for snow-covered terrain conditions (18 Dec. 1994 and 15 March 1995) and the other two for snow-free terrain (23 May 1993 and 30 April 1995). In this case, the digital land use/stem volume map was used as a reference. The reference data of forested areas was divided into 16000 blocks with varying stem volume and sized 4.5 ha on average. The semi-empirical model (1) was fitted into this block-wise processed data using three independent parameters: κ_e , σ_v and σ_g^o . 10% of the data were used for fitting and the rest for testing. The same blocks were used for all images.

Figure 2 shows the behavior of L-band σ^o for different conditions (four dates) together with C-band model fittings obtained for conditions as similar as possible to those of JERS-1 data acquisition. The C-band curves are determined as in Fig. 1 from sample plot-wise processed ERS-1 SAR observations. For L-band both the model fittings and the average JERS-1 SAR observations for six stem volume classes are depicted. The results of Fig. 2 show that the L-band σ^o always increases with the increasing stem volume, whereas the C-band σ^o can increase or decrease depending on soil/canopy conditions (or depict constant values).

On 18 Dec. 1994 soil was frozen and a thin dry snow layer covered the terrain (snow water equivalent < 5 mm, and consequently, snow layer thickness < 2 cm). Hence, L-band

JERS-1 observations show, similarly to C-band data, a low level of backscatter, but a stronger dynamic response to stem volume. The C-band model fitting shown in Fig. 2 is the curve obtained for 25 Nov. 1993, also presented in Fig. 1.

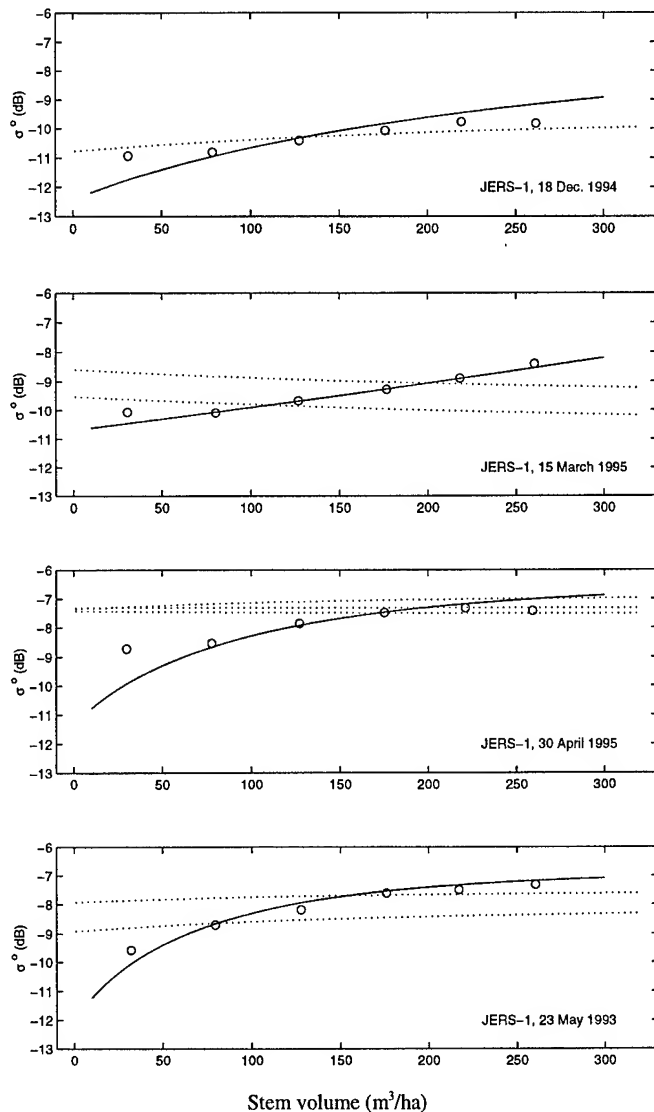


Fig. 2. Behavior of L-band σ^0 as a function of stem volume for different seasonal conditions. Open circles show the JERS-1 SAR observations and the solid lines the corresponding fittings of model (1) to JERS-1 data. The conditions for different cases are:

18 Dec. 1994: frozen soil with a thin dry snow cover

15 March 1995: refrozen snow cover

30 April 1995: wet soil and wet tree canopy

23 May 1993: dry soil.

Dotted lines depict the C-band responses obtained by fitting (1) into those ERS-1 observation dates that represent conditions similar to JERS-1 data acquisition.

On 15 March 1995 dry refrozen snow covered the forest floor (snow water equivalent varied from 40 to 60 mm). The JERS-1 observations for this date show a strong increase with the increasing stem volume, whereas the C-band observations for similar conditions show a clear decrease of σ^0 , respectively (ERS-1 images for 25 and 28 March 1993).

On 30 April 1995 terrain was snow-free and both the vegetation and ground were wet (rain and wet snow precipitation occurred prior and during the JERS-1 image acquisition date). Thus, σ^0 show the highest values for different stem volumes for this JERS-1 image. The ERS-1 images used for C-band curves shown in Fig. 2 do not correspond well the JERS-1 image of 30 April, since they represent summer conditions (19 July, 12 and 28 Aug. 1993). However, they are selected so that precipitation (and hence the canopy and soil moisture) has been considerable.

On 23 May 1993 precipitation did not occur during or prior the JERS-1 SAR image acquisition. Hence, the L-band backscatter from forest floor, σ_g^0 , shows low values. The increase of σ^0 as a function of stem volume is higher than that for other cases. The ERS-1 SAR-based results shown in Fig. 2 represent conditions quite similar to those of JERS-1 imaging (23 May 1995), even though the ERS-1 images are from summer and autumn (4 Aug. and 2 Oct. 1993).

FOREST BIOMASS RETRIEVAL

Applicability of the semi-empirical model

Even though the radar response to stem volume is much stronger at L-band than at C-band, the better usability of L-band radar e.g. for stem volume retrieval is not self-evident. This is demonstrated in Fig. 3 which depicts the best fits obtained between the model given by (1) and the L- or C-band SAR data (JERS-1 observations for 23 May 1993 and ERS-1 observations for 4 Aug. 1993). The model is fitted into JERS-1 and ERS-1 data (both processed forest block-wise) using three independent model parameters (κ_e , σ_v and σ_g^0). The results show that the model describes the average behavior of σ^0 more accurately at C-band than at L-band. This may be caused by the fact that trunk-ground reflection and coherent scattering effects not included in (1) may have a much larger effect at L-band.

Biomass retrieval experiment

The forest stem volume retrieval experiment was conducted using forest block-wise processed JERS-1 and ERS-1 SAR data (mean σ^0 -values for each block). The minimum size of the blocks for which the stem volume estimates were determined was varied in order to find out how the retrieval accuracy behaves as a function of the area size. 10% of the data were used for teaching, i.e. to estimate average κ_e , σ_v and σ_g^0 by fitting the semi-empirical model (1) into block-wise data using known (teaching) values for the stem volume. When multi-temporal/instrument data sets were employed this was performed separately for each image. In the second step, the stem volume

was estimated for the testing data set (90% of the total data). For multi-temporal/instrument data, this was conducted separately for each image, and the separate stem volume estimates obtained were combined using a linear regression equation determined using the teaching data set.

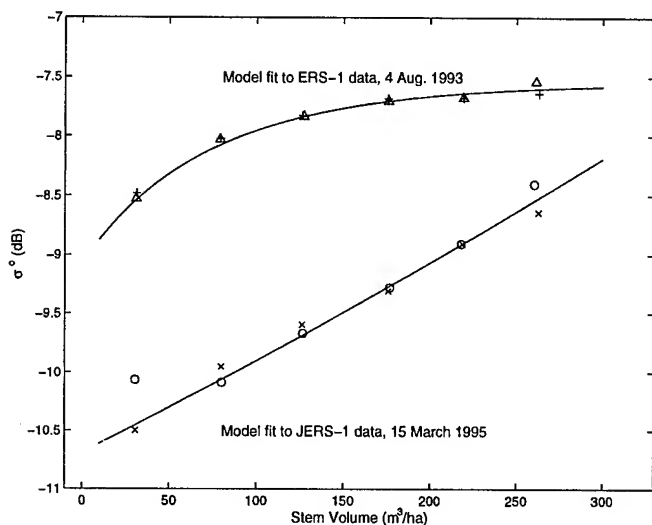


Fig. 3. Best fits (smallest rms differences) obtained between the semi-empirical model and (a) JERS-1 SAR images and (b) ERS-1 SAR images. Open circles/triangles show the mean SAR-derived σ^0 -values of different stem volume classes for the teaching data set (10% of the total data), whereas the crosses depict the average values for the test data set (90% of the data).

The stem volume retrieval results depicted in Fig. 4 show the results obtained using either two JERS-1 SAR images or two ERS-1 SAR images. The results show that relative accuracies of 25-30% can be obtained when the forest block size is larger than about 20 ha. L-band SAR appears to produce better retrieval accuracies for areas smaller than 20 ha, but for areas larger than 20 ha as good accuracies can be obtained using the optimal C-band images. As the block size was higher than 20 ha, the correlation coefficient (r) between the estimates and the reference values was from 0.65 to 0.85 for the JERS-1 data and from 0.60 to 0.65 for the ERS-1 data. The stem volume (reference data) had a mean value of 133 m³/ha with a standard deviation of 62 m³/ha. When a larger amount of SAR observations were employed, the retrieval results show even better accuracies. Using together 2 ERS-1 images and 4 JERS-1 images relative accuracies better than 25% were obtained.

CONCLUSIONS

Our results indicate that in the case of boreal forest zone:

- (a) Semi-empirical model given in (1) describes the behavior of σ^0 better at C-band than at L-band.
- (b) The dynamic response of σ^0 to change in stem volume (biomass) is higher at L-band than at C-band. At L-band, σ^0 always increases with increasing stem volume, which is not the

case at C-band.

(c) The freezing of soil in boreal forests can be well detected for different biomass classes and for deforested areas using C-band SAR data. The JERS-1 SAR data set (Fig. 2) indicates that the same applies at L-band.

(d) The stem volume retrieval experiment indicates good accuracies when the minimum size of the areas for which the estimates are determined is larger than about 10-20 ha. Moreover, the results indicate that using optimal C-band data solely as good results as using L-band data solely can be obtained as the size of the forest blocks is larger than about 20 ha. This may be caused by the fact that the semi-empirical model (1) describes the behavior of σ^0 better at C-band than at L-band.

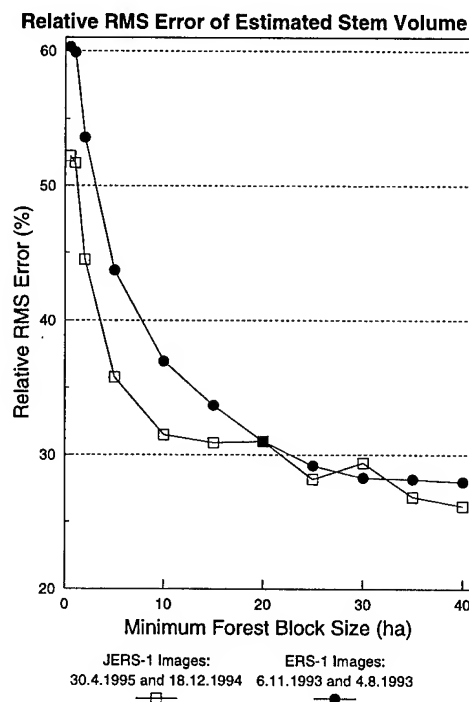


Fig. 4. Relative accuracy (rms error/average true value) of stem volume retrieval when two JERS-1 SAR images or two ERS-1 SAR images are used separately for inversion. The results are depicted as a function of the size of the area for which the estimates are determined.

REFERENCES

- [1] J. Pulliainen, P. Mikkilä, M. Hallikainen, J.-P. Ikonen, "Seasonal dynamics of C-band backscatter of boreal forests with applications to biomass and soil moisture retrieval," *IEEE Trans. Geosci. Rem. Sens.*, vol. 34, pp. 758-770, 1996.
- [2] E. Attema, F. Ulaby, "Vegetation modeled as water cloud," *Radio Sci.*, vol. 13, pp. 357-364, 1978.
- [3] Y. Oh, K. Sarabandi, F. Ulaby, "An empirical model and inversion technique for radar scattering from bare soil surfaces," *IEEE Trans. Geosci. Rem. Sens.*, vol. 30, pp. 370-381, 1992.
- [4] J. Pulliainen, K. Heiska, J. Hyypä, M. Hallikainen, "Back-scattering properties of boreal forests at the C- and X-bands," *IEEE Trans. Geosci. Rem. Sens.*, vol. 32, pp. 1041-1050, 1994.

Numerical Studies of Forest Backscatter in the VHF-band

L.M.H. Ulander, T. Martin

Defence Research Establishment (FOA)

P.O. Box 1165, S-581 11 Linköping, Sweden

Phone: (+46)-13-318044, Fax: (+46)-13-318100, email: ulander@lin.foa.se

Hans Israelsson

Chalmers University of Technology

Department of Radio and Space Science, S-412 96 Göteborg, Sweden

Phone: (+46)-31-7721000, Fax: (+46)-31-164513, email: hans.israelsson@emw.ericsson.se

Abstract -- The increasing interest for forest backscattering in the VHF band is stimulated by recent results from the CARABAS (20-90 MHz) SAR. Potential applications include forest biomass estimation and concealed target detection. For understanding the forest backscatter mechanisms it is important to develop scattering models and assess the limits of validity. Special consideration should be made to the fact that typical trunk and branch scattering is in the resonance region and that multiple scattering effects are important. A numerical method (FDTD) has been implemented which can be used to validate analytical scattering models. It features a five-layer PLM boundary condition, a far-field transformation method based on the reciprocity theorem, and an optional dielectric ground surface. It has been used to assess a coherent reflection model of a horizontal cylinder above dielectric ground. The results indicate an excellent agreement between the model and the FDTD method.

INTRODUCTION

The motivation for studying forest backscatter in the VHF-band is to support a number of potential applications of VHF SAR. Results using the CARABAS (20-90 MHz) SAR have demonstrated its unique capability for foliage penetration and detection of concealed man-made objects [1]. Although wave propagation at higher frequencies also allows for significant penetration, it is only below about 100 MHz when forest backscatter becomes sufficiently low to enable target detection with a low probability of false alarm. Recent results have also shown that VHF-band forest backscatter is sensitive to forest stem volume (or biomass) [2]. In contrast to higher frequencies, the measurement sensitivity does not seem to saturate and is high even for dense canopies.

The typical size of a tree and its major structures is of wavelength order, i.e. the scattering is in the resonance region. Furthermore, multiple scattering between tree structures will be significant since the separation distance is small compared to the wavelength. The ground interaction will also be important and significant interference between

the direct and reflected field will occur. Taken together, the modelling of VHF forest backscatter is a complex electromagnetic problem and its relation to existing simplified forest backscatter models needs to be assessed.

In this paper, we compare computational results from an approximate analytical model and a numerical method. The former is a coherent ground-reflection model based on the scattering model for a truncated cylinder [3], whereas the latter is based on the finite-difference time-domain (FDTD) method [4].

COHERENT REFLECTION MODEL

In most existing forest backscattering models, the forest canopy components are modelled by well-known geometrical structures, such as cylinders and discs. The trunks and branches are characterised by homogeneous dielectric cylinders. This approximation has been shown to give satisfactory results for microwave frequencies. In the VHF band, however, the radar wavelength matches the length of the trunks and the primary branches, and the validity of the approximation is in question.

For an infinitely long cylinder, the scattering problem is two-dimensional [5]. Hence, the solution for the scattered field can be exactly expressed in cylindrical Bessel functions. A long cylinder (in terms of wavelengths) can thus be approximately modelled from the two-dimensional solution. The equivalent electric current of the infinite cylinder is truncated at the end caps of the actual cylinder, and is then used to compute the three-dimensional radar-cross section. For long cylinders, this approach is nearly exact, in particular close to the specular direction. As the cylinder length-to-wavelength ratio decreases, however, the approximation is no longer valid. If the length-to-radius ratio is very large, on the other hand, the approximation remains valid as long as the radius is small compared to the wavelength [6].

The radar-cross section of a horizontal cylinder above a homogeneous dielectric ground surface has been modelled using the radar-cross section of a truncated infinite cylinder and including the interference of the direct and reflected

waves. The latter is determined using the Fresnel reflection coefficient. The cylinder axis is assumed parallel to the ground surface and perpendicular to the plane of incidence. The bistatic scattering amplitude includes four terms (corresponding to first-order ray tracing) with different phase angles due to different path lengths and reflections. The bistatic radar-cross section as a function of the incidence angle θ and scattering angle θ' is thus given by [3]

$$\begin{aligned} \sigma(\theta, \theta') = & \left| \sqrt{\sigma_c(\theta, \theta')} \right. \\ & + R(\theta) \sqrt{\sigma_c(\pi - \theta, \theta')} e^{-j2kh \cos \theta} \\ & + R(\theta') \sqrt{\sigma_c(\theta, \pi - \theta')} e^{-j2kh \cos \theta'} \\ & \left. + R(\theta) R(\theta') \sqrt{\sigma_c(\pi - \theta, \pi - \theta')} e^{-j2kh(\cos \theta + \cos \theta')} \right|^2 \end{aligned} \quad (1)$$

where σ_c is the free-space radar-cross section, R is the Fresnel reflection coefficient, k is the wavenumber and h is the cylinder height above the surface. Note that the total backscattered radar-cross section varies periodically with cylinder height due to the changing phase angles.

FDTD METHOD

In the numerical FDTD method, Maxwell's equations are discretised in both time and space. The incident plane wave is created within the computational volume by using the equivalence principle, i.e. the fields within a closed volume can be represented by equivalent magnetic and electric surface currents on the volume surface. This Huygens' surface is implemented in the FDTD-algorithm according to [7]. The technique implies that the total field exists in a closed volume within the computational volume, whereas only the scattered field exists outside the total field volume out to the outer boundary, see Fig. 1. The outer boundary is truncated using a 5-layer PML-boundary condition [8]. When considering scattering problems in free space, the incident plane wave can be created by equivalent surface currents expressed in a simple analytical form. When a conducting dielectric ground plane is present the field impinging on the object is composed of both an incident field and a reflected field, which has a complicated time-dependence. The incident, reflected and refracted field is therefore determined in the frequency domain, where the expressions for the reflected and refracted fields are well known, and then transformed into the time domain using an FFT. The equivalent surface currents can then be formed on the Huygens' surface.

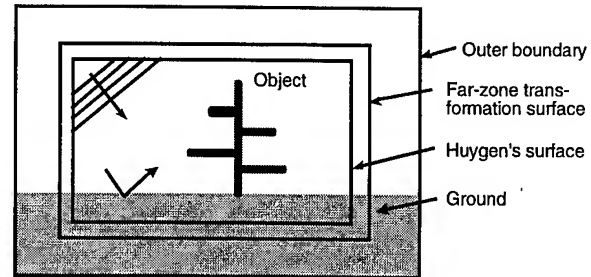


Figure 1. Illustration of the computational volume in FDTD.

In analogy with the equivalent surface currents for the incident field, the scattered field outside the Huygens' surface can be transformed into equivalent surface currents on a closed volume. These surface currents can be used to transform the scattered fields in the near-zone into the far-zone. For problems in free space this is done by integrating either the surface currents transformed into the frequency domain, multiplied with a free-space Green's function, or the time-domain surface currents convolved with a time-domain form of the free-space Green's function, see [9]. When a ground is present, however, matters become much more complicated. A near- to far-zone transformation with a ground present was recently reported which utilises the reciprocity theorem [10]. This type of transformation is also used in this study. A test-current filament \mathbf{J}_i is positioned in the far-zone where the scattered field is to be determined, and the reciprocity theorem gives the following equation

$$\int_V \bar{\mathbf{J}}_i \cdot \bar{\mathbf{E}}_s dV' = \int_V (\bar{\mathbf{J}} \cdot \bar{\mathbf{E}}_i - \bar{\mathbf{M}} \cdot \bar{\mathbf{H}}_i) dV' \quad (2)$$

where the $\bar{\mathbf{E}}_i$ - and $\bar{\mathbf{H}}_i$ - fields are created by the test-current filament and $\bar{\mathbf{J}}$ and $\bar{\mathbf{M}}$ are the currents creating the scattered field. By using the equivalence principle the only currents required in the integral are the equivalent surface currents representing the scattered field on a closed surface. If the test-current is a short line-current, the expression for the radar-cross section can be derived according to

$$\sigma = \frac{Z_o^2 k^2}{4\pi} \left| \oint_S \hat{\mathbf{n}} \cdot (\bar{\mathbf{H}}_s \times \bar{\mathbf{E}}_i + \bar{\mathbf{E}}_s \times \bar{\mathbf{H}}_i) dS' \right|^2 \quad (3)$$

RESULTS

An important test of the coherent ground-reflection model is to assess the accuracy when a dielectric ground is present. From a past study [11] of a horizontal dipole above ground it was concluded that the reflection coefficient approximation used in (1) is accurate within 1 dB for heights above $\lambda/6$. Figure 2 shows the results for a cylinder in free space, and above a dielectric ground surface at heights of 0.5 and 2 m, respectively. The results indicate very good agreement between the coherent reflection model and FDTD, indicating that first-order ray tracing is quite satisfactory for the branch scattering. Future work will also assess the trunk scattering in a similar manner.

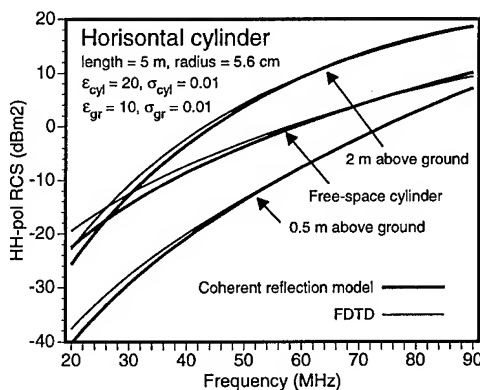


Figure 2. Broad-side mono-static radar-cross section for HH-polarisation and 60° incidence angle of a horizontal cylinder in free space and above a dielectric ground. Note the good agreement between the coherent reflection model and the FDTD method for all cases. The complex dielectric constant is given by $\epsilon_r + j \sigma / \omega \epsilon_0$.

REFERENCES

- [1] H. Hellsten et al., "Ultra-Wideband VHF SAR - Design and Measurements," Proc. Aerial Surveillance Sensing Including Obscured and Underground Object Detection, Orlando, FL, 4-6 April 1994, SPIE vol. 2217, pp. 16-25, 1994
- [2] H. Israelsson et al., "Retrieval of Forest Stem Volume using VHF SAR," IEEE Trans. Geosci. Remote Sensing, vol. 35, no. 1, pp. 36-40, 1997
- [3] H. Israelsson et al., "Modelling of VHF Radar Backscattering from Forests Based on Radiative Transfer," Proc. IGARSS'97, 1997

- [4] K.S. Yee, "Numerical Solution of Initial Boundary Value Problems Involving Maxwell's Equations in Isotropic Media," IEEE Trans. Antennas and Propagat., vol. 14, no. 3, pp. 302-307, 1966
- [5] G. T. Ruck et al., "Radar Cross Section Handbook," New York: Plenum, 1970
- [6] J.M. Stiles, and K. Sarabandi, "A Scattering Model for Thin Dielectric Cylinders of Arbitrary Cross Section and Electrical Length", IEEE Trans. Antennas and Propagat., vol. 44, no. 2, pp. 260-266, 1996
- [7] D. E. Merewether et. al., "On Implementing a Numeric Huygen's Source in a Finite Difference Program to Illuminate Scattering Bodies," IEEE Trans. Nuclear Science, vol. 27, no. 6, pp. 1829-1833, 1980
- [8] J.-P. Berenger, "A Perfectly Matched Layer for the Absorption of Electromagnetic Waves," J. Comp. Physics, vol. 114, pp. 185-200, 1994
- [9] A. Taflove, "Computational Electrodynamics, The Finite-Difference Time-Domain Method," Artech House, Boston, 1995
- [10] K. Demarest et al., "An FDTD Near- to Far-Zone Transformation for Scatterers Buried in Stratified Grounds," IEEE Trans. Antennas and Propag., vol. 44, no. 8, pp. 1150-1157, 1996
- [11] L.M.H. Ulander and Z. Sipus, "RCS of Dipoles used for Low-Frequency SAR Calibration," Proc. EUSAR'96, Königswinter, Germany, 26-28 March 1996, pp. 493-498, 1996

Estimating Soil Moisture in a Boreal Old Jack Pine Forest

Mahta Moghaddam, Sasan Saatchi, and Robert Treuhaft

Jet Propulsion Laboratory

MS 300-235, 4800 Oak Grove Drive, Pasadena, CA 91109

(818)354-1591, (818)393-3077 (FAX), Mahta.Moghaddam@jpl.nasa.gov

Abstract - Polarimetric L- and P-band AIRSAR data, corresponding model simulations, and classification algorithms have shown that in a boreal old jack pine (OJP) stand, the principal scattering mechanism responsible for radar backscatter is the double-bounce mechanism between the tree trunks and the ground [1]. The data to be used here were taken during six flights from April to September 1994 as part of the BOREAS project. The dielectric constants, or equivalently moisture contents, of the trunks and soil, can change rapidly during this period. To estimate these dynamic unknowns, parametric models of observed radar backscatter for the double-bounce mechanism are developed by using a series of simulations of a numerical forest scattering model. The resulting simulated data are used to derive polynomial fits of backscattering cross section as a function of the ground and trunk dielectric constants. Empirical and field data are used to relate the real and imaginary parts of the dielectric constants, and hence formulate the parametric model in terms of two unknowns only. Three data channels, P-HH, P-VV, and L-HH are used to solve of the two unknowns. A nonlinear optimization procedure is used to estimate the dielectric constants, and hence, in particular, soil moisture. Point ground measurements are used to verify the results of the estimation algorithm.

INTRODUCTION AND RATIONALE

The boreal ecosystem atmosphere research (BOREAS) project is a multidisciplinary effort to study the interactions between the boreal forest biome and the atmosphere to determine their role in global change. BOREAS is focused on two principle study areas in central Canada, one near the Prince Albert National Park in Saskatchewan, or the Southern study area (SSA), and the other near Thompson, Manitoba, or the Northern study area (NSA). During the time period of April 1994 to September 1994, several intensive and focused campaigns were carried out, in which several remote sensing instruments made measurements. In particular, the NASA/JPL airborne synthetic aperture radar (AIRSAR) collected polarimetric C-, L-, and P-band data during several flights in this time period. In this work, we concentrate on the data acquired over an old jack pine (OJP) stand in the SSA. The SSA contains several conifer forest types such as young and old jack pines and black spruce. There are also deciduous species such as aspen, as well as stands consisting of mixtures of these species.

A major goal of performing remote measurements, such as radar measurements using the AIRSAR, was to attempt to retrieve forest parameters that play significant roles in the functioning of the ecosystem. Previously, we have reported an algorithm to estimate the tree canopy moisture content for a young jack pine stand in the BOREAS SSA from AIRSAR data. Another important parameter is soil moisture under the forest canopy. Soil moisture content has implications in the rate of evapotranspiration, on water stress, and in the growth rate of forests. The latter is especially important in studying the factors limiting the growth of older trees.

In this work, an estimation algorithm was developed to obtain the soil moisture of an old jack pine stand for six different dates in the Spring and Summer of 1994. The site was chosen due to its specific structure, which, as described below, enabled a simplified modeling of the scattering process. As shown in [1] and further substantiated using the classification algorithm of [2], at P- and L-bands (P-HH, P-VV, and L-HH), the mechanism almost entirely responsible for the backscattered signal over the OJP site is double-bounce scattering between trunks and ground. For L-VV, the branch-ground interactions also become significant. Therefore, a parametric scattering model was derived in terms of the dielectric constant of the trunks and the dielectric constant of soil. This is distinguished from the estimation of tree canopy moisture in the young jack pine stand, where the dominant mechanism was volume scattering. The model was then used in a nonlinear algorithm to estimate the two dielectric values from P-HH, P-VV, and L-HH AIRSAR data. A few point comparisons of the results with ground-truth measurements were performed and good agreement observed. With the availability of further ground-truth data, more thorough validation will be performed.

SITE DESCRIPTION

The old jack pine stand is one of the four main flux tower sites of BOREAS southern study area. It is characterized by tall trunks resembling cylinders, a sparse crown layer, and a "smooth" floor covered by dry lichen. Some stand parameters are: tree density = $0.3/\text{m}^2$, trunk height = 15.1 ± 3.0 m, diameter at breast height = 13.0 ± 4.9 cm. These were measured directly during the summer of 1994.

AIRSAR DATA

AIRSAR data from several dates in the Spring and Summer of 1994 were used to estimate the soil moisture and assess its changes at the OJP site. The specific dates were April 17, 20, and 26, June 11, July 28, and September 20. The data channels used were P-HH, P-VV, and L-HH. Although the L-VV backscattered signal was also predominantly characterized as double-bounce, it included the scattering between the branch layer and ground, and therefore was not used in the estimation. Images and representative values of the above data will be shown at the presentation.

ESTIMATION

A two-step procedure [3] was used to estimate soil moisture, or equivalently, dielectric constant, from SAR data:

1. Derive a parametric scattering model from a numerical forest scattering model [4], with the dielectric constants of soil and tree trunks as the independent parameters. Empirical relations were used to relate the real and imaginary parts of soil and trunk permittivity, so that only one of them, in this case the real part, was taken as the parameter to be estimated. The other quantities which define the forest, and in particular, the double-bounce scattering process, are tree height and diameter distributions, trunk density, and soil roughness characteristics. Within the timeframe of this study, which spans about 5 months, this group of parameters can be assumed not to have changed, and therefore fixed in the derivation of the parametric models. The fixed values are those measured in the field and reported in Table 1. Model simulations are shown in Fig. 1(a)-(c). The parametric model is derived by fitting two-dimensional polynomials of higher-order to the curves shown. In this case, due to the smoothness and slow variations of the backscattered signals as shown, it was found that polynomials of third order are more than sufficient to describe the parametric model.
2. Use a nonlinear estimation algorithm to find the best set of parameters (soil and trunk dielectric constants) that describes the SAR data given the parametric model. The algorithm used here was an iterative one using the conjugate gradient method. The data covariances were included in the analysis, as well as prescribed parameter covariances to represent a regularization procedure.

RESULTS AND SUMMARY

The algorithm described above was applied to the six AIRSAR data sets, and soil dielectric maps produced over the

OJP site. From empirical measurements, the dielectric constant can be linearly related to soil moisture. Three of the six dielectric maps are shown in Fig. 2, where we observe the decreasing trend in soil moisture from a thawing day in April to late September. The OJP stand appears as the heart-shaped area, which is offset slightly from image to image. Point ground-truth dielectric constant and soil moisture measurements available using a TDR (available for the July data) were used for verification. More comprehensive results, a covariance analysis using synthetic data, and ground-truth comparisons will be shown at the presentation.

There are currently no means for completely validating the results of this algorithm, since a map of measured soil moisture over the entire OJP stand is not available. However, if a sufficiently varied number of ground points are used, the results can be considered validated for all the points within the range of the soil moisture values of those points. It should also be mentioned that the OJP forest was considered due to its structural simplicity. In general, the scattering process in a forest consists of several mixed mechanisms. A complete solution is left for future versions of this algorithm.

ACKNOWLEDGMENT

This work was performed by the Jet Propulsion Laboratory, California Institute of Technology, under contract from the National Aeronautics and Space Administration.

REFERENCES

- [1] Moghaddam and S. Saatchi, "Analysis of scattering mechanisms in SAR imagery over boreal forest: Results from BOREAS'93," *IEEE Trans. Geosci. Remote Sensing*, vol. 33, no. 5, pp. 1290-1296, 1995.
- [2] Freeman and S. Durden, "A three-component scattering model for polarimetric SAR data," *IEEE Trans. Geosci. Remote Sensing*, in press.
- [3] Moghaddam and S. Saatchi, "Monitoring tree moisture using an inversion algorithm applied to SAR data," *IEEE Trans Geosci. Remote Sensing*, submitted.
- [4] Durden, J. van Zyl, and H. Zebker, "Modeling and observation of the radar polarimetric signature of forested areas," *IEEE Trans. Geosci. Remote Sensing*, vol. 27, pp. 290-301, 1989.

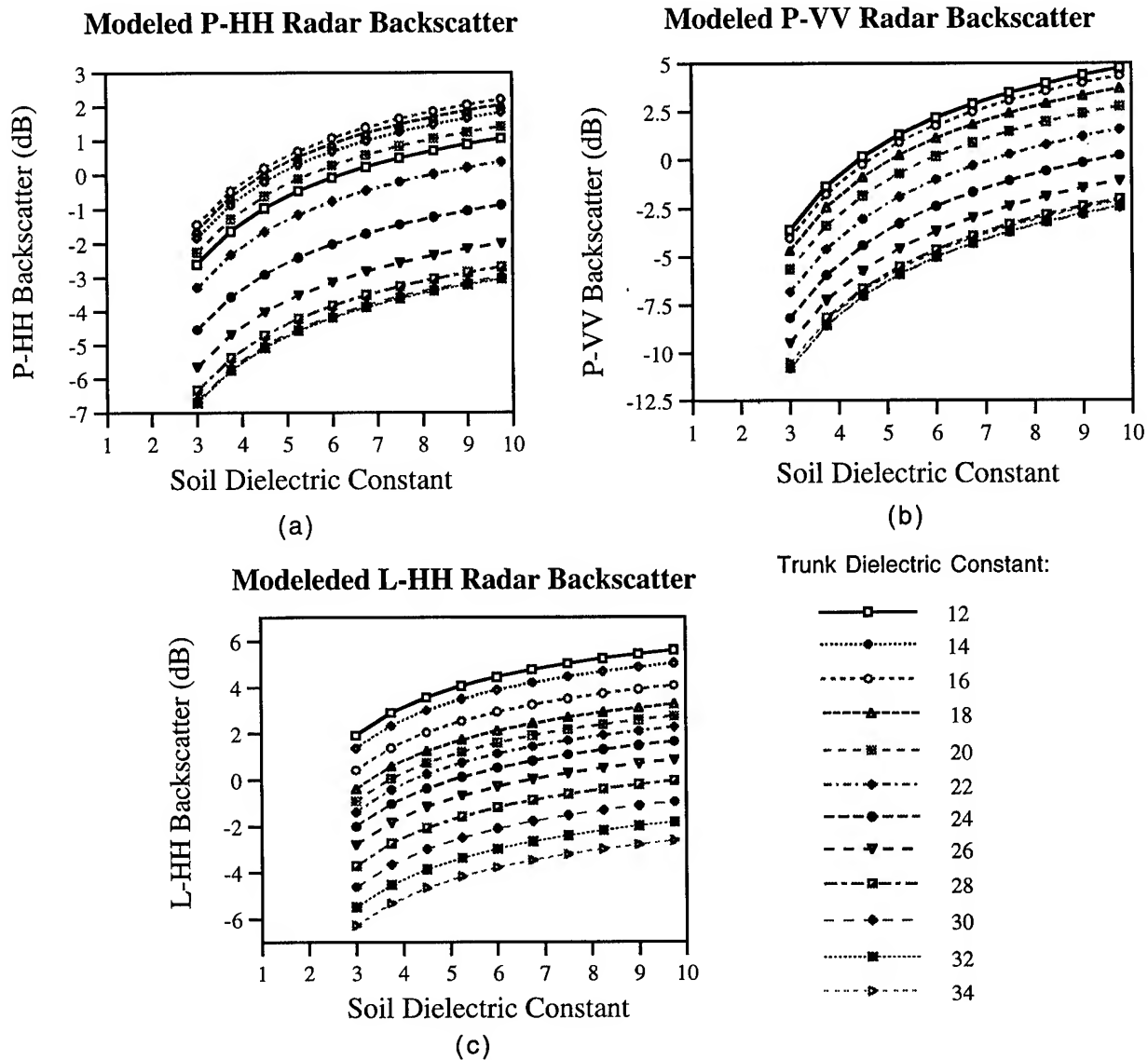


Figure 1. Radar backscatter curves from numerical forest scattering model for the BOREAS SSA OJP site.

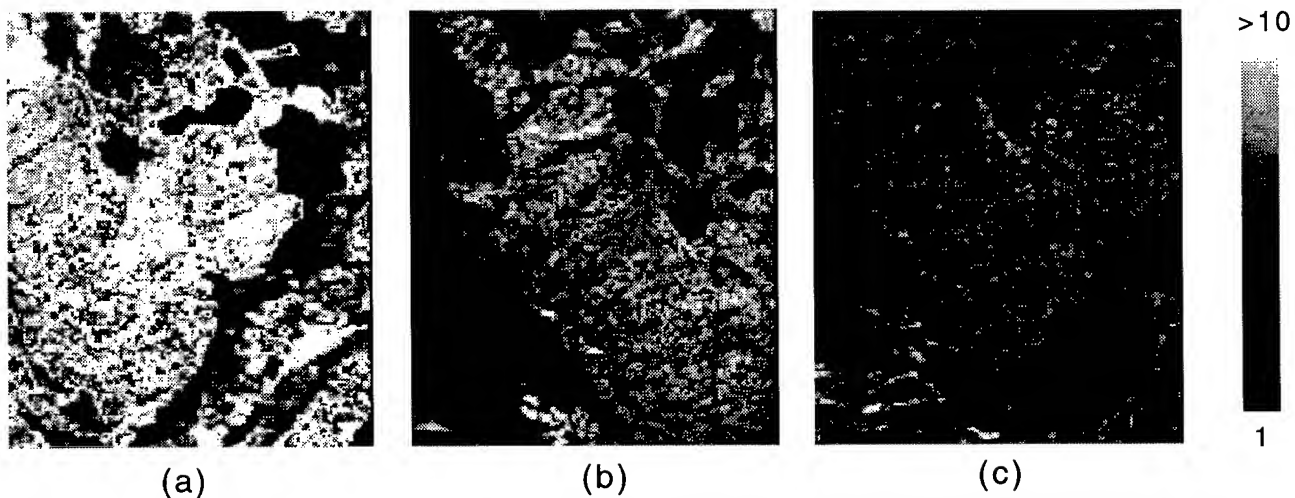


Figure 2. Estimated soil dielectric constant, linearly related to soil moisture, for the BOREAS SSA OJP site for (a) April 17, 1994, (b) July 28, 1994, and (c) September 20, 1994, using AIRSAR data.

Forest Vertical Structure from Multibaseline Interferometric Radar for Studying Growth and Productivity

Robert N. Treuhaft¹, Mahta Moghaddam¹, and Barbara J. Yoder²

¹Jet Propulsion Laboratory, MS 300-235
California Institute of Technology
4800 Oak Grove Drive
Pasadena, California 91109

Telephone: 818-354-6216 email: bob_treuhaft@radar-email.jpl.nasa.gov

²Oregon State University, Dept. of Forest Sci., Corvallis, OR 97331
Phone: 541-737-6110 email: yoderb@fsl.orst.edu

ABSTRACT

This paper describes the first quantitative attempt to estimate the vertical profile characteristics of forests from multibaseline interferometric radar (INSAR) data. In order to calculate the accuracy with which vertical characteristics can be estimated with INSAR, a simple, two-layer (subcanopy and canopy) forest is assumed to be observed by 4 baselines, most of which can be realized by current airborne systems. Calculations suggest that the height of the subcanopy layer, the total height of the forest, and the altitude of the underlying surface can be estimated with accuracies of 2-4 meters, with multiple baselines at C-band (wave length=0.056 cm). Extinction coefficients of each layer can be estimated with accuracies of 0.1 db/m. The estimation of height and extinction parameters from INSAR data is nonlinear, and accuracies therefore may depend heavily on the actual characteristics of the observed forest. This paper also discusses the application of vertical profile information estimated from INSAR to the identification of old-growth forests and their characteristics of growth and productivity. Because old-growth forests are characterized by layered vertical structures, the subcanopy and canopy characteristics discussed in this paper may enable identification and monitoring of old-growth stands, which in turn would facilitate ecosystem management and assessment of primary production on a global scale.

1. INTRODUCTION

For INSAR data taken over forests, the amplitude and phase of the complex cross-correlation depend on the vertical profiles of scatterer density and scattering amplitude. As shown in the next section, the cross-correlation can be expressed as an integral of functions of these profiles. Changing the INSAR baseline changes this integral. This paper begins to answer the following question: What is the accuracy of physical structure and scattering parameters estimated from a set of multibaseline INSAR measurements? A simple two-layer forest is treated in which the 6 estimated parameters (as shown in the next section) are 1) height-to-base-of-canopy (h_{tbc}), 2) total forest height (h_v), 3) subcanopy extinction coefficient (σ_{sc}), 4) canopy extinction coefficient (σ_c), 5) underlying surface topography (z_0), and 6) the canopy to subcanopy ratio of the product of the scatterer density and the squared backscattering amplitude (R). Expressions for the cross-correlation as a function of baseline and the 6 parameters are given in the next section. A simulation using 4 baselines, which can effectively be realized with current airborne systems, was performed and the derived parameter accuracies are presented in section 3. Section 4 discusses the application of these results to the identification and monitoring of old-growth forests.

2. THE INSAR CROSS-CORRELATION FOR A TWO-LAYER FOREST

In Appendix C, (C7) of [1], an expression is derived for the INSAR cross-correlation resulting from observations of a forest (volume scattering only) with arbitrary profiles of vertical density and scattering amplitude. The complex cross-correlation $\langle E(\vec{R}_1)E^*(\vec{R}_2) \rangle$ is proportional to:

The research described in this paper was carried out in part by the Jet Propulsion Laboratory, California Institute of Technology, under contract with the National Aeronautics and Space Administration.

$$\begin{aligned} & \langle E(\vec{R}_1)E^*(\vec{R}_2) \rangle \propto e^{ik(r_1-r_2)|_{z=z_0}} \\ & \times \int_0^{h_v} e^{i\alpha_z(\vec{B})z} \rho(z) < f_b^2(z) > \\ & \exp \left[\frac{-2}{\cos \theta_0} \int_z^{h_v} \sigma_x(z') dz' \right] dz \end{aligned} \quad (1)$$

where only the vertical z integration is shown (range and azimuth integrations are omitted here), because it is the only integration which depends on vegetation characteristics. In (1), \vec{R}_1 and \vec{R}_2 are the locations of the ends of the baseline vector \vec{B} , θ_0 is the incidence angle, k is the wavenumber, and h_v is the total height of the forest. In the first exponential term, $(r_1 - r_2)|_{z=z_0}$ is the difference in the pathlength to each end of the interferometer from a point with altitude z_0 at the forest floor, and this pathlength difference depends on \vec{B} . In (1), $\rho(z)$ is the number density of scatters at altitude z , $\langle f_b^2(z) \rangle$ is the average squared backscattering amplitude at z , and $\sigma_x(z)$ is the extinction coefficient at z , which also contains $\rho(z)$ [1]. The baseline dependence is explicitly called out in α_z , which is the derivative of interferometric phase with respect to altitude z . If the forest is assumed to be composed of two components, subcanopy (sc) and canopy (c), then with h_{tbc} the height-to-base-of-canopy:

$$\begin{aligned} & [\rho(z) < f_b^2(z) >] = [\rho_{sc} < f_{b_{sc}}^2 >]; \quad 0 < z < h_{tbc} \\ & [\rho(z) < f_b^2(z) >] = [\rho_c < f_{b_c}^2 >]; \quad h_{tbc} < z < h_v \\ & \text{and } R \equiv \frac{\rho_c < f_{b_c}^2 >}{\rho_{sc} < f_{b_{sc}}^2 >} \\ & \sigma_x(z) = \sigma_{sc}; \quad 0 < z < h_{tbc} \\ & \sigma_x(z) = \sigma_c; \quad h_{tbc} < z < h_v \end{aligned} \quad (2)$$

the normalized cross-correlation due to vegetation C_V can be written as:

$$\begin{aligned} C_V(\vec{B}) & \equiv \frac{\langle E(\vec{R}_1)E^*(\vec{R}_2) \rangle}{\sqrt{\langle E^2(\vec{R}_1) \rangle \langle E^2(\vec{R}_2) \rangle}} = \\ & \frac{C_{v1} + C_{v2}}{C_{v3} + C_{v4}} e^{ik(r_1-r_2)|_{z=z_0}} \quad \text{where} \\ C_{v1} & \equiv \frac{\exp[\frac{2\sigma_c h_{tbc}}{\cos \theta_0}]}{\alpha_z^2 + \frac{4\sigma_c^2}{\cos^2 \theta_0}} \left[\left(\frac{2\sigma_{sc}}{\cos \theta_0} \cos \alpha_z h_{tbc} + \alpha_z \sin \alpha_z h_{tbc} \right. \right. \\ & \left. \left. - \frac{2\sigma_{sc}}{\cos \theta_0} \exp\left[-\frac{2\sigma_{sc} h_{tbc}}{\cos \theta_0}\right] \right) + i \left(\frac{2\sigma_{sc}}{\cos \theta_0} \sin \alpha_z h_{tbc} \right. \right. \\ & \left. \left. + \alpha_z \exp\left[-\frac{2\sigma_{sc} h_{tbc}}{\cos \theta_0}\right] - \alpha_z \cos \alpha_z h_{tbc} \right) \right] \\ C_{v2} & \equiv \frac{R}{\alpha_z^2 + \frac{4\sigma_c^2}{\cos^2 \theta_0}} \left[\left(\frac{2\sigma_c}{\cos \theta_0} \exp\left[\frac{2\sigma_c h_v}{\cos \theta_0}\right] \cos \alpha_z h_v + \right. \right. \end{aligned}$$

$$\begin{aligned} & \alpha_z \exp\left[\frac{2\sigma_c h_v}{\cos \theta_0}\right] \sin \alpha_z h_v - \exp\left[\frac{2\sigma_c h_{tbc}}{\cos \theta_0}\right] \frac{2\sigma_c}{\cos \theta_0} \cos \alpha_z h_{tbc} \\ & \left. - \alpha_z \exp\left[\frac{2\sigma_c h_{tbc}}{\cos \theta_0}\right] \sin \alpha_z h_{tbc} \right) \\ & + i \left(-\alpha_z \exp\left[\frac{2\sigma_c h_v}{\cos \theta_0}\right] \cos \alpha_z h_v + \right. \\ & \left. \frac{2\sigma_c}{\cos \theta_0} \exp\left[\frac{2\sigma_c h_v}{\cos \theta_0}\right] \sin \alpha_z h_v + \alpha_z \exp\left[\frac{2\sigma_c h_{tbc}}{\cos \theta_0}\right] \cos \alpha_z h_{tbc} \right. \\ & \left. - \frac{2\sigma_c}{\cos \theta_0} \exp\left[\frac{2\sigma_c h_{tbc}}{\cos \theta_0}\right] \sin \alpha_z h_{tbc} \right) \Big] \\ C_{v3} & \equiv \exp\left[\frac{2(\sigma_c - \sigma_{sc})h_{tbc}}{\cos \theta_0}\right] \frac{\exp\left[\frac{2\sigma_{sc} h_{tbc}}{\cos \theta_0}\right] - 1}{\frac{2\sigma_{sc}}{\cos \theta_0}} \\ C_{v4} & \equiv R \frac{\exp\left[\frac{2\sigma_c h_v}{\cos \theta_0}\right] - \exp\left[\frac{2\sigma_c h_{tbc}}{\cos \theta_0}\right]}{\frac{2\sigma_c}{\cos \theta_0}} \end{aligned} \quad (3)$$

Although (3) is algebraically complex, the integrations required by (1), substituting (2), are elementary. In the next section, multiple baseline data are simulated to determine the accuracies with which the 6 parameters on which C_V depends can be estimated.

3. VERTICAL STRUCTURE PARAMETER ACCURACIES FROM MULTIBASELINE SIMULATIONS

In this section, the 6 parameters mentioned in the introduction, on which $C_V(\vec{B})$ depends, will be estimated from simulated data obtained by varying \vec{B} in (3). Four baseline lengths will be used: 2.5 m, 5 m, 10 m, and 20 m, all inclined at an angle of 66.25° to the horizontal, as in TOPSAR[2]. These baselines will be assumed to be at altitude of 8000 m, typical of TOPSAR, at an incidence angle of 35°. The physical TOPSAR baseline at C-band of 2.5 m can also be operated in "ping-pong" mode, in which signals are transmitted from alternate ends of the baseline, which produces an effective 5-m baseline. Because α_z in (1) and (3) depends on the ratio of baseline to altitude, the above baselines can effectively be realized by flying TOPSAR at 8000 m, 4000 m, and 2000 m in order to demonstrate the parameter estimation described in this paper. Given 6 values of the input parameters, (3) was used to calculate the amplitude and phase of the complex cross-correlations for the 4 baselines, i.e. 8 observations in all. Standard deviations used to Monte Carlo amplitude and phase were calculated following [3]:

$$\begin{aligned} \sigma_{|C_V|} & \approx \frac{1 - |C_V|^2}{\sqrt{2N}} \\ \sigma_\phi & \approx \frac{\sqrt{1 - |C_V|^2}}{\sqrt{2N}|C_V|} \end{aligned} \quad (4)$$

where N is the number of independent looks. These standard deviations, which represent "speckle noise," i.e. the random distribution of scatterers from look to look, with small corrections for the loss of correlation amplitude due to finite range resolution [1], were used to generate Monte Carlo data, which were then fed to a nonlinear least squares estimation procedure to extract distributions of the 6 parameters. Thermal noise, a small correction, was not included. The table below shows the mean \pm the standard deviation of the profile parameters for 50 and 100 radar looks, with the truth values for the simulation at the top of each column. For a roughly 5-m square look size, 50 and 100 looks correspond approximately to 35-m and 50-m square resolution, respectively.

From the table, it can be seen that the height-to-base-of-canopy, the total forest height, and the underlying topography were determined with accuracies of about 2-5 m, and the extinction coefficients of the two layers were determined at the 0.1-0.2 db/m level. The performance in the table will be tested with TOPSAR data in the coming year. Improvements to the performance calculation include accounting for correlations in speckle noise between baselines, accounting for the ground-trunk interaction and including polarimetry, and improving on the Monte Carlo nonlinear estimation procedure used here.

4. IDENTIFYING AND MONITORING OLD-GROWTH FORESTS WITH INSAR-ESTIMATED VERTICAL PROFILES

The definition of "old growth" is based largely on forest structure rather than tree age: old-growth forests are characterized by a multiple-story canopy that is structurally complex [4]. The estimation of the subcanopy and canopy parameters described in this paper may enable identification of forests with these structures. Identification, classification, and characterization of old-growth forests are particularly important in the Pacific Northwest of the United States. Management activities in the past have emphasized clearcut harvesting, causing severe loss in the

amount of old-growth habitat as well as extensive fragmentation of these habitats. These changes have led to significant declines in populations of animal species that depend on habitats characteristic of old growth forests. Negative impacts of past management practices on fisheries and other resources are also becoming increasingly clear.

Beyond basic classification, remote sensing offers the only realistic tool for predicting primary production on a global scale [5]. Measurements of the reflectance of visible and near-infrared radiation have produced predictions of primary productivity and transpiration of vegetation. However, algorithms based on reflected radiation significantly underestimate transpiration and primary production of old-growth stands. This is because the "conversion efficiency," or the amount of biomass growth per unit of absorbed solar energy, decreases as forests age. With the remotely sensed vertical structure information proposed here, it may be possible to adjust algorithms to account for age-related decline.

5. REFERENCES

- [1] R. N. Treuhaft, S. N. Madsen, M. Moghaddam, and J. J. van Zyl, "Vegetation Characteristics and Surface Topography from Interferometric Radar," *Radio Science*, **31**, 1449-1485, 1996.
- [2] H. A. Zebker, et al., "The TOPSAR Interferometric Radar Topographic Mapping Instrument," *IEEE Transactions on Geoscience and Remote Sensing*, **30**, 1992.
- [3] J. O. Hagberg, L. M. H. Ulander, and J. Askne, "Repeat-Pass SAR Interferometry Over Forested Terrain," *IEEE Trans. Geosci. Remote Sensing*, **33**, 331-340, 1995.
- [4] J. F. Franklin and T.A. Spies, "Ecological Definitions of Old-Growth Douglas-Fir Forests," in *Wildlife and Vegetation of Unmanaged Douglas-Fir Forests*, L. Ruggiero, ed., Gen. Tech. Rep. PNW-GTR-285, USDA Pacific Northwest Research Station, Portland, OR., 61-69, 1991.
- [5] H. A. Mooney and R.J. Hobbs, "Remote Sensing of Biosphere Function," *Ecological Studies*, R. J. Hobbs and H. A. Mooney, ed., **79**, Springer-Verlag, New York, 1-4, 1990.

Looks	h_{tbc} (m) (15)	h_v (m) (25)	σ_{sc} (db/m) (0.1)	σ_c (db/m) (0.3)	z_0 (m) (0)	R (2)
50	16.9 \pm 3.4	25.7 \pm 4.4	0.11 \pm 0.09	0.29 \pm 0.16	-0.8 \pm 4.2	3.3 \pm 1.8
100	16.2 \pm 2.3	25.5 \pm 3.2	0.12 \pm 0.08	0.32 \pm 0.12	-0.6 \pm 3.0	2.3 \pm 1.1

Simulation of Interferometric SAR Response to Deciduous and Coniferous Forest Stands

Kamal Sarabandi and Yi-Cheng Lin

Department of Electrical Engineering and Computer Science

The University of Michigan, Ann Arbor, MI 48109-2122

Tel : (313) 936-1575 FAX : (313) 647-2106 Email: saraband@umich.edu

Abstract – A coherent scattering model for tree canopies is employed in order to characterize the sensitivity of an interferometric SAR (INSAR) response to the physical parameters of forest stands. Combining the recently developed coherent scattering model for tree canopies and the INSAR Δk -radar equivalence algorithm, for the first time accurate statistics of the scattering phase center location of forest stands are obtained numerically. The scattering model is based on a Monte Carlo simulation of scattering from fractal generated tree structures, and therefore is capable of preserving the absolute phase of the backscatter. The model can also account for coherent effects and the inhomogeneous extinction. The location of the scattering phase center and the correlation coefficient are computed using the Δk -radar equivalence, simply by simulating the backscatter response at two slightly different frequencies. The model is successfully validated using the measured data acquired by JPL TOPSAR over a selected pine stand in Raco, Michigan.

INTRODUCTION

In recent years some experimental and theoretical studies have been carried out to demonstrate the potential INSARs in retrieving forest parameters. For example in [1] and [2] experimental data using ERS-1 SAR repeat-pass are employed to show the applications of SAR interferometry for classification of forest types and retrieval of tree heights. Also theoretical models have been developed to establish relationships between the interferogram phase and correlation coefficient to the physical parameters of vegetation and the underlying soil surface [3, 4]. Although these models give qualitative explanation for the measured data and provide a basic understanding of the problem, due to the oversimplified assumptions in the description of vegetation structure, they are not accurate enough for most practical applications. For example the shape, size, number density, and orientation distributions of vegetation in forest stands are nonuniform along the vertical direction. The nonuniform distributions of physical parameters of vegetation particles give rise to inhomogeneous scattering and extinction which significantly affects the correlation coefficient and the location of the vegetation scattering phase center.

Although there are a number of EM scattering models available for vegetation canopies, they are of little use with regard to INSAR applications due to their inability to predict the absolute phase of the scattered field. The absolute phase of the scattered field is the fundamental quantity from which the interferogram

images are constructed. The proposed model is basically composed of two recently developed algorithms: 1) a fully coherent scattering model for tree canopies based on a Monte Carlo simulation of scattering from fractal generated trees [5], and 2) extraction of the scattering phase center based on a Δk -radar equivalence relationship with INSAR [3].

MODEL DESCRIPTION

For an accurate estimation of the scattering phase center and the backscattering coefficients, the algorithm for generating desired tree structures must be capable of producing realistic tree structures and yet be as simple as possible. It has been shown that geometrical features of most botanical structures can be described by only a few parameters using fractal theory. To generate fractal patterns we use Lindenmayer systems which are versatile tools for implementing the *self-similarity* throughout a so-called rewriting process. For a tree-like structure, some essential botanical features must be added to the fractal process, including branch tapering in length and cross section, leaf placement, and randomizing the fractal parameters according to some prescribed probability density functions. The botanical features and the probability density functions must be characterized according to in-situ measurements of a given stand. Fig.1 (a) and (b) show the fractal maple and pine, respectively, generated by the fractal model in this study.

Once a tree structure is generated, the scattered field is computed by considering the tree structure as a cluster of scatterers composed of cylinders (trunks and branches) and disks/needles (leaves) with specified position, orientation, and size. The attenuation and phase shift due to the scattering and absorption losses of vegetation particles within the tree canopy are taken into account in the computation of the scattered field from individual particles. To the first order of scattering approximation, the backscatter from the entire tree is calculated from the coherent addition of the individual scattering terms. Hence, neglecting the multiple scattering among the scatterers, the total scattered field can be written as

$$\mathbf{E}^s = \frac{e^{ikr}}{r} \sum_{n=1}^N e^{i\phi_n} \mathbf{S}_n \cdot \mathbf{E}_o^i, \quad (1)$$

where N is the total number of the scatterers, \mathbf{S}_n is the individual scattering matrix of the n -th scatterer, and ϕ_n is the phase compensation accounting for the shifting of the phase reference from the local to the global phase reference, given by $\phi_n = k_0(\hat{k}_i - \hat{k}_s) \cdot \mathbf{r}_n$, where \mathbf{r}_n is the position vector of the n -th

scatterer in the global coordinate system. The individual scattering matrix S_n can be written as $S_n = S_n^t + S_n^{gt} + S_n^{tg} + S_n^{gg}$.

An INSAR system measures the backscatter of a scene at two slightly different look angles, and the phase difference between the two backscattered fields is used to derive the elevation information. In a recent study [3] it has been established that similar information can be obtained by measuring the backscatter of the scene at two slightly different frequencies provided that the look angle is known. For an INSAR system with known baseline distance (B) and angle α operating at frequency f_0 , the frequency shift (Δf) of an equivalent Δk -radar is given by $\Delta f = f_0 B \sin(\alpha - \theta) / mr$ where θ is the looking angle, $m = 1, 2$ for repeat-pass, and two-antenna INSAR configurations respectively, and r is the distance between the antenna and the scatterer. In Monte Carlo simulations, once the tree structure and the scattering configuration are determined, the backscatter signals are calculated twice at two slightly different frequencies. The backscatter at $f_1 = f_0$ and $f_2 = f_0 + \Delta f$ are represented by E_1 and E_2 respectively, which are computed from

$$E_1 = \sum_{n=1}^N e^{2ik_0 \hat{k}_i \cdot \mathbf{r}_n} S_n(k_0) \cdot \mathbf{E}_o^i, \quad (2)$$

$$E_2 = \sum_{n=1}^N e^{2i(k_0 + \Delta k) \hat{k}_i \cdot \mathbf{r}_n} S_n(k_0 + \Delta k) \cdot \mathbf{E}_o^i. \quad (3)$$

It is also shown that the height of the equivalent scatterer above the x-y plane of the global coordinate system can be determined from

$$z_e = \frac{-\Delta \Phi}{2\Delta k \cos \theta}, \quad (4)$$

where $\Delta k = 2\pi\Delta f/c$, and $\Delta \Phi = \angle(E_1^* E_2)$ represents the phase difference between E_1 and E_2 . For a random medium like a forest stand, the scattering phase center height (z_e) is a random variable whose statistics are of interest. Usually the mean value and the second moment of this random variable are sought. Based on a rigorous statistical analysis [3] it is shown that the statistics of $\Delta \Phi$ can be obtained from the frequency correlation function of the target by computing

$$\alpha e^{i\zeta} = \frac{\langle E_1^* E_2 \rangle}{\sqrt{\langle |E_1|^2 \rangle \langle |E_2|^2 \rangle}}, \quad (5)$$

where α is the correlation coefficient, and ζ is the coherent phase difference. Here $\langle \cdot \rangle$ denotes the ensemble averaging which is evaluated approximately using a sufficiently large number of realizations through the Monte Carlo simulation. The apparent height of the scattering phase center of a forest stand is proportional to ζ and can be obtained from

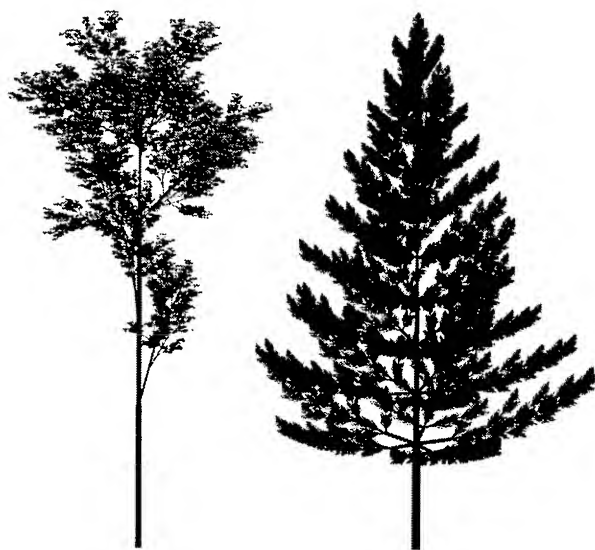
$$z_e = \frac{-\zeta}{2\Delta k \cos \theta}. \quad (6)$$

VALIDATION

The model predictions are compared with the JPL TOPSAR measurements over a selected pine stand, denoted as Stand 22. Stand 22 is a statistically uniform red pine forest located within Raco Airport, Raco, Michigan. This scene was selected for this study because the stand is over a large flat terrain which reduces the errors in the measured tree height due to possible surface topographic effects. In addition, the nearby runway provides a reference target at the ground level. Ground truth data for this stand have been collected since 1991 and careful in-situ measurements were conducted by the authors during the overflights of TOPSAR in late April, 1995. The JPL TOPSAR is an airborne two-antenna interferometer, operating at C-band (5.3 GHz) with vv polarization configuration. During this experiment, Stand 22 was imaged twice at two different incidence angles 39° and 53° .

Figure 2 shows a portion of the 39° radar image which includes the test stand. Each side of the dark triangle in this image is a runway of about 2 miles long. The measured height of the stand is obtained from the elevation difference between the stand and the nearby runway. The backscattering coefficient and the location of the scattering phase center as a function of the incidence angle were simulated at 5.3 GHz. As shown in Figures 3 and 4, excellent agreement between the model predictions and TOPSAR measurements is achieved. The simulated height of the scattering phase center of the same forest for an hh -polarized INSAR having the same antenna configuration and operating at the same frequency is also shown in Figure 3. It is shown that the estimated height at the hh -polarization configuration is lower than that obtained from the vv -polarization configuration. This result is usually true for most forest stands since the ground-trunk backscatter for hh -polarization is much higher than that for vv -polarization. Also noting that the location of the scattering phase center for a ground-trunk backscatter component is at the air-ground interface, the location of the scattering phase center of trees for hh -polarization is lower than that for vv -polarization.

The comparison between the simulated σ_{vv}^0 and the measured σ_{vv}^0 acquired by TOPSAR as a function of the incidence angle is shown in Figure 4. Also shown in this figure is the contribution of each scattering component (the direct backscatter σ^t and the ground-bounce backscatter σ^{gb}) to the overall backscattering coefficient. It was found that the contribution of the double ground-bounce component σ^{gg} was relatively small and for most practical cases can be ignored. In this case, at low incidence angles ($\theta_i < 30^\circ$) the ground-bounce backscatter is the dominant component, whereas at higher incidence angles the direct backscatter becomes the dominant factor. This trend is the cause for the increasing behavior of the scattering phase center height as a function of the incidence angle found in Figure 3. It is worth mentioning that the contribution of pine needles to the overall backscattering coefficient was found to be negligible compared to the contribution from the branches and



(a) Fractal Maple

(b) Fractal Pine

Figure 1: The Fractal trees simulated for (a) maple and (b) pine.

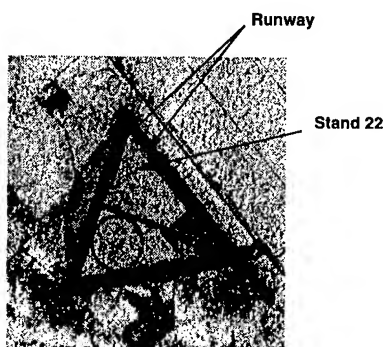


Figure 2: A portion of a TOPSAR C-band image (σ_{vv}^0), indicating Stand 22 at an airport near Racine, Michigan.

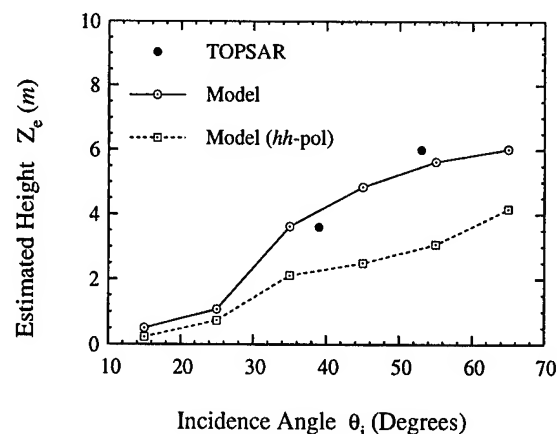


Figure 3: The estimated height of scattering phase center of Stand 22, compared with the data extracted from two TOPSAR images of the same stand.

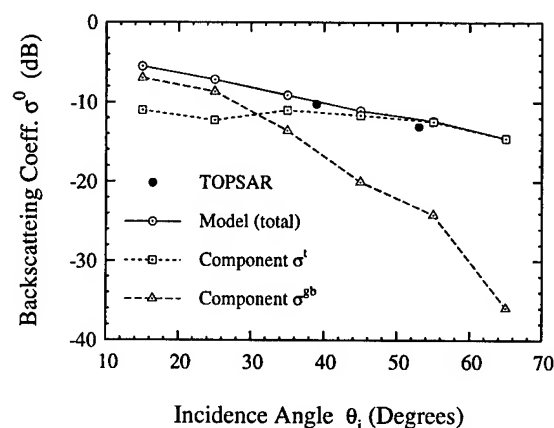


Figure 4: The simulated backscattering coefficient of Stand 22, compared with the measured σ_{vv}^0 extracted from two TOPSAR images of the same stand.

tree trunks. However, inclusion of the needles in the scattering simulation was necessary because of their significant effect on the extinction.

REFERENCES

- [1] J. O. Hagberg, L. M. H. Ulander, and J. Askne, "Repeat-pass SAR Interferometry over forested terrain," *IEEE Trans. Geosci. Remote Sensing*, Vol. 33, pp. 331-340, March, 1995.
- [2] U. Wegmuller and C. L. Werner, "SAR Interferometry Signature of Forest," *IEEE Trans. Geosci. Remote Sensing*, vol. 33, pp. 1153-1161, Sep. 1995.
- [3] K. Sarabandi, " Δk -Radar equivalent of interferometric SARs: a theoretical study for determination of vegetation height," in press.
- [4] R. N. Treuhaft, S. N. Madsen, M. Moghaddam, and J. J. van Zyl, "Vegetation characteristics and underlying topography from interferometric radar," *Radio Science*, Vol. 31, No. 6, pp. 1449-1485, 1996.
- [5] Y. C. Lin and K. Sarabandi, "A Monte Carlo Coherent Scattering Model For Forest Canopies Using Fractal Generated Trees," unpublished.

Processing and Analysis Techniques for Continental Scale Radar Maps of the Tropical Forest

Marc Simard^{1,2}, Gianfranco De Grandi¹, Sassan Saatchi³, Marc Leysen¹, Keith P.B. Thomson²

¹European Commission Joint Research Center, Space Applications Institute Monitoring Tropical Vegetation Unit TP 440, 21020 ISPRA (VA), Italia

²Centre de Recherche en Géomatique, Université Laval, Québec, Québec, Canada, E-Mail: simard@gmt.ulaval.ca, FAX: (418) 656-3607

³California Institute of Technology, Jet Propulsion Laboratory, Pasadena CA, USA

Abstract— A new avenue for radar mapping of the tropical forest at continental scale was recently proposed in the context of the European TREES (TRopical Ecosystem Environment monitoring by Satellites) project. The related issues ask for suitable approaches in the processing and analysis phases, which are the main focus of this paper. Some engineering aspects of the processing chain are described. Next the problem of information extraction from the mosaic with respect to the TREES thematic objectives is tackled. A first research topic is the ability to extract multi-scale structures of the tropical forest. The analysis was done using a technique based on the wavelet transform.

INTRODUCTION

We present a multi-resolution analysis and processing technique that is under investigation at the MTV unit of the Space Applications Institute at Ispra in the framework of the CAMP project (Central Africa Mosaic Project). CAMP is an attempt to bring space-borne SAR remote sensing into an entirely new perspective for global studies of the tropical ecosystem. The new approach called for the assemblage on demand and in a short turn around time of a vast amount of high resolution radar imagery from the SAR (Synthetic Aperture Radar) on-board the ESA ERS-1 satellite to obtain thematic information over the whole bio-geographical domain of Central Africa at several scales and with unprecedented completeness, spatial resolution and quality.

Using a high resolution radar sensor one can obtain information both at large geographical scale and at fine spatial detail; the access point to the data hierarchy - or the level of detail needed - is driven by the thematic application. The SAR sensor is therefore brought from the traditional role of gap filler or spatially limited hot spot analysis to the role of global mapping of an entire bio-geographical domain.

It is well known that radar sensors are useful for tropical forest mapping [1], [2], for cartography of drainage network, flooded regions [3], [4], [5], [6] and topographic features [5], [7]. But the passage from local to global area radar mapping entails peculiar scientific and engineering connotations. Large area coverage cannot be instantaneously obtained using an instrument with a narrow field of view and during an acquisition period (in the



Fig. 1. The ERS-1 SAR data of Sassandra site, Ivory coast. Two major classes of vegetation cover cannot be distinguished neither by intensity nor classical texture measures, the degraded (top left) and primary tropical forest (center left and bottom). The former class is characterised by large scale structures visible to the eyes. Features such as the river (dark line), the savannas (dark extended areas along the river), the town (group of white dots in the center right near the river) and agricultural fields (under the town) are also visible. ©JRC

present case roughly 2 months), spatio-temporal variations inevitably occur across the area. Ways to identify them and take them into account must be developed. Therefore contextual measures must be considered. Such a measure takes into account intensity values of neighbour pixels and their spatial variation: it is the image texture.

In the next sections, the Central Africa mosaic processing algorithm, based on the wavelet transform, is described whereby both low-resolution image versions and texture maps are produced. Indeed this technique is a first step towards an automatic classification of the large and thematically diversified Central Africa mosaic.

THE WAVELET TRANSFORM

In this section, the wavelet theory will not be described in detail since it has been done extensively in most related papers (see [8], [9]). The wavelet transform is a mathematical tool which allows for the decomposition of an image at different scales. Application of the theory to image decomposition is described in a paper by Mallat [8].

The original image is decomposed onto basis functions called the wavelets. The components of the image on the basis are called the wavelet coefficients $c_{a,b}$ and are defined as the inner product: $c_{a,b} = \langle f, \psi_{a,b} \rangle$, where a is

the scale of analysis and b is the spatial position. Intuitively, features in an image will be detectable from their size with respect to the scale of analysis a . The larger is $c_{a,b}$, the larger is the amount of structure in the image at position b and scale a . Therefore, by analysing the statistics and amplitude of those components one can describe the characteristics of an image at a given scale a and space location b . It is a multiscale measure of texture.

Many wavelet basis exist and one can choose according to the application and needs. We chose to use the cubic spline wavelet. Because of its large central lobe, smoothness and symmetry, we consider that it is well suited for homogeneous area texture analysis and characterisation.

MOSAIC PROCESSING

The original images supplied by ESA (over 450 images) are ERS-1 PRI at 25m resolution and a 12.5m pixel spacing; each file takes roughly 130 megabytes of disk storage. In order to manipulate the large amount of data and to respect the thematic goals of the project, a compromise on the resolution of the mosaic must be reached. Those considerations must always take into account the final goal which is the production of a classified thematic map of the tropical forest in Central Africa. Thus it is important to conserve all information that would allow for distinction between the different classes of targets, therefore the resolution of the mosaic should correspond to the scale at which we consider important structures to exist.

As a test case, we use the SAR image shown in Fig.1 taken over Sassandra, Ivory coast. The image contains two major classes, primary and degraded forest, which can not be classified on an intensity basis only, nor with classical texture measures, even though they are visually different in the texture content at large scale. In fact the degraded forest is a mosaic of small agricultural fields, savannas and patches of forests.

A first and classical approach to evaluate the scale at which structures can be used to identify targets, is to compute the power spectrum over different classes. The one dimensional range power spectrum was calculated for the primary and degraded tropical forest cases. In order to reduce noise the power spectrum was averaged over lines in azimuth. A total of 192 azimuth spectra were averaged. Fig.2 shows the resulting power spectra. Distinction in the spatial frequency content between the two targets is located in the low-frequency interval at scales greater than about 150m.

The mosaic processing is based on the wavelet decomposition algorithm developed by Mallat [8]. The algorithm that was used is shown in Fig.3. As mentioned earlier, the cubic spline wavelet is used as a basis. The wavelet transform is equivalent to a series of high and low-pass filtering steps followed by sub-sampling. The characteristics of the low-pass filter allow for conservation of low-frequency

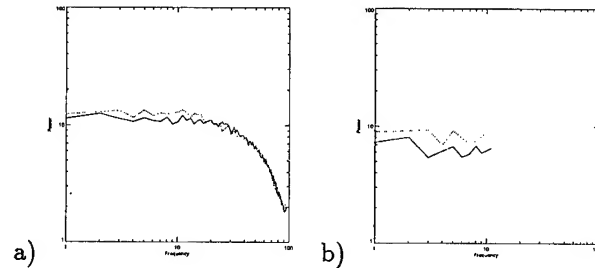


Fig. 2. a) Average power spectrum, with power amplitude in decibels and frequency on a logarithm scale in cycles/pixels (analysis window size=192 pixels, Nyquist=96) for primary tropical forest (dots) and degraded forest (full line). Distinction between the two classes is observed a low-frequency interval starting at 15 (about 150m). b) This figure shows the low-frequency conservation of the spline filtering, where the power spectrum is averaged over the same area at a resolution of 200m (Nyquist=12).

(large scale) content of the image to which we are interested. This is very important since this is where information for target distinction lies as seen from the power spectra.

As seen in the algorithm of Fig.3, we obtain to types of output. One is a low-pass version of the original image, which constitutes the base image for the construction of the Central Africa mosaic. The other type is the set of detail images. They are the wavelet coefficient images at a given scale (twice the scale of the input image) and contain the amount of structure at that scale; therefore they are an expression of texture. In order to build a texture map, the set of detail images, are added together to form an image which contains all structure at a given scale with no orientation bias. The sum is then normalised by the intensity low-pass image to produce a normalised scalogram [10], [11].

Because the wavelet transform acts as a band-pass filter and isolates a frequency interval, one can retrieve the important interval in the power spectrum where useful information exist. Fig.2(b) shows the power spectrum for the same regions as in Fig.2(a). It is readily seen that large scale structures are well conserved and that useful information is at a scale larger than 150m. Since the wavelet decomposition algorithm decomposes the original (12.5m pixel spacing) signal on a dyadic basis (octaves), we need to proceed to the 3rd and 4th decomposition levels, describing the image features of 100 and 200m in scale.

RESULTS AND CONCLUSIONS

The texture image (normalised scalogram) is shown on Fig.4 at a scale of 200m. The amount of structure (texture) is given by the value of the wavelet coefficients (or the normalised scalogram). Structure content at 200m of the degraded forest is seen to be larger than for the primary forest. The other detected structures are due to strong edges between forest targets, savannas and the river.

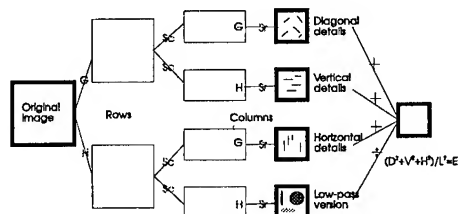


Fig. 3. The normalised scalogram (texture map) algorithm. The column and row filtering steps followed by subsampling by 2 correspond to Mallat's wavelet decomposition algorithm, where H is the low-pass filter and G the high-pass. The outputs are three detail images (3 orientations) and a low-pass version. The resulting wavelet coefficients are normalised by the low-pass intensity version which contains information orthogonal to the wavelet coefficients at the same scale. The wavelet coefficients are quadratically added to gather information in a single texture map E.

As a simple classification test, the normalised scalogram is averaged with a 3 by 3 window before applying a threshold. The averaging step constitutes the statistical first moment measure of the wavelet coefficient distribution. The resulting map is shown on Fig.4(b). Visual inspection and comparison of Fig.1 and Fig.4(b) shows the potential of the technique for classification of targets with the same first and second order statistics at small scales.

Targets such as the river and the savannas could easily be classified by their average intensity values. The agricultural areas are a more difficult case, since the backscattering varies with culture type and season. For example, they would be more easily classified from a multitemporal analysis over a dry season data acquisition. Classification of all targets could be improved by using a multiscale classification technique such as developed by Fau *et al.* [12].

In the future the multiscale measure will be used for continental scale classification algorithms for SAR thematic mapping of the Central Africa tropical forest, in the framework of JRC-CAMP and NASDA-GRFM (Global Rain Forest Monitoring) projects.

Image compression and noise reduction are other prospective applications of the wavelet decomposition algorithm.

ACKNOWLEDGMENTS

The stay of Marc Simard at the JRC was made possible because of the COLUTEC agreement and his grant from the Fond pour la Formation et Aide à la Recherche (FCAR), Québec. Additional support for Mr. Simard was also provided by Dr. Thomson's operating grant from the National Research Council for Science and Engineering of Canada (NSERC). He would also like to thank the support of the MTV unit staff at the JRC.

REFERENCES

[1] E. Nezry, E. Mougin, A. Lopes, J.P. Gastellu-Etchegorry, and Y. Laumonier, "Tropical mapping with combined visible and

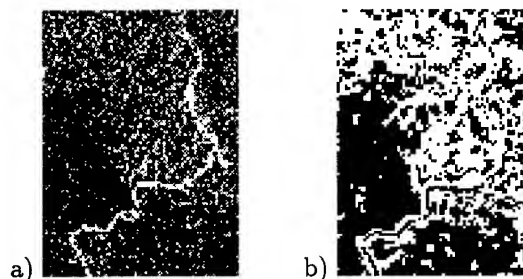


Fig. 4. (a) The normalised scalogram map is plotted to show structures (texture) which have a scale between 100 and 200m detected by ERS-1. (b) Threshold classified map of Sassandra region at 200m scale. In white are the degraded forest and non-forest areas while in black are the large primary tropical forests (left and bottom right). Also in black are the rivers and savannas which could be classified from average intensity alone. ©JRC

sar spaceborne data," *International Journal of Remote Sensing*, vol. 14, no. 11, pp. 2165, 1993.

[2] C.J. Oliver and R.G. White, "Optimum texture," *analysis of Synthetic aperture radar images*, vol. 2230, pp. 389, 1994.

[3] L.L. Hess, S. Filoso J.M. Melack, and Y. Wang, "Delineation of inundated area and vegetation along the amazon floodplain with sir-c synthetic aperture radar," *IEEE Transactions on Geoscience and Remote Sensing*, vol. 33, no. 4, pp. 896, 1995.

[4] L.L. Hess, J.M. Melack, and D.S. Simonett, "Radar detection of flooding beneath the forest canopy: A review," *International Journal of Remote Sensing*, vol. 11, no. 7, pp. 1313, 1990.

[5] H.J.H. Kux, F.J. Ahern, R.K. Raney, R.W. Pietsch, and B. Tittley, "The contribution of sarex'92 (south american radar experiment) campaign to the evaluation of natural resources in tropical rain forests: first results from test site acre, sw-amazonia, brazil," 16^e *Symposium canadien sur la télédétection et 8^e congrès de l'Association Québécoise de télédétection*, 1993.

[6] J.P. Ford and D.J. Casey, "Shuttle radar mapping with diverse incidence angles in the rainforest of borneo," *International Journal of Remote Sensing*, vol. 9, no. 5, pp. 927, 1988.

[7] Y. Rauste, Malingreau, and F. De Grandi, "Preliminary assessment of complementarity ers-1 jers-1 sar observations in the trees and grfm central africa mosaic projects," *Proceedings of the 3rd ERS-1 symposium, Florence, Italy*, 1997.

[8] S.G. Mallat, "A theory for multi-resolution signal decomposition: The wavelet representation," *IEEE Transactions on pattern and machine intelligence*, vol. 11, no. 7, pp. 674, 1989.

[9] O. Rioul and M. Vetterli, "Wavelets and signal processing," *IEEE SP magazine*, vol. 10, pp. 14, 1991.

[10] M. Simard, F. DeGrandi, K.P.B. Thomson, and G.B. Béné, "Analysis of speckle noise contribution on wavelet decomposition of sar images," *Submitted IEEE Transactions on Geoscience and Remote Sensing*, 1997.

[11] M. Simard, F. DeGrandi, K.P.B. Thomson, and M. Leysen, "Sensitivity analysis of ers-1 sar signal to multiscale structures of the tropical forest by means of the wavelet transform," *Proceedings of the 3rd ERS-1 symposium, Florence, Italy*, 1997.

[12] R. Fau, G.B. Béné, J.-M. Boucher, and D.-C. He, "Segmentation markovienne pyramidale d'images," *Journal canadien de télédétection*, vol. 20, no. 2, pp. 150, 1994.

Atmospheric Correction over a Composite Land and Water Surface

Tsutomu Takashima and Kazuhiko Masuda*

EORC/ NASDA, Roppongi First Bldg 14F, Roppongi 1-9-9

Minato-Ku, Tokyo 106, Japan

Phone: 81-3-3224-7084, Fax: 81-3-3224-7052

e-mail: tak@eorc.nasda.go.jp

and

Meteorological Research Institute, Tsukuba, Japan*

Abstract: An atmospheric correction algorithm for satellite visible data over a composite land and water surface is proposed. The proposed algorithm includes correction of the adjacency effect in an atmosphere-land (water surface) surface system. A typical numerical simulation is performed over the Tsukuba area in Japan at a wavelength of $0.56 \mu\text{m}$, which corresponds to the center wavelength of the second channel of AVNIR on ADEOS or the shortest channel of ASTER on EOS-AM1 (to be launched in 1998).

1. INTRODUCTION

One of the main objectives of the Advanced Visible and Near-infrared Radiometer (AVNIR) on the Advanced Earth Observing Satellite (ADEOS) is to derive surface reflection properties more precisely. The spatial feature of AVNIR to be stressed over other optical imagers is spectral data acquisition with a high spatial resolution of 16m. Quantization is performed at 8 bits/pixel; the swath width is 80km, corresponding to a satellite nadir angle of $\pm 2.86^\circ$ if the satellite altitude is 800km. Thus the observations are concentrated within very narrow nadir angles.

To derive the Earth surface (ocean) parameters more precisely, the effect of the atmospheric constituents is

eliminated. Furthermore, over land, the underlying terrain is composed of a variety of reflectances. In this case, the adjacency effect on satellite data due to the inhomogeneous surface should be included in the investigation of the atmospheric correction code.

Based on the simulation of atmospheric effects on the emergent radiation over a checkerboard type of terrain, an operational procedure for the atmospheric correction is described [1]. The upwelling radiation emerging from the top of the atmosphere is expressed as the sum of hemispherical integrals between the atmosphere and surface. The accuracy, however, depends upon the grid intervals rather than the number of interactions between the atmosphere and surface. The atmospheric correction over the Tsukuba area in Japan is performed as an example of a composite land and water surface. The land surface is assumed to be Lambertian, and the water surface is assumed to be a Cox & Munk model surface [2].

2. EMERGENT RADIATION OVER TSUKUBA

Fig.1 shows a topographical map of the Tsukuba area. The center is Kasumi-ga-Ura Lake, and the east side shows the coastal zone connecting to the Pacific ocean (Kashima Nada). The scattered urban areas are indicated by shading. The center vertical solid line is the

satellite orbit. Its swath is $\pm 40\text{km}$. The adjacency effect is considered within a distance of 30km from the subsatellite point. The Meteorological Research Institute is located at 36.05N , 140.13E . The solar azimuth is 20.8° from the satellite orbit. The solar zenith angle θ° between the summer solstice and the winter solstice is between 13° and 60° . Therefore, the computations were performed for 14.4° , 38.2° and 60° . The land surface is assumed to be Lambertian with an albedo of 0.4 , water surface is in accordance with the Cox & Munk model surface with a wind speed of 5m/sec , and the equivalent height of the atmosphere is assumed to be 7km . The atmosphere is assumed to be clear and hazy at a wavelength of $0.56\ \mu\text{m}$.

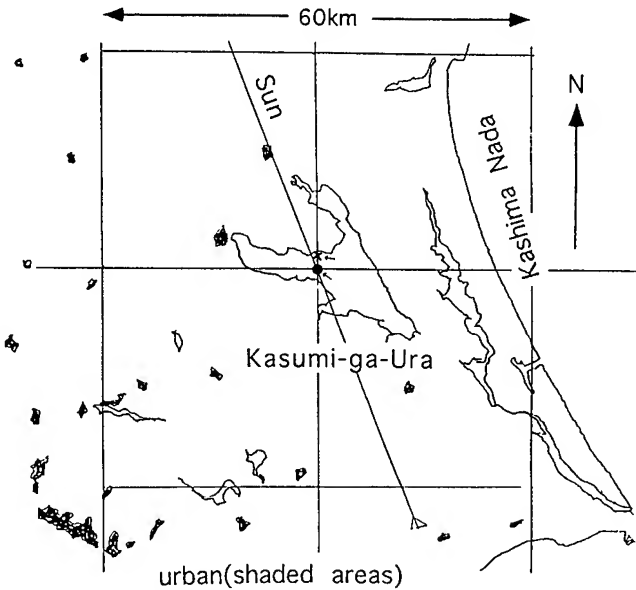


Fig. 1 Geographical Description of the Tsukuba Area. White areas indicate either lakes or rivers. Shading represents urban areas. The Pacific Ocean is located on the right hand side.

The optical thicknesses for molecular scattering and absorption are obtained by LOWTRAN7 [3] for the summer mid-latitude model. The aerosols are assumed to be the dust-like type provided by the

Radiation Commission, IAMAP [4]. Their size distributions are represented by lognormal distribution functions. The atmospheric total optical thicknesses adopted in this study are tabulated in Table 1.

3. EMERGENT RADIATION OVER THE LAKE

In the satellite observation direction, the radiation over the lake may be contaminated by radiation from the atmosphere and radiation reflected by the land. In general, the land reflectance is stronger than that of the water surface. Thus, over the lake, the radiance is not uniform. Furthermore, the effect of the land surface on the radiance over the lake may vary with the direction of the sun due to the water reflectance characteristics. The land surface effect decreases with increasing distance from the coast. The effect depends upon the atmospheric conditions, such as aerosol vertical distribution and scattering properties. To simplify the problem, the atmosphere is assumed to be homogeneously distributed up to an altitude of 7km . The effect of the surface was considered within a $20\text{km}\times 20\text{km}$ area. To begin with, the grid size is 1km . The contribution of the respective pixels to either the target pixel or the observation direction is calculated based on the reflection function and transmission function of the atmosphere. These numerical results are tabulated for frequent use to derive the emergent

Table 1 Optical thickness of molecules and aerosol at $0.56\ \mu\text{m}$. The aerosol is a dust-like aerosol with a single scattering albedo of 0.711 .

	Total	Aerosol (sct, abs)		Molecules (sct, abs)	
Clear	0.2330	0.0771	0.0229	0.0932	0.0398
Hazy	0.4821	0.2690	0.0799	0.0932	0.0398

radiation. Basically, the upwelling radiation from the top of the atmosphere can be computed based on the present model in accordance with the required accuracy. The upwelling radiance over the Lake was calculated at two points in the satellite orbit. These points are denoted by symbols x and ●. "x" is located 0.5km (3.7km) off the north (south) coast. "●" is located 2.5 km (1.7km) off the north (south) coast. The adjacency effect is shown in Table 2.

The land effect on the upwelling radiance over the lake decreases with increasing distance from the coast line. The "x" mark shows the location of a +13.88%(+23.13%) increase under clear (hazy) conditions. The "●" mark shows the location of a +0.21% (+0.70%) increase under clear (hazy) conditions. The "x" mark is 0.5km off the coast. Thus the effect of the land is large. However, the "●" is 1.7km off the coast. Thus the effect is small. Note that the present aerosol model shows substantial absorption of the incident radiation by the aerosol (albedo is 0.711). Therefore, the adjacency effect is not large if the observation target is located far from the coast. The effect is expected to be the larger if the aerosol albedo is larger. In Table 2, the effect of the land on the radiance over the lake depends on the solar zenith angle. It is large (small) for $\theta_0 = 38.2^\circ$ ($\theta_0 = 14.4^\circ$).

Table 2. Land effect on the radiance over the lake

Location	Atm	Solar zenith angle		
		14.4°	38.2°	60.0°
x	Clear	+3.22%	+13.88%	+11.62%
	Hazy	+6.39%	+23.13%	+17.45%
●	Clear	+0.07%	+0.21%	+0.18%
	Hazy	+0.28%	+0.70%	+0.53%

CONCLUSION

An algorithm for deriving the emerging radiation from the atmosphere bounded by a composite land and water surface was developed. An example of numerical simulation was performed over the Kasumi-ga-ura lake. The radiance changed when the lake was scanned in the lake cross-track direction due to the effect of the land reflectance. The radiance depends upon the zenith angle of the Sun and atmospheric conditions. The computational time can be reduced by preparing a look-up-table for parameters for frequent use. Thus the present method can be used as an atmospheric correction code for an operational system.

ACKNOWLEDGMENTS

We would like to express our appreciation to the US-Japan science team members of ASTER on EOS-AM1 who encouraged us to develop the present code.

REFERENCES

- [1] T. Takashima and K. Masuda, "Operational procedure of atmospheric correction on satellite visible data allowing for the adjacency effect", Remote Sens. Environ., 1997.
- [2] C. Cox and W. Munk, "Some problems in optical oceanography", J.Mar.Res., 14, 63-78, 1955.
- [3] F. X. Kneizys et al., "User's guide to LOWTRAN 7", Air Force Geophysics Lab., AFGL-TR-88-0177, 149p, 1988.
- [4] IAMAP, "A preliminary cloudless standard atmosphere for radiation computation", Section 2, pp 78-107, Boulder, Colorado, 1982.

Algorithms for Atmospheric Correction for Ocean Color data

S. Mukai, I. Sano and K. Masuda*

Kinki University, 3-4-1 Kowakae, Higashi-Osaka, Osaka 577, Japan
Tel.+81-6-721-2332 / Fax.+81-6-730-1320 / mukai@im.kindai.ac.jp

*MRI-JMA, Tsukuba, Ibaraki 305, Japan

Abstract — Atmospheric correction algorithms for ocean color data given by ADEOS/OCTS are shown here. Our atmospheric correction is based on radiative transfer process in an atmosphere-ocean model. In order to achieve better atmospheric correction, this paper proposes two subjects; one is how to determine aerosol characteristics by referring to polarization measurements, the other is new definition of atmospheric correction coefficients.

It is found that an oceanic aerosol model with the log-normal size distribution of ($\bar{r} = 0.24\mu m$, $\sigma = 2.0\mu m$) is a good candidate to describe the polarization data measured on July 29th in 1996 over the ocean in Seto Inland Sea in Japan. We also found that our atmospheric correction provides an improved chlorophyll map near the sea surface on September 3rd in 1996.

INTRODUCTION

Radiative transfer process in an atmosphere-ocean model is simulated to achieve an efficient atmospheric correction for ocean color data given by the Ocean Color and Temperature Scanner (OCTS) onboard the Advance Earth Observing Satellite (ADEOS).

We have introduced an idea of atmospheric correction coefficients, which represent the values of a ratio of the water leaving radiance to the observed radiance at the satellite [1]. Namely the atmospherically corrected images are obtained by multiplication of the calculated coefficients to the raw ocean color data. In this work two kinds of atmospheric correction coefficients are proposed. Difference of the two comes from each idea that the chlorophyll density near the sea surface is interpreted by the upward intensity just above the sea surface or that just below the sea surface.

ATMOSPHERIC CORRECTION FOR OCEAN COLOR DATA

Ocean color remote sensing is expected to progress not only with the OCTS but also with SeaWiFS of the USA in 1997 [2], ADEOS II/GLI of Japan in 1999 and so on. At this time we focus our attention on atmospheric correction for ocean color data from OCTS and POLDER onboard the satellite ADEOS. The POLarization and Directionality of the Earth's Reflectance (POLDER) also has ocean color bands and it is designed for polarization observations which will provide useful information on atmospheric aerosols [3].

Atmospheric correction is the process of removal of contaminated atmospheric light from space-borne data. In particular, atmospheric correction is a key process for ocean color analysis, since the contribution of atmospheric light to the space-borne data is about 80 to 90% in the visible wavelengths over the ocean. It is well known that efficiency of atmospheric correction strongly depends on how we can set up an appropriate aerosol model to the satellite-image concerned. Observations for radiance and degree of polarization of atmospheric aerosols were undertaken over the ocean with a portable photopolarimeter. By using these data, the optical properties of aerosols are retrieved based on simulations of the polarization field. Then our atmospheric correction including multiple scattering in the atmosphere-ocean system, which involves the retrieved aerosol models, is examined. Finally the expected chlorophyll map near the sea surface is derived through bio-optical algorithms.

POLARIMETRIC PROPERTIES OF AEROSOLS

Degree of polarization is a good indicator to derive optical properties of aerosols, because polarization features strongly depend on characteristics of scattering particles. The polarization degree and radiance of skylight were observed over the Seto Inland Sea on July 29th in 1996. These measurements were undertaken by a portable photopolarimeter (called PSR1000), which has six observing bands at wavelengths 0.443, 0.490, 0.565, 0.670, 0.765 and 0.865 μm . These wavelengths and their bandwidths are set up to correspond to the observing channels for the ADEOS/OCTS and POLDER. The dots in Fig.1 present the observed polarization degree. Roughly speaking degree of polarization decreases with wavelength.

These polarization data are used for retrieval of optical parameters of aerosols such as size and refractive index based on scattering simulations. A single scattering phase matrix is composed of Rayleigh scattering by molecular gases and Mie scattering by aerosols. The values of the phase matrix elements strongly depend on the characteristics of aerosols because of the uniform distribution of molecular gases.

One of the most widely used size distributions, the single-mode log-normal representation with two param-

ters, the mode radius (\bar{r}) and the width of the log-normal curve (σ) is considered here. Thus it becomes our purpose to retrieve (\bar{r}, σ) for the log-normal distribution. Based on our simulations it is found that oceanic type (OC) aerosols with ($\bar{r} = 0.2\mu\text{m}$, $\sigma = 2.4\mu\text{m}$) can explain the degree of polarization measurements. The dashed and solid curves in Fig.1 represent the calculated results for the retrieved OC type aerosols, respectively, by single and multiple scattering simulations, whose detail descriptions are cited in our paper [4].

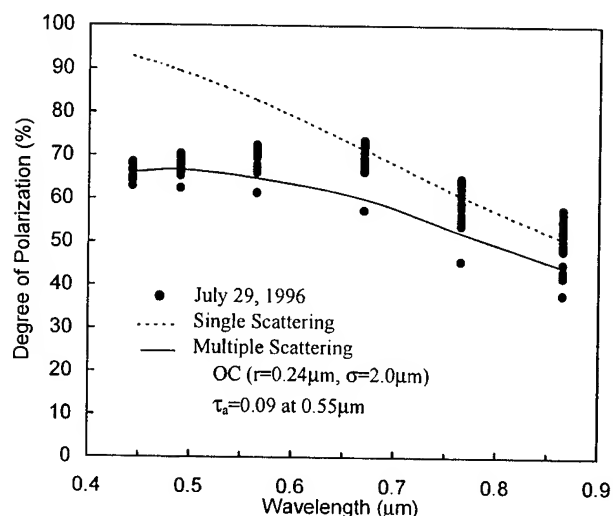


Fig. 1. Degree of polarization. The dots, and the dashed and solid curves represent the observed, and calculated values by single and multiple scattering simulations, respectively.

ATMOSPHERIC CORRECTION COEFFICIENTS

Our atmospheric correction is based on multiple scattering calculations in an atmosphere-ocean model. Fig.2 is an illustration of our atmosphere-sea surface-ocean model. The atmosphere model include the aerosol model derived in the previous section. Multiple scattering for the atmosphere-ocean model is solved by the adding-doubling method.

We consider two kinds of atmospheric correction coefficients $C1$ and $C2$ which represent a ratio of the upward intensity just above the sea surface and a ratio of the upward intensity just below the sea surface to that at the top of the atmosphere, respectively. Namely $C1 = I_A^+(\tau_A, \Omega)/I^+(0, \Omega)$ and $C2 = I_O^+(\tau_A, \Omega)/I^+(0, \Omega)$ by referring to Fig.2. The values of atmospheric correction

coefficients are obtained from multiple scattering calculations for an above mentioned atmosphere-sea surface-ocean model, and depend on the place of each pixel in an image as well as wavelength. The corrected image is obtained by multiplication of $C1$ or $C2$ values to the raw OCTS data.

Fig. 3 represents the expected chlorophyll map in units of $\mu\text{g/l}$. Here bio-optical algorithms by using ocean color data at wavelengths of 0.490, 0.520 and 0.565 μm are employed [5]. From this figure we found that our atmospheric correction based on the $C1$ -values provides an efficient chlorophyll map which is clearly demonstrated by the intrinsic stream of the Kuroshio Current in the Pacific Ocean in September.

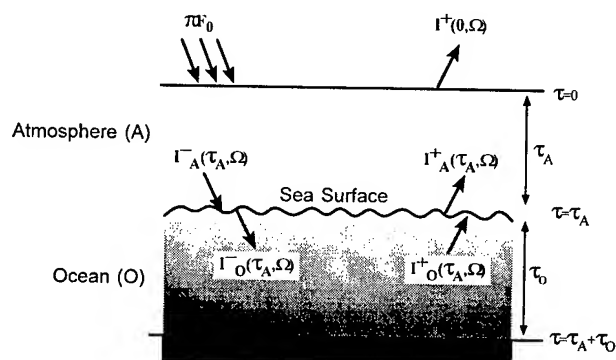


Fig. 2 An illustration of atmosphere-sea surface-ocean model.

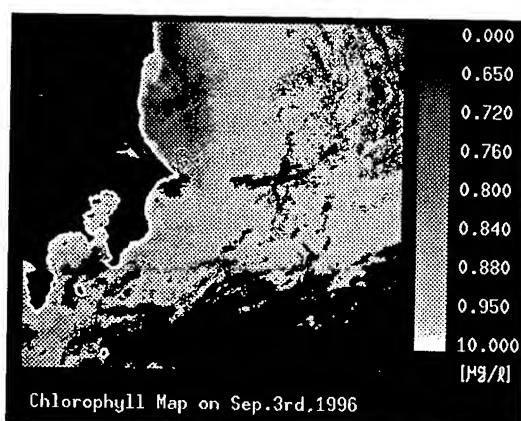


Fig. 3 Chlorophyll map on September 3rd in 1996.

DISCUSSIONS

It is found that an oceanic type aerosol with ($\bar{r} = 0.24\mu m$, $\sigma = 2.0\mu m$) can explain the polarization measurements in Seto Inland Sea, and our atmospheric correction involving the retrieved aerosol model provides an improved chlorophyll map of the sea surface near Japan by using ADEOS/OCTS ocean color data.

We can compare the upward radiance just below the sea surface (denoted by Below) with that just above the sea surface (Above) for two kinds of ocean model; one is clear water model (i.e. no hydrosols) denoted by the dashed curves and the other is an ocean model involving scattering type hydrosols (turbid) [6] denoted by the solid curves in Fig.4. It is found that the upward intensity at the sea surface level strongly depends upon the ocean model itself, and that just above the sea surface is different from that just below it. In this work two kinds of atmospheric correction coefficients, $C1$ and $C2$, have been proposed. At present it is difficult to determine which is better to interpret the chlorophyll density near the sea surface. At any rate, from a practical point of view, much more extensive measurements of atmosphere and ocean are desired to draw definite conclusions.

It is emphasized that satellite ocean color sensors should be mutually used with other sensors, e.g. combination use of OCTS and POLDER.

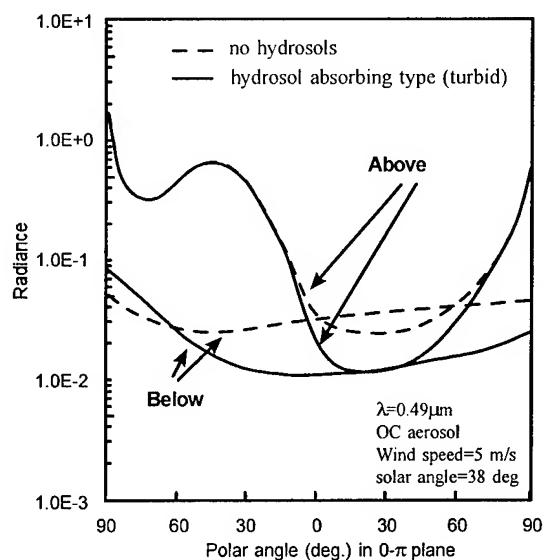


Fig. 4 Upward intensity at the sea surface level.

ACKNOWLEDGMENTS

The authors wish to express their thanks to Dr. Takashima of NASDA. This work was supported by NASDA (PSPC-18284), and also partially supported by scientific research funds from the Ministry of Education, Science and Culture of Japan (07640579).

REFERENCES

- [1] S. Mukai, I. Sano, K. Masuda and T. Takashima, "Atmospheric correction for ocean color remote sensing : Optical properties of aerosols derived from CZCS imagery," *IEEE Trans. Geosci. Remote Sensing*, vol.30, pp.818-824, 1992.
- [2] W. W. Gregg, F. S. Patt and R. H. Woodward, "Development of a Simulated Data Set for the SeaWiFS Mission," *IEEE Trans. Geosci. Remote Sensing*, vol.35, pp.421-435, 1997.
- [3] P. Y. Deschamps, F. -M. Bréon, M. Leroy, A. Podarie, A. Bricaud, J. C. Buriez and Sèze, "The POLDER mission: Instrument characteristics and scientific objectives," *IEEE Trans. Geosci. Remote Sensing*, vol.32, pp.598-615, 1994.
- [4] I. Sano, S. Mukai, M. Yasumoto, K. Masuda, M. Sasaki and H. Ishida, "Interpretation of Ground-based Measurements of Atmospheric Aerosols," *Proc. IEEE-IGARSS'97*, 1997.
- [5] NASDA, "ADEOS Reference Hand Book," Tokyo Japan, 1996.
- [6] M. Tanaka and T. Nakajima, "Effects of oceanic turbidity and index of refraction of hydrosols on the flux of solar radiation in the atmosphere-ocean system," *J. Quant. Spectrosc. Radiat. Transfer*, vol.18, pp.93-111, 1977.

An Atmospheric Correction Algorithm for Space Remote Sensing Data and Its Validation

A. Yamazaki, M. Imanaka, M. Shikada, T. Okumura, and Y. Kawata

Environmental Information Research Laboratory

Kanazawa Institute of Technology

Ogigaoka 7-1, Nonoichi, Ishikawa 921, Japan

Tel: 81-762-48-1100, Fax: 81-762-48-7753

E-mail: yamazaki@infor.kanazawa-it.ac.jp

Abstract -- In atmospheric correction for space remote sensing images, the atmospheric optical thickness at the time of satellite observation is critically needed and it is highly desirable to estimate this value from the satellite measured data itself. We presented an algorithm for estimating the meteorological range in the boundary layer from the measured satellite data. From the meteorological range value the atmospheric optical thickness can be found without difficulty. In this atmospheric correction algorithm we consider a one-dimensional vertically inhomogeneous radiative transfer model consisting of an atmosphere bounded by a flat Lambertian surface layer with a horizontally non-uniform albedo distribution. For the validation of atmospheric correction algorithm, we have made the simultaneous ground measurements of the surface reflectance and atmospheric optical thickness with the LANDSAT TM on Dec. 12, 1996. We found a good agreement between the measured and estimated albedo values in TM band 3 and 4, but it is acceptable in band 2.

INTRODUCTION

It is well known that the removal of atmospheric effects from the satellite image data is necessary. In this paper the atmospheric correction algorithm and the algorithm for estimating atmospheric optical thickness from the satellite image data set alone are presented. The validation results of these algorithms are also presented.

ATMOSPHERIC CORRECTION ALGORITHM

Let us consider the radiative transfer model in the

atmosphere bounded by a flat Lambertian surface layer with a horizontally non-uniform albedo distribution. Let (x, y) and z are rectangular coordinates defining ground target position and height position in the atmosphere, respectively. We assume that atmospheric model is a plane parallel homogeneous, vertically inhomogeneous, and anisotropically scattering atmosphere with optical thickness of τ , and parallel rays of a constant incident solar flux πF illuminates the top of the atmosphere ($z=z_0$) from direction of $\Omega_0 = (\theta_0 = \cos^{-1}\mu_0, \phi_0)$, where μ_0 and ϕ_0 are the cosine of the solar zenith angle and the solar azimuth angle, respectively. The upwelling diffuse intensity $I(z, x, y, -\Omega)$ at the top of the atmosphere in the direction of $-\Omega$ can be expressed by Eq.(1) [1], allowing for a single reflection of radiation by the target surface (x, y) and up to double reflections of radiation by the adjacent surface,

$$I(z, x, y, -\Omega) = \mu_0 FR(\tau, \Omega, \Omega_0) + A_t(x, y) \times (s \cdot \bar{A} + t) + (p - s)\bar{A}^2 + (q - t)\bar{A} \quad (1)$$

where $A_t(x, y)$, \bar{A} , and $R(\tau, \Omega, \Omega_0)$ are the albedo of the target, the mean albedo of the adjacent surface, and reflection function of the atmosphere, respectively. Reflection function $R(\tau, \Omega, \Omega_0)$ can be computed by the Doubling and Adding method [2]. Furthermore, p , q , s , and t in Eq.(1) are the radiation coefficients which can be expressed by the reflection and transmission functions of the atmosphere [1]. The mean emergent intensity at the top of the atmosphere can be given approximately by Eq.(2).

$$\bar{I}(z, x, y, -\Omega) = \mu_0 FR(\tau, \Omega, \Omega_0) + p \cdot \bar{A}^2 + q \cdot \bar{A} \quad (2)$$

The mean albedo and the target albedo are given by Eq.(3) and Eq.(4), respectively.

$$\bar{A} = \frac{\{-q + \sqrt{q^2 - 4p \cdot (\bar{I}_{obs} - \mu_0 FR(\tau, \Omega, \Omega_0))}\}}{2p} \quad (3).$$

$$A_i(x, y) = \frac{\{I_{obs} - (p - s) \cdot \bar{A}^2 - (q - t) \cdot \bar{A} - \mu_0 FR(\tau, \Omega, \Omega_0)\}}{s \cdot \bar{A} + t} \quad (4).$$

The atmospheric correction algorithm is given as follows[3]:

- (1) Adopt an appropriate atmospheric model and its optical parameters.
- (2) Compute the reflection and transmission functions, and the radiance coefficients, p , q , s , and t for a given incident solar illumination condition and a given wavelength band.
- (3) Compute the mean adjacent albedo \bar{A} from Eq.(3) by using \bar{I}_{obs} .
- (4) Compute $A_i(x, y)$ for each corresponding image pixel from Eq. (4) using the observed satellite-level intensity I_{obs} .
- (5) Repeat the above steps (2) to (4) and compute $A_i(x, y)$ for all image pixels in each wavelength band.

METEOROLOGICAL RANGE ESTIMATION

An algorithm for estimating the atmospheric optical thickness from the measured satellite image data itself is highly desirable, because it is not always possible to measure these parameters. In this study, we assume that an appropriate atmospheric optical thickness value can be deduced from the minimum radiance, $I_{obs.min}$, measured by the satellite sensor. In other words, we should have

$$\mu_0 FR_{path} = I_{obs.min} \quad (5),$$

with an appropriate atmospheric optical thickness. In this study, all atmospheric optical parameters, except for aerosol amounts in the boundary layer (altitudes: 0 - 2 km), are assumed to be kept constant and they are computed from MODTRAN code[4], by assuming the mid-latitude fall-winter model with the oceanic aerosol model. Since the aerosol optical thickness in the boundary layer can be found by inputting the meteorological range V at 0.55 μ m in MODTRAN code, we shall use V as a free varying atmospheric parameter, defining the atmospheric haze condition at the satellite observation time.

The estimation algorithm of V from the satellite data

is as follows:

- (1) First, compute a minimum observed radiance value within a given band image.
- (2) Compute the atmospheric path radiance by the Doubling and Adding method by changing value of V as a free parameter.
- (3) Find an appropriate value of V (or the aerosol optical thickness) which satisfies Eq.(5).

VALIDATION OF ALGORITHMS

We carried out the filed experiments for the validation of atmospheric correction algorithm at Heijogu(the Old Palace Site), near Nara City, Japan on Dec.12, 1996. We have made several simultaneous ground measurements of the atmospheric optical thickness and surface reflectance at LANDSAT overpassing time. The measurement results of the atmospheric optical thicknesses, the target's surface albedos are given in Fig. 1 and 2, respectively. The estimation study of the atmospheric optical thicknesses in bands 1, 2, 3, and 4 from the TM image data set has not finished yet at this moment, but the validation results of the atmospheric optical thickness will be presented at IGARSS'97 symposium. The estimation of the target's spectral albedo from the TM data set was done by applying our atmospheric correction algorithm by assuming $V=18$ km and the estimated target albedo values are plotted in Fig.2. The relative errors between the measurement and estimate values are 32.8%, 1.7%, and 8.3% in band 2, 3, and 4, respectively. The agreement in band 2 is rather poor, but it is good in other bands. The original TM image and estimated albedo image by our atmospheric correction algorithm are shown in Fig.3. The significance of the atmospheric correction is very clear by comparing two images (a) and (b).

CONCLUSIONS

We came to conclusions by this study as follows:

- (1) We presented an algorithm for estimating the meteorological range in the boundary layer from the measured satellite data.
- (2) The estimation of the target's spectral albedo from the TM data set was done by applying our atmospheric correction algorithm by assuming $V=18$ km. The relative errors between the measured and estimate albedo values are 32.8%, 1.7%, and 8.3% in band 2, 3, and 4, respectively.

(3) The significance of the atmospheric correction is shown clearly by comparing two images before and after the correction.

This study was supported by the Research Contract No. NASDA-PSPC-17710, National Aeronautics and Space Development Agency of Japan.

REFERENCES

[1] Y. Kawata, and et.al., "Radiometric Correction for Atmospheric and Topographic Effects on Landsat MSS

Images", Int. J. Remote Sensing, Vol.9, No.4, pp.729-748.

[2] J.E. Hansen, and L. Travis, "Light Scattering in Planetary Atmospheres," Space Sci. Review, vol. 16, pp. 527-610, 1974.

[3] Y. Kawata, and et.al., "Classification Accuracy for the MOS-1 MESSR Data Before and After the Atmospheric Correction", IEEE Trans. on GRE, Vol.28, No.4, pp.755-760.

[4] A. Berk, Bernstein, L.S., Robertson, D.C., "A Moderate Resolution Model for LOWTRAN 7", GL-TR-89-0122, 1989.

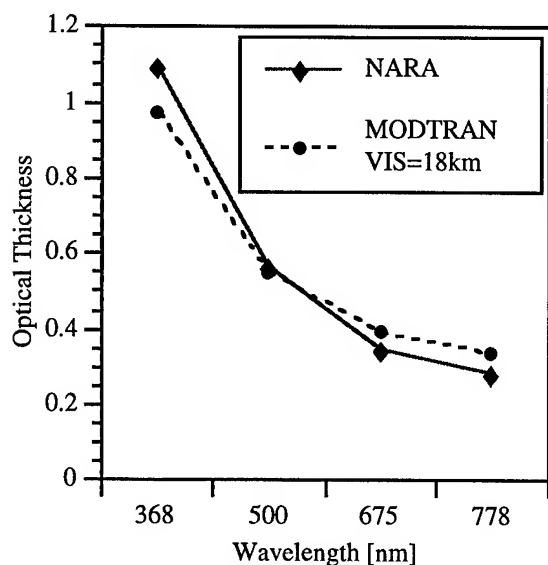


Fig.1. The atmospheric optical thickness data against the wave length, measured by the Sunphotometer PSF-100.

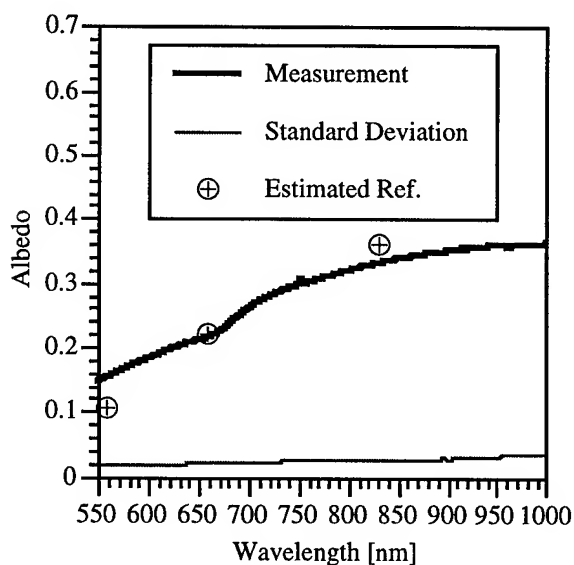
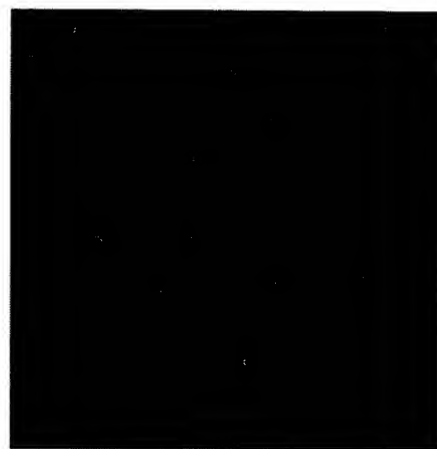
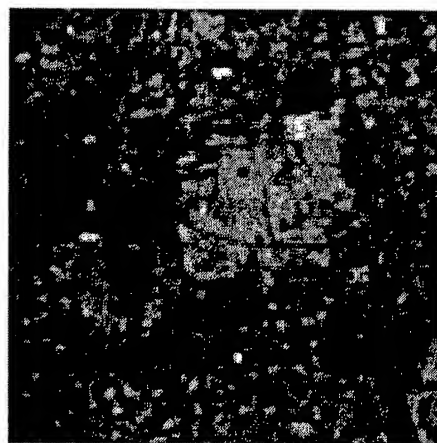


Fig.2. The spectral albedo of the target, measured by PS-1000 (Ocean Optics Co.LTD). The estimated albedo values from the TM images in bands 2, 3, and 4 are also plotted.



(a). Original TM image.



(b). Albedo image after the atmospheric correction.

Fig.3. The results of the atmospheric correction. The small subsection of the TM scene in band 4, including the target site (the Old Palace site), taken on Dec. 12, 1996. The significance of the atmospheric correction is very clear by comparing two images (a) and (b).

Estimation of Adjacent Effects in Polarization Measurements over the Coastal Zone

T. Kusaka, N. Taniguchi and Y. Kawata
Kanazawa Institute of Technology
7-1 Nonoichi-machi Ishikawa 921, Japan

Tel: +81-762-48-1100 Fax: +81-762-94-6727

E-mail: kusaka@manage.kanazawa-it.ac.jp

Abstract -- The polarization over the coastal zone observed by the airborne POLDER simulator, which was developed by CNES, France, is analyzed. It is shown that at the wavelength $\lambda=850\text{nm}$, the polarization degrees over the coastal zone become smaller than those over the sea surface at a long distance from the land, while at $\lambda=450\text{nm}$ the polarization pattern over the coastal zone is almost the same as that over the sea surface distant from the land. In this study, the adjacent effect that has influence on polarization measurements is evaluated by using a single scattering radiative transfer model. As a result, it is found that at $\lambda=850\text{nm}$, as adjacent effects arising from the radiation reflected by the land surface are more significant, the degree of polarization over the sea surface becomes smaller.

INTRODUCTION

The ADvanced Earth Observing Satellite (ADEOS) was successfully launched by the National Space Development Agency of Japan in 1996. It carries POLDER sensor developed by CNES, FRANCE. The POLDER sensor observes reflectances at 8 spectral bands in the visible and near infrared spectrum. In particular, the POLDER measures the polarized intensity at three different polarization angles at three of these channels (443, 670 and 865nm). The POLDER data sets are not yet available, and so Medimar data sets measured by the airborne POLDER simulator over Mediterranean Sea in 1991, which was developed by CNES to evaluate the POLDER data, are used in this study. The polarization over the sea and land surface measured by the airborne POLDER has been analyzed [1],[2],[3], but the polarization analysis in the coastal zone has not been done enough.

We first analyze the polarization over the coastal zone measured by the airborne POLDER, and show that the equi-polarization contours over the coastal zone are significantly different from those over the sea surface far away from the land at the wavelength $\lambda=850\text{nm}$. This indicates that at $\lambda=850\text{nm}$, the radiation reflected by the land surface has significant effects on the polarized intensity over the sea surface adjacent to the land surface. Therefore, we next simulate the linear polarization in the coastal zone by the single scattering radiative transfer

model including Stokes parameters. Finally, it is shown that at $\lambda=850\text{nm}$ the degree of polarization over the coastal zone becomes smaller, as compared with the polarization over the sea surface at a long distance from the land.

POLARIZATION OBTAINED FROM AIRBORNE POLDER

The airborne POLDER observes the polarized intensities at wavelengths 450 and 850nm. The flight altitude of the airborne sensor is 4700m, and the zenith angle of the sun is 38° and the azimuth angle 190° . The dimension of one image acquired by the airborne POLDER is 288×384 pixels area. The linear polarization (L_p) is obtained from the polarized intensities, I_1 , I_2 and I_3 , measured at three different polarization angles, i.e., $L_p = (2 * ((I_1 - I_2)^2 + (I_2 - I_3)^2 + (I_3 - I_1)^2))^{1/2} / (I_1 + I_2 + I_3)$. The contours of equi-polarization over the sea surface at a long distance from the land are shown in Fig.1. Fig.1 shows polarization degrees (%) at the wavelength $\lambda=850\text{nm}$. In Fig.2 the contours of equi-polarization over the coastal zone at $\lambda=850\text{nm}$ are shown. We can see from Figs.1 and 2 that at $\lambda=850\text{nm}$, the polarization pattern over the coastal zone is significantly different from that over the sea far away from the land. We also analyzed the 2-dimension pattern of polarization at $\lambda=450\text{nm}$. The result of it is not shown here, but it is found that the polarization pattern over the coastal zone is almost similar to that over the sea surface far away from the land. Figs.3 and 4 show the values of polarization (%) versus scattering angles on the principal plane in cases of Figs.1 and 2, respectively. As seen from Fig.3 and 4, at $\lambda=850\text{nm}$ the polarization degrees in the coastal zone become smaller than those over the sea surface far away from the land. On the other hand, at $\lambda=450\text{nm}$ the dependency of polarization degrees on scattering angles over the sea surface is almost the same in two cases (see Figs.3 and 4). This indicates that at $\lambda=850\text{nm}$, the radiation reflected by the land surface has a significant effect on the polarization over the sea surface adjacent to the land surface.

ADJACENT EFFECTS ON POLARIZATION MEASUREMENTS

The model of the radiance for evaluating adjacent effects on the land surface with non-uniform Lambertian reflectances is given by Kusaka, et.al [4]. In this study, we will extend the radiance model provided in [4] to the model described by Stokes' parameters, and estimate the linear polarization in the coastal zone. In this case, we assume that the sea surface is the flat and specular reflector provided by the Fresnel's formula and the land surface is the diffuse reflector given by the Lambert's law. It is also assumed that the atmosphere consists of Junge type aerosols and Rayleigh gas [3]. Since the optical thickness of the atmosphere is usually small at the near infrared band, it is assumed that the solar radiation will be scattered once in the atmosphere and reflected only once on the land and sea surface.

The Stokes vector $S (= [I, Q, U, V]')$ received by the sensor is given by

$$S = \mu_0 (R_s + R_b + R_a) F \quad (1)$$

where μ_0 is the cosine of the zenith angle of the incident solar radiation and R_s is the component transmitted directly to the sensor after the solar radiation has reflected off the sea surface, R_b the component scattered by the atmosphere after the solar radiation has reflected off the land surface, R_a the component transmitted diffusely in the atmosphere, and F is expressed by $F = [F, 0, 0, 0]'$ if πF is the incident solar irradiation. The linear polarization (L_p) is given by $L_p = (Q^2 + U^2)^{1/2} / I$. Adjacent effects due to the radiation reflected by the land surface will be evaluated in terms of R_b , and so only the R_b is expressed in detail.

Let's consider that the sensor receives the radiation reflected by the target point (x_0, y_0) on the sea surface. In this case, $R_b(x_0, y_0)$ is given by

$$R_b(x_0, y_0) = E_0 e^{-\tau/\mu} \iint A(x, y) k(x_0, y_0; x, y) dx dy \quad (2)$$

$$k(x_0, y_0; x, y) = \int_0^H \frac{z}{(z^2 + a^2)^{3/2}} \frac{P}{4\pi} \times \exp\left\{-\left(\frac{1}{\mu'} - \frac{1}{\mu_0}\right)\tau(z)\right\} \frac{\alpha(z)}{\mu} dz \quad (3)$$

In Eq.(2) $E_0 = \exp(-\tau/\mu_0)$ and μ is the cosine of the viewing angle of the sensor, τ the optical thickness of the atmosphere, $A(x, y)$ the reflectance at the point (x, y) on the land surface (see Fig.5). P is the single scattering phase matrix in the atmosphere. $\alpha(z)$ is the extinction coefficient at the height z and H is the altitude of the airborne sensor.

The boundary between the land and sea surfaces is not completely parallel to the principal plane as seen from Fig.2, but for simplicity R_b was computed under the assumption that the principal plane, i.e., yz -plane is parallel to the land. Moreover, for computational convenience, we approximated the

element P_{11} in the phase matrix for aerosols by Henyey-Greenstein phase function and $-P_{12}/P_{11}$ by the matrix element given by Rayleigh scattering. We computed L_p by changing the distance X to the land from the y -axis, provided that $A(x, y) = 0.25$ and $\tau = 0.12$. Fig.6 shows linear polarizations (%) versus scattering angles in cases of $X = 250m$, $1000m$ and infinity (no-land). We can see from Fig.6 that as X is smaller, the degree of polarization becomes smaller. This means that the polarization over the sea surface adjacent to the land becomes smaller than that over the sea surface at a long distance from the land, because of adjacent effects arising from the radiation reflected by the land surface.

CONCLUSIONS

We analyzed the airborne POLDER images over the coastal zone, and obtained the following results:

- (1) At the wavelength $\lambda = 850nm$, the polarization pattern over the coastal zone is significantly different from that over the sea surface far away from the land, while at $\lambda = 450nm$, the polarization over the coastal zone is almost the same as that over the sea surface far away from the land.
- (2) At $\lambda = 850nm$, the radiation reflected by the land surface has significant effects on the polarization measurements over the sea surface adjacent to the land

We would like to express our deep appreciation to Dr. Breon at Laboratoire de Modelisation du Climat et de l'Environnement, France for providing Medimar POLDER data. This work was supported by the Grand-in-Aid for Scientific Research on Priority Areas (No.08241222) of the Japanese Ministry of Education, Science, Sports and Culture.

REFERENCES

- [1] F.M.Breon and P.Y.Deschamps, Optical and Physical Parameter Retrieval from POLDER Measurements over the Ocean Using an analytical model, Remote Sens. Environ., Vol.43, pp.193-207, 1993
- [2] J.L.Deuze, et.al, Analysis of the POLDER Airborne Instrument Observation over Land Surface, Remote Sens. Environ., Vol.45, pp.137-154, 1993
- [3] A.Yamazaki, et.al, The Estimation of Aerosol Models by the Reflectance Analysis of the Airborne POLDER Data, Proc. IGARSS'96, Vol.2, pp.1250-1252, 1996
- [4] T.Kusaka, et.al, Removal of the Atmospheric Blurring from Remotely Sensed Earth Imagery, Proc.4th Int. Joint Conf. of Pattern Recognition, pp.931-935, 1978

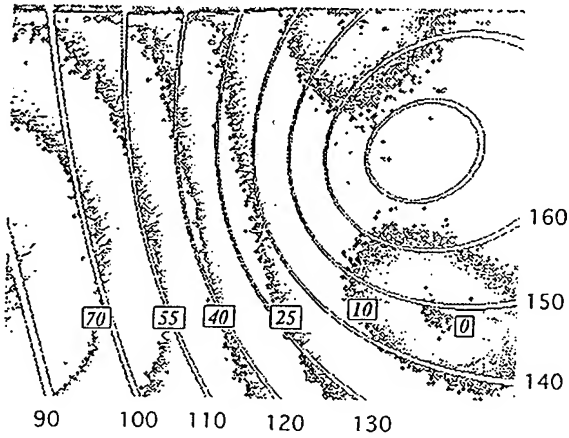


Fig.1 The contours of equi-polarization over the sea surface distant from the land. The number in the square shows the degree of polarization (%).

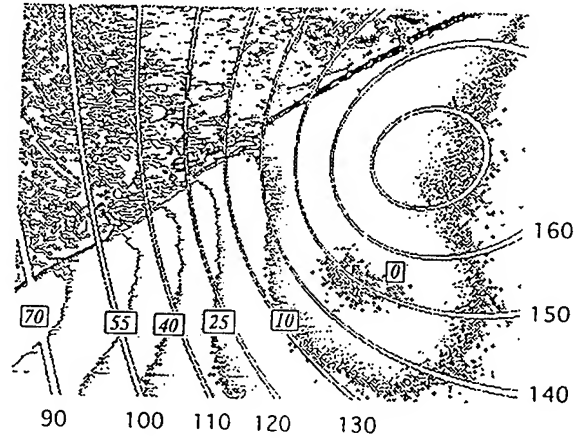


Fig.2 The contours of equi-polarization over the sea surface adjacent to the land. The number in the square shows the degree of polarization (%).

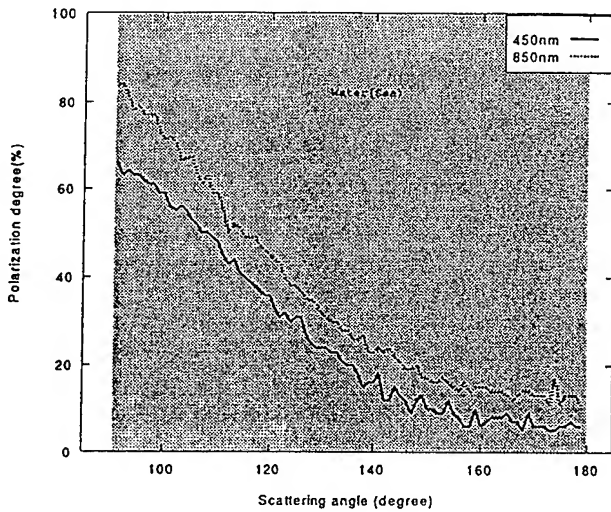


Fig.3 The polarization degrees (%) versus scattering angles on the principal plane in the case of Fig. 1

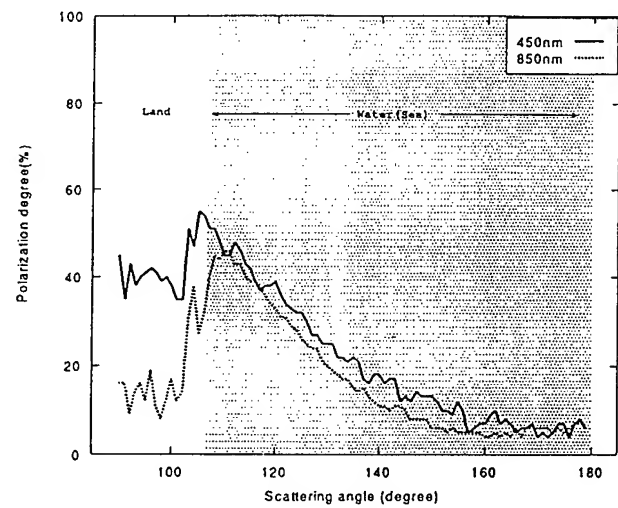


Fig.4 The polarization degrees (%) versus scattering angles on the principal plane in the case of Fig. 2

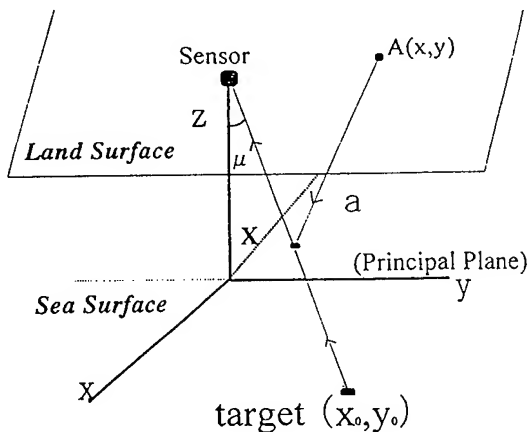


Fig.5 Geometry for the computation of adjacent effects

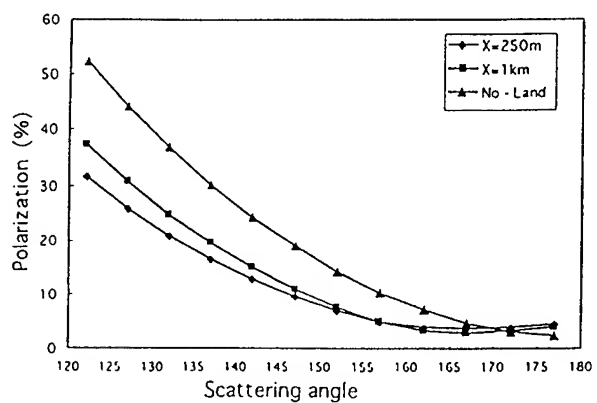


Fig.6 The polarization degrees (%) versus scattering angles at the distance to the land $X=250\text{m}$, 1000m and infinity (no land)

Information Content of Outgoing Reflected and Scattering Solar Radiation in UV and Visible Spectral Ranges*

Yu. M. Timofeyev, A. V. Vasilyev, V. V. Rozanov
Research Institute of Physics at St. Petersburg State University,
Ulyanovskaya 1, St. Petersburg-Petrodvorets, 198904, Russia,
tel.: +7-812-428-44-86, fax: +7-812-428-72-40, e-mail: tim@troll.niif.spb.su

Abstract – On the basis of the GOMETRAN radiative code, calculations of spectral covariance matrices of outgoing radiation in the 240-700 nm spectral range have been performed. It gave a possibility to examine the information content of measurement data simulated at different measurement designs (various measurement geometry and errors; different conditions of sun illumination and surface albedo) and to estimate the optimal number of measurement channels. The numbers of independently measurable parameters at measurement errors ranging from 0.1 to 1.0 % are 8-11, 1-2 for atmospheric content of the ozone and NO₂, respectively; 6-12 and 5-8, describing the aerosol optical characteristics and atmospheric density, respectively.

In the last few decades, a considerable amount of information on vertical profiles and total content of ozone on a global scale have been obtained by satellite method based on the measurements of outgoing reflected and scattering solar radiation in UV spectral range [1-3]. 12-channel SBUV spectrometer gives a possibility to retrieve the O₃ vertical profile, and 6-channel TOMS spectrometer is designed to mapping the two-dimensional fields of the total ozone. On April 1995, the GOME interferometer with more than 3500 channels in the 240 - 790 nm spectral range has been launched by ERS-2 satellite. This device allows to determine not only the ozone content but the content of other gaseous constituents of the atmosphere [4,5].

The necessity of permanent controlling the ozonosphere state and determining the spatial-temporal trends in the O₃ content due to human impacts on the ozone layer poses the problem of developing the new satellite devices for high-accuracy measurements of the ozone vertical profiles and total content. A study of optimal instrument designs (optimal number and spectral location of the channels) enabling the retrieval the maximum information available in the measurements is necessary part of such development.

To optimize the instrument spectral design spectral range, the V.P. Kozlov optimization method [6] may be applied. This method makes it possible a) to determine the number of independent parameters contained in the radiation measurements and the minimum number of measurement

channels required to derive this information; b) to estimate the information content of remote measurements; c) to calculate the optimal spectral measurement designs and to optimize the accuracy of remote sensing.

Present study is dedicated to analyzing the information content of the measurements of outgoing radiation in the 240-700 nm spectral range relative to different parameters of atmosphere and underlying surface.

To determine the number of independent information components is necessary to calculate the spectral covariance matrices of outgoing radiation K and define the eigenvalues μ_i and eigenvectors Ψ_i :

$$K \Psi_i = \mu_i \Psi_i. \quad (1)$$

The number of independent information components discernible by specific instruments in single satellite measurement is determined by Kozlov criteria:

$$\mu_i \geq \sigma^2, \quad (2)$$

where σ^2 is the RMS variance of measurement random noise.

The calculations of covariance matrices in the 240-700 nm spectral range with the step of 0.5 nm have been carried out on the basis of the GOMETRAN radiative code [4], taking into account the principal features of radiation transfer in the "cloudless atmosphere-surface" system (multiple molecular and aerosol scattering, molecular and aerosol absorption, reflection). There were assigned two types of underlying surface (sea and snow) and the following values of *a priori* variations of main atmospheric and surface parameters: O₃ - 50 %; NO₂ - 100 %, atmospheric density - 3 %; aerosol amount - 100 %, surface albedo - 20 %. The task of analyzing the information content was solved in the terms of relative radiance values because of strong variability of outgoing radiation in examined spectral range (a few orders). To do so, the values of outgoing radiation have been normalized to the average radiation spectrum and the criteria (2) has been formulated in the terms of relative measurement error.

*This work was supported in part by RFFI (Grant No.97-05-65492)

Table 1. The numbers of independent information components available in the measurements at various relative measurement errors σ (in %) and calculation scenarios

N	Varied parameters	Number of information components		
		$\sigma = 1.0$	$\sigma = 0.3$	$\sigma = 0.1$
1	All parameters	> 100	> 100	> 100
2	All, except albedo	13	15	19
3	Only O_3	8	10	11
4	Only NO_2	1	2	2
5	Only density	5	7	8
6	Only aerosol	6	8	10

An example of analyzing the information content of nadir outgoing radiation measurements in the 240 - 700 nm spectral range above sea at zenith Sun angle $\theta = 65^\circ$ is given in Table 1. When all atmospheric and surface parameters are varied, the number of independent information components N exceeds 100. The most part of those define the surface albedo under condition of cloudless atmosphere. It becomes evident when analyzing the variant 2 with non-variable albedo.

In this case, the numbers of information components defining the atmospheric variables are 13, 15 and 19 at measurement errors of 1.0, 0.3 and 0.1 %, respectively. The rest calculation variants describe the cases of varying the single atmospheric parameter and allow to estimate N for specific inverse problems - relative to O_3 (var. 3), NO_2 (var. 4), atmospheric density (var. 5) and optical characteristics of aerosol (var. 6).

Obtained data testify that the measurements of outgoing radiation in the 240 - 700 nm spectral range contain (depending on measurement errors) 8 - 11, 1 - 2, 5 - 8, and 6 - 10 independent components describing the vertical structure of the ozone content, the NO_2 content, the atmospheric density and aerosol optical characteristics, respectively. The level of measurement error influences essentially the opportunities of retrieving the O_3 content, atmospheric density and aerosol optical characteristics. The informativity of the inverse problem of NO_2 content retrieval is not too large and weakly depends on measurement error. Even the very precise measurements ($\sigma = 0.1$ %) shows promise of deriving only two independent parameters characterized the NO_2 vertical profile. This fact is caused by relatively small NO_2 absorption characterizing by the values of optical depth equal to about 0.005 in examined spectral range.

The data of Table 1 testify to a fairly rich information content of the measurements relative to the atmospheric density and aerosol optical characteristics. In the first case, this effect connects with considerable importance of

molecular scattering in outgoing radiation transfer in the short-wave spectral range (240 - 400 nm). The reasons of high possibility of retrieving the atmospheric aerosol are the significant aerosol influence on outgoing radiation in visible and near IR spectral range and rather wide spectral range (240 - 700 nm) under consideration. It is worth noting that N values, characterizing the possibility of aerosol retrieval, were obtained only for the specific atmospheric model involving the background stratosphere and sea tropospheric aerosol (23 km visibility range) [7] with variations of optical characteristics reaching to 100 %.

The analysis of Table 1 reveals the lack of additivity in N values. If N and N_i are the numbers of the independent information components for combine and special inverse problems, respectively, so $N < \sum_i N_i$. This peculiarity

testifies to noticeable interrelation between outgoing radiation variations caused by the changes in different atmospheric parameters. It is interesting to note that such additivity has been found when analyzing the problem of temperature-humidity sounding in the microwave range [8].

For analyzing the spectral features of the information components, the calculations of N have been also performed for the 240 - 310 and 240 - 440 nm spectral intervals separately. In Table 2, such data are given for both intervals (denoted as I and II, respectively) and the whole examined spectral range (III) for the case of nadir measurements above sea at relative measurement error of 0.3 % and zenith Sun angle of 65° .

It is seen from Table 2, that the narrowing of the measurement spectral range down to the 240 - 310 nm, covering only the Hartley-Huggins strong O_3 absorption band, leads to decrease of N for the complex inverse problem. It is a consequence of relatively weak influence of surface albedo on outgoing radiation and of excluding the NO_2 absorption bands. Addition of the 310 - 440 nm interval increases essentially the number of information components describing the aerosol, due to receiving the information on tropospheric aerosol, and gives a possibility to derive something about the NO_2 content.

Table 2. The numbers of independent information components available in the measurements in various spectral ranges under different calculation scenarios

N	Varied parameters	Number of information components		
		I	II	III
1	All parameters	9	88	> 100
2	All, except albedo	9	14	15
3	Only O_3	9	9	10
4	Only NO_2	0	2	2
5	Only density	6	7	7
6	Only aerosol	4	7	8

Table 3. Number of N for the GOME measurements

Calculation variant	2	3	4	5	6
N	19	10	3	8	12

It is known that relative error of outgoing radiation measurements in the 240 - 700 nm spectral range varies very strongly, first of all in UV region, because of the radiation intensity in different parts of the range differs by a few orders. For example, the signal / noise ratio, S/N, is 10 at $\lambda = 240$ nm and reaches to 6325 at $\lambda = 310$ nm in the GOME spectrometer [5]. In this connection, calculations of the number of independent informative components have been carried out with accounting the spectral dependence of S/N relevant to GOME spectrometer for 5 calculation scenarios similar to those in Tables 1,2.

Comparison of Tables 1 and 3 shows the N values for the GOME spectrometer similar to those for fixed S/N corresponding to relative measurement error of 0.1 %. Besides, 3 independent information components describing the NO₂ content are contained in the GOME measurements due to very high ratio S/N in the NO₂ absorption band (S/N = 4000 - 5124). This fact testifies to advisability of developing a special algorithm for interpreting the GOME measurement data to derive information on characteristics of NO₂ vertical distribution.

Performed study of information content of outgoing reflected and scattering solar radiation in the 240 - 700 nm spectral range makes possible to draw the following conclusions:

1. In the radiation measurements at various relative errors (1.0-0.1 %), there are contained 8 - 11 informative components describing the O₃ vertical profile, 5 - 8 - on atmospheric density, 6 - 12 - on aerosol optical characteristics and 1 - 2 - on NO₂ content.
2. The variations of outgoing radiation due to changes in the ozone content and atmospheric density are strongly correlated values, with a consequent non-additivity of the informative components of the complex and isolated problems of retrieving the atmospheric parameters. Because of this, the separation of information on the ozone content and atmospheric density present a stubborn problem. To enhance the accuracy of ozone sounding, it is appropriate to preset *a priori* values of the atmospheric density determined from independent measurements.
3. The surface albedo (sea, snow) does not noticeably influence the number of information components relating to different atmospheric variables.

4. The geometry of the measurements and conditions of illumination affect markedly the measurement informativity relative to atmospheric density and optical characteristics of atmospheric aerosol. The informativity enhances with increasing the atmospheric optical mass and Sun zenith and observation angles.
5. 3 informative components characterized the NO₂ content are contained in the GOME measurements and hence it would be useful to develop a special algorithm for retrieving the NO₂ vertical profile.
6. Optimal satellite sounder for deriving the O₃, NO₂ and aerosol content has to possess about 20 measurement channels in UV and visible spectral ranges. Optimal its spectral design is planned to be calculated at a later time.

REFERENCES

- [1] K.Yu. Kondratyev, Global Dynamics of Ozone. Moscow: Viniti, vol. 19, 1989, 212pp. (in Russian).
- [2] I.L.Karol, VV. Rozanov, and Yu.M. Timofeyev, Gaseous Admixtures in the Atmosphere. Leningrad: Gidrometeoizdat, 1983, 192 pp. (in Russian).
- [3] Yu.M. Timofeyev, "Satellite methods of study of gaseous content of atmosphere (a review)", Engl. transl. Izv., Atm. Ocean. Phys., vol.25, 1989, pp. 451-472.
- [4] V.V. Rozanov, Yu.M. Timofeyev, and J. Barrows, "Informativity of the measurements of outgoing UV, visible and near-IR solar radiation (GOME apparatus)", Earth Res. from Space, 6, 1995, pp.29-39 (in Russian).
- [5] Global Ozone Monitoring Experiment GOME, users manual European Space Agency, SP-1182, September 1995, 122 pp.
- [6] V.P. Kozlov, "On a problem of optimal planning the statistical experiment", Probab.Theor. and Appl., vol. 19, 1974, pp. 226-230, (in Russian).
- [7] F.X. Kneizys et al., Users Guide to Lowtran 7, AFGL-TR-86-0177, Environ.Res.Paper, 1010, 1988, 137 pp.
- [8] Yu.M. Timofeyev, A.V. Polyakov, A.V. Vasil'ev, E.M. Shul'gina, and R. McClatchey, "Microwave Temperature-Humidity Probing of the Atmosphere from Space", Engl. transl. Izv., Atm. Ocean. Phys., vol. 33, 1, 1997, pp. 46-53 [Izv.AN.Fizika Atm. i Okeana, pp. 53-61].

The Aerosol Optical Thickness Retrieval from GOME Spectra

Antonio Bartoloni*, Marina Mochi*, Claudio Serafini*
Marco Cervino**, Rodolfo Guzzi**, Francesca Torricella**

*Nuova Telespazio S.p.A.

Via Tiburtina 965 - 00156 Rome - Italy

phone: +39-6-40791 fax: +39-6-40793843

e-mail: antonio_bartoloni@telespazio.it marina_mochi@telespazio.it claudio_serafini@telespazio.it

**IMGA-CNR - Istituto per lo studio delle Metodologie Geofisiche e Ambientali

Via Gobetti 101 - 40129 Bologna - Italy

phone: +39-51-6398084 fax +39-51-6398132 e-mail: cervino@imga.bo.cnr.it

Abstract -- A prototype processor for the aerosol optical thickness retrieval and aerosol classification starting from GOME data has been developed. The aerosol classification is made choosing the minimum among the least squares residuals computed for different aerosol classes. For each pixel the output of processor gives the aerosol optical thickness, the aerosol classification, a relative retrieval residual and a flag that indicates if the pixel is cloudy. The results of some different GOME real data sets are shown.

1. INTRODUCTION

The determination of atmospheric aerosol load and classification on a global scale is a crucial item to refine the analysis of the Earth radiative balance.

Aerosols can be retrieved from data collected by GOME instrument, on board of the ERS-2 satellite, that collects radiation over the wavelength region from 240 to 790 nm.

The retrieving of both aerosol class and optical thickness is tested assuming that an aerosol layer is present in the Earth atmosphere. The retrieval algorithm has been implemented in a prototypal processor for the aerosol optical thickness and aerosol classification generation from GOME data (PGADP). This processor has been devised as a tool to be used for the development of an operational GOME data processing chain.

2. THE RADIATIVE TRANSFER MODEL GOMESIM

The adopted cloudless plane parallel atmospheric Radiative Transfer Model is GOMESIM [1], and it is based on the formulation proposed by Sobolev [2], in case of a pure scattering vertically homogeneous atmosphere bounded with a Lambertian reflecting surface. The reflectance is given by:

$$\rho = P(\gamma)\rho_1 + \Delta\rho \quad (1)$$

being $P(\gamma)\rho_1$ the single scattering coefficient $P(\gamma)$ the atmospheric scattering phase function and $\Delta\rho$ the higher order of scattering coefficient.

The contribution to the reflectance by radiation scattered only once is analytically computed taking into account the vertical optical non-uniformity, caused by the presence of an

aerosol layer bounded between two layers composed of molecules only ("Rayleigh layers"). Some assumptions and approximations have been done in defining the higher order of scattering coefficient: the scattering phase function is "smoothed" with a two-terms form (Legendre polynomial series); some approximations have been made on boundary conditions; approximations on the zenith dependence of the diffuse radiation have been introduced; the azimuth dependence of the reflection coefficient is due only to single scattering contribution. In order to take into account the atmospheric vertical non-uniformity, the following features have been added to the model computation of the higher order of scattering coefficient: an effective total (aerosol and molecules) scattering optical thickness is derived

$$\tau_s = \tau_1^R + \tau_2^R + \tau^{AS} \exp(-\tau_1^R \alpha) + \tau_3^R \exp\left(-\frac{\tau^{AS}}{\mu_0}\right) \quad (2)$$

where τ_i^R is the Rayleigh optical thickness of the i -th layer, from top to down, τ^{AS} is the aerosol scattering optical thickness, α is the sum of the secants of the sun and line-of-sight zenith angles, μ_0 is the cosine of the sun zenith angle; a two term scattering phase function, with a weighted (Mie and Rayleigh) asymmetry factor; aerosol absorption is parameterized by means of transmittance factors:

$$T^{AA} = \exp\left[-(1 - \omega_0)\tau^A \alpha\right] \quad (3)$$

where ω_0 is the aerosol single scattering albedo, τ^A is the aerosol extinction, scattering plus absorption, optical thickness.

Gas absorption can be ignored since wavelength at which it occurs will be avoided, see [1].

This approach has the advantage of considering the multiple scattering effects preserving the high speed of computation thank to the use of a few physical parameters.

3. PROTOTYPAL GOME AEROSOL DATA PROCESSOR

The main functions implemented by the prototypal processor for the GOME Aerosol Optical Thickness product generation (PGADP) are: GOME Reflectance Calculation, Cloud flag generation, Spectral Window Selection, Spectral

Reflectance Fitting, Ranking of the Aerosol Class, Surface Reflectance Calculation, Output Data Generation.

3.1 GOME Reflectance Calculation

The GOME instrument measures the following quantities:

- Earth-shine radiances
- sun irradiances

The reflectances calculation is performed using the formula

$$REF_{GOME} = \frac{\text{Earth-shine radiance} * \pi}{\text{sun irradiance} * \cos \theta_0} \quad (4)$$

where θ_0 is the zenith angle of the sun.

3.2 Cloud Flag Generation

In order to define the cloud detection algorithm of the AOT prototypal processor, the elaboration of the PMD, Polarization Measurements Device, data has been implemented following the line of the Cloud fractional Cover Algorithm (CCA) [3]. A PMD pixel is declared cloudy if:

$$PMD3 > \text{thre1} \quad \text{or} \quad \text{thre2} < PMD3 < \text{thre1} \quad \text{and} \quad PMD3/PMD2 > \text{thre3}$$

where PMD1, PMD2 and PMD3 are the reflectances measured respectively by three PMD channels.

The values currently assigned to these parameters are:

$$\text{thre1} = 0.12 \quad \text{thre2} = 0.05 \quad \text{thre3} = 0.5$$

3.3 Spectral Window Selection

In order to properly use GOME data for aerosol retrieval the influence of the absorption due to water, oxygen and ozone can be avoided in PGADP by selecting wavelength intervals in which gases absorption can be neglected and the spectral sensibility of the GOME can be fully exploited.

3.4 Spectral Radiance Fitting and Ranking of the Aerosol Class

The algorithm will be based on a fitting procedure of the GOME reflectances by the forward model GOMESIM. The maximum likelihood principle has been used in order to define the following objective function:

$$\min_{k \in \{1, \dots, 20\}} \left\{ \min_{\tau_{ext}^k} \left[\sum_{i=1}^m \ln(REF_ERR_{GOME}(\lambda_i)) + \frac{1}{2} \sum_{i=1}^m \left(\frac{REF_{GOME}(\lambda_i) - REF_{PM}^k(\lambda_i, \theta, \phi, \theta_0, \phi_0, \tau_{s,i}^k(\tau_{ext}^k), \omega_{0,i}^k)}{REF_ERR_{GOME}(\lambda_i)} \right)^2 \right] \right\} \quad (5)$$

where τ_{ext}^k , the retrieval parameter, is the extinction aerosol optical thickness of the aerosol class A_k at the reference wavelength 0.55 μm , $REF_{GOME}(\lambda_i)$ are the reflectances at the wavelength λ_i for $i=1, \dots, m$, $\tau_{s,i}^k$ is the scattering optical

thickness at the wavelength λ_i , for the aerosol class A_k , $\omega_{0,i}^k$ is single scattering albedo at the wavelength λ_i , for the aerosol class A_k .

The process is based on two nested minimization procedures. The inner minimization is performed on the extinction aerosol optical thickness of the aerosol class A_k at the reference wavelength 0.55 μm using a NAG routine based on a one-dimensional inverse quadratic interpolation. This process is repeated more then once in different values intervals in order to avoid local minima. The outer discrete minimization will be made choosing the minimum among the least squared residuals computed for different aerosol classes.

Assuming that the aerosol particles can be modeled by equivalent spheres of known refractive index, we use the Mie theory for the evaluation of the aerosol optical proprieties and aerosol phase function.

In the present version of PGADP the aerosol classes listed in Table I have been used.

3.5 Surface Reflectance Calculation

In order to introduce surface albedo in the aerosol retrieval scheme a parameterization of its spectral dependence is required. To this aim 5 spectral signatures have been used in

PGADP relative to the different surface types [4], that is: snow, vegetation, sand, soil and water.

Moreover for each pixel the following steps are performed in order to assign an albedo profile:

- minimization of the objective function (5) using each of the 5 spectral albedo profiles with a fixed tropospheric aerosol class;
- selection of the surface spectral albedo profile corresponding to the minimum residual value of the objective function.

3.6 Output Data Generation

The PGADP gives as output the geolocation information of the pixel processed and the following aerosol information: Aerosol class, that is a code for aerosol class identification, Table I; Aerosol Optical Thickness (at the reference wavelength 0.55 μm); Surface Albedo type, that is a code for the surface albedo identification; Relative Retrieval Residual.

Table I: Aerosol classes description

Aerosol Class	Description
1 - 4	Rural (RH=0%, 70%, 80%, 99%)
5 - 8	Urban (RH=0%, 70%, 80%, 99%)
9 - 10	Maritime (RH=0%, 70%, 80%, 99%)
13 - 16	Tropospheric (RH=0%, 70%, 80%, 99%)
17	Background Stratospheric
18	Aged Volcanic
19	Fresh Volcanic
20	Desert Wind-Carry

4. REAL GOME DATA PROCESSING RESULTS

The prototypal processor PGADP has been tested on a data set of real GOME data relative to 4 orbits in the period 29-31/01/97 covering the geographical area depicted in Fig 1 and Fig 2. In order to process this data set the PGADP parameters have been set as shown in Table II.

In Fig.1 the aerosol optical thickness values obtained by PGADP are shown regardless to the cloud information provided by the CCA algorithm. Fig.2 shows the results of considering as valid only the pixels over which no PMD is declared cloudy by the CCA algorithm. The effectiveness of the CCA in Cloud detection over Ocean has been also qualitatively tested against full disk Meteosat Image

5. CONCLUSIONS

The first results obtained on real GOME data show that the application of the CCA algorithm for the cloud flag generation seems to work over the Ocean where reasonable AOT values (<1) are calculated over a significant amount

Table II. The PGADP parameters chosen to process the data set

	SETTING
Aerosol Classes	1,2,3,4,9,10,11,12,13,14, 15,16,17,18,19,20
Wavelength Windows	- 0.36-0.43 μm - 0.751-0.757 μm - 0.775-0.785 μm
Surface Pressure	1013 hPa

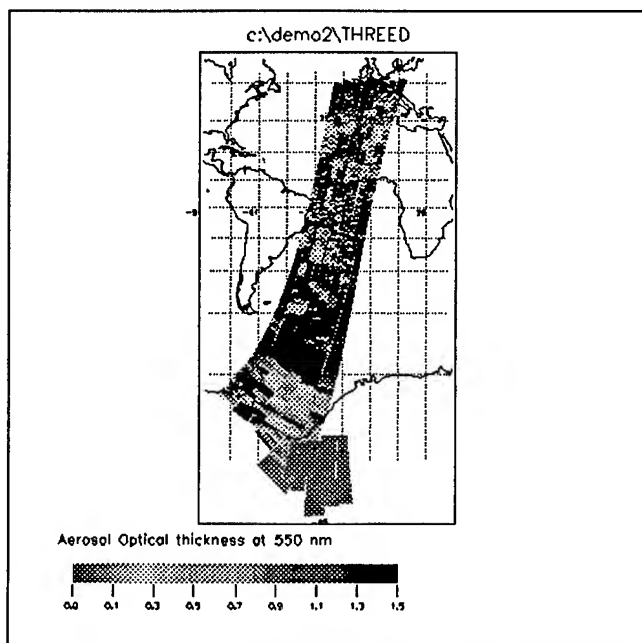


Figure 1: Aerosol Optical Thickness values obtained by PGADP

of pixels (65%). Nevertheless a more quantitative and sophisticated validation exercise has to be done in order to clearly establish the CCA effectiveness and to explain the presence of too high AOT value over clear open Ocean pixels. In conclusion the PGADP software is a useful tool for the assessment of the aerosol optical thickness retrieval algorithm from GOME data and we think that more problems and hopefully solutions will be found processing larger amount of data.

6. REFERENCES

- [1] R.Guzzi, M.Cervino, C.Levoni, F.Torricella, "GOME Cloud and Aerosol Data Product Algorithms Development," ESA Contract No. 11572/95/NL/CN, Modena, September 1996.
- [2] V.V.Sobolev, "A treatise on Radiative Transfer," Princeton, Van Nostrand C. Inc., 1963, pp.268-280.
- [3] Deschamps et al., "Study on the Effects of Scattering on the Monitoring of Atmospheric Constituents," Laboratoire d'Optique Atmospherique, Univeristé de Lille-1, University of Hamburg. ESA Contract No. 9740/91/NL/BI.
- [4] Bowker et al., "Spectral Reflectances of Natural targets for use in remote sensing studies," NASA Langley Research Centre, Hampton, Va., U.S.A., NASA report NASA-RP-1139, 1985.

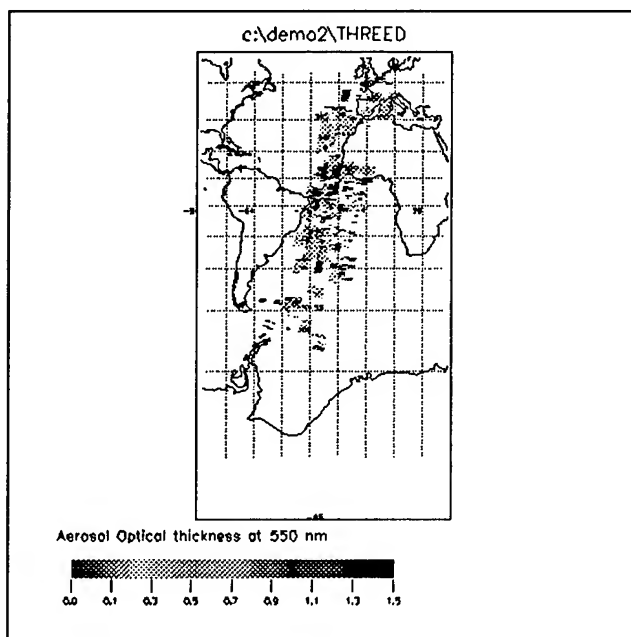


Figure 2: Aerosol Optical Thickness over pixels in which no PMD is declared cloudy by the CCA algorithm.

Aerosol Optical Thickness Over Ocean Areas and Its Relationship With Cloud Droplet Size

Qingyuan Han, Joyce Chou, and Ronald M. Welch

Institute of Atmospheric Sciences
South Dakota School of Mines and Technology
501 E. Saint Joseph Street
Rapid City, SD 57701-3995
Phone: (605) 394-2291; Fax (605) 394-6061
email: han@cloud.ias.sdsmt.edu

Abstract – This paper presents the results of retrieved aerosol optical thickness over ocean areas and its relationship with droplet sizes of water clouds. The aerosol optical thickness is retrieved from clear sky radiances of channel 1 of AVHRR from ISCCP dataset. The results show consistent distribution patterns of aerosol optical thickness with other authors' work. The aerosol optical thickness shows a negative relation with cloud droplet size, consistent with expected aerosol indirect effect.

INTRODUCTION

Satellite observations show that ocean radiances are linearly proportional to relative aerosol content and, thus, aerosol optical thickness for Landsat-1, -2 data [1] and for GOES-1 and NOAA-5 data [2] when effects of sunglint are avoided. Based on this relationship, it is assumed that changes in the emergent radiances at TOA are solely dependent on the atmospheric aerosol. Algorithms of remote sensing of aerosol optical thickness and relative aerosol content over ocean areas have been developed during the past two decades (e.g. Rao et al. [3] among others).

Due to the technique used in this study is a single wavelength intensity retrieval (channel 1 of AVHRR), assumptions have to be made about aerosol properties such as chemical composition, aerosol shape and size distribution. The chemical composition is assumed to be sulfate with refractive index $n=1.50-i0.0$. Junge distribution $n(r)=Cr^{-B}$ is used for aerosol size distribution with $B=3.0$ and particle shape is assumed to be sphere.

MODEL

Mie scattering is used to calculate the phase functions for different wavelengths (10 wavelengths are used within channel 1 of AVHRR spectrum interval). The phase functions at each wavelength are then used to calculate radiances for different aerosol optical thickness values from an adding-doubling radiative transfer program [4]. The radiances at different

wavelength are weighted according to instrument response function of AVHRR channel 1 to derive the radiance received by the satellite. Empirical bidirectional reflectance function for surface wind speed $\leq 5\text{m/sec}$ [5] is used in the model. Rayleigh scattering is included in the model according to the formula of Hansen and Travis [6]. Ozone and water vapor amount are from the American Standard Atmosphere. Sunglint areas are mostly screened out by nadir viewing geometry and further filtered away by the sunglint flag available in the CX data.

DATA

The dataset (ISCCP CX data) used to retrieve aerosol optical thickness over oceans is the ISCCP (International Satellite Cloud Climatology Project) analysis [7] at the individual pixel level. These CX data are a combination of ISCCP B3 data [8] and the cloud detection and radiative model analysis results that describe cloud and surface properties at original B3 image resolution. Specifically we use the results from AVHRR observations, which contain the radiances of all 5 AVHRR spectral channels. The atmospheric temperature and humidity profiles needed in our retrieval are taken from NOAA TOVS data. Details are described in Han et al. [4].

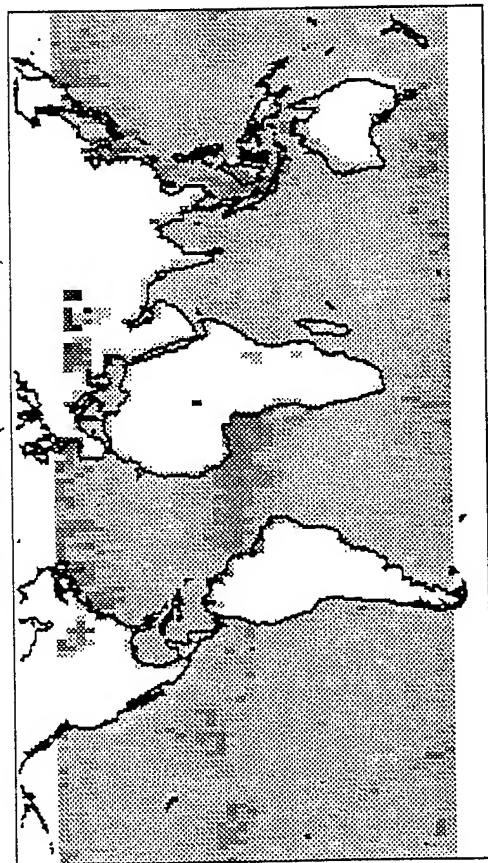
RESULTS

Figure 1 shows the distribution of aerosol optical thickness over ocean areas for 1987. The background aerosol optical thickness is around 0.04-0.05. Heavy dust blown from Africa is shown in all seasons. These patterns are consistent with other authors' results (e.g., Rao et al., 1989).

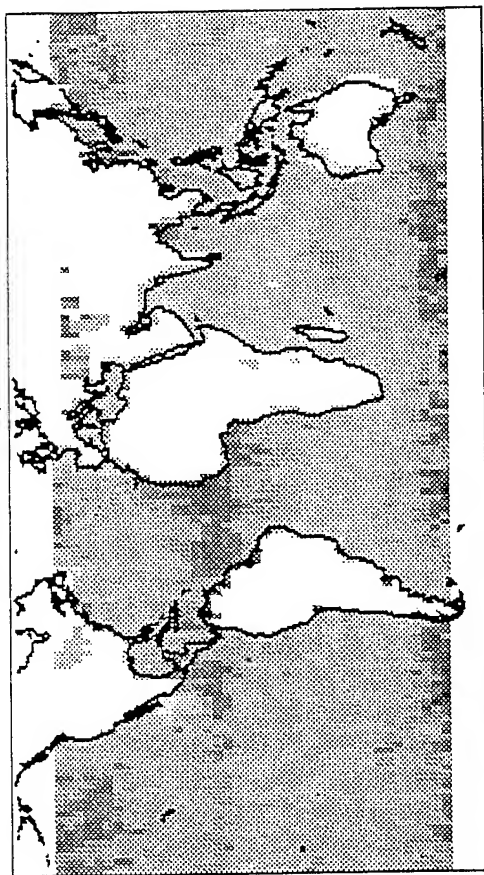
Figure 2 shows the relationship between aerosol optical thickness and water cloud droplet sizes. The droplet sizes are from our previous work (Han et al., 1994). It shows that a negative relationship exists between aerosol optical thickness and cloud droplet sizes, which is consistent with the predicted aerosol indirect effect.

Acknowledgments. This research was supported by NASA contract No. NAGW-3922 and NAGW-3788; was partially funded by DOE through the NIGEC Great Plain Regional Center at the University of Nebraska-Lincoln (DOE Cooperative Agreement No. DEFC03-90ER61010). Financial support does not constitute an endorsement by DOE of the views expressed in this paper. This research was also supported by the NASA Climate Program managed by Dr. Bob Curran.

JAN 1987 (NOAA-09)



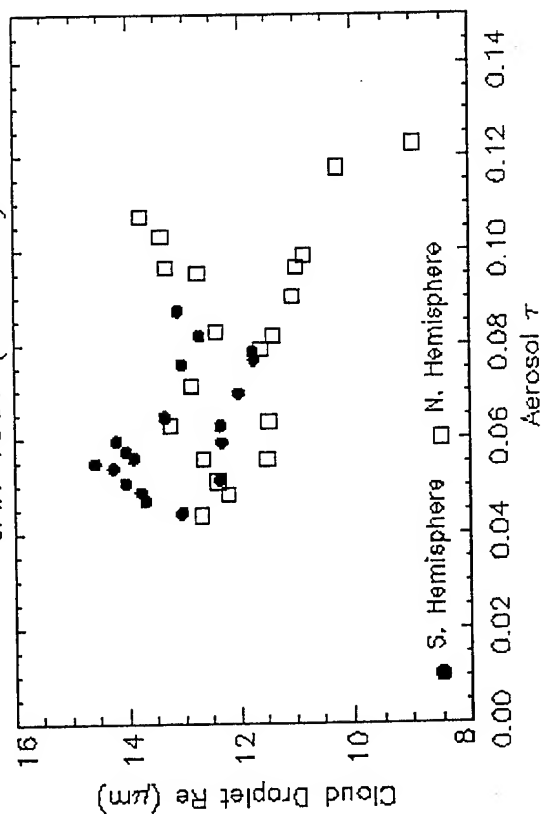
APR 1987 (NOAA-09)



0 3 6 9 12 15 21 27 30 x100

Fig. 1 Aerosol Optical Thickness Retrieved From NOAA-09

JAN 1987 (NOAA-9)



APR 1987 (NOAA-9)

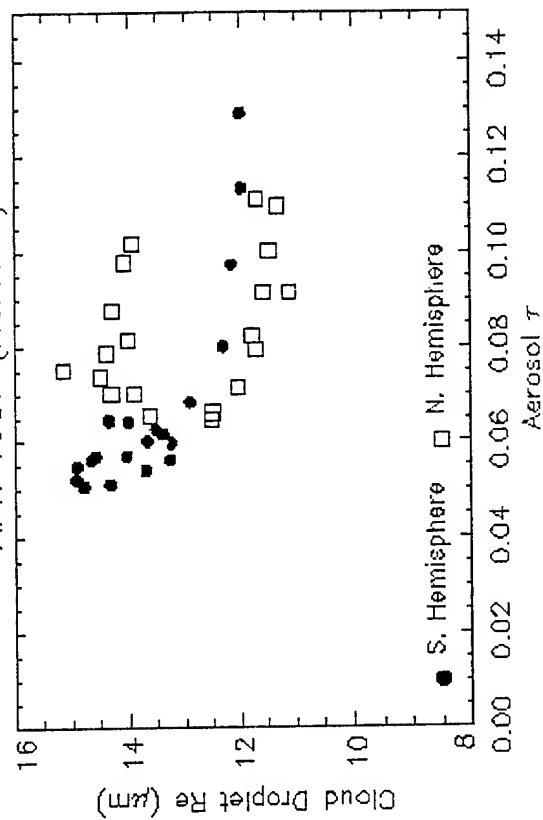


Fig. 2 Relation Between Cloud Droplet Size and Aerosol Optical Thickness.

REFERENCES

- [1] Griggs, M., 1975: Measurements of atmospheric aerosol optical thickness over water using ERTS-1 data. *J. Air Pollut. Control. Assoc.*, **25**, 622-626.
- [2] Griggs, M., 1979: Satellite observations of atmospheric aerosols during the EOMET cruise. *J. Atmos. Sci.*, **36**, 695-698.
- [3] Rao, C. R. N., L. L. Stowe, and L. L. McClain, 1989: Remote sensing of aerosol over the oceans using AVHRR data: Theory, practice, and applications. *Int. J. Remote Sensing*, **10**, 743-749.
- [4] Han, Q., W. B. Rossow, and A. A. Lacis, 1994: Near-global survey of effective droplet radii in liquid water clouds using ISCCP data. *J. Climate*, **7**, 465-497.
- [5] Cox, C. and W. Munk, 1954: Measurement of the roughness of the sea surface from photographs of the sun's glitter. *J. Opt. Soc. Amer.*, **44**, 838-850.
- [6] Hansen, J. E., and L. D. Travis, 1974: Light scattering in planetary atmospheres. *Space Science Review*, **16**, 527-610.
- [7] Rossow, W. B., and R. A. Schiffer, 1991: ISCCP cloud data products. *Bull. Amer. Meteor. Soc.* **72**, 2-20.
- [8] Schiffer, R. A., and W. B. Rossow, 1985: ISCCP global radiance data set: A new resource for climate research. *Bull. Amer. Meteor. Soc.*, **66**, 1498-1505.

Effects of Atmospheric Aerosol Models on the Single Scattering Point Spread Function in Optical Remote Sensing

Soo Chin Liew

Centre for Remote Imaging, Sensing and Processing, National University of Singapore

Lower Kent Ridge Road, Singapore 119260

Tel: (+65) 7715069, Fax: (+65) 7757717, Email: phyliew@nus.edu.sg

Abstract -- Light scattering by atmospheric aerosols produces blurring effects in remotely sensed images in the visible and near infrared wavelength bands. This blurring effect can be described by an effective scattering point spread function (PSF). In this paper, the single scattering PSF is derived from the radiation transfer equation assuming a plane parallel atmosphere with varying optical properties in the vertical direction. The PSF is computed for a given aerosol model and imaging geometry. The extinction coefficient, single scattering albedo and the scattering phase function are computed from the Mie theory. The effects of three different aerosol models (urban, maritime, continental) on the single scattering PSF are investigated.

INTRODUCTION

In the presence of atmosphere, absorption and scattering of the optical radiation by the constituent gases and aerosols in the atmosphere causes degradation of the remotely sensed image [1], most noticeably by the path radiance and the adjacency effect. Near to the boundary between two regions of different reflectance, the adjacency effect results in an increase in the apparent reflectance of the darker region while the apparent reflectance of the brighter region is reduced. This effect also produces blurring of the targets due to spreading of the reflected radiation by scattering, resulting in a reduced resolution image.

The adjacency effect can be modeled as the convolution of the surface reflectance with an effective scattering point spread function (PSF), which is dependent on the optical properties of the atmosphere and the geometry of image acquisition [1]. The PSF can, in principal, be derived from the theory of radiative transfer. However, evaluation of the exact PSF would require a considerable amount of computing resources. The computation of the PSF would permit the evaluation of the extent of blurring due to light scattering by the atmosphere for different imaging geometry and atmospheric conditions. If the blurring PSF is known, then it is also possible to restore the blurred image using the technique of deconvolution.

In this paper, we derive an expression for the scattering PSF from the radiative transfer equation using the single scattering approximation assuming a plane-parallel atmosphere. This model would be appropriate for relatively clear sky with an optical thickness of about 0.5 or less. The

PSF is then computed for various viewing geometry using the phase function for three aerosol models: urban, maritime and continental.

SINGLE SCATTERING POINT SPREAD FUNCTION

For a plane parallel atmosphere where the optical properties depend only on the vertical distance z above the ground, the optical parameters required to characterize the atmosphere are the extinction coefficient $\kappa_e(z)$, single scattering albedo $\omega_0(z)$ and the scattering phase function $P(\cos\theta; z)$ for scattering angle θ . The formal solution [2] of the radiative transfer equation along the direction of a vector s is

$$L(\tau) = L(0) \exp\left(\frac{-\tau}{u}\right) + \frac{1}{u} \int_0^\tau J(\tau') \exp\left(\frac{-(\tau-\tau')}{u}\right) d\tau' \quad (1)$$

where τ is the optical thickness at a height z ,

$$\tau(z) = \int_0^z \kappa_e(z') dz' \quad (2)$$

$J(\tau)$ is the scattering source function, u is the direction cosine of the vector s with respect to the z -axis. The vector s is assumed to be directed upward so that the direction cosine u is positive.

The imaging geometry is illustrated in Fig. 1. A sensor is located at P, at a height H above the ground. The direct line of sight of the sensor intercepts the ground at the point Q. The line QP makes an angle θ with the upward normal and the azimuth angle of QP is ϕ . The spatial distribution of the reflectance on the ground, assumed to be Lambertian, is $\rho(x,y)$. Due to the finite dimension of the sensor, the field of view of the sensor traces out a "footprint" on the ground which can be represented by a dimensionless function $f_0(x,y)$ which has a value of unity if the point (x,y) is inside the footprint and zero otherwise.

In a plane parallel atmosphere, the path radiance L_{path} due to scattering of sun light from the atmosphere is a constant independent of the ground reflectance, and will not be considered further. When the sensor at P is looking at the point Q having the coordinates (x, y) on the ground, the

irradiance at the sensor due to the direct reflected radiance (zero-scattering component) is

$$I_0(x, y) = \frac{E_i u e^{-\tau H/u}}{\pi s^2} \iint \rho(x', y') f_0(x - x', y - y') dx' dy' \quad (3)$$

where E_i is the total incident solar irradiance, $u = \cos \theta$ is the direction cosine of QP, $s = H/u$ is the distance QP and τH is the vertical optical thickness at P.

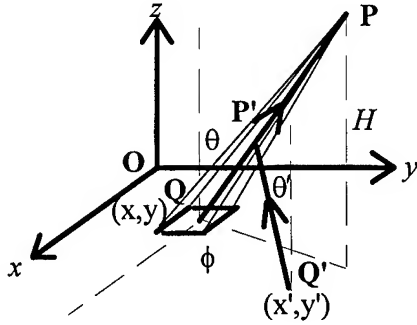


Fig. 1: Imaging geometry

If only single scattering at the atmosphere is considered, then the contribution to the adjacency effect is due to light coming from neighbouring points such as Q' at (x', y') reaching the sensor after one scattering event at a point P' along the line of sight of the sensor. The single scattering source function can then be expressed as

$$J_1(\tau) = \frac{\omega_0}{4\pi} \iint \frac{dx' dy' u'}{\pi r'^2} E_i \rho(x', y') e^{-\tau/u'} P(\cos \gamma) \quad (4)$$

where r' is the distance Q'P', $u' = \cos \theta'$ is the direction cosine of Q'P' and γ is the scattering angle. These variables are dependent on the coordinates of Q (x, y) and Q' (x', y') . If the height of P' above the ground is z' , and the azimuth angles of QP and Q'P' are ϕ and ϕ' respectively, then it can be shown that

$$r'^2 = [(x - x') + z' \tan \theta \cos \phi]^2 + [(y - y') + z' \tan \theta \sin \phi]^2 + z'^2 \quad (5)$$

$$u' = z' / r' \quad (6)$$

$$\tan \phi' = \frac{(y - y') + z' \tan \theta \sin \phi}{(x - x') + z' \tan \theta \cos \phi} \quad (7)$$

$$\cos \gamma = uu' + (1 - u^2)^{1/2} (1 - u'^2)^{1/2} \cos(\phi - \phi') \quad (8)$$

The single scattering irradiance at the sensor can then be expressed in a form similar to Eqn. (3),

$$I_1(x, y) = \frac{E_i u e^{-\tau H/u}}{\pi s^2} \iint \rho(x', y') f_1(x - x', y - y') dx' dy' \quad (9)$$

where

$$f_1(x - x', y - y') = \frac{\omega_0 A}{4\pi u} \int_0^H \frac{u'}{r'^2} e^{-\tau(1/u' - 1/u)} P(\cos \gamma) d\tau \quad (10)$$

The total irradiance at the sensor can then be expressed in the form of a convolution,

$$I(x, y) = \frac{E_i u}{4\pi s^2} e^{-\tau H/u} \rho(x, y) * (f_0(x, y) + f_1(x, y)) \quad (11)$$

Note that the blurring function $f_1(x, y)$ is due to the effects of single scattering from the atmosphere as well as the sensor's field of view. In fact, the scattering effect can be decoupled from the sensor's field of view by expressing f_1 as a convolution between $f_0(x, y)$ and a single scattering point spread function $h_1(x, y)$,

$$f_1(x, y) = f_0(x, y) * h_1(x, y) \quad (12)$$

with

$$h_1(x, y) = \frac{\omega_0}{4\pi u} \int_0^H \frac{u'}{r'^2} e^{-\tau(1/u' - 1/u)} P(\cos \gamma) d\tau \quad (13)$$

This single scattering PSF can be numerically evaluated. The equation (11) can be rewritten as

$$I(x, y) = \frac{E_i u}{4\pi s^2} e^{-\tau H/u} \rho(x, y) * h(x, y) * f_0(x, y) \quad (14)$$

where the effective point spread function is

$$h(x, y) = \delta(x, y) + h_1(x, y) \quad (15)$$

COMPUTATION OF SINGLE SCATTERING PSF

In this section, the results of computation of the single scattering PSF using Eqn. (13) are presented. The sensor is assumed to be flying at a height $H = 800$ km. Without loss of generality, the azimuth angle of the sensor line of sight is set at $\phi = 0$, i.e. the sensor is assumed to be looking parallel to the x-axis towards the negative direction. The zenith angle θ varies from 0 to 60 degrees. The extinction coefficient $\kappa_e(z)$ is assumed to vary with the height z according to an exponential relation,

$$\kappa_e(z) = \kappa_e(0) e^{-z/L} \quad (16)$$

where L is the characteristic height of the aerosol distribution and $\kappa_e(0)$ is the extinction coefficient at ground level which is related to the optical thickness at sensor height by

$$\tau_H = \kappa_e(0) L (1 - e^{-H/L}) \quad (17)$$

A value of 2 km is assumed for the characteristic height.

The phase functions, single scattering albedo and asymmetry for three aerosol models (continental, maritime and urban) were computed using the Mie routine from the 6S package [3]. For simplicity in the computation of the point spread function, the scattering phase function was modeled by the single parameter Henyey-Greenstein function using the asymmetry of the Mie phase functions computed for the respective aerosol models. The computed asymmetry and single scattering albedo for the aerosol models are shown in Table 1.

Table 1: Asymmetry (g) and single scattering albedo (ω_0) for the three aerosol models

	Continental	Maritime	Urban
g	0.6371	0.7425	0.5906
ω_0	0.8917	0.9890	0.6463

In the computation, the atmosphere is divided into 100 equal optical thickness layers from ground to the sensor height. The ground is divided into grid points equally spaced at 10 m intervals in both the x and y directions. At each grid point (x, y) , the value of the single scattering PSF $h_1(x, y)$ is computed using Eqn. (13). The trapezoidal rule is used in the computation of the integral.

The computed profiles of the single scattering PSF at a wavelength of 550 nm for three values of view angle ($\theta = 60^\circ, 25^\circ$ and 0°) for the three aerosol models are plotted in Fig. 2.

Since the sensor is viewing along the x -axis, and the ground is assumed to be Lambertian, the PSF must necessarily be symmetric about the x -axis. If the view angle is zero, i.e. the sensor is looking vertically down, then the PSF must have circular symmetry about the origin. However, for non vertical viewing, the PSF is asymmetric about the y -axis. In fact, it is seen that the peak of the PSF shifts towards the negative y -axis. The shift increases with increasing view angle. The PSF is also asymmetric about its peak. Generally, the slope is steeper on the side nearer to the origin, but the PSF decreases more gradually away from the origin resulting in a long 'tail'. The full width at half maximum generally increases with increasing view angle. The width ranges from about 30 m at zero view angle to more than 100 m at large view angles. Despite the different asymmetry and single scattering albedo for the three aerosol models, their PSF have similar shapes.

CONCLUSIONS

In conclusion, we have derived the single scattering point spread function from the radiative transfer equation. The PSF has been computed for various view angles for three aerosol models. The atmosphere was assumed to be plane-parallel. A single type of aerosols with an exponential vertical concentration profile was assumed. The computation was carried out at a single wavelength band. However, the model can be easily extended to include more than one type of aerosols, and computation for more than one wavelength band can also be done. The scattering phase function was modeled by the single parameter Henyey-Greenstein function using the asymmetry computed for the respective aerosol model. It is possible to replace the Henyey-Greenstein phase function by a look-up table generated from the Mie-calculation for a given aerosol model.

REFERENCES

- [1] Kaufman YJ (1989), The atmospheric effect on remote sensing and its corrections, in "Theory and applications of optical remote sensing", ed. by G. Asrar, John Wiley & Sons, New York, pp. 336-428.
- [2] Chandrasekhar S (1950), "Radiative transfer", Oxford Univ Press, UK; republished by Dover, New York (1960).
- [3]. Vermote E, Tanre D, Deuze JL, Herman M, and Morcrette JJ, Second simulation of the satellite signal in the solar spectrum (6S), distributed by NASA Goddard Space Flight Center, code 923, Greenbelt, MD 20771.

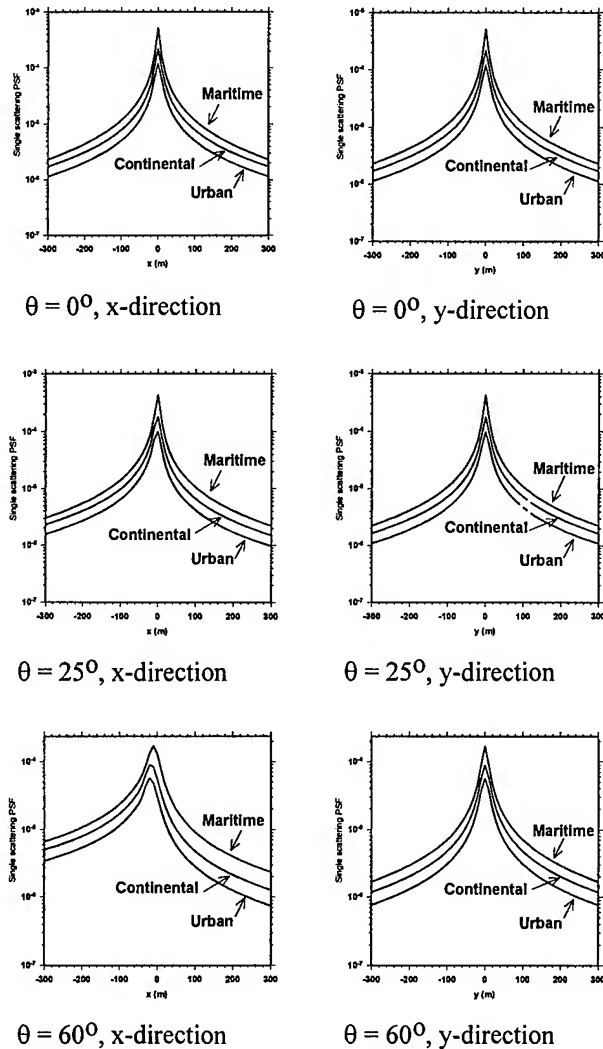


Fig. 2: Profiles of the single scattering point spread functions along the x and y directions.

AEROSOL RETRIEVAL USING SYNTHETIC POLDER MULTI-ANGULAR DATA

K.-S. Kuo*, R. C. Weger, and R. M. Welch

Institute of Atmospheric Sciences, South Dakota School of Mines and Technology
Rapid City, South Dakota

Abstract -- The POLarization and Directionality of the Earth's Reflectances (POLDER) instrument onboard the Japanese ADEOS satellite offers unique possibilities for the retrieval of aerosol parameters with its polarization and multi-angular capability. In this study we examine a technique that simultaneously retrieve multiple aerosol parameters, namely asymmetry factor, single-scattering albedo, surface albedo, and optical thickness, using simulated POLDER reflectances. It is found that, over dark or bright surfaces, simultaneous retrieval of multiple parameters is indeed possible, but not over surfaces with intermediate reflectivity. Among the four parameters, the single-scattering albedo is retrieved with the best accuracy and is the least vulnerable when the reflectance value is subjected to a 0.1% white noise.

INTRODUCTION

Atmospheric aerosol particles, both natural and anthropogenic, are important to the earth's radiative balance through their direct and indirect effects. They scatter the incoming solar radiation (direct effect) and modify the shortwave reflective properties of clouds by acting as cloud condensation nuclei (indirect effect). IPCC [1] estimates the radiative forcing of its direct effect to be -0.5 W/m^2 globally while the radiative forcing of the indirect effect ranges from 0 to -1.5 W/m^2 with much larger uncertainty. In order to understand the role that aerosols play in a changing climate, detailed and accurate observations are a prerequisite.

The retrieval of aerosol optical properties by satellite remote sensing has proven to be a difficult task, especially over land. The difficulty results mainly from the tenuous nature and variable composition of aerosols. To date, with single-angle satellite observations, we can only retrieve reliably against dark backgrounds, such as over oceans and dense vegetation. Even then, assumptions must be made concerning the chemical composition of aerosols, which may be highly variable. The best hope we have for aerosol retrievals over land surfaces are observations from multiple angles [2, such as those provided by the POLDER [3] and MISR [4] instruments.

In this investigation we examine the feasibility of simultaneous retrieval of multiple aerosol optical parameters using reflectances from three typical sets of twelve angles observed by the French POLDER instrument [3]. Specifically, angular sets 1, 2, and 3 in [3] are investigated; they correspond to, respectively, the nadir set, the backward set, and the forward set referred to in this study. The simultaneously retrieved aerosol optical

parameters consist of asymmetry factor, single scattering albedo, surface albedo, and optical thickness.

METHODOLOGY

Radiative Transfer Simulations

The Discrete Ordinate Model (DOM) developed by Stamnes *et al.* [5] is used to make the radiative transfer simulations in this study. First, a regular grid system is generated for the four-dimensional parametric space of asymmetry factor (g), single scattering albedo (ω_0), surface albedo (α), and optical thickness (τ). Specifically, g is varied from 0.6 to 0.8 at an interval of 0.025, ω_0 from 0.8 to 1 at an interval of 0.025, α from 0 to 0.72 at an interval of 0.06, and τ from 0.01 to 2.1 at an interval of approximately 0.13. The coordinate of a particular grid point is therefore specified by a 4-tuple of ($g, \omega_0, \alpha, \tau$). Using the components of the 4-tuple as inputs to DOM, model simulations are made for all grid points to obtain the *control* reflectance values at the three sets of observation angles. Reflectance values are also obtained for the same angles by randomly sampling the four-dimensional parametric space; these compose the *test* reflectance values.

The Henyey-Greenstein approximation is used to construct the phase functions from asymmetry factors for all simulations. The modeled atmosphere is assumed to contain only one homogeneous layer of aerosols. The modeled reflective surface is assumed to be Lambertian. A solar zenith angle of 45° is used in all simulations.

Polynomial Fitting

To estimate the optical parameters using the multi-angular reflectance values, we choose a least-squares polynomial fitting technique. If we denote the reflectance values at the K observational angles by r_i , where $i = 1, 2, \dots, K$, any of the optical parameter can be approximated by a d^{th} degree polynomial in the K variables of r_i . The coefficients of the polynomial are chosen to minimize the squares of errors at the grid points. The polynomial hence maps a hyper-surface in the K -dimensional reflectance space to a hyperplane in the four-dimensional optical parameter space. Note that, as d or K increases, the number of terms, N , in the polynomial increases much faster than linearly. The computational complexity of the present technique is roughly N^3 , therefore the computation cost increases dramatically when d or K get large.

RESULTS

It is found that using a third degree ($d = 3$) polynomial and every other angle ($K = 6$), one already approaches the limit of the retrieval accuracy; increasing the number of angles or the degree of the polynomial does not significantly improve the accuracy to warrant the extra computational cost. This is true for all three sets of angles investigated.

Using "pure" simulated data (i.e. without noise), the root-mean-square (rms) errors for the simultaneous retrieval of all four parameters are listed in Table 1 for the three sets of angles. It is rather interesting to find that g and ω_0 can be estimated with much higher confidence than α and τ . The retrievals of α and τ are more accurate using the nadir and backward sets of angles (sets 1 and 2), while the forward set yields better retrievals of g and ω_0 .

Since g and ω_0 can be accurately retrieved, a logical step to improvement is to fix g and ω_0 values and to apply the same polynomial fitting technique to α and τ . The original problem is equivalent to mapping a hyper-

surface in the reflectance space to a hyperplane in a four-dimensional space, while the current one maps to a straight line in a two-dimensional space. One would expect much better accuracy due to the reduced complexity of the problem. However, the results show that the improvement is quite negligible.

In Figure 1, we plot the reflectance values at every third angle of the twelve angles in the forward set (set 3) by varying α and τ but at fixed values of g and ω_0 . In the figure, μ is the cosine of the observation zenith angle and $\Delta\phi$ is the relative azimuth between the incident and observation directions. It is seen that, when α is small (large), the reflectance values increase (decrease) with increasing τ . However, when α assumes intermediate values (around 0.6), the reflectance values stay fairly constant across a wide range of τ , especially towards the large end of it. Similarly, when τ is large (>1.2) the reflectance values show no influence by the surface albedo. It is this ambiguity that results in large errors in the retrieval of α and τ . Indeed, if we assume that the surface albedo is known *a priori* and apply the same technique to simultaneously

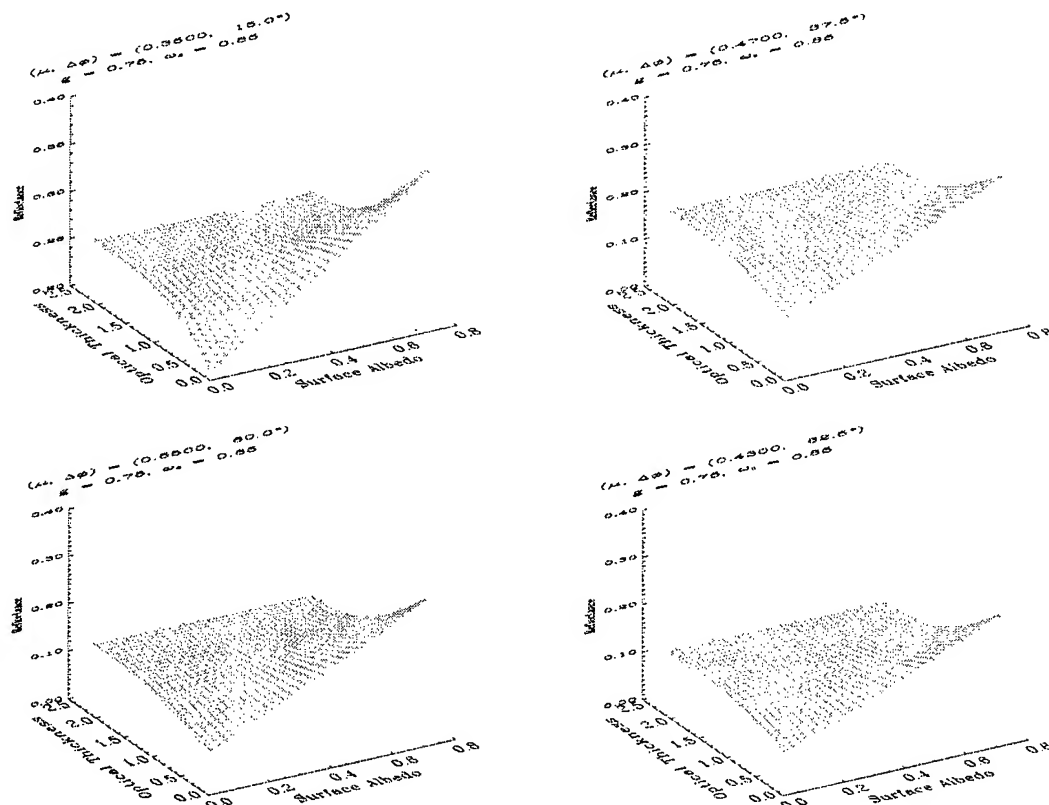


Figure 1. Reflectances (z-axis) as functions of surface albedo (x-axis) and aerosol optical thickness (y-axis) at $(\mu, \Delta\phi)$ of $(0.35, 15^\circ)$, $(0.47, 37.5^\circ)$, $(0.43, 82.5^\circ)$, and $(0.55, 60^\circ)$, clockwise from top left. The x-axis ranges from 0 to 0.8 while y-axis ranges from 0 to 2.5.

retrieve g , ω_0 , and τ , we find that much improved accuracy can be obtained for the retrieval of τ when α is smaller than 0.1 or larger than 0.6. There is no discernible improvement, however, for in-between values of α .

With 0.1% white noise added to the simulated data the rms error for the simultaneous retrieval worsens considerably. Table 2 lists these errors. Comparing Table 1 and 2, one observes that, again surprisingly, single-scattering albedo is the most accurate and the least vulnerable to the added noise.

When simultaneously retrieving g , ω_0 , and τ , by assuming α is known, the rms error for the retrieval of optical thickness in the presence of noise is about 3 to 4 times of that for the optical thickness retrieval without noise. Under no circumstance, i.e. low or high surface albedo, is the error better than 0.1.

Table 1. rms error for simultaneous retrieval from "pure" data

Set	α	g	ω_0	τ
1	0.076	0.006	0.004	0.126
2	0.085	0.008	0.004	0.166
3	0.101	0.003	0.002	0.211

Table 2. rms error for simultaneous retrieval from data with 0.1% white noise

Set	α	g	ω_0	τ
1	0.167	0.028	0.012	0.376
2	0.199	0.040	0.017	0.479
3	0.249	0.018	0.011	0.858

DISCUSSIONS AND CONCLUSIONS

We find that, using the chosen set of angles, the asymmetry factor and the single scattering albedo of an aerosol layer can be retrieved with high confidence. Due to ambiguity in the reflectance signal, surface albedo and aerosol optical thickness cannot be retrieved as accurately. However, when the surface reflectivity is low or high and its value is known, the simultaneous retrieval of the other three parameters improves.

The particular strength of the present technique is that it does not assume any *a priori* knowledge for the aerosol composition, i.e. the index of refraction. Using the present technique and the typical POLDER angles, one can retrieve single scattering albedo accurately at any wavelengths available from the instrument. The spectral dependence of single scattering albedo will no doubt give important clues to the chemical composition of aerosols. One can therefore make radiative transfer simulations with the correct chemical composition to yield better estimates of optical thickness.

ACKNOWLEDGMENT

The authors would like to thank Dr. Robert Curran of NASA Headquarters for his support and encouragement. Appreciation is extended to Connie Crandall for preparing the manuscript.

REFERENCES

- [1] J. T. Houghton, L. G. Meira Filho, B. A. Callander, N. Harris, A. Kattenberg, and K. Maskell, Eds., *Climate Change 1995 - The Science of Climate Change*. Cambridge: University of Cambridge, 1996, p. 21.
- [2] J. V. Martonchik, and D. J. Diner, "Retrieval of aerosol optical properties from multi-angle satellite imagery", *IEEE Trans. Geosci. Remote Sensing*, vol. 30, pp. 223-230, 1992.
- [3] P.-Y. Deschamps, F.-M. Breon, M. Leroy, A. Po-daire, A. Bricaud, J.-C. Buriez, and G. Seze, "The POLDER mission: Instrument characteristics and scientific objectives", *IEEE Trans. Geosci. Remote Sensing*, vol. 32, pp. 598-615, 1994.
- [4] Diner, D. J., *et al.*, "MISR: A multiangle imaging spectroradiometer for geophysical and climatological research from EOS", *IEEE Trans. Geosci. Remote Sensing*, vol. 27, pp. 200-214, 1989.
- [5] K. Stamnes, S. C. Tsay, W. Wiscombe and K. Jayaweera, "Numerically stable algorithm for discrete-ordinate-method radiative transfer in multiple scattering and emitting layered media" *Appl. Optics*, vol. 27, pp. 2502-2509, 1988.

Aerosol Optical Thickness and Scattering Phase Function Retrieval from Solar Radiances Recorded over Water : A Revised Approach

D. K. Paronis, J. N. Hatzopoulos

University of the Aegean, Dept. of Environmental Studies

Karadoni 17, 81100 - Mytilene, GREECE

Tel: ++30-251-42849 / Fax: ++30-251-23783 / E-mail: dpar@env.aegean.gr

Abstract -- The possibility of deriving aerosol optical thickness and phase function values for certain scattering angles from solar radiances recorded over the oceans is examined. Radiative transfer simulation results for the Advanced Very High Resolution Radiometer (AVHRR) and the Moderate Resolution Imaging Spectrometer (MODIS) instruments are presented. These results indicate that an iterative procedure should be used for the simultaneous determination of the two quantities.

INTRODUCTION

Aerosol optical thickness retrieval from solar radiances recorded over dark surfaces such as the oceans or land covered with dense vegetation, require accurate determination of the aerosol optical characteristics namely of the single scattering albedo and the single scattering phase function. Existing aerosol models have been proved to describe accurately the prevailing local conditions under certain circumstances [1]. Nevertheless, the uncertainties imposed by such an approximation may be large under extreme episodes or for large scale observations [2],[3].

Particle size and correspondingly phase function variability has been considered as a serious drawback in aerosol optical thickness retrievals. The problem was first addressed in [3] where a dual-channel method was proposed for the aerosol optical thickness estimation from measurements over the oceans using a variable phase function. The ratio of the measured radiances in the two solar channels of the Advanced Very High Resolution Radiometer (AVHRR) was used as a particle size index for the parametrization of the two-term Henyey-Greenstein phase function. Since this work, multi-channel algorithms have been proposed for the direct determination of the aerosol size distribution from AVHRR observations [4] and theoretical assessments have been carried out for future sensors such as the Moderate Resolution Imaging Spectrometer (MODIS) [5]. The problem of deriving the aerosol phase function from AVHRR observations over the oceans was addressed again in [6]. In this approach the AVHRR response was modeled for realistic marine aerosol models defined from in-situ measurements. More precisely, the possibility of deriving the marine aerosol phase function for certain scattering angles from the ratio of the measured radiances in the two solar AVHRR channels was investigated. It was finally concluded that for angles

between 80 and 110 deg. phase function retrieval is possible with sufficient accuracy.

Following this approximation, in the present work, radiative transfer simulation results are presented for AVHRR and MODIS instrument. As it is shown, the spectral ratio values recorded by both instruments depend not only on the phase function values but also on the aerosol optical thickness. In the frame of these results an iterative dual-channel algorithm is proposed for the simultaneous determination of the aerosol optical thickness and the single scattering phase function.

METHODOLOGY - RESULTS

The response of the first two AVHRR channels (0.58 - 0.68 μm , 0.7 - 1.1 μm) and the two MODIS channels centered at 0.55 μm and 0.659 μm was simulated by radiative transfer computations for various aerosol phase functions and different values of the aerosol optical thickness. The computations were performed with the aid of the 6S code which is an updated version of code 5S [7]. The set of phase functions was generated by assuming constant value for particle refractive index with real and imaginary parts equal respectively to 1.45 and 0.0 and a mono-modal size distribution with varying median radius and standard deviation of $\log r$. The underlying surface was assumed to be non-reflective ($\rho=0$), the scattering angle was set to 120 deg. while Rayleigh scattering was not taken into account.

Computation results are presented in Fig. 1 for both instruments in a form of scatter diagrams. In these diagrams, apparent reflectance in the visible is plotted against the apparent near infrared-to-visible reflectance ratio. In both diagrams contours of equal phase function value and of equal aerosol optical thickness are given.

These results indicate that quantities A_i and A_j/A_i can be used for the inversion of the aerosol optical thickness and the phase function value for the corresponding scattering angle. Additionally, from this set of contours it becomes evident that the two quantities depend on both the value of the phase function and the aerosol optical thickness. Thus, the spectral ratio measured by the sensors cannot be used alone for the phase function determination. For this to be possible, an iterative algorithm should be used.

Iterative Algorithm

Based on the set of the pre-computed values for MODIS

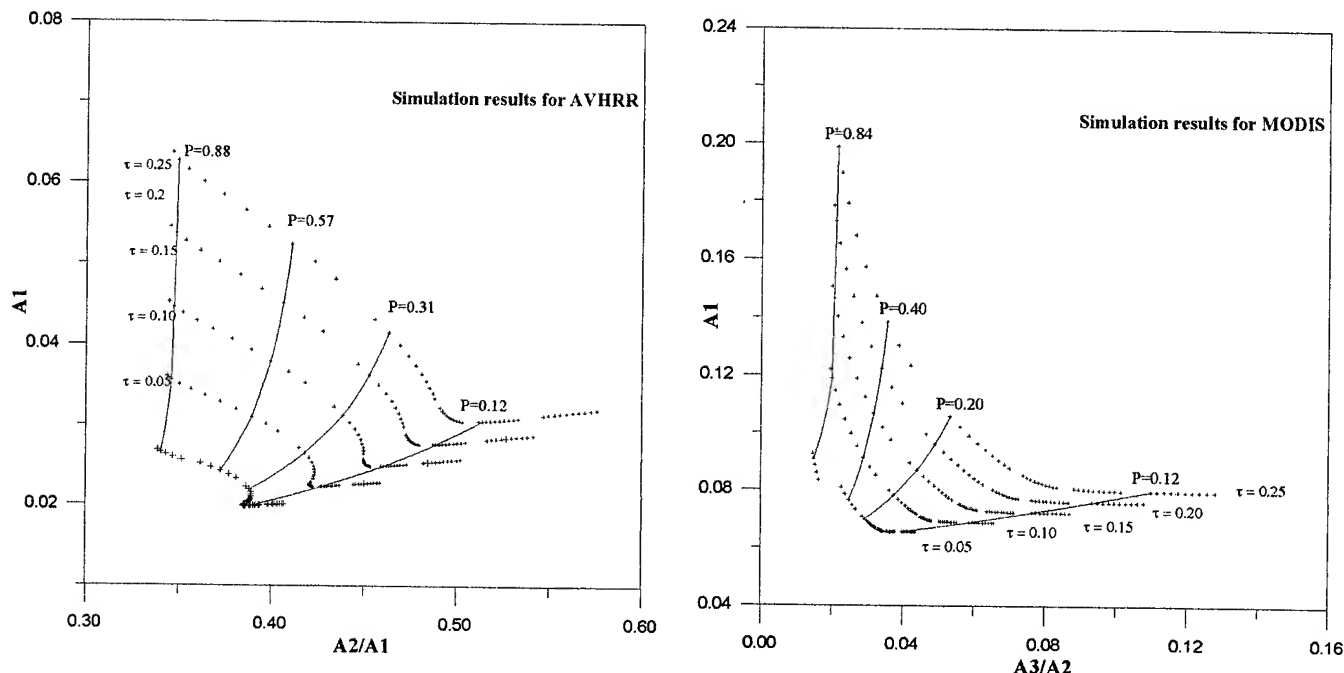


Fig. 1 : Simulation results plotted in the form of contours of equal aerosol optical thickness and of equal phase function value. X and Y axis represent respectively apparent near infrared-to-visible reflectance ratio and apparent reflectance in the visible. Computations were performed for scattering angle equal to 120 deg., refractive index $m = 1.45$ and surface reflectance $\rho = 0$.

instrument, an algorithm has been implemented for the simultaneous determination of aerosol optical thickness and phase function. The algorithm starts with an initial guess of the optical thickness value (τ^0). From the measured values of A_2 and A_3/A_2 a first guess of the phase function value (P^0) is defined by inverting the relation $A_3/A_2 = f(P, \tau^0)$. An estimation of the optical thickness (τ^1) is then defined by inversion of $A_2 = g(P^0, \tau)$ function. The procedure is repeated iteratively until convergence is attained. In the above procedure all the inversions are accomplished by using properly constructed Look Up Tables and linear interpolations through the pre-computed values. In Fig. 2 results of two different 'runs' of the algorithm for MODIS instrument are presented. True values (τ , $P(120)$) for the two 'runs' were (0.2, 0.17) and (0.15, 0.7) while initial guesses for the optical thickness were 0.18 and 0.25 respectively. For the first case, the solution is obtained after a few iterations and the estimation error is nearly zero. For the second case convergence is attained after about 30 iterations with somewhat greater estimation error as regards the phase function value.

CONCLUDING REMARKS

Radiative transfer simulation performed for a scattering angle equal to 120 deg. for AVHRR and MODIS channels, indicate that measurement of the apparent reflectance and of the near infrared-to-visible reflectance ratio over the ocean surface can be used for inferring simultaneously the aerosol

optical thickness and the value of the phase function for the specific angle through an iterative technique. Additional simulations for other scattering angles and different band combinations are needed in order the applicability and the limitations of this approach to be further investigated.

REFERENCES

- [1] F. Dulac, D. Tanré, G. Bergametti, P. Buat-Menard, M. Desbois, and D. Sutton, "Assessment of the African airborne dust mass over the Mediterranean Sea using Meteosat data," *J. Geophys. Res.*, 97, 2489-2506, 1992.
- [2] A. M. Ignatov, and L. L. Stowe, "Validation of the NOAA/NESDIS satellite aerosol product over the North Atlantic in 1989," *J. Geophys. Res.*, 100, 5123-5132, 1995.
- [3] P. A. Durkee, F. Pfeil, E. Frost, and R. Shema, "Global analysis of aerosol particle characteristics," *Atmospheric Environment*, Vol. 25A, No. 11, 2457-2471, 1991.
- [4] Y. J. Kaufman, R. S. Fraser, and R. A. Ferrare, "Satellite measurements of large-scale air pollution: Methods," *J. Geophys. Res.*, 95, 9895-9909, 1990.
- [5] D. Tanré, M. Herman, and Y. J. Kaufman, "Information on aerosol size distribution contained in solar reflected spectral radiances," *J. Geophys. Res.*, 101, 19043-19060, 1996.

- [6] J. N. Porter, A. D. Clarke, and P. Flament, "Deriving optical depths over the oceans from AVHRR Satellite: Modeling studies and Validations," in press.
- [7] D. Tanré, C. Deroo, P. Duhaut, M. Herman, and J. J. Morcrette, "Description of a computer code to simulate the satellite signal in the solar spectrum : the 5S code," Int. J. Rem. Sens., Vol 11, No. 4, 659-668, 1990.

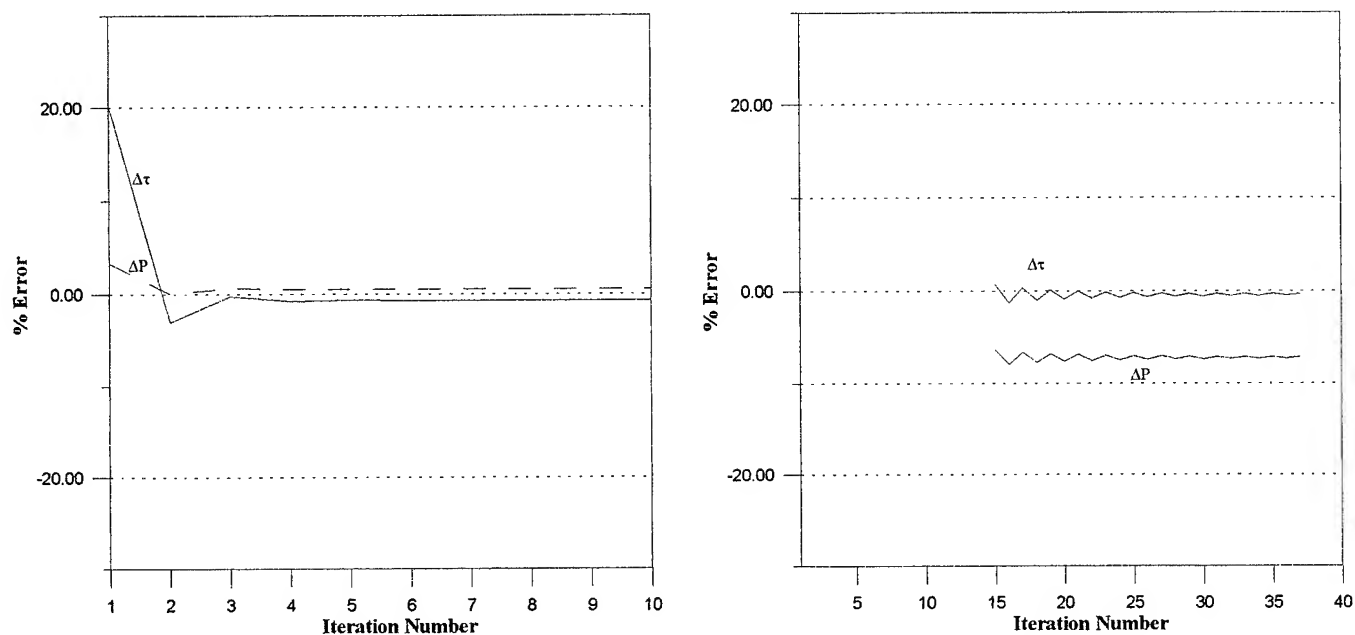


Fig. 2 : Estimation error of the iterative algorithm for two cases:

- a) $\tau=0.15$, $P(120)=0.7$, initial guess $\tau^0=0.18$,
- b) $\tau=0.2$, $P(120)=0.17$, initial guess $\tau^0=0.25$.

Satellite Remote Sensing of Fires, Smoke and Regional Radiative Energy Budgets

Sundar A. Christopher, Min Wang, Kristine Barbieri, and Ronald M. Welch
Institute of Atmospheric Sciences, South Dakota School of Mines and Technology
501 East Saint Joseph Street, Rapid City, SD 57701-3995

Shi-Keng Yang
Climate Prediction Center/NCEP
W/NMC53
World Weather Building, 5200 Auth. Road, #805
Washington, DC, 20233

Abstract -- Using satellite imagery, more than five million square kilometers of the forest and cerrado regions over South America are extensively studied to monitor fires and smoke during the 1985 and 1986 biomass burning season. The results are characterized for four major ecosystems, namely: (1) Tropical Rain Forest [TRF], (2) Tropical Broadleaf Seasonal [TBS], (3) Mild/Warm/Hot Grass/Shrub [MGS], and (4) Savanna/Grass and Seasonal Woods [SGW]. Using collocated measurements from the instantaneous scanner Earth Radiation Budget Experiment [ERBE] data, the direct regional radiative forcing of biomass burning aerosols are computed. The results show that more than 70% of the fires occur in the MGS and SGW ecosystems due to agricultural practices. The smoke generated from biomass burning has negative net radiative forcing values for all four major ecosystems within South America. The smoke found directly over the fires have mean net radiative forcing values ranging between -25.6 to -33.9 W/m^2 for 1985 and between -12.9 to -40.8 W/m^2 for 1986. These results confirm that the regional net radiative impact of biomass burning is one of *cooling*.

INTRODUCTION

Each year in the tropics, extensive areas of the forests and savannas are burned for agricultural purposes and to accommodate the needs of the expanding population [1]. The permanent removal of forests are replaced with grazing or crop land, while the land cleared for agricultural purposes is primarily used for shifting agriculture. Although burning takes place whenever there is plant material that is dry, biomass burning is concentrated between July and October in the Southern hemisphere, and between December and April in the northern hemisphere. In recent years, the effect of biomass burning on a global and regional scale has received due attention because of its effect on atmospheric chemistry, radiation budget, increasing greenhouse gases, loss of biodiversity, decreasing evapotranspiration and rainfall from altered general circulation patterns; increasing surface albedo and runoff; and spread of plant and human diseases via

colonization. The wide variety of satellite data from current and future instruments can be used to address these issues.

Although it has been well established that aerosols play a significant role on the radiation balance of the earth-atmosphere system, no comprehensive picture has yet emerged on how to obtain the radiative effects of aerosols on a global scale. The radiative effects of aerosols are often classified into two categories, namely, the "*direct effect*" [2] where the atmospheric aerosols scatter the incoming solar radiation, thereby reducing the amount of solar insolation to space and causing a "cooling effect", and the "*indirect effect*" [3] where the aerosols act as cloud condensation nuclei and modify the shortwave reflective properties of clouds. This effect could cause either "cooling" or "warming" depending upon the optical properties of clouds. Current estimates of the global direct effect of biomass burning range from -0.8 W/m^2 [2] to -0.2 W/m^2 [4].

We take a different approach to obtain the radiative forcing of aerosols which is similar to the cloud radiative forcing concept. In this method, narrowband measurements from the AVHRR are used to identify the smoke from biomass burning. Then, collocated measurements from the ERBE scanner are used to determine the TOA fluxes for both clear sky and aerosol regions. The difference between the clear and aerosol regions in the shortwave and longwave parts of the spectrum provide the "shortwave aerosol radiative forcing" and "longwave aerosol radiative forcing" respectively. These values are called "instantaneous radiative forcing values" because they are obtained during the time of the satellite overpass. In order to obtain a global mean value, sufficient spatial and temporal sampling must be available. The CERES/VIRS combination of instruments that will be available in the near-future from the TRMM platform is especially suited for obtaining global means of aerosol radiative forcing because the tropical regions will be sampled several times during any given day.

Acknowledgments: This research was supported by NASA Grant NAGW-3740 managed by Dr. Robert J. Curran, and by NASA New Investigator Program Grant NAGW-5195, managed by Dr. Ghassem Asrar.

DATA SETS, PREPROCESSING METHODS, AND REGION OF STUDY

The AVHRR LAC images from NOAA-9 are used in this analysis to map fires and smoke as a function of four major ecosystems. The period of study is between August to October, 1985 and July to October, 1986. Only daytime images during the ascending orbit (14:30 local solar time (LST)) are used. The ERBE scanner, which was operational between February 1985 and January 1987 on NOAA-9, are used to obtain the radiative fluxes at the top of atmosphere (TOA). The spatial resolution at nadir of the AVHRR and ERBE are about $1.1 \times 1.1 \text{ km}^2$ and $35 \times 35 \text{ km}^2$ respectively.

The region of study shown in Figure 1 in the enclosed rectangle between 10N to 30S and 40W to 80W encompasses four major ecosystems within South America. The four ecosystems [5] are: (1) Tropical Rainforest (TRF), (2) Tropical Broadleaf Seasonal (TBS) with dry or cool season, (3) Savanna/grass and seasonal woods (SGW), and (4) Mild/warm/ hot grass shrub (MGS).

METHODOLOGY

The detection of fires from AVHRR imagery is a well-established procedure. The physical principle behind the detection of fires from AVHRR imagery is the increased $3.7 \mu\text{m}$ channel response to fires when compared to the background. Robinson defines the amplification factor as the ratio of fire irradiance to the background irradiance. Calculations show that at $3.7 \mu\text{m}$, amplification factors of about 3200 and 20000 are predicted for cool (1000K) and hot fires (1800K) which makes the detection of fires possible from satellite imagery.

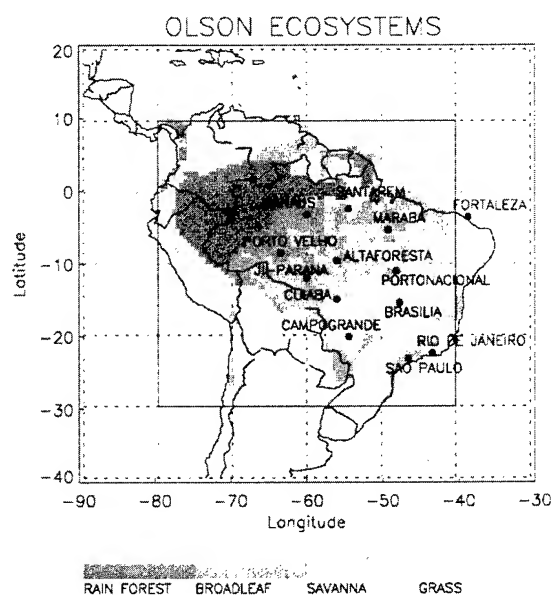


Fig. 1: Major ecosystems over South America.

Smoke pixels are identified by first locating fires within a collocated ERBE pixel. Within an ERBE pixel if fire and/or fires are present, then each AVHRR pixel is checked to ensure if the channel 4 temperatures are warmer than 273K. If this criteria is satisfied, then the ERBE pixel is classified as a "smoke pixel." This method captures the smoke directly above the fires that are warmer than 273K. Although it is possible to include clouds in this method, a visual examination of several images shows that directly above the fires, smoke predominates, as opposed to low level water clouds.

RESULTS

During August, September, and October 1985, a total of 211,580 fires were detected in all four ecosystems. Out of these, less than 1% of the fires were detected in the TRF. The percentage of fires detected by the TBS, MGS, and SGW ecosystems were 27%, 32%, and 40%, respectively. These results indicate that the majority of the fires are related to agricultural practices.

Figure 2 shows the temporal distribution of fires along with percent cloud cover values for July through October 1986. Peak fire activities are in late August and early September with more than 1500 fires detected for all ecosystems. A total of 9, 17, 17, and 22 images were used in this analysis for July, August, September, and October, and the number of fires detected were around 8851, 9622, 6253, and 11,548 respectively. There appears to be a well-defined relationship between the total number of fires and the clouds over this area which shows the difficulty in obtaining exact fire counts over the South American region.

Table 1 shows the SWARF, LWARF, and NE-TARF values for the four ecosystems. The SWARF values for all four ecosystems are negative, ranging from -25.3 to -40.6 W/m^2 . The TRF results should be

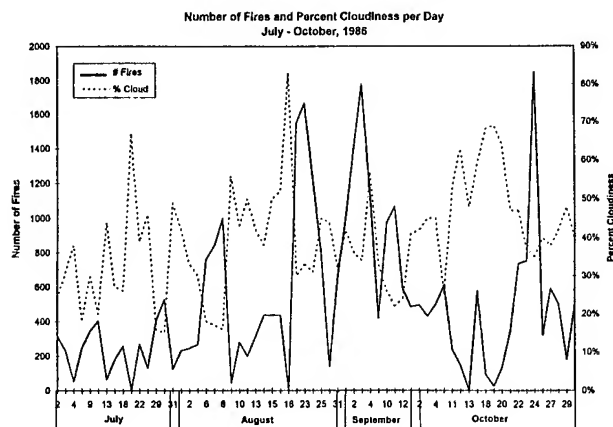


Fig. 2: Fire counts and percent cloud cover for the 1986 biomass burning season.

interpreted with caution because very few smoke pixels were identified during the period of study. The negative values indicate that the smoke pixels on the average reflect more of the incoming solar radiation as opposed to clear sky regions. These values are consistent with our previous study [7]. The mean LWARF values range from -0.3 to 6.7 W/m², with the MGS ecosystem having the only negative LWARF value. The NETARF, which is the sum of the SWARF and LWARF terms, therefore, shows the predominant effect of the reflective properties of smoke aerosols. The instantaneous net radiative forcing values are negative for all four ecosystems, with the TBS ecosystem having the largest NETARF values of about -35.3 W/m². Similar results are shown for 1986. These results show that the net radiative impact of aerosols for all four major ecosystems in South America is one of cooling.

Table 1

Mean shortwave, longwave, and net radiative forcing [W/m²] for four ecosystems for 1985 and 1986.

<u>1985</u>				
	TRF	TBS	MGS	SGW
SWARF	-40.6	-36.0	-25.3	-35.8
LWARF	6.7	0.7	-0.3	5.3
NETARF	-33.9	-35.3	-25.6	-30.5

<u>1986</u>				
	TRF	TBS	MGS	SGW
SWARF	-47.2	-36.6	-30.8	-32.6
LWARF	6.4	4.2	17.9	8.3
NETARF	-40.8	-32.4	-12.4	-24.3

SUMMARY

Collocated narrowband and broadband measurements are very useful in evaluating the direct radiative forcing of biomass burning aerosols on a regional scale. In this study, the 1985 and 1986 biomass burning season between July through October has been studied to monitor fires and smoke and to estimate the direct regional radiative impact of aerosols in four major ecosystems over South America. The AVHRR LAC data are used to detect fires and smoke. The broadband ERBE measurements are used to compute the instantaneous SW, LW and net radiative forcing of

biomass burning aerosols. The majority of the fires occur in the SGW and MGS ecosystems, which are broadly called the cerrado regions. The TRF ecosystem (selva) has less than 1% of the total fires that were detected. The smoke from biomass burning, which often spreads throughout the Amazon Basin, has a significant impact on the regional radiative balance. The average instantaneous radiative forcing of smoke for the four ecosystems that are studied are negative and range between -25.6 to -33.9 W/m² for 1985 and between -12.9 to -40.8 W/m² for the 1986 biomass burning season.

References

- [1] Andreae, M.O., Biomass burning: Its history, use, and its distribution and its impact on environmental quality and global climate, *In Global Biomass Burning*, J. S. Levine, ed., 1-21, 1991.
- [2] Penner, J.E., R.E. Dickinson, and C.A. O'Neill, Effects of aerosol from biomass burning on the global radiation budget, *Science*, 256, 1432-1434, 1992.
- [3] Schwartz, S.E., Are global albedo and climate controlled by marine phytoplankton, *Nature*, 336, 441-445, 1988.
- [4] Hobbs, P.V., J.S. Reid, R.A. Kotchenruther, R.J. Ferek, and R. Weiss, Direct radiative forcing by smoke from biomass burning, *Science*, 275, 1776-1778.
- [5] Olson, J.S., World Ecosystems (WE1.3 and WE 1.4) Digital Raster data on global Geographic (LAT/lon) 180X360 and 1080X2160 grids. Available from NOAA National Geophysical Data Center, Boulder, Colorado, 1991.
- [6] Robinson, J.M., Fire from space: Global fire evaluation using infrared remote sensing, *Int. J. Rem. Sens.*, 12[1], 3-24, 1991.
- [7] Christopher, S.A., D.V. Kliche, J. Chou, and R.M. Welch, First estimates of the radiative forcing of aerosols generated from biomass burning using satellite data, *J. Geophys. Res.*, 101, D16, 21265-21273, 1996.

Polarimetric Effects in Repeat-Pass SAR Interferometry

K. P. Papathanassiou and S. R. Cloude

DLR, Deutsche Forschungsanstalt für Luft- und Raumfahrt e.V.

P.O. Box 11 16, D-82230 Oberpfaffenhofen, Germany. Tel/Fax: +49-8153-28-2367/-1135

Email: kostas.papathanassiou@dlr.de , scloude@fges.demon.co.uk

Abstract - - In this paper we examine the role wave polarisation play in the interpretation of interferograms. We first propose a general formulation for vector wave interferometry and differential interferometry which includes the conventional scalar interferometry as a special subcase. Then we demonstrate how polarimetric target decomposition theory can be introduced in interferometry for the physical interpretation of the interferometric phase. The potential of polarimetric SAR interferometry (POL-InSAR) is demonstrated by first results from the evaluation of fully polarimetric interferometric SIR-C/X-SAR data.

INTRODUCTION

Repeat-pass SAR-interferometry (InSAR) with conventional radar-systems working with a single fixed polarisation has been successfully applied to measure surface topography and to monitor topographic displacements over time. One of the critical points in the interpretation of interferograms is the estimation of the location of the effective scattering center. As a typical example topography extracted over vegetated areas can differ significantly from the underlying surface topography polarisation and target parameters as vegetation type and terrain characteristics.

For the interpretation of interferograms the understanding and modeling of the coherent interaction of EM-waves with the scatterer is required. POL-InSAR will be a new challenge for the characterisation of the relation between interferograms and physical parameters of the scatterer.

VECTOR INTERFEROMETRY

Scalar repeat-pass interferometry involves forming the hermitian product of the received complex signals s_1 and s_2 for each resolution element from images I1 and I2 acquired at different times during two repeating passes over the same area. Of special significance is the hermitian positive semi-definite coherency matrix $[J]$ defined as

$$[J] = \left\langle \begin{bmatrix} s_1 \\ s_2 \end{bmatrix} \begin{bmatrix} s_1^* & s_2^* \end{bmatrix} \right\rangle = \left\langle \begin{bmatrix} s_1 s_1^* & s_1 s_2^* \\ s_2 s_1^* & s_2 s_2^* \end{bmatrix} \right\rangle \quad (1)$$

where * means complex conjugation. From $[J]$ we can ob-

tain the expression for the interferometric phase as

$$\tan(\phi_i) = \frac{\text{Im}(\langle s_1 s_2^* \rangle)}{\text{Re}(\langle s_1 s_2^* \rangle)} \longrightarrow \phi_i = \arg(\langle s_1 s_2^* \rangle) \quad (2)$$

and the expression for the interferometric coherence coefficient γ between s_1 and s_2 as

$$\gamma = \frac{|\langle s_1 s_2^* \rangle|}{\sqrt{\langle s_1 s_1^* \rangle \langle s_2 s_2^* \rangle}} \quad 0 \leq \gamma \leq 1 \quad (3)$$

Polarimetric radar systems measure the 2×2 complex scattering matrix $[S]$ for each resolution element in the image. In order to generalise the expressions for the interferometric phase and coherence we define a coherent scattering vector \underline{k} equivalent to the vectorisation of the scattering matrix $[S]$

$$\underline{k} = \text{Trace}([S]\Psi_P) = \frac{1}{\sqrt{2}}[S_{hh} + S_{vv}, S_{vv} - S_{hh}, 2S_{hv}]^T \quad (4)$$

T indicate the matrix transposition operation, S_{mn} ($m, n = h$ or v) is the complex scattering coefficient for m transmitted and n received polarisation in the HV -polarimetric basis and Ψ_P are the set of 2×2 complex Pauli basis matrices [1]. We consider here only the case of backscattering, i.e. $S_{hv} = S_{vh}$. For the vectorisation of $[S]$ different basis sets can be used. The advantage of the Pauli matrix basis is that the elements of the resulting scattering vector are closer to the physics of wave scattering and allow a better interpretation of the scattering mechanisms.

Using the hermitian products formed from the vectors \underline{k}_1 and \underline{k}_2 for images I1 and I2 we can construct a single hermitian matrix $[T_6]$ as following

$$[T_6] = \left\langle \begin{bmatrix} \underline{k}_1 \\ \underline{k}_2 \end{bmatrix} \begin{bmatrix} \underline{k}_1^{*T} & \underline{k}_2^{*T} \end{bmatrix} \right\rangle = \left\langle \begin{bmatrix} [T_{11}] & [\Omega_{12}] \\ [\Omega_{12}]^{*T} & [T_{22}] \end{bmatrix} \right\rangle \quad (5)$$

where $[T_{11}]$, $[T_{22}]$, and $[\Omega_{12}]$ are given by

$$[T_{11}] = \langle \underline{k}_1 \underline{k}_1^{*T} \rangle, [T_{22}] = \langle \underline{k}_2 \underline{k}_2^{*T} \rangle, [\Omega_{12}] = \langle \underline{k}_1 \underline{k}_2^{*T} \rangle \quad (6)$$

$[T_{11}]$ and $[T_{22}]$ are the standard 3×3 hermitian coherence matrices for the separate images [1]. $[\Omega_{12}]$ is a 3×3 complex

matrix which contains all the interferometric phase information between the polarimetric channels. It is important to note that while $[T_6]$ hermitian by definition, $[\Omega_{12}]$ is not hermitian. Possible temporal changes force us to assume that in general $\underline{k}_1 \underline{k}_2^{*T} \neq \underline{k}_2 \underline{k}_1^{*T}$.

The next step is to introduce two unitary complex vectors \underline{w}_1 and \underline{w}_2 which we may interpret as two scattering mechanisms. We can define the corresponding complex scattering coefficients by forming the projection of the scattering vector onto the complex vectors \underline{w}_1 and \underline{w}_2 :

$$\mu_1 = \underline{w}_1^{*T} \underline{k}_1 \quad \mu_2 = \underline{w}_2^{*T} \underline{k}_2 \quad (7)$$

These complex scalars form the basis for the generation of vector interferograms. Equation (7) can now be combined with equation (5) to generate an expression for the 2×2 hermitian matrix $[J]$ which decouples the w -vectors and the matrix $[T_6]$

$$[J] = \begin{bmatrix} \underline{w}_1^{*T} & \underline{0}^{*T} \\ \underline{0}^{*T} & \underline{w}_2^{*T} \end{bmatrix} \begin{bmatrix} [T_{11}] & [\Omega_{12}] \\ [\Omega_{12}]^{*T} & [T_{22}] \end{bmatrix} \begin{bmatrix} \underline{w}_1 & \underline{0} \\ \underline{0} & \underline{w}_2 \end{bmatrix} \quad (8)$$

where $\underline{0}$ is a 3×1 zero matrix. Using (8) we can derive the expression for the vector interferogram formation as

$$\mu_1 \mu_2^* = (\underline{w}_1^{*T} \underline{k}_1)(\underline{w}_2^{*T} \underline{k}_2)^{*T} = \underline{w}_1^{*T} < [\Omega_{12}] > \underline{w}_2 \quad (9)$$

From (9) we obtain the interferometric phase as

$$\phi_i = \arg(\underline{w}_1^{*T} \underline{k}_1 \underline{k}_2^{*T} \underline{w}_2) = \arg(\underline{w}_1^{*T} < [\Omega_{12}] > \underline{w}_2) \quad (10)$$

and also the generalised expression for the coherence γ as

$$\gamma = \frac{|\underline{w}_1^{*T} < [\Omega_{12}] > \underline{w}_2|}{\sqrt{< \underline{w}_1^{*T} [T_{11}] \underline{w}_1 > < \underline{w}_2^{*T} [T_{22}] \underline{w}_2 >}} \quad (11)$$

Equation (11) has been used to solve the optimisation problem involving maximisation of interferometric coherence [2].

VECTOR DIFFERENTIAL INTERFEROMETRY

Conventional differential InSAR has been successful applied to map displacements in the order of fractions of the radar wavelength. In the case of POL-InSAR we can apply this technique to separate the effective scattering centers of different polarised waves. To achieve true differential phase sensitivity, we first select a reference scattering mechanism \underline{w}_1 and form an interferogram in the sense of (9) with $\underline{w}_1 = \underline{w}_2$ for both images. Then we generate a second one, this time between scattering mechanism \underline{w}_1 in image I1 and a different mechanism \underline{w}_2 in image I2. Here in addition to the phase dependence on topography a phase component ϕ_{diff} related to the spatial separation of the scattering centers corresponding to \underline{w}_1 and \underline{w}_2 is included. Mathematically we have

$$[J_{diff}] = < X X^{*T} > \quad \text{where } X = \begin{bmatrix} \underline{w}_1^{*T} [\Omega_{12}] \underline{w}_1 \\ \underline{w}_1^{*T} [\Omega_{12}] \underline{w}_2 \end{bmatrix} \quad (12)$$

where $[J_{diff}]$ is a 2×2 hermitian matrix generated from the two complex interferograms. The phase of the differential interferogram results from (12) as

$$\phi_{diff} = \arg(\underline{w}_1^{*T} < [\Omega_{12}] > \underline{w}_1)(\underline{w}_1^{*T} < [\Omega_{12}] > \underline{w}_2)^{*T} \quad (13)$$

Note that both interferograms have the same baseline and so the differential interferogram results directly by their phase subtraction in the complex domain avoiding baseline induced errors. The limitation for this technique arises from the requirement for sufficient high coherence between w_1 and w_2 .

INTERFEROMETRIC PHASE DECOMPOSITION

In this section we will show how polarimetric target decomposition theory can be introduced in interferometry to advance the interpretation of the interferometric phase. The diagonalisation of the hermitian coherency matrix $< [T] >$ can be used to yield a basis invariant decomposition into orthogonal scattering processes [1]:

$$< [T] > = [U_3] < [\Sigma] > [U_3]^{-1} = \sum_{i=1}^3 \lambda_i \underline{e}_i \underline{e}_i^{*T} \quad (14)$$

$[\Sigma]$ is a 3×3 diagonal matrix with the eigenvalues λ_i of $< [T] >$ along the diagonal and the diagonalisation matrix $[U_3]$ has as columns the complex eigenvectors \underline{e}_i of $< [T] >$. The physical interpretation of each scattering component is related with its corresponding eigenvector and its relative contribution is given by its appropriate eigenvalue.

Based on (14) we can form the interferograms between scattering coefficients related to the same or different scattering mechanisms in the two images I1 and I2, by projecting the scattering vectors \underline{k}_1 and \underline{k}_2 onto the corresponding eigenvectors \underline{e}_i and \underline{e}_j :

$$\mu_1 \mu_2^* = (\underline{e}_i^{*T} \underline{k}_1)(\underline{e}_j^{*T} \underline{k}_2)^{*T} \quad (15)$$

The phase of the interferogram is given by

$$\phi_i = \arg(\mu_1 \mu_2^*) = \arg(\underline{e}_i^{*T} \underline{k}_1 \underline{k}_2^{*T} \underline{e}_j) \quad (16)$$

However, one note of caution is required. The absolute phase of the eigenvectors is not uniquely defined and so we must add to (16) a condition which fixes the phase difference between \underline{e}_i and \underline{e}_j uniquely. One approach would be to set the phase of one element of the eigenvectors to be zero, for example the first element. However this is not satisfying since in some circumstances this element may be zero. A better approach is to use (16) itself where the interferometric phase should all be contained in the vectors \underline{k}_1 and \underline{k}_2 and hence a sensible constraint to employ is $\arg(\underline{e}_i \underline{e}_j^*) = 0$.

EXPERIMENTAL RESULTS

We considered the scattering matrix SLC image pairs of the Tien Shan test site acquired from the SIR-C/X-SAR radar system on October 9 and 10, 1994 (data takes 122.20 and 154.20) and processed by NASA/JPL. The test area (see Fig.1) is near the southeastern edge of lake Baikal in Russia (lat. N 52.16°, long. E 106.67°)

The eigenvalue analysis of the data in L-band has shown that the forested areas of the image (which appear bright in the left and right part of the Fig. 1) are characterised by two large eigenvalues indicating two dominant scattering mechanisms. For each eigenvalue we form an interferogram using their appropriate eigenvector in the sense of (15). The phase difference of the two interferograms represents the difference between the phase centers of the two scattering mechanisms and is shown in Fig.2. The observed phase differences are equivalent to height differences of 25-35m. and are in accordance with our (poor) information about the tree heights in this region.

As a first result of POL D-InSAR we show in Fig.3 the phase image resulting by forming the differential interferogram between the HH and VV channel in L-band. In areas where surface scattering is dominant the coherence between HH and VV was high [3], and we can measure phase differences equivalent to height differences in the order of centimeters. Current activities are focused on modeling for the physical interpretation of the effects.

CONCLUSIONS

We have shown that with access to scattering matrix interferometric data we can determine the interferometric phase corresponding to any desired scattering mechanism in the images by forming the interferogram between the projections of the scattering vectors onto a corresponding unitary vector representation of the scattering mechanism. This can advance the estimation of the effective phase scattering center. The price to be paid is that fully coherent polarimetric data must be collected, for only then can scattering mechanisms be separated.

REFERENCES

- [1] S. R. Cloude and E. Pottier, "A Review of Target Decomposition Theorems in Radar Polarimetry", *IEEE Transactions on Geoscience and Remote Sensing*, Vol. 34 No. 2 March 1996, pp 498-518.
- [2] S. R. Cloude and K. P. Papathanassiou, "Coherence Optimisation in Polarimetric SAR Interferometry", Paper No. 97., *Proc. IGARSS'97, Singapore*.
- [3] K. P. Papathanassiou and J. R. Moreira, "Interferometric Analysis of Multifrequency and Multipolarisation SAR Data", *Proc. IGARSS'96, Lincoln, USA*, pp 1227-1229

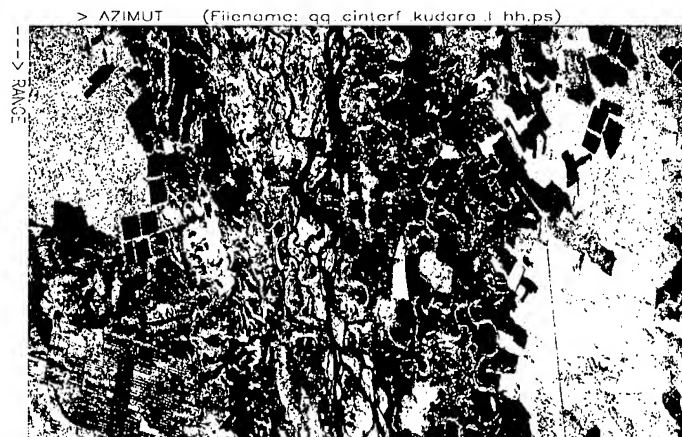


Figure 1: L-band SAR Image of the test site (HH Channel)

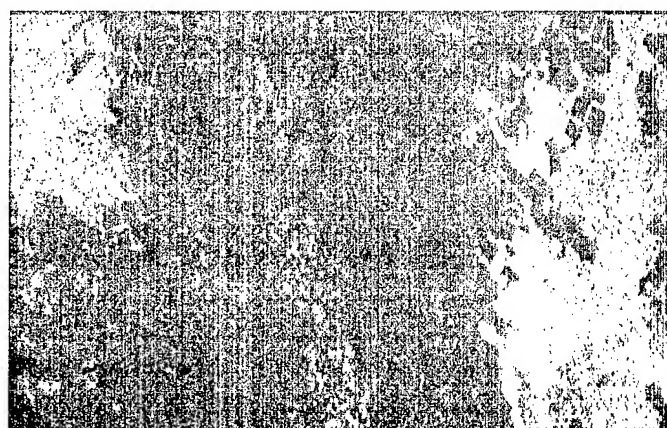


Figure 2: Phase difference between interferograms related to different scattering mechanisms



Figure 3: Phase of the differential interferogram between HH and VV Channel

HEIGHT MODEL GENERATION, AUTOMATIC GEOCODING AND MOSAICING USING AIRBORNE AeS-1 InSAR DATA

Francesco Holecz¹, João Moreira², Paolo Pasquali¹, Stefan Voigt², Erich Meier¹, and Daniel Nüesch¹

1 Remote Sensing Laboratories, University of Zurich, Winterthurerstrasse 190, CH - 8057 Zurich
Fax: +41 1 362 52 27, E-mail: franci@geo.unizh.ch

2 Aero-Sensing Radarsysteme GmbH, Münchenstrasse 20, D - 82234 Wessling
Fax: +49 8153 281543, E-mail: joao.moreira@dlr.de

ABSTRACT

The goal of this paper is to present the generation of high resolution digital surface models using airborne AeS-1 interferometric SAR data, their automatic geocoding and mosaicing. In order to be able to carry out these steps, high precision differential Global Positioning System data, high frequency attitude data of the platform, exact time synchronization and range delay of the system must be known. Since in the airborne case motion instabilities are large, due to dynamic properties of the aircraft and atmospheric turbulences, precise motion measurements of the platform are extracted and considered during the SAR processing. Once that all these basic requirements are fulfilled, one is able, using the processing reference tracks, and exploiting a forward - backward geocoding, to convert the phase differences to elevation data and to geolocate them by taking into account all geodetic and cartographic transforms. Results based on 400 MHz X-band InSAR data show that the derived surface model has a positioning accuracy in the order of 0.5m and a height accuracy better than 0.3m.

Keywords: Interferometric Synthetic Aperture Radar, Digital Surface Model, Geocoding, Mosaicing.

1. INTRODUCTION

It has been demonstrated and recognized that single-pass radar interferometry is an emerging method for the generation of Digital Surface Models (DSM) from Synthetic Aperture Radar (SAR) data. An important requirement within most applications, such as data fusion, integration of InSAR DSMs and/or SAR imagery in a Geographic Information System, is a precise geocoding.

The AeS-1 SAR system operates on board on a Cessna 207A and is currently able to collect single-pass interferometric X-band VV polarized data (Moreira et al., 1996). The maximum selectable system bandwidth of 400MHz allows the generation of high resolution digital surface data. These data can therefore be used to correctly calibrate the SAR data (Holecz et al., 1994) or for application purposes. However, the InSAR DSM and corresponding SAR data are in the original slant range geometry which is not convenient, since especially DSMs must be referred to a specific cartographic reference system.

A severe constraint of terrain geocoding is the availability of high resolution elevation data and precise ground control points (GCP). In fact, SAR products geometrically rectified using inaccurate ephemeris/flight path data, or low resolution Digital Elevation Model (DEM), or unreliable nominal range-Doppler parameters are not suitable for applications with high precision accuracy. The content of this paper focusses on one hand on the generation of high resolution DSM data, and on the other hand on the terrain geocoding of high resolution SAR/InSAR data without the aid of GCPs and considering solely precise nominal processing parameters. This will be demonstrated by utilizing single-pass InSAR data as well as by georeferencing SAR data taking into account an already existing high resolution digital photogrammetric surface model.

2. AeS-1 InSAR SYSTEM

This new airborne InSAR system has been designed and manufactured at Aero-Sensing Radarsysteme GmbH. The characteristics of the AeS-1 SAR system are shown in Table 1.

Frequency	9.6 (GHz)
Polarizations	VV
Bandwidth	100, 400 (MHz)
Normal baseline	1.5 (m)
Swath width	1.0 - 14.8 (km)
Incidence angle	30 - 80 (deg)
Acquisition modes	5 (A - E)
Resolution modes	3
PRF	1525 - 14000 (Hz)
Radiometric resolution	1.8 - 1.0 (dB)
S/N (4 km range)	25 (dB)
Positioning	DGPS and IMU

Table 1: Some AeS-1 system parameters.

In particular the following features of this InSAR system have to be considered:

- The maximum selectable system bandwidth allows a very high spatial resolution (0.5 meters).
- The platform is equipped with integrated real time Differential Global Positioning System (DGPS) and Inertial Motion Unit (IMU). This allows an extremely precise positioning of the platform in order of centimeters.
- The possibility to select 5 different acquisition modes from 1 to 14.8 km width also permits to have different geometric resolutions and map coverages.

3. PROCESSING CHAIN

The interferometric processor consists of the SAR focussing, interferometric, geocoding and calibration parts. In the SAR focussing step motion instabilities of the platform are extracted and compensated for. For this purpose two ideal flight paths are generated for the complete track considering the antenna baseline and the actual platform positions collected by the navigation system. Motion displacements are therefore calculated with respect to these ideal flight paths and successively compensated for.

The interferometric processing part can be summarized in the following steps: coregistration of the two slant range products, calculation of the interferometric phase and coherence, removal of flat terrain fringes, phase unwrapping, and computation of the interferometric height.

The phase unwrapping algorithm is based on a region growing approach (Reigber and Moreira, 1997). The advantage of this method is that the phase is unwrapped locally with a deterministic approach, so that no diffuse height distortions occur as in the case of global methods.

The phase to height conversion is carried out according to the method proposed by Schwäbisch (1995). This approach constructs a set of coefficients that relate the phase to height conversion for a coarse grid covering the full range swath and the complete track. For a set of ellipsoid heights h , a forward (Eq 1-3) backward (Eq 4-5) geocoding methodology is applied to calculate phase differences of the selected points, namely:

$$f_d = \frac{2}{\lambda} \cdot \frac{(\dot{P} - \dot{S}_1)(\dot{p}_p - \dot{p}_{s1})}{|\dot{P} - \dot{S}_1|} \quad (\text{Eq 1})$$

$$\dot{p}_1^2 = (\dot{P} - \dot{S}_1)^2 \quad (\text{Eq 2})$$

$$\frac{P_x^2 + P_y^2}{(a+h)^2} + \frac{P_z^2}{(b+h)^2} = 1 \quad (\text{Eq 3})$$

$$f_d = \frac{2}{\lambda} \cdot \frac{(\dot{P} - \dot{S}_2)(\dot{p}_p - \dot{p}_{s2})}{|\dot{P} - \dot{S}_2|} \quad (\text{Eq 4})$$

$$\dot{p}_2^2 = (\dot{P} - \dot{S}_2)^2 \quad (\text{Eq 5})$$

where, \dot{P} are the ground point positions, \dot{S} the master and slave antenna positions, \dot{p} the ranges, f_d the Doppler frequencies, a and b the semimajor and semiminor axis of the reference ellipsoid (in this case the WGS84 - World Geodetic System 1984 - ellipsoid). The advantage of this approach, as denoted in Small et al. (1996), is that it captures the true 3D baseline through image simulation, and consequently no baseline simplifications are introduced. To avoid Earth curvature effects, all the calculations are performed in WGS84 Cartesian reference system. In order to obtain absolute calibrated interferometric phase of the complete track one GCP is used. Subsequently, for each track part, absolute altitudes are iteratively computed considering the derived coefficients. In case of successive parallel tracks that must be mosaiced, the InSAR data are acquired with a slight overlay in range. The overlapping area allows, using correlation methods, to identify common points and therefore to avoid the necessity of having additional GCPs for the absolute phase calibration. In this way, even for large areas, the precise position of only one GCP is necessary.

In the final step the determined heights above the WGS84 ellipsoid are terrain geocoded by means of a forward geocoding (Eq 1-3) and converted into a desired cartographic reference system considering all geodetic and cartographic transforms. The accuracy of the track and attitude parameters allows to avoid the use of GCPs. Each track part is geocoded independently. Once that all the single scenes are geocoded and calibrated using topographic information, an automatic mosaicing procedure is performed. The results of the full processing chain are a surface model and a radar map of the area of interest.

In case that only magnitude data are acquired and/or a DEM or DSM is already existing, SAR data can be geocoded by applying a backward solution (Eq 4-5). Also in this situation the accuracy of the system is good enough to use solely nominal processing parameters, and therefore no GCPs must be employed.

4. TEST SITE AND DATA

The test site 'Limpach' is located between the cities of Solothurn and Berne in Northwest of Switzerland (47.1°N, 7.5°E) and covers an area of around 400 sqkm. This test area was chosen according to the following criteria:

- It shows flat to hilly terrain with height differences up to more than 100 meters and contains many different terrain features and ground cover types.
- DEM data (DHM25) of the Swiss Federal Office of Topography, having an original grid size of 25m and height resolution of 0.1m are available.
- Digital land registry data from 1 : 5000 scale are available.
- Digital photogrammetric surface (DPS) model data, collected on June 1994 and March 1997, having a grid size of 1m and height resolution of 0.1m are available.
- Digital laser scanner surface (DLS) model data, collected on May 1994, having a grid size of 2m and height resolution of 0.1m are available.

5. RESULTS

All Figures illustrate some results obtained from AeS-1 InSAR data acquired during the campaign in September 1996 in the test site 'Limpach'. Figure 1 shows for selected GCPs, measured with DGPS, the residual errors in x -, y -direction in the Swiss coordinate system (oblique Mercator projection). The geocoding of the GCPs is computed using a forward solution and nominal processing parameters (range and azimuth pixel spacing, and first pixel time delay). The deviations are for both images in sub-pixel domain, with a maximum residual error of 0.3 meters. Figure 2 depicts a perspective view of the generated InSAR DSM in the Swiss coordinate system, while Figure 3 exhibits the corresponding area overlaid with digital land registry data. The data in Figure 3, which are geocoded with a grid spacing of 0.5 by 0.5 m, demonstrate the perfect agreement between the two data sets. Note that this strong correspondence can only be achieved, if the derived elevation data is correct, otherwise displacements in x -, y -direction would be observed. Finally, Figure 4 illustrates a profile through the InSAR DSM, DHM25, DPS and DLS data. In order to compare all four data sets, they were resampled to 1m grid size. This plot shows the high concordance between the various models. For selected objects a height accuracy better than 0.3m was measured. Differences with the DHM25 data, which refer to the ground height, are remarkable in the forested area, where variations of around 20 meters are observed.

6. CONCLUSIONS

The obtained results lead to the following conclusions:

- It has been demonstrated that a rigorous solution of terrain geocoding based exclusively on nominal processing parameters exploiting a forward and/or backward approach is practicable. This is only possible if high precision DGPS and high frequency attitude data of the platform, exact time synchronization and range delay are known, and all geodetic and cartographic transforms are considered.
- Precise motion compensation and SAR/InSAR processing must be performed.
- Automatic generation of high resolution / high quality DSM data is feasible. The only constraint is that one GCP for the area of interest is still necessary, in order to obtain absolute calibrated interferometric phase.

Furthermore, it has to be pointed out, that the processing chain is sensor independent and operational. The computations are carried out on an array of 6 units of IBM PC Pentium Pro 200 MHz with 128 MB RAM each.

ACKNOWLEDGMENTS

Part of this work was supported by the Swiss Academy of Sciences and the Joint Research Centre, Ispra. The authors wish to thank Prof. A. Grimm (IGI GmbH) for the GPS support, Andreas Reigber (AeSR) for the development of the phase unwrapping algorithm, David Small (RSL), Wolfgang Goblirsch (RSL), Marcus Schwäbisch (AeSR), and Gianfranco Fornaro (IRECE) for fruitful discussions, Dr. Martin Suter (RSL) for the 3D visualization, the AeSR/RSL crews for the field campaign, and Gabriele Calastri for measuring the antenna positions. Thanks are due to the 'Vermessungsamt des Kantons Bern' for providing the digital land registry map, the Swiss Federal Office of Topography for the DHM25, and TopoSys GmbH for the DLS.

7. REFERENCES

- Holecz F., E. Meier, J. Piesbergen, D. Nüesch, and J. Moreira, 'Rigorous derivation of backscattering coefficient', IEEE Geoscience and Remote Sensing Society Newsletter, No. 92, 1994.
- Moreira J., 'Airborne SAR: Image generation and high precision DEM generation', Proceedings of XVIII ISPRS Congress, Vienna, 1996.
- Reigber A. and J. Moreira, 'Phase unwrapping by fusion of local and global methods', Proceedings of IGARSS Symposium, Singapore, 1997.
- Schwäbisch M., 'Die SAR-Interferometrie zur Erzeugung digitaler Geländemodelle', Forschungsbericht 95-25, DLR, 1995.
- Small D., P. Pasquali, and S. Fuglistaler, 'A comparison of phase to height conversion methods for SAR interferometry', Proceedings of IGARSS Symposium, Lincoln, 1996.

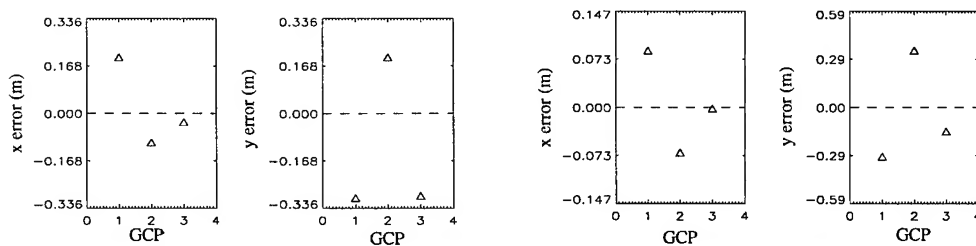


Figure 1: Residual errors for selected GCPs for master (left) and slave image (right) using forward solution

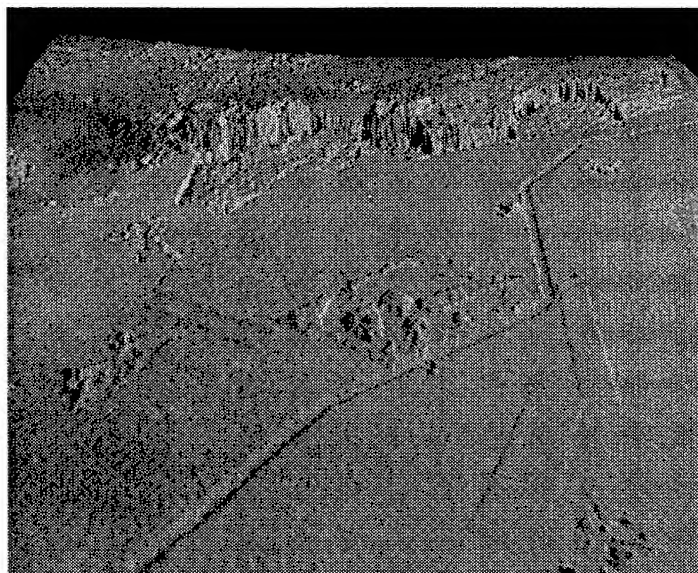


Figure 2: Perspective view of a terrain geocoded InSAR DSM data (0.5 x 0.5 m) in Oblique Mercator projection



Figure 3: Terrain geocoded magnitude data overlaid with GIS data

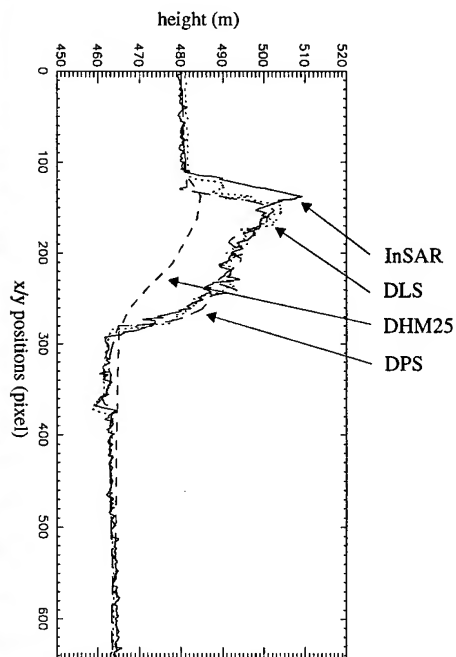


Figure 4: DEM and DSM profiles of segment AB

Coherence Optimisation in Polarimetric SAR Interferometry

S. R. Cloude and K. P. Papathanassiou

DLR, Deutsche Forschungsanstalt für Luft- und Raumfahrt e.V.

P.O. Box 11 16, D-82230 Oberpfaffenhofen, Germany. Tel/Fax: +49-8153-28-2367/-1135

Email: scloude@fges.demon.co.uk , kostas.papathanassiou@dlr.de

Abstract - In this paper we outline a general formulation for vector wave interferometry and then solve the optimisation problem involving maximisation of phase coherence. In this way we are able to show that wave polarisation effects play an important role in the extraction of information from Radar interferograms.

INTRODUCTION

Radar Interferometry is an important technique for space and airborne remote sensing, primarily because of its ability to provide all weather, high resolution digital elevation maps (DEM's) of terrain [1]. However, the quality of these maps is critically dependent upon the coherence between multiple images and this depends on several factors, including geometrical and temporal decorrelations, which in practice limit the achievable mapping accuracy [1].

One important source of decorrelation are statistical fluctuations in the surface or volume scattering mechanisms. In this letter we show that the assumption of white surface statistics [2] is often overly pessimistic and that practical optimisation algorithms can be developed which make use of the observed surface scattering data to maximise the coherence and hence improve the quality of the interferogram. The price to be paid for such improvements is that fully coherent polarimetric data must be collected, for only then can scattering mechanisms be separated.

SCALAR INTERFEROMETRY

Scalar Interferometry involves forming the hermitian product of complex scalars s_1 and s_2 from images I1 and I2. Of special significance is a hermitian coherency matrix $[J]$ defined in equation (1)

$$[J] = \left\langle \begin{bmatrix} s_1 \\ s_2 \end{bmatrix} \begin{bmatrix} s_1^* & s_2^* \end{bmatrix} \right\rangle = \left\langle \begin{bmatrix} s_1 s_1^* & s_1 s_2^* \\ s_2 s_1^* & s_2 s_2^* \end{bmatrix} \right\rangle \quad (1)$$

where $*$ is the complex conjugation operator. From $[J]$ we can obtain an estimate of the interferometric coherence coefficient between s_1 and s_2 by forming the scalar γ defined

as

$$\gamma = \frac{|\langle s_1 s_2^* \rangle|}{\sqrt{\langle s_1 s_1^* \rangle \langle s_2 s_2^* \rangle}} \quad 0 \leq \gamma \leq 1 \quad (2)$$

The higher the coherence the better the phase estimate between the complex variables s_1 and s_2 . We now consider the vector generalisation of this formulation with a view to optimising γ .

SCATTERING VECTOR FORMULATION FOR INTERFEROMETRY

We begin by defining a coherent scattering vector \underline{k} as shown in equation (3), where S_{mn} ($m, n = h$ or v) is the complex scattering coefficient for m transmit and n receive polarisation.

$$\underline{k} = [S_{hh}, \sqrt{2}S_{hv}, S_{vv}]^T \quad (3)$$

T indicate the matrix transposition operation. Under a change of scattering basis, \underline{k} transforms to \underline{k}' under a 3×3 complex unitary matrix $[U_3]$ as shown in (4).

$$\underline{k} = [U_3] \underline{k}' \quad (4)$$

Physically such transformations correspond to changes in the selected scattering mechanism in the image [3]. Such transformations have been used for interpretation and classifications of single look multi-polarisation SAR data. Here we examine their use for vector interferometry. There are 3 important hermitian products formed from the vectors for images I1 and I2 (\underline{k}_1 and \underline{k}_2):

$$[T_{11}] = \langle \underline{k}_1 \underline{k}_1^{*T} \rangle \quad [T_{22}] = \langle \underline{k}_2 \underline{k}_2^{*T} \rangle \quad [\Omega_{12}] = \langle \underline{k}_1 \underline{k}_2^{*T} \rangle \quad (5)$$

$[T_{11}]$ and $[T_{22}]$ are the standard 3×3 hermitian covariance matrices for the separate images [3]. $[\Omega_{12}]$ is a 3×3 complex matrix which contains all the interferometric phase information between polarimetric channels. The generalised image coherence is a function of these three matrices. In particular, we can construct a single hermitian matrix $[T_6]$ as in equation (6)

$$[T_6] = \left\langle \begin{bmatrix} \underline{k}_1 \\ \underline{k}_2 \end{bmatrix} \begin{bmatrix} \underline{k}_1^{*T} & \underline{k}_2^{*T} \end{bmatrix} \right\rangle = \left\langle \begin{bmatrix} [T_{11}] & [\Omega_{12}] \\ [\Omega_{12}^{*T}] & [T_{22}] \end{bmatrix} \right\rangle \quad (6)$$

We can use $[T_6]$ to obtain a generalised expression for the coherence. We begin by defining complex weights \underline{w}_1 and \underline{w}_2 to generate two complex scalars μ_1 and μ_2 as shown in (7)

$$\mu_1 = \underline{w}_1^{*T} \underline{k}_1 \quad \mu_2 = \underline{w}_2^{*T} \underline{k}_2 \quad (7)$$

These two scalars correspond to the complex scattering coefficients for scattering mechanisms \underline{w}_1 and \underline{w}_2 . Equation (5) can now be combined with equation (1) to generate an expression for the 2×2 hermitian matrix $[J]$ which decouples the w -vectors and the matrix $[T_6]$:

$$[J] = \begin{bmatrix} \underline{w}_1^{*T} & \underline{0}^{*T} \\ \underline{0}^{*T} & \underline{w}_2^{*T} \end{bmatrix} \begin{bmatrix} [T_{11}] & [\Omega_{12}] \\ [\Omega_{12}]^{*T} & [T_{22}] \end{bmatrix} \begin{bmatrix} \underline{w}_1 & \underline{0} \\ \underline{0} & \underline{w}_2 \end{bmatrix} \quad (8)$$

where $\underline{0}$ is a 3×1 zero matrix. We can now obtain a generalised expression for the interferometric coherence γ as

$$\gamma = \frac{|\langle \mu_1 \mu_2^* \rangle|}{\sqrt{\langle \mu_1 \mu_1^* \rangle \langle \mu_2 \mu_2^* \rangle}} \quad 0 \leq \gamma \leq 1 \quad (9)$$

Our task is to find \underline{w}_1 and \underline{w}_2 which optimise this expression based on estimates of the matrix $[T_6]$.

INTERFEROMETRIC COHERENCE OPTIMISATION

In order to solve the coherence optimisation problem, we must maximise the modulus of a complex Lagrangian function L defined as

$$L = \underline{w}_1^{*T} [\Omega_{12}] \underline{w}_2 + \lambda_1 (\underline{w}_1^{*T} [T_{11}] \underline{w}_1 - 1) + \lambda_2 (\underline{w}_2^{*T} [T_{22}] \underline{w}_2 - 1) \quad (10)$$

where λ_1 and λ_2 are multipliers introduced so that we can maximise the numerator of equation (9) while keeping the denominator constant. We can solve this maximisation problem by setting partial derivatives to zero. In this way we obtain two coupled complex equations as shown in (11)

$$\begin{aligned} \frac{\partial L}{\partial \underline{w}_1^{*T}} &= [\Omega_{12}] \underline{w}_2 + \lambda_1 ([T_{11}] \underline{w}_1 - 1) = 0 \\ \frac{\partial L}{\partial \underline{w}_2^{*T}} &= [\Omega_{12}]^{*T} \underline{w}_1 + \lambda_2 ([T_{22}] \underline{w}_2 - 1) = 0 \end{aligned} \quad (11)$$

We can solve these matrix equations and obtain estimates for \underline{w}_2 and \underline{w}_1 , the optimum scattering mechanisms in images I1 and I2 as

$$\begin{aligned} [T_{22}]^{-1} [\Omega_{12}]^{*T} [T_{11}]^{-1} [\Omega_{12}] \underline{w}_2 &= \lambda_1 \lambda_2^* \underline{w}_2 \\ [T_{11}]^{-1} [\Omega_{12}] [T_{22}]^{-1} [\Omega_{12}]^{*T} \underline{w}_1 &= \lambda_1 \lambda_2^* \underline{w}_1 \end{aligned} \quad (12)$$

It is important to realize that these are not the same optimum states as are well known in single imagery optimisation work. Here we have two 3×3 complex eigenvalue

problems for the vectors \underline{w}_1 and \underline{w}_2 . In the next section we show that matrices of the form $[T_{22}]^{-1} [\Omega_{12}]^{*T} [T_{11}]^{-1} [\Omega_{12}]$ have real eigenvalues.

INTERPRETATION AS A PRE-WHITENED SVD PROCESS

If we write the two hermitian matrices $[T_{11}]$ and $[T_{22}]$ in terms of their eigenvalue decompositions [3], then they and their inverses can be expressed in terms of square root matrices as shown in (13):

$$\begin{aligned} [T_{xx}] &= [U_x][\Sigma_x][U_x]^{*T} = [U_x]\sqrt{[\Sigma_x]}\sqrt{[\Sigma_x]}[U_x]^{*T} \\ &= \sqrt{[T_{xx}]}^{*T} \sqrt{[T_{xx}]} \\ [T_{xx}]^{-1} &= [U_x][\Sigma_x]^{-1}[U_x]^{*T} = [U_x]\sqrt{[\Sigma_x]^{-1}}\sqrt{[\Sigma_x]^{-1}}[U_x]^{*T} \\ &= \sqrt{[T_{xx}]^{-1}}^{*T} \sqrt{[T_{xx}]^{-1}} \end{aligned} \quad (13)$$

where $x = 1$, or 2 , $[U_x]$ is the matrix of eigenvectors and $[\Sigma]$ is a diagonal matrix with real diagonal elements. The significance of this result lies in the fact that we can transform the complex vector \underline{k} to a new basis defined by

$$\underline{k}'_x = \sqrt{[\Sigma_x]}[U_x] \underline{k}_x = \sqrt{[T_{xx}]} \underline{k}_x \quad (14)$$

This represents a shift into the orthogonal scattering mechanisms represented by the eigenvector matrix $[U_x]$, weighted in amplitude by the reciprocal of their respective eigenvalues. Physically this represents a whitening process for the vector \underline{k} .

We now apply this transformation to equation (12) to obtain for the optimum weight vector \underline{w}_2 the modified equation:

$$\begin{aligned} [T_{22}]^{-1} [\Omega_{12}]^{*T} \sqrt{[T_{11}]^{-1}}^{*T} \underline{w}'_2 &= \lambda_1 \lambda_2^* \sqrt{[T_{11}]^{-1}} \underline{w}'_2 \\ \rightarrow \sqrt{[T_{22}]} [T_{22}]^{-1} [\Omega_{12}]^{*T} \sqrt{[T_{11}]^{-1}}^{*T} \underline{w}'_2 &= \lambda_1 \lambda_2^* \underline{w}'_2 \\ (\sqrt{[T_{11}]^{-1}} [\Omega_{12}]^{*T} \sqrt{[T_{22}]^{-1}} \underline{w}'_2 &= \lambda_1 \lambda_2^* \underline{w}'_2 \\ (\sqrt{[T_{11}]^{-1}} [\Omega_{12}]^{*T} \sqrt{[T_{22}]^{-1}} \underline{w}'_2 &= \lambda_1 \lambda_2^* \underline{w}'_2 \\ \rightarrow [\Pi]^{*T} [\Pi] \underline{w}'_2 &= \lambda_1 \lambda_2^* \underline{w}'_2 \end{aligned} \quad (15)$$

where $[\Pi]$ is a 3×3 complex matrix. The final form of (15) is a classical hermitian eigenvalue problem for the eigenvectors \underline{w}'_2 . However, the eigenvalues of this matrix (which all must be real since $[\Pi]^{*T} [\Pi]$ is hermitian) are $\lambda_1 \lambda_2^*$, the same as those for the complex matrix $[T_{22}]^{-1} [\Omega_{12}]^{*T} [T_{11}]^{-1} [\Omega_{12}]$.

Hence we have shown that the eigenvalues in equation (12) are real and that the optimum value of the Lagrangian function L therefore corresponds to the maximum eigenvalue $\lambda_1 \lambda_2^*$. Note that in equation (15) we are essentially

solving the optimisation problem in a basis such that $[T_6]$ has the special form

$$[T_6] = \begin{bmatrix} [I_3] & [\Pi_{12}] \\ [\Pi_{12}]^{*T} & [I_3] \end{bmatrix} \quad (16)$$

where $[I_3]$ is a 3×3 identity matrix and $[\Pi]$ is defined in 16. In this case the modified Lagrangian function is

$$L = \underline{w}_1^{*T} [\Pi_{12}] \underline{w}_2 + \lambda_1(\underline{w}_1^{*T} \underline{w}_1 - 1) + \lambda_2(\underline{w}_2^{*T} \underline{w}_2 - 1) \quad (17)$$

which has the form of a classical singular value decomposition for the complex matrix $[\Pi]$. Physically we are then whitening the signals so as to perform speckle or 'noise' interferometry between the two images. The optimum values of interferometric coherence are then given by the singular values of the matrix $[\Pi]$.

EXPERIMENTAL RESULTS AND CONCLUSIONS

In order to solve the optimisation problem in equation 13 we first need an estimate of the matrix $[T_6]$. This we must obtain from the calibrated $[S]$ -matrix (complex scattering-matrix) data itself [3]. The estimates for these parameters are obtained by N -look complex averaging:

$$[T_{xx}] = \frac{1}{N} \sum_{i=0}^N \underline{k}_x \underline{k}_x^{*T} \quad [\Omega_{12}] = \frac{1}{N} \sum_{i=0}^N \underline{k}_1 \underline{k}_2^{*T}$$

To illustrate how changes in scattering mechanism lead to significant variations in coherence, we apply the optimisation method to full-polarimetric data (L- and C-band) acquired from the Space Shuttle-borne SIR-C/X-SAR radar system. Data from the Tien Shan test site (data takes 122.20 and 154.20) were provided by NASA/JPL as single-look complex SAR images. The test area is near the southeastern edge of lake Baikal in Russia (latitude: 52.16° , longitude: 106.67°). Fig. 1 show the interferometric coherence histograms of the optimum coherence (corresponding to the largest eigenvalue of 12), minimum coherence (corresponding to the smallest eigenvalue of 12) and as reference the coherence obtained by using the conventional hh -channel in the C-band. Fig. 2 show the histograms of the optimum coherence and as reference the coherence obtained by using the hh -channel in the L-band. We can see that there is significant difference between maximum and minimum coherence and hence conclude that polarimetry plays a significant role in determining the quality of Radar interferograms. Note that applying the proposed optimisation algorithm we do not only obtain the optimum value of phase coherence but we also obtain an estimate of the two scattering mechanisms in images I1 and I2 which generates this coherence. These may be

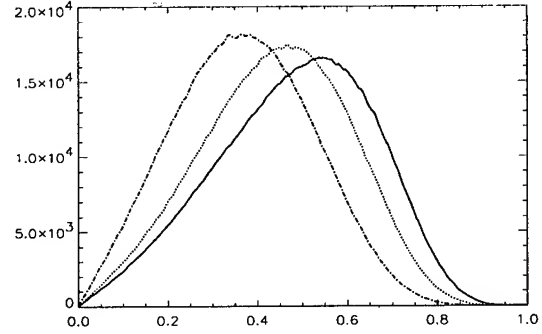


Figure 1: Coherence Histogram-Plots at C-band. Optimised (continuous), minimised (dashed), hh -channel (dotted)

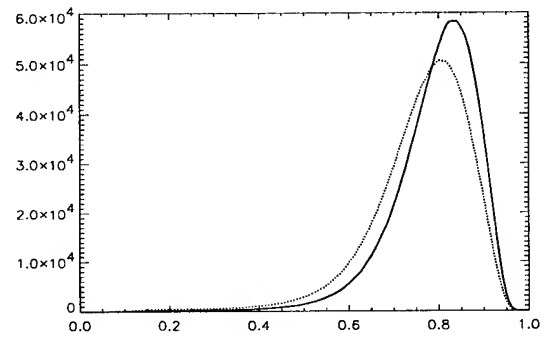


Figure 2: Coherence Histogram-Plots at L-band. Optimised (continuous) and hh -channel (dotted)

further exploited for classification and change detection purposes. Future work will concentrate on developing these techniques for applications in image classification and DEM generation.

REFERENCES

- [1] H. A. Zebker, J. Villasenor, "Decorrelation in Interferometric Radar Echoes", *IEEE Transactions on Geoscience and Remote Sensing*, Vol. 30 No. 5 September 1992, pp 950-959.
- [2] F. Gatelli, A. M. Guarnieri, F. Parizzi, P. Pasquali, C. Prati, F. Rocca, "The wavenumber shift in SAR Interferometry", *IEEE Transactions on Geoscience and Remote Sensing*, Vol. 32, No. 4, July 1994, pp 855-864.
- [3] S. R. Cloude, E. Pottier, "A Review of Target Decomposition Theorems in Radar Polarimetry", *IEEE Transactions on Geoscience and Remote Sensing*, Vol. 34 No. 2 March 1996, pp 498-518.

The X-Band SAR Demonstrator Development

R. Zahn*, H. Braumann*, M. Schlott**

* Dornier Satellite Systems, D-88039 Friedrichshafen, Germany
(Telephone: +49-7545-8-4959, Telefax: +49-7545-8-4177)

** DARA, D-53277 Bonn
(Telephone: +49-228-447-588, Telefax: +49-228-447-700)

Abstract - The technical and programmatic topics of the German / Swedish X-Band SAR Demonstrator development are described in the present paper. The aim of the project is to develop the technology of the next SAR generation in space.

INTRODUCTION

In preparation for a future international cooperation for a Multi Frequency/ Multi Polarization (MFMP) Earth monitoring space synthetic aperture radar (SAR) mission, the relevant X-band antenna technology is under development in Germany. Such a mission could be envisaged for a time scale about 2003. The technology development was started with the X-band Antenna Breadboard project which was carried out in cooperation with Sweden (SNSB) and was finished mid 1996.

The logical next step is the development of a Demonstrator to verify the electrical and mechanical system concept and the relevant technologies. DARA started this technology project in September 96 with Dornier Satellite Systems as a prime contractor, again in cooperation with Sweden (Saab Ericsson). For the future it is planned to broaden the international cooperation.

SAR SYSTEM REQUIREMENTS

Future spaceborne SAR instruments are required to implement highly flexible operational modes for example with respect to coverage and resolution. Only active phased arrays can fulfill this flexibility.

The main topics of the X-band SAR Demonstrator (**DESA**) development are the flight representative realization of one electrical panel of the active phased array antenna, main parts of the control and supply electronics, the control software and the test assembly. These activities can also be seen as a preparation of

a complete future SAR instrument. SAR system studies have been carried out to define a representative SAR design (SAR-R).

The present design (SAR-R) is a 12m x 0.7m SAR antenna with 30 rows in elevation and 30 columns in azimuth, giving 900 elements in total. The spacing in elevation allows an antenna pointing of ± 20 degrees while in azimuth only a limited scan capability is available due to the subarray size of 0.4m. The latter number also defines the size of the independent panels that form the core element of the antenna. The details of system design studies are given in separate IGARSS 97 presentations, see Ref. 1 and 2.

DESA TECHNICAL DESCRIPTION

The active front end of the SAR, also called active antenna, consists of a number of active and passive components: radiator, TR modules, data handling and control electronics, power distribution and conditioning networks and structures.

The radiation pattern is formed separately in transmit and receive, exploiting the full capabilities of active phased array antennas. While a fixed amplitude distribution is used for Tx, in Rx the pattern can be formed by phase and amplitude tapering. This scheme has the advantage that in Tx the amplifiers are operated at the highest possible efficiency and the sidelobes are lowered by using TR Modules with different output power in elevation. The present design shows good performance at X-Band. The radiated peak power is about 3 kW, the mass 440 kg, and the DC power consumption is 3.2 kW (this does not include central electronics functions).

The DESA block diagram is shown in Fig. 1. In the Central Electronics only a part of the later instrument will be build, while the RF electronics is completely replaced by the EGSE, using commercial lab equipment.

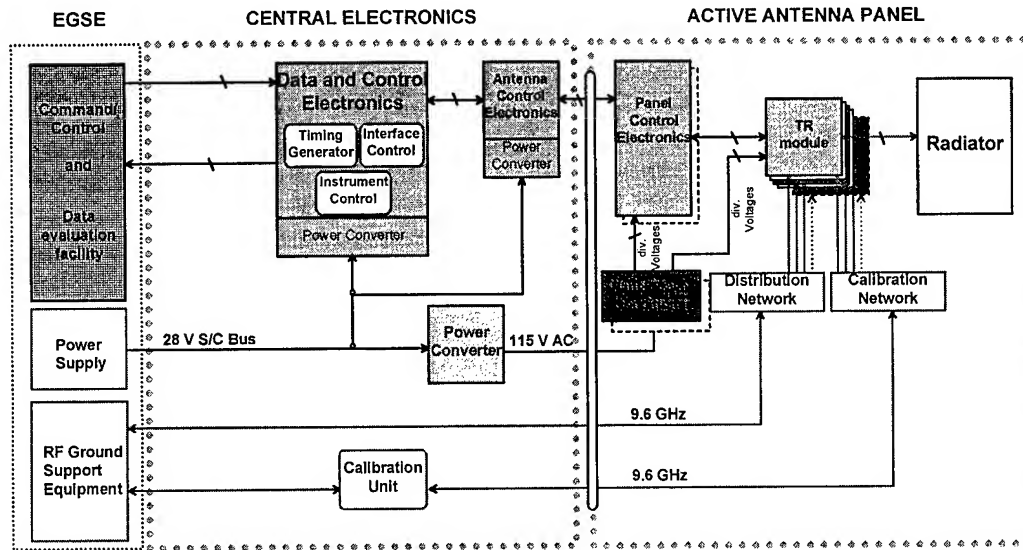


Fig. 1: X-Band SAR Demonstrator block diagram

The TR Modules are supplied by DASA/Ulm. MMIC technology together with a dedicated control logic is used. The modules include a self-correction for thermal amplitude and phase deviations. The main performance is:

Output power	7 W or 2 W
Noise figure	3.2 dB
Amplitude accuracy	0.5 dB
Phase accuracy	6°
Gain	30 dB
Mass	110 g

The antenna radiator for the DESA project will be a Waveguide type employing the Carbon Fibre Reinforced Plastics (CFRP) technology that was already used in the Space projects ERS-1, ERS-2 and X-SAR. For the multi-polarization capability, two radiators, one for H and one for V-pol, are used in the same antenna aperture. The waveguide technology shows also a very good performance

center frequency	9.6 GHz
polarization	dual linear
bandwidth	> 100 MHz
scan in elevation	+/- 20°
crosspolarization	< -25 dB
insertion loss	~ 0.5 dB

The mechanical design of one panel (out of 30) is shown in Fig. 2. This design is as far as possible flight representative, which means that a later mission design could be very similar. Carbon fibre technology is used for most of the mechanical structures. In the drawing electronic boxes for power and digital are shown within the panel, however, the respective cabling is missing. A compact design is achieved with a

panel mass of about 10 kg and a depth of less than 150 mm which is important for the stow volume.

The thermal design of the active antenna plays an important role, since approximately 3 kW of electrical power are consumed. The particular challenge is a completely passive thermal design, thus, setting difficult requirements to all components. A typical thermal profile over several orbits is shown in Fig. 3.

THE DESA SCHEDULE

The SAR Demonstrator project will last approximately 4 years (phase 1 and 2). In the first phase the system and subsystem requirements will be defined and the key technologies will be developed (dual polarized waveguide radiator and TR modules). In the second phase all subsystems, as listed above, will be build, integrated to an flight typical configuration and tested on system level.

PROGRAMMATIC OUTLOOK

An important requirement for a future SAR system will be the need that its application scenario will have to fit into a commercial frame. In future the following developments are needed:

- The manufacturing processes of the active antenna should on all levels rely widely on automatic production lines.
- The synergies of other radar development and manufacturing programs have to be exploited. Here for instance the X-Band Space SAR in Europe may well profit from current military onboard radar space and telecommunication programs.

- Moreover the direct access to SAR data products should be possible by implementation of SAR on board data processing and compression, which is presently studied within the DARA and ESA technology programs.
- Finally, the SAR instrument on one satellite should allow synchronous operation with the SAR payload on other satellites in order to reduce repeat cycles or to generate special SAR products on the basis of interferometric modes

References:

- [1] C. Heer, et. al., "An outlook for European Spaceborne SAR", Proc. IGARSS 97
- [2] E. Velten, C. Heer, "Future Operational Spaceborne SAR System Considerations", Proc. IGARSS 97
- [3] R. Zahn, et. al., "Advanced Antenna Technologies for X-Band SAR", Proc. IGARSS 95
- [4] R. Zahn, "The Design of a Future X-Band SAR", AEÜ, Int. J. Electron. Commun., 50 (1196) No.2, 85-91

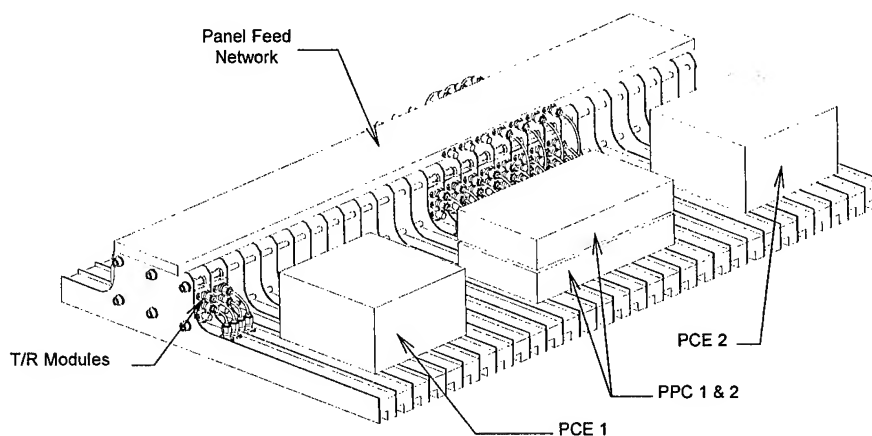


Fig. 2: Mechanical lay-out of the SAR Demonstrator

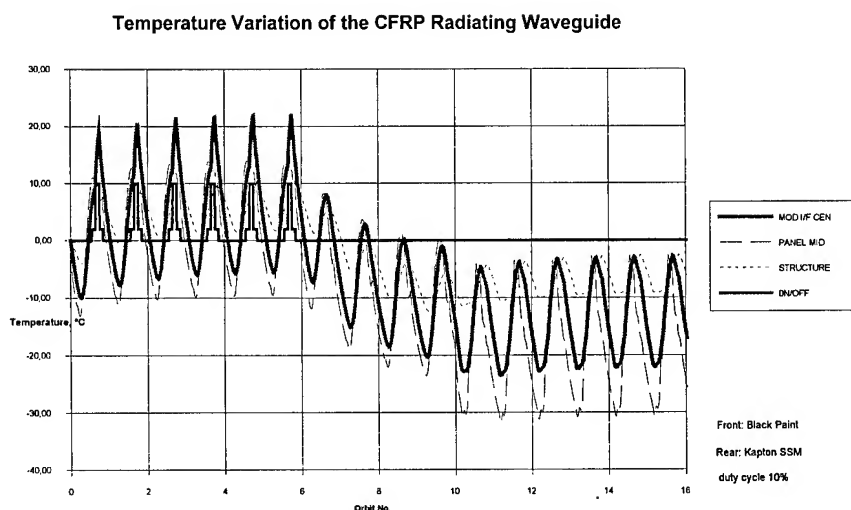


Fig. 3 Thermal behaviour of the SAR Front End

A Novel Model of the Platform Attitude Drift for SAR

Song Hongjun, Zhu Minhui, Senior Member, IEEE, Bai Youtian

Institute of Electronics, Academia Sinica (IEAS)

P.O.Box 2702-56, 100080, Beijing, P.R.China

Tel: (086)-010-62613849 Fax: (086)-010-62567363 Email: hjsong@ie0.ie.ac.cn

Abstract -- For Synthetic Aperture Radar(SAR) system, the platform attitude drift will affect the image qualities. During the system design of SAR, the computer simulation can be used to determine the attitude stability which can satisfy the users' demands. In the computer simulation, the first step is to create the mathematic model. General models of platform attitude drift are usually created in the time domain, such as the sinusoid one, and the model presented here is done in the frequency domain.

For each attitude angle (roll, yaw, pitch), the amplitude and phase values are first generated in the frequency domain. Because the attitude parameters are sampled with PRF(Pulse Repetition Frequency) in SAR system, the maximum frequency is set to $PRF/2$. The amplitude may be changed with the frequency (for example, inversely proportional to the square of frequency), while the phase may be uniformly distributed between 0 to 2π . Then the inverse Fourier transformation converts this data into the time domain. Because the phase center of the SAR's antenna is usually offset from the platform center, the attitude drift will change the slant range between the antenna's phase center and the target on the ground. These changes will affect the Doppler history in azimuth direction for the SAR. After these changes are simulated, the SAR raw data of a point target can be generated. With the general SAR procession, the simulated image is obtained. Using the analysis software, we can get the effects on the image qualities of the attitude drift. At last, the simulation steps and an example are also presented.

Keywords: SAR, Platform Attitude Drift, Simulation, Frequency Domain

1. INTRODUCTION

A stripmap airborne Synthetic Aperture Radar(SAR) is an active image radar which can generate the image of the terrain parallel to the flight path. In the range direction which is perpendicular to the flight path, the target position is determined by the two way propagation time of an impulse transmitted by the antenna and reflected by the targets on the ground. The geometric resolution in range direction is limited by the impulse bandwidth in frequency. In the azimuth direction which is parallel to the flight path, the fine geometric resolution is obtained by the large aperture length. For SAR, this length is realized mathematically by synthesizing an array antenna. Each element of this 'mathematic' array is lined up along the flight path. The

digital signal procession can be used to synthesize a large aperture as if the return signals of all elements were received simultaneously. This procession is also called azimuth compression. The array length is called synthetic length, while the corresponding time is synthetic time.

If the velocity is constant and the flight path is straight during the synthetic time, a fine resolution can be obtained. Actually, this assumption is not right. For airborne SAR, due to the turbulence, the velocity and the flight path, as well as the attitude, are always changed. The offset of velocity can be compensated on-line by changing the Pulse Repetition Frequency(PRF) so that the distance between each element of the synthetic array can keep constant. The flight path shift and the attitude drift which change two way propagation time can be corrected on-line by the range delay. Also all these errors can be corrected off-line during the digital signal procession on the ground. These errors are detected on the platform by the Inertial Measurement Unit(IMU). Because the IMU and in-line correcting units have limit precision, and the digital signal procession has also limit precision, all these errors can not be completely corrected. It will reduce the image qualities.

In this paper, the computer simulation is used to analyze the effects on the image qualities of the attitude drift. At first, the geometry of the SAR system and its procession are introduced, and then the mathematic model of the attitude drifts is created in the frequency domain, followed by the simulation steps. At last, some results and the discussion are presented.

2. SAR GEOMETRY AND ITS PROCESSION

Fig.1 illustrates the SAR geometry. The antenna is mounted on the platform with an offset length L , and the radar beam looks to the ground at an angle β . The slant range between antenna center and target is R . This geometry differs from others due to the fact that the antenna is usually not mounted on the platform center[1]. In this figure, it is obvious that if the platform attitude angle (roll, yaw or pitch) has some drift, it will change the slant range R .

In stripmap SAR, the radar transmits and receives signals pulse by pulse at PRF. When all the pulses in a synthetic time are received and stored, they are processed according to the history of changes in slant range. If the attitude drifts are not known exactly, these changes can not be compensated precisely. It will affect the impulse response of a point target.

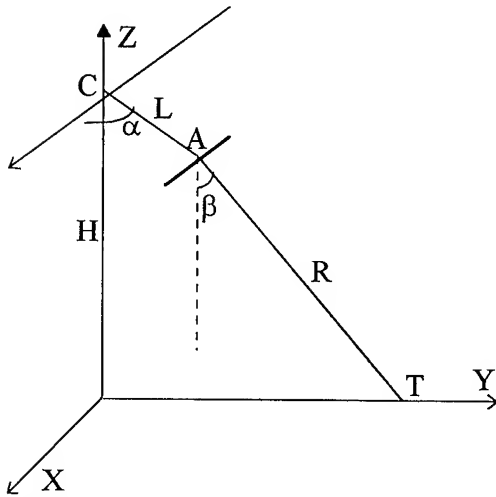


Fig 1. SAR Geometry, where C is platform center, A is antenna phase center, T is target on the ground, L is the offset between antenna and platform center, R is slant range. α is the antenna's mounted angle, β is the radar look angle.

3. ATTITUDE MODEL IN FREQUENCY DOMAIN

For airplane, the attitude often varies due to the turbulence which is not definite, thus the effects of attitude drift are difficult to analyze theoretically. On the other hand, the computer simulation is a good tool to analyze such random process, so it is selected to analyze these effects.

For simulation, the first step is to create the mathematic model. Ordinary methods are done in the time domain, such as using sinusoidal model or Taylor series. The model we presented here is done in the frequency domain. Using Fourier Analysis, the variables and their Fourier transformations have following relations[2]:

$$A(\omega) = F[a(t)] \quad (1)$$

$$B(\omega) = F[da(t)/dt] = j\omega A(\omega) \quad (2)$$

$$C(\omega) = F[d^2a(t)/dt^2] = -\omega^2 A(\omega) \quad (3)$$

where $F[\]$ represents the Fourier transform, $a(t)$ and $A(\omega)$ are the attitude values and their Fourier transformation, respectively, the $da(t)/dt$ and $B(\omega)$ are those of angular velocity, the $d^2a(t)/dt^2$ and $C(\omega)$ are those of angular acceleration.

For random signals, the Power Spectral Density(PSD) are often used to describe these signals. Because the PSD is the Fourier transformation of the autocorrelation, the PSD of a signal and its Fourier transformation have following relation:

$$PSD[a(t)] = |A(\omega)|^2 \quad (4)$$

In this paper, we use the PSD of the angular acceleration to describe the airplane attitude drift. Using physics theory, the angular acceleration is caused by moment of force. If the moment of force is assumed to be like a white noise, the PSD of the angular acceleration is constant in all frequency, as described in (5):

$$|C(\omega)|^2 = \text{Constant} \quad (5)$$

From (1), (2), (3), we can get following equations:

$$A(\omega) = x * \exp(j\phi)/\omega^2 \quad (6)$$

where ϕ is uniformly distributed from 0 to 2π .

In the computer simulation, the Discrete Fourier Transform (DFT) are often used. If we assume that the $a(n)$ and $A(n)$ are the series in time-domain and their DFT series, and the length is N, they have following relations:

$$A(n) = \text{DFT}[a(n)] = \sum a(i) * \exp(-j2\pi ni/N) \quad (7)$$

$$a(n) = \text{IDFT}[A(n)] = (1/N) * \sum A(i) * \exp(j2\pi ni/N) \quad (8)$$

$$\sum a(n) = A(0) \quad (9)$$

$$\sum |a(n)|^2 = \sum |A(n)|^2 / N \quad (10)$$

with (6), we have the following model of attitude drift:

$$A(n) = y * \exp(j\phi)/n^2 \quad (n > 0) \quad (11)$$

where ϕ is also uniformly distributed from 0 to 2π .

At the zero frequency, we assume its value is zero. From (9), it is easy to find that the mean value of the attitude drift is zero. Then, with (10), we can get the Mean Square Root Error (MSRE) δ as following:

$$\delta^2 = E[|a(n)|^2] = (\sum |a(n)|^2) / N = \sum |A(n)|^2 / N^2 \quad (12)$$

The MSRE δ is selected as the simulation parameter.

4. SIMULATION STEPS

Using the model mentioned above, the simulation steps are as following:

- input the simulation parameters (MSRE δ) for each attitude angle (roll, yaw, pitch);
- generate the Fourier transformation of each attitude angle according to the (12) and (11).
- do the inverse Discrete Fourier transformation to generate the values of each attitude angle in time domain.
- calculate the position of antenna's phase center during a synthetic time, and then the slant range as well.
- generate all the echoes of a point target in a synthetic time according to the slant range.
- do the azimuth compression using the reference signals with no attitude drift.
- measure the geometric resolution(-3db width), PSLR(Pulse SideLobe Ratio) and ISLR(Integrated SideLobe Ratio) of the point target response.
- loop the steps many times from b to g and calculate the mean values for the geometric resolution, PSLR and ISLR.

5. RESULTS AND DISCUSSION

An example is used to demonstrate the simulation steps. The platform and radar parameters are in Table 1.

In order to simulate the effects of different attitude angles, The roll, yaw or pitch angle is simulated independently, while the other angles are set to zero. Then all these angles are simulated at the same time. The results are shown in Table 2.

Table 1. Platform and radar parameters

platform height(H)	6 km
slant range(R)	10 km
platform velocity	150 m / s
Offset length of antenna(L)	1 m
antenna's offset angle(α)	45 degree
radar wave length(λ)	0.03 m
antenna length	1 m
antenna pattern	$\sin(x)/x$
synthetic time (Ts)	2 s
Pulse Repetition Frequency	400 Hz

The results in Table 2 show that with the increase of attitude drift, the geometric resolution (-3db width) becomes wider, while the PSLR and ISLR arise.

From Table 2, it is obvious that the effect of the roll angle is the most serious one. It is because with the parameters mentioned in Table 1, when the roll has an offset at 5 degree, the change of two way slant range is about 0.57λ , while 0.14λ for yaw angle and 0.11λ for pitch angle.

During the simulation, it is assumed that the azimuth compression is independent of the range direction, but actually the attitude drift will also cause the variance of the target position the range direction. This will affect the range migration correction procedure in the SAR signal procession. The coherency between range and azimuth direction is difficult to simulate. Further researches will be proceeded in this area.

For airplane, the trajectory of the platform center varies more seriously than the attitude angles. On the contrary, for spacecraft, the variation of attitude angles are more serious than that of trajectory. This model of attitude drift can also be used for spaceborne SAR.

Table 2. Attitude simulation results

Mean Square Root Errors of attitude angle (Deg)			3dbwidth (m)	PSLR (db)	ISLR (db)
Roll	Yaw	Pitch			
0	0	0	0.50	-19.3	-32.3
0	0	1.0	0.50	-19.3	-32.1
0	0	2.0	0.51	-19.2	-29.2
0	0	3.0	0.51	-16.4	-19.8
0	1.0	0	0.50	-19.3	-32.0
0	2.0	0	0.51	-18.8	-26.6
0	3.0	0	0.51	-14.1	-19.6
0.1	0	0	0.51	-19.0	-31.0
0.2	0	0	0.51	-18.1	-27.0
0.3	0	0	0.52	-17.0	-25.4
0.4	0	0	0.52	-12.8	-22.8
0.5	0	0	0.53	-9.3	-20.7
0.3	0.3	0.3	0.52	-16.7	-24.8
0.5	0.5	0.5	0.53	-8.9	-20.0

REFERENCES

- [1] Stefan Buckreuss, "Motion Errors in an Airborne Synthetic Aperture Radar System", European Trans. Telecomm. Related Technique, Vol. 2, pp. 655-664, Nov.-Dec. 1991
- [2] D.E. Newlanf, An Introduction to Random Vibrations and Spectral Analysis , Longman, 1975, pp. 48-50.

SIR-C polarimetric calibration by using polarization selective dihedrals and a polarimetric active radar calibrator

Masaharu Fujita, Toshihiro Masuda*, Yoshiyuki Fujino, and Makoto Satake
Communications Research Laboratory (*Toyo University, presently with RESTEC)
Koganei, Tokyo 184, Japan
tel: +81-423-27-7522/ fax: +81-423-27-6690/ e-mail: mfujita@crl.go.jp

Abstract – A novel approach to calibrate a polarimetric SAR is proposed and tested in the SIR-C/X-SAR experiment. The present technique needs one PARC (polarimetric active radar calibrator) and two PSD's (polarization selective dihedrals). Since PSD's have wide frequency coverage, only addition of another frequency PARC allows to calibrate a multi-frequency polarimetric SAR.

INTRODUCTION

A polarimetric SAR can measure a scattering matrix of a target with a high spatial resolution, with which we can completely describe the microwave backscattering process at the target. A measured scattering matrix, however, usually includes errors due mainly to radar hardware imperfections. This may cause an erroneous interpretation of the data in, for example, land use classification. Polarimetric calibration of a polarimetric SAR is therefore indispensable to effectively use the data for several possible applications.

The polarimetric calibration techniques are divided into two categories. The first one needs three reference targets having specific scattering matrices but needs no assumptions, while the other one needs assumptions on scene statistics and/or radar characteristics but needs one reference target. We propose in this paper an economic and need-no-assumption three-target technique for polarimetric calibration.

ALGORITHM

A scattering matrix S of a target is generally written as,

$$S = \begin{bmatrix} S_{hh} & S_{hv} \\ S_{vh} & S_{vv} \end{bmatrix}. \quad (1)$$

where the subscript ab shows a change of the polarization

state from a to b due to scattering. When the target is measured with a polarimetric SAR, a measured scattering matrix M is expressed by the following equation.

$$M = RST \quad (2)$$

where R and T denote the polarization transfer characteristics of the polarimetric SAR for reception and transmission, and a noise component is ignored for simplicity. If R and T are known, we can calculate the scattering matrix of a target from the measured scattering matrix as follows:

$$S = R^{-1}MT^{-1} \quad (3)$$

where the superscript -1 denotes matrix inversion. The polarimetric calibration means to estimate R and T , and invert M to find out the correct scattering matrix S of a target.

To estimate R and T , three targets having specific scattering matrices are deployed in the three-target technique. Among the techniques, Barnes [1] proposed to use the following scattering matrices using screened corner reflectors,

$$B_1 = \begin{bmatrix} 1 & 0 \\ 0 & 0 \end{bmatrix}, B_2 = \begin{bmatrix} 0 & 0 \\ 0 & 1 \end{bmatrix}, B_3 = \begin{bmatrix} 1 & 1 \\ 1 & 1 \end{bmatrix}. \quad (4)$$

However, multiple reflections between a screen and corner reflector surfaces caused undesired sequence of echoes, so it was hard to use the present technique. Freeman et al. [2] used polarimetric active radar calibrators (PARC's) to characterize the following scattering matrices,

$$F_1 = \begin{bmatrix} 0 & 1 \\ 0 & 0 \end{bmatrix}, F_2 = \begin{bmatrix} 0 & 0 \\ 1 & 0 \end{bmatrix}, F_3 = \begin{bmatrix} -1 & -1 \\ 1 & 1 \end{bmatrix}. \quad (5)$$

PARC's, however, are expensive to purchase, so the present technique has a disadvantage from an economical point of view.

Here, we propose a technique by combining the above two techniques. The first two scattering matrices in (1) of the

Barnes technique are realized by polarization selective dihedrals [3], and the third scattering matrix in (2) of the technique by Freeman et al. is provided by a PARC. A combination of the scattering matrices is thus as shown below.

$$B_1 = \begin{bmatrix} 1 & 0 \\ 0 & 0 \end{bmatrix}, B_2 = \begin{bmatrix} 0 & 0 \\ 0 & 1 \end{bmatrix}, F_3 = \begin{bmatrix} -1 & -1 \\ 1 & 1 \end{bmatrix} \quad (6)$$

Ratios of the row elements and of the column elements of R and T matrices are obtained by the B_1 - and B_2 -target data, and those of the diagonal elements are calculated from the F_3 -target data. The method of data processing for the

B_1 - and B_2 -targets or the F_3 -target is the same as that by Barnes [1] or Freeman et al. [2].

EXPERIMENT

A polarimetric calibration experiment [4] was carried out in the SIR-C/X-SAR program in 1994 at the Sarobetsu test site in a wild land where its surface was covered with short grass. The reference targets deployed at the site were three C-band PARC's, two horizontal PSD's, two vertical PSD's, two 22.5-degree rotated dihedrals and one trihedral. In the SRL-1 (shuttle radar laboratory-1) case in April, 1994, the test site was covered completely with snow, so all targets were placed directly on the snow cover. Since the surface condition was not suitable for azimuth angle measurement using, for example, a transit, we used a compass. Therefore, the azimuth setting included errors of more than several degrees because of unstable compass measurements. The elevation angle, on the other hand, was measured within 0.1-degree accuracy. In the SRL-2 case in October, 1994, on the other hand, the targets were placed on a sidewalk of a paved road. The surface condition allowed to measure the azimuth angle with 0.1-degree accuracy. The condition for elevation angle measurement was the same as in the SRL-1 case. In both cases, the distance between the adjacent targets was about 150 m.

In the following section, we calibrate three sets of full polarimetric data (DT8.1 and 28.5 in SRL-1, and DT556.1 in SRL-2) of the SIR-C C-band channel using the proposed technique, and compare with those using the 3-PARC

technique. The parameters of the data takes are summarized in Table 1.

Table 1. Date, time and incident angle of the SIR-C data takes.

Data take	Date in 1994	Time(JST)	Incident angle(deg.)
8.1, SRL-1	10 April	6:38	23.8
28.5, SRL-1	11 April	12:30	22.9
56.1, SRL-2	4 October	5:53	49.1

RESULT

The data are analyzed with the proposed technique to estimate the transmitting and receiving polarization transfer characteristics of the SIR-C C-band channel for each data take. Then, it is necessary to evaluate the validity of the above estimate. A normalized scattering matrix of a trihedral is theoretically written as follows:

$$S_{tri} = \begin{bmatrix} 1 & 0 \\ 0 & 1 \end{bmatrix} \quad (7)$$

This means that a trihedral reflects both vertically and horizontally polarized waves with the same radar cross section and does not depolarize an incident wave due to reflection. Thus it is possible to evaluate the validity of polarimetric calibration, especially for the amplitude and phase imbalance of the diagonal elements by inverting a measured scattering matrix of a trihedral and comparing it with (7). To save space, only the result for DT56.1, SRL-2 is shown here as an example. Since there are two pairs of PSD's, two corrected results are shown.

(measured)

(corrected)

$$\begin{bmatrix} 1 & 0 \\ 0 & 0.83 \angle 354.9 \end{bmatrix} \rightarrow \begin{bmatrix} 1 & 0.035 \angle 345.7 \\ 0.017 \angle 286.1 & 1.00 \angle 0.3 \end{bmatrix} \quad (8a)$$

$$\begin{bmatrix} 1 & 0.035 \angle 234.8 \\ 0.034 \angle 245.9 & 1.04 \angle 0.6 \end{bmatrix} \quad (8b)$$

The amplitude and phase imbalances are well corrected by inversion within 0.34 dB and 0.6 degrees in this case. However, the off-diagonal terms rather increase as compared to the measured scattering matrix probably due to imperfect polarization characteristics of the calibration targets. It remains almost -30 dB relative to the diagonal

terms. For comparison, the inversion result for the same data take using the 3-PARC technique is shown below.

(measured)

(corrected)

$$\begin{bmatrix} 1 & 0 \\ 0 & 0.83\angle 354.9 \end{bmatrix} \rightarrow \begin{bmatrix} 1 & 0.015\angle 20.8 \\ 0.065\angle 356.6 & 1.01\angle 3.6 \end{bmatrix} \quad (9)$$

There are no significant difference between the proposed technique result and the 3-PARC result.

To evaluate the polarimetric calibration for depolarization terms (off-diagonal elements), we next analyze the scattering matrix of the 22.5-degree rotated dihedral which has the following theoretical form:

$$S_{22.5} = \begin{bmatrix} 1 & -1 \\ -1 & -1 \end{bmatrix} \quad (10)$$

Again only the result for DT56.1, SRL-2 is shown below.

(measured)

(corrected)

$$\begin{bmatrix} 1 & 0.96\angle 90.5 \\ 0.96\angle 267.7 & 0.93\angle 175.2 \end{bmatrix} \rightarrow \begin{bmatrix} 1 & 0.96\angle 178.9 \\ 0.93\angle 183.6 & 1.22\angle 189.0 \end{bmatrix}$$

$$\begin{bmatrix} 1 & 1.06\angle 196.1 \\ 0.99\angle 187.5 & 1.17\angle 180.1 \end{bmatrix} \quad (11a \& b)$$

It can be clearly seen that the phase characteristics of the off-diagonal elements in the measured scattering matrix are well corrected to be within 3.8 degrees in the better case. The result with the 3-PARC technique is shown below.

(measured)

(corrected)

$$\begin{bmatrix} 1 & 0.96\angle 90.5 \\ 0.96\angle 267.7 & 0.93\angle 175.2 \end{bmatrix} \rightarrow \begin{bmatrix} 1 & 1.07\angle 181.3 \\ 1.09\angle 178.6 & 1.22\angle 183.6 \end{bmatrix} \quad (12)$$

Again there are no significant difference between the proposed technique result and the 3-PARC result. This proves the practical applicability of the proposed technique for calibrating a polarimetric SAR.

Since the proposed technique needs only one PARC in addition to two PSD's, there is an advantage over the 3-PARC technique from an economical point of view. Polarization selective dihedrals work over a wide frequency range, so only an addition of a different frequency PARC

allows to calibrate a multi-frequency polarimetric SAR.

CONCLUSION

A novel polarimetric calibration technique is proposed using two polarization selective dihedrals and one polarimetric active radar calibrator. The present technique works well as the 3-PARC technique not only for calibrating like polarization channels but also for depolarization terms including phase. Since the present technique needs only one PARC in addition to two PSD's, it is advantageous from an economical point of view than the 3-PARC technique. Capability of calibrating a multi-frequency polarimetric SAR by only addition of a different frequency PARC is another advantage of the present technique.

ACKNOWLEDGMENTS

The authors would like to express their gratitude to D. Evans, H. Ottl, and S. Wall for their support during the SIR-C/X-SAR program.

REFERENCES

- [1] R.H. Barns, "Polarimetric calibration using in-scene reflectors," MIT Lincoln Lab., Lexington MA, Rep.TT-65, Sept. 1986.
- [2] A. Freeman, Y. Chen, and C.L. Werner, "Polarimetric SAR calibration experiment using active radar calibrators," IEEE Trans. Geosci. Remote Sens., Vol.28, No.2, pp.224-240, 1990.
- [3] M. Fujita and T. Masuda, "A metal strip grating dihedral for polarimetric calibration," Radio Sci., Vol.30, No.2, pp.423-428, 1995.
- [4] M. Fujita, T. Masuda, Y. Fujino, and M. Satake, "SIR-C polarimetric calibration experiment using polarization selective dihedrals: A preliminary result," Proc. IGARSS'95, Florence, Italy, July 1995, Vol.II, pp.1591-1592.

Knowledge Based Weather Image Processing and Classification

Khalid J. Siddiqui,

Dept. of Computer Science, SUNY at Fredonia, NY 14063
Voice: 716-673-3193, Fax: 716-673-3446, Email: siddiqui@cs.fredonia.edu

Abstract: Satellite imagery of weather patterns and meteorological information are used to develop a Knowledge Based Weather Image processing and classification System (KB/WIS). Wavelet and fractal methods are used to extract features from weather images. The features extracted are used to represent various weather patterns. The system is statistically trained to characterize and interpret weather patterns. The system is a composite of four components: image acquisition, image pre-processing and enhancement, feature extraction and selection, and weather inference engine. Complete architecture of the KB/WIS system including its applications is described.

INTRODUCTION

Continuously influenced by the combined effects of earth's motions and the energy exchanges that continually occur between the atmosphere and the earth's surface and between the atmosphere and space, our planet's formless and invisible envelope of air reacts by producing an infinite variety of weather patterns. The methods available for weather information processing and forecasting can be roughly grouped into five approaches: analog, synoptic, numerical, statistical, and time-based dynamic forecasting methods. These methods can be used for various short-range to long-range weather forecasting [1].

Analog approaches match current conditions with records of similar past weather events with the idea that the succession of events in the past will be paralleled by current conditions. Synoptic methods are based on careful studies of the historic (synoptic) weather charts over a period of years, from which a set of empirical rules are established to forecast. Numerical methods use mathematical models to predict the evolution of physical processes in the atmosphere by the determinations of the conservation of mass, energy and momentum. The recent such techniques employ multi-level baroclinic models and include variables pertaining to pressure, wind directions and temperature as primary weather characteristics whereas the fronts are regarded as secondary features. Thanks to fast computers and large vector processors, vast amounts of computations which these models require has become possible to allow the preparation of a forecast map sufficiently ahead of the weather changes. Statistical techniques are now used to extrapolate and predict actual weather conditions. One such technique is Model Output Statistics (MOS) developed by the US National Weather Service. To predict for specific locations between the variable of interest a series of regression models are also developed [1]. Weather elements so predicted include daily maximum/

minimum temperature, 12-hour probability of precipitation of occurrences and precipitation amount, probability of frozen precipitation, thunderstorm occurrence, cloud cover and surface winds. Dynamic methods are being attempted at various weather centers using longer integration of medium-range models [1]. The object of weather forecasting, however, is not only to project the location and possible intensification of existing pressure system, but also to identify probable sites for the formation of the storm or severe weather centers.

The weather information processing procedures discussed above require human operator for interpretation and characterization which is cumbersome, labor-intensive and inefficient process. These methods often lead to inaccurate results. Though computer assisted forecasting using advanced mathematical models for the analysis of data has made greater strides, real-world weather situations often defy such modeling. Other advanced methods, such as pattern recognition and image/signal processing combined with the skills and experience of human (meteorologist), offer solutions to a large range of problems with much less investment of highly skilled personal and expensive computing resources [2]. Additionally, the solutions provided by such systems will be more reliable and robust as compared to their human counterpart or semi automated systems which must be operated by the trained personnel. Using PC-based computing environment we developed knowledge based pattern recognition method to model the weather patterns. Using these patterns the system learns to interpret and classify the weather. The weather pattern elements (features) from different weather images are automatically extracted to uniquely define weather patterns. To extract the hidden and occluded information wavelet and fractal methods are used.

OVERALL SYSTEM DESIGN

The KB/WIS system is a composite of four components (see Fig. 1). **Data acquisition** subsystem (DAS) performs three functions: data acquisition, data mapping and calibration, and image formation. It provides tools for image and multispectral data acquisition in various satellite formats including TIROS, DMSP, SGDB, GOES, GMS, and METEOSAT. It also includes the modules for low level smoothing and quality enhancement. A GUI-based user interface helps the user to acquire, display, and edit images/spectra and clean them as desired. **Image Preprocessing and Enhancement** subsystem (IP/ES) performs data ingest, conditioning and correction (noise elimination and enhancement to improve image to noise ratio; smoothing;

rectification of atmospheric effects and radiometric/geometric distortion; correction for skew, scan angle and time, orientation, and registration; normalization, etc.). Several routines to overlay, zoom, scale, rotate and loop (with direction controls) images providing functions for color/hue controls, resolution/brightness controls, etc., are available. High-level image processing and manipulation modules for both the point (pixel) operations and vector operations are developed to aid feature extraction. These modules are used to automatically process the image to correctly detect and delineate the desirable regions (clouds, image foreground/background, objects, geophysical boundaries, etc.) and other components of interest in digital images of weather maps: temperature, pressure, and moisture. Functions for image/region thresholding of gray scale; region growing/elimination; gray scale histogram construction; regional smoothing, enhancements, and sharpening using histogram equalization, edge detection, and filtering are also provided. **Feature Extraction and Selection:** This module constitutes a set of algorithms to extract the features from various image regions. The fractal algorithms are used to exploit and enhance the description and manifestation of complex and irregular regions. Considering the dependency of order one discrete wavelet transform (DWT) is also used to emphasize certain image regions and to extract extended (evolutionary) feature set from them. The number of features extracted may be too many to warrant efficient classification. Feature optimization modules to analyze and synthesize the extracted information are also developed [3]. This analysis determines the information contents each feature carries. The objective is to determine the most optimal parameters that could possibly be used for automatic classification of weather patterns. Using the optimal features each weather pattern is represented through a vector of selected features. Using clustering algorithms and discriminant analysis [4] visual tools are developed to allow the user to perform subjective analysis of features.

Using the selected features a set of samples describing three pattern classes representing three major factors, i.e., wind, cloud, and water which contribute most to weather formation were constructed. These weather patterns are used as reference patterns and are stored in the weather knowledge base (WKB). Additional meteorological knowledge in the form of rules that a meteorologist may use in identifying the weather patterns is also stored in WKB. For efficient retrieval and processing the WKB is organized as a tree of associated weather patterns (TAP). Structural proximity among weather patterns is used to determine the association. This organization helps in classifying a large set of weather classes using their own features without sacrificing the performance. In addition, the user will be able to analyze all weather patterns affecting a region as a hierarchy of candidate weather classes. **Weather Inference Engine (WINE):** Using the concept learning algorithm [4] WINE is trained to interpret the reference weather patterns which were

organized as TAP. A set of pattern recognition algorithms [4] which use the optimal features, classify and discriminate weather patterns, determine their identity, and hence interpret the oncoming weather. WINE automatically suggests a very small but definitive set of possible solutions along with level of confidence attached to each alternative.

SYSTEM METHODOLOGY

To demonstrate the potential of the KB/WIS a minimal subset of the system design was adopted. The methodology specifically used is described in this section. The DAS system reads the satellite data. Since the data from various satellites is received from 5/6 channels, it was mapped and calibrated. To create the multispectral weather images, the channels were scaled to one another. For example, to create a visible image from the TIROS two visible channels were calibrated so that for a particular pixel value (0-255 gray values), albedo values are the same. The DMSP data was inverted to occupy the same dynamic range as the visible data. The GOES infrared data was replicated to the equivalent visible resolution as was the input. The image formation is performed using histogram scaling which creates a colored visual image (RBG). To construct an image in the visual bands, for each pixel value two intensities (gun values) were evaluated. The gun values were computed based on the respective input image biases with respect to relative pixel values of both input images. The IP/ES performs histogram equalization to smooth and enhance the quality of the image displays.

Feature extraction is performed first by segmenting the image. The rules for segmentation are described in terms of HIS (hue, intensity, saturation) color space [5] by transforming from the RGB (Red, Green, Blue) color space. The intensity is described as, $I = R + G + B$, hue is described as,

$$H = \begin{cases} \theta & b \leq g \\ 360 - \theta & b > g \end{cases}$$

and the saturation is described as, $S = [1 - 3 \text{ Min } (r, g, b)] \times 100$ where, $\text{Min } ()$ is a function which selects the minimum of r, g , and b ; and r, g , and b are defined as

$$r = \frac{R}{I}, g = \frac{G}{I}, b = \frac{B}{I} \text{ and } \theta \text{ is given by,}$$

$$\theta = \cos^{-1} \left[\frac{2r - g - b}{\sqrt{6\{(r - \frac{1}{3})^2 + (g - \frac{1}{3})^2 + (b - \frac{1}{3})^2\}}} \right]$$

For different satellites different bands were considered as R, G , and B . For example, the bands 5, 4, and 1 were considered respectively as R, G , and B for TIROS data and transformed into HIS space. The advantages of dealing with data in HIS space is that it compensates for the dynamic range fluctuations of the scanned data and that it is useful for describing rules to extract objects from image data. Irregular and complex regions were treated using fractal and wavelet methods so that small details in the region may receive the same emphasis as the high

order components. Once the image is transformed, the components carrying weather information are extracted. For example, compared to the resolution of images from the individual satellites, the areas covering large water regions will be large. Selecting the band that transmits the most of the water related information, simple thresholding at some intensity of the selected band can detect the water regions. However, because of the HIS space, the dynamic range fluctuations of scanned data did not affect the water regions identification.

Modeling the Weather: Since weather varies with time and location, weather classification and effects analysis must be constantly appraised to retain its usefulness. To describe a weather model several parameters with associated level of confidence in 5 component areas were selected. They include, 1) meteorological event to be classified, 2) the sources of historical input variables, 3) current ground truth, 4) the size of the classification region, 5) the lead time and forecast period.

Meteorological events include moisture, temperature, pressure, winds, cloud cover, severe weather probability, and geographic parameters. Moisture describes, 1) the type of precipitation, i.e., rain, snow, freezing rain, etc., 2) estimate of precipitation amount, 3) probability of precipitation compared with regional thresholds, and, 4) estimated dew point. Temperature events includes expected temperature, probability of temperature compared with location thresholds, current temperature, and current and climatic temperature variations. The parameters pertaining to the pressure include expected barometric pressure, probability of pressure compared with location thresholds, current pressure, and current and climatic pressure variations. Wind events include expected wind direction, speed, and gust with confidence levels; probability of winds compared with location thresholds, current wind statistics; and current and climatic wind variations. Cloud cover is described using expected/current cover, ceiling, visibility, probability of a weather event compared with location thresholds. Cloud shape, type, size, orientation, were also considered. Severe weather parameters include probability of funnel clouds or tornado; probability of hail (& size), wind gusts, blizzard, cloud-to-ground lightning within specified grids, dust storms etc.

Geographic parameters refer to latitude/longitude, north/south hemisphere, and geophysical perimeters. Sources of climatic input variables include topographic/terrain data, periodic average on above parameters; etc.

Local model, single location model, or multiple location model is used to determine the size of the forecast region. The lead time is the amount of lag time between the time that the forecast model produces a forecast and the time that the valid period begins. The **valid period** is the time frame within which the forecast is valid.

A low level interpretation of multispectral image is performed using WINE. For example, an image region may be interpreted as: WATER: Water including lakes and rivers appear dark blue.

In case of brightness, it will be light blue, LAND: Land appear dark yellow with higher terrain becoming dark brown, or CLOUD: To show the depth various shades ranging from white to yellow will display the clouds.

CONCLUSION AND DISCUSSION

A weather image analysis, and interpretation system is designed. Preliminary results in enhancing and correctly classifying the major classes of water, land and cloud show the potential of the system. Complete system will implement full scale computer-enhanced decision making. The system increases the reliability, accuracy and consistency of identification and interpretation of weather images. Many benefits of this system can be mentioned including: 1) Accurate image acquisition, ingest, compression, storage, and dissemination of data using a smaller set of the most representative features. 2) Provide rapid and robust data processing. 3) Presents a comprehensive, yet user-friendly, hybrid decision-making facility combining meteorologist's expertise and computer synthesis of physical observations. The design of the system is highly modular and application independent and enhancements to the KB/WIS system will be possible. In addition the system will be able to adapt to other weather processing applications, e.g., identification of geographical locations; vegetation/crop analysis and estimation; object spotting; monitoring of environmental events processing and interpretation; dynamic object tracking and classification, etc., may be investigated in future.

REFERENCES

- [1] F.K. Lutgens, and E.J. Tarbuck, "The Atmosphere," 6th Edn., Prentice Hall, Englewood Cliffs, NJ, 1995.
- [2] K.J. Siddiqui, "Feature Selection in the Classification of Time-Variant Patterns, Ph.D. Thesis, Dept. of Computer Science, Concordia Univ., Montral, Canada 1994.
- [3] K.J. Siddiqui, Y.-H. Liu, D.R. Hay, and C.Y. Suen, "Optimal waveform feature selection using a pseudo-similarity method. Journal of Acoustic Emission, Vol. 9, No. 1, pp. 9-16, 1991.
- [4] K. Fukunaga, "Statistical Pattern Recognition." Academic Press, New York, 1990.
- [5] J.D. Foley and A. van Dam, Fundamentals of Interactive Computer Graphics, Reading, Mass., Addison-Wesley, 1982.

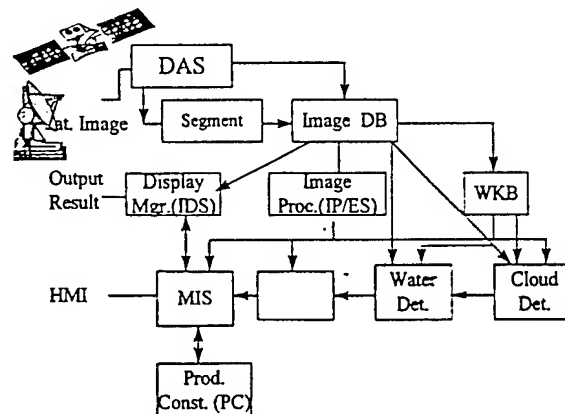


Fig. 1: Conceptual Structure of KB/WIS

Infectious Disease and Climate Change: Detecting Contributing Factors and Predicting Future Outbreaks

Ben Andrick, Bennett Clark, Kjell Nygaard, Antonette Logar, and Manuel Penaloza

Department of Mathematics and Computer Science

and

Ronald Welch

Institute of Atmospheric Sciences

South Dakota School of Mines and Technology

ABSTRACT

The spread of infectious diseases worldwide is a cause for concern in areas traditionally susceptible to these diseases and in areas where these diseases have been previously unknown. This work concentrates on diseases for which global infection rates have been increasing and which are transmitted by mobile agents, or vectors. For example, the mosquito is the vector responsible for the transmission of malaria, dengue and viral encephalitis. Identification of the factors, particularly environmental factors which can be detected from satellite imagery, which are highly correlated to outbreaks of these diseases is an important aspect of this research. Development of a system which will monitor these factors, as well as short term climate variations, such as El Nino events, is also necessary to provide risk assessments for susceptible regions so that intervention strategies may be employed to prevent or limit the impact of many vector-borne diseases. This paper describes a geographical information system that has been populated with climatic, geographic, and disease data used to distinguish correlations between the different data sets. The system provides a graphical user interface that allows for a spatial representation of the number of disease cases to be overlaid on a variety of satellite-derived parameters and geographic data. The Geographical Information System is the tool which, when combined with satellite-derived products, provides a framework for studying disease outbreaks.

I. INTRODUCTION

A vector-borne disease is one transmitted by mobile agents such as a mosquito. For example, the anopheline mosquito carries malaria in many areas of the world, which is one of the greatest health threats in the world. However, mosquitoes are only capable of survival above a given temperature. For example, the *Aedes aegypti* mosquito dies when the temperature drops below 0°C [1], with most of the larvae dying when the temperature is about 9°C [2]. Therefore, as temperatures vary with short-term climatic anomalies, and as temperatures rise globally due to increase concentrations of greenhouse gases, the mosquitoes are capable of migrating farther poleward, and of surviving at higher elevations [3][4]. This produces a threat of emerging diseases to areas that have been virtually free of those diseases in recent years. The overall warming of a certain area only needs to increase enough to allow for the breeding of the mosquito or other vectors. The increasing drug resistance of diseases and the insecticide resistance of mosquitoes present an increasing threat to many regions of the world, especially when combined with climatic fluctuations [5][6].

The period of time from which the mosquito is infected with a disease such as malaria, until the time the mosquito becomes infectious is known as the incubation period. At warmer temperatures, the incubation period is shorter in length [7]. Shorter incubation periods due to global warming and short-term fluctuations increase the risk of a potential epidemic. For example, the incubation period for type-2 dengue virus is 12 days at 30°C. This period

decreases to 7 days when the temperature rises only 2-5°C [8].

The purpose of the studies described by this paper is to evaluate the relationships between the spread of diseases, the characteristics of the vector spreading the disease, and the climatic factors affecting the vector. The model being developed to represent this system consists of several variables, which include climatic, geographic, and mosquito information. Since the system relies heavily on the use of geographic data, a Geographical Information System (GIS) was selected as the primary tool for this analysis. The GIS model being developed here will allow for queries to be made of the database entries, resulting in useful information from which decisions can be made for intervention. The ideal system will have the capabilities of producing accurate results while remaining efficient [9]. The following describes how the data was manipulated and organized to be informative, efficient, and generalized for further enlargements of the project. Note that the current system in development focuses upon the state of Texas. Future work will upgrade the system to cover the entire southern United States.

II. THE SYSTEM

The data selected for the system represents many of the variables affecting the spread of a vector-borne disease, specifically, climatic, elevation, and geographic data. In addition, information on reported cases of disease outbreaks was collected for the state of Texas by the Texas Department of Health and by the Center for Disease Control.

The geographic data provides detailed information about particular locations as well as the elevation of the land. The geographic data contains information on the locations of cities, county boundaries, and the United States border.

The type of climatic data collected was surface temperature and precipitation from the Tiros Operational Vertical Sounder (TOVS - NOAA-series satellite data) for 1985 until 1988. The surface temperature was the average temperature per day for each month covered over 1° by 1° regions.

The precipitation was the daily average in millimeters for each month and also covered 1 degree by 1 degree. More extensive daily values at 3-hour intervals will be available soon.

The system uses this data to evaluate relationships between vector-borne diseases and elevation, surface temperature, and precipitation. For example, in Texas the number of cases of malaria is expected to be greater in the warm summer months than in the winter. As expected, June and July are the months with the largest number of cases, while the winter months have the fewest cases. However, heat is not the only factor for mosquito breeding; moisture is also important. Thus, the maximum combination of these, rather than individual maximums, is the key search criteria. Also note that Texas ranges from sea level to over 8200 feet. All reported cases of malaria are located between sea level and 2000 feet, with the vast majority of cases in areas lower than 1000 feet in elevation. The system also highlighted anomalies. Given that mosquitoes do not breed above certain elevations, or below certain temperatures, the system could identify cases of malaria that were most likely not of local origin.

The analysis up to this point has been implemented using graphical overlays, which has supported the initial expectations of the project. Current efforts are concentrating on the development of intelligent search and correlation algorithms. Artificial neural networks, fuzzy logic, and case-based reasoning approaches are being tested. A fuzzy database and query language are most promising. For example, the user may want to view all cases of malaria that lie within a high altitude. The user may not know and, with the fuzzy interface does not need to know, what qualifies as a high elevation for a particular region in order to submit the query to the system [10].

Finally, another large component to this system is a World Wide Web interface. The interface provides access to the GIS and database and presents the user with images displaying the query results. Thus, a user anywhere in the world may ask about cases of malaria reported in Texas in the summer of 1994 that occurred at elevations below 1000 feet and have the results of the query displayed on a map of Texas

as well as in numerical form. The web site also provides information about each of the vector-borne diseases and hyperlinks to related web sites. Since some of the data is confidential, access to the disease outbreak information is not yet available to the general public.

III. CONCLUSION

Ultimately, the goal of this research is to provide a means of predicting vector-borne disease outbreaks. Then, the information can be passed on to public health officials and government agencies so preventive action could be taken. While it is unlikely that all the disease outbreaks can be predicted, a system such as this one will be capable of providing a risk assessment of a particular disease occurring in an approximate area. There are many countries that cannot afford to take all the precautionary steps to prevent disease outbreaks. If the country were provided with sufficient information of where and when to take preventive action, the country might be capable of preventing outbreaks from occurring.

IV. REFERENCES

- [1] Knipling, E.B., and W.N. Sullivan, "Insect Mortality at Low Temperatures", *J. Econ. Entomol.*, Vol. 50, pp. 368-369, 1957.
- [2] Smith, W.W. and G.J. Love, "Winter and Spring Survival of *Aedes Aegypti* in Southwestern Georgia", *Am. J. Trop. Med. Hyg.*, Vol. 7, pp. 309-311, 1958.
- [3] Shope, R., "Global Climate Change and Infectious Diseases", *Environ. Health Perspectives*, Vol. 96, pp. 171-174, 1991.
- [4] Patz, J.A., "Global Climate Change and Public Health", *International Perspectives in Environment, Development and Health*, G.S. Shahi, B. Levy, T. Kjellstrom, R. Lawrence and A. Binger, Eds., Springer Publications, NY, 1995.
- [5] Martens, W.J.M., T.H. Jetten, J. Rotmans, and L.W. Niessen, "Climate Change and Vector-Borne Diseases", *Global Environmental Change*, Vol. 5, pp. 195-209, 1995.

[6] Matsuoka, Y. and K. Kai, "An Estimation of Climatic Change Effects on Malaria", *J. Global Environ. Eng.*, Vol. 1, pp. 43-57, 1995.

[7] Longstreth, J. and J. Wiseman, "The Potential Impact of Climate Change on Patterns of Infectious Disease in the United States", in *The Potential Effects of Global Climate Change in the United States*, J.B. Smith, and D.A. Tirpak, Eds., Washington, DC, U.S. Environmental Protection Agency, Appendix G, Document 230-05-89-057, 1989.

[8] Watts, D. M. et al., "Effect of Temperature on the Vector Efficiency of *Aedes Aegypti* for Dengue 2 Virus", *Am. J. Trop. Med. Hyg.*, Vol. 36, pp. 143-152, 1987.

[9] Aronoff, Stan, "Geographical Information Systems, A Management Perspective", WDL Publications, 1995.

[10] Cox, Earl, "Fuzzy Fundamentals", *IEEE Spectrum*, October 1992.

V. DATA REFERENCES

Ten years (1985 through 1994) of disease data from the Center for Disease Control (CDC) covering the contiguous United States.

Twelve years (1984 through 1995) of disease data from the Texas Department of Health, Infectious Disease Epidemiology and Surveillance Division.

Political boundaries and populated places from United States Geographical Survey (USGS).

A digital elevation model of North America from EROS Data Center.

Surface temperature and precipitation from Tiros Operational Vertical Sounder (TOVS - NOAA - series satellite data.).

Infectious Disease and Climate Change: A Fuzzy Database Management System Approach

Manuel A. Penaloza¹ and Ronald M. Welch²

¹Department of Mathematics and Computer Science
email: mpenaloz@silver.sdsmt.edu

²Institute of Atmospheric Sciences
South Dakota School of Mines and Technology
501 E. St. Joseph Street
Rapid City, SD 57701-3995

Abstract--Infectious diseases are reemerging globally, many of them being climate-related. The integration of remote sensing and disease outbreak data along with GIS and artificial intelligence approaches provides the tools for predicting future disease outbreaks. A fuzzy database management system (FDBMS) has been constructed for this purpose, storing disease outbreaks and a variety of parameters such as precipitation, temperature, population density, elevation and other variables. The FDBMS is able to search the database and provide disease risk assessments based upon crisp and fuzzy conditions stated about spatial, temporal, climatic and other parameters. The fuzzy search is generated either by using a graphical user interface (GUI) or a fuzzy query language (FQL). FQL is an extension to the well-known relational Structural Query Language (SQL), and it allows the user to make complex queries. The FDBMS is able to display the locations of previous disease outbreaks on a world map in the system GUI. Currently, nine years of U.S. disease data from the Center for Disease Control (CDC) and from the state of Texas are stored in the database. A major expansion to global datasets is in progress, and international health agencies are asked to contribute to this effort.

1. INTRODUCTION

New and emerging infectious diseases are occurring all over the world, even in regions with no previous cases of these diseases [1]. Many of these disease outbreaks are climate related, especially with anomalous periods of precipitation and elevated temperatures and associated with El Nino/La Nina events.

The prediction of disease outbreaks due to environmental changes that the earth is experiencing require tools for storing and analyzing outbreak and climate parameter data. A Database Management System (DBMS) is a tool that defines, organizes and enables the search of data. Current DBMS use the relational model, due to the fact that it is easy to understand the model as well as it is easy to define and write queries. Searching in the relational model usually is performed by writing a query in Structured Query Language

(SQL). SQL enables any database user to express conditions with precise facts. A search for cases of malaria at locations with high temperatures and high precipitation rates requires crisp conditions such as:

"TEMPERATURE BETWEEN 28.5°C AND 40°C AND
PRECIPITATION > 5mm."

However, it seems more natural to search the database using fuzzy conditions such as

"HIGH TEMPERATURES AND HIGH PRECIPITATION."

Fuzzy logic was introduced by Zadeh[2] in the 60's to express and make decisions on vague concepts. The statement that "Peter is tall" in fuzzy logic associates a degree of membership of Peter in the set of tall persons. Without doubt Peter is tall if he is 7 feet high, but how about 5'9"? In fuzzy logic, the term tall is one of the states (or fuzzy set) of the fuzzy variable "height." Each state is represented by a membership function. The membership function indicates the degree of membership (DM) of an element into a set (or state). DM varies between 0 and 1, where 0 indicates the fact that x is not a member of a set A, whereas 1 represents full membership of x into set A.

Fuzzy logic has been used to extend the relational algebra and relational calculus query languages[3]. Unfortunately, programming in these languages is impractical. This paper describes a database system with a query language that enhances SQL by allowing the user to express fuzzy-based conditions as well as crisp conditions.

2. DATABASE CONTENT

The current database consists of a number of tables that contain nine years of disease data from the Center of Disease Control (CDC) and from the state of Texas. Data coming from international health agencies will be added in the future. A wide variety of satellite data has been used to derive surface properties such as temperature and precipitation.

Elevation data was provided by the NASA EROS data center. The elevation data has a resolution of 1x1 Km. The parameter data are stored in separate files. File names and associated data for these parameters are stored in a database table. Membership functions for each parameter are also stored in the database.

3. FUZZY DATABASE MANAGEMENT SYSTEM (FDBMS)

FDBMS is a Motif-based application that enables a user to manipulate data either by pressing the pushbuttons on the graphical user interface (GUI) or by expressing a query in an extended SQL called fuzzy query language (FQL).

The items in the application's menubar are pulldown menus that allows a user 1) to quit the application; 2) to insert, delete, update records in the database; 3) to query using FSQL; 4) to display the countries, continents, disease information; and 5) to get help about the different functions of the application.

To search the database using the GUI, the user generates the search conditions by pressing several of the search pushbuttons (DISEASE, CONTINENT, COUNTRY, PROVINCE/REGION, CITY, DATE, FUZZY). Pressing any the buttons will cause the display of an associated list of entries (e.g., a list of diseases). Then, the user selects one of the list entries and the application automatically enters it into the search condition list. Fuzzy conditions are entered into the search condition list by pressing the FUZZY button. This results in the display of a list of parameters and fuzzy sets. The search is submitted to the application when the SUBMIT pushbutton is pressed. The number of cases found are displayed in the results area of the GUI. The world map in the GUI allows a user to select a region on which he/she is interested on finding outbreak cases. All the search conditions are anded, except for the disease entries. Below is an example of a search condition list generated by pressing pushbuttons.

DISEASE: Malaria

OR: Dengue
SPATIAL: (34.2, -110.21) ,
(12.21, -95.50)
FUZZY : HIGH TEMPERATURE
AND: HIGH PRECIPITATION

The fuzzy conditions form a fuzzy rule with the implicit action SELECT. The implicit fuzzy rule is:

IF TEMPERATURE IS HIGH AND
PRECIPITATION IS HIGH THEN SELECT

The rule is satisfied when the rule's DT exceeds some threshold (e.g., 0.5). An outbreak case is selected when the information about the outbreak and the associated location parameter values satisfies each of the crisp conditions and if the fuzzy rule's DT exceeds 0.5. The results are stored in a file, and their locations are displayed as colored points in the world map.

The DT of the rule is computed by combining the DMs associated with each fuzzy condition using the minimum function. That is, the DT of a rule is the value of the weakest fuzzy condition's DM. For instance, assume that the input fuzzy variables *prec* (precipitation) and *stemp* (surface temperature) have the membership functions shown in Figure 1. Assuming input for *prec* is 5.6mm and *stemp* is 30°C (shown with dotted line in Figure 1), and the fuzzy rule:

IF *prec* is high AND *stemp* is high THEN select

This rule may indicate that we want to select a particular location with high precipitation and surface temperature. The computed DT for this rule provides the degree of confidence with the selection. From Figure 1, the DMs for the two fuzzy conditions are: DM(*prec* is high) is about 0.8 which is the intersection of the dotted line at *prec*=5.6 and the trapezoid for high precipitation; DM(*stemp* is high) is about 0.4. The DT for the rule is:

$$DT(\text{rule}) = \text{MIN}(0.8, 0.4) = 0.4$$

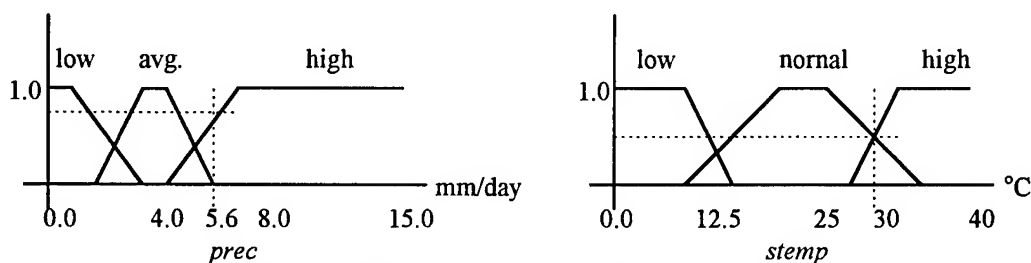


Figure 1. Membership functions for *prec* and *stemp*

To express a query using FQL, a user selects NEW of the Query pulldown menu and then the application brings a text window with a query template. The user writes the query by modifying this template. The template for FQL is:

```
SELECT [ * |
        [DISTINCT] list of attributes separated by comma
      ]
FROM [list of tables separated by comma]
[ WHERE
    [ crisp conditions
      [ AND ON LOCATIONS WITH
        fuzzy conditions ]
    ]
]
```

Terms enclosed on square brackets are optional. A '[' character indicates alternative selections. A '*' character tells the FDBMS to display all the attributes of the tables listed after FROM. Examples of queries using FQL are given below.

- a) SELECT DISTINCT COUNTY_CODE
FROM MALARIA
WHERE COUNT_CASES > 3
- b) SELECT DISTINCT COUNTY_CODE
FROM MALARIA, LOCATION
WHERE MALARIA.COUNTY_CODE =
LOCATION.COUNTY_CODE
AND MALARIA.COUNTY_CODE =
LOCATION.COUNTY_CODE
AND COUNT_CASES > 3
AND ON LOCATIONS WITH
HIGH PRECIPITATION
AND LOW TEMPERATURE

4. CONCLUSION

A database system with a fuzzy query language (FQL) is presented in this paper. FQL is an extension to SQL. This fuzzy database system enables a user to access and display disease outbreaks on a world map. A novice user may define a query using the pushbuttons and dialog windows of the GUI. A more experienced user may use the FQL to write a complex query.

This tool will be enhanced with artificial intelligence techniques that will predict area of risks for selected diseases. Then, the information can be passed to public health officials and government agencies so preventive actions could be taken.

ACKNOWLEDGMENTS

The authors wish to thank the Satellite Data Utilization Office (Code 910.4) and the Distributed Active Archive Center (Code 902.2) at Goddard Space Flight Center, Greenbelt, MD, 20771 for the production and distribution of the satellite data. These activities were sponsored by NASA's Mission to Planet Earth program.

We also would like to thank the Texas Department of Health and the Center for Disease Control (CDC) for providing the disease data used for this work.

REFERENCES

- [1] Colwell, Rita R., Global Climate and Infectious Disease: The Cholera Paradigm. *Science*, Vol. 274, December 20, 1996.
- [2] Zadeh, L. A., Fuzzy Sets. *Information and Control*, 1995, pp. 338-353.
- [3] Takahashi, J., 1993. Fuzzy Database Query Languages and Their Relational Completeness Theorem. *IEEE Transactions on Knowledge and Data Engineering*, Vol. 5, No. 1, Feb. 1993, pp. 122-125.

ENVIRONMENTAL MONITORING IN ITALY USING THE OPTICAL SENSORS OF THE PRIRODA MODULE

Neon A. Armand, Vsevolod V. Efremenko

Institute of Radio Engineering and Electronics of Russian Academy of Sciences

Mokhovaja str., 11 - 103907 Moscow - RUSSIA

Tel.: 007-095-2031433 - Fax.: 007-095-2038414 - E-mail: seva@mail.cplire.ru

Luca Pantani, Ivan Pippi

C.N.R.- I.R.O.E. "Nello Carrara"

Via Panciatichi, 64 - 50127 Florence - ITALY

Tel.: 0039-55-42351 - Fax.: 0039-55-410893 - E-mail: pippi@geodec.iroe.fi.cnr.it

ABSTRACT - In the field of the scientific co-operation between our two Institutes started in 1986, a common research program was developed for the analysis of the characteristics and the application of advanced spaceborne optical sensors for the remote sensing of the Earth.

This program has become a part of the international scientific project Priroda, which combines efforts of scientists from Belarus, Bulgaria, Czech Republic, France, Germany, Italy, Poland, Russia, Switzerland, Ukraine, and the USA. The space module Priroda is the technical base for the project. It was launched and attached to the inhabited space platform Mir in April 1996.

By means of the optical sensors placed on board of the Priroda module, we are going to study the geophysical parameters useful for environmental monitoring and resource evaluation in Italy.

Taking into account the characteristics of different sensors and utilising both experimental data available now and coming from similar sensors placed on aircraft or spacecraft and suitable models, we are estimating the possible applications of such new sensors over some test sites in the Tuscany region.

INTRODUCTION

A common activity between the Institute of Radioengineering and Electronics (I.R.E.) of the Russian Academy of Sciences and the Research Institute on Electromagnetic Waves (I.R.O.E.) "Nello Carrara" of the Italian National Research Council (C.N.R.) has been performed since 1986. In this field a research program is being carried out in order to analyse the characteristics and the possibilities of the spaceborne optical sensors operating at high and moderate spectral resolution for ecological, geophysical and resources investigations of the Earth [1].

This program has become a part of the international scientific project Priroda [2-3]. The space module Priroda, sketched in Fig.1, is the technical base for the project. It was

launched and attached to the inhabited space platform MIR in April 1996. The space station is orbiting at an altitude of 400 Km with an inclination of 51.6° , and 15.6 orbits per day.

At the beginning the data acquired from similar aerospace sensors and ground placed instrumentation have been utilised in the numerical simulation for estimation of the possibilities of the optical sensors placed on module Priroda to measure different environmental parameters. After one year of testing and calibration, the sensors of the Priroda module are ready to acquire data which will be compared with those coming from the ground segments.

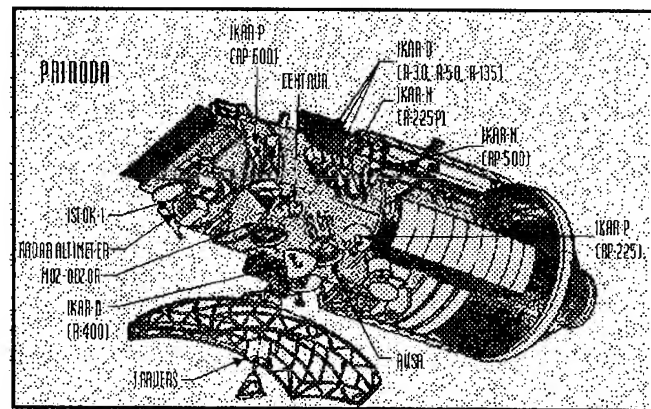


Fig. 1 - The space module Priroda.

SCIENTIFIC OBJECTIVES

The two Institutes are planning the following studies for the Priroda mission.

Coastal water characteristics investigation

In recent years more and more attention has been paid to coastal waters for their high productivity. However up to now we have only a poor knowledge of the horizontal distribution and temporal variation of the constituents and

the temperature field of coastal waters. Moreover the processes depend on the area of study.

The main water constituents and temperature fields can be determined by space optical remote sensing. The knowledge of suspended matter, phytoplankton, yellow substances and thermal distribution is the key for various ecological and resources studies in estuary and coastal zones.

The two Institutes intend to perform comparative studies of the spectral characteristics of water in coastal areas in the North Tyrrhenian Sea including the estuary of the Arno river and the Black Sea near Crimean.

Anthropogenic activity effects over the vegetation status

To study the regional peculiarities of the anthropogenic activity effects on the vegetation status it is necessary to combine the field measurements and the large scale data acquired from space sensors.

The I.R.O.E. has experience in lidars and imaging spectrometers as well as airborne multispectral scanner measurements [4-8]. The forest and the agriculture areas in the region of the Tuscany Apennines are under investigation. The acquired data show that the acid rains, coming from the industrial regions of North Italy, seem to be the main effect of the anthropogenic pressure on the environment. In order to verify this and other hypothesis the space remote sensing data are needed.

Spectral features in area of geothermal and volcanic activities

The geological processes in the active area throw as a rule into changes of structure and mineral composition on the Earth surface. Then the kind and structure of vegetation is changing too. These changes must appear also in the spectral signatures of the surfaces from visible to thermal infrared wavelengths.

These areas are interesting as potential thermal and mineral sources as well as danger zones. If these changes of spectral signatures can be defined by means of space remote sensing, the possibility of detection such areas as well as of monitoring the geological process will appear.

In the area of Tuscany there are two areas which can be utilised as test sites for space remote sensors. The first one is located in Larderello where a geothermal power station is situated and the second includes the Monte Amiata region where large number of high temperature water sources exist. Both areas are under geological studies and the related results are to be compared with the results of space investigations.

Atmospheric studies

Large scale atmospheric models are important and necessary tools for different studies and investigations. For example it is impossible to correct the results of space remote

sensing of the Earth surface or to make the weather-forecast without such models. For all these conveniences such models cannot unfortunately take into account the regional features and in some cases we have to develop regional models of atmosphere, which have not all the possibilities of the large scale ones. However the large scale models can be improved by including the regional models. Anyway in order to perform that improvement, data of atmospheric structure are needed.

For such investigations two different areas in Italy are chosen. The first one is located in Tuscany in the south side of the North Apennine mountains along the Arno river between the cities of Pisa and Florence. The region is characterised by a medium industrial activity, a specialised agriculture, a medium density of inhabitants and a low level of atmospheric pollution. The second area, placed between the Alps and Apennine mountains in the valley of the Po river, is a part of Lombardia and Emilia region with Milan in the centre. The related atmosphere is extremely polluted because of the high industrial activities and high density of inhabitants.

The comparison of the results of the space atmospheric sounding over these areas with the data of atmospheric structure measured from the ground and the results of large scale models will provide the improvement of such models and the performance of ecological analysis of the atmosphere over the areas together with the possible mutual influences.

THE PRIRODA OPTICAL SENSORS

In order to perform the goals mentioned above, the data from the following optical sensors, mounted on Priroda module, are utilised [9].

ISTOK-1

The instrument is a 64 channel infrared spectro-radiometer in the band of 4 - 16 μm to measure both the atmospheric transmittance spectrum by looking at the Sun and the thermal emission spectrum of the atmosphere and the Earth surface under different angles of pointing. In addition the instrument includes a TV CCD camera to observe the clouds and the Earth surface.

MOS-OBSOR

This imaging spectrometer is dedicated to the investigation of the reflected solar radiation in the atmosphere-Earth surface system in the visible and near infrared ranges. The apparatus consists of different optical blocks and is comprehensive of on-board data compression.

MOMS-2P

This modular optoelectronic multispectral stereo scanner consists of two subunits: a threefold stereoscopic imaging

system and a four-band multispectral camera with nadir orientation. The instrument parameters were designed in order to fill the gap between existing spaceborne system and airborne photography.

MSU-E

This electro-optical scanner is mainly devoted to investigate the reflected solar radiation in the "atmosphere-Earth surface" system at a spatial resolution of 25 m in three visible and near infrared spectral bands.

MSU-SK

This opto-mechanical scanner operates in four adjacent visible and near infrared bands at 120 m of spatial resolution plus one band in the thermal infrared region with 300 m of spatial resolution. An additional feature consists of the possibility to tilt the field of view of the scanner up to 30° in the plane normal to the flight direction.

GROUND EXPERIMENTS

During the Priroda mission truth measurements of different electromagnetic parameters will be performed by ground experiments for the remote sensing devices calibration and validation and for the development of new methods for geophysical parameters retrieving.

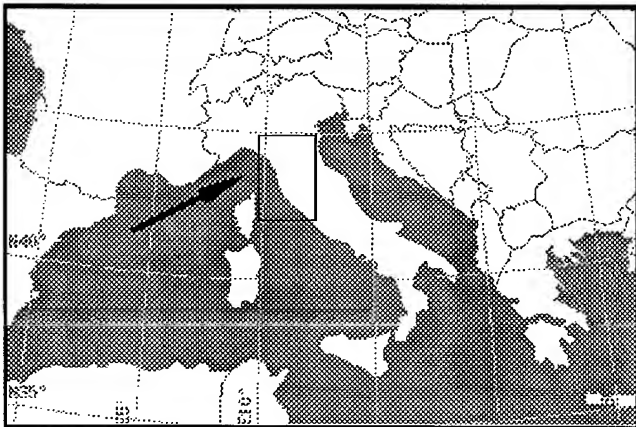


Fig. 2 - Preliminary test area location in Italy.

The preliminary location of the test areas regarding the goals of investigation are sketched in Fig.2. In these areas various field measurements will be performed utilising instrumentation such as spectroradiometers, pyranometers and lidar as well as the routine data coming from the environmental departments of regional and local authorities.

DATA EVALUATION

The sensors MSU-E and MSU-SK are also flown on RESURS-01 satellite into a solar synchronous orbit at an altitude of 680 Km. The data acquired in various areas are considered and the signal to noise ratio and the recursive noise was evaluated, also utilising the characteristic pattern of the FFTs, due to the conical scanning system of these sensors. Additional data coming from other aerospace sensors will be acquired.

CONCLUSIONS

This overview has shown the great potential of the instrumentation which is placed on the space station MIR. New algorithms are under development and the related software for remote sensing data processing are under implementation. In addition particular attention is paid to the evaluation and correction of the atmospheric effects on the signals detected by those sensors.

REFERENCES

- [1] R.A.S.-I.R.E., C.N.R.-I.R.O.E., "Proposal for Scientific Program: Common Experiments for Space Remote Sensing in Optical Band", International Project Priroda, December 1991.
- [2] Complex of Remote Sensing of the Earth: Priroda, Scientific program (Version 2 and Proposals of Bulgaria, Germany, Italy, Poland, Romania, USA, Czechoslovakia, France, Switzerland), Moscow 1993.
- [3] International Scientific Remote Sensing Project Priroda, Science Plan, Moscow 1995.
- [4] L.Pantani, I.Pippi, "Two Wavelength Lidars: Target Identification Through a Differential Reflectance Technique", *Optical Acta*, vol.30, pp.1473-1481, 1983.
- [5] P.Vujkovic, Cvijin, D.Ignjatijevic, I.Mendas, M.Sreckovic, L.Pantani, I.Pippi, "Reflectance Spectra of Terrestrial Surface Materials at CO₂ Laser Wavelengths: Effects on DIAL and Geological Remote Sensing", *Applied Optics*, vol.26, n.19, pp.4323-4329, 1987.
- [6] I.Pippi, B.Radicati, "Data Analysis of a Coastal Zone Remote Sensing Campaign by the NASA C130 Airplane", *Applications of Digital Image Processing X*, S.Diego, U.S.A., SPIE 829, pp.305-309, 1987.
- [7] A.Barducci, I.Pippi, "The I.R.O.E. Activity for the AVIRIS Campaign in Europe", *Proc. Third AVIRIS Workshop, Pasadena, U.S.A., NASA JPL 91-28*, pp.314-321, 1991.
- [8] A.Barducci, I.Pippi, "Temperature and Emissivity Retrieval from Remotely Sensed Images Using the 'Grey Body Emissivity' Method", *IEEE Trans. Geosci. Remote Sensing*, vol.34, n.3, pp.681-695, 1996.
- [9] Interkosmos (RGDS), "The Project Priroda", Moscow 1990 (in Russian).

A JOINT CHAIN BETWEEN THERMAL INERTIA MODEL AND GEOMETRIC OPTICAL MODEL OF BRDF*

Zhang Renhua

Institute of Geography, Chinese Academy of Sciences
Booieing , 100101, CHINA

Abstract -- This paper reveals the quantitative relationship between surface temperatures of the four components in the geometric optical model and soil thermal inertia, soil water content and micro-meteorologic parameters. The relations have been verified by using experiments. This work is a preparation for developing the geometric thermal model which is useful to study directional land surface temperature.

INTRODUCTION

In the thermal infrared remote sensing, the thermal inertia applications are major research content. Several thermal inertia models have been developed since 1970s [1][2][3]. There is common point for those model is the need of obtaining thermal information in more than two time-phases from remote sensing data. Generally, such two time-phases are the middle night and noon daytime. Because they can obtain maximum information. In fact, any time-phase can be used to calculate the thermal inertia, so long as there is a enough large difference of ground surface temperature of the two phases. If there are two adjacent ground surfaces whose diameters are from 0.1m to 10m and their soil physical properties are approximately identical. When two different solar radiations reach on the two surfaces, two different surface temperatures will be caused. No doubt, the temperature difference is similar to that of the two time-phases at the same surface and it contains information of the soil physical properties

A shadow of geometric object receives environment diffuse radiation only without direct solar radiation, so that a great temperature difference between the shadow and its adjacent sunlit surface can be occurred. Because position of the shadow is continually changed with sun zenith, the change of heated shortly by the different radiation can not result in the change of soil physical properties such as soil water content. The shadows projected by sparse forest, orchard, coarse soil surface, hills in the middle and low latitude region and so on satisfy basically above mentioned conditions.

As a result, a interesting research project can be developed, in which a thermal geometric model (TGM) should be established; more complicated inversion ought to

be conducted; more significant information can be abstracted from the inversion results.

The project may contributes to modelling of directional land surface temperature which is linking with the global change and regional sustainable development. This paper focus on discussing the function relationship of the temperature differences of shaded and sunlit ground and crown surfaces with soil water content and the other micro meteorologic parameters. The temperature difference considers as a joint chain between the thermal inertia model or plant water stress model and the geometric optical model (GOM) for developing the thermal geometric model. Particularly, the role of the shadows for the background and the crown will be pointed out in the thermal geometric model and its inversion. In order to verify the correction and feasibility for the idea presented this paper, experiments in the Yucheng Experimental Remote Sensing Site were carried out.

ESTABLISHING THE JOINT CHAIN

The geometric relationship of the GTM can be established by using the similar way in the geometric optical modelling. But, deducing quantitative functions of sunlit and shaded surfaces temperatures for crown and background are significant different from the GOM. The radiation balance principle is used for the GOM only, however, the GTM ought to be based on the principle of the heat balance.

The GOM for conifer forest presents a quantitative relationship of sunlit and shaded areas for crowns and background in a pixel with solar zenith, but view angle is nadir only.[4] Purpose of establishing GTM is for inverting application information from multi-angle thermal remote sensing data. For the inversion of the GTM, the information changed with view angle is more useful than with solar angle. Because the surface temperature will be changed when the solar angle is changed. Therefore, the use of information from the solar angle for inverting complicated matters considerably. In 1992, Li Xiaowen and A Strahler developed a geometric optical bidirectional reflectance model which assumes only two kind of surface over a

* The project is supported by NSFC of China

pixel [5]. However the GTM must know both area and surface temperature of all four components. The directional surface temperature of a pixel can be modeled as extension of their model:

$$T(i, v) = \frac{\iint_A [\sigma B(s) \epsilon(i, v) \cos \theta_i \cos \theta_v + (1 - \epsilon(i, v)) E] ds}{A \cos \theta_i \cos \theta_v} \quad (1)$$

where ds is a small surface element over area A of a pixel; $B(s)$ is black-body brightness temperature; i, v and s represent the directions of illumination, viewing and the normal to a surface element; $\cos \theta$ is cosine of the phase angle between two directions; θ is the zenith angle of a direction; $I_v(s)$ is indicator function equal to one if ds is viewed (I_v), zero otherwise; $\epsilon(i, v)$ is directional emissivity; E is environment irradiance over ds .

Li Xiaowen and A. Strahler did several excellent results in GOM in spite of the universal overlapping functions still needs to develop. The most of formulas for area of the four components in GOM can be adopted. But the surface temperatures of the four components in GTM should be modeled instead of the reflectances in GOM. It seems that the surface temperatures are more useful than areas of the four components for GTM. The propose of creating GTM is very clear: reveal the directional surface temperature distribution in term of the soil physical and micro-meteorological parameters; oppositely, estimate soil water content and plant water stress index according to inversion of multi-angle thermal remote sensing data. So far there are a lot of hard works to do in order to achieve the scientific goals

This paper focuses on discussing the quantitative relations between the four surface temperatures and micrometeorologic and soil physical parameters.

As well know, the heat balance equation for soil surface and leaf surface be written, for soil:

$$R_n = E + H + G \quad (2)$$

$$R_n = (S + D)(1 - \alpha) - \sigma(\epsilon_s T_s^4 - \epsilon_a T_a^4) \quad (3)$$

$$E = \frac{\rho_a C_p \Delta}{\gamma r_a} (T_s - T_a - \frac{d_a - d_s}{\Delta}) \quad (4)$$

$$H = \frac{\rho_a C_p}{r_a} (T_s - T_a) \quad (5)$$

where R_n is the net radiation; S and D are solar direct radiation and surrounding diffusion (including that of the sky and leaves) respectively; α is reflectivity of the soil surface; σ is the Stefan-Boltzmann constant; ϵ_s and ϵ_a is the soil and surrounding object emissivity

$$G = \rho_s C_s k \frac{(T_s - T_g)}{\delta z} = P k^{-1} \delta z \quad (6)$$

respectively; E is the latent heat flux, H and G are the sensitive heat and soil heat fluxes; ρ_a , ρ_s are the air and soil densities respectively; C_p , C_s are the air and soil specific capacities respectively; r_a is the air resistance; T_s , T_g and T_a are temperatures of at soil surface, at δz depth of soil and the air respectively; d_a and d_s are vapour saturation differences above and at soil surface; k is the soil heat conductivity, I_{th} is the thermal inertia which has a liner function with soil water content W , $I_{th}/(k\delta z) \approx aW + b$, where a , b are experimental coefficients.

When the changes for T_a , d_a , T_s , T_g and ϵ_s are not obvious, the temperature difference on the sunlit and shadow soil surface approximately are:

$$T_{s1} - T_{s2} = \frac{(1-P)(1-\alpha)(D+S) + \frac{\rho_a C_p}{\gamma r_a} (d_{s1} - d_{s2})}{\frac{\rho_a C_p (\gamma + \Delta)}{\gamma r_a} + \sigma \epsilon_s T_{SA}^3 + (aW + b)} \quad (7)$$

Where T_{s1} , T_{s2} , d_{s1} , d_{s2} are temperatures and vapour saturation differences of sunlit and shaded soil surfaces respectively; T_{SA} is average temperature of the sunlit and shaded soil surfaces; P is the gap possibility of the crown. When shadow is not very large, $d_{s1} - d_{s2} \approx 0$, otherwise $d_{s1} - d_{s2} = \Delta[F_1(T_{s1} - T_a) - F_2(T_{s2} - T_a)]$, where F_1 , F_2 are plant water stress index for sunlit and shaded soil surface.

For leaves, a similar expression can be obtained:

$$T_{L1} - T_{L2} = \frac{(1-\tau P')(1-\alpha_L)(D+S)}{\frac{\rho_a C_p}{\gamma r_a} + \frac{\Delta \rho_a C_p}{\gamma(r_a + r_c)} + \sigma \epsilon_L T_{LA}^3} \quad (8)$$

Where T_{L1} , T_{L2} are temperatures of sunlit and shaded leaf surfaces; T_{LA} is average temperatures of the two surfaces; τ and P' are the final transitivity and gap

possibility of upper level leaves, ε_L is emissivity of the leaf. r_c is stomatic resistance of the leaf. Therefore the temperature differences between sunlit and shaded surfaces depend not only on the optical properties, canopy structure and incident radiation which form radiation balance, but also on the sensitive heat flux, the latent heat flux and soil heat flux which are components of the heat balance together with the net radiation. In other words, the four components in GTM is final result of the heat balance on the soil or leaf surface. For this reason, in order to reveal the directional rule of the land surface temperature, one must know both area and temperature of the four surfaces. Fig.1 will show the relations of the surfaces of the four components and solar direct radiation, surface reflectivity, soil water content wind-speed and so on.

EXPERIMENTS FOR VERIFICATION

Experiments were conducted in the Yucheng Experimental Remote Sensing Site of Chinese Academy of Sciences in April, May 1996. There are two plots (each 10m x10m) of simulated pixel planed by pine with Poisson space distribution in the site. A 30m tall tower locates between the two plots whose soil water content can be controlled by a sprinkle irrigation system. The part of multiangle measurements in the principal plane can be carried out at various levels of the tower. Bowen ratio equipments were installed in the plots for measuring the sensitive, latent and soil heat fluxes. The temperatures and reflectances of four surfaces were observed by means of portable thermal infrared radiometer and CCD-portable spectral radiometer. The surface temperature differences inverted by multiangle measurements and its experimental validation will perform in next step. Verification in this paper focuses on the discussion of the joint chain between surface temperature of the four components and environmental parameters. It is primary to verify possibility of abstracting soil moisture from temperature differences of sunlit and shaded soil surface. From the experiments we obtained a data which show a good agreement with calculated values of (7) and (8) at Fig.2.

CONCLUSION AND DISCUSSION

It has been verified that the temperature differences of sunlit and shaded soil and leaf surfaces contains more environmental parameters information. Particularly soil thermal inertia or soil moisture may be abstracted by inversion of multiangle thermal remote sensing data. Establishment of GTM concerned with directional land surface temperature should add more heat balance consideration if GOM. is adopted as foundation.

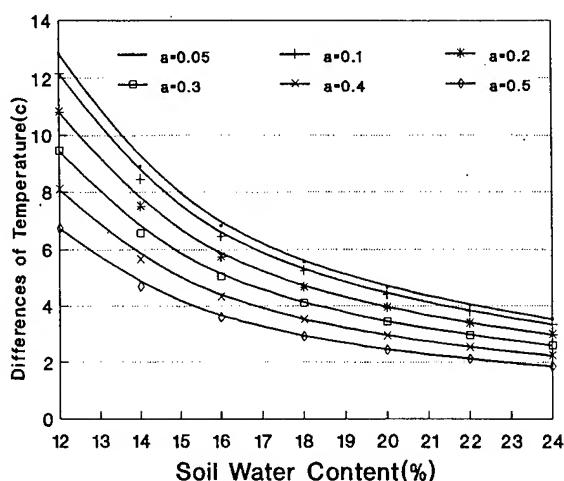


Fig.1 The relation between DOT and SWC.

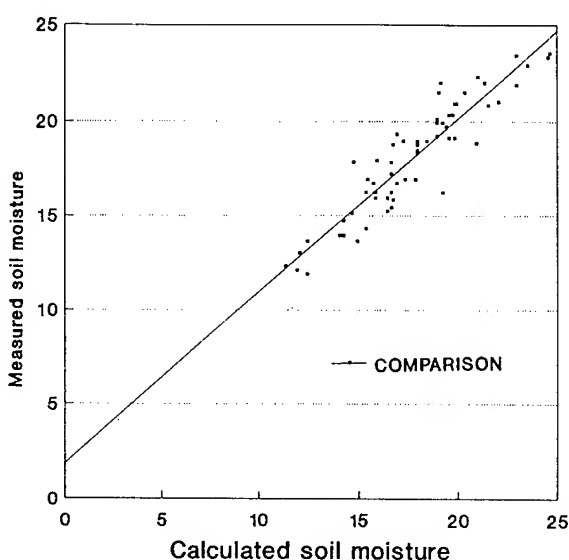


Fig.2 Correlation of calculations with measurements

REFERENCES

- [1] A. B. Kahle, "A simple thermal model of the earth's surface for geologic mapping by remote sensing", J. Geophys. Res., Vol. 82, pp.1673-1680,1977.
- [2] J.C. Price, "Thermal inertia mapping :a new view of the earth" J. Geophys. Res., Vol. 82, pp. 2582-2590,1977.
- [3] R.H. Zhang " A remote sensing thermal inertia model for soil moisture and its application", Chinese Science Bulletin, Vol.37: 4, pp.306-311, 1992.
- [4] X. Li and A.H. Strahler "Geometric-optical modeling of a coniferous forest canopy," IEEE Trans. Geosci.Remote Sensing, vol.GE-23,pp.207- 221,1985.
- [5] X. Li and Strahler " Geometric-optical bidirectional reflectance modelling of the discrete crown vegetation canopy: effect of crown shape and mutual shadowing. IEEE Trans. Geosci. Remote Sensing, vol.GE- 24,pp. 276-291,1992.

Retrieval of land surface temperature and water vapor content from AVHRR thermal imagery using an artificial neural network

Shunlin Liang (IEEE member)

Laboratory of Global Remote Sensing Studies
Department of Geography, University of Maryland,
College Park, MD 20742, USA
(301)-405-4556 (Phone), (301)-314-9299 (Fax)
sliang@geog.umd.edu

Abstract -- AVHRR thermal imagery is sensitive to both water vapor content (WVC) and land surface temperature (LST). A new algorithm based on MODTRAN simulations and neural network regression technique for estimating WVC and LST from the two AVHRR thermal channels is developed. The Navy climatological profiles and measured atmospheric profiles from TOGA COARE upper-air sounding archive were used to simulate AVHRR channels 4 and 5 radiances with different combinations of surface temperature, emissivity, viewing zenith angle. The simulated radiances were then converted to brightness temperatures. A feed-forward neural network was used to link those physical parameters with simulated brightness temperatures. This algorithm has been tested using measurements from BOREAS and HAPEX, and results indicate that this procedure performs reasonably well. The required improvements are also highlighted.

I. INTRODUCTION

There have been many techniques proposed and implemented for the retrieval of LST from remote observations. One common algorithm is the so-called split-window method, which has been used successfully for sea surface temperature retrievals. However, temperature derivation over land is more difficult than over the ocean because of the high spatial and temporal variability of surface emissivity and atmospheric water vapor.

The central part of most split-window algorithms is based on the assumption that the land surface temperature is linearly related to brightness temperature of two thermal channels. Recent studies show that nonlinear relation may improve the accuracy of land surface temperature retrieval [1]

[2]. In this study, an artificial neural network method is used to characterize this nonlinear relationship. A feed-forward neural network provides a flexible way to generalize linear regression functions. It can be seen as a way to parameterize a fairly general nonlinear function.

The basic procedure in this study consists of several steps: (1). atmospheric profiles are collected and the radiative transfer model is used to simulate radiance under different surface and atmospheric conditions; (2). a feed-forward neural network is used to link inputs and outputs; (3). the trained neural-network is then used for retrieving LST and WVC.

II. MODTRAN SIMULATION

Many earlier simulations were based on LOWTRAN. MODTRAN is the improved version of LOWTRAN. It provides the user with much higher accuracy although computation is a little more expensive. MODTRAN3.5 was used in this study.

Two major sources of atmospheric profiles were used. One is the Navy climatology model which contains monthly temperature and water vapor profiles in every 10° latitude zone. Since the total water vapor content in this dataset is not larger than 3.0 g/cm², the measured atmospheric profiles from the COGA-COARE (Tropical Ocean Atmosphere Coupled Ocean - Atmosphere Response Experiment) project [3] were also employed.

We varied the land surface temperature from $T_0 - 5$ to $T_0 + 20$ with increment of 5 °, where T_0 is the atmospheric temperature at the surface level, four viewing zenith angles: 10°, 25°, 40° and 55°,

and 48 emissivity combinations of channels 4 and 5 ranging from 0.9 to 1.0 with maximum two channel difference 0.02.

III. DATA ANALYSIS

The first step is to see how well the prediction is if we just use the following information: emissivities, viewing zenith angle and two brightness temperatures of channels 4 and 5. The results are presented in Fig. 1. Overall, the neural network approach did a pretty good job.

The next step is to see how the retrieval accuracy might improve by assuming we know WVC in the atmosphere. Fig. 2 illustrates the significant improvement, and the prediction errors are about 1° in most cases. We do notice some points that deviate the original temperature as large as 10° . It was found that those biggest errors are associated with high WVC (6.0 cm) and large difference between the land surface temperature and the air temperature.

If we do not input LST or air temperature, we can not predict water vapor content very accurately (Fig. 3) because of large variations in the atmospheric temperature profiles and combinations of air temperature and LST. It can be significantly improved only if we know both LST and air temperature (Fig. 4).

The neural network approach was compared with other split window algorithms using measurements from BOREAS and HAPEX. Those split window algorithms are believed best through a variety of testing [4]: Ulivieri et al. [5], Sobrino et al. [1], and Becker and Li [6]. Fig. 5 compares those algorithms using BOREAS ground measurements and we can see the neural network method performs not worse than other algorithms.

Although only a few points are available from HAPEX Fig. 6, the neural network algorithm performs the best. Ulivieri algorithm underestimates significantly. Both Sobrino (S1) and Becker-Li algorithms either underestimate or overestimate LST.

IV. CONCLUSION

It has been demonstrated that the neural network method is very promising. LST can be very reasonably retrieved, but water vapor content retrieval largely depends on our prior knowledge of LST and air temperature. In the current study, only limited atmospheric profiles were used, which are not representative for global applications. An extensive simulation is being carried out using four-dimensional assimilation data. Hopefully it can become an effective technique for retrieving LST and WVC operationally.

V. ACKNOWLEDGMENTS

The author likes to thank Dr. Kevin Czajkowski for providing BOREAS and HAPEX ground measurement data, and Drs. Sam Goward and Ralph Dubayah for helpful discussions.

VI. REFERENCES

- [1] J. A. Sobrino, V. Caselles and C. Coll, Theoretical split window algorithms for determining the actual surface temperature, *II Nuovo Cimento*, 16:219-236.
- [2] Liang S., S. Goward, J. Ranson, R. Dubayah, S. Kalluri, (1995), Retrieval of atmospheric water vapor and land surface temperature from AVHRR thermal imagery, *Proceedings of IGARSS'95*, 2:1959-1961.
- [3] Loehrer, S. M., T. A. Edmands, and J. A. Moore, (1996), TOGA COARE Upper-air sounding data archive: Development and quality control procedures, *Bulletin of the American Meteorological Society*, 77:2651-2671.
- [4] F. Becker, Z. L. Li, "Surface temperature and emissivity at various scales: Definition, measurement and related problems," *Remote Sensing Reviews*, vol. 12, pp. 225-253, 1995.
- [5] C., Ulivieri, M. M. Castronuovo, R. Francioni, and A. cardillo, "A split window algorithm for estimating land surface temperature from satellites, *Adv. Space Res.*, vol. 14, pp. 59 - 65, 1994.
- [6] F. Becker, and Z-L Li, "Towards a local split window method over land surface," *Int. J. Remote sens.*, vol. 3, pp. 369 - 393, 1990.

Fig.1 neural network, LST

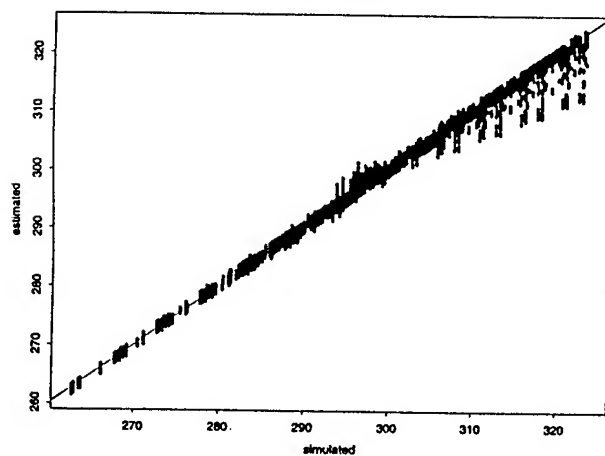


Fig. 2, neural network, LST given WVC

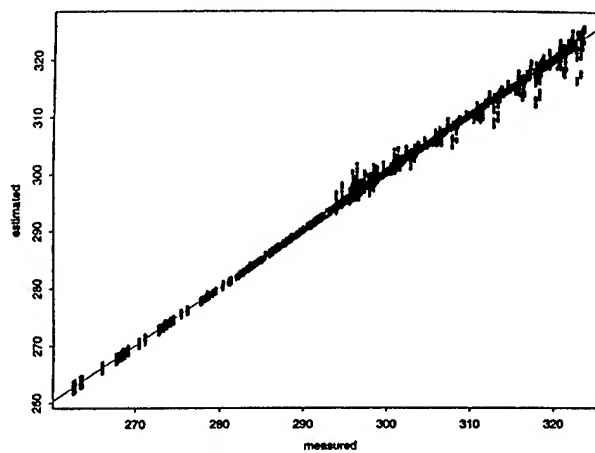


Fig.3, neural network, WVC

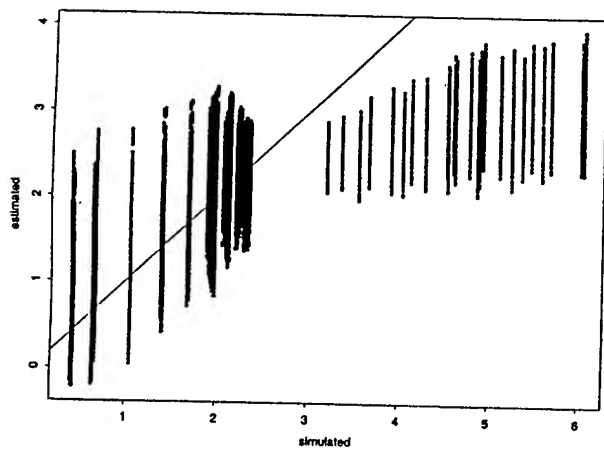


Fig. 4, neural network, WVC, given Ts & Ta

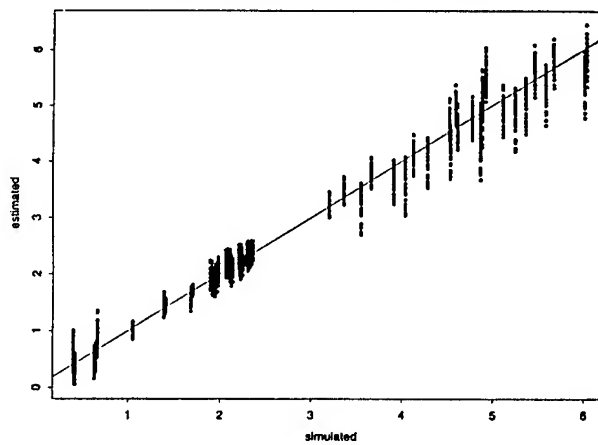


Fig 6, Comparison of neural network methods with split-window algorithms using HAPEX-Sahel data

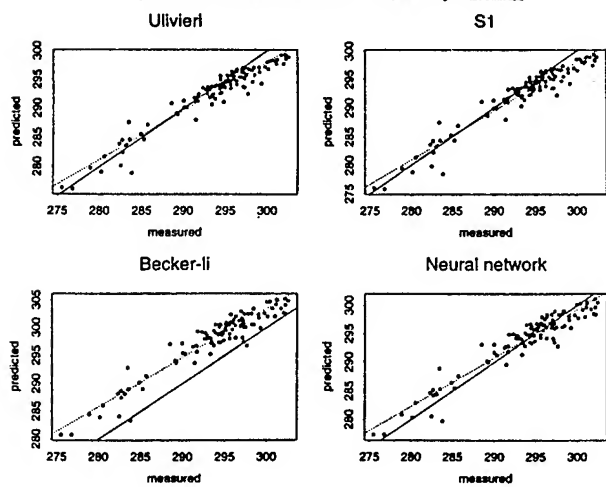
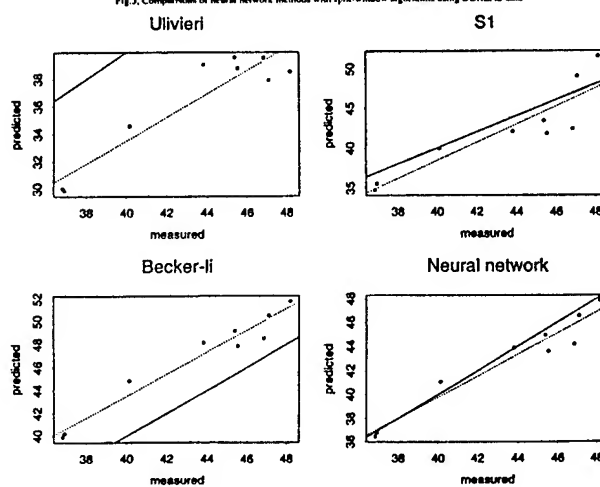


Fig.3, Comparison of neural network methods with split-window algorithms using BOREAS data



A Combined Temperature and Water Content Model for Bare Soil

Jan Kjellgren
Defence Research Establishment (FOA)
P.O. Box 1165
S-581 11 Linköping
Sweden
Tel: +46-13-318000, Fax: +46-13-318100
Email: jankje@lin.foa.se
Telex: 50073 FOATRE S

INTRODUCTION

We have developed a combined temperature and water content model for bare soil in one spatial dimension (depth) and time. The main purpose of the model is the study of the surface temperature variations due to a number of environmental parameters. In addition we also study the water content of the soil due to the great influence of evaporation. We characterize the soil by the thermodynamic and water tension properties. Experimental data have been used to support the model development.

MODEL DESCRIPTION

The core of the model is two coupled differential equations, one describing the temperature and the heat flow of the soil and one handling the water fraction and the soil water flow. The thermodynamic parameters of the heat flow depend on the water content. At the soil surface we model the heat exchange due to sun radiation, the thermal radiation exchange between the soil and the sky, the heat exchange due to air (and rain) convection and the exchange of sensible heat (mainly evaporation). We suppose no heat flow through the bottom surface. The main references when designing the model has been [1] and [2].

We simulate the temperature according to (1).

$$\rho_s[W]c_s[W]\frac{\partial T}{\partial t} = \frac{\partial}{\partial z}\left[k_T[W]\frac{\partial T}{\partial z}\right]; \quad (1)$$

with the boundary condition (2) at $z = 0$.

$$-k_T(W)\frac{\partial T}{\partial z} = \Phi_{sun} + \Phi_{therm} + \Phi_{conv} + \Phi_{lat}; \quad (2)$$

and the boundary condition (3) at $z = z_d$.

$$\frac{\partial T}{\partial z} = 0; \quad (3)$$

We simulate the water fraction according to (4).

$$\frac{\partial W}{\partial t} = -\frac{\partial}{\partial z}[Q_W]; \quad (4)$$

with

$$Q_W = k_W[W]\left\{\frac{\partial \psi[W]}{\partial z} + 1\right\}; \quad (5)$$

and with the boundary condition (6) at $z = 0$.

$$Q_W = Q_{rain} + Q_{lat}; \quad (6)$$

and the boundary condition (7) at $z = z_d$.

$$\Phi_W = 0; \quad (7)$$

We calculate the right hand terms of (2) according to (8).

$$\begin{cases} \Phi_{sun} = (1 - \alpha)I_{sun}; \\ \Phi_{therm} = \varepsilon(I_{sky} - \sigma T_0^4); \\ \Phi_{conv} = k_c[V](T_A - T_0) + Q_{rain}C_W(T_r - T_0); \\ \Phi_{lat} = k_c[V]k_{AW}\left(H_r e_A - e_s e^{-\frac{g\Psi M_W}{RT}}\right); \end{cases} \quad (8)$$

Symbols for variables and constants:

z	= depth below surface (m)
z_d	= depth of simulation (m)
t	= time (s)
T	= soil temperature (K)
k_T	= soil thermal conductivity ($\text{Wm}^{-1}\text{K}^{-1}$)
ρ_s	= density of soil ($\text{Jkg}^{-1}\text{K}^{-1}$)
c_s	= specific heat capacity of soil ($\text{Jkg}^{-1}\text{K}^{-1}$)
W	= soil moisture (% of volume)
k_W	= soil water conductivity (ms^{-1})
Ψ	= soil water pressure head (m)
Φ_{sun}	= absorbed sun radiation (Wm^{-2})
Φ_{therm}	= absorbed net thermal radiation (Wm^{-2})
Φ_{conv}	= absorbed convection heat (Wm^{-2})
Φ_{lat}	= absorbed latent heat (Wm^{-2})
Q_W	= soil water flow (ms^{-1})
Q_{lat}	= latent heat water flow (ms^{-1})
α	= soil albedo
ε	= soil emissivity
T_0	= soil surface temperature (K)
C_W	= volume heat capacity of water ($\text{Jm}^{-3}\text{K}^{-1}$)
T_r	= rain temperature, $\approx T_A$ (K)
σ	= Stefan-Boltzmann constant ($\text{W m}^{-2} \text{K}^{-4}$)
$k_c[V]$	= convection factor ($\text{W m}^{-2} \text{K}^{-1}$)
k_{AW}	= conversion constant (K Pa^{-1})
e_s	= saturation vapour pressure (Pa) at T_0
e_A	= saturation vapour pressure (Pa) at T_A
g	= earth acceleration (ms^{-2})
M_W	= molecular weight of water (kg mol^{-1})

R = gas constant ($\text{J mol}^{-1} \text{K}^{-1}$)
 Symbols for measured data files
 I_{sun} = total sun irradiance (W m^{-2})
 I_{sky} = thermal sky irradiance (W m^{-2})
 V = wind speed (m s^{-1})
 T_A = air temperature (K)
 Q_{rain} = rain intensity (ms^{-1})
 H_r = relative humidity

We use a discretised approximation of the depth dependance and use the internal discretisation of the program tool to solve for the time dimension, [3].

MODEL PARAMETER ESTIMATION

We roughly estimate the soil components clay, quartz and organic matter from the soil type and the dry volume weight. We calculate the specific heat and the density of the soil from the mixture of the components including the contents of water and air, c f. fig. 1. We have approximated the thermal conductivity separately for three soil types, sandy soil, clay soil and peat soil and prescribed a principal dependance upon water content, cf. [2, p 224]. We then approximate the thermal conductivity as a weighted mean. The procedure seems to give reasonable results, cf. fig. 2.

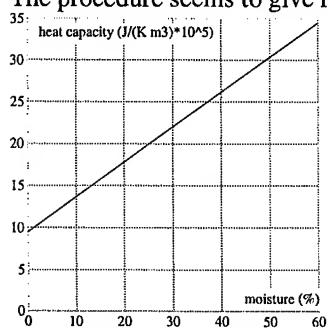


fig. 1 Soil heat capacity model as a function of soil moisture.

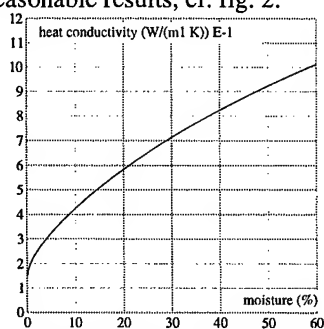


fig. 2 Soil heat conductivity model as a function of soil moisture

The reflection factor of the sun radiation (albedo) at the soil surface governs the heat absorption due to sun radiation.

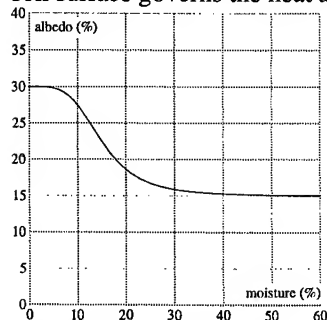


fig. 3 Model of albedo as a function of soil moisture.

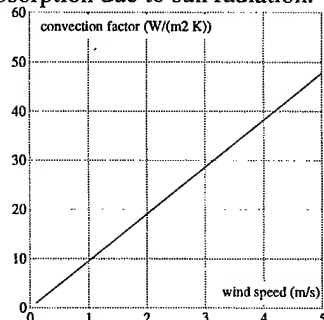


Fig. 4 Model of convection factor in neutral conditions as a function of wind speed.

The albedo normally depends on the water content, cf. [4]. We use a simple phenomenological approximation to model

the influence of the water content, cf. fig. 3.

For forced convection in neutral conditions we suppose a logarithmic increase of the wind speed with the height and calculate an aerodynamic resistance to heat, [2, p 118]. We estimate a roughness parameter from the mean height within the test area and the nearby surroundings, cf. [4, p 464] and [5, p 67]. We also estimate the zero velocity height plane, cf. [5, p 67]. We have used the settings 2 cm and 0.1 m for the roughness and the height plane respectively. For nonneutral conditions we adjust the convection factor regarding the buoyancy effect. We calculated the convection factor for temperature and wind speed measurements at different heights, 1.5 and 3 m respectively, cf. Fig. 4.

We have estimated the water retention properties of the soil by comparing the soil and its dry volume weight with the properties of measured soils in Sweden, cf. [7], and used the data from a similar soil (a clay soil), cf. [6, p 118, n:o 3] reproduced in fig. 5. We have estimated the soil water conductivity from the water retention curve supposing a capillary water flow, cf. [7, app. 1]. In these calculations we use an ad hoc setting of the tortuosity parameter. We then get an approximation of the soil water conductivity, cf. fig. 6.

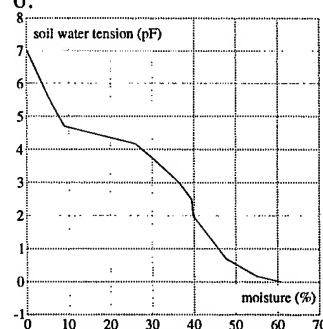


fig. 5 Model of soil water retention as a function of soil moisture.

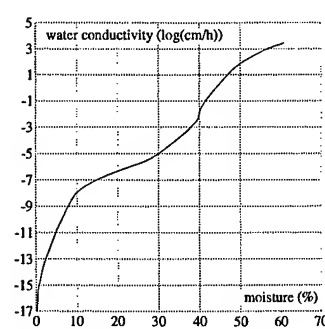


fig. 6 Model of soil water conductivity as a function of soil moisture

The soil is represented by a number of homogeneous layers (20-30) from the soil surface to a certain depth (60-70 cm). The thickness of the layers increases with very thin layers near the soil surface (<0.1 mm) and thick layers (≈ 5 -10 cm) at the bottom.

We estimated the initial values of the soil temperature and the soil moisture from the experimental observations of the soil temperature and bulk moisture. In addition we supposed an initial deep soil temperature (15°C).

ENVIRONMENTAL AND EXPERIMENTAL OBSERVATIONS

The experimental observations took place on August 27th to 29th 1991 during a period of slightly less than two days. We measured the environmental parameters sun and sky radiation, air temperature and humidity and wind speed using 3 min. time intervals. We also added rain intensity data using one hour intervals from a weather station, cf. fig. 7.

We also made isolated measurements of soil moisture, dry volume weight and surface height profile.

During the experimental observations we measured the soil temperature at three different depths below the surface (2, 5 and 15 cm). In addition we also measured the thermal radiation from the soil surface within two IR-bands (3-5 μm and 8-12 μm) and calculated a calibrated surface temperature, [9]. At the beginning of the simulation period the soil volume moisture was about 22%. A rain fall between 01⁰⁰ and 15⁰⁰ during day 2 increased the soil volume moisture to 33% measured at 10 hour.

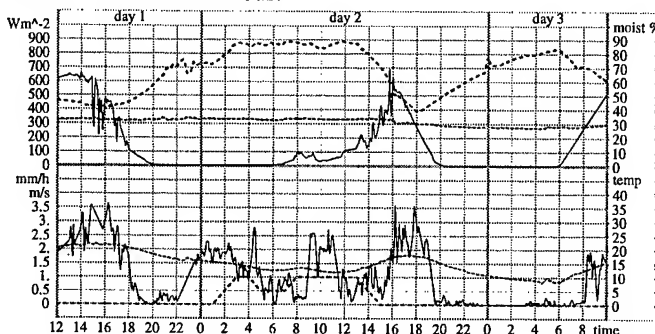


fig. 7 Measured data for the simulation period. The upper diagram shows total sun radiation (line), sky radiation (dotted line) and relative air humidity (thick dotted line). The lower one shows wind speed (line), air temperature radiation (dotted line) and rain intensity (thick dotted line).

SIMULATION AND EXPERIMENTAL OBSERVATIONS

From the simulation we separately present the emitted heat flux from the surface by evaporation, convection and thermal radiation ($-\Phi_L$, $-\Phi_C$, $-\Phi_T$). We notice the change from convection to evaporation as the dominant daytime term between the 1st and the 2nd day due to the corresponding change of the soil moisture, cf. fig. 8. We also notice the absence of convection and evaporation during the night between the 2nd and the 3rd day caused by the stable atmospheric conditions.

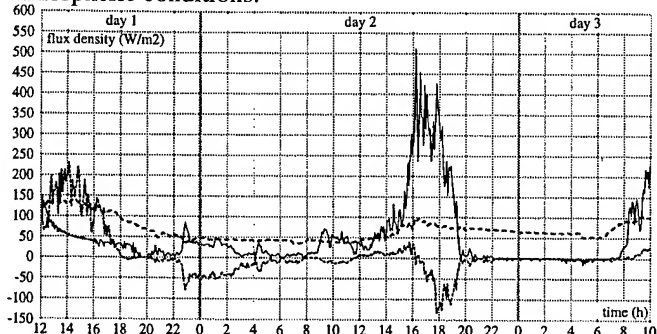


fig. 8 Simulation of the heat flux from the soil through evaporation (thin line), convection (thin dotted line) and thermal radiation (thick more dotted line).

The simulated soil moisture shows a steep gradient near the surface for evaporation periods with low soil moisture

conditions, cf. fig. 9. Around 18³⁰ in the evening of day 1 it became calm and the evaporation drops and the soil moisture near the surface starts to increase until the wind starts again around 22. Then the moisture drops and the gradient increases near the surface until the beginning of the rain. Integration of the simulated soil moisture for the upper 5 cm at 10 a'clock day 2 gives a value in reasonable correspondance with the measurement (33 %). After the rain, at 16 day 2 the simulated moisture of uppermost parts of the soil has increased to around 37 %. The simulated water conductivity of the soil has thereby increased significantly and the following large evaporation flux between 16 to 19 does not cause a steep soil moisture gradient at the surface.

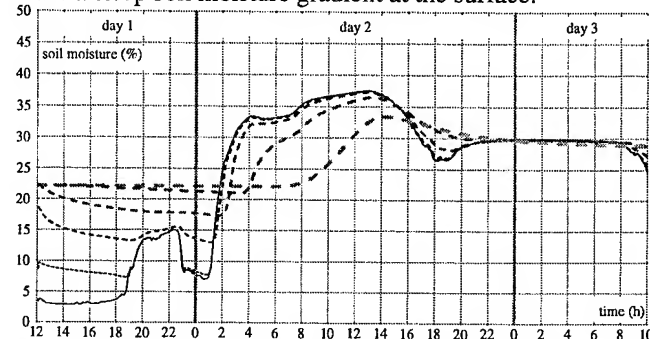


fig. 9 Simulation of soil moisture at the depths 20 (thin line) and 67 μm (thin dotted line) and at 1, 5, 10 and 50 mm (successively more dotted, thicker and grayer lines).

We compare the simulated surface temperature with the calibrated IR-measured temperatures. The RMS-difference between the simulated surface layer temperature and any of the measured surface temperatures was about 1° K. The measured temperatures also show an RMS-difference between each other of about 1° K. We notice an increased uncertainty during periods of strong solar radiation (12-16 day 1, 16-19 day 2, 8-10 day 3) and during stable atmospheric conditions (20 day 2 - 08 day 3).

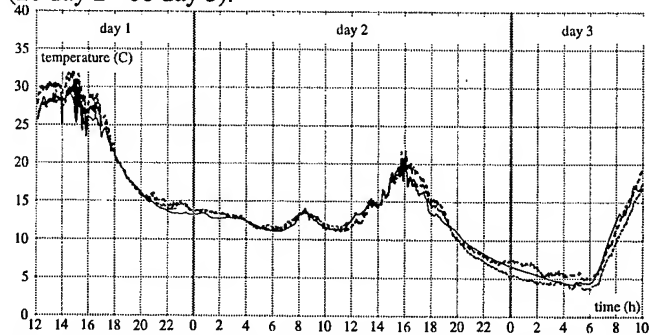


fig. 10 Simulation (line) and IR-measurements at 3-5 (thick dotted line) and 8-12 μm (dotted line) of the surface temperature.

We present the simulated soil temperature as a function of depth at four different times and compare them with piecewise linear functions related to the measured subsurface temperatures and the IR-measurements at 8-12 μm for the

surface temperature. The measured temperatures end at the depth of 15 cm. We notice the small variations for depths below 20 cm.

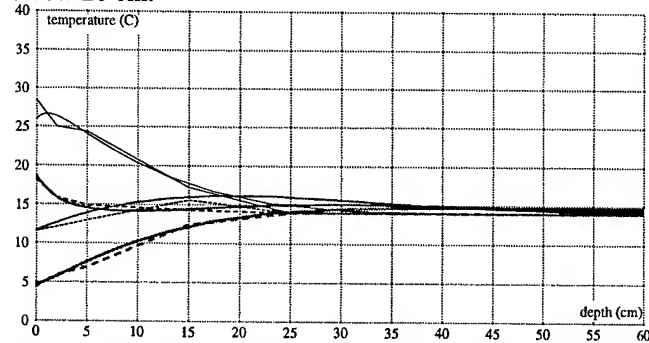


fig. 11 Simulated (curved lines) and measured (piecewise linear dotted lines) soil temperature depth profiles at the times day 1 hour 15, day 2 hours 5 and 15, day 3 hour 5 (successively thicker lines).

DISCUSSION

The modelling exercises indicate the need for more complete soil measurements and analysis to achieve a more accurate parameter estimation. We also need more complete measurements of the meteorological and aerodynamic conditions, especially in inhomogeneous areas. Within the model we have supposed only a liquid phase of the soil water flow neglecting the vapor phase. This will affect the result especially for low soil moisture conditions. In addition we also apply extremely thin plane surface layers in the model with no clear physical correspondance to the real more rough surfaces.

ACKNOWLEDGMENT

The collection of measurements and the calibration needed were carried through within the project 'IRmm - Models and model verification for the IR and mm-wavelength region', commissioned by the Swedish Program of Information Technology. Financial support has also been received from the Swedish Materiel Administration of the Armed Forces (FMV:RobotT). The efforts by Mr Hans Pettersson (FOA), Dr Lars Peterson and Dr Sune Axelsson (Saab Dynamics) are especially acknowledged. Informative communications with Prof. Per-Erik Jansson and Mrs Gunnel Alvenäs (Swedish University of Agricultural Sciences) are also acknowledged.

REFERENCES

- [1] P.-E. Jansson, "Simulation Model for Soil Water and Heat Conditions," Swedish University of Agricultural Sciences, Department of Soil Sciences, Division of Agricultural Hydrotechnics, Uppsala 165, 1991.
- [2] J. L. Monteith and M. H. Unsworth, *Principles of Environmental Physics*, 2 ed. London New York Melbourne Auckland: Edward Arnold, 1990.
- [3] S. Wolfram, *Mathematica*, 2.2.2 ed. Champaign: Wolfram Research Inc., 1991.
- [4] E. A. Glaser and C. H. M. V. Bavel, "The Effect of Soil Moisture upon Albedo," *Agricultural Meteorology*, vol. 27, pp. 17-26, 1982.
- [5] D. W. Hooch and R. A. Sutherland, "Obscuration Countermeasures," in *Countermeasure Systems*, vol. 7, *The Infrared and Electro-Optical Systems Handbook*, D. H. Pollock, Ed. Ann Arbor, Bellingham: Environmental Research Institute of Michigan, SPIE Optical Engineering Press, 1993, pp. 359-493.
- [6] J. O. Mattson, *Introduktion till Mikro- och Lokalklimatologi*. Malmö: LiberLäromedel, 1979.
- [7] S. Andersson and P. Wiklert, "Markfysikaliska Undersökningar i Odlad Jord: Om de Vattenhållande Egenskaperna i Odlad Jord," Swedish University of Agricultural Sciences, Department of Soil Sciences, Uppsala XXIII, 1972.
- [8] R. H. Brooks and A. T. Carey, "Hydraulic Properties of Porous Media," Colorado State University, Fort Collins Hydrology Papers 3, 1964.
- [9] H. Pettersson and L. Peterson, "Measurements of Natural Backgrounds in the Thermal IR Bands," National Defence Research Establishment (FOA), Linköping FOA Report A 30065-3.1, 1992.

The Use of Vegetation Indices in Forested Regions: Issues of Linearity and Saturation

Alfredo R. Huete, HuiQing Liu, Wim J.D. van Leeuwen

University of Arizona, 429 Shantz Bldg.#38, Tucson, AZ 85721, USA

Tel.: (1) 520 621 3228; fax: (1) 520 621 5401; ahuete@ag.arizona.edu

Abstract -- Numerous problems and difficulties have been reported with the use of vegetation indices in high biomass, forested regions. In this study we analyzed Landsat-5 Thematic Mapper (TM) scenes from various temperate and tropical forested biomes, representing needleleaf and broadleaf canopy structures in the Pacific Northwest (Oregon), Eastern U.S. (Harvard Forest), southern Chile, the Amazon, and Central America. The TM scenes were atmospherically corrected and reduced to MODIS surface reflectance data at 250 m pixel sizes. Various vegetation indices (VIs) were then computed including the normalized difference vegetation index (NDVI), simple ratio, soil-adjusted vegetation index (SAVI), enhanced vegetation index (EVI), and green vegetation index (GVI). The NDVI was also tested utilizing the green and middle-infrared (MIR) bands. All of the NDVIs were non-linear and were fairly saturated across the forested biomes. In contrast, the remaining indices remained sensitive to canopy structure variations over all of the forested biomes with minimal saturation problems. The high 'penetrating' capability of the near-infrared band through forested canopies was the dominant factor in vegetation index sensitivity and performance. We found that indices with higher weighting coefficients in the "near-infrared" to be the best approach in extending vegetation index performance over forested and dense vegetated canopies.

INTRODUCTION

The normalized difference vegetation index (NDVI), a non-linear transform of the near-infrared to red reflectance ratio, was developed to enhance the vegetation signal in low biomass conditions. Unfortunately, this enhancement is achieved at the expense of reduced sensitivity at the upper, or high biomass range of conditions. As a result, the NDVI often "saturates" in high biomass areas such as in forested biomes. Saturation occurs when the NDVI no longer responds to variations in green biomass. Changes in land use, land cover, biophysical vegetation parameters, and net primary production are difficult to detect in a 'saturated' mode. Studies have shown the NDVI to exhibit very little variation over canopies with low red reflectances (0.02 to 0.05) despite NIR reflectances which varied by over a factor of two [1].

This problem has been partially attributed to the highly-sensitive, chlorophyll-absorbing, "red" waveband, which saturates quickly with forest canopy closure. Several approaches have been proposed to improve upon the

performance of vegetation indices (VI) and achieve greater sensitivity in high biomass situations. These include use of the "green" band instead of the "red" band in the NDVI equation; (2) use of the "middle infrared" band for the "red" band in the vegetation index equation; and (3) use of more linear vegetation indices such as the Green Vegetation Index (GVI).

Gitelson [2] found a 'green' based NDVI to have a wider dynamic range and be five times more sensitive to chlorophyll-a concentration than the standard NDVI, since the green waveband remains sensitive to chlorophyll-a over a wider range of concentrations. This is of particular interest to the Moderate Resolution Imaging Spectroradiometer (MODIS) sensor, which has a narrower, more chlorophyll-sensitive red band (620 - 670 nm) relative to that of the broader-band, NOAA-AVHRR (550 - 680 nm).

Others have utilized Landsat TM bands 5 (1.55 - 1.75 μm) and 7 (2.08 - 2.35 μm) for discrimination of land cover types as well as variations in canopy structure in high biomass forest/grassland conditions. Red band imagery has been shown to saturate over Brazilian tropical forests which contained both primary and secondary forests in initial through advanced stages of regrowth. [3] In this study, we investigate vegetation index sensitivity in high biomass, forested canopies. The objectives of this analysis were: (1) to determine if vegetation index saturation is inherent to all, and (2) to determine if the 'green' and 'MIR' bands can be used to increase sensitivity over dense canopies.

METHODS AND STUDY SITES

We include forests with both broadleaf and needleleaf structures and evergreen and deciduous phenologies. In this paper we present the results obtained over two rainforests, a temperate evergreen broadleaf forest in southern Chile and a tropical evergreen broadleaf forest near Manaus, Brazil.

The TM images were first converted to 250m imagery using a fourier transform based, TM to MODIS program. The 250m images were calibrated with updated, vicarious-based calibration factors and then atmospherically corrected by use of an atmospheric radiative transfer code based on dark objects. The following vegetation indices were then calculated:

$$\text{NDVI} = (\rho_{\text{NIR}} - \rho_{\text{red}}) / (\rho_{\text{NIR}} + \rho_{\text{red}}), \quad (1)$$

$$\text{NDVI}_{\text{green}} = (\rho_{\text{NIR}} - \rho_{\text{green}}) / (\rho_{\text{NIR}} + \rho_{\text{green}}), \quad (2)$$

$$\text{NDVI}_{\text{MIR}} = (\rho_{\text{NIR}} - \rho_{\text{MIR}}) / (\rho_{\text{NIR}} + \rho_{\text{MIR}}), \quad (3)$$

$$SAVI = (1 + L) (p_{nir} - p_{red}) / (p_{nir} + p_{red} + L), \quad (4)$$

$$EVI = 2.5 (p_{nir} - p_{red}) / (1 + p_{nir} + 6 p_{red} - 7.5 p_{blue}) \quad (5)$$

$$GVI (6 \text{ band}) = -0.214 * p_{TM1} - 0.254 * p_{TM2} - 0.414 * p_{TM3} \\ + 0.812 * p_{TM4} + 0.046 * p_{TM5} - 0.239 * p_{TM7} \quad (6)$$

$$GVI (4 \text{ band}) = -0.5 * p_{TM3} + 0.806 * p_{TM4} - 0.02 * p_{TM5} \\ - 0.316 * p_{TM7} \quad (7)$$

The linear-based, GVI coefficients were derived with the use of an 'n-space' program [4].

RESULTS

Fig. 1 shows that there was very little variation in the red reflectance values over the forests of Chile (Fig. 1a) and Brazil (Fig. 1b). Yet there is considerable variation in the NIR reflectance values, associated with canopy structural conditions due to differences in forest species, regeneration stage, and LAI. There is also only slight variations in green reflectance values and slightly more variable middle-infrared reflectances, despite NIR variations from 0.10 to 0.40 (Fig. 1). This indicated that the use of the green and MIR bands would not result in significant sensitivity differences in the NDVI over these forests. Fig. 2 shows the resulting VI behavior over these forests. The NDVI was nearly saturated over both of the forests, including with the use of the green and MIR based, NDVI equations. The green band lowered the NDVI values slightly, while the MIR band raised them slightly. Thus, these additional bands did not result in a more sensitive NDVI equation. In contrast the SAVI and EVI remained sensitive to the variations in NIR reflectances. Similarly, the GVI equations also did not saturate and maintain sensitivity over these dense forests. This is seen in a crossplot of the GVI equations with the SAVI (Fig. 3). There was very little difference between the 6 - band and 4 - band GVI equations. Fig. 4 shows the ratio itself (NIR/red), remained sensitive to variations in the canopy, although with such low red reflectance values, the ratio was somewhat unstable with much scatter.

CONCLUSION

The structure of the NDVI equation, which is a non-linear transform of the simple ratio (NIR/red), was found to be the major cause for non-linearity and saturation in high biomass situations. As a result of the non-linear nature of the NDVI equation, the substitution of the "green" or "MIR" channels for the "red" had only slight but minimal improvements on NDVI sensitivity. The simple ratio, which is insensitive at low amounts of vegetation was found to remain sensitive to high biomass conditions without saturation. The ratio showed that there is still a significant "vegetation" signal present over dense forests. The GVI, EVI, and SAVI reduced the saturation problem considerably, remaining sensitive to

canopy variations over high biomass conditions. The high 'penetrating' capability of the near-infrared band through forested canopies was the dominant factor in vegetation index sensitivity and performance.

DISCUSSION

Although linear combination indices and other indices which are not "ratios" of wavebands performed better than the NDVI and NIR/red ratio indices, they would be more prone to noise associated with external factors such as calibration, cloud shadow, and topography than the ratio-based indices. However, in an era where atmospheric corrections and BRDF adjustments have progressed significantly, it is questionable whether we should still be relying on ratioing as a way to standardize data sets for routine, operational use.

ACKNOWLEDGMENTS

This work is supported by NASA/MODIS Contract No. NAS5-31364.

REFERENCES

- [1] Huete, A.R., Liu, H.Q., Batchily, K., van Leeuwen, W.J.D., 1997. A comparison of vegetation indices over a global set of TM images for EOS-MODIS. *Remote Sens. Environ.* 59:440-451.
- [2] Gitelson, A.A., Kaufman, Y.-J., Merzlyak, M.N., 1997. Use of a green channel in remote sensing of global vegetation from EOS-MODIS. *Remote Sens. Environ.* 58:289-298.
- [3] Moran, E.F., Brondizio, E., Mausel, P., Wu, Y., 1994. Integrating Amazonian vegetation, land-use, and satellite data. *BioScience* 44:329-338.
- [4] Jackson, R.D., 1983. Spectral indices in n-space. *Remote Sens. Environ.* 13:409-421.

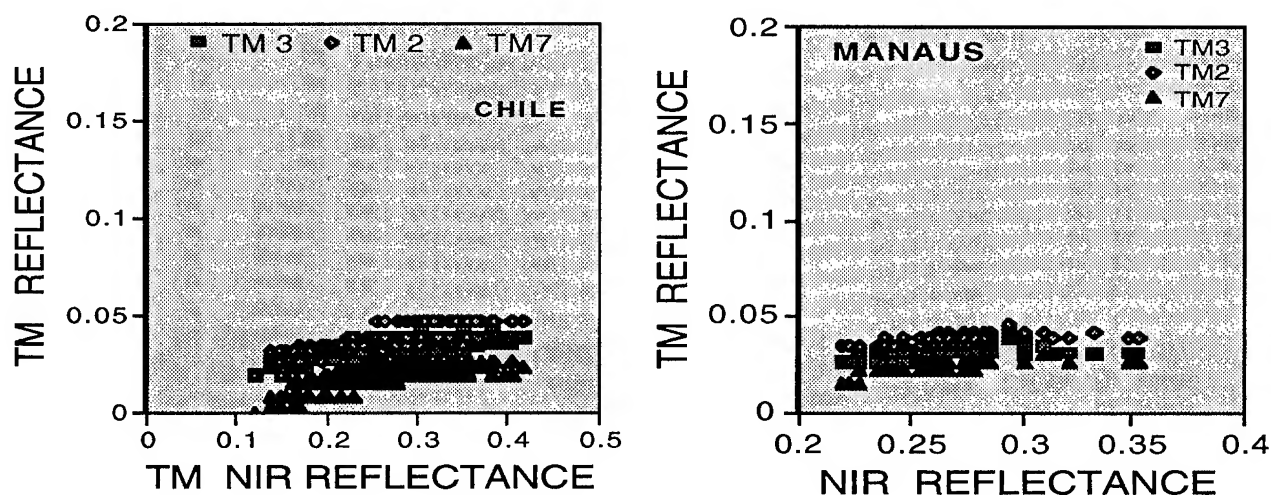


Fig. 1 Crossplots of green (TM2), red (TM3), and MIR (TM7) reflectances against NIR (TM4) reflectances for the (a) Chile forest and (b) Manaus forest.

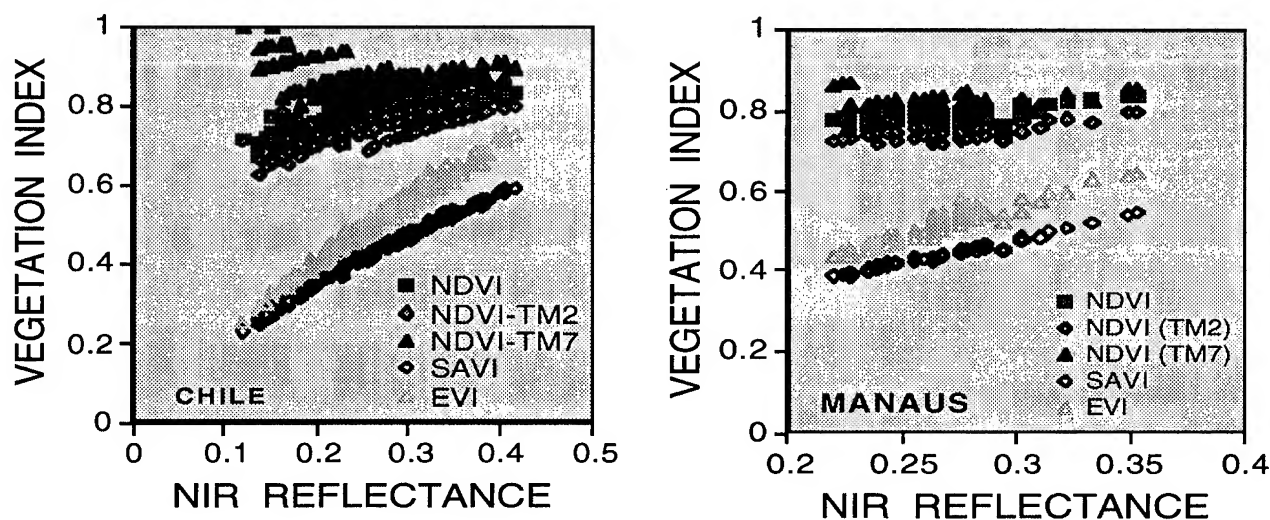


Fig. 2 Vegetation index behavior with NIR reflectance variations for (a) Chile and (b) Manaus.

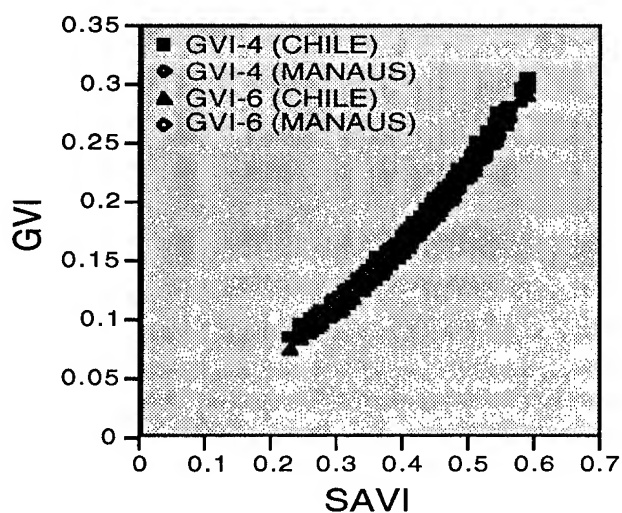


Fig. 3 4- and 6-band GVI equations plotted with the SAVI for Manaus and Chile.

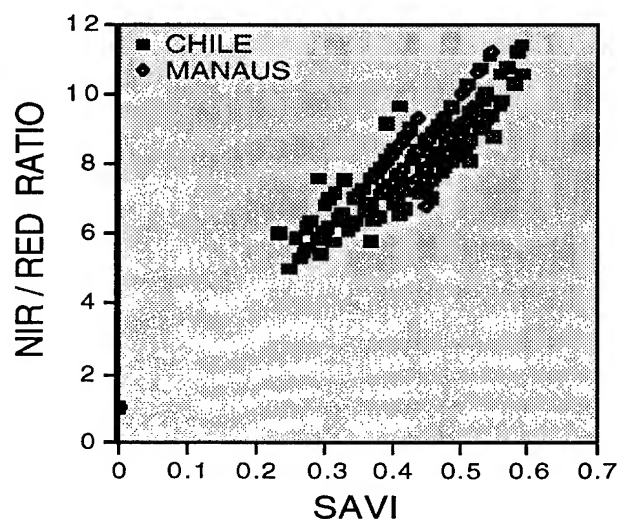


Fig. 4 NIR/red reflectance ratio plotted with the SAVI for Manaus and Chile.

Simultaneous Measurements of Water Vapor Profiles From Airborne MIR and LASE

J. R. Wang, P. Racette, and M. E. Triesky

Laboratory for Hydrospheric Processes

NASA Goddard Space Flight Center, Greenbelt, MD 20771, U. S. A.

Tel: 301-286-8949/FAX: 301-286-1762/e-mail: wang@sensor.gsfc.nasa.gov

E. V. Browell and S. Ismail

Atmospheric Sciences Division

NASA Langley Research Center, Hampton, VA 23681, U. S. A.

L. A. Chang

Futuretech Corporation, 14232 Masterpiece Lane, Gaithersburg, MD 20878, U. S. A.

ABSTRACT

A NASA ER-2 aircraft flight with both Millimeter-wave Imaging radiometer (MIR) and Lidar Atmospheric Sensing Experiment (LASE) was made over ocean areas in the eastern United States on September 25, 1995. The water vapor profiles derived from both instruments under both clear and cloudy conditions are compared in this paper. It is shown that good agreement is found between the MIR-derived and the LASE-measured water vapor profiles over the areas of clear-sky condition. In the cloudy areas, the MIR-retrieved values at the altitudes of the cloud layers and below are generally higher than those measured by the LASE.

INTRODUCTION

During September 9-26, 1996, a number of NASA ER-2 aircraft flights were conducted both over land and ocean surfaces in the eastern United States for the LASE validation experiment. LASE can provide measurements of high-precision water vapor profiles as well as profiles of scattering ratio that can be used to derive parameters associated with aerosols and cirrus clouds. On board the same aircraft is another instrument, MIR, that is capable of measuring atmospheric water vapor profiles under both clear and cloudy conditions [1-2]. Previously, the MIR-retrieved water vapor profiles could only be compared with those measured by the Raman lidar system and radiosondes at fixed times and locations. The simultaneous measurements of LASE and MIR on board the same aircraft provide the means of validating MIR-retrieved water vapor profiles over extended time and space.

MIR is a total-power cross-track scanning radiometer that measures millimeter-wave radiation at 9 frequency channels of 89, 150, 183.3 ± 1 , 183.3 ± 3 , 183.3 ± 7 , 220, 325 ± 1 , 325 ± 3 , and 325 ± 8 GHz [4]. It has a frequency-independent beamwidth of 3.5 degrees and provides brightness temperature images with an angular swath of 100 degrees

centered at nadir. The temperature sensitivities for the six low-frequency channels are ≤ 1 K based on a 70-msec integration time, while those for the three 325 GHz channels are on the order of 7-8 K. The measurements from the three high-frequency channels are not used in the present study.

MEASUREMENTS

The data presented below were acquired from the flight on September 25, 1995. Figure 1 shows the results from a 20-minute segment of the LASE measurements, expressed in gray scale; the top panel gives the aerosol backscatter and

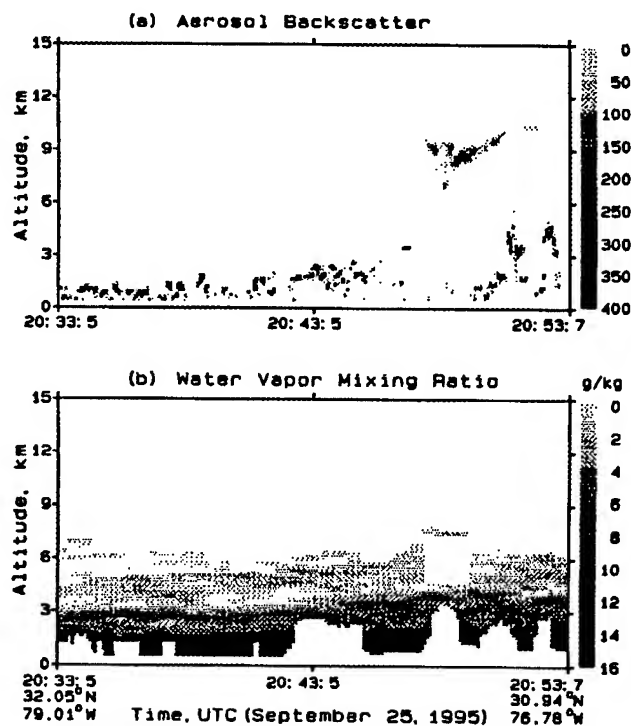


Figure 1. Profiles from the LASE measurements: (a) aerosol backscatter and (b) water vapor mixing ratio.

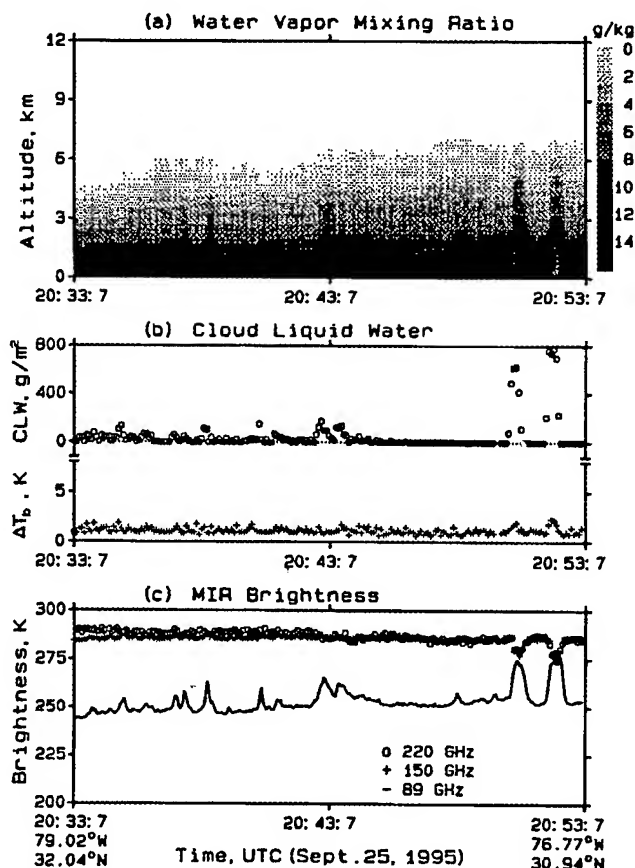


Figure 2. Results of MIR measurements: (a) profiles of water vapor mixing ratio, (b) estimated cloud liquid water and rms values of the retrievals, and (c) brightness temperature variations.

the bottom panel, the profiles of water vapor mixing ratio in g/kg. From the top panel we find that, between the period of 2033-2045 UTC, LASE sees aerosols or low-level clouds at altitudes below 3 km. Around 2048-2050 UTC, cirrus clouds are present between the altitudes of 8-10 km. After 2050 UTC there are two patches of clouds with cloud top of ~ 5 km. The profiles of mixing ratio in the bottom panel show a fine vertical resolution characteristic of lidar measurements [3]. However, for several areas where there are optically thick clouds or aerosols, the LASE measurements of water vapor are not effective in or below the cloud layers.

The corresponding profiles of water vapor mixing ratio retrieved from the MIR measurements are shown in Figure 2a. The plot shows that MIR measurements are capable of providing water vapor profiles under both clear and cloudy conditions. Figure 2b in the middle panel gives the cloud liquid water required in the retrieval process, and the parameter ΔT_b , which is the root-mean-square of the differences between the measured brightness temperatures

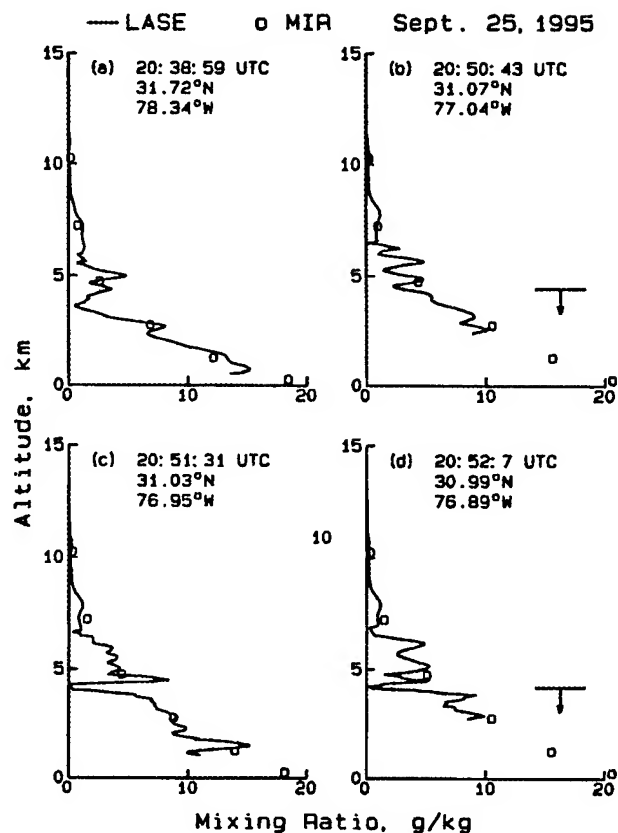


Figure 3. A comparison of water vapor profiles measured by MIR and LASE at four different times. Plots (a) and (c) are for clear condition, and plots (b) and (d), for cloudy conditions.

(T_b) and those calculated for all six channels from the final retrieved water vapor profile. ΔT_b indicates the condition of the retrieval; the retrieval is considered convergent and satisfactory when ΔT_b is ≤ 1 K. Figure 2c shows the T_b variations for the three window channels at 89, 150 and 220 GHz. T_b 's at 89 GHz are lower because of the partially transparent atmosphere and the low emissivity of the ocean surface. It is evident that this channel is also particularly sensitive to low-level clouds over the ocean surface.

COMPARISON OF LASE AND MIR RESULTS

Figure 3 gives a comparison of the mixing ratio profiles derived from LASE and MIR at four different times; LASE profiles are given by solid curves, while those of MIR, by open circles. Plots (a) and (c) are results under clear-sky condition and plots (b) and (d), cloudy condition. The horizontal bars and arrows in plots (b) and (d) indicate the heights of the cloud tops. The LASE measurements show the ability to capture the fine features of mixing ratio profiles. The MIR results generally give smooth profiles that are in good agreement with those of LASE. Under cloudy

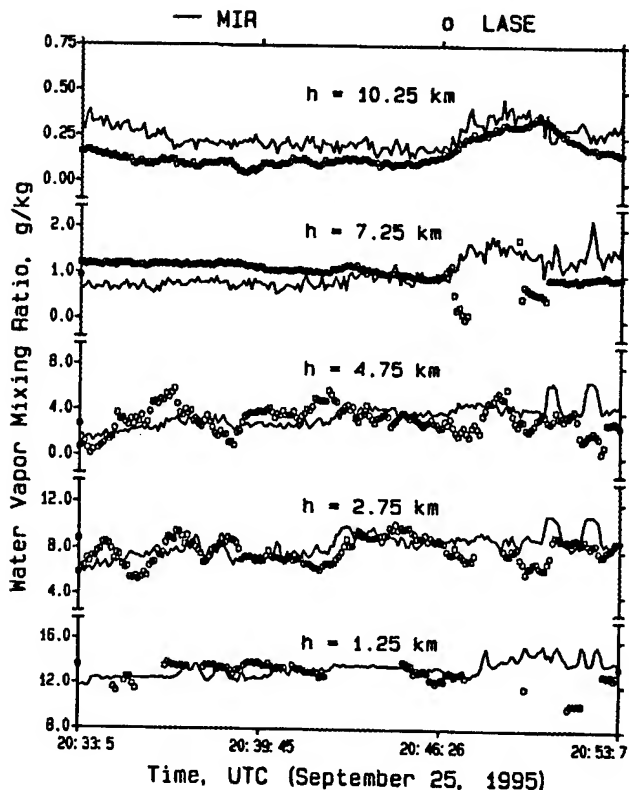


Figure 4. A comparison of LASE- and MIR-measured mixing ratios at five different altitudes.

conditions, LASE could not provide measurements like MIR, as shown in plots (b) and (d).

Figure 4 shows a comparison between LASE and MIR results at five different altitudes for the entire 20-minute interval displayed in Figure 2. At times after 2047 UTC the measurements are over areas covered with optically thick clouds and the LASE results are not reliable. Prior to 2047 UTC the measured mixing ratios from both instruments at three low altitudes of 1.25, 2.75, and 4.75 km appear to agree quite well. The MIR-retrieved values are generally smaller than those of LASE at 7.25 km altitude, and larger than those of LASE at 10.25 km. One of the reasons for this discrepancy could be due to the use of the model simulated temperature profiles, provided by the European Center for Medium-range Weather Forecast, in the retrieval process. The sensitivity of the temperature profile on the retrieval needs to be analyzed further.

CONCLUSION

Concurrent measurements of water vapor profiles over ocean surface were made by LASE and MIR on September 25, 1995. A very good agreement was found between the water vapor profiles measured by the two sensors. LASE is capable of providing profiles with a fine vertical resolution,

but faces difficulty in the areas covered by optically thick clouds. The MIR-retrieved profiles show a poor vertical resolution, but can be obtained in both clear and cloudy conditions. The measurements from these sensors are complementary to each other.

REFERENCES

- [1] J. R. Wang, S. H. Melfi, P. Racette, D. N. Whiteman, L. A. Chang, R. A. Ferrare, K. D. Evans, and F. J. Schmidlin, "Simultaneous measurements of atmospheric water vapor with MIR, Raman lidar, and rawinsondes," *J. Appl. Meteor.*, **34**(7), 1595-1607, 1995.
- [2] J. R. Wang, J. D. Spinhirne, P. Racette, L. A. Chang, and W. Hart, "The effects of clouds on water vapor profiling from the millimeter-wave radiometric measurements," *J. Appl. Meteor.*, in press, 1997.
- [3] D. N. Whiteman, S. H. Melfi, and R. A. Ferrare, "Raman lidar system for the measurements of water vapor and aerosols in the earth's atmosphere," *Appl. Opt.*, **31**(16), 3068-3082, 1992.
- [4] P. Racette, R. F. Adler, J. R. Wang, A. J. Gasiewski, D. M. Jackson, and D. Zacharias, "A millimeter-wave imaging radiometer for cloud, precipitation, and atmospheric water vapor studies," *J. Atmos. Ocean. Tech.*, **13**(3), 610-619, 1997.

Comparisons of Volume-Imaging Radar Observations of Atmospheric Boundary Layer Turbulence with Large Eddy Simulations

Brian D. Pollard, Stephen J. Frasier, Robert E. McIntosh

Microwave Remote Sensing Laboratory

University of Massachusetts, Amherst, MA 01003

Tel: 413.545.4492 Fax: 413.545.3690 email: pollard@alex.ecs.umass.edu

Abstract – The Turbulent Eddy Profiler (TEP) is a volume-imaging 915 MHz radar designed for atmospheric boundary-layer turbulence studies. The TEP system is a pulsed, phased-array radar that uses digital beamforming techniques in order to provide four-dimensional images of C_n^2 fluctuations and wind vectors on grid scales comparable to those of large-eddy simulations (LES).

In this paper we present results from an August 1996 deployment of TEP, including preliminary comparisons of TEP data and LES results. Vertical profiles of C_n^2 fluctuations are presented for a highly convective boundary layer. Those results are compared to published data simulated with LES from similar conditions. The measured variability of C_n^2 agrees well in the high signal-to-noise regions of the TEP data.

INTRODUCTION

In the recent history of the study of the atmospheric boundary layer (ABL), the continuously turbulent layer in contact with the earth's surface, the development of the successful direct-numerical simulation (DNS) and large-eddy simulation (LES) methods has made the field of atmospheric turbulence simulation highly accessible. An outstanding question in using DNS and LES, however, is how well they compare with experimental atmospheric data [1]. Established tools for probing the ABL such as wind profilers [2], sodars [3], and FM-CW radars [4] provide one-dimensional, vertical profiles of atmospheric structure, but the three-dimensional, time-varying fields produced by DNS and LES require three-dimensional experimental verification.

Volume-imaging lidars such as the one described in [5] are one method of providing three-dimensional atmospheric measurements. They provide velocity vector measurements over large volumes ($\sim 100\text{km}^3$), but are limited to relatively low pulse repetition rates (30 Hz) that result in scan times on the order of minutes. Lidars also scatter from aerosols rather than index of refraction irregularities, so that they are not capable of measuring the index of refraction structure function parameter C_n^2 in the ABL.

In order to provide high-resolution studies of C_n^2 and wind vector fields in the ABL, we have designed and

This work was supported by the US Army Research Office under Contract DAAL03-92-G-0110.

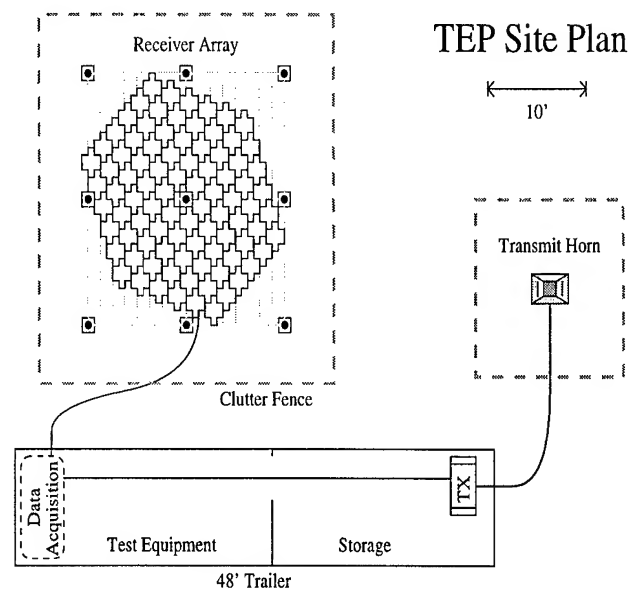


Fig. 1. TEP site plan.

developed the Turbulent Eddy Profiler (TEP) [6], [7]. TEP is a volume-imaging, 915 MHz radar with spatial and temporal resolution comparable to LES. This paper presents results from an August 1996 deployment, including structure-function parameter comparisons between TEP and LES data.

SYSTEM DESCRIPTION

The TEP system employs digital beamforming techniques to image a 25° cone above the array, from 200 m to 1500 m in altitude. The 90 element receiver array of microstrip patch antennas yields a focused beamwidth of 3.5° ; the focused beamwidth and the 30 m range resolution yield pixels of $30 \times 30 \times 30\text{m}^3$ at an altitude of approximately 500 m. With the full, 90 element array, approximately 50 beams can be formed in the 25° field of view, yielding a total of approximately 2100 volumetric pixels.

Figure 1 shows a site plan for TEP. A 25 kW peak-power transmitter feeds a corrugated horn antenna. Each antenna in the receive array has a separate microwave receiver, producing coherently averaged I and Q data. The data from each receiver is sent to a group of computers located in the 48' operations trailer, where the

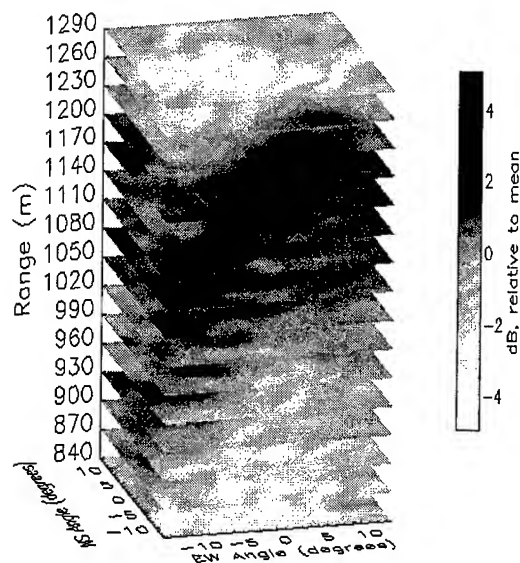


Fig. 2. A volume image of relative backscattered power.

data is stored to 8 mm tape. Beamforming and spectra are produced in post-processing; as all of the data from each receiver are available, multiple beams can be formed within the field of view simultaneously, substantially lowering the "scan" time of the instrument. Backscattered intensity and wind vector images can be produced up to ten times per minute. The backscattered intensity is used to calculate C_n^2 through the relationship of Ottersten [8],

$$\eta \approx 0.38 C_n^2 \lambda^{-1/3},$$

where η is the backscattered power per unit volume, and λ is the radar wavelength. Wind vectors are calculated using Doppler beamswinging techniques, summarized in [9].

In August 1996 TEP was deployed at the Rock Springs Meteorological Site of Pennsylvania State University. The data presented here is from the 22nd of August, from an mid-afternoon, highly convective boundary layer with low winds, typically less than 2 ms^{-1} , and very little cloud cover.

Figures 2 and 3 demonstrate the imaging capability of TEP. Figure 2 shows a typical volume image of relative backscattered power. The x and y-axes represent the angle from zenith in the East-West and North-South directions, respectively. The averaging time of the image is 5 seconds. The data presented is from approximately 15:20 on 22 August 1996, and the mean winds were from the West, or left to right on the image. The darker structure in the higher altitudes depicts an area of enhanced backscatter propagating through the image in the mean

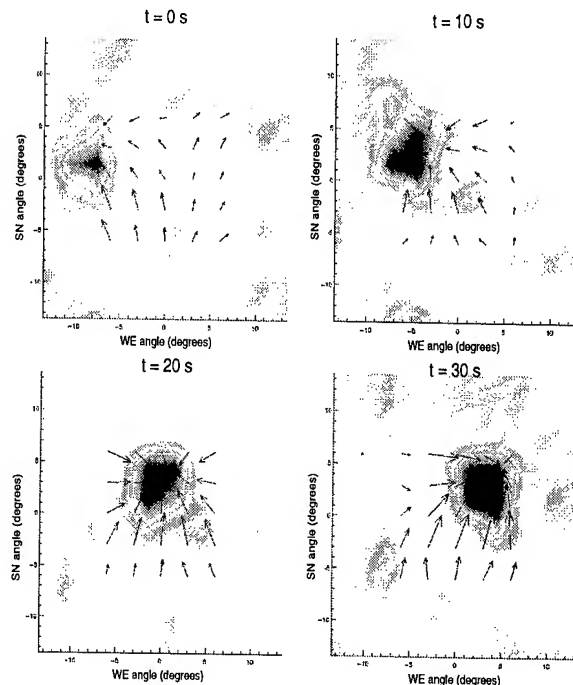


Fig. 3. Propagation of a turbulent eddy through a horizontal slice of the TEP's field of view.

wind direction. Figure 3 depicts a time-series of horizontal slices of backscattered power from an altitude of 1080 m. Horizontal wind vectors are overlaid on the images. The propagation of an updraft through the image from left to right is described by an area of high backscatter and by convergence of the local wind vectors. The spacing between successive images is 10 seconds.

The area of the horizontal slices in Figure 3 is $480 \times 480 \text{ m}^2$. In order to approximate the larger volumes of LES, vertical slices are taken through each image perpendicular to the wind direction and plotted as a function of time. Such an image can be thought of as a "volume" through the frozen turbulence hypothesis of Taylor [10], which assumes that areas of strong turbulence are frozen in space and time and advected over a sensor by the mean wind. Figure 4 shows such an image taken from TEP data, where the abscissa is time, or equivalently through multiplying by the mean wind, distance. Such volumes are used in the next section in structure-function parameter comparisons with LES.

COMPARISONS WITH LES

Peltier and Wyngaard [11] derived statistics of the structure-function parameters for humidity, C_Q^2 , humidity-temperature correlation, C_{TQ} , and temperature, C_T^2 for a moderately convective boundary layer using LES. Their results were presented in terms of a "flat-

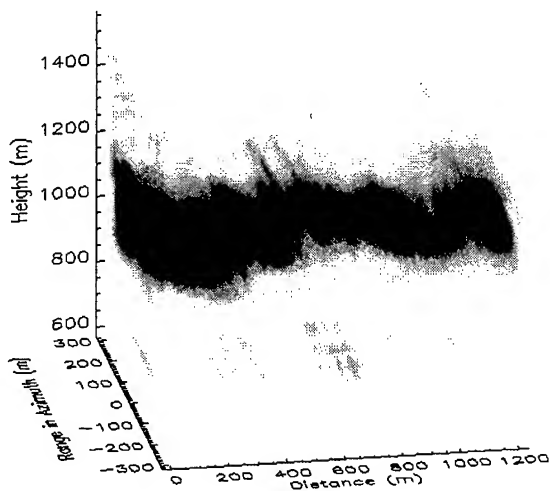


Fig. 4. A crosswind slice versus time rendered as a three-dimensional volume

ness factor", or normalized variance,

$$F_Q = \frac{\text{variance of } C_Q^2}{\text{squared mean of } C_Q^2},$$

computed over horizontal slices throughout the LES volume.

In order to compare TEP data to LES data, note from [12] that at microwave frequencies,

$$C_n^2 = \left(\frac{C_p}{\epsilon T^2} \right)^2 \alpha_m C_Q^2,$$

where α_m is a function of the change in humidity over the change in virtual temperature, p is the atmospheric pressure, T is the absolute temperature, and C and ϵ are constants. If, to first order, p , T , and α_m are constant in horizontal slices over the time taken to form Figure 4, then $F_Q \approx F_n$. As a normalized quantity, F_n is an attractive quantity for comparisons, as no absolute calibration of the instrument is necessary.

Figure 5 shows a comparison of the vertical profile statistics from the data from Figure 4 with the F_Q from [11]. Both data sets are scaled to the top of the boundary layer, z_i . The TEP data is scaled for finite beam efficiency and for the increase in pixel volume with height. While the TEP data volume is substantially smaller than the LES volume, and while the environmental conditions of the two data sets are different, there is quite good agreement between the two near z_i . Below z_i , as is suggested by the lack of structures at lower altitudes in Figure 4, the TEP system may be signal-to-noise limited.

FUTURE PLANS

The results presented in Figure 5 are preliminary but encouraging; there is good agreement with LES in the

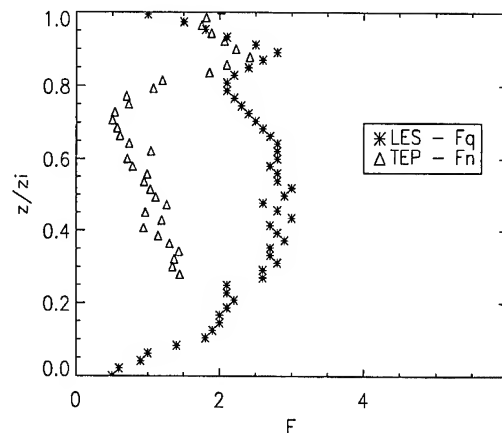


Fig. 5. A comparison of TEP and LES flatness factors.

high signal-to-noise regions of the TEP data. Ongoing research with the current data is focusing on examining longer data sets to better approximate LES volumes. Future plans include comparisons with more appropriate LES data, comparing not only structure-function parameters, but also velocity statistics.

REFERENCES

- [1] J. C. Wyngaard and L. J. Peltier, "Experimental micrometeorology in an era of turbulence simulation," *Boundary-Layer Meteorology*, vol. 35, 1995.
- [2] W. L. Ecklund, D. A. Carter, and B. B. Balsley, "A UHF wind profiler for the boundary layer: brief description and initial results," *J. Atmos. Oceanic Tech.*, vol. 5, p. 432-441, 1988.
- [3] W. D. Neff and R. J. Coulter, "Acoustic remote sensing," In Donald Lenschow, editor, *Probing the Atmospheric Boundary Layer*. American Meteorological Society, 1986.
- [4] F. D. Eaton, S. A. McLaughlin, and J. R. Hines, "A new frequency-modulated continuous wave radar for studying planetary boundary layer morphology," *Radio Sci.*, 30, p. 75-88, 1995.
- [5] E. W. Eloranta and D. K. Forrest, "Volume imaging lidar observations of the convective structure surrounding the flight path of a flux-measuring aircraft," *J. Geophys. Res.*, vol. 97, p. 18383-18393, 1992.
- [6] J. B. Mead, G. Hopcraft, B. D. Pollard, and R. E. McIntosh, "A digital beamforming radar profiler for imaging turbulence in the atmospheric boundary layer," In *International Geoscience and Remote Sensing Conference*, 1996.
- [7] J. B. Mead, G. Hopcraft, S. J. Frasier, B. D. Pollard, C. D. Cherry, D. H. Schaubert, and R. E. McIntosh, "A volume-imaging radar wind profiler for atmospheric boundary-layer turbulence studies," *J. Atmos. Oceanic Tech.*, in press.
- [8] H. Ottersten, "Atmospheric structure and radar backscattering in clear air," *Radio Sci.*, vol. 4, p. 1179-1193, 1969.
- [9] M. F. Larsen and J. Röttger, "The spaced antenna technique for radar wind profiling," *J. Atmos. Oceanic Tech.*, vol. 6, p. 920-938, 1988.
- [10] G. I. Taylor, "The spectrum of turbulence," *Proc. Royal Soc. London, Ser. A.*, vol. 164, p. 476-490, 1938.
- [11] L. J. Peltier and J. C. Wyngaard, "Structure-function parameters in the convective boundary layer from large eddy simulation," *J. Atmos. Sci.*, vol. 52, p. 3641-3660, 1995.
- [12] S. D. Burke, "Temperature and humidity effects on the refractive index fluctuations in the upper regions of the convective boundary layer," *J. Appl. Meteor.*, vol. 20, p. 717-721, 1981.

A tomographic infrared system for monitoring atmospheric pollution in urban areas

D. Giuli, F. Cuccoli, L. Facheris, S. Tanelli
Dipartimento di Ingegneria Elettronica - Università di Firenze
Via di S. Marta, 3 50139 Firenze - Italy

Abstract – This paper describes a feasibility study that has been carried out to define a measurement system able to estimate average concentration values of major species of pollutants over few km² areas. The system is based on laser diode semiconductor transmitters, and passive retroreflectors operating in the infrared region. Average concentrations are measured along rectilinear paths of 1 km maximum length, exploiting the infrared radiation absorption properties of pollutants. Measured data are then given as input to a tomographic reconstruction algorithm developed to retrieve space distribution of pollutants.

INTRODUCTION

In this paper we discuss the possibility to measure along rectilinear paths the average concentration of the fundamental molecular species of pollutants, with particular reference to CO, O₃ and nitrogen dioxides. This analysis was solicited by the fact that such measurement is the basis for the application of a tomographic reconstruction technique able to provide the distribution of concentration of pollutants. Such technique has been developed for rainfall field retrieval and tracking exploiting attenuation measurements along microwave links [1], nevertheless the data processing algorithm can be utilized unchanged for the problem discussed here. For a propagating electromagnetic wave with wavenumber ν (inverse of frequency) the Lambert-Beer law holds [2]:

$$dI(z, \nu)/dz = -\alpha(z, \nu) \cdot I(z, \nu) \quad (1)$$

where $I(z, \nu)$ is the power spectral density (W/cm²·Hz) at distance z along the wave propagation axis, and $\alpha(z, \nu)$ (cm⁻¹) is the attenuation coefficient, which is the sum of three terms:

$$\alpha = \alpha_R + \alpha_M + \alpha_G \quad (2)$$

where α_R and α_M account for attenuation due to Rayleigh effect, and to Mie effect, respectively, while α_G accounts for attenuation due to molecular absorption:

$$\alpha_G(\nu, z) = \sum_{i=1}^N \sigma_i(\nu) \cdot N_i(z) \quad (3)$$

where σ_i (in cm²) and N_i (molecules per cm³) are the absorption section and the concentration of the i -th molecular species, respectively. The molecular absorption is due to transitions between vibrational states that are peculiar of each molecular species. The characteristic frequency of each absorbing transition is the so-called absorption line. In standard pressure and temperature conditions (1 atm and 25°C, respectively) $\sigma_i(\nu)$ due to a single absorption line takes the typical Lorentzian form:

$$\sigma(\nu) = \frac{S}{\pi} \cdot \frac{\gamma_L}{(\nu - \nu_0)^2 + \gamma_L^2} \quad (4)$$

where ν_0 and γ_L are the center line wavenumber and width, respectively (cm⁻¹), and S the line amplitude (cm/molecule). The main molecular species of the atmosphere, be they pollutants or not, are characterized by a greater amplitude of the absorption lines in the wavelength interval 1-20 μ m. The greater variability with wavelength of α_G , with respect to both α_R and α_M , is exploited for measuring the concentration of molecular species by means of the so called "derivative method" [2],[3].

2. The measurement method

If a transmitter emits a monochromatic radiation with power P_{r0} , the residual power P_r collected by a receiver at distance L is obtained by integrating Eq. (1) along a path of the same length. If \bar{N} is the average concentration of the species of interest along the path of length L , and γ to account for all other attenuation effects, we have [2]:

$$P_r(\nu) = K P_{r0}(\nu) \cdot e^{-[\bar{N}L\sigma(\nu) + \gamma]} \quad (5)$$

where K is the optical efficiency. Assuming that K and P_{r0} are independent of the wavenumber, the ratio between the derivative of Eq. (5) with respect to the wavenumber and Eq. (5) itself provides:

$$\frac{1}{P_r(\nu)} \frac{dP_r(\nu)}{d\nu} = -\left[\bar{N}L \frac{d\sigma(\nu)}{d\nu} + \frac{d\gamma}{d\nu} \right] \quad (6)$$

If the wavenumbers are singled out for the species of interest, in correspondence of which the second term in the square parenthesis is negligible with respect to the first one, it is sufficient to perform power and power derivative measurements to obtain the average concentration along paths of known length.

3. The measurement apparatus

We describe here the measurement apparatus designed to directly provide an estimate of the left term of Eq.(6). The main devices that build up the proposed measurement apparatus are: infrared SDL (Semiconductor Diode Laser); passive retroreflector (corner cube reflector); infrared receiver; collimation and receiving electronics; electronic and control devices; pointing platform.

The average concentration measurement is performed by placing the devices according to the scheme of Fig. 2. The main reason for the adoption of semiconductor lasers as transmitters of infrared radiation are the following:

- the emission line width (about 1MHz), is small enough to resolve the molecular absorption figures [3];
- the emission power under unimodal propagation (about 100μW), allows one to measure average concentrations for transmitter-receiver distances up to about 1 km;

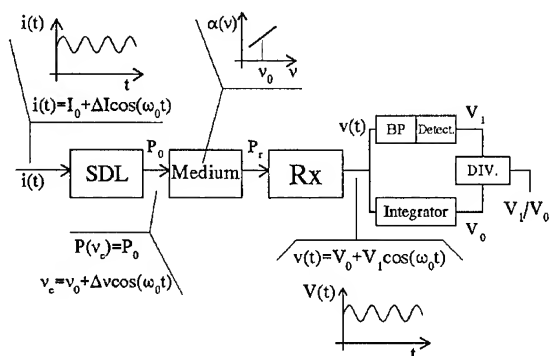


Fig. 1 - System configuration utilizable for measurements.

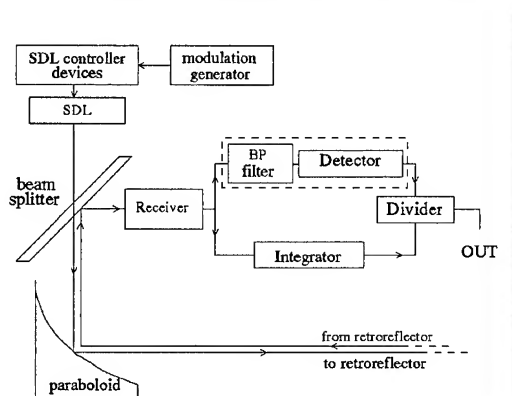


Fig. 2 - Arrangement of devices on the platform.

- the possibility to vary the emission frequency of the laser diode by means of the supply current allows one to measure the derivative of the received power [3]. The maximum value of the attenuation coefficient that still allows a significant power at the receiver's output was estimated based on SDL emission power, efficiency of the optical devices and effects of atmospheric turbulence [4] [5]. For 2 km two-way pathlength, a maximum attenuation coefficient has been estimated of about $2 \cdot 10^{-5} \text{ cm}^{-1}$. The left-hand quantity of Eq. (6) is measured (at the optimal wavelengths) by means of the scheme reported in Fig. 1. Therefore, the average concentration comes out to be:

$$\left. \frac{1}{P_r} \frac{dP_r}{dv} \right|_{v_0} \propto \frac{V_1}{V_0} \Rightarrow \bar{N} \propto \frac{V_1}{V_0}$$

4. Optimal wavelengths

To exploit the apparatus described, it is necessary to single out as many wavelengths (meeting the requirements posed by the derivative method) as the number of species whose the average concentration measurement is desired. Based on the HITRAN

database values [6] and on concentration values for the town of Florence provided by ARPAT-Italy, we searched for such optimal wavelengths by means of the characteristic parameters of the absorption lines (v_0 , γ_L and S), and of the minimum and maximum expected concentrations of the main molecules normally present in the atmosphere.

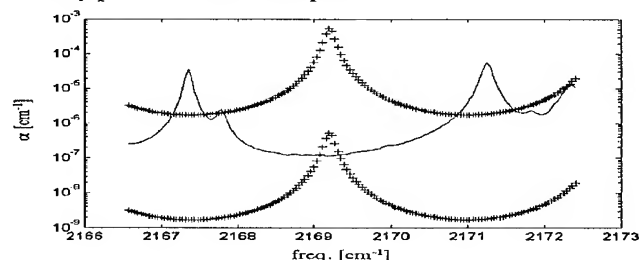


Fig. 3 Attenuation coefficient versus frequency (upper and lower + curves: due to 10 and 0.1 ppm CO concentration, respectively; continuous curve: due to all other molecules, at their maximum concentration)

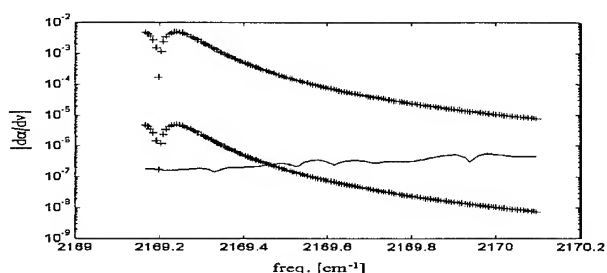


Fig. 4 Derivative of the absorption coefficient of Fig. 3, in the interval (2169.2,2170)cm⁻¹

Optimal wavelengths have been singled out for CO, O₃, N₂O, NO, NO₂. In particular, for CO we got the wavenumber interval (2169.2,2170)cm⁻¹ (corresponding to the wavelength interval (4.608,4.609) μm). Concentrations ranging from 0.1 and 10 ppm can be measured in such interval. Fig. 3 shows that in such frequency interval the absolute value of the derivative of the attenuation coefficient due to CO is always prevailing with respect to the total contribution of the other species. When CO concentration is high, it is advisable to utilize wavenumbers greater than 2169.5cm⁻¹. Figs. 3 and 4 were obtained by accounting for the contribution of the lines of all molecules with their centre line frequency v_0 included in the interval [2164,2174] cm⁻¹, that provide a significant level of absorption. As far as other molecules are concerned, we singled out an optimal frequency of 1057.77 cm⁻¹ (9.454 μm) for ozone, 2240.41 cm⁻¹ (4.45μm) for N₂O, 1900.04 cm⁻¹ (5.26μm) for NO, 843.71 cm⁻¹ (11.85μm) for NO₂.

5. Tomographic reconstruction of concentration fields

A network composed by an ensemble of transmitters, receivers and retroreflectors can provide a set of path-integrated attenuation measurements. These can be exploited as input to a

tomographic algorithm based on a stochastic approach, for which the reader is referred to [1]. Here we report synthetically some selected results.

For simulation purposes, we used the Gaussian Slender Plume model [7]. The model is valid under some quite restrictive conditions (see [7]); nevertheless, since the performance of the tomographic algorithm is practically independent of the field shape, the model served simply as reference to simulate plausible CO distributions due to point sources. The choice of CO is justified by the fact that its main sources (heating and internal combustion engines) can be modeled as point sources. Two different network topologies were used. NET01, with 5 transmitter-receiver pairs and 5 retroreflectors, provides an excellent coverage of the surface to be monitored. NET02, instead, is designed to minimize the number of transmitter-receiver pairs, and consequently the cost of the entire network, (transmitters' costs are remarkably higher). Simulations refer to 40 point sources randomly located in a 200x200m square surface, 0.5m above ground. The amplitude of each source ranges between 0.1 and 0.5 g/s (e.g. 40 car engines running at minimum). We considered a horizontal 0.3m/s wind speed. The concentration field is developed over a 500x500 m square surface located 5m above the sources. The results are reported in Figs. 4 and 5. Errors have been computed referring to the rectangular surface (strictly containing the measure network) plotted in the top-right frame of each figure. Notice that very low *me* values are observed in both cases; this is common to all simulations that have been performed. The spatial distribution is caught with appreciable fidelity; in particular, from the absolute error plots notice that zones with higher concentration are well individuated.

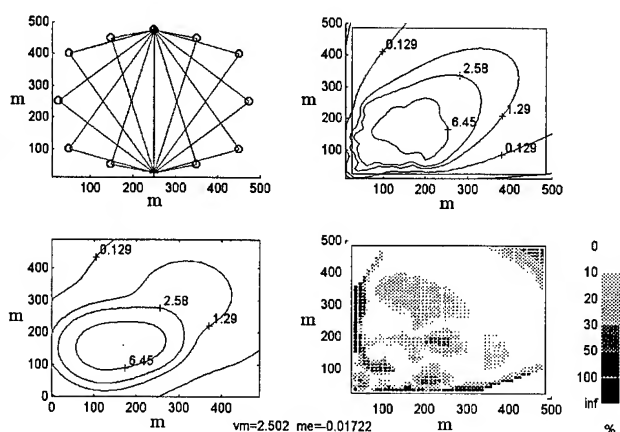


Fig. 4 - Reconstruction of a concentration of CO field (ppm) through NET01. Top left: measurement network; top right: simulated concentration field; bottom left: reconstructed concentration field; bottom right: error distribution; *vm*: mean value of reconstructed field; *me*: mean value relative error; +: transmitter-receiver pairs; o: retroreflectors

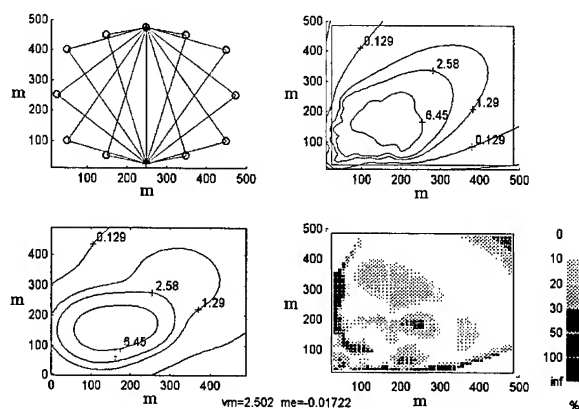


Fig. 5 - As Fig. 4, for NET02

6. Conclusions

The matter we have briefly synthesized in this paper is the result of a more general study that was carried out to assess the theoretical and technological feasibility of an air pollution monitoring system, which is particularly suitable for urban areas. Major difficulties were related to attenuation measurement principles and to their practical realizations, while the data processing algorithm for tomographic reconstruction was easily extended to the case under exam. The result is an affordable and flexible monitoring tool useful to provide, in particular if used jointly with a network of point sensors at ground, a complete and more reliable and detailed real-time information over the area.

References

- [1] D. Giuli, L. Facheris, S. Tanelli: "Stochastic technique for 2D tomographic reconstruction of rainfall fields through microwave measurements" Proc. Mathematical Methods in Geophysical Imaging IV, Denver, Colorado, August 1996, pp. 129- 139.
- [2] R.M. Measures "Laser remote sensing" Wiley Interscience, 1981
- [3] R.T. Ku, E. D. Hinkley, J. O. Sample, 1975 : "Long-path monitoring of atmospheric carbon monoxide with a tunable diode laser system " Applied Optics, vol. 14, n. 4, pag. 854-861
- [4] A. Ishimaru: "Wave propagation and scattering in random media" Academic Press, 1978
- [5] H. Beaumont, 1996: "Caractérisation de la turbulence atmosphérique et procédure d'amélioration des images pour des observations horizontales au dessus de la mer" These de Doctorat présentée au Département d'Astrophysique de l'Université de Nice-Sophia Antipolis.
- [6] L.S. Rothman: "AFGL trace gas compilation: 1982 version" Applied Optics, vol.22, n.11, pag. 1616-1625
- [7] J.H. Seinfeld, 1986: "Atmospheric chemistry and physics of air pollution" Wiley Interscience

Remote Sensing in China: Techniques and Applications

Guo Huadong
Institute of Remote Sensing Applications
Chinese Academy of Sciences
Beijing 100101, P. R. China
Tel: 86-10-64919740, Fax: 86-10-64915035
Email: Guohd@sun.ihep.ac.cn

Abstract - This paper consists of three parts. The first part introduces the Chinese remote sensing system, including remote sensing satellite, remote sensing ground receiving station, airborne remote sensing system and sensor development; the second part depicts the achievements of remote sensing in agriculture, forestry, geology and mineral exploration, oceanography, hazards and in other fields; finally, the progress of the development and application of new remote sensing techniques in China are briefly presented.

1.0 INTRODUCTION

Since the beginning of the 70's China has started researches on remote sensing and applications. The remote sensing satellites and polar-orbiting meteorological satellites have been launched, and an earth resource satellite is going to be in operation. many kinds of remote sensing instruments have been designed and manufactured, including those having international standard imaging spectrometer and multi-polarization synthetic aperture radar (SAR). Many large remote sensing application experiments have been organized. A very strong strength has been shown in the development of remote sensing technical system, acquisition of multi-source remote sensing data, analysis and process of remotely sensed data, and integrated applications of remote sensing data. Remote sensing applications were of preliminary use in the past and now are in practical stage. Many significant results have been achieved, and obvious economic effects have been gained in the field of agricultural resources, forest resources, mineral resources, surveillance of oceanic resources, engineering environment, city environment, as well as monitoring and assessment of floods and fire disasters, many achievements amongst them have become the basis for the national decision making and development. Remote sensing technology has been placed as one of the 35 important key technologies for advancing the development of China in the 1990s.

2.0 DEVELOPMENT OF REMOTE SENSING TECHNOLOGY

2.1 Remote Sensing Satellite

In April 1970, China launched the first man-made satellite. Twenty years since then, 15 satellites have been

launched, including 13 returnable satellite and 2 "FY-1" meteorological satellite.

2.1.1 Territory Satellite

In 1985 and 1986, China launched two Territory Satellite, the first one produced color infrared imagery, and the second one produced black-white panchromatic imagery. The satellite altitude was 175 to 210 km, and ran 16 cycles around the earth each day, the resolution was 10 to 15 m at center, and 45 to 55 m at margins.

2.1.2 Meteorological Satellite

The first meteorological satellite launched in China was called "FY-1", its major task was to acquire cloud imagery at night for the globe, and also to conduct remote sensing detection for oceanic water color. FY-1 was launched in September 1988 and placed at altitude of 901 km. In September 1990, the second satellite FY-1-B was launched. The high resolution scanning radiometer is its main sensor in which it consists of 5 channels, and its working bands range from 0.5 μ m to 12.5 μ m.

2.2 Remote Sensing Satellite Ground Receiving Station

In December 1986, China formally set up a Remote Sensing Satellite Ground Receiving Station which can receive Landsat MSS and TM data. Over 10 years since its establishment, the ground receiving station has achieved more than 100,00 Landsat TM scenes which cover 85% of Chinese territory and some regions of neighboring countries. The quality assessment for the data is very high. The station has provided more than 10000 items of services with remote sensing materials to near 500 organizations and remote sensing research teams, and has served more than 10000 researchers. From the end of 1993, the updated ground station can receive ERS-1 data of European Space Agency, and JERS-1 data of Japanese satellite. Data processing capability was also largely improved. At present, the station has signed agreement with Canada to receive Canadian Radarsat SAR data from 1997. The station will also receive data from Chinese Resources Satellite -1 in the near future.

2.3 Airborne Remote Sensing Satellite

As a preliminary system for spaceborne remote sensing, and to meet the real time needs of airborne remote sensing,

China has developed two sets of important airborne remote sensing systems.

2.3.1 High Altitude Airborne Remote Sensing System

The system is based on two Citation aircraft, and equipped with 13 sensors such as multi-spectrometry camera developed by the Chinese Academy of Sciences, infrared scanner, real aperture radar and SAR. The whole system is composed of three sub-systems: information acquisition, information processing, analysis and application. The system contains full remote sensing sensors, with wide spectrum coverage, and complete working modes. The service objects are for resources investigation, hazards monitoring and many other fields. The system is playing an increasing important role in many application fields.

2.3.2 All Weather Real Time Remote Sensing System

The system consists of information acquisition, information transmission and information processing sub-systems. The core of information acquisition sub-system is a Learjet aircraft, on which a 3 x 3 m SAR is loaded; the information transmission sub-system is to implement the transmission of SAR signals from aircraft-satellite-ground, i.e., transmitting SAR signal from aircraft to satellite, and then sending it to the ground; the information processing sub-system is to perform image processing on the ground. The major function of the system is to monitor those suddenly occurred natural hazards in all weather and real time conditions.

2.4 Development of Three Sensors

Three kinds of important sensors have been developed successfully in China

2.4.1 Imaging Spectrometer

An imaging spectrometer with 71 bands was successfully developed by the Shanghai Institute of Technology and Physics, Chinese academy of Sciences, in which there are 32 visible-infrared bands, 32 short-wave infrared bands and 7 thermal infrared bands. Correspondent working bands can be selected by different targets of applications.

2.4.2 Synthetic Aperture Radar

SAR was firstly developed in China in 1976. Ten years later, the Institute of Electronics, Chinese Academy of Sciences developed two generation X-band SAR systems from single band, single channel, single polarization to multi-band, multi-channel and multi-polarization.

2.4.3 Three Dimensional Imaging and Real Time Processing System

The conventional remote sensing technology is to directly acquire two dimensional remote sensing imagery, and then

produce 3D image with DEM data. This is neither time saving nor meeting the demands of real time data processing. The institute of Remote Sensing Applications, Chinese Academy of Sciences, collaborated with other agencies, have recently successfully developed a sample machine of 3D imaging system, which is an integrated system of scanner, GPS, laser distance measurer, attitude stable platform and other techniques. 3D imagery will be produced by data processing. This work has achieved preliminary success in the recent experiments.

3.0 APPLICATION OF REMOTE SENSING TECHNOLOGY

Remote Sensing application is a major purpose of developing space remote sensing technology. With the rapid improvement and development of modern science and technology, China has made very significant achievement in remote sensing applications.

In the applications to agriculture, national land use and resources investigation has been conducted. Crop yield estimation with remote sensing, in particular for wheat, has been received great attention by the government.

In the applications to forestry, a large scale remote sensing surveying for the "Three North" forest protection zone was conducted. Classification for forest types was made with remote sensing. Forest biomass estimation was also undertaken with radar remote sensing techniques.

In the applications to geology and mineral exploration, geological mapping with remote sensing was conducted. Especially, multi-sources remote sensing techniques have been applied to mineral exploration, and some gold deposits have been found with this technology. Some coal, oil and polymetallic ore deposits were also discovered with the aid of remote sensing.

In the applications to oceanography, remote sensing has provided information about the environment and navigation course of Chinese sea area. Monitoring of oil spill in the sea and sea water pollution were studied. Detection of topography under shallow sea was conducted with SAR data.

In the applications to hazard studies, flooding situation was monitored in real time with remote sensing. Monitoring of drought, forest fire, and snow disaster has also been studied. The loss caused by flooding, firing, earthquake and other hazards was estimated with remote sensing and GIS, the results were then provided to the decision making organization for their reference and use.

4.0 NEW GENERATION REMOTE SENSING TECHNOLOGY AND ITS APPLICATION

China is conducting a new remote sensing development and application program. In the year around 2000, a series of new research results will be obtained.

4.1 Remote Sensing Program

4.1.1 Radar Satellite (SAR Satellite)

China is going to launch a SAR satellite (SARSAT) about the year 2000. This satellite will work at L band with HH polarization, having two imaging modes with different resolution and variable look angles. At present, the SAR sample machine has been manufactured, which will lay an important foundation for the SARSAT.

4.1.2 Resources Satellite

Cooperated with Brazil, China has been developing a resource satellite since 1988. The Resources Satellite -1 will be launched in 1998, in which three imaging sensors will be loaded, they are wide angle imagery (WFI), high resolution CCD camera, infrared multi-spectrum scanner (IR-MSS). Resources Satellite-1 has three characteristics: CCD camera is resemble to TM bands, but resolution is higher than that of TM, CCD camera, similar to SPOT, has side imaging capability, the spatial resolution for WFI, IR-MSS and CCD are 256m, 156m, 78m, and 19.5m respectively.

4.2 New airborne system for earth observation

The new generation airborne system for earth observations, under the auspices of Information Acquisition and Processing subject of national 863 high-tech program, is a part of future development in China. The system is composed of airborne imaging spectrometer, dual-band multi-polarization high resolution SAR, and 3D information acquisition and real time processing systems. The imaging spectrometer has 128 channels, the spectral resolution of visible bands can be up to 5 nm. Three parts of visible -near infrared, short-wave infrared and thermal infrared can be operated separately in demands, or can be integrated to work together. SAR has L and X bands, and can image simultaneously with HH, HV, VV and VH polarizations, the spatial resolution of which can reach 1 to 3 meter. The 3D information system, integrated with scanner, laser distance measuring and GPS, can acquire real time 3D information of the earth surface. The successful development of above systems will advance the airborne system for earth observation in China.

4.3 New Remote Sensing Application Program

With the development of new remote sensing technology, China is undertaking a series of new remote sensing application programs. Remote sensing will be used for national land use and resources surveying, monitoring of

major crops and estimation of their yields, large scale mapping for urban and city, classification of terrain features, studies for oceanic preliminary production and oceanic dynamics, monitoring and assessment for natural hazards etc. Meanwhile, an operable Chinese resource and geographical information system is to be established. On the basis of more than 20 years research on remote sensing in China, the technology will be further oriented towards practical and industrialized development. Remote sensing will contribute much more than ever to the economic construction of China.

REFERENCE

- Guo Huadong, Progress of Space Remote Sensing and Applications in China, Progress of Space Science in China, pp. 259-295, 1995.
- Wang Xinmin, China Remote Sensing Satellite Ground Receiving Station, Remote Sensing in China, pp. 590-593, 1992.
- Fan Tianxi, FY-1 Satellite Data: Receiving, Processing and Applications, Remote Sensing of Environment, 6(2) 1991.
- Cao Shuhu, All-weather Real Time Airborne Remote Sensing transmission System and Its Application, Remote Sensing in China, pp. 180-182, 1996.
- He Xinnian, Operational High Altitude Airborne Remote Sensing System, Airborne Remote Sensing System, pp. 1-5, 1989.

Data Fusion of China Advanced Microwave Remote Sensor

Xiao Zhang, Jing-shan Jiang
MIRIT Lab, Center for Space Science and Applied Research
Chinese Academy of Sciences
P.O.Box 8701, Beijing 100080, P.R.CHINA
Phone: (86)10-62559944ext.3419, FAX: (86)10-62576921
Email: xiao@mimi.cnc.ac.cn jdidabao@public.east.cn.net

Abstract -- China Advanced Microwave Remote Sensor is a new sensor in which active and passive mode sensors are working simultaneously. There are three operation modes that are the combination of altimeter, scatterometer, and radiometer. The sensor generates various types of data from various measurement functions at the same time. It is very necessary to manage and process these data by data fusion techniques. With the fusion of this Multimode Microwave Remote Sensing data, we can get more information than single sensing mode, calibrate each other and meet multi-purpose missions.

1. INTRODUCTION

Because of the advantages of microwave remote sensing, such as less dependence on the weather, sensitive to the surface specification of planetary objects, it has been an important tool for observation from space. More and more advanced technologies have been developed and applied in the microwave remote sensor to improve the precision and ability. One of these development trends is the combination of different microwave remote sensing modes to get more valid information and to meet multi-purpose missions.

The Multimode Microwave Remote Sensor (M³RS), which is developed by the Laboratory for Microwave Remote Sensing and Information Technology (MIRIT Lab.), is a new synthetic microwave remote sensor in which active and passive modes are working simultaneously. It is designed for future China space projects. The main purpose of this sensor is ocean research, atmosphere research, and land soil moisture monitoring.

M³RS includes two active microwave remote sensing modes, altimeter and scatterometer, and one passive mode, microwave radiometers. The system is not the simple composition of these three modes one by one. It is the integration of all three modes. They use common units and resources in the sensor system as large percentage as possible, and these three sensing modes are operated at three operation modes that are performed by a unified System Controlling and Data Processing unit. The brief functional

block diagram is shown in Fig. 1.

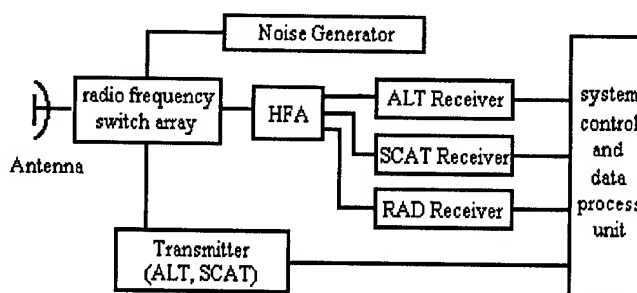


Fig.1. Brief Functional Block Diagram

Because of the integration of different remote sensing modes, M³RS gathers information from different sensing modes, same/different radio frequencies, same objects, and same route at the same time. These scientific data are relative indeed. The purpose of data fusion is to reach the maxim usage of all valid M³RS scientific data.

2. SYSTEM OPERATION AND MAIN SPECIFICATION OF M³RS

The all three operation modes are combined from three remote sensing modes, which are altimeter mode (ALT), scatterometer mode (SCAT), and radiometer mode (RAD). These combined operation modes are: ALT+RAD2-6, SCAT+RAD2-6, and multifrequency radiometer operating at all six frequencies (RAD1-6). The operation microwave frequency of Altimeter mode, Scatterometer mode, and one frequency of Radiometer (RAD1) is the same Ku-band frequency. In order to avoid the power release of active modes (SCAT and ALT) to RAD1 receiver, the ALT mode, SCAT mode and RAD1 mode are working time sequentially. The other five frequencies of Radiometer mode are ranging from 6.6GHz to 90GHz. The system control and data processing unit controls the selection of operation mode and pre-processes any necessary scientific data on line.

The main missions of multimode microwave remote sensor

are: significant wave high, mean sea level, ocean wind speed (for ALT mode), ocean wind field measurement (for SCAT mode), water content in atmosphere, snow coverage, sea surface temperature, and soil moisture (for RAD mode).

For Altimeter mode, the measurement accuracy after atmospheric correction is less than 10 cm, and the valid range of S.W. high is from 1 m to 20 m. For Scatterometer mode, the designed wind speed is ranged from 4m/s to 24m/s with accuracy of 2m/s or 10%. The wind direction measurement ranging from 0° to 360° has direction accuracy $\pm 20^\circ$. The radiation measurement accuracy of Radiometer mode is less than $\pm 0.5K$ with dynamic range from 80K to 400K. The Integration time is less than 100 ms.

3. DATA FUSION IN M³RS DATA PROCESSING

There are seven data sources involved in the data processing of Multi-mode Microwave Remote Sensors, which include (a) the three sensing modes of M³RS (ALT mode, SCAT mode, and RAD mode), (b) the platform data resource, (c) the other relative systems or instruments in the same platform, (d) the synchronized measurement on the ground or airplane, and (e) the Ground-based data library. The data from the first six data sources are fresh data because they are gathered from space or earth surface in real-time. Every data package generated by each mode of M³RS is marked with the unified time code, which is the basic label in pre-processing and data fusion processing. The data from sources (b) and (c) are also marked with the unified time code to identify their sampled time and space coordination. The calibration data from source (d) are labeled with both time and space coordination.

The schematic data processing procedure of M³RS is shown in Fig.2.

In the data processing procedure, there are many steps that need data fusion. The kinds of data fusion in M³RS data processing could be classified to five classes as following:

- 1). Original mode data+auxiliary data
- 2). mode data +data from library
- 3). data of same mode in different time
- 4). mode data +data from source (d)
- 5). data fusion of inter-mode data

These five kinds of data fusion are existed through the whole processing procedure. Some of them even appear in different phases in the M³RS data processing, such as pre-processing and post-processing.

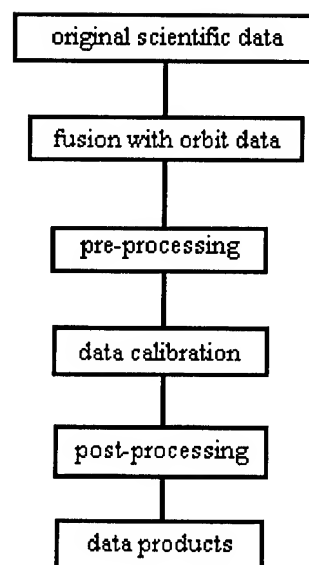


Fig.2. Schematic data processing of M³RS

The Auxiliary Data in the first kind of fusion comes from the sources (b) and (c). It includes attitude data and coarse space position data of platform, the precision orbit data from Precision Orbit-Determining System, and the space environment data, etc. These data are very useful in computing the geographical coordination of observed objects and also very useful in calibrating.

The data from previous missions or global data models, such as the weather data and atmospheric parameters, are defined as the data from library. The main purpose of this data fusion (Class 2) is to modify the deviation in propagation between the sensor and the observed objects.

Because the orbit repeats in a given period, it is interesting to compare with the data from the same geographical position in time sequence. With this kind of fusion, we could find out the changes of observed objects, analysis the result or reason of these changes, and even more forecast the trend.

In order to calibrate the remote sensing data from space sensors more precisely, it is necessary to apply the data fusion of Class 4. The match label of data in this kind of data fusion is both unified time code and geographical position codes. Considering various limits, it is difficult to measure the same object (such as the surface condition of a given ocean area) at the same time precisely enough by different sensors from different platforms. In a sense, the geographical position is more significant in this kind of data fusion.

As M³RS is an integrated multi-mode sensor, and some

modes (ALT, SCAT and RAD1) are operated at the same radio-frequency, there are many relationships between the data from each sensing mode. Fusion of inter-mode data can not only improve the utilization ratio of original sensor data, but also improve the precision of processed data effectively and help to analysis the instrument results of different measurement methods in real condition.

4. CONCLUSION

The modes integration of Multi-Mode Microwave Remote Sensor requires a large demand of data fusion to process the information gathered from different modes, different time, and different sources. As we pointed in the previous part,

the purpose of all these kinds of data fusion is that we wish to utilize the original scientific data more effectively, to improve the sensing precision of our remote sensing system in maxim possibility, and to find out the future development ways and methods by analysis.

REFERENCES

Jing-shan Jiang, Zhen-fan Zheng, He-guang Liu, Xiao Zhang, Zhong-fan Fan, "China Advanced Microwave Remote Sensor", The International Astronautical Federation Conference 1996, Beijing, P.R.China.

Research and Development on Synthetic Aperture Radar System in China

Zhu MinHui

Senior Member, IEEE

Institute of Electronics, Chinese Academy of Sciences

P.O.Box 2702, Beijing, 100080, P. R. CHINA

Tel: (086)-010-62554608 Fax: (086)-010-62567363 Email: mihzhu@ie0.ie.ac.cn

Abstract -- This paper presents the R&D activities of synthetic aperture radar (SAR) systems. Institute of Electronics, Chinese Academy of Sciences (IEAS) has engaged in this field since the end of 70's. It is not purely meant to be a testbed for testing new technologies and signal processing algorithms. In recent years, however, its airborne SAR (CASSAR) has advanced a main tool for microwave remote sensing application in china. In parallel, IEAS is responsible for the chinese spaceborne SAR which is being developed as a key geomatics data source. This data will be used to provide better monitoring of the dynamic events occurring on earth's surface to scientists, and resource managers, improve maps, and aid in assessing the impact of certain types of natural disasters. A multi-frequency, multi-polarization SAR programme will be considered.

INTRODUCTION

The Synthetic Aperture Radar is used to acquire high resolution large scale images of earth surface. The advantages of a SAR device are operations in all weather condition, and operations during the day and night cycles of an orbit in order to complement the existing optical sensors. It becomes a key tool of active microwave remote sensors for environment and resource survey and military application.

Since the end of 70's one major focus of development is informatics and as part of this activity China is developing geomatics capabilities aimed at supporting sustainable development and natural disaster mitigation. The Institute of Electronics Chinese Academy of Sciences (IEAS) started to study on imaging radar technology for radar system design and digital signal processing techniques at that time. Today, SAR systems both on airborne and spaceborne platforms form the major subjects in the institute, not only to demonstrate its technological feasibility, but also to develop SAR engineering projects and exploit some of its benefits to a range of application. IEAS heritage in SAR is, second to none in China.

THE AIRBORNE SYNTHETIC APERTURE RADAR CASSAR

Upon user's request, IEAS completed the first operational X-band airborne SAR with mono-polarization in early 80's. Then we published our first multi-swath and multi-

polarization airborne SAR imaging system (CASSAR) in the end of 80's. Fig. 1 shows a block diagram of CASSAR.

Antenna installations are in the bottom of aircraft with two pairs of slotted wave guide antennas attached on a four-axis (roll, pitch, yaw and tilt) steerable pedestal. It has been designed specially for operation on a Cessna Citation II. Here are phase coherent transmitter generated by klystron and receiver with a fast gain control including a STC for signal adaptation to two A/D converters, which digitize the inphase (I) and quadrature (Q) signal components. Very large amount of raw radar data depends on standoff range and swath width. The system offers the possibility to select number of polarizations (1/2/4). The latter choice leads to polarimetric observation. Fig. 2 and Fig. 3 show an example of CASSAR images with VV and VH polarization respectively. We have designed and performed the onboard real-time imaging processor with pipeline architecture of multi-processors. Since the range compression has been done by surface acoustic wave device in the receiver of CASSAR. The design uses the FFT fast correlation technique to perform azimuth pulse compression function. The produced image can be displayed and recorded onboard the aircraft in flight a real time. In addition a radio downlink and ground movable receiving station has been finished in the early of 90's. Therefore the produced images can be also displayed on ground monitoring system in time. This system dedicates to economic oriented applications, especially flooding monitoring and assessment of damage during the first half of 90's.

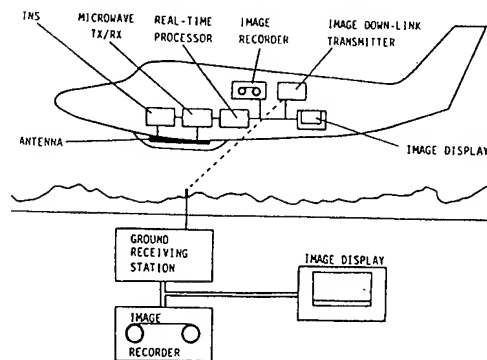


Figure 1 CASSAR Imaging Radar System
(with on-board real-time processor, image recorder & downlink, ground receiving station)

THE SPACEBORNE SYNTHETIC APERTURE RADAR L-SAR

At the end of 80's, we received a strong request of the national high technology program. It started our campaign work on the spaceborne SAR techniques. After the significant progresses of its key techniques, IEAS will complete the design of L-SAR, resulting in production of the major specifications to meet user's requirements. These include the subsystem specifications and those for the critical equipments. Hardware development is advanced. The instrument comprises two major functional groups, the central electronics and an active phased array antenna, which can be steered in one axis. In addition, spacecraft interface is also included. The central electronics modules which is composed of radio frequency electronics, the data handling and control electronics will be under its first airborne tests this summer. It will be developed a demonstration system for future spaceborne system. In meantime, it is intended to use for a wide range of possible applied researches. The active microstrip patch antenna models with deployed units will be verified by the beginning of next year.

Upon user community's requests, the planned Chinese SAR is designed L band, HH polarization, changeable incidence angle, two operating modes. It will be carried on a China made satellite with a circular sun-synchronized orbit.

IEAS does a lot of work on SAR processing both hardware and software. The fast imaging algorithms and massive parallel techniques are much emphasized. The groups from Beijing univ. Aeronautics & Astronautics and univ. of Electronic Science & Technology China have got good results on new SAR imaging algorithms and relevant SAR processing techniques.

CURRENT AND FUTURE WORK

Latest trends in airborne SAR systems are developing to SAR interferometry, which introduces the 3rd dimension to SAR imagery. CASSAR is used to implement the capability of two-pass interferometry. The evaluation of amplitude and phase of the two images yields the terrain height. The off-line SAR processing has provided first interferometric data in 1996.

Design and performance aspects in relation to a future dual frequency polarimetric spaceborne SAR instrument is currently being studied. It is expected that multiple parameter SAR instruments will be needed for a wide range of uses. We select full polarimetric operation, L and X bands, which allow simultaneous imaging. The next generation SAR instrument will be expected to improve spatial resolution, radiometric accuracy and stability. To provide SAR interferometric capabilities will be also included. Suitable design and performance modelling tools are studied.

REFERENCES

- [1] Zhu Minhui, Wei Zhongquan, Guo Kaidong, The Preliminary Study On Chinese Spaceborne SAR System, Report of UN/CHINA/ESA workshop on Microwave Remote Sensing Application. China Sep. 1994
- [2] Zhu Xixing, Zhu Minhui, The Development Of Onboard Imaging Processor For Airborne SAR In China, Proc. EUSAR'96, Konigswinter, Germany (1996)



Figure 2. CASSAR image with VV polarization



Figure 3. CASSAR image with VH polarization

A New Airborne Remote Sensing Platform for Generating Geocoding Image Without Ground Control Point

Li Shukai Xu Yongqi Liu Zhen

Institute of Remote Sensing Applications, Chinese Academy of Sciences
PBX 9718, Beijing 100101, PRC. Tel:+86-10-6491-9232 Email:sfdirs@public3.bta.net.cn

ABSTRACT--With the development of Global Position System and Inertial Navigation System(INS), the precise position and attitude parameters of airborne platform can be obtained. The new system, such as INSAR and Scanning Laser Ranger(SLR), are excellent equipment for acquiring the relative height of earth objects. At the same time optical remote sensing sensor make rapid progress. It is time to integrate these system into a new one, which can provide geocoding image without ground control points.

INTRODUCTION

The system, which integrates differential GPS receiver, INS, SLR and Infrared Sensor(IS), is loaded on a specially developed platform. The infrared axis of IS and optical axis of SLR are coupled in the same virtual optical axis, so every SLR point fit in a pixel of inferred image accurately. The integrated INS and GPS system can provide high accurate position and attitude parameters of the platform. DEM is generated from INS, GPS and SLR data. Because SLR point fit in a pixel of inferred image accurately, every DEM data have a corresponding image pixel. These points have the same function as the GCPs. It is easy to correct the error of images. The result of test in North China proves that good quality geocoding images can be obtained in 2 hours after flying. Obviously, the system can save much more money and job than the old method can. The system is a new development of surveying without GCPs.

PRINCIPLE OF THE SYSTEM

G , P is one point in space and ground respectively. If the coordinates $G(X_g, Y_g, Z_g)$ are given, and the vector \vec{GP} from G to P are given, then the coordinates of P can be obtained. The parameters of optical center are drawn from GPS data, INS provide three angle of the vector: sidespin α , angle of pitch ω and angle of yaw κ . SLR records the model of the vector: the ranger S is G to P , θ is the angle between scanning line and vertical line.

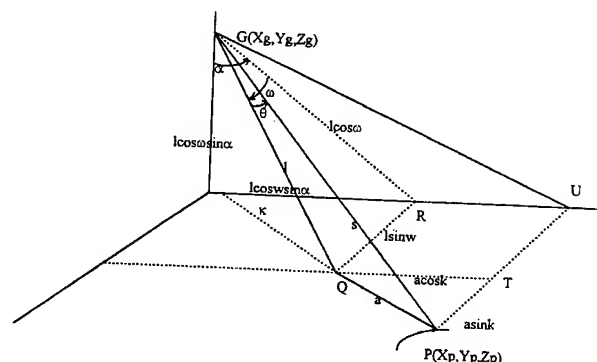


Figure 1 Principle of the System

STRUCTURE OF SYSTEM

The system includes two subsystem: System of Data Acquisition(SDA), System of Data Processing(SDP).

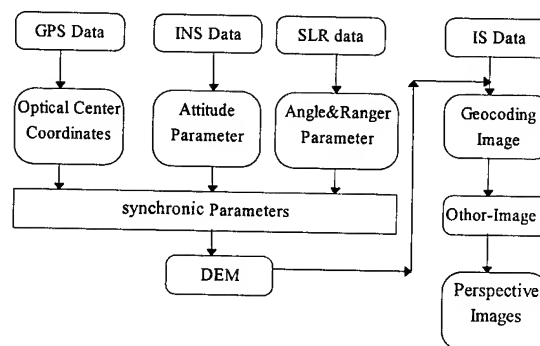


Figure 2 System Construct

SDA is composed of differential GPS receiver, INS, IS, SLR and a set of recorder and power system. A special platform was developed, on which sensors of SLR, IS, and INS were loaded. The deformation of the platform is limited in $15''$, so SLR, IS, and INS have the same parameters of position and attitude. The function of SDA is to receive, gather and record the data of GPS, INS, SLR, IS. The function of SDP is to input the data from DAS and to output different degree digital products, such as DEM, geocoding-image, ortho-image, 3D perspective image. The network, which is composed of Sun 20 workstation and 5 PCs, is the SDP

software platform. A special soft package was developed.

TEST AND RESULT

Test Site: Datangshan test site locate at Changping County, Beijing, north edge of North China plain, $116^{\circ}18'45''-116^{\circ}22'30''E$, $40^{\circ}10'40''-40^{\circ}12'30''N$. It cover 25 km. In test site there is a hill which is 120 meter high.

Parameters of Test

- Aircraft Type: Y - 5, Made in China
- Flying Altitude : 600 m
- Max Visual angle : 45°
- Frequency of IS : 10/20/40 (lines/second)
- Image Band : $8-12.5\mu m$
- Instant Field View : 3mrad
- Divergent Angle of SLR : 2.6
- Frequency of SLR : 1000Hz
- Model of SLR : Line

CONCLUSION AND DISCUSSION

The spatial quality of farm image(Picture 1) is very poor, it is impossible to correct the image by use of GCPs since at least over hundred GCPs need. Picture2 is geocoding images after



Picture 1 Datangshan Farm Image



Picture 2 Datangshan Farm Geocoding Image

correction by use of this system. The result is satisfied.

Eleven control point were used in evaluating the spatial accuracy of the system, the result is listed in table 1. It is conclude that there is obvious system error in flying direction, which is caused by the unsatisfied accuracy of the INS. The error of the system is bigger that aero-cameral, which is cause by the propagation and accumulation of error of sub-systems. There are a lot of research to be conducted:

- Improve the accuracy of INS, GPS .
- Analysis the how the error propagation and accumulation.

REFERENCES

- [1] Li Shukai, Xue Yongqi, Liu Zhen. "Report on Three Dimensional Information Gathering and Processing System - Test and Evaluation of Accuracy". Beijing, Feb.,1997.

ACKNOWLEDGEMENTS

We thanks all people conduct different research in this project, they are Prof. Xue Yongqi, Prof. Guo Huadong, Prof. Qian Yuhua, Mr. Liu Tong, Mr. You Hongjian, Dr. Jiang Yuesong, Mr. Chen Jiping, Mr. Shen Zaixun, Miss Ma Jingzhi, Mr. Jin Dondhua, Mr. Su Rong, Dr. Shao Hui, Mr. Liu Jianmin

Table 1										
Result of Test										
Point	GCP X	GCP Y	GCP Z	X	Y	Z	ΔX	ΔY	ΔH	
1	4449733.614	444846.962	47.458	4449718.310	444845.910	60.000	15.304	1.052	-12.542	
2	4449675.870	444850.906	47.171	4449659.910	444846.910	52.000	15.960	3.996	-4.829	
3	4449761.246	444819.062	47.228	4449761.880	444802.810	39.000	-0.634	16.252	8.228	
4	4449782.216	444810.624	47.430	4449784.660	444793.780	42.000	-2.444	16.844	5.430	
5	4449785.631	444613.399	47.523	4449771.780	444585.000	41.000	13.851	28.399	6.523	
6	4449808.606	444405.234	47.295	4449806.440	444386.970	41.000	2.166	18.264	6.295	
7	4449901.547	443970.519	47.624	4449878.720	443950.090	43.000	22.827	20.429	4.624	
8	4449570.782	444693.906	46.963	4449565.840	444693.590	41.000	4.942	0.316	5.963	
9	4449566.849	444635.971	46.723	4449571.780	444633.730	41.000	-4.931	2.241	5.723	
10	4449570.989	444560.703	48.228	4449573.750	444553.310	42.000	-2.761	7.393	6.228	
11	4449568.100	444838.376	47.219	4449560.910	444847.910	47.000	7.190	-9.534	0.219	
u(X)=6.497 u(Y)=9.605 u(H)=2.897				REMS: X=8.825 Y=10.695 H=6.002						

Reversible Compression of Multispectral Imagery Based on an Enhanced Inter-Band JPEG Prediction

B. Aiazzi*, P. S. Alba°, L. Alparone*, S. Baronti*

* Istituto di Ricerca sulle Onde Elettromagnetiche "Nello Carrara" - CNR, via Panciatichi, 64, I-50127 Firenze, Italy

Phone: +39-55-4235-275; Facsimile: +39-55-410893; E-mail: baronti@iroe.fi.cnr.it

° Dipartimento di Sistemi e Informatica, University of Florence, via S. Marta, 3, I-50139 Firenze, Italy

Phone: +39-55-4796-359; Fax: +39-55-4796-363; E-mail: alba@dsi.ing.unifi.it

* Dipartimento di Ingegneria Elettronica, University of Florence, via S. Marta, 3, I-50139 Firenze, Italy

Phone: +39-55-4796-372; Fax: +39-55-494569; E-mail: alparone@cosimo.die.unifi.it

Abstract -- A modified *inter-band* scheme based on the predictors used by lossless JPEG is proposed for lossless data compression of multispectral images. Basically, the value of the current pixel in the current band is predicted by the best JPEG predictor on the previously encoded band. Improvements are achieved by considering also the corresponding prediction error on the previous band. Coding performances, assessed on a variety of Landsat TM data, are better by about 3% than those of the basic *inter-band* scheme, and by 7% than those attained by lossless JPEG.

INTRODUCTION

Reversible image compression is growing in relevance for the remote sensing community. The availability of airborne and spaceborne multispectral imaging sensors with high spatial and radiometric resolutions allows new researches to be carried out on data compression [1-3].

Differential pulse code modulation (DPCM) schemes, like JPEG in *lossless* mode [4], are usually employed for error-free compression. Extension to multispectral image data, however, may lead to negligible benefits, or even to some performance penalty with respect to separate coding of individual bands, depending on whether *inter-band* correlation is larger than *intra-band* correlation or *vice-versa*, as well as by the noise [5,6]. The matter is to what extent reduction of *inter-band* redundancy destroys the underlying *intra-band* correlation.

Different approaches have been recently investigated based on the fact that space details are correlated along neighboring spectral bands [2,7]. Thus, the same spatial edge occurs in two adjacent bands, although the two bands may locally differ by a gain factor and an offset due to different sensor responses.

In a classical *intra-band* prediction, each image, say the k^{th} band, is raster scanned irrespective of the previous $(k-1)^{\text{st}}$ band. Considering a prediction support of unity size in L_1 metrics, prediction is possible only from *four* out of the *eight-neighbor* pixels (i.e., *causal neighborhood*), namely A_k , B_k , C_k , and D_k , as illustrated in Figure 1. An *inter-band* scheme is

achieved if the *spatial* prediction on the k^{th} band is driven by some *spectral* information derived from the $(k-1)^{\text{st}}$ band [2,7].

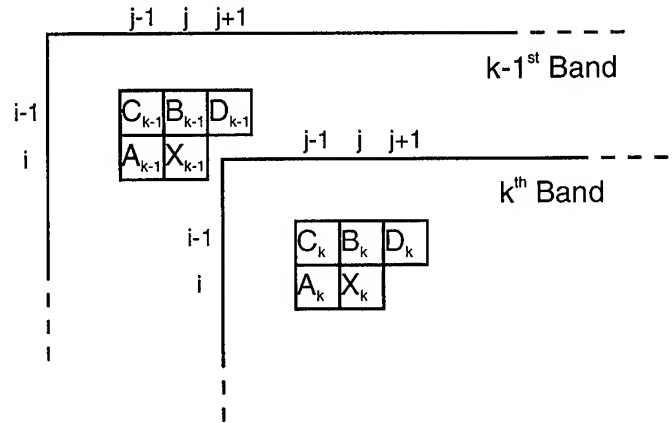


Figure 1. Causal neighborhood of pixel X in k and $k-1$ bands.

INTER-BAND LOSSLESS JPEG

A modified version of the Previous Closest Neighbor (PCN) algorithm [2] was recently defined from the standard set of eight predictors used by lossless JPEG.

Basically, an extension of the set of four zeroth order predictors used by PCN was introduced. Thus, a multispectral *lossless* JPEG was derived [7]. With reference to Fig. 1, prediction was achieved by means of the following set of 8 predictors, which have been standardized by JPEG:

$$\begin{aligned} \hat{X}_k^0 &= 0 & \hat{X}_k^4 &= A_k + B_k - C_k \\ \hat{X}_k^1 &= A_k & \hat{X}_k^5 &= A_k + \frac{B_k - C_k}{2} \\ \hat{X}_k^2 &= B_k & \hat{X}_k^6 &= B_k + \frac{A_k - C_k}{2} \\ \hat{X}_k^3 &= C_k & \hat{X}_k^7 &= \frac{A_k + C_k}{2} \end{aligned} \quad (1)$$

Standard *intra-band* lossless JPEG [4] consists of separately

applying each of the predictors (1) and choosing the one yielding minimum entropy over the whole image. Zeroth predictor is used only for extremely little correlated images.

The *inter-band* lossless JPEG [7] was stated as follows. Let \hat{X}_{k-1}^n , $n = 0, \dots, 7$, denote the set of predictors (1) at (i, j) evaluated in the $(k-1)^{\text{st}}$ band. Except for the first band which is coded in *intra* mode, optimum *inter-band* JPEG prediction at (i, j) in the k^{th} band, $k = 2, \dots, K$, is given by $\hat{X}_{k-1}^{\bar{n}}$, in which

$$\left| X_{k-1}(i, j) - \hat{X}_{k-1}^{\bar{n}}(i, j) \right| = \min_{n=0, \dots, 7} \left\{ \left| X_{k-1}(i, j) - \hat{X}_{k-1}^n(i, j) \right| \right\} \quad (2)$$

Thus, the algorithm turns out to be an adaptive lossless JPEG, in which prediction is driven by the previously encoded band.

ENHANCED INTER-BAND LOSSLESS JPEG

An *enhanced inter-band* lossless JPEG may be defined from considerations that when a band is being coded, prediction errors on the previous one are available and can be used to improve the current pixel prediction.

Prediction at (i, j) in the k^{th} band, $k = 2, \dots, K$, is given by

$$\hat{X}_k(i, j) = \hat{X}_k^{\bar{n}}(i, j) + \alpha_k [X_{k-1}(i, j) - \hat{X}_{k-1}^{\bar{n}}(i, j)] \quad (3)$$

in which $0 \leq \bar{n} \leq 7$ is still defined by (2), and α_k is a scaling factor independent of pixel position, introduced to adjust the gains of the imaging sensors. The simplest normalization is a variance equalization throughout bands:

$$\alpha_k = \sqrt{\frac{\sum_i \sum_j [X_k(i, j) - \bar{X}_k]^2}{\sum_i \sum_j [X_{k-1}(i, j) - \bar{X}_{k-1}]^2}} \quad (4)$$

in which \bar{X}_k denotes the global average of the k^{th} band. Notice that $\alpha_k=0$ yields the scheme reviewed in the previous section.

CODING RESULTS AND COMPARISONS

The test set comprises three Landsat Thematic Mapper (TM) 8-bit, 7-band images to be used for coding tests. One of which, of size 2560×1536 , relative to the site of Metaponto, in Southern Italy, was also used in the previous work by the authors [7]. The leftover two portray a zone near Trento, in Northern Italy, and one in the Sardinia isle. Both these latter images are details of size 512×512 .

In multispectral decorrelation algorithms, the order in which the bands are considered is essential for the coding success [2,3,5-7]. In fact, the different bands available should be arranged in a sequence that maximizes the average correlation

between any couple of consecutive bands. Such a sequence strongly depends on the multispectral imaging sensor; therefore, once it has been established, it will be the same also for most of the imaged scenes, notwithstanding they exhibit different land cover characteristics. Depending on the correlation coefficient (CC) between two bands, the second one might better be encoded *intra-band* than *inter-band*. Thus, a flag bit was added to each band in order to specify the decorrelation mode (*intra* or *inter*), along with either the label of the best JPEG predictor (1) (*intra*), or the index of the previously encoded band on which prediction relies (*inter*).

Inter-band correlation has been investigated also for the two new images. Correlation coefficients have been calculated and reported in Table 1. Band 6 has been discarded. Previous tests have demonstrated that, due to its resampling from a $120m \times 120m$ pixel size, *intra-band* prediction is far more suitable [7].

Band	1	2	3	4	5	7
1	-	0.96	0.94	0.27	0.67	0.81
2	0.93	-	0.97	0.36	0.75	0.88
3	0.89	0.98	-	0.27	0.72	0.89
4	0.63	0.81	0.80	-	0.74	0.48
5	0.77	0.89	0.92	0.87	-	0.91
7	0.79	0.90	0.94	0.80	0.98	-

Table 1. Correlation coefficients of two of the test Landsat images: *Sardinia* (lower triangle); *Trento* (upper triangle).

The above results suggest the best band-ordering to maximize correlation within pairs of successive bands. The optimum sequence of bands is 1 - 2 - 3 - 7 - 5 - 4, corresponding to correlation values between neighboring bands of 0.96, 0.97, 0.89, 0.91, and 0.74 for *Trento*, and of 0.93, 0.98, 0.94, 0.98, and 0.87 for *Sardinia*, as shown in Table 1.

The same sequence had been found also for the other TM image (Metaponto) [7]. Thus, results may be generalized.

The success of the present prediction strategy compared with the former one [7] will be assessed varying with the CC between two bands, not necessarily consecutive. Obviously, a threshold value on the CC exists above which *inter-band* prediction from the previous band is preferable to *intra-band* prediction performed standalone, and *vice-versa* below.

Table 2 reports bit-rates obtained from the novel scheme, when a TM band is either *intra* coded with lossless JPEG, or coded in *inter* mode from any one of the leftover bands. Notice that the rates may be larger for *inter* than for *intra* coding, depending on the correlation coefficient (see Tab. 1).

Figure 2 reports the bit rates for each band, except the 6th, varying with prediction: *intra* (JPEG), *inter* with $\alpha_k = 0$, as in [7] (IB0-JPEG), *inter* with $\alpha_k = 1$ (IB1-JPEG, without gain equalization), and *inter* with α_k as in Eq.(4) (EIB-JPEG). As expected, the variance normalization yields the best results for all bands in which *inter-band* prediction is employed.

Band	1	2	3	4	5	7
1	3.73	<u>3.56</u>	<u>3.60</u>	4.03	3.90	3.90
2	<u>2.90</u>	3.07	<u>2.38</u>	3.23	3.12	3.09
3	<u>3.39</u>	<u>2.82</u>	3.54	3.73	3.62	3.54
4	5.11	4.98	5.05	4.82	4.86	5.01
5	5.22	5.09	5.14	5.12	5.06	<u>4.61</u>
7	4.22	<u>4.05</u>	<u>4.05</u>	4.26	<u>3.63</u>	4.07

Table 2. BR's of Trento with band on i^{th} row predicted from band on j^{th} col. For $i=j$ (bold) *intra* JPEG prediction assumed. *Inter* < *intra* underlined.

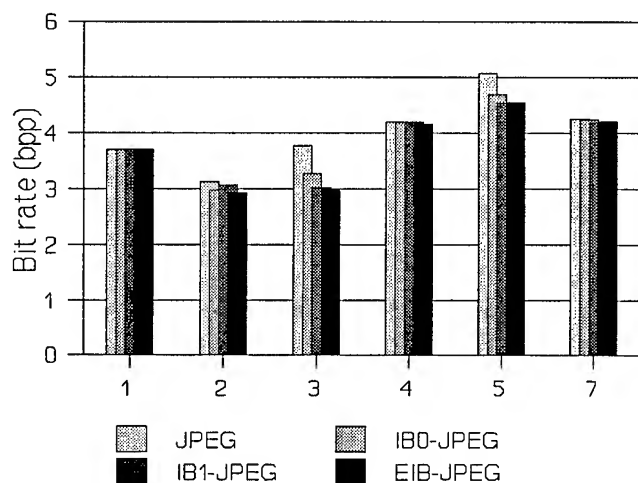


Figure 2. BR's (average on all test images) from the 6 coded bands: JPEG (*intra*), IB0-JPEG, IB1-JPEG, and EIB-JPEG.

Eventually, Figure 3 shows the global coding efficiency of EIB-JPEG compared with IB0-JPEG, equal to the former IB-JPEG [7], JPEG, and 4-pel auto regressive (AR) predictor [5].

CONCLUSIONS AND FUTURE TRENDS

This paper presented and discussed an enhanced version of an algorithm based on lossless JPEG, performing *inter-band* decorrelation for multispectral image compression.

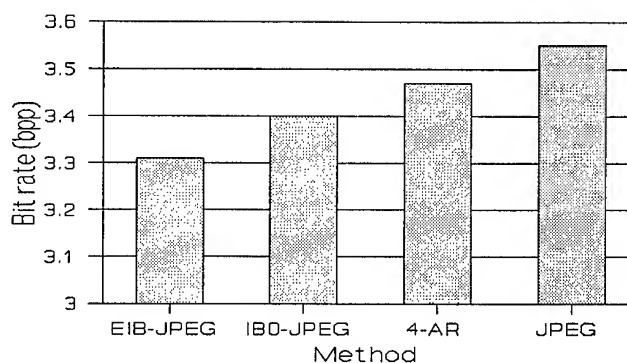


Figure 3. BR's averaged over the seven TM bands of Metaponto: 4 and 6 are always *intra* coded with JPEG. 4-pel AR and JPEG do not exploit *inter-band* correlation.

Extensive tests on Landsat TM 8-bit images have shown an average coding gain of about 3% with respect to the previous scheme, and of about 7% with respect to lossless JPEG. These results are expected to be improved when data with a larger number of bands will be considered, or when more advanced spatial predictors will be incorporated in the baseline of the 3D decorrelation method.

REFERENCES

- [1] V. D. Vaughn and T. S. Wilkinson, "System Considerations for Multispectral Image Compression Designs," *IEEE Signal Processing Magazine*, pp. 19-31, Jan. 1995.
- [2] N. D. Memon, K. Sayood, S. S. Magliveras, "Lossless Compression of Multispectral Image Data," *IEEE Trans. Geosci. Remote Sensing*, Vol. 32, No. 2, pp. 282-287, Mar. 1994.
- [3] R. E. Roger and M. C. Cavenor, "Lossless Compression of AVIRIS Images," *IEEE Trans. Image Processing*, Vol. 5, No. 5, pp. 713-719, May 1996.
- [4] W. B. Pennebaker and J. L. Mitchell, *JPEG: Still Image Compression Standard*, New York, NY: Van Nostrand Reinhold, 1993.
- [5] J. Wang and K. Zhang, "Spectral and Spatial Decorrelation of Landsat-TM Data for Lossless Compression," *IEEE Trans. Geosci. Remote Sensing*, Vol. 33, No. 5, pp. 1277-1285, Sept. 1995.
- [6] R. E. Roger and J. F. Arnold, "Reversible Image Compression Bounded by Noise," *IEEE Trans. Geosci. Remote Sensing*, Vol. 32, No. 1, pp. 19-24, Jan. 94.
- [7] B. Aiazzi, P. S. Alba, L. Alparone, S. Baronti, P. Guarnieri, "Reversible Inter-Frame Compression of Multispectral Images Based on a Previous-Closest-Neighbor Prediction," *Proc. IGARSS'96*, Lincoln, NE (US), pp. 460-462, 1996.

A DCT-based adaptive compression algorithm customized for radar imagery

A. Andreadis, G. Benelli, A. Garzelli, S. Susini

Department of Information Engineering, University of Siena, via Roma, 56, I-53100 Siena, ITALY

Phone: +39-577-263601; Fax: +39-577-263602; E-mail: garzelli@ing.unisi.it

Abstract -- In this paper an adaptive DCT-based image compression algorithm for radar images is proposed, tested and compared to JPEG and to classical coding algorithms for remote sensing imagery. The Modified Adaptive Discrete Cosine Transform (MADCT) scheme is proposed, which allows to classify each image block by means of a threshold criterion based on AC and DC activity. The strategy of transmission of the DCT coefficients, the recovering process of blocks incorrectly discarded, and the bit-allocation phase have been properly designed to provide high compression of two classes of images: X-band real-aperture radar images for ship traffic control, and SAR images for browsing applications. The experimental results, in terms of PSNR and compression ratio, prove the superiority of the novel scheme with respect to standard coding techniques.

INTRODUCTION

The JPEG DCT algorithm, even if optimized for noise-free color imagery, is frequently used for widespread image data reduction because at present it is a globally accepted image compression standard. By varying the bit allocation of the DCT coefficients of the transformed blocks, compression results can be greatly improved, when dealing with noisy and textured images. However, acceptable performance using JPEG on radar images can be achieved only on low-resolution data (having large look number and low speckle noise for SAR data), because the inter-pixel correlation decreases more slowly for browse images than for high-resolution images. Therefore, novel lossy compression schemes have to be designed when dealing with noisy and multi-textured images, in particular when high compression ratios are required. A higher degree of adaptivity is needed with respect to the standard compression schemes. This objective can be reached by using adaptive transform coding which employs a two-dimensional energy packing transformation (DCT) applied on small blocks of image data. Each transform block is classified into one of several classes on the basis of a block activity parameter and the transformed coefficients are then normalized, quantized and coded.

In this paper an adaptive image compression algorithm for radar images is proposed, tested and compared to JPEG and to classical coding algorithms for remote sensing imagery. The proposed scheme is a modified version of the ADCT algorithm [1], [2]: it selects n classes of blocks which are not

necessarily equipopulated. The DCT coefficients of the class having the lowest activity are not transmitted and a recovering process of blocks incorrectly discarded is performed in order to avoid target loss. The algorithm optimizes the block size, the bit assignment procedure and the parameter used to characterize the block activity, thus improving the adaptivity of the scheme and optimizing it for the image statistics. The strategy of transmission of the DCT coefficients, the recovering of misclassified blocks, and the bit-allocation phase are properly designed to fit with radar images.

THE MADCT ALGORITHM

The adaptive transform coding [1], [2] is a technique that can compress the image data to any user specified volume given that the associated image quality degradation is tolerable. The adaptive transform coding technique partitions the image data into small blocks (typically 16×16). Each block is then transformed by employing the Discrete Cosine Transform and then is classified into one of four classes on the basis of a block activity parameter, i.e., the ac energy.

In the proposed version (MADCT) of the compression technique, $N \times N$ (where $N=2^n$) blocks are DCT transformed to increase the degree of adaptivity of the scheme.

The blocks are classified by following an adaptive-threshold criterion based on two block-activity parameters. Further, the bit assignment procedure, which is based on the activity of each DCT coefficient, is modified to achieve higher compression ratios with the same quality assignments. Finally, the quantization process of the DCT coefficients is improved. Fig.1 illustrates the operations performed by the MADCT coder.

Block Classification

The blocks are classified into n groups according to the following measure of activity: for each block the ac energy E_{ac} , the dc energy E_{dc} , and the minimum, maximum and range values of E_{ac} and E_{dc} are computed.

As an example, for a classification into five classes, the following four thresholds

$$\begin{aligned} T_{ac}(i) &= \min_{ac} + \alpha_i \cdot \text{Range}_{ac} & i &= 1, 2 \\ T_{dc}(i) &= \min_{dc} + \beta_i \cdot \text{Range}_{dc} & i &= 1, 2 \end{aligned} \quad (1)$$

are computed, where $0 < \alpha_1 < \alpha_2 < 1$ and $0 < \beta_1 < \beta_2 < 1$.

Given that $E_{ac} < T_{ac}(1)$, a block is classified into class 0, 1 or 2 if

$$E_{dc} < T_{dc}(1) \quad (2)$$

or

$$T_{dc}(1) < E_{dc} < T_{dc}(2) \quad (3)$$

or

$$E_{dc} > T_{dc}(2), \quad (4)$$

respectively.

A block is classified into class 3 or 4 if

$$T_{ac}(1) < E_{ac} < T_{ac}(2) \quad (5)$$

or

$$E_{ac} > T_{ac}(2), \quad (6)$$

respectively, for any value of E_{dc} . It should be noted that the classes are not equally populated as in [1].

For the particular ship-traffic control application using X-band images, only three classes are selected, which correspond to sea clutter, ship bodies, and ship contours. According to the classification strategy adopted, only two coefficients α_1 and β_1 have to be defined, in particular they are set to the values $\alpha_1=0.25$ and $\beta_1=0.0715$. The blocks of class 0 are uniquely coded by their dc coefficients, if required, even if a better solution consists in assigning no bits to class 0, which represents the sea clutter. Conversely, the bit assignment to the DCT coefficients of the blocks of the other classes is determined by an adaptive procedure. Finally, isolated blocks of class 0 are recovered, i.e. promoted to class 1, in order to avoid undesirable loss of information into connected regions. This recovery process terminates the phase of generation of the classification map.

Bit Allocation and Quantization

Bit-allocation matrices are generated for the DCT coefficients of all classes except class 0. The bit assignment for each bit-allocation matrix is based upon a relationship from rate distortion theory: the number of bits is given by

$$N_{B_k}(u,v) = 1/2 \log_2(\sigma_k^2(u,v)) - \log_2(D) \quad (7)$$

where $(u,v) \neq (0,0)$ and $\sigma_k^2(u,v)$ is the variance of a transform sample and the parameter D controls the coding quality. In any case, 8 bits are always assigned to every dc coefficient. The bit-allocation matrices are then variable-length coded:

they represent the most significant part of the total overhead information.

The probability density functions of the normalized transformed ac coefficients have been modeled by Laplacian densities instead of Gaussian densities, as in the classical scheme [1]. Consequently, a non-uniform quantizer optimized for Laplacian statistics is used in order to quantize and reconstruct the normalized DCT coefficients. Huffman coding is finally adopted.

EXPERIMENTAL RESULTS AND COMPARISONS

The MADCT algorithm has been tested on simulated radar frames and on standard SAR images. In the case of real-aperture radar images, we used a proprietary radar simulator which allows to generate normal or critical scenarios in harbors or channels [3].

Performance has been evaluated in terms of Peak Signal-to-Noise Ratio ($PSNR=10 \log_{10}(255^2/MSE)$, where MSE is the Mean Squared Error) and Compression Ratio(CR).

Fig.2 shows an example of a radar image compared with three MADCT-reconstructed images corresponding to different values of compression ratios. Acceptable visual quality is achieved even for very high compression ratios, due to the classification phase which substantially removes the sea clutter.

The MADCT algorithm provides very interesting results also when only a small part of the radar image is represented by the sea clutter, as in Fig.3. In fact, both visual and numerical results show that satisfactory performance is assured, while standard coders like the JPEG algorithm (we used the PVRG version by Stanford University) are inadequate for the particular application.

Table 1 reports a comparison among MADCT, JPEG and ADCT for the compression of the SAR image *Airport*. PSNR values are indicated for the compression ratio CR=15.

CONCLUSIONS

An adaptive DCT image compression algorithm for radar images is proposed, which uses classification of $N \times N$ blocks based on AC and DC activity. The strategy of transmission of the DCT coefficients, the recovering of misclassified blocks, and the bit-allocation phase have been properly designed to fit with radar images. The results prove the superiority of the MADCT scheme with respect to JPEG and the classical ADCT algorithm when radar images have to be compressed.

Table 1. PSNR of reconstructed *Airport* SAR image (CR=15).

Algorithm	PSNR (dB)
JPEG	21.7
ADCT	25.2
MADCT	26.8

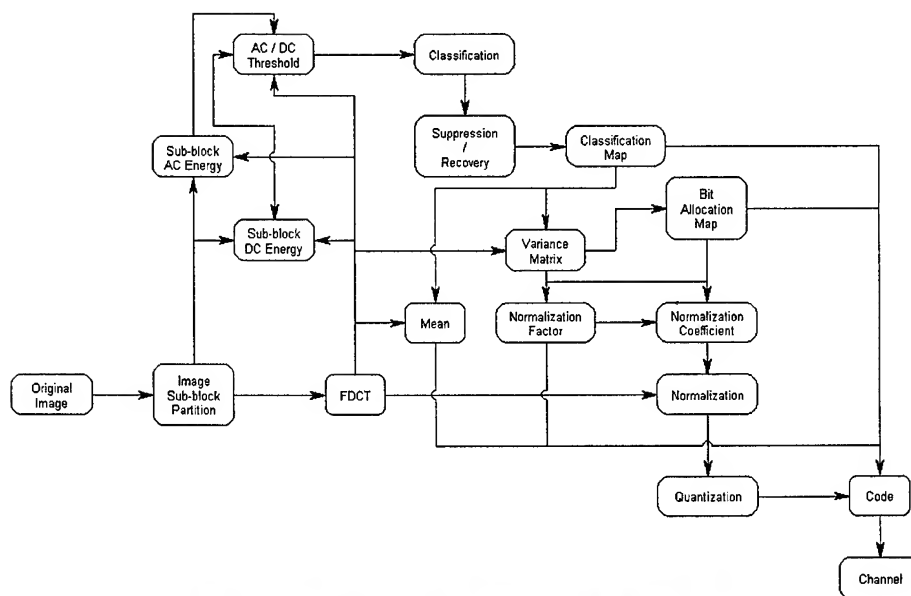


Fig. 1. Coding operations of the MADCT algorithm.

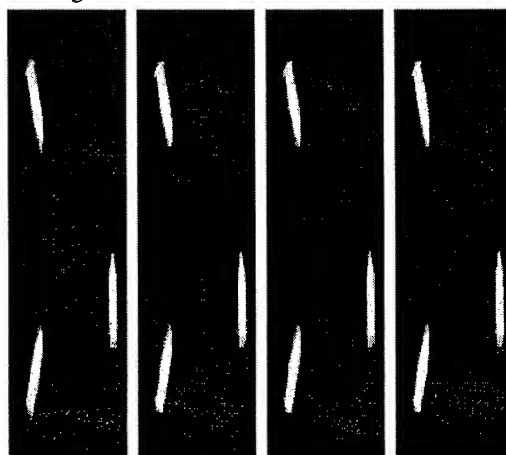


Fig. 2. From left to right: original image; decompressed images corresponding to CR=123.83 and PSNR=27.63dB; CR=167.51 and PSNR=27.69dB; CR=197.25 and PSNR=27.65dB.

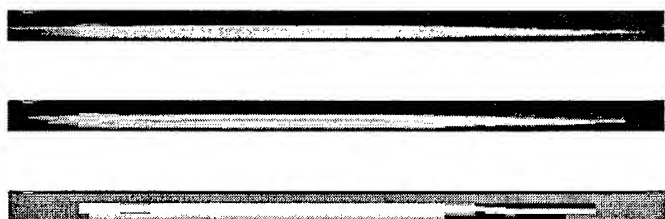


Fig.3. Original image (top); MADCT decoded image with CR=41 and PSNR=24dB (center); JPEG decoded image with CR=41 and PSNR = 15dB (bottom).

REFERENCES

- [1] W.H. Chen, C.H. Smith, "Adaptive coding of monochrome and color images", IEEE Trans. on Communications, vol.25, pp.1285-1292, Nov. 1977.
- [2] C.Y. Chang, R. Kwok, J.C. Curlander, "Spatial compression of Seasat SAR imagery", IEEE Trans. Geosc. and Remote Sensing, vol.26, pp.673-685, May 1988.
- [3] S. Bottalico, F. de Stefani, V. Sabbatino, M. Giubbolini, F. Leoni, R. Seu, "Simulation of maritime radar data", Proc. Int. Conf. Radar, Paris 1994, pp.528-533.

SPOT Image Compression Using Block Truncation Coding Techniques

Kai-Kuang Ma, Lei Huang, Shan Zhu, Anthony T.S. Ho

School of Electrical and Electronic Engineering
Nanyang Technological University
Nanyang Avenue, Singapore 639798
Republic of Singapore
Email: ekkma@ntu.edu.sg

ABSTRACT

Two most attractive block truncation coding methods, full-band *absolute moment block truncation coding* (AMBTC) and subband AMBTC (SAMBTC), are exploited to compress SPOT images in this paper. Results clearly show that SAMBTC is superior to full-band AMBTC on achieving better imaging quality, especially at low bit rates, plus other attractive system merits.

1. INTRODUCTION

With diversified and versatile applications utilizing the information extracted from remote sensing images captured by satellite, there has been increasing research interests and development in this field [1]. Unfortunately, transmission and/or storage of such images which usually consist of enormous amount of data can be quite costly, thus making image compression an attractive processing tool or functionality in the remote sensing field.

There are two fundamental categories of image compression methods: *lossless compression* and *lossy compression*. Generally, lossless compression can only achieve a small amount of compression ratio, typically about 2:1, without incurring any data loss, while lossy compression commonly yields much higher compression ratios and distortion, depending on application's requirements.

Besides the desired image quality, processing speed is another important factor to be considered. Considering some applications such as disaster mitigation, which requires efficient and even real-time transmission but with less demanding on information fidelity, a computationally simple and effective lossy compression scheme is therefore more suitable, and feasible, than lossless compression approach.

By deliberating the concerns as discussed previously, this paper experiments two most attractive block truncation coding methods, full-band *absolute moment block truncation coding* (AMBTC) [2][3] and *subband AMBTC* (SAMBTC) [4], to SPOT images. SAMBTC essentially exploits (AMBTC) into subband coding framework for gaining better

coding performance and other system merits at expense of more computation.

2. SUBBAND COMPRESSION METHODOLOGY

The principle of subband coding is based on the multi-resolution decomposition of the input signal into multiple subbands by a set of analysis filters at the encoder. Each subband is then maximally decimated and separately encoded. At the decoder, the encoded subbands are decoded, interpolated and then filtered by corresponding set of synthesis filters before being added together to reconstruct the original signal.

The proposed compression system, SAMBTC, consists of three components: (1) subband analysis and synthesis, (2) subband quantizer — AMBTC, and (3) subband dynamic bit allocation. Each subsystem is briefly described in the following subsections. For further details, refer to [4].

2.1 Subband Analysis and Synthesis

The analysis and synthesis filter banks are required to be designed in such way that the inevitable aliasing artifacts should be effectively eliminated. The *quadrature mirror filter* (QMF) bank [5] that fulfills this objective has been frequently used in subband coding.

By sequentially convoluting the QMF filters with the source image in both horizontal and vertical directions, four subbands are generated. The process can be repeatedly applied to the previously decomposed subbands to obtain more or higher levels of subband decomposition.

In this paper, Johnston's 32-tap QMF filter [5] is used to perform two-level equal-bandwidth subband decomposition. As a result, sixteen subbands are obtained.

2.2 Subband Quantizer: Absolute Moment Block Truncation Coding (AMBTC)

AMBTC has been proved to be the best 1-bit time-domain moment preserving quantizer from the aspects of computational complexity and mean-square error [5]. A fundamental requirement of AMBTC is that the input and output of this quantizer (i.e., before and after quantization)

should have identical *block mean* η and the *first absolute central moment* α , defined as follows:

$$\eta = \frac{1}{m} \sum_{i=1}^m x_i \quad (1)$$

$$\alpha = \frac{1}{m} \sum_{i=1}^m |x_i - \eta| \quad (2)$$

As pointed out in [3], AMBTC has two versions of algorithm. The version with advantages on computation and implementation is described as follows. First, the input image is divided into non-overlapping blocks. The pixels in each block are classified into two groups based on the *block mean* η using equation (1). To denote this pixel-group classification, the bitplane is generated. Two quantization levels, a and b , are computed as the mean intensities based on the pixels from the corresponding group independently. Each original pixel intensity is then quantized to a or b depending on the group it belongs to.

After quantization, only quantities a and b plus the bitplane of each block are required to be stored and/or transmitted. At the decoder, the decoding process simply substitutes levels a and b back to the corresponding pixel locations based on the bitplane information.

2.3 Subband Dynamic Bit Allocation

The image content of each subband image varies and thus results in different signal characteristics and statistical properties that affect the reconstructed image. Therefore, it is not effective to treat all the subbands equally. For that, dynamic bit allocation algorithm is designed to automatically allocate the available bits among the subbands. An optimum bit allocation algorithm subject to the Shannon rate-distortion bound using Lagrangian multiplier optimization technique was derived in [4] as follows.

For k equal subbands, the total B bits are allocated to the subbands according to the following formula:

$$b_j = \frac{B}{k} + \log_2 \left(\frac{p_j}{p_g} \right) \quad (4)$$

where b_j is the number of bits allocated to the j th subband. Quantity p_j is the average signal energy of the j th subband and defined as

$$p_j = \frac{1}{n \times n} \sum_{u=1}^n \sum_{v=1}^n I^2(u, v) \quad (5)$$

where $I(u, v)$ denotes the intensity of the pixel located at spatial index (u, v) . Quantity p_g is the *geometric mean* of the average signal energy of k subbands. That is,

$$p_g = \left(\prod_{j=1}^k p_j \right)^{1/k} \quad (6)$$

For practical concerns when using AMBTC as the subband quantizer, an optimum *sequential form* bit-allocation process is also derived in [4] and used in this paper for performance evaluation simulations.

3. SIMULATION RESULTS

The SPOT images we used in this paper were downloaded from the server of U.S. Geological Survey. They are four adjacent pictures of the map of Washington D.C. Metro. The original images are monochrome with size of 256×256 at 8 bpp. By using AMBTC and SAMBTC, they were encoded at various bit rates, and the decoded images are compared with the original ones.

The distortion is measured by the *peak signal-to-noise ratio* (PSNR):

$$PSNR = 10 \times \log_{10} \left(\frac{255^2}{MSE} \right) \text{ dB} \quad (5)$$

where MSE denotes the *mean-square error* between the original and reconstructed images. Results of independently using both full-band AMBTC and subband AMBTC coded at the same bit rates are documented in Table 1.

Note that the listed bit rates in Table 1 corresponds to full-band AMBTC window sizes at 4×4 , 8×8 , 16×16 and 32×32 , respectively. The bit allocation process as described in Section 2.3 dynamically determines the window sizes used in the subbands.

It has been reported in [4] that SAMBTC consistently and greatly outperforms AMBTC for real-world images, on both PSNR values and imaging quality, regardless the bit rates used for experiment. Due to inherited characteristics and image model of SPOT images, the results reported in Table 1 indicate that SAMBTC actually achieves slightly *lower* PSNR values than AMBTC at bit rates at 1.25 bpp and above. For the bit rates less than 1.25 bpp, SAMBTC has higher PSNR scores.

It is important to point out here that for the bit rate at 1.25 bpp and above, the SAMBTC decoded images, in fact, have better imaging quality subjectively than AMBTC counterparts, even though the corresponding PSNR values are slightly lower as mentioned above. This should not be a surprise since it is well known that the PSNR is a quantitative measurement that only approximately reflects the behavior and limitation of the human visual system. To illustrate, the reconstructed images using AMBTC and SAMBTC coded at 1.25 bpp are presented in Fig. 1. One might notice that some artificial black areas on the top of Figure 1(b) has been falsely created by the full-band AMBTC method. Overall Figure 1(c) is smoother but with less sharp edges.

For the reconstructed images coded at 1.0625 bpp and below, the SAMBTC image quality is clearly superior to the AMBTC.

Table 1: PSNR (in dB) comparison of AMBTC and SAMBTC

Image	Method	Bit-Rate, <i>bpp</i> (bits per pixel)			
		2.0	1.25	1.0625	1.01563
#1	AMBTC	28.22	25.93	24.35	23.31
	SAMBTC	27.62	25.80	25.32	25.10
#2	AMBTC	26.23	24.63	23.86	23.30
	SAMBTC	25.77	24.49	23.94	23.84
#3	AMBTC	28.94	26.81	25.60	24.73
	SAMBTC	28.38	26.71	26.37	26.20
#4	AMBTC	26.14	24.10	22.93	22.17
	SAMBTC	25.82	24.15	23.74	23.62

4. CONCLUSION

In this paper, we exploit two well developed and most attractive block truncation coding methods, *full-band* AMBTC and *subband* AMBTC (SAMBTC), to SPOT images and evaluate their coding performance in terms of the PSNR values as well as the resulting subjective image quality.

It clearly shows that SAMBTC achieves better performance than AMBTC. Most importantly, SAMBTC does not present blocking artifacts at low bit rates that might lead to misinterpretation of the image content. In addition, SAMBTC has certain attractive system merits, such as free of bit-rate lower bound, suitable for progressive image transmission, and so on [4]. Thus, SAMBTC is an attractive image coder for coding SPOT images.

REFERENCE:

- [1] R.M. Hord, *Digital Image Processing of Remotely Sensed Data*, New York: Academic Press Inc., 1982.
- [2] M.D. Lema, O.R. Mitchell, "Absolute Moment Block Truncation Coding and Its Application to Color Image," *IEEE Tans. Commun.*, vol. COM-32, no. 10, pp. 1148-1157, Oct. 1984.
- [3] K.-K. Ma, "Put Absolute Moment Block Truncation Coding in Perspective," *IEEE Trans. Commun.*, vol. 45, no. 3, pp. 284-286, Mar. 1997.
- [4] K.-K. Ma, S.A. Rajala, "Subband Absolute Moment Block Truncation Coding," *Optical Engineering*, Special Issue on Visual Communications and Image Processing, vol. 35, no. 1, pp. 213-231, Jan. 1996.
- [5] J.D. Johnston, "A Filter Family Designed for Use in Quadrature Mirror Filter Banks," *Proc. of the Int. Conf. on Acoust., Speech and Signal Proc.*, pp. 291-294, 1980.



(a)



(b)



(c)

Figure 1: Reconstructed image comparison of AMBTC and SAMBTC coded at 1.25 *bpp* using picture #1: (a) Original, (b) AMBTC with PSNR=25.93 dB, (c) SAMBTC with PSNR=25.80 dB.

Construction of Multi-resolution Terrain Models using Hierarchical Delaunay Triangulated Irregular Networks

Shu-Jeng Huang and Din-Chang Tseng

Institute of Computer Science and Information Engineering

National Central University

Chung-li, Taiwan 320

Email: tsengdc@ip.csie.ncu.edu.tw

Abstract -- For land planning or visualization, we need to model a large area of digital terrain in a graphics workstation and then display the 3-D terrain model at a general frame rate. However, the geometrical complexity of terrain models is far exceeding the capabilities of a general graphics workstation. Using a multi-resolution terrain model is one way to fit the requirement of the applications. Simplification or decimation algorithms are used to generate multiple terrain models at different detailed levels and then the models are selected to display for different situations such as distance or view scope. In this study, we concentrate on the triangulation and the level-of-detail generation of terrain models. In triangulation, we improve the performance of Palacios-and-Renuad triangulation algorithm. In level-of-detail generation, we give a new criterion to improve the accuracy of sequential multi-resolution terrain models based on the Schroder-and-Robbach, Schroeder *et. al.*, and Floriani-and-Puppo approaches. We also propose a new hierarchical structure of Delaunay triangulated models to represent multi-resolution terrain models. The hierarchical structure is a tree structure, and thus result in a better search performance than other approaches.

1. INTRODUCTION

Many applications depend on triangulated surface models to provide accurate 3-D representation of real-world objects. Applications on land planning, flight simulation, and vehicle navigation usually use triangulated surface models to model terrain for simulation, visualization, and analysis. More accurate representation and less amount of data are two important facts to these applications. In most cases, we always display a complex virtual world in a low-performance graphic workstation. If the geometric complexity of the world is far exceeding the graphic capabilities of the workstation, the display frame rate is always low. Using a multi-resolution model representation is one way to increase the frame rate. The level-of-detail models will improve the rendering performance and make real-time rendering possible, if we show a coarser model while the viewpoint is at a longer distance from terrain and a finer one while the viewpoint is at a shorter distance.

In the past few years, people have used triangulated irregular network (TIN) to describe terrain at different levels

of detail for various applications. In this paper, we propose a new criterion to generate different levels of detail for terrain models and use a hierarchical Delaunay triangulated irregular network (HDTIN) to represent these terrain models. A HDTIN is a tree structure, and has few slivery triangles. It gives good visual feeling with the help of texture mapping at any level of detail. On application, a hierarchical terrain model with n levels of detail is constructed based on the hierarchical Delaunay triangulation and a set (with n units) of predefined error threshold values, and the threshold values are defined on basis of view scope or view distance.

2. SEQUENTIAL MULTI-RESOLUTION TERRAIN MODELS

We use both Schroder and Robbach (abbreviated as S&R) [4] and Schroeder *et. al.* [5] and Floriani and Puppo [1] (abbreviated as S&FP) to generate multi-resolution terrain models. Since we want to use the multi-resolution terrain models in a terrain visualization system, the accuracy of the terrain models must be emphasized. Here, we proposed a new criterion, sliver, to enhanced these algorithms to improve the accuracy of the result multi-resolution terrain models.

As shown by Preparata and Shamos [3], if the triangle is as equiangular as possible, the interpolation will be more accurate. So we define a new weight value, *sliver*, as

P = perimeter of triangle T , and

A = area of triangle T .

$$\text{sliver}(T) = (P * P) / A \quad (1)$$

$$\text{normalized_sliver}(T) = \text{sliver}(T) / 20.78 \quad (2)$$

For an equiangular triangle, its sliver is 20.78; we use normalized sliver as defined in Eq.(2) in applications.

To generate more accuracy multi-resolution terrain models, we modify criteria of sequential level-of-detail generation proposed by S&R and S&FP with sliver enhanced criterion as following:

- (i) For criterion proposed by Schroder and Robbach [4], we modify their equations into Eqs. (3) and (4),

$$\bar{n}_{av} = \frac{\sum_{i=1}^{t_{no}} ((\bar{n}_i \cdot A_i) / S_i)}{\sum_{i=1}^{t_{no}} A_i}, \text{ and} \quad (3)$$

$$a_{max} = \max_{i=1}^{t_{no}} \left(\arccos \left(\frac{\bar{n}_{av} \cdot \bar{n}_i}{|\bar{n}_{av}| \cdot |\bar{n}_i|} \right) \right) / S_{ave}, \quad (4)$$

where

S_i is normalized_sliver of triangle i , and

$$S_{ave} = \sum_{i=1}^{t_{no}} S_i / t_{no}, \text{ and}$$

t_{no} is the triangle number of a TIN .

(ii) For criterion proposed by Schroeder *et al.* [5] and Floriani and Puppo [1], we change their equations into Eqs.(5) and (6)

$$d = |\bar{n} \cdot (\bar{v} - \bar{x})| / S_{ave}, \quad (5)$$

$$\bar{n} = \frac{\bar{N}}{|\bar{N}|}, \quad \bar{N} = \frac{\sum ((\bar{n}_i A_i) / S_i)}{\sum A_i}, \quad \bar{x} = \frac{\sum ((\bar{x}_i A_i) / S_i)}{\sum A_i}, \quad (6)$$

where

S_i is sliver of triangle i , and

$$S_{ave} = \sum_{i=1}^{t_{no}} S_i / t_{no}, \text{ and}$$

t_{no} is the triangle number of a TIN .

3. HIERARCHICAL MULTI-RESOLUTION TERRAIN MODELS

A *hierarchical Delaunay triangulated irregular network* ($HDTIN$) is a $HTIN$ with the further property that any triangulation in the hierarchy is a Delaunay triangulation. A HTM which comes from $HDTIN$ can have better approximation of terrain model than other $HTINs$.

Using a $HTIN$ to generate multi-resolution terrain model can merely replace part of terrain instead of whole terrain model. How to find a desired node in a $HTIN$ to replace part of the terrain model is main task in applications. Since we construct a $HTIN$ as a tree structure, it is easy to implement a $HTIN$ in applications by using any known tree-traverse algorithms to find a desired node to use, whether a depth-first search or width-first search can be used. The most disadvantage of a HT is its extra storage cost. It takes about 50% to 70% extra memory cost to store whole HT in real applications.

Before constructing a HT , we need to define a criterion to yield the refinement for each triangulation. One could build the HT by imposing that each triangles is refined into a triangulation containing no more than a maximum number of triangles. In this paper, we use a sequence of decreasing threshold values, indicated as $\varepsilon_1, \dots, \varepsilon_{level}$, to yield the refinement. This sequence of values also define the level number of detail; that is, a value corresponds to a level of

detail. We define a criterion function $Error(TIN)$ for each triangulation in a HT to compare with the sequence of threshold values to decide whether to stop or keep on the refinement.

We define $Error(TIN)$ as

$$Error(TIN) = \text{maximum error}_{\max}(t, v)$$

for all triangle t of TIN , where

$V(t) = \{v \mid \text{all vertices which its projection on } xy\text{-plane is inside the } xy\text{-plane-project triangle of triangle } t \text{ that is approximated by } f\}$,

$h(v)$ is the z value of vertex v ,

$f(v)$ is the approximating value of v by interpolating triangle t with f ,

$\text{error}(t, v) = \text{absolute value of } (h(v) - f(v))$, $v \in V(t)$, and

$\text{error}_{\max}(t, v) = \text{maximum error}(t, v)$, for all v in $V(t)$.

In order to get more precise multi-resolution terrain models, we use the defined sliver criterion to modify $Error(TIN)$. We replace $\text{error}(t, v)$ as

$$\text{error}(t, v) = \text{absolute value of } (v - v') *$$

normalized_sliver(t), $v \in V(t)$,

to improve the approximation of the original terrain model.

At first, we define a sequence of decreasing threshold values with dimension *level*, indicated as $\varepsilon_1, \varepsilon_2, \dots, \varepsilon_{level}$. The variable *level* also defines the level number of detail. These threshold values may be different for different DEM data.

We triangulate the origin DEM data to get first level triangulation tin_1 such that $\varepsilon_1 \leq \text{Error}(tin_1) < \varepsilon_2$. This triangulation is terrain model labeled as level 1, and is the root of the HDT . The Delaunay triangulation algorithm used here is proposed by Palacios-Velez and Renaud [2] and improved by our proposed speed-up method.

We keep on triangulating each triangle in tin_i to generate $tin_{(i+1)}$ until $\varepsilon_{i+1} \leq \text{Error}(tin_{(i+1)}) < \varepsilon_{i+2}$, for $i = 1$ to (*level*-1).

4. EXPERIMENTS AND EVALUATIONS

To show that our proposed sliver enhanced criteria can generate more accuracy models, we give four evaluation criteria used widely in geographical science for comparison: average absolute difference in elevation, root mean square error (*RMSE*), distribution of difference in elevation, and average sliver.

A *DEM* with 4347 vertices is used for demonstration. Four methods were compared on the basis of the above criteria: Method I is proposed by Schroeder *et al.* [5] and Floriani and Puppo [1], Method II is the same as method I but with sliver enhanced as described in Eqs.(5) and (6), Method III is proposed by Schroder and Robbach [4], and Method IV is the same method as method III but with sliver enhanced criterion

as described in Eqs.(3) and (4).

A few discussions were drawn based on the experiments:

- (i) The criteria functions that proposed by Schroeder *et al.* [5] and Floriani and Puppo [1] can get better approximation than the one proposed by Schroder and Robbach [4].
- (ii) Our proposed approaches with sliver enhanced criterion can really improve the accuracy of the result terrain models.
- (iii) According to normality and randomization values, we know that if we use approaches proposed by Schroeder *et al.* [5] and Floriani and Puppo [1], the vertices which are deleted from original terrain models distribute all over the models, not only cluster in a specific area, since their randomization and normality are smaller.

One ten-level experimental result of proposed hierarchical Delaunay triangulation is given to demonstrate the ability of the proposed approach. Partial multi-resolution terrain models are shown in Fig.1. The predefined refinement threshold values, indicated as ε_1 to ε_{10} , they are 98.405685, 73.968026, 59.449469, 51.985076, 46.782969, 42.829464, 30.078479, 21.860269, 15.073850, 9.581462.

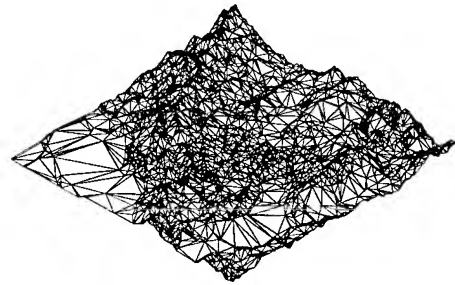
5. CONCLUSION

In this paper, we propose a hierarchical Delaunay triangulation algorithm to generate multi-resolution terrain models. With our sliver enhanced criteria, the generated terrain models can have a better approximation than by known algorithms. With our speed-up method while triangulating, we can improve the execution performance largely. However two problems still must be solved in the future :

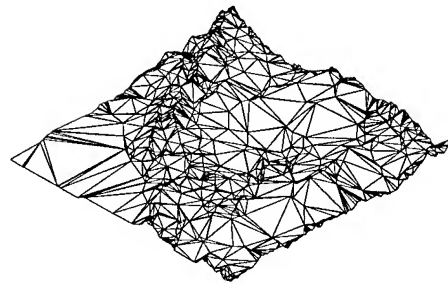
- (i) Because the proposed approach need extra memory to store the hierarchical triangulation, we can not have a real-time rendering result. How to solve this problem, we may have to limit the polygon numbers loaded into system at one time. The polygon numbers may be decided by the current frame rate while a rendering system running. In other hand, we may have to store an extra index file to make the search speed fast.
- (ii) The predefined refinement thresholds which are used to decided the level of detail are not defined automatically. How to solve this problem is still a research issue.

REFERENCES

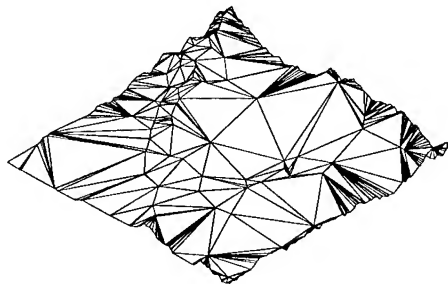
- [1] L. De Floriani and E. Puppo, "A hierarchical triangle-based model for terrain description," in *Theories and methods of spatio-temporal reasoning in geographic space*, Lecture Notes Computer Science 639, pp.236-251, 1992.
- [2] O. Palacios-Velez and B. C. Renaud, "A dynamic hierarchical subdivision algorithm for computing Delaunay triangulations and other closest-point problems," *ACM Transactions on Mathematical Software*, Vol.16, No.3, pp.275-292, 1990.
- [3] F. P. Preparata and M. I. Shamos, *Computational Geometry*. Springer-Verlag: New York, 1985.
- [4] F. Schroder and P. Robbach, "Managing the complexity of digital terrain models," *Computer & Graphics*, Vol.18, No.6, pp.775-783, 1994.
- [5] W. J. Schroeder, J. A. Zarge and W. E. Lorensen, "Decimation of triangle meshes," in *Proc. of SIGGRAPH '92, Computer Graphics*, Vol.26, No.2, Chicago, IL, Jul.26-31, 1992, pp.65-70.



Model with criterion ε_5 .



Model with criterion ε_2 .



Model with criterion ε_1 .

Fig. 1. Multi-resolution triangulated irregular networks.

WIND SPEED FORCING OF THE BULK-SKIN SEA SURFACE TEMPERATURE DIFFERENCE

W.J. Emery, C.J. Donlon. Colorado Center for Astrodynamic Research (CCAR), University of Colorado,
Boulder, Colorado, 80309

ABSTRACT

Recent studies (Wick, 1995; Donlon and Robinson, 1996) have shown that at high wind speeds the difference between bulk and skin sea surface temperature (ΔT) is constant at -0.1 K and there is no further dependence of ΔT on wind speed. To test this relationship for different seasons and a larger geographic region we examine moored buoy measurements in the Pacific of wind speed and bulk SST along with coincident estimates of the skin SST from infrared satellite measurements. In all seasons and for all locations nighttime ΔT is seen to be negatively correlated with wind speed up to 5 m/s. Above this wind speed the ΔT values cluster about a zero vertical line. During the day ΔT s for wind speeds below 5 m/s are less well correlated and the sign is positive; ΔT at wind speeds greater than 5 m/s shift from being generally positive values to generally negative values. Daytime ΔT values at higher wind speeds cluster about the vertical and lie mostly on the negative side of the zero line. Both day and night have similar RMS scatter (~ 0.35 K) for these vertical lines which is less than the RMS errors for both the strong nighttime correlations and the weaker daytime correlations.

INTRODUCTION

It is generally assumed that the difference between the bulk sea surface temperature (SST) measured at 1 m and the skin SST would be eliminated by the ocean turbulence generated at higher wind speeds. Thus, one should expect a direct relationship between wind speed and the bulk-skin temperature difference (ΔT) up to that point at which the upper layer is sufficiently well mixed to eliminate ΔT . Recently simultaneous measurements of skin and bulk SST have been examined with respect to coincident wind speeds (Wick, 1995; Donlon and Robinson, 1996). Wick (1995) found that ΔT was a function of both heat flux and wind speed with ΔT increasing with heat flux at constant wind speeds and ΔT decreasing with increasing wind speed at constant heat flux. Donlon and Robinson (1996) explored further the relationship of ΔT with wind speed concluding that at low wind speeds ΔT decreased with increasing wind speed. Above a wind speed

of 10 m/s they found that ΔT became a constant of -0.1 K with no further dependence of ΔT on changes in the wind speed. We explore the relationship between ΔT and wind speed using bulk temperatures measured by moored buoys and skin temperatures from nearly-coincident satellite overpasses from the global area coverage (GAC) data version of the Advanced Very High Resolution Radiometer (AVHRR).

DATA

The buoy data came from two sources: one was the Tropical Ocean Global Atmosphere (TOGA) buoys called the TOGA Atmosphere-Ocean (TAO) array. These data had been quality controlled and checked by the TAO office and the final results were available over the world wide web (WWW) at <http://141.142.3.76/SDG/IT94/Proceedings/EarSci/soreide/soreide.html>. The other buoy data were transmitted over the Global Telecommunication System (GTS) and are part of the NOAA's Coastal Environment Program (NCEP) Real-time Marine Observations and made available by Scott Woodruff of NOAA's Environmental Research Lab in Boulder, Colorado.

WIND SPEED VERSUS ΔT

After the filtering and processing of both the buoy and the AVHRR/GAC data we plotted the relationship between ΔT and wind speed as a scatter diagram. All of the nighttime data are plotted here in Fig. 1a with a regression line fit to the points between 0 and 5 m/s. As expected there is a moderate negative correlation between ΔT and wind speed. This is consistent with the view that under neutral conditions the skin SST is lower than the bulk SST which leads to the concept of the "cool skin" of the ocean. Above 5 m/s this relationship between wind speed and ΔT changes to scatter about 0.0 °C with an RMS value of 0.33 °C.

Switching to daytime (Fig. 1b) we see that below 5 m/s the slope of the line is now positive with most of the ΔT values being negative. In this case we can have an apparent "warm skin" which can occur when solar heating creates a diurnal

mixed layer and the net difference between the skin and the deeper bulk temperature becomes negative. The correlation for this regression line is much weaker than the negative nighttime correlation. In addition the RMS difference from the line was more than double the value for the nighttime conditions. Above 5 m/s the points again scatter about the 0.0 °C line. The RMS of the ΔT values from this line is 0.35°C which is slightly greater than the 0.33 °C RMS found for the overall nighttime comparison.

DISCUSSION

It is surprising how well the buoy and satellite data confirm aspects of the relationship between the skin and bulk SSTs (Wick, 1995) as derived from research measurements. We have extended these skin, bulk SST concepts to the study of routine measurements from moored buoys and infrared satellite sensors. The consistency of these results is clear evidence of the importance of the skin, bulk SST formation mechanisms. Furthermore the consistency between seasons for a large geographic area strongly suggests that these characteristics of the bulk-skin SST relationship hold true for all locations and seasons. These fundamental relationships are:

1. At wind speeds less than 5 m/s there is a moderate negative correlation between ΔT (bulk - skin) and the coincident wind speed for nighttime conditions. This indicates that the skin and bulk SSTs become similar as the wind increases to 5 m/s. At weaker winds (and indeed at calm conditions) the difference between bulk and skin SST are at their maximum reaching ΔT values as large as 1.8°C (cool skin).

2. During the day solar heating creates "warm skin" conditions when a thin diurnal layer is setup that causes the skin SST to be higher than the bulk SST measured below this diurnal layer. Thus the correlation between wind speed and ΔT is positive and weak due to the increased scatter from the variable daytime conditions.

3. Above 5 m/s the line bisecting the distribution of ΔT values is vertical about zero and the RMS deviation from this line is 0.35°C regardless of season. This is much smaller than any of the RMS values for the regression lines for the lower wind speeds.

CONCLUSIONS

The overall relationship between ΔT and wind speed is moderately inversely correlated at

night for weak winds and less well positively correlated during the day. Above 5 m/s ΔT values cluster about the zero line suggesting that increased turbulence caused by the higher winds is working to homogenize the upper ocean making ΔT zero. The scatter in ΔT for winds above 5 m/s is surprisingly. While there are some clear seasonal and latitudinal changes in both skin and bulk SST there appears to be relatively insignificant seasonal change in the relationship between ΔT and the wind speed.

ACKNOWLEDGMENTS

This study was supported by the National Aeronautics and Space Administration (NASA) under the Oceanography program of the Mission To Planet Earth (MTPE).

REFERENCES

Donlon and Robinson, 1996: Observations of the oceanic thermal skin in the Atlantic Ocean. *J. Geophys. Res.*, (in press)

Wick, G. A., 1995: Evaluation of the variability and predictability of the bulk-skin sea surface temperature difference with application to satellite-measure sea surface temperature, PhD dissertation, University of Colorado, Boulder, Co., 80309

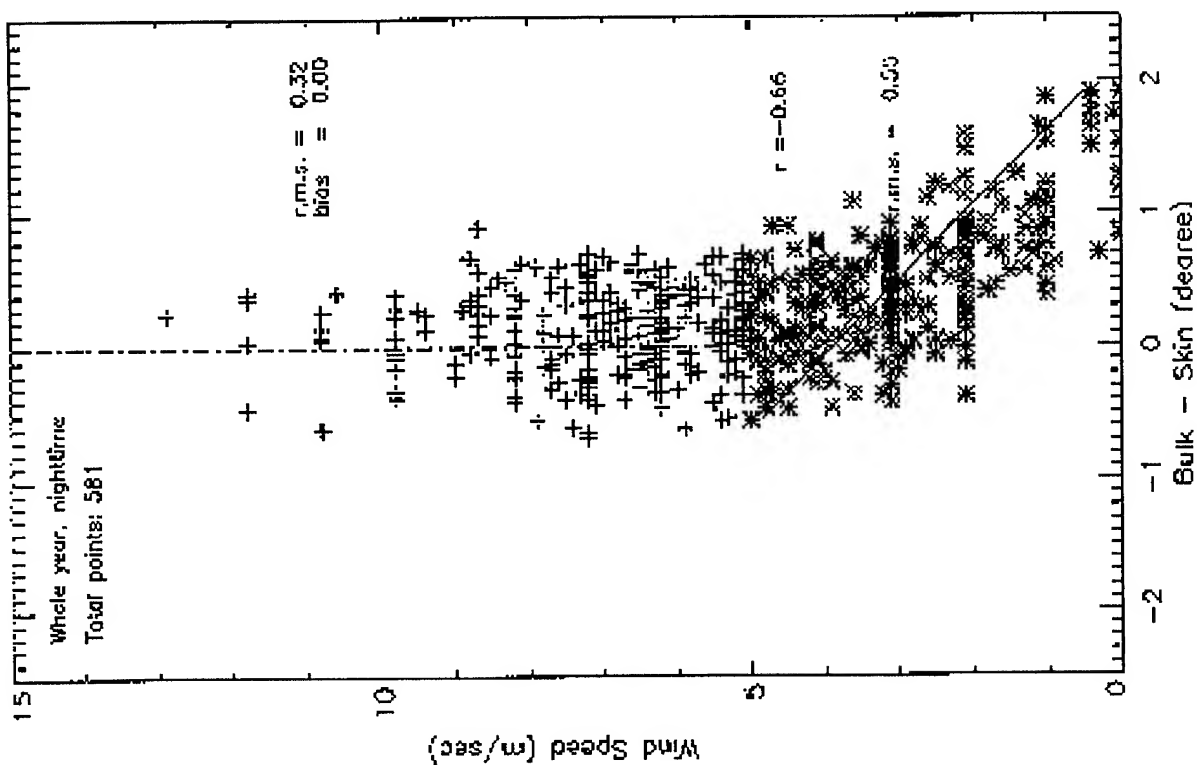


Fig. 1a. All seasons nighttime buoy wind speed versus bulk-skin SST difference (ΔT).

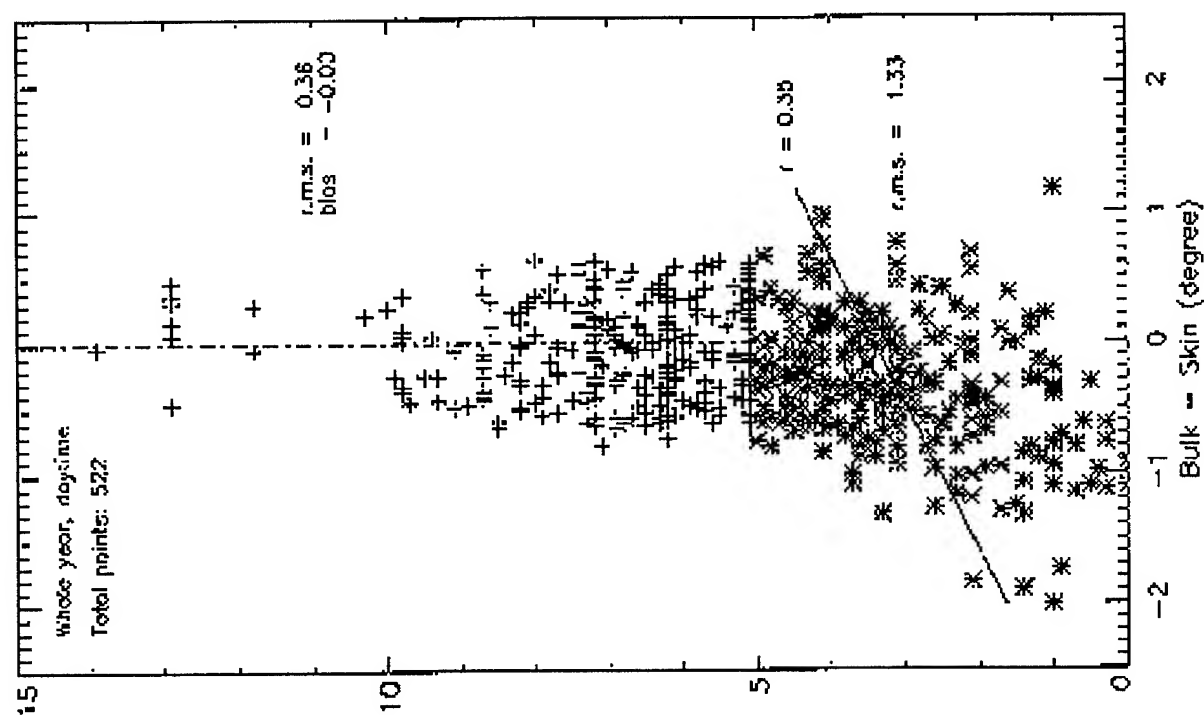


Fig. 1b. All seasons daytime buoy wind speed versus bulk-skin SST difference (ΔT).

Characteristics of the AVHRR-derived Sea Surface Temperature in the oceans around Japan

Hiroshi Kawamura and Yoshimi Kawai

Center for Atmospheric and Oceanic Studies, Faculty Of Science, Tohoku University
Sendai, 980 Japan

Tel:+81-22-217-6745/Fax:+81-22-217-6748/kamu@caos-o.geophys.tohoku.ac.jp

Abstract -- Examination of the AVHRR derived Sea Surface Temperature(SST) is carried out in the oceans around Japan. The MCSSTs(Multi-Channel SSTs) are compared with the in situ SSTs from various platforms, and revealed seasonal biases between them are discussed in detail.

INTRODUCTION

Sea surface temperature (SST) is one of the important factors influencing weather and climate, and SST is also controlled by atmospheric conditions. In order to monitor climate properly, it is necessary to obtain accurate SST data over the global oceans. The satellite observation of SST is indispensable for this purpose.

Various techniques have been proposed for deriving SST from infrared observations with satellite sensors (a comprehensive review is presented by [1]). The MCSST method[2][3] is the most popular technique. Many validation researchers have proven that the satellite SSTs derived through the MCSST algorithm agree well with in situ SSTs with rms (root mean square) errors of less than 0.7°C , and the bias between them is nearly zero over the global oceans[1].

MCSSTs IN THE OCEANS AROUND JAPAN

Sakaida and Kawamura[4] compared the MCSSTs derived from NOAA-11/AVHRR data with the in situ SSTs observed with the JMA (Japan Meteorological Agency) buoys moored in the oceans around Japan. They showed that the rms errors of the MCSSTs compared to the buoy SSTs are about 0.6°C and the coefficients determined from their data set are approximately the same as those given by NOAA/NESDIS.

On the other hand, Kawai and Kawamura[5] compared weekly averaged MCSSTs with weekly averaged in situ SSTs observed from ships and buoys in the oceans around Japan during November 1988 - May 1991. Both sets of SST data were averaged in 1° -grids. They discovered the existence of the large-scale spatial biases (the bias means an average of the difference, MCSST minus in situ SST) throughout the studied period in the regions north of the lateral 40°N , and the Tsushima and Tsugaru Warm Current regions. The biases in the former regions exceed -0.5°C , and in some areas, reach -1.0°C . Those in the latter regions are larger than $+0.5^{\circ}\text{C}$.

They[5] also found that the biases vary with a seasonal cycle in the former regions, where the biases are negative (positive) in winter (summer) and the amplitude of the seasonal bias variation is more than 2.0°C . Fig.1 shows the seasonal variations of the bias in the ocean around Japan.

The satellite infrared sensor measures the infrared radiation emitted from the surface skin of the ocean. In the SST algorithm tuning, drifting-buoy SSTs at 1m-depth are used to determine coefficients of the MCSST equations. The empirical determination is based on the assumption that the bulk-skin temperature difference is random and independent of time and space for daytime or nighttime, although the bulk-skin temperature difference, in fact, depends on many atmospheric factors, and varies.

In the oceans around Japan, a large amount of heat in the upper ocean is transferred to the cold and dry air generated over the Eurasian continent in winter, and the

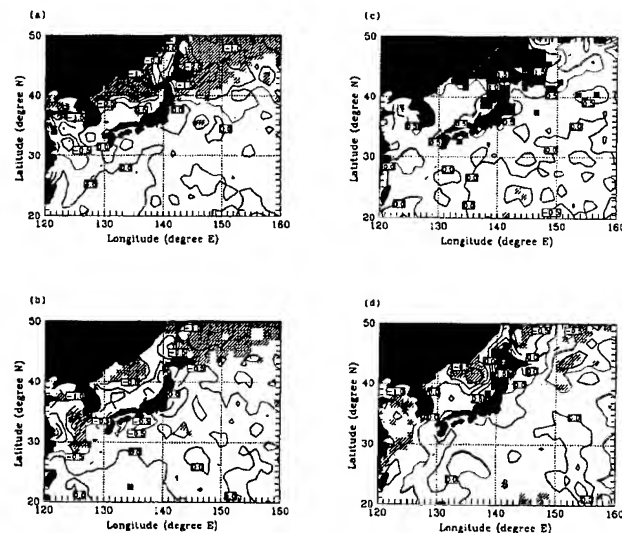


Figure 1 Seasonal variability of the bias between the daytime MCSSTs and the in situ SSTs(MCSSTs minus in situ SSTs) during November 1988-May 1991. (a)Winter (Jan.-Mar.), (b)spring (Apr.-June), (c)summer (July-Sep.), and (d)autumn (Oct.-Dec.). Positive and statistically significant biases are shaded, and negative and statistically significant biases are striped.

cold sea surface absorbs the strong solar radiation in summer. The active air-sea heat exchange over the oceans around Japan might cause a large bulk-skin temperature difference, and a large-scale spatial bias between satellite-derived and in situ SSTs is expected to appear[5].

We will investigate the reasons for seasonal and large-scale spatial biases in the oceans north of 40° N around Japan, paying particular attention to the relation between the biases and the vertical temperature structure of the sea surface layer.

DATA

In situ data

We have produced a data set consisting of pairs of SST values obtained by both methods at the same time and the same location.

We used the sea water temperature data observed with the eight thermistor-chains in the Sea of Okhotsk during July to November in 1992. Thermistor-chains are installed on moored buoys. The buoys are deployed along the coast of the Hokkaido Island on the Sea of Okhotsk, and the distance from each buoy to the seashore is about three kilometers. The locations of the eight buoys are shown in Fig.2. Sea water temperatures are measured at 1m, 3m, 5m, 10m, 15m, 20m, 25m, 30m, 35m, 40m and 45m depths, and the sampling interval of the temperatures is one hour.

Satellite data

The Center for Atmospheric and Oceanic Studies of Tohoku University has been receiving High Resolution Picture Transmission (HRPT) data from the NOAA satellites since April 1988[6][7]. We used the AVHRR data of NOAA-11, 12 received during July to November, 1992 to produce match-up sets of data. The coefficients given by NOAA/NESDIS are used. The MCSSTs derived from AVHRR using the NOAA coefficients were examined by [8].

Production of a match-up data set

The match-up data set used in this study is produced from the AVHRR scenes with cloud-free areas near the thermistor-chain locations. Cloudy pixels are eliminated by careful naked eye examination of the images. The infrared

data of 3×3 pixels around the thermistor-chain locations are sampled from the images, and averaged. Two in situ temperatures before and after the satellite observation are sampled. The temperature at the time of satellite observation is interpolated from the two in situ data. The averaged IR values and the zenith angle are coupled with the interpolated in situ temperature to produce a match-up data set.

The total number of match-up data in each month exceeds 40. In the present study, we do not discuss the dependence of the satellite-in situ temperature differences on the buoy locations. The daytime period, which is based on local times for sunrise and sunset, is 5:00-18:00 JST in July and August, 6:00-17:00 JST in September and October, 7:00-16:00 JST in November.

RESULTS

Fig.3 shows the monthly mean differences between the MCSSTs and the buoy temperatures calculated from all match-up data. The absolute values of the mean differences (biases) are almost larger than half-widths of their 95%-confidence intervals, and thus statistically significant. The scatters of the biases are larger during the day than during the night.

During the day in July and August, the difference at depths deeper than 1m increases with depth, indicating development of a temperature gradient in the surface layer. The mean MCSST is 0.5° C higher than the mean 1m-temperature only in August, while the former is lower than the latter in the other months. The bias between them is about 0.4~0.7° C in autumn. At night, the mean MCSST is always lower than the mean 1m-temperature. The bias between them is larger than that in the daytime, which is about 0.6~0.8° C in summer, 0.9~1.1° C in autumn. In the autumn, although the sea water temperatures deeper than 1m are nearly constant due to vertical mixing, there are large differences between the MCSSTs and the 1m-temperatures. Therefore, one might suggest that the difference results from the thermal structure in the layer from 0-1m in depth.

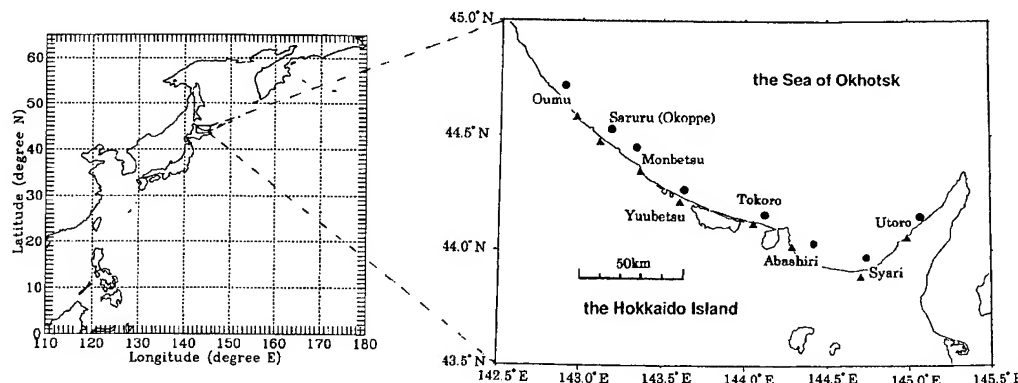


Figure 2. Locations of the eight buoys deployed in the Sea of Okhotsk (represented by solid circles, ●), and the AMeDAS stations on the Hokkaido Island (represented by solid triangles, ▲).

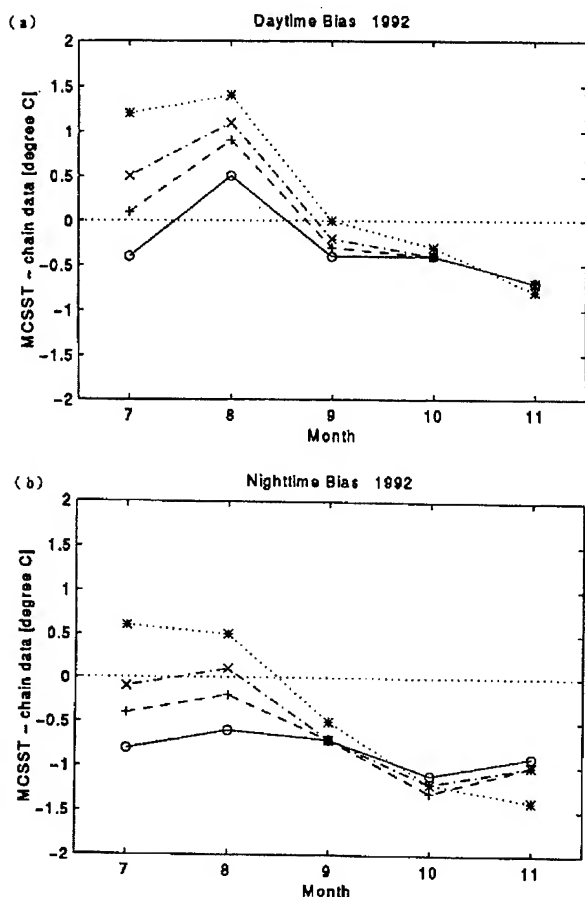


Figure 2. Variation of the monthly mean difference between the MCSSTs and the in situ sea water temperatures (a) during the day and (b) at night. The depths of the in situ observations are 1m(○), 3m(+), 5m(×) and 10m(*).

CONCLUSIONS

The analysis of the match-up data has shown seasonal and diurnal variations of the difference between the MCSST and the in situ temperature. These facts suggest that the vertical temperature gradient in the sea surface layer between 0m and 1m contributes to the MCSST-in situ SST differences, and the MCSSTs in the Sea of Okhotsk can easily be influenced by the sea surface heating or cooling.

When the 10m-temperature is regarded as the sea-truth, the biases have large values of more than 1°C and turn from positive in summer to negative in autumn. This is consistent with the result of the comparison of weekly 1° -grid data[5]. They used the SST data reported from voluntary ships, which usually observe the water temperature at depths much deeper than 1m.

ACKNOWLEDGMENTS

This study was supported by the international cooperative research program on GOOS (Global Ocean Observing System).

REFERENCES

- [1] I.J. Barton (1995): Satellite-derived sea surface temperatures: Current status. *J. Geophys. Res.*, 100, 8777-8790.
- [2] L.M. McMillin and D.S. Crosby (1984): Theory and validation of the multiple window sea surface temperature technique. *J. Geophys. Res.*, 89, 3655-3661.
- [3] E.P. McClain, W.G. Pichel and C.C. Walton (1985): Comparative performance of AVHRR-based multichannel sea surface temperatures. *J. Geophys. Res.*, 90, 11587-11601.
- [4] F. Sakaida and H. Kawamura (1992): Estimation of sea surface temperatures around Japan using the Advanced Very High Resolution Radiometer (AVHRR)/NOAA-11. *J. Oceanography*, 48, 179-192.
- [5] Y. Kawai and H. Kawamura (1997): Characteristics of the satellite-derived sea surface temperature in the oceans around Japan. *J. Oceanography*, 53, 161-172.
- [6] H. Kawamura, S. Kizu, F. Sakaida and Y. Toba (1993): The NOAA-HRPT data receiving system in the Center for Atmospheric and Oceanic Studies in the Tohoku University. *Tohoku Geophysical Journal (Science Reports of the Tohoku University, Series 5)*, 34, 89-102.
- [7] H. Kawamura, F. Sakaida and S. Kizu (1993): The AVHRR data processing system in the Center for Atmospheric and Oceanic Studies in the Tohoku University. *Tohoku Geophysical Journal (Science Reports of the Tohoku University, Series 5)*, 34, 103-114.
- [8] F. Sakaida and H. Kawamura (1992): Accuracies of NOAA/NESDIS sea surface temperatures estimation technique in the oceans around Japan, *J. Oceanogr.*, 48, 345-351.

Global and Regional Pathfinder SST Fields: Characterization and Validation

Kenneth S. Casey and Peter Cornillon

Graduate School of Oceanography, University of Rhode Island

Narragansett, Rhode Island 02882, United States of America

Telephone: (401) 874-6283, Facsimile: (401) 874-6728

E-mail: pcornillon@gso.uri.edu

Robert Evans and Guillermo Podesta

Rosenstiel School of Marine and Atmospheric Science, University of Miami

Miami, Florida 33149-1098, United States of America

ABSTRACT

As part of the National Aeronautic and Space Administration's and the National Oceanic and Atmospheric Administration's Pathfinder program in the United States, all of the five-channel Advanced Very High Resolution Radiometer (AVHRR) Global Area Coverage (GAC) data for the globe are being reprocessed to a consistent set of sea surface temperature (SST) fields. These fields, at a spatial resolution of 9.28 km and a temporal resolution of 12 hours, are available to the oceanographic community at no cost.

Following a description of the Pathfinder project our effort to validate the resulting global SST fields is presented. This effort evaluates climatologies of SST obtained from the global Pathfinder fields through a statistical comparison with the uppermost temperature value for hydrographic data in the 1994 World Ocean Atlas (WOA94) data set. The performance of the Pathfinder AVHRR climatologies is compared with that of previous climatologies and is shown to be superior to these in representing the mean SST state.

INTRODUCTION

Satellite-derived estimates of global SST from the five-channel Advanced Very High Resolution Radiometer (AVHRR) have been available for over 15 years, but their use in global change studies has been limited by time-varying biases and repeated modifications to the retrieval algorithms. The AVHRR Oceans Pathfinder project has undertaken the reanalysis of the calibration procedures and begun producing a long, consistent time-series of SST for use in climate and modeling studies. This reprocessing is based on the Non-Linear SST (NLSST) algorithm [1] and employs an extensive buoy match-up database [2] and improved cloud-clearing algorithms. Unlike the older Multi-Channel SST (MCSST) algorithm, the Pathfinder community-consensus procedures use all available retrievals and minimize sensor drift error. The Pathfinder algorithm yields both daytime and nighttime global images at a spatial resolution of 9.28 km, and upon

completion of the project images from late 1981 to present will be available.

These improvements to the satellite data set are found to produce a climatology that is better able to represent the SST field than previous in situ and blended SST climatologies. The evaluation method is based on comparisons between climatological SST and individual high-quality SST observations from research ships in the 1994 World Ocean Atlas (WOA94) data set [3]. In the following sections, the creation of the Pathfinder climatology and the means of evaluating it will be described, the results of the evaluation will be presented, and a brief discussion will be given. Several example climatological images will also be presented at the end of the paper.

METHODS

Nearly 3000 Version 1 Pathfinder fields from 1987 through 1990 were used to generate a satellite SST climatology. Version 4 Pathfinder data, which employs monthly rather than yearly coefficients and other revisions, is currently being developed but was not used in this study. Removal of cloud-contaminated pixels occurred in two steps. First, the standard Pathfinder cloud-masking routine, which is based on channel difference tests and a comparison to a reference field, was applied. Second, an "erosion" filter was applied. This filter further masks as cloudy any pixel immediately adjacent to a cloudy pixel, where the presence of the cloud edge may slightly reduce the apparent SST. The resulting fields were then averaged into calendar months to yield 12 monthly climatological fields. These 9 km monthly climatologies were nearly spatially complete for the entire globe. However, in areas of persistent cloudiness some small gaps remained. These gaps were filled using the median value of the surrounding pixels and simple linear interpolation between the previous and following monthly fields.

Several in situ and blended climatologies were also tested. The first is the Global Ocean Surface Temperature Atlas (GOSTA) which was created from volunteer observing ship data [4] and resolved to five degrees in latitude and longitude. The second in situ based climatology was the optimally-interpolated, Reynolds blended

Table 1: The standard deviation and the mean of the WOA94 anomalies for each climatology examined.

Climatology	Std. (°C)	Mean (°C)
Pathfinder, 9 km	1.49	-0.08
GISST, 1°	1.57	-0.15
WOA94, 1°	1.59	-0.10
Reynolds, 1°	1.60	-0.10
GOSTA, 5°	2.09	-0.29

SST analysis [5]. This climatology is resolved to one degree, and is based on 30 years of in situ data spanning 1950-1979 and AVHRR retrievals between 1982 and 1993. It is important to note that the AVHRR SST used in the Reynolds analysis is not Pathfinder AVHRR SST, but rather satellite SST determined using older algorithms. The third in situ climatology is comprised of high-quality, research ship-collected SST observations from the WOA94 dataset. This SST climatology also has a spatial resolution of one degree. The final climatology evaluated was Version 2.2 of the Global Sea-Ice and Sea Surface Temperature (GISST) data set [6]. This climatology blends AVHRR data and in situ observations in a manner similar to the Reynolds analysis to yield a one-degree climatology. Like the Pathfinder climatology, all of these climatologies are developed on a monthly basis.

Over 2.5×10^6 individual in situ observations between 1900 and 1993 from the WOA94 standard depth profiles were used in the evaluation of the climatologies. For each climatology being compared, the climatological SST values corresponding to the day and geographical location of the individual in situ observations were determined by linearly interpolating in time between the two closest climatological months and spatially weighting the four closest grid points in space. The high spatial resolution of the Pathfinder data obviated the need for spatial weighting, so only the temporal interpolation was performed on the satellite climatology. This process yielded daily SST anomalies for each climatology tested. The standard deviation of the anomalies for each climatology were then examined globally and by climatological monthly temperature class. The temperature classes were defined in one degree intervals by the climatological mean temperature at the location of the observation. For example, if the mean monthly climatological SST for a given observation was 18.5°C, then the anomaly was placed into the 18 to 19°C temperature class.

RESULTS

Table 1 lists the overall statistics for the comparisons made against the WOA94 in situ observations. All in situ minus daily climatological SST anomalies with a magnitude of less than 8°C, from all times and regions of the globe were incorporated into these statistics. The 9 km Pathfinder climatology anomalies have the smallest standard deviation at 1.49°C, while the GOSTA climatology anomalies have the largest standard deviation at 2.09°C.

The characteristics of each climatology are better illustrated by binning the anomalies by climatological temper-

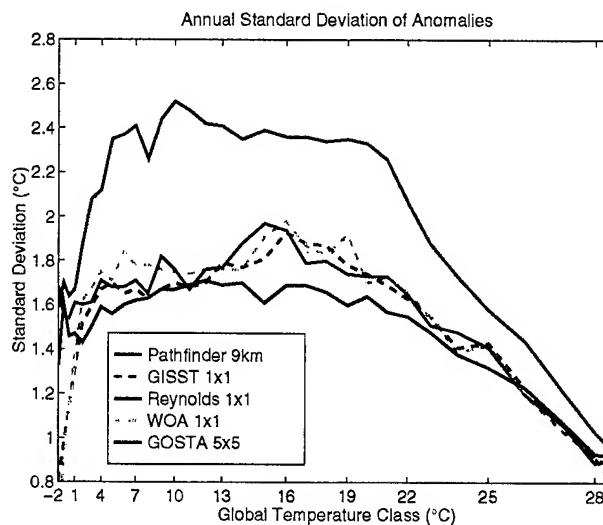


Figure 1: Annually averaged standard deviations of anomalies by temperature class.

ature class and plotting the standard deviations. Scaling the horizontal axis spacing by the relative number of observations in each class, as shown in Fig. 1, illustrates general trends toward higher standard deviations in the middle temperature classes and lower standard deviations in the warmest temperature classes for all climatologies. The Pathfinder standard deviations are significantly lower than the values for the three one-degree climatologies in all temperature classes between 1°C and 26°C, except for 8°C to 12°C where F-tests for significance indicate the Pathfinder and GISST values are not statistically different. The satellite and one-degree climatologies show much lower standard deviations than the five-degree GOSTA climatology everywhere. In temperature classes warmer than 26°C, the Pathfinder standard deviations are either not significantly different from, or slightly higher than the values for the one-degree climatologies.

DISCUSSION

The results of this study indicate the 9 km Pathfinder climatology is better able to minimize the anomaly standard deviations than the in situ and blended climatologies in all but the very warmest temperature classes. High water vapor content, persistent cloudiness, and atmospheric aerosols in the tropics may be contributing to the Pathfinder algorithm's relatively poor performance in those regions. Overall, however, the Pathfinder standard deviations are lower than those for the in situ climatologies by 0.08 to 0.60°C, and even in the warm tropical regions the Pathfinder climatology performs comparably to the one-degree climatologies.

ACKNOWLEDGMENTS

This research was performed with support from the National Aeronautic and Space Administration

(NAGW3009), and; from the State of Rhode Island and Providence Plantations through salary support to P. Cornillon. The satellite data processing software was developed by R. Evans, O. Brown, J. Brown and A. Li of the University of Miami. Their continued support is greatly appreciated.

REFERENCES

- [1] C.C. Walton. Nonlinear multichannel algorithms for estimating sea surface temperature with AVHRR satellite data. *Journal of Applied Meteorology*, 27:115-124, 1988.
- [2] G.P. Podesta, S. Shenoi, J.W. Brown, and R.H. Evans. AVHRR Pathfinder Oceans Matchup Database 1985-1993 (Version 18). Technical report, University of Miami Rosenstiel School of Marine and Atmospheric Science, 1995.
- [3] S. Levitus and T. Boyer. World Ocean Atlas 1994, Volume 4: Temperature. NOAA Atlas NESDIS 4, NOAA National Environmental Satellite, Data and Information Service, Washington, D.C., 1994. 117 pp.
- [4] M. Bottomley, C.K. Folland, J. Hsiung, R.E. Newell, and D.E. Parker. Global ocean surface temperature atlas (GOSTA). Technical report, Joint Meteorological Office/Massachusetts Institute of Technology Project, HMSO London, 1990.
- [5] Richard W. Reynolds and Thomas M. Smith. A high-resolution global sea surface temperature climatology. *Journal of Climate*, 8:1571-1583, 1995.
- [6] D.E. Parker, M. Jackson, and E.B. Horton. The 1961-1990 GISST2.2 sea surface temperature and sea-ice climatology surface temperature and sea-ice climatology. Technical Note 63, Hadley Centre for Climate Prediction and Research, Meteorological Office, London Road, Bracknell, Berkshire RG12 2SY, 1995.

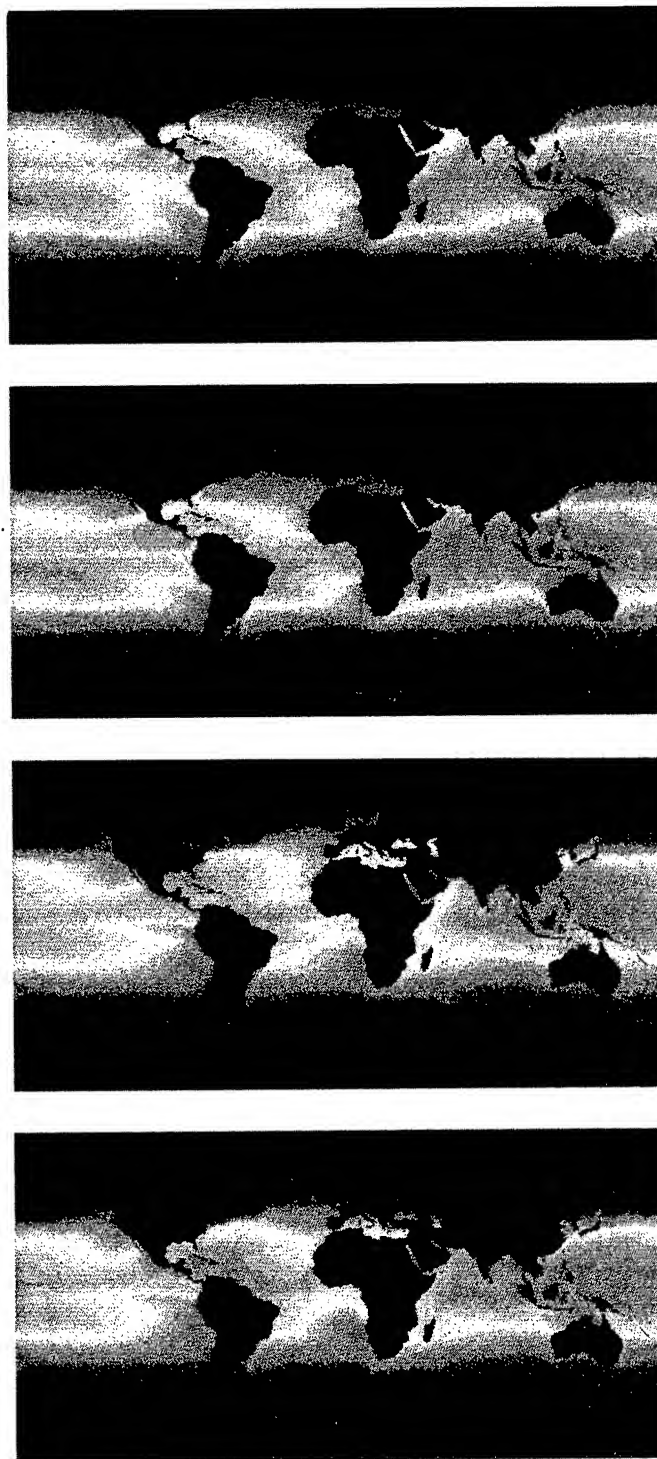


Figure 2: Pathfinder SST climatologies, from top to bottom, for January, April, July, and October

Measurement of Interferometer Instrument Line Shape

N C Atkinson and S H S Wilson

United Kingdom Meteorological Office (UKMO), Remote Sensing Branch
Building Y70, DERA Farnborough, Hampshire GU14 6TD, UK

Tel: +44-1252-395860 Fax: +44-1252-515523 Email: swilson@meto.gov.uk

Abstract – The UKMO has developed an airborne interferometer 'ARIES' to act as simulator for future satellite-based infrared sounders. In order to characterise anomalies in ARIES observations of atmospheric scenes, methods have been developed to experimentally determine interferometer Instrument Line Shape (ILS) rather than relying on simulation.

I. INTRODUCTION

A new generation of infrared satellite sounders are currently under development, to provide improved observations of atmospheric temperature and humidity profiles for operational meteorology. These new sounders, which include IASI, the Infrared Atmospheric Sounding Interferometer, offer considerably higher spectral resolution and spectral coverage than previous meteorological sounders, e.g. HIRS [1], with the intention of yielding both higher vertical resolution and accuracy in the retrievals. The feasibility of retrieving the improved data from such higher resolution sounders has been demonstrated experimentally, using HIS – the High-resolution Interferometer Sounder instrument mounted on the high-flying NASA ER-2 aircraft [2].

Recently, the UKMO has developed an infrared interferometer called ARIES – the Airborne Research Interferometer Evaluation System [3] as a simulator for the forthcoming satellite sounders, in particular IASI. At its heart, ARIES has a commercial interferometer (BOMEM MB200, $\sim 1 \text{ cm}^{-1}$ resolution). The system has two detectors; a Mercury Cadmium Telluride (MCT) detector is sensitive to the wavelength range $5.5 - 16 \mu\text{m}$ ($600 - 1800 \text{ cm}^{-1}$) and an Indium Antimonide (InSb) detector covers the range $3.3 - 5.9 \mu\text{m}$ ($1700 - 3000 \text{ cm}^{-1}$). A pointing mirror assembly has been developed to allow ARIES to view the scene at various angles, and to allow the instrument to view a pair of on-board calibration targets. ARIES can be used on the ground, but in its airborne role it is mounted on the UKMO C-130 research aircraft.

Through analysis of preliminary ARIES observations an anomaly was identified in the data from the MCT detector; no such problem was identified with data from the InSb detector. It was initially suspected that the anomaly resulted from a genuine optical characteristic of the instrument and therefore a number of techniques were developed to characterise the interferometer (i.e. measurement of instrument line shape, ILS). Ultimately, the cause of the anomaly was found to lie elsewhere, however this experience emphasises the need for thorough characterisation and testing

of an instrument before relying on the data. This is especially true for a space-borne instrument such as IASI.

II. DEFINITION

An important characteristic of interferometers is the Modulation Transfer Function (MTF) and the related Instrument Line Shape. In order to define these terms, it is helpful to consider the operation of a basic interferometer. The scene radiation incident onto such an instrument is partially reflected and partially transmitted by a beamsplitter. A variable optical path difference (OPD) is introduced between the reflected and transmitted paths, prior to recombination of the beams. The resulting interference pattern is monitored as a function of the path difference; this so-called 'interferogram' contains all the spectral information about the source, which can be recovered using the technique of Fourier transform. The instrument MTF describes the modulation of the interferometer signal as a function of OPD, by virtue of the design of the instrument. This is also known as the self-apodisation function, and is ideally uniform over the OPD range. The equivalent information in the spectral domain is known as the Instrument Line Shape (ILS).

III. MEASUREMENT OF ILS/MTF

Characterisation of the ILS/MTF is a basic requirement in the analysis of atmospheric spectra recorded using Fourier transform spectrometers. Frequently, a simulated line shape is assumed. This model line shape may be tested by comparison of atmospheric spectra with radiative transfer simulations, which assume that line shape. However, it would be more desirable to develop a direct, experimental method of characterising the ILS/MTF. For ARIES, a number of methods to determine this information have been attempted:

- Comparison of ARIES atmospheric measurements with line-by-line radiative transfer simulation (e.g. GENLN2/HITRAN).
- Comparison of ARIES measurements of spectral features from a single gas (i.e. in a gas cell) with those of a well characterised, higher resolution instrument or simulation.
- Direct measurement using a laser source as a well characterised input source.

Considering the first of these methodologies, fig. 1 shows part of the ARIES spectrum ($600 - 850 \text{ cm}^{-1}$) of the *upwelling* radiance, recorded during a high-level aircraft

run in clear-air at approximately 17000 ft (March '96, Southwest approaches to UK). Fig. 1 also shows another part of the ARIES spectrum ($750 - 950 \text{ cm}^{-1}$) of the *downwelling* radiance, recorded during the same run. The results of line-by-line radiative transfer simulations (GENLN2/HITRAN) are shown for comparison. The main spectral feature is due to CO_2 emission, centred at $\sim 670 \text{ cm}^{-1}$. It is clear that the amplitude of the sharp spectral features in the simulation is far greater than that observed experimentally. For the view of the downwelling radiance, the simulation predicts near-zero radiance in the atmospheric window region ($800 - 950 \text{ cm}^{-1}$), as expected. However, the experimental view shows oscillating negative radiances in this region. No such differences are observed for the ARIES InSb detector data. The amplitude discrepancy was originally thought to have resulted from an anomalous instrument ILS/MTF, and as such, spawned the measurement campaign described in this paper. The experimentally observed negative radiances in the atmospheric window region were thought to be unconnected to this problem and most likely explained in terms of poor calibration of very cold scenes. In truth, both of these assertions now appear to be incorrect, however the methods developed to probe the instrument ILS/MTF should be very useful elsewhere, and are now described.

III.1 Gas cell measurements

Here, lab-based single-gas ARIES spectra are recorded, using a gas cell. The intention is to compare the spectra with those recorded by a higher resolution, well characterised instrument (or simulation) in order to derive the ARIES ILS/MTF. Three experimental configurations were used:

1. Gas cell in emission: ARIES views a gas cell with a liquid nitrogen black-body target immediately behind the cell. Requires measurement of the gas cell temperature.
2. Gas cell in emission and absorption: ARIES views a gas cell with a warm black body behind the cell.
3. Gas cell in absorption: The gas cell is placed *inside* the optical head, immediately in front of the detector. Thus thermal emission from the gas cell does not contribute to the modulation of the measured interferogram.

In all three cases, the method involves taking readings with the cell containing the gas and then with the cell evacuated. By consideration of the optical components in the system, it can be shown that for cases 1 and 2, the transmission is given by:

$$T = \frac{R_{\text{gas}} - B}{R_{\text{vac}} - B} \quad (1)$$

where R_{gas} is the measured radiance with the gas cell full, R_{vac} is the measured radiance with the cell evacuated, and B is the Planck function at the temperature of the cell. The standard ARIES calibration procedure is described elsewhere [3]. For case 3, the transmission is given by:

$$T = \frac{S_{\text{gas}}}{S_{\text{vac}}} \quad (2)$$

where S is the raw spectrum obtained by Fourier transform of the interferogram. Having recorded the transmission spectrum by one of these methods, the MTF can be calculated as follows: select an appropriate spectral region, Fourier transform to the 'interferogram domain' and divide by the result obtained from a reference instrument/simulation treated in the same way. Note that this procedure requires that the reference spectrum is interpolated onto the same frequency grid as the ARIES spectrum. Also prior to the division, the spectra are squared to give a 'power' interferogram and smoothed to remove the sinusoidal component. The MTF itself is therefore the square root of the division result.

Measurements were carried out using a 90 mm long cell, with 47 mm diameter KBr windows. The gas cell was typically filled to a pressure of 50 mb; the gases used and relevant spectral bands are detailed below. Reference

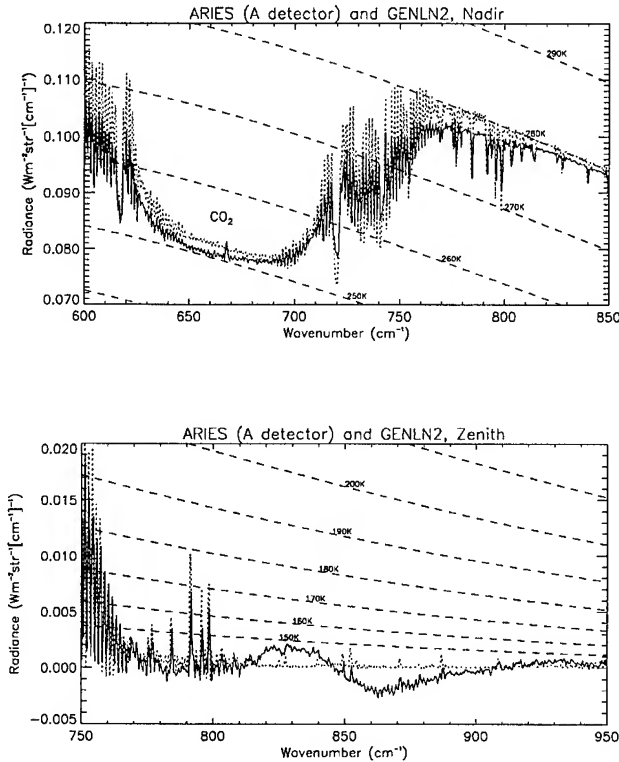


Figure 1: Nadir view (upper) and Zenith view (lower) spectra. In both cases, the ARIES spectrum is the solid curve and the GENLN2 simulation is shown dotted. Also shown are representative black-body temperature curves (dashed).

measurements using the same gas cell and gas fill were recorded using a Bruker IFS 120HR high resolution interferometer (resolution $\sim 0.1 \text{ cm}^{-1}$).

Gas	Spectral Bands (cm^{-1})
CO ₂	600-750, 2220-2420
N ₂ O	1100-1350, 2100-2300, 2400-2650
CH ₄	1150-1400, 2600-3200
CO	2000-2250

Fig. 2 shows the derived MTF from CH₄ gas cell measurements, for the ARIES MCT detector. This result is far from that expected; the MTF should be close to 1.0 near zero OPD, but in fact rapidly drops as low as 0.6. Results for the InSb detector showed no such anomaly.

III.2 Laser measurements

The gas cell technique described above has the advantage that spectral features are available to characterise most of the range of the ARIES detectors, however the method remains indirect, i.e. requiring a comparison. The use of a high resolution laser source affords direct measurement of the ILS/MTF, however the available sources in the thermal infrared are limited. In the measurements described here, a high resolution ($<0.1 \text{ cm}^{-1}$) CO₂ laser, operating at selected frequencies in the range 900 - 1100 cm^{-1} , was used. The laser was equipped with a monochromator, to allow selection of a single laser line.

In these experiments, the laser beam was expanded using a lens onto a screen; the beam size at the screen filled the ARIES acceptance cone. The laser power was attenuated such that the radiance was within the normal range observed by ARIES. In order to correctly allow for the presence of the thermal background in the interferogram signal, data were recorded with the laser off, both before and after the laser 'on' measurement. The 'difference' interferogram was obtained by averaging the two laser 'off' measurements (to allow for any drift) and subtracting from the laser 'on'

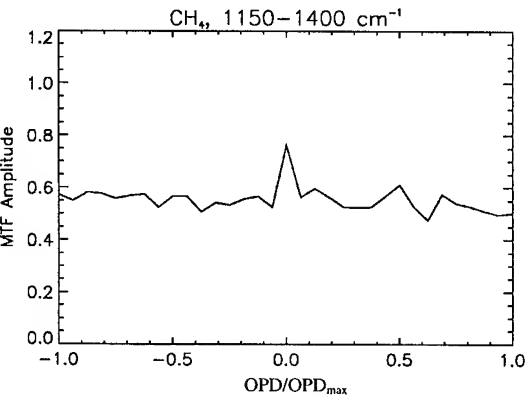


Figure 2: MTF derived from CH₄ transmission

measurement. The amplitude of the 'difference' interferogram is proportional to the MTF and can be normalised to unity at zero OPD if required.

Fig. 3 shows the unnormalised modulation amplitude as a function of OPD for various laser powers. There appears to be a feature at zero OPD, which is similar to that observed in the gas cell measurement. The feature is most apparent when the laser power is comparable with the thermal background, but diminishes as the laser power is further reduced. Fig. 4 shows an example of the results in the spectral domain. Note that there are unexpected differences between the laser 'on' and laser 'off' curves at frequencies well away from the main laser frequency (e.g. differences at 830 cm^{-1}).

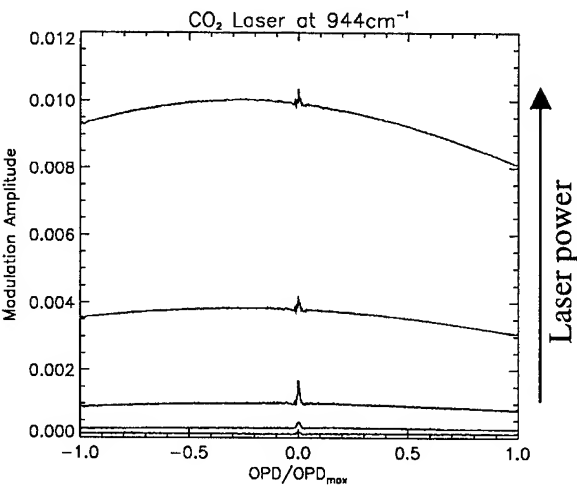


Figure 3: Modulation plots for ARIES viewing CO₂ laser source at various laser powers (increasing in vertical).

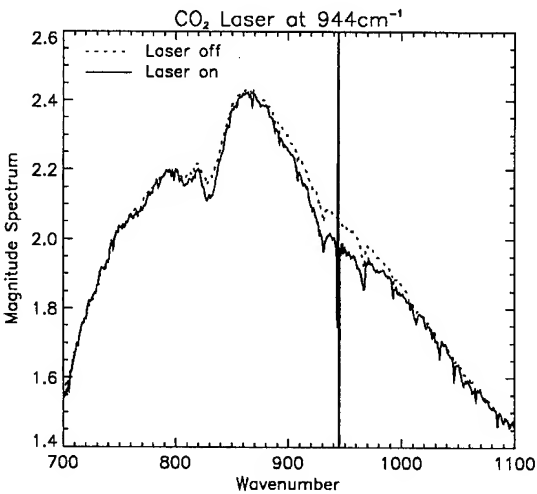


Figure 4: Raw spectrum observed for CO₂ laser 'on' (solid) and 'off' (dashed) measurements.

IV. ANOMALOUS MCT DETECTOR RESPONSE

The main results from the laser-based measurements indicate that the MTF anomaly varies with source power, being particularly important at low power, and that the thermal background is itself changed by the presence of the laser signal, at frequencies well removed from the laser line centre. These observations cannot be rationalised in terms of a simple optical characteristic of the instrument, as thought originally. It also became apparent that the observation of oscillating negative radiances in the atmospheric window measurement region of the aircraft spectra (§III) was potentially linked to the true source of the MTF anomaly rather than resulting from inadequate calibration of cold scenes.

A hypothesis was then made that the MCT detector/amplifier chain was nonlinear for small signals, showing a form of crossover distortion (reduced gain at low signal levels). Thus the interferogram centreburst would be unaffected, but the amplitude of the interferogram away from the centreburst would be reduced. This hypothesis was confirmed by direct injection of an electronic signal into the preamplifier. It was shown that the *digital* output from the analogue to digital converter (ADC) was interfering radiatively with the preamplifier input --- the signal could be seen to return to its 'correct' level at the end of each scan when the ADC was momentarily quiescent. Thus the cause of the anomaly was electronic in nature rather than optical, even though this was not apparent from the initial evaluation of the flight data. The instrument is now being modified by BOMEM in order to eliminate this interference.

A crude correction function has been formulated, based on these laboratory measurements. Fig. 5 shows the effect of applying the correction function to the ARIES interferograms used to generate Fig. 1. The agreement between ARIES and the GENLN2 simulation is considerably improved both in terms of the amplitude of the spectral features and the absence of oscillating negative radiances in the atmospheric window region (Zenith view). However, to derive an accurate MTF from the comparisons or from gas cell measurements it will be necessary to repeat the measurements with the ARIES electronics fixed.

V. CONCLUSIONS

Various methods for the measurement of interferometer ILS/MTF have been described. The most direct of these involves the use of an infrared laser as a well-characterised source. An alternative gas-cell based technique is less direct, but has the advantage of wide spectral coverage. Even though anomalies in the UKMO airborne interferometer data were not found to be due to genuine optical effects, the methods developed in this investigation should be useful for the experimental characterisation of other interferometer-based instruments.

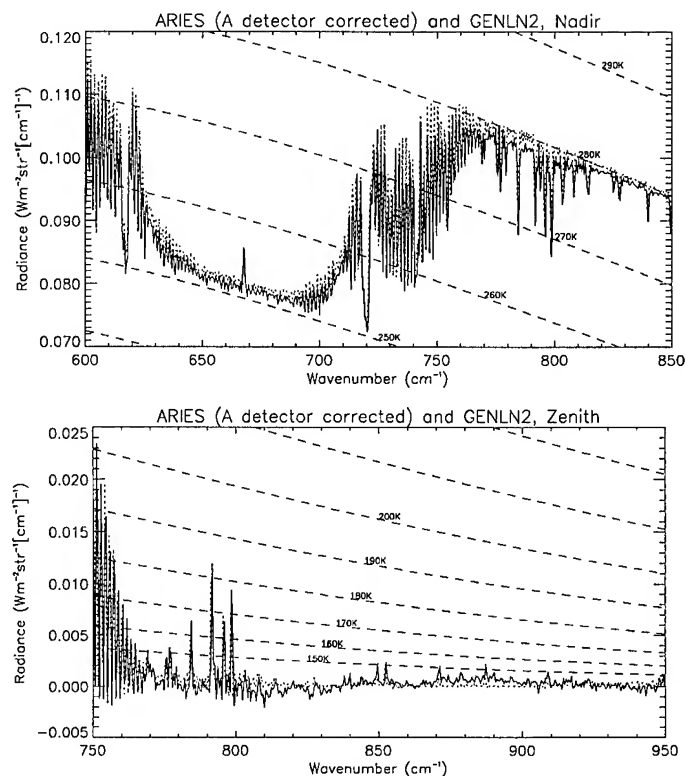


Figure 5: Nadir and Zenith ARIES data from the MCT detector (as fig. 1), corrected for amplifier nonlinearity.

ACKNOWLEDGEMENTS

We thank Drs J Ballard and D Newnham (Rutherford Appleton Laboratory) for assistance with the gas-cell measurements, Dr J M Vaughan (DRA Malvern) for provision of CO₂ laser facilities and M. J Giroux (BOMEM Inc.) for helpful discussions, particularly relating to the simulation of ILS/MTF. We also thank our colleagues at the Met. Office (Dr A C L Lee, Dr J A Smith and Mr P J Rayer) for their advice.

REFERENCES

- [1] J.R. Eyre, "The information content of data from satellite sounding systems: A simulation study," Q.J.R. Meteorol. Soc., vol 116, pp. 401-434, 1990.
- [2] H-L. Huang, W.L. Smith and H.M. Woolf, "Vertical Resolution and Accuracy of Atmospheric Infrared Sounding Spectrometers," J. Appl. Meteor., vol. 31, pp. 265-274, March 1992.
- [3] for full details of ARIES, see S.H.S. Wilson *et al*, "ARIES - a simulator for the next generation of spaceborne IR meteorological sounders," IGARSS 97, *in press*.

Progress on the SASAR System : First Results

M da Silveira¹, J Horrell², M Inngs², E Avenant¹

[1] Aerotek, CSIR

P.O. Box 395, Pretoria, South Africa, 0001

Phone : +27 12 841 4831 / Fax: +27 12 349 1766 / E-Mail : mdsilvei@csir.co.za

[2] Radar Remote Sensing Group, Dept. Electrical Engineering, UCT

Private Bag, Rondebosch, South Africa, 7701

Phone : +27 21 650 2792 +27 21 650 2799 / Fax : +27 21 686 7427

E-Mail : jhorrel@uct.ac.za mikings@eleceng.uct.ac.za

Abstract --The South African VHF SAR System (SASAR-1) has been successfully integrated and tested on the ground. Due to a required verification of the antenna mounting base design, the system could not yet be installed onboard the aircraft. A digital radio frequency memory (DRFM) was used to simulate a point target return from a certain range. This was used to measure the point spread function of the system. This paper reports on the progress of the system up to the first ground evaluation of the system and briefly discusses the new SASAR-2 system.

INTRODUCTION

The development, ground integration and system ground tests of the South African VHF SAR System (SASAR) has been completed successfully. The system will be installed on board a Boeing 707. This platform was chosen because of the following reasons:

- It can achieve a high altitude (33000 ft) allowing for long ranges.
- The wing is angled backwards relative to the velocity vector resulting in less reflection.
- There is no unknown propeller modulation,
- The platform is more stable making the creation of the long VHF synthetic apertures at long ranges easier.
- A high coverage rate is maintained because of the high speed of the platform.
- The antenna array is large, requiring a large fuselage diameter.
- The data can be combined with other sensors already installed in this platform.

The antennas will be installed on a mounting base which attaches to a number of already available mounting points on the left side of the aircraft. The South African Airforce (SAAF) Boeing 707 with the fitted antenna mounting base is shown in Fig. 1. The mounting base has been manufactured, but the SAAF requires additional safety verification before the antenna base can be used in flight. Indications are that the first test flight will only be in August.



Fig. 1 : Boeing 707 with Antenna Attached Mounting Base

This paper gives a technical overview of the current system, the ground test results as well as a brief discussion of the new SASAR-2 system.

SWATH CHARACTERISTICS

The system is designed for full polarimetric operation. Although only a single polarisation is currently implemented, an extension to the multi-polarisation capability is trivial as will be explained later. The swath characteristics of the system is shown in Table 1.

SYSTEM HARDWARE

The functional block diagram of the system is shown in Fig. 2. The system consists of the Transceiver Group, Signal Processor Group, Digital Recording Group, Systems Support Group and the Ground Support Group. Each of the functional groups will be briefly discussed below.

Transceiver Group

The transceiver consist of the T/R switch, transmitter, receiver, exciter, coherent oscillator and antenna. The bandwidth of whole transceiver group is 12 MHz. The antenna consists of an array of 3 (azimuth) x 2 (elevation)

Table 1 : Swath Characteristics

Parameter	Value
Best Resolution	13 m
Number of Range Bins	4096
Pixel Spacing Slant	10.55 m
Nominal Swath Start (from Nadir)	10 km
Swath Width (Slant)	43.2 km (single polarisation)
(at 13 m resolution)	14.4 km (full polarisation)
Coverage Rate (Single Pol at 400 knots)	556.8 km ² /min
Nominal Incidence Angle (Near)	45°
Nominal Incidence Angle (Far)	80°

elements. Each element consists of a horizontal and vertical monopole. The monopoles are inclined with respect to the ground plane normal. This increases the strength of the elements as well as fills in the null of the normal monopole pattern. The array depression angle is 22.5°, and the elevation and azimuth half power beamwidths are 48° and 50°, respectively.

The transmitter is a class A amplifier with a average power handling capability of 1 kW. A high power multi-polarisation T/R switch has been developed.

The receiver is fitted with a STC function and digital gain control. In order to limit the cost of the system, only a short monochrome pulse with a minimum length of 87.5ns is transmitted. This pulse length can achieve a range resolution of approximately 13 m.

Signal Processing and Recording Group

The signal processor group consists of an A/D converter, three high bitrate recorders (HBR's), a real-time processor

and a ground processor. The maximum sampling rate of the A/D cards is 25 MHz. The high bitrate recorders perform pre-summing of the data whereafter it is recorded on the hard disks at a required 640 kBytes/s. The recording capacity of the hard disks is two gigabyte, giving a recording time of just under one hour sustained. Auxiliary data (time stamping as well as PRI identification) is recorded together with the raw SAR data. The PRI ID data is required in order to verify afterwards that all the range lines were recorded. By increasing the PRF by three and using time multiplexing, only one receiver and A/D converter is used to generate the multi-polarisation data. The unambiguous range is also reduced by three when using this scheme. Currently only one A/D, one HBR and one hard drive is used. As soon as all the system tests are completed, two more HBR cards will be developed for a multi-polarisation capability.

The real-time processor (RTP) consist of a 266MHz DEC Alpha. The RTP is mainly used to ensure image quality and to select areas of interest for full resolution ground processing afterwards. The processor uses a quasi-focused algorithm without motion compensation. The RTP can achieve a resolution of 30 m in range and azimuth and has 1024 range bins which can be positioned across the swath.

Ground Support Group

The ground support group will consist of a data handling unit and the ground processor. The data handling system will be implemented at a later stage. The ground processor is based on the range-doppler algorithm. It will initially run on the DEC Alpha (also used for the RTP). The ground processor receives the raw data from the 2 GByte hard drive as well as the motion data which is recorded on the console system recorder.

Control and Interface Group

The control and interface group consists of the timing card and the console system. Control of the system is via the timing card. The radar user interface is the console system, which consist of a standard 486 PC. The inertial data is recorded on the console system recorder.

System Support Group

The system support group consists of the inertial platform, power supply system, mounting rack and other support items. The inertial measurement unit, a Marconi FIN31110 ring laser gyro, is supplied by Kentron. The power supply converts the 115 V of the aircraft to 220 V for the high power transmitter.

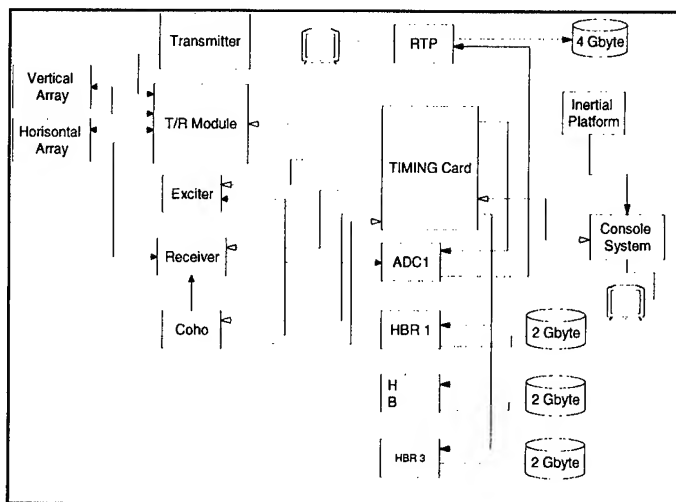


Fig. 2 : SASAR Functional Block Diagram

SYSTEM TEST RESULTS

The system was integrated at Simonstown. A large corner reflector antenna with a 40° beamwidth was used to direct the energy towards False Bay. Large interference was observed within the system band. After increasing the system average power (by increasing the pulse length) and setting the receiver gain just below saturation by the interference, the first range returns from the mountains in the vicinity of False bay were observed. Returns from mountains approximately 55 km away could also be observed.

The first tests indicated an unacceptable signal to interference ratio. Pulse compression is required to provide more average transmitted power and thus improve the signal to interference ratio. In order to further evaluate the system, it was decided to measure its point spread function using a DRFM. The DRFM has the capability to detect an incoming signal and sample this signal. The range to a point target can be programmed into the DRFM. It transmits the incoming signal back after a delay and with the phase associated with the programmed range. This procedure is repeated within every PRI for the whole synthetic aperture. The data is recorded on the HBR disk and processed afterwards. The point target will be visible within a certain number of range bins. Using this system, the point spread function from a ground range of 5 km, an aircraft speed of 236 m/s and a height of 10 km is shown in Fig. 4.

TEST AND DEDICATED FLIGHTS

The first test flight will probably be conducted in August 1997. It will be around the coastal area of Cape Town. The initial test flight will be the system structural qualifications, followed by the actual imaging flight. A number of dedicated

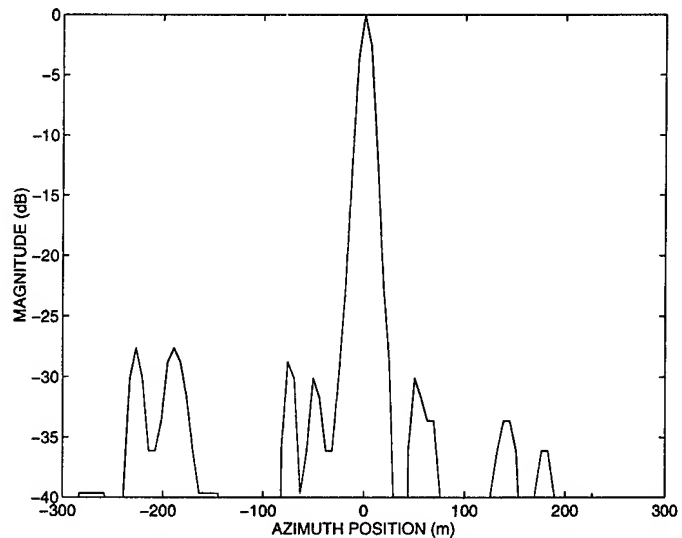


Fig. 4 : SASAR measured azimuth point spread function as generated by the DRFM

experiments will be conducted thereafter. The first experiment will be the first order system calibration. The other experiments will mainly be focused on foliage penetration, ground penetration, ship detection and target recognition applications.

SASAR-2 UPGRADE

The definition for the upgrade to the SASAR-1 system, called the SASAR-2 system has begun. The system will initially be a X-band system with long range, high resolution stripmap and spotlight capabilities. Thereafter, an L-band stripmap system will follow. Advanced features such as interferometry at X-band and MTI at L-band are planned. The X-band system planned development time is three years. The system will initially also be installed on the Boeing 707 platform, but it is designed to be used on any pressurized platform.

CONCLUSIONS

The development, integration and ground testing of the SASAR-1 system was completed successfully. Qualification of the antenna mounting base has delayed the first system test flights, which is now planned for August 1997. The definition phase of the new SASAR-2 system upgrade has begun.

ACKNOWLEDGMENTS

The authors wish to express their appreciation to S. Cronje and T. Küsel from Aerotek for their contribution towards generating the DRFM returns.

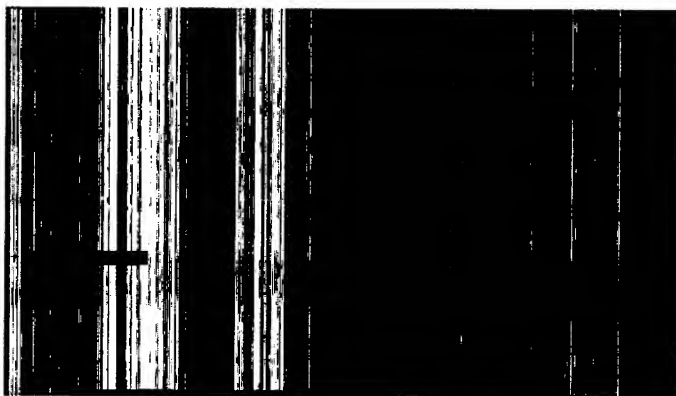


Fig. 3 : Range returns from the mountains in the vicinity of False bay as observed on the RTP

SASAR External Polarimetric Calibration Considerations

M da Silveira

Aerotek, CSIR

P.O. Box 395, Pretoria, South Africa, 0001

Tel : +27 12 841 4831/ Fax: +27 12 349 1766 / Email : mdsilvei@csir.co.za

Abstract -- SAR Polarimetric calibration at frequencies below 150 MHz presents unique challenges when compared to the higher frequency calibration procedures. Low frequency clutter based and point target calibration issues are discussed in this paper.

INTRODUCTION

The South African VHF SAR System (SASAR-1) has been successfully integrated and tested on the ground. Indications are that the first test flights will be undertaken in August 1997. Thereafter the polarimetric calibration of the system will proceed. The calibration considerations presented in this paper are the results of a study which was undertaken in 1996. The calibration goals used for the investigation are similar to that in [1]. The SASAR system is one of only a few systems operating at the low frequency of 141 MHz. The long operating wavelength (2.12m) poses several polarimetric calibration problems. It is the aim of this paper to highlight and discuss various low frequency clutter based and point target polarimetric calibration issues.

CLUTTER BASED CALIBRATION APPROACH

The clutter based approach uses only the statistical polarisation backscatter properties of randomly distributed targets (clutter) as well as a single point target [6]. The point target is usually a trihedral reflector, which is used to correct for the co-polarised channel imbalance as well as for the absolute radiometric calibration of the system. A number of targets must be placed across the swath in order to correct for the channel imbalance and conduct radiometric calibration across the swath. The clutter is used to correct the cross talk of the radar system. The clutter is normally spread over a large area and can thus be used for correction across the entire swath of the radar. The clutter based approach has a significant advantage over the point target approach in terms of calibration effort. It does not require the exact alignment required by the point target approach. In addition it requires only a number of trihedrals, which has a large beamwidth and alignment is simple. The calibration can also be done more often, as it can form part of every data collection and can be largely automated. The cost of this approach can be less than with the in-scene target approach.

However, the clutter backscatter has to conform to certain properties. Firstly, the clutter backscatter must be reciprocal. Natural targets will conform to this requirement, as opposed to active targets and plasma. Secondly, the co-polarised and cross-polarised backscatter must be uncorrelated. This is generally true at the higher frequencies (P-band and above) for thick vegetated terrain (such as forests). This property is not necessarily satisfied at frequencies below 150 MHz, as these wavelengths penetrate the tree canopy significantly. Except for trees with large thick branches, only the stems will produce a large backscattering. According to the author, the resultant backscatter tends to be predominantly VV polarised, thus not satisfying the second clutter criteria.

It is the view of the author that the backscatter properties of trees must be modelled as well as verified with measurements in order to ascertain whether there are trees that will actually satisfy the required backscatter polarisation criteria. Due to the uncertainties regarding the backscatter properties of distributed targets at the SASAR frequency, it was decided to investigate whether it is at all possible to conduct the polarimetric calibration using point targets.

IN-SCENE REFLECTOR CALIBRATION APPROACH

Procedure

The three point targets calibration approach has been described thoroughly in the literature [2]. Several types of point sources can be used including, trihedrals, dihedrals, dipoles above ground, active sources, polarised flat reflectors. The size of the reflectors is determined by the a required RCS above the clutter backscatter of 20 dB [3]. Even though the backscatter at 141 MHz is low for flat dry areas the required reflector size is still very large. The rest of the paper investigates the most suitable SASAR point targets for this approach.

Two Dihedrals and One Trihedral Approach

The signatures of the three targets are:

$$[S_a] = \begin{bmatrix} 1 & 0 \\ 0 & 1 \end{bmatrix} \quad [S_b] = \begin{bmatrix} 1 & 0 \\ 0 & -1 \end{bmatrix} \quad [S_c] = \begin{bmatrix} 0 & 1 \\ 1 & 0 \end{bmatrix} \quad (1)$$

where S_a is a trihedral, S_b a 0° dihedral, S_c a 45° dihedral. The dihedrals used by the DLR had a minimum leg length of 6λ [3]. This is a length of 12,72 m at 141 MHz, which is impractical. Using a smaller more practical leg length of 2λ will result in a pattern whose VV and HH scattering are not equal and change rapidly with angle. It is also affected by the reflection from the ground surface. An example of the RCS of a reflector with a leg length of 2λ at 141 MHz is shown in Fig.1 with no ground surface present. The RCS of the same reflector above a ground with dielectric constant of $4.13 + j0.27$ is shown in Fig.2, clearly showing the effect of the ground surface. The ripple in the pattern due to the small reflector size is also visible in both figures. The SASAR system has a high antenna cross polarisation component, and therefore this approach is not recommended [3].

Dipole Approach

In this case horizontal, vertical and slanted (about the radar line of sight) dipoles with the following scattering matrices are used [2]:

$$[S_a] = \begin{bmatrix} 1 & 0 \\ 0 & 0 \end{bmatrix} \quad [S_b] = \begin{bmatrix} 0 & 0 \\ 0 & 1 \end{bmatrix} \quad [S_c] = \begin{bmatrix} c & d \\ d & e \end{bmatrix} \quad (2)$$

Under perfect conditions $c=e=1$ and $d=0$. Under certain conditions such as alignment error or ground reflection component, $d \neq 0$ and thus $c \neq e$. This procedure is well suited for systems with a large cross-polarisation, since the calibration targets are highly polarised. The horizontal dipole gives a large RCS when it is a 0.5λ (or multiples thereof). Above the ground the RCS of the horizontal dipole is higher, where the RCS maximum angular position can be controlled by the dipole to ground spacing [4]. Unfortunately, the vertical and slanted dipoles are negatively affected by the ground reflection. A part of the horizontal component of the slanted dipole radiation is cancelled by the ground surface, with the result that a large difference between the horizontal and vertical components are generated which makes it unsuitable to use as the third calibration target.

Active Calibration Target Approach

A calibration procedure using active calibration targets was described in [5]. The required signatures are:

$$[S_a] = \begin{bmatrix} 0 & 0 \\ 1 & 0 \end{bmatrix} \quad [S_b] = \begin{bmatrix} 0 & 1 \\ 0 & 0 \end{bmatrix} \quad [S_c] = \begin{bmatrix} -1 & -1 \\ 1 & 1 \end{bmatrix} \quad (3)$$

These signatures are similar to the dipole approach signatures and are suitable for systems with poor cross-polarisation responses. With an active calibrator, a large RCS can be obtained from a physically small calibrator.

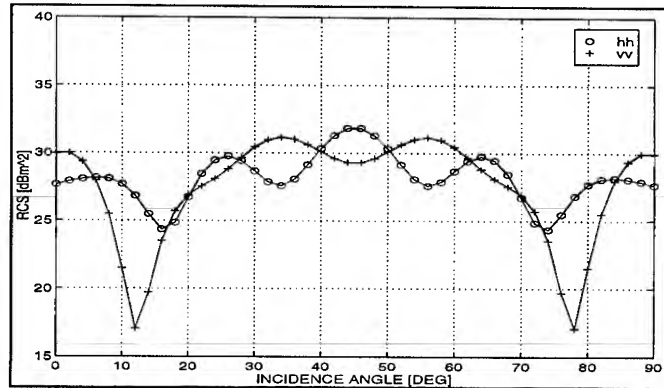


Fig. 1 : VV and HH RCS of 0° dihedral as a function of incidence angle with no ground present

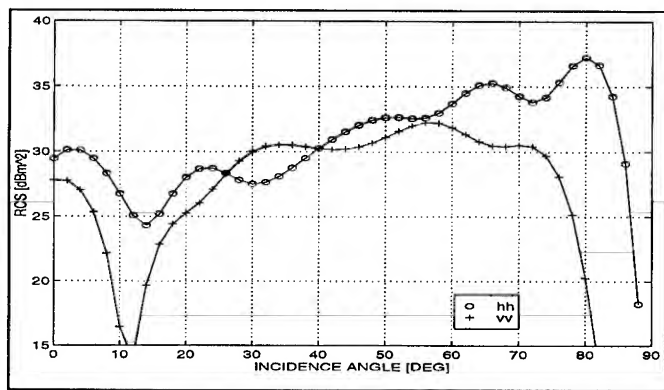


Fig. 2 : VV and HH RCS of 0° dihedral as a function of incidence angle above ground surface ($\epsilon_r = 4.13 + j0.27$)

However, a directive antenna is required in order to reduce the effects of the ground reflections. At 141 MHz this requires large antennas and since the calibrators must be calibrated themselves, makes this calibration approach not feasible for this frequency.

Polarised Flat Reflector Approach

The flat plate reflector gives a large RCS, but only over a very limited angular extend. Since the reflector has a large gain, the effect of the ground reflection component is less than with the other types of point targets. If an accurate alignment of the reflector combination and accurate flight path can be obtained, the flat plate reflectors seems to be the only viable point target at 141 MHz. The required signatures are:

$$[S_a] = \begin{bmatrix} 1 & 0 \\ 0 & 0 \end{bmatrix} \quad [S_b] = \begin{bmatrix} 0 & 0 \\ 0 & 1 \end{bmatrix} \quad [S_c] = \begin{bmatrix} c & d \\ d & e \end{bmatrix} \quad (4)$$

The first and second signatures can be obtained by arrays of closely spaced horizontal (Fig. 3) and vertical rods respectively. The third target consist of an array of 45° rotated closely spaced rods, as shown in Fig. 4. In all cases

the spacing (D) must be less than $0,125\lambda$. The RCS as a function of incidence angle and soil dielectric constant is shown in Fig. 5 for S_a . The RCS of reflector S_c for a ground dielectric constant of $2.9 + j0.1$ and for HH and VV polarisations is shown in Fig. 6. The best results is obtained when the dielectric constant of the soil is the lowest. Therefore it is essential to conduct the calibration procedure where the soil dielectric constant is low.

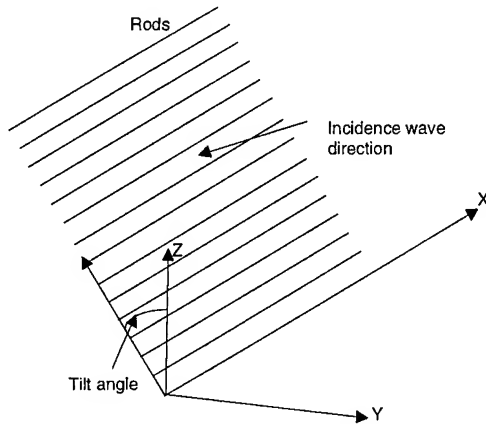


Fig. 3 : Horizontally polarised flat reflector

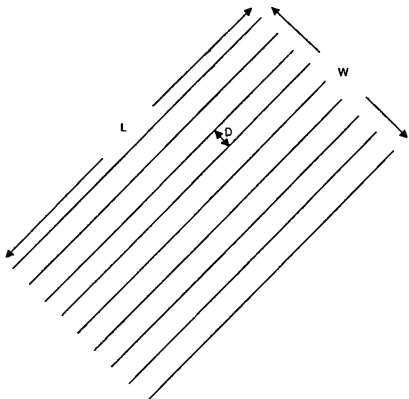


Fig. 4 : 45 ° flat polarisation reflector

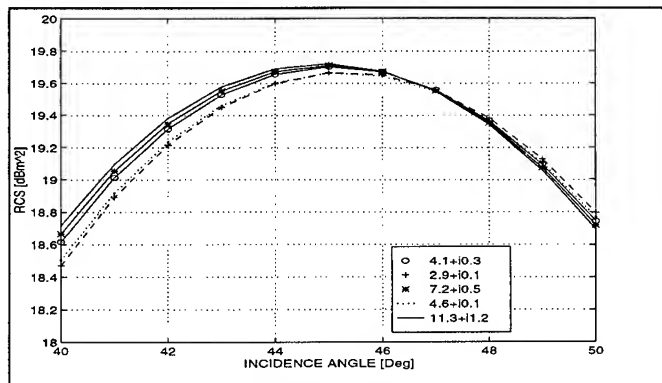


Fig 5 : RCS of horizontal flat reflector as a function of ground dielectric constant

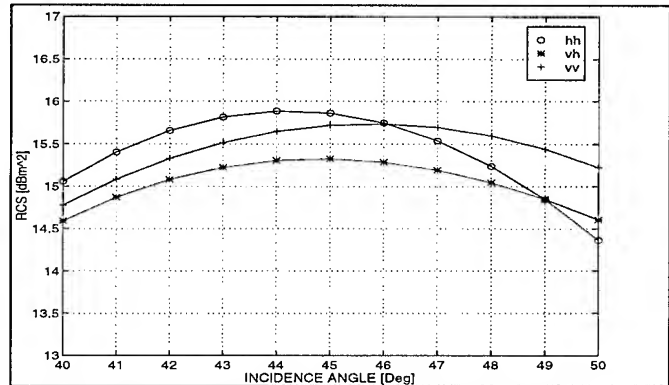


Fig. 6 : RCS of 45° flat reflector for $\epsilon_r = 2.9 + j0.1$

CONCLUSIONS

The clutter based polarimetric calibration approach is very attractive in terms of cost, number of reflectors, reflector alignment effort and calibration as part of every day data collection. However, it might be difficult to find the appropriate clutter target at frequencies below 141 MHz.

Point target RCS responses are severely deteriorated by ground reflection and small electrical size. The polarised flat reflector can be used, but alignment is extremely difficult.

REFERENCES

- [1] A.Freeman, Y. Shen, C.Werner, "SAR Calibration, An Overview", IEEE Trans. On Geoscience and Remote Sensing, Vol. 30, No. 6, pp. 1107-1121, Nov 1992.
- [2] S.Yueh, J.Kong "Calibration of Polarimetric Radars Using In-scene Reflectors", Journal of EM waves and Applications, Vol. 4, No. 1, pp 27-48, 1990.
- [3] M.Zink, "Cross-calibration Between Airborne SAR Sensors", DLR-FB 91-10.
- [4] L.Ulander, Z.Sipus, "RCS of Dipoles Used for SAR Calibration", EUSAR Conference, Koningswinter, Germany, pp. 439-498, June 1996.
- [5] A.Freeman, Y.Shen, C.Werner, "Polarimetric SAR Calibration Experiment Using Active Radar Calibrators", IEEE Trans. on Geoscience and Remote Sensing, Vol. 28, No 2, pp 224-240, March 1990.
- [6] J.van Zyl, "Calibration of Polarimetric Radar images Using Only Image Parameters and Trihedral Corner Reflector Responses", IEEE Trans. on Geoscience and Remote Sensing, Vol. 28, No. 3, pp 337-348, May 1990.

Spotlight SAR Processing Using the Extended Chirp Scaling Algorithm

Josef Mittermayer and Alberto Moreira

Institute of Radio Frequency Technology

German Aerospace Research Establishment (DLR)

D-82234 Oberpfaffenhofen, Germany

T: +49-8153-28-2373, e-mail: josef.mittermayer@dlr.de

Abstract -- This paper presents a new processing algorithm for spotlight SAR data processing. The spotlight mode offers the potential of achieving very high geometric resolution. The Extended Chirp Scaling (ECS) processing performs a subaperture approach combined with azimuth scaling and a new frequency scaling for range cell migration correction (RCMC). The subaperture processing and the effect of the frequency scaling are discussed. Simulation results demonstrate the precision processing in high resolution mode.

I. INTRODUCTION

Spotlight SAR offers a very high geometric resolution in azimuth [1]. In order to obtain a similar resolution in range, a high bandwidth chirp is transmitted. Due to the small range extension of spotlight scenes, dechirp on receive is used to reduce the range bandwidth before A/D conversion. Dechirp means to multiply the received range echoes by a chirp signal with inverted modulation rate centered at scene center position r_{ref} .

Some processing algorithms suitable for spotlight SAR processing are Chirp Scaling Algorithm, Polar Format Algorithm and Range Migration Algorithm. An advantage of the Chirp Scaling Algorithm is that it requires no interpolations. However, a linear frequency modulated range signal is necessary and must be recovered before processing. The Polar Format Algorithm is attractive since it requires only two FFT's, but two interpolations were needed in azimuth and range. The Range Migration Algorithm is able to process raw data dechirped in range by using three FFT's. The major advantage is the complete RCMC. One disadvantage is the need of the Stolt interpolation.

The ECS algorithm proposed in this paper works with chirped or dechirped raw data in range. Here we assume dechirped raw data. By means of a new frequency scaling, the RCMC is performed without interpolation and without the need of chirped signals in range. During range processing the spotlight aperture is divided into subapertures. This allows the use of short azimuth FFT's. Azimuth compression is performed using azimuth scaling and SPECAN. This combination overcomes the need of a very long reference function for azimuth compression without interpolation.

II. THE ECS ALGORITHM FOR SPOTLIGHT MODE

Fig. 1 shows the block diagram of the ECS algorithm. The spotlight SAR signal after dechirp, down-conversion and A/D-conversion can be expressed by (1). The distance be-

tween antenna and target at closest approach is r_0 , r is the azimuth dependent distance to the target, λ is the wavelength and c_0 the velocity of light.

$$s(t_a, t_r; r_0) = C \cdot \exp \left[-j \frac{4 \cdot \pi}{c_0} k_r (r(t_a; r_0) - r_{ref}) \left(t_r - \frac{2 \cdot r_{ref}}{c_0} \right) \right] \cdot \exp \left[j \frac{4 \cdot \pi}{c_0^2} k_r \cdot (r(t_a; r_0) - r_{ref})^2 \right] \exp \left[-j \frac{4 \cdot \pi}{\lambda} \cdot r(t_a; r_0) \right] \quad (1)$$

The azimuth time is t_a and the range time is t_r , while the range chirp rate is denoted by k_r and C is a complex constant. The processing starts with the subaperture formation. The raw data are divided into separate blocks with original range, but smaller azimuth extension. The subaperture processing is discussed in more detail in the next section.

After subaperture formation the raw data are transformed into the range Doppler domain by means of short azimuth FFT's. Here, the signals are range compressed but range cell migration is not yet corrected. This is performed by a new frequency scaling function (2), which is more explained in section 4. The frequency scaling function H_f has the same function as the well known chirp scaling function.

$$H_f(f_a, t_r; r_0) = \exp \left[j \frac{2 \cdot \pi \cdot k_r}{c_0} \cdot r_0 \cdot a(f_a) \cdot t_r \right] \quad (2)$$

The frequency scaling factor $a(f_a)$ in (3) is calculated similarly to the linear chirp scaling factor [3]. In equation (3) V is platform velocity and f_a is Doppler frequency.

$$a(f_a) = \frac{1}{\beta(f_a)} - 1; \quad \beta(f_a) = \sqrt{1 - \left(\frac{f_a \lambda}{2V} \right)^2} \quad (3)$$

Next, the data are transformed into two dimensional frequency domain by means of short range FFT's. This means, the full number of range samples, corresponding to the required range frequency resolution, is required just before the last range FFT. Then the residual video phase (RVP) correction is performed. The RVP arises during dechirp on receive and is discussed in section 4.

The next step is to transform the data again into range Doppler domain. Here, a small linear frequency modulation arising during frequency scaling is removed in order to avoid defocusing of the impulse response function (IRF) after the full range FFT. This full range FFT must have enough points to obtain a frequency sampling distance adequate for the range resolution.

Next, the azimuth scaling function H_a (4) transfers the hyperbolic phase history from the azimuth signals into a pure

quadratic one [2]. The resulting final Doppler rate $k_{a,sc1}$ means a linear frequency modulation constant with range. No resampling is needed after deramping and final azimuth FFT. More, the final sampling distance in azimuth can be adjusted by selecting a proper final Doppler rate.

$$H_a(f_a, f_r; r_o) = \exp\left[j\frac{4\pi}{\lambda} \cdot r_o \cdot \beta\right] \exp\left[j\frac{\pi}{k_{a,sc1}} \cdot f_a^2\right] \quad (4)$$

After azimuth scaling a range dependent azimuth phase is corrected which arises during the frequency scaling operation. The recombination of the subapertures is performed after short azimuth IFFT's in the range Doppler domain. After deramping, the data are finally transformed into the two dimensional frequency domain by full azimuth FFT's. As the length of the full range FFT's, the length of the full azimuth FFT's is determined by the azimuth resolution.

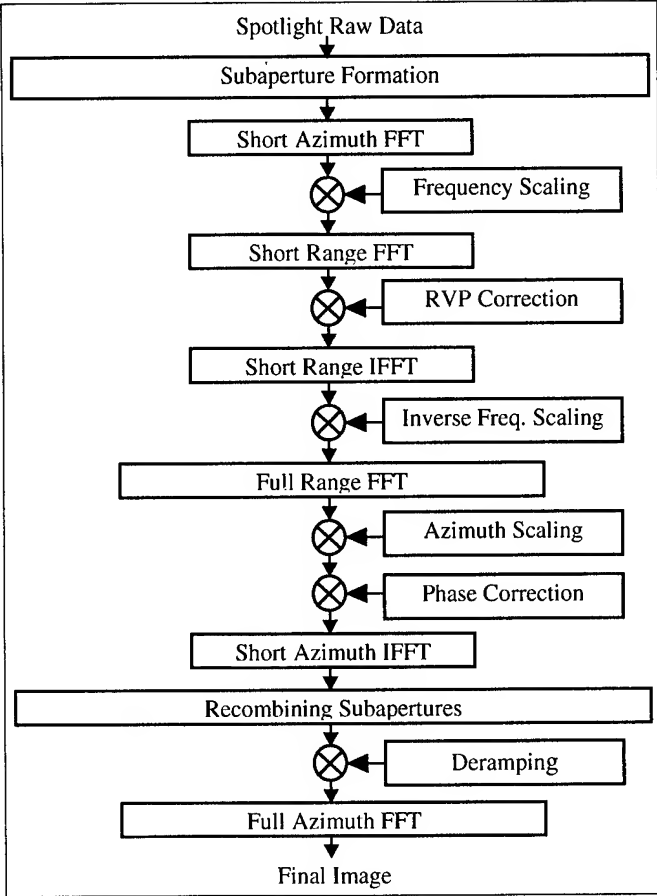


Fig. 1: Block diagram of the ECS algorithm

III. SUBAPERTURE FORMATION

The subaperture formation is shown in Fig. 2. The azimuth signals A and B with the Doppler rate $k_{a,near}$ belong to the azimuth end points of the imaged scene in near range. Bore-sight geometry is assumed and the scene size in azimuth Δa equals arbitrarily the spotlight aperture.

During range processing the instantaneous azimuth bandwidth B_a , which is the bandwidth of a single point target, has to be properly sampled. The maximum instantaneous azimuth bandwidth $B_{a,max}$ is the spotlight aperture T_{spot} times the near range Doppler rate $k_{a,near}$. The total azimuth bandwidth $B_{a,total}$ is higher than $B_{a,max}$ since the azimuth position of the targets results in a frequency offset. Thus, the total azimuth bandwidth $B_{a,total}$ is dependent on Δa :

$$B_{a,total} = B_{a,max} + k_{a,near} \cdot \Delta a / V \quad (5)$$

The spotlight raw data are separated into sub-blocks with duration T_{sub} at the beginning of the processing. For each subaperture processing the according f_{DC} value is used. After range processing including RCMC, the subapertures are recombined and the bandwidth B_a of each target is restored before azimuth processing. As can be seen in Fig. 2, the duration of the subapertures T_{sub} is determined by (6).

$$T_{sub} = \frac{PRF - B_{a,max}}{k_{a,near}} \quad (6)$$

To avoid a deterioration of the impulse response function there should be a small overlap between the subapertures.

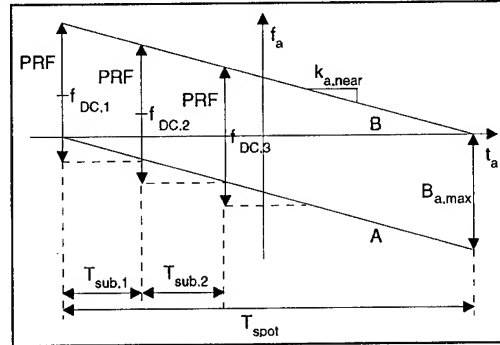


Fig. 2: Subaperture formation

IV. FREQUENCY SCALING

In Fig. 3 the frequency scaling operation is shown graphically. Plot 1 shows the range signals of three point targets after dechirp on receive. The targets are in near, reference and far range. The range time shift of the signals corresponds to the RVP. Plot 2 shows the frequency scaling function which is azimuth frequency dependent. The bold function is used for the range signals in the first plot.

The result of the frequency scaling can be seen in plot 3. The center frequencies of the range signals are shifted dependent on their range and azimuth positions. The azimuth position of a target results in an azimuth frequency and the frequency scaling is performed dependent on $a(f_a)$. In addition to the scaling of the center frequencies, a small linear frequency modulation is introduced which has to be removed later. The range signals after frequency scaling are represented in continuous line style while the range signals before frequency scaling are in dotted line style. Next, the RVP is removed. This can be interpreted as a scaling operation in

range frequency direction. The function for the removal is shown in plot 4. After the removal, the range signals are located at the same range time position as shown in plot 5. By multiplication with the inverse frequency scaling function, shown in plot 6, the small linear frequency modulation mentioned above is removed. Plot 7 shows the resulting range signals after complete frequency scaling. The frequency of the sinusoidal signal in far range is increased, in near range the frequency is decreased and the frequency at reference range is not changed (remains 0 Hz). After frequency scaling the range cell migration at all ranges is equalized to reference range. The bulk shift in range frequency for correcting the range cell migration of this reference range is already included in (2).

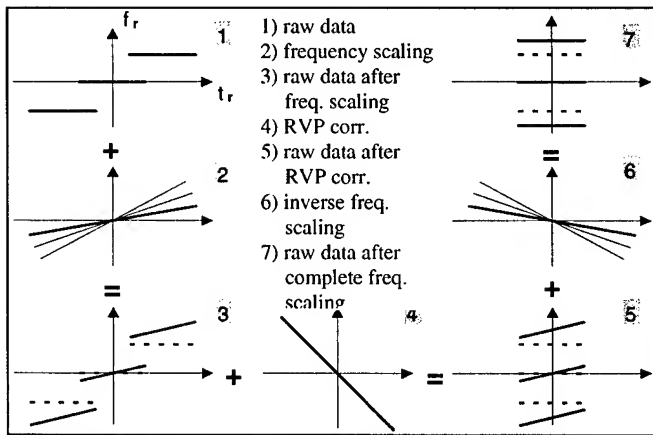


Fig. 3: Schematic representation of frequency scaling

V. SIMULATION RESULTS

Point target simulation was carried out to verify the validity of the proposed algorithm. The parameters during raw data generation and processing are listed in Tab.3. At the top in Fig. 4 a image gray level representation of six targets after processing is shown. At the bottom a contour plot of a single processed point target can be seen. The point target analysis results for the targets located at the right side are listed in Tab.1 and Tab. 2.

range [m]	ISLR [dB]	resolution[m]	res. Deviation
3500	-9.93	0.238	2.1 %
4500	-9.98	0.304	1.3 %

Tab. 1: Results of point target analysis in azimuth

range [m]	ISLR [dB]	resolution[m]	res. Deviation
3500	-10.13	0.733	1.7 %
4500	-10.08	0.733	1.7 %

Tab. 2: Results of point target analysis in range

The SLR of the first three sidelobes left and right are -13.2, -17.8 and -20.8 dB (± 0.1 dB) for all targets.

range chirp length	38.5 μ s
range chirp bandwidth	185 MHz
sampling freq. transmitted	200 MHz
sampling freq. after dechirp	40 MHz
reference range dechirp	4000 m
reference range azimuth scaling	4000 m
range scene size	1000 m
aircraft velocity	100 m/s
PRF	500 Hz
wavelength	0.03 m
length of spotlight aperture	2.003 s

Tab. 3: Parameters

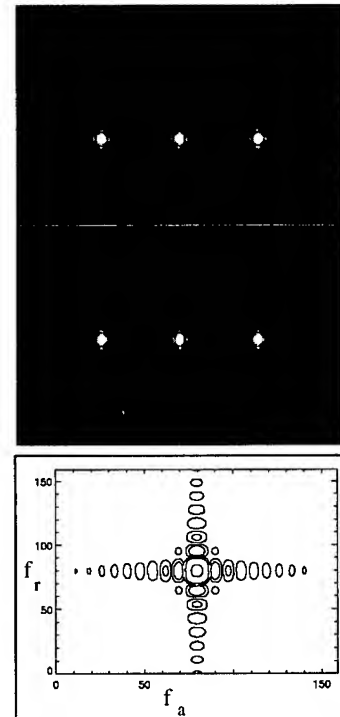


Fig. 4: Results

VI. CONCLUSION AND FUTURE ACTIVITIES

The ECS algorithm leads to a very precise and efficient processing since the algorithm is also suitable for dechirped raw data. Further, no interpolations are required and oversampling is only necessary before the final range and azimuth FFT's due to the use of subapertures. Future activities include the processing of E-SAR (Experimental airborne SAR system of DLR) data. The E-SAR has a very wide beam in azimuth and thus allows the simulation of spotlight mode. The phase errors in the different steps of the processing will be calculated in order to explore the limitations of the algorithm. The computational complexity will be evaluated and compared with other approaches suitable for spotlight processing.

REFERENCES

- [1] G. Carrara, R. S. Goodman, R. M. Majewski, "Spotlight Synthetic Aperture Radar", Artech House Boston, 1995.
- [2] Moreira, J. Mittermayer and R. Scheiber, "Extended Chirp Scaling Algorithm for Air- and Spaceborne SAR Data Processing in Stripmap and ScanSAR Imaging Modes", IEEE Trans. on Geosci. and Remote Sensing, Vol. 34, NO. 5, September 1996.
- [3] K. Raney, Runge, H., Bamler, R. Cumming, I. and Wong, F.: "Precision SAR Processing without Interpolation for Range Cell Migration Correction". IEEE Trans. on Geosci. and Remote Sensing, Vol.32, No.4, July 1994.

Wavelet Based Approaches for Efficient Compression of Complex SAR Image Data *

Michael Brandfaß, Wolfgang Cöster, Ursula Benz, Alberto Moreira
Institute of Radio Frequency Technology
German Aerospace Research Establishment (DLR)
D-82234 Oberpfaffenhofen, Germany

Abstract— New wavelet based approaches for efficient data compression of complex SAR images with high reconstruction quality are presented. These approaches utilize either a polar format representation to compress magnitude and phase information of the complex SAR images, separately by different compression schemes, or use a Fourier transform scheme to convert the complex image data format to a real data format before applying the wavelet decomposition technique. In both concepts the phase information of the compressed images is preserved in great extent. Additionally, a concept based on vector quantization is used, taking advantage of the correlation between polarization channels for data compression in multi-polarization channel modes. Therefore, these approaches are suitable for data compression in both interferometric and polarimetric applications. Finally, the quality of the reconstructed images are compared in terms of compression ratio and proved by image quality parameters.

INTRODUCTION

The continuously improved sensing of the past led to steadily rising data quantities. Therefore transmission and storage of these data quantities is often only possible using efficient data compression algorithms. Primarily, only real data formats are needed to compress arising data for the most applications. Considering synthetic aperture radar (SAR) images for interferometric purposes one has to deal with complex data formats. Thus, data compression of SAR images differ significantly from other applications. Additionally, the entropy of SAR signal data as well as SAR image data is much higher and relevant information is contained in both, the low frequency and the high frequency part of the spectrum. Unlike optical image data processing, which possesses a real data format, low entropy and for the most part only noise in the higher frequency spectrum, will not lead to sufficient image quality for SAR applications.

Especially for interferometric applications exist a high phase sensitivity preparing digital elevation models. Thus, a high phase accuracy and phase preservation is required, compressing complex data to prevent large errors in such elevation models. Therefore, compression of complex SAR

images make greater demands on reconstruction accuracy than in most other image compression applications. Up to now, only few algorithms exist in initial stages, dealing with compression of complex SAR data with sufficient quality for interferometric applications [1], but in general common methods lead to severe phase errors.

After a brief summary of discrete wavelet transform in chapter two, we continue in chapter three to prescribe common but often differently defined image quality parameters. Chapter four presents the compression schemes which enable polarimetric and interferometric applications for medium compression ratios

DISCRETE WAVELET TRANSFORM

Because of highly statistical symbol dependencies in image data one can partly split up these dependencies, through decorrelating orthogonal transforms as for instance with Fourier, Cosine or Walsh-Hadamard transform, which are common methods in image processing. The goal is to achieve high local energy concentrations within the transform domain, so that those spectral components which possess only small magnitudes are assumed to be of low importance. Therefore these components can be neglected before transmitting or storing the image data within the transform domain.

Within recent years also the wavelet transform became an important aspect in signal processing. Especially the application of data compression using discrete wavelet transform algorithms was successfully applied to signal and video data. In the initial iteration of the discrete wavelet algorithm the signal data is decomposed into a coarse and a detail component. In the next iteration stage the obtained coarse component of the previous iteration is decomposed into a further coarse and detail component, so that N decomposition iterations, yield N detail components and one coarse component of the analyzing signal. The coarse component of the decomposition can be understood as a low-pass filtered sub-signal and the detail components as the high-pass filtered sub-signals of the analyzing signal. The hierarchical coding scheme, which is provided by a multiresolution analysis [4] is a very powerful and efficient

* Presented at the International Geoscience and Remote Sensing Symposium, 4-8 August 1997, Singapore.

processing technique, because it enables high compression ratios using quantizer adapted to the subband statistics. In [2] is shown that the signal statistic of the high-pass filtered subbands of ECG data used for medical applications, is mainly focused around zero with probability distributions close to the generalized Gaussian distribution. We recognized that decomposed high-pass filtered subbands of intensity SAR image data also satisfies this statistical behavior. This gives rise to use a block adaptive Max quantizer [3], which is adapted to a gaussian distribution of a quantized signal statistic. The obtained subbands contain data of different importance with respect to image reconstruction. In general one can say that the data importance rises from iteration stage to iteration stage, i.e. the first high-pass decomposition band is of lowest importance and the resulting low-pass component of the final iteration stage is of greatest importance.

Multiresolution analysis also gives the fundamental framework to compute wavelet filter coefficients. For our numerical simulations presented in this paper we used the Daubechies-8 wavelet filter, which possesses a strictly compact support [5].

The low- and high-pass filtered subspaces are generated by dilation and translation of a scaling and a wavelet function, so that a set of scaling and wavelet functions constitute an orthogonal basis of the subspaces V_m and W_m , respectively, according to $\phi_{m,n}(x) = 2^{m/2} \phi(2^m x - n)$ and $\psi_{m,n}(x) = 2^{m/2} \psi(2^m x - n)$. The analyzing function $f(x)$ can be decomposed in each scale and reconstructed by its projections onto the subspaces W_m and V_m , as follows

$$f = \sum_n \langle f, \phi_{0,n} \rangle \phi_{0,n} + \sum_{m=0}^M \sum_n \langle f, \psi_{m,n} \rangle \psi_{m,n} \quad (1)$$

with M as the most upper scale, if the following orthogonality conditions are satisfied:

$$\langle \phi_{0,n}, \phi_{0,l} \rangle = \delta_{nl}; \quad \langle \psi_{m,n}, \psi_{k,l} \rangle = \delta_{mk} \delta_{nl} \quad (2)$$

Wavelets which satisfy these conditions, as for instance the daubechies-8, are called biorthogonal wavelets. The wavelet and the scaling function in (1) can be represented by the sequence of mutually complementary high-pass and low-pass filter coefficients h_{k-2n} and g_{k-2n} , respectively. Thus, the wavelet decomposition algorithm is given by

$$a_k^m = \sum_n h_{n-2k} a_n^{m+1}, \quad b_k^m = \sum_n g_{n-2k} a_n^{m+1} \quad (3)$$

with a_k^m and b_k^m as the coefficients of the low- and high-pass subspaces of the analyzing function $f(x)$, given by the samples a_n^{m+1} of the next upper subspace V_{m+1} . The reconstruction formula represented by the subband coefficients a_n^m, b_n^m is obtained in the same manner with the

aid of the corresponding wavelet and scaling filter coefficients:

$$a_k^{m+1} = \sum_n (h_{k-2n} a_n^m + g_{k-2n} b_n^m). \quad (4)$$

The filter coefficients have to be quadrature mirror filter coefficients, due to the fact that the wavelet and scaling functions span complementary orthogonal subspaces. Thus, they have to satisfy the relation $g_n = (-1)^{n+1} h_n (2N-1-n)$ $\forall n = 0, 1, \dots, 2N-1$ with $N=3$ for a Daubechies-8 filter.

IMAGE QUALITY PARAMETER

Image quality parameters are used to establish quantitative expressions, judging the image quality for compressed image data. For SAR image data we used the following parameters:

- Signal to noise ratio (SNR):

The SNR is a standard image quality parameter for data compression. It is defined as the ratio of the signal power of the uncompressed original image to the difference signal power of the original and the reconstructed image data after decompression in dB, i.e.

$$\text{SNR} = 10 \log_{10} \sum_i^L s_i^2 / (s_i - \tilde{s}_i)^2 \quad (5)$$

with s_i and \tilde{s}_i as the i th intensity image pixel of the original and the reconstructed image, respectively. The SNR is a global measure and cannot judge local variations of the reconstruction quality within the image. The PSNR is defined in the same way as the SNR, but instead of the mean signal power the largest pixel power of the original image is used.

- Histogram of image intensity:

The image intensity values can be classified and distinguished by their specific gray level distributions. Therefore, the histograms of the magnitudes of the SAR image data of the original and the reconstructed image after data compression are compared with each other.

- Mean phase error:

To give a measure of the reconstructed phase of complex SAR images after data compression, we consider the standard deviation of the phase (PSD) and the mean phase error (MPE)

$$\text{MPE} = \frac{1}{L} \sum_i^L |\phi_i - \tilde{\phi}_i| \quad (6)$$

with ϕ_i and $\tilde{\phi}_i$ as the phase of the original and the reconstructed SAR image.

COMPRESSION OF COMPLEX SAR IMAGE DATA

The new approaches presented in this paper can generally be distinguished in two different schemes. Both compression procedures lead only to small distortions in amplitude and phase of the reconstructed data.

In the first approach the complex image data is converted to a real data format using a FFT scheme without neglecting any phase information. Shifting the frequency spectrum by the half bandwidth to positive frequencies, one obtains a negative spectrum equal to zero. After applying the inverse Fourier transform, the resulting complex signal can be represented by its real part without loss of any information, since real and imaginary part of the signal are mutual Hilbert transforms. The sampling rate are doubled, but because of only using the real part of the converted signal the data amount is not risen. The particular advantage of this transformation is, that the wavelet decomposition and compression schemes can be applied as usual to ordinary intensity data. The reconstructed complex image data is received by undoing the FFT transformation scheme in reverse order.

In the second approach the complex image data is divided into magnitude and phase, applying two different compression techniques to both parts. The magnitude of the complex image data has the same properties as intensity SAR data and can be compressed, using the discrete wavelet transform and a compression scheme described below. The phase of the data is uniformly distributed and highly decorrelated, so that a nearly lossless compression technique has to be used. In this paper a vector quantizer [6] was chosen for that. The codebook of the vector quantizer is trained, using a typical image area of a similar image.

In both schemes a block adaptive Max quantizer was used with a fixed 5 bit quantization, either for the magnitudes of the image data in our first approach or for the real part of the converted complex image data in our second approach. Additionally, a vector quantizer is used on the Max-quantized data, grouping neighbouring image pixels to specific vectors. The phase of the image data in the second approach is always quantized by a vector quantizer without utilization of a block adaptive Max quantizer.

The complex SAR data set, we used for both compression methods, was taken in X-Band by the experimental SAR of DLR during a mission in 1996 and shows a part of Mount Etna. For each approach two numerical examples are given with different compression ratios (table 1). Both proposed schemes lead to good visual image quality as seen in figure 1, where only one compression example of each approach is depicted. The histograms of the reconstructed image magnitudes are also maintained with respect to their originals. The image quality parameters SNR and PSNR as well as the mean phase error (MPE) and phase standard deviation (PSD) for all the four examples are listed in the first table with their resulting compression ratios.

Additionally, the second approach is extended to multi-polarization mode. The magnitudes of four polarization channels are separately quantized using a block adaptive Max quantizer with a fixed 5 bit quantization as well. The low-pass component of the final wavelet decomposition was linearly quantized with maximum quantization. To exploit the high

correlation between the polarization channels a vector quantizer is used, putting the corresponding pixels of each polarization channel together, i.e. each pixel in each polarization channel of the same image area is grouped to a 4-element vector, so that N vectors are obtained for N image pixels of the 4-channel image. The considered polarimetric SAR image data set was taken in L-Band and shows a small detail of a countryside near Frankfurt. The reconstructed images of one of the co- and one of the cross-polarized channels (HH and VH) with the corresponding histograms of image magnitudes and the distributions of phase errors are presented in figure 2. The image quality parameters for all the 4 polarization channels are listed the second table. The results show that reasonable compression ratios can be achieved, exploiting the correlation between the polarization channels. Further enhancements of this compression ratio can be obtained, using a variable bit quantization, depending on the importance of each decomposition scale.

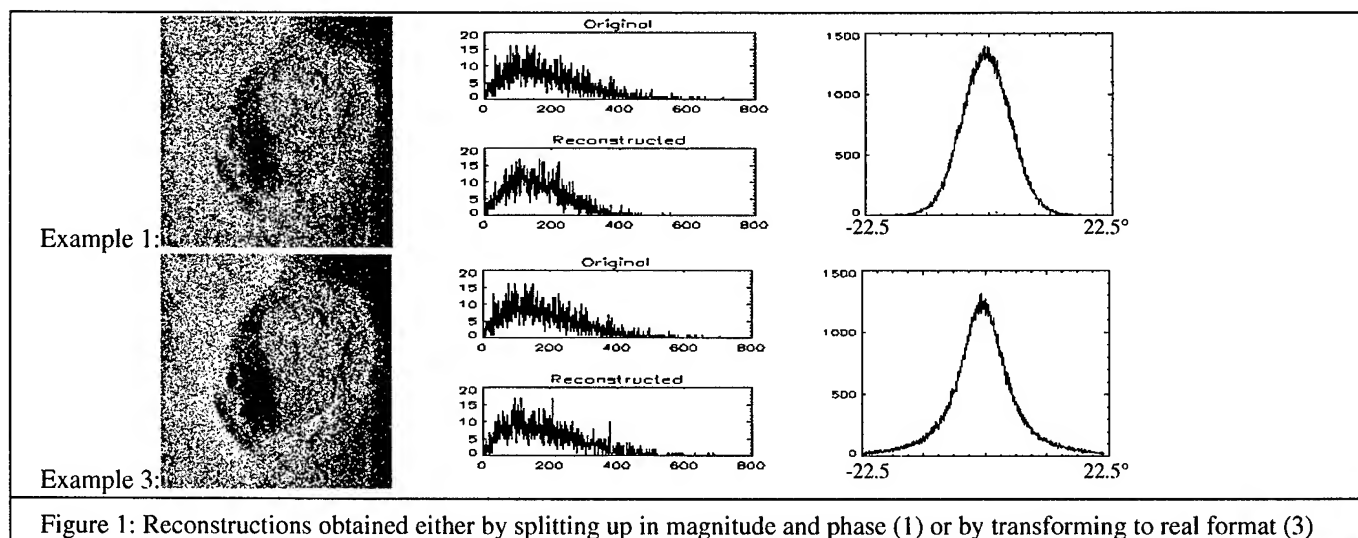
In all the presented cases only small distortions of the image data are visible. Additionally, the performances of the vector quantizers were increased by entropy coding of the stored codebook addresses for all the numerical examples in this paper.

SUMMARY

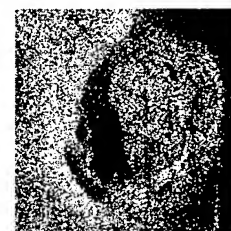
The presented results show, that compression of complex SAR data for polarimetric and interferometric applications is possible for medium compression ratios. They cannot be compared with those of intensity data, since the necessary phase preservation limits these ratios. In combination with wavelet transform, further improvements could be obtained, applying a fuzzy block adaptive quantizer, which is more flexible with respect to the data statistic.

REFERENCES

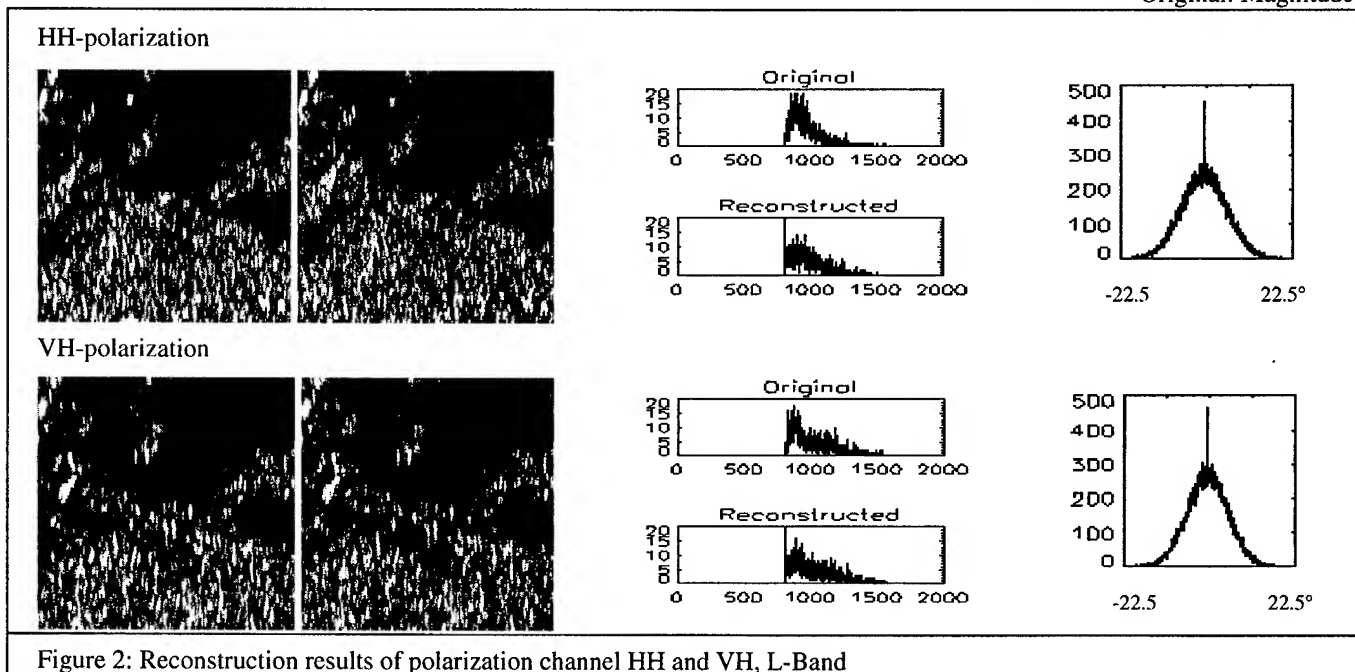
- [1] S. Werness, S. Wei, R. Carpinella: "Experiments with wavelets for compression of SAR data", *IEEE Trans. Geosci. Remote Sens.* **32**, 197-201 (1994).
- [2] J. Chen, S. Itoh, T. Hashimoto: "ECG data compression by using wavelet transform", *IEICE Trans. Inf. & Syst.* **76**, 1454-1461 (1993).
- [3] J. Max: "Quantizing for minimum distortion", *IRE Trans. Informat. Theory* **4**, 7-12 (1960).
- [4] S. Mallat: "Multiresolution representation and wavelets", Ph.D. Thesis, University of Pennsylvania, Philadelphia, USA (1988).
- [5] I. Daubechies: "Ten lectures on wavelets", SIAM, Pennsylvania, Philadelphia, USA (1992).
- [6] Y. Linde, A. Buzo, R. Gray: "An algorithm for vector quantizer design", *IEEE Trans. Commun.* **28**, 84-95 (1980).



Example	Compression Ratio	SNR [dB]	PSNR [dB]	PSD [deg]	MPE [deg]
1 Magn./Phase	9.2	9.5	23.8	4.68	3.65
2 Magn./Phase	13.2	6.9	21.2	7.12	5.4
3 FFT method	5.4	15.1	29.4	8.36	5.4
4 FFT method	8.9	12.7	27.0	12.0	8.2



Original: Magnitude



Polarization Channel	Total Compression Ratio	SNR [dB]	PSNR [dB]	PSD [deg]	MPE [deg]
HH	11.2	11.3	29.1	6.5	5.1
VV		9.0	25.6	6.5	4.9
HV		14.3	36.3	5.8	4.5
VH		14.5	36.2	5.8	4.5

A SAR Auto-Focus Technique Based on Azimuth Scaling

A. Moreira, J. Mittermayer and R. Scheiber

DLR, Deutsche Forschungsanstalt für Luft- und Raumfahrt e.V.

P.O. Box 11 16, D-82230 Oberpfaffenhofen, Germany. Tel/Fax: +49-8153-28-2360/-1449

Email: alberto.moreira@dlr.de

Abstract - - This paper proposes a new approach for automatic estimation of the Doppler rate during the SAR image formation process. The new technique is based on the scaling property in the azimuth direction applied to chirp signals. The measurement of the scaling error between two processed images with low resolution is used to estimate the effective sensor velocity. The achieved results show superior performance when compared to traditional auto-focus techniques. For a standard ERS-1 image, the velocity estimation can be performed with an accuracy better than 0.5 m/s.

INTRODUCTION

Auto-focus is commonly implemented in azimuth processing in order to estimate the sensor velocity with enough accuracy to focus the SAR image. This means that in addition to the wavelength and range distance, the effective sensor velocity must be estimated. Specially for airborne cases, the effective sensor velocity is not available with the required accuracy for processing. Since the correct velocity value leads to a well focused image, the approach to automatically estimate the effective sensor velocity from the radar data is denoted as auto-focus. The correct value of the Doppler rate leads to the best focusing in the azimuth compression for stationary targets and avoids quadratic phase errors in the impulse response function. Additionally, the azimuth looks are properly positioned for incoherent addition.

Common auto-focus techniques are based on the map-drift algorithm (e.g. Look Correlation or Shift And Correlate (SAC) approaches) and also on the Phase Gradient Algorithm (PGA) [1], [2]. The last one being more accurate but computationally very intensive. Due to the superior performance and the capability to estimate higher order phase error terms, the PGA has been mostly used for extremely high resolution images (e.g. Spotlight mode).

The mapdrift algorithm is based on the cross-correlation between adjacent looks. The resulting peak of the cross correlation gives information concerning the relative time shift between the looks which is used to estimate the correct velocity for processing.

The main drawback of the present techniques for auto-focussing are:

- *Speckle noise* - The speckle noise inherent in the SAR image is decorrelated between the two different looks. After the cross-correlation, the speckle leads to a noise floor which decreases the accuracy of the time shift determination.
- *Image Contrast* - A high image contrast is necessary to achieve a representative peak after the cross-correlation. In the case of poor scene contrast a false peak identification can occur which leads to a wrong time shift determination.
- *Target Fading* - Targets with high contrast can be affected by fading effect in the two different looks due to the different squint angle illuminations. This means that the backscattering behaviour of the target can be different from one look to the other which causes an erroneous peak location after cross-correlation.

The new proposed auto-focus technique works in a different way. The azimuth signal is processed twice by means of a simplified one-dimensional azimuth correlation. The first image corresponds to a medium resolution quick-look image with one look. The second image corresponds exactly to the same area of the first image but has a different geometric scaling factor in the azimuth direction. This scaling is applied prior to azimuth compression by means of a phase multiplication with a slowly varying quadratic phase function. The estimation of the scaling factor is used to calculate the effective sensor velocity.

This paper presents first the basic property of the azimuth scaling function in connection with the sensor velocity determination. Then, the main steps of the proposed auto-focus approach with azimuth scaling are discussed. In addition, a new technique is presented for determination of the scaling factor without use of image cross-correlation or interpolation. Finally, data from the ERS-1 sensor with corner reflectors are used to validate the proposed technique and to verify the achieved accuracy.

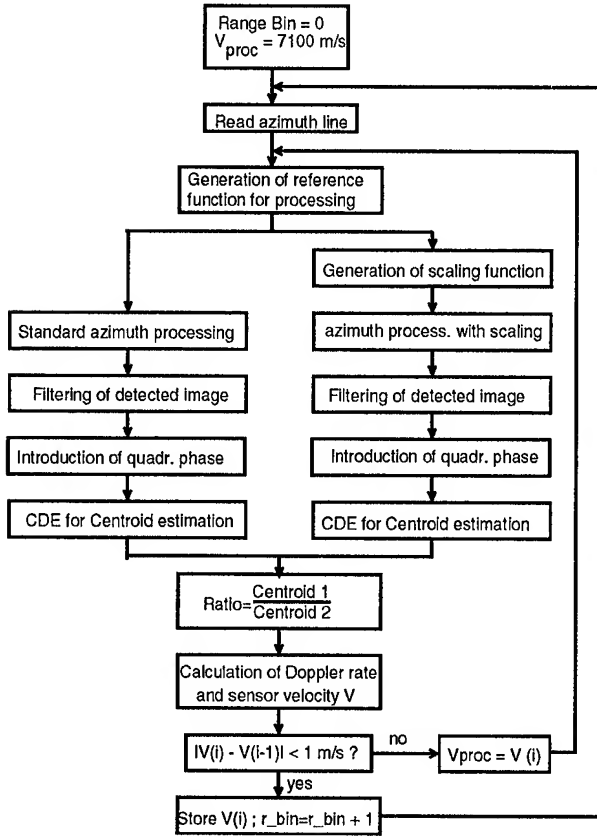


Figure 1: Block diagram of the proposed algorithm for for SAR auto-focus.

AZIMUTH SCALING

The azimuth chirp scaling technique has been proposed in [4] for automatic geometric scaling of the SAR image using the Extended Chirp Algorithm [3]. It can be also used for automatic azimuth co-registration of interferometric image pairs obtained in a multi-pass scheme with different PRF's and/or velocities. Defining a scaling factor α , the azimuth scaling function to be applied to the azimuth signal after range compression is given by

$$H_{scl}(t; r_o) = \exp[j \cdot \pi \cdot a_{scl} \cdot k_a(r_o) \cdot (t - t_{ref})^2] \quad (1)$$

whereby

$$a_{scl} = (1 - \alpha)/\alpha \quad (2)$$

and k_a is the azimuth Doppler rate, r_o is the range distance and t_{ref} is the reference time to the azimuth center position. The scaling function (1) has a small quadratic phase variation which when multiplied with the azimuth signal, causes a frequency shift of the chirp signals. This frequency shift increases linearly with the time $|(t - t_{ref})|$. Since the geometry of the final image is given by the Doppler zero position, there will be a linear scaling fixed

by the scaling factor α . If α equals to one, no scaling will occur.

Assuming that the used velocity for processing V_{proc} is not known with sufficient accuracy, there will be an error in the image scaling factor given by

$$\alpha = \frac{V}{V_{proc} \cdot a_{scl} + V} \quad (3)$$

Only for $V = V_{proc}$, (3) equals (2). This means that if the scaling factor α of the scaled image is measured with reference to the unscaled image, the effective sensor velocity V can be determined by using (3). It must be mentioned that the azimuth reference function for processing with a scaling factor has a slightly modified Doppler rate due to the multiplication of the azimuth signal with (1).

AUTO-FOCUS TECHNIQUE

Fig 1 shows the basic block diagram of the proposed approach. The main steps are summarized in the following. *Generation of reference function* - Initially a velocity value V_{proc} is assumed for the processing, which is updated as the algorithm works. The reference function for the first range bin r_{bin} is generated using V_{proc} .

Generation of scaling function - The scaling function is generated using a scaling factor near to one (e.g. $\alpha = 0.975$). The reference function for the processing with scaling has an adapted Doppler rate to the scaling factor, i.e. $k_{a_{scl}} = k_a \cdot (1 + a_{scl})$.

Image Processing - A simplified azimuth processing is performed to achieve one look images with low resolution (e.g. 1/3 of the maximum azimuth bandwidth).

Detection and filtering - Due to the azimuth scaling the processed bandwidth of the scaled image I_{scl} is slightly different to that of the unscaled image I_o . Both one-look intensity images are filtered to equalize the speckle information in both images.

Calculation of Scaling Ratio - A new method is proposed to calculate the scaling ratio between the two images. The first step is to multiply the two images I_o and I_{scl} by a quadratic phase function H_{ratio} which is given by:

$$H_{ratio} = \exp[\text{sgn}(t - t_{ref}) \cdot j \cdot \pi \cdot k \cdot (t - t_{ref})^2] \quad (4)$$

where $\text{sgn}(t)$ is the sign operator of the time variable. After the multiplication, the phase of the auto-correlation function of each image for a shift of one sample is calculated. This operation is similar to the CDE (Correlation Doppler Estimator) approach used for Doppler centroid estimation [5]. Here the ratio of the calculated phases of the auto-correlation function gives directly information of the scaling amount.

Calculation of Doppler Rate and Velocity - With the estimated scaling factor, the Doppler rate and the velocity

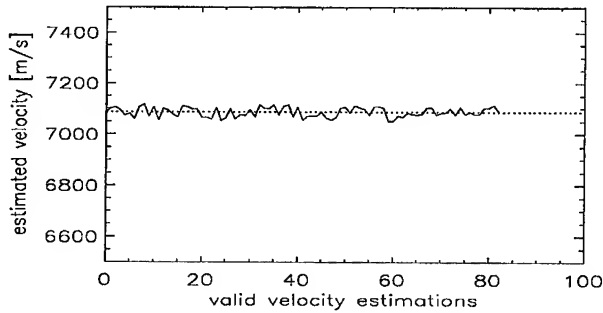


Figure 2: Estimated velocity values for a image block size of $2k \times 2k$ samples.

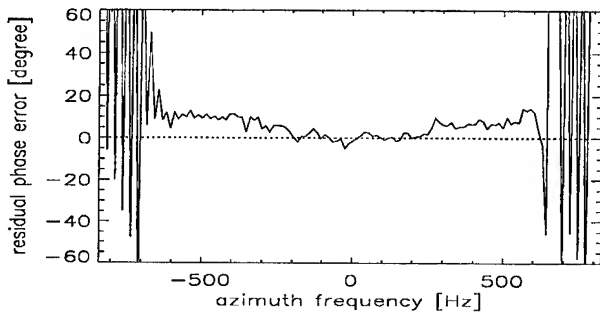


Figure 3: Analysis of residual phase error for a corner reflector. The processed bandwidth is limited to ± 600 Hz.

V can be estimated by using (3).

Check of Estimation Accuracy - If the difference between the estimated velocity V and the velocity for processing V_{proc} converges after two iterations, then the estimation is repeated until $|V(i) - V(i-1)|$ is smaller than the required velocity accuracy. For each iteration, the velocity for processing is updated by the estimated velocity value.

RESULTS OF VELOCITY ESTIMATION

Raw data of the ERS-1 sensor have been used to evaluate the accuracy of the new auto-focus technique. The image corresponds to the test site of Oberpfaffenhofen and has several corner reflectors for calibration purposes. Figure 2 shows the results of the estimation of velocity values for a block size of $2k \times 2k$ samples. There were 83 valid velocity values which converged in the calculation shown in fig. 1. The average value of all estimates is 7086.9 m/s with a standard deviation of 18.5 m/s.

If the velocity variations with range due to the earth curvature are compensated, the velocity values can be averaged and the standard deviation for a $2k \times 2k$ block is reduced to ca. 2 m/s. For the whole ERS-1 image, the standard deviation after averaging is lower than 0.5 m/s.

To demonstrate the achieved accuracy, the phase behaviour of a corner reflector in frequency domain has been analysed (see fig. 3). The mean velocity value of 7086.9 m/s with a standard deviation of 2 m/s has been used for processing. In the case of ideal focusing (no velocity error) the phase behaviour should be zero except for a constant value which was subtracted in fig. 3. The observed quadratic phase error has a maximum value of 10° which corresponds to a velocity error of 0.3 m/s.

DISCUSSION

The proposed algorithm for auto-focus has some important features which allows the velocity estimation with superior performance when compared to traditional techniques:

- *Less Sensitivity to Speckle Noise.* The use of the same processing bandwidth for both images means that the speckle behaviour in both images is the same. There is a slight change of the processing bandwidth due to the scaling function but this is compensated by the filtering of the detected image and by the iterative process in fig.1.
- *Less Requirement on Image Contrast.* Even targets with low contrast but with a good specular behaviour (point target behaviour) lead to a precise estimation of the velocity.
- *Less Sensitivity to Target Fading.* Since there is no squint angle variation between the two images, almost no target fading occurs.

Future work includes the extension of this algorithm for the velocity estimation of spotlight SAR data, which require an extremely precise estimation of the velocity which in several cases cannot be obtained from the aircraft navigation system with sufficient accuracy.

REFERENCES

- [1]-G.Carrara, R.S. Goodman, R.M. Majewski, "Spotlight Synthetic Aperture Radar", Artech House, 1995.
- [2]-F.K.Li et al., "Doppler parameter estimation for spaceborne synthetic aperture radars". IEEE Trans. Geosci. Remote Sensing, vol. GE-23, pp.47-55, Jan. 1985.
- [3]-A. Moreira, J. Mittermayer and R. Scheiber, "Extended Chirp Scaling Algorithm for Air- and Spaceborne SAR Data Processing in Stripmap and ScanSAR Imaging Modes". IEEE Trans. Geosci. Remote Sensing, vol. GE-34, pp.1123-1136, Sept. 1996.
- [4]-A. Moreira, R. Scheiber and J. Mittermayer, "Azimuth and Range Scaling for SAR and ScanSAR Processing". Proc. of IGARSS'96, pp.1214-1216.
- [5]-S.N.Madsen, "Estimating the Doppler Centroid of SAR Data". IEEE Trans. Aerosp. Electron. Syst., vol.25, no.2, 1989.

Speckle Reduction in SAR Images - Techniques and Prospects

G. Schwarz, M. Walessa, M. Datcu

German Aerospace Research Establishment DLR

German Remote Sensing Data Center DFD

Oberpfaffenhofen, D-82234 Weßling

Phone + 49 8153 28 1388, Fax + 49 8153 28 1448, Email {gschwarz, walessa, datcu}@dfd.dlr.de

Abstract: This paper presents a classification overview and a comparative study of despeckling algorithms. Almost all of the existing good speckle reduction algorithms show high computational complexity. Promising results giving a very good compromise between image enhancement and algorithm complexity are obtained using multiscale analysis techniques.

INTRODUCTION

Synthetic Aperture Radar (SAR) systems use coherent processing techniques to generate high resolution images of the terrain. However, SAR systems - like any coherent imaging system - are subject to speckling effects, which considerably reduce the detection of useful details within the acquired scenes. Furthermore, the resolution of SAR systems is comparable to the size of many of the objects of interest in the scene.

Consequently, research has been devoted to modelling speckle, and reducing its effects. The most commonly used model assumes that the received signal consists of reflections from many independent scatterers. This implies that the speckle at a single point is exponentially distributed (Gamma distributed when multiple looks are averaged) [9, 15]. Marginal or high order analysis has been used to derive algorithms for edge or texture detection, and image restoration. However, it has been noted that speckle often has significant correlation. Several methods indirectly include the effects of correlation by using locally averaged parameters [22].

A correlated speckle noise model can be used in an hierarchical modelling approach together with a region model depending on the class of terrain being imaged. Markov Random Field (MRF) models are used for both the underlying cross-section of the terrain, and the speckle process. The MRF model allows one to perform a Maximum A Posteriori (MAP) segmentation of SAR images, but it requires an estimation of the model parameters from the available noisy data [3, 13].

WHAT IS DESPECKLING?

The despeckling process is defined according to the assumed model for the SAR image formation. Two main classes can be defined: 1) under the assumption of multiplicative image noise, despeckling is an image restoration task and 2) under the

assumption of a SAR system imaging a scene, despeckling is defined as an inverse problem.

CLASSIFICATION OF DESPECKLING ALGORITHMS

In Diagram 1 we present an overview of speckle reduction algorithms based on the previous classification divided in two main classes depending on the type of SAR image representation: real or complex valued.

Multilook processing was and still remains an important and SAR-specific speckle reduction technique. The signal-to-noise ratio is enhanced at the cost of image resolution. Many applications demand the reduction of speckle while preserving the high resolution details. This requirement can be partly satisfied by local adaptation of the speckle filter. Variance driven measures are used [7, 14, 17], and for better preservation of the features the directionality is also checked [11]. The resulting algorithms are Minimum Mean Square Error (MMSE) estimators or approximations of it.

Geometrical filters are non-linearly combining the pixel values in an image window. This is done by iteratively applying a convex hulling algorithm [2]. The method relies on the correlation of the speckle process.

MAP estimation is a more accurate approach. It allows one to encapsulate the full knowledge about the SAR imaging system combined with prior information. Several methods have been developed investigating different prior models and degrees of refinement of the likelihood [16, 22]. A full Bayesian inversion is formulated in [8] and an application of the principle of Maximum Entropy is proposed in [27].

A classical homomorphic transform coupled with a Wiener filter was demonstrated recently [6] to give promising results.

The fields of multiresolution/multiscale signal modelling and analysis yield the best results for speckle removal and also reduce computational complexity. Heuristical multiresolution techniques based on the analysis of the noise variance at several resolutions are reported in [21, 24], de-noising techniques in the wavelet domain were investigated [10] with very good results. A new area emerged based on the theory of multiscale modelling of stochastic random fields [1, 18]. Recent results are presented in [5].

SAR images are intrinsically complex data. An approach which requires the least approximations in the modelling of SAR images relies on complex data and the complex nature of the SAR imaging system [3, 15]. Despeckling is formulated as an inverse problem. At least two formalisms have been investigated: a Bayesian inversion based on a prior expressed as a Gibbs random field [3, 12, 25], and a regularized inversion using the principle of Maximum Entropy [4].

EVALUATION OF THE IMAGE QUALITY

The quality of the despeckled images is an open topic. Several authors approach the problem from the SAR image quality point of view, others from the general perspective of image processing as the capability of preserving image features, and others from the application point of view measuring the quality of the classification process applied to the despeckled images [20, 26, 19]. None of the methodologies is fully satisfactory, and mainly for the model based methods, the image quality evaluation has to be approached from an information theoretic perspective.

More specifically, the most powerful despeckling algorithms are formulated as a scene understanding task: *to find the scene which best explains the observed data*. Such a problem is ill-posed. The scene inversion is a model based approach with regularization constraints. The solutions are model and regularization dependent. The models and sets of constraints carry our prior information and knowledge or encapsulate our assumptions. To deal in a systematic way with the *prior*, a consistent alternative is to investigate the inversion methods in the frame of the Bayesian inference and comparatively analyze the pure Bayesian approach with the methods of Maximum Entropy (MAXENT). These methods generally require to solve highly complex optimization problems with no or very difficult analytical representations. Their implementations result in stochastic relaxation methods.

Modelling plays an important role in information extraction. The performance of the solution critically depends on the descriptive accuracy of the model. The quality of the solution, i.e. the despeckled images can be interpreted as the quality of the used model.

Comparing models is a delicate task, more complex models can always fit better the data. Thus the maximum likelihood choice would lead us to implausible over-parameterized models that generalize poorly. It is the Bayesian approach that penalizes any unnecessarily complicated models; it favours the simpler and more precise ones.

From the strict perspective of information theory the accuracy of the models and implicitly of the despeckling algorithms can

be quantitatively measured in several ways. One can evaluate the relative entropy of finite dimensional distributions or the relative entropy rate of stochastic processes; one can compute the mutual information which quantifies the prior. This is directly related to the Occam factor [27] used for the model selection. One can also estimate the rate distortion function that quantifies the quality loss vs. the reduction of the information content, or the Pareto [28] frontier that characterizes the non-dominant solutions.

As a consequence, the modelling is no more a trivial task. Existing solutions are the decomposition of the sources which co-exist in the same process. Multiple models and cluster based modelling approaches are used; elegant solutions are hierarchical and multiscale modelling [3, 18, 23].

Gibbs Random Fields (GRF) are a rich class of models well suited for region processes and the description of textures. The limitations of GRF are due to the limited size of the neighborhood which can be described. The signals usually consist of features of physically significant structures at multiple scales; the sensors may provide signals of the same scene at several resolutions.

Multiscale stochastic models can describe a much larger class of images. GRFs represent a particular sub-class.

The image processing and analysis can be substantially enhanced and simplified computationally if they are designed to capture the multiscale nature of the data.

A different approach is cluster-based probability modelling. The method combines the techniques of generalization and summarizing.

PROSPECTS

We consider that improved modelling, simultaneous restoration and segmentation will lead to improved multiscale cluster based methods. At present, multiscale methods lack sufficient representation of image formation. We expect future developments that are faster than the present ones, however, we fear that these future systems will become more complicated.

TABLE 1: COMPARISON OF DESPECKLING ALGORITHMS

METHOD	QUALITY	LEVEL	RUN TIME
MULTILOOK	LOW	LOW	LOW
HOMOGEN	LOW	LOW	LOW
DIRECTIONAL	MEDIUM	LOW	LOW
GEOMETRICAL	MEDIUM	MEDIUM	MEDIUM
GAMMA MAP	MEDIUM	MEDIUM	MEDIUM
TEXTURES	MEDIUM	MEDIUM	MEDIUM
GIBBS	HIGH	HIGH	HIGH
MAXENT	VERY HIGH	HIGH	HIGH
WIENER	MEDIUM	MEDIUM	MEDIUM
MRES. HEUR.	MEDIUM	LOW	LOW
MULTISCALE	HIGH	HIGH	LOW

METHOD	QUALITY	LEVEL	RUN TIME
DENOISING	MEDIUM	LOW	LOW
ADAPTIVE	HIGH	LOW	LOW
MARKOV CPLX	VERY HIGH	HIGH	HIGH
MARTINGALE	HIGH	HIGH	HIGH
MAXENT CPLX	VERY HIGH	HIGH	HIGH

CONCLUSIONS

The best results are obtained by MAXENT or a full Bayesian approach when applied to complex data. That is mainly due to the accurate modelling of the SAR image formation in the complex domain. As an alternative, we consider the despeckling in the Bayesian approach and MAXENT for real valued images. However, all these algorithms are computationally complex. Very good suboptimal but much faster algorithmic solutions are obtained by wavelet based methods and multi-scale approaches. Several examples are presented in Figure 1.

SELECTED REFERENCES

[1] C.A. Bouman, M. Shapiro, 1994, "A Multiscale Random Field Model for Bayesian Image Segmentation", IEEE Tr. IP, Vol. 3, pp. 162-177.

[2] T.R. Crimmins, 1986, "Geometric Filter for Reducing Speckle", Applied Optics, Vol. 24, pp. 1438-1443.

[3] H. Derin, P.A. Kelly, G. Vezina, S.G. Labitt, 1990, "Modeling and Segmentation of Speckled Images Using Complex Data", IEEE Tr. GSRS, Vol. 28, pp. 76-87.

[4] B.R. Frieden, A.T. Bajkova, 1994, "Bayesian cross-entropy reconstruction of complex images", Applied Optics, Vol. 33, pp. 219-226.

[5] C.H. Fosgate, H. Krim, W.W. Irving, W.C. Karl, A.S. Willsky, 1997, "Multiscale Segmentation and Anomaly Enhancement of SAR Imagery", IEEE Tr. IP, Vol. 6, pp. 7-20.

[6] G. Franceschetti, V. Pascasio, G. Schirinz, 1995, "Iterative homomorphic technique for speckle reduction in synthetic-aperture radar imaging", J. Opt. Soc. Am., A12, pp. 686-694.

[7] V.S. Frost, K.S. Shanmugan, J.C. Holtzman, 1982, "A Model for Radar Images and its Application to Adaptive Digital Filtering", IEEE Tr. PAMI, Vol. 4, pp. 185-190.

[8] S. Geman, S. Geman, 1984, "Stochastic Relaxation, Gibbs Distributions, and the Bayesian Restoration of Images", IEEE Tr. PAMI, Vol. 6, pp. 721-741.

[9] J.W. Goodman, 1975, "Statistical Properties of Laser Speckle Patterns" in: Laser Speckle and Related Phenomena Edit. J.C. Dainty, Springer.

[10] H. Guo, J.E. Odegard, M. Lang, R.A. Gopinath, I.W. Selesnick, C.S. Burrus, 1994, "Speckle Reduction via Wavelet Shrinkage with Application to SAR based ATD/R", CML TR94-03, Rice University.

[11] W. Hagg, M. Sties, 1994, "Efficient Speckle Filtering of

SAR Images", Proc. IGARSS '94, pp. 2140-2142.

[12] H. Hetzheim, 1993, "Using Martingale representation to adapt models for non-linear filtering", Proc. ICSP93, pp. 32-35.

[13] P.A. Kelly, H. Derin, K.D. Hartt, 1988, "Adaptive Segmentation of Speckled Images Using a Hierarchical Random Field Model", IEEE Tr. ASSP, Vol. 36, pp. 1628-1641.

[14] J.S. Lee, 1980, "Digital Image Enhancement and Noise Filtering", IEEE Tr. PAMI, Vol. 2, pp. 165-168.

[15] J.S. Lee, K.W. Hoppel, A.R. Miller, 1994, "Intensity and Phase Statistics of Multilook Polarimetric and Interferometric SAR Imagery", IEEE Tr. GSRS, Vol. 32, pp. 1017-1027.

[16] A. Lopes, E. Nezry, R. Touzi, H. Laur, 1990, "Maximum a posteriori speckle filtering and first order texture models in SAR images", Proc. IGARSS '90, pp. 2409-2412.

[17] A. Lopez, R. Touzi, E. Nezry, 1990, "Adaptive Speckle Filters and Scene Heterogeneity", IEEE Tr. GSRS, Vol. 28, pp. 992-1000.

[18] M.R. Luetgen, W.C. Karl, A.S. Willsky, R.T. Tenney, 1993, "Multiscale Representation of Markov Random Fields", IEEE Tr. SP, Vol. 41, pp. 3377-3395.

[19] I. McConnell, C. Oliver, 1996, "Comparison of annealing and iterated filters for speckle reduction in SAR", Proc. SPIE Vol. 2958, pp. 74-85.

[20] G. F. McLean, M.E. Jernigan, 1991, "Indicator functions for adaptive image processing", J. Opt. Soc. Am., A8, pp. 141-156.

[21] P. Meer, R.-H. Park, K. Cho, 1994, "Multiresolution Adaptive Image Smoothing", CVGIP, Vol. 56, pp. 140-148.

[22] C.J. Oliver, 1991, "Information from SAR images", J. Phys. D, Vol. 24, pp. 1493-1514.

[23] K. Popat, R. W. Picard, 1997, "Cluster-Based Probability Model and Its Application to Image and Texture Processing", IEEE Tr. IP, Vol. 6, pp. 268-284.

[24] S. Ranganath, 1991, "Image Filtering Using Multiresolution Representations", IEEE Tr. PAMI, Vol. 13, pp. 426-440.

[25] E. Rignot, R. Chellappa, 1991, "Segmentation of synthetic-aperture-radar complex data", J. Opt. Soc. Am., A8, pp. 1499-1509.

[26] Y. Sheng, Z.-G. Xia, 1996, "A Comprehensive Evaluation of Filters for Radar Speckle Suppression", Proc. IGARSS '96, pp. 1559-1561.

[27] C. Toma, M. Datcu, 1992, "Maximum entropy and minimum cross-entropy methods in image processing", Proc. SPIE Vol. 1827, pp. 133-144.

[28] C. Toma, M. Datcu, 1994, "Genetic Algorithm for Maximum Entropy Image Restoration", Proc. SPIE, Vol. 2304, pp. 253-264.

[29] E.P. Simoncelli, E.H. Adelson, 1996, "Noise removal via Bayesian wavelet coring", Proc. 3rd IEEE Int. Conf. IP.

NOTE: The list of references is restricted due to the limited space.

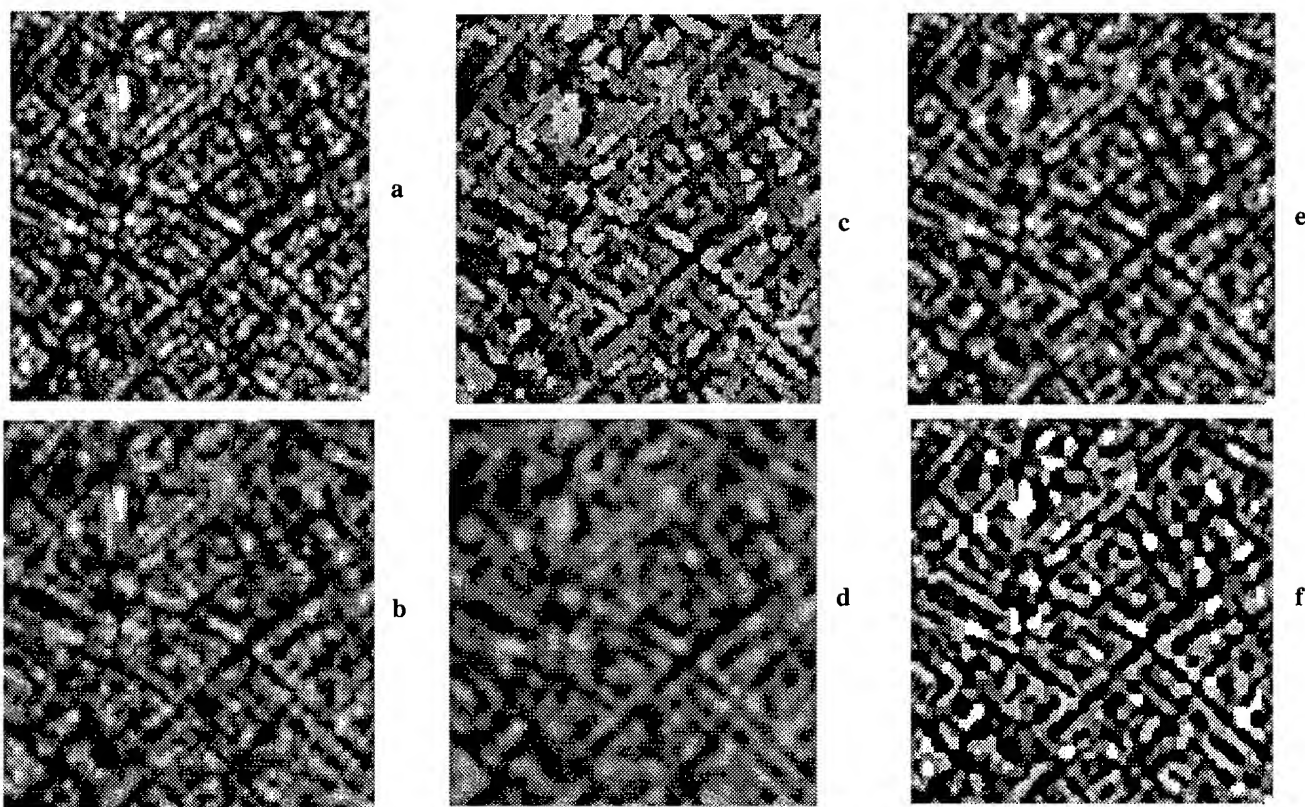
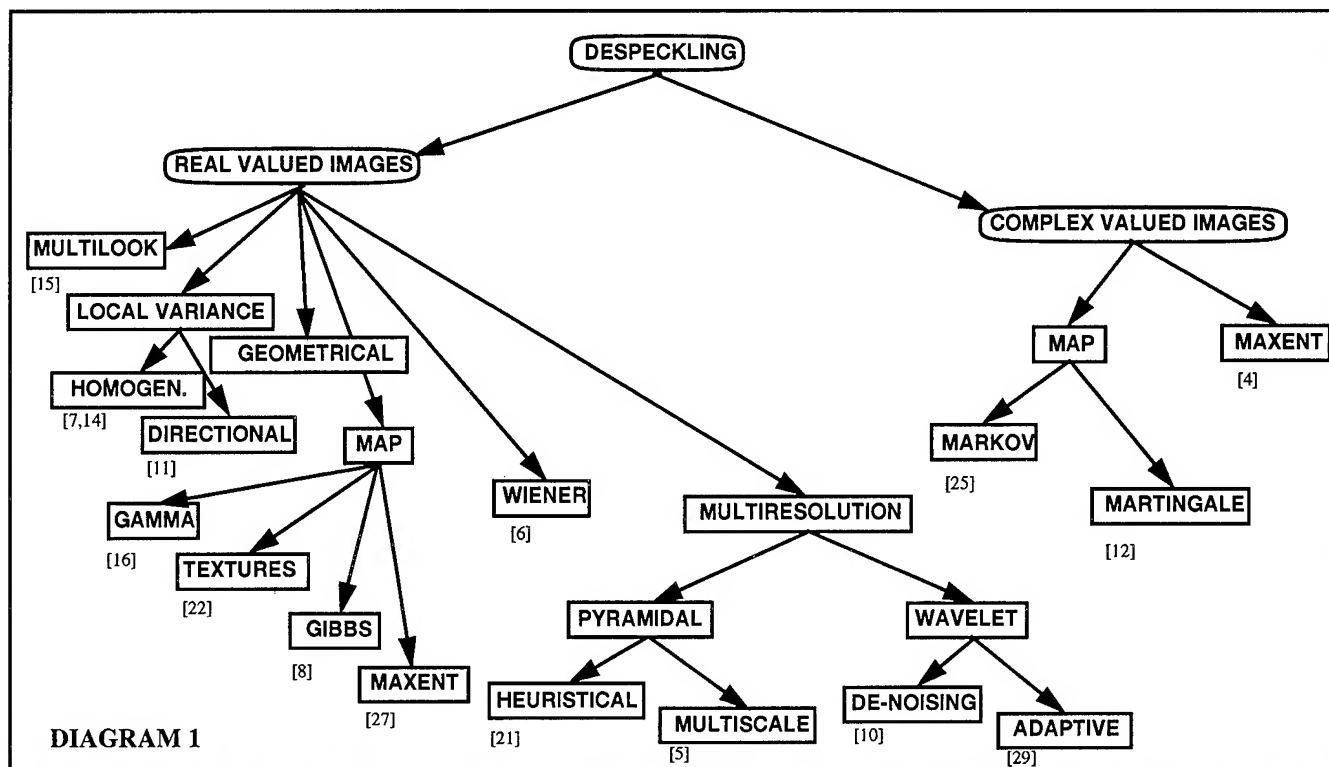


Figure 1: a) Original image (X-SAR, city of Munich), b) Wavelet based denoising [10], c) Edge Preserving Optimized Speckle filter [11], d) Gamma Maximum a Posteriori (GMAP) estimation [16], e) Maximum Entropy reconstruction [27], f) Stochastic Relaxation MAP reconstruction with Gibbs prior [8].

Early Identification and Surface Estimation of Agricultural Crops Using ERS SAR Images

Edmond Nezry

PRIVATEERS NV, Private Experts in Remote Sensing

42 De Weaver Drive, Philipsburg, Sint Marteen, Netherlands Antilles; c/o 21 via Carducci, 21027 Ispra, Italy

Phone/Fax: (+39) 332-781494; E-mail: via <http://www.treemail.nl/privateers/>

ABSTRACT

This paper outlines the operational feasibility of very early ERS SAR based acreage estimation of non-agriculture land (set-aside, fallow) and economically important crops in Europe, already during the winter season. To achieve this goal, a novel method for SAR time-series classification and interpretation has been developed. Results of a real-time ERS experiment are presented. Such results have been used for the first time in March 1995 to support the Rapid Estimates project of the European Union (EU). They are confronted here to the first SPOT based estimates from this project obtained only two months later.

1. INTRODUCTION

During the winter in Europe, and more generally in temperate zones, no or low agricultural vegetation cover is actually present on the ground. During most of this season, agricultural targets are principally the soils on which crops will grow later on, and it is generally not possible to identify directly crop species from the analysis of optical remote sensing images. For this reason, the first surface estimates are not available earlier than May, when weather conditions are favourable and crops start developing their plant structure. Nevertheless, already during the winter, the specific sensitivity of SAR's to important soil properties, such as surface roughness and moisture content can be exploited. These properties of soils as well as their evolution over time are not casual, as far as agricultural surfaces are concerned. Thus, a reasoning and processing methodology has been designed, to exploit the causal relationships existing between soil properties and crop cultivation. In order to understand and correctly interpret time-series of the ERS radar signal backscattered by non- or low-vegetated terrain, reasoning must involve solid knowledge regarding agriculture, SAR physics, as well as SAR image processing and classification.

To discriminate between non-cultivated and cultivated surfaces, and to identify the major crop types, a simple methodology for the winter monitoring of agriculture in Europe using ERS SAR images has been developed. Its concepts are based on the experience acquired from previous research regarding: the physical modelling of C-band SAR backscatter [1], the influence of meteorological effects on the ERS radar cross-section over time and the content of

agricultural information in ERS time series [2]. It is conceived to be robust regarding influences of meteorological factors on the ERS radar cross-section over time, and to emphasize the use of application-relevant information. The methodology combines multidisciplinary knowledge of:

1) The physics of interaction between the incident radar wave and natural media. The sensitivity of ERS backscattered amplitude (radiometry and to a lesser extent, texture) to soil roughness [e.g. 2-4] at the beginning of the agricultural season is of particular importance to achieve complete detection of prepared land. From February on, volume diffusion effects observable on the first growing crops [e.g. 3-5] are also exploited.

2) The agricultural practices and crop calendars at the site scale, which provide the interpretation clues for the identification of the most important crop types.

2. OVERALL METHODOLOGY

In practice, the implementation of this methodology using ERS time series for very early crop acreage estimates is as follows:

1) Specific SAR image processing is applied to the ERS PRI frames: full calibration, adaptive speckle filtering [6-7], and accurate co-registration.

2) Transformation of the time series (at least 3 acquisitions per-site, for topological correctness) into 3 synthetic channels, as uncorrelated as possible between each other. As shown in the next section, these channels are designed to provide an understandable picture of both the causes and the history of the ERS radar cross-section of agricultural targets during the observation period.

3) Spatial segmentation is then carried out through isodata clustering of the synthetic channels, a statistically objective method to identify natural data groupings.

4) The final crop (or group of crops) classes are identified through deductive interpretation of the synthetic channels using general knowledge regarding agriculture (main crops present on the area, their calendars and associated practices), physics (interaction wave/medium) and statistics (clusters structure). This way, the statistically defined clusters are recombined into well identified crops and land-use classes. Finally, separate detection and classification of structural elements [6] (built-up areas, main roads, rivers) improve the spatial accuracy of the final result.

3. SAR TIME-SERIES DECOMPOSITION

Classically, decomposition of a time series into uncorrelated channels is done using Principal Component Analysis (PCA). Unfortunately, this technique is too sensitive to particular environmental conditions affecting SAR images (e.g. rain) and not directly related to agriculture themes [2]. Furthermore, it generally hinders further physical interpretation of the evolution of radiometry in a time series. To preserve the physical and historical information meaningful to the current application, the following parameters are computed for every pixel:

- a) Mean backscattered amplitude during the period of observation ("backscatter" channel);
- b) Range of radar cross-section variation during the period of observation ("variation" channel).
- c) Date of maximum backscattered signal ("history" channel).

A previous study [2] showed that the two first channels provide a representation, in which urban, forest, grassland, bare soils and agricultural themes can already be separated using ERS time series.

For winter SAR observations, the third channel provides us with useful information regarding field preparation. Past experiments show that field preparation result in a very strong increase of ERS backscattered signal (up to more than 10 dB) whose effect remains visible for a timeframe of about one month [2]. This channel provides an additional discriminator for crop identification in relation to the knowledge of crop calendars provided that, as it is generally the case at test-site scale, all fields dedicated to the same crop are prepared at nearly the same time. If soil preparation occurred too long before the beginning of ERS observation (summer/early fall), crop phenology plays also a role that is registered by this channel as a relative maximum of the backscatter level at the end of observation (February), when the dense agricultural vegetation cover exceeds 20-50 cm (cf. rapeseed fields in Chartres), as observed and modelled in the literature [e.g. 4]. Variable environmental conditions are responsible for a general ensemble modulation of about 2 to 4 dB (depending on site and season) of the temporal crop signatures in ERS winter time series [2]. The major advantage of feature space selection is to filter this disturbing effect, allowing to exploit almost all SAR acquisitions. It is also well known that the choice of the appropriate feature space improves significantly the accuracy of clustering/classification results.

4. REAL-TIME OPERATION - TEST AREAS

A real-time pre-operational ERS project was carried out over 3 very different European test-areas (40x40 km each). Nineteen ERS frames were acquired from Nov. 1994 to Feb. 1995:

- Albacete (Spain): 4 dates, 5 frames acquired,

This test site was chosen to evaluate the method on a site presenting some difficulties in terms of both geomorphology and of agriculture. Important part of the site is mountainous, with altitude variations to more than 1000 m. In this test-area, arable land is being increasingly set aside for low rentability, and most cultivations require irrigation.

- Bologna (Italy): 7 dates, 7 frames acquired,

This test area includes most of the richest Italian agricultural region Emilia-Romagna. It is a flat plain, densely populated, located between the Po river and the Apennines mountains.

- Chartres (France): 4 dates, 7 frames acquired.

This site is located within one of the richest agricultural areas in Europe. Its monitoring is particularly important for the estimation of cereals production in France. The area is hilly, but with gentle slopes not exceeding 5 degrees.

Data were delivered within an average 10 days after acquisition, meeting the nominal delay constraints. The processing, interpretation and classification of SAR data were conducted as to make results available early in March.

5. RESULTS AND DISCUSSION

Examination of the classifications (available in [8]) shows that they present a good robustness to the relief characteristics within agricultural zones. Limitations regard mountainous areas where the clustering procedure is confused by the presence of strong relief. It is noteworthy that comparison with SPOT-based results shows that similar problems are met in the same areas using optical remote sensing data.

Comparisons between our ERS-based surface estimates and the SPOT-based estimates (using also ancillary information such as last year classifications, statistical trends, farmers declarations, etc.) of the operational EU project, are summarized in Tables 1 to 3. After running this project for 7 years, the EU claims for an accuracy superior to 85% for these estimations obtained in May.

Tables show that good agreement regarding the major land-use is generally found.

Crops (surfaces in ha.)	ERS-1, 7 dates 15/11/94- 17/2/95	SPOT, 2-dates 21/3/95 - 3/5/95
Non-cultivated	13029	13844
Rice	636	438
Perennial crops	23888	29280
Winter cereals	56139	43840
Sugar beets	23005	22295
Potato + maize	10463	10330
Spring crops	8729	7332
Non-agriculture	24109	32640

Table 1: Bologna test site. Surface estimates obtained using ERS (March) and SPOT (May) multi-temporal data.

Important differences can be noted on the Bologna test-area only, for the two following themes:

- non-agricultural surfaces, over estimated on the SPOT-based classification which includes part of the rice fields and spring cultivations in this class,
- winter cereals due to overestimation in the SPOT-based classification, and to residual confusion with perennial vegetation in our ERS classification.

For all other crops, estimations show good agreement, within the 15% uncertainty band of the SPOT-based estimations.

Crops (surfaces in ha.)	ERS-1, 4 dates 28/11/94- 10/2/95	SPOT, 2-dates 4/3/95 - 5/5/95
Non-cultivated	14225	11499
Winter wheat	68178	70622
Other cereals	5357	10015
Rape seed	12834	11360
Summer crops	24368	25784
Non-agriculture	35038	30720

Table 2: Chartres test site. Surface estimates obtained using ERS (March) and SPOT (May) multi-temporal data.

Crops (surfaces in ha.)	ERS-1, 4 dates 12/06/94-02/18/95	SPOT, 3-dates 03-04-05 / 1995
Non-cultivated	16576	not comparable
Vineyards and natural vegetation	35643	not comparable
Winter cereals	24791	27338
Other cereals	6412	6319
Sunflower	4226	3426
Maize / Corn	4062	5760

Table 3: Albacete test site. Surface estimates obtained using ERS (March) and SPOT (July) multi-temporal data.

6. CONCLUSION

Results show that very early ERS-based surface estimates of major crops and non-cultivated terrain can be carried out in operational conditions, when SAR data sources are reliable.

The method is technically simple and requires only state-of-the-art processing tools. Moreover, solid knowledge and understanding of SAR related physics and agriculture, as well as a solid experience in SAR data processing, are required.

It proved robust to geographical diversity, to site-landscape complexity, and to the effects not directly related to the agricultural use of soils (e.g. environmental effects). To achieve this robustness, the application-relevant ERS information is selected in the synthetic channels.

The agricultural targets of interest in ERS winter time series are identified using only general knowledge in physics and agriculture. They support an interpretation that is primarily based on a statistical analysis of the remote sensing data,

specifically oriented towards the identification of the agricultural themes of interest.

Good performances are obtained for the identification and surface estimation of major crops within a range of geomorphologic conditions similar to that on which optical remote sensing is successful. This range also coincides with the conditions for mechanized agriculture.

Finally, the method is economically valid, since the required data processing is inexpensive, and extensive ground survey is not a requirement. In addition, this method is conceived to provide, independently from other sources, very early crop surfaces estimations that represent an economically and/or financially valuable complementary information, about one month before crop prices are fixed on the short term market.

ACKNOWLEDGMENTS

Dr. J. Lichtenegger, Dr. G. Paci, Mrs. S. Rémondrière and Mr. G. Solaas (ESA/ESRIN), Mr. G. Genovese (JRC), and Dr. G. Kattenborn (Univ. Freiburg, FRG) contributed to the success of this work, within the ERS Pilot Project PE-FRNE.

REFERENCES

- [1] A. Beaudoin, T. Le Toan, S. Goze, E. Nezry, A. Lopes, E. Mougin, C.C. Hsu, H.C. Han, J.A. Kong, R.T. Shin, 1994: "Retrieval of forest biomass from SAR data", *Int. J. Rem. Sens.*, Vol.15, n°14, pp.2777-2796.
- [2] G. Kattenborn, E. Nezry, G. De Grandi, 1993: "High resolution detection and monitoring of changes using ERS-1 time series", *Proc. of the 2nd ERS-1 Symposium*, 11-14 Oct. 1993, Hamburg (FRG), ESA SP-361, Vol.1, pp.635-642.
- [3] F.T. Ulaby, M.C. Dobson, 1989: "Handbook of radar scattering statistics for terrain", Artech House Inc., Norwood (MA), USA.
- [4] E. Mougin, 1989: "Mesure et modélisation des effets des paramètres du couvert sur la propagation et la rétrodiffusion des ondes radar", Ph.D. dissertation, Institut National Polytechnique de Toulouse (France), 231 p.
- [5] H. Laur, 1989: "Analyse d'images radar en télédétection: Discriminateurs radiométriques et texturaux", Ph.D. dissertation, Univ. Paul Sabatier, (France), 250 p.
- [6] A. Lopes, E. Nezry, R. Touzi, H. Laur, 1993: "Structure detection and statistical adaptive speckle filtering in SAR images", *Int. J. Rem. Sens.*, Vol.14, n°9, pp.1735-1758.
- [7] E. Nezry, M. Leysen, G. De Grandi: "Speckle and scene spatial statistical estimators for SAR image filtering and texture analysis: Applications to agriculture, forestry and point targets detection", *Proc. of SPIE*, Vol.2584, pp.110-120, Sept. 1995.
- [8] E. Nezry, G. Aa. Solaas, S. Rémondrière, G. Genovese, G. Kattenborn, 1996: "Early crop identification and area estimation in Europe surfaces using ERS winter SAR images", submitted to *IEEE Trans. on Geosc. and Rem. Sens.*, unpublished.

Landcover Classification over the Mekong River Delta using ERS and RADARSAT SAR images

S. C. Liew^(a), S. P. Kam^(b), T. P. Tuong^(b), P. Chen^(a), V. Q. Minh^(c), and H. Lim^(a)

^(a)Centre for Remote Imaging, Sensing and Processing, National University of Singapore,
Lower Kent Ridge Road, Singapore 119260.
tel: (+65) 7715069, fax: (+65) 7757717, email: phylliew@nus.edu.sg

^(b)International Rice Research Institute, P.O. Box 933, 1099 Manila, Philippines

^(c)Department of Soil Science, Faculty of Agriculture, University of Can Tho, Can Tho, Vietnam

Abstract -- Unsupervised classification of the landcover in the rice growing area in the Mekong river delta was performed using a combination of the ERS and RADARSAT SAR data. The ERS SAR is VV polarized while the RADARSAT SAR is HH polarized. The advantages of multiple polarization SAR in landcover classification may be realized using data from these two satellites together. The study area for this work covers the Soc Trang and Bac Lieu provinces of Vietnam where a diversity of rice cropping systems is practiced. Rice crops at different growth stages exist in the area at any one time together with other non-rice vegetation. These classes can be discriminated using a combination of the two SAR images.

INTRODUCTION

Polarimetric synthetic aperture radar (SAR) has been reported to yield useful information for landuse classification [1]. Currently, multiple polarization SAR is not available on the existing remote sensing satellites. The SAR on the ERS satellite is VV polarized while the RADARSAT SAR is HH polarized. Furthermore, the ERS SAR has a fixed incident angle but the incident angle is variable for RADARSAT. By combining the ERS and RADARSAT SAR data acquired at approximately the same dates, the advantages of multiple polarization SAR with multiple look angles in landcover classification may be realized.

In this paper, we describe the results of landcover classification using SAR images acquired from the ERS and RADARSAT satellites in a rice growing area of the Mekong river delta. The study area for this work covers the Soc Trang and Bac Lieu provinces of Vietnam where a diversity of rice cropping systems is practiced [2]. Due to the varied rice planting systems, plots of rice crops at different growth stages exist in the area at any one time. Besides rice, there are also other types of vegetation such as fruit orchards, mangroves and Melaleuca forests in this area.

Our results indicate that by combining the two ERS and RADARSAT SAR images, rice in different growth stages as

well as non rice vegetation can be discriminated. Confusion exists if either image were used alone in the classification procedure.

METHODS

An ERS scene (September 22, 1996, descending mode) and a RADARSAT (September 17, 1996, S6 mode) of the study area were used in the study. The two scenes were co-registered using common ground control points and georeferenced to a 1:100,000 topographic map. The SAR scenes were first converted to 8-bit images by dividing the 16-bit digital numbers by 4 for the ERS scene, and by 100 for the RADARSAT scene. Both images had approximately the same means and standard deviations after conversion. The images were low-pass filtered using a 5x5 averaging window and then downsampled to 50-m pixel size. An edge-preserving speckle removal filter based on the adaptive Wiener filter for multiplicative noise was applied.

Unsupervised classification using the ISODATA algorithm (in the ERDAS IMAGINE software package) with 10 classes was performed, treating each image as a band in the two-band image. After classification, some classes were merged to obtain 8 final classes. The merged classes had significant overlapping histograms and occurred in proximity of each other in geographical locations. The results of classification were interpreted in relation to the results obtained in another study of the same area using multitemporal ERS SAR data [3].

Field surveys were carried on September 22 to ascertain the field conditions and crop stages in over 90 sampling plots within the test area.

RESULTS AND DISCUSSIONS

The result of classification is shown in Fig. 1 and the scatter plot of the class means is shown in Fig. 2. From the scatter plot, it can be seen that there is a general correlation between the digital numbers for the ERS and RADARSAT

images. However, there are also classes (1 and 6) where the DN is high in one image but low in the other image. The classes can be sorted in terms of their brightness in the two images, as shown in Table 1. The interpretations of the landcover types associated with these classes are listed in Table 2.

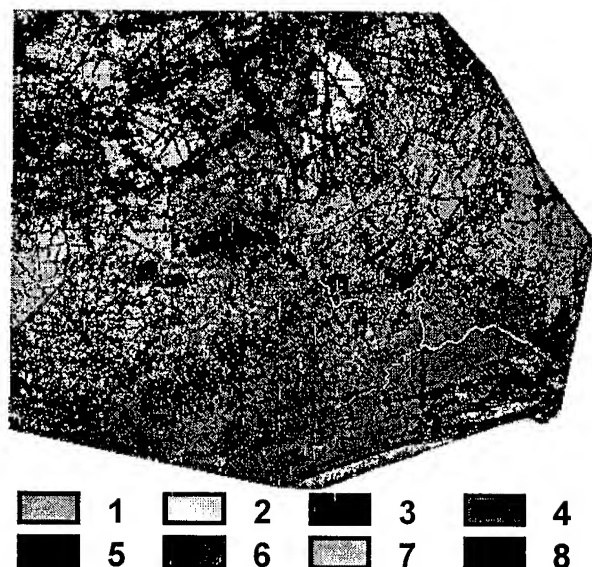


Fig. 1: Result of unsupervised classification using a pair of ERS and RADARSAT SAR images. The numbers in the legend are the class identification numbers.

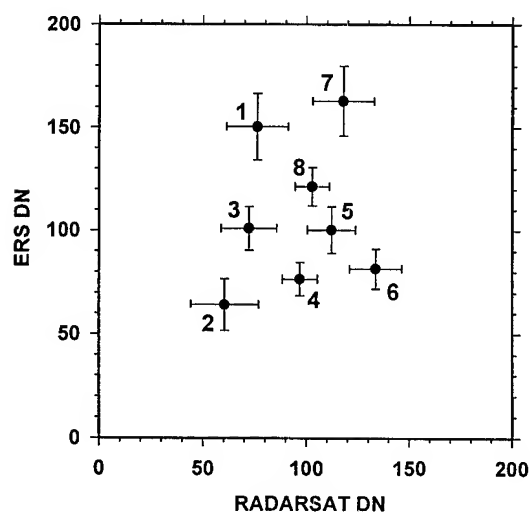


Fig. 2: Scatter plot of the class means for the classification map shown in Fig.1. The class standard deviations are plotted as error bars.

Table 1: Arrangement of the classes according to their ERS and RADARSAT image brightness

ERS High	Class 1	Class 7	
ERS Medium	Class 3	Class 5 Class 8	
ERS Low	Class 2	Class 4	Class 6
	RADARSAT Low	RADARSAT Medium	RADARSAT High

Table 2: Landcover Classes obtained from unsupervised classification of the ERS/RADARSAT composite image

Class Number	Landcover Type
1	uncertain
2	flooded fields
3	newly planted rice on flooded fields
4	rice in flowering/ripening stages
5	orchard trees, melaleuca forest
6	rice in booting stage
7	builtup area, moist rough soils (?)
8	non-rice vegetation, heterogeneous rice stages

The areas coloured black (class 5) in Fig. 1 are mainly associated with the non-rice vegetation along the canals and the melaleuca forests (black rectangular patch near the centre of the map). The backscattering coefficient is about -7 dB in the ERS image.

The yellow areas (class 2) in Fig. 1 have low backscatter in both the ERS and RADARSAR images. They are very likely the flooded fields in low-lying areas, i.e. with standing water, little or no vegetation. They occur both in the irrigated (upper half of the image) and the rainfed (lower left) double cropping areas. The first crop has been harvested before flooding and the second crop starts only after the flood subsided. The brown areas (class 3) have low backscatter (similar to class 2) in the RADARSAT image, but higher backscatter in the ERS image. They are probably flooded fields with newly planted rice. The higher ERS backscatter may be also be due to partially exposed soils because of land preparation.

The red areas (class 6) have high RADARSAT, but low ERS backscatter. They are very distinctly associated with the rainfed single crop region along the coast. The rice crop was in the booting stage during the field check on Sep 22.

The magenta areas (class 4) are quite widespread. Near to the coast, they occur in areas more inland from the red areas.

Normally these areas have their salinity flushed out earlier than the red areas, so the rice crop is expected to be planted slightly earlier and hence should be more advanced than the booting stage of the red class. In the more inland rainfed double cropping areas (top of the image), the magenta areas (class 4) are also in the flowering/ripening stages. It is interesting to note that the RADARSAT backscatter is distinctly higher for the booting stage and then seem to drop as the reproductive stage of the crop advances.

The blue areas (class 8) associated with the linear features along the canals, and also in areas near to the coast (at lower right corner of map) are non-rice areas since their backscatter is relatively stable temporally in our previous study using multitemporal SAR [3]. However, class 8 also occurs within the rice areas. During the field check, these areas were in the transition between the harvest of the first crop and planting of the second crop and the fields were heterogeneous. Some plots were in the ripening stage while an adjacent plot could be newly planted with the second crop.

Class 1 (coloured cyan) and Class 7 (coloured green in Fig. 1) have high ERS backscatter, but low to medium RADARSAT backscatter. In our sampling sites near to the middle of the map, the area had mainly newly planted rice crop. However, the field conditions for the cyan/green areas near to the right of the map were uncertain. It is interesting to note that the builtup areas like the towns of Soc Trang, Bac Lieu and Phung Hiep have high backscatter in the ERS image, as expected, but the RADARSAT backscatter is only in the medium range. In fact, these towns could not be discriminated easily from the surrounding rice areas by visual inspection of the RADARSAT image. These builtup areas are classified into class 7 (green areas in Fig. 1). The town of Bac Lieu is especially noticeable in Fig. 1 as a green dot surrounded by the red areas near to the bottom of the map.

Unlike the previous study [3] using multitemporal ERS SAR data which allows delineation of rice cultivating systems in the Mekong delta, the present study using only two images acquired in September (5 days apart) would not be able to yield information about rice cultivating system, which requires the knowledge of the temporal pattern of the radar backscatter. The two SAR images only give information about the landcover types at the time of acquisition.

The broad spread in the scatter plot of the class means show that the SAR data from ERS and RADARSAT complement each other well in landcover classification. For example, Classes 4 and 6 (low to medium ERS brightness) would not be discriminated in the ERS image, but they are well separated in the RADARSAT image. Classes 4, 5, 7 and 8 appear to have similar medium level brightness in the RADARSAT image, but they can be discriminated with the addition of the ERS image in the classification.

Due to the differences in polarization and incident angles between RADARSAT and ERS SAR, the response of RADARSAT SAR as a function of the rice plant growth stage is expected to be different. Our observations seem to indicate that the RADARSAT backscatter increases initially with growth stage, but decreases as the reproductive stage advances. Controlled experiments and numerical modelling of the effects of incident angles and polarization need to be done to better understand this observation.

CONCLUSIONS

We have performed an unsupervised classification of the landcover in the rice growing areas of the Mekong river delta. Our results indicate that different stages of the rice crops can be discriminated by combining ERS and RADARSAT SAR images. A scatter plot of the class means show that the classes would not be distinguished if either one of the images were to be used alone.

REFERENCES

- [1] L. E. Pierce, F. T. Ulaby, K. Sarabandi, and M. C. Dobson, "Knowledge-based classification of polarimetric SAR images," *IEEE Trans. Geosci. Remote Sensing*, vol. 32, pp. 1081-1086, 1994.
- [2] T.P. Tuong, C.T. Hoanh and N.T. Khiem. 1991. "Agro-hydrological factors as land qualities in land evaluation for rice cropping patterns in the Mekong Delta of Vietnam," in P. Deturck and F.N. Ponnampetuma (eds.) *Rice Production on Acid Soils of the Tropics*. Institute of Fundamental Studies, Kandy, Sri Lanka.
- [3] S. C. Liew, S. P. Kam, T. P. Tuong, P. Chen, V. Q. Minh, L. Balababa, and H. Lim, "Delineation of rice cropping systems in the Mekong river delta using multitemporal ERS synthetic aperture radar," *Proc. 3rd ERS Symposium*, Florence, Mar. 17-21, 1997 (in press).

Comparison Between Classified Result of Paddy Field and Statistic Data of the Production

Tsukasa Hosomura and Ceballos Silva Alejandro P.

Kanazawa Institute of Technology

Ohgigaoka 7- 1, Nonoichi- machi, Ishikawa 921, Japan

Tel:+81- 762- 94- 6708/Fax:+81- 762- 94- 6709/E- mail:hoso@infor.kanazawa- it.ac.jp

Abstract -- Advances in remote sensing (RS) and computer technology have given the tools needed to monitor and assess the status of natural resources like natural vegetation and agroecosystems. The scientific bases of the potential usefulness of multispectral reflectance in agriculture and natural resources is based on the fact that different objects as well as different organisms reflect the energy of sun in different way. Several RS techniques has been used for several applications, including: identifying crops, evaluating grassland condition and productivity, monitoring vegetation and providing indicators of the yield of crops. The objective of this study is to classy the type of crops and to estimate their production using Landsat image for Kanazawa area. The estimation of crop production will be compare with the available statistics data for this zone.

INTRODUCTION

Detailed agricultural statistics are essential for an adequate monitoring and an eventual improvement of Agricultural Policy specially in countries where production food is a vital problem. The diversity of agricultural areas prevents the exclusive use of field surveying due to the large sampling effort that would be required for high accuracy.

The analysis of satellite and airborne remotely sensed imagery has introduced a notable improvement in agricultural statistics⁽⁷⁾. Besides the complexity of agriculture landscapes make it necessary that the information is cartographically and ultimately integrated in a geographical information system (GIS). Such an integration would facilitate the analysis within an environmental and social context. The technology of GIS provides a means of introducing information and knowledge from other data sources into the decision- making process and help in handling and manipulating the classified remotely- sensed data.

Although in some studies using a single date supervised

classification approach confusion between different crops was observed ⁽²⁾, the potential of the RS techniques has been recognized as a means to prepare dynamic land use maps, spatially and accurately, at various levels of confidence ⁽¹⁾.

The full potential of RS has, however, yet to be realized especially in terms of providing information on ecological classes that may be of value for conservation purposes ⁽⁴⁾, and to identify land for future expansion potential for agriculture .

On the other hand information on crop production is fundamentally important for the decision makers of a country. The earlier and more reliable this information is the greater is its value, ⁽⁵⁾ ⁽⁸⁾ and satellite remote sensing data has a dominant role in provide information reliable.

METHOD USED IN THIS STUDY

Basic Concepts

Multispectral classification is the process of sorting pixels into a finite number of individual classes or categories of data, based on their data files values. If a pixel satisfies a certain set of criteria, the pixel is assigned to the class that corresponds to that criteria ⁽³⁾.

Classification of remotely sensed data is used to assign corresponding levels with respect to groups with homogeneous characteristics, with the aim of discriminating multiple objects from each other within the image ⁽⁶⁾.

Classification generally can be made according to the following procedures:

- 1) Definition of classification classes
- 2) Selection of features
- 3) Sampling of training data
- 4) Estimation of Universal statistics
- 5) Classification. There are several popular techniques including,

Maximum Likelihood classifier.

6) Verifications of results.

Description of Classification Process

The classification process was carried out using enhancement Landsat image of 1991 for Kanazawa area, and consisted of the following step:

a) Preprocessing

(1) Training area

First step was accomplished in the procedure of Training Area selection which were defined and delimited the classes representative in the image. Polygons were built distributed at random in each one of the considerate classes.

(2) After that the procedure Get Training Data by Supervised Learning was carried out.

b) Classification

The classification was accomplished by using Maximum Likelihood Classifier.

c) Post processing

(1) Create Color Code Data

In this stage the Color Codes were built for each one of the classes defined in the (a.1) step, to help its visual identification.

(2) Color Code Image

Finally using the procedure Create Color Code Image, an image in which each class was identified with a different color was generated.

Estimation of Production

Once the process of classification finish the following step will be to digitize the administrative boundaries of the Kanazawa area. After that it is accomplished to overlap this information to the Landsat image using GIS software. We will determine the precision of the estimation of the production using remote sensing data, comparing the statistics data with estimated data.

AGRICULTURAL APPLICATIONS OF RS TECHNIQUES

Agricultural Applications Overview

When one considers the components involved in studying the worldwide supply and demand for agricultural products, the applications of RS in general are indeed many and varied. The scope of the physical, biological, and technical problems facing modern agriculture is an extremely broad one that is

intimately related with worldwide problems of population, energy, environmental quality, climate and weather. These facts are in turns influenced by human values and traditions and economic, political and social systems.

Crop Type Classification

Crop type classification through air photo interpretation is based in the premise that specific crop types can be identified by their spectral response patterns and photo texture. Successful identification of crops requires a knowledge of the developmental stages of each crop in the area to be inventoried. Because of changes in crop characteristics during the growing cycle can be very useful in the interpretation process.

Crop Condition Assessment

Deleterious conditions that can be assessed include crop disease, insect damage, plant stress from other causes and disaster damage. The most success applications have utilized large scale color infrared aerial photographs.

It would also be more difficult to differentiate among the effects of disease, insect damage, nutrient deficiencies or drought from variations caused by plant variety, plant maturity, planting rate or background soil color differences. The best conditions for detecting crop stress by air photo interpretation exist when the stress occurs over wide areas, instead of in isolated fields and is systematic in nature.

Other optimum conditions are when the crop canopy is well enough developed that the vegetation response predominates over that of the soil background. Because many stress effects are most apparent during dry spells, photographs should not be taken soon after rainy weather.

Crop Yield Estimation

In principal, the process is simple and straightforward. In a given study area, the interpreter needs to determine the area of each crop type and estimate the yield per unit area of each crop. The total yield is then a simple product of the area times the yield per unit area.

Beyond yield estimation, crop yield prediction can also be assisted through the interpretation process. Successful crop yield prediction must consider climatic and meteorological conditions. Valuable input to the determination of these conditions can be obtained from meteorological satellite data.

EXPERIMENT

Methodology

The classification process was carried out using enhancement LANDSAT TM image of November 1991. The classes representative of each features were defined and delimited, for example: rice, forestry, shadow s forestry, other kind of vegetation, bare ground, urban area, river and sea. The classification was accomplished by using Maximum Likelihood Classifier.

Results of Experiment

The classification process was carried out using original Landast image. It can be seen the area of Kanazawa including forestry, urban and rice production areas, also it can be seen mountain Hakusan , river , Japan sea and bare ground area. Bands considered in this experiment were : Red, Green, Blue and Infra Red, because in general these bands represent vegetation.

In the classified image, it can be appreciated forestry, the urban areas in color brown, river and Japan sea in blue color and different kind of vegetation in yellow color (Class1) and orange color (Class2) .

Estimation of the total area of rice, using Class1 and Class2, it was very similar in the areas considerate, except in the area of Kanazawa and Tatsunokuchi.

The data of estimated area of the Class1, Class2 and statistic data were normalized in order to seeing clearly the differences between both classes and as a rule, we observed that the behavior of the Class2 was nearby to statistic data however now it can not be indicated which Class represents to rice production area.

The percentage of variation of the Class2 with respect to statistics data, did not indicate so much differences between both data. It was observed values from - 21.3 to + 16.3.

The former results indicated that may be Class2 is associate with area of production of rice. The estimation of production was carried out using the Class2 data and the percentage of variation with respect to the statistic data indicated similar behavior to the previous result , due to the fact that was used estimated area data to calculate estimated production.

CONCLUSIONS

a) Class1 and Class2 include another kind of vegetation, not

only rice field.

b) It must be used an image of another season (May- August) in order to classify rice field.

c) It is necessary to get ground truth data to compare with estimated area.

ACKNOWLEDGMENTS

The authors are grateful to The Ishikawa Prefecture Agricultural Research Center staff, specially Mr. Takao Miyashita for provision of the statistics data.

REFERENCES

- [1] J.Adinarayana and N. Rama Kirshna, I ntegration of Multi- seasonal remotely- sensed images for improved landuse classification of a hilly watershed using geographical information systems , Int. J. Remote Sensing, Vol.17, No.9,pp.1679- 1688,1996
- [2] V.K.Dadhwai, J.S. Parihar, T.T.Medhavy, D.S. Ruhai, S.D.Jarwal and A.P.Khera, C omparative performance of thematic mapper middle- infrared bands in crop discrimination , Int. J. Remote Sensing, Vol.17, No.9, pp.1727- 1734, 1996
- [3] Erdas Inc., F ield Guide. Second edition. Version 7.5 , July, Atlanta, USA, 1991
- [4] G.M. Foody and R.A.Hill, C lassification of tropical forest classes from Landsat TM data , Int. J. Remote Sensig, Vol.17, No.12, pp.2353- 2367,1996
- [5] D.Hamar, C.Ferencz, J. Lichtenberger, G Tarcsai and I. Ferencz- Arkos, Y ield estimation for corn and wheat in the Hungarian Great Plain using Landsat MSS data , Int. J. Remote Sensing, Vol.17, No.9, pp.1689- 1699, 1996
- [6] Japan Association on Remote Sensing, R emote Sensing Note , 1993
- [7] A. Lobo, O Chic and A. Casterad, C lassification of Mediterranean crops with multisensor data: per pixel versus per- object statistics and image segmentation , Int. J. Remote Sensing, Vol.17, No.12, pp.2385- 2400, 1996
- [8] K.Okamoto and M.Fukuhara, E stimation of paddy field area using the area ratio of categories in each mixel of Landsat TM , Int. J. Remote Sensing Vol.17, No.9, pp.1735- 1749,1996

WINTER CROPS CLASSIFICATION USING SATELLITE DATA

O.Kryvobok

Ukrainian Research Hydrometeorological Institute

37 Nauki str., Kyiv 252028 Ukraine

Tel: 370(044)2658664, fax:370(044)2655363

e-mail: bel@ozsol.kiev.ua

Abstract -- The technique of winter crops classification using satellite data is suggested, which to separate winter crops in depending from their conditions. The technique based on textural measures computed using Gray Level Difference Vector approach (GLDV). The present study compares classification results derived by visual analyses of investigated area from low-flying plane and from GLDV approach using satellite data. It is found that GLDV approach produces accuracy equivalent to those obtained from visual interpretation.

INTRODUCTION

Satellite-based remote sensing is an effective tool for observing and monitoring agricultural crops. The main advantages of this technology are: repeat coverage, objectively, accuracy. Due to such advantages obtaining the crop condition assessment (CCA) from space is very perspective. The investigation [1] has proved that there is a close connection between the CCA and future yield. Today in Ukraine there is an aerovisual technique of CCA (five-mark grading system). The CCA is depend on structure, color and mottledness of stand of grass. This is an integral assessment. We have tried to quantify these notions by textural analyses. Although the GLDV approach suffers a slight degradation in classification accuracy but has a considerable saving in run time and in storage requirements compares with another approach [2]. Images obtained from high-resolution satellite instruments are ideal in realization textural analyses, because such object as agricultural fields consist from 400 or more pixels (field size is about 1*1 km).

ANALYSES OF DATA

a) Data description

The KOSMOS-1939 satellites provide extremely high spatial-resolution data in several spectral bands. The multispectral scanner (MSU-E) has a nominal spatial resolution of 45m with three narrow spectral bands centered at 0.55, 0.65, 0.85 μm wavelengths. Data have been recorded on the 10 of May 1992 under Sofievka of Dnepropetrovsk region (DR), Ukraine. Sofievka is a wheat growing area of south part DR (N47° 50', E 33° 50'), and is about 2000 hectares (40*20km) in size, and is covered by KOSMOS-1939, circuit N21951. Data were obtained from "Planeta" Russian remote sensing center in the form of multispectral images 1600*1200 pixels. Data from plane were collected throughout the area for 60 selected fields during the wheat season and recording detailed agronomic information with the assistance of the district agronomist. Thirteen fields were in satisfactory,

thirty eight - in good and nine - in perfect conditions. Each field was precisely plotted on the map for location in the KOSMOS images.

b) Calibration of satellite data

The calibration of satellite data is a conversion from gray level N to radiance and reflectance. Spectral radiances $G\lambda$ is given by

$$G\lambda \text{ (W /m}^2\text{/ sr/ } \mu\text{m)} = (N - N_0) / S \quad (1)$$

where N_0 is the intercept value, S is the spectral sensitivity of instrument N_0 and S were taken from [3]. Reflectance R is calculated from

$$R = (\pi * G\lambda) / (S\lambda_0 * \cos\theta) \quad (2)$$

where $S\lambda_0$ is the extraterrestrial solar spectral flux and θ solar flux angle. Spectral solar flux was corrected for elliptical path of the earth around the sun [4].

c) Atmospheric correction of satellite data

Data were corrected for atmospheric effects using the model developed by author [3]. The special computer code was created. Inputs to the code include: the type of radiometer, observational geometry, meteorological data from standard observations, ground reflectance. A primary output of the program is an at-satellite reflectance. The program run calculation for each shotwave channels of radiometer beginning with ground reflectance of 0.0 and proceeding to 1.0 in increment of 0.1, thus forming a look-up table. In order to find the ground reflectance corresponding to actually measured reflectance of the unit area it is necessary to go through the look-up table until find ground reflectance giving correspondence between measured and calculated reflectances.

TEXTURAL FEATURES

a) The GLDV approach

The GLDV approach is a statistical model that describes texture by statistical rules governing the distribution and relation of gray levels in local neighborhoods. GLDV is based on the absolute differences between pairs of gray levels at a distance d apart at angle ϕ . The difference vector density function $P(M)$ is defined for $M = |I - J|$, where I and J are the gray levels separated by distance d with relative orientation ϕ of the pixels. It is normalized by dividing the gray level frequencies of occurrence by the total frequencies [2].

Dropping subscripts d and ϕ , making dependence on d and ϕ implicit, the GLDV textural features are defined as:

$$\text{Mean} = \sum_M MP(M) \quad (3)$$

$$\text{Standard Deviation} = \left\{ \sum_M M^2 P(M) \right\}^{1/2} \quad (4)$$

$$\text{Contrast} = \sum_M M^2 P(M) \quad (5)$$

$$\text{Angular Second Moment} = \sum_M \{P(M)\}^2 \quad (6)$$

$$\text{Entropy} = - \sum_M P(M) \log P(M) \quad (7)$$

$$\text{Local Homogeneity} = \sum_M P(M) / \{1 + M\}^2 \quad (8)$$

b) Computing textural measure

Satellite data were transformed to Ratio Vegetation Indexes (RVI). RVI is expressed as follows

$$RVI = CH(0.85\mu m) / CH(0.65\mu m) \quad (9)$$

where $CH(0.85)$ is spectral reflectance of near infrared channel and $CH(0.65)$ is spectral reflectance of visible channel. Using the expressions (3-8), textural measures were computed as function of pixel separation d at five spatial resolutions. Pixel separation was 1, 2, 3, 4, 5, corresponding to distances 45, 90, 135, 180 and 225 m. Computations have been made at angles 0° , 45° , 90° , 135° . Computations have been made for each field, corresponding to different CCA. Mean value of each measure for appointed CCA has been defined. After that correlation between each average textural measures and CCA have been computed (Tab.1), using following expression

$$f = \left(\sum_i f_i \right) / N \quad (10)$$

where f_i is a correlation at each pixel separation, $i=1, N$

Three textural measures that has f more than 0.5 were chosen. These are ASM, ENTRO and CONTR. Fig.1 shows two textural measures (CONTR, ENTRO) as function of pixel separation d at four angles determining directionality. Fig.1 shows textural measures for two cases: a) CCA is 5 (perfect condition); b) CCA is 3 (satisfactory condition).

Table 1. Correlation coefficients between appointed CCA and textural measures

Textural measures	CCA			
	0°	45°	90°	135°
MEAN	0.43	0.35	0.26	0.37
STD	0.27	0.22	0.25	0.31
CONTR	0.73	0.54	0.48	0.49
ASM	0.66	0.61	0.45	0.51
ENTRO	0.72	0.68	0.53	0.41
HOMOG	0.41	0.38	0.31	0.37

CLASSIFICATION PROCEDURE

Thirty-six fields have been chosen to compute mean textural measures for different CCA, as described before, the remainder has been used as test data to determine the accuracy of classification. Textural measures of investigated field were compared with the same mean values of different CCA. Classifying of fields has been realized according to the following rule

$$\sum_i |F_{mi} - F_i| = \min \quad (10)$$

where F_{mi} mean value of textural measures (ASM, ENTRO, CONTR) of different CCA and F_i is the same value of investigated field.

Tab.2 shows the classification results for this procedure

Tab.2 Accuracy of classification

Actual CCA	Classified		
	3	4	5
3(satisfactory)	4	1	0
4(good)	1	14	2
5(perfect)	0	2	3
overall accuracy %	87.5%		

CONCLUSION

This paper has demonstrated high classification accuracies of GLDV approach in CCA. This technique will be able to substitute aerovisual interpretations in observing and monitoring winter crops.

REFERENCES

1. Dmitrenko V.P. Trudy UHMI, v.84,1969 (Russian edition)
2. Welch et al. Cloud Field classification based upon high spatial resolution textural features. J.Geoph..Res.,vol.94, N12, pp 14749-14765,1989.
3. Kryvobok O.,Atmospheric correction of satellite images.Proccedings of 4th Ukrainian-China-Russian Symposium of Space Science and Technology.
4. Paltridge,G.W., and C.M.Platt,1976: Radiative Processes in Meteorology and Climatology, Elsevier Sci.Publ.Co.,318pp.

case: A

case : B

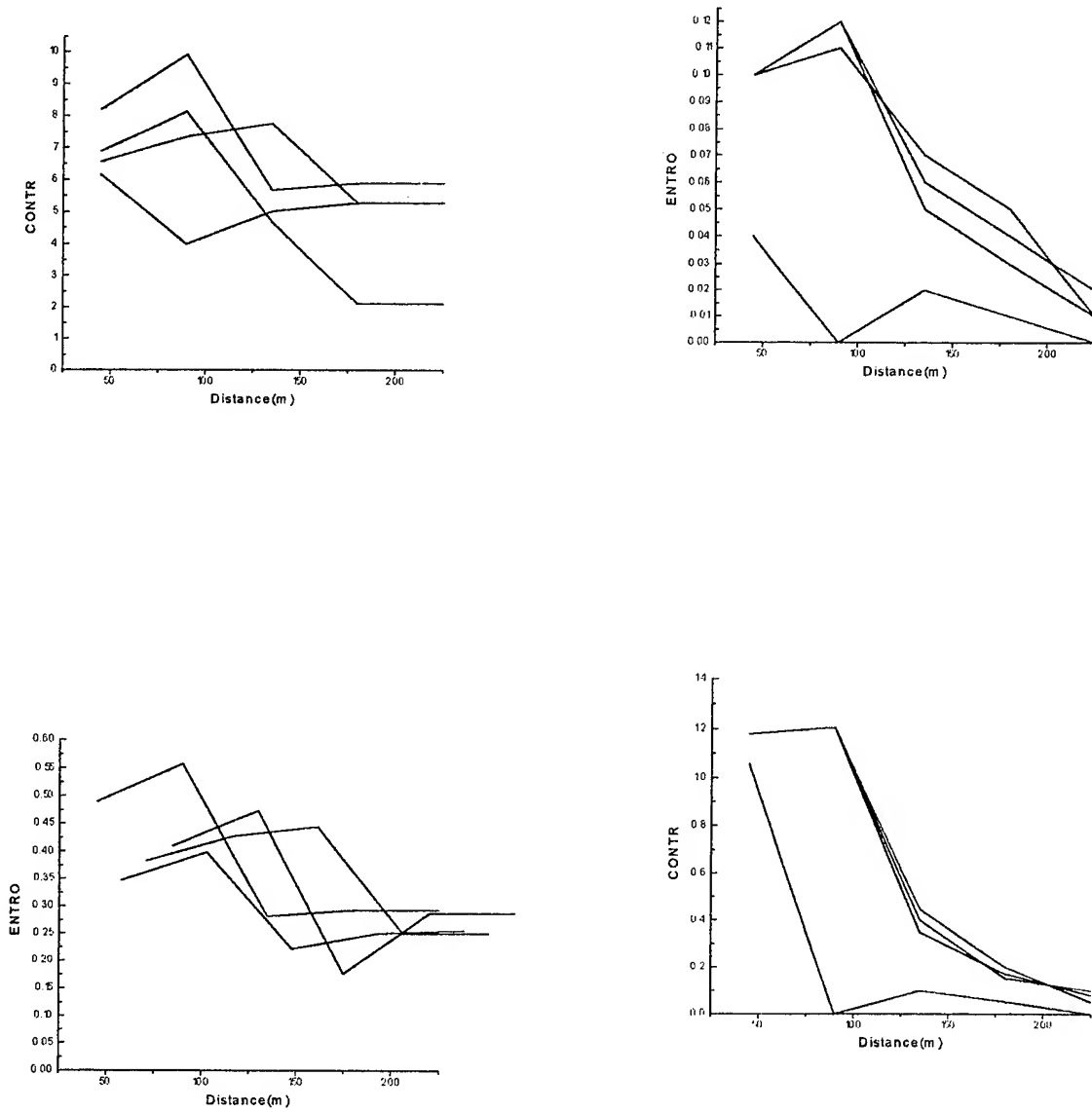


Fig.1 CONTR and ENTRO as function of distance d ; $0^\circ, 45^\circ, \dots, 90^\circ, 135^\circ$.

Shortperiodic Variability of Different Landscapes in MM-Wave Range

Y.F.Vasilyev, B.D.Zamaraev, V.L.Kostina, A.N.Roenko

Institute of Radiophysics & Electronics
National Academy of Sciences of Ukraine
Proskura St.12, Kharkov 310085, UKRAINE
T:0572-44-85-65, F:0572-44-11-05,
E-m:ire@ire.kharkov.ua

In our paper, presented at IGARSS Conference [1], we discussed in details some characteristics of radar backscattering signal intensity in mm-wave range, such as seasonal, angular, spatial dependences for different types of Earth surfaces. But, it's necessary to stress that in some cases one of the most influential reason on backscattering intensity is the shortperiodic variability - during month, weeks, days and also hours, especially in summer, when it's connected with yield ripening.

Well, let's discuss the radar backscattering intensity variability from different ploughing fields, fields covered with perennial grass, wheat, barley and potato during one week in the second half of July. At this period the regular simultaneous measurements of backscattering intensity, temperature and soil moisture were conducted. Radar measurements were made using airborne (helicopter) side-scan radar.

According to the values of backscattering intensity three potato fields and field, covered with grass, were combined in one type of surfaces. It was made on the base of visual estimation of this covers by operator on helicopter board, as a "green" fields. Such estimation shows rather large percent value of soil covering by vegetation and may be considered as characteristic of vegetation state.

The ploughing fields were estimated as a "black" fields. The fields, covered with wheat and barley were estimated by operator as "yellow" fields. Except the

subjective operator estimation in classification of mentioned covers, visually equal character in shortperiodic variability of backscattering intensity of this covers were given into consideration.

The weather during the measurement cycle was changed from calmy to rather windy, sometimes it was raining.

According to the analysis of radar backscattering signal, intensity we may dispose the mentioned covers in the following sequence:

a) potato and perennial grass;
b) cereals, which value of backscattering intensity is 3-4dB below;

c) bare soil, ploughing field - according to soil moisture it's close to type a) or b).

Type c) covers are characterized by the most great variability of backscattering intensity - the changes are quick and deep; type a) - on the contrary is characterised by smooth and slow changes; type b) - is situated between a) and c).

The measurements conducted at good, sunshine, windy weather after raining made it possible to say that the value of backscattering signal intensity in the morning was 3-4dB greater than in the evening. This fact may be explained as decreasing of vegetation water content and soil moisture values.

The comparison of backscattering intensity with soil moisture values for different covers is presented. It's shown, that value of backscattering intensity from ploughing field is fully determined by soil moisture (permittivity of the soil) at the

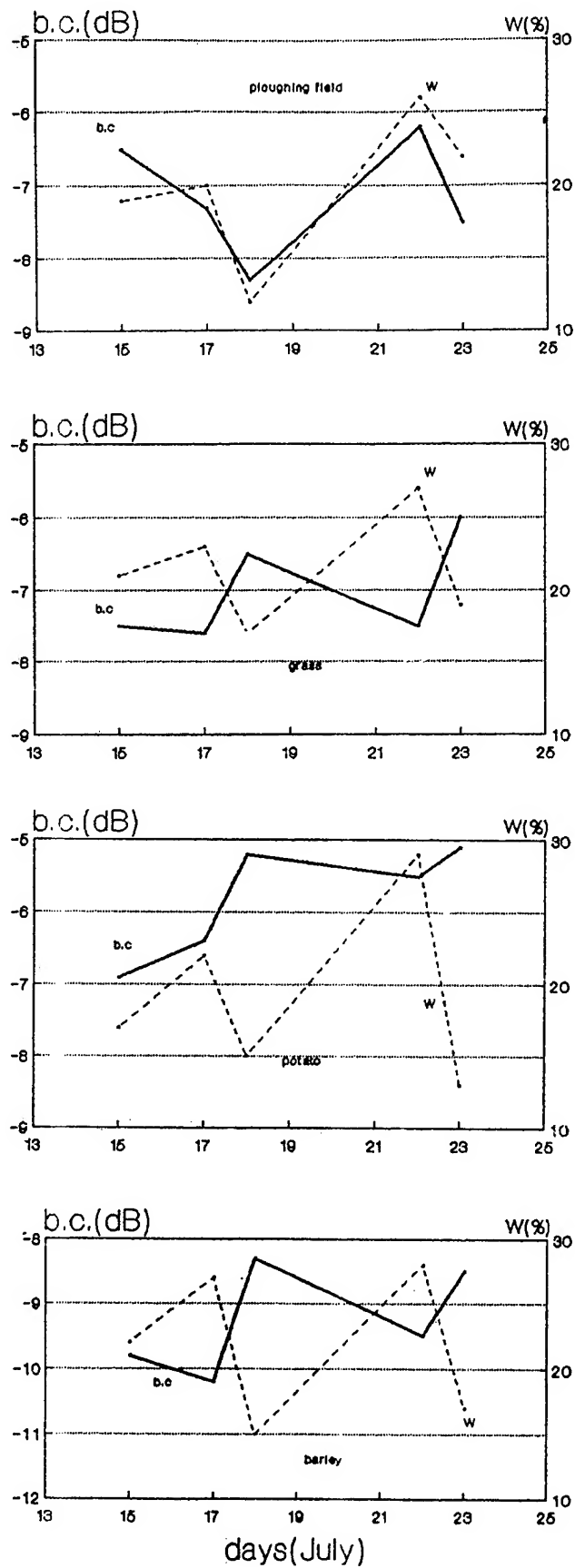


Fig.1

stable roughness conditions. For another fields we didn't find significant correlation between radar backscattering signal intensity and soil moisture. In that case it's necessary to find correlation between backscattering signal intensity and water content of biomass.

Investigations of biomass water content influence on radar backscattering signal intensity were conducted during 4 year cycle with the help of ground-based scatterometer. The surface covered with grass was investigated. In details equipment and methodics of this measurements were presented in [2]. According to the results of this investigations we may divide the growth cycle of the plants on two parts: the period of intensive biomass growth and the period of ripening and withering. The first period is characterised by significant correlation between the changes of backscattering intensity and full water content of biomass. Then, in the period of ripening, when the biomass quantity reaches some definite value, the full water content becomes a secondary influential factor. The main influence on

changes of backscattering intensity at that period are given by the changes of relative free water content of the plants upper leaves.

In the period of wheat ripening, when the water content of biomass changes from 70% to approximately 30%, the value of radar backscattering signal intensity from the field with dense vegetation decreases on 5-10dB, and at further decreasing of water content to 20%, when the harvest begins, decreasing of the value of backscattering intensity is not so noticeable.

References

- [1] Y.F.Vasilyev, B.D.Zamaraev, V.L.Kostina, A.N.Roenko
"Investigation & catalogization of backscattering characteristics of different Earth covers in mm-wave band", Proc. IGARSS'96, 1996.
- [2] F.V.Kivva, A.N.Roenko, Y.F.Vasilyev, B.D.Zamaraev
"Angular & seasonal dependences of the backscattering coefficients from vegetation at 35GHz", Tr.J. of Physics, v.19, N8, 1995, p.p.970-975.

Monitoring Crop Growth on China Plains by Using SSM/I Data

Ya-Qiu Jin

Wave Scattering and Remote Sensing Center
and Department of Electronic Engineering
Shanghai, China 200433

Abstract - Scattering and polarization indices at SSM/I channels are defined for monitoring crop growth. Examples are analyzed by using SSM/I observations over China Plains. These indices and their temporal variations are characteristic parameters during crop growth.

INTRODUCTION

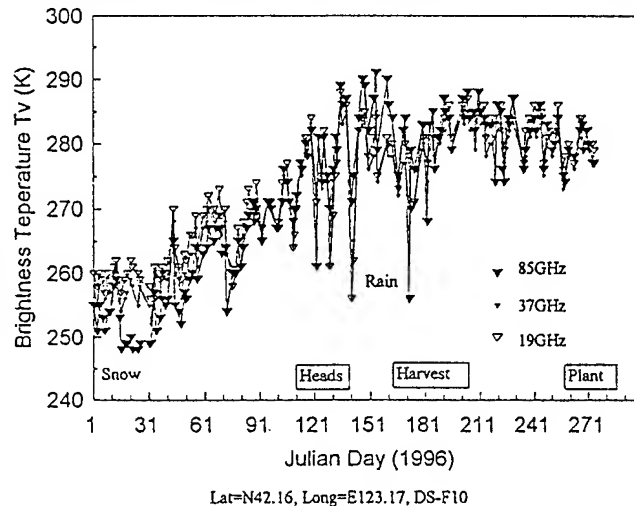
One of most interesting problems in agriculture remote sensing is how to monitor and evaluate crop growth. Satellite-born microwave radiometers are primary tools for global surface monitoring because of the potential of microwave to observe the earth surfaces through clouds and to provide information of the internal properties of surface covers. However, microwave measurements by satellite-born radiometers have not been well applied for this purpose. Thermal emission from crop fields observed by satellite sensors is governed by crop growth, underlying soil moisture, land surface roughness, atmospheric precipitation and water vapor, physical temperature of atmosphere and land surface, etc. Information of crop growth in temporal and spatial variation is usually not easy to be identified from observable brightness temperature (TB) by satellite-born radiometers. Effect of increasing soil moisture after rainfall usually dominates the emission from crop land. How to use microwave data from satellite-born radiometers to monitor crop growth and to understand quantitative relationship between crop growth and observable TB remain to be studied.

In this paper, we define some scattering and polarization indices by SSM/I data. These indices can be employed to demonstrate monotonously crop growth process. Numerical simulation of the vector radiative transfer (VRT) for a layer of vegetation canopy at SSM/I channels is also obtained [1]. As an example, the SSM/I data of 1996 over the China north and northeastern plains are analyzed.

SSM/I DATA OVER CHINA PLAINS

Fig.1 shows temporal variation of the vertically polarized TB at SSM/I 19, 37, 85 GHz channels over the China northeastern plain (42.16°N, 123.17°E) during January-

September 1996. Seasonal variation of TB is governed by the physical temperature of atmosphere and land surface.



Lat=N42.16, Long=E123.17, DS-F10

Fig.1 SSM/I data of T_{Bv} over crop field of China northeastern plain.

The scattering index $SI_v \equiv T_{B22v} - T_{B85v} > 0$ is used as a rule to detect snowpack and rains. The polarization index $PI_{19} \equiv T_{B19v} - T_{B19h}$ is usually defined for monitoring plain surface wetness. SI_v and PI_{19} from SSM/I observations of Fig.1 are given in Fig.2. It can be seen that snow melting and rains can increase PI due to increase of plain surface wetness. During crop growth, crop canopy might gradually darken the surface PI. However, change of the plain surface wetness and water bodies can dominate variation of surface emission. It can be seen in Fig.2 that PI is significantly increased after rains in March. Since soil wetness, especially, enhances the horizontally-polarized surface reflectivity around satellite observation angle 54° , we define another scattering index as $SI_h \equiv T_{B37h} - T_{B85h}$ to monitor change of surface wetness.

Fig.3 gives temporal variation of PI_{19} , PI_{85} , SI_h . The days for seeding, growth and harvest are indicated in the figure. It can be seen that as wetness increases after rains or irrigation, PI_{19} is increased and $SI_h < 0$. At harvest, full crops might darken both PI_{19} and PI_{85} .

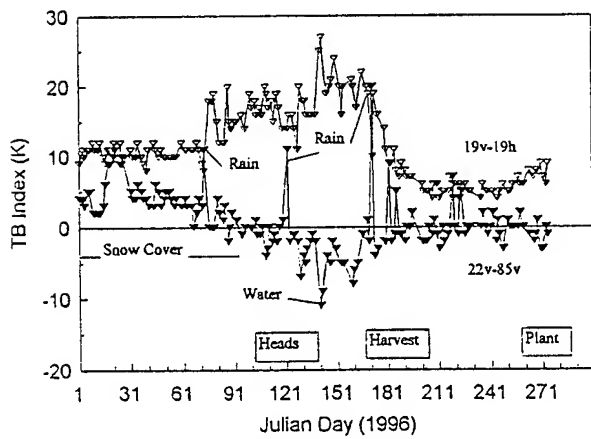


Fig.2 Temporal variation of SI and PI.

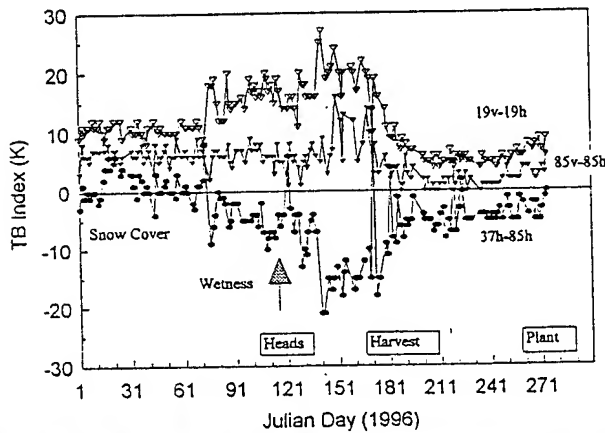


Fig.3 Temporal variation of PI_{19} , PI_{85} and SI_h .



Fig.4 Spatial variation of the difference ΔSI_h between May and January 1996.

Fig.4 shows spatial variation of SI_h difference between May and January. It can be seen that significant increase of surface wetness happened in May irrigation around the China northeastern plain. Effect from surface wetness always dominates TB of plain areas.

To see the correlation of TB and crop growth, we define a crop index as $CI \equiv PI_{19} + SI_h$. We found that the index CI can minimize the dominant influence from surface wetness and show monotonously crop growth process. CI can be seen as a characteristic index for monitoring crop growth. Fig.5 shows temporal variation of CI. The same results are also obtained in our analysis of SSM/I data over China north plain [2].

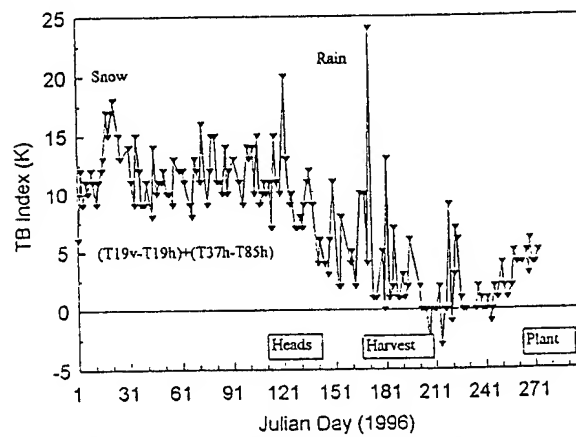


Fig.5 Temporal variation of crop index CI.

TB INDICES AND VRT SIMULATION

Atmospheric radiative transfer with no rains is written as

$$T_{Bp}^{SSM/I} = e_{vp} T_s e^{-\tau_a} + T_a (1 - e^{-\tau_a}) (1 + r_{vp} e^{-\tau_a})$$

where $p = v, h$; v is frequency; τ_a is atmospheric opacity; T_s, T_a are the surface and atmospheric effective temperature, respectively. The term $e_{vp} T_s$ is the emission from surface canopy, and $r_{vp} = 1 - e_{vp}$. If we simply take $T_0 \approx T_s \approx T_a$, we might have

$$PI_{19} \approx (r_{19h} - r_{19v}) e^{-2\tau_{19a}} T_0$$

$$SI_h \approx (r_{85h} e^{-2\tau_{85a}} - r_{37h} e^{-2\tau_{37a}}) T_0$$

As surface wetness increases, r_{19h} is significantly increased more than the change of r_{19v} . It causes PI_{19} increasing. Variation of τ_{19a} and T_0 can cause fluctuation of PI_{19} . Since r_{85h} is less than r_{37h} and $\tau_{85a} > \tau_{37a}$ generally, increasing surface wetness will cause $SI_h < 0$. On very rough surface with small difference of r_{37h} and r_{85h} , SI_h might approach to zero.

We have developed a VRT model for vegetation canopy at SSM/I channels. Theoretical derivation and discussion can be referred to Ref. [1]. Fig. 6 shows simulations at four cases: (1) snowpack with snow depth =10 cm; (2) crop height $d=40$ cm, surface volumetric wetness $M_v = 0.1$; (3) $d=40$ cm, $M_v = 0.3$ (4) full crop before harvest, $d=120$ cm, $M_v = 0.1$. Parameters in calculations can be seen in Ref. [1].

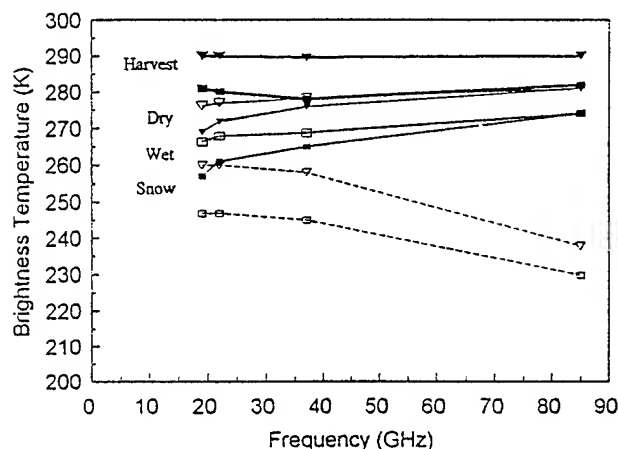


Fig.6 VRT simulation from crop field.

CONCLUSIONS

In this paper, we discussed several scattering and polarization indices from SSM/I observations. It is applied to monitoring crop growth. A new crop index CI can be seen as a characteristic parameter to monitor crop growth process. Numerical VRT simulation at SSM/I channels is also developed. Some examples from SSM/I observations over China Plains are discussed. It shows great potential of microwave data in applications of agricultural management.

ACKNOWLEDGMENT

This work was supported by the China National Science Foundation and the Shanghai Research Center for Applied Physics.

REFERENCES

- [1] Y.Q. Jin (1997), "Radiative transfer of snowpack /vegetation canopy at SSM/I channels and satellite data analysis", Remote Sensing of Environment, in press.
- [2] Y.Q. Jin (1997), "Analysis of SSM/I data for monitoring crop growth of China north and northeastern plains", Journal of Remote Sensing (in chinese), in press.

An Exploration of Features for SAR Classification

Leland Pierce

The University of Michigan, Radiation Lab
Ann Arbor, MI 48109-2122 USA

FAX: +1-313-747-2106 email: lep@eecs.umich.edu

ABSTRACT

Classification of SAR images usually is constrained by the choice of features to use. Often the powers, in dB, for several frequencies and polarizations are used. However, there are very many other features one could use, some that include the spatial variability between neighboring pixels. This paper explores the utility of using some of these non-standard features in a standard Bayesian classification framework.

Some features make the frequency relationships explicit by forming gradients of the standard powers in the frequency domain. Others use the differences between the polarizations and the same or different frequencies. Still others form statistics based on some small neighborhood surrounding each pixel. One such is called texture which is the standard-deviation without the contribution from speckle. Others use the geometrical relationship between the pixels, examples are: lacunarity, grey-level co-occurrence matrices, others?....

For full-polarimetric data there is also available the co-pol phase-difference statistics, which are known to correlate well with the scattering mechanisms associated with the target.

There are also less well-known features: (1) polarization for maximum power, (2) polarization for minimum power, (3) power image calculated based on maximum separability between 2 classes, (4) Eigenvalues and vectors of the scattering matrix

For interferometric data there are also some other features: (1) Coherence, (2) Statistics of height information, (3) Differences in height information between different polarizations and frequencies,

Each of these features will be evaluated for its usefulness to classification and various optimum scenarios will be presented for different sensor combinations.

Segmentation of Radar Imagery Using Gaussian Markov Random Field Models and Wavelet Transform Techniques*

Yunhan Dong¹, Bruce Forster¹ and Anthony Milne²

¹School of Geomatic Engineering, The University of New South Wales, Sydney 2052, Australia

Telephone: +61 2 9385 4209, +61 2 9385 4172, Facsimile: +61 2 9313 7493

Email: y.dong@unsw.edu.au, b.forster@unsw.edu.au

²Office of Postgraduate Studies, The University of New South Wales, Sydney 2052, Australia

Telephone: +61 2 9385 2731, Facsimile: +61 2 9385 3733, Email: t.milne@unsw.edu.au

Abstract — This paper presents segmentation of radar imagery by two steps: 1. initial segmentation using wavelet transform techniques and watershed method; 2. segment merging using the Gaussian Markov random field models. The method can be applied to both single-channel and multi-channel images.

INTRODUCTION

With its penetration through clouds, and high spatial resolution, SAR (synthetic aperture radar) has shown its potential for classifying and monitoring geophysical parameters. Many researchers have concentrated on SAR image classifications for both natural and built targets [1-5]. However, the classification of SAR images based on the information provided by individual pixels cannot generally give satisfactory results because the images are highly speckled due to coherent processing. Segmentation segments an image into disjointed regions corresponding to objects, or parts of objects that differ from their surroundings, and thus enables further classification to be performed based on the information provided by clusters rather than individual pixels.

Various methods for image segmentation have been developed based on textures and statistical values, such as the mean, standard deviation and covariances [6-7]. The Gaussian Markov random field (GMRF) model has been shown to be an accurate and compact representation for a range of images. The GMRF model discriminates segments based on the region information not only up to the second order statistics but also the spatial relationships (referring to Equations (1)-(2)). In other words, the GMRF model considers two regions are different if one or more than one of the following conditions is true.

1. The first order statistics (the mean value for a single channel image or the mean vector for a multi-channel image) are different;
2. The second order statistics (the variance for a single channel image or the covariance matrix for a multi-channel image) are different;
3. the spatial relationships (textures) are different.

GAUSSIAN MARKOV RANDOM FIELD MODEL

When an area, illuminated by radar, contains many elementary scatterers which are randomly distributed in

terms of size, orientation and location, the measurements of backscattering intensity for the area have a Gaussian distribution [6]. For a cluster S , represented by the GMRF model, the conditional probability of all the pixels in S belonging to S is the product of conditional probability of each pixel in S [7]:

$$p(\mathbf{X}_s|S; s \in S) = \prod_{s \in S} p(\mathbf{X}_s|S) \\ = \prod_{s \in S} \frac{1}{(2\pi)^{n/2} |\mathbf{C}|^{1/2}} \exp\left\{-\frac{1}{2} \mathbf{E}_s^T \mathbf{C}^{-1} \mathbf{E}_s\right\} \quad (1)$$

where n is the number of channels, \mathbf{E}_s is a zero mean Gaussian noise vector in which each of its element is a linear combination of noise errors corresponding to its spatial neighboring pixels within the same channel.

$$e_i = (x_{i0} - \bar{x}_i) - \sum_{k=1}^{N_i} t_{ik} (x_{ik} - \bar{x}_i) \quad i = 1, 2, \dots, n \quad (2)$$

where x_{i0} denotes the i th channel measurement at the current pixel position, \bar{x}_i is the mean value of the i th channel for cluster S , and $x_{ik} - \bar{x}_i$, $k = 1, 2, \dots, N_i$, denotes the measurement error at the neighborhood position k for the i th channel measurement. Reference [8] discussed the choices of the neighborhood sets. t_{ik} is the model parameters. C_{ij} , the element of the covariance matrix \mathbf{C} , is the expected value of e_i and e_j , i.e., $C_{ij} = E\{e_i e_j\}$. Reference [9] shows that,

$$\prod_{s \in S} p(\mathbf{X}_s|S) = \left[(2\pi)^{n/2} |\mathbf{C}|^{1/2}\right]^{-M_s} \exp\left\{-\frac{1}{2} M_s \cdot n\right\} \quad (3)$$

where M_s is the number of pixels in the cluster S . Finding the maximum conditional probability in (1) is equivalent to finding the minimum determinant of \mathbf{C} . Therefore the model parameters t_{ij} should be chosen in such a way that the determinant $|\mathbf{C}|$ achieves a minimum, which can be obtained by letting $\partial|\mathbf{C}|/\partial t_{ik} = 0$.

INITIAL SEGMENTATION

Initial segmentation is essential to use the GMRF model segmenting images, as the model parameter estimation requires cluster statistics. Because the GMRF method features merging only, it is very important to ensure each initial segment to be only part of (or whole of) one cluster.

*This work was supported by the Australian Research Council.

Each pixel belongs definitely to only one cluster, but this is not considered to be as the so called the initial segmentation, as its statistics cannot be computed. Reference [7] suggests to divide a whole image into small square blocks, say 4×4 pixels as the initial segmentation. What are used for the initial segmentation in this paper are the techniques of wavelet transform and watershed. A smooth image can be obtained after speckle is greatly suppressed by a wavelet lower frequency filtering algorithm [10]. Edges are detected by a substitute of the high frequency filter for the low frequency filter. The detected edges are generally not closed. The watershed method [11] is applied to form the closed edges as segmentation requires. The initial segmentation is generally conservative in order to ensure each segment to belong to no more than one cluster.

SEGMENT MERGING

The criterion used for the segment merging is similar to an approach used in [7]. The maximum likelihood probability is defined as the product of the the maximum probabilities of all segments.

$$p(\mathbf{X}|\mathbf{S}) = \prod_k p(\mathbf{X}_s|S_k; s \in S_k) \quad (4)$$

Consider the two spatially adjacent segments S_p and S_q to be merged. If they belong to the same cluster, their covariance matrices should be very close to each other. As a result, the maximum likelihood probability post merging will be close to the the maximum likelihood probability before merging. On the other hand, if the two segments belong to different clusters, an attempt to merge them will cause a collapse in the maximum likelihood probability post merging. A threshold, therefore, can be selected either automatically or manually during the merging iteration to determine segment merging.

EXAMPLES

In short, the procedures are:

1. Perform an initial segmentation;
2. Compute statistics and model parameters for all segments;
3. Merge any two spatially adjacent segments if they satisfy the merging criterion;
4. Repeat Step 3 until no further merger takes place.

A synthetic 512×512 radar image consisting of five clusters is shown in Fig. 1. The values of the mean and standard deviation for the up-left/bottom-right corners, the up-right/bottom-left corners and the central circle are (0.0800, 0.0231), (0.0906, 0.0260), and (0.0906, 0.0370), respectively. It is worth noting that the up-right/bottom-left corners and the central circle have the same mean. The difference is only their standard deviation. To segment such a speckled image using their original grey values, an accuracy of 95% requires the mean difference between clusters to be about 5.7 dB. But the mean differences in the image are

only 0.5 dB and 0 dB. Fig. 2 shows the initial segmentation, and the final segmentation is presented in Fig. 3. As the true segments are known, the accuracy can be easily assessed. The accuracy for all segments are more than 97% in this case.

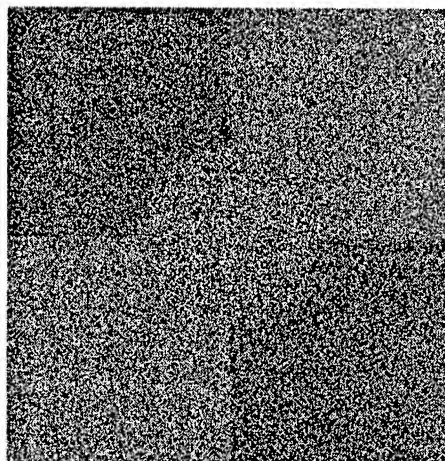


Figure 1: A synthetic 512×512 pixel radar image contains five clusters. The up-right/bottom-left corners and the central circle have a same mean but different standard deviation.

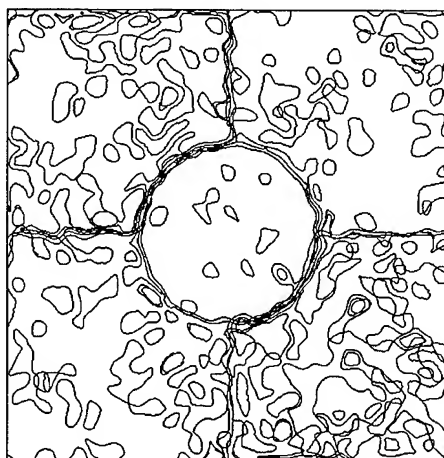


Figure 2: The initial segmentation of Fig. 1.

A 512×512 NASA/JPL AirSAR C-band HH polarization intensity image, acquired from the South Alligator River region, Northern Territory, Australia, is shown in Fig. 4. It mainly contains three types of land covers: the central bright region representing a wet *Melaleuca* swamp, the surroundings representing mixed woodland, and the darkest areas little vegetated soil. The initial segments and the final segments are shown in Figs. 5 and 6, respectively.

REFERENCES

- [1] J. J. Van Zyl, "Unsupervised classification of scattering behavior using radar polarimetry data," IEEE

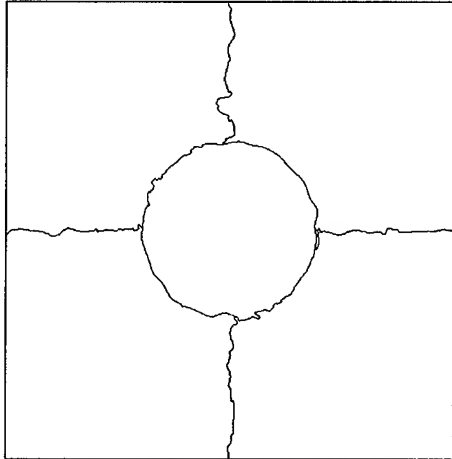


Figure 3: The final segmentation of Fig. 1.

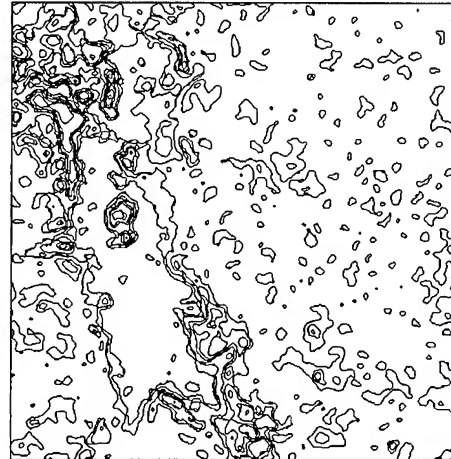


Figure 5: The initial segmentation of Fig. 4.

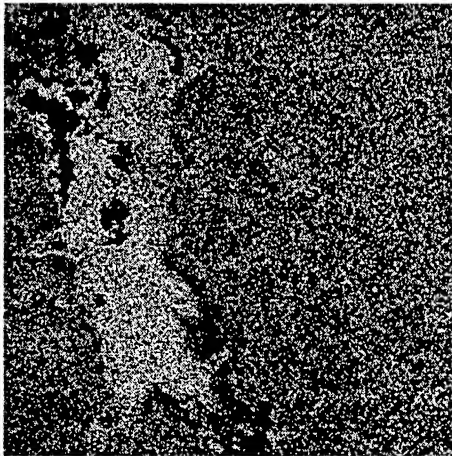


Figure 4: A 512×512 pixel NASA/JPL AirSAR C-band HH polarization intensity image, acquired from the South Alligator River region, Northern Territory, Australia in 1993.

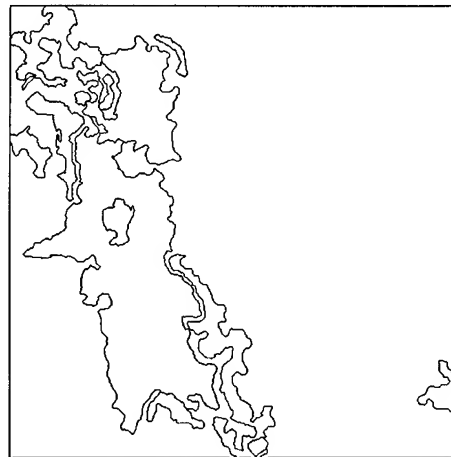


Figure 6: The final segmentation of Fig. 4.

- Trans on Geoscience and Remote Sensing, vol. 27, pp. 36-45, 1989.
- [2] A. Freeman, and S. Durden, "A three-component scattering model to describe polarimetric SAR data," Proceedings of SPIE Radar Polarimetry: 23-24 July 1992, San Diego, California, pp. 213-224, 1992.
 - [3] L. E. Pierce, F. F. Ulaby, K. Sarabandi, and M. C. Dobson, "Knowledge-based classification of polarimetric SAR images," IEEE Trans on Geoscience and Remote Sensing, vol. 32, pp. 1081-1086, 1994.
 - [4] M. C. Dobson, L. E. Pierce, and F. T. Ulaby, "Knowledge-based land-cover classification using ERS-1/JERS-1 SAR composites," IEEE Trans on Geoscience and Remote Sensing, vol. 34, pp. 83-99, 1996.
 - [5] Y. Dong, B. C. Forster and C. Ticehurst, "Decomposition and interpretation of radar polarization signatures," Proceedings of IGARSS '96, pp. 1556-1558, 1996.
 - [6] E. Rignot, and R. Chellappa, "Segmentation of polarimetric synthetic aperture radar data," IEEE Trans on Image Processing, vol. 1, pp. 281-300, 1992.
 - [7] D. K. Panjwani, and G. Healey, "Markov random field models for unsupervised segmentation of textured color images," IEEE Trans on Pattern Analysis and Machine Intelligence, vol. 17, pp. 939-954, 1995.
 - [8] R. Kashyap, R. Chellappa, and N. Ahuja, "Decision rules for choice of neighbors in random field models of images," Computer Graphics and Image Processing, vol. 15, pp. 301-318, 1981.
 - [9] Y. Dong, and B. C. Forster, "Segmentation of radar imagery using Gaussian Markov random field models," unpublished.
 - [10] Y. Dong, B. C. Forster, A. K. Milne, and C. Ticehurst, "The Application of wavelet transform for speckle suppression in radar imagery," Proceedings of IGARSS' 97.
 - [11] E. Dougherty, An Introduction to Morphological Image Processing. Bellingham: SPIE Optical Engineering Press, 1992.

Efficient Calculation in the Map Domain of SAR Layover and Shadow Masks

David Pairman and Stephen McNeill

Landcare Research - Manaaki Whenua

PO Box 69, Lincoln, New Zealand

Ph: 64 3 325 6700 Fax: 64 3 325 2418 Email: PairmanD@Landcare.cri.nz

Abstract -- Layover and shadow are two phenomena common in synthetic aperture radar imagery of steep terrain areas. While little can be done to mitigate backscatter estimates in layover or shadow areas, a mask is often required to exclude them from any backscatter based analysis.

This paper presents an algorithm for detecting both shadow and layover areas directly in the map domain rather than converting to the slant range image domain (and back) to effect the calculation. Furthermore the algorithm presented uses a straightforward search through the map image and thus avoids the complex and inherently inefficient buffering required to search along lines of constant azimuth.

As the method can be considerably simplified by assuming a constant bearing to the satellite and constant local incident angle to the local geoid, an analysis of the errors produced by making these assumptions is given. Results show that the differences are insignificant for many applications of satellite data. For aircraft SAR imagery, it is not practical to assume a constant incidence angle. However, interpolation of incidence angle has been found to give adequate results for aircraft SAR.

INTRODUCTION

Unlike optical remote sensing instruments, the viewing geometry of synthetic aperture radar (SAR) imagery is significantly side-looking. We illustrate this in figure 1 where the off-nadir viewing angle is typically in the range 15° - 60° . A SAR instrument emits radar pulses and records the time, frequency and phase of the scattered return. The Doppler history of returns is used to determine the position in the azimuth (along path) direction, and the echo time to determine the range (across track) position. In its initial "slant range" form an image across-track dimension represents the true range from the instrument rather than a range along the ground.

Images can be routinely converted to a "ground range" on the assumption of a smooth surface. However, as elevated terrain is closer to the instrument than its corresponding point projected on a local geoid, such terrain appears displaced towards the sensor. Thus, mountains appear to lean toward the sensor in both slant range and ground range imagery. If elevation information is available, for instance from a digital elevation model (DEM), then corrections can be made for terrain displacement and an orthorectified image product can be produced on a given map projection.

One consequence of the side-looking geometry shown in figure 1 is that regions of shadow and layover can form in the vicinity of steeper terrain. These phenomena are discussed in the next section and it will be shown that the extent of shadows

and layover can be found by searching along lines of constant azimuth, which is at right angles to the instrument's flight line. A backscattered signal within these regions cannot practically be related to ground characteristics of interest [1]. Therefore, layover and shadow masks are required to exclude these regions from any further analysis. This is important since the accuracy of layover and shadow masks is often not critical, provided all affected areas are within the masked regions.

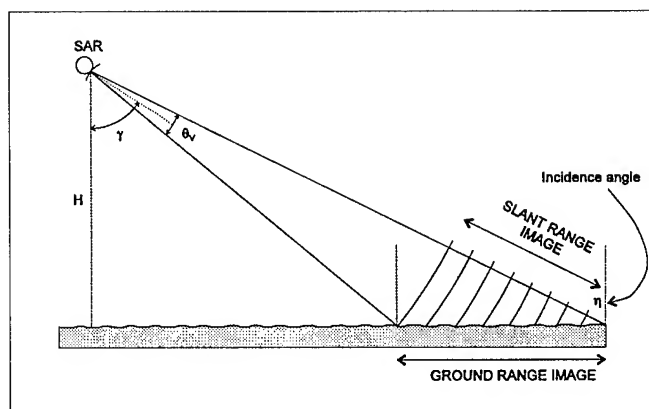


Figure 1 SAR side looking geometry (from [1])

SHADOW AND LAYOVER

Shadow is the simplest of these two phenomena to understand as it relates directly to our everyday experience of electromagnetic radiation behaviour as visible light. Recalling that the SAR geometry is side looking and referring to figure 2, it is easy to see that some areas on the ground will not be illuminated by the radar signal. These areas are "shadowed" by higher terrain that is closer to the SAR instrument. The region E-F in figure 2 is in shadow, and as no backscatter will be returned from this region, a dark patch will be seen in the SAR image whether its form is slant range, ground range, or orthorectified. Any terrain with slopes away from the sensor of more than $\pi/2 - \eta$ where η is the incidence angle (with the local geoid) will contain shadow regions.

Layover is a less familiar phenomena caused by the downward-looking component of the SAR geometry. As the across-track image dimension is actually a range from the sensor, backscatter returns from elevated terrain arrive earlier, making it appear displaced towards the sensor. Where there are regions with slopes towards the sensor greater than η , the backscatter from the top of the region (point C in Figure 2), will arrive before that from points lower down the slope. Returns

for the high-slope region (B-C in figure 2) and the area in front of and behind this region will become mixed, resulting in a bright return with no practical method of separating the contributions from different points on the ground.

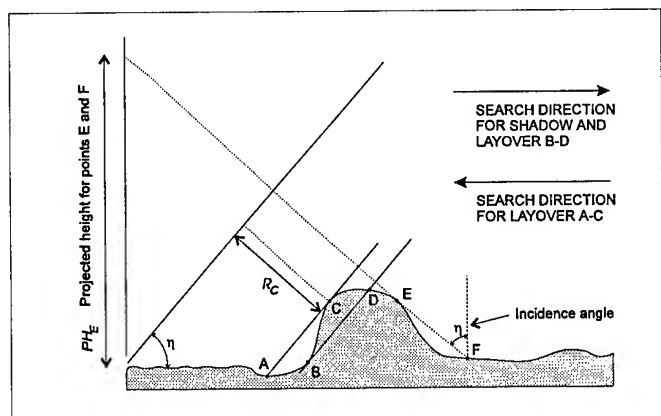


Figure 2 Shadow and layover search algorithm

In identifying regions of shadow and layover in the image domain, a two-pass, one dimensional search in the range direction is clearly sufficient. Referring to figure 2, one can project each point back toward the sensor to produce a projected height at the edge of the image. In figure 2 this is illustrated as PH_E for point E and is the same value for point F. If the search is from left to right, only the highest projected value so far encountered need be stored, and if the current point's projection is below this maximum, it will be in radar shadow. In figure 2, the region between E and F will have a lower projected height than that of point E.

Similarly, a record of the distance back to a plane of slope η intersecting the edge of the image can be kept. This is illustrated as distance R_C for point C in figure 2. If the search is from left to right, points closer to this plane than a previously found maximum will be affected by layover. For instance, the region B-D is closer to the plane than point B. A search in the opposite direction is required to detect the layover affected region A-B by maintaining the minimum of the distance to the plane. In this search the region A-C will be further from the plane than the minimum previously found at C.

In both the shadow and layover calculation, the incidence angle η to the local geoid is not constant. Modifications can easily be made to the method to account for this. However, at satellite heights the variation is small and, as will be shown in later, an exact solution may be unwarranted.

It is clear from the above description that shadow and layover masks can both be generated from two passes across an elevation model image transformed into the original satellite image projection. If each line represents data at a constant azimuth, then the image can be processed a line at a time. Conversely, if the image columns represent a constant azimuth, we can still efficiently process the image by maintaining arrays of maxima/minima values with an element of the array for each column.

MAP DOMAIN METHOD

The methods described so far have one major drawback in that the DEM information needs to be transformed to the original satellite projection and resulting masks need to be transformed back to the map domain. Lines of constant azimuth, or even arrays of such lines, could be followed in the map domain to affect the process described above. This is effectively doing the transformation "on the fly" and, for large images, accessing portions of the image in the order required is inefficient.

It has already been illustrated that an array containing maxima/minima values can be "swept" across a DEM in the image domain to identify shadow and layover. Furthermore, it has been shown that, although not efficient in implementation, this can also be done in the DEM map domain where the "sweeping array" (SW) will be oriented at an arbitrary angle to the image as shown in figure 3.

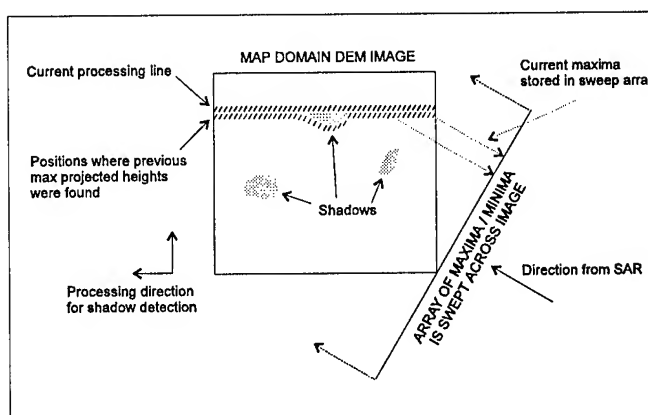


Figure 3 Detecting shadow in the map domain

A more efficient method in the map domain can be carried out by realising that not all parts of the sweeping array need be at an equivalent range at any stage. That is, the sweeping array's progress across the image need not be at right angles to the range direction or even a straight line. As each new point is compared with the current maxima/minima array element appropriate that point's azimuth value, it is only necessary that other points with the same azimuth value but closer to the SAR have already been swept over by the array. Finally it can be seen that the image can be traversed in a line-by-line and pixel-by-pixel manner while still maintaining this condition. Depending on the direction of the SAR track, it may be necessary to process top-to-bottom or bottom-to-top and, within each line, left-to-right or right-to-left as appropriate to maintain this condition. As before, two sweeps are required, one away from the sensor and one towards the sensor to identify shadow and all of the layover affected areas.

The algorithm described above is very efficient as it requires no complex buffering and, in its simplest form, only involves interpolation in a single dimension. Points in the DEM image will not generally be positioned exactly on a constant azimuth line represented by an element in the sweep array. Interpolation

into the sweeping array is therefore necessary to compare with the previous maximum or minimum. Interpolating between these array elements, which in theory could come from significantly separated points in the image, seems inappropriate. Therefore, for each array element we store not only the maximum (or minimum), but also the slope on either side to allow accurate interpolation from the single element.

ACCURACY OF MASKS

In the above discussion, several assumptions have been made that are not strictly accurate. The magnitudes of errors caused by these assumptions are investigated in this section and where appropriate refinements described. To illustrate the problem, we refer to a typical JERS-1 (Japan Earth Resources Satellite) SAR image of the Taranaki region. The region is about 39° south and it contains a volcanic cone rising to about 2500m.

The satellite path may not be a straight line in the map projection, meaning that the constant azimuth lines are not exactly parallel or even straight. Although map projection and latitude dependant, this effect is likely to be very small over a single SAR image. For a typical JERS-1 SAR scene (75x75 km) at mid latitude, the satellite path varies by $<0.1^\circ$. In an aircraft mounted SAR, orientation variations between a processed image product and a map should be insignificant.

The previous discussion has also assumed a constant radar incident angle with respect to the local geoid. From figure 1 this is clearly not so especially for an aircraft mounted SAR instrument. For JERS-1 SAR images, the local incidence angle varies from 36.4 to 41.9° which could make as much as 20% difference to the layover influence of a given terrain feature. Local incidence for an aircraft mounted instrument such as NASA's AIRSAR vary between 25 to 65° over a 10km swath.

The problem can largely be avoided by continuously adjusting the incident angle η as we progress through the image. A simple linear interpolation can be used, although for improved accuracy, it is preferable to interpolate $\tan \eta$, which is linear in ground range to a first approximation, rather than η itself. As the current maxima/minima held are only relative quantities, the method automatically compensates for a slowly varying incident angle.

Variation in incidence angle from one ground range pixel to the next is insignificant and can be ignored. A larger difference in incident angle may be expected between the ends of lengthy shadow or layover regions where direct comparisons are still being made. The length of shadow/layover regions is dependent on the terrain and SAR characteristics. In our JERS-1 Taranaki image, the effect is more pronounced for layover and the longest region found was ~1km. Over this distance the incidence angle varies by $<0.08^\circ$, resulting in an error in the layover region length of ~3m. For an AIRSAR image, a 1km layover region could have a variation in incidence angle of around 3.5° resulting in an error up to 150m for the projected edge.

Depending on terrain, this accuracy may not be sufficient for aircraft applications. However, more sophisticated approaches

can be taken to improve this error, even to the point of modelling the actual range back to the spacecraft/aircraft for an exact solution. In the context of generating shadow and layover masks, this seems unnecessary. These masks are generally used to exclude bad backscatter data from later processing. In most applications simply growing the masks by a couple of pixels to account for any errors in the method and to allow for any misregistration within the orthorectified imagery is a more practical approach. It should also be realised that identification of shadow/layover is often limited by DEM accuracy.

CONCLUSIONS

A simple and efficient algorithm has been developed to identify layover and shadow regions in the map domain using a DEM. This algorithm avoids the need to either re-project the DEM into the original satellite image domain or to do complex buffering while searching along lines of constant azimuth.

An analysis of errors due to simplifying assumptions shows that the small variation in satellite track across the image can be safely ignored. The same cannot be said for the variation in incident angle. However, this angle can be varied using interpolation. Once this is done, it will also have negligible effect due to the nature of the search method.

Masks of layover and shadow are required to exclude "bad" data in many studies using radar backscatter. Such studies include classification (*cf.* [2]); the determination of physical quantities such as wood volume (*cf.* [3]); and studies of backscatter relationships to the terrain itself (*cf.* [4]). In such studies the algorithm described is more than accurate enough to identify regions to exclude from the analysis.

ACKNOWLEDGEMENTS

Funds for this research were provided by the New Zealand Foundation for Research, Science and Technology under Contract 96-LCR-09-4826.

REFERENCES

- [1] J.C. Curlander, and R.N. McDonough, *Synthetic aperture radar : systems and signal processing*. John Wiley & Sons Inc, ISBN 0-471-85770-X., 1991.
- [2] K.M. Bergen, L.E. Pierce, M.C. Dobson, and F.T. Ulaby, "A multi-temporal classifier for SIR-C/X-SAR imagery," *Proc IGARSS'96*, (Lincoln), May 1996, pp 1568-1570.
- [3] K.M. Bergen, M.C. Dobson, and L.E. Pierce, "Carbon dynamics in northern forests using SIR-C/X-SAR imagery," *Proc IGARSS'96*, (Lincoln), May 1996, pp 1580-1582.
- [4] D. Pairman, S.E. Belliss, and S.J. McNeill, "Angular dependence of SAR backscatter around Mt Taranaki, New Zealand," *Proc IGARSS'96*, (Lincoln), May 1996, pp 1839-1841.

Different Approaches to Multiedge Detection in SAR Images

Roger Fjørtoft^{1,2}

Armand Lopes¹

Philippe Marthon²

Eliane Cubero-Castan³

¹CESBIO (UMR 5639 CNES/CNRS/UPS), 18 avenue Edouard Belin, Bp 2801, 31401 Toulouse cedex 4, France
Phone: (33) 5-61-55-85-39 Fax: (33) 5-61-55-85-00 E-mail: Roger.Fjortoft@cesbio.cnes.fr Armand.Lopes@cesbio.cnes.fr

²ENSEEIH (LIMA-IRIT-URA CNRS 1399), 2 rue Camichel, Bp 7122, 31071 Toulouse cedex 7, France
Phone: (33) 5-61-58-83-53 Fax: (33) 5-61-58-83-53 E-mail: Philippe.Marthon@enseeiht.fr

³CNES – French Space Agency (DGA/SH/QTIS), 18 avenue Edouard Belin, 31401 Toulouse cedex 4, France
Phone: (33) 5-61-27-46-12 Fax: (33) 5-61-27-31-67 E-mail: Eliane.Cubero-Castan@cnes.fr

Abstract -- Edge detection is a fundamental issue in image analysis. The presence of speckle, which can be modelled as a strong multiplicative noise, complicates edge detection in Synthetic Aperture Radar (SAR) images. Several statistical edge detectors have been developed specifically for such images, based on the hypothesis that only one step edge is present in the analyzing window. We here concentrate on the spatial aspect of edge detection in SAR images. Depending on the scene type and the size of the analyzing window, the monoedge hypothesis is violated more or less frequently. We present and compare three approaches to edge detection in a multiedge context: an optimum non-adaptive operator, a spatially adaptive operator and multiscale analysis.

INTRODUCTION

SAR images and images from other imaging systems relying on coherent illumination are characterized by strong intensity fluctuations known as speckle. In SAR imagery speckle is generally modelled as a multiplicative, Gamma-distributed random noise with unity mean and variance equal to the inverse of the Equivalent Number of Independent Looks (ENIL) [3].

Gradient-based edge detectors, developed for optical images, perform poorly when applied to SAR images. This is mainly due to the multiplicative nature of speckle. A basic experience is that gradient-based operators, which basically compute a difference of local mean values on opposite sides of the central pixel, detect more false edges in areas of high reflectivity than in areas of low reflectivity. To overcome this problem, several statistical edge detectors have been developed for SAR images based on the multiplicative noise model and the restrictive hypothesis that only one step edge is present in the analyzing window. Well-known examples of such monoedge detectors are the Ratio Of Averages (ROA) operator [1] and the Likelihood Ratio (LR) operator [2], which both yield a Constant False Alarm Rate (CFAR). The ROA operator coincides with the optimum LR operator when only the analyzing window is split in two equally sized halves.

The monoedge model is, however, not very realistic. To sufficiently suppress the influence of the speckle, relatively large analyzing windows must be used, and for most scene types several edges may then co-occur within a half-window. There are several ways of taking this situation into account.

MULTIEDGE DETECTORS

The computationally most efficient approach is to use a non-adaptive operator designed for the multiedge case. We recently proposed a CFAR edge detector for SAR images which is optimum in the Minimum Mean Square Error (MMSE) sense for a stochastic multiedge model [4]. This operator computes a Ratio Of Exponentially Weighted Averages (ROEWA) on opposite sides of the central pixel in the horizontal and vertical

directions. The slope of the exponential weighting function is controlled by a parameter b , which depends on the reflectivity mean and variance, the ENIL and the mean region width [4]. To make the operator independent of the scanning direction, we normalize each ratio to be superior to one by taking the maximum of the measured ratio and its inverse. The magnitude of the horizontal and vertical components yields an edge strength map, from which local maxima are extracted and attributed to edges.

The ROA operator is basically designed for the monoedge case, but by making the size and shape of the window scene adaptive it can face a multiedge situation. We have chosen an approach which is slightly different from the one proposed in [1]. We first fix the Probability of False Alarm (PFA), i.e. the probability of detecting an edge in a zone of constant reflectivity. The corresponding detection thresholds for all window sizes in the range of interest are calculated. We compute the ratio in the horizontal, vertical and diagonal directions, and take the maximum of each measured ratio and its inverse. To facilitate the comparison of results for windows of different sizes, each ratio is divided by the appropriate detection threshold. Normalized ratios superior to one thus indicate the presence of an edge. The overall maximum value, which is the strongest indication of an edge across the scales, is retained as the edge strength of the pixel. Local maxima of the edge strength map are considered as the most probable edge localizations.

Multiscale analysis consists in detecting characteristic scale-space signatures. When using the continuous wavelet transform, the Haar wavelet is optimum for edge detection in signals with multiplicative noise [6]. However, such wavelet-based detection schemes do not yield a CFAR, so we use a ratio rather than a difference of arithmetic averages on each scale. Each scale corresponds to a certain window size, and we suppose that the monoedge hypothesis is verified at least for some of the smaller windows. The identification of the characteristic signature by correlation is quite complicated for a two-dimensional signal, so we propose a far simpler detection method [5]. We first employ the ROA operator over a wide range of window sizes, normalizing by the detection threshold as in the adaptive case. Pixelwise averaging of the results on different scales gives the edge strength map.

The watershed algorithm [7] can be used to obtain closed, skeleton boundaries running through local maxima of the edge strength map. To suppress false edges due to speckle more efficiently, we introduce a threshold under which local maxima are ignored [8], or basin dynamics [9].

COMPARISON

The test image we have used to compare the different approaches is composed of vertical lines of gradually increasing width from 1 to 10 and with contrast ratio 4. The ideal image

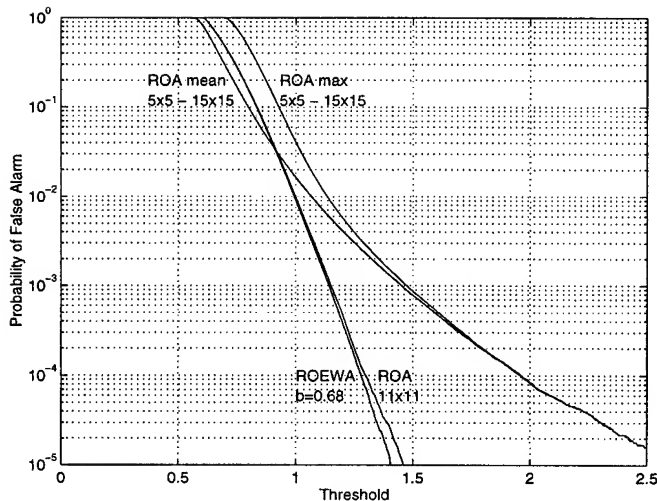


Figure 1. PFA versus detection threshold.

is multiplied by white noise with unity variance and mean to obtain a simulated 1-look image. As all edges are vertical, we compute ratios only in the horizontal direction. We take the ROA operator with window size 11×11 as a reference. The PFA was set to 1%, and the ratios were divided by the corresponding detection threshold as described above. We found the ROEWA operator with $b = 0.68$ to have the same speckle reduction capacity as the ROA operator with window size 11×11 , and normalized the ratios of exponentially weighted averages by the same threshold. $b = 0.68$ corresponds to the theoretical optimum [5] for a mean region width of 5. The adaptive operator and the multiscale operator both used windows of size 5×5 through 15×15 .

The experimental PFAs as a function of the threshold for all four methods are plotted in Fig. 1. We first note that threshold 1.0 as expected corresponds to a PFA of 1% for the fixed scale ROA operator. The PFA of the ROEWA operator coincides with that of ROA operator. Taking the mean ratio of arithmetic averages over several window sizes reduces the PFA for low thresholds, but for higher thresholds the PFA is higher than for the fixed scale operators. A threshold of 1.07 corresponds to a PFA of 1%. For the adaptive method, which takes the maximum ratio across the scales, the PFA graph lies above those of the other methods, but it converges towards that of the multiscale operator for high thresholds. According to Fig. 1, the threshold should be set to 1.13 for the adaptive operator to have the same PFA. Refer to [5] for information on the PFA in the multidirectional case.

A line of the ideal image is illustrated in Fig. 2. If we average a block of 11 speckled lines centered on a certain sample line, we obtain the intensities shown in Fig. 3. This illustrates the detection problem in the horizontal direction for the 11×11 ROA operator. Figs. 4 through 7 show the edge strengths obtained with the different operators centered on the sample line. The ideal edge positions are indicated by dotted vertical lines, and the threshold corresponding to a PFA of 1% is indicated by a horizontal dashed line in each case.

Let us now suppose that we retain local maxima over the threshold as edges, cf [8]. We see from Fig. 4 that the 11×11 ROA operator detects edges between lines of width 5 or higher. When the region width becomes smaller than the width of a half-window, the edge responses get much weaker, so that the edges are not detected with the PFA we have fixed. The ROEWA operator detects some edges at finer line widths, but some intermediate edges are lost and there is a spurious edge in

pixel position 32. It should be noted that the test image is not a typical realization of the stochastic process corresponding to the multiedge model for which the ROEWA operator is optimum. When retaining the maximum ratio across the scales, we detect edges systematically down to line width 2, as can be seen from Fig. 6. For the operator which takes the mean ratio over different window sizes, we also detect edges down to line width 2, as shown in Fig. 7. As far as the edge localization precision is concerned, no significant differences can be observed between the two latter methods, but they both perform better than the ROEWA operator.

CONCLUSION

In this article we compare three simple approaches to multiedge detection in SAR images. Tests on a simulated SAR image indicate that the two methods which rely on normalized ratios of arithmetic averages computed on different scales can detect edges that are closer together than the fixed-scale ROEWA operator with the same PFA. We have here only considered watershed thresholding of edge strength maps. To improve the edge detection, the expected evolution of an edge across the scales should be taken into account explicitly. The normalized ROA operator computed on different scales has a characteristic ridge as edge signature. A more advanced detection algorithm could follow this ridge from coarse scales and good noise reduction to finer scales and better edge localization.

ACKNOWLEDGMENTS

This work is part of contract 833/CNES/96/0574/00. We thank the French Space Agency CNES for financial support.

REFERENCES

- [1] R. Touzi, A. Lopès, and P. Bousquet, "A statistical and geometrical edge detector for SAR images," *IEEE Trans. Geosci. Remote Sensing*, vol. 26, no. 6, pp. 764-773, November 1988.
- [2] C. J. Oliver, D. Blacknell, and R. G. White, "Optimum edge detection in SAR," in *IEE Proc. Radar Sonar Navig.*, vol. 143, no. 1, February 1996.
- [3] F. T. Ulaby, R. K. Moore, and A. K. Fung, *Microwave Remote Sensing*, vol. 3, Dedham, MA: Artech House, 1986.
- [4] R. Fjørtoft, P. Marthon, A. Lopès, and E. Cubero-Castan, "Multiedge detection in SAR images," in *Proc. ICASSP*, vol. 4, Munich, Germany, April 1997, pp. 2761-2764.
- [5] R. Fjørtoft, P. Marthon, and A. Lopès, "Multiresolution edge detection in SAR images," in *Proc. NORISIG*, Tromsø, Norway, May 1997.
- [6] M. Chabert, J. Y. Tournet, and Gilles Mesnager, "Edge detection in speckled SAR images using the continuous wavelet transform," in *Proc. IGARSS*, Lincoln, Nebraska, May 1996, pp. 1842-1844.
- [7] L. Vincent and P. Soille, "Watersheds in digital spaces: An efficient algorithm based on immersion simulations", *IEEE Trans. PAMI*, vol. 13, no. 6, pp. 583-598, 1991.
- [8] P. Marthon, B. Paci, and E. Cubero-Castan, "Finding the structure of a satellite image," in *Proc. EurOpto Image and Signal Processing for Remote Sensing*, vol. SPIE 2315, Rome, Italy, 1994, pp. 669-679.
- [9] M. Grimaud, "A New Measure of Contrast: Dynamics," in *Proc. Image Algebra and Morphological Processing III*, vol. SPIE 1769, San Diego, July 1992, pp. 292-305.

Reprints of our communications can be downloaded from URL <http://www.enseiht.fr/Recherche/Info/Vision/Membres/RF/>

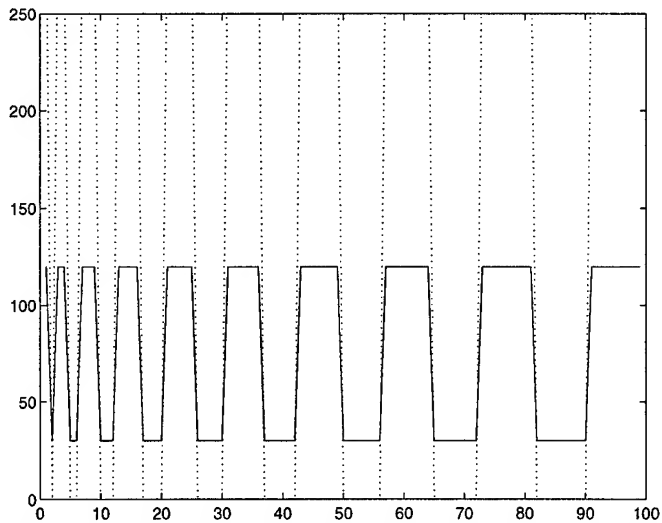


Figure 2. Intensities of a sample line of the ideal test image.

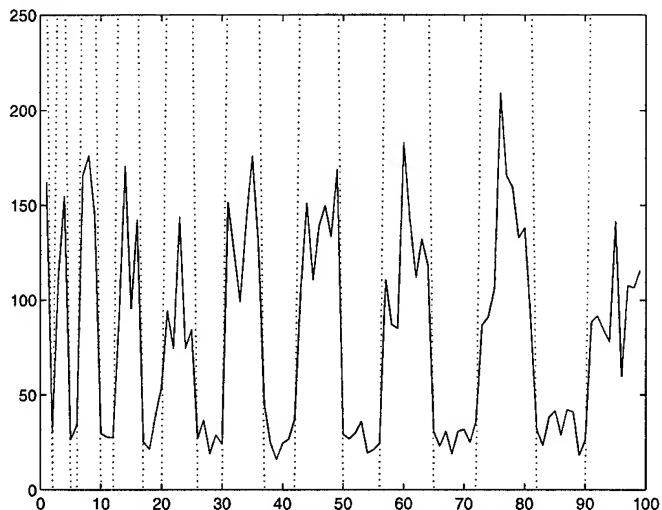


Figure 3. Average intensities of a block of 11 lines of the speckled test image.

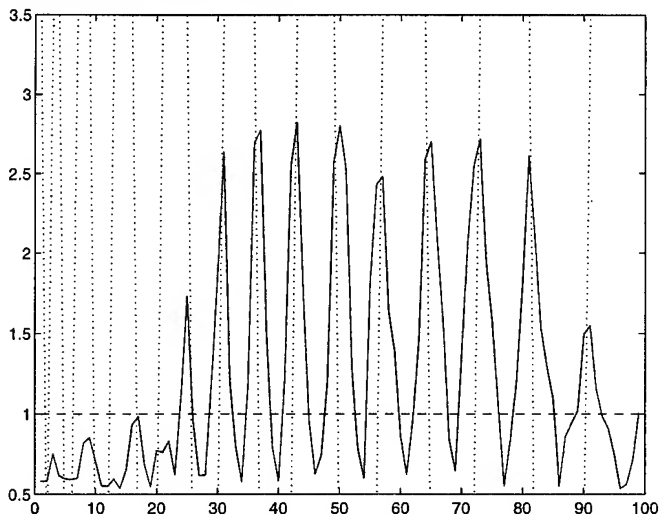


Figure 4. Normalized ratios for a 11×11 window centered on the sample line.

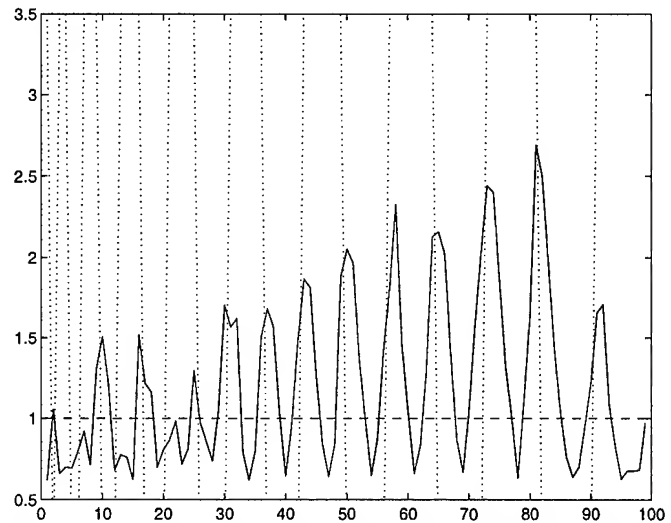


Figure 5. Normalized ratios for the ROEWA operator with $b = 0.68$ centered on the sample line.

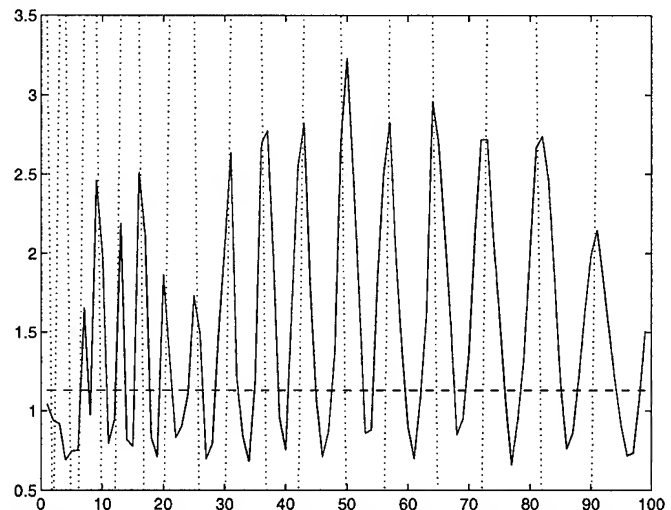


Figure 6. Maximum of normalized ratios for 5×5 to 15×15 windows centered on the sample line.

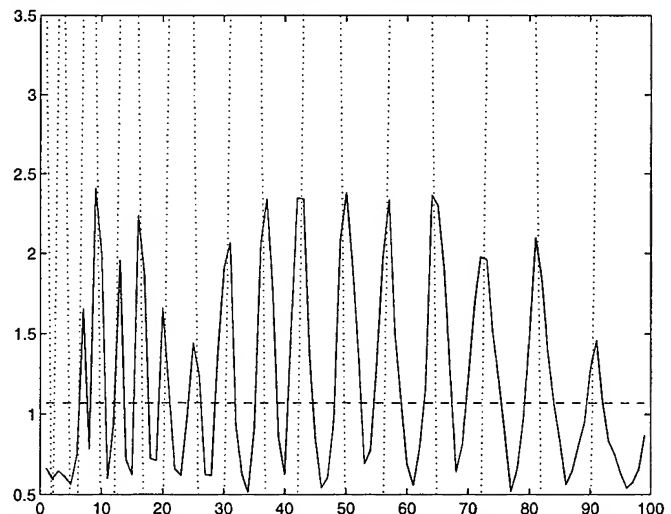


Figure 7. Average of normalized ratios for 5×5 to 15×15 windows centered on the sample line.

Terrain classification via texture modelling of SAR and SAR Coherency images

Jonathan P. Meagher, John Homer, Rupert Paget and Dennis Longstaff

Department of Electrical and Computer Engineering,

The University of Queensland, Brisbane, Qld 4072, Australia and

Cooperative Research Centre for Sensor Signal and Information Processing

Ph: +61 7 3365 3683, Fax: +61 7 3365 3684, Email: homerj@elec.uq.edu.au

Abstract – In this paper we investigate the use of the SAR coherence image and SAR intensity images for terrain classification. In particular, we present two algorithms which utilise both the coherence and intensity images, to produce an improved classification map. A kernel-based density estimation Markov Random Field methodology is employed for texture modelling.

INTRODUCTION

In this paper we consider the application of a newly developed image classification technique which relies on higher order statistical information, to SAR images and SAR coherency images. The aim is to achieve improved terrain classification from the technique via “fusion” of the two image types. The classification technique is based on a non-parametric Markov Random Field (MRF) approach. In particular, the technique provides a set of probability maps, each map indicating the probability that the image texture, on a local scale, is the same as that of a model texture. The model texture is that generated from a window of pixels containing a given terrain type.

METHODOLOGY

The procedure requires two single look complex SAR images, which we denote S_1 and S_2 , and involves; (i) co-registration, (ii) generation of the corresponding coherency image, (iii) application of a MRF based classifier. We consider three different approaches to step (iii).

Co-registration

Co-registration of the two SAR images was carried out by the procedure recommended in [3]. This procedure allows for a slight rotation and a slight stretching of one image relative to the other as well as a translational offset between the two images. The suitability of this procedure relies on the flight paths from which the images are acquired, having a relatively small baseline and being almost parallel. This is the typical situation for repeat passes of SAR imagery satellites, such as the ERS-1 satellite.

Coherency Image Generation

The coherency value for each pixel site (i, j) was determined from the local sampled coherency (1):

$$C = \frac{\sum_N [S_1 S_2^* \exp(-j\varphi)]}{\sqrt{\sum_N [|S_1|^2] \sum_N [|S_2|^2]}} \quad (1)$$

where the summation is over N neighbouring pixels and φ is a terrain slope dependent phase term which is included to compensate for changes in the relative phase of the two images with terrain topography. As recommended

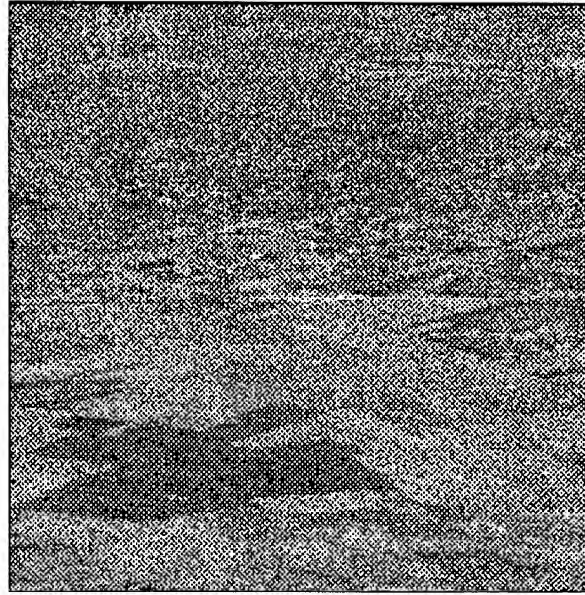


Figure 1: Intensity image of S_1

in [3], φ is estimated using local derivatives of the phase difference image, $\varphi_1(r, s) - \varphi_2(r, s)$, where $\varphi_k(r, s)$ is the phase value of pixel (r, s) in image k .

Texture Based Terrain Classification

A density estimation Markov Random Field approach, proposed by [2], is used for texture modelling.

Consider a test image Φ_{ij} , $1 \leq i, j \leq N_\Phi$, which we would like to classify w.r.t. a pre-defined texture sample Ψ_{ij} , $1 \leq i, j \leq N_\Psi$. In addition, assume that the images are Markov Random Fields, such that the joint Probability Density Function of each image can be determined by its Local Conditional Probability Density Functions [1]. This allows the images to be considered as a set of independent neighbourhoods. Following the results of [2], we use overlapping 3×3 neighbourhoods for density estimation, such that the test image Φ is covered by N_Φ^2 3×3 overlapping neighbourhoods. We denote each neighbourhood by ϕ , bold-faced to signify a multi-dimensional variable. Similarly, we cover the texture sample Ψ with a set of N_Ψ^2 neighbourhoods, each denote by ψ .

Following the methodology of [4], we employ Gaussian kernel-based density estimation to evaluate the probability of a given neighbourhood ϕ_{rs} occurrence in the texture sample Ψ :

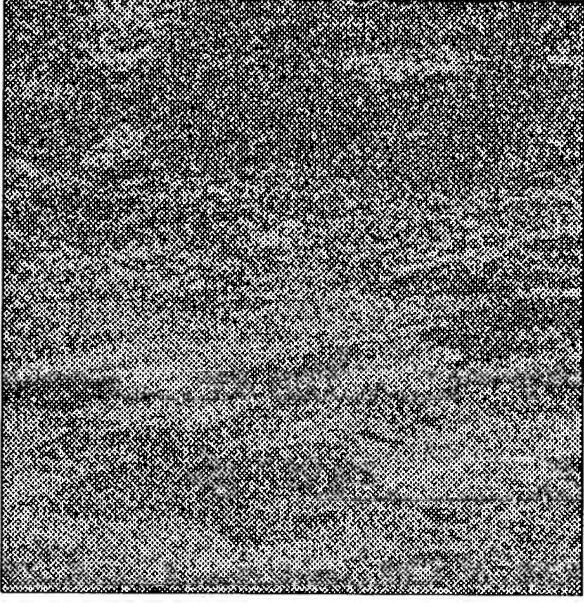


Figure 2: Coherence image generated from S_1 and S_2

$$P(\phi_{rs}|\Psi) = \frac{1}{N_\psi h} \sum_{i,j=1}^{N_\psi} K\left(\frac{1}{h}(\phi_{rs} - \psi_{ij})\right) \quad (2)$$

Here K is the Gaussian kernel function and h is a normalising constant.

Density estimation is applied, as it is impractical to construct histograms for such Probability Density Functions. These would be sparse given the dimensionality and amount of data available. We instead construct matrices of density estimates which are samples of the PDF only. Hence we need to apply a statistical test on the two populations of PDF estimates to determine whether they have the same underlying PDF. We present three methods which all utilise the MRF Gaussian kernel-based density estimation scheme as described above.

Single image classification

Single image classification involves the classification approach of [2]. It entails two stages. Firstly, a matrix Υ of density estimates $P(\phi_{rs}|\Psi)$ is calculated for the entire test image Ψ . A similar matrix Ξ of density estimates $P(\psi_{rs}|\hat{\Psi})$ is calculated for the texture sample. $P(\psi_{rs}|\hat{\Psi})$ is the probability that the neighbourhood ψ_{rs} is from the texture sample $\hat{\Psi}$, ($\hat{\Psi} \subset \Psi$, $\psi_{rs} \notin \hat{\Psi}$).

$$P(\psi_{rs}|\hat{\Psi}) = \frac{1}{(N_\psi - 1)h} \sum_{ij=1, ij \neq rs}^{N_\psi} K\left(\frac{1}{h}(\psi_{rs} - \psi_{ij})\right) \quad (3)$$

The matrix Ξ is a set of density estimates for the probability density function associated with the MRF representation of the texture sample Ψ , and provides a measure of the density of the clustering of the texture sample in the 9 dimensional space (associated with the 3x3 neighbourhood).

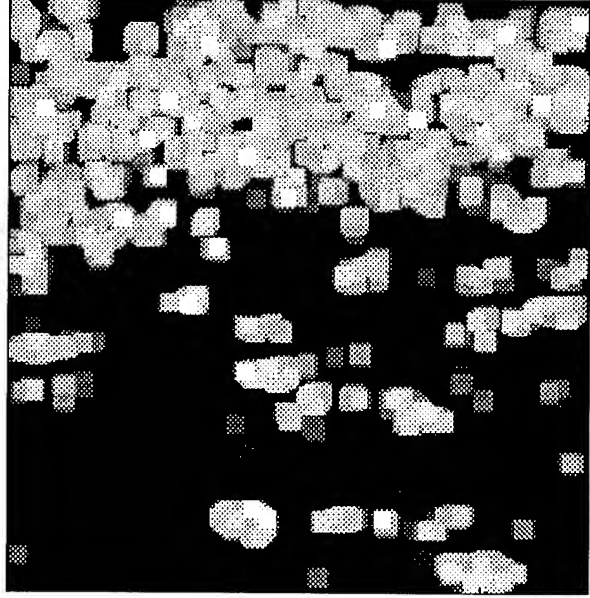


Figure 3: Classification map of $|S_1|$ figure 1, w.r.t. the texture sample taken from the middle top of the image

The second stage involves the application of the Kruskal-Wallis (K-W) test, to determine the probability that the neighbourhood ϕ under question is correctly labelled L_Ψ , as being of the texture class encompassed in Ψ . To this end, the matrix Υ is considered on a neighbourhood by neighbourhood basis, this time 7x7 neighbourhoods are used and denoted as ν . The Kruskal-Wallis test (K-W) evaluates the null hypothesis that the different classes (ν, Ξ) of density estimate samples come from identical populations. We use the confidence value from the test for the probability $P(L_\Psi|\phi)$

$$P(L_\Psi|\phi) = \text{K-W}(\nu, \Xi) \quad (4)$$

Fusion of classification maps

With the coherence image C and either of the SAR intensity images ($A = |S|$). Classification may be carried out via maximization of $P(L_\Psi|c, a)$. Where c and a are co-located neighbourhoods in the images C and A . If we assume that A and C are Gaussian and uncorrelated, it can be shown that,

$$\begin{aligned} P(L_\Psi|c, a) &= \frac{P(L_\Psi|c) P(L_\Psi|a)}{P(L_\Psi)} \\ &\cong P(L_\Psi|c) P(L_\Psi|a) \end{aligned} \quad (5)$$

In this the second of the three MRF based classification algorithms, we also assume that $P(L_\Psi)$ is uniformly distributed. Thus classification is achieved via the product of the two single image classification maps $P(L_\Psi|c)$ and $P(L_\Psi|a)$.

Multi-image classification

We can denote all three images S_1 , S_2 , and C as Φ^k , $k = 1, 2, 3$ respectively, and their corresponding texture

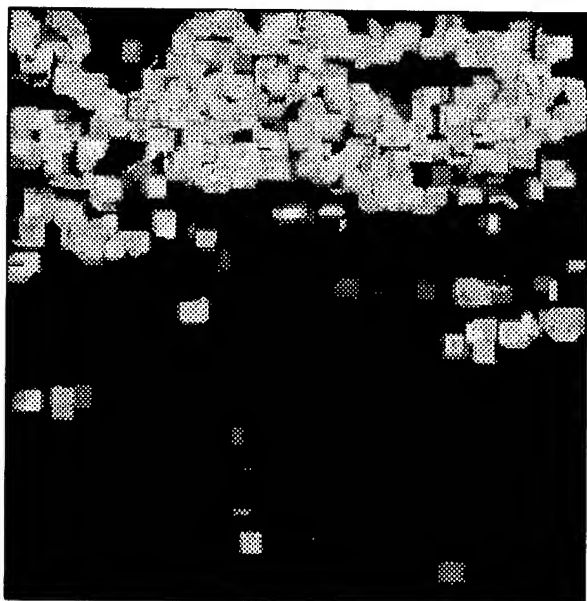


Figure 4: Composite classification map, from fusion of classification maps S_1 and C

samples as Ψ^k . For multi-image terrain classification, we calculate the density estimates matrices Υ^k and Ξ^k . Here $\Upsilon_{rs} = P(\phi_{rs}^k | \Psi^k)$ and $\Xi_{rs} = P(\psi_{rs}^k | \Psi^k)$, both being third order vectors. We treat these as 3 dimensional independent random data and hence calculate density estimates these of,

$$\Gamma_{rs} = P(\Upsilon_{rs} | \Xi^k) = \frac{1}{N_{\Xi} h} \sum_{i,j=1}^{N_{\Xi}} K \left(\frac{1}{h} (\Upsilon_{rs} - \Xi_{ij}) \right) \quad (6)$$

$$\begin{aligned} \Theta_{rs} &= P(\Xi_{rs} | \Xi^k) \\ &= \frac{1}{(N_{\Xi} - 1)h} \sum_{ij=1, ij \neq rs}^{N_{\Xi}} K \left(\frac{1}{h} (\Xi_{rs} - \Xi_{ij}) \right) \end{aligned} \quad (7)$$

Next we consider the density estimate matrix Γ , on a 7×7 neighbourhood basis γ and perform the Kruskal-Wallis test as for the signal image classification case.

$$P(L_{\Psi} | \phi^k) = \text{K-W}(\gamma, \Theta) \quad (8)$$

RESULTS

We applied the three classification algorithms to two complex valued SAR images S_1 and S_2 acquired by the ERS-1 satellite over Bonn, Germany. Fig. 1 is a 245×245 intensity image of S_1 . Fig. 2 is the corresponding coherence image, after the two SAR images have been co-registered. Figs 3-5 detail the classification maps produce by the three different algorithms, in the order they are presented in the text. The training texture sample Ψ , for this example was selected from the top-middle of the scene. All three methods are able to differentiate between

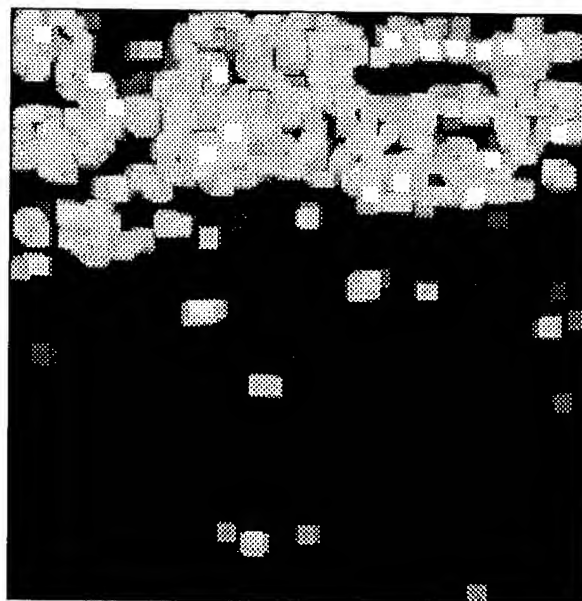


Figure 5: Multi-image classification map

the texture present in the top third of the scene w.r.t. the other major texture types present. With the two multi-image algorithms, classifying very few neighbourhoods in the lower two-thirds of the scene, as being of the same type as the texture training sample.

CONCLUSIONS

In this paper we have presented three MRF Gaussian kernel-based density estimation classification algorithms. These may be applied to pairs of single look complex images and their corresponding coherence image. The application of these methods to ERS-1 acquired SAR data sets indicates they are all capable of terrain classification. The multi-image methods are found to be more discriminating than the single image method. However, without the use of a test series of ground-truthed images qualitative conclusions can only be drawn. Such a set of ground-truthed images would allow quantitative analysis of the different algorithms performance over a number of different scenes.

REFERENCES

- [1] J. Besag. On the statistical analysis of dirty pictures. *Journal of the Royal Statistical Society*, 48(3):259-302, 1986.
- [2] R. Paget and D. Longstaff. Texture synthesis via non-parametric markov random field. In *Conference Proceedings DICTA-95, Digital Image Computing: Techniques and Applications*, pages 547-552, 1995.
- [3] C. Prati. Report on ers-1 sar interferometric techniques and applications. Technical report, ESA Study Contract Report, June 1994.
- [4] B. W. Silverman. *Density Estimation for Statistics and Data Analysis*. Chapman and Hall, 1986.

Adaptive Texture-Preserving Filtering of Multitemporal ERS-1 SAR Images

B. Aiazzi*, L. Alparone°, S. Baronti*, R. Carlà*

*Istituto di Ricerca sulle Onde Elettromagnetiche "Nello Carrara" - CNR, via Panciatichi, 64, I-50127 Firenze, Italy
Phone: +39-55-4235-275; Facsimile: +39-55-410893; E-mail: baronti@iroe.fi.cnr.it

°Dipartimento di Ingegneria Elettronica, University of Florence, via S. Marta, 3, I-50139 Firenze, Italy
Phone: +39-55-4796-372; Fax: +39-55-494569; E-mail: alparone@cosimo.die.unifi.it

Abstract -- A novel approach is proposed to adaptive filtering of multi-temporal images. A transformation aimed at decorrelating data is defined on the set of images taken at different times. Adaptive filtering is performed on the new set of data which are then transformed back. Results on ERS-1 multi-temporal SAR images show effectiveness in reducing speckle, while the intrinsic texture, edges and point targets are better preserved than by filtering each observation separately.

INTRODUCTION

Speckle noise typically occurs in imaging systems operating with coherent radiation, such as Synthetic Aperture Radar (SAR). It is originated by the random scattering of objects within elementary resolution cells and appears as a granular *signal-dependent* noise, whose effect is to degrade the appearance of images and to decrease the performance of image interpretation and classification algorithms.

Several techniques have been developed for speckle suppression [1]. Adaptive spatial filtering based on local statistics is widely used. In multi-frequency polarimetric SAR, several images in various polarizations and/or frequencies can be combined to produce a less noisy version (polarimetric filtering, or principal component -PC- analysis). When registered multi-temporal images of the same area are available, speckle processing can be designed in order to take advantage of *temporal correlation*. A viable strategy would be considering PC transformation of the original data, as suggested by Lee and Hoppel for polarimetric data [2]. This approach looks attractive, but noise statistics changes after transformation. In particular, it can no longer be assumed that the noise is multiplicatively related to the signal, since the mean of the images in the PC domain is zero. Such filters as Kuan's LLMMSE [3] and Meer's [4], cannot be directly used, since local variation coefficient (C_v , ratio of the square root of local variance to the local mean) loses its significance.

In this work, a new despeckle algorithm is proposed, which exploits the correlation of spatially registered multi-temporal data. A reversible transformation, which approximately maintains the noise model, is applied to a set of multi-temporal ERS-1 SAR images. Adaptive filtering is performed in the new domain; then data are inversely transformed.

MULTI-TEMPORAL TRANSFORMATION

The transformation which lies at the basis of the algorithm can be defined depending on the number of multi-temporal images available. In the case of only two images, their pixel-by-pixel average and difference constitute an example of reversible transformation with attractive properties. In fact, the average weakens the uncorrelated component of the observed signal, thus resulting in a higher SNR, while the difference removes the correlated component and strengthens noise, which can thus be heavily filtered without losing information [5]. Seasonal changes, which are also present in the difference image, are not deeply altered, appearing as correlated spatial structures. Unfortunately, the difference image is zero-mean and all the considerations on local statistics filters still apply.

A possible variant is to take the geometric mean and the ratio of the two images:

$$\begin{aligned} F_0(i,j) &= \sqrt{f_0(i,j)f_1(i,j)} \\ F_1(i,j) &= \frac{f_0(i,j)}{f_1(i,j)} \end{aligned} \quad (1)$$

$f_0(i,j)$ and $f_1(i,j)$ are the original images while $F_0(i,j)$ and $F_1(i,j)$ the transformed ones. Again, the former exhibits higher SNR, while the latter mostly contains noise or seasonal changes, and can be thus strongly filtered. The ratio image features unit-valued mean, and all filters for signal-dependent noise are applicable [6]. The reverse transformation can be easily found:

$$\begin{aligned} f_0(i,j) &= F_0(i,j)\sqrt{F_1(i,j)} \\ f_1(i,j) &= \frac{F_0(i,j)}{\sqrt{F_1(i,j)}} \end{aligned} \quad (2)$$

By assuming that $f_0(i,j)$ is identical to $f_1(i,j)$, apart from noise and small seasonal variations, that the noise affecting $f_0(i,j)$ is uncorrelated with the noise affecting $f_1(i,j)$ and of unity mean and same standard deviation σ_u , it stems that

$$\begin{aligned} \sigma_{U0} &= \frac{\sigma_u}{\sqrt{2}} \\ \sigma_{U1} &= \sqrt{2} \sigma_u \end{aligned} \quad (3)$$

where σ_{U0} , σ_{U1} are noise standard deviations of $F_0(i,j)$, $F_1(i,j)$.

The standard deviation of noise can be estimated on homogeneous areas by computing C_v , also denoted as speckle index. Alternatively, the mode of C_v histogram is a good estimate of the standard deviation of noise [4]. Although such a measurement is biased in excess for textured images, due to areas in which speckle is not fully developed, it is interesting to plot C_v 's for original and transformed images. The modes of the histograms of Figure 1 are distributed in a good agreement with (3). Slight differences are mainly due to signal changes between $f_0(i,j)$ and $f_1(i,j)$ which introduce a spatial correlation in F_l , whilst weakening correlation in F_o .

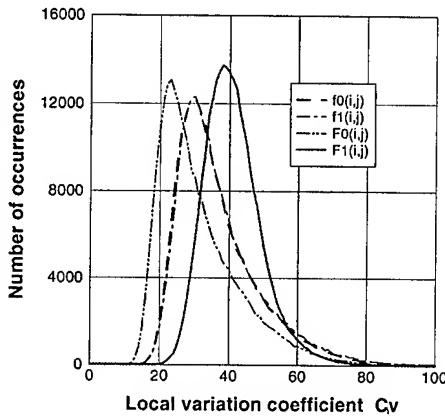


Figure 1. - Histograms of C_v , computed for a pair of multitemporal SAR images, their geometric mean and ratio.

The despeckle algorithm consists of processing $F_0(i,j)$ and $F_l(i,j)$ each with an adaptive filter suitable for multiplicative noise. Once σ_u has been estimated, σ_{u0} , σ_{ul} are given by (3).

The transformation defined by (1) and (2) can be easily generalized to deal with more than two images, whenever available, to obtain further SNR benefits. If the number of images N is a power of two, let $\{f_n(i,j), n = 0, \dots, N-1\}$ denote a set of consecutive multitemporal spatially overlapped observations. Apply (1) to couples of images, thus producing $N/2$ geometric means and $N/2$ ratios. Then, retain the latter terms and apply again (1) to couples of the former terms, and so on, recursively. The overall transformation will be

$$F_0 = \sqrt[N]{\prod_{n=0}^{N-1} f_n(i,j)}$$

$$F_k = \sqrt[\frac{N}{m}]{\prod_{n=(2l)N/m}^{(2l+1)N/m-1} f_n(i,j)} \quad k = 1, \dots, N-1 \quad (4)$$

$$m = 2^{\lceil -\log_2 k \rceil}$$

$$l = k \bmod (m/2)$$

Notice that the term F_0 has the highest SNR, terms from F_l to

$F_{N/2-1}$ are ratios of geometric means and have SNR's greater than or equal to that of any of the f_n , while the last $N/2$ terms are plain ratios and thus have SNR lower by about 3 dB.

RESULTS

The advantages of the proposed multitemporal approach to speckle removal are assessed by comparing the images obtained by straightforward filtering of the originals and by means of the gain in speckle index of the various images. Lee's filter, as generalized by Kuan *et al.* [3], was chosen.

Figure 2 shows two 256×512 ERS-1 images extracted from the processed area. Time difference is about one month (27 Nov. 1995 and 1 Jan. 1996). The archaeological site of Pisticci, Southern Italy, is visible on the low left corner, while the town of Pisticci Scalo appears in the upper part of the image. The two images have been combined according to (1) and shown in Figure 3. The correlated component (left) looks less noisy than each original while the ratio image (right) seems affected by speckle noise mainly. Few small objects appear, which are present in either of the two images only.

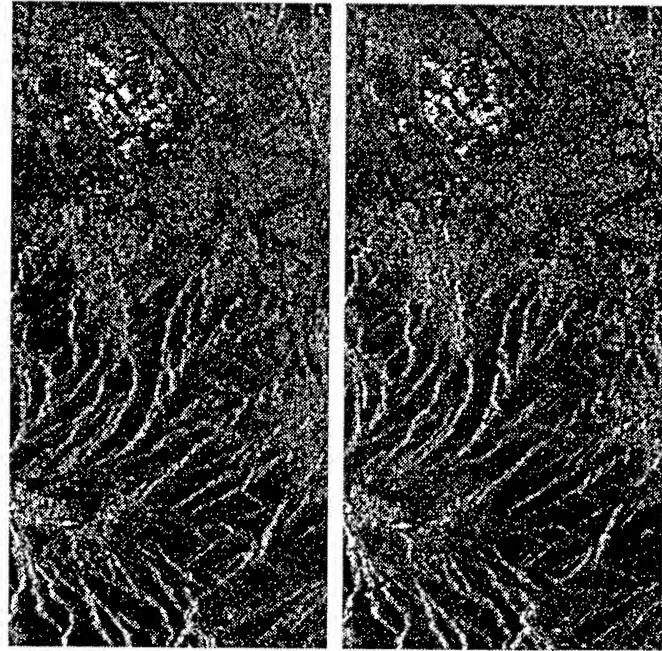


Figure 2. - Details of size 256×512 from the ERS-1 images.

These two components have been processed by Lee's filter (working with $\sigma_{u0} = 0.13$ and $\sigma_{ul} = 0.38$, respectively) and further recombined according to (2). Figure 4 (top) illustrates the results for a detail of the first image (left) and of the second (right), respectively. Notwithstanding the heavy reduction of noise, point targets, edges and textured areas have been well preserved. Results of the Lee's filter, separately applied to the same details, are also shown (bottom).

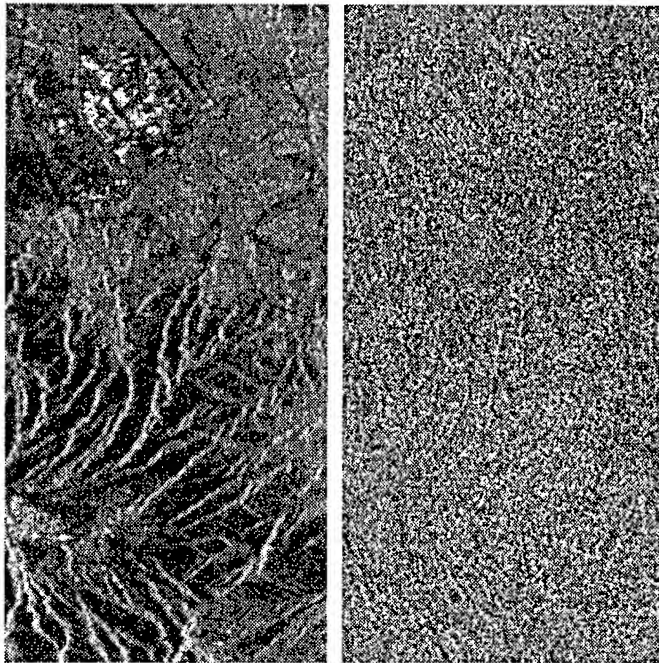


Figure 3. - Geometric mean (left) and ratio (right) of the images in Fig. 2. The ratio is rescaled for display convenience.

The noise standard deviation was set $\sigma_n = 0.19$ (roughly $0.13\sqrt{2}$) in order to guarantee the same filtering effect. Images on the right of Fig. 4 appear rather blurred when compared to those on the left. In addition, despeckle is less effective in homogeneous areas, and texture is not as well preserved.

The gain obtained for speckle index by directly filtering the originals with Lee's algorithm is estimated to be about 35%. With the proposed algorithm, this gain is about 40%, but with the advantage of a better visual quality.

CONCLUSIONS

The approach of defining a reversible transformation, which involves at least two images, and removing noise in the transformed domain has been introduced. If the transformation is suitably defined in order to separate noise from signal by increasing SNR in some of the transformed component, the advantages are apparent. Image denoising is more efficient than traditional filtering in term of speckle index. In addition, filtered images exhibit a greater sharpness, edge and point target are less blurred, texture is effectively preserved.

ACKNOWLEDGMENT

Work carried on under grants of CNR -Research Council of Italy- within the "National Project on Cultural Heritage".

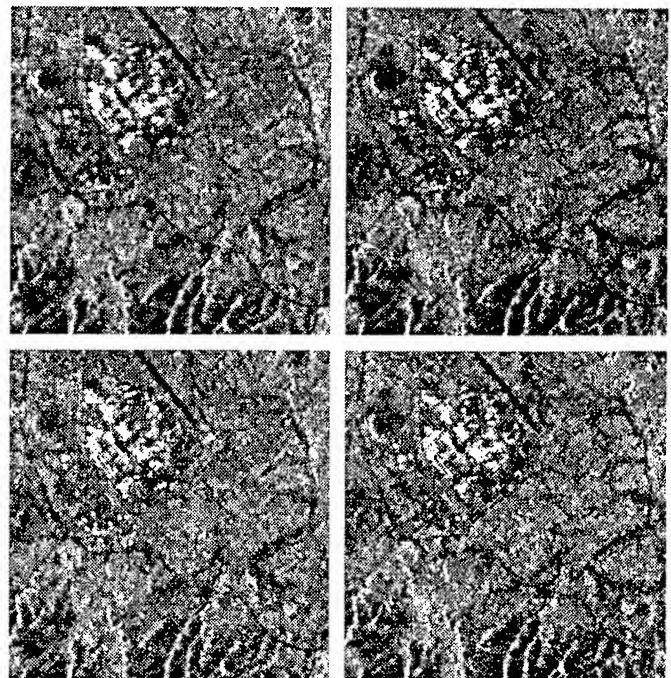


Figure 4. - Details of test images of Fig. 2 (256×256) filtered by means of Lee's filter: (top) with the multitemporal transformation; (bottom) each observation separately.

REFERENCES

- [1] J.-S. Lee, I. Jurkevich, P. Dewaele, P. Wambacq, A. Oosterlinck, "Speckle Filtering of Synthetic Aperture Radar Images: A Review," *Remote Sensing Reviews*, Vol. 8, pp. 313-340, 1994.
- [2] J.-S. Lee, K. Hoppel, "Principal Component Transformation of Multifrequency Polarimetric SAR Imagery," *IEEE Trans. Geosci. Remote Sensing*, Vol. 30, No. 4, pp. 686-696, 1992.
- [3] P. Meer, R.-H. Park, K. Cho, "Multiresolution Adaptive Image Smoothing," *CVGIP: Graphic Models Image Process.*, Vol. 56, No. 2, pp. 140-148, 1994.
- [4] D. T. Kuan, A. A. Sawchuck, T. C. Strand, P. Chavel, "Adaptive Noise Smoothing Filter for Images with Signal-Dependent Noise," *IEEE Trans. Pattern Anal. Machine Intell.*, Vol. 7, No. 2, pp. 165-177, 1985.
- [5] J. D. Villasenor, D. R. Fatland, L. D. Hinzman, "Change Detection on Alaska's North Slope Using Repeat-Pass ERS-1 SAR Images," *IEEE Trans. Geosci. Remote Sensing*, Vol. 31, No. 1, pp. 227-236, 1993.
- [6] E. M. Rignot, J. J. van Zyl, "Change Detection Techniques for ERS-1 SAR Data," *IEEE Trans. Geosci. Remote Sensing*, Vol. 31, No. 4, pp. 896-906, 1993.

Internal Waves Detection from ERS-1 SAR Images using the 2-D Wavelet Transform

J. A. Ródenas, D. Cabarrocas, R. Garello

Ecole Nationale Supérieure des Télécommunications de Bretagne, Dpt. ITI

Technopôle de Brest-Iroise, BP 832, 29285, Brest, Cedex, France

Tel: (+33) 2 98 00 10 60 ; Fax: (+33) 2 98 00 10 98

E-mail: {Josep.Rodenas, David.Cabarrocas, Rene.Garello}@enst-bretagne.fr

Abstract – In this paper, the utility of wavelet analysis as a tool for automatic oceanic internal wave detection from SAR ocean images will be examined using the 2-D wavelet transform. A method for coastline detection based on a sequence of basic-processing procedures followed by a contour tracing algorithm will be also introduced in order to have sea-land separation to enhance the internal wave detection problem. Then, the image will be wavelet transformed with various scales to finally extract the internal wave structures based on the first and second order statistics. The results from this study show that wavelet analysis is an excellent tool to detect and locate internal waves from SAR ocean images against background noise.

INTRODUCTION

Simultaneous satellite images, in-situ measurements from moorings and ship operations, and wind records from buoys and meteorological stations can be used to detect and monitor the ocean environment. By using repeated satellite coverage, the mesoscale features, such as internal waves, can be tracked through multitemporal satellite data analysis leading to an important data product: satellite derived maps for tracking mesoscale features in the coastal zone.

The extraction of mesoscale ocean feature information from satellite images usually results from human interpretation of the greytone patterns visible in the image. With the proliferation of oceanographic analyses that utilize satellite data, it becomes highly desirable for certain applications to move from labor-intensive manual interpretation of satellite images, toward a capability for automated interpretation of these images. Thus, this paper develops an automatic method for internal wave detection in which dark spots with a high probability of being an internal wave are automatically identified.

The automated analysis of satellite imagery has been formulated conceptually to consist mainly of three levels: image segmentation, feature labeling and synthesis, and oceanographic expert system. In our case, the algorithm will consist of two parts: (i) separation of sea-land and classification; and (ii) extraction and detection of the internal wave structures. The first problem in the detection system is to distinguish sea from land in a SAR image. One potential technique is presented here by using digital maps to locate islands and coastlines. This level involves image segmentation using con-

ventional image processing techniques. The second problem is to locate the significant internal wave structures using the relatively new tool for analyzing geophysical data, the *wavelet transform*. This transformation is inherently localized in both time and frequency, and as such is a valuable tool when analyzing nonstationary data, i.e. SAR images. The wavelet transform gives spectral decomposition via the scale concept. The 2-D wavelet transform is a highly efficient bandpass filter, which can be used to separate various scale processes and to show their relative phase/location information [1].

Our goal in this work will be to detect and locate internal wave signatures from SAR ocean images, including land detection to avoid false alarms from land features. An initial approach for internal wave detection from ERS-1 SAR images, using the 1-D wavelet transform, was introduced last year [2]. In that work, the detection of internal waves and wavelength estimation from SAR image profiles, using a new constructed wavelet based on a soliton analytical model, was presented. This paper tends to be the continuation of the problem of automatic detection and characterization of internal wave signatures from remote sensing images.

INTERNAL WAVES ON SAR IMAGES

Internal waves become visible on radar images because they are associated with variable surface currents which modify the surface roughness patterns via current-wave interaction. The radar is a surface sensor: the higher the roughness, the higher is the radar return and the brighter is the image in intensity [3]. Internal wave forms are associated with rough and smooth bands and show up bright and dark bands in the image (Fig. 1).

The Strait of Gibraltar connects the Atlantic Ocean with the Mediterranean Sea. The water body in the Strait of Gibraltar and its approaches consists of a lower layer of saltier Mediterranean water and an upper layer of less dense Atlantic water. The mean flow is composed of two counter-flowing layers: the surface layer flows eastwards towards the Mediterranean (Alboran Sea), and the lower layer westwards towards the Atlantic. This mean flow is modulated by (predominantly semidiurnal) tidal current and by wind and atmospheric pressure changes. Internal waves are primarily generated in the Strait by interaction on the tidal current with prominent underwater bottom features, primarily with the Camarinal Sill. Recently, surface

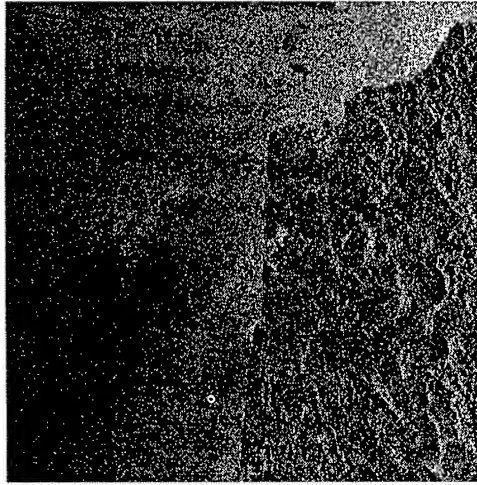


Figure 1: ERS-1 SAR image acquired on September 10, 1993, at 11:05 UTC at the Strait of Gibraltar. It shows an area of approximately 100 km x 100 km (composed of frame 2889 and orbit 11261, and centered at 36.50°N, 6.0°E).

roughness patterns associated with internal wave forms have been delineated on radar images acquired over the Strait of Gibraltar and the Alboran Sea by SAR aboard the European ERS-1 satellite [4].

SEA-LAND SEPARATION AND CLASSIFICATION

In order to detect and characterize internal waves from SAR ocean images, a first algorithm for land detection, to avoid false alarms from land features, should be developed. The lack of contrast between the ocean and nearby land area makes the ordinary edge detection methods inferior. Ocean areas in SAR images, however, are much more homogeneous in grey levels than land areas and features reflecting the "roughness" of an image can be very useful for sea-land separation. A coastline detector has been introduced by Lee and Jurkevich [5]. The

merit of this approach is its simplicity in the sense that it consists of a sequence of widely-used basic image-processing operations. Based on this consideration, a coastline detector using an appropriate selection of the threshold, used for land-sea segmentation, followed by contour tracing, and a refinement for contour precision, is proposed in Fig. 2. The main difference between the Lee *et al.* method and the one proposed here is the introduction of a majority filter and a binary image edge detector [6], instead of the classical Robert's edge detection filter, in order to enhance the precision of the detected contour. In the detection process, a *manual threshold* is estimated from the image histogram. A choice of $1.5 \cdot \sigma$, where σ is the standard deviation of the image, gave in general good results for most of the tested SAR ocean images.

Fig. 3(a) shows the detected coastline when overlaid on the original image. The refined coastline matches that of the original image to within a pixel or two. From here, a classification of the sea and land areas can be easily obtained (Fig. 3(b)).

INTERNAL WAVES FEATURE EXTRACTION

The 2-D wavelet transform is a relatively new technique for decomposition of an image with orthogonal (or non-orthogonal) basis functions and is becoming widely used in image detection. The use of orthonormal bases of compactly supported wavelets to represent a discrete signal in two dimensions yields a localized representation for coefficient energy [1]. The wavelet coefficients are a measure of the intensity of the local variations of the signal for the scale under concern. The value of a coefficient will be large when the dilation of the mother wavelet is close to the scale of the heterogeneity causing the signal to be irregular. On the contrary, the coefficients are negligible when the local signal is regular (smooth) for this particular scale. Hence the value of a coefficient for a particular location and at any scale can be understood as a characterization of the structures having this scale and present at this geophysical location.

Based on this principle, the proposed method to detect and extract the significant internal wave structures from SAR ocean images is the following:

First, we apply the 2-D wavelet transform on the speckleless original image using the Least Asymmetric Daubechies wavelet of order $N=4$ [7]. Normally a 4-level image decomposition contains most of the significant structures to be extracted. Then, we estimate the most significant wavelet sub-images from the study of the maximum and minimum energies in the decomposition. Only those subbands containing relevant energies will be considered for the reconstruction process. Since we know beforehand that the internal wave patterns are quasi-periodic signals whose dominant frequencies are located on the middle frequency channels, thus we apply two manual thresholds ($\min=1.0 \cdot \sigma$, and $\max=3.0 \cdot \sigma$) to the only considered subbands in order to keep the significant structures from the center of the wavelet sub-image histograms [8]. Very large pixel values are associated to noise and contours, and very low

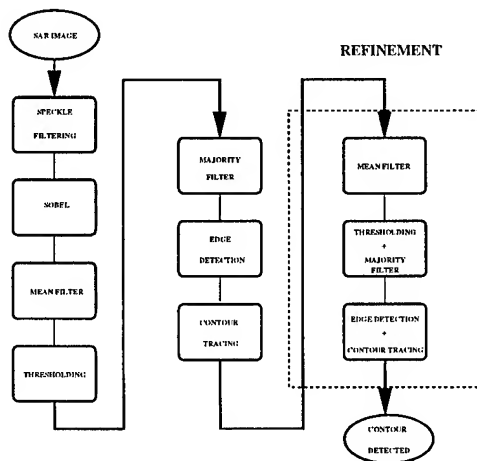


Figure 2: Schematic for sea-land separation and classification.

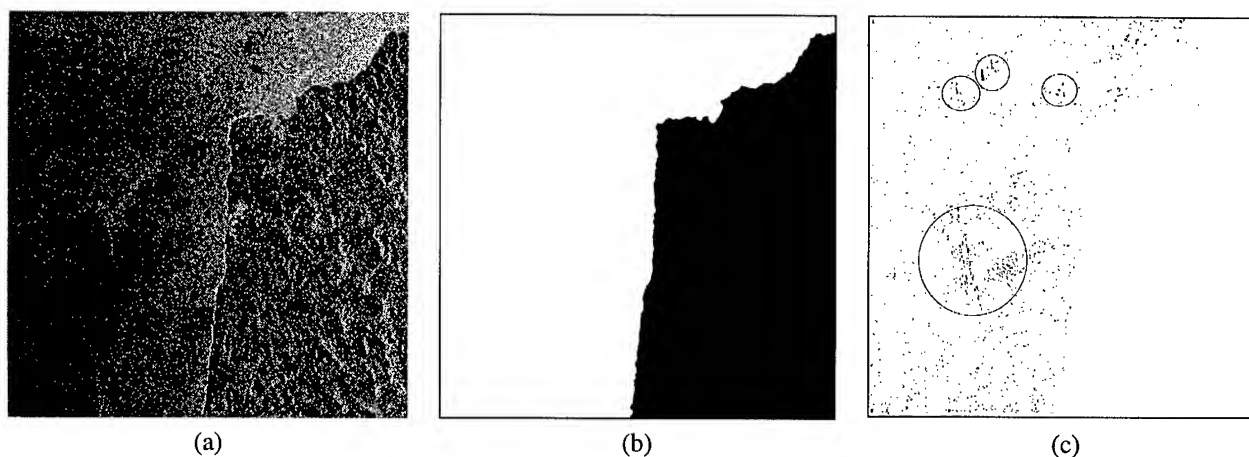


Figure 3: Internal wave feature detection. (a) Detected coastline overlaid on the original image. (b) Sea-land separation and classification. (c) Most significant extracted internal wave structures.

pixel values correspond to homogeneous regions. Thus, for the internal wave detection problem, we are only interested in the middle pixel values. At this step, we verify whether the considered pixel energy belongs to the sea class or not. If it belongs, then it is considered as a significant feature. If not, it is discarded. Finally, we reconstruct the considered energies using the 2-D inverse wavelet transform. A binary image is also obtained in order to reduce the data volume.

Fig. 3(c) shows the detected internal wave structures from the original ERS-1 SAR image using the proposed method. We can observe that internal wave patterns are quite well located against background noise. However, the signatures associated to the absence of backscattering due to bad SAR image formation, which appear as black areas in the SAR images, are also detected. Furthermore, this kind of noise is located on the same frequency channels that the internal wave structures. Thus, a way to enhance this detection could be to introduce a new class in the classification scheme which will allow to reject this kind of noise from the feature extraction scheme.

CONCLUSIONS AND FUTURE WORK

An efficient computational framework has been discussed for the extraction of mesoscale features present in SAR images. Selected coastlines coincide quite well with the true situation when overlaid on the original image. Direct thresholding techniques based on the mean and variance from the study of the wavelet coefficients give good results for the problem of internal wave signature extraction from SAR ocean images. Internal wave structures were quite well located against background noise by means of wavelet analysis methods.

Our future research directions will be to introduce a third part in the system, called internal wave characterization, which will include the determination of internal wave parameters such as: orientation, number of peaks in the packet, wavelengths, amplitudes, etc. The current work here serves as a motivation and explanation for the ongoing work on the understanding of internal waves from satellite data.

ACKNOWLEDGMENTS

The authors would like to thank Dr. W. Alpers, Hamburg University, Germany, for providing us with the ERS-1 SAR images. This work was supported by the MAST-III (MORSE) Programme of EC, under the contract MAS3-CT95-0027.

REFERENCES

- [1] Mallat S. G. A theory for multiresolution decomposition: The wavelet representation. *IEEE Trans. on Pattern Analysis and Machine Intelligence*, 11(7):675–681, 1989.
- [2] Rodenas J. A. and Garello R. Detection and location of internal waves in ocean sar images by means of wavelet decomposition analysis. In *Proceedings of IGARSS'96*, volume IV, pages 1953–1955, Lincoln, may 1996.
- [3] Alpers W. Theory of radar imaging of internal waves. *Nature*, 314:245–247, 1985.
- [4] Alpers W. and La Violette P. E. Tide-generated nonlinear internal wave packets in the strait of gibraltar observed by the synthetic aperture radar aboard the ers-1 satellite. In *Proc. First ERS-1 Symposium - Space at the Service of our Environment*, pages 753–758, 1992.
- [5] Lee J-S. and Jurkevich I. Coastline detection and tracing in sar images. *IEEE Trans. on Geoscience and Remote Sensing*, 28(4):662–668, 1990.
- [6] Schowengedt R. A. *Techniques for Image Processing and Classification in Remote Sensing*. New York: Academic Press, London, 1983.
- [7] Daubechies I. *Lectures on Wavelets*. Academic Press, New York, 1992.
- [8] Donoho D. L. and Johnstone I. M. Ideal spatial adaptation by wavelet shrinkage. Technical report, Stanford University, Dpt. of Statistics, Avril 1993.

Results of CAL/VAL and Preliminary Scientific Results of ADEOS

Haruhisa Shimoda

Earth Observation Research Center*

National Space Development Agency

1-9-9, Roppongi, Minato-ku, Tokyo, 106, Japan

TEL:+81-3-3224-7054, FAX:+81-3-3224-7051, e-mail:shimoda@eorc.nasda.go.jp

Abstract

ADEOS was successfully launched on August 1996. It carries 8 sensors on board to measure atmosphere, ocean and land of the Earth for better understanding of global change. The spacecraft and all the 8 sensors on board are functioning well and we can expect good scientific results from ADEOS. Initial calibrations of most of the sensors are finished and performances are the same or better than expected.

INTRODUCTION

ADEOS has been successfully launched from Tanegashima Space Center by H-II launcher on 17, August 1996. ADEOS carries 8 sensors on board, which measure geophysical parameters of atmosphere, ocean and land. The mission concept of ADEOS is to contribute to the better understanding of global change, especially global warming and stratospheric ozone depletion.

Spacecraft as well as on board sensors are functioning well, and excellent scientific results are expected. Here, status of ADEOS including mission instruments, results of CAL/VAL and preliminary scientific results are described.

BUS STATUS

ADEOS was put into planned orbit with smallest maneuvers. Other critical components such as solar paddles, batteries, attitude and orbit control system, mission data recorders etc. are functioning well and the spacecraft will remain operational more than 5 years.

As for the mission operation, there exists some restrictions caused by command capacity and power limitations. Commands of ADEOS are dealt by a on board computer(OBC) and the number of commands(macro command) allowed for single revolution is 100. This limitation sometimes cause a restriction of operation such as direct down link of AVNIR data. Other restriction come from the power restriction, and IMG and OCTS cannot be simultaneously operated in eclipse.

SENSOR STATUS AND CAL/VAL

AVNIR

AVNIR (Advanced Visible and Near Infrared Radiometer) is functioning well. Spatial resolution, radiometric performance, signal to noise ratio(S/N), etc. are all within the specification.

Slight problems still remain in the ground processing of

* Permanent address: Tokai University Research & Information Center

2-28-4, Tomigaya, Shibuya-ku, Tokyo, 151, Japan

TEL:+81-3-3481-0611, FAX:+81-3-3481-0610, e-mail:smd@keyaki.cc.u-tokai.ac.jp

AVNIR. One problem is the existence of striping noise in ocean images of panchromatic mode. This phenomena is caused by the sensitivity difference between proto-flight test and in space. This problem will be fixed soon after examining detector sensitivities.

Another problem is caused by the same reason. AVNIR has another detectors called navigation band to measure slight attitude variation. The correlation calculation between main detectors and navigation detectors is not so good because of the striping noise. This problem will also be fixed soon.

The radiometric calibration of AVNIR will be done using mainly under flight data of AVIRIS on board NASA ER-2 over California desert. The first flight and second flight was done on November, 1996 and February 1997. Results from these data will be presented in the symposium. Similar under flight experiments will be conducted twice a year.

OCTS

OCTS(Ocean Color and Temperature Scanner) also functions well although several problems have occurred. Two anomalies were detected after launch. One is an anomaly of tilting mirror. OCTS is equipped with a tilting mirror to avoid sun glitter. Electric oscillation has occurred at the limit switch. This phenomena has been stopped by changing the tilting angle from $\pm 20^\circ \pm 19^\circ$.

Another anomaly was the degradation of sensitivity of thermal infrared detectors. In order to recover the sensitivity, baking operations were applied in February, and the sensitivities was recovered to the initial state. However, detector sensitivities has started degradation again, and some periodical baking operations may be needed.

The radiometric calibration of OCTS in visible and near infrared channels are conducted by vicarious calibrations. Two methods are mainly used. One is similar to that of AVNIR, i.e., utilizing AVIRIS under flight. Another method

is measurements on the sea surface.

IMG

IMG(Interferometric Monitor for Greenhouse Gases) has experienced several anomalies. First anomaly was found at the time of initial operation. IMG is a Michelson Fourier interferometer and the moving mirror is suspended by a magnetic bearing. At the first time, this moving mirror could not be floated. This was caused by lower surrounding temperature compared to expected before launch. This anomaly was corrected by raising surrounding temperature.

Another problem is degradation of interferometric efficiency. IMG employs a dynamic alignment system of moving mirror alignment using phase lock loop(PLL) with laser phase differences. Sometimes this PLL slips and the output of IMG decreases. This phenomena was mainly caused by estimation error of cyclic transfer function of magnetic suspension under 0 G environment. This problem will be mostly solved by inserting auto alignment operation every day.

ILAS

ILAS(Improved Limb Atmospheric Sounder) functions well. The only anomaly is related to the sun edge sensor, which causes a difficulty in the estimates of tangential heights. The reason is rather complex, but the actual impact will not so large after the modification of ground processing algorithm for sun edge sensor.

RIS

RIS(Retroreflector In Space) is a large aperture corner mirror and will be used long distance absorption measurements using ground based lasers. There is no problem for the mirror. The first infrared spectrum was measured in January with a rather large noises. The S/N will be improved after the modification of the ground laser system.

NACAT

NSCAT(NASA Scatterometer) is functioning very well. Initial calibrations was finished and also initial validation was almost finished.

TOMS

TOMS(Total Ozone Mapping Spectrometer) is also functioning very well. The calibration and validation will be finished soon.

POLDER

POLDER(Polarization and Directionality of Earth's Reflectance) is functioning well. However, the calibration process is rather slow and the initial calibration will be finished on October.

PRELIMINARY SCIENTIFIC RESULTS

Ozone

Antarctic ozone holes in 1996 were measured by ADEOS sensors, i.e. TOMS, ILAS and IMG. Although detailed discussions using all 3 sensors have not yet been done, it is very hopeful that these sensor suite will give us 3 dimensional understanding of ozone depletion.

The ozone depletion in Arctic areas in 1997 spring is also a very interesting phenomena, and we expect a good study of this new phenomena using ADEOS sensors.

Ocean Color and Temperature

The global ocean color and temperature data sets are now being regularly generated weekly and monthly basis from OCTS. This regular data set generation will bring us new insight of ocean biological phenomena.

Aerosols

A global aerosol map from OCTS was generated by T.Nakajima from CCSR(Center for Climate System Research) of University of Tokyo. OCTS measures the upwelling radiance from the ocean, but 90% of the radiance measured at spacecraft comes from the atmosphere.

The obtained optical thickness and angstrom exponent of global aerosol show far better results compared to NOAA operational aerosol maps. These data will be very useful for the better understanding of global warming.

Sea Surface Winds

Sea surface winds data from NSCAT are tested for inputs to the numerical weather prediction models, and the results show these data will improve the accuracy of weather prediction.

Another advantage of NSCAT wind vector is its higher ground resolution with the same accuracy than expected(25km to 50km). This higher spatial resolution will give us a detailed surface wind understanding.

Sea Ice

An unexpected results from NSCAT is back scattering coefficient from land surface give us information of land. Especially, it has been proved that NSACT is very useful for monitoring sea ice and may be also useful for snow.

Until now, sea ice concentration measurements over Arctic and Antarctic were done using microwave radiometer like SSM/I on DMSP. However, sea ice images derived from NSCAT data show far better spatial resolution than microwave radiometer. Sea ice monitoring using NSCAT will come to one of the largest contribution to global change monitoring.

OCTS (Ocean Color and Temperature Scanner)

Hiroshi Kawamura^{*,+}, Masanobu Shimada^{*}, Hisashi Nakamura^{*}, Hiromi Oaku^{*}, Yasushi Mitomi^{*}
and Akira Mukaida^{*}

^{*}OCTS team, Earth Observation Research Center/NASDA,
Roppongi First Building, 1-9-9, Roppongi, Minato-ku, Tokyo 106, Japan
Tel: +81-3-3224-7040/Fax: +81-3-3224-7051

⁺Center for Atmospheric and Oceanic Studies, Faculty of Science, Tohoku University, Sendai, 980 Japan
Tel: +81-22-217-6745/Fax: +81-22-217-6748/kamu@caos-o.geophys.tohoku.ac.jp

Abstract--Ocean Color and Temperature Scanner(OCTS) is a visible and infrared radiometer devoted to frequent global measurement of Chlorophyll-a (Chl-a) and sea surface temperature. After a long break of the global ocean-color observation, OCTS reopened it since November, 1996. Initial check of the sensor and preliminary results of cal/val have demonstrated availability of the OCTS data for global ocean color research.

INTRODUCTION

CZCS(Coastal Zone Color Scanner) onboard the Nimbus-7 satellite were operated from 1978 to 1986. It has been the main source of ocean color data for a long time, and contributed in understanding the marine environment and its biological, biochemical and physical processes in the ocean[1]. CZCS had four visible, one near IR, and one thermal infrared bands. CZCS is the first-generation ocean color sensor, and its successor, one of the second-generation global ocean color sensors, is OCTS onboard the ADEOS(Advanced Earth Observing Satellite). The ADEOS was launched on 17 August, 1996, and the OCTS started the continuous global observation from November, 1996.

The OCTS main targets are 1)Chl-a, 2)Sea Surface Temperature(SST) in the global ocean, and 3)Vegetation index on the grounds. Because of the unique characteristics of the ADEOS mission, OCTS may contribute to the progress of oceanography.

OCTS INSTRUMENTS

OCTS has eight visible and near-infrared channels and four thermal infrared channels, and achieves highly sensitive spectral measurement with these channels. The detail of the OCTS bands are listed in Table 1. The sensor swath is about 1400km(± 40 degrees), which covers the earth surface within 3 days. Its spatial resolution is 700m at the surface. An example of the OCTS global coverage in a day and the operation gains for ocean and land are shown in Fig.1.

OCTS has Course Data Transmission(DTL) system at UHF band for quick delivery of 4 bands (443 nm, 565 nm, 665 nm, 11.0 μ m) with 6 x 6-km spatial resolution.

Table 1. Spectral Characteristics of OCTS

Band (μ m)	Radiance (W/m ² /sr/ μ m)	S/N
0.402-0.422	145	450
0.433-0.453	150	500
0.480-0.500	130	500
0.510-0.530	120	500
0.555-0.575	90	500
0.655-0.675	60	500
0.745-0.785	40	500
0.845-0.885	20	450

Band (μ m)	NEDT Target Temperature @300K
3.55-3.88	0.15K
8.25-8.80	0.15K
10.3-11.4	0.15K
11.4-12.5	0.20K

Initial check of the OCTS sensor had been carried out from

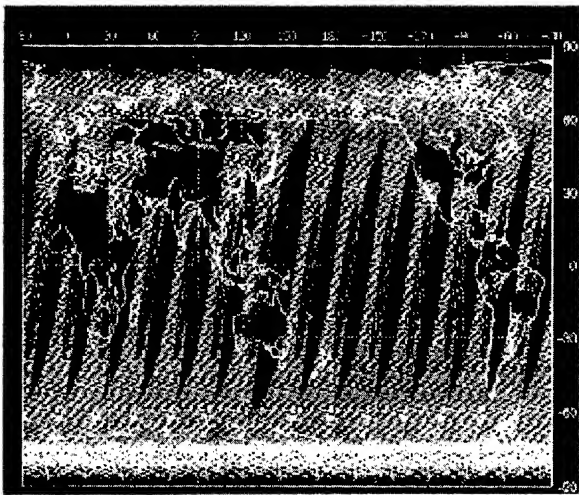


Figure 1 OCTS coverage on 25 February, 1997. Blue swath shows regions of ocean-high gain, yellow ocean-normal gain and red land gain.

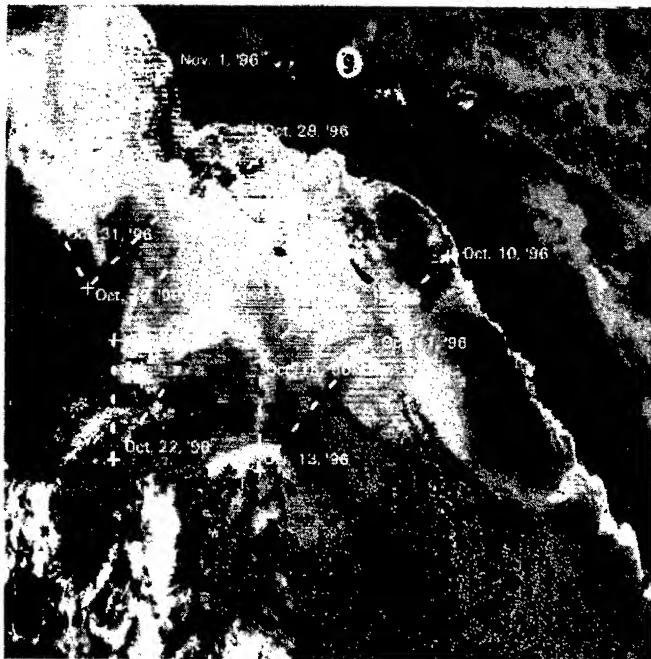


Figure 2 OCTS Chl-a image off California on 1 November, 1996. Tracks of the Chl-a observation cruise are superimposed.

September to November, 1996, and it is proved that the OCTS instrument is almost performing at or beyond engineering specifications.

ALGORITHM

In order to retrieve the ocean color information from the OCTS observations, atmospheric correction and in-water algorithms are required. "CZCS-type" atmospheric correction algorithm modified by Fukushima and Toratani[2] had been applied to process the OCTS data from November, 1996 to March, 1997. "OCTS-type" algorithm, which is based on the SeaWiFS algorithm[3] and modified by Fukushima, Nakajima and Toratani, is used since April, 1997. In-water algorithm is based on empirical relationships between the ratio of three-bands of water leaving radiance and water properties including, pigment concentration, chlorophyll concentration, and diffusion coefficient[4]. Split window algorithm is used for the sea surface temperature.

Through a vicarious calibration using data from the optical buoys, the OCTS algorithms are tuned preliminarily. The validation of the estimated Chl-a is made using the in situ observation data obtained off California by G.Mitchell. Fig.2 shows the image of the estimated Chl-a image, where the track of the observation cruise are superimposed. The observed Chl-a values from 10 October to 1 November are presented in Fig.3. Corresponding values estimated from the OCTS data through the new algorithm and vicarious calibration are shown in Fig.4. Both agree quite well except for several points near the coast.

The algorithms are now examined in detail, and will be fixed in September, 1997. Vicarious calibration of the sensor with data from ship, buoy[5],[6], and airplane is ongoing. The Chl-a data are intensively collected in the oceans around Japan for validation of the OCTS products.

CONCLUDING REMARKS

Standard products are distributed to PIs from NASDA, but they are not validated. Intensive LAC project, which started in December, 1996, is a new scheme to distribute the daily images of OCTS Chl-a and SST with the highest spatial resolution through the internet. Anybody can obtain the

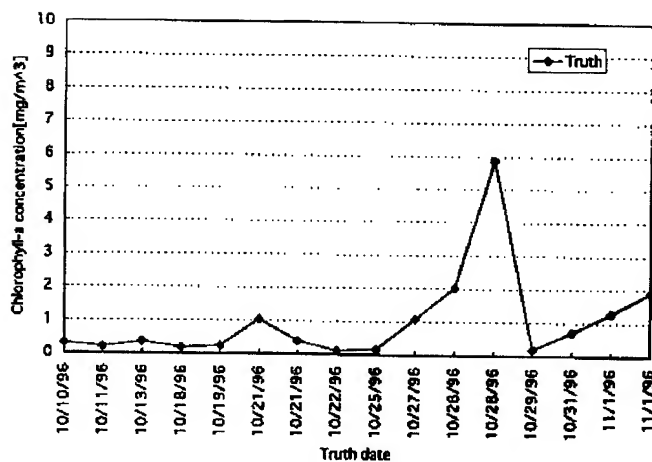


Figure 3 The in situ Chl-a obtained in the ocean off California in October – November, 1996.

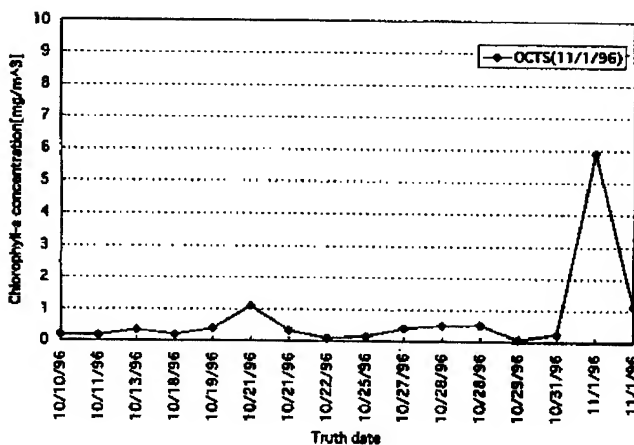


Figure 4 The estimated Chl-a from the OCTS data obtained on 1 November, 1996.

OCTS images in the oceans around Japan from [www.HomePage of EORC \(Earth Observation Research Center\) of NASDA](http://www.eorc.nasda.go.jp) (<http://www.eorc.nasda.go.jp>). Further information of the OCTS/ADEOS is available through [NASDA EOC HomePage](http://www.eoc.nasda.go.jp) (<http://www.eoc.nasda.go.jp>) and [NASDA EORC HomePage](http://www.eorc.nasda.go.jp).

REFERENCE

- [1] V. Barale and P. M. Schlittenhardt, eds. (1993): Ocean colour: Theory and applications in a decade of CZCS experience, Kluwer Academic Pub., 367pp.
- [2] H. Fukushima and M. Toratani (1997): Asian dust aerosol: Optical effect on satellite ocean color signal", *Journal of Geophysical Research*, In press.
- [3] H. R. Gordon and M. Wang (1996) "Retrieval of water-leaving radiance and aerosol optical thickness over the oceans with SeaWiFS: a preliminary algorithm, *Applied Optics*, 33, 443-452, 1997.
- [4] M. Kishino, M., T. Ishimaru, K. Furuya, T. Oishi, and K. Kawasaki (1995): Development of Underwater Algorithm (in Japanese), Institute of Physical and Chemical Research (Riken). Wako, Saitama, 90pp, 1995.
- [5] J. Ishizaka, I. Asanuma, N. Ebuchi, H. Fukushima, H. Kawamura, K. Kawasaki, M. Kishino, M. Kubota, H. Masuko, S. Matsumura, S. Saitoh, Y. Senga, M. Shimanuki, N. Tomii and M. Utashima (1997): Time series of physical and biological parameters off Shimane, Japan, during fall of 1993: First observation by moored optical buoy system for ADEOS data verification", *Journal of Oceanography*, In press.
- [6] M. Kishino, J. Ishizaka, S. Saitoh, Y. Senga and M. Utashima (1997): Verification plan of OCTS atmospheric correction and phytoplankton pigment by moored optical buoy system", *Journal of Geophysical Research*, In press.

Atmospheric trace species measurements by ILAS and RIS

Yasuhiro Sasano and Nobuo Sugimoto
National Institute for Environmental Studies
Tsukuba, Ibaraki 305 Japan
Tel: +81-298-50-2444/Fax: +81-298-50-2569
E-mail: sasano@nies.go.jp

Abstract--The Improved Limb Atmospheric Spectrometer (ILAS) launched on board the Advanced Earth Observing Satellite (ADEOS) in August 1996 has been normally working and acquiring data with the solar occultation method for the stratospheric ozone layer in the northern and southern high latitude regions. The data from ILAS is processed to derive profiles of ozone and other gas species as well as profiles of temperature and aerosol information, archived at ILAS & RIS Data Handling Facility (ILAS & RIS DHF) at National Institute for Environmental Studies (NIES), and distributed to science communities.

The Retroreflector in Space (RIS) on board the ADEOS is a corner cube mirror with an effective diameter of about 50 cm, which is used for earth-satellite long path laser absorption measurements of atmospheric gas species concentration.

Brief introduction of the ILAS and RIS and some preliminary results of the measurements are presented.

INTRODUCTION

The Improved Limb Atmospheric Spectrometer (ILAS) instrument [1] for monitoring physical and chemical behavior of the stratospheric ozone layer from space was developed by Environment Agency (EA) of Japan and installed on board the Advanced Earth Observing Satellite (ADEOS). The Retroreflector in Space (RIS), another instrument developed by EA for the ADEOS, is a corner-cube retroreflector, which is used for earth-satellite long path laser absorption measurements of atmospheric gas species concentration [2].

The ADEOS was launched on August 17, 1996 from Tanegashima Space Center by National Space Development Agency of Japan (NASDA), and was renamed as "Midori". ILAS initial checkouts were carried out intermittently from September 17 to the beginning of November 1996. Through the initial checkouts, the instrument was found to work as expected. The RIS experiments using a laser transmitter/receiver station in Tokyo started just after the launch of the ADEOS and initial tunings of the ground laser transmitter and receiving system have been made since then.

Routine operation of the ADEOS satellite and the ground segments at NASDA were announced to start on November 26, 1996. The ILAS & RIS Data Handling Facility (ILAS & RIS DHF) at National Institute for Environmental Studies (NIES) also began routine operation on the same day.

ILAS

Measurement principle and instrument [3]

The principle of ILAS measurements is based on the solar occultation technique, which has been used for SAGE, SAGE-II, and HALOE sensors on board the U. S. satellites and proved quite effective and stable for measurements of the stratospheric trace species. The ILAS instrument has an infrared (IR) and a visible spectrometer. Main targets of the ILAS measurements using the IR channel data are vertical profiles of ozone (O_3) and ozone-related species such as nitric acid (HNO_3), nitrogen dioxide (NO_2), nitrous oxide (N_2O), methane (CH_4), and water vapor (H_2O). Other minor gases such as N_2O_5 , CFC11 and CFC12 will be also tried to derive. Profiles of aerosol extinction coefficients at some IR wavelengths are also derived. From the visible channel data that gives absorption spectra due to oxygen molecules, temperature and pressure profiles are obtained. Aerosol extinction profile is also derived from the visible channel signal in the wavelength range of no absorption due to oxygen molecules.

The altitude range for data analysis is from the cloud-top to about 60 km, depending on retrieved parameters, and the instantaneous field of view has a 2 km height resolution. Since the solar occultation technique is employed as the measurement principle and the ADEOS satellite has a sun-synchronous polar orbit (the inclination angle is 98 degrees and the altitude is about 800 km), the measurement region of the ILAS is over high latitude regions (58-73 N and 65-90 S), which changes according to the season. The ILAS gives quite unique measurement opportunities, which generate daily height-longitude cross sectional maps of the atmospheric parameters.

The ILAS instrument [4,5] consists of the following

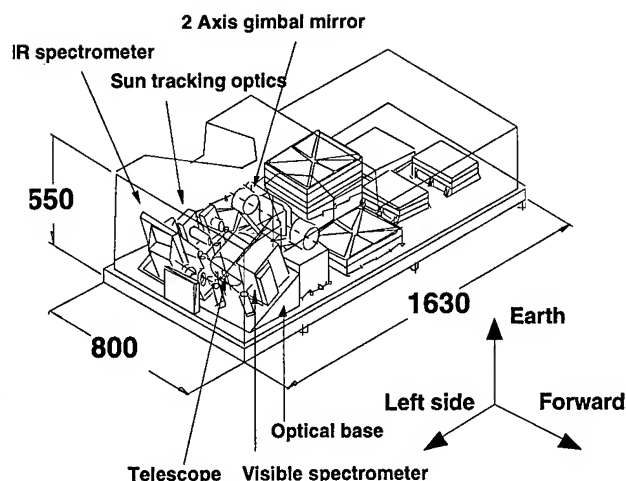


Fig. 1 Overview of the ILAS instrument

seven major components: (i) a mirror with 2-axis gimbals that is controlled to track a radiometric center of the sun, (ii) a 12 cm diameter Cassegrain telescope, (iii) a beam splitter and transfer optics, (iv) an IR spectrometer, (v) a visible spectrometer, (vi) a sun-edge sensor, and (vii) signal processing units. Fig. 1 shows the overview of the ILAS instrument. The sun light passes through two cutaways; one is for sunrise direction and the other is for sunset direction. A plane mirror mounted on the 2-axis gimbals reflects the sun light into the 12 cm telescope mounted on the slanted optical base. The light passes through the rectangular slit at the primary focal point, and is then split using the dichroic mirror and transfer optics into the IR and visible spectrometers. Table 1 summarizes the characteristics of the ILAS hardware.

ILAS Data Processing

The raw data that the ILAS instrument generates in orbit are outputs from the visible and IR spectrometers and from the sun-edge sensor, which are converted to 11 bit digital signals. This data, with additional ephemeris data such as time and satellite position, is called "Level 0" data and is transferred from NASDA Earth Observation Center (NASDA/EOC) to the ILAS & RIS DHF for further processing. "Level 1" data are generated from Level 0 data, by extracting data for effective measurements, screening and correcting outlier and missing data, and converting the data to transmittance by dividing them by the exoatmospheric signal.

Algorithms [6] for data retrieval from Level 1 to "Level 2" have been developed to generate vertical profiles of target species by the ILAS project staff scientists with help of the

Table 1 ILAS hardware characteristics

Grating Spectrometers with Linear Array Detectors	
IR detector	44-pixel pyro-electric detector
Visible detector	1024-pixel MOS photo-diode array
Spectral Coverage / Resolution	
IR	850 - 1610 cm^{-1} (6.21 - 11.77 μm)
	0.129 μm resolution
Visible	753 - 784 nm
	0.15 nm resolution
IFOV	
2 km Vertical x 13 km Horizontal in the IR channel	
2 km Vertical x 2 km Horizontal in the visible channel	
Positioning	
Track radiometric center of the sun from 0 to 200 km	
IFOV position measurement from the top edge of the sun	
with a resolution of 8 arc seconds by 1024-pixel linear array detector	
Data Rate	12 Hz, 517 kbps
Weight	130 kg
Power	78 W (maximum)
Size	800 x 1630 x 550 (XYZ in mm)

ILAS Science Team members. The basic concept is the non-linear least square (NLSQ) fit of theoretically synthesized signal to the observed signal (forward method). Vertical profiling is done by the onion peeling procedure.

Aerosol and PSCs information can be retrieved from extinction coefficient profiles from "aerosol window" channels signal in the IR region and in the visible region. The extinction coefficients at a finite number of wavelength are used for characterizing aerosol/PSCs types and size distribution parameters. These are used for estimating aerosol/PSCs effects for the whole wavelength range of the IR transmission spectrum.

Level 0' data are generated from the raw data directly acquired at NASDA/EOC, and transmitted to ILAS & RIS DHF on a semi-real time basis. The Level 0' data differ from the Level 0 data in that the Level 0' data include predicted satellite position data while the Level 0 data contain satellite position data which were determined using tracking data. Level 0' data are processed to Level 2' products for quick-look purposes.

ILAS validation experiments

Validation experiments have already started [7]. The first validation data from ozonesondes were gathered at Syowa station in the Antarctic last November. Since then, various

validation experiments were conducted by the ILAS project and by cooperative researchers. A balloon campaign at Kiruna, Sweden, was conducted in cooperation between EA and CNES, in which a lot of scientists participated from several countries by bringing their own instruments for balloon flights.

Validation analysis is being carried out by the experiment data providers as well as by the ILAS Science Team members. Revision of data processing algorithms and software is also being made.

Preliminary results from ILAS measurements

Fig. 2 shows some ozone profiles obtained along a latitude circle of 70 S on November 17, 1996, when an ozone hole was still existing. Some profiles were for inside of the ozone hole and some are for outside, the difference of which can be interpreted from the location difference relative to the polar vortex (ozone hole).

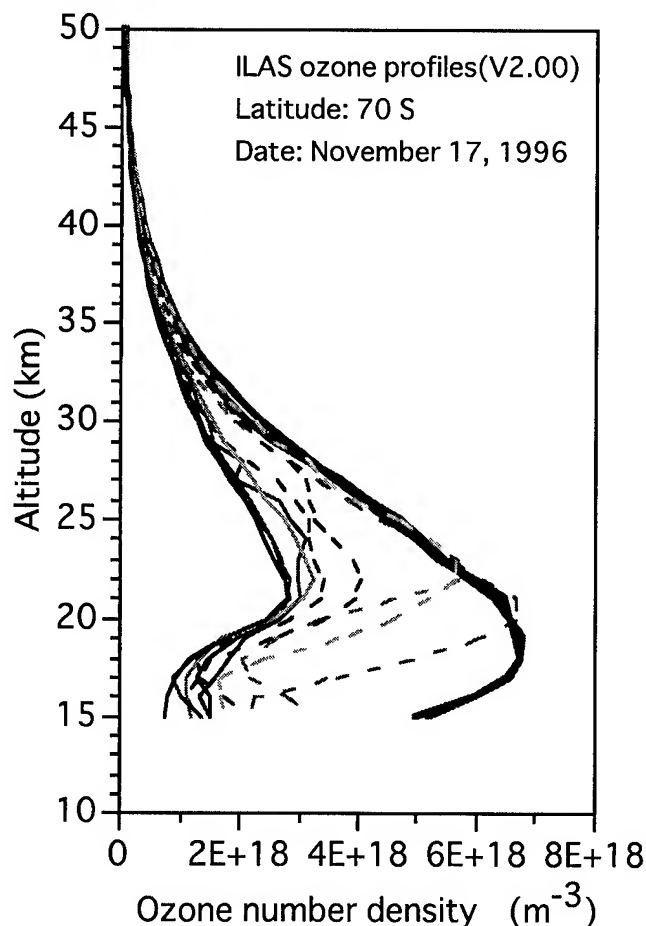


Fig. 2 Ozone profiles along a latitude circle of 70 S, obtained on November 17, 1996. Bold and thin curves (solid) represent profiles outside and inside the ozone hole, respectively. Dashed curves are for a transient region.

RIS

Principle of RIS measurements

The RIS is a single element cube-corner retroreflector for earth-satellite-earth laser long-path absorption measurements of atmospheric trace species. The RIS has a hollow structure with an effective diameter of 0.5 m. A spherical mirror with a very small curvature is used for one of the three mirrors forming the corner cube, to optimize the ground pattern of the beam reflected by the RIS on the ADEOS, which moves with a velocity of approximately 7 km/s. In the RIS experiments a laser beam is transmitted from a ground station, reflected by the RIS, and received back at the ground station. The absorption of the intervening atmosphere is measured in the round-trip optical path. The column contents and vertical profiles of atmospheric trace species are obtained from the measured spectra. The RIS experiment is performed when the ADEOS passes over one of the ground tracks within 1000 km from the ground station. The satellite overpasses the measurement region approximately once a day on alternately ascending (nighttime) and descending (daytime) orbital paths. One measurement lasts approximately 200 seconds each time.

Ground station

The ground system at the Communications Research Laboratory located in Koganei-city, Tokyo consists of an optical satellite tracking system and a laser transmitter and receiver system for spectroscopic measurements. An active satellite tracking method using the image of the RIS lit by a second-harmonics (SH) of Nd:YAG laser at 532 nm is used simultaneously with the programmed tracking method to achieve the tracking accuracy requirement for the experiments. Two single-longitudinal-mode TEA-CO₂ lasers are used for the spectroscopic measurements. One of the TEA laser is used to measure absorption of atmospheric trace gases, and the other is used to record a reference signal. The method using the Doppler shift of reflected beam caused by the satellite movement is used in the RIS experiment to measure spectrum of the atmosphere.

Preliminary results of RIS experiment

After the launch of the ADEOS, efficiency of the reflection of RIS was tested with a SH Nd:YAG laser, and it was confirmed that the efficiency was close to the theoretical value. Active tracking of the RIS was established with an ICCD camera in a Coude system. An accuracy of

approximately 30 μrad has been achieved.

Experiment on the spectrum measurement was started in December 1996. Fig. 3 shows the first spectrum taken with the Doppler shift method. The two TEA CO_2 lasers are tuned to 10R(24) line of $^{13}\text{CO}_2$ and 9P(24) line of $^{12}\text{CO}_2$, respectively. The vertical axis of Fig. 3 indicates logarithm of the ratio of the signal intensity for the primary laser to that for the reference laser. The horizontal axis indicates time that corresponds to wavelength of the return light. The absorption feature seen in Fig. 3 is that of ozone. The lower panel shows a theoretically simulated spectrum generated with the HITRAN line absorption database. The measured spectrum agreed with the simulation; however the error in the measurement was larger than expected. It was found that the dominant cause of the error was the difference between the beam patterns of the two TEA CO_2 lasers. On the basis

of the error analysis, we improved the transmitter optics using a spatial filter which consists of lenses and a pinhole. The accuracy of the spectrum measurement has been improved approximately 5 times. We are continuing experiments with the improved transmitter system.

ACKNOWLEDGMENTS

The authors wish to express their sincere thanks to all the people involved in the ILAS and RIS projects of EA and NASDA/ADEOS projects.

REFERENCES

- [1] Y. Sasano, Y., M. Suzuki, T. Yokota, H. Kanzawa, "Improved limb atmospheric spectrometer (ILAS) project: ILAS instrument, performance and validation plan," SPIE, Vol. 2583, 1995, pp. 193-204.
- [2] N. Sugimoto and A. Minato, "Data Reduction Method for the Laser Long-Path Absorption Measurement of Atmospheric Trace Species Using the Retroreflector in Space," IEICE Trans. Commun. E78-B, 1995, pp. 1585-1590.
- [3] ILAS Project, "ILAS User's Handbook", edited by Y. Sasano, 1997 [Available from the authors at National Institute for Environmental Studies].
- [4] M. Suzuki, Y. Sasano, T. Ishigaki, N. Kimura, N. Araki, A. Matsuzaki, "Improved Limb Atmospheric Spectrometer, ILAS," SPIE Vol. 2268, 1994, pp. 103-110.
- [5] M. Suzuki, A. Matsuzaki, T. Ishigaki, N. Kimura, N. Araki, T. Yokota, Y. Sasano, "ILAS, the Improved Limb Atmospheric Spectrometer, on the Advanced Earth Observing Satellite," IEICE TRANS. Commun., E78-B, 1995, pp. 1560-1570.
- [6] T. Yokota, "ILAS: Monitoring of high-latitude ozone layer: Part 2 Data Retrieval Algorithm, Ozone Layer Observation by Satellite Sensors," Proc. of Int. Workshop Global Environ. Earth Obs. Satellite Sensors, Tokyo, 8-9 December 1993, edited by Y. Sasano and T. Yokota, 1994, pp. 52-53 [Available from the authors at National Institute for Environmental Studies].
- [7] H. Kanzawa, Y. Kondo, C. Camy-Peyret, Y. Sasano, "Balloon campaigns at Kiruna-Esrange planned in ILAS Correlative Measurements Program," Proc. 12th ESA Symp. European Rocket and Balloon Programmes and Related Research (Lillehammer, 29 May - 1 June 1995), ESA SP-370, 1995, pp. 345-349.

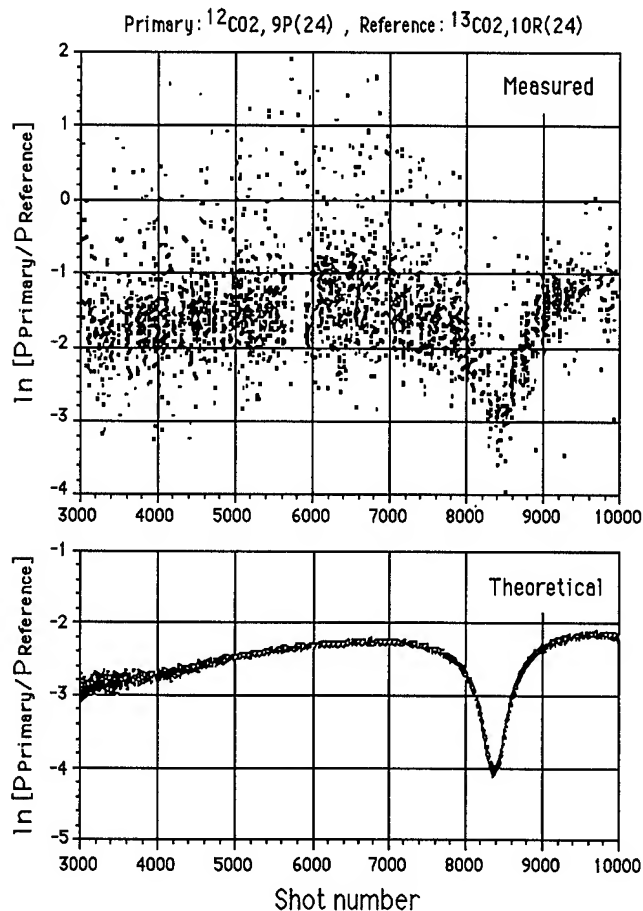


Fig. 3 The first spectrum measured with the RIS (upper), and simulated spectrum (lower) for ozone

Studies of Atmospheric and Oceanic Phenomena with the NASA Scatterometer

W. Timothy Liu

Jet Propulsion Laboratory 300-323

California Institute of Technology

Pasadena, CA 91109, U.S.A.

(Tel: 1-818-354-2394; Fax: 1-818-393-6720; email: liu@pacific.jpl.nasa.gov)

INTRODUCTION

The ocean and the atmosphere are coupled by the transport of momentum which is governed by the wind shear, but measurements of wind are sparse over most of the ocean. The ocean and the atmosphere are turbulent fluids with non-linear interaction; processes at one scale affect processes at other scales. Spaceborne sensors are the only potential means of measurement at adequate temporal and spatial scales.

A few decades ago, marine radar operators encountered noise on their radar screens which obscured small boats and low-flying aircraft. They termed the noise "sea clutter". This clutter was the backscatter (reflection) of the radar pulses by the rippling waves on the ocean's surface. The idea of remote sensing of ocean surface winds was based on the belief that these surface ripples are in equilibrium with the local winds. The microwave scatterometer sends microwave to the ocean surface and measures the backscatter from which ocean surface wind speed and direction are derived.

The ocean surface is largely covered by clouds, but the atmosphere and its cloud are almost transparent to microwave and the scatterometer can measure wind under both clear and cloudy conditions. While the radiometer, a passive sensor, can measure wind speed, the scatterometer, an active sensor, has the proven capability of measuring both wind speed and direction at the broadest range of conditions.

NASA SCATTEROMETER

The National Aeronautics and Space Administration (NASA) Scatterometer (NSCAT) was successfully launched into a near-polar, sun-synchronous orbit on the Japanese Advanced Earth Observing Satellite (ADEOS) in August 1996 from Tanegashima Space Center in Japan. The six antennas of NSCAT send microwave pulses at a frequency of 14 GHz to the Earth's surface and measure the backscatter. The antennas scan two 600-km bands of the ocean which are separated by a 330-km data gap. From NSCAT observations, surface wind vectors can be derived at 25-km spatial resolution, covering 77% of the ice-free ocean in one day and 97% of the ocean in two days.

TYPHOON AND EXTRATROPICAL TRANSITION

During its first few days of the ocean observing mode, starting 15 September 1996, NSCAT monitored the evolution of the twin typhoons Violet and Tom in the western North Pacific. They moved north from the tropical ocean where they were born, acquiring the features of mid-latitude storms, with developing frontal structures, increasing asymmetry, and introduction of dry air into the core of the typhoons. While Violet hit Japan, causing destruction and death, Tom merged with a mid-latitude trough and evolved into a large extratropical storm with gale-force winds [1].

By superposing NSCAT wind field on the maps of integrated water vapor from the Special Sensor Microwave / Imager (SSM/I), Tom can be distinguished from the extratropical cyclones by the high water vapor (and diabatic heating generated by latent heat release) concentrated in the core, from 15th to 17th of September. During this period, NSCAT also observed vigorous cyclogenesis at 35°N, north of Tom. These activities were missed largely by the numerical weather forecasts of the National Oceanic and Atmospheric Administration because of their coarse resolution. The spacebased data show much less water vapor in these extratropical cyclones compared with Tom, with higher value in the warm sector between the fronts, but not at the core. Tom speeded up on the 18th and moved toward the northeast. On September 19, it moved into the trough at 35°N. It lost much of the water vapor during this process, but still kept unusually high water vapor at the frontal location, compared with previous extratropical cyclones. This high water vapor was clearly observed by SSM/I in the next few days as the system resulting from Tom moved east. NSCAT data also indicate strong winds above 25 m/s for this extratropical system that resulted from Tom.

We understand relatively little of the extratropical transition of tropical cyclones because of the complex thermodynamics involved. Since the transition usually occurs over the ocean, there has been very little measurements of it. Yet the mid-latitude storms resulting from tropical cyclones usually have strong winds and heavy precipitation. The transition is a fascinating science problem, but it also

has important economic consequences. The transition occurs over the busiest trans-ocean shipping lane, and when the resulting storms hit land, they usually cause devastation to populated areas. Spaceborne microwave scatterometer and radiometer help to reveal the large amount of energy carried over from the tropical cyclone to the extratropical regions.

MONSOON

Monsoons are the seasonal changes of winds forced by continent-ocean temperature contrast. Their onset, intensity, and retreat vary greatly, and the variation has strong economic impact and may cause severe human suffering. Over land the consequences of monsoon are, perhaps, well observed, but the breeding ground over the ocean has been insufficiently monitored, and scatterometer has the potential of making a contribution. The Asian monsoon has a strong influence over a large portion of the world's population, yet it is much less studied and understood than the Indian Monsoon [2].

The annual variation of monsoons at two locations on 19°N, one in the Bay of Bengal at 90E and the other in the South China Sea at 115°N are examined. Time series, starting 1992, of wind speed and direction from NSCAT and ERS-1 scatterometer are plotted with the precipitable water from SSM/I and sea surface temperature derived by blending observations of the Advanced Very High Resolution Radiometer (AVHRR) with in situ measurements. In the Bay of Bengal, the wind direction changes gradually from northerly during winter to southwesterly in summer, with moistening of the atmosphere and warming of the ocean. The strength of the wind increases dramatically in June, signifying the onset of summer monsoon, with sharp increase in precipitable water but slight cooling of the ocean. There is a relative quick reversal of direction in September and drop in strength, but only gradual drying and cooling of the ocean. In the South China Sea, there is a much clearer and more dramatic onset of the winter monsoon in late September or early October, with large increase in wind speed, decrease in precipitable water and sea surface temperature. The wind direction changes sharply from south / southwesterly to northeasterly. The onset of summer monsoon appears to be more gradual, over a period February to April. In the South China Sea, the winter monsoon is much steadier than the summer monsoon; in summer the monsoon is often interrupted by storms.

EQUATORIAL KELVIN WAVES

The main advocacy of the scatterometer used to come from the oceanographers who want to study wind-driven ocean

circulation. One of the most interesting areas to study wind-driven ocean circulation is the equatorial waveguide, where the wind effect is directly felt. The equatorial Pacific has received much attention because winds has been postulated as the precursor of an important climate signal - the El Nino and Southern Oscillation [3]. The climatological annual cycles were removed from three types of spacebased data to compute the interannual anomalies. NSCAT zonal wind components show that there are strong westerly wind anomalies around the date-line in late December, 1997. It started a downwelling Kelvin waves traveling east across the equatorial Pacific which was observed as positive sea level anomalies by the TOPEX/Poseidon altimeter. When the Kelvin waves reach the eastern Pacific, anomalous sea surface temperature anomalies were observed by the AVHRR.

ACKNOWLEDGMENTS

This study was performed at the Jet Propulsion Laboratory, under contract with the National Aeronautics and Space Administration (NASA). It was supported by the NASA Scatterometer Project, the Earth Observing System Interdisciplinary Science and the Physical Oceanograph Program of NASA's Mission to Planet Earth.

REFERENCES

- [1] Liu, W.T., W. Tang, R.S. Dunbar, "NASA Scatterometer observes the extratropical transition of Pacific typhoons", *Eos Transaction of Amer. Geophys. Union*, in press.
- [2] Liu, W.T. and W. Tang, "Spaceborne scatterometer in studies of atmospheric and oceanic phenomena from synoptic to interannual time scales". *Space Remote Sensing of Subtropical Ocean*. C.T. Liu (ed.), Elsevier Press, Amsterdam, in press.
- [3] Liu, W.T., W. Tang, and L.L. Fu, 1995: Recent Warming Event in the Pacific May Be an El Nino *Eos Trans of Amer. Geophys. Union*, 76, 429-437, 1995

The Analysis of the POLDER Data

Y. Kawata, A. Yamazaki, K. Takemata* and T. Kusaka

Environmental Information Research Laboratory

Kanazawa Institute of Technology

and

Kanazawa Technical College*

Ogigaoka 7-1, Nonoichi, Ishikawa 921, Japan

Tel: 81-762-48-1100, Fax: 81-762-48-7753

E-mail: kawata@infor.kanazawa-it.ac.jp

Abstract -- The ADvanced Earth Observing Satellite(ADEOS) was successfully launched by the National Space Development Agency of Japan(NASDA), last summer. The POLDER is one of eight sensors on board of the ADEOS and it has an ability to measure both the directional reflectance and polarization from the earth atmosphere-surface system. Since the ADEOS/POLDER data sets are not available yet, the analysis results using the airborne POLDER data sets were given here, in stead. We have made analyses on both the Medimar campaign data over the Medeterranean Sea in 1991 and the La Crau campaign data over the land in the southeast of France in 1990.

INTRODUCTION

The airborne version of a POLDER sensor has been implemented and several airborne POLDER campaigns have been conducted by CNES and Laboratoire d'Optique Atmosphérique (LOA), Université des Sciences et Technologies de Lille (USTL) since 1990.

The POLDER consists of wide-field-of-view telecentric optics, a rotating wheel with spectral and polarizing filters and a two dimensional CCD detector array. In the Medimar airborne POLDER experiment, polarization and reflectance measurements were done at two wavelengths of 0.45 [μm] and 0.85 [μm]. The directional measurements cover up to 52 degrees in the cross-track direction and up to 44 degrees in the along-track direction (one observed image consists of 384x288 pixels). The solar zenith angle and flight altitude of the airborne POLDER were $\theta_0=38^\circ$ and $h=4700$ [m], respectively. The measured aerosol optical thickness values were $\tau_a=0.12$ at 0.85 [μm] and $\tau_a=0.314$ at 0.45 [μm]. The measured sea surface wind speed and its direction were $V=14.4$ [m/s] and NNW, respectively[1].

As for the airborne La Crau POLDER data over the land, the solar zenith and azimuthal angles at the time of the observation were $\theta_0=43^\circ$ and $\phi_0=104^\circ$, respectively. The flight altitude was 5900 m. In addition, the aerosol optical thickness values were $\tau_a=0.20$ at 0.85 [μm], and $\tau_a=0.40$ at 0.55 [μm]. The refractive index of aerosols were estimated to be $m=1.50-i0.005$, and the Junge type size distribution with $v=3.0$ were estimated from sky measurements[2].

The preliminary analyses on the Medimar and La Crau campaign data have been already made by CNES and USTL researchers [1] and [2], respectively.

ANALYSIS OF MEDIMAR DATA

We have made the multiple scattering analysis on the Medimar data over the Medeterranean Sea measured by the airborne POLDER in the spring of 1991. The preliminary analysis results were presented at the previous IGARSS'96 [5]. Assuming an atmosphere-ocean system with an anisotropic Cox-Munk type reflecting sea surface[3], the theoretical reflectance and the polarization values versus the viewing angle are computed by the adding and doubling method[4] for 10 aerosol models, namely, the Haze M, five Junge type functions with $v=3.0, 3.5, 4.0, 4.5$ and 5.0 , and the Water-Soluble, Oceanic, Maritime and Continental models. In this analysis we assumed that the radiation contribution from the underwater is negligible at 0.85 [μm]. Since we considered 9 different refractive indices ($m=1.33, 1.33-i0.01, 1.33-i0.05$; $m=1.5, 1.5-i0.01, 1.5-i0.05$; $m=1.75, 1.75-i0.01$, and $1.75-i0.05$), and 15 wind speeds (from $V=8.0$ [m/sec] to $V=15.0$ [m/sec] in increments of 0.5 [m/sec]), there are 135 different combinations of the refractive index and wind speed for the Haze M and the five Junge type models. The refractive indices of $m=1.33, 1.5$, and 1.75 correspond to those of water, dust, and soot aerosols, respectively. We examined 135 cases for the

Haze M and the five Junge type models and 15 wind speed cases for the Water-Soluble, Oceanic, Maritime and Continental models as to whether any could explain the 3.0 and 5.0, the Oceanic, Maritime and Continental models could not satisfy the above constraint for any combination of the assumed refractive index and wind speed valued. We found that the Junge type models with $v = 3.5, 4.0$, and 4.5 and the Water-Soluble model could satisfy the observed reflectance data when an appropriate wind speed was assumed. They are as follows: the Junge type function with $v = 3.5$ and $m = 1.5 - i0.01$ (referred to as aerosol model A) for $10.5[\text{m/sec}] \leq V \leq 13.0[\text{m/sec}]$, that with $v = 4.0$ and $m = 1.33$ for $10.5[\text{m/sec}] \leq V \leq 11.5[\text{m/sec}]$ (referred to as aerosol model B), that with $v = 4.0$ and $m = 1.75 - i0.05$ for $11.0[\text{m/sec}] \leq V \leq 12.5[\text{m/sec}]$, that with $v = 4.5$ and $m = 1.33 - i0.01$ for $10.0[\text{m/sec}] \leq V \leq 12.5[\text{m/sec}]$, and that $v = 4.5$, $m = 1.75 - i0.05$ for $10.0[\text{m/sec}] \leq V \leq 12.5[\text{m/sec}]$, and the Water-Soluble model for $12.0[\text{m/sec}] \leq V \leq 13.5[\text{m/sec}]$. As for the linear polarization, we found that these candidate models can satisfy the observed linear polarization features in the forward scattering direction, but they can not explain the observed polarization features in the backward scattering direction. The theoretical linear polarization values in the backward scattering direction are much smaller than the ones observed one. The case of the aerosol model A (Junge type function with $v = 3.5$ and $m = 1.5 - i0.01$) is shown in Fig.1, as one of such examples.

ANALYSIS OF LA CRAU DATA

We have analyzed the reflectance data of the La Crau data set over the land to estimate the BRDFs for selected land cover types. The accurate atmospheric correction is required for such analysis. Our atmospheric correction algorithm, applicable to the POLDER type snap shot image, were described previously[6], we will not repeat it again, here. We applied our atmospheric correction algorithm to the La Crau scenes and we, thus, obtained the corresponding spectral albedo images for all scenes.

In our previous paper[7] we selected 22 target areas (River, Pond, City, Road, Rice Field, Forest, Orchard, Vineyard and Marsh) whose locations lie along near the flight pass and the estimation results of the BRDFs for these were tabulated by using Deuze's BRDF model [2]. The BRDFs for water surface covers are, more or less, isotropic with respect to the viewing zenith angle. We can compute

the spectral BRDFs for target surface covers, using the parameter values of Table 2 in [7]. The spectral BRDFs for the forest target are shown in Fig.2, as one of such examples. We can notice from Fig.2 that the BRDF for the forest is nearly flat against the viewing zenith angle at $0.50 [\mu\text{m}]$, with showing a very slight increase in the back scattering direction, whereas it shows clearly a large albedo increase (hot spot) in the back scattering direction at $0.85 [\mu\text{m}]$.

CONCLUSIONS

Since the ADEOS/POLDER data is not available yet, the analysis results using the airborne POLDER data were Presented. The main results are summarized as follows:

- (1) We found several aerosol models which can satisfy the observed reflectance data over the ocean.
- (2) Such aerosol models explained the observed polarization data over the ocean in the forward scattering direction, but they failed to satisfy it in the backward scattering direction.
- (3) The BRDFs for several land cover types were successfully made, using a series of the ground albedo images that were estimated by our atmospheric correction method.

We would like to express our deep appreciation to Profs. Herman and Deschamps at LOA, Universite des Sciences et Technologies de Lille, France and Dr. Bréon at Laboratoire de Modelisation du Climat et de l'Environnement, France for kindly providing La Crau POLDER data.

This study was supported by the Research Contract No. NASDA-PSPC-17710, National Aeronautics and Space Development Agency of Japan.

REFERENCES

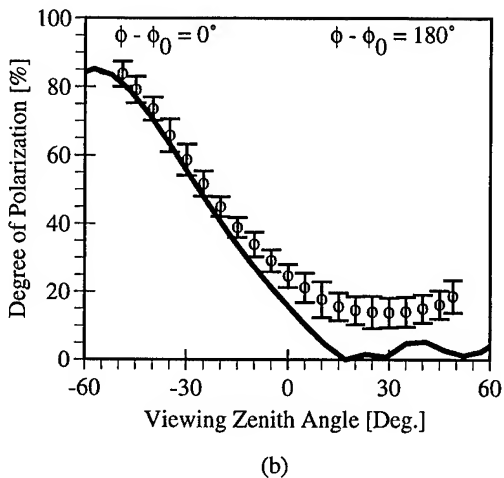
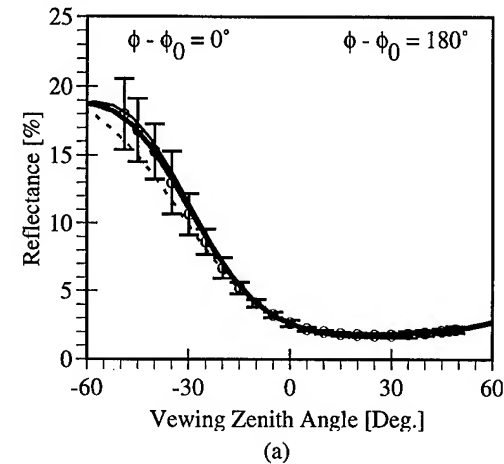
- [1] Breon, F.M., and Deschamps, P.Y., 1993, "Optical and Physical Parameter Retrieval from POLDER Measurements over the Ocean Using an Analytical Model", *Remote Sens. Environ.*, Vol.43, pp. 193-207.
- [2] J. L. Deuze et al., 1993. "Analysis of the POLDER Airborne Instrument Observations over Land Surfaces", *Remote. Sens. Environ.*, no.45, pp.137-154.
- [3] Cox, C., and Munk, W., 1954, "Measurement of Roughness of the Sea Surface from Photographs of the Sun's Glitter", *J. Opt. Soc. Amer.*, Vol.44, pp. 838-850.
- [4] Hansen, J.E., and Travis, L., 1974, "Light Scattering in Planetary Atmospheres", *Space Sci. Review*, Vol.16, pp.

527-610.

[5] Yamazaki,A. ,Ueda, K. , Kawata,Y., and Kusaka,T., 1996,"The Estimation of Aerosol Models by the Reflectance Analysis of the Airborne POLDER Data", IEEE IGARSS' 96, Vol.2, , pp. 1250-1252.

[6] Takemata, K. and Kawata, Y. 1995, "Estimation of land surface BRDF by using airborne POLDER image data", IEICE Trans. Commun., vol. E78-B, no. 12. pp.1591-1597.

[7] Takemata, K., Yonekura,T. ,Asae, M., and Kawata,Y., 1996,"Estimation of BRDF from Land Surfaces Using Airborne POLDER Data", IEEE IGARSS' 96, Vol.2, , pp. 1666-1668.



o Observed Data — 11.0 [m/sec]
 — 10.5 [m/sec] - - - 13.0 [m/sec]

Fig.1. Reflectance (a) and Polarization (b) versus viewing zenith angle in the principal plane. Lines are for the cases of the anisotropic Cox-Munk model with $V=13.0$ [m/s], 11.0 [m/s] and 10.5 [m/s] and wind direction of NNW.

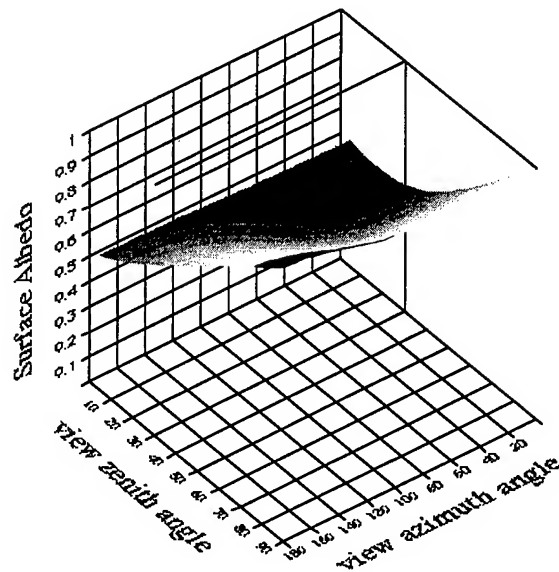
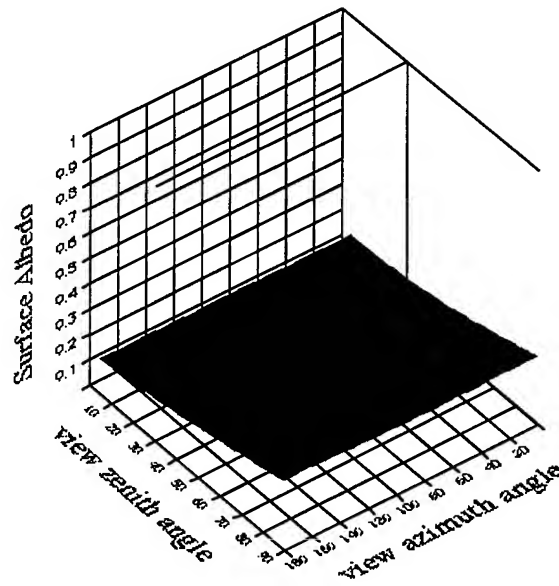


Fig.2. 3 Dimensional representation of the BRDF for the forest target.

Cloud Classification and Retrieval from Spaceborne Microwave Radiometry Using a Simulated Cloud Database

G. d'Auria¹, F. S. Marzano¹, N. Pierdicca¹, R. Pinna Nossai¹, P. Basili², and P. Ciotti³

¹ Dipartimento di Ingegneria Elettronica, Università "La Sapienza" di Roma (Italy)
Via Eudossiana, 18 - 00184 Roma (Italy); Fax: +39-6-4742647; gioda@palatino1.ing.uniroma1.it

² Istituto di Elettronica, Università di Perugia (Italy)
Via G. Duranti, 1 - 06131 Perugia (Italy); Fax: +39-75-5852654; E-mail: basili@mozart.istel.unipg.it

³ Dipartimento di Ingegneria Elettrica, Università di L'Aquila (Italy)
Poggio di Roio - 67040 L'Aquila (Italy) - Fax: +39-862-432537; E-mail: cpiero@dsaq1.ing.univaq.it

Abstract -- A database of cloud genera is illustrated in terms of statistical distributions of hydrometeor vertical profiles. Since it is mainly derived from a microphysical model, it keeps both the microphysical consistency and the meteorological meaning. A simulated database of brightness temperatures, observed both from a spaceborne radiometer as the Special Sensor Microwave Imager and from a ground-based radiometer, is produced. An automatic classifier of cloud genera is proposed and its performances analyzed. Comparisons among SSM/I data, ground-based measurements and meteorological information are also described.

INTRODUCTION

Infrared and visible radiometers aboard geostationary satellites have been widely used so far to map cloud coverage. However, these passive sensors cannot probe inside the clouds, and information on their properties can only be gained indirectly and with many ambiguities. Multichannel microwave passive observations have been recognized to be promising tool for atmospheric studies since information on the cloud structure and microphysics can be extracted from brightness temperature measurements [1]. It is well known that few experimental data exist in literature for setting up a reliable cloud database to be used in an inversion algorithm. Thus one has very often to rely on models strictly based on the microphysics of clouds, which generally refer to specific storm clouds [2].

The microphysical description of clouds is essentially based on the knowledge of the hydrometeor vertical profiles. Cloud genera can be determined by a variety of hydrometeor profiles. All the possible realizations of a cloud genus must be known in order to proceed to find its microwave signature. Hopefully, its radiative responses should be clearly distinguished one from the other in order to identify them.

In this work we have used a rather extensive database of hydrometeor vertical profiles for various cloud genera together with a radiative transfer model to obtain the corresponding brightness temperatures for both satellite-based and ground-based radiometers. This database can be applied to train a

supervised classifier in order to derive automatically cloud maps from spaceborne microwave imagery, like those of the Special Sensor Microwave Imager (SSM/I).

CLOUD GENERA AND RADIATIVE TRANSFER

The input for the generation of the database is the microphysical model known as the University of Wisconsin Nonhydrostatic Modeling System (UW-NMS) [2]. This model is three-dimensional and time-dependent and considers four different categories of hydrometeors: precipitating liquid water (raindrops), non precipitating liquid water (cloud droplets), precipitating ice (graupel particles) and non precipitating ice (ice crystals and aggregates).

Each profile of the original microphysical model is ascribed to a given genus of cloud and sometimes even to a species or attribute of the cloud genus itself. The guidelines for this recognition are based on some basic points: the vertical extension (top and bottom altitudes), the concentration of each hydrometeor species at the various altitudes, the intensity of rainfall (if any) and the evolution stage [3]. The first column of Table 1 lists the modeled cloud genera and species.

Once the subdivision into cloud genera is performed, the statistical parameters of each class can be calculated. Each profile is described by a vector g of dimension D , given by the four hydrometeor equivalent water contents (EWC's) multiplied by the number of samples along the altitude. For an easier handling of each data base, further simplifications are introduced. The vertical structure constituted by 41 layers (the original sampling resolution) are reduced to 7-layers by a staircase approximation. A covariance matrix C_g around its mean vector m can be associated to each cloud genus. These quantities can be used to enlarge the statistical database. Indeed, we have increased from 774 to 4500 the number of realizations of all the cloud genera. This is particularly necessary for certain classes which contain a small number of elements. By assuming a Gaussian density distribution defined by matrix C_g and vector m , it is possible to perform a pseudo-random generation of realizations, which will result

Gaussian distributed and limited only to positive values of the parameters [1]. During the generation, we have supposed the cloud levels to be random and the meteorological parameters to be randomly variable around the climatological profile. As an example, Fig.1 shows the mean vertical structure of a nimbostratus in terms of integrated EWC's within each layer for the four hydrometeor species.

The solution of the radiative transfer equation (RTE) has been carried out numerically following the Eddington approximation, specifying the top and bottom boundary conditions and the continuity conditions at the layer interfaces [4]. For the Earth's surface conditions, both specular sea and Lambertian land surfaces have been considered. The phase function has been assumed as an expansion of Legendre polynomials, but limited to the first order. All the hydrometeors have been assumed to be spherical thus using the Mie formulation to compute asymmetry factors and extinction coefficients. The gaseous absorption has been calculated by the Liebe model. Single-scattering coefficients have been averaged over the size distribution and the results of the radiative simulation have been found fairly dependent on the assumed distribution.

Fig.2 shows the scatterplot of the simulated 85 GHz T_B against 19 T_B , centered around the climatological clear-air T_B values, for a cumulonimbus, cumulonimbus with incus and a nimbostratus, as observed by a multifrequency spaceborne radiometer. As an example of ground-based applications, Fig.3 shows the histogram of 36 GHz T_B (again centered around the clear-air value) for various cloud genera.

CLOUD SUPERVISED CLASSIFICATION

The simulated data base of genus cloud structures and brightness temperatures allows us to design an automatic classifier, based on the Maximum Likelihood (ML) criterion. This criterion consists of maximizing the multivariate probability of the brightness temperature vector conditioned to the considered class. In order to make a simulated independent test, the whole data base consisting of 4500 points (500 for 9 cloud genera) has been subdivided into a training set and a test set.

We have generated 8 brightness temperature data bases, i.e. over land and sea for spring, summer, autumn and winter meteorological conditions. The surface emissivity has been assumed to be fixed for this application. For the classification we have considered only the T_B frequencies at 19, 37 and 85 GHz (including polarizations for sea-background cases).

Tests have been performed by adding to the T_B test set a Gaussian error with 1 K standard deviation [3]. Results for spaceborne observations show that the mean error (defined as the average of the classification errors obtained for each class) is much lower over the sea (about 17%) than over land (about 27%). This result was expected since, on one hand, over the

sea optically thin clouds are much more separated in terms of radiometric signature and, on the other hand, over the sea the measurement vector has a dimension which is double with respect to the land case. Both over land and sea the cumuliiform clouds are well classified with errors less than 25% over land and less than 15% over the sea, even though the classifier often confuses cumuli congesti for nimbostrati. The largest misclassification errors are made on stratus clouds which are frequently confused with altocumuli and cumuli mediocres. The latter considerations also apply to ground-based radiometric observations.

SSM/I TESTS AND GROUND-BASED MEASUREMENTS

Although an exhaustive validation of the simulation results is not within the scope of this work, we have tested the produced cloud- T_B database in different ways [3]. Objective difficulties arise when a direct comparison with the cloud truth is attempted and information taken from other sensors cannot always solve the ambiguities.

The second column of Table 1 shows the results of the cloud genus classification in terms of per-cent occurrence obtained by applying the ML classifier to a flood case. The case is relative to the Liguria (Italy) event which took place on September the 27th, 1992 and whose images were acquired by SSM/I at 1555 UTC [5]. The storm system was characterized by convective cells with a strong vertical development and a high surface rainfall rate with measured raingauge values up to 50 mm/h. During a cold front the abrupt lifting of warm air causes cumulonimbus formation in the very passage accompanied with nimbostrati and cumuli ahead and behind the front. The SSM/I overpass in Liguria caught only the last stage of the frontal system when the strongest cumulonimbi have already extinguished. Indeed, it is worth noting that Table 4 indicates a considerable presence of nimbostrati with cumuli congesti and cumulonimbi with incus.

Ground-based radiometric measurements at 36 GHz have been also undertaken together with visual inspection of cloud coverage to test the cloud classification accuracy. The third column of Table 1 shows the percentage occurrence of cloud genera as classified by means of ML during the months of June and July 1996. In this case, a radiosounding set acquired in Rome during summer has given the climatological clear-air conditions. Preliminary comparisons carried out by using visual classification mean errors of 25%.

CONCLUSIONS

In this work we have used a database of hydrometeor profiles of clouds and of the corresponding simulated brightness temperatures for each type of cloud, defined according to a classification into genera and species. In this way we remain within the framework of a classification which

is widely studied and recognized by the meteorological scientific community. Tests have been mainly carried out examining SSM/I imagery and ground-based radiometric measurements.

Acknowledgments. This work has been partially supported by ASI and MURST. The SSM/I data have been provided by DAAC of NASA's Marshall Space Flight Center (MSFC).

REFERENCES

- [1] N. Pierdicca, F.S. Marzano, G. d'Auria, P. Basili, P. Ciotti, and A. Mugnai, "Precipitation retrieval from spaceborne microwave radiometers using maximum *a posteriori* probability estimation", IEEE Trans. Geosci. Remote Sensing, vol. 34, pp. 1-16, 1996.
- [2] E.A. Smith, A. Mugnai A., H.J. Cooper, G.J. Tripoli, and X. Xiang, "Foundations for statistical-physical precipitation retrieval from passive microwave satellite measurements. Part I: Brightness temperature properties of a time dependent cloud-radiation model", J. Appl. Meteorol., vol. 31, pp. 506-531, 1992.
- [3] G. d'Auria, F.S. Marzano, N. Pierdicca, R. Pinna Nossai, P. Basili, and P. Ciotti, "Remotely sensing cloud properties by microwave radiometry using a modeled cloud database", presented at Fifth Specialist Meeting on Microwave Radiometry and Rem. Sens. of Env., Boston (MA, USA), 4-6 Nov. 1996 and submitted to Radio Sci..
- [4] R. Wu, and J.A. Weinman, "Microwave radiances from precipitating clouds containing aspherical ice, combined phase, and liquid hydrometeors", J. Geoph. Res., vol. 89, pp. 7170-7178, 1984.
- [5] V. Levizzani, F. Porcù, F.S. Marzano, A. Mugnai, E.A. Smith, and F. Prodi, "Investigating a SSM/I microwave algorithm to calibrate Meteosat infrared instantaneous rainrate estimates", Meteorol. Appl., vol. 3, pp. 5-17, 1996.

Table 1 Results for SSM/I test (Liguria case) and ground-based measurements in terms of per-cent occurrence.

Cloud genera and species	SSM/I Liguria data	Ground-based 36 GHz data
<i>Cumulus mediocris</i>	0 %	10.8 %
<i>Cumulus congestus</i>	28.6 %	0 %
<i>Cumulonimbus</i>	1.2 %	0 %
<i>Cumulonimbus incus</i>	12.3 %	0 %
<i>Stratus</i>	0 %	0 %
<i>Nimbostratus</i>	57.9 %	0 %
<i>Altostratus</i>	0 %	6.7 %
<i>Altostratus</i>	0 %	23.0 %
<i>Cirrus</i>	0 %	59.5 %

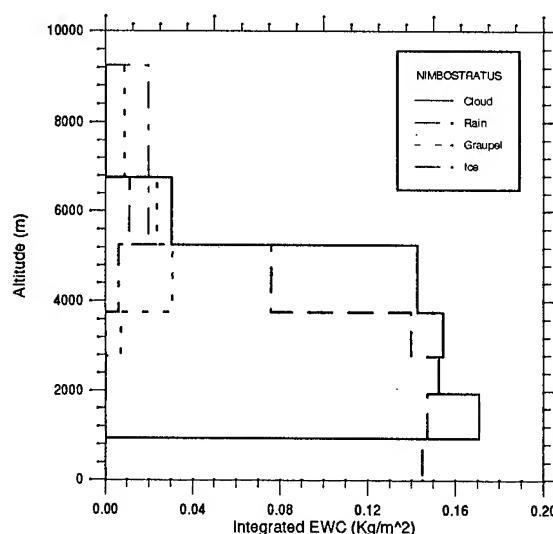


Fig.1 Mean vertical structure of a nimbostratus.

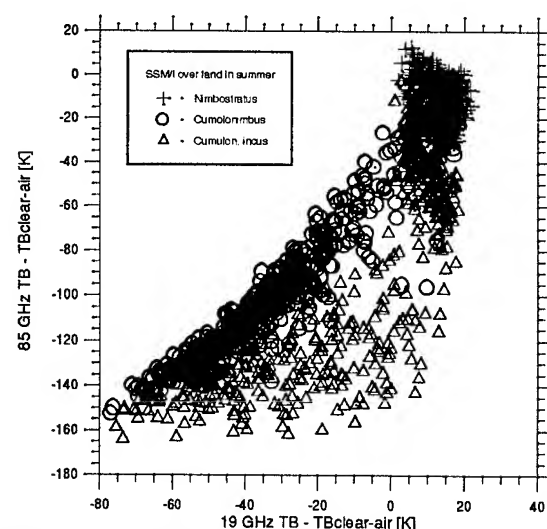


Fig.2 Scatterplot of simulated TB's over land from space.

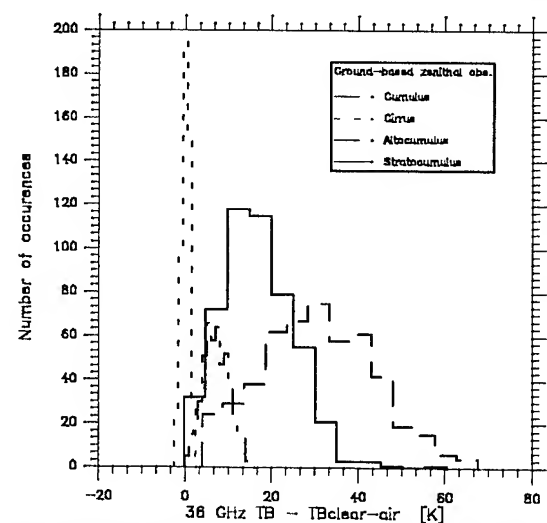


Fig.3 Histogram of simulated 36 GHz TB from ground.

On the Measurement of Stratus Cloud Properties with a Cloud Radar and Microwave Radiometer

A. S. Frisch*, T. Uttal**, C.W. Fairall**, and J.B. Snider***

* Cooperative Institute for Research in the Atmosphere
Colorado State University/NOAA
Environmental Technology Laboratory
Boulder CO 80303 USA

** NOAA Environmental Technology Laboratory, Boulder, CO 80303 USA

*** Cooperative Institute for Research in Environmental Sciences
University of Colorado/NOAA
Boulder, CO 80303 USA

TEL: 303-497-6209; FAX: 303-497-6978; EMAIL: sfrisch@etl.noaa.gov

Abstract -- Algorithms have been developed to calculate the vertical profiles from cloud radar reflectivity measurements and microwave radiometer measurements of integrated liquid water. In addition, the algorithms calculate the effective radius profiles, and the total number of cloud droplets. When drizzle is present, radar reflectivity, vertical velocity and the spread of the vertical velocity can be used to calculate vertical profiles of liquid water, liquid water flux, effective radius, and droplet number. When there is no drizzle, we can use the Doppler capability to profile various vertical velocity turbulence parameters, such as the vertical velocity spectra, variance, and skewness. All parameters are important in the development of cloud models. Data taken during ASTEX (Atlantic Stratocumulus Transition Experiment) have been used to study the behavior of stratus clouds at Porto Santo Island, Madeira, Portugal.

INTRODUCTION

Stratus clouds are important in boundary layer dynamics and global climate. Most measurements of stratus clouds have been made with aircraft [1, 2, 3]. However, aircraft measurements are expensive, and cannot be used for long term monitoring at a single location. The development of the cloud sensing radar

[4] gives us the opportunity to monitor the cloud reflectivity, and when the antenna is pointed vertically and the radar has Doppler capability it can also measure the vertical velocity structure of the cloud droplets. Frisch et al. [5] showed how the cloud radar measurements of reflectivity could be combined with the integrated liquid water measurements from a microwave radiometer to retrieve cloud properties using a log-normal cloud droplet model.

We can show that for vertical liquid water profiles, a log-normal droplet distribution assumption is not necessary which makes the earlier method [5] more general.

We can use any droplet distribution where we can relate the 6th moment to the 3rd moment. Then using radar reflectivity and integrated liquid water from the radiometer we can calculate the profile of liquid water. In addition, if the radar calibration is off by a constant value, then the liquid water profile retrieval is independent of this calibration offset.

METHOD

The reflectivity Z (m^3) is given by

$$Z(z) = 10^{(dBZ(z) - 180)/10} \quad (1)$$

This work was funded by NOAA and the Department of Energy Atmospheric Radiation Measurement (ARM) program.

and if the measured value of dBZ* is given by dBZ+k, where k is the calibration offset and dBZ is the measured backscattered power in mm⁶m⁻³ then,

$$Z(z) = 10^{k/10} Z^*(z). \quad (2)$$

The liquid water is given by

$$q_l(z) = \frac{4}{3} \pi N(z) \rho_w \langle r^3(z) \rangle \quad (3)$$

where z is the height, ρ_w is the water density, (the brackets denote the moment of the radius over an arbitrary distribution), and N is the number of droplets.

Now if we can relate the higher moment to the lower, i.e. if $\langle r^6 \rangle = k^2 \langle r^3 \rangle^2$, then the reflectivity is

$$\begin{aligned} Z(z) &= 2^6 N(z) \langle r^6(z) \rangle \\ &= 2^6 N(z) k^2 \langle r^3 \rangle^2 \end{aligned} \quad (4)$$

and the liquid water becomes

$$q_l(z) = \frac{0.52}{k} \rho_w N(z)^{1/2} Z(z)^{1/2}. \quad (5)$$

Aircraft observations in stratus clouds have shown that the number density is approximately constant with height [1, 2, 3].

Now the total water as measured by the radiometer is the sum of $q_l(z_j)$ over all heights or

$$\begin{aligned} Q_l &= \int_{z=0}^{z=\infty} q_l(z) dz_j \\ &= \frac{0.52 \rho_w N^{1/2}}{k} \int_{z=0}^{z=\infty} Z(z) dz \end{aligned} \quad (6)$$

and the liquid water at a height, z, is

$$q_l(z_j) = \frac{\overline{Q_l} Z(z)^{1/2}}{\int_{z=0}^{z=\infty} Z(z)^{1/2} dz} \quad (7)$$

If we substitute the relationship $z = 10^{k/10} Z^*$, we have

$$q_l(z) = \frac{\overline{Q_l} Z^*(z)^{1/2}}{\int_0^\infty Z^*(z)^{1/2} dz} \quad (8)$$

This shows that the retrieval is independent of the calibration when it is shifted by a constant. However, when we go to determine the effective radius and the number of cloud droplets, then we need to pick a distribution and have the calibrated reflectivity (for further discussion see [5].)

EXAMPLE OF CLOUD LIQUID WATER RETRIEVAL

As an example, we used some data taken during ASTEX, the Atlantic Stratocumulus Transition Experiment held in the North Atlantic in June 1992. The radar was the National Oceanic and Atmospheric Administration (NOAA) Environmental Technology Laboratory (ETL) K_a-band cloud radar. The microwave radiometer used at ASTEX was developed at ETL [6] and is a three-frequency system for the simultaneous measurement of atmospheric water vapor and liquid water in clouds. Figure 1 shows a liquid water profile calculated from data taken on June 5, 1992 on the Island of Porto Santo, Madeira, Portugal. The data were taken over a 23 minute period.

REFERENCES

[1] S. Nicholls, "A model of drizzle growth in warm, turbulent, stratiform clouds," *Quart. J. Roy. Meteor. Soc.*, **113**, 1141-1170, 1987.

[2] A. Slingo, S. Nicholls, and J. Schnetz, "Aircraft observations of marine stratocumulus during JASIN," *Quart. J. Roy. Meteor. Soc.*, **108**, 833-856, 1982a.

[3] A. Slingo, R. Brown, and C. L. Wiench, "A field study of nocturnal stratocumulus; III. High resolution radiative and microphysical observations," *Quart. J. Roy. Meteor. Soc.*, **108**, 145-166, 1982b.

[4] F. Pasqualucci, B.W. Bartram, R.A. Kropfli, and W.R. Moninger, "A millimeter-wavelength dual-polarization Doppler radar for cloud and precipitation studies," *J. Climate Appl. Meteor.*, **22**, 758-765, 1983.

[5] A.S. Frisch, C.W. Fairall, and J.B. Snider, "Measurement of Stratus Cloud and Drizzle Parameters in ASTEX with a K_a -band Doppler Radar and Microwave Radiometer," *J. Atmos. Sci.*, **52**, 2788-279, 1995.

[6] D.C. Hogg, F.O. Guiraud, J.B. Snider, M.T. Decker, and E.R. Westwater, "A steerable dual-channel radiometer for measurement of water vapor and liquid in the atmosphere," *J. Appl. Meteor.*, **22**, 789-906, 1983.

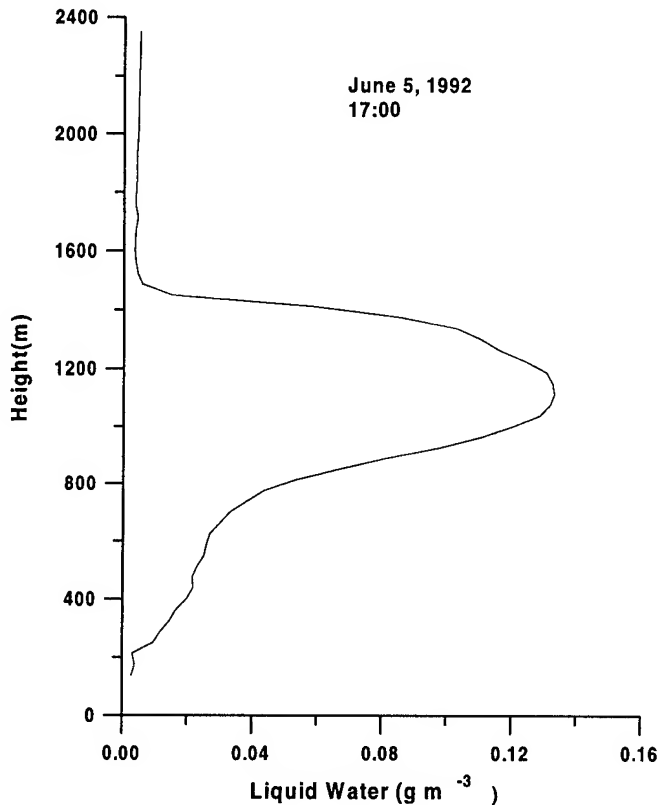


Figure 1. Example of a retrieved liquid water profile derived from cloud radar and microwave radiometer data.

Remote Sensing of Boundary-Layer Temperature Profiles by a Scanning 5-mm Microwave Radiometer and RASS: A Comparison Experiment

E. R. Westwater, Y. Han, V. G. Irisov, and V. Leuskiy
CIRES
University of Colorado/NOAA
Environmental Technology Laboratory
325 Broadway, MS R/E/ET1
Boulder, Colorado, 80303-3228 USA
Tel: (1) 303-497-6527
Fax: (1) 303-497-3577
email: ewestwater@etl.noaa.gov
corresponding author: E. R. Westwater

E. N. Kadyrov and S. A. Viazankin
Central Aerological Observatory
Microwave Remote Sensing Laboratory
Pervomajskaya St. 3 Dolgoprudny
Moscow Region, 141700, RUSSIA
Phone/Fax: (7) (095)40877-58
email: attex@adonis.iasnet.com

Abstract --Two techniques for deriving low-altitude temperature profiles were evaluated at an experiment conducted from November 1996 to January 1997 at the Boulder Atmospheric Observatory (BAO). The first used a scanning single wavelength 5-mm (60 GHz) microwave radiometer to measure vertical temperature profiles. The second was a Radio Acoustic Sounding System (RASS) that operated at 915 MHz. Typically, radiometric profiles were produced every 15 min; those from RASS were hourly. The BAO has an instrumented 300-m tower with 5-min measurements of temperature and relative humidity available at the surface and at altitudes of 10, 50, 100, 200, and 300 m. The tower measurements were occasionally supplemented with radiosonde releases and with hand-held meteorological measurements taken on the tower elevator. Data from this experiment are presented and plans for future deployments of these instruments are discussed. In addition, a new quality control algorithm for the RASS system is presented and evaluated.

INTRODUCTION

Remote sensing of low-altitude temperature profiles is important for a variety of studies, including air pollution, air/sea interaction, and short-term meteorological forecasting. Two techniques show promise for routine unattended sensing of profiles during non-precipitating conditions. The first uses a scanning single wavelength 5-mm (60 GHz) microwave radiometer to measure temperature and temperature gradient profiles. These radiometers have wide bandwidth (4 GHz) and excellent sensitivity (0.03 K rms @ 1 s). The second uses a Radio Acoustic Sounding System (RASS) that operates at 915 MHz [1]. The RASS system has range gates centered at 135m, 195m, ..., each with a vertical resolution and spacing of 60 m; for our comparisons we interpolated these data to tower levels. For all practical purposes, the maximum range of this RASS system was 615 m. In addition, RASS measures profiles of virtual temperature T_v ,

rather than kinetic temperature T . Typically, radiometric profiles are produced every 15 min while those of RASS are hourly.

During November 1996 to January 1997, several remote sensing and in situ measurements were operated at the Boulder Atmospheric Observatory (BAO), near Erie, Colorado, USA. The BAO has an instrumented 300-m tower with 5-min measurements of temperature and relative humidity available at the surface and at altitudes of 10, 50, 100, 200, and 300 m. The tower measurements were occasionally supplemented with radiosonde releases and with hand-held meteorological measurements taken on the tower elevator. In addition to the elevator, the tower also has a carriage that is moveable from the bottom to the top of the tower. In the first month of the experiment, both a discrete scanning radiometer operated by the Central Aerological Observatory (CAO) and one operated by the Environmental Technology Laboratory (ETL) were operated at about the same altitude (10 m). The CAO radiometer was a commercially available instrument from the Russian firm ATTEX [2], [3]. ETL deployed a continuously scanning radiometer with a receiver similar to that of the first [4]. The ETL radiometer was suspended from the carriage on a boom at the 10-m level, while the ATTEX radiometer was located on a trailer about 25 m away.

Data from both the ATTEX and the ETL radiometers were used to derive temperatures at the tower levels so that they could be compared directly with the *in situ* measurements. The ATTEX radiometric system had its own calibration reference, consisting of an *in situ* measurement of temperature at the height of the radiometer. This reference therefore constrained the brightness temperature measured when the radiometer pointed in the in the horizontal direction to be equal to the reference temperature. The ETL system did not have an associated *in situ* measurement; therefore, with the radiometer mounted at the 10-m tower level, we used the tower temperature measurement as the horizontal reference.

Two profile retrieval algorithms were used to derive profiles from the 5-mm radiometer brightness temperature data. The first, used on the ATTEX radiometer data, was a variation of the Twomey-Tikhonov retrieval algorithm [5]. The second, used on the ETL data, used a variation of linear statistical retrieval [6] that derives lapse rate profiles from a projection of angular brightness temperatures on a set of empirical orthogonal functions.

RESULTS

Time Series

Fig. 1 shows a time series of temperature at the 200-m level for the ATTEX radiometer, RASS, and tower sensor. In preparing the RASS data for this figure, strict quality control methods (QC) were applied (see the following section). In addition, the RASS T_v values have been converted to T by use of the tower humidity measurements. Note the roughly 20 °C range in temperatures during this 8 day time period and the rapid drop in temperature during 4 - 5 and 9-10 January. Similar comparison time series were developed for the ETL radiometer and the tower with the quality of the comparisons being about the same.

Statistical Comparisons with Tower Sensors

In the first half of the experiment, the ETL radiometer was operated at the 10 m tower level; during the second half, the radiometer was elevated to the 300-m level and scanned the atmosphere above and below. Therefore, the sample size available for simultaneous comparisons of all upward-looking instruments was limited. In addition, the sample size of RASS data was reduced by about 25 % due to QC criteria. Nevertheless, we think the available data were able to give at least a rough estimate of the accuracy of the systems. Statistical comparisons are shown in Table 1.

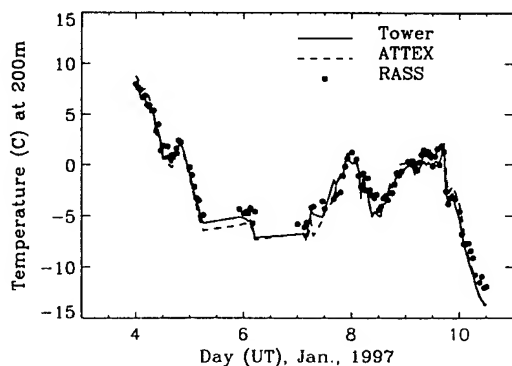


Fig. 1. An 8-day time series of temperature at 200 m as measured by the ATTEX radiometer, by the *in situ* sensor on the tower, and by RASS. January 4 to 11, 1997.

Table 1. Statistical comparisons between ATTEX, ETL, RASS, and BAO tower temperature measurements in °C

TOWER LEVEL (m)	ETL rms bias n	ATTEX rms bias n	RASS rms bias n
10	0.00 0.00 2351	0.89 0.28 2103	
50	1.04 0.04 2351	0.85 -0.25 2103	
100	1.19 -0.60 2351	0.88 -0.07 2103	
200	1.04 -0.37 2351	0.81 -0.07 2103	0.92 0.42 166
300	1.24 -0.17 2351	1.31 -0.33 2103	1.34 0.56 162

QUALITY CONTROL METHOD FOR RASS

The RASS data were available for us on the ETL web site, and formed a portion of the data base for a regional air pollution experiment also conducted by ETL. These data from the web site had already been corrected for vertical wind velocities and a consensus average quality control had been applied to the data. However, even after the application of these methods, several large outliers remained. Discussions with an ETL scientist knowledgeable about RASS indicated that a recently installed commercial radio communications transmitter was giving radio frequency interference. Previous results [1] had yielded accuracy results of 0.5 °C rms. In Fig. 2, we show a scatter plot of RASS measurements, converted from T_v to T and interpolated to the 200-m tower level, vs. the *in situ* measurements. It is obvious that without some additional QC these data would be inadequate for most meteorological purposes. Since our radiometric comparisons with all of the tower levels were quite encouraging, we used the scanning radiometer to develop a QC method for RASS. Our method was quite straightforward: from the radiometer data, we had estimates, at each tower level, of the accuracy of the T retrieval; i.e., the rms error σ and bias, as well as the regression line and its statistics. We also use surface humidity and pressure measurements to estimate T_v . If a RASS measurement, adjusted for bias, fell within a $\pm 3 \sigma$ level of the estimated T_v , then the measurement was accepted; if not, the measurement was rejected. The scatter plot for the 200-m tower level, after QC is applied, is shown in Fig. 3 and a statistical summary is shown in Table 2. The improvement in every aspect is apparent.

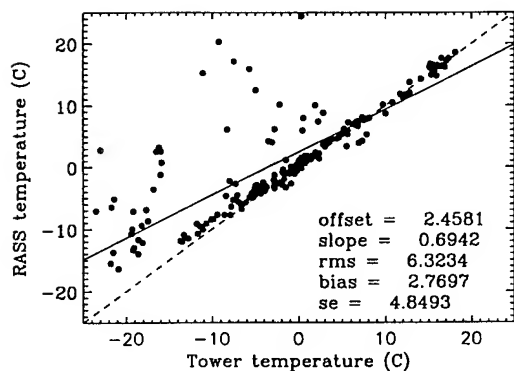


Fig. 2. Scatter plot of RASS vs. BAO tower measurements at 200 m without quality control. Sample size = 215.

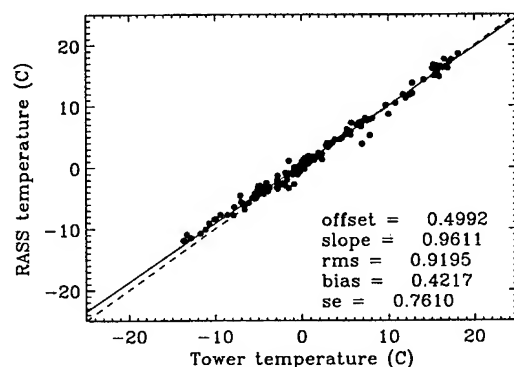


Fig. 3. Scatter plot of RASS vs. BAO tower measurements at 200 m using ATTEX radiometric temperature retrievals for quality control. Sample size = 166.

Table 2. Statistical comparisons between RASS and BAO tower measurements in °C						
TOWER LEVEL (m)	BEFORE QC			AFTER QC		
	rms	bias	N	rms	bias	N
200	6.32	2.77	215	0.92	0.42	166
300	5.51	2.55	212	1.32	0.56	162

RADIOMETRIC RETRIEVALS ABOVE 300 M

The top level of the BAO tower was 300 m, although both the 5-mm radiometers and RASS both gave measurements above this level. We realized that attenuation of the intervening atmosphere caused the radiometric retrievals to degrade with altitude. However, accuracy estimates of the radiometer at 400 and 500 m were around 1.0 K rms. To evaluate the accuracy of the radiometer at these levels, we simply compared the radiometric retrieval with RASS

measurements that had been subject to quality control. In addition, to convert from T_v to T , we assumed that the mixing ratios at 400 and 500 m were equal to their measured values at 300 m. After screening for obvious outliers, we compared RASS and radiometric retrievals at the two upper levels and achieved rms differences of 0.87 and 1.07 °C. The scatter plots of the comparisons are shown in Figs. 4 and 5. Note the diminished sample size from the 300-m comparisons; this is due to the limited availability of the RASS measurements at the 400- and 500-m levels.

COMBINED RADIOMETRIC-RASS RETRIEVALS

The prospects for combining RASS and radiometric retrievals from the scanning radiometer are excellent. The ability of the radiometer to measure temperature from the surface to 300 or 400 m, the region of overlap between radiometer and RASS, and the potential of RASS to probe much higher than the radiometer, all suggest that such a combination would be fruitful. In Fig. 6, we show temperature profiles from the radiometer, RASS, and the tower. There is a region of overlap where the retrievals agree well with other, as well as non-intersecting regions, where each system could independently contribute information. A variety of retrieval algorithms could be used to combine such data, if the accuracies of the data; i.e., their error covariance matrices, are known [5], [6].

As another measure of how well a RASS could supply additional information to the radiometer, we determined the relative hourly sample sizes, before quality control, which were produced by RASS. Ref. [1] has discussed how 915 MHz RASS is subject to an appreciable amount of acoustic attenuation that limits its upper altitude coverage. For the system deployed by ETL during this experiment, the relative frequency of data availability is given in Table 3. Relative sample sizes were roughly cut in half for each range gate above 495 m.

Table 3. Relative sample size N achieved by RASS during BAO experiment as a function of height (m)							
h(m)	135	195	255	315	375	435	495
N	250	268	251	204	187	131	92

CONCLUDING REMARKS

The 5-mm scanning radiometers, both of ATTEX and of ETL, gave excellent comparisons during winter conditions at the BAO 300-m tower; several days of data were obtained during a snow storm, with no degradation of the quality of the data. A limited number of comparisons with the 915 MHz RASS, showed the ability of the radiometer to derive temperature profiles to about 500 m. During these experiments, the RASS system was subject to severe radio frequency interference; to eliminate spurious data, a

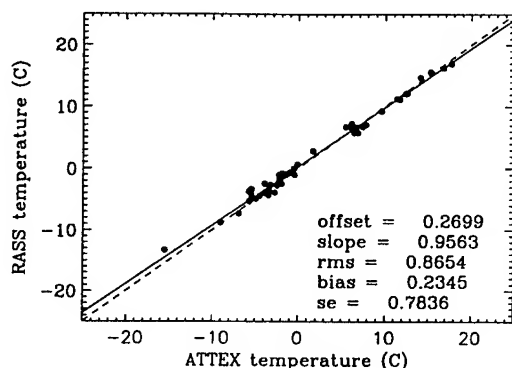


Fig. 4. Scatter plot of ATTEX radiometer vs. RASS temperature measurements at 400 m. RASS T_v measurements have been converted to T by use of tower humidity measurements at the 300-m level. Sample size = 58.

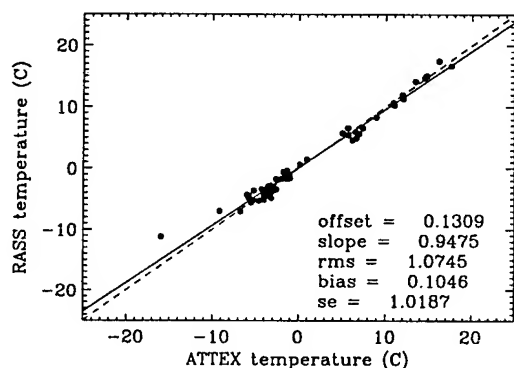


Fig. 5. Scatter plot of ATTEX radiometer vs. RASS temperature measurements at 500 m. RASS T_v measurements have been converted to T by use of tower humidity measurements at the 300-m level. Sample size = 58.

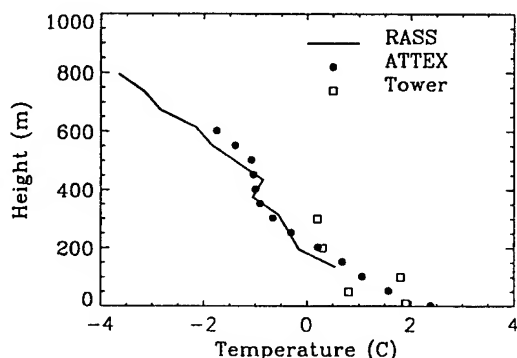


Fig. 6. Profiles of temperature as measured by the ATTEX radiometer, RASS, and BAO *in situ* sensors. January 7, 2100 UTC.

quality control method, based on radiometric temperature soundings, was developed and successfully applied to the data. About 75% of the RASS data passed the QC criterion and yielded accuracies, relative to tower measurements, of better than 1.3 °C rms.

As a part of the U. S. Department of Energy's Atmospheric Radiation Program (ARM), an ATTEX radiometer was purchased and will be deployed in their new facility on the North Slope of Alaska (NSA). To derive profiles above 500 m, ARM is also considering RASS systems at 915 and at 449 MHz. We believe that the quality control method that we derived here would be applicable to RASS, and that RASS and radiometers could make a useful combined remote sensing system.

ACKNOWLEDGMENTS

This study was partially supported by the Environmental Sciences Division of the Department of Energy as a part of their Atmospheric Radiation Measurements Program. The authors thank J. A. Shaw and J. R. Jordan for useful comments on the manuscript.

REFERENCES

- [1] May, P.T., R.G. Strauch, K.P. Moran, and W.L. Ecklund, "Temperature sounding by RASS with wind profiling radars," IEEE Trans. Geosci. Remote Sens., vol. 28, pp. 19-28, 1990.
- [2] Troitsky, A. V., K. P. Gaikovich, V. D. Gromov, E. N. Kadyrov, and A. S. Kosov, "Thermal sounding of the atmospheric boundary layer in the oxygen band center at 60 GHz," IEEE Trans. Geosci. Remote Sensing, vol. 31, no. 1, pp. 116-120, 1993.
- [3] Kadyrov, E., B. Zak, K. Stamnes, J. Simmons, A. J. Alkezweeny, and R. Storvold, "A microwave temperature profiler and a tethered sonde: a comparative study in interior Alaska," Proc. Seventh ARM Science Team Meeting, March 3-7, 1997, San Antonio, Texas (in press).
- [4] Trokhimovskiy, Yu. G., E. R. Westwater, Y. Han, and V. Ye. Leuskiy, "Air and Sea Surface Temperature Measurements Using a 60 GHz Microwave Rotating Radiometer," IEEE Trans. Geosci. Remote Sensing, (in press).
- [5] S. Twomey, Introduction to the mathematics of inversion in remote sensing and indirect measurements, New York: Elsevier, 1977, 243 pp.
- [6] Westwater, E. R., "Ground-based Microwave Remote Sensing of Meteorological Variables," Chapter 4 in Atmospheric Remote Sensing by Microwave Radiometry, Michael A. Janssen, ed., J. Wiley & Sons, Inc., 1993, pp. 145-213.

A Neural Network Algorithm for the Retrieval of Atmospheric Profiles from Radiometric Data

F. Del Frate and G. Schiavon

DISP — Università "Tor Vergata" — Via di Tor Vergata — I-00133 Roma — Italy
delfrate@utovrm.it, schiavon@disp.utovrm.it

Abstract — The potentiality of neural networks for retrieving vertical profiles of atmospheric temperature and vapor is investigated. Inputs to the net are the brightness temperatures measured by a ground-based multichannel microwave radiometer and the surface measurements of temperature and relative humidity. A neural network algorithm has been tested comparing its retrievals with those obtained by means of a linear statistical inversion applied on the same data sets. The analysis has been limited to the case of profiles with clouds to test the ability of the neural network to face non-linear problems. The technique has proven to be flexible, showing a good capability of exploiting information provided by other instruments, such as a laser ceilometer. A fault tolerance evaluation has also been considered, which showed interesting properties of robustness of the algorithm.

INTRODUCTION

The knowledge of profiles of atmospheric variables, such as temperature and water vapor is relevant to several applications in the fields of meteorology, telecommunications, radio astronomy, air traffic safety, etc.

Such profiles are commonly obtained from radiosonde measurements, launched every 12 hours from meteorological stations. However, it is often desired to have continuous measurements in real time, to follow the evolution of the state of the atmosphere. To this aim, ground-based microwave radiometry has already proven to be a powerful tool to perform continuous atmospheric sounding [1] and neural networks have been effectively used for the inversion of temperature profiles [2].

In this paper we present a new neural network based technique for the retrieval of atmospheric profiles of temperature and vapor from radiometric data. The generic atmospheric quantity $F(z)$ (temperature or vapor), discretized in N height levels, can be expressed through the following equation:

$$F(z_i) = \langle F(z_i) \rangle + F'(z_i) \quad i = 1, 2, \dots, N \quad (1)$$

where $\langle F(z_i) \rangle$ represents the *a priori* information contained into the mean climatological profile, and $F'(z_i)$, which has zero mean, the deviation from $\langle F(z_i) \rangle$. Then the eigenvectors $[u_k]$ (of elements $u_k(z_i)$) of the covariance matrix associated to the unknown vector $[F']$ (of elements $F'(z_i)$) can be calculated.

*This work has been partially supported by ASI (Agenzia Spaziale Italiana). Radiosonde data have been provided by the Meteorological Service of the Italian Air Force.

Their ensemble is a complete set of orthogonal functions, known as NOF (Natural Orthogonal Functions) [3], and the profiles of deviations can be expanded in terms of the functions of this set:

$$F'(z_i) = \sum_{k=1}^N c_k u_k(z_i) \quad (2)$$

only a few natural functions are required if we are not interested in the small-scale variations of the profile. Then, we can consider the following approximation for $F(z_i)$

$$F(z_i) \approx \langle F(z_i) \rangle + \sum_{k=1}^M c_k u_k(z_i) \quad (3)$$

with $M < N$. At this point a neural network is used for the computation of the coefficients c_k appearing in (3).

The topology of the net, which estimates the coefficients straight from the brightness temperatures and the ground measurements, is a standard feed forward perceptron with one hidden layer [4]. The activation function of each node of the perceptron has been the logistic function. The net has been trained using the back-propagation algorithm which easily run on a medium speed CPU (the complete training process never took more than few hours).

INPUT AND OUTPUT DATA

We assumed to measure the brightness temperature of the atmosphere with a ground-based microwave radiometer aiming at zenith at the following seven frequencies: 22.235, 23.87, 31.65, 51.25, 52.85, 53.85, 54.85 GHz. These values define the actual channels of a new generation radiometer for remote sensing of atmosphere designed and developed under a ESA (European Space Agency) contract by Officine Galileo (Florence, Italy) [5].

Two sets (*training* and *evaluation*) of profiles of temperature and water vapor have been considered. They belong to sets of actual radiosonde-measured profiles over various locations in Italy. These profiles have been used to compute the brightness temperatures as would be measured at the various frequencies by the described radiometer, by using Liebe's Millimeter-wave Propagation Model (MPM) [6]. To simulate noise in the radiometric channels, random fluctuations with 0.5 K standard deviation have been added to the brightness temperature data. Ground measurements of surface temperature and relative humidity have also been considered and as a further optional piece of information we used the height of the base of the cloud, which can be

measured by a laser ceilometer. Its considered vertical resolution was 15 m. To test the intrinsic ability of neural networks to face non-linear problems, we have restricted our analysis to the case of profiles with clouds, where the non-linearities of the inversion problem are stronger.

RESULTS

The *training* set of profiles has been used to evaluate the NOF and the coefficients of the corresponding expansion. These coefficients constituted the output layer of the neural network in its training phase, while the inputs were the seven brightness temperatures and the ground measurement of the variable to be retrieved. The algorithm has then been tested on the *evaluation* set. The expansion (3) has been limited to six terms ($M = 6$). The retrieval of the coefficients for more terms did not improve significantly the performances, due to noise contribution and to the poor sensitivity of the radiometers to the small-scale variations of profiles. The profiles of r.m.s. error of the estimate with the proposed algorithm are reported in Figure 1, compared to those of a linear statistical inversion (trained and tested on the same data sets). The standard-deviation curve gives the *a priori* profiling accuracy without measurements. We see that the neural network based technique displays better performances, especially for the temperature profile, where at various height levels the improvements is around 20 %.

Of particular interest is the case of the inclusion of the height of the base of the cloud, provided by the ceilometer, in the input vector. This seems to positively affect the neural estimation procedure (Figure 2), this time especially for water vapor, for which, for the lower part of the profile, the performance improvement is again around 20 %. The same doesn't occur using the linear statistical inversion which is not able to take a significant advantage of the information provided by the ceilometer as the neural network does. We may say that the neural network algorithm shows good properties of flexibility and portability being able of effectively managing the measurements provided by a combined instrumentation.

We also analyzed the algorithm from the point of view of its fault tolerance. To this aim we simulated a set of masked fault conditions which wouldn't be detected by a standard quality control procedure. In fact, some thresholds can be set to define acceptable physical ranges for the brightness temperatures measured by each channel of the radiometer. The detection of values outside these ranges can activate a recovery procedure which, for instance, makes use of an alternative algorithm for less channels, perhaps offline, or discards corrupted data. However, if the fault is such that the outputted data are within the set ranges, it can't be detected. One at the time the brightness temperature of all seven channels was then permanently set to a value within an acceptable physical range, but very close to either its upper or its lower bound, thus simulating a saturation problem. In Figure 3 we plotted the overall averaged r.m.s. error profile resulting from all the fourteen cases. It can be noted that, even though for the simulated worst cases the performances of the algorithm

are considerably degraded, they nevertheless show a much better behaviour than that of the linear statistical inversion method.

As a final step we refined the algorithm including a pruning procedure [7] for the nets that were determined after the training phase. This procedure showed that some of the connections of the nets, as defined by the initial feed-forward configuration, were completely ineffective and could be removed. We were able to eliminate more than 20 % of the initial connections with no loss of information provided by the net. We also noted that the removal didn't alter the property of robustness of the net.

REFERENCES

- [1] D.C. Hogg, M.T. Decker, F.O. Guiraud, K.B. Earnshaw, D.A. Merrit, K.P. Moran, W.B. Sweezy, R.G. Strauch, E.R. Westwater, and C.G. Little, "An automatic profiler of the temperature, wind and humidity in the troposphere," *J. Clim. Appl. Meteorol.*, vol. 22, pp. 807–831, 1983.
- [2] J.H. Churnside, T.A. Stermitz, and J.A. Schroeder, "Temperature profiling with neural network inversion of microwave radiometer data," *J. Atmos. Oceanic Technol.*, vol. 11, pp. 105–109, 1994.
- [3] A.M. Obukhov, "The statistically orthogonal expansion of empirical functions," *Translated by the American Geophysical Union*, pp. 288–291, Nov. 1960, [*Izviya Acad. Sci. USSR, Geophysics Series*, pp. 432–439, 1960].
- [4] D.E. Rumelhart, G.E. Hinton, and R.J. Williams, "Learning internal representations by error propagation," *Parallel Distributed Processing*, D.E. Rumelhart and J.L. McClelland, Eds., The MIT Press, pp. 318–362, 1986.
- [5] E. Battistelli, C. Capitani, A. Culebras, F. Del Frate, G. Schiavon, B. Arbesser-Rastburg, and J.P. Baptista, "A multifrequency mm-wave radiometer (MFR): instrument description and retrieval algorithm," *Microwave Radiometry and Remote Sensing of the Environment*, D. Solimini, Ed., VSP Press, Utrecht, The Netherlands, pp. 529–536, 1995.
- [6] H.J. Liebe, G.A. Hufford, and M.G. Cotton, "Propagation modeling of moist air and suspended water/ice particles at frequencies below 1000 GHz," *AGARD 52nd Specialists' Meeting of the Electromagnetic Wave Propagation Panel*, Palma De Mallorca, Spain, pp. 3-1–3-10, 1993.
- [7] C.M. Bishop, *Neural Networks for Pattern Recognition*, Clarendon Press, Oxford, 1995, pp. 359–362.

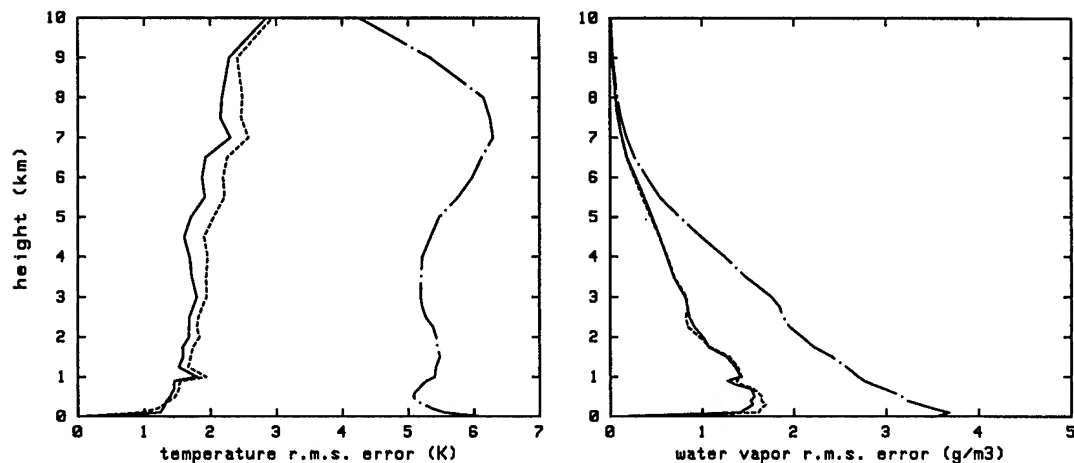


Fig. 1. Profiles of r.m.s. error of retrieved temperature (left) and vapor (right). Solid line: neural network; dashed line: linear regression; dash-dotted line: standard deviation of profiles from their means. Simulated input data: 7 brightness temperatures.

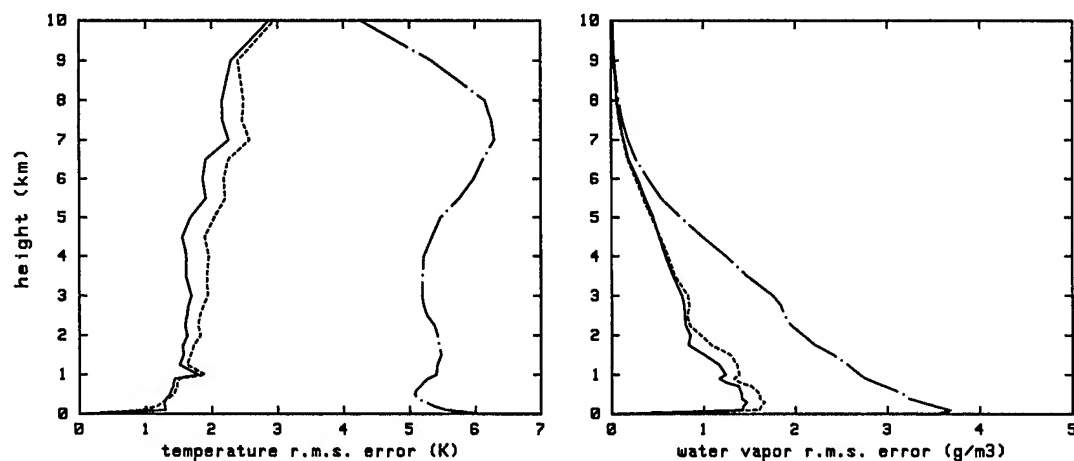


Fig. 2. Profiles of r.m.s. error of retrieved temperature (left) and vapor (right). Solid line: neural network; dashed line: linear regression; dash-dotted line: standard deviation of profiles from their means. Simulated input data: 7 brightness temperatures and height of base of cloud.

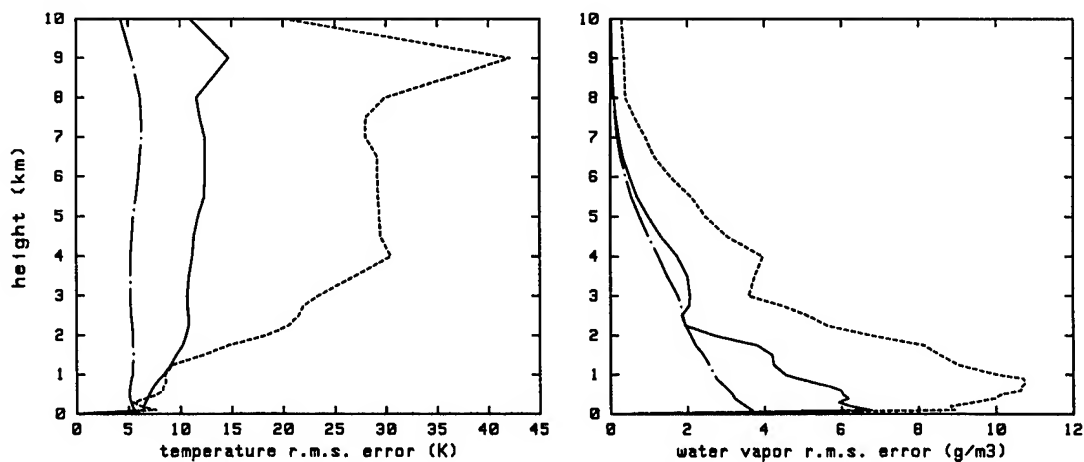


Fig. 3. Profiles of r.m.s. error of retrieved temperature (left) and vapor (right) averaged over 14 cases of fault simulation. Solid line: neural network; dashed line: linear regression; dash-dotted line: standard deviation of profiles from their means. Simulated input data: 7 brightness temperatures.

The Role of a priori Information in Designing Retrieval Algorithms for Microwave Radiometric Profiling of the Atmosphere

°°°P. Basili, °°P. Ciotti, °G. d'Auria, °F. S. Marzano, °N. Pierdicca, and °°°S. Bonafoni

°°°Inst. of Electronics, Univ. of Perugia, via Duranti 1/A1 06143, Perugia, Italy
ph.: +39755852653, fax: +39755852654, E-mail: basili@istel.ing.unipg.it

°°Dep. of Electrical Engineering, Univ. of L'Aquila, 67040 Poggio di Roio, L'Aquila, Italy
ph.: +39862434412, fax: +39862434414, E-mail: cpiero@dsiaq1.ing.univaq.it

°Dep. of Electronics Engineering, Univ. of Rome "La Sapienza", via Eudossiana 18, 00184 Roma, Italy
ph.: +39644585847, fax: +3964742647, E-mail: gioda@palatino.ing.uniroma1.it

Abstract -- This paper considers the relevance of *a priori* information in the retrieval of atmospheric temperature profiles in terms of time and space evolution models. Different retrieval algorithms (ordinary and ridge linear regressions, Kalman filtering and neural networks) are compared, when applied to both synthetic and real SSM/T measurements.

INTRODUCTION

Microwave radiometers have been used for many years, both from ground and satellite platforms, for profiling atmospheric parameters such as temperature, water vapor and even cloud liquid [1,2]. Unfortunately, the vertical resolution and the accuracy of profiles obtained from radiometric measurements by using standard linear regression retrieval algorithms do not meet the requirements of meteorological applications. On the other hand, these limits are directly related to the insufficient information content of the measurements and to the ill-posed nature of the inverse problem. A possible way to overcome these difficulties is to increase the amount of information brought by the measurements (by combining all kind of available measurements), and to take profit of the accessible *a priori* information (including temporal and spatial correlation of the atmospheric parameters), by developing retrieval algorithms making use of the entire history of measurements and, possibly, of suitable evolution models.

In this paper, we have considered the problem of atmospheric temperature profiling by satellite microwave radiometry. We start by examining the relevance of the *a priori* information about atmospheric parameters, associated to temporal and spatial evolution models, derived statistically from a database of radiosoundings (RAOB's). Then, on the basis of synthetic brightness temperatures, computed at the SSM/T frequencies from radiosounding data, we compare the performances of several retrieval algorithms: linear regressions, Kalman filtering and neural network based algorithms. Finally, we consider the application of the algorithms to SSM/T measurements.

TIME AND SPACE CORRELATIONS

Time and space correlation of atmospheric temperature profiles can be considered as useful *a priori* information to be exploited in retrieval algorithms. To assess the relevance of this information we have performed a study, based on RAOB's, to develop a simple evolution model and verify the time and space predictability of temperature profiles.

Time transition matrices

A temporal evolution model has been designed, for summer conditions in Rome (Italy), in terms of a transition matrix Φ_T according to the expression:

$$t(k+1) = \Phi_T(k,k+1) t(k) \quad (1)$$

where t is the temperature profile and the arguments $k, k+1$ define two successive instants. Matrix Φ_T has been computed by using a standard regression technique (OLS), by ridge regression (RLS) [3] or, alternatively, by OLS applied to 8 principal components of the expansion of the original 92-level temperature profiles into empirical orthogonal functions [4,5]. We considered couples of radiosoundings separated by an interval of 6 hours as described in Tab. I, where the climatological variability and the accuracy of prediction of a profile, given the profile measured 6 hours before, are also reported, in terms of profile-averaged rms error $\langle \text{RMS} \rangle$, for the training set.

The results of the test of matrix Φ_T , determined by means of the three techniques, on an independent set of profiles are reported in Tab. II. Fig. 1 shows how *a priori* information lasts for successive time intervals separated by multiples of 6 hours from the initial profile.

Tab. I. Training set, Rome, May-Sept. 1988-93

	h: 00->06	h: 06->12	h: 12->18	h: 18->24
$\langle \text{RMS} \rangle$	239 RAOB	218 RAOB	245 RAOB	266 RAOB
Clim.	3.68	3.66	3.51	3.68
OLS	1.31	1.18	1.16	1.54

Tab. II. Test set, Rome, June 13-28, 1996 (117 RAOB's)

<RMS>	00->06	06->12	12->18	18->24
OLS	2.31	2.90	2.27	2.81
RLS	1.74	2.00	1.58	2.26
OLS_PC	2.42	2.52	2.23	2.66

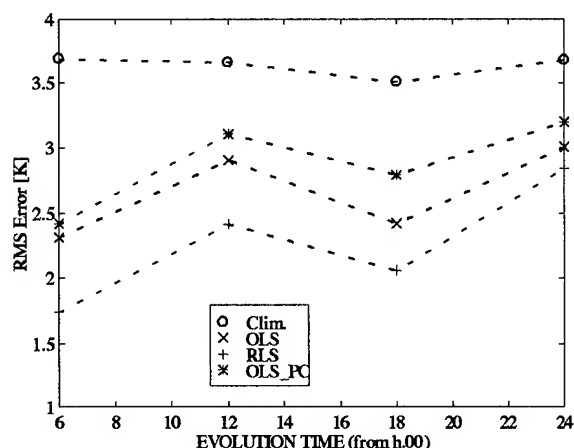


Fig. 1. Profile-averaged rms prediction error due to successive 6-hour projections, performed by differently computed matrix Φ_T .

Space transition matrices

Similarly to the temporal evolution, we have designed a spatial evolution model, still for summer conditions, in terms of a transition matrix Φ_s between couples of contemporaneous profiles of Rome and Milan. Tab. III describes the RAOB data sets and Tab. IV the accuracy of prediction when using Φ_s matrices computed by the above mentioned techniques. The accuracy of prediction of the different computation algorithms can be better appreciated in Fig. 2, where vertical profiles of rms errors are shown.

RETRIEVAL ALGORITHMS

In this section the performances of linear regressions, Kalman filtering [6,7,8] and neural network [9] based on principal components for temperature profile retrieval are

Tab. III. RAOB data set for Rome to Milan transition

	Year	Month	Launch time	RAOB's
Training	1988 & 1990	05-09	00-06-12-18	658
Test	1984	06-09	12	87

Tab. IV. Average rms errors for Rome to Milan transition

	Clim.	OLS training	OLS test	RLS test	OLS_PC test
<RMS>	3.85	2.45	2.85	2.52	2.77

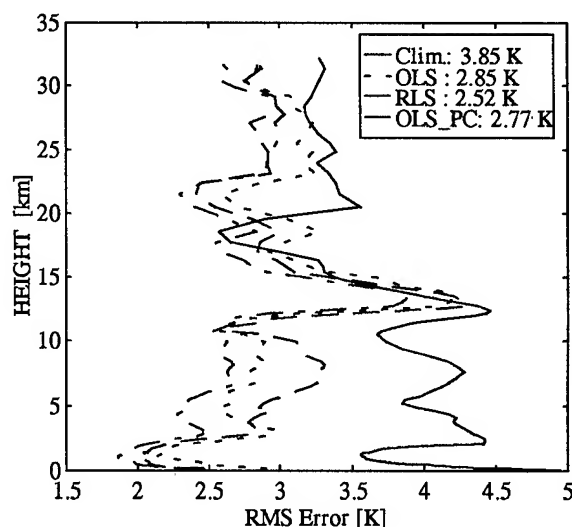


Fig.2. Vertical profiles of rms errors for Rome to Milan transition (test set)

compared on the basis of synthetic brightness temperatures, computed by means of the Liebe's model [10] at the 5 atmospheric sensing SSM/T frequencies (59.4, 58.825, 58.4, 54.9, 54.35 GHz). For the training of the algorithms we have used the RAOB's data set described in Tab. I, while the comparison was performed on the test set described in Tab. II. As an example of the results, Fig. 3 shows profiles of rms errors produced by the different algorithms, for temperature profiles measured in Rome at 0600 and 1200 GMT.

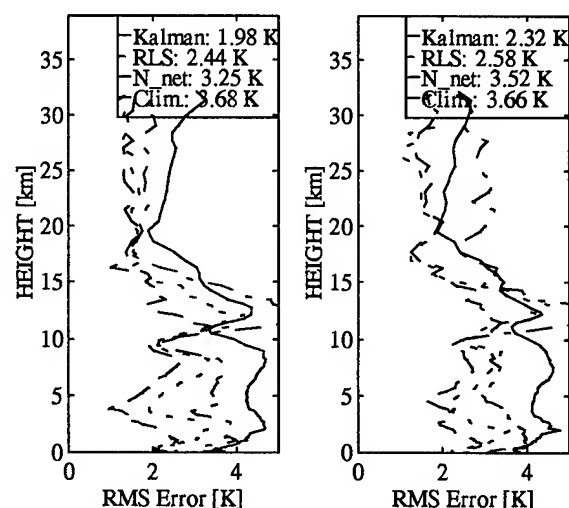


Fig.3. Profiles of rms errors, by using different algorithms, for temperature profiles measured in Rome, June 1996, at 0600 GMT (left panel) and at 1200 GMT (right panel).

APPLICATION TO SSM/T DATA

The above mentioned retrieval algorithms have been applied to a sequence of SSM/T measurements acquired over Rome and described in Tab. V.

Fig. 4 shows the results for the last two SSM/T passes of Tab V. Only RLS and Kalman estimates (that produced the most accurate profiles) are presented. It is worth mentioning that the Kalman filter has been recursively applied, starting from the first measurement of June the 11th, considering time steps of 6 hours referred to 00, 06, 12 and 18 GMT. For time steps when close SSM/T measurements were not available, only an *a priori* Kalman estimate was computed by a projection of the preceding estimate, operated by the transition matrix Φ_T .

CONCLUSIONS

The study performed in this work has shown that time and space correlations of temperature profiles are useful *a priori* information, that can be exploited when developing statistical retrieval algorithms. In particular, we have presented results relative to the temporal evolution of the atmospheric profiles and the Kalman filtering approach has

Tab. V. Data relative to SSM/T measurements over Rome used in the case study.

Day (June '96)	11	12	13	14	15
Time (GMT)	5:32	5:20	16:35	16:22	16:10
Off nadir angle.	13.6°	13.6°	13.6°	0°	13.6°

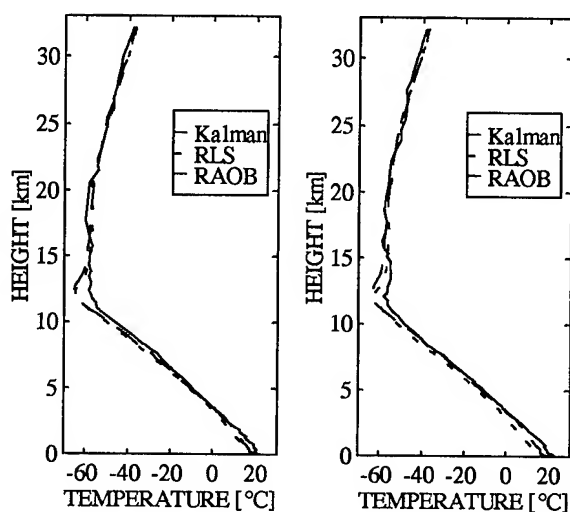


Fig. 4. Example of temperature profiles retrieved from SSM/T measurements acquired over Rome: angle = 0°, 1622 GMT, 14/6/96 (left panel); angle = 13.6°, 1610 GMT, 15/6/96 (right panel).

resulted the most performing algorithm, thanks to its recursive scheme, where information brought by the measurements and information associated to the *a priori* knowledge are blended together. As far as the neural network algorithm is concerned, even if it produced the best results (considering all the techniques) on the training set, the estimation accuracy on independent test sets has appeared poor. Finally, an application to real SSM/T measurements has confirmed the outcomes of the study performed on synthetic data.

ACKNOWLEDGEMENTS

This work has been partially supported by ASI, MURST and National Project for Antarctic Researches of CNR. The SSM/T data have been provided by DAAC of NASA's Marshall Space Flight Center (MSFC).

REFERENCES

- [1] J. I. H. Askne and E. R. Westwater, "A review of ground-based remote sensing of temperature and moisture by passive microwave radiometers," *IEEE Trans. Geosci. and Remote Sensing*, GE-24, pp. 340-352, 1986.
- [2] H. E. Fleming, N. C. Grody and E. J. Kratz, "The forward problem and corrections for the SSM/T satellite microwave temperature sounder," *IEEE Trans. Geosci. and Remote Sensing*, vol. 29, pp. 571-583, 1991.
- [3] L. J. Crone, L. M. McMillin and D. S. Crosby, "Constrained regression in satellite meteorology," *J. of Appl. Meteor.*, vol.35, pp. 2023-2035, 1996.
- [4] W. W. Cooley and P. R. Lohnes, *Multivariate Data Analysis*, New York, John Wiley and Sons, 1971, 364.
- [5] W. L. Smith and H. M. Woolf, "The use of eigenvectors of statistical covariance matrices for interpreting satellite sounding radiometer observations," *J. of Atmos. Sci.*, vol. 33, pp. 1127-1140, 1976.
- [6] K. Brammer and G. K. Siffing, *Kalman-Bucy Filters*, chapter 5, 6. Artech House, Norwood, MA, 1989.
- [7] W. H. Ledsham and D. H. Staelin, "An extended Kalman-Bucy filter for atmospheric temperature profile retrieval with a passive microwave sounder," *J. of Appl. Meteor.*, vol.17, pp. 1023-1033, 1978.
- [8] P. Basili, P. Ciotti, and D. Solimini, "Inversion of ground-based radiometric data by Kalman filtering," *Radio Sci.*, vol.16, pp. 83-91, 1981.
- [9] M. H. Hassoun, *Fundamentals of Artificial Neural Networks*, MIT Press, 1995.
- [10] H. Liebe, "MPM - An atmospheric millimeter-wave propagation model," *Int. J. IR & MM Wave*, vol. 10, pp. 631-650, 1989.

Developmental Studies for Remote and In-Situ Detection of Halogenated Compounds by Laser-Induced Photofragmentation/Fragment Detection Spectrometry

R.C. Sausa

U.S. Army Research Laboratory, AMSRL-WT-PC, Aberdeen Proving Ground, Maryland 21005

Voice: (410) 278-7070, Fax: (410) 278-7333, Email: Sausa@ARL.MIL

and

J.B. Simeonsson

University of Iowa, Department of Chemistry, Iowa City, IA 52242

Voice: (319) 353-2277, Fax: (319) 353-1270, Email: jbsimeon@blue.weeg.uiowa.edu

Abstract: The analytical capabilities of a one-color, laser-induced photofragmentation/fragment detection technique for the remote and *in situ* detection of halogenated compounds is reported. For brominated compounds, 260.634-nm laser radiation is used to fragment the target compound and also excite the characteristic Br atom photofragment by means of its two-photon $4p^4 5p^4 D^{\circ}_{3/2} \rightarrow 4p^5 \ ^2P^{\circ}_{3/2}$ transition, whose absorption cross section is estimated to be $3.8 \times 10^{-43} \text{ m}^4$. Detection is accomplished by (2+1) resonance-enhanced multiphoton ionization, as well as, laser-induced fluorescence and stimulated emission from the $4p^4 5p^4 D^{\circ}_{3/2} \rightarrow 4p^5 \ 5s^4 P_{3/2,3/2}$ transitions at 844 and 751 nm, respectively. The SE signal is distinct from the LIF signal in that it is coherent, bidirectional, and propagates coaxially with the laser beam. It is also approximately two orders of magnitude greater than the LIF signal at 844 nm because of photophysical amplification. The technique has been demonstrated for CH_3Br , CHClBr_2 , and CHBr_3 at total gas pressures of 1-760 Torr with detection limits in the parts-per-billion.

INTRODUCTION

In recent years there has been considerable interest in developing fast, sensitive, and cost effective devices for the remote and *in-situ* detection of trace volatile halogenated organic compounds. Much of this interest stems from concerns related to the safety of humans, wildlife, and the environment. Laser photofragmentation/fragment detection (PF/FD) techniques offer real-time monitoring capabilities with high sensitivity and selectivity, and can be used for either point or remote sensing [1]. The PF/FD approach is particularly useful for large molecules which are weak fluorophors or predissociate with the absorption of laser radiation. One-color PF/FD is based on the use of a single laser operating at a fixed frequency to photofragment the target compound into characteristic atomic or diatomic fragments, and to facilitate their detection by resonance-enhanced multiphoton ionization (REMPI), laser-induced fluorescence (LIF), or stimulated emission (SE). The detection of these fragments by such methods is feasible because they possess favorable combinations of strong optical transitions, and sharp, well-resolved spectral features. Reported

in this paper are studies of PF/FD techniques for measuring trace levels of brominated compounds.

RESULTS/DISCUSSION

The PF/FD approach for brominated compounds consists of the following processes: (1) precursor excitation at 260.63-nm by means of its $n \rightarrow \sigma^*$ transition, which is localized on the Br atom; (2) photofragmentation, yielding Br atoms in their ground ($^2P^{\circ}_{3/2}$) and first excited ($^2P^{\circ}_{1/2}$) states; and (3) Br-atom detection by (2+1) REMPI using miniature electrodes, and by LIF or SE using a photomultiplier tube coupled to a monochromator or narrow band interference filter. The precursor excitation and photofragmentation processes, and the Br excitation process occur at the same laser frequency and in the duration of the laser pulse, approximately 20 nsec. The SE signal, unlike the LIF signal, is coherent, bidirectional, and propagates coaxially with the laser beam. Also, it is approximately 100 times larger than LIF because it is photophysically amplified.

An estimate of the magnitude of the two-photon absorption cross section for the Br $4p^4 5p^4 D^{\circ}_{3/2} \rightarrow 4p^5 \ ^2P^{\circ}_{3/2}$ transition is obtained by the following expression [2]:

$$\sigma_0^{(2)}(\omega) = \frac{\pi e^4}{8\epsilon_0^2 m^2 c^2} \frac{\omega_l^2}{\omega_1 \omega_2} \frac{f_1 f_2}{(\omega_1 - \omega)^2} \quad (1)$$

where e is the electronic charge (C), m is the mass of the electron (kg), ϵ_0 is the permittivity of free space ($\text{C}^2/(\text{N m}^2)$), c is the speed of light (m/s), ω_i ($i=1,2$) is the angular frequency of the radiation (s^{-1}), and f_i ($i=1,2$) is the absorption oscillator strength of the strongest transitions between the appropriate states. Substitution of the appropriate energies and oscillator strengths ($f_1=0.199$, $f_2=0.513$) into (1) yields a value of $3.8 \times 10^{-43} \text{ m}^4$. For comparison, McIlrath et al. have reported the two-photon cross section for O atoms at 226 nm as $7.0 \times 10^{-44} \text{ m}^4$ [2]. This value is in good agreement with those predicted by more rigorous quantum mechanical methods which include contributions from multiple intermediate states. The above expression is an approximation that is effective when the two-photon cross section is dominated by a single intermediate

state. Lesser contributions by additional intermediate states are best accounted for by explicit quantum mechanical approaches, although such calculations require extensive computational capabilities.

Presented in Fig. 1 are REMPI, LIF, and SE excitation profiles of Br from CHClBr_2 at 100 Torr and 1 atm. In the case of each technique, the profile is broadened at 1 atm. The broadening is greatest for the ionization and least for the SE profiles. The narrowness of the SE profile relative to the LIF and ionization is expected due to the exponential gain of the medium, which leads to a spectral narrowing of the profile. The reason for the difference in the widths of the LIF and ionization profiles is as yet unknown.

The PF/REMPI signal dependence on the laser intensity for CH_3Br is nonlinear, suggesting that increases in the laser intensity could lead to significant increases in the Br ionization signal. As the excitation of the Br atoms is a (2+1) REMPI process, the power dependence might be expected to be as high as 4. A plot of the Br ion signal (generated from CH_3Br) as a function of the laser intensity at 260.634 nm reveals a power dependence of 1.5, indicating the possible saturation of at least one of the photoexcitations of the precursor molecule and/or the Br fragment. A power dependence study of 1.5 was also observed by PF/LIF, which similarly indicates partial saturation of one of the photoexcitations of the PF/LIF processes.

Shown in Fig. 2 are the Br signal dependencies for the REMPI, LIF, and SE techniques as functions of the total cell pressure. It is important to note that for each pressure indicated

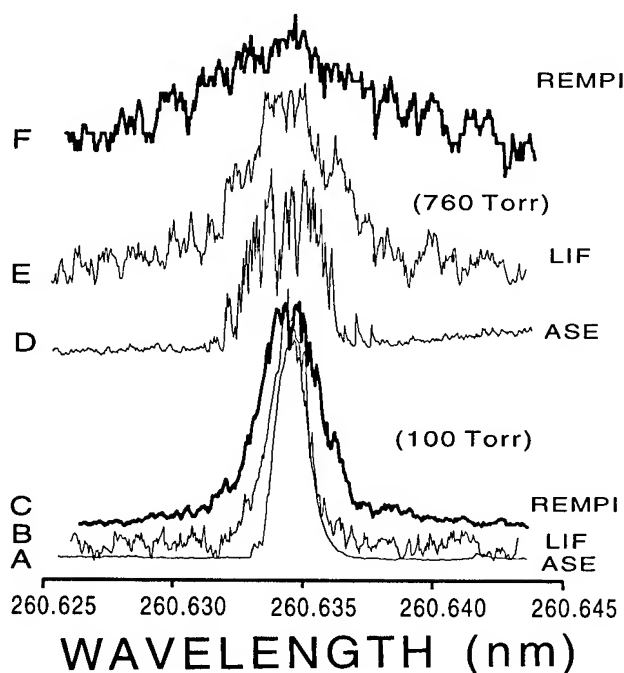


Fig. 1. Normalized excitation profiles of Br atom generated from CHClBr_2 at 100 and 760 Torr for PF/REMPI, PF/LIF, and PF/SE.

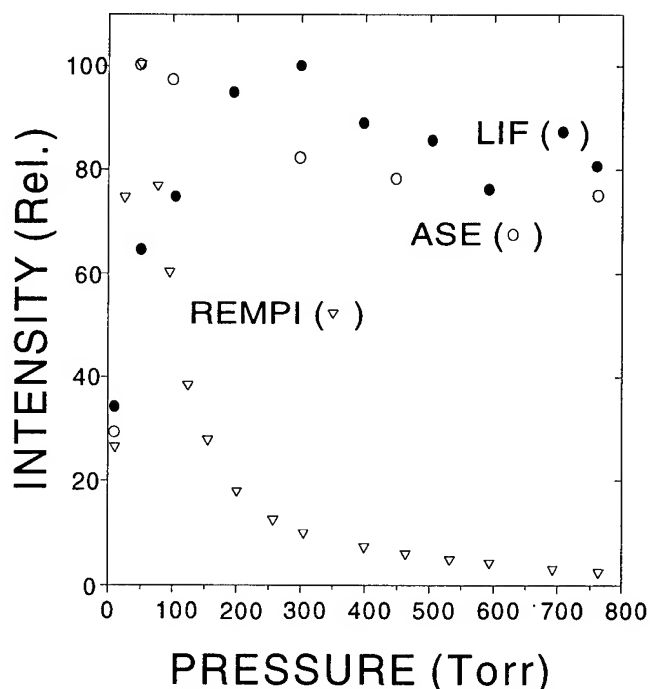


Fig. 2. Pressure dependence of normalized signals for PF/REMPI (open inverted triangles), PF/LIF (filled circles) and PF/SE (open circles) techniques.

in the figure, the mixing ratio of sample is constant, i.e. the sample (analyte) density changes with the pressure. It is observed that increased pressures reduce the sensitivities, although pressure influences the individual techniques differently. In the case of ionization, the signal is at a maximum at relatively low pressures (near 50 Torr) and then falls rapidly at higher pressures. The increase in signal at low pressures is believed to be due to charge amplification by the buffer gas, whereas its decrease at higher pressures is due to combined effects of quenching and transfer losses of the ions/electrons to the collection electrodes. In the cases of LIF and SE, it is seen that the pressure dependencies of these two techniques are similar, although the SE signal shows a steeper rise at lower pressures and faster decay at higher pressure than the LIF. The different pressure dependencies for LIF and SE are related to the effects of collisions on the SE lineshape, where increased collisions broaden the linewidth and reduce the gain.

Detection limits ($S/N=3$) of CH_3Br , CHBr_3 and CHClBr_2 are presented in Table I. Noise in this study is defined as the standard deviation of 16 independent measurements of the background signal in N_2 measured off resonance at 260.64 nm. As shown in Table I, high sensitivities in the ppb were observed using the PF/REMPI technique for CHClBr_2 , CHBr_3 , CH_3Br , with the first two compounds having a sensitivity of approximately 60 times greater than the last. Apparently, the efficiency in the photodissociation pathways leading to the formation of Br is better for CH_3Br and CHBr_3 than for CHClBr_2 . In addition, the stoichiometry favors the production

Table I. Detection limits (ppb) of CH₃Br, CHBr₃, and CHClBr₂ using ~ 100μJ of 260.635-nm radiation.

	PF/REMPI	PF/LIF ^a	PF/SE ^b
CHBr ₃	2.5	350	20
CHClBr ₂	2.2	250	10
CH ₃ Br	130	-	-

^a Detection at 5 cm from sample
^b Detection at 2 m from sample

of more Br atoms on a per mole-atom basis for CHClBr₂ and CHBr₃ than the singly substituted CH₃Br. For a comparison of our PF/REMPI results, Arepalli et al. have also used this technique and estimated a detection limit of 0.4 ppb for Br atoms as generated from HBr and other compounds [3]. It should be noted, however, that the HBr (and other species) was sampled in pure form and at much lower pressures (mTorr) than were used in the present studies, and extrapolation of their results to dilute samples in a buffer gas matrix is difficult. Nonetheless, in both studies the absolute number of Br atoms detected at the LOD are very similar (on the order of 10⁴-10⁶).

Table I also reveals that the sensitivities obtained from the PF/REMPI approach are two and four orders of magnitude greater than the LIF and SE techniques, respectively. The high sensitivities achieved using the PF/REMPI approach demonstrates the strong potential of the method, and suggests the approach will be most effective when efficient fragmentation of the parent molecule is assured. For fluorinated and chlorinated compounds, however, this may only be possible by using a separate fragmentation source, that is, a dual laser approach. The PF/REMPI approach is susceptible to high background noise as well as the highest degree of interference (due to nonresonant multiphoton ionization). Experimentally, it was observed that the magnitude of the background near 260 nm represented as much as 50% of the total ionization signal when the laser is in resonance with the Br transition, indicating that alternative ionization processes originating from parent molecule and/or other daughter fragments are operative. For this reason, the technique appears to be limited to relatively low laser pulse energies. It should be possible to eliminate all the ionization interferences by using mass spectrometric detection. However, due to the limited sample throughput of most spectrometers, these systems may suffer lower sensitivity, which would limit their applicability to sample environments that require mass selectivity.

The PF/LIF approach as implemented here has lower sensitivity relative to PF/REMPI, as shown in Table I. This difference in sensitivity results primarily from the high background and laser scatter inherent in these PF/LIF measurements, and is not necessarily characteristic of the

technique. The analytical capability of this approach can be improved, however, by better system design, i.e. the addition of light baffles, signal collection optics, and/or spectrometer.

As shown in Table I, the PF/SE technique has the lowest sensitivity. However, it also has a strong analytical potential. Unlike REMPI and LIF, the background noise of the SE approach is low and can be made even lower with appropriate shielding of the detector. Furthermore, since the signal is coherent and the background emission is incoherent, increasing the laser intensity to saturation conditions will greatly enhance the sensitivity without compromising the signal-to-noise ratio. The SE signal has other attributes that are unique due to its coherent nature. While the SE signal is coaxial with the laser, it can easily be separated with filters or prisms and, as it is bidirectional, it only requires "one window access" to the sample environment. This has important implications for accessing remote or hostile environments and also for coupling to fiber optic probes. For these reasons, it is believed that the SE technique potentially has great utility for Br atom monitoring applications.

CONCLUSION

One-color, laser-induced photofragmentation/fragment detection spectrometry at 260.634 nm using ionization, fluorescence and stimulated emission techniques have been employed to detect brominated compounds under ambient conditions. These techniques have been evaluated as to their relative analytical capabilities for trace level determinations. The PF/REMPI technique is demonstrated as having the highest sensitivity with detection limits for CHBr₃ and CHClBr₂ in the low ppb range. Detection limits for the LIF and SE approaches are in the ppm range for the same compounds. Much higher sensitivities are projected with an increase in laser energy and improved system design. It is anticipated that the SE method will have several advantages over conventional methods for rapid and convenient measurements of ppm levels of Br atoms in gaseous environments.

ACKNOWLEDGMENTS

The authors thank Ms. Joyce E. Newberry and Dr. John Vanderhoff (ARL) for their technical assistance and valued discussions.

REFERENCES

- [1] J. Simeonsson and R. Sausa, *Applied Spectroscopy Reviews*, **31(1&2)**, 1, 1996, and references therein.
- [2] T.J. McIlrath, R. Hudson, A. Aikin and T.D. Wilkerson, *Appl. Optics* **18**, 316, 1979.
- [3] S. Arepalli, N. Presser, D. Robie and R.J. Gordon, *Chem. Phys. Lett.* **117**, 64, 1985.

Conference Author Index

A

Abdou, W. 1743
 Abenant, E. 2015
 Abou-El-Magd, A.M. 1458
 Adair, M. 380
 Adam, N. 1341
 Adamovic, M. 1066, 1382
 Adragna, F. 1533
 Adrian, V. 1150
 Afifi, M.S. 133
 Ahmad, S. 1418
 Ahmed, I. 1627
 Aiazzi, B. 1054, 1990,
 Ainsworth, T.L. 1371, 1407, 1716
 Al-Ghamdi, A.G. 133
 Alba, P.S. 1990
 Aler, J. 1015
 Alexandrov, V. 1681
 Alparone, L. 1054, 1184, 1990, 2066
 Alpers, W. 1162, 1518, 1521, 1527
 Alumbaugh, D.L. 929, 933
 Anbazhagan, S. 29
 Andreadis, A. 1993
 Andrianasolo, H.H. 1627
 Andrick, B. 1947
 Angino, G. 15, 374, 990
 Antar, Y.M.M. 1594
 Antonischki, G. 1805, 1820
 Aoki, S. 1582
 Arai, K. 553
 Arkhipkin, O. 281
 Armand, N.A. 347, 1953
 Arnold, D.V. 386
 Arthern, R.J. 1823
 Askari, F. 1521
 Askne, J. 793, 800
 Asmus, V. 1681
 Aspinall, R.J. 269
 Atkinson, N.C. 1395, 2011
 Auer, T. 1224
 d'Auria, G. 2087, 2100
 Awaka, J. 1633
 Axelsson, S.R.J. 79, 317

B

Bachelier, E. 1606
 Baerwald, W. 1022
 Bai, Y. 1938
 Bakar, S.B.A. 1069
 Baker, J. 1796
 Bakhanov, V.V. 350
 Balababa, L. 1084
 Baldina, E.N. 347
 Baldini, L. 1454
 Baldy, S. 6
 Bali, S. 948
 Bamler, R. 865, 1710
 Bang, K. 237
 Banik, B. 1066, 1382
 Baquero, M. 1871
 Barbieri, K. 1923
 Barczy, J.F. 784, 787
 Barducci, A. 888
 Baraldi, A. 67
 Barni, M. 1184
 Baronti, S. 1054, 1990, 2066
 Bartoloni, A. 325, 1908, 1853
 Basili, P. 2087, 2100
 Bauer, P. 1275
 Beaudoin, A. 784, 787
 Benediktsson, J.A. 501, 913, 1026, 1669
 Benelli, G. 1993
 Benger, S.N. 272
 Bennett, J.C. 1211
 Benz, U. 322, 2024
 Berendes, T. 32
 Bergen, K.M. 1072
 Berthod, M. 1347
 Bertoia, C. 402
 Bessafi, M. 6
 Betti, M. 1184
 Betty, C.L. 1600
 Beyth, M. 743
 Bhatia, R.C. 1129
 Bhogal, A.S. 670, 677
 Bicheron, P. 165, 556
 Bickel, D.L. 1545
 Bittner, M. 1495
 Blanchard, A.J. 643
 Blindow, N. 227
 Bobylev, L.P. 830, 1681
 Bodechtel, J. 533, 743
 Boechl, R. 1022
 Boehnke, K. 1823, 1826
 Boerner, W.M. 1401, 1591
 Bogatyrev, S.D. 350
 Boisvert, J. 1376
 Bolen, S. 1114
 Bonafoni, S. 2100
 Bonn, F. 122, 189
 Borderies, P. 1606
 Borgeaud, M. 898, 1606
 Borri, G. 1054
 Bostater, Jr., C. R. 881
 Botti, J.A. 692
 Bradley, Q. 677
 Bradshaw, B. 1766
 Brandfaß, M. 2024
 Braumann, H. 1935
 Breit, H. 465
 Brennan, K. 1624
 Breton, E. 652
 Brewster, A. 1766
 Bricaud, A. 825
 Bringi, V.N. 954, 1114, 1458
 Brisco, B. 1376, 1430
 Browell, E.V. 1969
 Brown, C.G. 353, 1847
 Bruegge, C. 1743
 Brummer, B. 1162
 Bruniquel, J. 1044, 1560, 1868
 Brunzell, H. 1285

Bruzzzone, L. 764, 1202
 Buckley, J.R. 1015
 Bullock, M.E. 1350
 Burgess, D.W. 1075
 Burnett, C.N. 84
 Buscaglione, F. 18
 Busu, I. 1398

C

Cabarrocas, D. 2069
 Caetano, M. 240, 680
 Calahan, R.F. 1444
 Caldararu, F. 607
 Caldararu, M. 607
 Calhoun, J. 922
 Calkoen, C. 1320
 Calvet, J-C. 1090
 Campagnolo, M.L. 680
 Campbell, W. 819
 Caraglio, Y. 784
 Carla, R. 2066
 Carswell, J.R. 1001
 Casanova Roque, J.L. 87
 Casarano, D. 719, 898, 1272
 Casciati, F. 113
 Casey, K. 2008
 Castagnas, L. 784
 Castanie, F. 293
 Castel, T. 784, 787
 Cavalieri, D.J. 1291
 Ceballos Silva, A.P. 2041
 Ceccato, P. 1569
 Celani, C. 325
 Cervino, M. 1908
 Chae, H.S. 517, 528
 Chan, H.L. 484, 487
 Chan, P. 1255
 Chan, T-K. 1138
 Chandrasekar, V. 954, 1114, 1458
 Chane-Ming, F. 581
 Chang, A.T.C. 625
 Chang, L.A. 1969
 Chang, L.Y. 1424
 Chang, P. 1009
 Chanzy, A. 1090
 Chapman, B. 104
 Charlebois, D. 670
 Chellappa, R. 171
 Chen, A.J. 1424
 Chen, C.F. 1424
 Chen, C.H. 1190
 Chen, C.T. 1199
 Chen, F-C. 1474
 Chen, J. 1862
 Chen, J.M. 165
 Chen, K-S. 806, 1199, 1208, 1365,
 1368, 1424
 Chen, P. 963, 1084, 2038
 Chen, S. 938
 Chenierie, I. 1606
 Cheng, P. 839

Cherniakov, M. 1282
 Chesters, D. 984
 Chew, W.C. 938, 945, 1474
 Chiu, T. 901
 Choi, H-K. 136
 Choi, K-H. 524
 Choi, S.D. 1492
 Chou, J. 32, 1760, 1911
 Christopher, S.A. 32, 116, 1923
 Chu, A. 1358
 Chuah, H.T. 1069, 1421, 1427
 Chuah, T. 996
 Chubb, S.R. 1317, 1521, 1692
 Chuideri, A. 1663
 Cihlar, J. 165
 Ciotti, P. 2087, 2100
 Clark, B. 1947
 Clemente-Colon, P. 505
 Cloude, S.R. 1411, 1591, 1926, 1932
 Cloutier, C. 1382
 Colandrea, P. 1853
 Coll, C. 1233
 Collaro, A. 433
 Coltelli, M. 1022
 Comiso, J.C. 857, 1300
 Conel, J.E. 1743
 Connors, V.S. 116
 Console, E. 646
 Cook, M.S. 1814
 Cooley, J.H. 1666
 Cooley, T. 1654
 Cooley, T.W. 1666
 Cooper, A.L. 1317, 1692
 Coppo, P. 904
 Cornillon, P. 2008
 Corsini, G. 1536
 Costamagna, E. 655
 Coster, W. 2024
 Cottis, P.G. 1379
 Cracknell, A.P. 1398
 Crawford, M.M. 457, 667
 Croci, R. 18
 Crowther, P. 328, 1689
 Cubero-Castan, E. 2060
 Cuccoli, F. 1975
 Cumming, I. 725, 731, 1704

D

Dai, X. 243, 1029, 1763
 Daida, J.M. 1808, 1811
 Daley, N. 670, 677
 Dall, J. 1018
 D'Amelio, C. 1853
 Dams, R.V. 1350
 Danduran, P. 1678
 Daniels, D.J. 1278
 Dano, E. 1168
 Dargaud, G. 833
 Darovskikh, A. 1675
 da Silva, J.C. 1335
 Datcu, M. 255, 258, 411, 616, 767, 2031

Davidson, G.W. 865
 Davis, A. 1444
 Davis, C.H. 397
 Davis, H.B. 692
 De Carolis, G. 719, 862
 De Grandi, G. 1038, 1047, 1371, 1414, 1725, 1890
 Dech, S.W. 1495, 1505
 Deering, D. 165, 1787
 Del Frate, F. 2097
 Dell'Acqua, F. 1463
 Dellepiane, S.G. 737, 907, 1174
 Demarez, V. 1566
 Deng, Y. 367
 Derksen, C. 1672
 Derooin, J-P. 1612
 Desjardins, R. 207, 252
 Desnos, Y-L. 722
 Diani, M. 1536
 Dias, J.M.B. 773
 Dinardo, S.J. 1466
 Dinesh, M.S. 521
 Ding, K.H. 919
 Dionisio, C. 987
 Dmitriev, W.V. 1480
 Dobson, M.C. 119, 1072, 1180, 1621, 1719
 Doi, K. 1582
 Donald, G.E. 275
 Donato, T. 1521
 Dong, Y. 891, 1057, 2054
 Donlon, C.J. 2002
 Donnelly, W.J. 1001
 Douglass, A.R. 542
 Downey, I.D. 370, 1569
 Dozier, J. 628, 1451
 Du, L.J. 1407
 Ducrot, D. 1566
 Dupont, S. 1347
 Durden, S.L. 1466, 1639, 1642
 Dymond, J.R. 1075

E

Early, D.S. 1838, 1844
 Eck, T. 165
 Ecklund, W.L. 1753
 Edelstein, W.N. 1466
 Edwin, J.M. 29
 Efremenko, V.V. 1953
 Eibert, T.F. 227
 Eineder, M. 1341
 El-Khattib, H.M. 197
 El-Mowelhi, N.M. 197
 El-Salam, A.A. 197
 Emery, W.J. 1502, 1509, 2002
 Emmett, C.F. 1557
 Endoh, T. 414
 Engdahl, M. 1081
 England, A.W. 1096
 Engman, E.T. 1093, 1269
 d'Entremont, R. 1220

Erbe, E. 625
 Erickson, J. 1654
 Ermakov, S.A. 1335, 1530
 Escalante, B. 38
 Espedal, H.A. 1165, 1168
 Esteban, H. 1871
 Estevan de Quesada, R. 1361
 Evans, D.L. 1734
 Evans, R. 2008
 Evtuchenko, A. 1126
 Ewe, H.T. 1069, 1427

F

Facheris, L. 1975
 Fairall, C.W. 2090
 Fedor, L.S. 1001
 Feng, Y. 216
 Ferger, O. 21
 Fermont, A. 95
 Fernandez, D.M. 1808, 1811, 1814
 Ferrazzoli, P. 1618
 Fetterer, F. 402
 Fischer, H. 1686
 Fischer, K. 1808
 Fishtahler, L.E. 1249
 Fjortoft, R. 2060
 Flasse, S.P. 1569
 Fleig, A. 171
 Fleury, D. 1678
 Flood, B. 1214
 Floury, N. 784, 787, 1560, 1868
 Fornaro, G. 433, 451, 878
 Forster, B. 891, 1057, 1576, 2054
 Fortuny, J. 1871
 Foster, J.L. 625
 Franceschetti, G. 433, 878, 1701
 Franchois, A. 925
 Fraser, D. 1657
 Frasier, S. 1539, 1972
 Freeman, T. 104
 Frei, M. 743
 French, J. 1460
 Frisch, A.S. 2090
 Frison, P-L. 1832
 Frolind, P-O. 436, 797, 1214
 Fuchs, J. 714
 Fujimura, S. 658, 975
 Fujino, Y. 1941
 Fujisaka, T. 966
 Fujita, M. 1941
 Fujiwara, S. 1585
 Fukuda, S. 1187
 Fullerton, K. 1660
 Fung, A.K. 702, 1144, 1308, 1365, 1376, 1600
 Fung, T. 836
 Furseth, D.A. 1063
 Furuya, K. 481
 Fusina, R.A. 1317

G

Gabella, M. 3
 Gader, P. 643
 Gage, K.S. 1753
 Gaillard, C. 122, 1787
 Gaiser, P.W. 1009
 Gaitley, B.J. 1743
 Galati, G. 833, 1123
 Galloway, J. 1012, 1460
 Gamba, P. 113, 655, 1463
 Garcia, F. 38
 Garello, R. 1515, 1678, 2069
 Garzelli, A. 1184, 1993
 Gasiewski, A.J. 1001, 1006
 Gastellu-Etchegorry, J.P. 1566, 1787
 Gautam, N.C. 1775
 Gelautz, M. 468
 Georges, T.M. 1802
 Ghinelli, B.M.G. 1211
 Gibeaut, J.C. 457, 667
 Giorgi, F. 113
 Giorgini, F. 737
 Giros, A. 652
 Giuli, D. 1454, 1975
 Goblirsch, W. 439
 Goetz, A.F.H. 1385
 Gogineni, S.P. 996, 1305
 Goh, K.C. 813
 Goldblat, V.Y. 1530
 Gong, P. 895
 Gonzales, A.E. 246
 Gonzalez-Alonso, F. 87
 Goodberlet, M. 1012
 Goodenough, D.G. 84, 664, 670, 677
 Goodison, B. 1672
 Gorishnya, Y.V. 1105
 Goto, S. 210
 Gough, P.T. 471, 1588
 Gowda, K.C. 521
 Grandell, J. 622
 Greidanus, H. 1078, 1320
 Grim, R.J.A. 1078
 Grinder-Pederson, J. 1018
 Grischenko, V.D. 1681
 Grunes, M.R. 1038, 1716
 Guerreiro, L. 1618
 Guglielmi, V. 293
 Guillevic, P. 1787
 Guneriussen, T. 631, 634
 Guo, H. 746, 749
 Guo, Y. 731, 845
 Gurgel, K-W. 1805, 1820
 Gustavsson, A. 797, 1214
 Gutierrez, R. 457
 Gutman, G. 1252
 Guzzi, R. 1908
 Gwyn, J. 128

H

Ha, Y-L. 524
 Haboudane, D. 128, 189

Haddad, Z.S. 1639, 1642
 Haefner, H. 640
 Hagen, J.O. 634
 Haimov, S. 1460
 Hall, D.K. 619, 625
 Hallikainen, M. 622, 637, 803, 1081, 1314, 1597, 1874
 Haltrin, V.I. 296, 299, 595
 Hamran, S-E. 634
 Hamre, T. 1681
 Han, Q. 1760, 1911
 Han, Y. 2093
 Hanada, T. 1486
 Hanado, H. 1645
 Hansen, P.E. 1808, 1811
 Hansen, V. 227
 Hanssen, R. 1710
 Hara, Y. 966, 1392
 Hardin, P.J. 511, 1557, 1563, 1835
 Harlan, J.A. 1802
 Hartnett, J. 328
 Hatzopoulos, J.N. 1920
 Hausknecht, P. 1022
 Hauteceur, O. 556, 1230
 Hawkins, D.W. 471
 Hawkins, R.K. 1066, 1382
 Hay, G.J. 84, 664
 He, Y. 356
 Heer, C. 990, 993
 Heidebrecht, K.B. 1385
 Heikkonen, J. 1660
 Hellmann, M. 1411
 Hellsten, H. 797, 1214
 Helmlinger, M.C. 1743
 Heng, A. W-C. 734
 Heng, W-C. 1518
 Hennings, I. 1320
 Hensley, S. 628, 1358
 Hensley, W.H. 1545
 Herland, E-A. 1344
 Herries, G.M. 1032
 Herzog, A. 951
 Heygster, G. 58, 61, 1675
 Hiernaux, P. 1832
 Hill, M.J. 269, 275
 Hilliard, L. 984
 Hilmarsson, O. 1026
 Hirosawa, H. 1187
 Ho, A.T.S. 1996
 Hock, L. 1512, 1850
 Hodges, J. 1227
 Hoeben, R. 1365, 1368
 Hoekman, D.H. 1078, 1728, 1731
 Holden, H. 610, 809, 885
 Holecz, F. 448, 1929
 Holloway, P.E. 1331
 Homer, J. 1579, 2063
 Honda, K. 1829
 Hong, D. 237
 Hong, S. 89, 92, 1793
 Hook, S. 1233
 Hope, A. 1766

Horie, H. 1645
 Horn, R. 1022
 Hornbostel, A. 1126
 Horrell, J. 2015
 Hoyano, A. 1239
 Hsieh, C-Y. 702
 Hsu, A. 1266, 1269
 Hsu, M-K. 70, 806
 Hu, B. 1220
 Huadong, G. 50, 1978
 Huang, C. 171
 Huang, K-Y. 1196
 Huang, S. 1999
 Huang, X. 249
 Huang, Y. 536
 Huete, A.R. 98, 341, 1966
 Hugh, Q. 128
 Huimin, P. 1477
 Hunewinkel, T. 417
 Hunt, B.R. 1588
 Hwang, L. 1996
 Hwang, P.A. 1156, 1171
 Hyman, A. 1227
 Hyyppa, H. 1081
 Hyyppa, J. 1081

I

Ignatov, A. 1252
 Iguchi, T. 1111, 1117, 1633, 1636
 Iino, A. 1239
 Iisaka, J. 916
 Im, E. 1642
 Imanaka, M. 1899
 Imhoff, M.L. 1624
 Impagnatiello, F. 15, 374
 Inanaga, A. 125, 969
 Inggs, M. 490, 2015
 Ingimundarson, J.I. 913
 Inkinen, M. 1081
 Iodice, A. 1701
 Irion, Jr., H.G. 1132
 Irisov, V.G. 2093
 Irisov, V.I. 1001
 Isaac, M. 613
 Ishida, H. 9
 Ishimaru, A. 1138
 Ismail, S. 1969
 Israelsson, H. 800, 1878
 de Iulis, M. 1275
 Ivanov, A.Y. 539
 Iwamoto, M. 966

J

Jackman, C.H. 542
 Jackson, T.J. 1093, 1099
 Jacobs, G.A. 1156, 1171
 Jaja, J. 174
 Jansen, R.W. 1317
 Jefferies, W.C. 1063
 Jenkins, A.D. 1165

Jensen, R.R. 1557, 1563, 1835
 Jensen, V. 1165, 1698
 Jenstrom, D. 984
 Jezek, K. 1305
 Jha, R. 1382
 Jia, X. 778
 Jiang, J. 392, 1609, 1981
 Jiang, X. 816
 Jiang, Z. 474
 Jianguo, N. 55
 Jin, M.Y. 477
 Jin, Y-Q. 405, 567, 2050
 Johannessen, J.A. 1153, 1165, 1168
 Johannessen, O.M. 1153, 1165, 1168,
 1681, 1698
 Johnsen, H. 631
 Johnsen, K-P. 1675
 Johnson, D.R. 688, 699
 Johnson, P.E. 1847, 1856
 Jonsson, T. 797, 1214
 Jung, I-S. 524, 584
 Jyo, Y. 1205

K

Kadygrov, E.N. 2093
 Kahn, R. 698, 1743
 Kalb, M. 688, 699
 Kalluri, S.N.V. 171, 174
 Kalma, J.D. 1263
 Kam, S.P. 1084, 2038
 Kamble, V.P. 1129
 Kamiya, Y. 1392
 Kanagaratnam, P. 1305
 Kanellopoulos, I. 1660
 Kanellopoulos, J.D. 1379
 Kanevsky, M.B. 1530
 Kao, M. 377
 Karaev, V.Y. 1530
 Karlinsky, T.W. 386
 Kasilingam, D. 35, 1193, 1512, 1524,
 1527, 1695, 1850, 1862
 Kato, Y. 481
 Kattenborn, G. 1087
 Kattleman, R. 1451
 Kaufmann, H. 743
 Kawabata, K. 966
 Kawai, Y. 2005
 Kawamura, H. 1499, 1865, 2005, 2075
 Kawanishi, T. 1630
 Kawata, Y. 210, 1790, 1899, 1902, 2084
 Kazakov, V.I. 350
 Kellndorfer, J. 1180, 1719
 Kelly, R. 1460
 Kemarskaya, O.N. 350
 Kemppinen, M. 1224
 Kennedy, K.D. 957
 Kennedy, W.D. 938
 Kerr, Y. 1090
 Khazenie, N. 685
 Khoo, V. 35, 127, 151, 845, 848, 1512,
 1695, 1850

Khorram, S. 243, 1029, 1763, 1769
 Kijashko, S.V. 1335
 Kim, J. 89
 Kim, K-O. 24, 584
 Kim, K.E. 528
 Kim, K.H. 331
 Kim, K.S. 200
 Kim, M.S. 200, 850
 Kim, S.J. 517
 Kim, T. 1492
 Kim, Y. 1358, 1404
 Kimura, F. 1865
 Kimura, H. 442
 Kindel, B. 1385
 Kitiyakara, A. 1639
 Kiyasu, S. 975
 Kjellgren, J. 1962
 Klein, A.G. 619
 Kliche, D.V. 32, 116
 Kloster, K. 1681
 Knapp, E. 1001
 Knight, D. 809
 Knizhnikov, Y.F. 347
 Knulst, J.C. 1168
 Kobayashi, T. 570, 1389
 Koike, K. 1582
 Kojima, M. 1630
 Komiyama, K. 481
 Kondo, N. 1392
 Kong, J.A. 787
 Koponen, S. 1314
 Korsbakken, E. 1153, 1165
 Koskinen, J. 44, 637
 Kostina, V.L. 2047
 Kozu, T. 1111, 1117, 1630, 1636
 Kravtsova, V.I. 347
 Kriebel, S.K.T. 1035
 Krishnan, P. 598
 Krovotyntsev, V.A. 1681
 Kryvobok, O. 2044
 Kubo, M. 414
 Kudo, J-I. 1499
 Kuga, Y. 1138, 1141
 Kumagai, H. 1111, 1633
 Kuo, K-S. 32, 1917
 Kuroiwa, H. 1630
 Kurvonen, L. 622, 1874
 Kusaka, T. 210, 972, 1902, 2084
 Kusanobu, S. 649
 Kutuza, B.G. 1126
 Kuze, H. 55
 Kwarteng, A.Y. 119
 Kwok, L.K. 151, 213, 249, 454, 813,
 1257, 1548
 Kwok, R. 505

L

Ladd, D.N. 1648
 Lahtinen, J. 1597
 Laing, T.W. 341
 Lakshmi, V. 1102

Lam, J.H. 380
 Lanari, R. 433, 451, 878
 Lang, R. 925
 Larsson, B. 797, 1214
 Lau, W.K.M. 1438
 Laurore, L. 21
 Lawrence, G. 1350
 Lawrence, W.T. 1624
 Le Caillec, J.M. 1515
 Le Toan, T. 719, 784, 787, 898, 1272,
 1560, 1606, 1868
 Le Vine, D.M. 377
 Leberl, F. 468
 Leblanc, S.G. 165
 Ledebuer, W.C. 1743
 LeDrew, E. 610, 809, 885, 1672
 Lee, B.G. 331
 Lee, C.W. 92
 Lee, H-G. 575, 850
 Lee, J-H. 331, 524
 Lee, J-Y. 524
 Lee, J. 89, 1793
 Lee, J.S. 1038, 1047, 1199, 1371, 1407,
 1414, 1716
 Lee, J.T. 92
 Lee, K-H. 588
 Lee, K. 200, 850
 Lee, S. 661
 Legarsky, J. 996
 Leggeri, G. 374
 Lei, Q. 533
 Lemmings, M.J.P.M. 423
 Leon, D. 1460
 Leone, A. 3
 LeQuere, P. 207, 252
 Leroy, M. 165, 556, 1230, 1787
 Leshkevich, G.A. 505
 Lettvin, E. 1859
 Leung, P.S. 380
 Leusky, V. 2093
 Leveau, J. 581
 Leysen, M. 1047, 1725, 1890
 Li, F. 1466, 1639
 Li, G. 498, 511, 740
 Li, L. 1009
 Li, M. 249, 389
 Li, S. 427, 683, 999, 1987
 Li, X. 1220
 Li, Z-J. 1144
 Li, Z. 408
 Liang, S. 174, 1781, 1959
 Liao, J. 746
 Liao, M. 204
 Lichtenthaler, H.K. 1799
 Liew, S.C. 734, 813, 848, 963, 1084,
 1548, 1560, 1914, 2038
 Lightstone, L. 154
 Likht, F.R. 601
 Lim, H. 213, 454, 734, 813, 1084, 1518,
 1527, 1548, 2038
 Lim, I. 445
 Lim, O.K. 213

Lim, P. 722
 Lim, T.K. 35, 1527, 1695
 Lin, C.C. 548, 1150
 Lin, C.S. 302
 Lin, I-I. 35, 151, 845, 1512, 1527, 1695, 1850
 Lin, Y-C. 151, 1887
 Liou, Y-A. 1096
 Litovchenko, K.T. 539
 Liu, A.K. 505, 1441
 Liu, H. 1749, 1966
 Liu, J. 1120
 Liu, Q.H. 942, 1147
 Liu, W.T. 1435, 2082
 Liu, Y.S. 389
 Liu, Z. 427, 683, 999, 1987
 Llewellyn-Jones, D. 308, 311
 Lobanov, V. 806
 Logar, A. 1947
 Loh, K.F. 1418
 Lolli, S. 904
 Lombardini, F. 1536
 Long, D.G. 246, 353, 386, 1557, 1563, 1835, 1838, 1841, 1844, 1847, 1856, 2063
 Longstaff, I.D. 1282, 1579
 Looyen, W. 370, 1078
 Lopes, A. 758, 761, 1044, 2060
 Lopez, J.M. 1361, 1871
 Lopez, J.R. 38
 Lord, R.T. 490
 Lou, Y. 1358, 1404
 Lu, D. 1120
 Lu, Y.H. 445
 Luca, D. 411
 Luchinin, A.G. 1335
 Lucht, W.W. 1220
 Luckman, A. 1796
 Lukowski, T.I. 1066, 1382
 Lunden, B. 317
 Luneberg, E. 1401, 1591
 Luntama, J.P. 1314
 Luo, R. 160
 Luscombe, A.P. 154, 1063
 Lyu, J-W. 1489
 Lyzenga, D. 1168

M

Ma, K.K. 1996
 Macelloni, G. 940, 1260
 Madsen, S.N. 1018, 1358
 Mahdi, S. 990
 Mahmood, A. 1217
 Mahmood, N.N. 1418
 Mahootian, F. 695, 854
 Makynen, M. 637, 803
 Maldonado, L. 1404
 Malingreau, J.P. 1725
 Mancini, M. 1263, 1365, 1368
 Mango, S.A. 1521
 Manian, V. 335

Marandi, S.R. 493
 Marazzi, A. 113, 655, 1463
 Marcus, T. 1291
 Marinelli, L. 21
 Marshak, A. 1444
 Marthon, P. 2060
 Martin, T. 1878
 Martin-Neira, M. 1470
 Martonchik, J.V. 1743
 Martuccelli, A. 737
 Marzano, F.S. 2087, 2100
 Massonnet, D. 652, 1338, 1533
 Mastropietro, R. 616
 Masuda, K. 9, 1893, 1896
 Masuda, T. 1941
 Masuko, H. 570, 1389
 Mathieu-Marni, S. 171
 Matsuura, K. 73, 414
 Mattia, F. 719, 898, 1272
 Mattikalli, N.M. 1093
 Matwin, S. 670
 Maupin, P. 207, 252
 Mavrocordatos, C. 1470
 Mayaux, P. 1725
 Mazzetti, P. 1454
 McIntosh, R.E. 1001, 1460, 1466, 1539, 1753, 1972
 McNeill, S. 2057
 Meagher, J. 2063
 Mecocci, A. 113, 655
 Meier, E. 1929
 Meisner, R.E. 1495, 1505
 Melentyev, V.V. 1681
 Meloni, G.P. 67
 Melville, W.K. 711
 Mendez, R. 38, 128
 Meneghini, R. 1636
 Metternicht, G.I. 95, 338, 674
 Miao, J. 58, 61
 Miche, J.A. 1799
 Michel, T. 448
 Micoso, A.G. 125
 Migliaccio, M. 1701, 1853
 Milekhin, L.I. 359
 Milekhin, O.E. 1681
 Miller, T. 1404
 Milne, A. 1057, 2054
 Milne, A.K. 1433, 1573, 1624
 Miner, G.F. 386
 Minh, V.Q. 1084, 2038
 Mirbagheri, M. 1576
 Mishkin, V. 41
 Mitchell, B.G. 825
 Mitchell, G. 1060
 Mitnik, L. 70, 601, 806
 Mitnik, M.L. 70
 Mitomi, Y. 2075
 Mitteregger, E. 468
 Mittermayer, J. 2021, 2028
 Miura, T. 98
 Mochi, M. 1908
 Moctezuma, M. 38

Moghaddam, M. 1881, 1884
 Molinaro, F. 581
 Moller, D. 1539
 Moran, M.S. 98
 Moreira, A. 451, 2021, 2024, 2028
 Moreira, J. 869, 1929
 Morisette, J.T. 1769
 Mott, H. 1401
 Mouchot, M.C. 207, 252, 646, 1678
 Mougin, E. 1832
 Mourad, P.D. 1159
 Moyssidis, M.A. 1379
 Muchoney, D.M. 1227
 Mukai, S. 9, 1896
 Mukaida, A. 2075
 Muller, G. 1162
 Muller, H.J. 1603
 Mura, F. 987
 Murakami, M. 1585
 Muralikrishna, I.V. 1772,
 Murali Krishna, I.V. 1778
 Muramoto, K. 73
 Muratova, N. 281
 Myers, R.J. 692

N

Nagabhushan, P. 521
 Nahamura, H. 1585, 2075
 Nakaoka, N. 649
 Natarajan, M.P. 613
 Nativi, S. 1454
 Nault, J. 819
 Navarro, A. 240
 Navarro, P. 1569
 Nazarenko, D.M. 1060
 Nedlin, G.M. 1692
 Nemoto, Y. 1392
 Nerushev, A.F. 359
 Nesti, G. 904, 1361, 1871
 Neuenschwander, A.L. 667
 Newman, G.A. 929, 933
 Nezry, E. 758, 1044, 1051, 1087, 2035
 Ng, C.S. 445
 Ng, J. 848
 Nghiem, S.V. 505
 Nichol, J. 278, 813
 Nicolaescu, D. 607
 Niemann, K.O. 84, 664
 Nirchio, F. 325
 Nishii, R. 649, 658
 Nitta, K. 1585
 Nogami, Y. 1205
 Nolf, S. 116
 Nonin, P. 1347
 Noon, D.A. 1282
 Nualchawee, K. 1829
 Nuesch, D. 1929
 Nygaard, K. 1947

O

O'Leary, E. 1404
 O'Neill, K. 1135, 1288
 O'Neill, P. 1099, 1266, 1269
 Oaku, H. 1389, 2075
 Odegard, R. 634
 Oelke, C. 1311, 1686
 Oguma, H. 978
 Oh, Y. 708
 Ohkura, T. 125
 Ohno, C. 1392
 Iwamoto, M. 1392
 Oikawa, K. 1630
 Oikawa, S. 308
 Okamoto, K. 1633, 1636
 Okumura, T. 1899
 Oleson, K.W. 1509
 Omatu, S. 1205
 Omura, M. 1582
 Ong, J.T. 1757
 Onstott, R.G. 177, 1294, 1808, 1811
 Oricchio, M. 987
 Oristaglio, M.L. 945
 Oury, S. 1651
 Ozawa, S. 1585

P

Padoin, M. 1454
 Paduan, J.D. 1814
 Paek, K.N. 528
 Paget, R. 2063
 Pairman, D. 2057
 Paloscia, S. 1260
 Pampaloni, P. 904, 1260
 Pan, R. 498
 Pantani, L. 1953
 Papathanassiou, K.P. 1022, 1411, 1716, 1926, 1932
 Paraschiv, A. 607
 Pariman, D. 1075
 Park, M.E. 92
 Park, S.K. 136
 Parkes, I. 308, 311
 Parlange, M.B. 1099
 Parmiggiani, F. 67, 862
 Paronis, D.K. 1920
 Pasquali, P. 448, 1929
 Pasquariello, G. 719, 1272
 Patrascu, S. 607
 Pavan, G. 833, 1123
 Pavlakis, P.J. 1332
 Pazmany, A. 1460
 Pelinovsky, E. 1331
 Pellegrini, P.F. 981
 Peloquin, S. 128, 189
 Penaloza, M. 1947, 1950
 Pendlebury, S.F. 1689
 Peng, R. 1645
 Perez, C. 397

Perona, G. 3
 Peterson, D.L. 957
 Petrenko, B.Z. 359, 383
 Petrou, M. 737
 Pettersson, L.H. 1681
 Philpot, W. 1243
 Phinn, S. 1766
 Piau, P. 293
 Piazza, E. 981
 Picard, G. 787
 Pichel, W.G. 505
 Pichon, G. 1347
 Pick, D.R. 1395
 Piepmeier, J.R. 1001, 1006
 Pierce, L. 1072, 1180, 1246, 1621, 2053
 Pierdicca, N. 2087, 2100
 Piesbergen, J. 640
 Pilorz, S.H. 1743
 Pineiro, Y. 925
 Pinelli, G. 1536
 Pinna Nossai, R. 2087
 Pippi, I. 888, 1953
 Podesta, G. 2008
 Poiars Baptista, J.P.V. 1275
 Pollard, B.D. 1972
 Porter, D.L. 1539
 Posa, F. 719, 898, 1272
 Poujade, V. 21
 Preston, M.I. 770
 Pritt, M.D. 872, 875
 Provvedi, F. 18
 Puglisi, G. 1022
 Pulliainen, J. 622, 637, 803, 1874

Q

Quegan, S. 770, 781, 1041
 Quek, W. 963
 Quigley, D. 711
 Quinones, M.J. 1728

R

Ra, J-W. 136, 1489
 Racette, P. 984, 1737, 1969
 Raimadoya, M.A. 1569
 Ramasamy, S.M. 29
 Ramesh Babu, I. 1778
 Randriambelo, T. 6
 Rango, A. 625
 Ranson, J. 1269
 Ranson, K.J. 460, 1722
 Rao, S.R. 1129
 Rawls, W.J. 1099
 Rayer, P.J. 1395
 Reagan, J.A. 1749
 Redley, I. 308
 Regas, D. 714
 Rehrauer, H. 255
 Reigber, A. 869, 1022, 1716
 Remond, A. 1612

Remund, Q.P. 1841
 Renouard, L. 1347
 Reulke, R. 1022
 Ribbes, F. 1560
 Ricard, M.R. 667
 Riccio, D. 1701
 Richards, S.L. 1847
 Riggs, G.A. 619
 Rim, S. 89, 1793
 Ritter, M. 711
 Rivard, L.A. 128
 Robertson, A.E. 386
 Rodenas, J.A. 2069
 Rodin, A. 41
 Roenko, A.N. 2047
 Romanov, A. 41
 Romeiser, R. 1320, 1326
 Romero, G. 1404
 Rondal, J.D. 125
 Rosen, P.A. 1585
 Rouvier, S. 1606
 Royer, A. 189
 Rozanov, V.V. 1905
 Rozenberg, A. 711
 Rudolf, H. 1551
 Ruisi, R. 904
 Rundberg, W.B. 957
 Russo, G. 833
 Ruzek, M. 688, 699
 Ryu, J.A. 517

S

Saatchi, S. 104, 1881
 Sadowy, G.A. 1466
 Saito, H. 73
 Sakaida, F. 1499
 Sakane, M. 972
 Sakurada, Y. 55
 Sakurai-Amano, T. 916
 Samuel, P. 1698
 Sandven, S. 1681
 Sano, E.E. 98
 Sano, I. 9, 1896
 Sansosti, E. 433, 451, 878
 Santalla del Rio, V. 1594
 Santos, J. 240
 Sarabandi, K. 901, 1887
 Sasaki, M. 9
 Sasano, Y. 2078
 Satake, M. 570, 1389, 1941
 Satalino, G. 1272
 Sato, T. 1477, 1645
 Satoh, C. 966
 Sattchi, S. 1890
 Sausa, R.C. 2103
 Scarchilli, G. 1123
 Schaaf, C.B. 1220
 Schattler, B. 465
 Scheele, M. 1022
 Scheiber, R. 451, 1022, 1554, 2028
 Schiavon, G. 1618, 2097

Schistad Solberg, A.H. 157
 Schlick, T. 1805
 Schlott, M. 1935
 Schlueter, N. 61
 Schmidt, R. 417
 Schmitt, K. 1713
 Schmugge, T. 1099, 1233, 1236
 Schmullius, C.C. 1734
 Schneider, T.L. 1466
 Schnepf, N.G. 1808, 1811
 Schoeberl, M.R. 542
 Schou, J. 1041
 Schroeder, M. 258
 Schroth, A. 1126
 Schuler, D. 1047, 1371, 1407, 1414
 Schumann, R.L.G. 1829
 Schwarz, G. 2031
 Scott, J.C. 1335
 Seguin, G. 536
 Seidel, K. 255, 258, 411, 616
 Sekelsky, S.M. 1753
 Selige, T.M. 101, 1032, 1784
 Serafini, C. 1908
 Sergievskaya, I.A. 1335, 1530
 Serpico, S.B. 764, 1202
 Sery, F. 761, 1044
 Shaari, A.T. 1069
 Shah, A. 180
 Shan, Y.Y. 1757
 Shay, E.L. 692
 Shay, L.K. 1817
 Shchegol'kov, Y.B. 1335, 1530
 Shepherd, J.D. 1075
 Shi, J. 628, 1193, 1269, 1451
 Shih, S.E. 919
 Shikada, M. 210, 1899
 Shimada, M. 570, 1389, 1585, 2075
 Shimoda, H. 2072
 Shin, J. 1793
 Shmalenyuk, A.S. 347
 Siddiqui, K.J. 1944
 Sieber, A.J. 1361, 1551, 1871
 Sigismondi, S. 1260
 Silberstein, D. 1444
 Silva, T.A.M. 773
 da Silveira, M. 2015, 2018
 Simaan, M.A. 261, 559
 Simard, M. 1725, 1890
 Simeonsson, J.B. 2103
 Singh, K. 213, 454, 1548
 Singhroy, V. 752
 Siqueira, P. 104
 Sisk, T.D. 1624
 Sivaprakash, S. 848
 Skiles, J.W. 957
 Skotnicki, W. 1404
 Slatton, K.C. 457
 Slob, S. 192
 Small, D. 448
 Smirnov, V.G. 1681
 Smith, G. 793
 Smith, J. 1395

Smits, P.C. 737, 907, 1174
 Snider, J.B. 2090
 Soh, L.-K. 1177
 Solaiman, B. 207, 252
 Solberg, R. 631
 Solhaug, J. 1681
 Sommer, S. 189
 Song, H. 1938
 Song, J. 474
 Song, Y.S. 528
 Souleres, E. 545
 Souma, T. 311
 Souyris, J.C. 719, 898, 1272, 1606, 1868
 Spivak, L. 281
 Srivastava, S.K. 1063, 1066, 1382
 St-Onge, B. 207, 252
 St.Germain, K. 1009, 1291
 Stacy, N.J.S. 728
 Standley, L. 1654
 Staples, G.C. 1060
 Stapleton, N. 1335, 1530
 Steel, A. 1660
 Steinbrecher, U. 465
 Steinnocher, K. 910
 Stenstrom, G. 797, 1214
 Stephen, H. 1829
 Stephens, G.L. 1466
 Stephens, K. 180
 Stephenson, J.R. 370
 Stephenson, R. 370
 Stephenson-Hawk, D. 180
 Stevens, D. 722, 725
 Stickley, G.F. 1282
 Stock, L. 1300
 Stockman, S. 685
 Stone, R.N. 505
 Stow, D. 1766
 Strahler, A. 1220, 1227
 Straka, M. 945
 Stramski, D. 821, 825
 Strapp, J.W. 1458
 Strobl, P. 1022
 Strözzi, T. 790
 Sturm, J.M. 705
 Stussi, N. 454, 813, 1548, 1560
 Su, Z. 1365, 1368
 Subhash, N. 1799
 Sugimoto, N. 2078
 Sugita, M. 284
 Suinot, N. 545, 548, 1150, 1470
 Sultan, N. 536
 Sun, B. 24
 Sun, G. 460, 1269, 1722
 Sun, X. 168
 Supit, I. 1051
 Susini, S. 1993
 Susskind, J. 1102
 Suzuki, Y. 210
 Sveinsson, J.R. 501, 913, 1026, 1669
 Swift, C. 1001, 1012, 1297

T

Tadross, M. 862
 Takagi, M. 916
 Takamata, K. 2084
 Takashima, T. 1893
 Takemata, K. 1790
 Takemura, K. 1477
 Takeuchi, N. 55
 Takeuchi, S. 107, 969, 1707
 Talipova, T. 362, 1331
 Tamba, S. 305, 308, 311
 Tan, B.T.G. 734
 Tan, F.Y. 963
 Tanaka, D. 55
 Tanaka, S. 658
 Tanelli, S. 1975
 Taniguchi, N. 1902
 Tanner, A.b. 1466
 Tarchi, D. 904, 1551
 Tassan, S. 825
 Tateiba, M. 184, 1486
 Taylor, V. 1404
 Teague, C.C. 1808, 1811
 Teague, W.J. 1156, 1171
 Teany, L.D. 1382
 Teixeira, F.L. 945
 Tennant, K. 1350
 Teo, N.L. 848
 Terehov, A. 281
 Tesauro, M. 433, 451, 878, 1554
 Testud, J. 1651
 Thames, P.S. 1509
 Thepaut, I. 1678
 Thompson, D.G. 386
 Thomson, K.P.B. 1890
 Thurai, M. 1648
 Ticehurst, C. 891, 1057, 2054
 Tikhonov, V.V. 1108
 Timchenko, A.I. 230, 1105
 Timofeyev, Y.M. 562, 1905
 Tishkovets, V.P. 230
 Tjuatja, S. 1144, 1308, 1600
 Tobita, M. 1585
 Todo, M. 442
 Toh, J. 845
 Tomiyasu, K. 1615
 Tommasini, M. 981
 Torma, M. 44
 Torre, A. 990
 Torricella, F. 1908
 Toutin, T. 839
 Townshend, J.R.G. 171, 174, 1781
 Trang, A.H. 1132
 Tretter, W. 743
 Treuhaft, R.N. 1881, 1884
 Trichon, V. 1566
 Triesky, M.E. 1969
 Trinder, J.C. 1576
 Troch, P.A. 1263, 1365, 1368
 Trohkimovski, Y. 1323
 Tsai, F. 1243

Tseng, D. 264, 1999
Tseng, R-S. 806
Tseng, W.Y. 505, 1441
Tseng, Y.C. 1208
Tulin, M.P. 714
Tungalagsaikhon, P. 1505
Tuong, T.P. 1084, 2038
Tuzlukov, V.P. 139
Tzeng, Y.C. 1096, 1199

U

Ulaby, F. 119, 1072, 1180, 1621, 1719
Ulander, L. 436, 797, 800, 1214, 1878
Um, G-M. 588
Umehara, T. 1389
Usai, S. 1542
Uttal, T. 2090

V

Vaccaro, R. 1174
Vali, G. 1460
van Leeuwen, W.J.D. 341, 1966
Van Zyl, J. 1358, 1404
Vandemark, D.C. 1001
Vanska, T. 803
Varfis, A. 1660
Vasilyev, A.V. 1905
Vasilyev, Y.F. 2047
Vasquez, R. 335
Vazouras, C.N. 1379
Velten, E. 993
Vernazza, G. 764
Vesecky, J. 1811, 1808, 1859
Vincent, N. 545, 548, 1470
Viswanathan, G. 1129
Vogelzang, J. 1320
Voigt, S. 1929
Volden, E. 157, 631
Volkov, A.M. 1681
Vuorela, A. 1344

W

Wadhams, P. 862
Wahl, T. 47
Walessa, M. 767, 2031
Walker, J.P. 1263
Wan, W. 1657
Wang, C. 746, 749
Wang, D.W. 1171
Wang, H. 142
Wang, J. 895, 1269, 1737, 1969
Wang, L. 1609
Wang, M. 116, 1923
Wang, T. 945
Wang, X. 749
Warner, R.A. 819
Waseda, T. 714
Wasrin, U.R. 1560
Watanabe, M. 125
Weger, R.C. 1917
Wegmuller, U. 790

Wehrman, M.J.G. 101
Weiss, J.M. 32, 160
Welch, R.M. 32, 116, 160, 1760, 1911, 1917, 1923, 1947, 1950
Welch, S. 714
Wensink, G.J. 1320
Wenzel, O. 1799
Wergin, W. 625
Werner, C. 790
West, J.C. 705
Westwater, E.R. 1001, 2093
Wever, T. 743
Weydahl, D.J. 287
Wiesbeck, W. 1713
Wiesmann, A. 1675
Wigner, J.P. 1090
Willgoose, G.R. 1263
Williams, J.B. 370
Williams, M.L. 755
Williams, R.N. 328, 1689
Wilson, C.L. 1648
Wilson, S.H.S. 1395, 2011
Wilson, W.J. 1466
Winebrenner, D.P. 1823
Winker, D.M. 1740
Wiscombe, W. 1444
Wismann, V. 1823, 1826
Wolfe, J. 1382
Wong, F. 722, 725, 731
Wood, E.F. 1266
Wu, J. 24, 1609
Wu, P. 1865
Wu, S-H. 1144
Wu, S.Y. 1441
Wu, T.D. 1365
Wynn, W.M. 1483

X

Xia, Y. 743
Xiao, W. 216
Xinqiao, L. 50
Xu, K. 389
Xu, W. 1704
Xue, Y.L. 389, 1987

Y

Yakam-Simen, F. 758, 1051
Yamagata, Y. 978
Yamanouchi, T. 73
Yamazaki, A. 1899
Yamazaki, Y. 2084
Yang, K. 171
Yang, S-K. 1923
Yang, X. 219
Yang, Y.K. 584
Yanow, G. 951, 960
Yanquen, X. 55
Yasumoto, M. 9
Yasuoka, Y. 284
Ye, C-S. 588
Ye, J.P. 402
Yeo, T.S. 445, 484, 487

Yin, Z. 677
Ying, X. 145, 232
Yocky, D.A. 1545
Yoder, B.J. 1884
Yokoyama, R. 305, 308, 311
Yonezawa, C. 107, 1707
Yoshida, M. 125
Yoshikawa, M. 658, 1205
Yu, H. 145, 232
Yu, J.J. 781
Yun, C. 816
Yun, S. 50, 1430

Z

Zagolski, F. 122, 1051, 1566, 1787
Zagorin, G.K. 359
Zahn, R. 1935
Zamaraev, B.D. 2047
Zelli, C. 15, 18
Zeng, Q. 408
Zhang, C.B. 445
Zhang, G. 1141
Zhang, L. 1120
Zhang, Q. 222
Zhang, R. 35, 168, 222, 1695, 1956
Zhang, X. 1981
Zhang, Y. 392, 842
Zhang, Z. 174, 204, 845
Zhao, J. 356
Zhao, K. 58
Zhao, L. 963
Zhou, B. 1524
Zhou, N. 389
Zhou, P. 1144
Zhu, M. 740, 1938
Zhu, M.H.
Zhu, S. 1996
Zhu, X. 498, 740
Zhu, Z. 168
Zion, M. 1266
Ziskin, D.C. 1255
Zuikova, E.M. 1335, 1530
Zwally, H.J. 857